

Ghenadii Korotcenkov *Editor*

# Handbook of II-VI Semiconductor-Based Sensors and Radiation Detectors

Vol. 3: Sensors, Biosensors and  
Radiation Detectors

 Springer

# Handbook of II-VI Semiconductor-Based Sensors and Radiation Detectors

Ghenadii Korotcenkov  
Editors

# Handbook of II-VI Semiconductor-Based Sensors and Radiation Detectors

Vol. 3: Sensors, Biosensors and Radiation  
Detectors

 Springer

*Editor*

Ghenadii Korotcenkov  
Department of Physics and Engineering  
Moldova State University  
Chisinau, MD-2009, Moldova

ISBN 978-3-031-23999-1      ISBN 978-3-031-24000-3 (eBook)  
<https://doi.org/10.1007/978-3-031-24000-3>

© The Editor(s) (if applicable) and The Author(s), under exclusive license to Springer Nature Switzerland AG 2023

This work is subject to copyright. All rights are solely and exclusively licensed by the Publisher, whether the whole or part of the material is concerned, specifically the rights of translation, reprinting, reuse of illustrations, recitation, broadcasting, reproduction on microfilms or in any other physical way, and transmission or information storage and retrieval, electronic adaptation, computer software, or by similar or dissimilar methodology now known or hereafter developed.

The use of general descriptive names, registered names, trademarks, service marks, etc. in this publication does not imply, even in the absence of a specific statement, that such names are exempt from the relevant protective laws and regulations and therefore free for general use.

The publisher, the authors, and the editors are safe to assume that the advice and information in this book are believed to be true and accurate at the date of publication. Neither the publisher nor the authors or the editors give a warranty, expressed or implied, with respect to the material contained herein or for any errors or omissions that may have been made. The publisher remains neutral with regard to jurisdictional claims in published maps and institutional affiliations.

This Springer imprint is published by the registered company Springer Nature Switzerland AG  
The registered company address is: Gewerbestrasse 11, 6330 Cham, Switzerland

# Preface

Binary and ternary semiconductors of II–VI group (ZnS, ZnSe, ZnTe, CdS, CdSe, CdTe, HgTe, HgS, HgSe, HgCdTe, CdZnTe, CdSSe and HgZnTe) are very popular among researchers because of their remarkable physical and chemical properties, which, as a group, are unique. II–VI compounds possess a very wide spectrum of electronic and optical properties. Most materials of group II–VI are semiconductors with a direct band gap and high optical absorption and emission coefficients. In addition, binary II–VI compounds are easily miscible, providing a continuous range of properties. As a result, the II–VI semiconductors possess band gap, varying over a wide range. Therefore, II–VI compounds can serve as efficient light emitters such as light diodes and lasers, solar cells, and radiation detectors operated in the range from IR to UV and X-ray. II–VI compound-based devices can also cover terahertz range. Besides common photovoltaic applications, II–VI semiconductors are also potential candidates for a variety of electronic, electro-optical, sensing and piezoelectric devices. In particular, nanoparticles of II–VI semiconductors, such as quantum dots, one-dimensional structures and core-shells structures, can be used for the development of gas sensors, electrochemical sensors and biosensors. These semiconductors, when downsized to nanometer, have become the focus of attention because of their tunable band structure, high extinction coefficient, possible multiple exciton generation and unique electronic and transport properties. It is important that II–VI semiconductors can be easily prepared in high-quality epitaxial, polycrystalline and nanocrystalline films. The concentration of charge carriers can also vary in II–VI semiconductors in a wide range due to doping. Thus, the use of II–VI films represents an economical approach to the synthesis of semiconductors for various applications. It should be noted that the range of technical applications for II–VI compounds goes beyond the better-known semiconductors such as Si, Ge and some of the III–V compounds.

Formally, metal oxides such as CdO and ZnO also belong to II–VI compounds. However, we will not cover them in this book. In recent years, these compounds have been allocated to a separate group “Metal oxides,” and many books have been devoted to their discussion, in contrast to other II–VI compounds. In particular, for

those who are interested in exactly these compounds, we can recommend the *Metal Oxides* series which is published by Elsevier.

The aim of this three-volume book is to provide an updated account of the state of the art of multifunctional II–VI semiconductors, from fundamental sciences and material sciences to their applications as various sensors and radiation detectors, and, based on this knowledge, to formulate new goals for further research. The proposed book provides an interdisciplinary discussion of a wide range of topics, such as synthesis of II–VI compounds, their deposition, processing, characterization, device fabrication and testing. Topics of the recent remarkable progresses in the application of nanoparticles, nanocomposites and nanostructures consisting of II–VI semiconductors in various devices are also covered. Both experimental and theoretical approaches were used for this analysis.

Currently, there are already published books on II–VI semiconductors. However, some of them were published too long ago and they cannot reflect the current state of research in this area. Other published books focus on a limited number of topics, from which topics related to various sensor applications such as gas sensors, humidity sensors and biosensors are almost completely excluded. When considering photodetectors, the focus is also only on the analysis of IR photodetectors. However, sensors operated in the visible, ultraviolet and X-ray ranges also hold great promise for applications. With these books, we will try to close this gap.

Proposed our three-volumes book *Handbook of II–VI Semiconductor-Based Sensors and Radiation Detectors* is the first to cover both chemical sensors and biosensors and all types of photodetectors and radiation detectors based on II–VI semiconductors. It contains a comprehensive and detailed analysis of all aspects of the application of II–VI semiconductors in these devices. This makes these books very useful and comfortable to use. Combining this information in three volumes, united by common topics, should help readers in finding the necessary information on the required subject.

Chapters in *Handbook of II–VI Semiconductor-Based Sensors and Radiation Detectors. Vol. 1: Materials and Technologies* describe the physical, chemical and electronic properties of II–VI compounds, which give rise to an increased interest in these semiconductors. Technologies that are used in the development of various devices based on II–VI connections are also discussed in detail in this volume.

*Handbook of II–VI Semiconductor-Based Sensors and Radiation Detectors. Vol. 2: Photodetectors* focuses on the consideration of all types of optical detectors, including IR detectors, visible and UV detectors. This consideration includes both the fundamentals of the operation of detectors and the peculiarities of their manufacture and use. An analysis of new trends in the development of II–VI semiconductors-based photodetectors is also given.

*Handbook of II–VI Semiconductor-Based Sensors and Radiation Detectors. Vol. 3: Sensors, Biosensors and Radiation Detectors* describes the use of II–VI compounds in other fields such as radiation detectors, gas sensors, humidity sensors, optical sensors and biosensors. The chapters in this volume provide a comprehensive overview of the manufacture, parameters and applications of these devices.

We believe that these books will enable the reader to understand the present status of II–VI semiconductors and their role in the development of a new generation of photodetectors, chemical sensors, biosensors and radiation detectors. I am very pleased that many well-known experts with extensive experience in the development and research of II–VI semiconductor sensors and radiation detectors were involved in the preparation of the chapters of these books.

The target audience for this series of books are scientists and researchers working or planning to work in the field of materials related to II–VI semiconductors, i.e. scientists and researchers whose activities are related to electronics, optoelectronics, chemical and biosensors, electrical engineering, biomedical applications, etc. I believe this three-volume book may also be of interest to practicing engineers or project managers in industries and national laboratories who would like to develop II–VI semiconductor-based photodetectors, radiation detectors and sensors but do not know how to do it, and how to select the optimal II–VI semiconductor for specific applications. With numerous references to an extensive resource of recently published literature on the subject, these books can serve as an important and insightful source of valuable information, providing scientists and engineers with new ideas for understanding and improving existing II–VI semiconductor devices.

I believe that these books will be very useful for university students, doctoral students and professors. The structure of these books offers the basis for courses in materials science, chemical engineering, electronics, optoelectronics, environmental control, chemical sensors, photodetectors, radiation detectors, biomedical applications and many others. Graduate students may also find the book very useful in their research and understanding of the synthesis of II–VI semiconductors, study and application of this multifunctional material in various devices. We are confident that all of them will find the information useful for their activities.

Finally, I thank all the authors who contributed to these books. I am grateful that they agreed to participate in this project and for their efforts to prepare these chapters. This project would not have been possible without their participation. I am also very grateful to Springer for the opportunity to publish this book with their help. I would also like to inform that my activity related to editing this book was funded by the State Program of the Republic of Moldova project 20.80009.5007.02.

I am also grateful to my family and wife, who always support me in all my endeavors.

Chisinau, Moldova

Ghenadii Korotcenkov

# Contents

## Part I X-Ray Radiation Detectors

<b>1</b>	<b>Basic Principles of Solid-State X-Ray Radiation Detector Operation</b> .....	<b>3</b>
	M. Zahangir Kabir	
<b>2</b>	<b>CdTe-/CdZnTe-Based Radiation Detectors</b> .....	<b>35</b>
	A. Opanasyuk, D. Kurbatov, Ya. Znamenshchikov, O. Diachenko, and M. Ivashchenko	
<b>3</b>	<b>ZnS-Based Neutron and Alpha Radiation Detectors</b> .....	<b>75</b>
	Ghenadii Korotcenkov and Michail Ivanov	
<b>4</b>	<b>ZnSe- and CdSe-Based Radiation Detectors</b> .....	<b>109</b>
	Shweta Jagtap, Madhushree Bute, Sapana Rane, and Suresh Gosavi	
<b>5</b>	<b>Medical Applications of II-VI Semiconductor-Based Radiation Detectors</b> .....	<b>137</b>
	Ghenadii Korotcenkov and Sergiu Vatavu	

## Part II Electric and Electronic Chemical Sensors

<b>6</b>	<b>Introduction in Gas Sensing</b> .....	<b>161</b>
	Ghenadii Korotcenkov and Vladimir Brinzari	
<b>7</b>	<b>II-VI Semiconductor-Based Thin Film Electric and Electronic Gas Sensors</b> .....	<b>177</b>
	Stella Vallejos and Chris Blackman	
<b>8</b>	<b>Nanocomposite and Hybrid-Based Electric and Electronic Gas Sensors</b> .....	<b>201</b>
	Roman B. Vasiliev, Artem S. Chizhov, and Marina N. Rumyantseva	



<b>9</b>	<b>II–VI Semiconductor-Polymer Nanocomposites and Their Gas-Sensing Properties</b> . . . . .	233
	Chandan Kumar, Satyabrata Jit, Sumit Saxena, and Shobha Shukla	
<b>10</b>	<b>Nanomaterial-Based Electric and Electronic Gas Sensors</b> . . . . .	253
	Andrea Gaiardo, Barbara Fabbri, and Matteo Valt	
<b>11</b>	<b>II–VI Semiconductor-Based Humidity Sensors</b> . . . . .	281
	Ghenadii Korotcenkov, Michail Ivanov, and Vladimir Brinzari	
<b>Part III Optical Sensors</b>		
<b>12</b>	<b>II–VI Semiconductor-Based Optical Gas Sensors</b> . . . . .	307
	Savita Sharma, Ayushi Paliwal, Pragati Kumar, and Nupur Saxena	
<b>13</b>	<b>Spectroscopic Gas Sensing Systems</b> . . . . .	335
	Zhenhui Du and Jinyi Li	
<b>14</b>	<b>Luminescence and Fluorescence Ion Sensing</b> . . . . .	361
	Faheem Amin, Yasir Iqbal, and Ghenadii Korotcenkov	
<b>15</b>	<b>Photoelectrochemical Ion Sensors</b> . . . . .	393
	Alka Pareek and Pramod H. Borse	
<b>16</b>	<b>II–VI Semiconductor-Based Optical Temperature Sensors</b> . . . . .	417
	Nupur Saxena and Pragati Kumar	
<b>Part IV Biosensors</b>		
<b>17</b>	<b>Introduction to Biosensing</b> . . . . .	441
	Ghenadii Korotcenkov, Rabiul Garba Ahmad, Praveen Guleria, and Vineet Kumar	
<b>18</b>	<b>Fluorescent Biosensors Based on II–VI Quantum Dots</b> . . . . .	475
	Nguyen Thu Loan, Ung Thi Dieu Thuy, and Nguyen Quang Liem	
<b>19</b>	<b>QDs-Based Chemiluminescence Biosensors</b> . . . . .	509
	Fahimeh Ghavamipour and Reza H. Sajedi	
<b>20</b>	<b>Electrochemiluminescent Biosensors Based on II–VI Quantum Dots</b> . . . . .	531
	Xiao-Yan Wang, Zhi-Yuan Che, and Shou-Nian Ding	
<b>21</b>	<b>Electrochemical Biosensors</b> . . . . .	551
	Mayank Garg, Arushi Gupta, Amit L. Sharma, and Suman Singh	
<b>22</b>	<b>Photoelectrochemical Biosensors</b> . . . . .	567
	Sirlon F. Blaskievicz, Byanca S. Salvati, Alessandra Alves Correa, and Lucia Helena Mascaro	
<b>23</b>	<b>II–VI Semiconductor QDs in Surface Plasmon Resonance Sensors</b> . . . . .	589
	Hina F. Badgujar and Anuj K. Sharma	

**24 Biomarkers and Bioimaging and Their Applications** ..... 615  
Suchismita Ghosh and Kaustab Ghosh

**25 Biosensors Based on II–VI Semiconductor Quantum Dots  
for Health Protection** ..... 633  
Suria Mohd Saad and Jaafar Abdullah

**26 Application of II–VI Semiconductor-Based Biosensors  
in Nanomedicine and Bioanalysis** ..... 653  
Bruno Gabriel Lucca and Jacqueline Marques Petroni

**27 Specific Applications of II–VI Semiconductor Nanomaterials-Based  
Biosensors for Food Analysis and Food Safety**..... 673  
Xiaodong Guo, Jiaqi Wang, Mengke Zhang, and Marie-Laure  
Fauconnier

**Index**..... 697

## About the Editor



**Ghenadii Korotcenkov** received his PhD in physics and technology of semiconductor materials and devices in 1976 and his doctor of science degree (doctor habilitate) in physics of semiconductors and dielectrics in 1990. He has more than 50-year experience as a teacher and scientific researcher. Long time he was a leader of gas sensor group and manager of various national and international scientific and engineering projects carried out in the Laboratory of Micro- and Optoelectronics, Technical University of Moldova, Chisinau, Moldova. International foundations and programs such as the CRDF, the MRDA, the ICTP, the INTAS, the INCO-COPERNICUS, the COST and NATO have supported

his research. From 2007 to 2008, he carried out his research as an invited scientist in Korea Institute of Energy Research (Daejeon). Then, from 2008 to 2018, Dr. G. Korotcenkov was a research professor in the School of Materials Science and Engineering at Gwangju Institute of Science and Technology (GIST) in Korea. Currently, G. Korotcenkov is a chief scientific researcher at Moldova State University, Chisinau, Moldova.

Scientists from the former Soviet Union know the results of G. Korotcenkov's research in the study of Schottky barriers, MOS structures, native oxides and photo-receivers based on III–Vs compounds such as InP, GaP, AlGaAs and InGaAs. His current research interests since 1995 include material sciences, focusing on metal oxide film deposition and characterization ( $\text{In}_2\text{O}_3$ ,  $\text{SnO}_2$ ,  $\text{ZnO}$ ,  $\text{TiO}_2$ ), surface science, thermoelectric conversion and design of physical and chemical sensors, including thin film gas sensors.

G. Korotcenkov is the author or editor of 45 books and special issues, including 11-volume *Chemical Sensors* series published by Momentum Press, two-volumes *Handbook of Gas Sensor Materials* published by Springer, 15-volume *Chemical Sensors* series published by Harbin Institute of Technology Press, China, three-volumes *Porous Silicon: From Formation to Application* issue published by CRC

Press, three-volumes *Handbook of Humidity Measurements* published by CRC Press, three-volumes *Handbook of II-VI Semiconductor-based Sensors and Radiation Detectors* published by Springer, and 6 proceedings of the international conferences published by Trans Tech Publ., Elsevier and EDP Sciences. In addition, currently he is a series editor of *Metal Oxides* book series published by Elsevier. Since 2017, more than 35 volumes have been published within this series.

G. Korotcenkov is the author and coauthor of more than 675 scientific publications, including 34 review papers, 62 book chapters, more than 200 peer-reviewed articles published in scientific journals ( $h$ -factor = 43 (Web of Science),  $h = 45$  (Scopus) and  $h = 60$  (Google scholar citation), 2022). He is the holder of 17 patents. He presented more than 250 reports on national and international conferences, including 17 invited talks. G. Korotcenkov, as a cochairman or member of program, scientific and steering committees, has participated in the organization of more than 40 international scientific conferences. Dr. G. Korotcenkov is a member of editorial boards in five scientific international journals. His name and activities have been listed by many biographical publications including Who's Who. G. Korotcenkov have also been listed as one of the "World's Ranking Top 2% Scientists" in Applied Physics/Analytical Chemistry in the Physics and Astronomy Cluster. His research activities have been honored by the National Prize of the Republic of Moldova (2022), the Honorary Diploma of the Government of the Republic of Moldova (2020), an Award of the Academy of Sciences of Moldova (2019), an Award of the Supreme Council of Science and Advanced Technology of the Republic of Moldova (2003); the Prize of the Presidents of the Ukrainian, Belarus, and Moldovan Academies of Sciences (2004); Senior Research Excellence Award of Technical University of Moldova (2001; 2003; 2005), the National Youth Prize of the Republic of Moldova in the field of science and technology (1980), among others. Some of his research results and published books have won awards at international exhibitions. G. Korotcenkov also received fellowships from the International Research Exchange Board (IREX, United States, 1998), Brain Korea 21 Program (2008–2012) and BrainPool Program (Korea, 2007–2008 and 2015–2017). <https://www.scopus.com/authid/detail.uri?authorId=6701490962> <https://publons.com/researcher/1490013/ghenadii-korotcenkov/> <https://scholar.google.com/citations?user=XR3RNhAAAAAJ&hl> [https://www.researchgate.net/profile/G\\_Korotcenkov](https://www.researchgate.net/profile/G_Korotcenkov)

**Part I**  
**X-Ray Radiation Detectors**

# Chapter 1

## Basic Principles of Solid-State X-Ray Radiation Detector Operation



M. Zahangir Kabir

### 1.1 Introduction

X-rays are electromagnetic waves, whose photon energies range roughly from 0.1 keV to 125 keV. The X-rays are classified as soft X-rays (from 0.1 keV to 10 keV) and hard X-rays (10 keV to 125 keV). X-rays are used in various types of imaging purposes; for examples, diagnostic medical X-ray imaging cover photon energies from 10 keV up to 120 keV, crystallography uses X-ray photons of energy around 10 keV, security scanning uses photon energies from 80 to 140 keV, and X-ray microscopy and fluorescence spectroscopy cover photon energies ranging from 0.1 to 3 keV, as shown in Fig. 1.1. Different applications require different specialized detectors having different suitable photoconductors and detector designs.

A radiation detector is a device that converts the energy (or part of the energy) of the incident radiation into a measurable electrical signal. In other words, it can measure the presence of a particular type of radiation. There are two types of X-ray detectors: (1) scintillation detectors and (2) solid-state semiconductor detectors. In scintillator detectors, X-ray energy is converted into light photons in the scintillator layer and these light photons are then detected by a photodetector. In solid-state semiconductor detectors (also known as the direct conversion detector), X-ray photons directly generate electron and hole pairs (EHPs) in the photoconductor layer, which are collected on electrodes. Semiconductor X-ray radiation detectors are the most important class of detectors for detecting and measuring this type of radiation because of their solid-state structure, higher resolution, and efficiency. These semiconductor radiation detectors are also used as imaging detectors and capture X-ray images by arranging them in arrays. A simplified functional classification of

---

M. Z. Kabir (✉)  
Department of Electrical and Computer Engineering, Concordia University,  
Montreal, QC, Canada  
e-mail: [zahangir.kabir@concordia.ca](mailto:zahangir.kabir@concordia.ca)

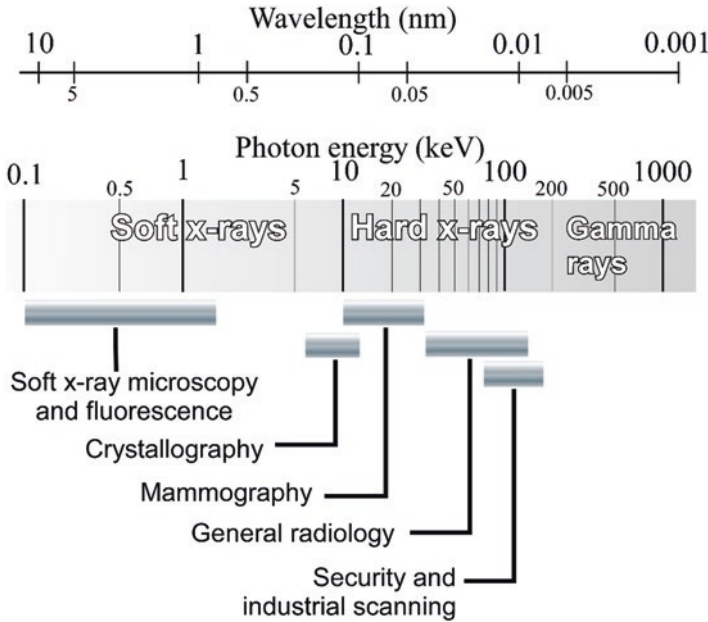


Fig. 1.1 The X-ray spectrum and applications over various spectral regions. (Idea from Ref. [1])

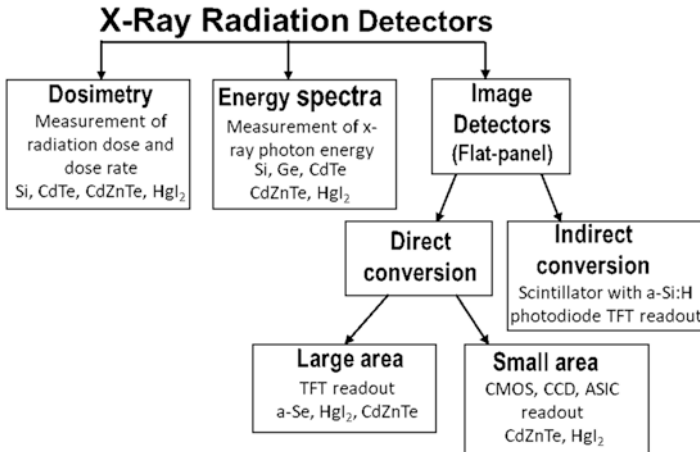
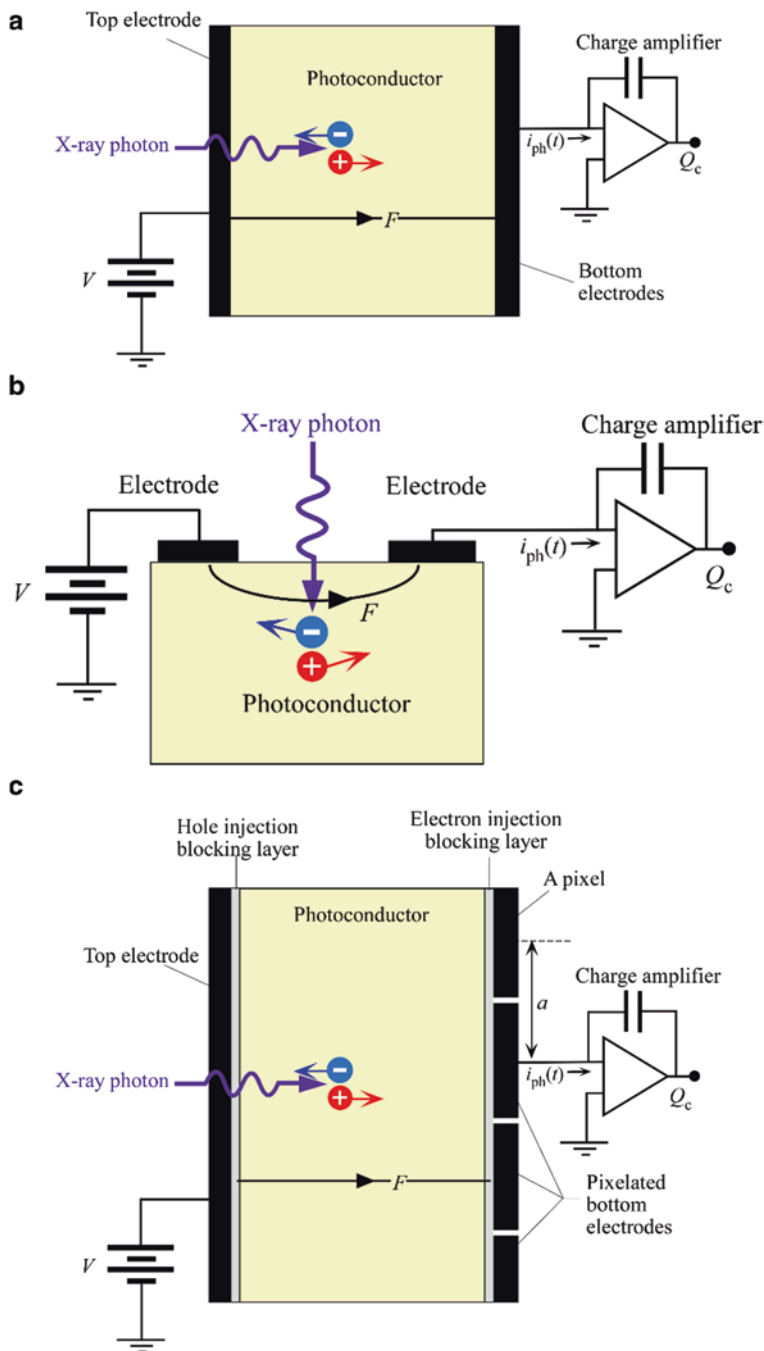


Fig. 1.2 A simplified classification of X-ray radiation detectors with corresponding photoconductor materials. (Idea from Ref. [2])

semiconductor X-ray detectors is shown in Fig. 1.2. Only semiconductor detectors will be discussed in this chapter.

The semiconductor detectors have one of three common configurations shown in Fig. 1.3, depending on the applications. The planar configuration (Fig. 1.3a) is the



**Fig. 1.3** Simplified cross-sectional structures of three basic X-ray detectors: (a) single element planar detector, (b) co-planar detector, and (c) pixelated detector for imaging applications. Here  $Q_c$  is the collected charge and  $i_{ph}(t)$  is the instantaneous photocurrent



most common and simplest configuration for implementation, where a photoconductor layer is sandwiched between two electrodes. The co-planar configuration (Fig. 1.3b) can provide higher spectral resolution. The top electrode is a continuous metallic plate, and the bottom electrode is segmented into 2D arrays of pixels in imaging detectors (Fig. 1.3c). The photoconductor layer can have several compositions such as  $p$ - $n$ ,  $p$ - $i$ - $n$ , or simply metal/photoconductor/metal type. The metal/photoconductor/metal type detectors are often called photoconductive detectors. Detectors based on the  $p$ - $n$  junction or a Schottky junction are reverse-biased to ensure a wider depletion layer and strong electric field in the depletion region though the field is not uniform. Therefore,  $pin$  devices are preferred not only because of their wider  $i$ -layer, or depletion layer width, but also ensuring a relatively uniform field in this depletion layer.

The top electrode is biased with a voltage source to establish a relatively uniform electric field along the photoconductor layer in the photoconductive detectors. The bulk part of the photoconductor layer used in photoconductive detectors is either intrinsic or close to intrinsic (slightly  $p$  or  $n$ -type). The X-ray absorption, ionization (EHP generation), and charge transport occur mainly in the nearly intrinsic photoconductor layer where both holes and electrons can drift by the influence of the applied electric field  $F$ . The X-ray generated holes and electrons drift following the electric field and induce photocurrent  $i_{ph}$  in the external circuit, which corresponds to the radiation received by the detector. An additional current, named as the dark current, continuously flows in the external circuit because of the adequate electric field in the absence of the radiation. The dark current must be as small as possible because it acts as a noise.

The detector is designed in such a way that the dark current can be minimized. There are two main sources of dark current [3, 4]: (i) thermal generation of charge carriers in the photoconductor layer and (ii) carrier injection from the contacts. The thermal generation of carrier in high bandgap semiconductors is negligibly small and its contribution to the dark current is also very small. The electrode-semiconductor contacts are blocking (e.g., Schottky junction) in nature in photoconductive detectors to minimize the carrier injection from the metallic contacts, but allow photogenerated charge carrier flow from the photoconductor layer to the electrodes to eliminate carrier accumulation at the interfaces. A very thin blocking layer is often inserted between the bulk photoconductor layer and the electrode in order to minimize the carrier injection from the electrode as shown in Fig. 1.3c. The non-injecting blocking contacts may not require if the resistivity of the photoconductor is sufficiently high [3]. The carrier injection from the metal contacts is insignificant in reverse-biased  $p$ - $n$  or  $pin$  detectors and the dark current is controlled by the thermal generation current in the depletion region.

The fundamental concepts related to X-ray detectors such as X-ray interaction with the solid-state materials, EHP creation mechanism, signal formation principles, general requirements, and materials for X-ray detectors are described in Sect. 1.2. Two very important applications of X-ray radiation detectors in spectroscopic and flat-panel imaging are described in Sects. 1.3 and 1.4, respectively. A brief introduction to X-ray interaction position sensitive semiconductor detector structures and their implication on charge collection are given in Sect. 1.5.

## 1.2 X-Ray Photoconductivity

### 1.2.1 X-Ray Interactions with Photoconductor

X-rays interact with the photoconductor which occurs mainly by three different mechanisms. The types of interactions are the photoelectric effect, Rayleigh scattering, and Compton scattering. The incident X-rays can be completely absorbed in the medium (photoelectric effect) or scattered (Rayleigh or Compton scattering). *Rayleigh* scattering involves an elastic (coherent) scattering of X-rays by orbital electrons. The energy of the scattered X-ray is identical to that of the incident X-ray. There is no exchange of energy from the X-ray to the medium. However, the scattered X-ray experiences a change in its trajectory relative to that of the incident X-ray, and this has an adverse effect in imaging detectors, where the detection of scattered X-rays is undesirable. However, this type of interaction has a low probability of occurrence in the diagnostic X-rays. In general, the average scattering angle decreases with increasing incident X-ray energy  $E$ .

*Compton* scattering involves an inelastic (incoherent) scattering of an X-ray photon by an atomic electron. Compton scattering typically occurs when the energy of the X-ray photon is much greater than the binding energy of the atomic electron. Therefore, the Compton effect occurs with the outer-shell electrons. This interaction includes an electron of kinetic energy  $E''$ , an ionized atom, and a scattered X-ray photon of energy  $E'$  that is lower than the incident photon energy  $E$ . Thus, some energy is imparted to the medium in Compton scattering event. The imparted energy depends on the scattering angle which is random. The probability of Compton absorption per unit mass is approximately proportional to  $E^{-0.5}$  [5].

In photoelectric interaction, the incident X-ray interacts with an orbital electron in the atom, and all its energy is transferred to the electron. Part of this energy is used to overcome the binding energy of the electron, and the remaining fraction becomes the kinetic energy  $E_k$  of the photoelectron. If the energy of the incident X-ray is higher than the binding energy of the electron, the electron is removed from its shell and a vacancy is created in that shell. The ejected electron is most likely one whose binding energy is closest to, but less than, the incident photon energy. For example, for photons whose energies exceed the *K*-shell binding energy, photoelectric interactions with *K*-shell electrons are most probable. The binding energy associated with the *K*-shell is called the *K-edge* and so on. This vacancy is usually filled by an electron from an outer shell, leaving a vacancy in the outer shell that in turn may be filled by an electron transition from a more distant shell. This series of transitions is called an electron cascade. The energy released by each transition is equal to the difference in binding energy between the original and final shells of the electron. This energy may be released by the atom as characteristic X-rays or Auger electrons. The probability of photoelectric absorption per unit mass is approximately proportional to  $Z^4/E^3$ , where  $Z$  is the atomic number. Emissions from transitions exceeding 100 eV are called *characteristic* or *fluorescent* X-rays. The *characteristics* X-rays are named as *K*-fluorescent, *L*-fluorescent, etc. based on the electron receiving shell.

### 1.2.2 Ionization Energy and Signal Formation

Energetic primary electrons created by photoelectric effect or Compton scattering travel in the solid can cause ionization along its track and create many electron-hole pairs (EHPs). As a result, a single X-ray photon can create thousands of EHPs. However, on average, a certain portion of X-ray photon energy is not absorbed in the medium because of various scattering events. The average energy absorbed in the medium by the primary X-ray interaction can be determined and is described by the linear attenuation coefficient  $\alpha$  and energy absorption coefficient  $\alpha_{\text{en}}$ . Thus,  $(\alpha_{\text{en}}/\alpha)E$  is the average absorbed energy  $E_{\text{ab}}$  by the primary X-ray interaction per attenuated X-ray photon of energy  $E$ . For sufficiently thick medium, the escaped radiations from the primary interaction site can interact with atomic electrons of the medium like primary X-rays but at different points. Therefore, the actual average absorbed energy per attenuated X-ray photon of energy  $E$  in a very thick detector is higher than  $(\alpha_{\text{en}}/\alpha)E$  and closer to  $E$ .

The average number of EHP creation per absorbed photon,

$$N_i = \frac{E_{\text{ab}}}{W_i} \quad (1.1)$$

Where  $W_i$  is the ionization energy of the medium, which is the average absorbed energy required to create a single EHP. In this case, the maximum collected charge in the external circuit would be  $Q_i = eN_i$  if there is no loss of charge carriers in the detector, where  $e$  is the elementary charge. Klein [6] developed a formula to calculate the ionization energy, which is,

$$W_0 \approx CE_g + E_{\text{phonon}} \quad (1.2)$$

where  $E_g$  is the bandgap energy,  $C = 2.8$  and  $2.2$  for crystalline and amorphous semiconductors, respectively, [6, 7]. Here  $E_{\text{phonon}} = m\hbar\omega_p$ , where  $m$  is the average number of optical phonon emission per ionization and  $\hbar\omega_p$  is the optical phonon energy. The value of  $E_{\text{phonon}}$  is in the range of 0.1–0.5 eV. Note that the ionization energy obtained from Klein's formula is denoted by  $W_0$ . In most semiconductors, the ionization energy follows Eq. (1.2) and thus  $W_i \approx W_0$ . However, there are few exceptional semiconductors (e.g., amorphous selenium, *a*-Se) where the actual ionization energy  $W_i \gg W_0$  and depends on the electric field and photon energy [8–10]. In those cases, the Klein's formula serves as the lowest theoretical limit for the ionization energy [11].

Since the photoconductors have relatively higher resistivity and thus there is inadequate reservoir of free carriers available to surround the photogenerated carriers and maintain local charge neutrality within the time scale of interest, the photogenerated drifting carriers instantaneously induce charges at the electrodes. The rate of change of this induced charge creates current in the external circuit. Therefore, the currents resulting from the photogeneration of mobile carriers into the

photoconductive detector are due entirely to induction. The Shockley-Ramo's theorem provides a convenient way to calculate the induced current flowing through an electrode of multielectrode detectors (e.g., pixelated image detector) due to the motion of charge carriers in the detector (Fig. 1.4). The induced current  $I_j$  and charge  $\Phi_j$  on an electrode  $j$  by a moving elementary positive charge  $e$  at  $x$  are given by [12–14],

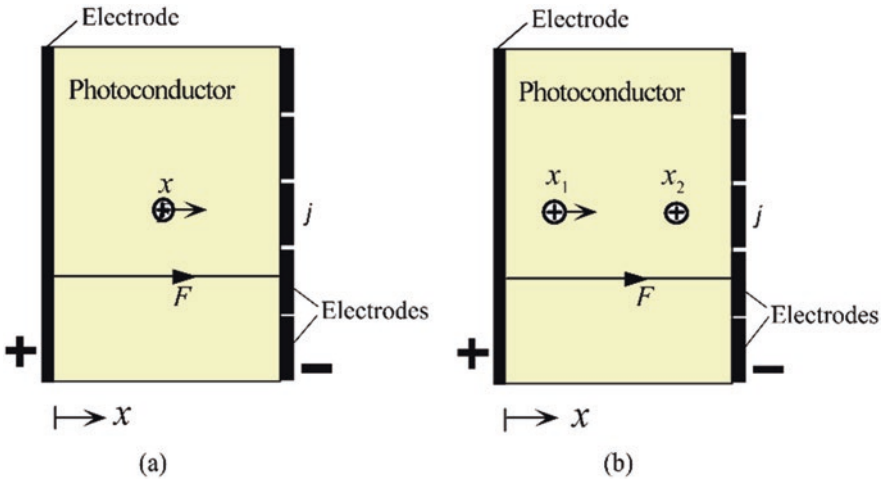
$$I_j = ev \cdot F_{wj}(x) \tag{1.3}$$

$$\Phi_j = -eV_{wj}(x) \tag{1.4}$$

where  $v$  is the instantaneous velocity of charge  $e$ ,  $F_{wj}(x)$  and  $V_{wj}(x)$  are the weighting field and potential of electrode  $j$ .  $F_{wj}(x)$  and  $V_{wj}(x)$  are the electric field and potential that would exist at charge  $e$ 's instantaneous position  $x$  if the electrode of interest ( $j$ ) is raised to unit potential and all other electrodes kept at zero potential and all charges removed.  $V_{wj}$  is unitless and the unit of  $F_{wj}$  is  $m^{-1}$ . An analytical expression for the weighting potential in pixelated detectors having finite square pixels has been derived in literature [15].

Let a positive point charge be moving from  $x_1$  to  $x_2$ .  $\Phi_{j1}$  and  $\Phi_{j2}$  are the induced charges at electrode  $j$  when the charge is at  $x_1$  and  $x_2$ , respectively. The induced charges,  $\Phi_{j1} = -eV_{wj}(x_1)$  and  $\Phi_{j2} = -eV_{wj}(x_2)$ . The collected charge at electrode  $j$  for moving a positive point charge from  $x_1$  to  $x_2$  is given by,

$$Q_j = -(\Phi_{j2} - \Phi_{j1}) = e[V_{wj}(x_2) - V_{wj}(x_1)] \tag{1.5}$$



**Fig. 1.4** A cross section of a multielectrode detector: (a) an elementary positive charge at  $x$  is drifting by an applied field  $F$ . (b) An elementary positive charge is moved from point  $x_1$  to  $x_2$

For a large area single-element detector,  $F_w(x) = 1/L$ ,  $V_w(x) = x/L$ , and thus current,  $i = ev/L$  [16], where  $L$  is the photoconductor thickness. In this case, the collected charge at the electrode for moving a positive point charge from  $x_1$  to  $x_2$  is simply,

$$Q_j = -(\Phi_{j2} - \Phi_{j1}) = e \frac{(x_2 - x_1)}{L} \quad (1.6)$$

If there is carrier trapping, only a fraction of photogenerated charge is collected in the external circuit. Consider an electron and a hole (an EHP) are generated at  $x$  and drift under the influence of the electric field. The average electron and hole photocurrents are  $i_e(t) = (ev_e/L)\exp(-t/\tau_e)$  for  $t < t_e$  and  $i_h(t) = (ev_h/L)\exp(-t/\tau_h)$  for  $t < t_h$ , respectively; where  $v_e = \mu_e F$ ,  $v_h = \mu_h F$ ,  $t_e = x/v_e$ ,  $t_h = (L-x)/v_h$ ,  $\mu$  is the carrier mobility, and  $\tau$  is the carrier lifetime. The subscripts  $e$  and  $h$  on  $\mu$  and  $\tau$  refer to electrons and holes, respectively. Both types of carrier drifts produce currents of the same polarity at any electrode. Therefore, the collected charge at any electrode is the sum of the contributions of both types of carrier transports. The average collected charge for applying a positive bias at the top electrode (the electric field is along the positive  $x$  direction) is,

$$\begin{aligned} Q_c(x) &= \int_0^{t_e} i_e(t) dt + \int_0^{t_h} i_h(t) dt \\ &= \frac{e\mu_e\tau_e F}{L} [1 - e^{-x/\mu_e\tau_e F}] + \frac{e\mu_h\tau_h F}{L} [1 - e^{-(L-x)/\mu_h\tau_h F}] \end{aligned} \quad (1.7)$$

where  $t_e = x/\mu_e F$  and  $t_h = (L-x)/\mu_h F$  are the electron and hole transit times, respectively. Eq. (1.7) is the well-known *Hecht equation* for calculating the average collected charge. The maximum collected charge,  $Q_c = e$ , when the lifetime of both holes and electrons is infinity. Therefore, the charge collection efficiency,

$$\eta_{cc}(x) = \frac{\mu_e\tau_e F}{L} [1 - e^{-x/\mu_e\tau_e F}] + \frac{\mu_h\tau_h F}{L} [1 - e^{-(L-x)/\mu_h\tau_h F}] \quad (1.8)$$

Equation (1.8) is the charge collection efficiency for a free EHP generation at  $x$ , which depends not only on the charge carriers transport properties (mobility-lifetime of both holes and electrons) and electric field, but also on the location where the charge is created. For exponential absorption throughout the photoconductor layer (which is the case for X-rays), the average charge collection efficiency [17, 18],

$$\eta_{cc} = x_h \left[ 1 + \frac{(e^{-1/x_h} - e^{-1/\Delta})}{(\Delta/x_h - 1)\eta} \right] + x_e \left[ 1 - \frac{(1 - e^{-1/\Delta - 1/x_e})}{(\Delta/x_e + 1)\eta} \right], \quad (1.9)$$

where  $x_e = \mu_e \tau_e F/L$ ,  $x_h = \mu_h \tau_h F/L$ ,  $\Delta = 1/\alpha L$  and  $\eta = 1 - \exp(-1/\Delta)$  is the quantum efficiency of the photoconductive detector. Therefore, the actual collected charge  $Q_c = Q_i \eta \eta_{cc}$ , where  $Q_i$  is the X-ray generated free charges,  $\eta$  accounts for the average fraction of the X-rays that are attenuated within the photoconductor thickness. Though Eq. (1.9) applies under small signal conditions under uniform electric field, the equation shows much resilience even under strong injection and errors are not as large as one may anticipate [19]. Further, Eq. (1.9) assumes that the carrier transport properties (i.e.,  $\mu\tau$  do not vary across the sample). It is still possible to use Eq. (1.9) in cases where the carrier ranges are not uniform in the sample by suitably defining effective carrier ranges as discussed in [18]. The charge collection efficiency for a given photoconductor depends on  $x_e$  and  $x_h$  and hence on the applied field. Most semiconductors have asymmetric  $\mu\tau$  products. Ensuring that the carrier with the longer range is drifted towards the bottom electrode can provide a better charge collection efficiency [15].

### 1.2.3 X-Ray Photoconductors

The following are the general properties of the X-ray photoconductor [20] used in X-ray detectors:

1. Most of the incident X-ray radiation should be absorbed within a practical photoconductor thickness. This means that, over the energy range of interest, the attenuation depth  $\delta$  (inverse of the attenuation coefficient  $\alpha$  of the photoconductor) of the X-rays must be substantially less than the photoconductor layer thickness  $L$ . Higher atomic number materials give higher attenuation.
2. The photoconductor should have high intrinsic X-ray sensitivity, i.e., it must be able to generate as many collectable (free) EHPs as possible per unit of incident radiation. This means the ionization energy,  $W_i$ , (amount of radiation energy required to create a single free EHP) must be as low as possible.
3. The photoconductor should have good charge carrier transport properties. That means the product of carrier drift mobility ( $\mu$ ) and carrier lifetime ( $\tau$ ) should be high so that the charge collection efficiency is close to unity.
4. The properties of the photoconductor should not change with time because of repeated exposure to X-rays, i.e., X-ray fatigue and X-ray damage should be negligible.
5. The detector should preferably operate at around room temperature.

Both elementary (Si, Ge, or Se) and compound semiconductors are used in radiation detectors. Si detectors are used for low energy X-rays (<30 keV) [21]. They are mechanically and chemically robust. High purity Ge detectors have high resolution and efficiency for detection of hard X-rays. Both Si and Ge detectors often need to operate at low ambient temperature to decrease the dark current from thermally generated charge carriers [22]. Compound semiconductors are mostly derived from

groups III and V (e.g., GaAs, GaN, InP) and groups II and VI (e.g., CdTe) of the periodic table. The compound semiconductors have few distinct advantages as their electronic and chemical properties can be modified by band-gap engineering for specific applications in radiation detectors. For example, adding a few percent Zn into the CdTe lattice strengthens the lattice of CdTe, increases the band gap [23], decreases the conductivity, and hence reduces the dark current. A few selected compound semiconductors such as CdTe, CdZnTe ( $\text{Cd}_{0.92}\text{Zn}_{0.08}\text{Te} - \text{Cd}_{0.9}\text{Zn}_{0.1}\text{Te}$ ), and  $\text{HgI}_2$  are already used in commercial X-ray and  $\gamma$ -ray spectroscopic detectors. They do not need cooling and can be used at room temperature, which is a distinct advantage. Their properties have been extensively reviewed in the literature [21, 22, 24–29] and in recent book [3] and chapters [30, 31]. A comprehensive description of the photoconductors for large area medical X-ray image detectors can be found in Refs. [32, 33].

Group II-VI materials attract special attention for radiation detectors because they can provide continuous broad range of bandgaps (e.g., 0.15 eV for HgTe to 4.4 eV for MgS). These compounds are formed by combining a Group IIb metal (such as Zn, Cd, and Hg) with a Group VIa cation (usually S, Se or Te). They have high effective Z and thus provide high stopping power (i.e., high attenuation). The high stopping power enables thinner detector. All II-VI binaries have direct bandgaps. The typical main compounds are CdTe and HgTe. They are alloyed with Zn, Se, Mn, or Cd to create ternary compounds (e.g.,  $\text{Cd}_{(1-x)}\text{Zn}_x\text{Te}$ ,  $\text{Cd}_{(1-x)}\text{Mn}_x\text{Te}$  and  $\text{Hg}_{(1-x)}\text{Cd}_x\text{Te}$ ) for commercial radiation detectors. Group II-VI semiconductors can also be created in quaternary forms, although less common than III-V varieties.

There are many experimental semiconductors that have good commercial potential. For example, GaAs *p-i-n* X-ray detectors for spectroscopy have been demonstrated [34]. GaAs arrays have been also demonstrated for X-ray spectroscopy with high resolution [35]. SiC is another possible X-ray detector material that has favorable properties for X-ray spectrum measurements and can be used in harsh environments [36, 37]. GaN-based X-ray radiation detectors are more suitable at high temperature and high radiation field operation [38, 39]. The electronic properties of typical materials used in dosimetry and spectroscopic detectors are summarized in Table 1.1. The materials for imaging detectors are described in Sect. 1.4.

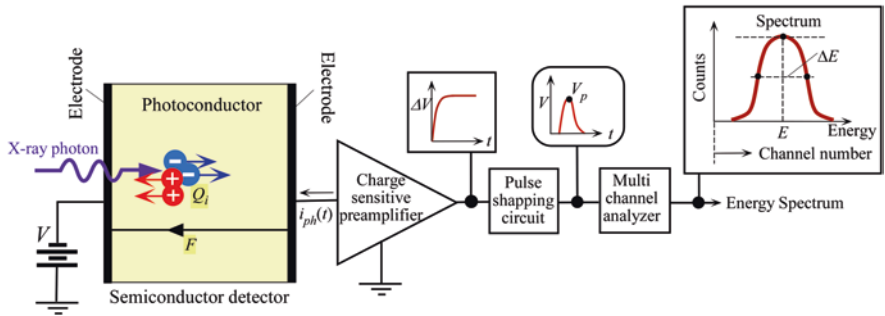
### 1.3 X-Ray Spectroscopic Detectors

The measurement of the energy distribution of the incident radiation is known as radiation spectroscopy. The basic principle of spectroscopy measurement set up using a semiconductor detector is illustrated in Fig. 1.5. The fundamental properties of a radiation detector are often determined by its pulse height spectrum. To construct a pulse height spectrum, a stream of monoenergetic photons is irradiated within the detector. Photons are sufficiently separated so that one photon at a time is absorbed and the collected charges from the individual photons can be separately processed and stored in the multichannel analyzer. The preamplifier integrates the

**Table 1.1** Selected examples of *single crystal* semiconductors for use in X-ray detectors for the measurement of dose or energy spectra. If the detector type is not fully known, metal/semiconductor/metal is shown. HPGe is high purity Ge

Semi-conductor	Detector type	Density (g cm <sup>-3</sup> )	E <sub>g</sub> (eV)	W <sub>i</sub> (eV)	F <sub>N</sub>	Typical mobility-lifetime
Si	<i>pn</i> , <i>pin</i> or Schottky junction	2.33	1.12	3.62	0.08–0.13	$\mu_e\tau_e \approx 1 \text{ cm}^2/\text{V}$ , $\mu_h\tau_h \approx 1 \text{ cm}^2/\text{V}$
Ge Ge (Li)	<i>pin</i> -like, metal/HPGe/metal	5.33	0.72	2.96	0.06–0.11	$\mu_e\tau_e \approx 1 \text{ cm}^2/\text{V}$ , $\mu_h\tau_h \approx 1 \text{ cm}^2/\text{V}$
GaAs	<i>pin</i>	5.32	1.43	4.18	0.14	$\mu_e\tau_e \approx 10^{-4} \text{ cm}^2/\text{V}$ , $\mu_h\tau_h \approx 4 \times 10^{-6} \text{ cm}^2/\text{V}$
CdTe	Schottky, <i>pin</i> , and metal/CdTe/metal	5.85	1.44	4.43	0.06–0.09	$\mu_e\tau_e \approx 10^{-3} \text{ cm}^2/\text{V}$ , $\mu_h\tau_h \approx 10^{-4} \text{ cm}^2/\text{V}$
CdZnTe	Schottky, <i>pin</i> , and metal/CdTe/metal	5.8	1.57	4.6	0.10	$\mu_e\tau_e \approx 10^{-3} \text{ cm}^2/\text{V}$ , $\mu_h\tau_h \approx 10^{-4} \text{ cm}^2/\text{V}$
HgI <sub>2</sub>	Metal/HgI <sub>2</sub> /metal	6.4	2.15	4.2	0.12	$\mu_e\tau_e \approx 3 \times 10^{-4} \text{ cm}^2/\text{V}$ , $\mu_h\tau_h \approx 4 \times 10^{-5} \text{ cm}^2/\text{V}$
4H-SiC	Metal/HgI <sub>2</sub> /metal	3.29	3.27	7.28	0.128	$\mu_e\tau_e \approx 4 \times 10^{-4} \text{ cm}^2/\text{V}$ , $\mu_h\tau_h \approx 8 \times 10^{-5} \text{ cm}^2/\text{V}$
InP	Metal/InP/metal	4.79	1.34	4.2	0.13	$\mu_e\tau_e \approx 2 \times 10^{-5} \text{ cm}^2/\text{V}$ , $\mu_h\tau_h \approx 10^{-5} \text{ cm}^2/\text{V}$

Source: Data are typical values quoted in the literature as in Refs. [3, 28]



**Fig. 1.5** The basic principle of photon energy spectrum measurements using a semiconductor detector

transient current pulse to produce a voltage step  $\Delta V$  proportional to collected  $Q_c$ . The pulse shaping circuit converts the preamplifier output signal into a form suitable for measurements, producing an output voltage pulse with pulse height  $V_p$  proportional to  $Q_c$ . However, a statistical variation in  $Q_c$  is observed for different incident photons and so does in voltage pulse height  $V_p$ . The multichannel analyzer sorts out incoming voltage pulses according to their output pulse height and stores the number of pulses (count) of a particular charge level (channel number). We can



suitably calibrate the measurement system for a known photon energy so that we can convert the  $Q_c$  to photon energy  $E$  and plot the number of occurrences (counts) against the photon energy  $E$  which is called a pulse height spectrum. The detailed analyses of the various components of spectroscopic measurement technique are described in radiation detection and measurement textbooks such as in references [40, 41]. In the ideal case, we would find a Gaussian distribution with a mean that corresponds to  $E$  and a full width between half maximum (FWHM),  $\Delta E$ . If  $\sigma$  is the standard deviation of the Gaussian profile, then  $\Delta E = 2.35\sigma$ .

There are several potential sources of fluctuation for the observed  $\Delta E$ . These include any drift of the operating characteristics of the detector during the measurements, sources of random noise within the detector and instrumentation system (electronic noise), and statistical noise arising from the discrete nature of the measured signal itself. The third source represents the minimum amount of fluctuation that will always be present in the detector signal, which sets an important limit on detector performance.

The overall observed variance can be written as

$$\sigma^2 = \sigma_{\text{con}}^2 + \sigma_{\text{cc}}^2 + \sigma_e^2, \quad (1.10)$$

Where  $\sigma_{\text{con}}$  is the standard deviation owing to carrier generation,  $\sigma_{\text{cc}}$  is the standard deviation owing to incomplete charge collection, and  $\sigma_e$  is the standard deviation owing to leakage current and amplifier noise. The electronic noise is a lumped value incorporating the noise associated with the leakage current of the detector and the noise due to the electronic chain, starting with the preamplifier, to the final output.

As mentioned earlier, the energy transfer of an X-ray photon energy to the matter occurs through the creation of an energetic primary electron. This energetic primary electron slows down by transferring energy in a cascade of energy transfer processes to electrons and the lattice. The conversion process of an absorbed photon to the number of carriers has fluctuations about its mean value  $N_i$  due to the randomness of this whole processes. If the conversion (the ionization of the medium by the primary electron) was a string of independent events, the conversion statistics would be a Poisson distribution so that the variance of the conversion process would be  $N_i$ . In fact, the energy conversion events are correlated by energy conservation. Therefore, the variance in the number of charge carrier generation is modified by a Fano factor  $F_N$  [42], and thus the actual variance of conversion is  $F_N N_i$ . If  $\Delta E_{\text{con}}$  is the FWHM in the pulse height spectrum in Fig. 1.5 from the statistics of the conversion process alone, then this would be

$$\Delta E_{\text{con}} = 2.355\sqrt{F_N E W_i} \quad (1.11)$$

The Fano factors for many semiconductors are typically less than 1 and are listed in Table 1.1.  $F_N < 1$  is accounted by the fact that the spread in the collected number of carriers is less than that expected from Poisson statistics. A reliable experimental measurement of  $F_N$  requires that the photogenerated carriers suffer no trapping (all

are collected) and the electronic noise in the measurement circuit is suppressed. Fano factor also has temperature and photon energy dependence [3].

The second important broadening mechanism is the effect of charge carrier trapping during the drift of the carriers towards their collection electrodes. Some of charge carriers can be trapped during their drift towards the electrodes and are not fully collected, so the measured charge is less than  $Q_c$ . There are two intermingled fluctuations in charge collection. First is that not every photon is absorbed at  $x$ , so there will be fluctuations in  $x$  and hence in  $Q_c$ . The absorption probability of a photon along the sample follows an exponential distribution  $\exp(-\alpha x)$  where  $\alpha$  is the linear attenuation coefficient of the medium. The variance of charge collection efficiency for the fluctuation on interaction distance  $x$  can be found in Ref. [43, 44]. Second, charge carrier trapping during drift is a stochastic process and there will be fluctuations in  $\eta_{cc}$  even if each photon was absorbed exactly at  $x$ . The signal variance for the fluctuation in  $\eta_{cc}$  owing to charge carrier trapping for photon interaction at  $x$  is given in Ref. [45].

The resolution of a spectroscopic detectors is nominally quoted in terms of the FWHM width  $\Delta E$  at the photon energy  $E$ . Obviously, the smaller is  $\Delta E$ , the better is the resolution of the detector in discriminating different energy photons. High purity Ge detectors operated at low temperatures have especially high spectral resolution. For example, if the electronic noise can be reduced by special techniques, then a resolution of 345 eV at 59.5 keV or 0.57% is achievable at 100 K [46], though typical quoted values in various tables have been 670 eV at 77 K [3]. Typically, the energy resolution with compound semiconductor detectors at room temperature is approximately 2% or more, but less at low temperatures as discussed in references [28]. Tables 9.5, 4, and 3 in references [3, 26, 28], respectively, provide the best values that are observed for a range of semiconductors at energies 5.9 keV and 59.5 keV.

## 1.4 Flat-Panel X-Ray Image Detectors

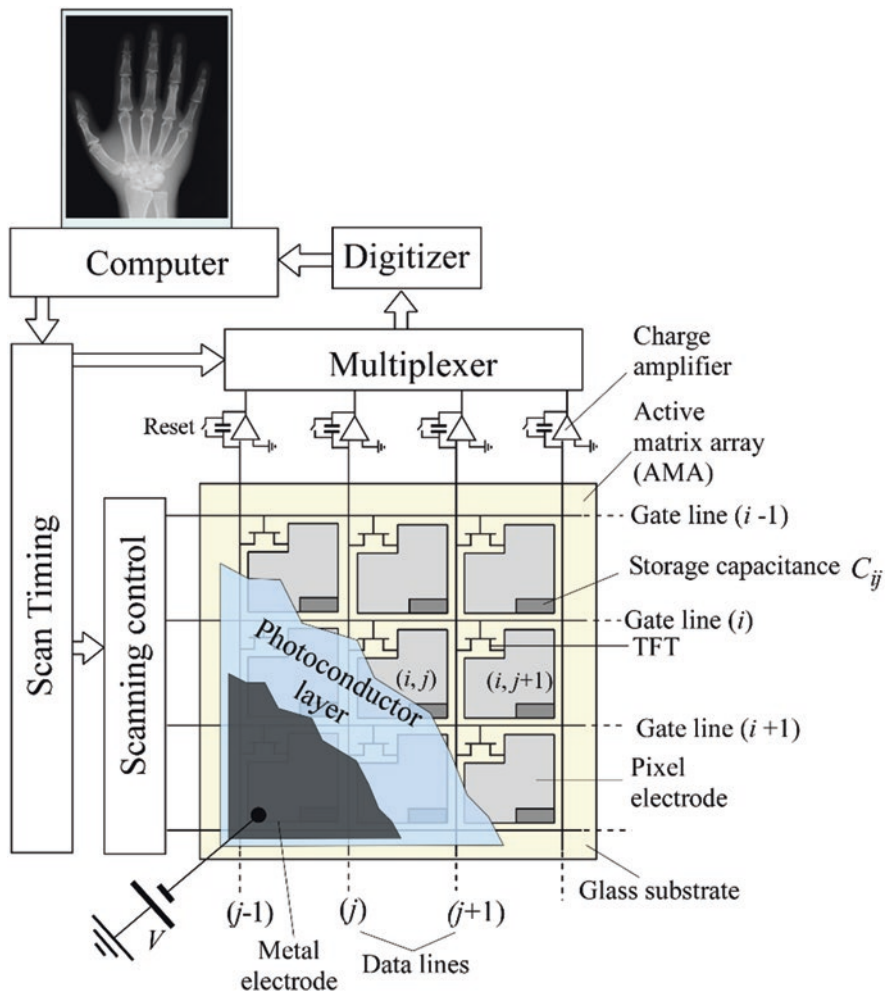
### 1.4.1 Materials and Structures

The flat-panel X-ray imagers (FPXIs) are, at present, the most successful digital X-ray detectors for screening medical imaging such as mammography and general radiography [47–50]. The last few decades have seen a nearly full transformation of X-ray imaging to modern digital imaging. Digital X-ray image sensors have two major parts; the detector where X-rays are absorbed and charge carriers are generated and collected, and the peripheral electronics (including a two-dimensional active-matrix arrays, AMA) that scan and process the collected charge from the detector for display or other form of readable information [51]. An AMA is a two-dimensional large array of pixels as shown in Fig. 1.6. The requirements on the digital detector technology have become more and more demanding as medical X-ray imaging today is not only about projection imaging, but involves real-time imaging

(fluoroscopy) and tomosynthesis, among other imaging enhancements such as dual energy imaging, photon counting, etc., each of which has its own demands on the detector technology [52–58]. The FPXIs are generally either phosphor-based (indirect conversion) or photoconductor-based (direct conversion). In indirect method, X-ray energy is converted into light photons in phosphor layer (mostly cesium iodide, CsI) and these light photons are then detected by a photodiode. In direct method, X-ray photons directly generate EHPs in the photoconductor layer, which are collected on electrodes. The typical single pixel structures of both direct and indirect conversion FPXIs with TFT are shown in Fig. 1.7. A comprehensive and detailed review of flat-panel image detectors, both direct and indirect, has been given by Rowlands and Yorkston [59]. A drawback of indirect method is that the light photons are scattered and blur the image. The direct conversion detectors produce much sharper images than the indirect conversion detectors [48]. The focus of this section is on the properties and the performance of direct conversion X-ray image detectors.

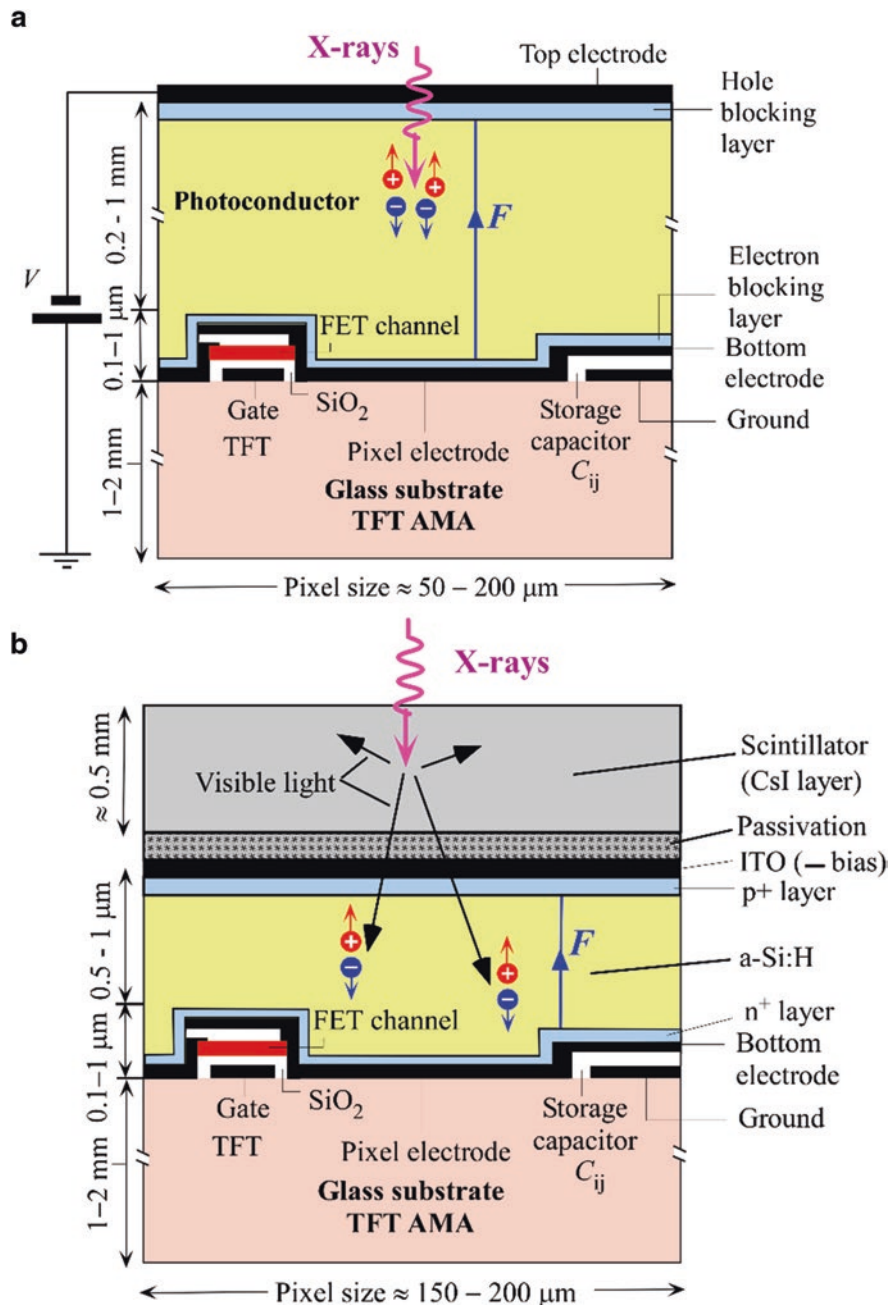
For large area detectors, each pixel has a thin film transistor (TFT) and a charge storage capacitance. The TFT gate (G) is for the control of the “on” or “off” state of the TFT and connected to a particular address line  $i$ , the drain (D) is connected to a pixel electrode and a pixel storage capacitor, the source is connected to a particular data line  $j$ . The AMA has  $M \times N$  number of gate and data lines, where  $M$  and  $N$  can be several thousand. The intrinsic read-out resolution of the detector is determined by the pixel pitch, which is typically 50–100  $\mu\text{m}$ . The TFT array is laid out on a suitable flat rectangular glass substrate and is purchased by the detector manufacturing company as a component onto which the semiconducting photoconductor is coated. The TFT-AMA substrate makes use of the well-established hydrogenated amorphous silicon ( $a\text{-Si:H}$ ) technology for displays. A photoconductive layer is deposited on top of the AMA substrate (Fig. 1.7). A suitable electrode is deposited on the top surface to apply a bias voltage, which establishes a field in the photoconductor. Upon absorption of X-ray photons through the top surface, electrons and holes are generated in the photoconductor layer and these carriers drift and give rise to an X-ray photocurrent. Each pixel stores an amount charge in the storage capacitor based on the radiation received on top of that pixel. The stored charge from the capacitors can be read through properly addressing the TFT ( $i,j$ ) via the gate ( $i$ ) and source ( $j$ ) lines. The electrical signals from pixels are amplified, multiplexed, and digitized so that the image can be conveniently displayed in a computer screen. The signal scanning technique is adequately described in these Refs. [51, 59, 60].

In the case of small area imaging detectors, the TFT in AMA can be replaced by CMOS, CCD or, a particular ASIC (Application Specific Integrated Circuit) pixelated read-out chip. For direct conversion detectors, an X-ray photoconductor such as CdZnTe crystals are usually indium bump-bonded (equivalent to “cold welding”) to electrodes on a CMOS [61]. CdZnTe crystals have also been bonded to ASIC read-out chips and CCDs using indium bumps to produce high resolution detectors for slot scanning X-ray imaging [62, 63]. Direct coating of the CMOS with a photoconductor has also been tried, for example,  $a\text{-Se}$  directly evaporated onto a defined area of the CMOS [64]. In recent years, advances have been made in increasing the



**Fig. 1.6** The structure of a typical direct conversion active-matrix array-based flat panel X-ray imager. (Idea from Ref. [51])

effective imaging area of wafer-size CMOS chips through stitching and tiling [65]. In another application, polycrystalline layer of  $HgI_2$  was grown directly on a CMOS chip ( $10\text{ cm} \times 10\text{ cm}$ ) to construct an X-ray imager [66]. There are several distinct advantages to using crystalline photoconductors on CMOS read-out chips. First is that the pixel size can be made very small and the whole operation can be very fast compared to TFT arrays. The second is that most CMOS imaging chips have on-pixel MOS transistors that provide on-pixel amplification to improve the imaging performances. Presently, the largest area commercial CMOS sensors are about  $11\text{ cm} \times 14\text{ cm}$  and use indirect conversion as described in [67]. Manufacturers such as Dexela and Teledyne-DALSA also offer CMOS-tiled detectors for specific X-ray



**Fig. 1.7** A typical pixel structure of the TFT-based flat-panel detector: (a) a pixel element of the direct conversion FPXI, and (b) a pixel element of the indirect conversion FPXI

imaging applications that include not only medical imaging but also industrial imaging (e.g., nondestructive testing).

Stabilized *a*-Se is currently the only photoconductor for large area commercial X-ray image sensors, especially for mammography [51, 68]. Stabilized means that *a*-Se has been alloyed with 0.2–0.5%. As to prevent the crystallization of pure *a*-Se and then doped with Cl in the ppm amounts to control the charge transport (see [69] and recent review in [70]). The commercial *a*-Se detector is *n-i-p* or *p-i-n* type, where bulk *i*-layer is the stabilized *a*-Se layer [5]. These *p*-like and *n*-like layers do not have conventional *p*- or *n*-layer definitions in crystalline semiconductor theory based on electron and hole concentrations or the position of the Fermi level, rather they have a very high concentration of deep trap centers for oppositely charged carriers. In the *p*-like layer, the holes are relatively mobile, but electrons get easily trapped, and similarly in the *n*-like layer, electrons are mobile, but the holes get trapped easily. The thickness of these *p*- or *n*-like layers is few microns, whereas the *i*-layer thickness is at least few hundred microns. The thin *p*- or *n*-like layers act as “blocking layers”. The trapped charge carriers in these blocking layers reduce the electric field at the contacts and, hence, reduce the carrier injection from the electrodes, which reduces the dark current [71]. The *p-i-n* structure was the key to the success of the *a*-Se-based FPXI because it allowed the dark current to be extinguished to an innocuous level [72–74].

*A*-Se is the most preferred photoconductor for direct-conversion X-ray detectors because of its low dark current, convenient low-temperature deposition over a large area, and good charge-transport properties. There is one remarkable drawback of *a*-Se, which is its lower intrinsic X-ray sensitivity (i.e., large  $W_i$ ) ionization energy as compared to its competitors, such as polycrystalline  $\text{HgI}_2$  or  $\text{CdZnTe}$  [32]. For example, the typical value of the electric field used in *a*-Se detectors is  $10 \text{ V}/\mu\text{m}$  where the value of  $W_i$  is about 45 eV; the value of  $W_i$  is 5–6 eV for polycrystalline mercuric iodide (poly- $\text{HgI}_2$ ) and poly- $\text{CdZnTe}$ . The imaging properties of *a*-Se based FPXIs for various medical imaging modalities have been well-examined and analyzed; see for example [75–80]. There have been a number of other photoconductors, such as polycrystalline layers of  $\text{TlBr}$  [81, 82],  $\text{PbI}_2$  [83–86],  $\text{HgI}_2$  [60, 87–91],  $\text{CdTe}$  [92],  $\text{CdZnTe}$  [93, 94],  $\text{PbO}$  [95–98], and various hybrid organic–inorganic perovskite (e.g., methylammonium lead halides, MA Pb-halides) [99–105] that have been investigated to replace *a*-Se. Some of these, particularly  $\text{HgI}_2$  and  $\text{MAPbI}_3$  [60, 106], have shown much potential for use in commercial FPXI applications. MA Pb-halide perovskites, in polycrystalline form, can be easily and cheaply prepared in large areas from solution (in contrast to vacuum deposition) and have already shown very good performance in photovoltaics and photodetector applications [107, 108]. The basic underlying problem with most of these semiconductors is that they exhibit either an unacceptably large dark current under high fields needed to extract all X-ray generated charges or they possess significantly incomplete charge collection, and its consequences such as low resolution and image lag because they need to be operated at a low field to prevent a large dark current [32, 51]. Another drawback of polycrystalline materials is the adverse effects of grain boundaries in limiting charge transport and the nonuniform response

of the sensor due to large grain sizes. Grain boundaries in the polycrystalline material are expected to create trapping levels within the band gap and introduce potential barriers between neighboring grains [109, 110]. Table 1.2 provides a summary of the properties of current photoconductive layers that either are used or have potential for use in large area FPXIs. Photoconductors for large area X-ray imaging have been recently reviewed in [33, 111].

## 1.4.2 Metrics of X-Ray Imaging Performances

X-ray sensitivity, resolution in terms of modulation transfer function (MTF), detective quantum efficiency (DQE), image lag, and ghosting are often considered as the metrics of imaging performances. For most practical applications, the spatial-frequency-dependent ( $f$ -dependent) detective quantum efficiency,  $DQE(f)$ , is the appropriate metric of overall system performance and is unity up to the Nyquist frequency for an ideal FPXI.

### 1.4.2.1 X-Ray Sensitivity

The *X-ray sensitivity* is an important selection criterion of a photoconductor for its use in X-ray detectors, which is defined as the collected charge per unit area per unit exposure of radiation. If  $\Phi_0$  is the photon fluence per Roentgen, the X-ray sensitivity can be written as [112],

$$S = \frac{eE\Phi_0}{W_i} \left( \frac{\alpha_{en}}{\alpha} \right) \eta \eta_{cc} = \frac{8.72 \times 10^{-6}}{(\alpha_{air} / \rho_{air}) W_i} \left( \frac{\alpha_{en}}{\alpha} \right) \eta \eta_{cc} \quad (CR^{-1} cm^{-2}) \quad (1.13)$$

Where  $\alpha_{air}$  and  $\rho_{air}$  are the energy absorption coefficient of air and its density ( $\alpha_{air}/\rho_{air}$  is in  $cm^2/g$  and  $W_i$  is in eV). Note that the expression of X-ray sensitivity in Eq. (1.13) does not consider the secondary photon reabsorption. For a thin detector where the probability of secondary photon reabsorption is low, Eq. (1.13) is still good. However, in thick detectors where most of the secondary photons are reabsorbed in the detector volume, the X-ray sensitivity for uniform excitation becomes,

$$S = \frac{8.72 \times 10^{-6}}{(\alpha_{air} / \rho_{air}) W_i} \eta \eta_{cc} \quad (CR^{-1} cm^{-2}) \quad (1.14)$$

The X-ray sensitivity is basically controlled by  $W_i$ ,  $\eta$  and  $\eta_{cc}$ . Typical X-ray sensitivities of various photoconductive X-ray detectors are given in Ref. [33].

**Table 1.2** Properties of a few selected large area X-ray photoconductors. PVD is physical vapor deposition and SP is screen printing

Photoconductor State Preparation	Density (g/cm <sup>3</sup> )	$\delta$ at 20 keV $\delta$ at 60 keV	$E_g$ (eV)	$W_i$ (eV)	Electron $\mu_e \tau_e$ (cm <sup>2</sup> /V)	Hole $\mu_h \tau_h$ (cm <sup>2</sup> /V)
a-Se Amorphous Vacuum deposition	4.3	49 $\mu\text{m}$ 998 $\mu\text{m}$	2.2	45 at 10 V/ $\mu\text{m}$ 20 at 30 V/ $\mu\text{m}$	$3 \times 10^{-7} - 10^{-5}$	$10^{-6} - 6 \times 10^{-5}$
Cd <sub>0.95</sub> Zn <sub>0.05</sub> Te Polycrystalline Vacuum deposition	4.3	80 $\mu\text{m}$ 250 $\mu\text{m}$	1.7	5	$\sim 2 \times 10^{-4}$	$\sim 3 \times 10^{-6}$
HgI <sub>2</sub> Polycrystalline PVD	6.3	32 $\mu\text{m}$ 252 $\mu\text{m}$	2.1	5	$10^{-5} - 10^{-4}$	$10^{-6} - 10^{-5}$
HgI <sub>2</sub> Polycrystalline SP	6.3	32 $\mu\text{m}$ 252 $\mu\text{m}$	2.1	5	$10^{-6} - 10^{-5}$	$\sim 10^{-7}$
PbI <sub>2</sub> , Polycrystalline Normally PVD	3–5	28 $\mu\text{m}$ 259 $\mu\text{m}$	2.3	5	$7 \times 10^{-8}$	$\sim 2 \times 10^{-6}$
PbO, Polycrystalline Vacuum deposition	5.8	12 $\mu\text{m}$ 218 $\mu\text{m}$	1.9	8–20	$10^{-9} - 5 \times 10^{-7}$	$4 \times 10^{-8}$
CH <sub>3</sub> NH <sub>3</sub> PbI <sub>3</sub> Perovskites Polycrystalline SP	4.8	52 $\mu\text{m}$ 365 $\mu\text{m}$	1.6	5	$\sim 10^{-6}$	$10^{-6} - 10^{-4}$
TlBr Polycrystalline Vacuum deposition	7.5	18 $\mu\text{m}$ 317 $\mu\text{m}$	2.7	6.5	Small	(1.5–3) $\times 10^{-6}$

Source: Data combined from various sources

### 1.4.2.2 Spatial Resolution

The spatial resolution of an imaging device/system can be described in terms of the modulation transfer function (MTF), which is the relative response of the system as a function of spatial frequency. The FPXI is a rotationally symmetric system, and therefore, MTF is also rotationally symmetric and can be expressed in terms of single radial frequency  $f$ , which is the Fourier transform of the line spread function (LSF). When an imaging system is stimulated with a signal along a line, the LSF is constructed by evaluating the system response perpendicular to the line. The size of the pixel in an imaging detector sets a theoretical limit on the image resolution. While images with small pixels have the potential to deliver high spatial resolution, many other factors also affect spatial resolution, and in many cases, those other factors limit the spatial resolution. The shape of pre-sampling MTF contains all the information on signal blurring of the detector, which can be described as a cascade of several independent stages where the overall MTF is simply the product of the



MTFs of all the individual stages. The pre-sampling MTF of an image detector can be expressed as,

$$MTF(f) = MTF_m(f) \times MTF_{tr}(f) \times MTF_a(f), \quad (1.15)$$

where  $MTF_m = p_{pe}MTF_{pe} + p_kMTF_k + p_cMTF_c$  is the weighted MTF including the MTFs due to the range of the primary photoelectron,  $K$ -fluorescence reabsorption, and Compton Scattering [113],  $MTF_{pe}$  is due to the range of the primary photoelectron,  $MTF_k$  is due to the  $K$ -fluorescence reabsorption,  $MTF_c$  is due to Compton scattering,  $MTF_{tr}$  is due to the charge carrier trapping, and,  $p_{pe}$ ,  $p_k$ , and  $p_c$  are the relative probabilities of the released charge carriers being from the photoelectric primary electron interaction,  $K$ -fluorescent X-ray reabsorption, and Compton scattered photon, respectively.  $MTF_a$  is the modulation transfer function associated with the aperture function of the pixel electrodes. The aperture in FPXI is approximately a square with a dimension  $a$ , and thus,

$$MTF_a(f) = \left| \text{sinc}(af) \right| = \left| \frac{\sin(\pi af)}{\pi af} \right| \quad (1.16)$$

The spatial resolution in direct conversion FPXIs is usually high and closer to  $MTF_a$ , as compared to phosphor-based FPXI [48]. The signal blurs due to the range of primary photoelectron and Compton scattered photons are insignificant for diagnostic X-rays (up to 100 keV) [17, 113]. Therefore, the charge carrier trapping and the reabsorption of  $K$ -fluorescent X-ray photons at different points from the primary X-ray interaction point are the two dominant mechanisms responsible for the loss of resolution [114, 115] in direct conversion FPXI. The loss of resolution due to fluorescence reabsorption is maximum (although not very substantial) just above the  $K$ -edge of the photoconductor material. This effect can be ignored when (i) the incident X-ray photon energy is lower than the  $K$ -edge of the photoconductor, or (ii) the mean energy of the X-ray beam and the  $K$ -edge occurs at widely different energies [17, 114]. The theoretical method for calculating  $MTF_k$  can be found in oxy-Refs. [113, 116]. The charge carrier trapping has a significant effect on the resolution of these direct conversion X-ray image detectors, which is discussed below.

The top electrode in direct conversion FPXI is a continuous metal plate and the electrode on the other side of the photoconductor is segmented into an array of individual square pixels of size  $a \times a$ . Since the effective fill factor (the effective fraction of pixel area used for image charge collection) of a photoconductive flat-panel detector is close to unity [117, 118], the *effective* pixel aperture width  $a$  is virtually identical to the pixel pitch (center to center distance between two pixels). Some of the X-ray generated carriers become captured by deep traps in the bulk and blocking layers during their drift across the photoconductor. These trapped carriers induce charges not only on the corresponding pixel electrode, but also on neighboring pixel electrodes and consequently there is a lateral spread of signal and hence a loss of image resolution [2]. An analytical expression for the MTF due to distributed carrier

trapping in the bulk of the photoconductor has been described in [119]. If all charge carriers are trapped right at the interface between the photoconductor and blocking layer only, then its corresponding MTF can be calculated by a simple analytical expression [115, 120]. In fact, some of X-ray generated carriers are trapped in the *i*-layer (i.e., the bulk trapping) and the rest are trapped (or recombine with oppositely charged trapped carriers) in the blocking layers or reach at the corresponding electrode. A mathematical model for calculating MTF due to this distributed trapping (bulk plus blocking layer trapping) is described in Ref. [121]. The effect of bulk trapping is more important in thicker detectors. The charge carrier trapping/recombination (in both bulk and blocking layer) mostly determines the resolution of the chest radiographic detectors, whereas the charge carrier trapping/recombination in the blocking layer and *K*-fluorescence reabsorption mainly control the resolution of the amorphous selenium mammographic detectors [121].

### 1.4.2.3 Noise and DQE

Detective quantum efficiency (DQE) measures the ability of the detector to transfer signal relative to noise from its input to its output. The image signal is generated in the detector and passes through the read out and peripheral electronics such as self-scanning devices, amplifiers, and analog-to-digital converters. These read out and peripheral electronics contribute to noise, which is commonly termed as the electronic noise. Again, the random nature of charge carrier generation and transport properties gives rise to random fluctuations in image signals contributing to image formation and hence creates random noises, which is termed as the quantum noise. The resultant image relative to noise components is partially degraded by various sources of statistical fluctuations, which arise along the imaging chain. The relative increase in image noise through an imaging system as a function of spatial frequency  $f$  is expressed quantitatively by  $DQE(f)$ . The  $DQE(f)$  is defined as

$$DQE(f) = \frac{SNR_{\text{out}}^2(f)}{SNR_{\text{in}}^2(f)}, \quad (1.17)$$

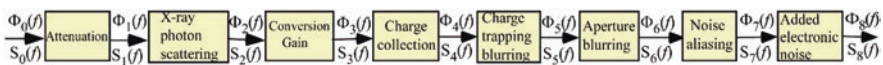
where  $SNR_{\text{in}}$  and  $SNR_{\text{out}}$  are the signal to noise ratio at the input and output stages of an image detector, respectively.  $DQE(f)$  is unity for an ideal detector. The  $SNR(f)$  is a function of the MTF and the noise power spectrum (NPS). The input noise in the number of X-ray quanta incident on the detector follows a Poisson process and thus, input noise variance is,  $\sigma^2 = \Phi_0$  and the input  $NPS(f)$ ,  $S_0 = \sigma^2 = \Phi_0$ , where  $\Phi_0$  is the average number of X-ray photons incident on the detector. Therefore, input  $SNR_{\text{in}}^2(f) = \Phi_0^2 / \Phi_0 = \Phi_0$ .

The  $DQE(f)$  is conveniently calculated by developing an appropriate cascaded linear system model [122, 123]. In the cascaded linear system model, an imaging system is described as cascades of several independent elementary stages. The effects of various phenomena, such as charge carrier trapping, *K*-fluorescence, and

electronic noise, on  $DQE(f)$  in the imaging chain have been examined in Refs. [45, 116, 124]. The cascaded linear system model of Kabir et al. [116] is the most comprehensive one, which combines both series and parallel processes [125]. However, one can get quite similar result using a much simpler cascaded linear system model consisting of only series branches as described in [17, 126].

The linear system model for the calculation of  $DQE(f)$  of a photoconductive detector consists of eight stages: (1) X-ray attenuation, (2) scattering of X-ray photons before EHP creation, (3) the generation of charge carriers (conversion gain), (4) charge collection, (5) blurring due to charge carrier trapping, (6) aperture blurring, (7) noise aliasing, and (8) the addition of electronic noise. The flow chart shown in Fig. 1.8 illustrates these eight separate stages and the signal and noise in different stages. Each of these stages can be categorized as one of the following five processes: (i) stochastic gain, (ii) stochastic blurring, (iii) deterministic blurring, (iv) aliasing, and (v) addition. The first, third, and fourth stages in Fig. 1.8 are considered as the stochastic gain stage. The stochastic gain enhances the noise associated with the quanta because the amplifying mechanism is stochastic in nature. The second and fifth stages are the stochastic blurring stages. Stochastic blurring is caused by random scattering of quanta. The integration of signal onto individual pixels in a digital detector is the deterministic blurring stage (sixth stage). The details of the signal and noise propagation through various stages are described in [17]. This cascaded linear system model has been applied to several different photoconductive detectors [114, 127].

High conversion gain ( $\sim E/W_i$ ) and high charge-collection efficiency are required to improve the DQE performance of an X-ray image detector. The conversion gain is solely a material property of the photoconductor. The charge collection efficiency can be improved by increasing  $F$  and improving the  $\mu\tau$  products of the carriers. However, increasing  $F$  also increases the dark current dramatically and, thus, there is a practical limitation on  $F$ . The quantum noise limited SNR decreases with increasing dose. On the other hand, the electronic noise is usually independent of the incident radiation dose. Therefore, the detector could be quantum noise limited if the incident dose is sufficiently high to overcome the effect of the electronic noise. When the incident dose is reduced to very low levels (e.g., fluoroscopy and tomography), the detector performance is mainly controlled by the electronic noise. The schemes for reducing the electronic noise or increasing the internal signal gain become essential for low-dose imaging applications [128–130]. Recently, there has been an intense attempt to develop solid state flat-panel direct and indirect conversion sensors utilizing avalanche selenium detectors for low-dose medical X-ray imaging [131–134]. The avalanche multiplication can increase the signal strength and improve the signal to noise ratio in low-dose X-ray imaging applications.



**Fig. 1.8** The block diagram shows the propagation of signal and NPS through the eight stages of a direct conversion X-ray imaging detector

There are several electronic noise sources associated with the read-out technology used, e.g., TFT vs. CMOS or passive pixel vs active pixel. The noise is expressed as root-mean-square number of electrons. The dominant sources of electronic noise are the TFT reset noise or  $kTC$  noise (typical value is 600 e) and the data line noise (typical value is 800–2000 e in passive pixel) per pixel. The data line noise has two important noise contributions: the charge amplifier and the data line. These noise sources are lumped into a single quantity and quoted as a number of electrons referred to the input of the charge amplifier. Each of the component sources of noise is independent. Therefore, the total noise power is the sum of the noise powers of all the sources. In general, the data line noise dominates all other noise sources in passive pixel TFT arrays. This large noise can be reduced by using a source follower or an amplifier at the pixel level, which makes the pixel an active pixel, rather than passive with just a TFT switch. Active pixel architectures in which the pixel has an embedded amplifying transistor can reach sub-500 electrons per pixel for  $a$ -Si:H TFTs and below 200 e for CMOS sensors. Active pixel sensors (APS) have shown improved SNR with respect to passive pixel sensors (PPS, with only a TFT switch) [135–138]. It is important to mention that nearly all sensitive CMOS imaging chips already have on-pixel amplification. The CMOS sensors show low electronic noise when the pixel size is very small ( $\sim 25$   $\mu\text{m}$ ) [129]. However, larger CMOS APS sensors show relatively higher electronic noise [65]. Moreover, the APS sensors are vulnerable to the radiation damage [139].

#### 1.4.2.4 Image Lag and Ghosting

The detectors should be free of noticeable image lag and ghosting. When the photoconductor is exposed to X-rays, a transient photocurrent starts to flow that reaches almost a steady value at the carrier transit time [140]. Ideally, the current should be present as long as the detector is subjected to X-ray exposure and, once the radiation is stopped, it should diminish to zero. In reality, some of the drifting carriers are trapped at various levels of defect states within the bandgap of the photoconductor layer and the subsequent release of these trapped carriers lead to a transient decaying current for several hundreds or thousands of seconds after the cessation of the excitation [141]. This is known as the residual current or the lag signal and has been modeled for  $a$ -Se detectors in [142]. For most applications, this is an undesirable phenomenon because when part of the current from a previous exposure combines with the next one, the resulting image can be inaccurate, particularly when images are acquired in a fast sequence, e.g., in fluoroscopy. The image lag signal has been measured in most of the potential photoconductive detectors. The amount of image lag signal in  $a$ -Se detectors has been found to be negligible, whereas it is quite significant in some of other polycrystalline detectors [32].

The X-ray exposure can change the X-ray sensitivity of the exposed area and thus lead to a shadow impression of a previously acquired image which becomes visible in subsequent uniform exposure, which leads to what is called “ghosting” [143]. Ghosting can severely affect the diagnostic value of X-ray images. The

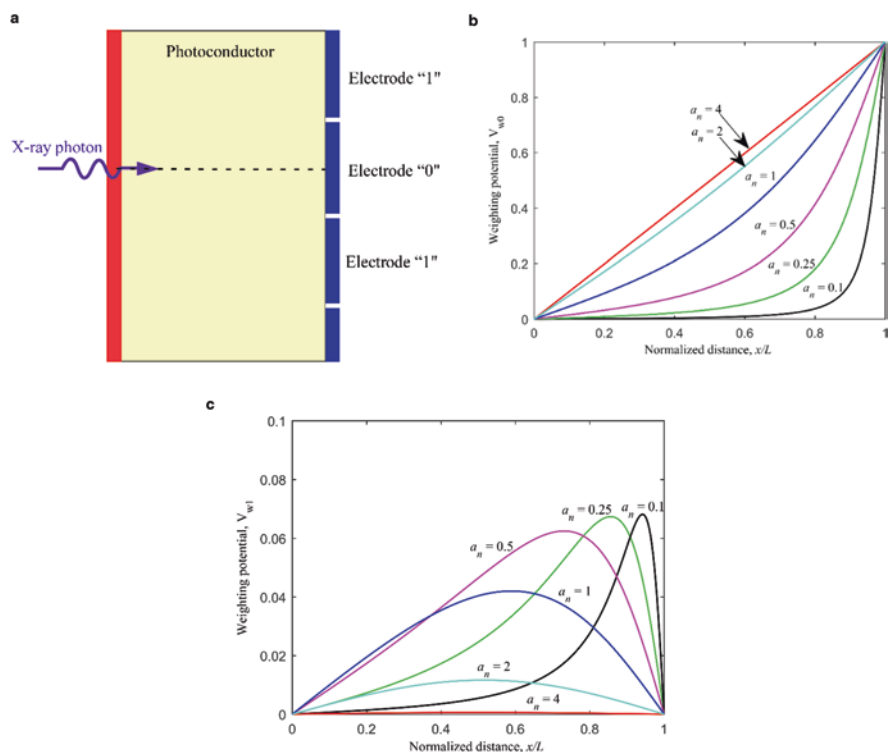
causes of change in X-ray sensitivity and resolution, and their recovery mechanisms in *a*-Se detectors, have been systematically investigated in the last decade [144, 145]. Although the relative amounts of changes in sensitivity and resolution, arising from repeated exposure in commercial *a*-Se detectors, are below the tolerance level, they are due to the following probable mechanisms: (i) recombination of drifting carriers with oppositely charged trapped carriers [141], (ii) creation of X-ray induced metastable trap centers [146, 147], and/or (iii) reduction of the free carrier generation due to space charge (i.e., due to a nonuniform electric field) [145, 148]. It is expected that the ghosting phenomenon may also be present in other photoconductive (e.g., HgI<sub>2</sub>, CZT, PbO, and PbI<sub>2</sub>) detectors, although a very limited number of reports are available in literature [104].

## 1.5 Position-Sensitive Semiconductor Detectors

Many semiconductors have asymmetric transport properties of holes and electrons. To overcome the effects of severe trapping of one type of charge carriers (e.g.,  $\mu\tau$  of holes in polycrystalline CdZnTe is two orders of magnitude inferior to electrons), few special detector structures have been developed in which the collected charge is sensitive only to the other type of charge carriers [3]. These techniques are called single polarity charge sensing, which can alleviate the charge trapping problem if the schubwegs ( $\mu\tau F$ ) of just one type of charge (such as electrons) can be larger than the photoconductor thickness. The charge collection efficiency of Frisch grid [149] and coplanar detectors [150] depends only on one type of charge carriers. The response of a pixelated detector for X-ray imaging, the so-called small pixel effect [151], provides unique advantage by favoring one type of carrier (that moves towards the pixels) over the other.

The small pixel effect on the charge collection at the corresponding electrode or the neighboring electrodes can be easily understood by the help of Shockley-Ramo's theorem (Eq. 1.4) and the shape of the weighting potentials of the pixelated electrodes. Let us assume an X-ray interaction occurs along the center of any pixel (named as "0" pixel in Fig. 1.9a). Then, the weighting potentials of the central pixel ( $V_{w0}$ ) and the next neighboring pixel ( $V_{w1}$ ) as a function of interaction position  $x$  for various normalized pixel widths ( $a_n = a/L$ ) are shown in Fig. 1.9b, c. For small pixels, the weighting potential  $V_{w0}$  rises very slowly until very close to the pixel electrodes (near-field region); then rises upwards sharply [15]. On the other hand, the weighting potential  $V_{w0}$  is almost linear for large pixels,  $a_n \gg 1$ , (e.g.,  $a_n = 4$  curve in Fig. 1.9a). The large pixel case, i.e.,  $a_n \geq 4$ , is equivalent to the case of a single-element detector. The weighting potentials of neighboring pixels are zero at both ends of the detector as shown in Fig. 1.9b. As a result, the neighboring pixels don't receive any signal if there is no trapping. In practice, the neighboring pixels may receive some signals depending on the trapping rates of both types of charged carriers (electrons and holes) [119]. The nonlinearity of the weighting potential of the next neighboring pixel  $V_{w1}$  increases with decreasing normalized pixel width  $a_n$ .

In smaller pixels, i.e.,  $a_n \leq 0.2$ , the motion of charge carriers close to the pixel electrodes (near-field region) can produce almost full signal (collected charge) strength in the external circuit and the motion of charge carriers outside this region induces very little signal. The reason is that the induced charge on a particular pixel electrode by a moving charge is very small when the charge is far away (the distance to the pixel is much greater than the pixel dimension) due to charge sharing among many pixel electrodes and increases rapidly when the charge is in the vicinity of this pixel. As a result, the change in induced charges in pixel electrodes due to the carrier motion through the near-field region is much higher than their motion in the outside of the near-field region (this change in induced charge produces electric current in the external circuit and the integration of this current is the collected charge). A very small fraction of carriers moves through the near-field region for the carriers that move towards the top electrode because of exponential absorption profile across the photoconductor thickness and the irradiation occurs through the top electrode. The induced signals due to the carrier drift towards the top electrode should decrease with decreasing the normalized pixel width. Since the charge collection efficiency of pixelated detectors mainly depends on the transport properties (mobility and



**Fig. 1.9** (a) X-ray interaction occurs along the center of a pixel (named as the pixel electrode “0”). The next nearest pixel electrodes are named as electrode “1”. (b) The weighting potential of the center pixel and (c) The weighting potential of the next nearest pixels

lifetime) of the charges that move towards the pixel electrodes, the effects of poor transport properties of other type of carriers can be eliminated by having smaller pixels. Some of the potential photoconductors (e.g.,  $\alpha$ -Se, CdZnTe, and HgI<sub>2</sub>) for X-ray image detectors have asymmetric transport properties (mobility-lifetime products) for electrons and holes. Therefore, the charge collection efficiency of pixelated detectors can be improved by ensuring that the carrier (electron or hole) with the higher mobility-lifetime product is drifted towards the pixel electrodes.

## References

1. Bushberg JT, Seibert JA, Leidholdt EM Jr, Boone JM. The essential physics of medical imaging. 3rd ed. Wolters Kluwer; 2012. p. 19.
2. Kasap SO, Kabir MZ. Chapter 20: X-ray detectors. In: Rudan M, et al., editors. Springer handbook of semiconductor devices. Cham: Springer Nature; 2022.
3. Owens A. Semiconductor radiation detectors. Boca Raton: CRC Press; 2019.
4. Kabir MZ. Dark current mechanisms in amorphous selenium-based photoconductive detectors: an overview and re-examination. *J Mater Sci Mater Electron*. 2015;26:4659–67.
5. Martz HE, Logan CM, Schneberk DJ, Shull PJ. X-ray imaging: fundamentals, industrial techniques, and applications. Boca Raton: CRC Press; 2017.
6. Klein CA. Bandgap dependence and related features of radiation ionization energies in semiconductors. *J Appl Phys*. 1968;39:2029–38.
7. Que W, Rowlands JA. X-ray photogeneration in amorphous selenium: geminate versus columnar recombination. *Phys Rev B*. 1995;51:10500–7.
8. Blevins I, Hunt DC, Rowlands JA. Measurement of X-ray photogeneration in amorphous selenium. *J Appl Phys*. 1999;85:7958–63.
9. Mah D, Rowlands JA, Rawlinson JA. Sensitivity of amorphous selenium to x rays from 40 kVp to 18 MV: Measurements and implications for portal imaging. *Med Phys*. 1998;25:444–56.
10. Bubon O, Jandieri K, Baranovskii SD, Kasap SO, Reznik A. Columnar recombination for X-ray generated electron-holes in amorphous selenium and its significance in  $\alpha$ -Se X-ray detectors. *J Appl Phys*. 2016;119:124511.
11. Kabir MZ, Arnab SM, Hijazi N. Electron-hole pair creation energy in amorphous selenium: geminate versus columnar recombination. *J Mater Sci Mater Electron*. 2019;30:21059.
12. Shockley W. Currents to conductors induced by a moving point charge. *J Appl Phys*. 1938;9:635–6.
13. Ramo S. Current induced by electron motion. *Proc IRE*. 1939;27:584–5.
14. He Z. Review of the Shockley-Ramo theorem and its application in semiconductor gamma-ray detectors. *Nucl Instr Meth Phys Res A*. 2001;463:250–67.
15. Kabir MZ, Kasap SO. Charge collection and absorption-limited X-ray sensitivity of pixelated X-ray detectors. *J Vac Sci Technol A*. 2004;22:975–80.
16. Kasap SO. Optoelectronics and photonics: principles and practices. Upper Saddle River: Prentice-Hall; 2001, Ch. 5.
17. Kabir MZ. Effects of charge carrier trapping on polycrystalline PbO X-ray imaging detectors. *J Appl Phys*. 2008;104:074506.
18. Kasap SO, Kabir MZ, Ramaswami KO, Johanson RE, Curry RJ. Charge collection efficiency in the presence of non-uniform carrier drift mobilities and lifetimes in photoconductive detectors. *J Appl Phys*. 2020;128:124501.
19. Ramaswami K, Johanson R, Kasap S. Charge collection efficiency in photoconductive detectors under small to large signals. *J Appl Phys*. 2019;125:244503.

20. Kasap SO, Kabir MZ, Rowlands JA. Recent advances in X-ray photoconductors for direct conversion X-ray image sensors. *Curr Appl Phys.* 2006;6:288–92.
21. Mirzaei A, Huh J-S, Kim SS, Kim HW. Room temperature hard radiation detectors based on solid state compound semiconductors: an overview. *Electron Mater Lett.* 2018;14:261.
22. Pennicard D, Pirard B, Tolbanov O, Iniewski K. Semiconductor materials for X-ray detectors. *MRS Bull.* 2017;42:445–50.
23. Capasso F. Band-gap engineering: from physics and materials to new semiconductor devices. *Science.* 1987;235(4785):172–6.
24. Takahashi T, Watanabe S. Recent progress in CdTe and CdZnTe detectors. *IEEE Trans Nucl Sci.* 2001;48:950–9.
25. Szeles C, Cameron SE, Ndap J-O, Chalmer WC. Advances in the crystal growth of semi-insulating CdZnTe for radiation detector applications. *IEEE Trans Nucl Sci.* 2002;49:2535.
26. Owens A, Peacock A. Compound semiconductor radiation detectors. *Nucl Instr Methods Phys Res A.* 2004;531:18–37.
27. Sellin PJ. Recent advances in compound semiconductor radiation detectors. *Nuclear Instr Methods Phys Res A.* 2003;513:332–9.
28. Owens A. Semiconductor materials and radiation detection. *J Synchrotron Radiat.* 2006;13:143–50.
29. Sordo SD, Abbene L, Caroli E, Mancini AM, Zappettini A, Ubertaini P. Progress in the development of CdTe and CdZnTe semiconductor radiation detectors for astrophysical and medical applications. *Sensors.* 2009;9:3491–526.
30. Szeles C. CdZnTe and CdTe crystals for medical applications. In: Iwanczyk JS, editor. *Radiation detectors for medical imaging.* Boca Raton: CRC Press; 2016. p. 1–28.
31. Owens A. Photovoltaic materials. In: Kasap SO, editor. *Photovoltaicity and photovoltaic materials.* Chichester: Wiley & Sons; 2022.
32. Kabir MZ, Kasap SO. Photoconductors for direct conversion X-ray image detectors. In: Kasap SO, Capper P, editors. *Springer handbook of electronic and photonic materials*, 2nd edition. Springer Academic Publishers; 2017. p. 1125–47.
33. Kabir MZ. X-ray photoconductivity and typical large area X-ray photoconductors. In: Kasap SO, editor. *Photovoltaicity and photovoltaic materials.* Chichester: Wiley & Sons; 2022. p. 613–42.
34. Lioliou G, Meng X, Ng JS, Barnett AM. Characterization of gallium arsenide X-ray mesa p-i-n photodiodes at room temperature. *Nucl Instr Methods Phys Res A.* 2016;813:1–9.
35. Owens A, Bavdaz M, Peacock A, Poelaert A. High resolution X-ray spectroscopy using GaAs arrays. *J Appl Phys.* 2001;90:5376.
36. Lees JE, Barnett AM, Bassford DJ, Stevens RC, Horsfall AB. SiC X-ray detectors for harsh environments. *J Instrum.* 2011;6:1–9. <https://doi.org/10.1088/1748-0221/6/01/C01032>.
37. Bertuccio G, Caccia S, Puglisi D, Macera D. Advances in silicon carbide X-ray detectors. *Nucl Instr Methods Phys Res A.* 2011;652:193–6.
38. Wang J, Mulligan P, Brillson L, Cao LR. Review of using gallium nitride for ionizing radiation detection. *Appl Phys Rev.* 2015;2:031102.
39. Duboz JY, Lauegt M, Schenk D, Beaumont B, Reverchon JL, Wieck AD, Zimmerling T. GaN for X-ray detection. *Appl Phys Lett.* 2008;92(26):263501.
40. Knoll GF. *Radiation detection and measurement.* 3rd ed. New York: Wiley; 2000.
41. Tsoufanidis N, Landsberger S. *Measurement and detection of radiation*, 4th Edition. Boca Raton: CRC Press; 2015.
42. Fano U. Ionization yield of radiations. II. The fluctuations of the number of ions. *Phys Rev.* 1947;72:26.
43. Kabir MZ, Kasap SO. Dependence of the DQE of photoconductive X-ray detectors on charge transport and trapping. *SPIE Proc.* 2002;4682:42–52.
44. Ruzin A, Nemirovsky Y. Statistical models for charge collection efficiency and variance in semiconductor spectrometers. *J Appl Phys.* 1997;82:2754–8.



45. Mainprize JG, Hunt DC, Yaffe MJ. Direct conversion detectors: the effect of incomplete charge collection on detective quantum efficiency. *Med Phys.* 2002;29:976–90.
46. Barton P, Amman M, Martin R, Vetter K. Ultra-low noise mechanically cooled germanium detector. *Nucl Instr Methods Phys Res A.* 2016;812:17–23.
47. Markus K, Weber CH, Wirth S, Pfeifer K-J, et al. Advances in digital radiography: physical principles and system overview. *Radiographics.* 2007;27:675–86.
48. Spahn M. Flat detectors and their clinical applications. *Eur Radiol.* 2005;15:1934.
49. Cowen AR, Kengyelics SM, Davies AG. Solid-state, flat-panel, digital radiography detectors and their physical imaging characteristics. *Clin Radiol.* 2008;63:487–98.
50. Spahn M. X-ray detectors in medical imaging. *Nucl Instr Methods Phys Res A.* 2013;731:57–63.
51. Kasap SO, Frey JB, Belev G, Tousignant O, Mani H, Greenspan J, et al. Amorphous and polycrystalline photoconductors for direct conversion flat panel X-ray image sensors. *Sensors.* 2011;11:5112.
52. Yorkston J. Recent developments in digital radiography detectors. *Nucl Instr Methods Phys Res A.* 2007;580:974–85.
53. Karim K. Active matrix flat panel imagers. In: Iniewski K, editor. *Medical imaging.* New York: Wiley & Sons Inc; 2009. p. 23–58.
54. Seco J, Clasié B, Partridge M. Review on the characteristics of radiation detectors for dosimetry and imaging. *Phys Med Biol.* 2014;59:R303–47.
55. Vedantham S, Karellas A, Vijayaraghavan GR, Kopans DB. Digital breast Tomosynthesis: state of the art. *Radiology.* 2015;277:663–84.
56. Panetta D. Advances in X-ray detectors for clinical and preclinical computed tomography. *Nucl Instr Methods Phys Res A.* 2016;809:2–12.
57. Zhao W. Ch. 3: Detectors for tomosynthesis. In: Reiser I, Glick S, editors. *The tomosynthesis imaging.* Boca Raton: CRC Press; 2017.
58. Fredenberg E. Spectral and dual-energy X-ray imaging for medical applications. *Nucl Instr Methods Phys Res A.* 2018;878:74–87.
59. Rowlands JA, Yorkston J. Ch.4: Flat panel detector for digital radiography. In: Beutel J, Kundel HL, Van Metter RL, editors. *Handbook of medical imaging, vol. 1.* Bellingham, Washington: SPIE Press; 2000. p. 225–313.
60. Jiang H, Zhao Q, Antonuk LE, El-Mohri Y, Gupta T. Development of active-matrix flat panel imagers incorporating thin layers of polycrystalline HgI<sub>2</sub> for mammographic X-ray imaging. *Phys Med Biol.* 2013;58:703–14.
61. Veale MC. Ch. 3: CdTe and CdZnTe Small pixel imaging detectors. In: Awadalla S, editor. *Solid-state radiation detectors: technology and applications.* Boca Raton: CRC Press; 2015.
62. Yin S, Tümer TO, Maeding D, Mainprize J, Mawdsley G, Yaffe MJ, Gordon EE, Hamilton WJ. Direct conversion CdZnTe and CdTe detectors for digital mammography. *IEEE Trans Nucl Sci.* 2002;49:176–81.
63. Mainprize JG, Ford NL, Yin S, Gordon EE, Hamilton WJ, Tümer TO, Yaffe MJ. A CdZnTe slot-scanned detector for digital mammography. *Med Phys.* 2002;29:2767–81.
64. Hellier K, Benard E, Scott CC, Karim KS, Abbaszadeh S. Recent progress in the development of a-se/CMOS sensors for X-ray detection. *Quantum Beam Sci.* 2021;5:29.
65. Farrier M, Achterkirchen TG, Weckler GP, Mrozack A. Very large area CMOS active-pixel sensor for digital radiography. *IEEE Trans Electron Devices.* 2009;56:2623–31.
66. Hartsough NE, Iwanczyk JS, Nygard E, Malakhov N, Barber WC, Gandhi T. Polycrystalline mercuric iodide films on CMOS readout arrays. *IEEE Trans Nucl Sci.* 2009;56:1810–6.
67. Konstantinidis AC, Szafraniec MB, Speller RD, Olivo A. The Dexela 2923 CMOS X-ray detector: A flat panel detector based on CMOS active pixel sensors for medical imaging applications. *Nucl Instr Methods Phys Res A.* 2012;689:12–21.
68. Yaffe MJ. Ch. 2: Detectors for digital mammography. In: Bick U, Diekmann F, editors. *Digital mammography. Medical radiology.* Berlin, Heidelberg: Springer; 2010.

69. Kasap SO, Koughia KV, Fogal B, Belev G, Johanson RE. The influence of deposition conditions and alloying on the electronic properties of amorphous selenium. *Semiconductors*. 2003;37:789–94.
70. Kasap SO. Doped and stabilized amorphous selenium single and multilayer photoconductive layers for X-ray imaging detector applications. In: Kasap SO, editor. *Photoconductivity and photoconductive materials*. Chichester: Wiley; 2022. p. 715–80.
71. Mahmood SA, Kabir MZ, Tousignant O, Mani H, Greenspan J, Botka P. Dark current in multilayer amorphous selenium X-ray imaging detectors. *Appl Phys Lett*. 2008;92:223506.
72. Polischuk BT, Jean A. Multilayer plate for X-ray imaging and method of producing same. US Patent 5,880,472; 1999.
73. Frey JB, Belev G, Tousignant O, Mani H, Laperriere L, Kasap SO. Dark current in multilayer stabilized amorphous selenium based photoconductive X-ray detectors. *J Appl Phys*. 2012;112:014502.
74. Frey JB, Sadasivam K, Belev G, Mani H, Laperriere L, Kasap SO. Dark current–voltage characteristics of vacuum deposited multilayer amorphous selenium-alloy detectors and the effect of X-ray irradiation. *J Vac Sci Technol A*. 2019;37:061501.
75. Matsuura N, Zhao W, Huang Z, Rowlands JA. Digital radiology using active matrix readout: amplified pixels for fluoroscopy. *Med Phys*. 1999;26:672–81.
76. Pang G, Lee DL, Rowlands JA. Investigation of a direct conversion flat panel imager for portal imaging. *Med Phys*. 2001;28:2121–8.
77. Pang G, Rowlands JA. Development of high quantum efficiency flat panel detectors for portal imaging: intrinsic spatial resolution. *Med Phys*. 2002;29:2274–85.
78. Zhao W, Ji W, Debie A, Rowlands JA. Imaging performance of amorphous selenium based flat panel detectors for mammography: characterization of small area prototype detector. *Med Phys*. 2003;30:254–63.
79. Hunt DC, Tousignant O, Rowlands JA. Evaluation of the imaging properties of an amorphous selenium-based flat panel detector for digital fluoroscopy. *Med Phys*. 2004;31:1166–75.
80. Zhao W, Hunt DC, Tanioka K, Rowlands JA. Amorphous selenium flat panel detectors for medical applications. *Nucl Instr Methods Phys Res A*. 2005;549:205–9.
81. Destefano N, Mulato M. Influence of multi-depositions on the final properties of thermally evaporated TlBr films. *Nucl Instr Methods Phys Res A*. 2010;624:114–7.
82. Bennett PR, Shah KS, Cirignano LJ, Klugerman MB, Moy LP, Squillante MR. Characterization of polycrystalline TlBr films for radiographic detectors. *IEEE Trans Nuclear Sci*. 1999;46:689–93.
83. Yun M, Cho S, Lee R, Jang G, Kim Y, Shin W, Nam S. Investigation of PbI<sub>2</sub> film fabricated by a new sedimentation method as an X-ray conversion material. *Jpn J Appl Phys*. 2010;49:041801–5.
84. Shah KS, Street RA, Dmitriyev Y, Bennett P, Cirignano L, Klugerman M, Squillante MR, Entine G. X-ray imaging with PbI<sub>2</sub>-based *a*-Si:H flat panel detectors. *Nucl Instr Methods Phys Res A*. 2001;458:140–7.
85. Zhu X, Sun H, Yang D, Wangyang P, X. Gao: Comparison of electrical properties of X-ray detector based on PbI<sub>2</sub> crystal with different bias electric field configuration. *J Mater Sci Mater Electron*. 2016;27:11798–803.
86. Street RA, Ready SE, Lemmi F, Shah KS, Bennett P, Dmitriyev Y. Electronic transport in polycrystalline PbI<sub>2</sub> films. *J Appl Phys*. 1999;86:2660–7.
87. Zhao Q, Antonuk LE, El-Mohri Y, Wang Y, Du H, Sawant A, Su Z, Yamamoto J. Performance evaluation of polycrystalline HgI<sub>2</sub> photoconductors for radiation therapy imaging. *Med Phys*. 2010;37:2738–48.
88. Du H, Antonuk LE, El-Mohri Y, Zhao Q, Su Z, Yamamoto J, Wang Y. Investigation of the signal behavior at diagnostic energies of prototype, direct detection, active matrix, flat-panel imagers incorporating polycrystalline HgI<sub>2</sub>. *Phys Med Biol*. 2010;53:1325–51.
89. Zentai G, Partain LD, Pavlyuchkova R, Proano C, Virshup GF, Melekhov L, et al. Mercuric iodide and lead iodide X-ray detectors for radiographic and fluoroscopic medical imaging. *SPIE Proc*. 2003;5030:77. <https://doi.org/10.1117/12.480227>.

90. Street RA, Ready SE, van Schuylenbergh K, Ho J, Boyec JB, Nysten P, Shah K, Melekhov L. Comparison of  $\text{PbI}_2$  and  $\text{HgI}_2$  for direct detection active matrix X-ray image sensors. *J Appl Phys.* 2002;91:3345–55.
91. Park JC, Jeon PJ, Kim JS, Im S. Small-dose-sensitive X-ray image pixel with  $\text{HgI}_2$  photoconductor and amorphous oxide thin-film transistor. *Adv Healthc Mater.* 2015;4:51–7.
92. Lee S, Kim JS, Ko KR, Lee GH, Lee DJ, Kim DW, et al. Direct thermal growth of large scale Cl-doped CdTe film for low voltage high resolution X-ray image sensor. *Sci Rep.* 2018;8:4810.
93. Tokuda S, Kishihara H, Adachi S, Sato T. Improvement of temporal response and output uniformity of polycrystalline CdZnTe films for high-sensitivity X-ray imaging. *Proc SPIE.* 2003;5030:861–70. <https://doi.org/10.1117/12.479938>.
94. Tokuda S, Kishihara H, Adachi S, T. Sato: preparation and characterization of polycrystalline CdZnTe films for large-area, high-sensitivity X-ray detectors. *J Mater Sci Mater Electron.* 2004;15:1–8.
95. Simon M, Ford RA, Franklin AR, Grabowski SP, Mensor B, Much G, et al. Analysis of lead oxide (PbO) layers for direct conversion X-ray detection. *IEEE Trans Nucl Sci.* 2005;52:2035–40.
96. Semeniuk O, Grynko O, Decrescenzo G, Juska G, Wang K, Reznik A. Characterization of polycrystalline lead oxide for application in direct conversion X-ray detectors. *Sci Rep.* 2017;7:8659.
97. Reznik A, Semeniuk O. Ch. 7: Lead oxide as material of choice for direct conversion detectors. In: Ray A, editor. *Oxide electronics*. Chichester: Wiley; 2021.
98. Grynko O, Reznik A. Ch. 17: Progress in Lead oxide X-ray photoconductive layers. In: Kasap SO, editor. *Photoconductivity and photoconductive materials*. Chichester: Wiley; 2022.
99. Gill HS, Elshahat B, Kokila A, Li L, Mosurkald R, Zygmanski P, Sajob E, Kumar J. Flexible perovskite based X-ray detectors for dose monitoring in medical imaging applications. *Phys Med.* 2018;5:20–3.
100. Yakunin S, Sytnyk M, Kriegner D, Shrestha S, Richter M, Matt GJ, et al. Detection of X-ray photons by solution-processed lead halide perovskites. *Nat Photonics.* 2015;9:444–9.
101. Wei H, Fang Y, Mulligan P, Chuirazzi W, Fang H, Wang C, et al. Sensitive X-ray detectors made of methylammonium lead tribromide perovskite single crystals. *Nat Photonics.* 2016;10:333–9.
102. Kim Y, Kim KH, Son DY, Jeong DN, Seo JY, Choi YS, et al. Printable organometallic perovskite enables large-area, low-dose X-ray imaging. *Nature.* 2017;550:88–92.
103. Lin Q. Metal halide perovskites for photodetection. In: Kasap SO, editor. *Photoconductivity and photoconductive materials*. Wiley; 2022. p. 781–806.
104. Shrestha S, Fischer R, Matt G, Feldner P, Michel T, Osvet A, et al. High-performance direct conversion X-ray detectors based on sintered hybrid lead triiodide perovskite wafers. *Nat Photonics.* 2017;11:436–40.
105. Li Y, Adeagbo E, Koughia C, Simonson B, Pettipas RD, Mishchenko A, et al. Direct conversion X-ray detectors with  $70 \text{ pA cm}^{-2}$  dark currents coated from an alcohol-based perovskite ink. *J Mater Chem C.* 2022;10:1228–35.
106. Rowlands JA. Material change for X-ray detectors. *Nature.* 2017;550:47–8.
107. Deumel S, Breemen A, Gelinck G, Peeters B, et al. High-sensitivity high-resolution X-ray imaging with soft-sintered metal halide perovskites. *Nat Electron.* 2021;4:681–8.
108. Wang H, Kim DH. Perovskite-based photodetectors: materials and devices. *Chem Soc Rev.* 2017;46:5204–36.
109. Greuter F, Blatter G. Electrical properties of grain boundaries in polycrystalline compound semiconductors. *Semicond Sci Technol.* 1990;5:111.
110. Chowdhury MH, Kabir MZ. Electrical properties of grain boundaries in polycrystalline materials under intrinsic or low doping. *J Phys D Appl Phys.* 2011;44:015102.
111. Sellin PJ. Thick film compound semiconductors for X-ray imaging applications. *Nucl Instr Methods Phys Res A.* 2006;563:1–8.

112. Kasap SO. X-ray sensitivity of photoconductors: application to stabilized *a*-Se. *J Phys D Appl Phys.* 2000;33:2853–65.
113. Que W, Rowlands JA. X-ray imaging using amorphous selenium: inherent spatial resolution. *Med Phys.* 1995;22:365–74.
114. Panneerselvam D, Kabir MZ. Evaluation of organic perovskite photoconductors for direct conversion X-ray imaging detectors. *J Mater Sci Mater Electron.* 2017;28:7083–90.
115. Kabir MZ, Kasap SO, Zhao W, J.A. Rowlands: direct conversion X-ray sensors: sensitivity, DQE & MTF. *IEE Proc. (CDS: Special Issue on Amorphous and Microcrystalline Semiconductors).* 2003;150:258–66.
116. Kabir MZ, Rahman MW, Shen WY. Modelling of DQE of direct conversion X-ray imaging detectors incorporating charge carrier trapping and K-fluorescence. *IET Circuits Devices Syst.* 2011;5:222–31.
117. Hunt DC, Tousignant O, Demers Y, Laperriere L, Rowlands JA. Imaging performance of amorphous selenium flat-panel detector for digital fluoroscopy. *Proc SPIE.* 2003;5030:226–34. <https://doi.org/10.1117/12.480131>.
118. Pang G, Zhao W, Rowlands JA. Digital radiology using active matrix readout of amorphous selenium: geometric and effective fill factors. *Med Phys.* 1998;25:1636–46.
119. Kabir MZ, Kasap SO. Modulation transfer function of photoconductive X-ray image detectors: effects of charge carrier trapping. *J Phys D Appl Phys.* 2003;36:2352–8.
120. Zhao W, Rowlands JA. Digital radiology using active matrix readout of amorphous selenium: theoretical analysis of detective quantum efficiency. *Med Phys.* 1997;24:1819–33.
121. Kabir MZ. Effects of blocking layers on image resolution in multilayer photoconductive imaging detectors: application to amorphous selenium X-ray detectors. *Radiation* 2022;2:91–99.
122. Rabbani M, Shaw R, Van Metter R. Detective quantum efficiency of imaging systems with amplifying and scattering mechanisms. *J Opt Soc Am A.* 1987;4:895–901.
123. Cunningham I. Ch. 2: Applied linear systems theory. In: Beutel J, Kundel HL, Van Metter RL, editors. *Handbook of imaging*, vol. 1. Bellingham: SPIE Press; 2000.
124. Kabir MZ, Kasap SO. DQE of photoconductive X-ray image detectors: application to *a*-se. *J Phys D Appl Phys.* 2002;35:2735–43.
125. Cunningham IA. Linear-systems Modeling of parallel cascaded Stochastic processes: the NPS of radiographic screens with reabsorption of characteristic X radiation. *Proc SPIE.* 1998;3336:220–30.
126. Sengupta A, Zhao C, Konstantinidis A, Kanicki J. Cascaded systems analysis of *a-se/a-Si* and *a-InGaZnO* TFT passive and active pixel sensors for Tomosynthesis. *Phys Med Biol.* 2019;64:025012.
127. Arnab SM, Kabir MZ. Impact of charge carrier trapping on amorphous selenium direct conversion avalanche X-ray detectors. *J Appl Phys.* 2017;112:134502.
128. Parsafar A, Scott CC, El-Falou A, Levine PM, Karim KS. Direct-conversion CMOS X-ray imager with  $5.6 \mu\text{m} \times 6.25 \mu\text{m}$  pixels. *IEEE Trans Electron Devices.* 2015;36(5):481–3.
129. Arvanitis CD, Bohndiek SE, Royle G, Blue A, Liang HX, Clark A, et al. Empirical electro-optical and X-ray performance evaluation of CMOS active pixels sensor for low dose, high resolution X-ray medical imaging. *Med Phys.* 2007;34(12):4612–25.
130. Hunt DC, Kenkichi Tanioka JA, Rowlands. X-ray imaging using avalanche multiplication in amorphous selenium: investigation of depth dependent avalanche noise. *Med Phys.* 2007;34(3):976–86.
131. Scheuermann JR, Miranda Y, Liu H, Zhao W. Charge transport model in solid-state avalanche amorphous selenium and defect suppression design. *J Appl Phys.* 2016;119:024508.
132. Arnab SM, Kabir MZ. Impact of Lubberts effect on amorphous selenium indirect conversion avalanche detector for medical X-ray imaging. *IEEE Trans Radiat Plasma Med Sci.* 2017;1(3):221–8.
133. Imura S, Mineo K, Honda Y, Arai T, Miyakawa K, Watabe T, Kubota M, Nishimoto K, Sugiyama M, Nanba M. Enhanced image sensing with avalanche multiplication in hybrid structure of crystalline selenium photoconversion layer and CMOSFETs. *Sci Rep.* 2020;10:21888.

134. Arnab SM, Kabir MZ. A novel amorphous selenium direct conversion avalanche detector structure for low dose medical X-ray imaging. *IEEE Trans Radiat Plasma Med Sci.* 2020;4:319–26.
135. Matsuura N, Zhao W, Huang Z, Rowlands JA. Digital radiology using active matrix readout: amplified pixel detector array for fluoroscopy. *Med Phys.* 1999;26:672–81.
136. Karim K, Nathan A, Rowlands JA. Amorphous silicon active pixel sensor readout circuit for digital imaging. *IEEE Trans Electron Devices.* 2003;50:200–8.
137. Koniczek M, Antonuk LE, El-Mohri Y, Liang AK, Zhao Q. Theoretical investigation of the noise performance of active pixel imaging arrays based on polycrystalline silicon thin film transistors. *Med Phys.* 2017;39:3491–503.
138. Zha C, Kanicki J. Amorphous in-Ga-Zn-O thin-film transistor active pixel sensor x-ray imager for digital breast tomosynthesis. *Med Phys.* 2014;41:091902.
139. Bogaerts J, Bart D, Guy M, Dirk U. Total dose and displacement damage effects in a radiation-hardened CMOS APS. *IEEE Trans Electron Devices.* 2003;50(1):84–90.
140. Loustauneau V, Bissonnette M, Cadieux S, Hansroula M, Massona E, Savarda S, Polischuk B, Lehtimaki M. *Proc SPIE.* 2003;5030:1011.
141. Mahmood SA, Kabir MZ, Tousignant O, Greenspan J. Investigation of ghosting recovery mechanisms in selenium X-ray detector structures for mammography. *IEEE Trans Nucl Sci.* 2012;59:597.
142. Siddiquee S, Kabir MZ. Modeling of photocurrent and lag signals in amorphous selenium X-ray detectors. *J Vac Sci Tech A.* 2015;33:041514.
143. Loustauneau V, Bissonnette M, Cadieux S, Hansroul M, Masson E, Savard S, Polischuk B. Ghosting comparison for large-area selenium detectors suitable for mammography and general radiography. *Proc SPIE.* 2004;5368:162–9. <https://doi.org/10.1117/12.535812>.
144. Manouchehri F, Kabir MZ, Tousignant O, Mani H, Devabhaktuni VK. Time and exposure dependent X-ray sensitivity in multilayer amorphous selenium detectors. *J Phys D Appl Phys.* 2008;41:235106.
145. Kabir MZ, Chowdhury L, DeCrescenzo G, Tousignant O, Kasap SO, Rowlands JA. Effect of repeated X-ray exposure on the resolution of amorphous selenium based X-ray imagers. *Med Phys.* 2010;37:1339–49.
146. Kasap SO, Yang J, Simonson B, Adeagbo E, Walornyj M, Belev G, Bradley MP, Johanson RE. Effects of X-ray irradiation on charge transport and charge collection efficiency in stabilized *a*-Se photoconductors. *J Appl Phys.* 2020;127:084502.
147. Simonson B, Johanson RE, Kasap SO. Effects of high-dose X-ray irradiation on the hole lifetime in vacuum-deposited Stabilized *a*-Se photoconductive films: implications to the quality control of *a*-Se used in X-ray detectors. *IEEE Trans Nucl Sci.* 2020;67:2445.
148. Hoq A, Panneerselvam D, Kabir MZ. Sensitivity reduction mechanisms in organic perovskite X-ray detectors. *J Mater Sci.* 2021;32:16824.
149. McGregor DS, He Z, Seifert HA, Wehe DK, Rojas RA. Single charge carrier type sensing with a parallel strip pseudo-Frisch-grid CdZnTe semiconductor radiation detector. *Appl Phys Lett.* 1998;72(7):792–5.
150. Luke PN. Unipolar charge sensing with coplanar electrodes – application to semiconductor detectors. *IEEE Trans Nucl Sci.* 1995;NS-42:207–13.
151. Barrett HH, Eskin JD, Barber HB. Charge transport in arrays of semiconductor gamma-ray detectors. *Phys Rev Lett.* 1995;75:156–9.

# Chapter 2

## CdTe-/CdZnTe-Based Radiation Detectors



A. Opanasyuk, D. Kurbatov, Ya. Znamenshchykov, O. Diachenko,  
and M. Ivashchenko

### 2.1 Introduction

Processes accompanied by nuclear radiation are widely used in energy, industry, medicine, and scientific research [1, 31]. Their application opens up unlimited prospects, but requires a special approach to process control and ensuring personnel safety. The study of radioactivity showed that the human body has a limited set of natural receptors. Such a significant factor of danger, as hard radiation during nuclear decay, can be perceived by a person only after long-term interaction with body tissues, which sometimes causes irreparable damage to the body. Therefore, almost from the moment of the discovery of “invisible rays”, the question arose of developing ionising radiation detectors that would allow measuring the intensity and determining the energy spectrum of radiation.

To register and measure the characteristics of nuclear irradiation, many instruments can be used, such as ionisation cameras, proportional counters, Geiger-Muller counters, scintillation counters, diffusion cameras, Wilson cameras, bubble and spark cameras, Cherenkov counters, etc. In addition, nuclear irradiation can also be registered using special photographic emulsions. Recently, nuclear irradiation solid-state semiconductor detectors have also been developed for these purposes.

Semiconductor detectors are similar to gas ionisation chambers in terms of the physical principle of operation. Semiconductor materials suitable for the development of effective radiation detectors must meet the following requirements: they must have (i) a high resistivity ( $<10^{10}$  ohm•cm), (ii) a low value of the average energy expended by a quant of irradiation to create a pair of charge carriers, (iii) low

---

A. Opanasyuk · D. Kurbatov (✉) · Y. Znamenshchykov · O. Diachenko  
Department of Electronics and Computer Technics, Sumy State University, Sumy, Ukraine  
e-mail: [dkurbatov@sci.sumdu.edu.ua](mailto:dkurbatov@sci.sumdu.edu.ua)

M. Ivashchenko  
Konotop Institute, Sumy State University, Sumy, Ukraine

value of the rate of recombination of the created charge carriers, and hence the high value of their lifetime, (iv) high value of the velocity of positive and negative charge carriers, and (v) large average of an atomic number of atoms ( $Z$ ) forming a compound for sufficient absorption capacity of the material. In most cases, these requirements are best met by single-crystal semiconductors, in which carrier transport is not limited by scattering at grain boundaries. But the number of semiconductor materials with high atomic numbers that can be obtained in the form of large single crystals with the required electro-physical properties and high chemical and mechanical stability is significantly limited. Unfortunately, only some semiconductor materials meet the abovementioned requirements at room temperature.

In recent decades, numerous attempts have been made to develop semiconductor detectors of various constructions based on many materials capable of operating at low and room temperatures [1, 42]. The initial goal of these studies, formulated as early as 1970, was the development of proportional detectors. To solve this problem, well-studied and technologically advanced electronic materials such as silicon (Si) and germanium (Ge) were used. But it turned out that these materials have disadvantages that significantly limit their use. Germanium has a low band gap and a high conductivity. Therefore, detectors developed on its basis must operate at liquid nitrogen temperature (77 K) to limit the influence of intrinsic noise. At the same time, detectors based on silicon doped with lithium have a low efficiency of detecting hard X-rays and  $\gamma$ -rays due to the low atomic number of material. Significant successes in creating uncooled radiation detectors operating at room temperature have been achieved only with the use of new semiconductor materials such as  $\text{HgI}_2$ , CdTe,  $\text{Cd}_{1-x}\text{Zn}_x\text{Te}$  (CZT),  $\text{Cd}_{1-x}\text{Mn}_x\text{Te}$  (CMT), etc.

High-resistance Cl-doped single crystals of cadmium telluride (CdTe:Cl) have been widely used as a base material to manufacture detectors of various types of hard-radiation [13, 33, 91, 98, 103, 105]. In recent years, the tendency to substitute CdTe:Cl on triple-component solutions has been observed, especially Zn-based solutions. It may be caused by the following benefits of  $\text{Cd}_{1-x}\text{Zn}_x\text{Te}$  (CZT) compound against bi-component solution: high value of the materials' resistivity, increased charge carriers' mobility and lifetime, band gap ( $E_g$ ) variation ability due to composition changing, increasing stability due to the higher band gap value and to the harder interactions between the components atoms, etc. [6, 15, 21, 24, 59]. However, the structural and electric homogeneity of this solid solution of single crystals was unsatisfactory due to the zinc segregation coefficient of  $k = 1.35$  [70, 84, 102, 106]. So, in recent times, as an alternative way for traditional CZT solid solution to manufacture hard-irradiation room-temperature detectors, the usage of  $\text{Cd}_{1-x}\text{Mn}_x\text{Te}$  (CMT) compound has been proposed [16, 39, 53, 65, 95]. As a result, a problem of growing the massive single crystal cadmium telluride samples and its solid solutions to obtain high-efficiency irradiation detectors with homogeneity and well-controlled electrical characteristics was formed [13, 33, 38, 49, 60, 67].

One more way to improve the structural quality of CdTe and CZT single crystals is the Se implementation into materials with a segregation coefficient value close to 1 [70, 80, 106]. It was estimated that Se (this material has an opposite segregation tendency) added into CZT may result in samples with stable lattice constant value

and electro-physical characteristics by ingot volume [29, 70, 78]. Therefore, the development of methods for obtaining single-crystal solid solutions of  $\text{Cd}_{1-x}\text{Te}_{1-y}\text{Se}_y$  (CTS) and  $\text{Cd}_{1-x}\text{Zn}_x\text{Te}_{1-y}\text{Se}_y$  (CZTS) has been started [20, 29, 70, 78, 80, 106]. The study determined that obtained single crystals of these materials had a high homogeneity; they had practically absent defects, often present in CdTe and CZT single crystals [20, 70, 78, 80, 106].

To decrease the cost of irradiation detectors in recent times, thick (close to 100  $\mu\text{m}$ ) structural perfect single crystal and polycrystalline films were proposed instead of bulk single crystals [54]. As an analogue, CdTe films may be used as CZT, CMT, CTS, CZTS solid solution layers. However, the possibility of using the thick layers of chalcogenide compounds for detecting hard irradiation in recent times is practically not studied, and related papers connected to the fabrication of the film detectors are almost absent.

This work is generally devoted to using CdTe and CZT compounds as detector materials.

## 2.2 Types of Hard Irradiation Detectors

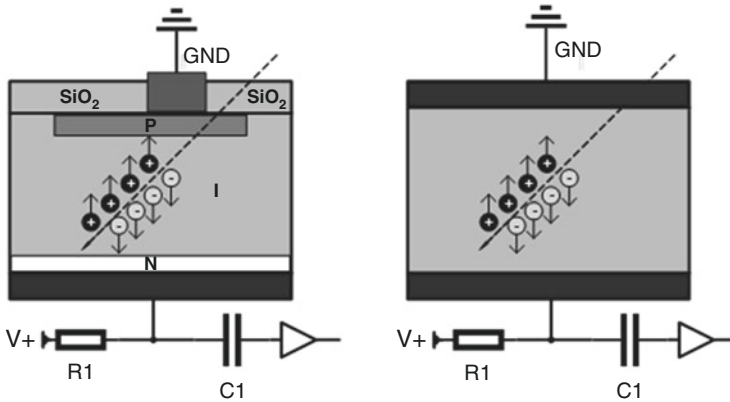
Nuclear irradiation detectors are devices for the registration of  $\alpha$ -particles and  $\beta$ -particles, X-rays and  $\gamma$ -irradiation, neutrons, protons, etc. They are used for determining the irradiation composition, calculating their intensity, measuring the quantum particles energy spectra, studying the processes of interactions between fast particles and atomic nucleus, and studying the processes of decay of the non-stable particles. Registering process is based on the interactions between irradiation or particles and substance.

All nuclear radiation detectors can be divided into particle counters, path detectors, and detectors that change their measurement properties during the irradiation.

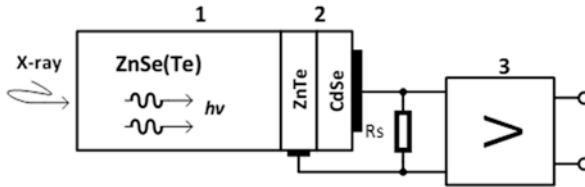
Irradiation detectors have the following main characteristics: efficiency (probability of particle registering during its getting to the detector), time distinction (a minimal time of fixation two separate particles by detector), death time, or time of reveal (time during which detector after the registering process losses the ability to register the next particle or significantly worsens their characteristics). In case of additional determination, the particle energy, or their coordinates, a detector is also characterised by energy distinction (particle energy determination precision) and spatial distinction (particle coordinates determination precision).

Semiconductor detectors are worked by the principle of generation of the non-equilibrium charge carriers in material under the influence of different types ( $\alpha$ ,  $\beta$ , X-ray,  $\gamma$ ) of nuclear irradiation with their following separation (Fig. 2.1). Such detectors are actively studied and improved in recent time due to their following advantages: compactness, a wide range of detection irradiation energies, low energy consumption, direct transformation of irradiation energy on electric signal, functional ability at room temperatures, high efficiency, and energy distinction. Moreover, the unique properties of semiconductor detectors make it possible to solve problems that are inaccessible to other types of detectors [1, 42].





**Fig. 2.1** Scheme of hard irradiation spectrometer based on semiconductor detector with (a) *p-i-n* structure or (b) ohmic contacts. (Idea from Grinev et al. [28])



**Fig. 2.2** Typical view of a detector with (1) ZnSe scintillator (Te), (2) *p*-ZnTe—*n*-CdSe photo-receiver, and (3) registration system. (Idea from Grinev et al. [28])

In most cases, a semiconductor detector is presented as a single crystal deposited onto opposite facets of metal contacts, so it represents a “metal-semiconductor-metal” structure [1, 42]. Electro-physical and detecting characteristics of this structure depend on the semiconductor material properties and the properties of the metal-semiconductor section boundary, material’s properties, and contact fabrication technique.

During the hard irradiation fabrication, semiconductor detectors use two types of contacts: rectifier (barrier) and ohmic contacts [42]. Ohmic contacts are intended for passive semiconductor connection to an external electrical field, so they must have a constant and limitless low electrical resistivity. Rectifier contacts (Schottky barriers) are active elements of electronic circuits. They are characterised by non-linear current-voltage characteristics (*I-V* curve) and are primarily analogue to diodes based on homojunction and heterojunctions [79, 81]. The best energy distinction during the registration of  $\gamma$ -quants has detectors with barrier contacts due to their low values of losses currents and the low values of noise levels. Constructions of detectors with homojunction and heterojunctions are also presented.

Another type of solid-state detector is the “scintillator-photoreceiver” system (Fig. 2.2) where the electron-hole pairs are created under the influence of hard

irradiation following their recombination and further luminescence in the range of photoreceiver-sensitive wavelengths.

So, hard irradiation in a scintillator is transformed into electro-magnetic irradiation with a lower frequency value and is further transformed into an electrical signal in a photoreceiver [28].

### 2.3 General Criteria for Choosing the Optimal Material for Solid-State Detectors

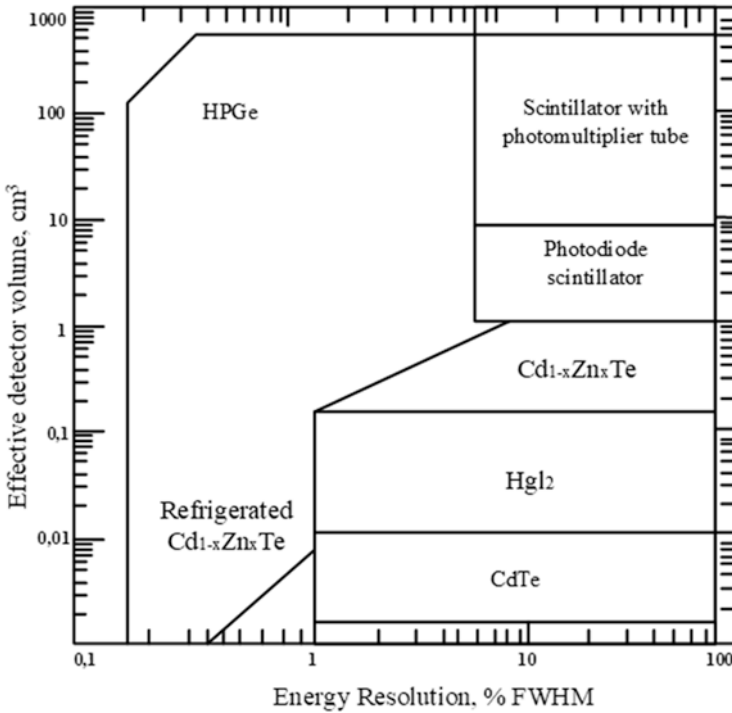
To satisfy the above-described characteristics, the material for fabrication of the hard irradiation detectors must have the following range of physical parameters [1, 2, 42, 58]:

- High-density  $\rho_m$  and large average atomic number  $Z$ , which ensures efficient absorption of ionising radiation quanta in a fairly small volume.
- A low value of energy formation in the electron-hole pairs leads to the creation of more free carriers during the absorption of ionised irradiation quant. It facilitates the registration and increases the precision of quant energy determination.
- High transport properties of free charge carriers (multiplication of the mobility on lifetime  $\mu_\tau$ ) of electrons (e) and holes (h) in material, which provide a formation of the qualified output signal without spectral distortions and efficiency losses.
- A high value of resistivity  $\rho$ , which provides a minimal loss current and decreases an own detector.
- Possibility of forming the ohmic and blocking contacts that makes a possibility to realise a necessary detector's construction.
- Manufacturability allows obtaining a quality material and manufacturing detectors with a given shape and size.
- Stability of parameters during long-term storage and operation.

Atomic number  $Z$  of detecting material is the main parameter which might be maximised. It reduces the depth of radiation absorption and increases its detection efficiency. The same effect can be achieved if at the same efficiency to reduce the thickness of the detector or at the constancy of both values to increase the maximum resolution energy of  $\gamma$ -irradiation. It is well known that the depth of absorption of this irradiation very much ( $\sim Z^5$ ) depends on the material's atomic number. Therefore, in [2], as a parameter characterising the absorption capacity of a semiconductor, it is proposed to use the  $\rho_m Z^5 / \mu$  where  $\rho_m$  is the density of the material and  $\mu_0$  is its molar mass. Effective volumes of irradiation absorption of  $\gamma$ -detectors of different designs and based on many materials are given in Fig. 2.3.

Wide band gap  $E_g$  is one of the most necessary semiconductor's characteristics influencing the detector's quality. For example,  $E_g$  determines the carriers mobility  $\mu_{e,h}$ , which, as a rule, changes inversely proportional to the wide band. It also determines a resistivity  $\rho$  which increases during increasing  $E_g$ .

Semiconductor band gap also determines the energy of electron-hole pairs formation, which are created under irradiation due to Klein ratio  $E_p = 2.8E_g + 0.606$



**Fig. 2.3** Sizes of spectrometric detectors and their energetic distinction for  $\gamma$ -irradiation with the energy of 662 keV. (Reprinted with permission from (Lund et al. [52]. Copyright 1995: IEEE)

(Fig. 2.4) [58] ( $E_p = 2.67E_g + 0.87$  by another data [42]). Dark currents and detector noises also depend on  $E_g$  intensively decreasing during band gap increasing.

It is well known [79, 81] that resistivity  $\rho$  is inversely proportional to free charge carriers' concentration that is estimated by the following equation:

$$n_i = \sqrt{N_c N_v} \exp(-E_g / 2kT), \tag{2.1}$$

where  $N_c, N_v$  are the number of quantum states in conduction and valence bands;  $k$  is Boltzmann constant.

However, in real semiconductors, as a rule, there are uncontrolled impurities that act as donors and acceptors and determine the amount of thermally generated carriers, and hence the material's resistance. These media are responsible for dark currents and detector noise.

The signal of a semiconductor detector is proportional to the absorbed energy, and the number of generated electron-hole pairs during single-photon absorption is calculated by the expression  $N = E/E_p$  where  $E$  is the radiation energy. The average statistical deviation of this value is equal to  $\sigma = \sqrt{N}$  or in energy units  $E_{rms} = E_p \sqrt{N} = \sqrt{E \cdot E_p}$ . The half-height peak width in the spectrum (energy

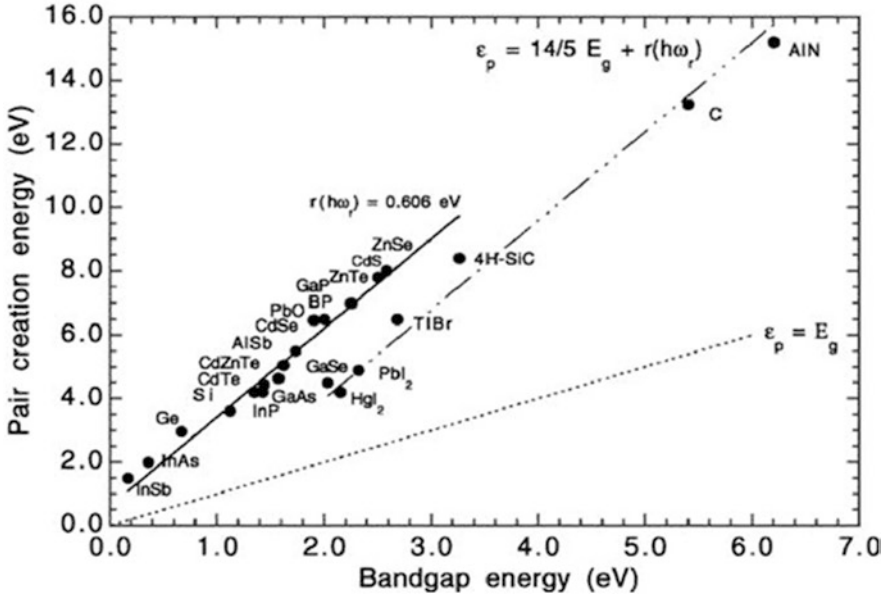


Fig. 2.4 The average energy needed for creating single electron-hole pair in different semiconductor materials depends on their wide band gap. (Reprinted with permission from Owens and Peacock [58]. Copyright 2004: Elsevier)

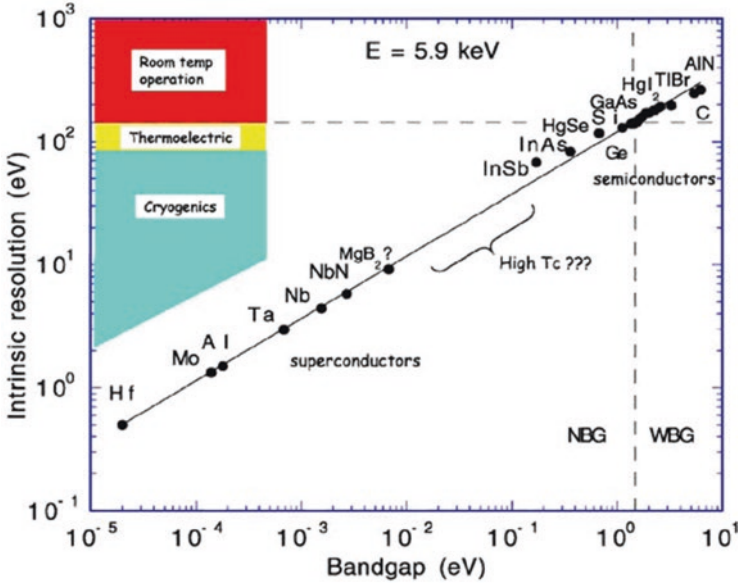
difference, see Fig. 2.5) can be written as follows  $E_{\text{FWHM}} = \Delta E = 2.35\sqrt{E \cdot E_p}$ . In practice, the equation  $E_{\text{FWHM}} = \Delta E = 2.35\sqrt{E \cdot E_p \cdot F}$  where  $F$  is the Fano factor is used to estimate the limit of the difference due to statistical processes. This factor is always less than one, and for the most studied semiconductors, such as Si and Ge, it is 0.250–0.415 [48, 58].

As we can see, while choosing a semiconductor based on the value of the band gap  $E_g$ , a compromise is needed to maximise  $\mu_{e,h}$ ,  $\rho$  and other material parameters simultaneously. Available empirical and theoretical data suggest that the optimal values of  $E_g$  should be in the range of 1.7–2.2 eV [58].

The following ratio determines the efficiency of charge carriers collecting in the detector:

$$\text{CCE} = \frac{Q}{Q_0} = \frac{\lambda_e}{L} \left[ 1 - \exp\left(-\frac{(L-x_0)}{\lambda_e}\right) \right] + \frac{\lambda_h}{L} \left[ 1 - \exp\left(-\frac{x_0}{\lambda_h}\right) \right] \quad (2.2)$$

As follows from the relationship, this efficiency depends not only on the free path length  $\lambda_e$  and  $\lambda_h$ , but also on the localisation of the charge that occurs when irradiated. Since the place of interaction of photons with matter is essentially random, it can be described by the classical exponential law of absorption; as a result, the width of the peak in the energy spectrum is determined by the ratios  $\lambda_e/L$  and  $\lambda_h/L$ .



**Fig. 2.5** Minimum resolution of devices based on semiconductors and superconductors at radiation energy of 5.9 keV as a function of the band gap of the material  $E_g$ . The graph is based on the average Fano factor of 0.14 for semiconductors and 0.22 for superconductors. (Reprinted with permission from Owens and Peacock [58]. Copyright 2004: Elsevier)

$$\lambda_{e,h} = \tau_{e,h} \mu_{e,h} E,$$

$$\lambda / L = \mu_{e,h} \tau E / L = \mu_{e,h} \tau \rho J_T / L, \quad (2.3)$$

where  $\lambda$  is the length of the charge carriers;  $L$  is the thickness of the detector;  $\tau$  is a lifetime of charge carriers;  $E$  is an electric field strength in the detector;  $J_T$  is the dark current density. To improve charge collection, the product  $\mu_{e,h} \tau \rho$  should be as large as possible. The value of  $J_T$ , however, is limited by the requirement of low noise level in the detector (in the case of sufficient electrical strength of the material).

Thus, to assess the ability of the detector material to store and record radiation-induced charges, it makes sense to use the product of three factors  $\mu_{e,h} \tau \rho$ , preferring the material with the maximum value of this product (other things being equal). Other parameters (energy of electron-hole pair formation, melting temperature, etc.) are not the primary factors and may not be considered in the first stage of detector material selection.

In the second stage of semiconductor selection for ionising radiation detectors, it is necessary to consider the possibility of practical production of the material, including the growth process of the single crystal. Parameters such as the required level of purity of the starting materials, melting temperature, pressure at which crystals are grown, chemical stability of the compound, the possibility of long-term operation and storage of the device, etc. are also subject to analysis.

To numerically compare the efficiency of detector materials in the future, we will use the products of  $\mu_{e,h}\tau\rho$  and  $\rho_m Z^2/\mu$  and then we will separately characterise the material in terms of its manufacturability. Some important from the point of view of detector properties parameters of some semiconductor materials are given in comparative Table 2.1 [2, 42, 58].

Subsequently, we used them to determine the above products and select semiconductor materials with the best characteristics for detecting hard irradiation. The results of the corresponding calculations for materials of *n*- and *p*-types are shown in Fig. 2.6.

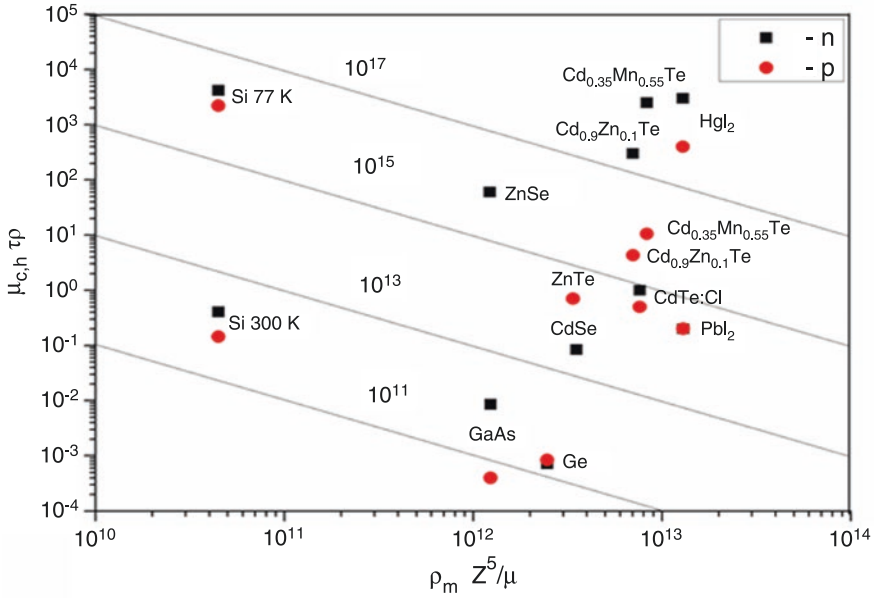
It has been shown from Fig. 2.6 and Table 2.1 that the best detective properties have the following materials: CMT, HgI<sub>2</sub>, CZT, ZnSe, CdTe, ZnTe, CdSe, and others. The results of the calculation of the efficiency of detecting hard irradiation of different energy by detectors based on some of these materials are shown in Fig. 2.7.

As already mentioned, it is necessary to use materials with optimal parameters to create high-performance hard radiation detectors with high spectral resolution and recording speed. Such parameters include the high atomic number value required for the effective interaction of atoms with radiation. At the same time, a significant value of the band gap and the product of the parameters of mobility-lifetime ( $\mu_{e,h}\tau$ ) are required to obtain high resistance and low dark currents of the detector, respectively. In addition, for a high sensitivity and efficiency of detectors, you need to use base layers with a large thickness, which provides conditions for the absorption of the maximum number of incident photons. The need for homogeneity and low density of structural defects in the detecting material is due to the need for efficient charge transfer of generated charge carriers, low dark currents, and the lack of additional conductive circuits between detector contacts that can cause short circuits.

Taking into account all the above requirements, only some semiconductor materials are suitable for use as detectors: Si, Ge, GaAs, HgI<sub>2</sub>, TlBr, CdTe and CZT, CMT, etc. Among these semiconductor materials, silicon and germanium are the most studied and technologically developed. It was on their basis that the first semiconductor detectors of hard radiation were created [1]. Detectors made of these materials have good transport properties and are pretty perfect and cheap.

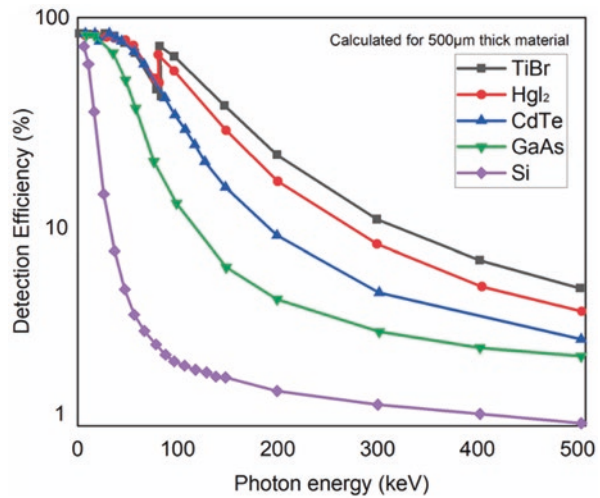
**Table 2.1** Parameters of some semiconductor materials that characterised their detecting properties

Parameter	CdTe:Cl	Cd <sub>0.9</sub> Zn <sub>0.1</sub> Te	Cd <sub>0.35</sub> Mn <sub>0.55</sub> Te	
Atomic number <i>Z</i>	50	49.1	49	
Density, $\rho_m \cdot 10^3$ (kg/m <sup>3</sup> )	5.85	5.78	5.80	
Working temperature (K)	300	300	300	
$E_g$ (eV)	1.46	1.57	1.73	
Fano Factor, $\Delta E_{FWHM}$ keV at 60 keV	0.3	0.393	0.53	
The formation energy of <i>e-h</i> pair, eV	4.43	4.64	2.12	
Drift mobility $\mu$ (cm <sup>2</sup> /V·sec)	<i>e</i>	1000–1100	1000–1100	–
	<i>h</i>	100	120	–
The average lifetime of carriers $\tau$ (sec)	<i>e</i>	10 <sup>-7</sup> –3·10 <sup>-6</sup>	8·10 <sup>-7</sup> –3·10 <sup>-6</sup>	–
	<i>h</i>	1.2·10 <sup>-7</sup> –5·10 <sup>-6</sup>	6·10 <sup>-8</sup> –1.2·10 <sup>-6</sup>	10 <sup>-7</sup>
$\mu\tau$ (cm <sup>2</sup> /V)	<i>e</i>	10 <sup>-4</sup> –3·10 <sup>-3</sup>	8·10 <sup>-4</sup> –9·10 <sup>-3</sup>	>10 <sup>-6</sup>
	<i>h</i>	10 <sup>-5</sup> –4·10 <sup>-4</sup>	3·10 <sup>-6</sup> –1.2·10 <sup>-4</sup>	–



**Fig. 2.6** Characterisation of semiconductor materials in case of the hard irradiation detecting efficiency. (Idea from Abyzov et al. [2])

**Fig. 2.7** Dependence of hard irradiation detecting efficiency on the energy of different materials devices. (Idea from Lowe et al. [51])



Nevertheless, these materials have certain disadvantages that limit their use in this field. Germany has a small band gap  $E_{gGe} = 0.67$  eV at  $T = 300$  K, and, consequently, a high specific conductivity. Therefore, germanium detectors to limit the influence of intrinsic noise can work only at low operating temperatures

( $E_{g\text{Ge}} = 0.74$  eV at  $T = 77$  K). Detectors based on silicon ( $E_{g\text{Si}} = 1.1$  eV at  $T = 300$  K), in addition to this disadvantage, have a relatively low efficiency of detection of quanta with energies above 60 keV due to low atomic number.

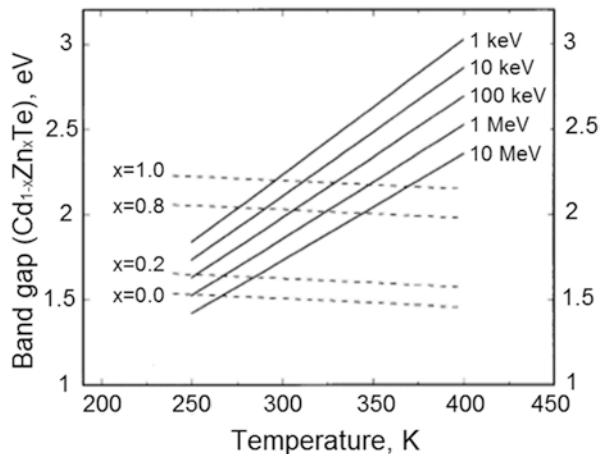
The most attractive semiconductor materials that are suitable for detectors with high recording efficiency and good energy resolution, operating even at room temperature, are based on CdTe and solid solutions. These materials combine a relatively high resistivity and one of the most significant known values of the product  $\mu_{e,h}\tau$ . Due to this fact, CdTe, CZT, and CMT are materials that require the most negligible thickness (0.5 mm) at an applied voltage of 100 V and must absorb 90% of radiation under the action of radiation with an energy of 60 keV. Such indicators are very close to the ideal detector material [23].

The advantage of using solid solutions is the ability to vary their physical properties in a wide range, which allows you to optimise their characteristics for use as a detector material. The growing interest in radiation detectors that can operate at room temperature has led to the development of technologies using semiconductor compounds with a wider band gap compared to Si and Ge [58]. In turn, the main advantage of solid solutions of CZT, CMT over CdTe is the ability to obtain a material with a more significant band gap and, accordingly, greater resistivity and leakage current.

Theoretical calculations show [92] that for effective detection of radiation with energies of about 10 keV at room temperature, it is necessary to use a solid solution of CZT with significant concentrations of zinc ( $x = 0.8$ ) (Fig. 2.8), while the concentration of manganese in CMT solution can be twice as small.

In the following, we will focus on the review of the main physical characteristics of cadmium telluride and its solid solutions.

**Fig. 2.8** Optimal wide band gap depending on the temperature and photon energy for CZT solid solution with different zinc compositions





## 2.4 Main Physical Characteristics of CdTe, ZnTe, and CZT and Their Application

In the general case, a standard iodine radiation detector based on CdTe (ZnTe, CZT) consists of a base layer made of its own semiconductor, where incident photons are absorbed, and electron-hole pairs are generated, as well as electrical contacts. The electrical signal is removed from the ohmic contact (e.g. Pt), while the other contact is blocking (e.g. In), which reduces the dark currents of the device. It is possible to further reduce the influence of dark currents on the detector output signal by creating a  $p-i-n$  junction.

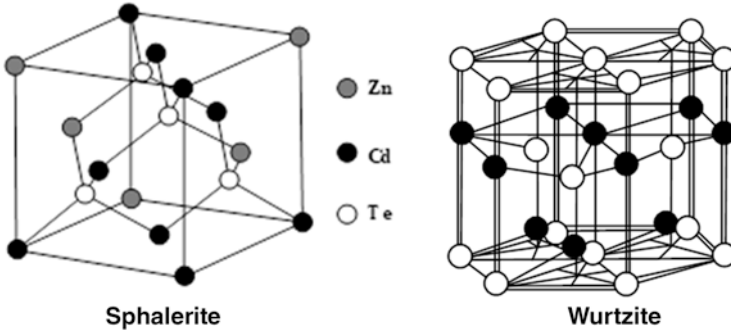
Due to the unique physical properties of II-VI-group compounds, especially – cadmium telluride, this compound is a perspective material for fabrication on its basis of a wide range of high-efficiency nuclear energetic devices, solar energy instrumentations, optical, and acoustic electronic [3, 21, 46, 66, 99, 104]. It is a wide band gap semiconductor with a high transmission coefficient value (~70%) of electro-magnetic irradiation in the range of wavelengths of  $\lambda = (2.0-30.0) \mu\text{m}$ . These properties allow its usage to fabricate the corresponding spectra filters and electronic and optical modulators in near-IR and IR areas [91, 104]. A significant interest of researchers has the luminescent properties of CdTe. It may be caused by direct interactions between the valence and conduction gaps through the shallow acceptor levels that lead to the formation of irradiation in infra-red spectra [104].

Cadmium telluride is one of the promising materials for manufacturing X-ray and  $\gamma$ -irradiation semiconductor detectors that can work at room temperatures. As a rule, to detect the low-energy X-ray irradiation, low-ohm  $n$ -CdTe is used. In contrast, it is necessary to register the high-energy irradiation to use the semi-isolated material with a resistivity of  $\rho = (10^8-10^{10}) \text{ Ohm}\cdot\text{m}$  [3, 5, 46, 56].

Such wide usage of CdTe is due to its extremal physical properties. Besides, cadmium telluride is the heaviest compound of II-VI semiconductors ( $\mu = 240 \cdot 10^{-3} \text{ kg/mole}$ ). The ionicity by Phillips ( $I_{\text{ph}} = 0.717$ ) is also bigger among these compounds.

Cadmium telluride is the single material in II-VI group compounds that can be obtained in both types of semiconductor conductivities. It is usually crystallised in a sphalerite (zinc blend) structure, which lies in a cubic symmetry group and consists of two face-centred cubic lattices (FCC), shifted each other on the quarter of the space-diagonal of the crystallographic cell. Each sub-lattice is formatted by cadmium of tellurium atoms as shown in Fig. 2.9. So, four neighbouring atoms that belonged to another FCC sub-lattice surround each atom in a materials lattice. Neighbouring atoms situated in tetrahedron form, simultaneously creating covalent connections, distribute four valence electrons.

Hexagonal (wurtzite) modification of CdTe (Fig. 2.9) is metastable and is occurred in crystals and films obtained in super non-equilibrium conditions. Sphalerite and wurtzite modifications differ from each other only by alternating densely packed atomic layers. Sphalerite phase CdTe lattice constant is the biggest among all II-VI compounds with an analogue crystalline structure.



**Fig. 2.9** Crystalline structure of sphalerite phase of CdTe and CZT (left), and wurtzite phase of CdTe (right) compound

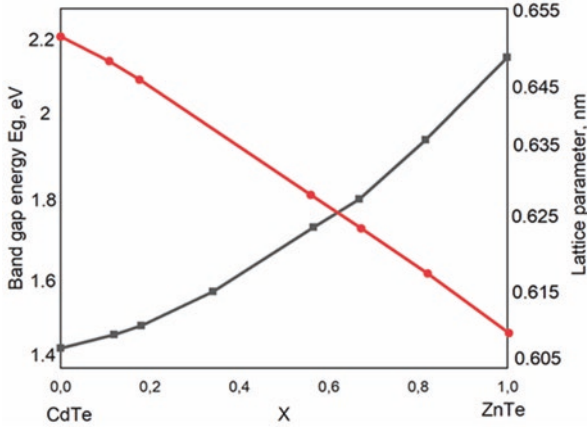
Electro-physical properties of this material are estimated by parameters and configuration of its band gap, and its value is the smallest among II-VI compounds [96].

Cadmium telluride has a high value of vapour pressure close to the melting point. This fact is complicated to grow the crystals from the melt, but formatted the favourable conditions for grown crystals and thin films from the vapour phase. During the evaporation procedure, CdTe is dissociated, and its gas phase is a mixture of compound components vapours. Moreover, there is observed an absence of chalcogenides molecules. Cadmium vapour in the mixture is single-atomic; simultaneously tellurium may be presented in single-atomic as a double-atomic state, and the first state prevails.

Zinc telluride is a wide bandgap semiconductor which has a bandgap value of  $E_g = 2.26$  eV at room temperature and  $E_g = 2.39$  eV at  $T = 4.2$  K. Its melting point is  $T_m = 1513$  K; its density is  $\rho_m = 5.633 \cdot 10^3$  kg/m<sup>3</sup>. Its sublimation heating is  $Q = 119.2$  kJ/mole; its formation enthalpy value is  $\Delta H = -117.5$  kJ/mole. In thermodynamically equilibrium conditions, zinc telluride is crystallised in a cubic sphalerite structure. The compound's lattice constant is  $a = 0.61033$  nm, and the distance between Zn and Te atoms is 0.363 nm. The thermal coefficient of linear expansion at room temperature is  $\alpha_0 = 8.4 \cdot 10^{-6}$  K<sup>-1</sup> [82].

ZnTe presence area in a temperature range from room temperature (RT) to melting point (MP) lays from the tellurium side. ZnTe stoichiometric composition at 300 K corresponds to 66.12 mass. % of Te and to 33.98 mass. % of Zn (50.0048 at. % of Te) [8, 10, 22, 25, 34, 57, 82]. Phase diagram features lay the effect of consisting in ZnTe the tellurium excess. As a result, it has an electro-conductivity with only hole type regardless of the obtaining conditions and type of compound doping [10, 12, 34]. Holes' mobility in material is  $\mu_p = 110$  cm<sup>2</sup>/V·sec and their effective mass is  $m_{hp} = 0.154 \cdot m_0$ ,  $m_{hp} = 0.695 \cdot m_0$  [10, 25, 34].

CZT ternary semiconductor compound is a solid solution of cadmium telluride (CdTe) and zinc telluride (ZnTe). It is a direct gap semiconductor with  $p$ -type conductivity. Wide band-gap of this material is varied from 1.46 eV (CdTe) to 2.26 eV (ZnTe) depending on the zinc concentration (Fig. 2.10). CZT as CdTe is crystallised as sphalerite structure based on cubic symmetry group and consists of two FCC



**Fig. 2.10** Variation of wide band gap (filled circle) and lattice constant (filled square) at room temperature depending on the  $x$  solid solution concentration

cubic sub-lattices shifted each other onto quarter crystallographic cell spacing diagonals. Cadmium (Cd), zinc (Zn), or tellurium (Te) atoms form each of these sub-lattices. In general conditions, the solid solutions grown mechanism is revealed in mutual substitutions of atoms by metal sub-lattice (Cd, Zn). In contrast, the concentration of the atoms in the chalcogenide sub-lattice (Te) is constant; the principle of Cd, Zn, and Te atoms positioning in solid solution crystal lattice is shown in Fig. 2.9 (left). So, the general physical parameters of solid ternary solutions may have intermediate properties corresponding to the pure binary compounds [94].

The effect of zinc atoms impurity on CdTe lies in decreasing the lattice constant and increasing the band gap. The value of CZT lattice constant may be determined using the Vegard linear approximation [18, 75]:

$$a(\text{Cd}_{1-x}\text{Zn}_x\text{Te}) = a(\text{CdTe}) \cdot (1-x) + a(\text{ZnTe}) \cdot x, \quad (2.4)$$

where  $a(\text{CdTe})$  and  $a(\text{ZnTe})$  are CdTe and ZnTe lattice constant values – 0.64810 nm and 0.61026 nm, correspondingly.

In the case of a crystalline material, the relation Eq. (2.5) determines the dependence of the band gap CZT on  $x$  [4]. Corresponding dependencies have been shown in Fig. 2.10.

$$E_g(x) = 1.48 + 0.70 \cdot x - 0.38 \cdot x(1-x). \quad (2.5)$$

Fabrication of the high-quality irradiation detectors requires a material with high values of resistivity and charge carrier lifetime multiplication  $\mu\tau$  [17]. Increasing the zinc concentration in CZT solid solution leads to increasing its resistivity (Table 2.2), which, as a result, decreases the device's dark current and increases the detecting efficiency [19].

On the other hand, increasing the zinc concentration can decrease crystalline quality due to lattice deformation [63, 64, 83]. This effect is the reason why the Zn

**Table 2.2** The main characteristics of CdTe, ZnTe and CZT

Material	CdTe	Cd <sub>0.9</sub> Zn <sub>0.1</sub> Te	ZnTe
Crystalline structure	Cubic (sphalerite)	Cubic (sphalerite)	Cubic (sphalerite)
Atomic number, $Z$	48; 52	48; 30; 52	30; 52
Density (kg/cm <sup>3</sup> ), $\rho_m$	$6.2 \cdot 10^{-3}$	$5.78 \cdot 10^{-3}$	$5.63 \cdot 10^{-3}$
The wide band gap (eV), $E_g$	1.46	1.57	2.26
Resistivity (Ohm $\times$ cm), $\rho$	$10^9$	$10^{10}$	$10^{10} - 10^{12}$
$\mu_c \tau_c$ (cm <sup>2</sup> /V)	$10^{-3}$	$10^{-3} - 10^{-2}$	$10^{-3} - 10^{-2}$
$\mu_h \tau_h$ (cm <sup>2</sup> /V)	$10^{-4}$	$10^{-5}$	$10^{-5}$

Source: Data extracted from Berchenko and Sredin [8], Berger [9], Bhargava [10], Del Sordo et al. [17], Kasap and Capper [34], Novoselova [57], Schlesinger [76], Georgobiani [25]

concentration in the CZT solid solution of most detectors does not exceed  $x = 0.20$  and most often lies in the range  $x = 0.04-0.10$  [17].

The main physical properties of CZT in the case of  $x = 0.10$  and their comparison to the physical properties of pure CdTe and ZnTe are presented in Table 2.2.

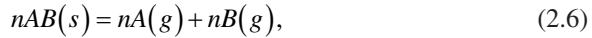
## 2.5 Methods of Growth of the Bulk CdTe Crystals and Solid Solutions on Their Base

### 2.5.1 II-VI Compounds Phase Diagrams Features

The complexity of the technology of growing single crystals of II-VI compounds, which includes cadmium telluride, and especially solid solutions based on them, is due to the following reasons: high melting points and strong dissociation of the melt, the tendency to unilateral deviation from stoichiometry, segregation of components, and also the ability of these compounds in the synthesis to crystallise in various modifications.

To select the conditions for growing single crystals and determine the conditions of their annealing point to change certain properties, it is necessary to know the phase diagrams of such compound. The phase equilibrium in the system of II-VI compounds is usually characterised by three parameters: temperature ( $T$ ), pressure (where  $P$  is the sum of the partial pressures of the components), and phase composition ( $x$ ). It can be described by a conventional bio-component system (AB), where only one compound is formed. For such systems, in the case of the crystal growth process, it is interesting to consider two types of equilibrium – the equilibrium of a solid compound with a gas phase (GP), the equilibrium of a ternary-component system – a solid compound, liquid and gaseous phase (TLG). The latter determines the equilibrium conditions for growing the compound from the melt.

In contrast to the constituent components, II-VI compounds are more refractory and have significantly lower vapour elasticity. The peculiarity of these materials is their decomposition or dissociation at elevated temperatures, which is described by the following equilibrium reaction:



where  $s$  is a solid state,  $g$  is a gas state.

Numerous mass-spectrometric studies show that the gas phase of the elements of VI group of the table of elements consists mainly of diatomic molecules ( $n = 2$ ).

Equation (2.7) indicates that the partial pressures of the components of the compounds are interrelated. They are interconnected by the following equilibrium constant:

$$K_p = P_A^n P_{Bn}, \quad (2.7)$$

Where activities are estimated is a partial pressure.

In the case of pressure measurements, the KP is usually determined for all materials. The minimal pressure in the melting point condition of stoichiometric composition may be assumed from the following equation:

$$P_{\min} = \frac{3}{2} \sqrt[3]{2K_p}. \quad (2.8)$$

During the “solid state-liquid-gas” system description, we have the three analysed components: temperature, pressure (as a sum of two components pressures), and composition. Inert gas pressure has not practically influenced the system’s equilibrium. Two surfaces describe the phase equilibrium in three-dimensional space with  $P$ ,  $T$ , and  $x$  coordinates. For a more informative demonstration of the ternary phase, the surfaces of liquids and solids are usually projected on bi-dimensional areas. It leads to obtaining the three types of phase diagrams:  $P - x$ ,  $T - x$ ,  $P - T$ . On  $P - x$  and  $T - x$  diagrams, the solid state is usually described as a separate vertical line.

The phase diagrams shown in Figs. 2.11 and 2.12 estimate a connection between pressure and temperature for CdTe and ZnTe compounds. The upper curve is characterised by the cadmium (zinc) vapour pressure and estimates the highest boundary of the solid CdTe (ZnTe) stability area. The pure tellurium pressure (Figs. 2.11b and 2.12b) determines the lowest curve.

For practical usage, the higher interest of researchers represents the value of minimal pressure ( $P_{\min}$ ) close to the maximal melting point ( $T_{\max}$ ). In the case of CdTe and ZnTe, these values are  $4.8 \times 10^{-3}$  Pa (0.23 atm.) and  $10^{-2}$  Pa (0.64 atm.), respectively.

The possibility of controlling the electrical properties of any material is determined by its homogeneity area. It can be seen in Fig. 2.11a that the CdTe presence area is quite asymmetric. In the case of a temperature more than 1000 K, the more significant part of the compound presence area lies on the cadmium side. In the case of a temperature lower than 1000 K, this area is shifted onto the tellurium side [3]. So, cadmium telluride crystal growth temperature determines their point defects, which prevail in materials. Because they are charged, they have estimated a type of material’s conductivity. In most cases, during the single crystal growth and the

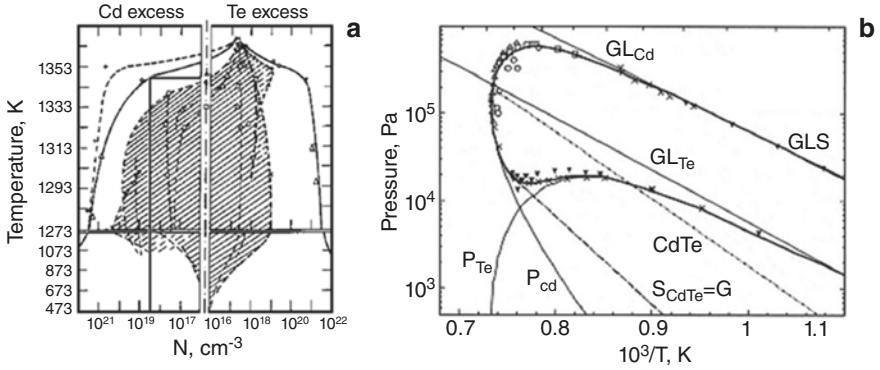


Fig. 2.11 CdTe compound phase diagrams: (a) –  $T - x$ , (b) –  $P - T$ . (Idea from Kreger [45])

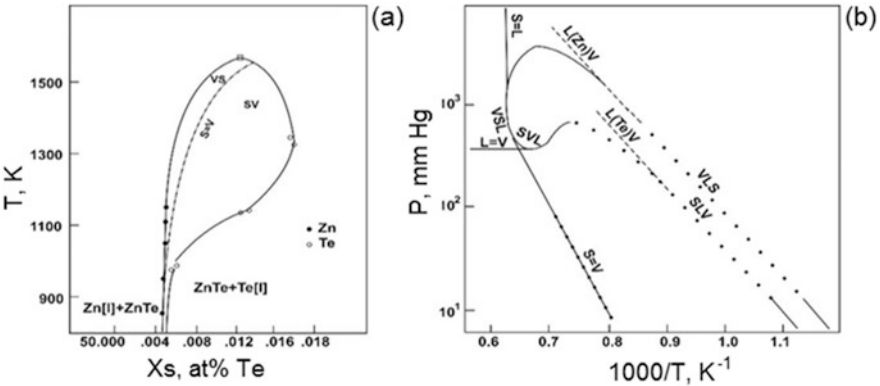


Fig. 2.12 ZnTe compound phase diagrams: (a) –  $T - x$  (a), (b) –  $P - T$ . (Reprinted with permission from Feltgen et al. [22]. Copyright 2001: Elsevier)

deposition of undoped films of this compound, they have a  $p$ -type conductivity because the preferred defects in the material are single-charged cadmium vacancies ( $V_{Cd}^-$ ) [71] or interstitial tellurium atoms ( $Te_i^-$ ) [7].

### 2.5.2 Methods of Single Crystals Growth

Modern methods of growing crystals of II-VI compounds can be divided into three main groups: growth from the gas phase, growth from solutions, and crystallisation from the melt [44]. Each of these groups has many varieties and methods of growth. Criteria for choosing the method of obtaining crystals, taking into account at least three parameters: the nature of the substance to be crystallised, the nature of melting; presence of phase transitions, chemical activity, etc.; technical and economic indicators of the method (complexity and cost of equipment, type of construction

materials, etc.); requirements for the actual structure, geometric configuration, and dimensions of the grown single crystal. In addition, some authors used to obtain crystals of chalcogenide compounds by other methods such as electrolytic precipitation, hydrothermal synthesis, chemical precipitation, etc. [14, 15]. However, these methods are not widespread in our time.

It was previously thought that II-VI compounds have relatively high melting points and sublime well, so it is most convenient to use the method of growing from the gas phase. However, the results of later studies were the most acceptable method of rising from the melt under inert gas pressure. Thus, the highest quality large crystals of CdTe and CZT can be grown only by melting under pressure.

### 2.5.2.1 Vapour Phase Growth

Relatively perfect chalcogenide crystals are obtained from the gas state, but epitaxial films are most often applied in this way [30]. Existing methods of growing single crystals of II-VI compounds from the gas phase can be divided into two main groups [40, 47]: synthesis from elements and the sublimation method of powdered compounds in a vacuum. The chemical transport method is the synthesis of elements that can be carried out either in an inert atmosphere or in an atmosphere of chemically active gas. The main requirement in the growth of samples from the gas phase is the continuous supply of a pair of compound components in the reaction zone and the crystal's growth. Depending on the method of transportation of crystal-forming elements, crystallisation methods from the gas phase can be divided into dynamic and static. Dynamic methods use a carrier gas that passes continuously through the system. In static methods, transport is provided by the diffusion of components through the gas phase. The source of steam, in this case, is a compound of the desired composition in powder form, which is at a high temperature. The pair of components formed during the dissociation of the compound diffuses into the cold zone, where the crystals grow [47].

It should be noted that during growing from the gas phase, crystals of very high quality of many compounds can be obtained, but their growth rates are usually very low [40]. In addition, the growth rate also decreases during synthesis due to the deterioration of heat dissipation from the growing crystal. The situation is somewhat better for hexagonal compounds, but growth is often limited to one orientation [40]. Low temperatures of the growth process contribute to high quality, especially in those compounds in which the phase transition occurs below the melting point (ZnSe, ZnS).

The use of the method of gas transport reactions is possible only if a certain amount of transporting agent is introduced into the crystal. Halogens are the only possible agent for the growth of crystals of II-VI compounds, so the presence of some donors in the resulting material should be expected. In some cases, growth temperatures are pretty low, less than 1073 K. At such temperatures, quartz ampoules remain rigid and almost inert. Another advantage is that the desorption from the furnace elements is low. If the contact of the growing crystal with the ampoule walls

is excluded, then using very low gradients (below 5 degrees per cm), it is possible to obtain samples practically free from thermoelastic stresses.

### 2.5.2.2 Solution Growth

One of the most common methods of growing crystals from solution is the method of zone melting (moving heater). The narrow zone of the tellurium melt passes through the rod of the source polycrystalline material CdTe or ZnTe. Suppose the temperature gradients are selected correctly, and the area moves slowly. In that case, the material will dissolve in the lower part of the zone and precipitate as a single crystal in the upper. This method combines the advantages of solution growth and zone cleaning and low temperatures (923–1123 K), which are used to eliminate corrosion of the crucible material virtually. However, solid recrystallisation is used to cultivate single crystals of II-VI compounds to a limited extent [41].

### 2.5.2.3 Melting Growth

The method of growing crystals from the melt is widespread. The primary condition for obtaining single crystals by this method is congruent melting of the substance, the absence of polymorphic transitions and, preferably, its sufficient chemical inertness. The main advantage of melt growth is the high growth rate, resulting from which large single crystals can be obtained relatively quickly. At the same time, speeds of a few millimetres per hour are typical; however, when crystals of high quality with a high-quality structure are to be obtained, much lower rates are often used. The melt has already received crystals of all zinc and cadmium chalcogenides, considering the sufficiently high sulfite vapour pressure. Only cadmium telluride can be melted under relatively mild conditions, so a sealed quartz ampoule can be used as a crucible. Usually, higher temperature compounds are grown in graphite or, in some cases, in ampoules of pyrolytic boron nitride.

In recent years, gradient cooling (or Tamman's method) is gaining popularity for high-volatile compounds. Nowadays, the vertical Bridgman method and its modification are becoming more and more widespread for the cultivation of single crystals of II-VI compounds, which is associated with improving the design of growth chambers [35, 36, 78, 87]. This method allows the melt to be well preserved, as the free surface from which evaporation occurs is kept to a minimum. In the case of tellurides, the vapour pressure is moderate. The stoichiometry of the compounds can be controlled through a reservoir with a heated electrode (modified Bridgman method). In the case of CdTe and ZnSe crystals, the popularity of the low-growth gradient method is periodically reviving.

Bridgman's horizontal method for the cultivation of II-VI compounds is rarely used. The large melt area that arises contributes to its rapid evaporation. However, the relatively low volatility of CdTe has made progress in this method in terms of reducing thermomechanical stresses in the samples.



The Czochralski method, quite common for cultivating single crystals of other materials, has hardly been used to cultivate chalcogenide compounds. Only polycrystalline CdTe ingots were obtained using  $B_2O_3$  as a flux [72].

At the same time, the zone melting method is often used to grow CdTe crystals [73, 93]. This method is similar to Bridgman's method, except that only a tiny portion of the charge melts at a given time. It reduces the crucible material's corrosion and the melt's rate of evaporation. The sharp temperature zones used in this method are well combined with the volatility of compounds in the growth setup [30, 73, 93].

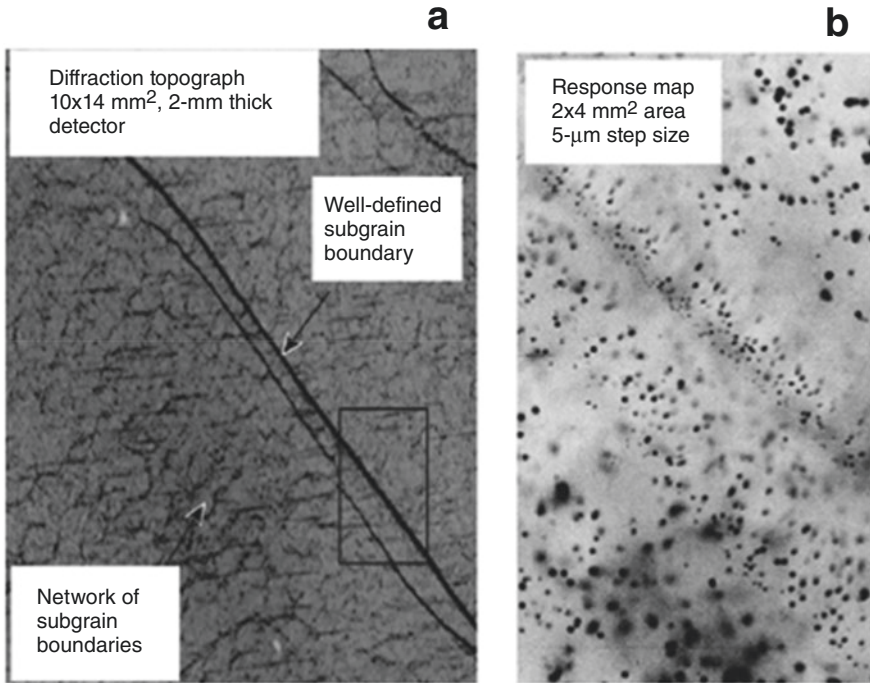
Comparative analysis of the main methods of growing crystals of II-VI compounds shows that the best structural characteristics of single crystals can be obtained using vapour-phase methods that ensure crystal growth without contact with the ampoule walls and the solution-melt method of moving heater (tellurium for CdTe). However, only growth methods from the melt (Bridgman, zone melting, gradient cooling, and their modifications) combine high crystal growth rates with sufficiently good crystallinity and purity of the material. In addition, only these methods nowadays provide the possibility of obtaining crystals of large sizes and, accordingly, high productivity of technological equipment.

### ***2.5.3 Structural Features of Single Crystals of CdTe and Its CZT Solid Solutions***

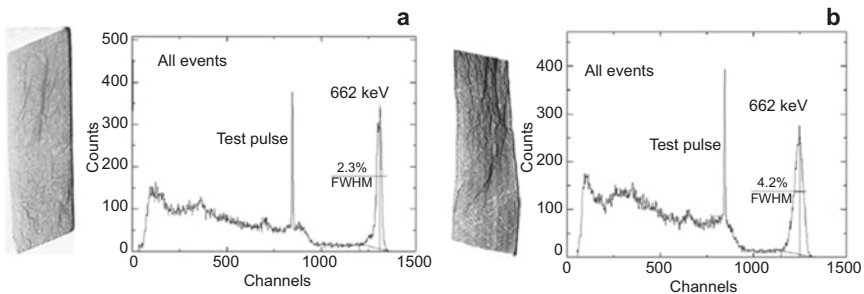
High-quality CdTe and CZT single crystals are required in hard radiation detectors. However, they are challenging to grow due to the constituent components' high melting points and volatility [69]. The obtained single crystals, as a rule, contain a large number of structural defects. The performance of detectors based on these compounds is primarily limited by the presence of such internal crystal defects as networks of subgrain boundaries and a high concentration of tellurium (Te) inclusions (Fig. 2.13). These defects lead to a deterioration of the conditions of charge carrier transport, especially for holes, and the spatial heterogeneity of the transfer parameters, which leads to a deterioration of the energy resolution of detectors in the amplitude-pulse spectra (Fig. 2.14).

It has been estimated that Te inclusions are the main centres of hole capture in CdTe and CZT single crystals, and crystal defects, such as subgrain boundaries and their connections, are the primary centres for isolating these inclusions. Isolation of tellurium precipitates during crystal growth is due to the peculiarities of their  $T - x$  phase diagram, where most of the region of solid solutions is shifted towards excess tellurium (Fig. 2.15). At the same time, with increasing zinc content in CdTe at the growth temperature of single crystals increases the amount of excess tellurium. When the crystals are cooled to room temperature, excess tellurium is released in the form of precipitates due to retrograde solubility. Typical concentrations of precipitates in CdTe and CZT crystals are shown in Table 2.3.

Inclusions of tellurium can be removed by post-growth annealing of single crystals in Cd vapour. However, this process can lead to the formation of star-shaped

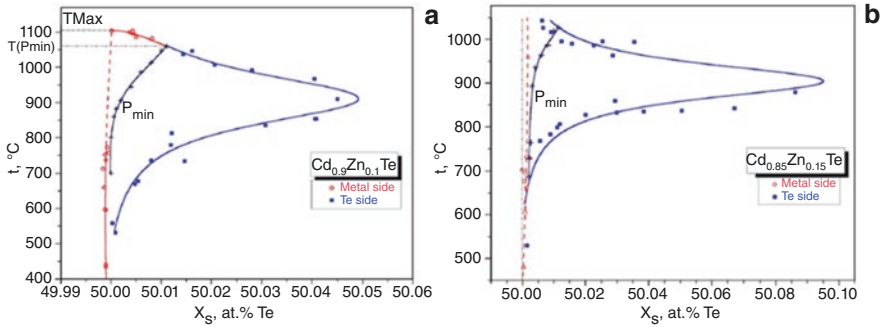


**Fig. 2.13** CZT single crystal micrograph for detecting the signals obtained by (a) the X-ray diffraction topography and (b) the X-ray crystal card obtained in high-resolution conditions. (Reprinted with permission from Bolotnikov et al. [11]. Copyright 2013; Elsevier)



**Fig. 2.14** (a) X-ray topography and (b) amplitude Frisch grid-detector spectra based on CZT crystals with different sub-grain boundary concentrations. Sample dimensions:  $6 \times 6 \times 15 \text{ mm}^3$ . (Reprinted with permission from Bolotnikov et al. [11]. Copyright 2013; Elsevier)

defects, which, in turn, can capture electrons and reduce the response to hard radiation (Fig. 2.16) [101]. Subgrain boundary networks are usually randomly distributed in the CdTe / CZT matrix, causing spatial severe heterogeneity in the quality of the single crystal in volume and amplifying its poor spectral quality.



**Fig. 2.15**  $T-x$  projection of CZT solid solutions phase diagrams of different compositions: (a) –  $\text{Cd}_{0.9}\text{Zn}_{0.1}\text{Te}$ , (b) –  $\text{Cd}_{0.85}\text{Zn}_{0.15}\text{Te}$ . (Reprinted with permission from Greenberg and Guskov [27]. Copyright 2006: Springer Nature)

**Table 2.3** Typical concentrations of Te precipitates in CdTe and CZT crystal designed for detector application

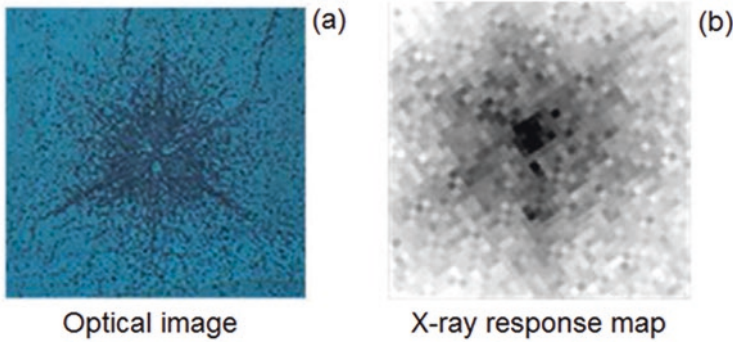
Material	Temperature ( $^{\circ}\text{C}$ )	$X$ (at.%)	Typical Te precipitations concentration ( $\text{cm}^{-3}$ )
CdTe	$\sim 900$	50.014	$7 \cdot 10^4$
$\text{Cd}_{0.90}\text{Zn}_{0.10}\text{Te}$	$\sim 900$	50.052	$2.8 \cdot 10^5$
$\text{Cd}_{0.85}\text{Zn}_{0.15}\text{Te}$	$\sim 900$	50.100	$2.8 \cdot 10^5$

In addition, CZT crystals grown using the high/low-pressure Bridgman method create inhomogeneity of zinc concentration along the length of the ingot due to the high segregation coefficient  $\text{Zn} \sim 1.35$  [68]. Including 10% Zn in CdTe can increase the material's band gap by 2%, indicating the importance of uniformity of the distribution of Zn along the length of the grown crystal. Heterogeneity in zinc concentration leads to the growth of very poor crystals [68]. Only about 30% of the total length of the grown CZT ingot has the crystalline quality of the detector class, which significantly increases the cost of production of these detectors. Thus, using single crystals CdTe and CZT as detector material requires a significant improvement in their structural quality.

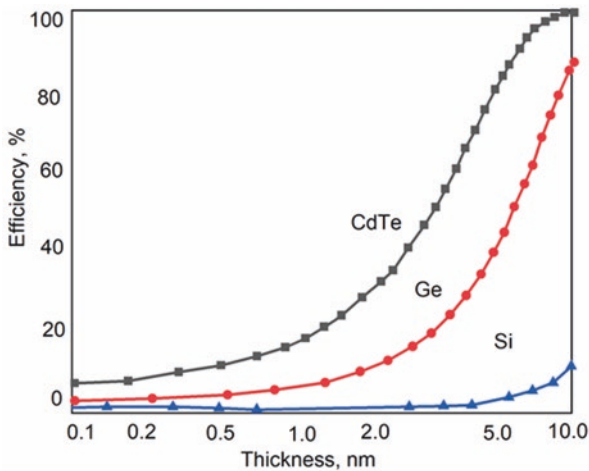
## 2.6 Hard Irradiation Detectors Based on CdTe and CZT Single Crystals

### 2.6.1 X-Ray and Gamma Irradiation Detectors Based on Cadmium Telluride

Unlike gamma-ray detectors, X-ray detectors do not have to be thick. Due to the high ability to inhibit ionising radiation and absorb X-rays in the area near the input electrode, the efficiency of collecting charge carriers generated by radiation can be reduced to the efficiency of collecting particles of only one sign, characterised by



**Fig. 2.16** (a) Star-wise effect in annealed CZT single crystal determined by the optical microscopy after chemical treatment, and (b) a card of carrier's collection efficiency. (Reprinted with permission from Yang et al. [101]. Copyright 2006: Springer Nature)



**Fig. 2.17** Gamma irradiation detection efficiency with the energy of 100 keV depending on CdTe, Si, and Ge detection layer thickness. (Reprinted with permission from Takahashi et al. [85]. Copyright 2009: IEEE)

greater mobility – i.e. electrons. Due to this, detectors made of CdTe have a high quantum detection efficiency (Fig. 2.17).

The high value of the average atomic number of cadmium telluride ( $Z(\text{CdTe}) = 50$ ) and its density provide good absorption of ionising radiation. A wide band gap ( $E_g(\text{CdTe}) = 1.46 \text{ eV}$  at  $T = 300 \text{ K}$ ) allows it to be used at room temperature because, in these conditions, the material has reasonably high resistivity [42, 58]. Cadmium telluride was probably the first broadband material to be used to make non-cooling gamma-ray detectors. However, the low electrical resistivity of its crystals is the cause of increased leakage currents, which limits the actual energy resolution of CdTe-based detectors. That is why chlorine is introduced into the material to compensate for electrically active impurities, both own (Cd vacancies) and uncontrolled. However, even with a special alloying Cl impurity, the resistance of CdTe crystals does not exceed  $\rho = (10^8 - 3 \times 10^9) \text{ Ohm}\cdot\text{cm}$  [42, 97, 104].

It was found that Cl-doped single crystals of cadmium telluride have all the characteristics of very pure semiconductor material if the criterion of purity is the concentration of electrically active impurities. Indeed, such crystals have a resistivity  $\rho \sim (10^8\text{--}10^9)$  Ohm (i.e. very close to their resistance), a long lifetime of carriers ( $\tau \sim 5 \times 10^{-6}$  sec), and high mobility of charge carriers of both types. The conductivity in these crystals is determined by only one impurity level ( $\sim E_v + 0.60$  eV) with an impurity concentration  $N = (10^{12}\text{--}10^{13})$  cm<sup>-3</sup>. These high parameters are difficult to explain by compensating for shallow donor and acceptor levels when doped with chemical impurities. According to Verger et al. [97] and Zanio [104], the high purity of chlorine-doped material is a consequence of the so-called “self-purification” of crystals, which is associated not with the direct separation of impurities from the crystal, but with the deactivation of electrically neutral impurities and intrinsic defects. The decontamination mechanism is an almost complete chemical interaction of impurities and their defects with the formation of stable electrically neutral complexes, the energy levels located outside the forbidden zone of the material [97].

The grown alloy crystals are cut into plates of the required thickness, ground, polished, and treated in a chemical herb to create detectors. After these operations, apply electrical contacts. As electrode materials, metals with low (Al, In) and high electron yield (Au, Pt, Ir) are used. In addition to surface barrier structures, metal-oxide-semiconductor and *p-i-n* structures are also used to improve contact properties. The task of obtaining optimal and reproducible contacts is essential because it is closely related to polarisation in chlorine-doped crystals, limiting detectors’ capabilities based on CdTe [42].

Recently, a material doped with impurities with an unfilled d-band is also used to create hard radiation detectors, giving localised states near the middle of the material’s band gap: V, Cr, etc. It allows compensating for residual impurities and obtaining a material with high resistivity [26, 97].

Detectors based on chlorine-doped CdTe single crystals have high spectrometric properties, but at the same time, they are characterised by changes in signal amplitude and collection efficiency over time. The degradation of amplitude spectra over time is due to polarisation. The problem of polarisation could be solved entirely by growing CdTe crystals with their conductivity without doping with compensating impurities. Indeed, with the help of the mobile heater method, it is possible to obtain un-doped CdTe crystals from very well-purified starting materials, in which the polarisation effect is almost absent. However, even at the lowest growing temperatures, crystals obtained in this way have a relatively low resistivity of  $\rho \sim (10^4 - 10^6)$  Oh-m, which does not allow them to be used effectively in large-volume detectors.

A significant step towards overcoming this problem was the production of CdTe crystals from the Bridgman melt under high pressure (HPV), which was first carried out by San Diego Semiconductors, Inc., USA [62]. The high inert gas (argon) pressure of up to 100 atm used in this method significantly suppresses the dissociation of CdTe molecules in the melt, thus reducing the number of intrinsic defects in the solid material. As a result, it was possible to raise the resistivity of cadmium telluride crystals to  $10^9$  Ohms without doping impurities. In addition, the size of the

crystals grown by the method of HPV can reach 100 mm in diameter, significantly reducing the cost of such material.

Over the last decade, CdTe and CdTe:Cl single crystals have been widely used in ionising radiation detectors production, IR-filter substrates, and non-linear optics for various industries: medicine, nuclear power plant control, X-ray and gamma-ray imaging equipment, security, etc. [13, 33, 67, 77, 91]. However, improving the performance of existing devices based on these materials has slowed down in recent years. Modern electronics devices require the creation of structurally perfect single crystals of new promising materials with controlled optical and electrical properties and the ability to create reliable electrical contacts. One of the effective methods of controlling the structurally sensitive characteristics of cadmium telluride is isovalent impurities introduction and the formation of solid solutions based on it. The introduction of the third, and sometimes the fourth element, into the binary compound, allows changes in such essential parameters of the material as the lattice period, electron affinity, band gap, conductivity, etc.

In recent years, attempts have been made to replace such detector materials as CdTe and CdTe:Cl with solid solutions CZT, CMT, and CZTS, which have much better characteristics (higher resistivity, higher mobility of charge carriers, the ability to change the band gap of the material by introducing impurities, lower concentration precipitates, two-dimensional and point defects, etc.), and the structural characteristics of the material along the single-crystal ingot are more uniform (Table 2.3). It increases the yield of high-quality detector material significantly, thus reducing the cost of the detectors themselves.

### 2.6.2 Detectors Based on CZT Solid Solutions

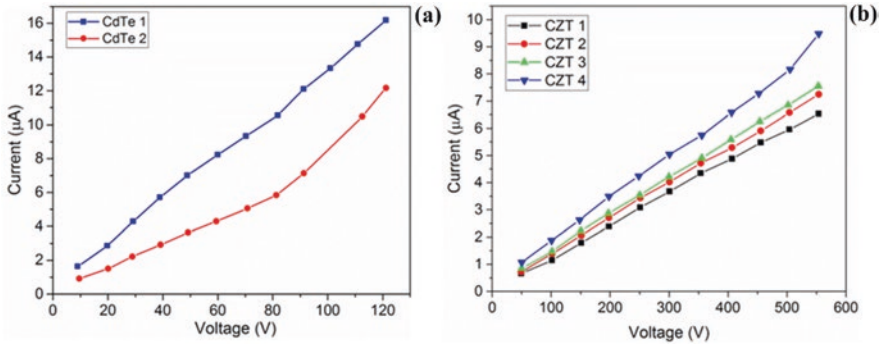
A positive result in the semiconductor detectors of hard irradiation gave the transition from CdTe to solid solutions CZT, where  $x = 0.05\text{--}0.20$ , proposed by experts from Aurora Technologies Corp., San Diego, USA. As they showed in [19], such a crystalline material has a resistivity of ( $10^{10}\text{--}10^{11}$ ) Ohm without additional doping. As a result, the loss currents in the metal-semiconductor-metal system used to detect radiation are significantly reduced. It substantially improves the performance of detectors based on CZT crystals. It makes it possible to obtain an actual energy resolution for  $^{137}\text{Cs}$  radiation ( $E = 662$  keV) at room temperature, which is close to the resolution of germanium detectors at liquid nitrogen (77 K). In the general case, CZT crystals proved suitable for manufacturing compact X-ray sensors in the range of 10 keV–1 MeV, operating at room temperature.

Since 1992, significant efforts have been made to develop ionising radiation detectors based on CZT material grown by the Bridgman method of high pressure (HPV) [42]. The Zn vapour pressure at the melting point is lower than Cd, so introducing Zn into CdTe within (5–20) % at a pressure of 100 atm leads to the improved stoichiometry of the obtained semiconductor material without the need for additional doping with impurities. As a result of growing CZT by the HPV method, it is

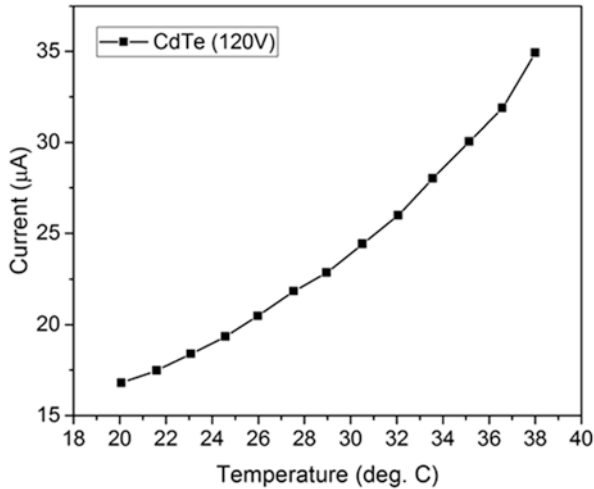
possible to get a material with a resistivity of  $10^{11}$  Ohm $\times$ cm, which is almost two orders of magnitude larger than that of CdTe crystals. Since leakage currents are reduced in a material with a higher resistivity, using CZT crystals allows detectors with larger dimensions of the sensitive element both in thickness and area of the component. The diameter of the crystals grown by the HPV method can reach 10 cm and a weight of 10 kg.

Along with the increase in the width of the band gap and the resistance of the detector material, the introduction of Zn has negative consequences concerning the transfer of holes. As can be seen from Table 2.3, the transport properties (characterised by the product of mobility  $\mu$  for the lifetime of carriers  $\tau$ ) of CZT material improve compared to CdTe concerning electron transfer but deteriorate in the hole component. On average, the lifetime of holes in CZT detectors is much shorter than in detectors based on chlorine-doped CdTe crystals. The reason for this is not yet clear; perhaps it is due to non-stoichiometry and more defects in the crystal. The advantage of the HPV method is the possibility of obtaining large CZT ingots, but their homogeneity is not yet sufficient and needs to be improved. The higher resistivity CZT of the material compared to CdTe (hence lower loss currents) makes it possible to produce better spectrometers from this material for the low-energy region because at relatively low energies of ionising radiation, quanta induced charge in the case of irradiation of the detector with the transfer of electrons, not holes. Lower loss currents of CZT detectors also make it possible to use these detectors at higher temperatures. The loss currents of CdTe and CZT detectors operating at room temperatures affect the energy resolution to a greater extent than the electronic noise of the previous and main charge-sensitive amplifiers connected to the detectors. Detector loss currents increase nonlinearly with increasing temperature. Since the capacitance of the detectors is usually very small (about 1 pF), the contribution of noise to the half-width of the spectral line in the first approximation can be estimated as proportional to the square root of the product of the loss current at the time of signal amplification. If the detector is directly connected to the preamplifier, a significant DC component of the loss current may limit the amount of inverse resistance of the preamplifier. But the lower the feedback resistance, the higher the electronic noise of the preamplifier. When the ambient temperature changes during the detector's operation, the noise will change, negatively affecting the spectral resolution and efficiency of counting pulses in a given energy range.

In Eisen and Shor [21], loss currents were measured on many CdTe and CZT detectors depending on the temperature and the applied electric voltage at different bias polarities. The variation in loss current values for detectors of the same material did not exceed  $\pm 15\%$ . After applying a voltage to CdTe or CZT detectors at the initial stage, a slight decrease in the loss current was observed, and then it stabilised. For CdTe detectors, the stabilisation time was (10–15) minutes, and for CZT detectors – less than 1 minute. Longer stabilisation times for CdTe detectors indicate the presence of deeper traps for charge carriers near the electrodes. Loss currents depending on the applied voltage ( $I$ - $V$  curves) are shown in Fig. 2.18 for several different CdTe and CZT detectors. In some CdTe detectors, there was an asymmetry in the loss currents when voltages of varying polarity were applied. It indicates the existence of barriers of different heights at two opposite contacts in such detectors. In the case of



**Fig. 2.18** Loss currents at 300 K depending on the bias voltage in the case of (a) CdTe detectors and (b) CZT detectors. All listed samples (CdTe 1–2, CZT 1–4) have detector quality but belong to different manufacturers. (Reprinted with permission from Eisen and Shor [21]. Copyright 1998: Elsevier)

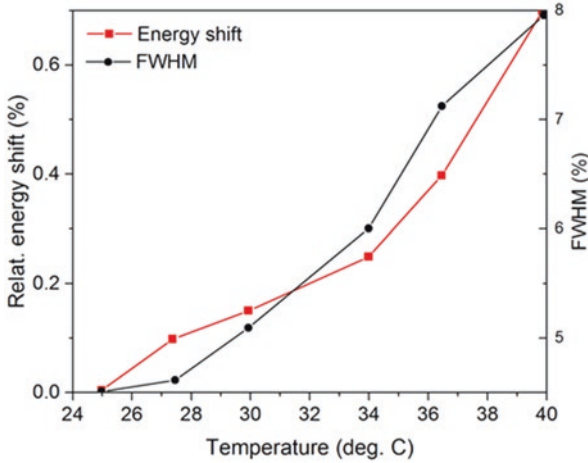


**Fig. 2.19** Temperature dependence of the loss current of a typical CdTe detector during the bias voltage of 120 V. (Reprinted with permission from Eisen and Shor [21]. Copyright 1998: Elsevier)

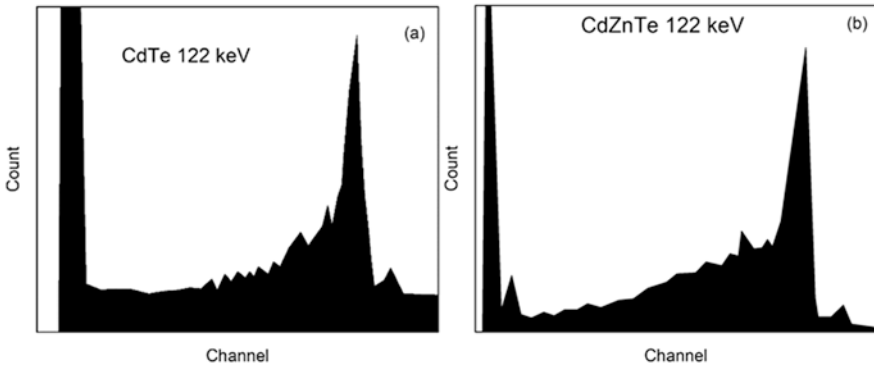
CZT detectors, there is complete symmetry in the loss currents. In addition, the  $I$ - $V$  curves of these detectors in the range of applied voltage  $U = (10\text{--}500)$  V are linear. The temperature dependence of the loss current of one of the CdTe detectors studied by Eisen and Shor [21] is shown in Fig. 2.19. The technical characteristics of most CdTe detectors after their continuous operation for a week at a voltage of 120 V and a temperature of 303 K remained satisfactory. Only in some detectors was an increase in the loss current, and in some, there was even a breakdown.

Figure 2.20 shows the change in the half-width temperature of the 122 keV line and its energy temperature offset (recorded signal height) for a typical CZT detector with an operating offset of 500 V. The detector was DC connected to the preamplifier, and the amplifier signal generation time was set as 2  $\mu\text{s}$ . For this value of the





**Fig. 2.20** Temperature dependence of the line half-width at 122 keV and shifting by energy for a typical CZT detector at a bias voltage of 500 V. (The idea of Korbutyak [42])



**Fig. 2.21** Spectrums were obtained by (a) CdTe detector with a bias voltage of 120 V and (b) CZT detector with a 500 V bias voltage. The time of forming signals was 3  $\mu$ sec. Reprinted with permission from Eisen and Shor [21]. Copyright 1998: Elsevier)

operating voltage, the half-width and energy position of the line change slightly with temperature. Therefore, the detector can function satisfactorily in the temperature range up to 309 K.

Let us analyse the spectra of these planar CdTe and CZT detectors (for example, in the case of  $^{57}\text{Co}$  radiation source, see Fig. 2.21) obtained without additional correction of charge collection (by special electronics, modified electrode configuration, etc.). We can determine which parameters are responsible for the difference between these spectra:

1. CZT detectors at an operating bias of 500 V have a better energy resolution than CdTe-based detectors with a potential difference of 120 V. If we characterise the resolution of the half-width line (as a percentage of line position). For the time of signal amplifier 3  $\mu$ sec, it is 4.7% for CZT and 7.2% for CdTe detectors. Its

best value in CZT detectors is due to the low level of current losses. With less signal generation time, the resolution of CdTe-based detectors becomes much better.

2. The average efficiency of converting incident radiation into photocurrent on CdTe detectors with a thickness of 2 mm is approximately the same as on CZT detectors with a thickness of 3 mm. An incomplete collection of media in detectors due to trapping holes is more pronounced in the spectra of CZT detectors. Although the energy resolution of CZT detectors is better than that of CdTe detectors, the holes contribute to the photo peak only from a small part of the detector's working area.
3. The efficiency of converting incident radiation into photocurrent in CdTe detectors increases very strongly with increasing applied voltage, while in most CZT detectors, this growth is very slow. It means that the CZT signals are very short-lived, and the contribution to the total induced signal of the hole's component is insignificant. Moreover, the traps for holes in CZT detectors are more profound than in CdTe detectors.
4. The efficiency of converting incident radiation into photocurrent in CdTe detectors increases significantly with increasing amplifier signal generation time, while in most CZT detectors, this increase is slow. It again indicates a more significant contribution of holes in the case of CdTe detectors than CZT detectors and the ability to compensate for the non-ballistic process of hole transfer by increasing the pulse generation time, which leads to a long time of signal growth. The contribution of holes in most CZT detectors is very small, and increasing the time of pulse formation within reasonable limits cannot compensate for the effect of too long a flight time of the holes.

## **2.7 Main Methods of Obtaining and Using CdTe, CZT, and CMT Films as Radiation Detectors**

### **2.7.1 Main Methods of Deposition of CdTe, CZT, and CMT Films**

As it was already mentioned, it has recently been proposed to use thick films of CdTe and its solid solutions to create hard radiation detectors.

Currently, the following methods are most widely used to obtain CZT and CMT films: organometallic epitaxy from the gas phase [54], organometallic chemical deposition from the gas phase [83], pulsed laser deposition [4], thermal evaporation [38], magnetron sputtering [107], molecular beam epitaxy [74], and hot wall epitaxy [86]. Among these methods of evaporation, close-spaced vacuum sublimation (CSVS) technique can be considered a promising low-cost film deposition technology [43]. As a rule, CZT and CMT films by CSVS are produced by evaporation of the charge of particular chemical composition [100] or sequential application of layers of individual elements of the compound, followed by annealing of the

multilayer structure [89]. Using co-evaporation of CdTe and ZnTe, MnTe from different sources can be even more promising because, in this case, we can expect precise control of the concentration of impurities in the material.

A characteristic feature of films of solid solutions of CZT, CMT is their more defective structure compared to massive materials. That is, in most cases, the films contain a large number of extended defects (dislocations, pores, grain boundaries, inclusions). It is especially true of polycrystalline films grown on non-orienting substrates. It affects semiconductors' structural, optical, and electrical properties. Defective film structure is susceptible to material production technology and can be optimised by determining the optimal growing conditions [43].

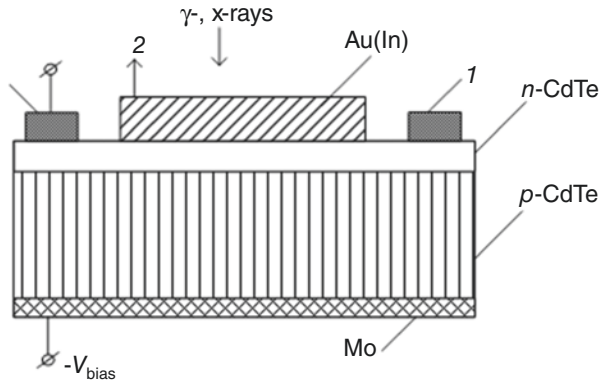
A detailed study of the structural and optical properties of the CZT and CMT layers was performed in [83, 88]. It was shown that the method and physical and technological conditions of application, changes in chemical composition, and defective structure of the material influence the properties of films.

### 2.7.2 Usage of the CdTe and CZT Films in Ionising Radiation Detectors

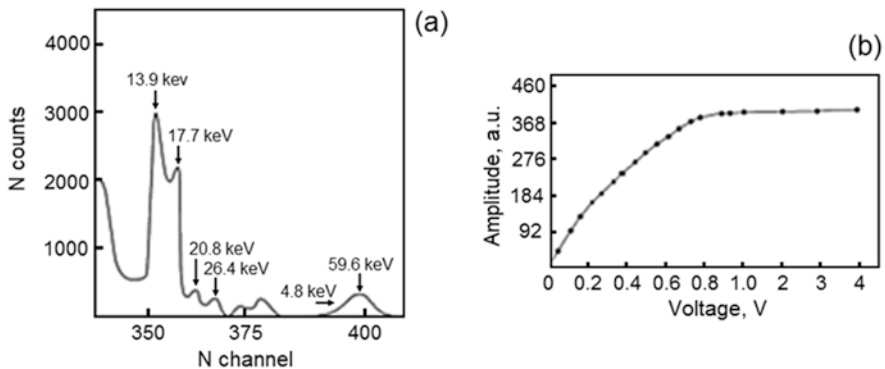
CdTe thick films as a detector material have only recently begun with scientists in Japan and Korea [37, 50, 54, 55, 90]. For this purpose, monocrystalline films obtained on oriented substrates [54] are mainly used nowadays because the grain boundaries of polycrystalline layers are effective recombination and trap centres that significantly affect the electrical characteristics of detectors. However, many authors [55, 77] used coarse-grained polycrystalline layers as detector material. To do this, they must have a columnar grain structure and crystallite sizes that significantly exceed the diffusion-free path length of charge carriers  $D \gg \lambda$  [42]. For example, in [55], CdTe films 300  $\mu\text{m}$  thick and with an average grain size of 10  $\mu\text{m}$  were obtained on glass and quartz substrates by sublimation in a closed volume at  $T_s = (713\text{--}823)$  K. These films had a  $p$ -type conductivity and resistivity of  $\rho \sim 10^{10}$  Ohm $\cdot\text{cm}$ , but a small value of  $\mu\tau$ . The authors did not study the detector properties of the material.

The first detectors based on thick  $d = (30\text{--}150)$   $\mu\text{m}$  CdTe films were developed by [105]. The primary material was polycrystalline  $p$ -CdTe films with a columnar structure, obtained by sublimation in a hydrogen stream on molybdenum substrates. The film's grain size was  $D = (30\text{--}150)$   $\mu\text{m}$ . They had a resistivity of  $\rho = 10^3\text{--}10^7$  Ohm $\cdot\text{cm}$ , and the lifetime of non-equilibrium charge carriers in the layers was  $\tau = (50\text{--}70) 10^{-6}$  sec. To create detectors in a single cycle, the structure of  $p$ -CdTe- $n$ -CdTe- $n$ -CdO-Au (In) was formed (see Fig. 2.22).

It was shown that the method and physical and technological conditions of application, changes in chemical composition, and defective structure of the material influence the properties of films. Dependence of signal from the bias voltage shown in Fig. 2.23b for film detector indicates high homogeneity and perfection of sensitive areas of detectors formed by a set of independent parallel crystallites. All



**Fig. 2.22** Construction of a hard irradiation detector based on CdTe thick films. 1 are defending electrodes, 2 is a signal to the electronic system



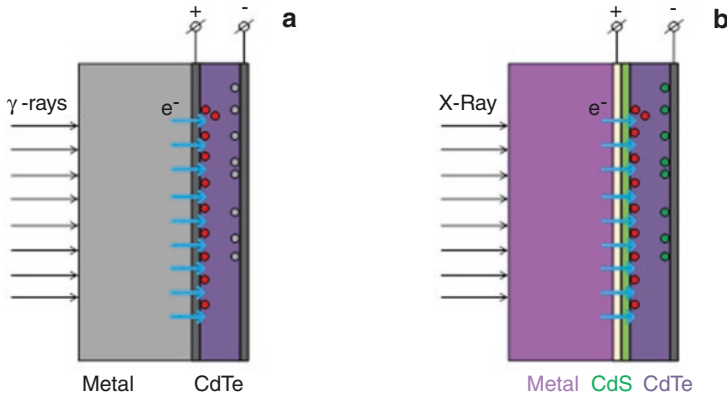
**Fig. 2.23** (a) Amplitude spectra of  $^{241}\text{Am}$  source, determined by CdTe-film detector at  $T = 293$  K. The bias voltage was  $U = 4.3$  V,  $N_{\text{ch}}$  is the channel's number; (b) dependence of channel's amplitude on the bias voltage. (Source – public domain)

detectors based on CdTe films had stable parameters even after two months of storage at  $T = 293$  K.

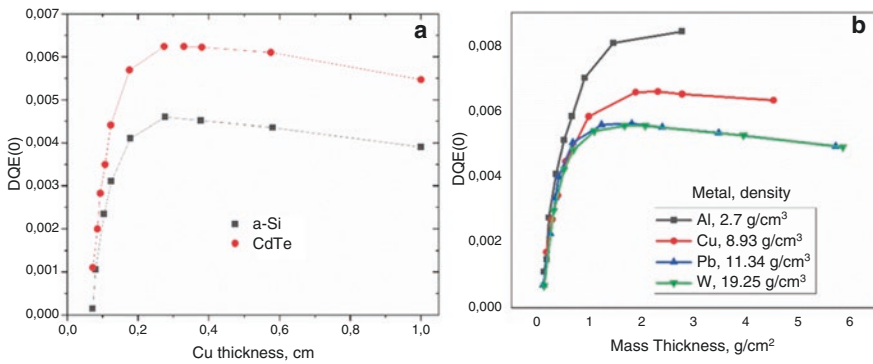
In Kang [32], some different methods of recording hard irradiation by a detector based on CdTe films were used. Compton electrons knocked out of the metal through which the detector material is irradiated are registered in the proposed designs. The corresponding designs are shown in Fig. 2.24.

Because of the simulation, irradiated lead or copper is the optimal metal for use as a conversion layer through the detector. The thickness of this layer should be 2 mm, with a thickness of the CdTe absorption layer varying from 30 to 300  $\mu\text{m}$ .

The results of comparing the characteristics of Compton electron detectors with a base layer of amorphous silicon and CdTe film with copper contacts of different thicknesses when irradiated with quanta with  $E = 6$  MeV and the characteristics of the detector based on CdTe film depending on the contact material are shown in Fig. 2.25.



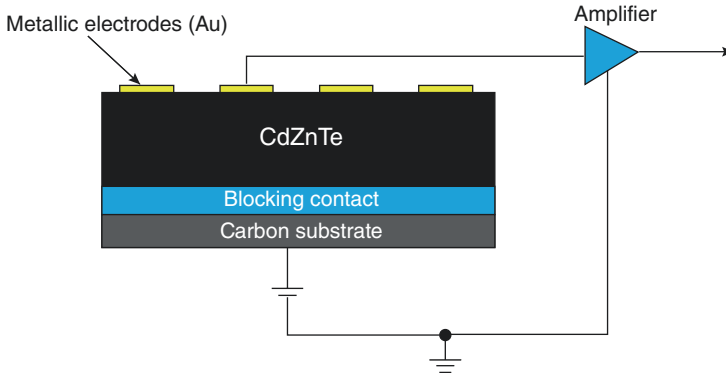
**Fig. 2.24** Designs of hard irradiation detectors based on CdTe thick films that registered Compton electrons: (a) Sketch of the proposed CdTe thin-film detector with metal converter. Fat arrows represent the secondary electrons generated in the converter. The dark and light dots are the electrons and holes generated in CdTe and separated to the opposite faces of the CdTe structure (b). (Reprinted with permission from Parsai et al. [61]. Copyright 2010: John Wiley & Sons)



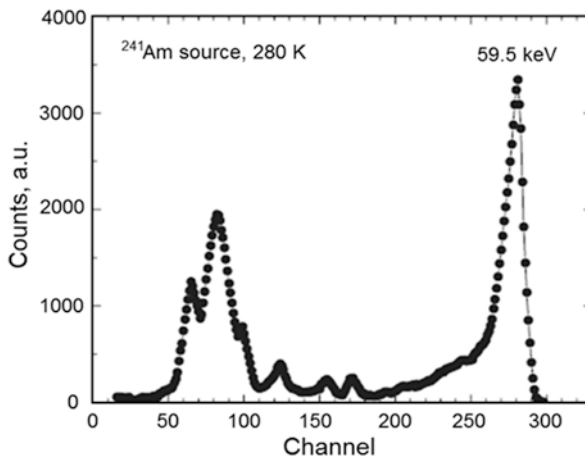
**Fig. 2.25** (a) Comparison of the characteristics of Si- and CdTe-based detectors ( $d = 30 \mu\text{m}$ ) with different thicknesses of copper contacts (irradiation with  $E = 6 \text{ MeV}$ ); (b) the detector's characteristics based on CdTe film depending on the conversion layer type of material. (Reprinted from Kang [32])

Detectors of ionising irradiation based on CZT thick films have been successfully developed in Kim et al. [38], Tokuda et al. [91], Won et al. [98]. Typically, such transducers consist of an absorbing layer, a blocking contact to reduce dark currents of the device, a carbon substrate, and metal contacts (Fig. 2.26). Due to the low output signal level, the detector must be connected to an amplifier.

The best results were achieved when CZT thick films doped by analogy to single crystals with donor impurities (Cl, Sn) [38] were used as the absorption layer. Introducing these impurities allowed compensation for the fine acceptors in the solid solution of  $p$ -type conductivity. In turn, this led to a significant increase in resistivity, which in its value approached the values inherent in its semiconductors



**Fig. 2.26** A design of a hard irradiation detector based on CZT thick film



**Fig. 2.27** Gamma irradiation spectrum of  $^{241}\text{Am}$  detector based on  $\text{Cd}_{0.96}\text{Zn}_{0.04}\text{Te}:\text{Cl}:\text{Sn}$  *n*-type thick film. (Reprinted with permission from Kim et al. [38]. Copyright 2008: Elsevier)

and the inversion of the material's conductivity. As a result, the resolution of film detectors has reached the level of devices based on CZT single crystals (Fig. 2.27).

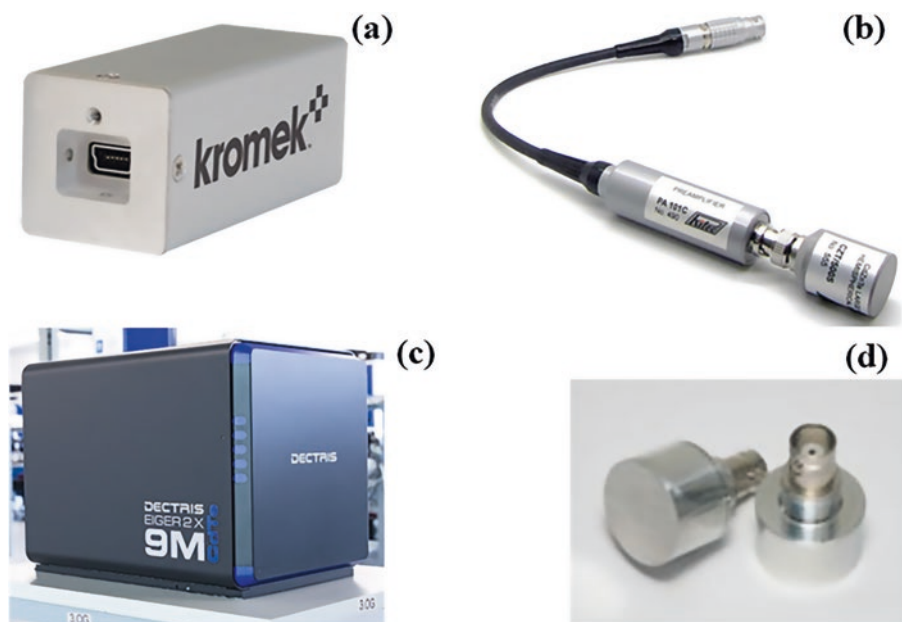
CdTe- and CZT-based hard irradiation detectors have found their practical application in the nuclear industry, medicine, astrophysical research, and radiation safety. Manufacturers of these detector systems are many innovative companies around the world, including the United States, Korea, Japan, and the European Union, including Kromek Group (UK), Dectris (USA), Baltic Scientific Instruments (BSI) (Latvia), Eurorad (France), and others.

The main parameters of individual real detector systems based on CdTe and CZT are given in Table 2.4, and their general appearance is given in Fig. 2.28.

**Table 2.4** The main parameters of real detector systems based on CdTe and CZT

Name	Producer	Detector material	Energy range	Energy resolution FWHM (keV)	Dimensions (mm <sup>3</sup> )	Applications
GR1	Kromek	CZT	30 keV–3.0 MeV	13–16	10 × 10 × 10	Control of nuclear materials, environmental monitoring, self-contained portable spectrometer
μSPEC	BSI	CZT	20 keV–3.0 MeV	16–23	25 × 25 × 70	Control of nuclear materials, environmental monitoring
EIGER2 R	Dectris	CdTe	8 keV–25 keV	4–11	77 × 38 × 0.75	Macromolecular crystallography, X-ray powder diffraction
S.5.5.3	Eurorad	CdTe	<6 keV	8–12	5 × 5 × 3	X-ray diffraction, X-ray fluorescence, bone densitometry, surgical probes, custom inspection systems

Source: [www.kromek.com](http://www.kromek.com); <http://bsi.lv>; [www.dectris.com](http://www.dectris.com); [www.eurorad.com](http://www.eurorad.com)



**Fig. 2.28** General view of irradiation detectors based on CdTe and CZT: GR1 ([www.kromek.com](http://www.kromek.com)) (a), μSPEC (<http://bsi.lv>) (b), EIGER2 R ([www.dectris.com](http://www.dectris.com)) (c), S.5.5.3 ([www.eurorad.com](http://www.eurorad.com)) (d)

## References

1. Abramov AI, Kazansky YA, Matushevich ES. Physical foundations of the operation of nuclear radiation detectors. Fundamentals of experimental methods of nuclear physics. Moscow: Atomizdat; 1977.
2. Abyzov AS, Azhazha VM, Davydov LN, Kovtun GP, et al. Selection of semiconductor material for gamma radiation detectors. *Technol Des Electron Equip.* 2004;3:3–6.
3. Armani N, Ferrari C, Salviati G, Bissoli F, Zha M, Zappettini A, Zanotti L. Defect-induced luminescence in high-resistivity high-purity undoped CdTe crystals. *J Phys Condens Matter.* 2002;14(48):13203.
4. Aydinli A, Compaan A, Contreras-Puente G, Mason A. Polycrystalline Cd<sub>1-x</sub>Zn<sub>x</sub>Te thin films on glass by pulsed laser deposition. *Solid State Commun.* 1991;80(7):465–8.
5. Bassani F, Tatarenko S, Saminadayar K, Bleuse J, Magnea N, Pautrat JL. Luminescence characterisation of CdTe: in grown by molecular beam epitaxy. *Appl Phys Lett.* 1991;58(23):2651–3.
6. Bavdaz M, Peacock A, Owens A. Future space applications of compound semiconductor X-ray detectors. *Nucl Instrum Methods Phys Res, Sect A.* 2001;458(1–2):123–31.
7. Bell SJ, Baker MA, Duarte DD, Schneider A, Seller P, et al. Comparison of the surfaces and interfaces formed for sputter and electroless deposited gold contacts on CdZnTe. *Appl Surf Sci.* 2018;427:1257–70.
8. Berchenko N, Krevs V, Sredin V. Semiconductor solid solutions and their usage. Moscow: Voenizdat; 1982.
9. Berger LI. Semiconductor materials. Boca Raton: CRC Press; 2020.
10. Bhargava R. Properties of wide bandgap II-VI semiconductors. London: INSPEC; 1997.
11. Bolotnikov AE, Camarda GS, Cui Y, Yang G, Hossain A, Kim K, James RB. Characterisation and evaluation of extended defects in CZT crystals for gamma-ray detectors. *J Cryst Growth.* 2013;379:46–56.
12. Bose DN, Bhunia S. High resistivity in-doped ZnTe: electrical and optical properties. *Bull Mater Sci.* 2005;28(7):647–50.
13. Brambilla A, Renet S, Jolliot M, Bravin E. Fast polycrystalline CdTe detectors for bunch-by-bunch luminosity monitoring in the LHC. *Nucl Instrum Methods Phys Res, Sect A.* 2008;591(1):109–12.
14. Brytan V. An influence of atomic hydrogen impurities on electrical and optical properties of CdTe and Cd<sub>1-x</sub>Zn<sub>x</sub>Te single crystals grown by sublimation method (PhD dissertation, Odessa); 2014.
15. Carcelén Valero V. Growth and characterization of Cd<sub>0.85</sub>Zn<sub>0.15</sub> crystals doped with Bi: 10<sup>19</sup> at/cm<sup>3</sup> (PhD Thesis, Universidad Autónoma de Madrid, Madrid); 2010.
16. Cross AS, Knauer JP, Mycielski A, Kochanowska D, Wiktowska-Baran M, et al. (Cd, Mn) Te detectors for characterisation of X-ray emissions generated during laser-driven fusion experiments. *Nucl Instrum Methods Phys Res, Sect A.* 2010;624(3):649–55.
17. Del Sordo S, Abbene L, Caroli E, Mancini AM, Zappettini A, Ubertini P. Progress in the development of CdTe and CdZnTe semiconductor radiation detectors for astrophysical and medical applications. *Sensors.* 2009;9(5):3491–526.
18. Denton AR, Ashcroft NW. Vegard's law. *Phys Rev A.* 1991;43(6):3161–4.
19. Doty FP, Butler JF, Schetzina JF, Bowers KA. Properties of CdZnTe crystals grown by a high-pressure Bridgman method. *J Vac Sci Technol B.* 1992;10(4):1418–22.
20. Duff MC, Hunter DB, Burger A, Groza M, Buliga V, et al. Characterisation of heterogeneities in detector-grade CdZnTe crystals. *J Mater Res.* 2009;24(4):1361–7.
21. Eisen Y, Shor A. CdTe and CdZnTe materials for room-temperature X-ray and gamma ray detectors. *J Cryst Growth.* 1998;184:1302–12.
22. Feltgen T, Greenberg JH, Guskov AN, Fiederle M, Benz KW. P–T–X phase equilibrium studies in Zn–Te for crystal growth by the Markov method. *Int J Inorg Mater.* 2001;3(8):1241–4.



23. Fiederle M, Feltgen T, Meinhardt J, Rogalla M, Benz KW. State of the art of (Cd, Zn) Te as gamma detector. *J Cryst Growth*. 1999;197(3):635–40.
24. Franc J, Höschl P, Belas E, Grill R, Hlidak P, et al. CdTe and CdZnTe crystals for room temperature gamma-ray detectors. *Nucl Instrum Methods Phys Res, Sect A*. 1999;434(1):146–51.
25. Georgobiani AN. Wide-band II-VI semiconductors and the prospects of their application. *Soviet Phys Uspekhi*. 1974;17(3):424.
26. Gnatenko YP, Bukivskij PM, Piryatinski YP, Faryna IO, et al. The effect of impurity and intrinsic defects on the energy structure and dynamic of electronic processes CdTe:V and Cd<sub>1-x</sub>Hg<sub>x</sub>Te:V crystals. *Funct Mater*. 2008;15(1):23–9.
27. Greenberg JH, Guskov VN. Vapor pressure scanning of non-stoichiometry in Cd0.9Zn0.1Te1±δ and Cd0.85Zn0.15Te1±δ. *J Cryst Growth*. 2006;289(2):552–8.
28. Grinev BV, Ryzhikov VD, Seminozhenko VP. Scintillation detectors and radiation control systems based on them. Kyiv: Naukova dumka; 2007.
29. Holloway PH, McGuire GE. Handbook of compound semiconductors: growth, processing, characterisation, and devices. Park Ridge; 1995.
30. Kalinkin IP, Aleskovskij VB. Epitaxial films of A<sub>2</sub>B<sub>6</sub> compounds. Leningrad: LGU Publishing; 1978.
31. Kamae T. Developments in semiconductor detector technology and new applications—symposium summary. *Nucl Instrum Methods Phys Res, Sect A*. 1999;436(1–2):297–303.
32. Kang J. Thin film CdTe as high energy x-ray detector material for medical applications (PhD thesis, University of Toledo); 2008.
33. Kang S, Jung B, Noh S, Cho C, Yoon I, Park J. Feasibility study of direct-conversion x-ray detection using cadmium zinc telluride films. *J Instrum*. 2012;7(01):C01010.
34. Kasap S, Capper P. Springer handbook of electronic and photonic materials. Berlin: Springer; 2017.
35. Kikuma I, Furukoshi M. Formation of defects in zinc selenide crystals grown from the melt under argon pressure. *J Cryst Growth*. 1978;44(4):467–72.
36. Kikuma I, Matsuo M, Komuro T. Growth and properties of ZnSe crystals by a modified Bridgman method. *Jpn J Appl Phys*. 1991;30(11R):2718.
37. Kim TW, Park HL, Lee J. Structural and optical properties of a strained CdTeGaAs heterostructure grown by temperature-gradient vapor transport deposition at low temperature. *Thin Solid Films*. 1995;259(2):253–8.
38. Kim K, Cho S, Seo J, Won J, Hong J, Kim S. Type conversion of polycrystalline CdZnTe thick films by multiple compensation. *Nucl Instrum Methods Phys Res, Sect A*. 2008;584(1):191–5.
39. Kim K, Cho S, Suh J, Hong J, Kim S. Gamma-ray response of semi-insulating CdMnTe crystals. *IEEE Trans Nucl Sci*. 2009;56(3):858–62.
40. Kolesnikov NN, Timonina AV. An universal technology of wide band gap II-VI compounds growth. *Izvestija vysshshykh uchebnykh zavedenij. Materialy elektronnoi tekhniki*. 2010;2:24–8.
41. Koohpayeh SM. Single crystal growth by the traveling solvent technique: a review. *Prog Cryst Growth Charact Mater*. 2016;62(4):22–34.
42. Korbutyak DV. Cadmium telluride: impurity-defect states and detecting properties. Kyiv: Ivan Fedorov; 2000.
43. Kosyak V, Opanasyuk A, Bukivskij PM, Gnatenko YP. Study of the structural and photoluminescence properties of CdTe polycrystalline films deposited by close-spaced vacuum sublimation. *J Cryst Growth*. 2010;312(10):1726–30.
44. Kozlova OG. Growth and morphology of crystals. Moscow: Moscow State University Publishing; 1980.
45. Kreger F, et al. Chemistry of non-ideality crystals. Moscow: Mir; 1969.
46. Krustok J, Collan H, Hjelt K, Mäddasson J, Valdna V. Photoluminescence from deep acceptor-deep donor complexes in CdTe. *J Lumin*. 1997;72:103–5.
47. Kulchitskij NA, Naumov AV. The modern state of CdTe, ZnTe and Cd<sub>1-x</sub>Zn<sub>x</sub>Te fabrication. *Izvestija vysshshykh uchebnykh zavedenij. Materialy elektronnoi tekhniki*. 2010;2:17–24.

48. Kutniy DV, Prokhorets IM, Rybka AV, Nakonechny DV, et al. Technique for measuring electro-magnetic radiation by semiconductor detectors. Questions of atomic science and technology; 2006.
49. Kwon JS, Shin DY, Choi IS, Kim HS, Kim KH, et al. Growth of polycrystalline Cd<sub>0.8</sub>Zn<sub>0.2</sub>Te thick films for X-Ray detectors. *Phys Status Solidi B*. 2002;229(2):1097–101.
50. Lee HS, Lee KH, Kim JS, Park HL, Kim TW. Rapid thermal annealing effects on the optical properties in strained CdTe (100)/GaAs (100) heterostructures. *J Mater Sci*. 2004;39(23):7115–7.
51. Lowe BG, Sareen RA. Semiconductor X-ray detectors. Boca Raton: CRC Press; 2014.
52. Lund JC, Olsen R, Van Scyoc JM, James RB. The use of pulse processing techniques to improve the performance of Cd<sub>1-x</sub>Zn<sub>x</sub>Te gamma-ray spectrometers. *IEEE Nucl Sci Symp Med Imag Conf Rec*. 1995;1:126–30.
53. Mycielski A, Kowalczyk L, Gałazka RR, Sobolewski R, Wang D, Burger A, et al. Applications of II–VI semimagnetic semiconductors. *J Alloys Compd*. 2006;423(1–2):163–8.
54. Niraula M, Yasuda K, Uchida K, Nakanishi Y, Mabuchi T, Agata Y. MOVPE growth of thick CdTe heteroepitaxial layers for X-ray imaging detectors. *Phys Status Solidi C*. 2004;1(4):1075–8.
55. Niraula M, Yasuda K, Takagi K, Kusama H, Tominaga M, Yamamoto Y, Suzuki K. Development of nuclear radiation detectors based on epitaxially grown thick CdTe layers on n+-GaAs substrates. *J Electron Mater*. 2005;34(6):815–9.
56. Nishizawa H, Ikegami K, Takashima K, Usami T, Hayakawa T, Yamamoto T. Development of multi-layered CdTe semiconductor detectors. *Hoshasen*. 1996;22(3):27–36.
57. Novoselova AV, Lazarev VB. Physical and chemical properties of semiconductor substances: a reference. Moscow: Nauka; 1979.
58. Owens A, Peacock A. Compound semiconductor radiation detectors. *Nucl Instrum Methods Phys Res, Sect A*. 2004;531(1–2):18–37.
59. Owens A, Buslaps T, Gostilo V, Graafsma H, Hijmering R, Kozorezov A, et al. Hard X- and  $\gamma$ -ray measurements with a large volume coplanar grid CdZnTe detector. *Nucl Instrum Methods Phys Res, Sect A*. 2006;563(1):242–8.
60. Park SJ, Kim KH, Park YJ, Yuk SW, et al. X-ray response of Polycrystalline-CdZnTe. *IEEE Symp Conf Rec Nucl Sci*. 2004;7:4428–32.
61. Parsai EI, Shvydka D, Kang J. Design and optimisation of large area thin-film CdTe detector for radiation therapy imaging applications. *Med Phys*. 2010;37(8):3980–94.
62. Raiskin E, Butler JF. CdTe low level gamma detectors based on a new crystal growth method. *IEEE Trans Nucl Sci*. 1988;35(1):81–4.
63. Reno JL, Jones ED. Determination of the dependence of the band-gap energy on composition for Cd<sub>1-x</sub>Zn<sub>x</sub>Te. *Phys Rev B*. 1992;45(3):1440.
64. Rodríguez ME, Alvarado-Gil JJ, Delgadillo I, Zelaya O, et al. On the thermal and structural properties of Cd<sub>1-x</sub>Zn<sub>x</sub>Te in the range 0<x<0.3. *Phys Status Solidi A*. 1996;158(1):67–72.
65. Rohatgi A, et al. High efficiency cadmium and zinc telluride-based thin film solar cells, Final Subcontract Report DE91002112; 1990.
66. Romeo A. Growth and characterisation of high efficiency CdTe/CdS solar cells (Doctoral dissertation, ETH Zurich); 2002.
67. Rossa E, Bovet C, Meier D, Schmickler H, Verger L, et al. CdTe photoconductors for LHC luminosity monitoring. *Nucl Instrum Methods Phys Res, Sect A*. 2002;480(2–3):488–93.
68. Roy UN, Weiler S, Stein J, Cui Y, Groza M, Buliga V, Burger A. Zinc mapping in THM grown detector grade CZT. *J Cryst Growth*. 2012;347(1):53–5.
69. Roy U, Camarda G, Cui Y, Gul R, Hossain A, Yang G. Cadmium zinc telluride selenide (CdZnTeSe) a promising low cost alternative to cadmium zinc telluride (CdZnTe) for medical imaging and nuclear detector applications. New York: Brookhaven National Lab; 2017.
70. Roy UN, Camarda GS, Cui Y, Gul R, Yang G, Zazvorka J, et al. Evaluation of CdZnTeSe as a high-quality gamma-ray spectroscopic material with better compositional homogeneity and reduced defects. *Sci Rep*. 2019;9(1):1–7.

71. Rudolph P. Fundamental studies on Bridgman growth of CdTe. *Prog Cryst Growth Charact Mater.* 1994;29(1–4):275–381.
72. Rudolph P. Prosperity and difficulty of bulk crystal growth of semiconductor compound (a review). *Funct Mater.* 2007;14(4):411–25.
73. Rudolph P, Engel A, Schentke I, Grochocki A. Distribution and genesis of inclusions in CdTe and (Cd, Zn) Te single crystals grown by the Bridgman method and by the travelling heater method. *J Cryst Growth.* 1995;147(3–4):297–304.
74. Sakr GB, Yahia IS. Effect of illumination and frequency on the capacitance spectroscopy and the relaxation process of p-ZnTe/n-CdMnTe/GaAs magnetic diode for photocapacitance applications. *J Alloys Compd.* 2010;503(1):213–9.
75. Schenk M, Hähner I, Duong LTH, Niebsch HH. Validity of the lattice-parameter Vegard-rule in  $\text{Cd}_{1-x}\text{Zn}_x\text{Te}$  Solid Solutions. *Cryst Res Technol.* 1996;31(5):665–72.
76. Schlesinger TE. *Semiconductors for room temperature nuclear detector applications.* San Diego: Academic Press Inc; 1995.
77. Sellin PJ. Thick film compound semiconductors for X-ray imaging applications. *Nucl Instrum Methods Phys Res, Sect A.* 2006;563(1):1–8.
78. Sen S, Johnson SM, Kiele JA, Konkel WH, Stannard JE. Growth of large-diameter CdZnTe and CdTeSe boules for  $\text{Hg}_{1-x}\text{Cd}_x\text{Te}$  epitaxy: status and prospects. *MRS Online Proceedings Library (OPL).* 1989;161.
79. Sharma BL. *Semiconductor heterojunctions.* Moscow: Soviet Radio; 1979.
80. Shim M, Kim YM, Lee HH, Hong SJ, Lee JH. Separation behavior of impurities and selenium reduction by the reactive zone refining process using high-frequency induction heating to purify Te. *J Cryst Growth.* 2016;455:6–12.
81. Simashkevich AV. *Heterojunctions based on AII BVI semiconductor compounds;* 1980.
82. Singh HP, Dayal B. Lattice parameters and thermal expansion of zinc telluride and mercury selenide. *Acta Crystallogr Sect A: Cryst Phys, Diffraction, Theor Gen Crystallogr.* 1970;26(3):363–4.
83. Stolyarova S, Edelman F, Chack A, Berner A, Werner P, et al. Structure of CdZnTe films on glass. *J Phys D Appl Phys.* 2008;41(6):065402.
84. Strzałkowski K. The composition effect on the thermal and optical properties across CdZnTe crystals. *J Phys D Appl Phys.* 2016;49(43):435106–12.
85. Takahashi T, Watanabe S. Recent progress in CdTe and CdZnTe detectors. *IEEE Trans Nucl Sci.* 2001;48(4):950–9.
86. Takahashi J, Mochizuki K, Hitomi K, Shoji T. Growth of  $\text{Cd}_{1-x}\text{Zn}_x\text{Te}$  ( $x \sim 0.04$ ) films by hot-wall method and its evaluation. *J Cryst Growth.* 2004;269(2–4):419–24.
87. Thomas RN, Hobgood HM, Ravishankar PS, Braggins TT. Melt growth of large diameter semiconductors. *Solid State Technol.* 1990;33(5):121–8.
88. Tirado-Mejía L, Marín-Hurtado JI, Ariza-Calderón H. Influence of disorder effects on  $\text{Cd}_{1-x}\text{Zn}_x\text{Te}$  optical properties. *Phys Status Solidi B.* 2000;220(1):255–60.
89. Tobeñas S, Larramendi EM, Purón E, De Melo O, Cruz-Gandarilla F, et al. Growth of  $\text{Cd}_{1-x}\text{Zn}_x\text{Te}$  epitaxial layers by isothermal closed space sublimation. *J Cryst Growth.* 2002;234(2–3):311–7.
90. Tokuda S, Kishihara H, Adachi S, Sato T. Improvement of the temporal response and output uniformity of polycrystalline CdZnTe films for high-sensitivity X-ray imaging. In: *Medical Imaging 2003: Physics of Medical Imaging*, Vol. 5030; 2003, pp. 861–870.
91. Tokuda S, Kishihara H, Adachi S, Sato T. Preparation and characterisation of polycrystalline CdZnTe films for large-area, high-sensitivity X-ray detectors. *J Mater Sci Mater Electron.* 2004;15(1):1–8.
92. Toney JE, Schlesinger TE, James RB. Modeling and simulation of uniformity effects in  $\text{Cd}_{1-x}\text{Zn}_x\text{Te}$  gamma-ray spectrometers. *IEEE Trans Nucl Sci.* 1998;45(1):105–13.
93. Triboulet R, Marfaing Y. Growth of high purity CdTe single crystals by vertical zone melting. *J Electrochem Soc.* 1973;120(9):1260.

94. Triboulet R, Siffert P. CdTe and related compounds; physics, defects, hetero- and Nanostructures, crystal growth, surfaces and applications: physics, CdTe-based nanostructures, CdTe-based Semimagnetic Semiconductors, defects. Elsevier; 2009.
95. Trivedi SB, Wang CC, Kutcher S, Hommerich U, Palosz W. Crystal growth technology of binary and ternary II–VI semiconductors for photonic applications. *J Cryst Growth*. 2008;310(6):1099–106.
96. Turkevych I. High temperature properties of CdTe (Doctoral dissertation, Prague); 2004, 188 p.
97. Verger L, Baffert N, Rosaz M, Rustique J. Characterisation of CdZnTe and CdTe: Cl materials and their relationship to X- and  $\gamma$ -ray detector performance. *Nucl Instrum Methods Phys Res, Sect A*. 1996;380(1–2):121–6.
98. Won JH, Kim KH, Suh JH, Cho SH, Cho PK, et al. The X-ray sensitivity of semi-insulating polycrystalline CdZnTe thick films. *Nucl Instrum Methods Phys Res, Sect A*. 2008;591(1):206–8.
99. Wu X. High-efficiency polycrystalline CdTe thin-film solar cells. *Sol Energy*. 2004;77(6):803–14.
100. Xu H, Xu R, Huang J, Zhang J, Tang K, Wang L. The dependence of Zn content on thermal treatments for Cd<sub>1-x</sub>Zn<sub>x</sub>Te thin films deposited by close-spaced sublimation. *Appl Surf Sci*. 2014;305:477–80.
101. Yang G, Bolotnikov AE, Camarda GS, Cui Y, Hossain A, Yao HW, James RB. Internal electric field investigations of a cadmium zinc telluride detector using synchrotron x-ray mapping and Pockels effect measurements. *J Electron Mater*. 2009;38(8):1563–7.
102. Yazdi S, Alinejad M, Tajabor N. Growth of Cd<sub>0.96</sub>Zn<sub>0.04</sub>Te single crystals by vapor phase gas transport method. *Iran J Phys Res*. 2006;6(1):1–5.
103. Zaiour A, Ayoub M, Hamié A, Fawaz A, Hage-ali M. Preparation of high purity CdTe for nuclear detector: electrical and nuclear characterisation. *Phys Procedia*. 2014;55:476–84.
104. Zanio K. Semiconductors and semimetals. New York: Academic Press; 1978.
105. Zaveriukhin BN, et al. Film detectors of nuclear irradiation based on cadmium telluride. *Tech Phys Lett*. 2003;29(22):80–7.
106. Zhang N, Yeckel A, Burger A, Cui Y, Lynn KG, Derby JJ. Anomalous segregation during electrodynamic gradient freeze growth of cadmium zinc telluride. *J Cryst Growth*. 2011;325(1):10–9.
107. Zhou H, Zeng D, Pan S. Effect of Al-induced crystallisation on CdZnTe thin films deposited by radio frequency magnetron sputtering. *Nucl Instrum Methods Phys Res, Sect A*. 2013;698:81–3.

# Chapter 3

## ZnS-Based Neutron and Alpha Radiation Detectors



Ghenadii Korotcenkov and Michail Ivanov

### 3.1 Introduction

Neutrons are subatomic elemental particles with no electric charge and approximately the same mass as a proton. Neutron has a rest mass  $m_n = 1.008665$  Da, spin  $S = \hbar/2$  (intrinsic mechanical moment), and magnetic moment  $\mu_n = -1.9130 \mu_N$ , where  $\mu_N$  is a nuclear magneton. It has a huge internal field and zero external. The neutron has an electromagnetic bound mass in the form of a conglomerate of an electron and a proton with a zero external electric field. Free neutrons are one kind of ionizing radiation.

The sources of neutron are:

1. Radionuclide sources based on spontaneous fission of radionuclides or various nuclear reactions.
2. Nuclear reactors. The generation of neutrons occurs in the process of controlling a chain reaction in a nuclear reactor based on the fission of heavy nuclei  $^{235}\text{U}$ ,  $^{239}\text{Pu}$  with an average energy of  $\approx 2.0$  MeV.
3. Accelerators of charged particles. As a result of the collision of charged particles with energies of hundreds of MeV, neutrons are generated.
4. Another source of neutrons is the impact of high-energy cosmic rays on atoms high in the atmosphere.

Different sources produce neutrons with different energies. Neutrons emitted from an atomic nucleus by fission or alpha particle bombardment have a broad distribution of energies, anywhere from about 0.01 to 15 MeV, though most have energies between 0.5 and 5 MeV. Different classifications exist, an example of one is given in Table 3.1. The given values of the boundary energies are, of course, rather conditional. Moreover, it is generally considered that the neutrons are “slow” when

---

G. Korotcenkov (✉) · M. Ivanov

Department of Physics and Engineering, Moldova State University, Chisinau, Moldova

**Table 3.1** Classification of neutron in function of the energy ranges

Category	Energy	Average wavelength, cm
Ultracold	$<10^{-7}$ eV	$9.10^{-6}$
Cold	$10^{-7}$ – $5.10^{-3}$ eV	$9.10^{-8}$
Thermal	$5.10^{-3}$ – $0.1$ eV	$2.10^{-8}$
Epithermal	$0.1$ – $10$ eV	$3.10^{-10}$
Intermediate	$10$ eV– $100$ keV	$3.10^{-11}$
Fast	$100$ keV– $100$ MeV	$<10^{-12}$
High-energy	$>100$ MeV	$<10^{-13}$

Source: Data extracted from Aza et al. [3]

**Table 3.2** Moderating powers and ratios of selected materials

Moderator	Moderating ratio
Water (H <sub>2</sub> O)	58
Heavy water (D <sub>2</sub> O)	21,000
Graphite (C)	200
Polyethylene	122

Source: Data extracted from Ref. [29]

they have a kinetic energy of less than 0.5 eV (cadmium cut-off energy) and “fast” when they have energy higher than this value.

As stated earlier, when neutrons are emitted from a nucleus, they typically have an energy of a few MeV and a speed that is a few percent of the speed of light [68]. These fast neutrons tend to pass through most materials without being absorbed, but when they collide with nuclei, they lose some of their energy and speed with each collision. The process of slowing down neutrons in multiple collisions is called moderation. Neutrons lose the most energy when colliding with light nuclei such as the hydrogen nucleus. Water and most plastics contain a lot of hydrogen, and these materials are also good neutron moderators (Table 3.2). After several tens of collisions with hydrogen nucleus in the moderator, the neutrons are slowed down to speeds close to the speed of atomic vibrations from thermal motion. Such slow neutrons are called thermal neutrons. Thermal neutrons are much easier to detect than fast neutrons. Therefore, in studies of condensed matter, slow neutrons are mainly used

There are currently seven main application areas where neutron detectors are required. They are listed below [58]:

1. *Fusion*: Neutron detection and neutron spectrometry provide fusion specialists with a valuable set of diagnostic tools to analyze the state of the plasma [26].
2. *Nuclear power*: modernization of the design and operation of reactors. Neutron detectors make it possible to “display” the spatial distribution of the neutron flux in the reactor core [61].

3. *Security*: control of arms and radioactive materials, monitoring of storage sites for nuclear fuel waste, and movement of radioactive materials across the borders of states, as well as decontamination and decommissioning of nuclear power facilities [20, 84].

The primary purpose of neutron detection for national security is to help identify nuclear threats and distinguish materials used in “dirty bombs” from other radioactive materials such as industrial, medical, and natural sources of gamma radiation. One important reason for detecting neutrons is that gamma rays from special nuclear materials (SNM) can be shielded. Gamma rays from plutonium are mostly low energy and can be absorbed by less than an inch of lead or other heavy metals, shielding the SNM from gamma detection. Neutrons are not absorbed by these materials, so lead-shielded plutonium can still be detected by neutron emission. Of course, neutrons can also be shielded by neutron-moderating materials such as plastic and water, but this requires too thick layers of these materials.

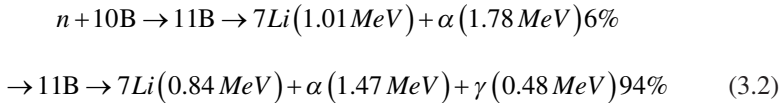
4. *Fundamental science*: study of cross sections for nuclear reactions, dark matter, exotic nuclei, neutron beams, and space physics, including antineutrino experiments [5, 19, 21]. For example, neutron detectors can be used in high-energy physics as part of ionization calorimeters to detect neutrons produced by the interaction of high-energy particles (electrons and/or hadrons) with the material of the calorimeter.
5. *Dosimetry*: personnel protection, radiotherapy (medicine) [44].
6. *Applied research*: study of material properties using neutron scattering, diffraction, radiography, and tomography [51, 65].
7. Industrial application: petroleum industry, construction, and agriculture.

## 3.2 Neutron Detection

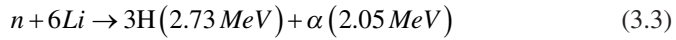
Neutrons do not have an electric charge and do not leave traces (tracks) of ionized and excited particles, the appearance of which is detected by most particle detectors. However, the interaction of neutrons with the substance of the detector can cause a variety of nuclear reactions with the formation of charged particles and  $\gamma$ -quanta. This secondary radiation can already be detected by conventional detectors. To detect neutrons, various types of neutron-nucleus interactions can be used. However, reactions of interaction of neutrons with three isotopes are usually used for these purposes. These isotopes include helium-3 ( $^3\text{He}$ ), lithium-6 ( $^6\text{Li}$ ), and boron-10 ( $^{10}\text{B}$ ) [68]. The concentration of these isotopes in nature is 0.00014%, 7.50%, and 19.80% for  $^3\text{He}$ ,  $^6\text{Li}$ , and  $^{10}\text{B}$ , respectively.



$$5333 \text{ barn} @ 1.8 \text{ \AA} \sim 0.025 \text{ eV}$$



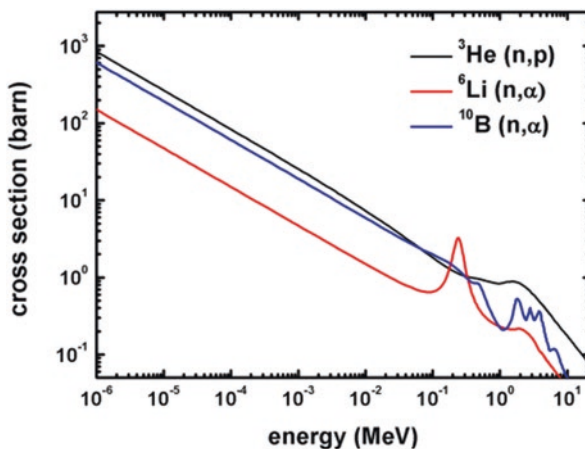
3838 barn @ 1.8 Å



941 barn @ 1.8 Å

The choice of  ${}^3\text{He}$ ,  ${}^6\text{Li}$ ,  ${}^{10}\text{B}$  nuclei as a converter is due to the large neutron capture cross section of these nuclei (Fig. 3.1). There are a few isotopes of elements that absorb thermal neutrons about 1000 times more than most materials do. Table 3.3 provides the examples of cross sections for capture of thermal neutrons ( $\sim 0.025\text{ eV}$ ) for common isotopes used in neutron detection.

As we can see, the interaction of neutrons with isotopes  ${}^3\text{He}$ ,  ${}^6\text{Li}$ , and  ${}^{10}\text{B}$  is accompanied by the formation of charged alpha particles ( ${}^4\text{He}$ ), triton ( ${}^3\text{H}$ ), and  $\gamma$ -quanta (during the interaction of neutrons with  ${}^{10}\text{B}$ ). Consequently, the neutron detector, in addition to the converter, whose nucleus interacting with neutrons generate charged particles and  $\gamma$ -quanta, must contain a detector that registers them. It is important to note that these reactions (3.1, 3.2, and 3.3), which are exothermic and proceed with heat release, are maximally efficient only at thermal neutron energies ( $5 \times 10^{-3} - 0.5\text{ eV}$ ). As the neutron energy  $E_n$  increases, the efficiency decreases:  $\varepsilon \sim 1/(E_n)^{1/2}$  for  $E_n < 0.1\text{ MeV}$ . Therefore, if there are fast neutrons in the radiation, then to register them, neutron detectors are surrounded by a hydrogen-containing substance, in which neutrons are moderated (read Sect. 3.8)



**Fig. 3.1** Cross section as a function of incident neutron energy for  ${}^3\text{He}$  (n,p),  ${}^6\text{Li}$  (n,α), and  ${}^{10}\text{B}$  (n,α) reactions. (Reprinted from <http://atom.kaeri.re.kr/cgi-bin/endlplot.pl>)



**Table 3.3** Thermal neutron capture cross sections for isotopes common to neutron detection

Isotope	Cross section, barns	
	Capture	Scattering
Hydrogen-1	0.33	30
Helium-3	5300	3.9
Lithium-6	940	0.78
Boron-10	3800	2.3
Cadmium-113	20,000	25
Gadolinium-157	250,000	1000

### 3.3 Scintillation Detectors

Currently, neutron detectors can be grouped into four main classes: gas detectors, scintillation detectors, proportional detectors, and semiconductor detectors. Each of them has its own advantages and disadvantages. At present, proportional counters based on helium-3 are the most common as thermal neutron detectors. They consist of large area  $^3\text{He}$  counters, usually of two tubes, 2 meters long per module [33]. The great advantage of this type of detector is a large cross section for  $^3\text{He}$  (n,p) reaction over a wide range of neutron energy (the cross section for 0.025 eV neutron energy is 5330 barns), as well as negligible sensitivity to gamma-rays, which is a problem only in a very large radiation field.  $^3\text{He}$  counters are simple in design and are characterized by a stability over a wide range of environmental conditions, not being degraded over years of operation. Today,  $^3\text{He}$  counter is the standard for calibrating other neutron detectors

Despite a number of advantages, such as insensitivity to gamma radiation, a rather high efficiency of thermal neutron detection (~60–90%), solid-state thermal neutron detectors based on various scintillators are beginning to play an increasingly important role [34]. The reason for this substitution of  $^3\text{He}$  counters by scintillator detectors is the sharply increased deficit of the  $^3\text{He}$  isotope after 2001 due to the crisis in its production. Other disadvantages of helium-based neutron counters include (i) leakage of helium from existing counters, leading to temporary parameter instability, (ii) the high price of helium counters (the price of helium has risen from \$100 to \$2000 per liter in recent years), and (iii) the need for high voltage sources to operate the detectors

The luminescent method of dosimetry is based on the ability of ionizing radiation to excite the atoms and molecules. The transition of atoms and molecules from an excited state to the ground state is accompanied by the emission of light (visible or ultraviolet). This phenomenon is called luminescence, the substances in which luminescence occurs are called phosphors or scintillators, and devices using this effect are called scintillation detectors [34]. The scintillation method of particle registration is one of the oldest registration methods. As early as 1919, in experiments on the scattering of charged particles by nuclei, E. Rutherford and coworkers

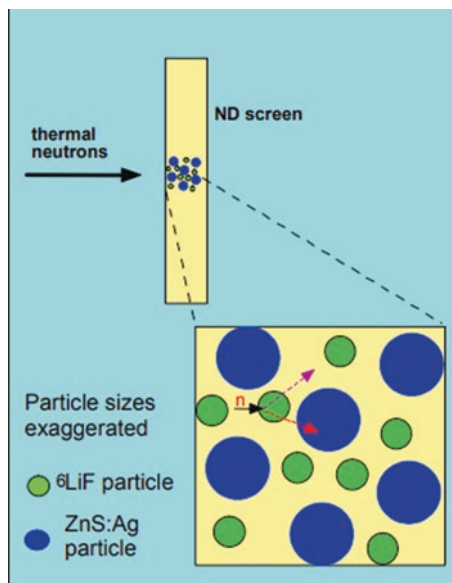
registered  $\alpha$ -particles by visually observing flashes of light in ZnS(Ag). However, the scintillation method for detecting particles was widely developed only after the invention of photomultiplier tubes (PMT), devices capable of detecting weak flashes of light. As a rule, the number of photons emitted is approximately proportional to the energy absorbed by the scintillator, which makes it possible to obtain radiation energy spectra. Scintillation detectors also compare favorably with gas discharge counters in response speed [34]

All scintillators can be divided into three classes: organic, inorganic, and gaseous [34, 43]. Of the organic compounds, liquid and solid solutions of aromatic compounds or single crystals of anthracene, stilbene, tolane, etc. are most often used. Organic scintillators have much shorter flash times (on the order of a few to tens of nanoseconds) compared to inorganic ones (tenths of microseconds), but they have a lower light yield. Light yield is the number of photons emitted by the scintillator when a certain amount of energy is absorbed. Gas scintillators also have flash times in the nanosecond range. However, the light yield in gas scintillators due to the low density of gases is relatively low even in comparison with organic scintillators

With regard to inorganic scintillators, three types of scintillators are commonly used to detect thermal neutrons [81, 89]. These are a GS20(Ce) glass scintillator, europium-activated lithium iodide ( ${}^6\text{LiI}(\text{Eu})$ ), and a ZnS(Ag)/ ${}^6\text{Li}$  scintillator. The ZnS(Ag)/ ${}^6\text{Li}$  scintillator is a granular compressed mixture of ZnS(Ag) and  ${}^6\text{Li}$ . The parameters of scintillators based on these materials are given in Table 3.4. All of these materials use  ${}^6\text{Li}$ , which has a large thermal neutron absorption cross section (see Fig. 3.1) and enters into the  $(n,\alpha)$  reaction when neutrons are absorbed. As shown in reaction (3.3), the absorption process leads to the decay of  ${}^6\text{Li}$  with the formation of charged alpha particles and tritons. The large  $Q$  value of this reaction ( $Q = 4.8$  MeV) is released in the form of the kinetic energy of the reaction products (alpha particles and tritons), which provides a significant “per act” energy transfer in the scintillator during their interaction. Detectors based on a glass scintillator have a high neutron detection efficiency and a good pulse pair resolution of  $\sim 70$  ns. However, they have both a high sensitivity to gamma radiation and a high intrinsic detector background. In contrast, ZnS/ ${}^6\text{Li}$  scintillation detectors can exhibit both extremely low gamma sensitivity and inherent detector background. However, the 2  $\mu\text{s}$  resolution of the pulse pair of these detectors is only moderate. The processes occurring in the  ${}^6\text{LiF}/\text{ZnS}(\text{Ag})$  neutron detection screen are shown in Fig. 3.2. As for  ${}^6\text{LiI}(\text{Eu})$ , the crystals of this scintillator are hygroscopic and require sealing. In addition, the  ${}^6\text{LiI}(\text{Eu})$  scintillator is less sensitive than the  ${}^6\text{LiF}/\text{ZnS}(\text{Ag})$  scintillator

**Table 3.4** Classical slow neutron detectors

Material	${}^6\text{Li}$ atom concentration, $\text{cm}^{-3}$	Scintillator efficiency	Photon wavelength, nm	Neutron light yield (ph/n)	Decay time, ns
${}^6\text{Li}$ -glass (Ce)	$1.75 \times 10^{22}$	0.45%	395	$\sim 7000$	70
${}^6\text{LiI}(\text{Eu})$	$1.83 \times 10^{22}$	2.8%	470	$\sim 51,000$	1400
${}^6\text{LiF}/\text{ZnS}$	$1.18 \times 10^{22}$	5–9.2%	450	$\sim 160,000$	100–1000



**Fig. 3.2** Diagrammatic representations of physical processes occurring in a physical processes occurring in a  ${}^6\text{LiF}/\text{ZnS}$  neutron detection screen. (Reprinted from <https://scintacor.com/>)

The choice of  ${}^6\text{LiF}$  and  $\text{ZnS}(\text{Ag})$  for use in a neutron detector is based on the fact that each component in this mixture represents “best in class” performance (i.e., neutron absorption and luminescence, respectively). In the case of neutron absorption, the  $\text{LiF}$  crystal structure offers one of the highest densities of  $\text{Li}$  active sites in the solid state and therefore maximizes the probability of interacting with a neutron when it is enriched in  ${}^6\text{Li}$ . The relative content of  ${}^6\text{Li}$  in nature is 7.59% and the highest content of  ${}^6\text{Li}$  in  $\text{LiF}$  is currently 95%. Usually, this material is used in a neutron detector. In a number of works, when developing neutron detectors, instead of  ${}^6\text{LiF}$ ,  ${}^{10}\text{B}$  is used in the form of  ${}^{10}\text{B}_2\text{O}_3$  [9] or  $\text{H}_3{}^{10}\text{BO}_3$  [35]. Compared to  ${}^{10}\text{B}$ , the thermal neutron capture cross section of  ${}^6\text{Li}$  is about 4 times lower, but the energy released in the nuclear reaction (3.3) involving  ${}^6\text{Li}$  is 1.73 times greater than in the nuclear reaction (3.2) involving  ${}^{10}\text{B}$ . An additional advantage of reaction (3.3) involving  ${}^6\text{Li}$  is the absence of a gamma background. The advantages of the  $\text{ZnS}(\text{Ag})/{}^{10}\text{B}_2\text{O}_3$  scintillator include the fact that the content of the  ${}^{10}\text{B}$  isotope in natural boron is about 20%. This means that enrichment with the  ${}^{10}\text{B}$  isotope may not be used to develop the boron light composition, which greatly simplifies the fabrication process.

With regard to luminescence,  $\text{ZnS}(\text{Ag})$  is one of the brightest known phosphors (see Fig. 3.3) and remains unsurpassed in its emission under the action of alpha particles and tritons (i.e., the products of neutron capture by  ${}^6\text{Li}$ ) [42]. To improve fluorescence,  $\text{ZnS}$  is doped with  $\text{Ag}$  atoms, which act as an activator.  $\text{ZnS}(\text{Ag})$  has a very efficient emission due to the donor-acceptor transition: the donor level is due to the addition of aluminum or chlorine, and the acceptor level is due to silver [8].

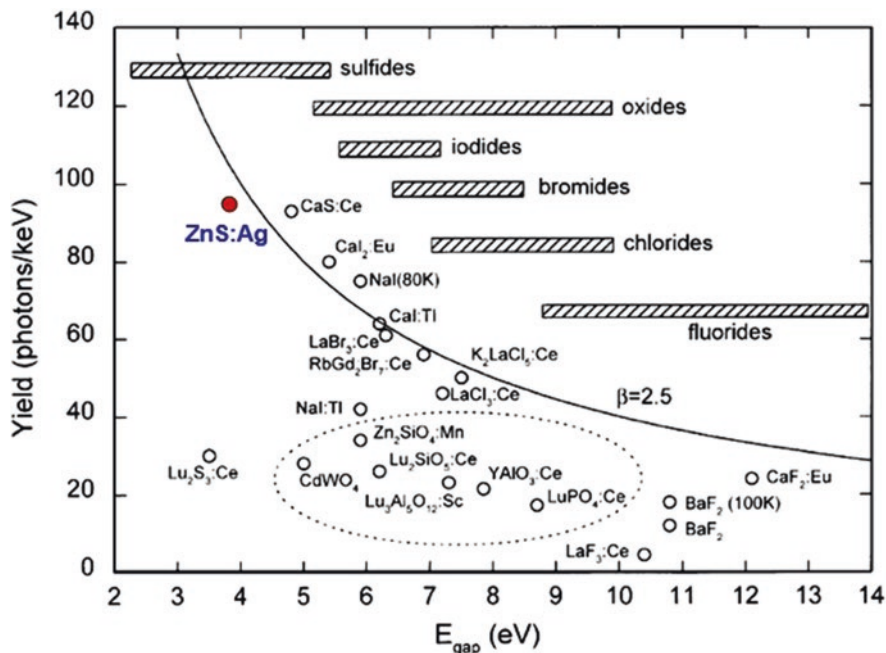


Fig. 3.3 Light yield of scintillators and cathode ray tube phosphors. (Reprinted with permission from Dorenbos [17]. Copyright 2002: Elsevier)

If we analyze the available information, it turns out that most of the personal alpha monitors (PAM) that are used in laboratories for the detection of alpha particles are built from ZnS(Ag) due to its potentially large area and low cost. ZnS is also widely used in its undoped form in “glow in the dark” paints and products due to its long lasting phosphorescence. It should be noted that in some cases ZnS(Cu) is used instead of ZnS(Ag). ZnS(Cu) is also a good phosphor that emits in the longer wavelength region of the spectrum. If the emission maximum of the ZnS:Ag scintillator is at a wavelength of  $\sim 450$  nm, then for ZnS(Cu) the emission maximum is observed at a wavelength of  $\sim 520$  nm.

The process of interaction of charged particles with ZnS can be described as follows (see Fig. 3.4). Charged particles move in the phosphor material for several tens of microns (approximately 6–12  $\mu\text{m}$  for  $\alpha$  particles and 30–70  $\mu\text{m}$  for triton [93] in opposite directions). These particles scatter on ZnS(Ag) atoms, leading to excitation or ionization. The resulting free charge carriers will cause secondary and tertiary free carriers as they thermalize at the bottom of the conduction band. The population of free carriers migrates in the conduction band until it is captured by the luminescent center, which then relaxes to form a photon [66, 67]. The content of  ${}^6\text{LiF}$  in the  ${}^6\text{LiF}/\text{ZnS:Ag}$  composite can vary within 10–60% of the mass used. For example, the 70% efficient thermal neutron counter, developed by Marin et al. [38], contained up to 42%  ${}^6\text{LiF}$  in the composite. The fact that the detector uses a thin scintillator

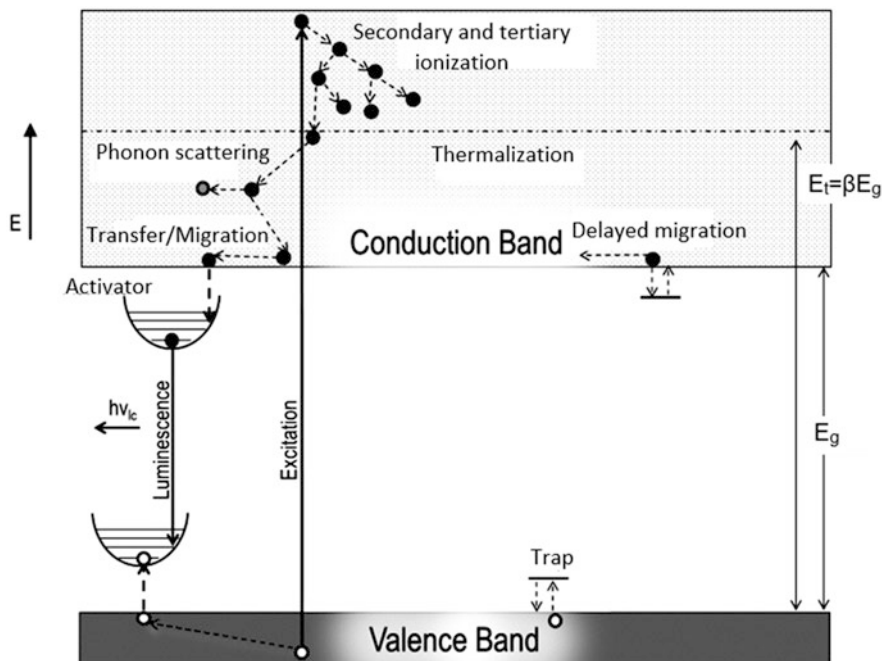


Fig. 3.4 Schematic of scintillation process in inorganic crystal via impurities/defects. (Idea from Castle [10])

layer with a relatively low  $Z$  causes its extremely low sensitivity to gamma radiation. The estimates made show that the  $\text{ZnS}(\text{Ag})/{}^6\text{LiF}$  scintillator has a sensitivity to gamma quanta at a level of  $10^{-6}$  [85] and a light yield of  $\sim 95,000\text{--}160,000$  photons per neutron [59]. This is due to the fact that in  $\text{ZnS}(\text{Ag})$  the formation of one photon requires 27 eV, while  $\alpha$ -particles have an energy of more than 4 MeV (reaction 3.3). As a result, in a suitably designed detector, the ionization caused by charged  $\alpha$ -particles and triton can make a signal that is distinctly larger than the signal from electrons produced by gamma rays. Therefore, if a large signal is detected, it is counted as a neutron; if the signal is small, it is either ignored or counted separately as a gamma ray. Thus, the combination of  ${}^6\text{LiF}$  and  $\text{ZnS}:\text{Ag}$  forms a neutron scintillator composite (NSC) material with exceptional efficiency.

Of course, when developing a neutron scintillator, it would be possible to use  $\text{ZnS}$  single crystals with better luminescent properties, on the surface of which a  ${}^6\text{LiF}$ ,  ${}^{10}\text{B}_2\text{O}_3$ , or  $\text{H}_3{}^{10}\text{BO}_3$  converting layer was deposited [41]. But, the solution of many problems of radiation registration requires large-area scintillators. The manufacture of detectors of this type from single crystals is a very difficult task, requiring significant material costs, since there is no well-established technology for growing  $\text{ZnS}$  single crystals of the required sizes. This problem can be solved by using a scintillation matrix of single crystals. However, in this case, it is impossible to avoid the laborious selection of matrix elements, which must be uniform in their

scintillation parameters. The experiment showed that the best way out of this situation is to use the neutron scintillator composite material discussed above. In addition, composite facilitates the transfer of energy from the converter to the scintillator. However, it must be said that layer-by-layer deposition of a scintillator and a converter is in some cases used to expand the functionality of commercial ZnS(Ag) screens. For example, Morris et al. [46] used commercial ZnS(Ag) screens ([www.eljentechnology.com](http://www.eljentechnology.com)) with  $3.25 \pm 0.25$  mg/cm<sup>2</sup> phosphor, vacuum-coated with  $20 \pm 5$  nm boron enriched up to 95% <sup>10</sup>B, for ultracold neutron (UCN) detection. They found that the thinner <sup>10</sup>B coating provided higher efficiency and several times more light than ~120 nm thick coatings.

Unfortunately, the neutron scintillator composite, when composed of such granular mixtures, is subject to optical loss due to light scattering at internal interfaces and absorption of light as it passes through the composite. The latter is facilitated by ZnS:Ag, which itself can absorb its own luminescence. Since the ZnS:Ag scintillator is weakly transparent to its own luminescent radiation, the light radiation coming out only from its surface layer is actually recorded. These loss mechanisms cause restrictions on the thickness of the scintillator screen: an increase in the thickness of the composite material above a certain threshold value (for example, about 0.3–0.5 mm for <sup>6</sup>LiF/ZnS:Ag mixtures) does not provide additional light yield, despite the additional neutron absorption capacity.

There is another problem with the ZnS(Ag)/<sup>6</sup>LiF scintillator. Since the refractive index of light for most scintillators is quite large, a significant part of the light that arises in the scintillator experiences total internal reflection on its surface. The refractive index for a ZnS crystal is about 2.4, and for LiF about 1.3. Therefore, to ensure good optical contact (and, consequently, to increase light collection), a binder material can be added to the composite that is transparent in the range of wavelengths of photons emitted by the scintillator and has a certain refractive index, consistent with the material of the neutron scintillator. This significantly reduces internal absorption and scattering, thus enhancing the light yield of the neutron scintillator. As a result, the number and intensity of optical pulses reaching the photosensitive element increase, which, in turn, significantly improves the efficiency of neutron detection. Such a binder may be polymethylmethacrylate (C<sub>5</sub>O<sub>2</sub>H<sub>8</sub>)<sub>n</sub>, polydimethylsiloxane (C<sub>2</sub>H<sub>6</sub>OSi), or polyethylene (C<sub>2</sub>H<sub>4</sub>).

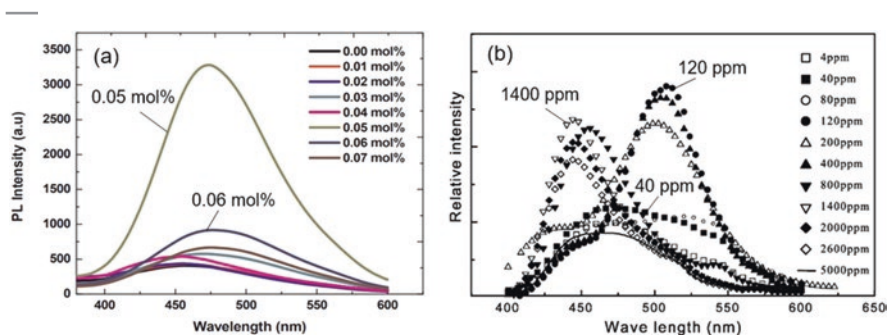
Regarding the particle sizes of ZnS(Ag) and <sup>6</sup>LiF in the ZnS(Ag)/<sup>6</sup>LiF composite, it is considered that 5–9 μm for ZnS, 0.6–0.8 μm for LiF, and less than 2 μm for H<sub>3</sub><sup>10</sup>BO<sub>3</sub> particles are optimal [10, 35]. When these conditions were met, a noticeable improvement in the light yield and an increase in the efficiency of thermal neutron detection were observed. The experiment showed that the particle size of the <sup>6</sup>LiF converter (0.6–0.8 μm) provides a high probability of neutron absorption and a high yield of secondary radiation. At a converter particle size below 0.6 μm, the probability of neutron absorption in the converter decreases, and an increase in the <sup>6</sup>LiF grain size above 0.8 μm leads to a decrease in the light yield and energy of secondary radiation (α-particles and tritons). This takes place due to absorption of α-particles and tritons in LiF grains, even before they will fall into the scintillator. This leads to a decrease in the efficiency of neutron detection. The particle size of

the ZnS(Ag) scintillator of 7–9  $\mu\text{m}$  provides a large proportion of the energy loss of  $\alpha$ -particles in the scintillator and, as a result, a high light yield. The experimental data correlate well with the computer simulation data given in [10].

### 3.4 ZnS-Based Phosphors

Manufacturers of ZnS-based scintillators do not describe the technology of synthesis and post-synthesis treatments of ZnS(Ag) particles. However, based on the available information, it can be concluded that in order to achieve a high efficiency of neutron detectors, the ZnS(Ag) particles used to manufacture the scintillator must be optically transparent, have high luminescence efficiency, low decay time, and high temporal stability of parameters. Many studies have been carried out to solve these problems. They showed that ZnS(Ag)-based phosphores used in the fabrication of neutron detectors can be synthesized using a wide variety of methods [18] from chemical vapor deposition (CVD) [40], solid state procedure [36], sol-gel technology [69] and chemical precipitation [16, 60], to hydrothermal technique [23]. A description of these technologies can be found in Chap. 11 (Vol. 1). ZnS scintillator is conventionally made by adding  $\text{AgNO}_3$  and  $\text{NH}_4\text{Cl}$  to make ZnS:Ag,Cl, resulting in blue emission (2.80 eV, 450 nm) [91] with a decay time of 5 ns ( $\gamma$ -ray) to 100 ns ( $\alpha$ -particle) [7].

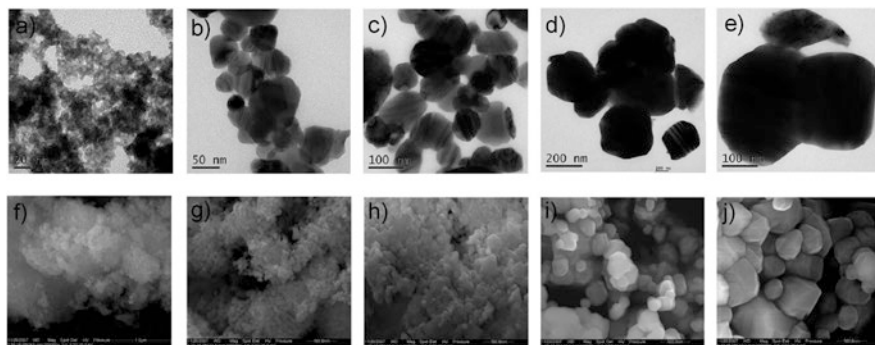
The optimal concentration of Ag in ZnS is usually at the level of 0.05 mol% [1, 4]. This concentration provides the best luminescent properties of the synthesized ZnS(Ag) (see Fig. 3.5a). With a deviation towards a greater or lesser concentration of the activator, the luminescence intensity decreases. The same situation is observed when doping ZnS with Cu. When doped with copper, the maximum photoluminescence was also observed at doping concentrations below 0.25% [48]. For example, Kotera and Naraoka [32] studied ZnS(Ag) and ZnS(Cu) with activator



**Fig. 3.5** (a) PL spectra for ZnS doped with different concentration of Ag. (Reprinted with permission from Ref. [1]. Copyright 2018: Elsevier); (b) The cathodoluminescence spectra of ZnS:Cu:Cl phosphors with various Cu-doped concentrations. (Reprinted with permission from Ref. [12]. Copyright 2001: Elsevier)

concentration varying between 0.1 and 0.0001 mol%. In the ZnS(Cu) samples studied by Davies et al. [16], the concentration of Cu was 0.01–0.005 mol.%. As we can see in Fig. 3.5b, the maximum luminescence at a wavelength of  $\sim 520$  nm is observed for samples with a Cu concentration of 120 ppm, which corresponds to 0.012% [12]. As the Cu concentration increases, the luminescence maximum shifts to the short wavelength region, and its intensity decreases. However, it should be noted that there are also works in which the decrease in the ZnS(Cu) photoluminescence intensity begins at a Cu concentration exceeding 2% [57].

To stabilize properties, control grain sizes, and improve optical transparency, the synthesized material is typically annealed at 800–1200 °C [11, 16, 32]. Annealing is accompanied by an increase in crystallite size (see Fig. 3.6), which starts at  $T \sim 400$  °C and accelerates at  $T > 600$  °C [82]. When choosing the optimal annealing conditions, the luminescence intensity increases as well [92]. Lu and Chu [36] observed the maximum photoluminescence of ZnS after annealing at  $T = 1100$  °C. Annealing also makes persistent phosphorescence shorter [32, 82]. Annealing in an oxygen containing atmosphere was accompanied by the formation of ZnO and a decrease in the luminescence intensity [74]. Therefore, in order to exclude the oxidation and transformation of ZnS into ZnO, annealing is carried out in an atmosphere of an inert gas (Ar, N<sub>2</sub>) or an atmosphere containing sulfur vapor. For example, in [77], samples of ZnS(Ag) and ZnS(Cu) were fired at 1020 °C for 40 min in argon atmosphere. To improve the temporal stability of ZnS:Ag phosphors, it is also proposed to use a surface coating with a thin layer of In<sub>2</sub>O<sub>3</sub> or ITO (In<sub>2</sub>O<sub>3</sub>:Sn) [55, 70]. Surface encapsulation also makes it possible to reduce the amount of sulfur species out-gassing from the ZnS and thus reduce the degradation of ZnS:Ag phosphorus [55]. At that, Souriau et al. [70] note that when solving the problem of stability of phosphors, one has to find a compromise between luminous efficiency and stability.



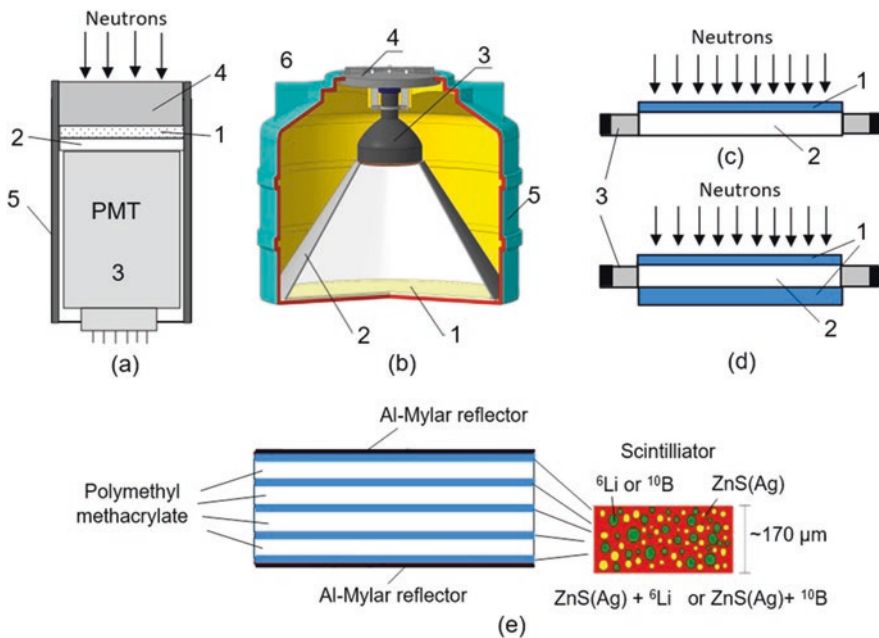
**Fig. 3.6** (a–e) TEM and (f–j) SEM images of ZnS NCs (f) samples after annealing: (a, g) –  $T_{\text{an}} = 600$  °C, (b, g) –  $700$  °C, (d, i) –  $800$  °C, (e, j) –  $900$  °C. (Reprinted with permission from Ref. [82]. Copyright 2011: RSC)



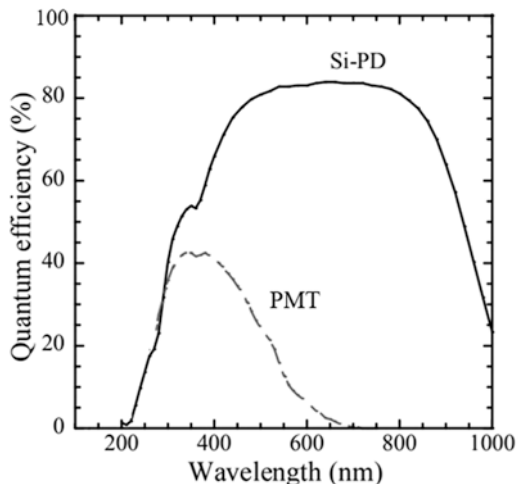
### 3.5 Neutron Detectors

Scintillator-based neutron detectors can be configured in a variety of ways. The main elements of such detectors are a scintillator, a photomultiplier tube (PMT) or a semiconductor photodetector that converts the emitted light into a current pulse, and an optical system for combining the scintillator and photodetector. Some examples of neutron detectors are shown in Fig. 3.7.

As a photoreceiving device in neutron detectors, PMTs are mainly used, the spectral sensitivity of which is matched with the emission wavelength of the scintillator. But there are also devices using silicon avalanche photodiodes (Si-APD),



**Fig. 3.7** (a) The design of a neutron detector with a small effective working area using a moderator: 1 – scintillator, 2 – light guide-light mixer, which simultaneously serves as a neutron reflector, 3 – PMT, 4 – polyethylene moderator, 5 – polyethylene case; (b) Design of a neutron detector with an increased sensitive area: 1 – ZnS(Ag)/  $^6\text{LiF}$  (30 mg/cm<sup>2</sup>) scintillator, 2 – reflective cone, 3 – PMT, 4 – cover; 5 – housing for light shielding. (Reprinted from Ref. [9]. Published by Moscow State University as open access); (c, d) Configuration of a planar neutron detector with (c) one and (d) two scintillator layers: 1-scintillator; 2 – flat light guide (organic glass) or WLS fibers; 3 – PMT or Si-PM; (e) Internal configuration of the planar detectors with multilayer structure. The detector's sensitive area is composed of five transparent ~170  $\mu\text{m}$ -thick layers of a mixture of ZnS(Ag) and 95%  $^{10}\text{B}$  enriched boron. These layers are arranged in four plates of PMMA sizing 23 × 36 × 0.635 cm for the N-15 and 120 × 15.2 × 0.635 cm for the N-48 detector. The PMMA function is twofold, as light guide and as neutron moderator. All is surrounded by ~8  $\mu\text{m}$  thick aluminum mylar as light reflector. Detector has an outer moderator made of high density polyethylene (0.94 g cm<sup>-3</sup>) with thickness 24–48 mm. (Reprinted from Ref. [22]. Published by EDP Sciences as open access)



**Fig. 3.8** Quantum efficiency (%) plotted against the wavelength (nm). (Adapted with permission from Ref. [88]. Copyright 2013: Elsevier)

often referred to as Si-PM [38, 47]. Figure 3.8 represents the quantum efficiencies of PMT and Si-APD. Although the quantum efficiency of Si-APD is higher than PMT, which allows them to detect even single-photon events, PMT allows for a much higher multiplication gain of up to  $10^6$ . That is why PMTs are used in most neutron detectors. When using Si-APD, there is also a risk of signal suppression by the thermal noise of the avalanche photodiode (Si-PM). Marin et al. [38] propose to suppress noise by cooling the photodiodes or by applying a timing coincidence circuit. Marin et al. [38] showed that the use of the signal coincidence scheme from two Si-PM makes it possible to exclude even weak noises.

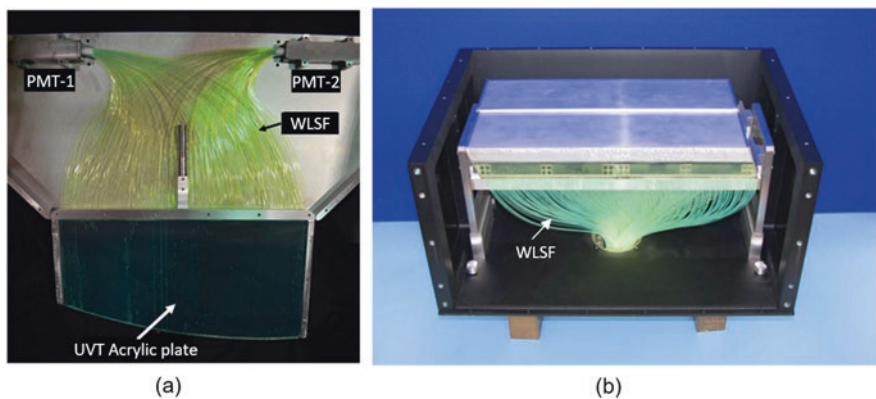
The simplest version of the neutron detector is the one proposed by Lucas [37] for counting alpha-emitting radon and progeny. A modern version of the Lucas Cell typically consists of a clear plastic cylinder with an interior coating of ZnS(Ag) on the walls, but not on the bottom of the cylinder. The ratio of cylinder diameter to length is from 1:8 to 1:24. Cylinder is then placed in a light-tight enclosure containing a photomultiplier tube connected to an electronic counter. This simple, relatively inexpensive alpha counter has been widely used for assessment of radon concentrations. To turn the alpha detector into a neutron detector, it is enough to replace the ZnS(Ag) scintillator with a  ${}^6\text{LiF/ZnS:Ag}$  composite. The geometry of the sensitive volume of the detector, in which the length is much greater than the width, is favorable for light collection, but does not allow the creation of compact high-performance neutron detectors with a large sensitive surface.

To solve this problem, detectors using flat scintillation screens are more suitable. The collection of scintillation light from the surfaces in such detectors is carried out using a wave length shifting plate (WLSP), at the ends of which photomultipliers are installed. Efficient collection of light is possible provided that the length of the plate is much greater than the width, which is determined by the diameters of the PMT. The design of the detector makes it possible to create neutron detectors with

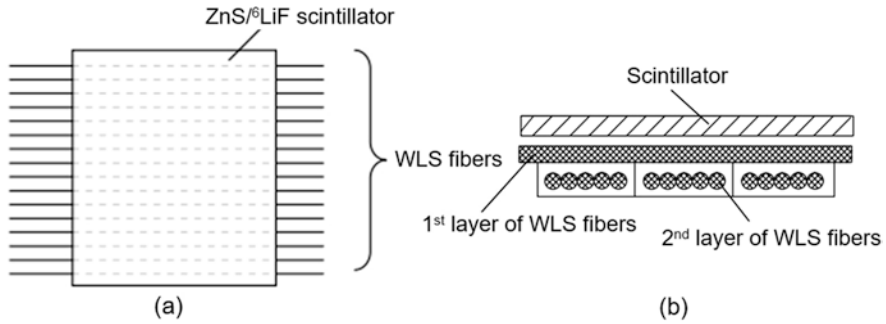
a large sensitive surface by increasing the width of the wave length shifting plate and the number of PMTs installed at its ends. However, an increase in the number of photomultipliers used complicates the design of the detector and significantly increases its power consumption. Another disadvantage of such detector is the low efficiency of scintillation light collection, since the scintillation light is collected only from the end of the WLSF. Wave length shifting optical fibers (WLSFs) (Fig. 3.9) can be used instead of a WLS plate, which are placed close to each other on the surface and optically coupled to PMT [27, 46]. Since the optical fiber re-radiates only about 4% of the light, PMTs are used to pick up the signal. It is important to note that optical fibers are sensitive to gamma rays, which requires additional electronics to isolate neutron events.

To increase the efficiency of neutron detection, several layers of light guide plates and scintillation screens can be used. The efficiency of neutron detection by a detector with layered phosphorus can reach 30–50%. But this leads to an increase in the thickness of the detector and the need to use light concentrators, which leads to an increase in the dimensions of the detector. The efficiency of the detectors can also be improved by using the configuration shown in Fig. 3.7b. The scintillator is scanned by a single photomultiplier tube [9] with a photocathode diameter of 15 cm. To improve light collection, a light-reflecting cone with a diffuse surface is used, made of 5 mm thick foil-wrapped polyethylene foam [9].

The use of optical wavelength shifting (WLS) fibers for signal pickup, on the one hand, complicates the process of manufacturing sensors, and, on the other hand, makes it possible to manufacture position-sensitive neutron detectors. The most efficient way to make a linear one-dimensional position sensitive neutron detector has been described in [49]. The detector consists of a planar scintillator, WLS fibers,



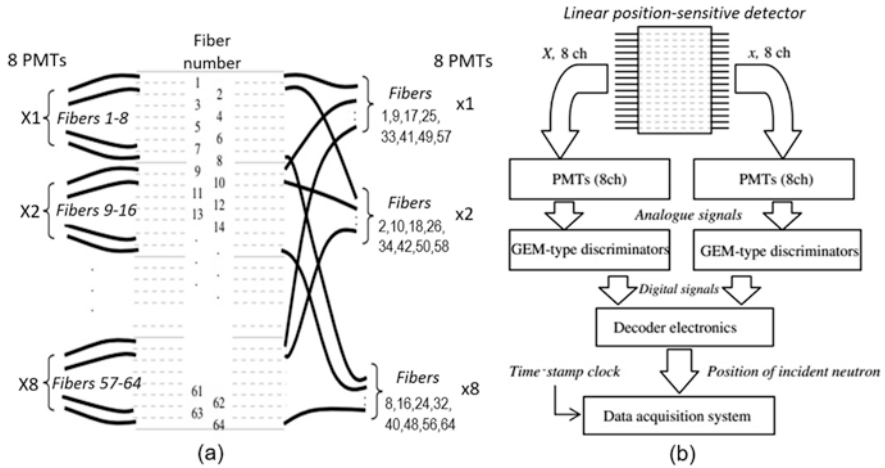
**Fig. 3.9** (a) Photographs of the detector, showing the phototube housings (PMT), the wave length shifting fiber light (WLSF) transport. An array of wave length shifting fibers, WLSFs, glued into an ultra-violet transmitting acrylic plate. Alternate fibers were directed into one of two photomultiplier tubes (PMTs). (Reprinted with permission from Ref. [46]. Copyright 2017: AIP Publishing); (b) Prototype ZnS:Ag/<sup>6</sup>LiF scintillation detector for Imaging and Materials Instrument (IMAT, ISIS Facility): 200 pixels, 100 × 4 mm, 64-channel flat panel PMT. (Reprinted from <https://www.isis.stfc.ac.uk>)



**Fig. 3.10** (a) Schematics of the neutron-sensitive scintillator and the array of WLS fibers in one-dimensional position sensitive detector. The neutron-sensitive area of the prototype detector was  $32 \times 70$  mm. ZnS/<sup>6</sup>LiF scintillator was 0.4 mm thick and had a density of  $96 \text{ mg/cm}^2$ , where the weight ratio of ZnS to <sup>6</sup>LiF was 4:1. WLS fibers had diameter 0.5 mm. (Reprinted with permission from Ref. [49]. Copyright 2009; Elsevier). A schematic of the scintillator and fibers arrangement in a two-dimensional neutron detector. (Reprinted with permission from Ref. [15]. Copyright 2004; Elsevier)

multi-anode PMTs, ISIS GEM type discriminators, and position decoding electronics. Neutrons are detected by detecting light from a ZnS/<sup>6</sup>LiF scintillator sent to the PMT via WLS fibers. Figure 3.10 shows schematics of a neutron-sensitive scintillator and WLS fibers array. When irradiated with neutrons, the ZnS:Ag scintillator emits blue light after being excited by secondary particles. The fibers can collect blue scintillation light efficiently because the scintillator is located close to the WLS fibers array. WLS fibers with 300 ppm dye concentration change the wavelength of the incoming light from blue to green, and the green light propagates to the PMT through the fibers. This wave length shift avoids self-absorption of re-emitted light in the fiber. The fiber pitch is about 0.55 mm. In order to achieve a high spatial resolution, both the diameter of WLSF and the fiber pitch should be kept low. However, a smaller diameter fiber can, in general, receive less light from the scintillator resulting in a lower light collection. Thin optical dividers can be placed in between the fibers to prevent absorption of light by adjacent fibers. However, it should be kept in mind that small pixels due to fiber diameter and fiber pitch can significantly increase the cost of detectors, especially in the case of detectors with a large sensitive area.

WLS fibers are encoded in such a way as to reduce the number of PMTs and associated electronic circuits. Figure 3.11a shows the fiber coding scheme used in a detector containing 64 fibers. The specialized electronics of the decoder makes it possible to determine the position of the incident neutron on the basis of the received information (Fig. 3.11b). To do this, the decoder analyzes the propagation of light along several fibers using a special lookup table. Compared to the individual fiber readings used in early positional detectors, the use of this fiber optic encoding greatly reduces the number of PMTs and related electronics required to read all detector channels. For example, 256 detector channels can be read by 32 PMTs instead of 256 PMTs, and 1024 detector channels can be read by 64 PMTs. Such fiber coding is very advantageous when creating a large detector with small pixels.



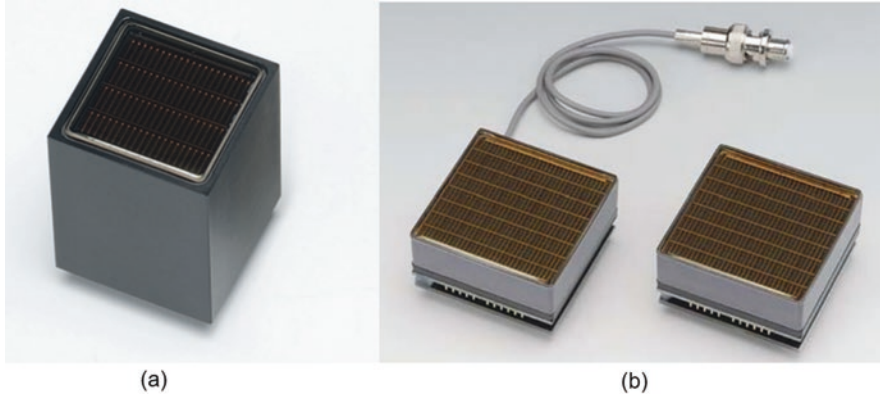
**Fig. 3.11** (a) The fiber-coding scheme in the prototype linear WLS fiber detector. The fibers were coded into groups of eight fibers; (b) Block diagram of the prototype detector system. (Reprinted with permission from Ref. [49]. Copyright 2009: Elsevier)

However, in this case, a trade-off between the count rate and the number of PMTs is necessary. Reducing the number of PMTs reduces the speed of signal processing.

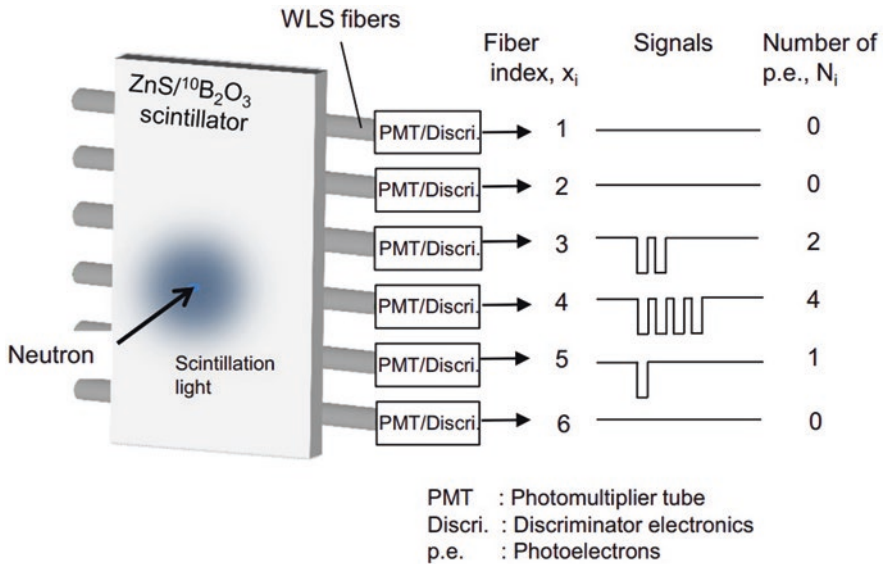
It was shown that a developed detector in which the fiber array was sandwiched between two  $\text{ZnS}/^6\text{LiF}$  scintillators (see Fig. 3.7d) exhibited a spatial resolution of 0.5 mm, a detection efficiency of 35% for 1 Å neutrons, and a gamma sensitivity of less than  $10^{-7}$ . According to Nakamura et al. [49], this type of detector would be useful where a sub-millimeter spatial resolution is required with large detector coverage such as in neutron reflectometers. It is important to note that the technology of coded fiber optic connections was proposed in 1997 by Rhodes et al. [64]. They, using coded fiber optic connections between the scintillator and photomultiplier tubes, have developed a pixel scintillation detector ( $^6\text{Li}/\text{ZnS}$ ) that can distinguish a total of 348 pixels using only 12 PMTs. Subsequently, X-Y neutron detectors were developed using this technology [15, 39, 52]. To do this, a second layer of WLS fibers was added to the detector design, located perpendicular to the first one (see Fig. 3.10b), and two additional decoders.

Another important breakthrough in the development of position-sensitive neutron detectors for large scientific projects was the development of multi-anode PMTs (Fig. 3.12a) and flat-panel multi-anode PMTs (FP-PMTs) (Fig. 3.12b). These technologies have allowed the development of new cost-effective approaches to the development of multipixel detectors. By combining WLSF with fiber coding technology, the requirements for the number of PMTs, high voltage sources, electronics, and cables are greatly reduced.

It was the advent of multi-anode PMTs that allowed Nakamura et al. [53] to develop a two-dimensional neutron scintillation detector that operates with an extremely simple detection scheme without any fiber coding. Figure 3.13 shows the block diagram of the scintillator and the structure of the detector with WLS fibers.



**Fig. 3.12** (a) Multi-anode PMTs assembly H12445 series: Affective area  $\sim 23 \times 23$  mm;  $4 \times 4$  multi-anode;  $\lambda_{\text{max}} - 400$  nm. The multiple-anode PMT is equivalent to incorporating multiple PMTs in a single housing. An output pin protrudes from the base of the housing for each of the 32 anodes, which means that each anode is externally accessible. The uniqueness of the multiple-anode PMT is in the electron-multiplication section—it is distributed throughout the housing; (b) Flat panel type multi-anode PMT assembly H12700 and H14220 series: Affective area  $\sim 48.5 \times 48.5$  mm; Pixel size:  $6 \times 6$  mm/anode;  $\lambda_{\text{max}} - 380$  nm (H12700) and  $420$  nm (H14220). (Reprinted from <https://www.hamamatsu.com>)

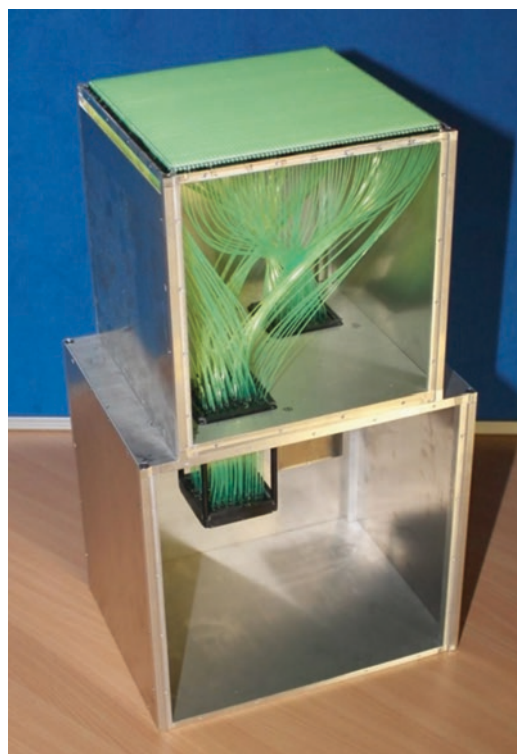


**Fig. 3.13** Schematic diagram of the scintillator and wavelength-shifting (WLS) fiber detector (only the WLS-fibers array in the x direction is presented for simplicity). (Reprinted with permission from Ref. [53]. Copyright 2015: Elsevier)

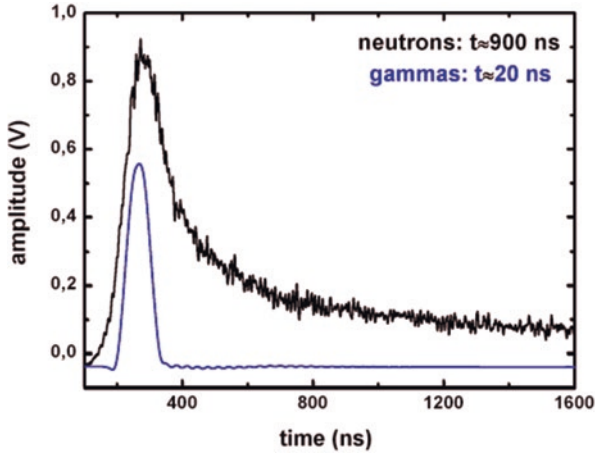
The detector consists of 256 fibers (128 in each of 2 layers) and electronics channels. The detector has a  $320 \times 320$  mm neutron sensitive scintillator. This detector used four 64-channel multi-anode PMTs (H8804 from Hamamatsu). A simple calculation algorithm allows to speed up the processing of information and make the detector faster than previously described.  $\text{ZnS}/^{10}\text{B}_2\text{O}_3$  scintillation screens 0.2 and 0.4 mm thick are located above and below the array of WLS fibers, respectively. The thickness of the scintillation screens was chosen to maximize the detection efficiency of the thermal neutron detector [51].

Using multi-anode PMTs, one can also implement an even simpler detector configuration, where each fiber forms a separate pixel. Such a detector is shown in Fig. 3.14. It was developed for the single crystal diffractometer installed at ISIS Neutron and Muon source (<http://www.isis.rl.ac.uk>). In its manufacture, fibers with a diameter of 1 mm were used. The signal was recorded using  $64 \times 64$  fiber array and two 64-channel FP-PMTs.

It should be noted that the detector based on  $\text{ZnS}(\text{Ag})$  is sensitive not only to thermal neutrons, but also to gamma rays, which is mainly due to the sensitivity of thin plastic fibers to gamma radiation. However, this problem of the sensitivity of neutron detectors to gamma radiation can be solved using pulse shape processing techniques. Differences in the excitation processes associated with neutron and



**Fig. 3.14** Neutron detector for single crystal diffractometer: Active area  $-192 \times 192$  mm<sup>2</sup>;  $64 \times 64$  fibers; Pixel size  $-1.5 \times 1.5$  mm<sup>2</sup>; Efficiency 67% at 1.8 Å. (Reprinted from <http://www.isis.rl.ac.uk>)



**Fig. 3.15** Averaged, gated pulses recorded with BC-704 scintillation screen irradiated with gamma-rays and neutrons. (Reprinted from <http://www.crystals.saint-gobain.com>)

gamma rays interactions make it possible to separate these particles using the pulse shape recognition (PSD) method [25]. Light pulses from  $\gamma$ -rays and neutrons are shown in Fig. 3.15. The differences in decay time constants are extremely large – for  $\gamma$ -rays it is at the level of nanoseconds, while for neutrons a light pulse has a decay time of microseconds or fractions of a microsecond [7].

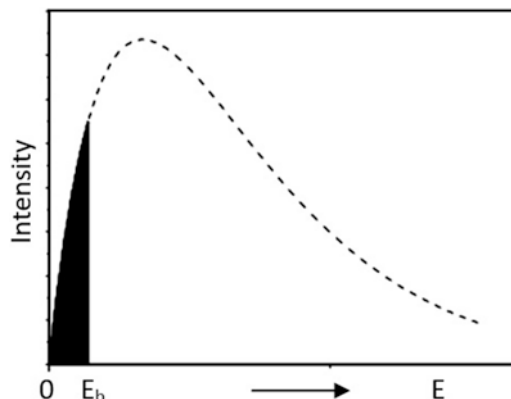
### 3.6 Filters for Neutron Detectors

If we need to measure the flux of only thermal neutrons in radiation containing fast neutrons and  $\gamma$ -rays, then in this case various filters can be used (see Fig. 3.16). Table 3.5 gives the cut-off wavelengths ( $\lambda_b$ ) and corresponding cut-off neutron energies ( $E_b$ ) for some filters used in practice.

The great advantage of polycrystalline filters is that they have the highest light-gathering power compared to monochromators. However, on the other hand, they have a significant drawback: a large blurring of the spectral line from the side of long wavelengths ( $\Delta E/E \sim 40\text{--}50\%$ )

Along with polycrystalline filters, single-crystal filters are also used, which have small absorption and incoherent elastic scattering cross sections. These filters attenuate the thermal neutron flux to a small extent, but at the same time significantly attenuate unwanted accompanying radiations, such as fast neutrons and  $\gamma$ -rays. For example, a quartz single-crystal filter 27.5 cm long, cooled with liquid nitrogen, attenuates the flux of fast neutrons by 25 times, resonant neutrons by 2000 times,  $\gamma$ -rays with an energy of 2 MeV by 30 times, and thermal neutrons by only 2.5 times. It is important to note that filters that cut-off fast neutrons and  $\gamma$ -rays also help to reduce radiation damage in the scintillator, and thus improve the stability of the detector parameters.





**Fig. 3.16** Energy spectrum of filtered neutrons (shaded area).  $E_b$  is the boundary energy of neutrons corresponding to the cut-off wavelength  $\lambda_b$ . The dotted line shows the spectrum of neutrons incident on the filter

**Table 3.5** The cut-off wavelengths and corresponding cut-off neutron energies for some filter

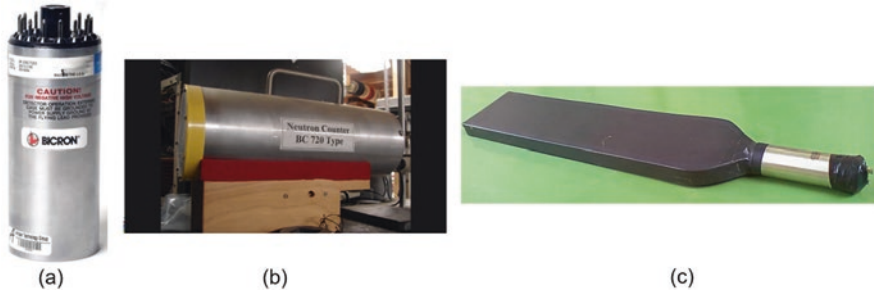
Filter material	$\lambda_b$ , nm	$E_b$ , eV
Beryllium	0.395	0.0052
Beryllium oxide	0.44	0.0042
Lead	0.57	0.0025
Graphite	0.669	0.00183
Bismuth	0.80	0.00128

### 3.7 Market of Neutron Detectors

Currently, ZnS-based scintillators are manufactured by several companies. For example, Saint-Gobain Crystals offers several variants of such scintillators. The BC-702 plastic scintillator is an efficient thermal neutron detector with excellent ability to separate neutrons from gamma background radiation. The BC-702 scintillator (Fig. 3.17a) is made on the basis of a lithium compound (up to 95% enriched in lithium  $^6\text{Li}$ ) mixed with phosphorus powder based on ZnS(Ag). The BC-702 scintillator is available as a 6.35 mm thick disc and 38 mm, 50 mm, 76 mm, and 127 mm diameters. The disc can be mounted directly on a photomultiplier tube or light guide.

The plastic scintillator BC-720 (Fig. 3.17b) is specially designed to detect fast neutrons (energy above 1 MeV) due to its insensitivity to gamma radiation. The BC-720 scintillator is made in the form of a disc 15.9 mm thick and 38 mm, 50 mm, 76 mm, and 127 mm in diameter. As in other detectors, the maximum emission is at a wavelength of 450 nm. The disc can be mounted directly on a PMT or light guide.

Plastic scintillators BC-704 and BC-705 are designed for neutron radiography. The detectors consist of successive layers of a  $6\text{LiF}/\text{ZnS}$  scintillation screen and an array of optical fibers. The scintillation light in the BC-704 is produced in ZnS(Ag), absorbed and re-emitted in the WLS fibers, through which it is transported to the



**Fig. 3.17** Photos of ZnS-based scintillators of BC-700 type manufactured by Saint-Gobain Crystals: **(a)** BC-702 (Diameter: 2 inches; Length: 2.5 inches); **(b)** BC-720; **(c)** BC-704. (Reprinted from <http://www.crystals.saint-gobain.com>)

**Table 3.6** Performances of ZnS-based scintillators of BC-700 type

Type	Decay time, ns	Sensitivity to $\gamma$ -rays	Isotope	Application	Integrated design
BC-702	250	Very low	$^6\text{Li}$	Thermal neutron detectors	Integrated with a photomultiplier tube (PMT)
BC-704				Thermal neutron detectors, neutron radiography	
BC-705					
BC-720			H	Detectors of fast neutrons	

Source: Data extracted from <https://www.crystals.saint-gobain.com/>

photomultiplier tube. The wavelength at the emission maximum is 450 nm (blue light). The BC-704 scintillator (Fig. 3.17c) is a flat, usually rectangular, nonhygroscopic screen (no more than 300 × 300 mm in size) placed on an aluminum plate 1 mm thick. The composition and properties of the BC-705 scintillator are the same as those of the BC-704 scintillator, except that the zinc sulfide is doped with copper, i.e., ZnS(Cu), which allows the BC-705 to have emission maximum at 525 nm (green light), which is most suitable for use with certain types of electron-optical converters. Table 3.6 below shows the characteristics of these plastic scintillators.

It is important to note that the neutron detectors developed by some groups outperform those offered by Saint-Gobain Crystals (Bicron) (<http://www.crystals.saint-gobain.com>). For example, parameters of detectors developed by the team of Katagiri [27] compared to commercial products (Bicron, BC-704) are shown in Table 3.7. It is seen that the developed ZnS/ $^6\text{LiF}$  scintillator (indicated as “standard”) exhibited a detection efficiency of 40.7% for thermal neutrons, which was about 1.5 times higher than that of BC-704. According to Katagiri [27] estimations, the main reason of such difference is the transparency of the scintillators. This means that although the configuration of the detector affects its performance, the main way to increase the performance of the neutron detector is still to use a scintillator with higher transparency and luminescence efficiency.

**Table 3.7** Neutron detection efficiencies for the phosphor/neutron converter scintillators for thermal neutrons

Scintillator	ZnS/ <sup>6</sup> LiF, standard	ZnS/ <sup>6</sup> LiF, 2 times <sup>6</sup> LiF	ZnS/ <sup>10</sup> B <sub>2</sub> O <sub>3</sub> heated up to 500 °C	Y <sub>2</sub> SiO <sub>5</sub> :Ce <sup>3+</sup> / <sup>6</sup> LiF	Bicron, BC-704 ZnS/ <sup>6</sup> LiF,
Neutron detection efficiency, %	40.7	43.5	29.0	37.1	26.4

Source: Reprinted with permission from Ref. [27]. Copyright 2004: Elsevier

**Table 3.8** Parameters of ZnS-based neutron detection screens

Screen type	ND	NDg
Formulation	<sup>6</sup> LiF/ZnS:Ag	<sup>6</sup> LiF/ZnS:Cu, Al
Phosphor type	Particulate blend	Particulate blend
Emission color	Blue	Green
Peak emission	450 nm	530 nm
Decay to 10%	80 μm	85 μm
Afterglow	Low level	Low level
X-ray absorption	Very low	Low
UV absorption	Broad band	>220 nm into visible

Source: Data extracted from [www.Scintacor.com](http://www.Scintacor.com)

Several companies offer ZnS-based neutron detection screens. In particular, Tables 3.8 and 3.9 list the parameters of neutron detection screens developed in company Applied Scintillation Technologies “Scintacor” ([www.Scintacor.com](http://www.Scintacor.com)) for detection and imaging of thermal neutrons. According to Scintacor, the standard ND screen is a blue emitting screen with unique low sensitivity to background gamma, and the green emitting NDg screen is ideal for CCD imaging

Market analysis of ZnS-based neutron detection screens shows that the nominal neutron detection efficiency of most designed ZnS/<sup>6</sup>Li-based screens is in the range of 23–36% [71, 72, 76, 85]. However, as indicated in Table 3.7, there are reports of screen development with detection efficiency up to 43.5% [27, 30]. The performance achieved is the result of many years of research to optimize screen composition and thickness [15, 31]. Many believe that the achieved neutron detection efficiency for ZnS/<sup>6</sup>Li screens is close to the theoretical limit, and improving the light output of the screens will not increase the probability of detecting neutrons, since this improvement does not increase the number of neutrons captured by <sup>6</sup>Li. [2]

The theoretical capture efficiency for <sup>6</sup>LiF/ZnS(Ag) screens depends on their thickness and the ratio of <sup>6</sup>LiF to ZnS. A typical layer with a molecular ratio of 1:2 and a thickness of 250 μm has a capture probability of about 26% per neutron crossing according to the manufacturer’s data. Therefore, a significant improvement can come only by increasing the probability of neutron capture. Previous studies aimed at increasing the probability of neutron capture by increasing the thickness or

**Table 3.9** Features of ZnS-based neutron detection screens developed by Scintacor

Parameter	Description
Shapes	The screens can be manufactured in a range of shapes from flat sheets to more complex designs such as ridge/ grooved tiles and conformed cylindrical surfaces. Most types of screens are heat formable.
ZnS: <sup>6</sup> LiF mass ratio	The following mass ratios are available: 4:1 for maximum light output; 2:1 for maximum <sup>6</sup> Li density and detection efficiency.
Dimensions	The neutron detection screens are readily available up to 500 × 500 mm but larger sizes can be manufactured to special order.
Substrates	Scintacor neutron detection screens are available either on a 250 μm white polyester substrate or free standing (i.e., without any substrate). Additional substrates are available on demand.
Construction	A wide range of mountings and support materials are available, such as aluminium plates. Wall thickness, tolerances can be agreed on demand.

Source: Data extracted from [www.Scintacor.com](http://www.Scintacor.com)

**Table 3.10** Performances of ZnS/<sup>6</sup>LiF and ZnS/<sup>10</sup>B<sub>2</sub>O<sub>3</sub> ceramic scintillators

Parameter	ZnS/ <sup>6</sup> LiF	ZnS/ <sup>10</sup> B <sub>2</sub> O <sub>3</sub>
Detector efficiency for 1 Å (%)	50	60
Multicount ratio (%)	0.6 ± 0.3	0.3 ± 0.3
Gamma sensitivity (× 10 <sup>-7</sup> )	2 ± 1	1.5 ± 1
Quiet count rate (/s/cm <sup>2</sup> )	2.1 ± 0.3	6.9 ± 0.3

Source: Reprinted with permission from Ref. [50]. Copyright 2009: Elsevier

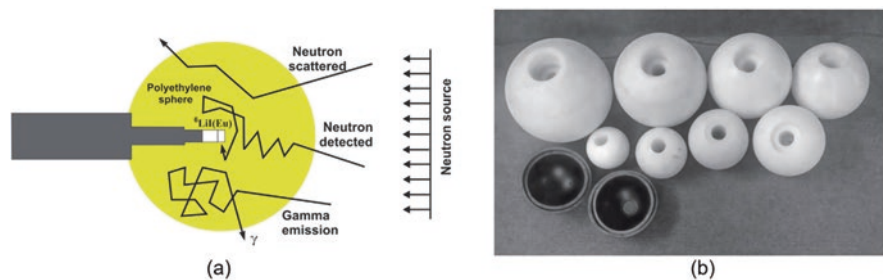
content of <sup>6</sup>Li in the screen have shown that these changes have a negative effect on light output: neutron detection efficiency is reduced, as a greater percentage of captured neutrons go undetected [71, 85]. Therefore, in recent years, research has been carried out aimed at finding solutions that will overcome the difficulties that have arisen. In particular, efforts continue to improve the efficiency of ZnS-based neutron detectors by using <sup>10</sup>B, which has a higher probability of neutron capture [10, 22, 24, 27, 53]. For example, Nakamura et al. [50] based on a comparison of the parameters of a fiber-coded linear position-sensitive neutron detector equipped with a ZnS/<sup>6</sup>LiF and ZnS/<sup>10</sup>B<sub>2</sub>O<sub>3</sub> ceramic scintillators concluded that the neutron detection efficiency of ZnS/<sup>10</sup>B<sub>2</sub>O<sub>3</sub>-based detector at 1 Å was 1.2-fold higher than that of a similar detector based on a ZnS/<sup>6</sup>LiF scintillator (Table 3.10). At that both detectors exhibited similar gamma sensitivities. Nakamura et al. [50] believe that the detector efficiency could be further improved by increasing the light yield of the ZnS/<sup>10</sup>B<sub>2</sub>O<sub>3</sub> scintillator or optimizing the thickness or <sup>10</sup>B content in the screen. An additional benefit to use screens based on boron and ZnS(Ag) is the potential cost-savings due to the difference in price between <sup>10</sup>B and <sup>6</sup>Li. In addition, the optimal ratio of converter (<sup>10</sup>B) and scintillator (ZnS) in neutron screen is likely to require significantly less boron by weight

### 3.8 Fast Neutron Detectors

As mentioned earlier, the higher the energy of the neutrons, the less likely it is that the neutron will be absorbed. Therefore, when the purpose of the measurement is simply to count fast neutrons without measuring their energy, then it is sufficient to use a material that will slow down (or “moderate”) fast neutrons to the energy of thermal neutrons. To slow down fast neutrons, hydrogen or compounds containing hydrogen are often used, on which fast neutrons experience elastic scattering during deceleration. As a result, a fast neutron loses part of its initial kinetic energy in the moderator and reaches the detector in the form of a low-energy thermal neutron, the detection efficiency of which is much higher by the previously presented detectors. Moderators based on compounds containing hydrogen perform their function well at neutron energies below 10 MeV. If the neutron energy is greater than 10 MeV, then neutron registration is usually carried out in two stages. At the first stage, as a result of the interaction of fast neutrons, for example, with lead nuclei, several tens of neutrons with many times lower energies are formed. And already at the second stage, these neutrons are slowed down in hydrogen-containing media to thermal energies sufficient for their registration using the slow neutron detectors considered earlier. The disadvantage of detectors of this type is the dependence of the efficiency on the neutron energy. In addition, they do not provide information about the energy of neutrons, although the solution of many scientific and technical problems requires knowledge of the energy of the incident neutron, since the energy of the reaction products depends significantly on the energy of the incident neutrons.

The simplest solution to this problem is to use the Bonner Sphere Spectrometer (BSS). It consists of a thermal neutron detector located in the center of a set of spherical polyethylene moderators of different diameters. Spherical geometry results in an isotropic response. In order to measure the neutron energy spectrum at a specific location, measurements must be made with each individual sphere, which acts as an “integral” device. Because of their different diameters, the spheres have different response functions and thus can give different energy-integrated responses in the same neutron field. The inclusion of lead or another highly atomic element in the sphere increases the response to high-energy neutrons (up to GeV) due to the spallation reaction, in which the response of ordinary polyethylene spheres tends to decrease: the elastic scattering cross section decreases at energies above 20 MeV. In addition, a cadmium shell insert is used to reduce the sensitivity of detector in the thermal energy region in order to have independent response functions. The choice of thermal detector and the number of spheres depends on the application. For example, CERN BSS consists of seven spheres: five polyethylene spheres with external diameters of 81, 108, 133, 178, and 233 mm, complemented by two other spheres, nicknamed Ollio and Stanlio, where cadmium and lead inserts have been introduced. The configuration and appearance of a standard BSS is shown in Fig. 3.18.

It should be noted that detectors based on other converters have also been developed to detect fast neutrons. In particular, Yamane et al. [87] and Mori et al. [45]



**Fig. 3.18** (a) Bonner sphere system for a  ${}^6\text{LiI}(\text{Eu})$  neutron radiation detector. (Reprinted from Ref. [56]. Published by InTech as open access. Fig. 10); (b) Eight Bonner Spheres with diameters from 5" (12.7 cm) to 12" (30.48 cm), and four 1-cm-thick lead half shells (bottom left). The lead half shells can be combined to form either a 1-cm or a 2-cm-thick lead shell surrounding the 6" Bonner Sphere. (Reprinted with permission from Ref. [14]. Copyright 2016: IOP)

demonstrated the measurement of 14.1 MeV neutrons using a  ${}^{232}\text{Th}$  converter and a  $\text{ZnS}(\text{Ag})$  scintillator placed at the tip of a single optical fiber. This converter uses a fast fission reaction and a neutron energy threshold of 1.1 MeV.

### 3.9 Devices Based on $\text{ZnS}/{}^6\text{LiF}$ Scintillators

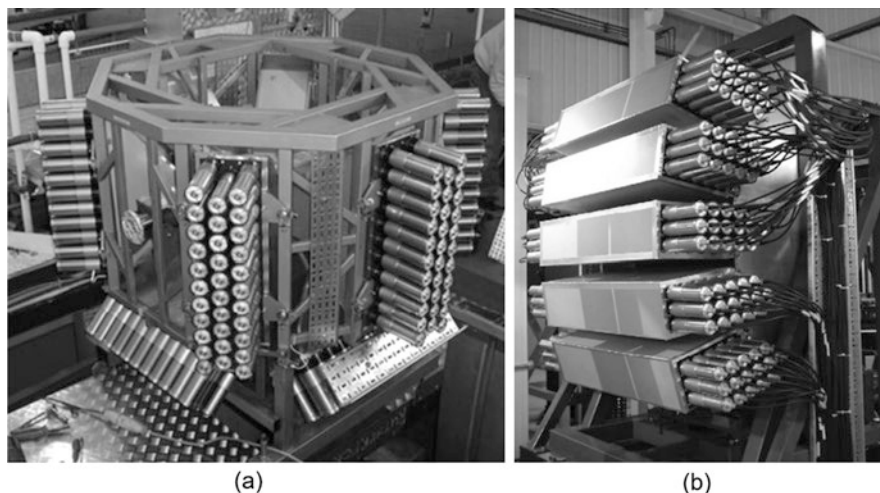
Based on neutron detectors, in addition to portable devices for radiation monitoring (Fig. 3.17c) and stationary devices for monitoring the movement of radioactive materials (see Fig. 3.19) [33], a variety of instruments have been developed for major international and national scientific projects carried out in various scientific centers.

High-intensity pulsed-neutron facilities that have been under construction in the USA (Spallation Neutron Source (SNS), <http://neutrons.ornl.gov>, NIST Neutron Imaging Facility (NIF), <https://www.nist.gov>), Japan (Japan Proton Accelerator Research Complex (J-PARC), <http://j-parc.jp>), Europe (The European Organization for Nuclear Research (CERN), <https://cerncourier.com>, the European Spallation Source (ESS), <https://europeanspallationsource.se>), the UK (Rutherford Appleton Laboratory (RAL) (<http://www.isis.rl.ac.uk>), and Russia (Frank Laboratory of Neutron Physics (<http://flnph.jinr.ru/en/facilities/ibr-2>), Institute for Nuclear Research, <https://www.inr.ru/>) have started producing neutrons. Such facilities require a large variety of neutron detectors, including position-sensitive neutron detectors [24, 54, 75]. In particular, the Japan Atomic Energy Research Institute (JAERI) is developing a range of  $\text{ZnS}/{}^6\text{LiF}$  and  $\text{ZnS}/{}^{10}\text{B}_2\text{O}_3$ -based instruments for J-PARC aimed at creating two-dimensional pixel detectors for single crystal and biological sample diffraction in the J-PARC beamline. These systems give position resolutions from a few  $\text{mm}^2$  to  $0.5 \text{ mm}^2$  [27, 28]. At the IBR-2 reactor in Russia, a detector of this type has been developed for the Fourier strain diffractometer. Here, the flexibility of the fibers has been used to develop a detector geometry that closely



**Fig. 3.19** Neuport and NeuTruck portal detection systems разработанные на основе ZnS/6LiF BC-704 detector. (Reprinted from <http://www.crystals.saintgobain.com>)

mimics the instrument's focusing surface [6]. Crow et al. [15] have developed a prototype WLS fiber detector based on ZnS:Ag/<sup>6</sup>LiF scintillator for the SNS. This detector has an active area of  $480 \times 200 \text{ mm}^2$  with a position resolution of  $6 \times 40 \text{ mm}$ . WLS crossed fiber detectors are planned as the detectors for the powder diffractometer POWGEN3 and the engineering diffractometer VULCAN on the SNS. At the present time, approximately half of the neutron instruments at the neutron and muon scattering ISIS facility in the United Kingdom employ ZnS:Ag/<sup>6</sup>LiF-based neutron detectors [65]. The ISIS neutron scattering instruments comprise of diffractometers, such as GEM, HRPD, LAD, SXD, OSIRIS, POLARIS, HiPr, LOQ, ENGIN-X, and SANDALS, and spectrometers such as MARI, eVS, HET, TFXA, IRIS, and PRISMA, together with the neutron reflectometers CRISP and SURF [62, 63, 65]. Linear position sensitive ZnS:Ag/<sup>6</sup>LiF-based detectors have been used on many of indicated powder and single crystal diffractometers. These detectors allow large solid angle coverage, provide 3–5 mm position resolution and 50% neutron detection efficiency at 1 Å. Also, ZnS/<sup>6</sup>LiF-based neutron detectors are currently being developed for DREAM and HEIMDAL powder diffractometers intended for installation in the ESS [73]. To give you an idea of the dimensions of these instruments, Fig. 3.20a shows a photograph of the single crystal diffractometer, SXD, and Fig. 3.20b shows the ENGIN-X detector array that has been constructed using similar linear position sensitive fiber-coded ZnS/<sup>6</sup>Li scintillation detectors. This linear position sensitive detector array was designed for General Materials Diffractometer (GEM). The entire ENGIN-X detector array comprises of 2400 detector elements and covers an area of 1.4 m<sup>2</sup>.



**Fig. 3.20** (a) The single crystal detector array at ISIS. The sample sits in the center of the octagonal frame and is viewed by eleven detector modules. Each of these modules has 4096  $3 \times 3$  mm<sup>2</sup> pixels. Quad coincident fiber optic coding allows each module to be readout by just 32 PMTs. (Reprinted from <https://www.isis.stfc.ac.uk/>); (b) The south bank of the ENGIN-X detector array. (Reprinted with permission from Ref. [65]. Copyright 2004: Elsevier)

### 3.10 Phoswich Detector

For radiation monitoring during accidents at nuclear power plants such as Fukushima Daiichi, radiation detectors are needed not only for gamma photons, but also for alpha and beta particles, since nuclear fission products emit beta and gamma photons, and mixed oxide fuel containing plutonium emits alpha particles [86]. In environments with nuclear contamination, in addition to gamma photons, it is also necessary to control alpha and beta particles. Monitoring of gamma photons is relatively simple and is usually done with scintillation detectors. However, alpha and beta particles are difficult to control due to their short range, and most of these particles are absorbed in the entrance window of radiation detectors. Currently, there are radiation detectors for individual measurement of alpha and beta particles and gamma photons. Thin scintillation detectors based on ZnS (Ag), such as TCS-232 B, Hitachi-Aloka Medical Co., Japan, are the most common instruments for detecting alpha particles. Plastic scintillation detectors such as TCS-316 H, Hitachi Aloka Medical Co., Japan, are used to detect beta particles. To detect gamma photons, the NaI(Tl) scintillation detector is most often used, for example, TCS-171 B, Hitachi-Aloka Medical Co., Japan.

However, the use of three types of scintillation detectors for monitoring is uneconomical and can lead to increased radiation doses in heavily contaminated areas, since measurements with three detectors are time-consuming. To solve this problem, phoswich technology was proposed, on the basis of which detectors were

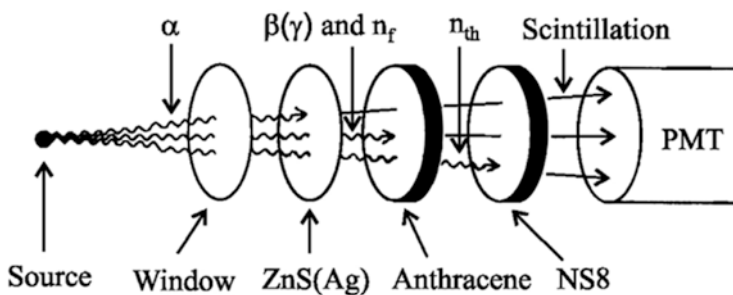


developed for the simultaneous monitoring of alpha and beta particles. ZnS(Ag) and plastic scintillators were used for their manufacture [78, 90]. A similar phoswich detector is commercially available (TCS-362, Hitachi-Aloka Medical Co., Japan). It contains two photomultipliers (PMT) for simultaneous measurement of alpha and beta particles. There is a problem with such a detector: a plastic scintillator for detecting beta particles also registers gamma photons. Therefore, the phoswich method was later extended to a three-layer configuration, which allowed measurements of three different types of radiation. One phoswich detector used a ZnS(Ag) scintillator for alpha particles, a plastic scintillator for beta particles, and NaI(Tl) or  $\text{Bi}_4\text{Ge}_3\text{O}_{12}$  (BGO) for gamma photons [79]. Another phoswich detector used ZnS(Ag) for alpha particles,  $\text{CaF}_2$  for beta particles, and NaI(Tl) for gamma detectors [13, 83]. However, due to the high light output of ZnS(Ag) scintillator and the high energy of most alpha particles (5–8 MeV), differences in the pulse amplitude were found between the scintillators, which complicates signal processing. The detection of gamma photons in beta particle scintillators also requires a solution.

Usuda et al. [80] demonstrated that a phoswich detector comprised ZnS(Ag) anthracene, and  $^6\text{Li}$ -glass scintillators are capable of separately identifying the interactions of beta radiation (electrons), alpha particles, fast neutrons, and thermal neutrons (Fig. 3.21). Discrimination is achieved as follows:

- Alpha radiation interacts only within the ZnS(Ag).
- Electrons interact in both the ZnS(Ag) and the anthracene due to their longer range.
- Fast neutrons interact via proton recoil only in the anthracene.
- Thermal neutrons interact via neutron capture only in the  $^6\text{Li}$ -glass.

As materials used in the development of such phoswich detectors, scintillators such as EJ-440, EJ-442, and EJ-444 offered by Eljen Technology (<https://eljentechnology.com>) can be used. These materials are based on silver-activated zinc sulfide (ZnS:Ag) and are designed to detect alpha particles. EJ-440 consists of highly uniform ZnS:Ag deposited on one side of a 0.25 mm thick pure polyester sheet. The density of the fluorescent layer is sufficient to completely absorb ordinary alpha particles, such as those from Americium-241. The uniformity of alpha sensitivity



**Fig. 3.21** Arrangement of a ZnS(Ag)/anthracene/NS8 phoswich for simultaneous counting of  $\alpha$ -,  $\beta$ ( $\gamma$ )-rays and neutrons. (Reprinted with permission from Ref. [80]. Copyright 1997: Elsevier)

from batch to batch is constant and has a spread within 1.5%. Like EJ-440, EJ-442 consists of highly uniform ZnS:Ag deposited on one side of a thick, inflexible base material. Most often, acrylic plastic plates are used as a basis, having a thickness of 1.5–5 mm with a maximum size of up to 300 × 300 mm. The EJ-444 consists of an EJ-212 thin plastic scintillator with a ZnS:Ag layer on one side. The main area of application of the EJ-444 is the registration of alpha and beta particles in environmental monitoring devices. In EJ-444, the ZnS:Ag layer is, on the one hand, thick enough to completely trap all known alpha particles; on the other hand, it allows most of the beta particles to pass into the plastic scintillator to be registered in it.

**Acknowledgments** This research was funded by the State Program of the Republic of Moldova, project 20.80009.5007.02.

## References

1. Abdalla AM, Ali AM, Al-Jarallah M. Characterization and radiation detection application of ZnS(Ag) nanoparticles. *Physica B*. 2018;550:235–43.
2. Abreu Y, Amhis Y, Arnold L, Ban G, Beaumont W, Bongrand M, et al. A novel segmented-scintillator antineutrino detector. *J Instrum*. 2017;12:1–18.
3. Aza E, Dinar N, Manessi GP, Silari M. A Bonner sphere spectrometer for pulsed fields. *Radiat Prot Dosim*. 2016;168:149–53.
4. Bachman CH, Sawner ML, Allen WM. Spectral energy distribution curves of ZnS:Ag and ZnCdS:Ag after thermal vacuum treatment. *J Electrochem Soc*. 1956;103(2):117–22.
5. Ban G, Beaumont W, Buhour JM, Coupé B, Cucoanes AS, D'Hondt J, et al. SoLid: search for oscillations with Lithium-6 detector at the SCK-CEN BR2 reactor. *Nucl Part Phys Proc*. 2016;273–275:2690–2.
6. Belushkin AV, Kuzmin ES, Shvetsov VN. Status of the FLNP project on neutron position-sensitive detectors. *Nucl Instrum Methods Phys Res A*. 2004;529:249–53.
7. Birks JB. The theory and practice of scintillation counting. Oxford: Pergamon Press; 1964.
8. Blasse G, Grabmaier BC. Luminescent Materials. Berlin: Springer; 1994.
9. Bouchama I, Dmitrieva AN, Gromushkin DM. Study of the properties of neutron detector based on ZnS(Ag)+6LiF for monitoring of radiation situation near nuclear setups. *Mosc Univ Phys Bull*. 2018;4:1840202. (in Russian)
10. Castle B. Improved neutron detection using Zinc Sulfide with Boron. PhD thesis, Merton College, University of Oxford, UK; 2018.
11. Chander H, Shanker V, Haranath D, Dudeja S, Sharma P. Characterization of ZnS:Cu, Br electroluminescent phosphor prepared by new route. *Mater Res Bull*. 2003;38:279–88.
12. Chen YY, Duh JG, Chiou BS, Peng CG. Luminescent mechanisms of ZnS:Cu:Cl and ZnS:Cu:Al phosphors. *Thin Solid Films*. 2001;392:50–5.
13. Childress NL, Miller WH. MCNP analysis and optimization of a triple crystal phoswich detector. *Nucl Instrum Methods Phys Res A*. 2002;490:263–70.
14. Chu MC, Fung KY, Kwok T, Leung JKC, Lin YC, Liu H, et al. Development of a Bonner sphere neutron spectrometer from a commercial neutron dosimeter. *JINST*. 2016;11:P11005.
15. Crow ML, Hodges JP, Copper RG. Shifting scintillator prototype large pixel wavelength-shifting fiber detector for the POWGEN3 powder diffractometer. *Nucl Instrum Methods Phys Res A*. 2004;529:287–92.
16. Davies DA, Silver J, Vecht A, Marsh PJ, Rose JA. A novel method for the synthesis of ZnS for use in the preparation of phosphors for CRT devices. *J Electrochem Soc*. 2001;148(10):H143–8.

17. Dorenbos P. Light output and energy resolution of Ce<sup>3+</sup>-doped scintillators. *Nucl Instrum Methods Phys Res A*. 2002;486:208–13.
18. Fang X, Zhai T, Gautam UK, Li L, Wu L, Bando Y, et al. ZnS nanostructures: from synthesis to applications. *Prog Mater Sci*. 2011;56(2):175–287.
19. Feldman WC, Barraclough BL, Fuller KR, Lawrence DJ, Maurice S, Miller MC, et al. The lunar prospector gamma-ray and neutron spectrometers. *Nucl Instrum Methods Phys Res A*. 1999;422:562–6.
20. Gozani T. The role of neutron based inspection techniques in the post 9/11/01 era. *Nucl Instrum Methods Phys Res B*. 2004;213:460.
21. Gromushkin DM, Alekseenko VV, Petrukhin AA. Registration of the thermal neutron flux near the Earth's surface. *Izvestiya RAN, ser. Phys*. 2009;73(3):425–7. (in Russian)
22. Guzman-Garcia KA, Vega-Carrillo HR, Gallego E, Gonzalez-Gonzalez JA, Lorente A, Ibañez-Fernandez S. <sup>10</sup>B+ZnS(Ag) as an alternative to <sup>3</sup>He-based detectors for radiation portal monitors. *EPJ Web Conf*. 2017;153:07008.
23. Hoa TTQ, Vu LV, Canh TD, Long NN. Preparation of ZnS nanoparticles by hydrothermal method. *J Phys*. 2009;187:012081.
24. Hosoya T, Nakamura T, Katagiri M, Birumachi A, Ebine M, Soyama K. Development of a new detector and DAQ systems for iBIX. *Nucl Instrum Methods Phys Res A*. 2009;600:217–9.
25. Iwanowska J, Swiderski L, Moszynski M, Wolski D, Kniest F, Catto G The BC-704 scintillation screen with light readout by wavelength shifting fibers as a highly efficient neutron detector. In: *Proceedings of 2011 IEEE nuclear science symposium conference record, NP1.M-210*, 2011. p. 423–426.
26. Johnson LC, Barnes C, Krasilnikov A, Marcus FB, Nishitani T. Neutron diagnostics for ITER. *Rev Sci Instrum*. 1997;68:569.
27. Katagiri M. Development status of position-sensitive neutron detectors for J-PARC in JAERI—a comprehensive overview. *Nucl Instrum Methods Phys Res A*. 2004;529(2004):254–9.
28. Katagiri M, Nakamura T, Ebine M, Birumachi A, Sato S, Schooneveld EM, Rhodes NJ. High-position-resolution neutron imaging detector with crossed wavelength shifting fiber read-out using two ZnS/<sup>6</sup>LiF scintillator sheets. *Nucl Instrum Methods Phys Res A*. 2007;573(2007):149–52.
29. Knoll GF. *Radiation detection and measurement*, vol. 3. Hoboken: Wiley; 2000.
30. Kojima T, Katagiri M, Tsutsui N, Imai K, Matsubayashi M, Sakasai K. Neutron scintillators with high detection efficiency. *Nucl Instrum Methods Phys Res A*. 2004;529:325–8.
31. Koontz PG, Keepin GR, Aahley JE. ZnS(Ag) phosphor mixtures for neutron scintillation counting. *Rev Sci Instrum*. 1955;26(4):352–6.
32. Kotera Y, Naraoka K. Electrophotoluminescence of zinc sulfide phosphors. *Bull Chem Soc Jpn*. 1960;33(6):721–6.
33. Kouzes RT, Ely JH, Erikson LE, Kernan WJ, Lintereur AT, Siciliano ER, et al. Neutron detection alternatives to <sup>3</sup>He for national security applications. *Nucl Instrum Methods Phys Res A*. 2010;623:1035–45.
34. L'Annunziata MI. Solid scintillation analysis. In: L'Annunziata MI, editor. *Handbook of radioactivity analysis*, vol. 1. Oxford: Academic; 2020. p. 899–1045.
35. Litvin VS, Belyaev AD, Ignatov SM, Nedorezov VG, Sadykov RA, Alekseev AA, et al. Application of scintillators based on ZnS(Ag)/<sup>6</sup>LiF and LiI(Eu) in combination with silicon photomultipliers in thermal neutron detectors with high coordinate and time resolution. *Proc Russ Acad Sci Ser Phys*. 2009;73(2):230–2. (in Russian)
36. Lu H-Y, Chu S-Y. The mechanism and characteristics of ZnS-based phosphor powders. *J Cryst Growth*. 2004;265:476–81.
37. Lucas HF. Improved low-level alpha-scintillation counter for radon. *Rev Sci Instrum*. 1957;28:680–3.
38. Marin VN, Sadykov RA, Trunov DN, Litvin VS, Aksenov SN, Stolyarov AA. A new type of thermal neutron scintillation detectors based on ZnS(Ag)/LiF and avalanche photodiodes. *Lett JTF*. 2015;41(18):96–101. (in Russian)

39. Mauri G, Sykora GJ, Schooneveld EM, Rhodes NJ. Enhanced position resolution for ZnS:Ag/6LiF wavelength shifting fibre thermal neutron detectors. *Eur Phys J Plus*. 2021;136:286.
40. McCloy JS, Bliss M, Miller B, Wang Z, Stave S. Scintillation and luminescence in transparent colorless single and 3 polycrystalline bulk ceramic ZnS. *J Lumin*. 2015;157:416–23.
41. McGregor DS, Vernon SM, Gersch HK, et al. Self-biased Boron-10 coated high-purity epitaxial GaAs thermal neutron detectors. *IEEE Trans Nucl Sci*. 2000;NS-47:1364–70.
42. Medvedev MN. Scintillation detectors. Moscow: Atomizdat; 1977. (in Russian)
43. Milbrath AD, Peurrung AJ, Bliss M, Webe WJ. Radiation detector materials: an overview. *J Mater Res*. 2008;23(10):2561–81.
44. Miller BW, Gregory SJ, Fuller ES, Barrett HH, Bradford BH, Furenlid LR. The iQID camera: An ionizing-radiation quantum imaging detector. *Nucl Instrum Methods Phys Res A*. 2014;767:146–52.
45. Mori C, Uritani A, Miyahara H, Iguchi T, Shiroya S, Kobayashi K, et al. Measurement of neutron and  $\gamma$ -ray intensity distributions with an optical fiber-scintillator detector. *Nucl Instrum Methods Phys Res A*. 1999;422:129–32.
46. Morris CL, Adamek ER, Broussard LJ, Callahan NB, Clayton SM, Cude-Woods C, et al. A new method for measuring the neutron lifetime using an in situ neutron detector. *Rev Sci Instrum*. 2017;88:053508.
47. Mosset J-B, Stoykov A, Greuter U, Hildebrandt M, Schlumpf N, Van Swygenhoven H. Evaluation of two thermal neutron detection units consisting of ZnS/<sup>6</sup>LiF scintillating layers with embedded WLS fibers read out with a SiPM. *Nucl Instrum Methods Phys Res A*. 2014;764:299–304.
48. Murugadoss G. Synthesis and photoluminescence properties of zinc sulfide nanoparticles doped with copper using effective surfactants. *Particuology*. 2013;11(5):566–73.
49. Nakamura T, Schooneveld EM, Rhodes NJ, Katagiri M, Toh K, Sakasai K, Soyama K. A half-millimetre spatial resolution fibre-coded linear position-sensitive scintillator detector with wavelength-shifting fibre read-out for neutron detection. *Nucl Instrum Methods Phys Res A*. 2009;606:675–80.
50. Nakamura T, Schooneveld EM, Rhodes NJ, Katagiri M, Sakasai K, Soyama K. Evaluation of the performance of a fibre-coded neutron detector with a ZnS/<sup>10</sup>B<sub>2</sub>O<sub>3</sub> ceramic scintillator. *Nucl Instrum Methods Phys Res A*. 2009b;600:164–6.
51. Nakamura T, Kawasaki T, Hosoya T, Toh K, Oikawa K, Sakasai K, et al. A large-area two-dimensional scintillator detector with a wavelength-shifting fibre readout for a time-of-flight single-crystal neutron diffractometer. *Nucl Instrum Methods Phys Res A*. 2012;686:64–70.
52. Nakamura T, Toh K, Kawasaki T, Honda K, Suzuki H, Ebine M, et al. A scintillator-based detector with sub-100- $\mu$ m spatial resolution comprising a fibre-optic taper with wavelength-shifting fibre readout for time-of-flight neutron imaging. *Nucl Instrum Methods Phys Res A*. 2014;737:176–83.
53. Nakamura T, Toh K, Kawasaki T, Ebine M, Birumachi A, Sakasai K, Soyama K. A two-dimensional scintillation-based neutron detector with wavelength-shifting fibers and incorporating an interpolation method. *Nucl Instrum Methods Phys Res A*. 2015;784:202–7.
54. Nakamura T, Kawasaki T, Tohi K, Harjo S, Sakasai K, Alzawa K. Two-dimensional scintillation neutron detector for TAKUMI diffractometer in J-PARC MLF. *JPS Conf Proc*. 2021;33:011097.
55. Ollinger M, Craciun V, Singh RK. Nano-encapsulated ZnS:Ag phosphors for field emission flat panel display applications. *MRS Proc*. 2002;704:W8.4.1–6.
56. Ortiz-Rodríguez JM, del Rosario Martínez-Blanco M, Cervantes Viramontes JM, Vega-Carrillo HR. Robust design of artificial neural networks methodology in neutron spectrometry. In: Suzuki K, editor. *Artificial neural networks: architectures and applications*. London: INTECH; 2013. p. 83–111.
57. Peng WQ, Cong GW, Qu SC, Wang ZG. Synthesis and photoluminescence of ZnS:Cu nanoparticles. *Opt Mater*. 2006;29:313–7.

58. Peurrung AJ. Recent developments in neutron detection. *Nucl Instrum Methods Phys Res A*. 2000;443:400–15.
59. Pino F, Stevanato L, Cester D, Nebbia G, Sajo-Bohus L, Viesti G. Study of the thermal neutron detector ZnS(Ag)/LiF response using digital pulse processing. *JINST*. 2015;10:T08005.
60. Polte J. Fundamental growth principles of colloidal metal nanoparticles – a new perspective. *CrystEngComm*. 2005;17:6809–30.
61. Price WJ. *Nuclear radiation detection*. 2nd ed. New York: McGraw-Hill; 1964.
62. Rhodes NJ. Scientific reviews: status and future development of neutron scintillation detectors. *Neutron News*. 2006;17(1):16–8.
63. Rhodes NJ, Johnson MW, van Eijk CWE. The future of scintillator detectors in neutron scattering instrumentation. *J Neutron Res*. 1996;4:129–33.
64. Rhodes NJ, Wardle AG, Boram AJ, Johnson MW. Pixelated neutron scintillation detectors using fibre optic coded arrays. *Nucl Instrum Methods Phys Res A*. 1997;392:315–8.
65. Rhodes NJ, Schooneveld EM, Eccleston RS. Current status and future directions of position sensitive neutron detectors at ISIS. *Nucl Instrum Methods Phys Res A*. 2004;529:243–8.
66. Rodnyi PA. *Physical processes in inorganic scintillators*. London: CRC Press; 1997.
67. Rodnyi PA, Dorenbos P, van Eijk CWE. Energy loss in inorganic scintillators. *Phys Status Solidi B*. 1995;187(1):15–29.
68. SAVER. The neutron-detecting personal radiation detectors (PRDs) and spectroscopic PRDs market survey report. The National Urban Security Technology Laboratory, U.S. Department of Homeland Security, Science and Technology Directorate; 2015.
69. Shionoya S, Yen WM, Yamamoto H. *Phosphor handbook*. 2nd ed. London: Taylor & Francis Group; 2006.
70. Souriau J-C, Jiang YD, Penczek J, Paris HG, Summers CJ. Cathodoluminescent properties of coated SrGa<sub>2</sub>S<sub>4</sub>:Eu<sup>2+</sup> and ZnS:Ag, Cl phosphors for field emission display applications. *Mater Sci Eng B*. 2000;76:165–8.
71. Spowart AR. Measurement of the absolute scintillation efficiency of granular and glass neutron scintillators. *Nucl Instrum Methods*. 1969;75:35–42.
72. Spowart A. Measurement of the gamma sensitivity of granular and glass neutron scintillators and films. *Nucl Instrum Methods*. 1970;82:1–6.
73. Stefanescu I, Christensen M, Fenske J, Hall-Wilton R, Henry P, Kirstein O, et al. Neutron detectors for the ESS diffractometers. *J Instrum*. 2017;12:01019.
74. Swart HC, Greeff AP, Holloway PH, Berning GLP. The difference in degradation behaviour of ZnS:Cu,Al,Au and ZnS:Ag,Cl phosphor powders. *Appl Surf Sci*. 1999;140:63–9.
75. Sykora J, Schooneveld EM, Rhodes NJ. Development and future prospects of wavelength shifting fibre detectors at ISIS. *Proceedings of the conference: international collaboration on advanced neutron sources XXI, Mito, Japan; 2014*. p. 410–320.
76. Tojo T, Nakajima T. Preparation of thermal neutron scintillators based on a mixture of ZnS(Ag), <sup>6</sup>LiF and polyethylene. *Nucl Instrum Methods*. 1967;53:163–6.
77. Tripathi LN, Chaubey BR, Mishra CP. Luminescence in ZnS: (Cu, Tb) and ZnS: (Ag, Tb) phosphors. *Phys Stat Sol A*. 1980;60:185–92.
78. Usuda S. Development of ZnS(Ag)/NE102A and ZnS(Ag)/Stilbene phoswich detectors for simultaneous  $\alpha$  and  $\beta(\gamma)$  counting. *J Nucl Sci Technol*. 1992;29:927–9.
79. Usuda S, Abe H, Mihara A. Phoswich detectors combining doubly or triply ZnS(Ag), NE102A, BGO and/or NaI(Tl) scintillators for simultaneous counting of  $\alpha$ ,  $\beta$  and  $\gamma$  rays. *Nucl Instrum Methods Phys Res A*. 1994;340(3):540–5.
80. Usuda S, Sakurai S, Yasuda K. Phoswich detectors for simultaneous counting of  $\alpha$ -,  $\beta(\gamma)$ -rays and neutrons. *Nucl Instrum Methods Phys Res A*. 1997;388(1–2):193–8.
81. van Eijk CWE. Inorganic scintillators for thermal neutron detection. *IEEE Trans Nucl Sci*. 2012;59(2012):2242–7.
82. Wang X, Shi J, Feng Z, Li M, Li C. Visible emission characteristics from different defects of ZnS nanocrystals. *Phys Chem Chem Phys*. 2011;13:4715–23.

83. White L, Miller WH. A triple-crystal phoswich detector with digital pulse shape discrimination for alpha/beta/gamma spectroscopy. *Nucl Instrum Methods Phys Res A*. 1999;422(1–3):144–7.
84. Wilhelm K, Nattress J, Jovanovic I. Development and operation of a  ${}^6\text{LiF}:\text{ZnS}(\text{Ag})$ —scintillating plastic capture-gated detector. *Nucl Instrum Methods Phys Res A*. 2017;842:54–61.
85. Wu C, Tang B, Sun ZJ, Zhang Q, Yang Z, Zhang J, et al. A study of  $\text{ZnS}(\text{Ag})/{}^6\text{LiF}$  with different mass ratios. *Radiat Meas*. 2013;58:128–32.
86. Yamamoto S, Hatazawa J. Development of an alpha/beta/gamma detector for radiation monitoring. *Rev Sci Instrum*. 2011;82:113503.
87. Yamane Y, Linden P, Karlsson JK-H, Pazsit I. Measurement of 14.1 MeV neutrons with a Th-scintillator optical fibre detector. *Nucl Instrum Methods Phys Res A*. 1998;416:371–80.
88. Yanagida T. Study of rare-earth doped scintillators. *Opt Mater*. 2013;35:1987–92.
89. Yanagida T. Inorganic scintillating materials and scintillation detectors. *Proc Jpn Acad Ser B*. 2018;94:75–97.
90. Yasuda K, Usuda S, Gunji H. Development of scintillation-light-transmission type phoswich detector for simultaneous alpha- and beta (gamma)-ray counting. *IEEE Trans Nucl Sci*. 2000;47:1337–40.
91. Yen WM, Weber MJ. Inorganic phosphors: compositions, preparation and optical properties. Boca Raton: CRC Press; 2004. p. 302.
92. Yoshiro O. On the crystal growth of zinc sulfide phosphor. *Bull Chem Soc Jpn*. 1959;32(8):804–8.
93. Ziegler JF, Ziegler M, Biersack J. SRIM – the stopping and range of ions in matter. *Nucl Instrum Methods Phys Res B*. 2010;268(11–12):1818–23.

# Chapter 4

## ZnSe- and CdSe-Based Radiation Detectors



Shweta Jagtap, Madhushree Bute, Sapana Rane, and Suresh Gosavi

### 4.1 Introduction

Radiation is energy or particles that originate from source and can travel through space [1]. Radiations are of two types, namely ionizing or non-ionizing, depending upon its energy to knock out the electron from an atom or has capability to break the covalent bond. The studies proved that non-ionizing radiation, namely, radio and microwave energy are harmful, if used at very high doses. UV radiations are also non-ionizing type and can cause damage to DNA molecules causing cancer. The radiation that unstable atoms emit while releasing energy, to attain a more stable state, is known as ionization radiation and is more of a health threat to human beings as it causes the change in structure of the atoms in cells, and more specifically the DNA molecules inside the cells [1]. Besides these harmful side effects of radiation, it is used in several fields such as medicine, academics, and industry for the benefit humankind. Also, radiation has useful applications in various areas such as archaeology, space exploration, agriculture, geology, and law enforcement [2–4].

Radiation detectors are devices which sense and measure radiation emissions and/or levels of radiation produced by a source. Radiation detectors are used for two purposes, namely, protection of human being and radiation measurement

---

S. Jagtap

Department of Electronic and Instrumentation Science, Savitribai Phule Pune University, Pune, India

M. Bute

Department of Environmental Science, Savitribai Phule Pune University, Pune, India

S. Rane

Department of Electronics, Mamasahab Mohol College, Pune, India

S. Gosavi (✉)

Department of Physics, Savitribai Phule Pune University, Pune, India  
e-mail: [swg@physics.unipune.ac.in](mailto:swg@physics.unipune.ac.in)

applications. Radiation dosimeter is one of the examples of detection and measurement of radiation. The badges are utilized to detect high-energy radiation. These badges aware about protection from the most harmful effects of radiation exposure through informing the amount of radiation they have been exposed to along with its health effects [5]. Radiation detectors can be categorized depending on the type of radiation or by their underlying operating principles. They can be categorized broadly as: Gas-filled radiation detectors, Solid-state radiation detectors, and Scintillation radiation detectors. Scintillation radiation detectors use the light energy produced when the material interacts with radiations and eventually find the level of radiation. The scintillator light pulses can be of small-time span that enables the device and detection of large particle number in short time duration. Scintillating materials can be liquids or solids. The incoming radiation strikes the scintillating material that results into emission of photons followed by amplification of the signal using photomultiplier tube. The resulting output pulse is proportional to the amount of light energy entering the tube and to be detected. The Scintillation radiation detectors usually provide information on a variety of data about the source, incident radiation, their charges, particles, energies, etc. [6].

Scintillators are very important type of radiation detector in various nuclear technologies and radiation applications such as medical imaging, well logging, homeland security, marine and space exploration, and high-energy physics [7]. Scintillators are classified into two categories, namely, organic scintillators and inorganic scintillators. The selection of scintillator used for radiation detection is decided on the basis of radiation particles to be detected and their applications. Liquid organic scintillators have an outstanding ability to discriminate between gamma rays and neutrons or alpha particles based on detected pulse shape. Hence, it can be prominently used to detect neutrons or accelerated charged particles [6, 8]. The limitations of organic scintillators are their low density and detection efficiency, due to which inorganic scintillators are preferred for measuring X-rays or gamma rays. Inorganic scintillators can be operated at higher temperature than their organic counterparts [7, 9, 10]. Ionic solids composed of high-density crystals are used in inorganic scintillators that are mainly of two types, namely, single-crystal and polycrystalline ceramics. Single crystals exhibit efficient optical properties at low fabrication costs and hence are ideal in fields with extreme conditions of detection and in measuring high-energy radiation under harsh conditions. Polycrystalline ceramics has poor optical properties (transparency) and hence used for lower energy radiation detection applications [7]. The process of scintillation occurs in three steps, where in first step, the energy of incident radiation is transformed to electron-hole pairs, and as the energy is higher, massive number of electron-hole pairs is generated. The second step involves the energy gain of luminescent ions from these electron-hole pairs and lastly, in third step this energy is released in the form of photons when the ions undergo a transition from excited state to ground state. The conversion in first step is due to Compton scattering and photoelectric effect and the electron-hole formation is due to radiative decay, Auger process, and inelastic electron/electron scattering. The thermalization process helps to produce phonons resulting in the formation of low-energy electrons at the lower edge of conduction band and



holes at the upper edge of valence band. The entire process takes less than 1 psec and an energy loss is expected on the account of non-radiative transitions followed by luminescence due to electron and hole recombination at the luminescence centre.

The efficiency of luminescence can be studied by following Eq. (4.1):

$$\eta = \Upsilon SQ \quad (4.1)$$

Where,  $\eta$  is the luminescence efficiency,  $\Upsilon$  is the conversion process efficiency,  $S$  is transfer process efficiency, and  $Q$  is quantum efficiency of luminescence centre [8].

G. Bizarre [9] has also discussed the scintillation process using the following equation, wherein  $N_{\text{ph}}$  is the number of scintillation photons,

$$N_{\text{ph}} = \frac{E}{\beta E_{\text{gap}}} SQ \quad (4.2)$$

Here,  $E$  = Energy absorbed by the scintillator,  $E_{\text{gap}}$  = Band gap energy, and  $\beta$  = Average energy required to produce one thermalized electron-hole pair.

#### 4.1.1 Parameters Characterizing Scintillation Radiation Detectors

The efficiency ' $\eta$ ' is an important factor for the selection of good scintillators. The other affecting factors are decay time, afterglow of the luminescent signal, and radioluminescence after the excitation of ions.

The important terms associated with scintillators are as follows [11]:

- (i) Light yield: light yield can be defined as the ratio of number of scintillation photons to the energy deposited. Light yield can also be termed as light output and scintillation response.
- (ii) Decay time: The decay time of a scintillator is defined as the period it requires for the intensity of the light pulse to revert to  $1/e$  of its greatest value. Most scintillators have multiple decay times, and the effective average decay time is generally specified. The decay time is essential for quick counting and/or timing applications.
- (iii) Afterglow: Afterglow is the amount of scintillation light that remains after the X-ray excitation has stopped for a given amount of time. Afterglow can continue for hours in lengthy decay time components and can start within a millisecond.
- (iv) Radioluminescence: The wavelength distribution of scintillation light when triggered by ionizing radiations is referred to as radioluminescence. Generally, ionizing radiation interacts with materials to produce radioluminescence. The examples of this radiations are  $\alpha$  or  $\beta$  particles, and cosmic rays or photons such as  $\gamma$ -rays or X-rays. Also, the materials that show radioluminescence are designated as scintillations.

The decay time should be small for attaining fast response time. A linear response of the light yield is expected so as to maintain the proportionality with the irradiation. Inorganic scintillators proved to be of better use, taking into consideration their high efficiency and greater light yield compared to the conventional scintillators.

The high light yield of these detectors enables to detect radiations of low energy (or intensity) with a high signal-to-noise ratio (S/N). Taking in account the excitation energy, number of emitted photons per unit energy differs and this relation is nonproportional to the scintillation performance. This is important factor of consideration for practical applications and most suitable scintillator should be selected for the target energy. The scintillation decay time is directly related to the timing resolution of radiation detectors. The decay time is mainly affected by the speed of transfer of free electrons and holes from an ionization track to the emission centre and the lifetime of the luminescence state of the activator. The timing resolution parameter is of utmost importance for high counting-rate applications, such as PET. Further to detect high-energy photons, dense materials possessing high effective atomic numbers are preferred [11].

#### ***4.1.2 Materials Used in the Manufacture of Scintillation Radiation Detectors***

Till date, several studies have been carried out using inorganic alkali-halide crystals such as sodium iodide (NaI: Tl) and caesium iodide (CsI: Tl) activated with thallium, NaI: Tl, CsI: Tl. These materials, however, suffer large decay times and low radiation stability. Bismuth germanium oxide,  $\text{Bi}_4\text{Ge}_3\text{O}_{12}$  (BGO), and gadolinium orthosilicate,  $\text{Gd}_2\text{SiO}_5$ : Ce (GSO:Ce) make oxide-based scintillators that provide good mechanical strength and immunity to humidity [12]. Further, it also exhibits high stopping power, good density, and increased radiation absorption efficiency compared to alkali-halide [13, 14]. However, these two oxide-based scintillators exhibited very low light yield as compared to the two alkali-halides [14, 15]. In order to overcome these limitations, compounds belonging to the II–VI semiconductor group are being anticipated and investigated. In this article, the attempt is made to review and discuss the research development/advancement in the field of radiation detectors employing compounds belonging to the II–VI semiconductor group, particularly ZnSe and CdSe. These compounds are endorsed with a series of excellent properties such as good light output, better thermal and radiation stability, mechanical strength, rapid decay times, and non-hygroscopicity [16] that make them suitable in various applications [17, 18].

## 4.2 Crystal-Based Solid Scintillation Detectors

These scintillation detectors are simply crystals with refractive index between 1.4 and 2.5. Crystal-based solid scintillation detectors offer a variety of properties and wide range of characteristic parameters in a density scale of 2.5–7.9 g/cm<sup>3</sup>. Moreover, diverse array of decay time is available in this crystal family providing both slow and fast decay. Extensive stretch is observed in the light yield of these crystals from  $1.1 \times 10^4$  to  $7.5 \times 10^4$  photons/MeV. NaI crystal, possessing moderate values of majority of characteristic parameters among this family, is commonly chosen for employment [19]. The whole crystal surface, other than the part in contact with analyser photomultiplier tube, is coated with aluminium to protect the crystal from atmospheric moisture and obstruct the external light. When a crystal is used for high-energy radiations, the aluminium layer also blocks alpha and low-energy beta radiations. In order to enhance the reflection of visible light, this aluminium is whitened or layered with reflector materials such as MgO. These multiple reflections help reach the visible light to the analyser photomultiplier tube efficiently. On the ground of this efficiency, three types of crystal-based scintillation detectors are considered, namely, (1) planar, (2) well-type, and (3) through-hole detectors. Design change in the cylindrical structure of NaI crystal changes the radiation exposure of detector affecting counting geometry.

### 4.2.1 Planar Detector

One of the two flat surfaces in cylindrical NaI crystal is exposed to the radiations and remaining one is connected to the analyser through a light pipe relieved with light-transmittance grease. Nonetheless, this type can only deal with around half of the total possible radiation emission that it can perceive only 180° exposure out of all 360° radiation emission. This geometry of crystal is cited as  $2\pi$  counting geometry which proved not to be enough for the further analysis. The aluminium coating depleted is around 0.5 mm thick in this type of crystal detectors. When experimented with the design of crystal and set the results side by side, planar designs proved to be barely advantageous due to lower detection efficiencies. This experimentation gave birth to the next type of detectors.

### 4.2.2 Well-Type Detector

As the name suggests, a well-type crater is drilled at the centre of cylindrical crystal and aluminium is coated inside of the crater. The aluminium coating on this crystal is 0.25–0.5 mm thick in order to achieve maximum counting geometry. This modification helps in increasing the exposure to the radiation emission, further

enhancing the counting efficiency. The crater is called detector well, in which the counting sample is encompassed within a plastic or glass tube. This arrangement makes it feasible to receive more radiations. The encircling detector crystal possibly receives more radiation emissions from its  $360^\circ$  neighbourhood, objecting a  $4\pi$  counting geometry. However, if the sample tube slips in the well, it can result in a blemished or damaged detector. Additional concern related to well-type detectors is the position of sample so as to receive the objected maximum radiation. This sample should be placed at the exact centre of detector to attain optimal counting geometry. However, it is proven that this crystal design can approach to  $4\pi$  geometry closely but is incapable of achieving it efficiently and thus, the experimentation progressed towards next type of detectors.

### ***4.2.3 Through-Hole Detector***

To hold the sample volume at the centre of detector, the crater is elongated and turned into a through-hole design by boring past the well depth and keeping the aluminium coat similar to that of well-type. This design becomes an encircling hollow cylinder allowing the sample tube to be shifted up or down from the bottom of the detector. In this type, it is possible to put an integral number of detectors without disturbing one's performance. Evidently, this design achieves  $4\pi$  geometry and proves accommodative to a practical set up with different sample volumes [19].

## **4.3 Single and Polycrystalline ZnSe- and CdSe-Based Scintillators**

Wide-bandgap II–VI materials are expected to yield high performance when its application towards radiation detectors is considered. In modern technology, various methods are reinvented and/or modified in order to tailor and fine tune the growth mechanism and therefore the desired properties of crystals of wide-bandgap II–VI compounds can be achieved while growing. For example, ZnSe has a wide bandgap of 2.7 eV and CdSe has 1.74 eV. As per the specific need, these semiconductor crystals can be grown in the form of thin films and bulk crystals. Recently, use of quantum dots has also shown the potential for the scintillator application. In case of crystal grown method, various techniques are modified for growth control according to need of required layer structure, uniformity, and dopant level. Impurities and native defects, purity, and quality of the grown semiconductor compound play vital role in deciding the fundamental characteristics of the material and therefore considered as very important in deciding the key features. Crystals of II–VI compounds can be grown from all three phases of the desired materials compositions and dopants. Among them, chemical vapour transport (CVT) and physical vapour

transport (PVT) methods use vapour phase of the material as suggested by their names. But liquid phase is used in melt growth technique. However, melt grown technique is extensively known to produce bulk crystals in relatively short growth time. Also, molecular beam epitaxial growth and surfactant soft template are some of the popularly used methods for controlled synthesis of nanostructures for scintillation application. In this chapter, the details of melt growth technique and quantum dots for ZnSe and CdSe scintillators are discussed in brief.

### ***4.3.1 Melt Growth Technique-Based Scintillators***

The brief history of crystal growth revealed that crystal growth of the group II and VI semiconductor compounds deals with several challenges. Resolving stagnation in this field is very critical due to the various properties of materials, such as congruent melting points, considerable partial pressure in the compounds and volatility, high melting point of the constituent ingredients, low thermal conductivity and stacking fault energy, high tendency for twinning, and solid-solid phase transition. Today's modern radiation detector technology completely relies on very high-quality semiconductor materials. More prominently, every application demands very specific characteristics properties to be possessed by semiconductor material in use. To serve this purpose, doping of these semiconductor materials came in to existence. Unfortunately, the vapour transport technique can serve in this situation in a very limited manner because incorporation mode of dopant and compensation effect are strongly influenced by transport agents. Therefore, growth from near stoichiometry melts can be generously useful to solve the purpose. After realization of these facts, at the beginning, few attempts were demonstrated to achieve crystal growth from solution growth techniques, in which use of vertical travelling heater method (THM) [20], selenium rich melt-solution growth technique [21], and controlled vapour pressure technique [22] are being tested for its application in crystal growth. These methods are found to be reasonably handicapped showing unacceptable slow rate of deposition with impurities' inclusion. On the basis of empirical data and theoretical knowledge, few modifications in the melt growth method are put forward to avoid these practical implications. At the beginning, two variations in Bridgman (BR) method are suggested as high pressure and close space. In case of high-pressure technique, inevitable stoichiometry deviation and material deposition outside crucible are observed [23–25]. In another variation in Bridgman technique, prime requisite is a close system [26]. Having close system avoids mass transportation and deposition of dopant and semiconductor to the cooler regions [27, 28]; this also maintains stoichiometry [29]. Appropriate choice of container is crucial since it should sustain at high temperature and pressure. Usually, a quartz ampoule encapsulated in graphite crucible [26, 30, 31] is very suitable for this technique. In BR technique, shape of solid-liquid interface is determined by ratio of  $G/R$  [(Temperature) Gradient/(growth) Rate]. Experimental data [32, 33] suggested that  $G/R$  ratio in the range of 57–175 K/cm<sup>2</sup> gives fairly good quality ZnSe crystal growth, while 83 K/

$\text{cm}^2$  is considered to give optimum results. Moreover, it is also demonstrated that the growth conditions as 76 K overheating above 1797 K of melting temperature, i.e. temperature gradient of 30 K/cm and growth rate of 3.6 mm/hr., are capable of producing high quality twin-free ZnSe [28, 29]. Further the development of low-pressure Bridgman method is also established, which is configurable as vertical or horizontal forms, affecting the crystal properties. In order to grow radiation detector grade semiconductor crystals, various modifications in BR method are ascertained to achieve specific condition suitable for tuning crystal properties during its growth from the melt. Depending on slow or rapid cooling during solidification, most of the electric properties are determined. If solidification is followed by slow cooling, then the electrical properties are driven by impurity concentration and vapour overpressure, whereas in case of rapid cooling of ingot electric properties are driven by overpressure or quench temperature. If ultrahigh purity starting materials are used, High Pressure Bridgman (HPB) method has proven its capability to grow crystals with best spectroscopic grade properties, specifically when design is for large volume detectors.

From the material perspective, group II–VI crystal properties are enhanced and tuned specifically for various radiation detectors. ZnSe and CdS doped with isoelectronic Te are grown using BR technique nearly with 50 mm diameter and height [34]. Comparative studies of those crystals revealed that CdSTe could be used for gamma-ray spectroscopy, the emission shows peak at 640 nm attributed to decay of exciton trapped at Cd interstitial and S vacancies, while incorporation of Te enhanced defects. Further, by considering the different shaping time for the detector amplifier, an accountability for the presence of slow component is made and the comparative analysis of CdSTe, CsI (TI), and  $\text{CdWO}_4$  crystals for absolute light yield is presented. The red intense light yield of CdSTe crystal is approximately  $1.7 \times 10^4$  photons per MeV of absorbed gamma-ray energy and the decay time is described with a sum of two exponential decay components of  $18 \pm 6$  ns and  $270 \pm 40$  ns. However, the light yield for  $\text{CdWO}_4$  and CsI (TI) crystals is noted as  $1.1 \times 10^4$  and  $5.7 \times 10^4$  photons per MeV, respectively. However, for ZnSeTe, the measured decay time is large which is roughly 50  $\mu\text{s}$ , but shows comparable light yield (55,000 ph/MeV) to that of well-known red light emitting CsI (TI). The observations are made that, due to low Z of the ZnSeTe, it is not suitable for gamma-ray spectroscopy but shows significant application in low-energy X-ray detection, its scintillation intensity in the  $\mu\text{s}$  time scale is comparable to the  $\text{CdWO}_4$  crystal [34]. It is learned eventually that the scintillation properties very much depend on stoichiometry of the crystals, which can be tailored using various growth mechanisms and annealing methods. Further experimentation shows that when ZnSe crystal is grown using HPB technique, it can possibly be used for high temperature ( $25^\circ\text{C} \leq T \leq 160^\circ\text{C}$ ) solid state X-ray or gamma-ray detector [35]. However, in this studies, ZnSe crystal with heavy dislocation densities is observed due to ZnSe phase transformation just below the melting point from a hexagonal to cubic structure. A Comparative study between HPB and high-pressure vertical zone melting (HPVZM) growth processes is carried out to assess its feasibility for the growth of CdZnTe, CdSe, and ZnSe crystals for its respective application in large-volume ionizing

radiation detectors, large diameter polarizers, and multispectral optics (from visible to middle IR region) [36]. HPVZM process is offering distinct advantages compared to HPVB, by allowing controlled deviation from the stoichiometric composition or pre-set deviation from stoichiometry and thus also encompassing its scope in further extension of the method in development of more zinc and cadmium chalcogenides crystal preparation.

ZnSe:Te,O crystals are grown using modified BR–Stockbarger technique in a vertical compression furnace. Change in the optical band gap energy of ZnSe (2.608 eV) and ZnSe:Te,O (2.555 eV) crystals is observed owing to the impurities in defect level in ZnSe:Te,O crystals with maximum wavelength of the emission spectrum at 630 nm [37]. Exposure of ZnSe:Te,O scintillator to  $^{137}\text{C}_{\gamma}$ -ray gives the 11.9% energy resolution and produces 2.167 times higher light output than CsI (TI) with afterglow as 0.023% after 5 ms [38]. The ZnSe:Te,O scintillator decay curves consist of two components, 27  $\mu\text{s}$  and 83  $\mu\text{s}$  [39, 40]. In X-ray inspection scanners, scintillators with different atomic number and densities can be used to work in the energy range 20 keV–10 MeV for non-destructive testing. Similarly, low afterglow and short decay time of detectors allow rapid counting from large number of detectors. Initially the material like CsI (TI) with light yield  $5.5 \times 10^4$  photons/MeV and afterglow about 0.3–2% after 20 ms is considered, but the later development preferred afterglow up to 0.01–0.001% after 10 ms.  $\text{CdWO}_4$  meet this expectation but light output is very less. Therefore, the problem persists to tailor the material characteristics appropriately to meet the requirement in case of scintillators. Assessment of CdS(Te) crystal unequivocally indicated that the  $\text{Cd}_1$  (600 nm) and  $V_s$  (730 nm) participate in radiation emission and light output and afterglow properties are not meeting up to requirements. Soon, the development in the X-ray digital radiography offered the solution of incorporation of dual-energy detection systems and this is based on the effective differentiation between the materials with similar density but with varied effective atomic numbers. To address this issue, doping of ZnSe crystal is considered. However, previously, for this application, ZnSe(Te) crystal-based scintillator is not usable due to intrinsic properties of the crystal like long decay time, low density, and  $Z_{\text{eff}}$  along with poor transparency to own emission. Nevertheless, due to the development in the dual energy inspection scanners, ZnSe(Te) crystals turned out to be best suitable for low-energy array detectors, providing the ace of simultaneous identification and imaging of dangerous objects or substances and thus development of detectors for non-destructive testing of organic inclusions and cargo inspection proceeded. The Bridgman method is used for the ZnSe(Te) crystals growth [41]. Defect engineering in this case is very crucial. It is postulated that the tailoring of emission spectra range is possible by adding isovalent defects in such a way that the ionic radius and electronegativeness of these defects species differ substantially from the atom to be replaced with defects. Further, the analytical and experimental data suggested that inclusion of Te isovalent defects enhances defect formation in Zn sublattice, and the augmentation of Zn vacancies ( $V_{\text{Zn}}$ ) concentration is favoured. Thus, it is also observed that principle working band in case of ZnSeTe scintillator produces the luminescence around 630–640 nm. The addition of Te stimulates two processes, one is formation of stable

association of  $V_{Zn}$  and  $Te_{Se}$  (concentration of isovalent Te defects used to replace Se) and second is formation of mobile interstitial Zn. These processes make main elements of radiative recombination centre. The light yield of ZnSeTe is better than CsI (Tl), light yield is approximately  $7.5 \times 10^4$  photons/MeV, after glow is 0.05% after 20 ms, and decay time is 50–150  $\mu$ s.

The formation of luminescence centres for formation of radiation band in the range 630–640 nm is achieved according to the difference in the electronegativity of Zn metal and chalcogenides (Se, Te, O). Also, to alter the luminescence centre domination type, the introduction of oxygen in its active forms ( $O^0$ ,  $O^-$ ) and metals of group III (Al, In, Ga) in the quantity about 1/5 of Te concentration, in ZnSe is proposed. This makes alteration possible in the luminescence maxima in the range 590–610 nm, light yield about  $5 \times 10^4$  photons/MeV, after glow is 0.005% after 20 ms. The material with these properties shows potential of application in multi-energy X-ray microscopy and tomography. Consequently, combined use of ZnSe(Te) and CsI(Tl) in two energy detector array shows significant improvement in non-destructive testing of organic inclusions.

Along with the other scintillation properties, low reflection coefficient of ZnSe for electrons makes it suitable for the application in medium energy gamma radiation and beta particles detection. ZnSe shows that the presence of deep levels and optical transitions aroused from this results in luminescence band peaked at 600–630 nm. An intentional stability in the defect level can be tuned in to the iso electronically Te doped ZnSe crystal using Bridgman–Stockbarger method in a vertical compression furnace under argon gas [40]. The luminescence range 1.9–2.1 eV is achieved for ZnSeTe single crystals, which is advantageous for its application as scintillator. Further improvement in as-formed ZnSeTe single crystals can be brought in by thermal annealing in different environments, for example vacuum, zinc, tellurium, and selenium; the treatment is used to develop luminescence comprised of two strong overlapping bands at 2.15 and 1.95 eV, which are resulted out of stable defect complexes and hence capable of acting as efficient emission centres useful in scintillation detectors for medium energy gamma radiation and beta particles [40].

Bridgman–Stockbarger method is also adopted for the development of  $ZnSe_{(1-x)}S_x$  mixed crystals [41]. On varying the x concentration, the energy levels of radiative recombination centres in the band gap of  $ZnSe_{(1-x)}S_x$  crystals change easily. The crystal shows formation of sphalerite lattices, for which luminescence spectral band maximizes in the range 590–595 nm at room temperature. Light output usually in case of ZnSe(Te) is produced only after the crystal annealing in Zn environment and reported to yield increase up to value 1. While in case of  $ZnSe_{(1-x)}S_x$  mixed crystals when sulphur content in the crystal increases up to  $x = 0.3$  due to the optimum content of ternary complexes  $O_{Se}V_{Zn}Zn_i$ , it produces light yield up to 0.65 which further increases up to 1.05–1.09 after the crystal annealing in Zn environment. Similarly, short decay time of 0.001 ms offers better energy resolution and speed of the detector. Short afterglow as 0.002% after 20 ms offers effective range of the amplitudes of recorded signals in a detector. As-formed  $ZnSe_{(1-x)}S_x$  mixed crystals exhibit light output comparable to ZnSe(Te) ‘classic scintillator’ with better transparency to their



own radiation and better thermal stability (for energy of emitted photons  $h\nu \sim 2$  eV), indicating the possibility of futuristic development of  $\text{ZnSe}_{(1-x)}\text{S}_x$ -based X-ray and  $\gamma$ -ray detectors even at higher intensity of radiations.

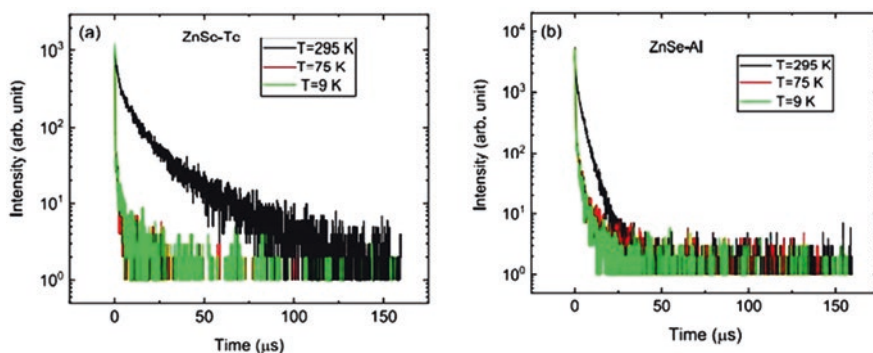
ZnSe with its relatively wide direct bandgap (2.70 eV) and broad transmission window has proven its scintillator application in X-ray and gamma-ray detection and often the isoelectronic elements like Te, S, O, or Al are doped to enhance scintillation performance. However, use of ZnSe in Large mass bolometer is also proposed to search for rare event, which includes neutrinoless double beta decay ( $0\nu$ -DBD) and Dark Matter interactions. This is because ZnSe contains  $^{82}\text{Se}$ , which is one of the most perspective materials in this field. For this, appropriate characteristics of ZnSe crystal are achieved using melt growth technique and further setting optimal annealing conditions [42, 43], due to which it is possible to achieve intentional enhancement in deep-level-related emissions specifically capable of detecting medium energy  $\beta$  and  $\gamma$  radiation and also for X-ray introscopy and tomography. ZnSe shows different scintillation properties for  $\alpha$  particles, and  $\beta$  and  $\gamma$ , which generate considerably different light/heat signatures and further imply discriminating emissions due to  $\alpha$  particles as background.

Also, use of ZnSe crystal for Dark matter detector (DMD) is exploited by studying the light emitted by nuclear recoils and  $\beta$  and  $\gamma$  interactions at 100 keV. In case of bolometers, 'The Light Yield of  $\beta/\gamma$  events ( $\text{LY}_{\beta/\gamma}$ ), defined as the amount of detected light per particle energy, does not depend on the energy'. The experimental data show that the Light Yield of  $\alpha$  particles ( $\text{LY}_{\alpha}$ ) is  $26.62 \pm 0.86$  keV/MeV which is higher than  $\text{LY}_{\beta/\gamma} = 6.416 \pm 0.008$  keV/MeV unlike in other known scintillating crystals [44]. This behaviour is not yet fully understood. However, this difference in light yield of  $\alpha$  and  $\beta/\gamma$  is further exploited and within the region of interest background due to  $\alpha$  particles is rejected.

LUCIFER (Low-background Underground Cryogenic Installation for Elusive Rates) is the experiment which is used to search for  $0\nu$ -DBD for which the feasibility of the cryogenic scintillating bolometers is demonstrated wherein  $\text{Zn}^{82}\text{Se}$  crystal highly enriched with the  $^{82}\text{Se}$  (95.5%) isotope is used. The performances of a ZnSe crystal functioned within the LUCIFER R&D is tested on the ground of energy resolution and discrimination capability of  $\alpha$  particles to avoid background noise. Further development in  $0\nu$ -DBD and DMD involved use of  $^{100}\text{Mo}$  embedded in  $\text{ZnMoO}_4$  crystal and  $^{82}\text{Se}$  embedded ZnSe crystal and the radiopurity of these crystals gives better energy resolution [45]. From few preliminary cryogenic tests, it is clear that the ZnSe crystals grown from the melt exhibit excellent bolometric performance; however, the precise designing of growth conditions plays very crucial role which is well established and described in the past [45]. For the construction of a bolometer/scintillation detector designed to study  $0\nu$ -DBD, large quantity of high-perfection large volume ZnSe is needed. Also, this demands particular information of point defects presented in the crystals in use. To achieve this, use of Bridgman technique to grow  $^{82}\text{Se}$  isotope is reported to give better results when high-purity starting materials are used [46]. For the production of enriched  $\text{Zn}^{82}\text{Se}$  crystal, specific growth conditions are practiced to control and manipulate defect formation

during crystal growth. It is worth mentioning here that the enriched  $\text{Zn}^{82}\text{Se}$  crystals grown using chemical vapour (CVD) and physical vapour (PVD) do not exhibit scintillation in as grown form. However, in this case at low temperature, enriched  $\text{Zn}^{82}\text{Se}$  crystals (grown using BR method) exhibit two intense luminescence bands positioned at 540 nm and 620 nm. The analysis of this could not identify the defect source responsible for first band (540 nm), but the second band is assigned to ‘A centre luminescence associated with close  $V_{\text{Zn}} - D_{\text{Zn}}$  pairs’. Further thermal annealing treatment of as-formed  $\text{ZnSe}$  crystal (BR method) increases crystal homogeneity and reduces microcracks, but despite of this,  $\text{ZnSe}$  without thermal treatment evidently produces better scintillation efficiency owing to the larger (order of ppm) existence of Zn vacancies and Al shallow donors pairs in the as-formed material, and which are the very cause of strong luminescence/scintillation in the red spectral region ( $\sim 620$  nm). Thus, the Bridgman technique provides a controlled way of defect engineering of closed donor-acceptor pairs (DAPs) of the order of a few ppm; therefore, grown enriched  $\text{Zn}^{82}\text{Se}$  material shows excellent material properties with high electron mobility at low temperatures and makes it a suitable candidate for bolometer/scintillation detector.

Similarly, for ionizing radiations, cryogenic scintillation detectors use  $\text{ZnSe}$  doped with Al or Te and is reported to give a fast response and higher light yield [47]. These results are presented in Fig. 4.1. The crystal grown using BR technique is reported to exhibit an emission band at 600 nm ( $\text{ZnSe-Al}$ ) and 640 nm ( $\text{ZnSe-Te}$ ). The red-light emission is subjected to radiative recombination of electrons which are originated from shallow donor centres and also due to the variety of impurity complexes and defects formed in the crystal [39]. Theoretical and empirical data come up with interesting fact that formation of those oxygen impurities and defects around ubiquitous Zn vacancies are generically featured in crystals during their growth, when BR technique is employed, thus the method is known to impact luminescent property of the crystal and therefore provides a way of engineering the material electronic properties to make it suitable for planned application [48]. The X-ray luminescence spectra and decay curves of  $\text{ZnSe-Te}$  and  $\text{ZnSe-Al}$  are analysed in



**Fig. 4.1** Decay performance of (a)  $\text{ZnSe-Te}$  and (b)  $\text{ZnSe-Al}$  scintillators. (Reprinted with permission from Ref. [47]. Copyright 2021: Elsevier)

the temperature range 77–295 K. An order of magnitude decrease in the effective decay time constant is observed, i.e. in ZnSe–Al, from 1.9 to 0.32  $\mu\text{s}$  and in ZnSe–Te from 4.5 to 0.46  $\mu\text{s}$ . The scintillation performances of Te-doped ZnSe and Al-doped ZnSe are analysed in the temperature range 9–295 K, when excited by  $\alpha$ -particles. The empirical data show that the light output of this scintillator at 75 K increases by  $80 \pm 5\%$  in case of Al-doped ZnSe and  $95 \pm 5\%$  in case of ZnSe–Te than room temperature. However, cooling to 9 K almost doubles the response of both scintillators. Importantly, the response time is also observed to be improving. This journey of continuous efforts towards good quality crystal growth is still an ongoing. Based on all empirical data and theoretical understandings, continuous efforts are put forward by research community to refine device development protocols, in order to tune growth dynamics and achieve desired qualities in semiconductor crystals.

### 4.3.2 *Quantum Dot-Based Scintillators*

With progressive research on radiation detectors using scintillation, it is proven that quantum dot-based nanostructured materials have shown efficient scintillation properties compared to conventional scintillating materials. These efficient properties are the result of high photon count, higher quantum efficiency, adjustable band gap, emission in visible region, high photon output, and superior work performance at room temperature. There had been some conventional radiation detectors such as cadmium-zinc-telluride performing efficiently at room temperature, although their crystal size was measured to be in centimetres in each direction. Quantum confinement provided a solution for this particular drawback. Quantum confinement regime shows difference in electronic and optical properties of materials due to radically small scale structure of energy bands. The distinctive length-scale for II–VI group semiconductor is 1–25 nm. This results in quantum-size effect and decreasing confinement width with decreasing particle size. The mentioned change in confinement width explains emission wavelength shifting towards blue region. Taking this shift direction in account, structures are grouped into 1D (quantum well), 2D (quantum wire), and 3D (quantum dot confinements). These quantum dots are zero-dimensional semiconductor crystals, in which decreasing size increases the energy band gap. This fine-tuning of band gap energy in visible region results in improved coupling with photomultipliers and gives efficient photon count. This improved photon output efficiency at room temperature is not seen in conventional scintillators. Moreover, unlike conventional scintillators, quantum dot scintillators show high-energy resolution and have a wide choice of photon transducers and photomultipliers. The photomultiplier tube used with conventional scintillators have quantum efficiency less than 25% as their output wavelengths are in UV and blue regions. Nevertheless, the property of quantum dots to adjust output wavelengths in visible region provides an advantage of increased scintillation efficiency up to 70% [49]. It is difficult to explain the multicolour photon visuals in scintillation with

conventional scintillators as they show indefinite resolution in emission peaks in the photoluminescence plot. The properties of quantum dots are hence proved to be efficient for scintillation over the conventional scintillation; however, their properties change depending upon the materials and their structures which vary with their synthesis.

Quantum dots differ in scintillation properties relative to their synthesis process. The synthesis processes were studied on different levels where a combination of skills and considerable amount of research was required for higher quantum yield. Along with quantum yield, high optical quality and well-defined size and shape were principle parameters to attain higher scintillation efficiency. From continuous experimentation and timely evolutions, it is proven that these parameters can be optimized using particular synthesis processes. Further, Létant and Wanga [50] reported in their study of semiconductor quantum dot scintillators under alpha and gamma radiation that optical parameters such as quantum efficiency and emission wavelength play key role to decide scintillation ability of the nanomaterials. These parameters can be controlled on molecular level with appropriate choice of synthesis methods. The luminescence that advances the scintillation property of materials is tuned with the help of modern synthesis methods. This kept researcher going with their experiments of new synthesis techniques and use of quantum dots in both industrial and academic fields. In the early days, the research for synthesis methods with higher quantum yield and the products having higher quantum efficiency was accelerated. Initially, synthesis of quantum dots was reported with cadmium series by aqueous and organometallic methods. These two methods were known to give highest possible yield with high-quantum-efficiency and emissions in visible or near-infrared regions advantageous for scintillation. Furthermore, Hines et al. [51] recorded ~20–50% quantum yield of luminescent ZnSe quantum dot scintillators with improved luminescent properties and better crystallinity. Reports by Suemune et al. [52] state that, owing to the scintillation efficiency of CdSe with ~20–30% of PL quantum productivity and broad emission spectra, this improved synthesis of ZnSe quantum dots was carried out for better results. As comparatively narrower band gap of CdSe gave better luminescence in red to green emission region, wider band gap ZnSe quantum dots provided expected blue emission on the grounds of quantum size effect. In many quantum dot synthesis methods, two processes are involved, namely, nucleation and growth of quantum nuclei. For example, in organometallic synthesis method, the organometallic precursors are nucleated and slowly processed to grow in a hot alkylamine coordinating solvents such as trioctylphosphine oxide (TOPO)-hexadecylamine (HDA) mixture. Time involved for these individual processes changes the size dispersion and optical properties of resulting quantum dots. Thus, the size of quantum dots can be varied by changing the growth time and thus, changes in optical properties are observed. After much evolution of ZnSe quantum dot synthesis processes via aqueous, organometallic, microwave synthesis, hot-injection method, sol-gel routes the highest quality quantum dots for scintillation with better luminescence were resulted through green synthesis route, as developed by Chen [53]. The method is proven to be cheaper and environment-friendly as it avoids the use of expensive, toxic, and air-sensitive chemicals like

phosphine and oleic acid that are commonly used in organometallic synthesis. In addition to it, properties and morphology of resulted quantum dots were desirable for enhanced scintillation efficiency. The resultant quantum dots also preserved their own crystallinity and tuneable range of wavelengths. Prior to the green synthesis techniques, the poor luminescence properties of quantum dots were treated with shelling them up or creating an alloy from the same.

Marie-Eve Delage et al. [49] studied the characteristics of quantum dot concentration for scintillation purpose and scintillation efficiency was plotted as a function of quantum dot concentration. It was seen that the scintillation output was linear function of quantum dot concentration when measured with different energy irradiation and different integration times. In this study, the photoluminescence properties of ZnSe quantum dots were in fine agreement with the estimated quantum size measurements obtained by AFM. These quantum dots were in the range of 11 nm of diameter with zinc-blend crystalline structure. The same study agreed to the reports of changing the size of quantum dots with changing growth time, thus showing the favourable wavelength shift in emission spectra due to quantum confinement. Ryzhikov et al. [54] studied the scintillation characteristics of ZnSe quantum dots to find out the parameters with practically efficient values. The studied ZnSe quantum dots with effective atomic number 33 were recorded to have density as  $5.4 \text{ g/cm}^3$ . For same sample, the conversion efficiency was reported to be 19.4 with decay time of 5–7 microseconds. After 10 milliseconds of radiation removal, the glow seemed to be 0.05%. On irradiating with X-rays with  $\lambda_m$ , the attenuation coefficient was  $0.1\text{--}0.3 \text{ cm}^{-1}$ . Refractive index for this wavelength was recorded to be 2.4 and the emission wavelength changed to maximum 610 nm at 300 K. Other irradiation such as gamma rays showed the radiation stability limit of ZnSe to be  $10^8 \text{ rad}$ . All these observations were in a good agreement to the expected values with good quantum efficiency of 19.4%, thus making ZnSe the best choice for scintillation applications highly effective in energy ranges 20–80 KeV.

#### 4.4 Performance of Doped ZnSe- and CdSe-Based Radiation Detectors

Scintillation is the process of absorption of incident ionizing radiation followed by emission of characteristic spectrum where the wavelength of the emitted radiation is generally longer than that of absorbed radiation. Scintillating materials or luminescent materials utilize this phenomenon to emit light in the visible region after absorption of high-energy radiation like alpha particles, beta particles, gamma rays, neutron rays, or X-rays. Several organic compounds exhibit inherent fluorescence on absorption of photon by virtue of their conjugated nature and electronic transitions occurring between energy levels of a lone molecule. Moreover, organic scintillators can exist in the form of pure organic crystals, organic solutions (solvent containing organic scintillator), or plastic scintillators. It is well understood that, in

pure crystals, the bandgap represents a band of energies that an electron can never occupy. However, when electrons gain sufficient energy by absorption of incident radiation, it undergoes a transition from valence band to conduction band by overcoming the bandgap and leave a hole in the valence band. This excited electron eventually de-excites back to the valence band by emission of photon. The process of photon emission in this case is, however, an inefficient one. The loss of energy is governed by other mechanisms such as non-radiative emissions and inelastic electron-electron scattering. Moreover, for pure crystals, the energy emitted during de-excitation does not lie within the visible range on account of wider bandgaps.

Doping of ZnSe and CdSe with suitable materials known as activators is an effective way of overcoming these problems. Dopants are so chosen that the process introduces additional energy levels within the forbidden bandgap of the pure crystal. Thus, the emitted photons are of lower energy (in the visible region of the electromagnetic spectrum) as the electrons de-excite to the valence band through these metastable energy states. In addition, doping also causes crystal lattice point defects, which dictates the radiation characteristics of doped radiation detectors or scintillators [55, 56]. Improved conversion efficiency and better radiation stability have also been reported for doped II–VI semiconductor compounds [55, 57]. Therefore, the creation of defects in the surrounding sublattice of pure crystal is stimulated by an isovalent dopant (IVD) atom as it differs from the substituted atom in terms of its ionic radius and electronegativity. Further, these isovalent dopants for II–VI semiconductor compounds can be characterized into two types. The first category consists of IVD that introduces localized energy states into the band—isolated energy levels or exciton levels on an isoelectronic dopant centre. The isoelectronic doping alters the recombination properties of the material by introducing new recombination channels which act as electron traps and provide high scintillation efficiency. The second type of IVD creates energy levels in the form of non-forbidden (allowed) energy bands.

Despite the fact that the IVD has the same valency as that of the replaced atom in the parent lattice, critical properties such as ionic radii, covalent radii, ionization energy, ionizing property with surrounding atoms of the lattice, and electronegativity might differ significantly. The bond energy of donor (D) or acceptor (A) dopants is of higher order than that of IVD charge carriers. However, the charge localization on the IVD is comparatively higher. This combination causes the development of isolated local states inside the band gap (after the first kind of IVD is introduced), with energy levels functioning as foci of quenching or emission, or changes in the zone spectrum of permissible bands (IVD of the second type). When the first and second type IVDs are introduced together, the band gap may be varied; at about the same rate, local levels are formed, generating emission centres. Ryzhikov et al. [58, 59] reported that tellurium (Te)-doped ZnSe improved the defect formation in ZnSe lattice structure. It was observed that the addition of Te as a dopant prompts the formation of recombination centres responsible for efficient emission. Lee et al. [60] investigated the radiation properties of oxygen-doped ZnSe photodiode for alpha-, beta-, and gamma- ray detection. The resolution for gamma quanta was observed to be 6.3% and hence study concluded that  $\alpha/\gamma$  nearly equal to one along

with sufficiently high resolution, good light output makes this photodiode a good candidate for alpha-, beta-, and gamma-ray detection. Cho et al. [56] also compared the performance of conventionally utilized CsI(Tl) scintillator with oxygen and tellurium-doped ZnSe (ZnSe(O) and ZnSe(Te) respectively). The results showed that O and Te-doped ZnSe scintillators exhibit exceptional properties such as excellent light yield, low afterglow, and high conversion efficiency. Also, ZnSe(O) showed promising radiation detection properties in the range of 20–200 KeV. Pranciškus et al. [61] studied the photoluminescence spectra of Te, O, and O-Al co-doped ZnSe. Te and O-doped ZnSe exhibited higher luminous intensity (by a factor of  $\approx 40$ ) than undoped ZnSe which was further found to be increased after O and Al co-doping. The authors concluded that, despite the fact that aluminium cannot function as an activator, it appears that adding this impurity to the ZnSe crystal tends to increase oxygen incorporation and, as a result, the formation of higher densities of defect centres responsible for efficient emission. With such a significant rise in photoluminescence intensity, there is a good chance of a significant increase in radiative recombination via the impurity energy levels developed because of suitable doping. More recently, colloidal quantum dots (cQDs) have gained a lot of interest in the scientific community as potential radiation detectors primarily because they exist in the nanometer scale leading to the phenomenon of 3D quantum confinement effect of cQDs that can be tuned as a function of size which results in greater light output than their bulk counterparts [62]. Lecavalier et al. [63] synthesized water dispersed multi-layered core-shell CdSe–CdS–Cd<sub>0.5</sub>Zn<sub>0.5</sub>S–ZnS cQDs for radiation detection. The observation indicates a linear relationship between the luminescent intensity and dose of ionizing radiation, rendering it as a promising candidate for scintillator application.

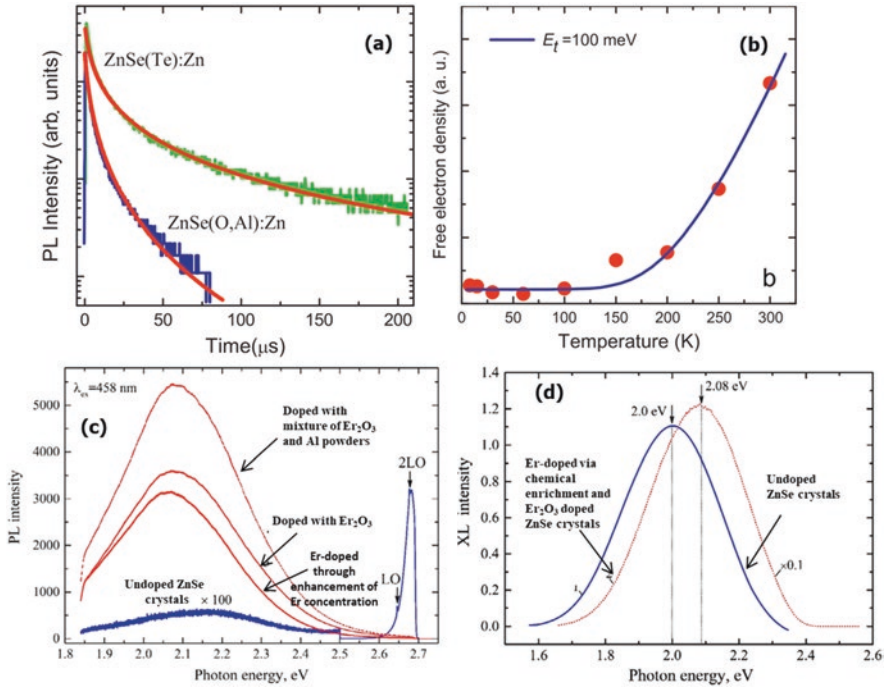
Groeneveld et al. [64] used ZnTe seed clusters for the synthesis of (Zn,Cd)Te/CdSe colloidal hetero-nanowires. The growth of the nanowires is attributed to the inclusion of CdSe. The emission spectra for the synthesized hetero-nanowires were in the range of 530–760 nm with high quantum yield. Also, tuning the composition of (Zn,Cd)Te/CdSe could successfully control the optical properties of the hetero-nanowires [64]. Hence, doping with suitable activators will enhance the scintillating properties of ZnSe/CdSe material to a great extent. The quality of scintillating materials has been demonstrated to be influenced by factors such as doping, annealing, and heavy ion irradiation. Kim et al. [65] reported synthesis of zinc selenide (ZnSe:O) single crystals doped with 2 wt% oxygen and annealed using excess Zn conditions. The XRD investigation demonstrated that the lattice constant drops after annealing at 1290 K with increase in oxygen impurities. While the energy band gap of annealed ZnSe:O single crystals reduces from 2.60 to 2.58 eV with excessive Zn, it does not alter for ZnSe single crystal structure. The radioluminescence of the annealed ZnSe:O scintillator stimulated by X-rays has a highest emission wavelength at 595 nm. The annealed ZnSe:O scintillator has a comparative light output of approximately 1.277 times that of the CsI:Tl scintillator. The annealed ZnSe:O scintillator also exhibited comparatively high relative light output of (1.28 times) than CsI:Tl and good afterglow level (0.012%) after 5 ms. Additionally, it was observed that, when exposed to Cs 662 KeV gamma rays, the energy precision of

the heated ZnSe:O scintillator was 7.4%. These findings showed that the annealed ZnSe:O scintillator not only have higher afterglow level and a higher relative light output than the CsI:Tl scintillator, but its timing characteristics make it ideal for detection in an introscope device. As a result, the annealed ZnSe:O scintillator is predicted to be suitable for X-ray detectors in military surveillance systems.

It was observed in the previous decade that the optical transitions deliberately insert deep levels in the band gap of Te-doped ZnSe and result in at least two significantly continuous luminescence bands. This deep level of emission is expected to be created by co-doping of iso-electronically doped ZnSe crystals, which could have a major impact on emission efficiency and other characteristics crucial for the crystals' employment in scintillation detectors. Based on this, Shevchenko et al. [66] evaluated the luminescence characteristics of ZnSe scintillation crystals co-doped with oxygen (O) and aluminium (Al) to those of typical tellurium (Te)-doped ZnSe scintillators in continuous-wave and pulsed irradiation in the range of temperature of 8–300 K. As the temperature reaches room temperature (RT), a significant increase in the low-energy element of the deep-level-related emission is detected. The higher density of recombination centres is important for the improved low-energy emission component in the co-doped crystals, according to donor–acceptor pair (DAP) recombination. However, high-energy (HE) charged electrons are primarily collected by the previous centres, contributing to the strengthening of the HE band. On the other hand, thermal ionization of the donors in the DAPs is responsible for the HE band and this leads in suppression of this band at extreme temperature (see Fig. 4.2a). A portion of the ionizing electrons recombine non-radiatively, while the remainder are grabbed by the LE band recombination centres and assist to its amplification. This improvement is stronger in ZnSe(O,Al):Zn crystals with a large density (see Fig. 4.2b). Similarly, Hizhiny et al. [67] studied scintillation effects of Al and Te-doped ZnSe. Their findings showed that doping ZnSe crystals with Te or Al reduces resistivity significantly (from  $10^{12}$  to  $10^9$  and  $10^{12}$  to  $10^8$   $\Omega\text{cm}$ , respectively). Both TeSe and AlZn defects form hole traps, but AlZn generates a deep trap, whereas TeSe produces a shallow trap, which is unstable at RT. ZnSe, ZnSe(Te), and ZnSe(Al) showed a 5–8 order of magnitude drop in resistivity when exposed to annealed zinc vapours. The creation of deep hole traps on interstitial defects  $\text{Zn}_i$ , as well as the destruction of zinc vacancies, contributes to the enhancement in conductivity of the samples following annealing in zinc vapours. Also, the trapping characteristics of doping-related point defects vary when  $V_{\text{Zn}}$  is destroyed and this action offers an innovative mechanism for annealing-induced conductivity gain.

On the other side, Ryzhikov et al. [54] revealed variations in scintillation and optical characteristics of ZnSe (Te,O) crystal-based scintillators when exposed to the gamma, electron, proton, and neutron ionizing radiations. The analysis indicates that when crystals are irradiated with neutrons, light output improves by 20–150%, with significant improvements in optical properties in the visible and infrared (IR) spectrum regions. Light output of gamma-irradiated scintillator crystals ZnSe (Te,O) decreases by less than 10–12% under dosages of 100 Mrad. Similar properties were observed in case of samples irradiated with electrons. It was observed that, the biggest dramatic loss of scintillation characteristics of ZnSe (Te,O) crystals was





**Fig. 4.2** (a) The temperature dependence of PL intensity of free electron density and (b) Photoluminescence decay kinetics of LE band (at 1.95 eV) measured in ZnSe (O,Al):ZnSe and ZnSe(Te):Zn samples at 8 K. (Reprinted with permission from Ref. [66]. Copyright 2013: Elsevier); (c) Room-temperature photoluminescence spectra of undoped and Er doped (3 ways) ZnSe crystals. LO and 2LO are the first – and second-order of longitudinal optical phonon mode in ZnSe. Excitation wavelength is 458 nm and (d) X-ray luminescence spectra of undoped Er-ZnSe crystals at 80 K. (Reprinted with permission from Ref. [68]. Copyright 2014: Elsevier)

caused by proton irradiation, with selective absorption spectrum arising in the IR (4–7  $\mu\text{m}$ ) range. Owing to the role of light output and the minimum afterglow level, this model is excellent choice for tomographs and current X-ray introsopic technologies. Also, it can be used as dosimeters for detection of  $\gamma$ - and  $\beta$ -radiation at high dose rates [66].

According to literature, the scintillator ZnSe (Te) has efficiently filled the void in the ‘scintillator-photodiode’ detector family for advanced radiation introsopes. For example, in comparison to CsI crystals, scintillators fabricated by isovalently doped ZnSe crystals have 4–7% greater translation efficiency and a  $10^3$ – $10^4$  times greater radiation stability (TI) [69]. It is also well known that some complex molecules based on broad-band substances (for examples, p-ZnTe–n-CdSe heterostructures) exhibit good photosensitivity in the visual spectra [70]. Photoreceivers based on heterostructures created directly on the surface of this scintillator should be possible because of a unique combination of semiconductor and scintillation capabilities of crystals ZnSe(Te,O). Also, small dimensions, compactness, high operational

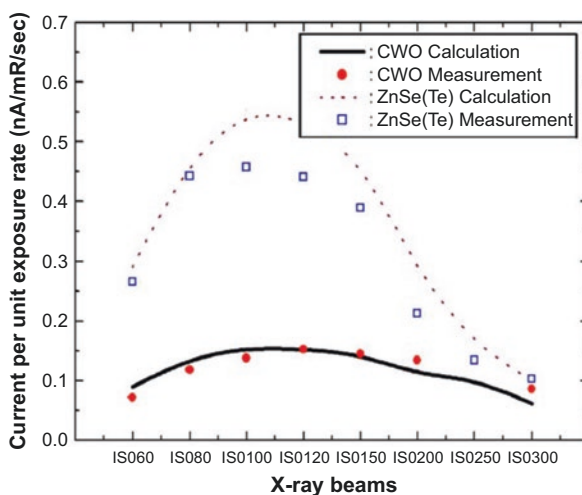
characteristics, and design simplicity are the advantages of solid state combined detectors (CD). These CD consist of a scintillator and a barrier layer photocell. In addition, such CD detector does not require power sources. Thus, Focsha et al. [70] developed a photosensitive heterostructure – semiconductor scintillator type CD – ZnSe(Te,O)/p-ZnTe–n-CdSe. The cumulative impact of ZnSe (Te)/ p-ZnTe–n-CdSe revealed strong radiation sensitivity owing to the close contact of the scintillator and the HP, which reduced reflected losses as well as exhibited high spectrum coherence factor (0.62–0.98). In addition, the short-circuit current in the output circuit of the combine detector (CD) is linearly proportional to the X-ray radiation dose rate in the interval of 360 R/min and the CD can work at temperatures in the range of RT–100 °C. The heterostructures–photoreceiver has a response time of  $10^{-5}$  s that is the same as the scintillator flash duration. Doping of rare-earth in isovalent dopant results in the creation of an acceptor level, which offers an extra releasing channel for electron traps [71]. In particular, emissions in the visible area are detectable in ZnSe with a high Er content. In order to use ZnSe single crystals as efficient scintillation radiation detectors, the research of defect structural alteration produced by Er-doping and processes of Er-stimulated radiative recombination are essential. Thus, Nasieka et al. [68] investigated the effects of Er-doping on the transparency, luminescence, and structural characteristics of ZnSe single crystals. Er was carried out in three different ways: (1) by inserting  $\text{Er}_2\text{O}_3$  powder; (2) by chemically enhancing Er concentration; and (3) by injecting  $\text{Al}_2\text{O}_3$  and  $\text{Er}_2\text{O}_3$  oxide mixture. The resonant Raman Scattering (RS) spectrum of undoped ZnSe crystals and crystals doped with Er atoms in diverse manners were also studied. According to RS spectra, Er dopant (10–3 wt.%) causes significant disordering of the initial crystal lattice due to the integration of rare-earth atoms with large radii, which causes significant lattice deformation. It results into broadening and decrease in intensity of vibrational spectra. Also, additional absorbance band was observed in case of Er doping. At the same time, Er-doping enhances the effectiveness of laser-excited luminescence (>100 times) and X-ray luminescence (>10 times) (see Fig. 4.2c, d). The maximum photoluminescence intensity is attained by co-doping ZnSe with  $\text{Er}_2\text{O}_3$  and aluminium particles in laser-driven luminescence. Though Al cannot operate as an accelerator, its presence appeared to increase oxygen integration into the ZnSe crystal, resulting in the production of a larger density of defect centres necessary for efficient emission. The impact of Er-doping on luminescence effectiveness suggested that rare earth metal doping in ZnSe crystals can be effectively used for scintillation purposes.

QDs have recently been integrated into liquid scintillators to control the emission spectrum. This procedure also presents a worthwhile enhancing performance of the battery. In this context, Xu et al. [72] reported CdSe/ZnS quantum dots (QDs) (made in various CdSe/ZnS ratios) as an Emulsifier-Safe liquid scintillator. As additional QDs were incorporated in Emulsifier-Safe liquid scintillator, the colour of the combination changed from blue to blue-green followed by deep yellow-green seen from RL emission spectra. In addition, as the number of CdSe/ZnS QDs increased, the relative luminescence intensities at 520 nm raised exponentially with decreased relative intensities at 420 nm. In addition, as the fraction of QDs in the combined

solution increases, the transmittance reduces. Finally, it was determined that in the case of liquid scintillation, QD doping is utilized to adjust the emission spectrum, hence improving spectrum coupling and matching. This synergistic strengthen effect can be used in a variety of optical monitoring and detecting applications [73].

## 4.5 Comparison of ZnSe/CdSe with Traditional Scintillators

The II–VI semiconductor compounds, particularly ZnSe and CdSe, are the preferred material for low-energy detectors among identified scintillators. ZnSe and CdSe have outstanding scintillation properties since they have excellent mechanical strength, non-hygroscopicity, and no cleavages. Further, they show remarkable physical properties such as decay time, light output, and radiation stability. As a result, they were shown to be more appropriate for detecting low-energy gamma radiation, alpha- and beta-particles than traditional scintillators [74]. For example, Ryzhikov et al. [75] built linear-array detector modules based on traditional  $\text{CdWO}_4$  (CWO) and new ZnSe (Te) scintillator modules for use in X-ray monitoring systems. In the low-energy X-ray system, ZnSe (Te) outperformed other materials in terms of photocurrent and detective quantum efficiency (DQE). Also, ZnSe (Te) performed better in the low-energy X-ray system and was comparable to CWO in the high-energy X-ray system in terms of photocurrent and detective quantum efficiency (DQE) [76]. Similarly, Kwak et al. [76] reported the comparative study between ZnSe(Te) and traditional CWO using linear-array detector modules. The results indicated that, photocurrents of ZnSe(Te) detectors per unit illumination rate were two to three times larger than those of CWO detectors (Fig. 4.3). Furthermore, it was observed that ZnSe(Te) exhibited better results when the depth of scintillator is optimized. In contrast, it was discovered that combining ZnSe (Te) and CsI(Tl)



**Fig. 4.3** Photocurrent comparison between CWO and ZnSe(Te). (Reprinted with permission from Ref. [76]. Copyright 2005: Elsevier)

crystals in a two-energy detector array significantly enhanced the effectiveness of technology developed to detect organic inclusions [77, 78].

Scintillating films are utilized in image capturing to convert X-ray and gamma radiation to visible light. CsI(Tl) layers produced in a vacuum are commonly used in image formation technologies in medical instruments [79]. The primary characteristics of the system are its high conversion capacity for high-energy radiation, the ease of thermal vacuum deposition, and the columnar shape of the developing layer, which increases its resolving power. Later, as a scintillating material, ZnSe (Te) was introduced, and its properties were found to be relevant. It has a conversion efficiency that is closely similar or maybe better than CsI(Tl) and it has higher radiation hardness and less hygroscopicity than CsI(Tl). As a result, it appears acceptable to produce vacuum-condensed ZnSe(Te) layers and compare their properties to those of CsI(Tl). Fedorov et al. [79] have compared crystalline structure, morphology, and scintillation properties of these ZnSe(Te) and CsI(Tl) layers. They used physical vapour deposition in a vacuum to create both CsI(Tl) and ZnSe(Te) layers in this investigation since this technique results into an identical deposited layer of dopant and initial source. The morphological analysis revealed that CsI(Tl) layers produce a columnar-like morphology, which is considered to be important since the columns operate as a sort of light guide, ensuring improved resolving power in collected images. The layered cross sections of ZnSe(Te) were dependent on the layer deposition rate, whereas the layer cross sections of CsI(Tl) were independent on the layer deposition rate. As a result of this, higher deposition rate resulted in poor directed growth. However, 0.4 wt.% Te in vacuum-deposited ZnSe(Te) layers did not exhibit significant scintillation characteristics in their initial condition. However, annealing in Zn environment significantly increases scintillation capabilities by promoting the production of defect complexes around the Te dopant, which behave as light emitting centres under radiation exposure.

Apart from ZnSe and CdSe nanomaterials, Yoneyama et al. [80] presented a comprehensive investigation of inorganic scintillators including  $Gd_3A_{12}Ga_3O_{12}$ : Ce (GAGG),  $Gd_2O_2S$ : Tb (GOS), CsI:Tl (CsI),  $Lu_3A_{15}O_{12}$ : Ce (LuAG), and  $Y_3A_{15}O_{12}$ : Ce (YAG). The results revealed that GOS showed maximum light yield, followed by CsI, GAGG, CWO, YAG, LuAG, and BGO. The best spatial resolution of micro X-ray radiography pictures was achieved with GAGG and LuAG, followed by CsI, CWO, and YAG. Except for GOS, the visual quality was nearly identical. These findings suggest that with a low X-ray flux source, CsI is acceptable for micro X-ray radiography and computerized tomography, while GAGG and LuAG are suitable with a high X-ray flux source.

## 4.6 Applications

Scintillators or radiation detectors have consistently been in demand over the past decades in various industries and areas of research. Some of the high temperature scintillators can also be utilized in extreme operating conditions of high temperature

and pressure. The well logging industry where digging of extremely deep oil wells is done to extract fuels generally has temperatures of around 175 °C and pressure of  $\approx 20,000$  psi [81]. Therefore, robust scintillators that exhibit good mechanical strength and are able to sustain under extreme conditions are utilized in this industry. ZnSe- and CdSe-based scintillators also find applications in diverse areas such as medical science, X-ray tomography, high-energy physics (HEP), and nuclear and space science. These materials have been proven to offer significant benefits over other conventionally used detectors for detecting alpha, beta, and low-energy gamma radiation. Moreover, they also demonstrate excellent performance at considerably high temperature and high dose loads [43]. In comparison to photon beam radiotherapy, proton therapy is useful in treating malignancies as it can provide highly precise dosages to tumours while decreasing radiation exposure to normal organs. The tendency of a proton beam to concentrate on a specific spot necessitates accurate equipment and treatment dosage monitoring. Scintillators can be here utilized for indirect dosage monitoring and equipment quality control along with direct primary proton beam tracking. Computer X-ray tomography is another useful technology for detecting diseases before they become serious, especially those that require surgery. Explosives are distinguished from organic materials using ZnSe crystals in security applications. Gamma-ray detectors used in gamma-ray spectroscopy are frequently employed in space exploration to study cosmic phenomenon and composition of various celestial bodies and are subjected to high radiation conditions resulting from sources such as solar flares and cosmic rays. Thus, scintillators with high detection efficiency, good energy resolution, and reliability are preferred in this field.

## 4.7 Conclusion

This book chapter focuses mainly on ZnSe- and CdSe-based scintillation detectors. The phenomenon of scintillation can be described as the emission of characteristic spectrum known as luminescence on absorption of incident radiation. This luminescent property can be observed in various organic and inorganic materials. Several studies show that, although numerous organic materials inherently exhibit this interesting property, inorganic scintillators are generally preferred for high-energy radiation detection. This is due to the fact that inorganic materials exhibit properties such as high detection efficiency and satisfactory decay time and are able to sustain high operating temperature conditions rendering them suitable for efficient radiation detection. More particularly among the inorganic class of materials, ZnSe- and CdSe-based detectors are better suited for radiation detection application as compared to conventionally used scintillating materials, for instance,  $\text{PbWO}_4$  and  $\text{CdWO}_4$  (CWO). Here, we also discuss the closed space vapour transport technique, R-CVY method, melt growth technique, molecular beam epitaxial growth, and surfactant soft template method used for single and polycrystalline ZnSe and CdSe synthesis. It was observed that the size, quality, and morphology of ZnSe and CdSe

nanostructures can be modified by controlling the various reaction parameters, namely, temperature, deposition rate, and substrate type.

Moreover, this chapter offers a comprehensive review on the effect of doping in ZnSe and CdSe with suitable activator materials such as O, Te, Al, and Zn. The process of doping helps to tune the bandgap of the parent material, thereby improving its scintillating performance to a great extent. Additionally, the application of radiation detectors in diverse areas, such as medicine and health care, space exploration, and high-energy physics, is also discussed in detail.

## References

1. Tonnessen BH, Pounds L. Radiation physics. *J Vasc Surg.* 2011;53(1):6S–8S.
2. Delage M-È, Lecavalier M-È, Larivière D, Allen CN, Beaulieu L. Dosimetric properties of colloidal quantum dot-based systems for scintillation dosimetry. *Phys Med Biol.* 2019;64(9):095027.
3. <https://www.nrc.gov>.
4. Marques L, Vale A, Vaz P. State-of-the-art mobile radiation detection systems for different scenarios. *Sensors.* 2021;21(4):1051.
5. Frame PW. A history of radiation detection instrumentation. *Health Phys.* 2005;87(2):111–35.
6. Knoll GF. Radiation detection and measurement. 4th ed. Hoboken: Wiley; 2010. p. 223–58.
7. Kim C, Lee W, Melis A, Elmughrabi A, Lee K, Park C, et al. A review of inorganic scintillation crystals for extreme environments. *Crystals.* 2021;11(2021):669.
8. Kim C, Yeom J-Y, Kim G. Digital n- $\gamma$  pulse shape discrimination in organic scintillators with a high-speed digitizer. *J Radiat Prot Res.* 2019;44(2):53–63.
9. Gu P, Wang P, Guan W, Zheng L, Zhou Y. Research progress on LYSO:Ce scintillation crystals. *J Cryst Growth.* 2010;50(10):1858.
10. Cherepy NJ, Kuntz JD, Roberts JJ, Hurst TA, Drury OB, Sanner RD et al. Transparent ceramic scintillator fabrication, properties and applications. In: Proceedings of international society for optics and photonics, the hard X-ray, vol. 7079. Gamma-Ray, and Neutron Detector Physics X; 2008. p. 70790X.
11. Takayuki Y. Inorganic scintillating materials and scintillation detectors. *Proc Jpn Acad Ser B.* 2018;94:75–97.
12. Linardatos D, Konstantinidis A, Valais I, Ninos K, Kalyvas N, Bakas A, et al. On the optical response of tellurium activate Zinc Selenide ZnSe:Te single crystals. *Crystals* 2020. 2020;10(11):961.
13. Valais I, Michail C, David S, Nomicos CD, Panayiotakis GS, Kandarakis I. A comparative study of the luminescence properties of LYSO:Ce, LSO:Ce, GSO:Ce and BGO single crystal scintillators for use in medical X-ray imaging. *Phys Med.* 2008;24(2):122–5.
14. van Eijk CWE. Inorganic scintillators in medical imaging. *Phys Med Biol.* 2002;47(8):R85–R106.
15. Holl I, Lorenz E, Mageras G. A measurement of the light yield of common inorganic scintillators. *IEEE Trans Nucl Sci.* 1988;35(1):105–9.
16. Jagtap S, Chopade P, Tadepalli S, Bhalerao A, Gosavi S. A review on the progress of ZnSe as inorganic scintillators. *Opto-Electron Rev.* 2019;27(1):90–103.
17. Ryzhikov V, Chernikov V, Gal'chinetskii L, Galkin S, Lisetskaya E, Opolonin A, et al. The use of semiconductor scintillation crystals AII-BVI in radiation instruments. *J Cryst Growth.* 1999;197(3):655–8.
18. Czirr JB, MacGillivray GM, MacGillivray RR, Seddon PJ. Performance and characteristics of new scintillators. *Nucl Instrum Methods Phys Res, Sect A.* 1999;424(1):15–9.

19. L'Annunziata MF. Solid scintillation analysis. In: L'Annunziata MF, editor. Handbook of radioactivity analysis. Cambridge: Academic; 2012. p. 1021–115.
20. Triboulet R, Rabago F, Legros R, Lozykowski H, Didier G. Low-temperature growth of ZnSe crystals. *J Cryst Growth*. 1982;59(1–2):172–7.
21. Bhargava RN. Materials growth and its impact on devices from wide band gap II–VI compounds. *J Cryst Growth*. 1988;86(1–4):873–9.
22. Unuma H, Higuchi M, Yamakawa Y, Kodairi K, Okano Y, Hoshikawa K, et al. Liquid encapsulated flux growth of ZnSe single crystals from Se solvent. *Jpn J Appl*. 1992;31(4A):L383.
23. Fischer AG. Preparation and properties of ZnS –type crystals from the melt. *J Electrochem Soc*. 1959;106(9):838.
24. Kulakov MP, Kulakovskii VD, Fadeev AV. Twinning in ZnSe crystals grown from melt under pressure. *Inorg Mater*. 1976;12(10):1536–8.
25. Kikuma I, Furukoshi M. Direct observation of the 3C-2H transformation in ZnSe by high-temperature x-ray diffraction. *J Cryst Growth*. 1985;71(1):136–40.
26. Holtan WC, Watts RK, Stinedurf RD. Synthesis and melt growth of doped ZnSe crystals. *J Cryst Growth*. 1969;6(1):97–100.
27. Omino A, Suzuki T. Bridgman growth of ZnSe crystals with a PBN crucible sealed in a molybdenum capsule. *J Cryst Growth*. 1992;117(1–4):80–4.
28. Wang JF, Omino A, Isshiki M. Melt growth of twin-free ZnSe single crystals. *J Cryst Growth*. 2000;214–215:875–9.
29. Wang J, Omino A, Isshiki M. Growth and conductive type control of ZnSe single crystals by vertical Bridgman method. *J Cryst Growth*. 2001;229(1–4):69–73.
30. Fischer AG. Methods of growing crystals under pressure. In: Pamplin BR, editor. Crystal growth. Oxford: Pergamon; 1975. p. 357–93.
31. Fischer AG. Techniques for melt-growth of luminescent semiconductor crystals under pressure. *J Electrochem Soc*. 1970;117(2):41C.
32. Wang JF, Omino A, Isshiki M. Bridgman growth of twin-free ZnSe single crystals. *Mater Sci Eng*. 2001;83(1–3):1185–91.
33. Rudolph P, Schäfer N, Fukuda T. Crystal growth of ZnSe from the melt. *Mater Sci Eng Rep*. 1995;15(3):85–133.
34. Schotanus P, Dorenbos P, Ryzhikov VD. Detection of CdS(Te) and ZnSe(Te) scintillation light with silicon photodiodes. *IEEE Trans Nucl Sci*. 1992;39(4):546–50.
35. Eissler EE, Lynn KG. Properties of melt-grown ZnSe solid-state radiation detectors. *IEEE Trans Nucl Sci*. 1995;42(4):663–7.
36. Kolesnikov NN, James RB, Berzigiarova NS, Kulakov MP, Kolesnikov NN, James RB, et al. HPVB and HPVZM shaped growth of CdZnTe, CdSe and ZnSe crystals. *Proc SPIE*. 2002;4784:93–104.
37. Lee WG, Kim YK, Kim JK, Starzhinskiy N, Ryzhikov V, Grinyov B. Properties of ZnSe:Te,O crystals grown by Bridgman-Stockbarger method. *J Nucl Sci Technol*. 2008;5:579–81.
38. Kim YK, Kim JK, Lee WG, Kim SY, Kim BI, Ha JH. Properties of semiconductor scintillator ZnSe:O. *Nucl Instrum Methods Phys Res*. 2007;580:258–61.
39. Semnozhenko VP, Ryzhikov VD, Apolonin AD, Lysetska OK, Galkin SN, Voronkin EF, et al. ZnSe(Te)- based crystals for nondestructive testing and Cargo inspection. *Proc SPIE*. 2006;6319:63191B.
40. Ryzhikov V, Tamulaitis G, Starzhinskiy N, Gal'chinetskii L, Novickovas A, Kazlauskas K. Luminescence dynamics in ZnSeTe scintillators. *J Lumin*. 2003;101:45–53.
41. Trubaieva OG, Chaika MA, Lalayants AI. The growth, structure and luminescence properties of ZnSe<sub>1-x</sub>S<sub>x</sub> materials. *Lith J Phys*. 2018;58(3):254–60.
42. Beeman JW, Bellini F, Cardani L, Casali N, Dafinei I, Di Domizio S, et al. Performance of a large mass ZnSe bolometer to search for rare events. *J Instrum*. 2013;8:P05021.
43. Ryzhikov V, Grinyov B, Galkin S, Starzhinskiy N, Rybalka I. Growing technology and luminescent characteristics of ZnSe doped crystals. *J Cryst Growth*. 2013;364:111–7.

44. Tretyak VI. Semi-empirical calculation of quenching factors for ions in scintillators. *Astropart Phys.* 2010;33(1):40–53.
45. Beeman JW, Bellini F, Benetti P, Cardani L, Casali N, Chiesa D, et al. Current status and future perspectives of the LUCIFER experiment. *Adv High Energy Phys.* 2013;2013:237973.
46. Silva BC, de Oliveira R, Ribeiro GM, Cury LA, Leal AS, Nagorny S, et al. Characterization of high-purity  $^{82}\text{Se}$ -enriched ZnSe for double-beta decay bolometer/scintillation detectors. *J Appl Phys.* 2018;123(8):085704.
47. Galkin S, Rybalka I, Sidelnikova L, Voloshinovskii A, Kraus H, Mykhaylyk V. Performance of ZnSe-based scintillators at low temperatures. *J Lumin.* 2021;239:118360.
48. Ryzhikov VD, Starzhinskiy NG, Gal'chinetskii LP, Silin VI, Tamulaitis G, Lisetskay EK. The role of oxygen in formation of radiative recombination centers in  $\text{ZnSe}_{1-x}\text{Te}_x$  crystals. *Int J Inorg Mater.* 2001;3(8):1227–9.
49. Delage MÈ, Lecavalier M-È, Larivière D, Allen CN, Beaulieu L. Characterization of a binary system composed of luminescent quantum dots for liquid scintillation. *Phys Med Biol.* 2018;63(17):175012.
50. Létant SE, Wanga TF. First study of nano-composite scintillators under alpha irradiation. *Appl Phys Lett.* 2005; 1–12
51. Hines MA, Sionnest PG. Bright UV-blue luminescent colloidal ZnSe nanocrystals. *J Phys Chem B.* 1998;102(19):3655–7.
52. Suemune I, Tawara T, Saitoh T, Uesugi K. Stability of CdSe and ZnSe dots self-organized on semiconductor surfaces. *Appl Phys Lett.* 1997;71:3886–8.
53. Chen L, Jiang Y, Wang C, Liu X, Chen Y, Jie J. Green chemical approaches to ZnSe quantum dots: preparation, characterization and formation mechanism. *J Exp Nanosci.* 2010;5(2):106–17.
54. Ryzhikov VD, Silin VI, Starzhinsky NG. A new  $\text{ZnSe}_{1-x}\text{Te}_x$  scintillator: luminescence mechanism. *Nucl Tracks Radiat Meas.* 1993;21(1):53–4.
55. Ryzhikov V, Starzhinskiy N. Properties and peculiar features of application of iso- electronically doped A2B6 compound – based scintillators. *J Korean Assoc Radiat.* 2005;30(2):77–84.
56. Cho YH, Park SH, Lee WG, Ha JH, Kim HS, Starzhinskiy N. Comparative study of a CsI and a ZnSe(Te/O) scintillation detector's properties for a Gamma-ray measurement. *J Nucl Sci Technol.* 2008;45(5):534–7.
57. Baltramiejunas R, Ryzhikov VD, Raciukaitis G, Gavryushin V, Juodzbališ D, Kazlauskas A. Centres of radiative and nonradiative recombination in isoelectronically doped ZnSe:Te crystal. *Physica B.* 1993;185(1–4):245–9.
58. Ryzhikov V, Starzhinskiy N, Gal'Chinetskii L, Gashin P, Kozin D, Danshin E. New semiconductor scintillators ZnSe(Te,O) and integrated radiation detectors based thereon. *IEEE Trans Nucl Sci.* 2001;48(3):356–9.
59. Ryzhikov VD. Scintillation crystals of A2B6 semiconductors. Moscow: NIITEHIM; 1989. (in Russian)
60. Lee WG, Kim YK, Kim JK, Sec HJ, Ryzhikov V, Starzhinskiy N. Particularities of ZnSe-based scintillators for a spectrometry of charged particles and gamma quanta. *J Korean Phys Soc.* 2006;48(1):47–50.
61. Pranciškus V, Gintautas T, Shevchenko D, Žukauskas A, Starzhinskiy N, Katrunov K. Luminescence study of ZnSe based scintillators in frequency domain. *Lith J Phys.* 2008;48(3):243–7.
62. Berends AC, de Mello Donegá C. Ultrathin one- and two-dimensional colloidal semiconductor nanocrystals: pushing quantum confinement to the limit. *J Phys Chem Lett.* 2017;8(17):4077–90.
63. Lecavalier M-E, Goulet M, Allen CN, Beaulieu L, Larivière D. Water-dispersible colloidal quantum dots for the detection of ionizing radiation. *Chem Commun.* 2013;49(99):11629–31.
64. Groeneveld E, van Berkum S, van Schooneveld MM, Gloter A, Meeldijk JD, van den Heuvel DJ, et al. Highly luminescent (Zn,Cd)Te/CdSe colloidal heteronanowires with tunable electron-hole overlap. *Nano Lett.* 2012;12(2):749–57.



65. Kim K, Kim JK, Lee WG, Kim SY, Kim BI, Ha JH, et al. Properties of semiconductor scintillator ZnSe:O. *Nucl Instrum Methods Phys Res Sect A*. 2007;580(1):258–61.
66. Shevchenko D, Gavryushin V, Mickevičius J, Starzhinskiy N, Zenya I, Zhukov A, et al. Emission properties of ZnSe scintillation crystals co-doped by oxygen and aluminium. *J Lumin*. 2013;143:473–8.
67. Hizhnyi YA, Nedilko SG, Borysiuk VI, Chornii VP, Rybalka IA, Galkin SM, et al. Effect of annealing in zinc vapours on charge trapping properties of ZnSe, ZnSe(Te) and ZnSe(Al) scintillation crystals: revealing the mechanisms by DFT computational studies. *Opt Mater*. 2019;97:109402.
68. Nasieka I, Boyko M, Strelchuk V, Kovalenko N, Gerasimenko A, Starzhinskiy N, et al. Optical characterization of Er-doped ZnSe for scintillation applications. *Opt Mater*. 2014;38:272–7.
69. Atroshchenko LV, Burachas SF, Gal'chinetskii LP, Grinev BV, Ryzhikov VD, Starzhinskiy NG. Scintillator crystals and detectors of ionizing radiation on their basis. Kiev: Naukova Dumka; 1998. p. 167–310. (in Russian)
70. Focsha AA, Gashin PA, Ryzhikov VD, Starzhinskiy NG, Gal'chinetskii LP, Silin VI. Properties of semiconductor scintillators and combined detectors of ionizing radiation based on ZnSe(Te,O)/pZnTe–nCdSe structures. *Opt Mater*. 2002;19(1):213–7.
71. Katrunov K, Starezhinskiy N, Malyukin Y, Silin V, Zenya I, Tamulaitis G. Effect of rare-earth elements on luminescence properties of ZnSe-based chalcogenide scintillators. *Nucl Instrum Methods Phys Res Sect A*. 2010;622(1):139–41.
72. Xu Z, Zhang Z, Gamage KAA, Liu Y, Ye H, Tang X. Synergistic enhancement of CdSe/ZnS quantum dot and liquid scintillator for radioluminescent nuclear batteries. *Energy Resour*. 2021;45(8):12195–202.
73. Ryzhikov VD, Starzhinskiy NG, Gal'chinetskii LP, Guttormsen M, Kist AA, Klamra W. Behavior of new ZnSe(Te,O) semiconductor scintillators under high doses of ionizing radiation. *IEEE Trans Nucl Sci*. 2001;48(4):1561–4.
74. Xu Z, Zhang Z, Gamage KAA, Liu Y, Ye H, et al. Synergistic enhancement of CdSe/ZnS quantum dot and liquid scintillator for radioluminescent nuclear batteries. *Int J Energy Res*. 2021;45(8):12195–202.
75. Ryzhikov VD, Opolonin AD, Pashko PV, Svishch VM, Volkov VG, Lysetskay EK, et al. Instruments and detectors on the base of scintillator crystals ZnSe(Te), CWO, CsI(Tl) for systems of security and customs inspection systems. *Nucl Instrum Methods Phys Res A*. 2005;537:424–30.
76. Kwak S-W, Cho G, Kim B-H, Kim I, Jae MS. Comparative study of CWO and ZnSe(Te) scintillation detector on the performance of X-ray imaging system. *Nucl Instrum Methods Phys Res A*. 2005;537:449–53.
77. Ryzhikov VD, Opolonin AD, Pashko PV, Svishch VM, Volkov VG, Lysetskaya EK. Instruments and detectors on the base of scintillator crystals ZnSe(Te), CWO, CsI(Tl) for systems of security and customs inspection systems. *Nucl Instrum Methods Phys Res, Sect A*. 2005;537(1–2):424–30.
78. Hamers S, Freyschmid J. Digital radiography with an electronic flat-panel detector: first clinical experience in skeletal diagnostics. *Medicamundi*. 1998;42(3):2–6.
79. Fedorov A, Katrunov K, Lalayants A, Lebedinsky A, Shiran N, Mateychenko P. Properties of vacuum deposited CsI(Tl) and ZnSe(Te) scintillator layers. *IEEE Trans Nucl Sci*. 2009;56(3):955–7.
80. Yoneyama A, Baba R, Kawamoto M. Quantitative analysis of the physical properties of CsI, GAGG, LuAG, CWO, YAG, BGO, and GOS scintillators using 10-, 20- and 34-keV monochromated synchrotron radiation. *Opt Mater Express*. 2021;11(2):398–411.
81. Beeman JW, Bellini F, Cardani L, Casali N, Dafinei I, Di Domizio S. Performances of a large mass ZnSe bolometer to search for rare events. *J Instrum*. 2013;8:P05021.

# Chapter 5

## Medical Applications of II-VI Semiconductor-Based Radiation Detectors



Ghenadii Korotcenkov and Sergiu Vatavu

### 5.1 Introduction

Currently, radiation detectors based on II-VI compounds, mainly cadmium-tellurium (CdTe) and cadmium-zinc-tellurium (CZT), are widely used in various fields. On their basis, various systems for visualization of X-ray and gamma radiation are being developed, including medical computed tomography (CT) systems, modern systems of single-photon emission computed tomography (SPECT), and positron emission tomography (PET) [10, 33, 65, 66]. Radioactive waste monitoring [37], as well as control of territories with radioactive contamination, including remote control using unmanned aircraft systems [62] can be carried using CdTe and CZT detectors. CdTe and CZT detectors are also used in devices for nondestructive quality control of various materials [22], for control of nonproliferation of nuclear weapons (IAEA), and border control devices for detecting cases of unauthorized traffic in radioactive materials. Gamma and X-ray spectrometry and the development of X-ray and gamma telescopes are also important applications for CdTe and CZT detectors [20]. However, in this chapter, we will limit ourselves to considering only the medical field of application of radiation sensors based on II-VI compounds.

### 5.2 Nuclear Medicine

Nuclear medicine (NM) is a branch of clinical medicine that uses radionuclide pharmaceuticals [69]. Nuclear medicine dates back to the first scientific experiments with radioactive isotopes in the 1910s and 1920s. Since the 1990s, NM began to

---

G. Korotcenkov (✉) · S. Vatavu

Department of Physics and Engineering, Moldova State University, Chisinau, Moldova

© The Author(s), under exclusive license to Springer Nature  
Switzerland AG 2023

G. Korotcenkov (ed.), *Handbook of II-VI Semiconductor-Based Sensors and  
Radiation Detectors*, [https://doi.org/10.1007/978-3-031-24000-3\\_5](https://doi.org/10.1007/978-3-031-24000-3_5)

develop into the largest industry in noninvasive diagnosis and therapy, playing a vital role in various fields and disciplines of clinical medical practice, contributing to the improvement of the quality of patient care. The essence of nuclear medicine is that certain types of radiopharmaceuticals (RFP) are injected into a biological organism. Then, due to the vital activity of the organism, they pass through the organs under study and are retained in them. Moreover, the accumulation of pharmaceuticals can occur both in normal tissues and in pathological foci. The radioactivity of individual zones is recorded using detectors. The received signals are processed by modern technical means of electronics and are stored, recorded, and visualized. Currently, diagnostic methods of nuclear medicine are the most relevant studies of the internal structure of an object, especially a person. Nuclear research methods are used in cardiology, oncology, neurology, pulmonology, and endocrinology. Several million cases of malignant neoplasms are diagnosed in the world every year. And it is nuclear medicine that can increase the early detection of malignant tumors and increase the chances of recovery. Currently, according to the World Nuclear Association (WNA), more than 40 million radionuclide procedures are performed in the world on the basis of more than 10 thousand clinics per year, of which 90% are diagnostic tests and 10% are therapeutic procedures. Visualization of the distribution of radiopharmaceuticals in the body is carried out using gamma cameras, single-photon emission computed tomography (SPECT), or positron computed tomography (PET).

### ***5.2.1 Single-Photon Emission Computed Tomography (SPECT)***

Single-photon emission computed tomography (SPECT) is a method of nondestructive volumetric examination of the internal structure of an object, in which a radionuclide that emits gamma quanta is used to obtain an image [68]. The radionuclide is part of a radiopharmaceutical. Radiopharmaceuticals for diagnostics are administered intravenously, after which a SPECT examination is performed. This method is applicable in the diagnosis of various diseases such as epilepsy, Alzheimer's disease, and traumatic brain injury, in the diagnosis of oncological diseases, and is widely used for examining patients after a heart attack and for examining blood flow in the cardiovascular system.

SPECT consists of two movable blocks. The first unit is a detection system that consists of one, two, three, or more gamma cameras that rotate around the patient to obtain a tomographic image. The second block is a table moving in a horizontal plane. Radiation detectors can change the relative position for the convenience of removing information from different sides of the object.

### 5.2.2 *Positron Emission Tomography (PET)*

Positron emission tomography (PET) is a method of radioisotope diagnostics that allows to obtain information about the functioning of a selected organ or the whole body by studying the metabolic processes occurring in it [47, 51, 69]. PET uses isotopes that emit positrons, which are elementary particles equal in mass to an electron and positively charged. PET is actively used in clinical oncology for the imaging of tumors and metastases, for the clinical diagnosis of certain brain diseases (dementia). PET is also an important research tool for imaging the human heart.

The positron emission tomograph consists of a fixed ring of detectors and a movable table on which the patient is placed. The first PET scanner (positron emission tomograph) was created in 1961 [50]. But in recent years, there has been significant progress in their development. All PET components, including radiation sensors, are under continuous improvement. Modern commercial preclinical PET systems have achieved FWHM (spatial resolution analog) values of 0.55 mm. Existing commercial PET clinical imaging systems have FWHM values of less than 4 mm with extremely high contrast sensitivity, allowing visualization of the objects with even smaller sizes [84].

The most promising PET technologies are time-of-flight (TOF) and the so-called “whole body PET”. TOF technology takes into account not only the coincidence of gamma quanta emitted in opposite directions after annihilation, but also those minimal differences in time with which each of them reached its crystal in detector. New clinical PET systems have an extremely low temporal resolution of coincidence (about 210 ps). The first PET of the whole body (EXPLORER PET / CT) with a spatial resolution of 2.9 mm was introduced in 2018. Its axial field of view is 194 cm, which allows it to obtain images of the entire human body at one time (<https://explorer.ucdavis.edu>), necessary for the correct application of kinetic models in dynamic studies [5]. PET remains a relatively expensive technique, which limits its mass adoption, but at the same time provides new opportunities for the more affordable SPECT technology. In recent years, commercial SPECT preclinical systems have achieved very high spatial resolution, sometimes even higher than PET. For example, the U-SPECT from MILabs (<https://www.milabs.com/u-spect>), positioned as a dynamic isotope microscopy instrument, has an FWHM of 0.25 mm. However, it should be noted that in addition to “whole body PET”, systems are currently being developed for the analysis of individual organs. For example, Morimoto et al. [47] developed a 3D brain PET scanner.

### 5.2.3 *Computed Tomography (CT)*

Computed tomography is a diagnostic technique that uses X-rays to produce an image. At present, Computed Tomography (CT) market represents one of the major diagnostic modalities in the medical imaging markets worldwide. The computed

tomograph consists of two units: fixed and movable. The stationary unit includes an annular detection system and an X-ray source – an X-ray tube moving in a circle around the patient to obtain one tomographic slice. The movable unit includes a table on which the patient is placed. The information obtained as a result of scanning goes to the computer, where the image is restored and a three-dimensional picture of the investigated area is built. CT makes it possible to accurately establish the localization and prevalence of the pathological process, as well as to evaluate the results of treatment. It is used in the study of almost all areas of the human body. It also provides information about blood vessels (CT angiography) and the work of the heart muscle in “real time” (CT angiography of the heart – fast imaging combined with a large number of slices of the area of interest).

### ***5.2.4 Detectors for CT, PET, and SPECT***

Various approaches are used to visualize CT, PET, and SPECT results. Now, the most widely used in digital radiography is the sensor technology for converting X-ray radiation into light using Si-based photomultiplier tubes (SiPM) and a scintillator. For example, SPECT and PET imaging systems were originally developed for general use with full body imaging [3]. Therefore, such scanners typically use scintillation detectors, which can be large [76]. However, solid state radiation detectors are also used in the development of CT, PET, and SPECT systems [24]. For example, in recent years, there has been a significant increase in interest in SPECT systems for individual organs, especially in the field of cardiology. Due to the rise in heart disease among the world’s population, the demand for myocardial perfusion imaging has increased dramatically. The same situation is observed in the development of PET systems [47]. In this case, due to the relatively small field of view required for these systems, solid state technology becomes particularly cost-effective.

Improvements in the technical characteristics of semiconductor detectors used in CT, PET, and SPECT have significantly reduced body scan time and improved spatial resolution. The use of the technology of semiconductor detectors of ionizing radiation makes it possible to produce up to 300 frames per second during one shooting. These frames are combined into a single multilayered panoramic image of high quality and clarity, while blurring the image disappears, and the clarity and contrast of the image are increased by 300% [72]. As a result, the image obtained using semiconductor detectors was much sharper and more contrasting than that obtained with scintillators. The flexibility in sizing and precise layout of semiconductor detectors not only improves spatial resolution, but also provides information on the depth of interaction. High-energy resolution is expected to reduce scatter in detected signals and improve the accuracy of reconstructed images [47].

Germanium (Ge) has the highest resolution among semiconductor detectors; however, the small band gap and low resistivity allow this material to operate only at very low temperatures, which severely limits its use in portable devices. Silicon

(Si) detectors have a similar disadvantage. CdTe and CdZnTe are heavier materials than Si and Ge and can be used for absorption of higher energy photons and particles. With the widest bandgap of the three materials, they have the best ability to absorb X-ray and Gamma radiation. Thus, CZT-based detectors operate at room temperature and can process more than  $2 \times 10^6$  photons per second per  $\text{mm}^2$ . The unique combination of spectroscopy and very high counting rates at room temperature makes CdTe and CZT very good materials for nuclear radiation detectors [18]. The high energy and spatial resolution, as well as the response time of the sensors, makes these materials much more promising for imaging diagnostics than scintillation materials [1, 41]. Until recently, there was a problem of obtaining large CZT single crystals [24], which significantly increased the cost of detectors. But studies aimed at improving the quality of grown single crystals of large sizes, carried out in many laboratories, have yielded good results (read the Chap. 9, Vol. 1). Solid state radiation detectors based on CdTe and CdZnTe (CZT) [20] are gradually conquering the market as their production becomes cheaper [6, 23, 77].

The first CdTe medical imaging system, NUCAM, was presented by Eisen et al. [21] aiming to replace the Anger type  $\gamma$  cameras. NUCAM is a small field  $16 \times 16$  cm camera equipped with  $40 \times 32$  CdTe:Cl detectors with Pt contacts and a pixel size of  $4 \times 4$  mm, each one connected to a low-noise preamplifier and an amplifier-shaper. Continuous clinical trials of the NUCAM camera were carried out for more than 2 years in various hospitals in Israel and USA for different clinical procedures, such as cardiac Tl and Tc perfusion, Tc MIBI gated perfusion, Tc MUGA, thyroid, breast, and children organs. The performance of the NUCAM was comparable to that of the Anger camera, with contrast resolution due to scatter rejection better for the NUCAM camera.

Digital Corporation (San Diego, USA) has developed the first small  $\gamma$ -camera based on CZT detectors, Digirad 200t Imager, which till now is on market. It has an active area of  $21.6 \times 21.6$  cm made of  $64 \times 25 \times 25 \times 5$  mm CZT detector modules. Each module is an  $8 \times 8$  array of pixels with an electrode configuration that reduces trapping problems [14]. The system can be mounted on a special rotation chair to carry out heart SPECT studies. Clinical using has shown that Digirad camera has comparable or better performance than that of conventional Anger cameras, allowing better imaging geometries in some clinical procedures such as breast imaging.

As for the first commercial instruments for clinical usage, the first such SPECT using the CZT detector (Spectrum-dynamics, Haifa, Israel) began shipping in 2008 in the United States [6, 23]. D-SPECT exterior is shown in Fig. 5.1a. D-SPECT (Spectrum Dynamics, Haifa, Israel). D-SPECT uses pixelated CZT detector arrays in 9 vertical columns mounted in a  $90^\circ$  gantry geometry. The parallel hole high sensitivity collimators are made of tungsten. The use of the CZT detector made it possible to increase the quality of the resulting image and reduce the diagnostic time by 5 times. This means that the use of semiconductor detectors of ionizing radiation can significantly reduce the level of radiation exposure to the patient [29]. Ogawa et al. [52–54] showed that CdTe-based SPECT detectors can have an ultra-high-resolution. Such systems are in great demand for small animal imaging applications and studies of individual organs [56]. Another revolutionary SPECT system is the



**Fig. 5.1** (a) Appearance of D-SPECT developed by Dynamic Medical. Spectrum Dynamics combines the CZT modules in a proprietary and patented column design. These detector columns swivel during a SPECT scan acquisition, while the gantry is in a fixed position and close to the patient. There is no perceivable motion for the patient during the scanning session. (<https://spectrum-dynamics.com>); (b) A dedicated cardiac Discovery NM 530c gamma camera with Alcyone Technology that combines CZT detectors, focused collimation, stationary data acquisition, and 3D reconstruction to improve workflow, dose management, and overall image quality ([www.gehealthcare.com](http://www.gehealthcare.com))

Discovery NM 530c (Fig. 5.1b), developed by GE Healthcare ([www.gehealthcare.com](http://www.gehealthcare.com)). This system is based on multi-pinhole collimator system and an array of nineteen CZT pixelated detectors. Spatial resolution was reported better in GE Discovery (6.7 vs 8.6 mm); count sensitivity is higher in DSPECT (850 vs 460 counts per second per MBq). Both parameters are better than the mean values for conventional SPECT (15.3 mm of spatial resolution and sensitivity of 130 counts per second per MBq) [32].

Ben-Haim et al. [9] also found that the improved spectral performance of the CdTe detector compared to conventional scintillation detectors provides improved scatter suppression. They also showed that in such systems it is possible to organize the simultaneous acquisition of images from several indicators. This approach ensures that these images are spatially aligned, which can reduce the number of outpatient visits and the time to make a diagnosis. In their research, Ben-Haim et al. [9] used hyperspectral CdTe-based detectors  $2 \times 2$  cm, which had  $80 \times 80$  pixels with a step of  $250 \mu\text{m}$  and a three-sided docking structure, which made it possible to form larger arrays. The detectors are called hyperspectral because they measure the energy of each photon that interacts in the CdTe to give full spectroscopic information from 5 to 200 keV in each pixel. The SPECT system developed was capable of resolving spatial elements with a size of 2 mm. These characteristics are superior to alternative detectors currently used in SPECT clinical systems. Russo et al. [63] also compared imaging performance of compact gamma cameras equipped by a  $\text{LaBr}_3\text{:Ce}$  scintillator and semiconductor detectors based on CdTe. They have shown that the intrinsic imaging performance of the small field of view CdTe camera is superior to the  $\text{LaBr}_3\text{:Ce}$  camera for applications using detectors with small volume.

Ueno et al. [80] and Morimoto et al. [47] have shown that CdTe-based detectors can also be used in the development of a PET scanner. This prototype scanner used CdTe detectors. The detector channel consisted of four CdTe elements (two radial and two transaxial). It was shown that a PET scanner using this detector module improves the volumetric resolution of images and allows the implementation of human PET with a spatial resolution better than 3.0 mm. In 2011, Hitachi introduced a PET brain scanner with 155,024 CdTe detectors ([www.hitachi-medical.co.jp](http://www.hitachi-medical.co.jp)). The Spanish Voxel Imaging PET (VIP) project is currently developing a PET detector with 6.3 million channels using CdTe pixel detectors connected to specialized readout electronics (<https://www.ifae.es/projects/vip/>). The Stanford Group has also made very impressive strides in creating a PET scanner for small animals using CZT detectors (<https://stanfordhealthcare.org/>). However, problems remain. In particular, each PET camera requires millions of pixels (more than an order of magnitude more than SPECT requires), which means that for PET cameras, the main problem is the cost of the detector [33].

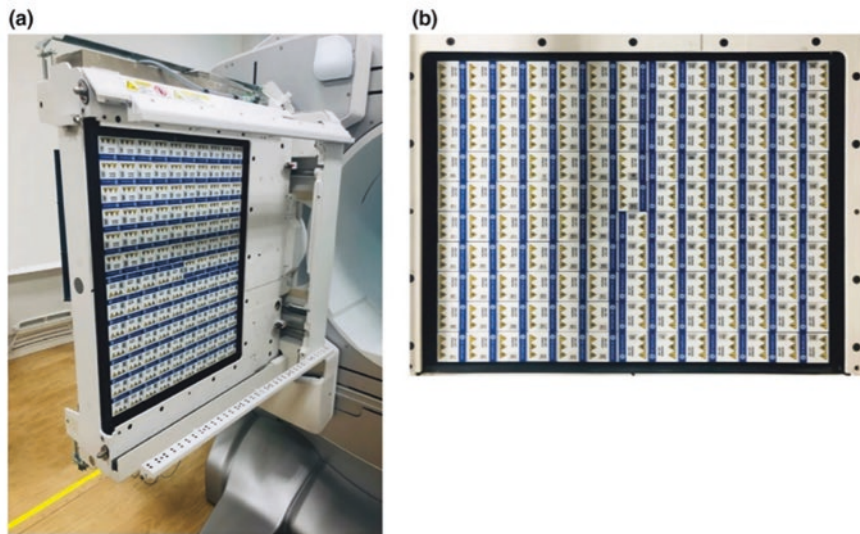
As for computed tomography (CT), after the first mention of the use of CdTe or CdZnTe detectors in X-ray computed tomography applications in 1985 [75], very little additional information appeared in the literature [90]. One of the limitations of using CdTe / CdZnTe detectors was the rather long afterglow [35]. Research showed that by changing the structure of detectors and contacts, as well as improving the quality of the material used, progress can be made in reducing photo decay in X-ray detectors based on CdTe and CdZnTe [87]. As a result, there have been reports of the use of CdTe and CdZnTe detectors for spectral clinical CT and nondestructive testing (NDT) applications [7]. However, despite significant progress made in improving the parameters of CZT, problems remain with the development of commercial-grade CT scanners based on CZT [33].

However, recent studies have shown that CZT devices can be successfully integrated into computed tomographs [34]. The example of a general-purpose CZT device (Fig. 5.2), coupled with a Computed Tomography (CT), was introduced by General Electric (GE) Healthcare. The clinical CZT devices have been tested for anatomically specific cardiac examinations. Several clinical studies using this device have been reported, covering different aspects including the reduced radiation burden due to higher sensitivity, verification of dual-radionuclide imaging, and short-time acquisition using Tc-99m and I-123 in myocardial blood flow tests.

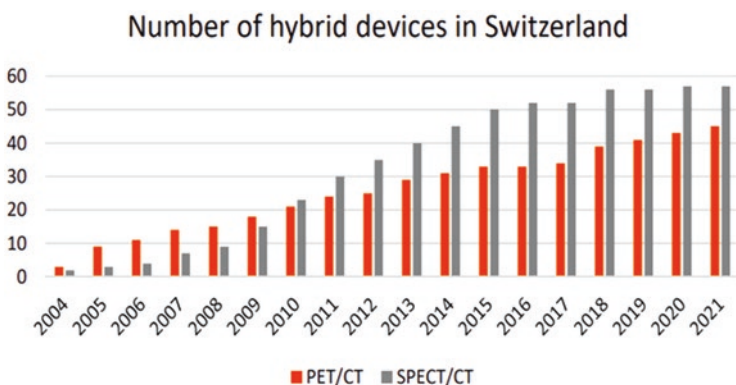
### 5.2.5 Multimodal Systems

In modern medicine, combined SPECT/CT, PET/CT, and PET/MRI (magnetic resonance imaging) systems are increasingly used. For example, in Switzerland, from 2004 to 2014, the number of such installations increased more than tenfold (Fig. 5.3). They are designed in a modular manner, when the 4 main subsystems, PET, SPECT, CT, or magnetic resonance imaging (MRI), can be connected and assembled by the manufacturer at the request of the customer (this approach is currently offered by





**Fig. 5.2** (a) External appearance of a CZT detector. (b) Detector arrangement. There are 13 detectors placed in the x direction and 10 in the y direction. (Reprinted from [34]. Published 2021 by Wiley as open access)



**Fig. 5.3** Number of PET/CT and SPECT/CT in Switzerland. (Reprinted from Van der Meulen et al. [81]. Published 2021 by MDPI as open access)

the Hungarian company Mediso <https://mediso.com/global/en>) [69]. This is because SPECT and PET provide scanty anatomical information. CT and MRI are used to fill this gap. In such systems, first, a SPECT (PET) image is obtained, and then the table is advanced into the CT or MRI unit and CT or MRI images are obtained. The advantage of the combined system is that in one procedure, both the anatomical picture and information about the nature of the spread of the pathological process are obtained. In other words, such systems make it possible to combine the

structural analysis of an organism with a functional one. In addition, this makes it possible to shorten the time for a complete examination of the patient, and, which is very important, to minimize the radiation exposure.

The first PET/CT system with time-of-flight (TOF) technology was introduced in 2006 and has been continuously improving its performance since then. Examples of new aligned CZT-based tomographs are the GE 870 CZT radiodiagnostic tomograph (<https://www.gehealthcare.co.uk>) with planar arrays of pixelated detectors and Spectrum Dynamics VERITON-CT with 12 independent detectors and 360° coverage (<https://spectrum-dynamics.com/products/veriton-series>) (see Fig. 5.4). This is most important for cardiac studies, as fast 3D data collection allows myocardial blood flow values to be calculated in much the same way as PET. PET/MRI technology is currently marketed in two models from Siemens (<https://www.siemens-healthineers.com>) and GE (<https://www.gehealthcare.com>), which allow full body examinations. The main advantages of such systems are the expanded capabilities of MRI in soft tissue imaging, which is most important in various pathologies with damage to the liver, prostate, head, and neck region [45]. There is also a SPECT/CT system on the market using advanced Cadmium Zinc Telluride (CZT) technology (<https://www.gehealthcare.co.uk/>). StarGuide brings together a variety of technologies and productivity tools to help physicians lead the way to effective healthcare while still delivering suitable imaging solutions in difficult clinical conditions.



**Fig. 5.4** NM/CT 870 CZT is the third generation of general purpose digital SPECT/CT system designed with CZT detection technology. An important capability unique to NM/CT 870 CZT is the ability to image low energy and medium energy isotopes with energies up to 250 keV. Accessibility to the Medium Energy High Resolution & Sensitivity (MEHRS) collimator, via collimator exchange, expands the full-service SPECT/CT offering to include theranostics applications and potentially eliminate the need for a supplemental NaI-based SPECT system. Combined with the latest Xeleris™ quantitative applications and CT advancements that include a 32-slice overlapped reconstruction capability, the latest dose reduction technologies and Smart MAR, the NM/CT 870 CZT system changes entire nuclear medicine experience. (<https://www.gehealthcare.co.uk/>)

### 5.3 Radionuclide and Radiation Therapy

Radiation therapy (RT) is one of the leading methods of treating patients with malignant neoplasms and some nonneoplastic diseases. As an independent method or in combination with surgery and chemotherapy, radiation therapy is recommended in more than 80% of patients with malignant neoplasms. The wide indications for radiation therapy using are explained by the possibility of using it in both operable and inoperable forms of the tumor, as well as the steadily increasing effectiveness of various methods of radiation therapy. The success of radiation therapy is also associated with the development of diagnostic and therapeutic techniques, with the emergence of new designs of devices, with the development of clinical dosimetry, and with numerous radiobiological studies that reveal the mechanism of tumor regression under the influence of radiation.

One of the most important factors in RT is the accuracy with which the radiation dose can be delivered to the tumor. In the process of radiation therapy, various types of radiation can be used, such as high-energy X-rays, gamma rays, and irradiation with fast electrons, protons and neutrons. In all cases, it is necessary to control the direction of radiation and the dose of radiation. Typically, the accuracy of dose delivery to the target should be 2–3%. This is exactly what can be done using various semiconductor radiation sensors [61]. Semiconductor dosimeters are an excellent choice for these applications, because of the following reasons:

- (a) They provide much higher sensitivity (18,000 times) than ionizing chambers of the same volume due to their higher density and ionization energy, which is about 10 times less, what is required in gas;
- (b) They have a small dosimetric volume;
- (c) They provide dosimetry with high spatial resolution;
- (d) They have good mechanical stability;
- (e) And most importantly, radiation dosimetry can be performed in real time in vivo, which is critical for improving clinical outcomes of treatment.

Nuclear medicine doctors are demanding improved spatial resolution every year. These factors make new CdTe and CZT detectors more and more attractive for use in radiation therapy. Currently, radiation therapy apparatus is equipped with real-time systems for creating portal images. The most commonly used positioning system is a “simulator” equipped with a high-resolution detector and software to superimpose the generated image on the patient. Portal imaging allows real-time monitoring of the patient’s position under the radiation therapy beams. Among the advantages of CdTe and CZT-based detectors developed for radiation therapy [46, 86], this is the compactness of the sensor and scanner mechanism, which makes it easy to upgrade most of the existing linear accelerators.

As we indicated earlier, X-ray radiation, gamma radiation, as well as irradiation with fast electrons, protons, and neutrons can be used in radiation therapy. Previous consideration has shown that sensors based on II-VI compounds are effective detectors of X-ray, gamma, and proton radiation. They are distinguished by their small

size, excellent energy resolution in nuclear spectroscopy, ease of pixelation for high spatial resolution, and the possibility of integration with readout electronics [61]. It is important to note that for these purposes, in addition to CdTe and CZT, other II-VI compounds, such as ZnSe [12, 58], ZnS [19], and CdS [60], can be used. For example, it was found that the sensitivity (optical intensity) of the ZnS scintillator detector [19] was flat during detection of dose rates from 50 cGy/min to 800 cGy/min. This was a broad dose rate range, which covers the ranges normally implemented in radiotherapy. This means that the ZnS-based detector is a powerful candidate for radiotherapy applications [19]. At the same time, in terms of their parameters, II-VI compounds in a number of cases exceed the parameters of many traditional scintillators. For example, Linardatos et al. [40] compared ZnSe:Te, bismuth germanium oxide (BGO) and gadolinium orthosilicate (GSO:Ce) crystals ( $10 \times 10 \times 10$  mm). They have established that the linearity of ZnSe:Te, BGO, and GSO:Ce light signals to X-ray exposure were 99.79%, 99.86%, and 99.6%, respectively. However, ZnSe:Te had the highest sensitivity to exposure (i.e.,  $10.382 (\mu\text{W}/\text{m}^2)/\text{mR}$ ) compared to BGO ( $3.378 (\mu\text{W}/\text{m}^2)/\text{mR}$ ) and GSO:Ce ( $8.021 (\mu\text{W}/\text{m}^2)/\text{mR}$ ). Studies have shown that electron flux dosimetry [15],  $\beta$ -particles [59] and  $\alpha$ -particles [71] can also be performed using detectors based on compounds II-VI compounds.

Because of the performed studies, it was found that CdZnTe-based detectors can also be used to register thermal neutrons. Fast neutrons are produced in linear accelerators and nuclear reactions during the bombardment of targets in cyclotrons designed to produce radioisotopes. However, their thermalization with light materials is accompanied by the formation of thermal neutrons [11]. Thermal neutrons have a large capture cross-section and this property makes it possible to detect fast neutrons without damaging the material of the detectors by high-energy neutrons. This is achieved by placing a screen of lightweight materials of a certain thickness in front of the detector. Martin-Martin et al. [44] have developed CdZnTe thermal neutron detectors based on semiconductor gamma spectrometers containing neutron conversion elements. CdZnTe (CZT) detectors with a size of  $3 \times 10 \times 10$  mm with a coplanar grid without a moderator were tested for detecting neutrons close to an electron accelerator and a proton PET cyclotron. As a result, a fairly high efficiency of neutron detection was found. One of the main advantages of using this neutron detector is that the same device can be used to simultaneously register neutron and gamma radiation with good spectrometric characteristics and without cryogenic cooling [8]. Martin-Martin et al. [44] believe that the ability of the CZT detector to measure gamma and neutron radiation inside the cyclotron vault gives these sensors significant advantages, because the use of CZT detectors provides quick results on the received dose prior to the reading of the passive dosimeter worn by the operator.

Treating tumors using particle therapy such as carbon (C-ion) [2] is another area where detectors based on II-VI compounds can be used. C ion radiation therapy has several advantages such as better radiobiological and physical properties, as explained in detail in [42]. Yogo et al. [89] showed that the dosimetric method using a ZnS scintillator for three-dimensional dose distribution of C ions is an alternative and, in some cases, a more effective dosimetric instrument in comparison with other

methods used for these purposes. The ZnS scintillator was faster, less dependent on linear energy transfer (LET), and had a more accurate depth dose profile compared to conventional gadolinium-based scintillators [89].

### 5.3.1 Nuclear Probes

Nuclear probes are an important attribute of nuclear medicine. One example of such probes is shown in Fig. 5.5a. Miniature probes are used in two areas of application: preoperative localization of small (tumor) masses and continuous monitoring of physiological functions during operations. These probes are used as a homing device. A targeting agent, usually a monoclonal antibody labeled with a low-energy gamma or beta-ray emitter, is administered to the patient prior to surgery. The ideal targeting agent binds specifically to malignant tissue, while the unbound fraction is gradually cleared from the bloodstream and from normal tissues. The characteristics of an ideal probe can be found in Refs. [28, 43, 73]. Nuclear probes are widely used in operations related to colorectal cancer and cancer of the prostate and lymph nodes [4]. Examples of nuclear probes developed on the basis of II-VI compounds and their comparative characteristics with probes developed on the basis of other materials are given in [12, 74]. These detectors were developed based on CdTe and CZT. They can be both single detector devices and multi-detector devices. One example of such devices is the CdTe camera with a sensitive area as small as  $\sim 2 \text{ cm}^2$  and an active detector thickness as small as 1 mm, which was developed by Russo et al. [63]. According to Russo et al. [63], this camera has the characteristics most suitable for applications, where the basic requirements are the ultrahigh spatial



**Fig. 5.5** (a) An example of a miniaturized probe used for radioguided surgery. SGDP Medical probe with planar detector with volume  $0.25 \text{ cm}^3$  developed by ZRF RITEC SIA (<http://www.ritec.lv/>). (b) Micro-sized Gamma Spectrometer (The MGS series), fully integrated instrument based on a CdZnTe (CZT) crystal ( $0.06$  or  $0.5 \text{ cm}^3$ ) operated at room temperature from IMS Innovation & Measurement Systems. (<https://www.imsrad.com/CdZnTe-spectrometers.php>)

resolution and compactness. They are used, in particular, in preoperative and intraoperative radio-controlled surgery, in detectors for imaging small animals, and in sensors for intracavitary imaging. In the last case, an application could be the detection of prostate tumor via transrectal examination by positioning the detector close to the organ in order to minimize the effect of the high background concentration of pharmaceutical in the bladder. Examples of other miniature CdTe and CZT detectors that can be used as nuclear probes can be found in review prepared by Heller and Zanzonico [28], and on the websites of companies specializing in the production of various radiation detectors ([www.kromek.com](http://www.kromek.com); [www.gehealthcare.co.uk](http://www.gehealthcare.co.uk); <http://bsi.lv/en>; [www.eurorad.com](http://www.eurorad.com), [www.imsrad.com](http://www.imsrad.com), et al.). An example of such a microspectrometer is shown in Fig. 5.5b.

## 5.4 Digital Radiography

Following the rapid advances in X-ray computed tomography (CT) technology, intensive research began in the mid-1970s to develop new radiographic imaging techniques such as digital radiography (DR), using the latest advances in electronics and computer technology [10, 65]. These efforts were an attempt to improve the quality of X-ray diagnostics by reducing the patient's radiation dose and improving the quality of the resulting image [26, 88]. For film emulsions based on silver halide, a sufficiently large radiation dose is required due to the low quantum efficiency (DQE = 4%). In addition to reducing the radiation dose to the patient, DR has many advantages over film radiography. These include high dynamic range, fast acquisition and display of images, the ability to see the smallest changes in one image, no need for consumables and storage space for reagents and film boxes, the ability to create an electronic archive, to display saved images without degradation of quality, extended data analysis, and image processing capabilities [48, 70].

It should be noted that digital radiography, like the systems previously discussed, uses detectors that convert X-ray radiation into an electrical signal [26, 35, 88]. Planar digital detectors, developed for radiological techniques such as radiography and fluoroscopy, consist of large-area pixel arrays that use matrix addressing to read the charges resulting from the absorption of X-rays in the detector environment. As with PET, CT, and SPECT systems, there are two approaches to fabricating panel imaging sensors, direct and indirect methods. In an indirect method [88], the phosphor converter absorbs the incident X-ray radiation and emits visible light, which is converted by the photodiode into an electronic image. However, the indirect method is ineffective and can lead to increased image noise, especially with weak signals. Another approach, the direct method [88], uses solid-state radiation detectors that directly convert the absorbed X-rays into an electrical signal, which is subsequently read by an array of active matrices. The direct method has a higher intrinsic resolution than the indirect method because it avoids the step of converting X-rays to light.

Currently, digital radiography is widely used in the following areas [65, 66]:

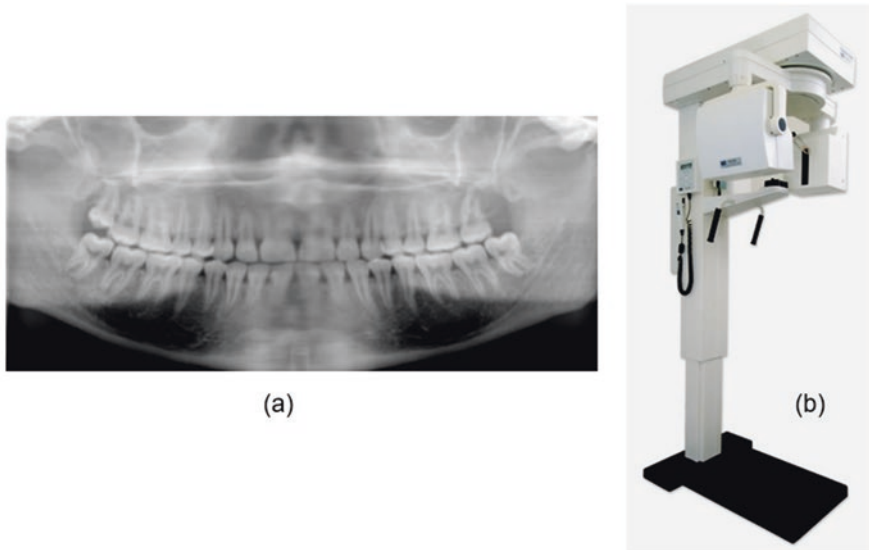
- Chest X-ray imaging.
- High-resolution dental digital radiography systems.
- Mammography.
- Bone densitometry.

#### ***5.4.1 Chest X-Ray Imaging***

Chest X-ray is one of the most common uses for digital radiography principles [66]. The first publications on the use of radiation detectors based on II-VI compounds appeared back in 1993 [78, 79]. In their designs, they used either an array of 32 CdTe detectors or a linear array of 256 CdTe detectors with platinum electrodes. Subsequently, a device was proposed that consisted of an X-ray tube and a position-sensitive CdTe matrix containing  $512 \times 8$  elements located with a pitch of  $250 \mu\text{m}$  and a gap of  $70 \mu\text{m}$  [64]. The experimental device has been validated on patients in a clinical setting and has shown better results than conventional film-based methods. Subsequently, such devices, based on the principles of digital radiography, became predominant in the X-ray market [25].

#### ***5.4.2 High-Resolution Dental Digital Radiography Systems***

Dental applications require very low cost and good performance at high-count rates. Therefore, high-resolution dental digital radiography system is another successful application for semiconductor radiation detectors [38, 82] as smaller fields of view can be used with smaller arrays. With digital radiography, the start of treatment is not delayed due to film processing. In addition, due to the significantly lower radiation dose during digital radiography, several images can be taken during treatment without endangering the patient's health. As a result, there are many digital X-ray systems available on the market today, including systems using CdTe and CZT-based detectors. The first experimental devices used a CdTe:Cl matrix with a size of  $64 \times 64$  pixels with a pitch of  $100 \mu\text{m}$  [16]. Each detector cell was connected to the input pad of the silicon chip via an indium contact. The spatial resolution of the developed system has been described as being higher than that of existing systems using a scintillation screen connected to a CCD imaging system. In later developments, a small pixel spectroscopic CdTe detectors consisted of  $80 \times 80$  pixels on a  $250 \mu\text{m}$  pitch with  $50 \mu\text{m}$  inter-pixel spacing [85]. Example of panoramic image obtained using CdTe radiation detectors is shown in Fig. 5.6.



**Fig. 5.6** An original panoramic image (a) obtained with a PanoACT-1000 panoramic unit ([www.nissin-dental.com](http://www.nissin-dental.com)) (b) that used a CdTe (cadmium telluride) semiconductor detector and a sophisticated digital signal-processing technique based on tomosynthesis. (Reprinted from Ogawa et al. [53]. Published 2010 by the British Institute of Radiology as open access)

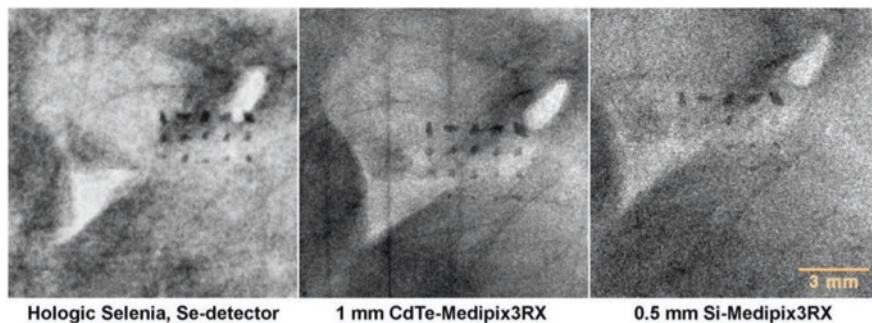
### 5.4.3 Mammography

Mammography, an X-ray method for examining the mammary glands, is currently the most commonly used imaging method in breast cancer screening because it allows rapid imaging of the breast with high resolution and relatively low radiation dose. Mammograms will show lesions such as calcifications, calcium buildup associated with cancerous processes, fibro adenomas, benign lesions that tend to enlarge, and fluid-filled cysts that are not related to cancer. Computer mammography, developed on the principles of digital radiography, automatically analyzes a digital image to look for pathological changes.

However, mammography has its limitations. It is widely accepted that mammography sensitivity and specificity are significantly reduced in women with radiologically dense breasts [17, 36, 57]. Therefore, in parallel with mammography, other methods are being investigated, such as positron emission tomography, molecular imaging of the breast (MBI), and single photon emission computed tomography (SPECT), which can complement or replace mammography for some patient groups [39, 83]. An overview of various breast-imaging techniques can be found in [27, 30]. The benefits of functional techniques are widely recognized as evidenced by the development of dedicated breast PET systems [49].

Regarding the possibility of using CZT sensors, van Roosmalen et al. [83] compared a photomultiplier tube scintillation detector using a solid NaI (Tl) crystal with





**Fig. 5.7** Comparison of the section of the human breast tissue phantom between Hologic Selenia Se-detector, CdTe-Medipix3RX and Si-Medipix3RX. The dose was reduced by 55% compared to the standard dose. The image quality of the CdTe-Medipix3RX is superior to the other detectors in terms of spatial resolution, contrast, and noise. (Reprinted from (Procz et al. [58]. Published 2020 by IEEE as open access)

a cadmium-zinc telluride detector. They showed that the main advantage of NaI (Tl) photomultiplier gamma detectors is their much lower price. At the same time, CZT detectors can provide better spatial and energy resolution than NaI (Tl) photomultiplier detectors. The same result was obtained after comparison between the clinical mammography detector of the Hologic Selenia system and a Medipix3RX-based detector with CdTe- and Si-sensors (see Fig. 5.7). Therefore, CZT detectors are often selected for planar molecular breast imaging (MBI) for high-resolution functional breast imaging [31].

#### 5.4.4 Bone Densitometry

Bone densitometry is an important tool for the diagnosis and follow-up of osteoporosis and for determining the risk of fractures [38]. The testing procedure measures the bone density of the spine, pelvis, forearm, and thigh. Bone density testing can be performed using X-rays, dual-energy X-ray absorptiometry (DEXA or DXA), or quantitative computer scans using specific software to determine the density of the hip or spine. Research has shown that CZT detectors are ideal for high performance DEXA systems. For example, arrays of CdTe detectors began to be used in commercially available devices designed for these applications more than 40 years ago [55, 67]. The first devices were developed using a 64-element linear CdTe: Cl detector array. Their use in clinics has demonstrated their reliability and reproducibility of the results obtained. The devices made it possible to measure bone mineral density in less than 15 sec with an accuracy of better than 1%. Currently, Kromek Dual Energy X-ray Absorptiometry (BMD, DEXA) gamma detectors are used for these purposes (<https://www.kromek.com>). Kromek makes a range of CZT based detectors for medical OEMs to use on their BMD, DEXA scanners. Bone densitometry

uses an ultra-stable dual-energy X-ray source to quantify small changes, ~1%, in a patient's bone mineral density. This application requires an X-ray photon energy discriminating sensor (a perfect job for CZT) that has high efficiency, high energy resolution, high count rate performance and exceptional long-term stability to enable Dual Energy X-ray Absorptiometry (DEXA). This successful application of CZT has revolutionized bone densitometry systems.

**Acknowledgments** This research was funded by the State Program of the Republic of Moldova, projects 20.80009.5007.02 and 20.80009.5007.12.

## References

1. Abbaspour S, Mahmoudian B, Islamian JP. Cadmium telluride semiconductor detector for improved spatial and energy resolution radioisotopic imaging. *World J Nucl Med.* 2017;16(2):101–7.
2. Ando K, Kase Y, Matsufuji N. Light ion radiation biology. *Compreh Biomed Phys.* 2014;7:195–210.
3. Anger HO. Scintillation camera. *Rev Sci Instrum.* 1958;29:27–33.
4. Arnold MW, Schneebaum S, Berens A, Mojzicik C, Hinkle G, Martin EW. Radioimmunoguided surgery challenges traditional decision making in patients with primary colorectal cancer. *Surgery.* 1992;112:624–9.
5. Badawi RD, Shi H, Hu P, Chen S, Xu T, Price PM, et al. First human imaging studies with the EXPLORER total-body PET scanner. *J Nucl Med.* 2019;60(3):299–303.
6. Bai C, Babla H, Kindem J, Cornwell R. Evaluation of a cardiac SPECT system using a common set of solid-state detectors for both emission and transmission scans and an ultra-low dose lead X-ray transmission line source. *IEEE Nucl Sci Symp Conf Rec.* 2009;M13-81:3606–10.
7. Barber WC, Wessel JC, Nygard E, Iwanczyk JS. Energy dispersive CdTe and CdZnTe detectors for spectral clinical CT and NDT applications. *Nucl Instrum Methods Phys Res A.* 2015;784:531–7.
8. Bell ZW, Cristy SS, Lamberti VE, Burger A, Woodfield BF, Niedermayr T, et al. Neutron detection with cryogenics and semiconductors. *Phys Status Solidi C.* 2005;2:1592–605.
9. Ben-Haim S, Kacperski K, Hain S, Van Gramberg D, Hutton BF, Erlandsson K, et al. Simultaneous dualradionuclide myocardial perfusion imaging with a solid-state dedicated cardiac camera. *Eur J Nucl Med Mol.* 2010;37(9):1710–21.
10. Besch HJ. Radiation detectors in medical and biological applications. *Nucl Instrum Methods Phys Res A.* 1998;419:202–16.
11. Bramblett RL, Ewing RI, Bonner TW. A new type of neutron spectrometer. *Nucl Instr Methods.* 1960;9:1–12.
12. Britten AJ. A method to evaluate intra-operative gamma probes for sentinel lymph node localisation. *Eur J Nucl Med.* 1999;26:76–83.
13. Brodyn S, Degoda VY, Sofienko AO, Kozhushko BV, Vesna VT. Monocrystalline ZnSe as an ionising radiation detector operated over a wide temperature range. *Radiat Meas.* 2014;65:36–44.
14. Butler JF, Lingren C, Fruesenhahn SJ, Doty FP, Ashburn WL, Conwell RL, et al. CdZnTe solid-state  $\gamma$  camera. *IEEE Trans Nucl Sci.* 1998;NS-45:359–63.
15. Cavallini A, Fraboni B, Dusi W, Auricchio N, Chirco P, Zanarini M, Siffert P, Fougères P. Radiation effects on II-VI compound-based detectors. *Nucl Instrum Methods Phys Res A.* 2002;476(3):770–8.

16. Cuzin M, Glasser F, Mermet R, Meunier N, Peyret C, Rambud P. Preliminary characterization of a new hybrid structure with CdTe: X-ray imaging capabilities. *SPIE*. 1994;2278:21–7.
17. Carney PA, Miglioretti DL, Yankaskas BC, Kerlikowske K, Rosenberg R, Rutter CM, et al. Individual and combined effects of age, breast density, and hormone replacement therapy use on the accuracy of screening mammography. *Ann Int Med*. 2003;138:168–75.
18. Darambara D, Todd-pokropek A. Solid state detectors in nuclear medicine. *Q J Nucl Med*. 2002;46:3–7.
19. Debnath SBC, Fauquet C, Tallet A, Goncalves A, Lavandier S, Jandard F, et al. High spatial resolution inorganic scintillator detector for high-energy X-ray beam at small field irradiation. *Med Phys*. 2020;47(3):1364–71.
20. Del Sordo S, Abbene L, Caroli E, Mancini AM, Zappettini A, Ubertini P. Progress in the development of CdTe and CdZnTe semiconductor radiation detectors for astrophysical and medical applications. *Sensors*. 2009;9:3491–526.
21. Eisen Y, Shor A, Gilath C, Tsabarim M, Chouraqui P, Hellman C, et al. A  $\gamma$  camera based on CdTe detectors. *Nucl Instr Methods Phys Res A*. 1996;380:474–8.
22. Eisen Y, Polak E. An array of CdTe detectors for imaging applications. *Proc Mater Res Soc Symp*. 1993;302:487–95.
23. Gambhir SS, Berman DS, Ziffer J, Nagler M, Sandler M, Patton J, et al. A novel high-sensitivity rapid-acquisition single-photon cardiac imaging camera. *J Nucl Med*. 2009;50:635–43.
24. Gasanov AA, Kuznetsov MS, Naumov AV. Domestic crystals manufacturing for devices used in photonics. Part 2 – semiconductor ionizing radiation detectors. *Photonics Russia*. 2018;12(5):514–9. (in Russian)
25. Gelaw SM. Screening chest X-ray interpretations and radiographic techniques. IOM guidelines. Global Radiology Coordination and Teleradiology Centre, Makati city, Philippines; 2015.
26. Giakos GC, Vedantham S, Chowdhury S, Odogba J, Dasgupta A, Guntupalli R, et al. Timing characteristics of a Cd<sub>1-x</sub>Zn<sub>x</sub>Te detector-based X-ray imaging system. *IEEE Trans Instrum Meas*. 1999;48(5):909–14.
27. Fowler AM. A molecular approach to breast imaging. *J Nucl Med*. 2014;55:177–80.
28. Heller S, Zanzonico P. Nuclear probes and intraoperative gamma cameras. *Semin Nucl Med*. 2011;41:166–81.
29. Henzlova MJ, Duvall WL. The future of SPECT MPI: time and dose reduction. *J Nucl Cardiol*. 2011;18:580–7.
30. Hruska CB, O'Connor MK. Nuclear imaging of the breast: translating achievements in instrumentation into clinical use. *Med Phys*. 2013;40:050901.
31. Hruska CB, Weinmann AL, O'Connor MK. Proof of concept for low-dose molecular breast imaging with a dual-head CZT gamma camera. Part I. Evaluation in phantoms. *Med Phys*. 2012;39(6):3466–75.
32. Imbert L, Poussier S, Franken PR, Songy B, Verger A, Morel O, et al. Compared performance of high-sensitivity cameras dedicated to myocardial perfusion SPECT: a comprehensive analysis of phantom and human images. *J Nucl Med*. 2012;53(12):1897–903.
33. Iniewski K. CZT detector technology for medical imaging. *JINST*. 2014;9:C11001.
34. Ito T, Matsusaka Y, Onoguchi M, Ichikawa H, Okuda K, Shibusaki T, Shishido M, Sato K. Experimental evaluation of the GE NM/CT 870 CZT clinical SPECT system equipped with WEHR and MEHRS collimator. *J Appl Clin Med Phys*. 2021;22:165–77.
35. Jahnke A, Matz R. Signal formation and decay in CdTe X-ray detectors under intense irradiation. *Med Phys*. 1999;26:38–48.
36. Kolb TM, Lichy J, Newhouse JH. Comparison of the performance of screening mammography, physical examination, and breast US and evaluation of factors that influence them: an analysis of 27825 patient evaluations. *Radiology*. 2002;225:165–75.
37. Kwak S-W, Choi J, Park SS, Ahn SH, Park JS, Chung H. Comparison of experimental results of a Quad-CZT array detector, a NaI(Tl), a LaBr<sub>3</sub>(Ce), and a HPGe for safeguards applications. *J Instrum*. 2017;12:C11011.

38. Langlais R, Katsumata A, Naidoo S, Ogawa K, Fukui T, Shimoda S, Kobayashi K. The cadmium telluride photon counting sensor in panoramic radiology: gray value separation and its potential application for bone density evaluation. *Oral Surg Oral Med Oral Pathol Oral Radiol.* 2015;120(5):636–43.
39. Lee CH, Dershaw D, Kopans D, Evans P, Monsees B, Monticciolo D, et al. Breast cancer screening with imaging: recommendations from the society of breast imaging and the ACR on the use of mammography, breast MRI, breast ultrasound, and other technologies for the detection of clinically occult breast cancer. *J Am Col Radiol.* 2010;7:18–27.
40. Linardatos D, Konstantinidis A, Valais I, Ninos K, Kalyvas N, Bakas A, et al. On the optical response of tellurium activated zinc selenide ZnSe: Te single crystal. *Crystals.* 2020;10:961.
41. Lopes MI, Chepel V. Detectors for medical radioisotope imaging: demands and perspectives. *Rad Phys Chem.* 2004;71:683–92.
42. Malouff TD, Mahajan A, Krishnan S, Beltran C, Seneviratne DS, Trifiletti DM. Carbon ion therapy: a modern review of an emerging technology. *Front Oncol.* 2020;10:82.
43. Mariani G, Vaiano A, Nibale O, Rubello D. Is the “ideal”  $\gamma$ -probe for intraoperative radioguided surgery conceivable? *J Nucl Med.* 2005;46(3):388–90.
44. Martin-Martin A, Iniguez MP, Luke PN, Barquero R, Lorente A, Morchon J, et al. Evaluation of CdZnTe as neutron detector around medical accelerators. *Rad Protect Dosimetry.* 2009;133(4):193–9.
45. Mayerhoefer ME, Prosch H, Beer L, Tamandl D, Beyer T, Hoeller C, et al. PET/MRI versus PET/CT in oncology: a prospective single-center study of 330 examinations focusing on implications for patient management and cost considerations. *Eur J Nucl Med Mol Imaging.* 2019;47(1):51–60.
46. Mc Gann WJ, Cirignano L, Entine G, Biggs P. A new solid-state detector for radiation-therapy imaging. *Nucl Instr Methods A.* 1990;299:172–5.
47. Morimoto Y, Ueno Y, Takeuchi W, Kojima S, Matsuzaki K, Ishitsu T, et al. Development of a 3D brain PET scanner using CdTe semiconductor detectors and its first clinical application. *IEEE Trans Nucl Sci.* 2011;58(5):2181–9.
48. McParland BJ. A study of patient radiation doses in interventional radiological procedures. *J Radiol.* 1998;71:175–85.
49. Miyake KK, Matsumoto K, Inoue M, Nakamoto Y, Kanao S, Oishi T, S., et al. Performance evaluation of a new dedicated breast PET scanner using NEMA NU4-2008 standards. *J Nucl Med.* 2014;55:1198–203.
50. Moses WW, Derenzo SE, Budinger TF. PET detector modules based on novel detector technologies. *Nucl Instr Meth A.* 1994;353:189–94.
51. Nestle U, Weber W, Hentschel M, Grosu AC. Biological imaging in radiation therapy: role of positron emission tomography. *Phys Med Biol.* 2009;54:R1–25.
52. Ogawa K, Muraishi M. Feasibility study on an ultra-high-resolution SPECT with CdTe detectors. *IEEE Trans Nucl Sci.* 2010;57:17–24.
53. Ogawa K, Langlais RP, McDavid WD, Noujeim M, Seki K, Okano T, et al. Development of a new dental panoramic radiographic system based on a tomosynthesis method. *Dentomaxillofac Radiol.* 2010;39:47–53.
54. Ogawa K, Ohmura N, Iida H, Nakamura K, Nakahara T, Kubo A. Development of an ultra-high resolution SPECT system with a CdTe semiconductor detector. *Ann Nucl Med.* 2009;23:763–70.
55. Ohtsuchi T, Tsuitsui H, Ohmori K, Baba S. X-ray imaging sensor using CdTe crystals for dual energy X-ray absorptiometry. *IEEE Trans Nucl Sci.* 1994;NS-41:1740–5.
56. Park SJ, Lee CL, Cho HM, Kim HJ. Ultra high resolution SPECT with CdTe for small animal imaging applications: Monte Carlo simulation study using voxelized phantom. *J Korean Phys Soc.* 2012;60:1145–9.
57. Pisano ED, Hendrick RE, Yaffe MJ, Baum JK, Acharyya S, Cormack JB, et al. Diagnostic accuracy of digital versus film mammography: exploratory analysis of selected population subgroups in DMIST. *Radiology.* 2008;246:376–83.

58. Procz S, Roque G, Avila C, Racedo J, Rueda R, Santos I, Fiederle M. Investigation of CdTe, GaAs, Se and Si as sensor materials for mammography. *IEEE Trans Med Imaging*. 2020;39(12):3766–78.
59. Ramírez M, Martínez N, Marcazzó J, Molina P, Feld D, Santiago M. Performance of ZnSe(Te) as fiberoptic dosimetry detector. *Appl Radiat Isot*. 2016;116:1–7.
60. Román RJ, Ruiz García I, Escobedo Araque P, Palma López AJ, Guirado Llorente D, Carvajal MA. Light-dependent resistors as dosimetric sensors in radiotherapy. *Sensors*. 2020;20(6):1568.
61. Rosenfeld AB. Semiconductor detectors in radiation medicine: radiotherapy and related applications. In: Tavernier S, Gektin A, Grinyov B, Moses WW, editors. *Radiation detectors for medical applications*. New York: Springer; 2006. p. 111–47.
62. Royo P, Pastor E, Macias M, Cuadrado R, Barrado C, Vargas A. An unmanned aircraft system to detect a radiological point source using RIMA software architecture. *Remote Sens*. 2018;10(11):1712.
63. Russo P, Mettivier G, Pani R, Pellegrini R, Cinti MN, Bennati P. Imaging performance comparison between a LaBr<sub>3</sub>:Ce scintillator based and a CdTe semiconductor based photon counting compact gamma camera. *Med Phys*. 2009;36:298–317.
64. Sato K, Sato N, Ukita M, Adachi S, Inoue T, Tokuda S et al. Development of multichannel CdTe radiation detectors, In: *Proceedings of 9th Workshop on Radiation Detectors and Their Uses*, 17–19 January 1995, Tsukuba, pp. 208–218; 1995.
65. Scheiber C, Giakos GC. Medical applications of CdTe and CdZnTe detectors. *Nucl Instrum Meth Phys Res A*. 2001;458:12–25.
66. Scheiber C. New developments in clinical applications of CdTe and CdZnTe detectors. *Nucl Instrum Methods Phys Res A*. 1996;380:385–91.
67. Schneider P, Bomer W. Peripheral quantitative computed tomography for bone mineral measurement with a new special purpose QCT-scanner. *Fortschr Rontgenstr*. 1991;154:292–9.
68. Scuffham JW, Wilson MD, Sellar P, Veale MC, Sellin PJ, Jacques SDM, Cernik RJ. A CdTe detector for hyperspectral SPECT imaging. *JINST*. 2012;7:P08027.
69. Sergienko VB, Ansheles AA. Nuclear medicine and molecular imaging in clinical practice: yesterday, today and tomorrow. *Terapevticheskii Arkhiv*. 2021;93(4):357–62. (in Russian)
70. Speller R, Royle G, Scannvini MG, Horrocks J. Impact of new digital X- and gamma ray imaging systems upon patient doses. *Appl Radiat Isot*. 1999;50:153–63.
71. Sun M, Zhao D, Yin Z, Yang F, Jie W, Wang T. Material properties and device performance of CdSe radiation detectors. *Nucl Instrum Methods Phys Res A*. 2019;959:163487.
72. Takahashi T, Watanabe S. Recent progress in CdTe and CdZnTe detectors. *IEEE Trans Nucl Sci*. 2001;48(4):950–9.
73. Martin EW, editor. *Surgery in the detection and treatment of colorectal cancer*. Landes Company; 1994. p. 42.
74. Tiourina T, Arends B, Rutten H, Lemaire B, Muller S. Evaluation of surgical gamma probes for radioguided sentinel node localization. *Eur J Nucl Med*. 1998;25:1224–31.
75. Tomasov AA, Arkad'eva EN, Zelenina N, Karpenko VP, Maslov LV, Matveev OA, Yazykov NN. CdTe X-ray detector for computed tomography. *Zh Tekh Fiz*. 1985;55:897–901.
76. Townsend DW. Positron emission tomography/computed tomography. *Semin Nucl Med*. 2008;38:152–66.
77. Tsuchiya K, Takahashi I, Kawaguchi T, Yokoi K, Morimoto Y, Ishitsu T, et al. Basic performance and stability of a CdTe solid state detector panel. *Ann Nucl Med*. 2010;24:301–11.
78. Tsuitsui H, Ohtsuchi T, Ohmori K, Baba S. X-ray energy separation method using a CdTe semiconductor X-ray imaging sensor and photon counting method. *IEEE Trans Nucl Sci*. 1993;NS-40:40–4.
79. Tsuitsui H, Ohtsuchi T, Ohmori K, Baba S. Fabrication and characteristics of a submillimeter detector element formed on a CdTe single-crystal wafer as a multichannel detector array applicable to diagnostic imaging with energy information. *Jpn J Appl Phys*. 1993;32:228–33.

80. Ueno Y, Morimoto Y, Tsuchiya K, Yanagita N, Kojima S, Ishitsu T, et al. Basic performance test of a prototype PET scanner using CdTe semiconductor detectors. *IEEE Trans Nucl Sci.* 2009;56:24–8.
81. Van der Meulen NP, Strobel K, Miranda Lima TV. New radionuclides and technological advances in SPECT and PET scanners. *Cancers.* 2021;13:6183.
82. Van der Stelt PF. Filmless imaging: the uses of digital radiography in dental practice. *J Am Dent Assoc.* 2005;136:1379–87.
83. Van Roosmalen J, Goorden MC, Beekman FJ. Molecular breast tomosynthesis with scanning focus multi-pinhole cameras. *Phys Med Biol.* 2016;61:5508–28.
84. Van Sluis J, de Jong J, Schaar J, Noordzij W, van Snick P, Dierckx R, et al. Performance characteristics of the digital biograph vision PET/CT system. *J Nucl Med.* 2019;60(7):1031–6.
85. Veale MC, Bell SJ, Seller P, Wilson MD, Kachkanov V. X-ray micro-beam characterization of a small pixel spectroscopic CdTe detector. *JINST.* 2012;7:P07017.
86. Verger L, Boitel M, Gentet M, Hamelin R, Mestais C, Mongellaz F, et al. Characterization of CdTe and CdZnTe detectors for gamma-ray imaging applications. *Nucl Instrum Methods Phys Res.* 2001;458:297–309.
87. Wurm P, Hage-Ali M, Koebel JM, Siffert P. Study of the photodecay in CdTe X-ray detectors. *Mater Sci Eng B.* 1994;28:47–50.
88. Yaffe MJ, Rowlands JA. X-ray detectors for digital radiography. *Phys Med Biol.* 1997;42:1–39.
89. Yogo K, Tsuneda M, Horita R, Souda H, Matsumura A, Ishiyama H, et al. Three-dimensional dose-distribution measurement of therapeutic carbon-ion beams using a ZnS scintillator sheet. *J Radiat Res.* 2021;62(5):825–32.
90. Zelenina NK, Ignatov SM, Karpenko VP, Maslova LV, Matveev OA, Popov DA, et al. A study of CdTe MSM structures. *Nucl Instrum Methods Phys Res A.* 1989;283(2):274–8.

**Part II**  
**Electric and Electronic Chemical Sensors**

# Chapter 6

## Introduction in Gas Sensing



Ghenadii Korotcenkov and Vladimir Brinzari

### 6.1 Introduction

The atmospheric air in which we live contains many different chemicals of natural and artificial origin. Some of these substances are vital to our lives, while many others can harm our health. At present, industrial production in a wide range carries out the synthesis and use of highly hazardous substances, in particular toxic, flammable, and explosive gases. Despite tight control over technological processes, accidental emissions of these gases inevitably occur, which pose a potential hazard to the industrial enterprise, its employees, and people living nearby. Around the world, incidents of asphyxiation, explosions, and deaths caused by toxic and explosive gases are a constant reminder of this problem. Therefore, the introduction of gas sensors that provide continuous monitoring of gaseous media and the surrounding atmosphere can significantly improve the control of technological processes and help prevent the occurrence of the aforementioned incidents [1–3]. Table 6.1 shows which gases should be controlled in various fields of applications.

Environmental monitoring, that is, control of air pollution from industrial plants and exhaust gases from cars, is also necessary to solve the problem of air pollution [3, 4]. The development of industry and the increase in the number of cars on the road is accompanied by a significant worsening of the condition of surrounding atmosphere (see Fig. 6.1). As a result, toxic gases, dangerous to health, appear in the atmosphere. The main gases that cause air pollution are nitrogen oxides,  $\text{NO}_x$  ( $\text{NO}$  and  $\text{NO}_2$ ), carbon monoxide ( $\text{CO}$ ), sulfur oxides ( $\text{SO}_x$ ), natural gas or methane ( $\text{CH}_4$ ) as the most important component, and ozone ( $\text{O}_3$ ). Since  $\text{NO}_x$  gases with sulfur oxides ( $\text{SO}_x$ ) emitted from coal-fired power plants cause acid rain, the increase

---

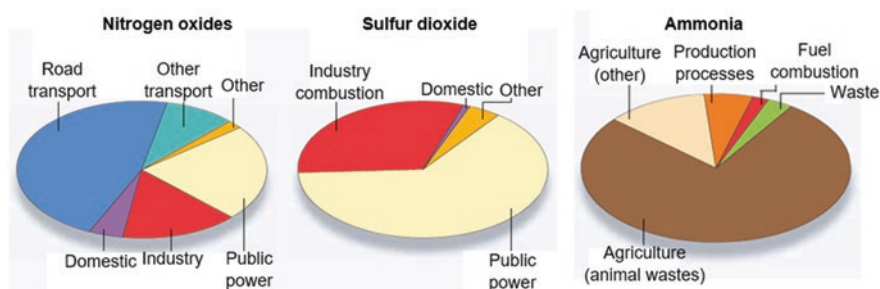
G. Korotcenkov (✉) · V. Brinzari  
Department of Physics and Engineering, Moldova State University,  
Chisinau, Republic of Moldova



**Table 6.1** Some examples of gas sensor applications

Field of application	Examples of detected gases	
Environment	CO, CH <sub>4</sub> , humidity, CO <sub>2</sub> , O <sub>3</sub> , NO <sub>x</sub> , VOCs, SO <sub>x</sub> , HCs, NH <sub>3</sub> , H <sub>2</sub> S	
Safety at work	Indoor air quality, toxic gases, combustible gases, O <sub>2</sub>	
Domestic safety/Household application	CO, CH <sub>4</sub> , humidity, CO <sub>2</sub> , VOCs	
Safety in car	CO, CH <sub>4</sub> , LPG, VOCs	
Public security	Indoor air quality, toxic gases, combustible gases, O <sub>2</sub>	
Medical/clinical	O <sub>2</sub> , NH <sub>3</sub> , NO <sub>x</sub> , CO <sub>2</sub> , H <sub>2</sub> S, H <sub>2</sub> , Cl <sub>2</sub> , anesthesia gases	
Agriculture	NH <sub>3</sub> , amines, humidity, CO <sub>2</sub> ,	
Food quality control	Humidity, CO <sub>2</sub> , etc.	
Utilities/automotive/Power plants	O <sub>2</sub> , CO, HCs, NO <sub>x</sub> , SO <sub>x</sub> , CO <sub>2</sub> , H <sub>2</sub> , HCs	
<i>Industry:</i>	Petrochemical	HCs, conventional pollutants
	Steel	O <sub>2</sub> , H <sub>2</sub> , CO, conventional pollutants
	Water treatment	Cl <sub>2</sub> , CO <sub>2</sub> , O <sub>2</sub> , O <sub>3</sub> , H <sub>2</sub> S, CH <sub>4</sub>
	Semiconductor	H <sub>2</sub> , CH <sub>4</sub> , HCl, AsH <sub>3</sub> , BCl <sub>3</sub> , PH <sub>3</sub> , CO, HF, O <sub>3</sub> , H <sub>2</sub> Cl <sub>2</sub> Si, TEOS, C <sub>4</sub> F <sub>6</sub> , C <sub>3</sub> F <sub>8</sub> , GeH <sub>4</sub> , NH <sub>3</sub> , NO <sub>2</sub> and O <sub>2</sub>
	Oil and gas	HCs, H <sub>2</sub> S, CO
Defense/military	Agents, explosives, propellants	
Aerospace	H <sub>2</sub> , O <sub>2</sub> , CO <sub>2</sub> , humidity	
Traffic/tunnels/car parks	CO, O <sub>3</sub> , NO <sub>x</sub> , SO <sub>2</sub> , CH <sub>4</sub> , LPG	

HCs hydrocarbons, VOCs volatile organic compounds

**Fig. 6.1** Sources of NO<sub>x</sub>, SO<sub>2</sub>, and NH<sub>3</sub> emissions in UK, 2001

in the concentration of CO<sub>2</sub>, CH<sub>4</sub>, and O<sub>3</sub> contributes to global warming, and the appearance of smog as a result of a photochemical reaction, they must be detected and, if necessary, the population warned about the existing hazard. We must not forget about organic compounds such as formaldehyde (HCHO), which are widely used in building materials and furniture production. Formaldehyde has been found to be the most hazardous indoor air pollutant. Studies have shown that gas sensors can monitor the aforementioned hazardous gases and vapors both in the atmosphere

and in living quarters [2], and therefore the widespread use of gas sensors is one of the tools that can improve our quality of life.

Control of combustion processes is another important application for gas sensors [3, 5]. This task is a priority in many industries. It has been found that controlling the content of CO, NO<sub>x</sub>, O<sub>2</sub>, CO<sub>2</sub>, hydrocarbons (HC), and volatile organic compounds (VOC) in combustion products allows for better control of the combustion process, which leads to a decrease in toxic emissions, more efficient use of fuel, and subsequent energy savings.

Gas sensors can also be used to characterize food aroma as part of food quality control during preparation and storage. The most suitable instruments for this function are electronic noses, which are developed on the basis of gas sensors. As you know, the sense of smell plays a fundamental role in human development and bio-social interactions. An electronic nasal system usually consists of a multisensor array, an information processing unit such as an artificial neural network (ANN), software with digital pattern recognition algorithms, and reference library databases [6–9]. As sensor technology advances, such gas sensor arrays will become commonplace in chemical and food processing lines, and more sophisticated sensors will be incorporated into automated process monitoring and control systems. In addition to the food industry, electronic noses can be applied in industries such as the automotive, packaging, cosmetics, pharmaceutical, and biomedical industries. There electronic noses can be used to control the quality of raw materials and finished products, freshness and ripeness of fruits, shelf life studies, assessing the authenticity of premium products, classifying fragrances and perfumes, detecting microbial pathogens, etc. In agriculture, gas sensors can be used to diagnose animal and plant diseases, detect contaminants and pathogens in milk, meat and other food products, and determine product quality such as the ripeness and taste of fruits and vegetables in the field [10].

Medicine and pharmaceuticals is another important application for gas sensors. The movement towards continuous patient monitoring drives emerging requirements for sensors in healthcare. Respiration analysis is one of the possible medical applications of gas sensors. Under these conditions, feedback on patient status and therapy results can be obtained without the delays associated with traditional intermittent measurements and the use of central laboratories for chemical and biochemical analysis [11, 12].

## 6.2 Gas Sensors Classification

Currently, there are a wide variety of devices based on various materials and operating on different principles that can be applied to gas detection. Taking into account transduction mechanisms, all of these devices can be classified into six main groups, which are the following: (1) electrochemical sensors, (2) electrical sensors, (3) mass-sensitive sensors, (4) optical sensors, (5) calorimetric sensors, and (6) magnetic sensors [13, 14].

*Electrochemical sensors* such as amperometric, potentiometric, and conductometric sensors are based on the detection of electroactive particles involved in chemical recognition processes and use charge transfer from a solid or liquid sample to an electrode, or vice versa [14–16].

*Electrical sensors*, which work by interaction of the surface with the target gas, unite a large group of gas sensors such as semiconductor conductometric sensors, capacitance sensors, work function type sensors, Schottky barrier-, MOS-, and FET-based sensors [13].

*Mass-sensitive gas sensors* such as microcantilever, quartz crystal microbalance (QCM), and surface acoustic waves (SAW) operate based on the disturbance and change in the mass of the sensor surface during interaction with chemicals [17]. Mass-sensitive devices transform the mass change at a specially modified surface into a change in some property of the support material. The change in mass is caused by the accumulation of the analyte during interaction with the sensitive layer applied to the mechanical resonator [13].

*Optical gas sensors* transform changes in optical phenomena that result from an interaction of the analyte with the receptor part. More generally, optical gas sensors detect changes in visible light or other electromagnetic waves during interactions with chemicals [14].

*Thermometric (calorimetric) sensor* devices convert the temperature changes, which are generated by chemical reactions into electrical signals such as the change of the resistance, current, and voltage. The catalytic sensors widely known as “catalytic bead” or “pellistors” are the most known and used type of these gas sensors [18, 19]. Thermoelectric, pyroelectric, and thermoconductivity-based devices are other representatives of thermometric gas sensors [13]. The advantages and disadvantages of all of the above sensors are described in sufficient detail in [3, 13, 14].

*Magnetic gas sensors* are based on changes in the paramagnetic properties of the analyzed gas. These are represented by certain types of oxygen monitors [20]. It was found that oxygen has a relatively high magnetic susceptibility as compared to other gases such as nitrogen, helium, argon, etc. and displays a paramagnetic behavior.

It should be noted that our classification of gas sensors is only one possible alternative. The detection principles can also be used to classify gas sensors. According to the principles of detection, commonly used gas sensors can be divided into the following three groups: (i) gas reactivity sensors; (ii) a sensor based on the physical properties of the gas; and (iii) gas sorption sensors. Gas sensors can also be classified according to the approach taken when designing gas sensors. According to this approach, gas detectors come in two main types: portable devices and fixed gas detectors. According to technology used for gas sensor fabrication, they can be classified as ceramic, thin film, and thick film gas sensors. Micromachined gas sensors, which were designed during last decades, also can be referred to this principle of classification. Gas sensors can also be grouped according to their operating temperature. This classification approach yields two broad groups: “hot sensors” and “cold sensors”. “Cold sensors”, unlike “heat sensors”, operate at ambient

temperature. A more detailed description of gas sensors, including design and operating principles, can be found in already published reviews and books [3, 13, 14].

It is clear that not every device that responds to changes in the gas atmosphere can be considered as a sensor suitable for the market [3]. The main purpose of any gas sensors is to provide reliable information on the chemical composition of the environment in real time. Therefore, ideally, a device designed to measure gas should operate continuously and reversibly without disturbing the sample. An ideal gas sensor should be inexpensive, reliable, and operate with ideal and instantaneous selectivity for a specific target gas that is present in the environment [21]. Ease of manufacture, fast response, minimum measurement error, insensitivity to relative temperature and humidity, high resistance to contamination and poisoning, and low noise levels are also essential requirements for gas sensors developed for the gas sensor market. Chou [22] believes that the ideal sensor should be portable enclosed in a small, explosion-proof housing, making it suitable for use in hazardous locations and harsh environments. For portable applications, the ideal gas sensor should be small and have low energy consumption. In addition, minimal specialized training is required to manage the operation and maintenance of the sensor. Gas sensors must provide repeated measurements of analytes over a long period of time at multiple or remote locations while maintaining environmental monitoring [23]. An ideal sensor should operate continuously and reliably without requiring recalibration for at least 30 days. Such a gas sensor must operate in an industrial environment for at least 2 years or longer and must be replaceable or renewable at a reasonable cost. In addition, the gas sensor must be easily positioned in a multipoint system, and the controller or controlled distribution system must be able to easily control its operation. The necessary degree of quantitative reliability, such as precision and accuracy, must also be ensured. However, we have to point out that there is no such ideal gas sensor on the sensor market today, despite the great strides that have been made over the past decades [3, 13, 14], which leads to the emergence of numerous studies in this area.

### 6.3 II-VI Compounds as Gas-Sensitive Material and Their Gas Sensor Applications

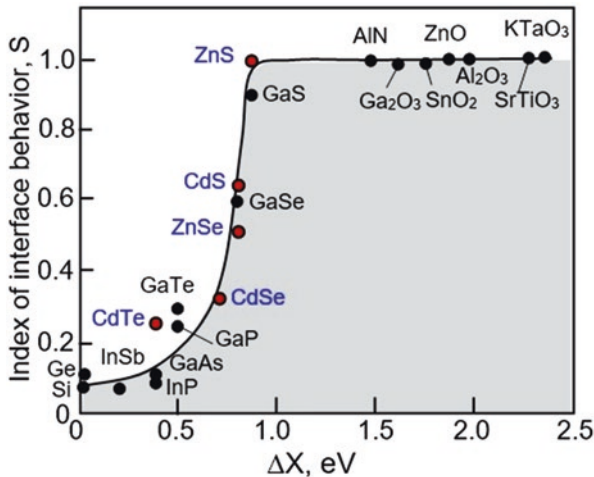
The results of numerous studies have shown that, in theory, any material can be used in the design of a solid state gas sensor, regardless of its physical, chemical, structural, or electrical properties [3, 13, 14, 24]. As a result, prototypes of gas sensors based on covalent semiconductors, semiconducting metal oxides, solid electrolytes, polymers, noble metals, ionic membranes, carbon-based materials, organic semiconductors, and ionic salts have been already tested [25–30].

However, in practice, it turned out that metal oxides are the most suitable for the development of gas sensors intended for operation in aggressive environments. These materials are characterized by high manufacturability, good stability of

parameters, and the absence of intrinsic surface states in the band gap [31]. These are important parameters as good stability makes it possible to work in aggressive atmospheres. Moreover, the low density of surface states excludes the pinning of the Fermi level, which can limit the change in the position of the surface Fermi level during the interaction of a gas-sensitive material with a gaseous atmosphere. The latter is necessary to achieve high sensitivity of most gas sensors on the market. As for the high manufacturability of metal oxides, it provides (i) the possibility to form thin films, thick films, and powders with required parameters, (ii) the possibility to use various deposition and processing methods, specific for standard microelectronic technologies, and (iii) the possibility to modify structural, electrophysical, and chemical properties [31].

Studies have shown that II-VI semiconductor compounds, such as ZnS, ZnSe, CdS, CdSe, also have the necessary manufacturability and stability of parameters in an oxygen atmosphere. The experiment showed that, for the most stable ZnS and CdS compounds, the transition to the oxide phase, depending on the duration of heat treatment in an oxygen atmosphere and the crystallite size, occurs at temperatures of 400–500 °C [32, 33]. However, it should be recognized that the change in the electrical and structural properties of these compounds can begin at lower temperatures [34, 35]. Compounds II-VI and especially ZnS, as well as metal oxides, do not have the surface Fermi level pinning (see Fig. 6.2).

It has been recognized that semiconductors can be classified into two broad groups based on the properties of the semiconductor - metal interface. “Ionic” materials display little or no Fermi-level stabilization at the interface; “covalent” materials display virtually complete stabilization. Figure 6.2 illustrates this statement. The slope =  $\frac{d\Phi_{Bn}}{dX_M}$ , which is inversely correlated to the extent of Fermi-level



**Fig. 6.2** Influence of electronegativity ( $X$ ) on the value of  $S$  in  $\Phi_{Bn} = S \Delta X$ . (Data extracted from [36])

stabilization, was found to be  $=1$  (no Fermi-level stabilization) for “ionic” materials and  $=0.1$  (nearly complete Fermi-level stabilization) for “covalent” materials. As we can see for II-VI compounds, the slope  $S$  is varied from 0.3 for CdTe and CdSe to 1.0 for ZnS. This means that the surface Fermi-level position, i.e., the band bending in these semiconductors, can be changed in wide range, contributing to achievement of high sensor response due to interaction with gas surrounding. For comparison, for conventional semiconductors such as Si, GaAs, and InP, the surface Fermi level is firmly pinned within their band gap due to the high surface state density. That is what causes the low sensitivity of the gas and humidity sensors based on these materials.

### 6.3.1 II-VI Semiconductor-Based Conductometric Gas Sensors

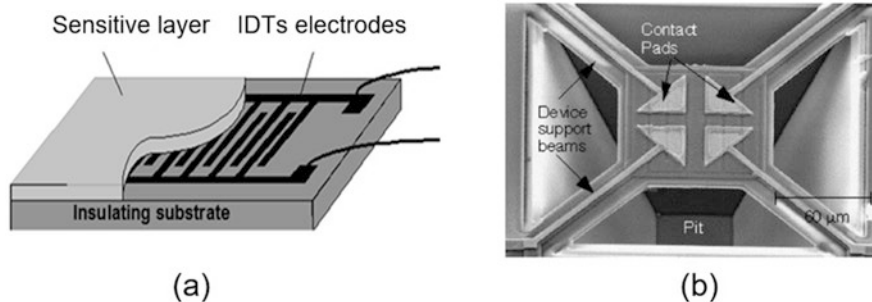
Experiment showed that the most successful specific surface properties of II-VI semiconductor compounds can be realized in conductometric gas sensors. In addition, II-VI semiconductor compounds have other properties important for gas-sensitive materials used in conductometric sensors [37]. These materials have (1) acceptable conductivity because we control the change in conductivity, (2) a band-gap wide enough to operate at elevated temperatures; (3) the ability to form structures with high gas permeability to achieve high sensitivity and fast response; and (4) specific surface properties to interact with the target gas. Some of these parameters are shown in Table 6.2. In addition, just like metal oxides, II-VI semiconductors can be synthesized as powders, single crystals, epitaxial and polycrystalline films, and 1D, 2D and 3D nanostructures.

Conductometric (resistive) sensors, in which semiconductor II-VI compounds can find the greatest application, have a simple design [38]. Gas sensors contain two electrodes, gas-sensitive layer, dielectric substrate, and heater to generate the desired temperature in the active region. The main advantages of chemiresistive gas sensors are ease of manufacture, ease of operation, and low manufacturing cost, which means that well-designed metal oxide conductometric sensors can be mass-produced at a reasonable cost. Conductometric sensors can be manufactured using different approaches. They can be fabricated using thin-film or thick-film technology. They

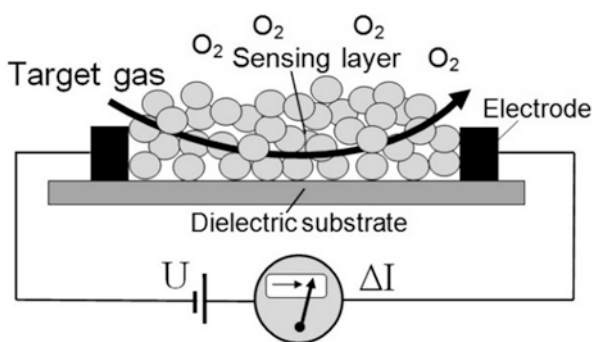
**Table 6.2** Parameters of chalcogenides used in gas sensors

Semiconductor	$E_g$ , eV	$T_{\text{melting}}$ , °C	$T_{\text{sublimation}}$ , °C	$T_{\text{oxidation}}$ , °C
ZnS	3.54–3.91	1827–1850	1178	<500
ZnSe	2.7–2.721	1525	800–900	<300
ZnTe	2.25–2.27	1238–1290	~600	
CdS	2.42–2.46	1475–1750	980	<450–500
CdSe	1.74–1.751	1268	600–700	
CdTe	1.49–1.51	1092	~500	

Source: Reprinted with permission from [30]. Copyright 2013: Springer



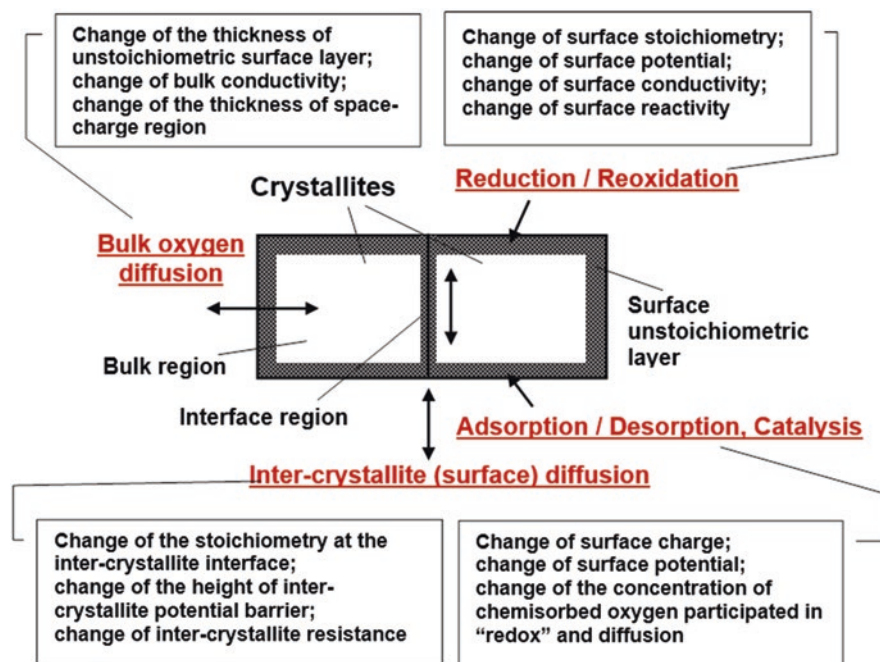
**Fig. 6.3** (a) Conventional platform, (b) micromachining hot-plate platforms. (Reprinted with permission from [39]. Copyright 2001: Elsevier)



**Fig. 6.4** Diagram illustrating construction and working principle of conductometric gas sensors. (Reprinted with permission from [40]. Copyright 2017: Elsevier)

can be manufactured on conventional platform (Fig. 6.3a) or micro-processing platform with extremely low power dissipation (Fig. 6.3b). The latter makes it possible to embed such sensors into ICs. Conductivity sensors are compact and durable, have excellent sensitivity and very short response times, and are very well suited for the design of portable alarm systems and electronic nose. These advantages of conductometric sensors make it possible to develop low-cost portable devices that can be effectively used for gas detection in various locations, including in situ monitoring.

The principle of operation of conductometric gas sensors is based on the fact that their electrical conductivity (or electrical conductance) can be controlled by the presence or absence of certain chemicals in the surrounding atmosphere (see Fig. 6.4), such as toxic and flammable gases and vapors that come into contact with the device [38]. It should be noted that, despite the simple principle of operation of conductometric gas sensors based on metal oxides, the involved gas detection mechanism is rather complicated. This process involves physical and chemical adsorption, desorption, chemical reactions, surface catalysis, surface and volume diffusion occurring on the surface, or in the volume of the sensitive layer. As a result, the gas detection effect is controlled by a large number of parameters of the sensitive material, such as thickness, grain size, porosity, crystallite faceting,



**Fig. 6.5** Diagram illustrating processes taking place in polycrystalline semiconductors during gas detection and their consequences for semiconductor properties. (Reprinted with permission from [41]. Copyrights 2007: Elsevier)

agglomeration, grain network, neck size, active surface area, band gap, adsorption/desorption parameters, catalytic activity, bulk conductivity, surface and bulk stoichiometry, surface architecture, etc. (see Fig. 6.5). The analysis showed that the influence of the above-mentioned parameters on the gas characteristics occurs through a change in such parameters as the effective area of inter-grain and inter-agglomerate contacts; energy parameters of adsorption/desorption processes; number of sites; concentration of charge carriers; initial surface potential; coordination number of metal atoms on the surface, etc. Such a complex relationship between the parameters of gas-sensitive effects and the magnitude of the sensor response significantly complicates the search for conditions that provide optimal sensor parameters. A more detailed description of the mechanisms of interaction of gases with the surface of the gas-sensitive layer, explaining the appearance of the conductometric signal, can be found in numerous reviews and books [42–45].

It is important that the response of II-VI-based gas sensors of conductometric type for various semiconductors changes according to the value of the  $S$  from Fig. 6.2. For example, in the couple CdS and CdSe, CdS-based sensors had much better sensitivity to vapors of water, ethanol, ammonia, acetone, and iodine [46]. It should also be noted that all the laws were established for metal oxides and generalized in Korotcenkov [47] work in gas sensors based on II-VI [48]. This means that for better sensitivity, II-VI semiconductor compounds should be porous with small



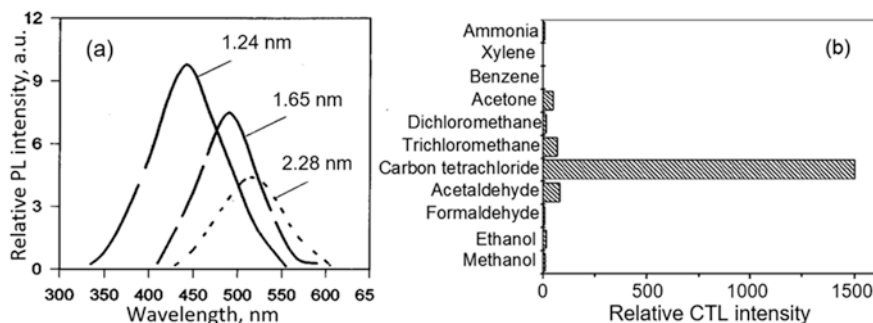
grain sizes and diameters of nanowires or nanofibers [49]. Thinner films also showed higher sensitivity and faster response times [50]. Higher operating temperatures reduce response and recovery times [50]. Surface modification, including modification with noble metals, also improves the selectivity and sensitivity of II-VI semiconductor compounds [37, 51]. A more detailed description of conductometric sensors of various types based on II-VI compounds and their composites can be found in the following Chap. 8, Vol. 3.

### 6.3.2 *II-VI Semiconductor-Based Optical Gas Sensors*

Optical gas sensors are another very promising field of application for II-VI compounds. Chapters 12, 13, 14, and 15, Vol. 3, will focus on this topic. Optical sensors can be designed using different principles of operation [14, 52]. For example, gas sensors can use optical gas detection techniques such as optical absorption, reflection, UV fluorescence, chemiluminescence, light scattering, refraction, and photoionization, which can be implemented as IR sensors, luminescence sensors, fiber-optical sensors, refractometric- and interferometric-based sensors, integrated optical sensors, and devices based on colorimetry principles [14, 52].

Currently the most commonly developed optical gas sensors are sensors that use indicator dyes (external sensor) to convert the concentration of a target gas into a measurable optical signal. In such sensors, the indicator or molecular recognition element is the main sensing element, because it is the indicator that is exposed to the system being measured, and its interaction with the analyte can provide selective sensing. This interaction causes a change in the measured optical properties, and the degree of this change is determined by the concentration of the analyte. Due to their simple visual readout, detection systems based on indicator dyes can be very inexpensive and are therefore widely used. The most commonly used methods include indicator-mediated luminescence and absorption spectroscopy [53–56]. The promise of II-VI compounds for the design of such sensors is because these compounds have high photoconductivity and luminescence characteristics that are sensitive to various adsorbates from gas and liquid phases [37]. These properties make it possible not only to develop optical detectors for various purposes based on these materials (read Vol. 2), but also to use them for surface functionalizing of other gas-sensitive materials. The discussion of this topic can be found in the Chap. 8 (Vol. 3).

In this regard, the use of Quantum Dots (QD's) based on II-VI compounds is especially promising. Semiconducting nanocrystals, otherwise known as Quantum Dots (QD's), were first discovered in the early 1980s [57]. Since then, interest in QD's as alternatives to traditional organic dyes has increased dramatically [58–60]. Typically, QD's are colloidal nanocrystalline particles roughly spherical, with particle diameters typically ranging from 1 to 12 nm [61]. At such small sizes (close to or smaller than the dimensions of the exciton Bohr radius within the corresponding



**Fig. 6.6** (a) Photoluminescence spectra of ZnS QDs in zeolite Y ( $\lambda_{\text{exc}} = 280$  nm). (Reprinted with permission from [64]. Copyright 1997: American Institute of Physics). (b) Selectivity of the carbon tetrachloride ZnS-based gas sensor. Conditions: wavelength, 460 nm;  $T_{\text{oper}} = 335$  °C; gas concentration, 4.5  $\mu\text{g/ml}$ , and air flow rate, 210 ml/min. (Reprinted with permission from [65]. Copyright 2009 Elsevier)

bulk material), these nanostructured materials behave differently from bulk solids, because of quantum-confinement effects [62].

It was established that quantum dots, in contrast to organic dyes, have broad absorption spectra, higher quantum yields, better chemical and photoluminescence stability, reduced photobleaching, and narrow emission spectra without red tailing [63]. Moreover, QD's have the size-dependent nature of the emission wavelength (see Fig. 6.6a), which is related to the three-dimensional quantum confinement of their charge carriers. The smaller the dot, the greater is the blue shift observed relative to the typical  $E_g$  of the bulk semiconductor. This means that by controlling the growth of the nanocrystal, the emission wavelength can be tailored. In fact, QD can be made to emit luminescence from the ultraviolet to the near-infrared spectral region. In particular, depending on the particles size, the emission of CdSe quantum dots can be continuously tuned from 465 to 640 nm, corresponding to a size ranging from 1.9 to 6.7 nm (diameter), respectively. For CdTe QDs, the emission is observed in the red range from 600 to 725 nm. Higher-energy emission is possible with CdS and ZnS QDs (350–550 nm).

The possibility of using QDs in gas sensors is due to the fact that luminescence of QDs is very sensitive to their surface states and this sensitivity is much stronger than that of bulk material. Figure 6.6b shows how sensitive and selective such sensors can be. It was found that emission processes in QDs are the result of electron-hole recombination and strongly depend on the competition between such radiative processes and the mechanisms of non-radiative recombination. Non-radiative processes occur mainly at defects located at the nanocrystal surface. In this context, the large surface/volume ratio of QDs allows one to obtain enhanced quantum yields by controlling the chemical composition of their surface and passivating surface defects [59]. This means that possible chemical or physical interactions between given

chemical particles with the surface of nanoparticles can lead to changes in the surface charges of QDs and very significantly affect the emission of QD photoluminescence [66].

It is important that all mentioned above features of QDs are highly attractive for both optical fiber and planar platforms applications. Experiment confirmed this prediction and, despite a relatively recent area of research, a number of sensing applications have emerged recently. It was established that while most dyes present severe photodegradation when illuminated by energetic radiation, quantum dots have demonstrated their photostability in most situations. Although photobleaching of bare dots has been reported, nanocrystals with an adequate protective shell are known to remain extremely bright even after several hours of exposure to moderate to high levels of UV radiation. On the other hand, the luminescence emission of common dyes can vanish completely after a few minutes [59].

An analysis of the available literature shows that mainly gas sensors were designed on the base of CdSe QDs, with intense light-emitting properties [67–69]. However, other II-VI compounds, such as CdS, CdTe, or ZnS, are also used [70]. A major drawback of the cadmium selenide dots is their toxicity. Zinc sulfide quantum dots could be much less toxic than cadmium selenide. However, ZnS does not possess the level of light emission intensity as cadmium selenide. Recent studies have shown that this disadvantage can be partially overcome by doping zinc sulfide quantum dots with a suitable metal ion such as manganese and lanthanides [71].

The experiment showed that the use of core-shell structures based on II-VI compounds embedded in gas permeable polymer matrix also contributes to a significant improvement in the characteristics of sensors [68, 72]. The reasons for surface capping and embedding in polymer are mainly to prevent aggregation of the QD's and to passivate dangling bonds at the surface. Surface passivation involves coating the core QD with a substance that has a larger band gap such as ZnS or CdS. It was found that the overcoating of the nanocrystal core (CdSe, CdTe) with an outer shell of a higher bandgap semiconductor (ZnS, CdS) is a successful strategy to produce materials with high quantum efficiencies (in the 50% range). Besides the increased brightness, core-shell systems provide increased photostability and chemical resistance [73]. More recently, highly luminescent CdSe core nanocrystals capped with a multi-shell layer (CdS and ZnS) have been reported, displaying quantum yields in a 70–85% range [74]. It is necessary to note that the increased photostability of core-shell QDs is a key feature important for sensor applications. A more detailed discussion of core/shell nanoparticles including their synthesis and properties can be found in review prepared by Chaudhuri and Paria [75]. Embedding in gas permeable polymer also improves sensor stability [67, 68].

**Acknowledgments** G.K. and V.B. are grateful to the State Program of the Republic of Moldova, project 20.80009.5007.02, for supporting their research.

## References

1. Cleaver KD. The analysis of process gases: a review. *Accred Qual Assur.* 2001;6(1):8–15.
2. Yamazoe N. Toward innovations of gas sensor technology. *Sens Actuators B Chem.* 2005;108:2–14.
3. Korotcenkov G, editor. *Chemical sensors: comprehensive sensor technologies.* Vol. 6, Sensors application. New York: Momentum Press; 2011a.
4. Fine GF, Cavanagh LM, Afonja A, Binions R. Metal oxide semiconductor gas sensors in environmental monitoring. *Sensors.* 2010;10:5469–502.
5. Docquier N, Candel S. Combustion control and sensor: a review. *Prog Energy Combustion Sci.* 2002;28:107–50.
6. Kowaiski BR, Bender CF. Pattern recognition: a powerful approach to interpreting chemical data. *J Am Chem Soc.* 1972;94:5632–9.
7. Gardner JW. Detection of vapours and odours from a multisensor array using pattern recognition: principal component and cluster analysis. *Sens Actuators.* 1991;4:109–15.
8. Gardner JW, Bartlett PN. *Electronic noses. Principles and applications.* Oxford, UK: Oxford University Press; 1999.
9. Korotcenkov G, Stetter JR. Chemical gas mixture analysis and the electronic nose: current status, future trends. In: Korotcenkov G, editor. *Chemical sensors: comprehensive sensor technologies.* Vol. 6. Chemical sensors applications. New York: Momentum Press; 2011. p. 1–56.
10. Wilson AD, Baietto M. Applications and advances in electronic-nose technologies. *Sensors.* 2009;9:5099–148.
11. Kharitonov SA, Barnes PJ. Clinical aspects of exhaled nitric oxide. *Eur Respir J.* 2000;16:781–92.
12. Cao W, Duan Y. Breath analysis: potential for clinical diagnosis and exposure assessment. *Clin Chem.* 2006;52(5):800–11.
13. Korotcenkov G. *Chemical sensors: comprehensive sensor technologies.* Vol. 4: Solid state devices. New York: Momentum Press; 2011.
14. Korotcenkov G. *Chemical sensors: comprehensive sensor technologies.* Vol. 5: Electrochemical and optical sensors. New York: Momentum Press; 2011.
15. Korotcenkov G, Han S-D, Stetter JR. Review of electrochemical hydrogen sensors. *Chem Rev.* 2009;109(3):1402–33.
16. Stetter JR, Korotcenkov G, Zeng X, Tang Y, Liu Y. Electrochemical gas sensors: fundamentals, fabrication and parameters. In: Korotcenkov G, editor. *Chemical sensors: comprehensive sensor technologies.* Vol. 3: Electrochemical and optical sensors. New York: Momentum Press; 2011. p. 1–123.
17. Fanget S, Hentz S, Puget P, Arcamone J, Matheron M, Colinet E, Andreucci P, Duraffourg L, Myers E, Roukes ML. Gas sensors based on gravimetric detection—A review. *Sens Actuators B.* 2011;160:804–21.
18. Miller JB. Catalytic sensors for monitoring explosive atmospheres. *IEEE Sensors J.* 2001;1(1):88–93.
19. Korotcenkov G. Practical aspects in design of one-electrode semiconductor gas sensors: status report. *Sens Actuators B Chem.* 2007;121:664–78.
20. Merilainen PT. A differential paramagnetic sensor for breath-by-breath oximetry. *J Clin Monit.* 1990;6(1):65–73.
21. Ho CK, Robinson A, Miller DR, Davis MJ. Overview of sensors and needs for environmental monitoring. *Sensors.* 2005;5:4–37.
22. Chou J. *Hazardous gas monitors: a practical guide to selection, operation and application.* New York: McGraw-Hill; 2000.
23. Potyrailo RA, Mirsky VM. Combinatorial and high-throughput development of sensing materials: the first 10 years. *Chem Rev B.* 2008;108:770–813.
24. Korotcenkov G, editor. *Chemical sensors: fundamentals of sensor materials,* vol. 1-3. New York: Momentum Press; 2010.

25. Sadaoka Y. Organic semiconductor gas sensors. In: Sberveglieri G, editor. Gas sensors. Dordrecht: Kluwer Academic; 1992. p. 187–218.
26. Monkman G. Monomolecular Langmuir-Blodgett films—Tomorrow’s sensors? *Sensor Rev.* 2000;20:127–31.
27. Talazac L, Brunet J, Battut V, Blanc JP, Pauly A, Germain JP, Pellier S, Soulier C. Air quality evaluation by monolithic InP-based resistive sensors. *Sens Actuators B Chem.* 2001;76:258–64.
28. Eranna G, Joshi BC, Runthala DP, Gupta RP. Oxide materials for development of integrated gas sensors: a comprehensive review. *Crit Rev Solid State Mater Sci.* 2004;29:111–88.
29. Adhikari B, Majumdar S. Polymers in sensor applications. *Prog Polym Sci.* 2004;29:699–766.
30. Korotcenkov G. Handbook of gas sensor materials, vol. 1 and 2. New York: Springer; 2013.
31. Korotcenkov G. Metal oxides for solid state gas sensors. What determines our choice? *Mater Sci Eng B.* 2007;139:1–23.
32. Shanmugam N, Cholan S, Kannadasan N, Sathishkumar K, Viruthagir G. Effect of annealing on the ZnS nanocrystals prepared by chemical precipitation method. *J Nanomater.* 2013;2013:351798.
33. Eom NSA, Kim T-S, Choa Y-H, Kim W-B, Kim BS. Surface oxidation behaviors of cd-rich CdSe quantum dot phosphors at high temperature. *J Nanosci Nanotechnol.* 2014;14:8024–7.
34. Maticic N, Kukk M, Spalatu N, Potlog T, Krunks M, Valdna V, Hiie J. Comparative study of CdS films annealed in neutral, oxidizing and reducing atmospheres. *Energy Procedia.* 2014;44:77–84.
35. Zajac AT. On the thermally oxidized CdS as a photoactive material. *New J Chem.* 2019;43:8892–902.
36. Kurtin S, McGill TC, Mead CA. Fundamental transition in the electronic nature of solids. *Phys Rev Lett.* 1969;22:1433–6.
37. Seker F, Meeker K, Kuech TF, Ellis AB. Surface chemistry of prototypical bulk II–VI and III–V semiconductors and implications for chemical sensing. *Chem Rev.* 2000;100:2505–36.
38. Korotcenkov G, Sysoev V. Conductometric metal oxide gas sensors. In: Korotcenkov G, editor. Chemical sensors: comprehensive sensor technologies. Vol. 4. Solid state devices. New York: Momentum Press; 2011. p. 53–186.
39. Semancik S, Cavicchi RE, Wheeler MC, Tiffany JF, Poirier GE, Walton RM, et al. Microhotplate platform for chemical sensor research. *Sens Actuators B Chem.* 2001;77:579–91.
40. Korotcenkov G, Cho BK. Metal oxide composites in conductometric gas sensors: achievements and challenges. *Sens Actuators B.* 2017;244:182–210.
41. Korotcenkov G, Brinzari V, Stetter JR, Blinov I, Blaja V. The nature of processes controlling the kinetics of indium oxide-based thin film gas sensor response. *Sens Actuators B Chem.* 2007;128:51–63.
42. Barsan N, Schierbaum K, editors. Gas sensors based on conducting metal oxides, Elsevier metal oxide series. Korotcenkov G, editor. Cambridge, MA: Elsevier; 2018. ISBN: 9780128112243.
43. Brinzari V, Korotcenkov G. Kinetic approach to receptor function in chemiresistive gas sensor modeling of tin dioxide. Steady state consideration. *Sens Actuators B.* 2018;259:443–54.
44. Brinzari V, Korotchenkov G, Dmitriev S. Theoretical study of semiconductor thin film gas sensitivity: attempt to consistent approach. *J Electron Technol.* 2000;33:225–35.
45. Korotcenkov G, editor. Chemical sensors: simulation and modeling. Vol. 2: Conductometric gas sensors. New York: Momentum Press; 2012.
46. Nesheva D, Aneva Z, Reynolds S, Main C, Fitzgerald AG. Preparation of micro - and nanocrystalline CdSe and CdS thin films suitable for sensor applications. *J Optoelectron Adv Mater.* 2006;8(6):2120–5.
47. Korotcenkov G. The role of morphology and crystallographic structure of metal oxides in response of conductometric-type gas sensors. *Mater Sci Eng R.* 2008;61(2008):1–39.
48. Lantto V, Golovanov V. A comparison of conductance behaviour between SnO<sub>2</sub> and CdS gas-sensitive films. *Sens Actuators B Chem.* 1995;24-25:614–8.
49. Xu L, Song H, Zhang T, Fan H, Fan L, Wang Y, Dong B, Bai X. A novel ethanol gas sensor-ZnS/cyclohexylamine hybrid nanowires. *J Nanosci Nanotechnol.* 2011;11(3):2121–5.

50. Afify HH, Battisha IK. Oxygen interaction with CdS based gas sensors by varying different preparation parameters. *Ind J Pure Appl Physics*. 2000;38(2):119–26.
51. Miremadi BK, Colbow K, Harima Y. A CdS photoconductivity gas sensor as an analytical tool for detection and analysis of hazardous gases in the environment. *Rev Sci Instrum*. 1997;68(10):3898–902.
52. Korotcenkov G. Handbook of humidity measurement: methods, materials and technologies. Vol. 1: Spectroscopic methods of humidity measurement. Boca Raton: CRC Press; 2018.
53. Wolfbeis OS. Fiber optic chemical sensors and biosensors, vol. 1 and 2. Boca Raton: CRC Press; 1991/1992.
54. Lakowicz JR. Principles of fluorescence spectroscopy. 2nd ed. New York: Kluwer Academic/Plenum Press; 1999.
55. Valeur B, Brochon JC, editors. New trends in fluorescence spectroscopy: applications to chemical and life sciences. Berlin: Springer; 2001.
56. Baldini F, Chester AN, Homola J, Martellucci S, editors. Optical chemical sensors. Dordrecht: Springer; 2006.
57. Ekimov AI, Efros AL, Onushchenko AA. Quantum size effect in semiconductor microcrystals. *Solid State Commun*. 1985;56:921–4.
58. Costa-Fernandez JM. Optical sensors based on luminescent quantum dots. *Anal Bioanal Chem*. 2006;384:37–40.
59. Jorge P, Martins MA, Trindade T, Santos JL, Farahi F. Optical fiber sensing using quantum dots. *Sensors*. 2007;7:3489–534.
60. Callan JF, De Silva AP, Mulrooney RC, McCaughan B. Luminescent sensing with quantum dots. *J Incl Phenom Macrocycl Chem*. 2007;58:257–62.
61. Smith AM, Nie S. Semiconductor nanocrystals: structure, properties, and band gap engineering. *Acc Chem Res*. 2010;43(2):190–200.
62. Alivisatos AP. Semiconductor clusters, nanocrystals, and quantum dots. *Science*. 1996;271:933–7.
63. Jaiswal JK, Simon SM. Potentials and pitfalls of fluorescent quantum dots for biological imaging. *Trends Cell Biol*. 2004;14:497–504.
64. Chen W, Wang Z, Lin Z, Lin L, Efros AL, Rosen M. Absorption and luminescence of the surface states in ZnS nanoparticles. *J Appl Phys*. 1997;82:3111–5.
65. Luo L, Chen H, Zhang L, Xu K, Lv Y. A cataluminescence gas sensor for carbon tetrachloride based on nanosized ZnS. *Anal Chim Acta*. 2009;635:183–7.
66. Chen Y, Rosenzweig Z. Luminescent CdS quantum dots as selective ion probes. *Anal Chem*. 2002;74:5132–8.
67. Nazzal AY, Qu L, Peng X, Min XM. Photoactivated CdSe nanocrystals as nanosensors for gases. *Nano Lett*. 2003;3(6):819–22.
68. Potyrailo RA, Leach AM. Selective gas nanosensors with multisize CdSe nanocrystal/polymer composite films and dynamic pattern recognition. *Appl Phys Lett*. 2006;88(13):134110.
69. Vassiltsova OV, Zhao Z, Petrukhina MA, Carpenter MA. Surface-functionalized CdSe quantum dots for the detection of hydrocarbons. *Sens Actuators B Chem*. 2007;123:522–9.
70. Norhayati AB, Aidhia R, Akrajas AU, Muhamad MS, Yahaya M. Fluorescence gas sensor using CdTe quantum dots film to detect volatile organic compounds. *Mater Sci Forum*. 2010;663–665:276–9.
71. Mohanta D, Nath SS, Mishara NC, Choudhury A. Irradiation induced gain growth and surface emission enhancement of ZnS:Mn/PVOH semiconductor nano particles by  $Cl^{+9}$  ion impact. *Bull Mater Sci*. 2003;26:289–94.
72. Xu H, Wu J, Chen C-H, Zhang L, Yang K-L. Detecting hydrogen sulfide by using transparent polymer with embedded CdSe/CdS quantum dots. *Sens Actuators B Chem*. 2010;143:535–8.
73. Hines MA, Guyot-Sionnest P. Synthesis and characterization of strongly luminescing ZnS capped CdSe nanocrystals. *J Phys Chem*. 1996;100:468–71.
74. Xie R, Kolb U, Li J, Basché T, Mews A. Synthesis and characterization of highly luminescent CdSe-core CdS/Zn<sub>0.5</sub>Cd<sub>0.5</sub>S/ZnS multishell nanocrystals. *J Am Chem Soc*. 2005;127:7480–8.
75. Chaudhuri RD, Paria S. Core/shell nanoparticles: classes, properties, synthesis mechanisms, characterization, and applications. *Chem Rev*. 2012;112:2373–433.

# Chapter 7

## II-VI Semiconductor-Based Thin Film Electric and Electronic Gas Sensors



Stella Vallejos and Chris Blackman

### 7.1 Introduction

Materials based on II-VI semiconductors have been applied to sensing various gases and vapors. Specifically, intrinsic II-VI semiconductors in the form of thick or thin films composed of particles or low-dimensional structures have shown part-per-million (ppm) sensitivity to nitrogen dioxide, carbon monoxide, ethanol, and isopropanol. Other less common species detected include gasoline, liquefied petroleum gas (LPG), or formic acid. The gas responses of these materials have been stimulated by heat or light, and their readouts have been enabled by transducing elements that usually comprise resistive principles.

The gas sensing properties of II-VI semiconductors are connected with their morphological, structural, electronic, and chemical properties. The vast number of studies on gas-sensitive II-VI semiconductors have consistently shown that these materials must meet essentially the same requirements as gas-sensitive metal oxides (the most common materials in gas sensing). These requirements mainly include small grain size, high porosity, optimal charge carrier concentration, and high chemical surface activity. Hence, the study of II-VI semiconductors as gas sensors has a strong dependence on synthesizing and tuning their physical and chemical features. The most popular synthesis methods for this group of semiconductors in gas sensing include chemical bath, precipitation, and hydrothermal routes, followed by other redeposition methods that integrate the synthesized materials over the appropriate transducing platforms.

---

S. Vallejos (✉)

Instituto de Microelectrónica de Barcelona (IMB-CNM), Consejo Superior de Investigaciones Científica (CSIC), Bellaterra-Barcelona, Spain  
e-mail: [stella.vallejos@imb-cnm.csic.es](mailto:stella.vallejos@imb-cnm.csic.es)

C. Blackman

Department of Chemistry, University College London (UCL), London, UK

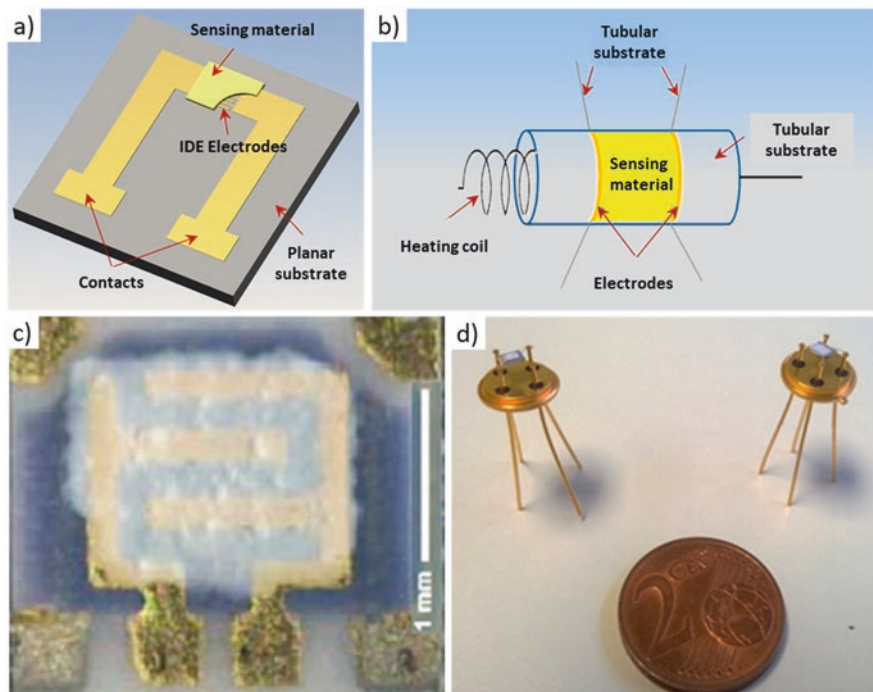
Currently, there is little systematized information on the gas sensing properties of II-VI semiconductor films and their actual functionality. In the literature, there are a considerable number of reports on gas-sensitive II-VI semiconductors, although mainly on CdS and ZnS. A small number of studies also refer to CdTe and CdSe, and there is almost no information regarding the gas sensing properties of ZnSe. In part, this may be due to CdS and ZnS being relatively more stable in air and presenting wider bandgaps than the other II-VI semiconductors; both properties are essential, particularly in conductometric gas sensors operating under thermal activation at elevated temperatures. Hence, this chapter primarily discusses the findings reported for CdS and ZnS as representative gas-sensitive materials from the II-VI group of compound semiconductors focusing on intrinsic thick or thin II-VI semiconductors films, their possible gas sensing mechanism(s), the factors that may influence their sensing properties, and the metrics of their functionality.

## 7.2 Synthesis of Gas-Sensitive II-VI Semiconductors Films and Gas Sensor Fabrication

The gas sensing properties of II-VI semiconductors have been exploited predominantly using electrically transducing platforms in resistive configuration due to the simplicity, ease of fabrication and operation, and feasibility of miniaturization of such sensors. These sensors, also known as chemoresistive sensors, are bipolar devices fabricated on either planar substrates or tubular substrates containing electrodes. The electrodes may be integrated as simple contacts or with interdigitated (IDE) configuration, as shown in the schematic images in Figs. 7.1a, b. Classical chemoresistive sensors integrate a heating element electrically isolated from the electrodes to activate the interactions of the gas and the sensing material. State-of-the-art microfabrication processes based on micro-electro-mechanical systems (MEMS) technology have led to miniaturizing further these devices facilitating the incorporation of heaters with low thermal losses (micro-hotplates) or light-emitting diodes (micro-light plates) to photoactivate the gas sensing response of semiconductors [1, 2]. However, to date, the study of II-VI semiconductors as gas-sensitive films has generally been performed on classical substrates based on bulk silicon or alumina, as shown in Table 7.1.

The synthesis of II-VI semiconductors and their integration with the substrate is critical for sensor fabrication. These procedures define the material characteristics (e.g., grain size, porosity, grain boundaries, and crystallinity) and its chemical, surface, and electric properties. Generally, gas-sensitive II-VI semiconductors are integrated with the substrate via direct or transfer methods [1]. The first (direct methods) involves the direct and selective deposition of the material over the substrate. In contrast, the second (transfer method) employs pre-synthesized powders that are redeposited over the substrate in the form of pastes or slurries. Synthesis methods such as chemical bath, flame-assisted spray pyrolysis, chemical vapor deposition, or





**Fig. 7.1** Schematic figure of a (a) planar and (b) tubular chemoresistive gas sensor. Adapted with permission from references [3, 4], respectively. Copyright 2018 and 2017: Elsevier. (c) Photograph of a planar chemoresistive sensor with the sensing film (CdS) integrated. (d) Photograph of a planar sensor bound and packaged. (Adapted from reference [5]. Published 2016 by MDPI as open access)

sputtering are among the most popular routes to integrate II-VI semiconductors directly with the substrate. The II-VI semiconductors integrated by these methods usually acquire the form of films (with hundreds of nanometers to tens of microns in thickness) comprised of particles or low-dimensional structures such as flakes. Specifically, chemical bath routes have been demonstrated for growth of gas-sensitive ZnS and CdS thin films containing particles of tens of nanometers using chemical solutions based on  $\text{ZnSO}_4$  [6, 7] and  $\text{CdSO}_4$  [8, 9], respectively. Similarly, flame-assisted spray pyrolysis has been used to deposit ZnS thin films composed of aggregates of particles with sizes in the order of units of nanometers by using solutions based on  $\text{Zn}(\text{NO}_3)_2$  and  $\text{Na}_2\text{S}$  [10]. Other routes, including CVD, pulsed laser deposition, physical evaporation, and sputtering, also reported the direct integration of CdS [3, 11, 12], ZnSe [13], and CdSe [14] films containing particles of tens of nanometers, respectively; the starting materials for these routes were based on powders or targets of the materials themselves.

The II-VI semiconductors integrated by transfer methods are generally produced via wet-chemistry synthetic routes such as precipitation or hydrothermal processes. Precipitation routes have mainly been reported for the synthesis of spherical CdS

**Table 7.1** Comparative table showing the synthetic methods and main characteristics of gas-sensitive II-VI semiconductors

Synthetic method	Sem.	As-synthesized morphology	Features	Substrate	Electrodes	Integration method	Ref.
ChB	CdS		N/A	<sup>P</sup> Glass	N/A	Direct	[8]
	ZnS		$T = 210 \text{ nm}$	<sup>P</sup> SAW	N/A IDE	Direct	[6]
	ZnS		$T = 410 \text{ nm}$ $CS = 50 \text{ nm}$ $PS = 50 \text{ nm}$	<sup>P</sup> Glass	N/A	Direct	[7]
	CdS		$T = \text{N/A}$ $PS = \sim 40 \text{ nm}$	<sup>P</sup> Glass	N/A	Direct	[9]
FASP	ZnS		$PS = 8 \text{ nm}$	<sup>P</sup> Si/SiO <sub>2</sub>	Ag Cs	Direct	[10]
CVD	CdS		$T = 25 \mu\text{m}$ $FT = 20 \text{ nm}$	<sup>P</sup> Si/SiO <sub>2</sub>	Au IDE	Direct	[3]
	CdS		$T = 25 \mu\text{m}$ $FT = 20 \text{ nm}$	<sup>P</sup> Si/SiO <sub>2</sub>	Ag/Pd IDE	Direct	[11]
PLD	CdS		$T = 500 \text{ nm}$ $PS = 9 \text{ nm}$	<sup>P</sup> Si/SiO <sub>2</sub>	Pt IDE	Direct	[12]
PE	ZnSe		$T = 50 \text{ nm}$ $CS = 10 \text{ nm}$ $PS = 30 \text{ nm}$	<sup>P</sup> Glass	In CTs	Direct	[13]
DC-ST	CdSe		$T = 600 \text{ nm}$ $CS = 17 \text{ nm}$	<sup>P</sup> N/A	Al IDE	Direct	[14]
P	CdS		$d = 100 \text{ nm}$	<sup>P</sup> Al <sub>2</sub> O <sub>3</sub>	Au IDE	Screen printing	[5]
	CdS		$d = 21 \text{ nm}$ $CS = 21.2 \text{ nm}$	<sup>T</sup> Al <sub>2</sub> O <sub>3</sub>	Au CTs	Paste coating	[4]
	CdS		N/A	<sup>P</sup> Al <sub>2</sub> O <sub>3</sub>	N/A	Screen printing	[15]
HP	ZnS		$d = 200 \text{ nm}$ $CS = 28 \text{ nm}$	<sup>T</sup> Al <sub>2</sub> O <sub>3</sub>	Au CTs	Paste coating	[16]
	ZnS		$d = 500 \text{ nm}$	<sup>T</sup> Al <sub>2</sub> O <sub>3</sub>	Au CTs	Paste coating	[17]
	ZnS		$d = 200 \text{ nm}$ $FT = 50 \text{ nm}$	<sup>T</sup> Al <sub>2</sub> O <sub>3</sub>	Pt Cs	Paste coating	[18]
	CdS		$d = 1400 \text{ nm}$	<sup>T</sup> Al <sub>2</sub> O <sub>3</sub>	Au CTs	Paste coating	[19]
	CdS		N/A	<sup>T</sup> Al <sub>2</sub> O <sub>3</sub>	Au CTs	Paste coating	[20]
	CdS		$L = 6000 \text{ nm}$	<sup>P</sup> Al <sub>2</sub> O <sub>3</sub>	Au IDE	Spin coating	[21]
SG	CdS		$d = 128 \text{ nm}$	N/A	N/A	N/A	[22]

*P* Precipitation; *PLD* Pulsed Laser Deposition; *DC-ST* DC Sputtering; *PE* Physical Evaporation; *ChB* Chemical Bath; *HP* Hydrothermal Process; *SG* Sol gel; *FASP* Flame-Assisted Spray Pyrolysis; *CVD* Chemical Vapor Deposition; *TE* Thermal Evaporation; *SAW* Quartz-based Surface Acoustic Wave platform; *d* diameter; *CS* Crystal Size; *T* Thickness; *PS* Particle Size; *FT* Flake thickness; *CTs* Contacts; *N/A* data not available

particles (tens or hundreds of nanometers) produced from  $\text{Cd}(\text{OOCCH}_3)_2 \cdot x\text{H}_2\text{O}$  (cadmium acetate hydrate) and  $\text{CH}_3\text{CSNH}_2$  (thioacetamide) [5, 15]. However, particles with flake-like and brick-like morphology were also formed via alternate precipitation and sonication steps by using  $\text{CdCl}_2 \cdot 5\text{H}_2\text{O}$  (cadmium chloride pentahydrate) and  $\text{NH}_2\text{CSNH}_2$  (thiourea) as precursors for Cd and S, respectively [4]. Hydrothermal synthetic routes have been used for the formation of solid [16] and hollow [17] spherical particles of ZnS, as well as other spherical particles containing nanoflakes over the surface (so-called ‘urchin-like’ structures) [18]. The sizes of the resulting particles vary in a range of hundreds of nanometers to a few microns according to the specific hydrothermal route employed. The routes frequently start from  $\text{ZnAc}_2 \cdot 2\text{H}_2\text{O}$  (zinc acetate) as the Zn precursor and either thiourea, thioacetamide, or  $\text{C}_5\text{H}_{12}\text{N}_2\text{S}_2$  (1-pyrrolidine dithiocarboxylic acid ammonium) as the S precursor. Hydrothermal routes have also been used for synthesis of CdS with varied morphologies. For instance, CdS urchin-like structures were synthesized by a hydrothermal route based on  $\text{Cd}(\text{OOCCH}_3)_2 \cdot 2\text{H}_2\text{O}$  (cadmium acetate dihydrate) and thiourea [19]. On the other hand, dendrite-like or leaf-like CdS structures were achieved by using  $\text{CdCl}_2 \cdot x\text{H}_2\text{O}$  (cadmium chloride hydrate) mixed with KSCN (potassium thiocyanate) [20] or thiourea [21]. Other synthetic routes for the formation of CdS powders and subsequent transfer onto the substrate involve using sol-gel [22] and thermal evaporation processes [11].

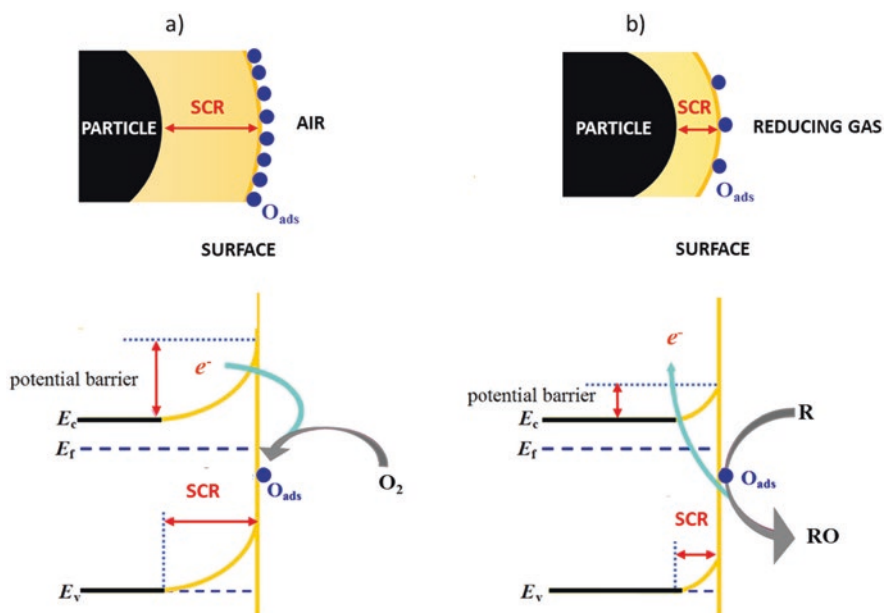
Table 7.1 summarizes the synthetic methods, morphologies, and primary features reported for gas-sensitive II-VI semiconductors films. The variety of available synthetic methods for II-VI semiconductors, mainly based on chemical bath, precipitation, and hydrothermal synthesis routes, is evident from the survey. The recurrence of these methods may be related to their simplicity compared to other procedures requiring particular infrastructure (vacuum systems, high temperatures, reactants in the gas phase, or other elements for handling reactants/by-products).

### 7.3 II-VI Semiconductors and their Gas Sensing Mechanisms

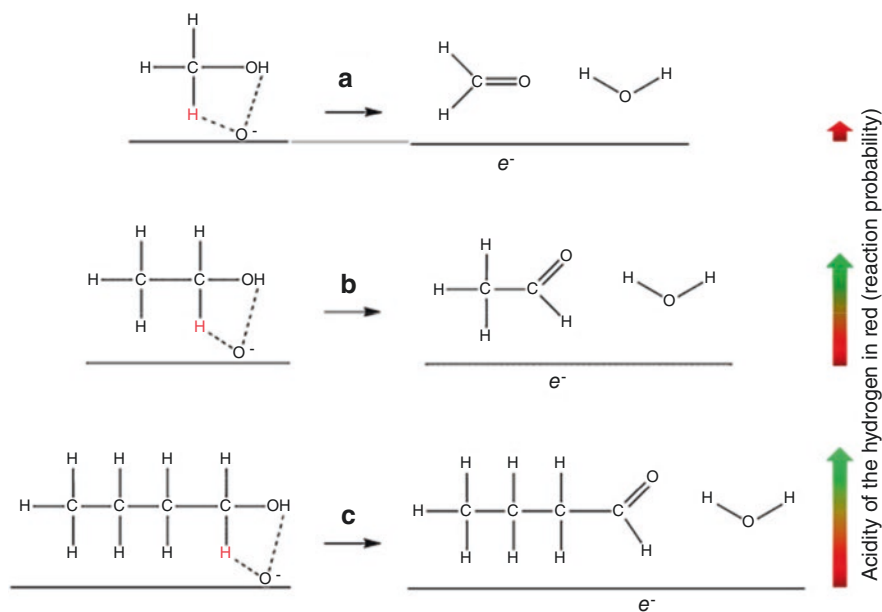
The II-VI semiconductors are responsive to gases due to their ability to change their surface Fermi-level position in relatively wide ranges, similar to most common gas-sensitive metal oxides [23]. This ability correlates inversely with the interface behavior index obtained from classic experiments that measure the barrier energy at metal-semiconductor interfaces as a function of the electronegativity of the metals employed [24]. As a reference, well-known gas-sensitive metal oxides, such as  $\text{SnO}_2$  and ZnO, have high indexes ( $\sim 1$ ). In contrast, poor gas-sensitive semiconductors, such as Si, GaAs, or InP, have low indexes, close to zero, as they experience surface Fermi-level pinning due to their high density of surface states. In II-VI semiconductors, these indexes vary between 0.2 and 1, with the highest index

reported for ZnS ( $\sim 1$ ) followed by CdS ( $\sim 0.6$ ), ZnSe ( $\sim 0.5$ ), CdTe ( $\sim 0.3$ ), and CdSe ( $\sim 0.3$ ). Subsequently, the gas sensing mechanisms of II-VI semiconductors are usually attributed to classic space-charge-region models [4, 9–12, 19, 20, 22, 25, 26]. These models suggest the adsorption of oxygen at the surface with the subsequent formation of oxygen species ( $O_2^-$ ,  $O^{2-}$ ,  $O^-$ ) and an electron-depleted layer, which is then compensated by electrons or further electron depleted during interaction with reducing or oxidizing gases, respectively (Fig. 7.2).

A specific sensing mechanism for interaction of alcohols with CdS films has also been proposed, based on the dehydrogenation of alcohols by pre-adsorbed oxygen ions (Fig. 7.3). The proposed mechanism and experimental results determined a proportional relation between the length of the alkyl chain and its reaction efficiency at the gas-sensitive surface, with higher response to n-butanol followed by ethanol and then methanol. This was attributed to an increment of the acidity in the hydrogen of the  $CH_2$  group closest to the OH group as the chain becomes longer, increasing the probability of the reactions shown in Fig. 7.3 to occur compared to other possible reactions. Hence, higher responses were obtained experimentally for the CdS films to n-butanol than ethanol or methanol [25].



**Fig. 7.2** Gas sensing mechanism based on surface space-charge-region models. Scheme of an n-type semiconducting particle and its surface band bending when exposed to (a) air and (b) reducing gas. SCR Surface Charge Region;  $E_f$  Fermi level;  $E_c$  Conduction band minimum;  $E_v$  Valence band maximum;  $O_{ads}$  Adsorbed oxygen



**Fig. 7.3** Gas sensing mechanism for alcohols, from top to bottom: (a) methanol, (b) ethanol, and (c) n-butanol. The arrow on the right of each reaction indicates qualitatively the acidity of the hydrogen in red, which is proportional to the reaction probability. (Adapted with permission from reference [25]. Copyright 2015: Elsevier)

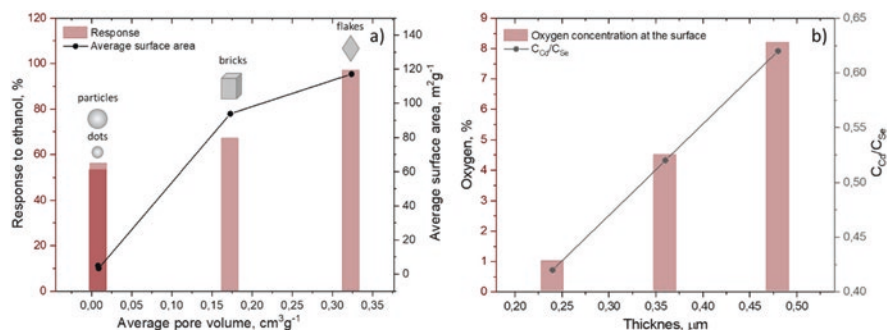
## 7.4 Factors that Influence the Gas Sensing Properties of II-VI Semiconductors

### 7.4.1 Size, Morphology, and Structure

Since the efficacy of a gas-sensitive material is surface-dependent, previous investigations, albeit mainly on metal oxides, have demonstrated that the sensing properties are dependent on characteristics such as the size, morphology, and microstructure of the material [23, 27, 28]. As a rule, it has been found that nanoscale morphological shapes and high surface-to-volume ratio improve the sensing performance due to their increased relative number of active sites at the surface. Similarly, II-VI semiconductors have been demonstrated to possess enhanced sensing properties when their morphology is structured and reduced in size. For instance, hierarchical 3D micro/nanostructures of CdS with leaf-like morphology showed higher responses and faster dynamic response compared with CdS microspheres to various gases, including diethyl ether, methanol, acetone, and isopropanol [21]. The highest response difference was obtained with methanol, which registered four times more response with the hierarchical micro/nanostructures than with the microspheres.

The advantage of using mesoporous hierarchical nanostructures instead of solid nanospheres was also reported for ZnS where mesoporous hierarchical nanostructures with three-fold higher specific surface area ( $\text{m}^2\text{g}^{-1}$ ) and approximately two-fold larger pore volume ( $\text{cm}^3\text{g}^{-1}$ ) registered almost four-fold higher response to 100 ppm of gasoline at  $290^\circ\text{C}$  [16]. Similarly, other comparative studies on CdS nanocrystals, including flakes, bricks, particles, and quantum dots (QDs), revealed enhanced ethanol sensing properties for flake-like structures [4]. The most remarkable differences in response were obtained between the nanoflakes and QDs, with almost 60% higher ethanol response for the nanoflakes than the QDs at  $270^\circ\text{C}$ . These results [4] were connected with the differences in specific surface areas and pore volumes, as is evidenced in Fig. 7.4a which displays the correlation of the surface area, pore-volume, and response to ethanol. The improved performance of the CdS nanoflakes was also related to the presence of extra defect states associated with sulfur vacancies, which contribute to the adsorption of oxygen from the environment enhancing the response to gases. These defect states in CdS were inferred from the nanoflakes' photoluminescence spectrum that contained an additional emission peak at 675 nm.

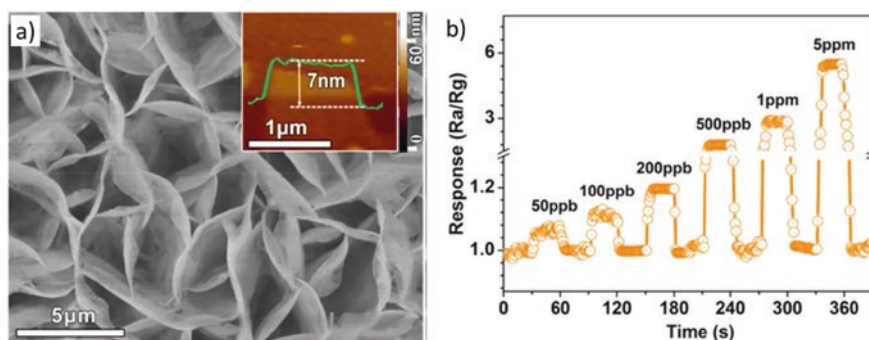
Other investigations highlight the influence of the film thickness on the sensing properties of II-VI semiconductors. For instance, studies on CdSe and CdS films demonstrated an enhanced oxygen sensitivity as the film thickness of these materials increased (Fig. 7.4b) [14, 29, 30]. Detailed evaluation of the film surface properties using X-ray photoelectron spectroscopy (XPS) and secondary ion mass spectroscopy (SIMS) revealed that this behavior was related to the increment of relative Cd-content on the film surface. This Cd enrichment was found to occur during the growth of CdSe and CdS films and be correlated with the adsorption of oxygen species and hence the sensitivity to oxygen of resistive sensors based on CdSe and CdS films [29, 30]. Further investigations on the thickness dependence of CdSe sensitivity to carbon monoxide reported consistent results by showing an increment in CdSe sensitivity as its thickness increased from 350 to 500 nm [14].



**Fig. 7.4** (a) Correlation of the average pore volume, average surface area analyzed, and response to ethanol for different CdS-like morphologies (data extracted from reference [4]). (b) Correlation of the CdS film thickness, the ratio of the Cd to Se concentration at the surface, and concentration of surface oxygen adsorbed. (Data extracted from reference [29])

The effect of ZnS thickness on the response of surface acoustic wave sensors also indicated an improved performance towards ammonia by increasing the film thickness from a few nanometers (<42 nm) to 210 nm. These results were attributed to the higher specific surface area and active sites on the surface of the films with 210 nm. However, the results are not conclusive on whether the chemistry or structure of the ZnS films was modified by the film thickness [6] as seen for CdS and CdSe films [29, 30].

Studies of the phase and defect-dependent gas sensing performance of ZnS also indicate sensitivity improvements connected with the crystalline structure, especially with the presence of the wurtzite phase in ZnS. It was observed that ZnS with high contents of wurtzite crystals increased the response of ZnS to hydrogen sulphide compared to ZnS with high contents of zinc blend phase. Wurtzite-structure ZnS tends to form flake-like shapes, which expose S-terminated planes increasing the relative number of sulfur vacancies and promoting the adsorption of both oxygen and target gases [18]. Something similar occurs for CdS, which has improved sensing properties to various volatile organic compounds (VOC), particularly isopropanol, when the morphology has a flake-like shape and is characterized by a wurtzite phase and S-terminated surface (Fig. 7.5) [11]. Specifically, the polar {0001} planes of wurtzite-structure in CdS flakes have an S-terminated (00 $\bar{1}$ ) surface that usually contains sulfur vacancies and dangling bonds (due to their low formation energy), which has been shown to enhance the adsorption of gaseous molecules [11]. Accordingly, the structure of crystalline gas-sensitive II-VI semiconductors and the nature of the surfaces exposed to the gases are essential in the sensing mechanism and the overall sensing performance. These results are consistent with those generally found on crystalline gas-sensitive metal oxides, which demonstrated a dependency of the gas sensing activity on the crystal shape [28]. Hence, research on the controlled growth of nanocrystalline structured materials (generally classified as 1D, 2D, and 3D structures) has increased significantly in



**Fig. 7.5** (a) Correlation of the average pore volume, average surface area analyzed, and (b) response to ethanol for different CdS-like morphologies. (Adapted with permission from reference [11]. Copyright 2016: American Chemical Society)

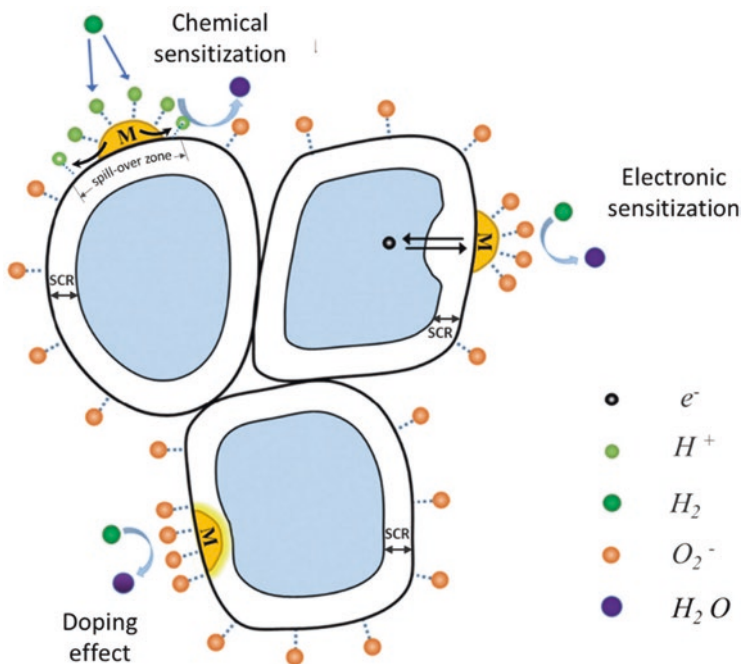
recent years. Further discussion on the recent advances of these types of structures based on II-VI semiconductors is addressed in Chap. 10, Vol. 3.

### **7.4.2 Modifications: Doping, Surface Decoration, and Mixture of Components**

Materials modification, achieved by loading or incorporating second-phase constituents (e.g., ions, metals, or other inorganic or organic materials), has been shown to be generally effective in improving gas sensing properties such as sensitivity, selectivity, speed of response, and operating temperature [31–33]. These modifications can influence the gas sensing properties by increasing the density of active sites (e.g., defects, sulfur vacancies) or charge carriers (doping effect), or the modification can lead to a chemical sensitization by promoting the ‘spill-over’ of active chemical species over the gas sensing (‘support’) material and/or to an electronic sensitization characterized by the formation of heterojunctions and tuning of interfacial potential barrier energy and charge carrier transfer. The modification of materials can also promote synergistic behavior, as each constituent material serves a different purpose that is complementary to the other so that the synergistic effect of the constituents is greater than the effect of a single element [31–33]. Figure 7.6 illustrates the possible effects derived from the modification of gas-sensitive materials.

Hence, II-VI semiconductors have been modified with various material types to improve their gas sensing properties. The most common modifications incorporate doping atoms such as Zn, Ni, or Mn or decorating metals such as Au or Pd. The use of Zn as a dopant has been shown as one of the simple routes to modify CdS due to its similar crystal structure to ZnS. Doping of CdS with Zn has been shown to enhance the sensitivity of CdS to reducing gases such as methanol, ethanol, methylbenzene, formaldehyde, and acetone. The incorporation of the smaller  $\text{Zn}^{2+}$  ion in the CdS structure modifies the bond length/strength in the CdS crystal so that the concentration of S vacancies, which act as electron donors, decreases [35]. Doping of CdS with Zn also leads to a drop in the carrier concentration of the film, allowing a higher ratio of free carriers to take part in the surface reactions [36], hence the report of enhancing sensitivity to reducing gases [35] despite the loss of active sites due to the decrease of S vacancies in the doped structure. Something similar occurs with the doping of CdS with  $\text{Ni}^{2+}$  ions, which has been shown to improve the sensitivity of CdS to LPG [37]. A combination of Ni-doping and Au-decoration in ZnS nanospheres has also shown important changes in the sensing properties of ZnS to formaldehyde and other gases such as ethanol and ammonia [38], increasing the response of ZnS by 60% and reducing the time of response by 15% when the concentration of formaldehyde was 5 ppm. The improvements were associated with the charge transfer modification in the doped system and chemical sensitization mechanisms of the Au nanoparticles at the Ni-doped ZnS nanospheres surface. Doping of





**Fig. 7.6** Schematic diagram showing the possible effects derived from the bulk doping or surface modification (Chemical sensitization and Electronic sensitization) of gas-sensitive materials. M second-phase constituent modifying the 'support' material; SCR Surface Charge Region. (Adapted with permission from reference [34]. Copyright 2018: Elsevier)

ZnS with  $Mn^{2+}$  ions has also led to improved oxygen sensing [39]. These doped structures with dual-emission from ZnS (445 nm) and Mn (590 nm) possessed a linear decrease of their fluorescence intensities with increasing oxygen concentration, which was attributed to a rapid capture of photogenerated carriers as the oxygen was adsorbed causing a temporary deactivation of surface luminescence centers.

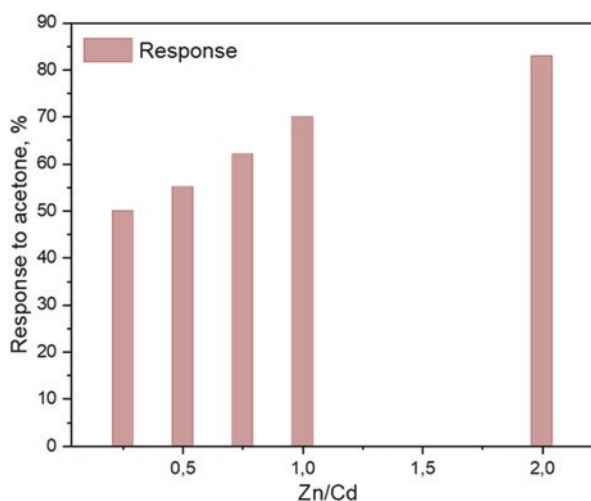
Another strategy for modifying II-VI semiconductors included the incorporation of small amounts of metals such as Au [40] or Pd [41]. The decoration of ZnS with Au nanoparticles, for instance, enhanced response to various gases (including nitrogen dioxide, ammonia, ethanol, carbon monoxide, and hydrogen sulfide) at room temperature as compared to the equivalent system without nanoparticles decoration [40]. The sensitivity of this decorated system was found to be further improved by exciting the material with UV light. A similar study on Pd-decorated ZnS nanoparticles also showed significant enhancement to nitrogen dioxide sensing, compared to undecorated ZnS, under UV illumination [41]. The following section discusses the influence of photoactivation in the gas sensing properties of non-modified and modified II-VI semiconductors.

Much research has also focused on studying the gas sensing behavior of modified II-VI semiconductors that contain heterojunctions between one or more kinds

of II-VI semiconductors, for instance, ZnS and CdS. This modified system with different molar ratios of Zn/Cd was investigated for sensitivity to gases such as ammonia and acetone [42]. Generally, CdS modified with ZnS reported an increment of the response as the Zn/Cd ratio increased from 0.25 Zn/Cd to 2 Zn/Cd. Simultaneously, the modified systems reported a slight decrease of the bandgap of CdS, from 2.40 eV (CdS) to 2.38 eV (for 0.75 Zn/Cd) and 2.35 eV (for 1.0 Zn/Cd). Figure 7.7 displays a graphical summary of the response to acetone and its correlation with the Zn/Cd ratio in the samples. Other modified II-VI semiconductors with heterojunctions include those that incorporate metal oxides [41–49], conductive polymers [50], or carbon-based materials [51]. Among them, the use of semiconducting metal oxides, particularly ZnO, to modify the II-VI semiconductor is the most popular in the literature. A more detailed discussion of the modification of II-VI semiconductors with other semiconducting materials is addressed in Chap. 9.

### 7.4.3 Thermal and Light Activation

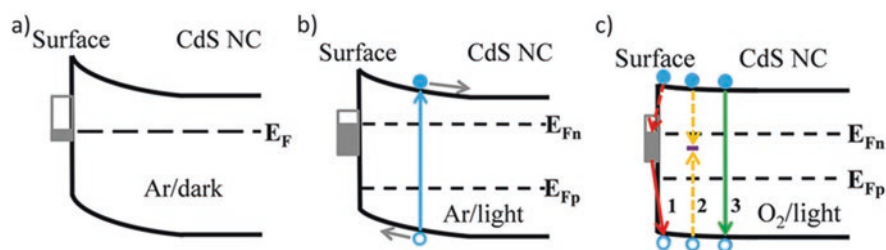
The usual operation for II-VI semiconductors in gas sensor devices is in resistive mode activated thermally by external or local heating elements that raise the temperature to hundreds of degrees Celsius (70–300 °C) [4, 7, 11, 16–18, 20–22, 25, 26, 50, 51]. However, II-VI semiconductors have also been reported to have a resistive or optical gas response at room temperature (with or without photoactivation) [3, 6, 10, 12, 15, 52–55]. The operation at room temperature is mainly related to the physical adsorption of oxygen molecules at the surface, and frequently the responses under this operation mode are low. In contrast, the operation under photoactivation usually relates to the formation of photogenerated free electrons that finally participate in the chemical interactions at the surface [2]. Previous studies on



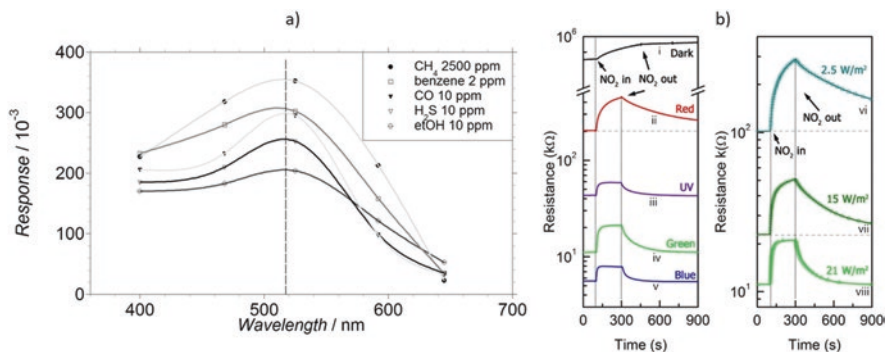
**Fig. 7.7** Dependence of the response to acetone as a function of the Zn/Cd ration in ZnS-modified CdS films. (Data extracted from reference [42])

light- (467 nm) activated CdS crystals suggested photo-assisted oxygen adsorption [54]. This means that in the presence of light, oxygen is chemisorbed on the surface of CdS as negatively charged ions by taking electrons from surface states or the conduction band of CdS. These studies also determined a significant influence of oxygen adsorption on the photoconductivity, with oxygen reducing the photoconductivity due to effective surface passivation of CdS. In contrast, tests in vacuum or argon led to more effective charge separation of the photogenerated electron-hole pairs and increased photoconductivity. Figure 7.8 illustrates this behavior in terms of energy band bending at the CdS surface.

CdS films also showed photoconductivity changes to other gases, including methane, benzene, carbon monoxide, hydrogen sulphide, and ethanol [15, 56]. These changes (responses) showed wavelength dependence, suggesting bandgap-resonant behavior that maximizes both the photoconductivity (in agreement with other works on CdS [59]) and the surface chemical activity. Thus, the maximum changes were found for the wavelength (525 nm – green; 2.36 eV), near the bandgap energy of CdS (2.40 eV), see Fig. 7.9a. Detection of gases by measuring other parameters in green light-activated CdS sensors, such as photosensitivity, dark resistance, or phase angle, has also demonstrated potential for analytical identification of various gases, which include carbon monoxide, hydrogen, ethanol, acetone, and methanol [60]. Green light-activated CdS sensors have also been shown to be sensitive to nitrogen dioxide, providing not only higher responses than those recorded under other wavelength excitations but also faster responses and recovery times [3]. It is worth noting that tuning of both parameters, i.e., response and speed of response and recovery, depends on the light irradiance, as can be observed in Fig. 7.9b. CdS-based sensors were also found to be suitable for operation under



**Fig. 7.8** Electronic energy band gap of CdS nanocrystals (NC). (a) in dark with Ar atmosphere, (b) in light with Ar atmosphere, and (c) in light with  $O_2$  atmosphere.  $E_F$ ,  $E_{Fn}$ , and  $E_{Fp}$  are the Fermi level in equilibrium and the quasi-Fermi level of electrons (holes) under illumination, respectively. The blue arrow in panel (b) indicates the optical transition of electrons from valence band to conduction band upon absorption of photons. The filled and empty blue circles denote the photoexcited electrons (holes). Gray arrows indicate the dissociation of excitons after generation by the built-in electric field near the surface. The arrows in panel c indicate three possible channels for the recombination of electron-hole pairs: (1) recombination from surface trap states to the valence band (red); (2) Shockley–Read–Hall recombination (dashed yellow); (3) inter-band recombination (green). The defect levels that serve as recombination centers are represented by a short purple line in panel (c). (Adapted with permission from reference [54]. Copyright 2014: American Chemical Society)



**Fig. 7.9** (a) Response of CdS films to various gases as function of the exciting light wavelength (adapted with permission from reference [58]. Copyright 2004: AIP Publishing). (b) Response of CdS nanoflakes to 5 ppm of  $\text{NO}_2$  as function of the exciting light wavelength and green light irradiance (adapted with permission from reference [3]. Copyright 2018: Elsevier)

fluorescent lamps and natural solar light, suggesting potential for operating with low power consumption sources [3].

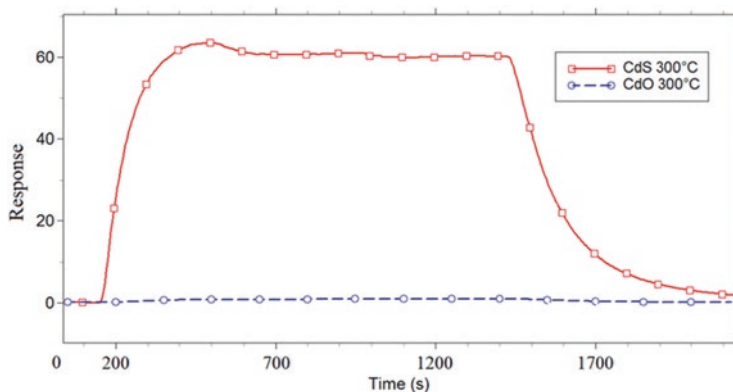
Other studies also show that gas-sensitive II-VI semiconductors activated by light can be tuned by their modification with second phase constituents. The formation of interfaces and concomitant band bending has been demonstrated as a fundamental step in photo-stimulated chemical sensing. Band bending can reduce the electron-hole pair recombination and promote their separation and migration to the surface, making it chemically more reactive [2]. For instance, band bending due to metal-semiconductor interfaces facilitates the separation of photogenerated charge carrier pairs where the photoexcited electrons can be trapped in the metal, while the photoexcited holes enrich the semiconductor. This is the main reason for the enhancement of photoactivity in metal-semiconductor interfaces. Simultaneously, the metal participating in the interface may also provide chemical sensitization to the semiconductor [31, 33], as discussed in the previous section. An example in the literature of the UV-activated sensing performance of ZnS decorated with Pd demonstrated significant improvements in the ZnS response to nitrogen dioxide [41]. The response of ZnS to nitrogen dioxide (1 ppm) registered three times higher response values when decorated with Pd nanoparticles and also faster recovery time, showing a decrease from 100 s to 80 s, with respect to unmodified ZnS.

Band bending due to semiconductor-semiconductor interfaces can also promote the separation of photogenerated charge carrier pairs and make the surface chemically more reactive. In this interface type, the band alignment and type of conductivity of each constituent (n- or p-type) influence the charge separation. The literature has shown that semiconductor-semiconductor interfaces with a staggered gap are usually more advantageous for light activation [2], and currently most of the examples in the literature involving II-VI semiconductor-semiconductor interfaces usually incorporate ZnO in the system.

Generally, these systems have shown improved responses to nitrogen dioxide [43, 61–64] or ethanol [65, 66].

#### 7.4.4 Stability and Operational Conditions

In practical sensor devices, the operational conditions may also influence the final sensing properties of II-VI semiconductors. In particular, the operation of gas sensors in atmospheric ambient imposes the need for gas-sensitive materials that are stable not only in the presence of oxygen, but also under thermal and light excitation. Compared to typical gas-sensitive materials based on metal oxides, II-VI semiconductors bring certain disadvantages concerning their stability. This is because II-VI semiconductors tend to oxidation processes that may change their chemical and electronic properties and, in turn, their sensing performance. For instance, ZnS has been found to oxidize easily to ZnO upon heating in the open air [67–70]. The formation of ZnO is usually reported to occur at temperatures above 400 °C [62–64]. However, this onset temperature has proved to decrease further, to about 300 °C, upon downsizing the ZnS particles to sizes between 3 and 5 nm [62, 65]. In some study cases, this temperature approaches those employed to activate ZnS's gas sensing response [7, 16]. CdS may also form oxidized phases from Cd-O-S, Cd(S<sub>2</sub>O<sub>7</sub>), or CdSO<sub>4</sub> upon heating in open air at 400 °C. Other oxidized forms, including Cd<sub>5</sub>S<sub>3</sub>O<sub>6</sub> and Cd<sub>3</sub>SO<sub>6</sub>, have also been found at temperatures between 500 and 600 °C [71]. The oxidation of CdS to CdO has also been shown to occur upon heating in air at 400 °C [72]. This phase change, i.e., from CdS to CdO, has shown to be disadvantageous in gas sensing as the sensitivity of thermally activated CdO is significantly lower compared to that of CdS (Fig. 7.10) [5]. These results suggest that the functionality of II-VI semiconductors with high temperature activation may not be reliable for practical applications.



**Fig. 7.10** Comparative response of CdS and CdO films to 5 ppm of ethanol at 300 °C. (Adapted with permission from reference [5]. Copyright 2016: MDPI)

## 7.5 Key Metrics of Intrinsic II-VI Semiconductor-Based Gas Sensors

Intrinsic II-VI semiconductors in the form of thick or thin films composed of particles or low-dimensional structures have shown part-per-millions (ppm) sensitivity to various gases and vapors. Table 7.2 displays examples of the maximum responses registered from the most successful II-VI semiconductor-based sensors reported in the literature to specific gases, concentrations, and operating conditions. Overall, the responses are in units or tens of magnitude and the speed of response/recovery in units or tens of seconds. It is worth noting that both characteristics, i.e., response

**Table 7.2** Major gas responses recorded by II-VI semiconductor films to various gases and vapors

Sem.	P	M	Activation	Gas	C	R	$t_r/t_r$	Ref.
ZnS	Resistive	MPs	<sup>T</sup> 290 °C	Gasoline	100 ppm	25	7 s/5 s	[16]
		TF	<sup>T</sup> 270 °C	Chlorine	N/A	1.2	N/A	[7]
		NPs	<sup>T</sup> 160 °C	Hydrogen sulphide	50 ppm	18	18 s/12 s	[18]
		MSfs	<sup>T</sup> 160 °C	Ethanol	100 ppm	4.5	2 s/21 s	[17]
		TF	<sup>T</sup> 373 K	LPG	200 ppm	0.16	N/A	[10]
CdS	SAW	TF	<sup>RT</sup> 25 °C	Ammonia	20 ppm	1.2 <sup>Rf</sup>	23 s/148 s	[6]
	Resistive	TF	<sup>T</sup> 300 °C	Butanol	5 ppm	90	N/A	[25]
		NFls	<sup>T</sup> 270 °C	Ethanol	1 ppm	1.6	3 s/5 s	[4]
		ULs	<sup>T</sup> 230 °C	Ethanol	100 ppm	20	1 s/ 1 s	[52]
		Dts	<sup>T</sup> 260 °C	Formic acid	50 ppm	30	19 s/26 s	[20]
		NFls	<sup>T</sup> 230 °C	Isopropanol	5 ppm	6	N/A	[11]
		LLSs	<sup>T</sup> 210 °C	Isopropanol	100 ppm	63	6 s/15 s	[21]
		MNPs	<sup>T</sup> 180 °C	Nitric oxide	1 ppm	9	13 s/37 s	[26]
		NPs	<sup>T</sup> 70 °C	Nitrogen dioxide	20 ppm	273	N/A	[22]
		TF	<sup>T</sup> 38 °C	Nitrogen dioxide	100 ppm	1.4	50 s/720 s	[9]
		TF	<sup>T</sup> 20 °C	LPG	1000 ppm	0.7	N/A	[12]
		NPs	<sup>GL</sup> N/A	Methane	2500 ppm	3.5	N/A	[15]
		NCs	<sup>BL</sup> 19 mW/cm <sup>2</sup>	Oxygen	10%	35	5 s/N/A	[54]
		NFls	<sup>GL</sup> 21 W/m <sup>2</sup>	Nitrogen dioxide	5 ppm	1.9	44 s/113 s	[3]
CdSe	Resistive	TF	<sup>T</sup> 277 °C	Carbon dioxide	1000 ppm	0.23	N/A	[53]
		TF	<sup>RT</sup> N/A	Ethanol	N/A	40	N/A	[55]
		MPs	<sup>XL</sup> 350 W	Ethanol	200 ppm	3.8	N/A	[56]
CdTe	SAW	TF	<sup>RT</sup> N/A	Carbon monoxide	N/A	25 <sup>Rf</sup>	N/A	[57]

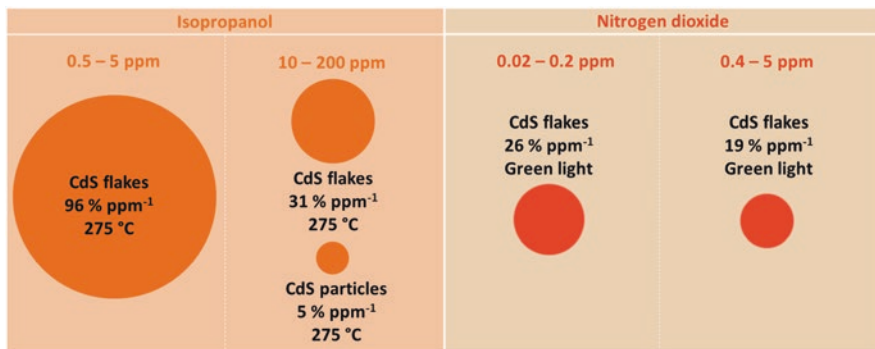
*Mat* Material; *P* Principle; *C* Concentration; *T* Temperature; *RT* room temperature; *Rf* Response in Kilo Hertz (KHz); *GL* Green light *BL* Blue light; *XL* Xenon lamp (visible light); *R* response defined as  $R_a/R_g$  for reducing gases and  $R_g/R_a$  for oxidizing gases; *N/A* data not available; *NFls* nanoflakes; *LLSs* Leaf-like structures; *TF* Thin film; *NCs* Nanocrystals; *Dts* Dendrites; *MPs* Mesoporous structure; *MSfs* Microspheres; *NPs* Nanoparticles; *MNPs* Micro/nanoparticles; *ULs* Urchin-like structures; *LPG* Liquefied petroleum gas

and speed of response/recovery, depend directly on the gas and concentration. Most of the gas-sensitive II-VI semiconductors in the literature report resistive operation mode and thermal stimulation at temperatures above 70 and below 300 °C. However, operation at room temperature with or without light stimulation has also proved feasible, as noticed in Table 7.2.

The evaluation of the middle/long-term stability of these responses under controlled ambient suggested relatively good stability of II-VI semiconductors such CdS and ZnS for periods of 20 to 110 days. For instance, the response of CdS nano-flakes to 200 ppm isopropanol was found to be stable, with slight change from a response of 76 to response of 71 over a period of 20 days [11]. However, other reports on CdS sensitivity to NO<sub>2</sub> observed the need for an aging period (~20 days) before the response entered a stable period [9]. Further tests on CdS-based sensors demonstrated even more extended periods of stability, from 42 days to 60 days, when exposed to gases such as ethanol [5], and several VOCs [4], and LPG [12]. Tests of ZnS exposed to LPG also suggested good stability operating at room temperature over a period of 30 days [10]. CdS nanoflakes operating under green light also showed long periods of nitrogen dioxide response stability with a loss of the response of only 10% in a period of 110 days [3].

An account of the sensitivity (i.e., the response variation as a function of a change in a gas concentration) of II-VI semiconductors in the literature is complex as only a few works report this characteristic. Nevertheless, an estimation of the sensitivity from the calibration curves recorded in different works may provide an indication of the metrics of this parameter. The fact is that calibration curves for intrinsic II-VI semiconductor films are limited, and the available curves refer preferentially to CdS-based sensors. This could be related to the significant number of literature reports on CdS gas sensing. Alternatively, it could be connected to the fact that the sensitivity of intrinsic II-VI semiconductor films is relatively low and, consequently, has not reported significant response changes to gas concentration variations.

Indeed, the metrics of sensitivity from the available data for II-VI semiconductor-based sensors report values of only tenths of % ppm<sup>-1</sup> to gases such as ethanol [10], isopropanol [4], isopropanol [21], or nitrogen dioxide [9] in concentrations between 1 and 100 ppm. Among the most representative sensitivity metrics for intrinsic CdS films, one can find those recorded for sensors based on CdS with flake-like morphology. These types of sensors reported sensitivity to low concentrations of isopropanol (0.5–5 ppm) in the order of various tens % ppm<sup>-1</sup> under thermal stimulation (275 °C) [11]. Similarly, CdS films with flake-like morphology registered tens % ppm<sup>-1</sup> to nitrogen dioxide (0.02–5 ppm) under light excitation [3]. Figure 7.11 displays a graphical view of the representative sensitivity metrics for CdS. Note that these data only refer to intrinsic CdS films. The modification of intrinsic II-VI by tuning the morphology from films to 1D structures (e.g., rods) and/or by incorporating catalyst on their surface may certainly improve these metrics. A selected example of the sensitivity metric of light-activated intrinsic ZnS nanorods indicates that its sensitivity to nitrogen dioxide (1–5 ppm) can reach a value of 93% ppm<sup>-1</sup> and increase further to 306% ppm<sup>-1</sup> by decorating the ZnS nanorods with Pd nanoparticles [41].



**Fig. 7.11** Estimation of the sensitivity of CdS flakes and particles as reported in references [3, 11]

Another crucial metric in gas sensors is the sensor's selectivity or ability to identify (discriminate) a particular analyte in a complex mixture, avoiding interfering responses from other analytes. Literature reports usually analyze this characteristic through comparative studies of responses to selected analytes so that the degree of cross-response is determined. Table 7.3 summarizes the cross-responses reported to selected gases for various intrinsic II-VI semiconductors.

The bottom and top of the table display the type of II-VI semiconductor, activation type, and gas concentrations annotated in each reference. The color codes from blue to red and numbers from 1 to 10 along each column show the response to each gas analyte and its load in percentage for the highest response (colored in red and labelled as 10). Thus, for instance, the first column of Table 7.3 indicates that ZnS particles respond preferentially to Cl<sub>2</sub> (red 10) [7]. However, they may experience high interferences from CO<sub>2</sub> (light-green 6), H<sub>2</sub>S (light-green 6), and H<sub>2</sub> (green 5), but only moderate interference from LPG (turquoise 2), NH<sub>3</sub> (light-blue 1), and ethanol (light-blue 1). Similarly, other ZnS systems suggest better selectivity to ethanol (among methanol, dichloromethane, and benzene) [17] or ammonia (among ethanol, hydrogen, carbon monoxide, hydrogen sulphide, and nitrogen dioxide) [6]. The modification of ZnS by doping its structure with Ni and decorating it with Au nanoparticles indicates improving the formaldehyde response [38]. However, the selectivity for both systems (i.e., non-modified and modified) is relatively low as the response of these systems presents high interferences from ethanol, ammonia, or toluene. CdS have also shown selective responses to reducing gases such as ethanol [4, 19], isopropanol [11], and n-butanol [5] with a moderate probability of interferences among them. In addition, CdS systems have also reported high responses to nitrogen dioxides (NO<sub>x</sub>) [3, 9, 26] with apparently negligible interferences from other gas responses (e.g., ethanol, ammonia, hydrogen, or carbon monoxide). Overall, II-VI semiconductors' selectivity is partial and relative to the set of interfering gases, as for other gas-sensitive materials (e.g., metal oxides).



**Table 7.3** Cross-responses to different gases and vapors recorded using II-VI semiconductors. The color codes and numbers in each column of the table represent the load of response for the referenced material towards the same gas concentration of various tested analytes

	270 °C – 500 ppm	160 °C – NR	25 °C – 100 ppm	27 °C – Vconc.	27 °C – Vconc.	300 °C – Vconc.	270 °C – Vconc.	230 °C – 100 ppm	NR – 500 ppm	180 °C – 30 ppm	38 °C – 100 ppm	200 °C – 25 ppm	Green light – 5 ppm	300 °C – Vconc.	RT – 1000 ppm	
Ethanol	1	10	1	8	8	8	10	10	3	1	2	0	0	7		
Methanol		6					1	5	0					1		
Acetone				2	1	0	3					2	0	0		
Isopropanol									10			10				
n-butanol							10							10		
Methane						0				1				0		
Benzene		3											0	0		
Toluene			8	4			0	2					0			
Formaldehyde			10	10			3									
Acetaldehyde						1								1		
Dichloromethane		4														
LPG	2														10	
Cl <sub>2</sub>	10										2					
NH <sub>3</sub>	1		5	7	6		2	3			2		1			
H <sub>2</sub>	5		1			0				0				0	4	
CO			1							1						
CO <sub>2</sub>	6							2							3	
H <sub>2</sub> S	6		1							2	5		1	0	4	
SO <sub>2</sub>						0				1				0		
NO										10				0		
NO <sub>2</sub>			1			0					10		1	2		
	ZnS Ps [7]	ZnS MSFs [17]	ZnS MuSs [6]	Ni doped ZnS NSFs [39]	Ni doped ZnS NSFs [39]	Au@Ni doped ZnS NSFs [39]	CdS Ps [25]	CdS NFIs [4]	CdS UCsS [19]	CdS NFIs [11]	CdS MPs [27]	CdS TFs [9]	CdS LSs [21]	CdS NFIs [3]	CdS PW [5]	CdS@SiO <sub>2</sub> TFs [12]



RT room temperature; Vconc. cross response to gases with different concentrations; Ps Particles; MSFs Microspheres; MuSs Mucosal-like structures; NSFs Nanospheres; NFIs nanoflakes; UCsS Urchin-like structures; MPs Microparticles; TFs Thin films; LSs Leaf-like structures; PW Powder; NR Not reported

## 7.6 Conclusions

This chapter focused on the fabrication processes, synthetic routes, and gas sensing properties of II-VI semiconducting films. The discussion addressed the most common factors influencing II-VI semiconductors' gas sensing properties, including morphology tuning, surface modification, and thermal/photoactivation. The survey showed that ZnS and CdS are the main II-VI semiconducting compounds in gas sensing and usually integrated into sensors as thin layers containing spherical-like particles or other hierarchical structures in the form of flakes or dendrites. These low-dimensional or hierarchical structures reported superior gas responses than traditional spherical-like particles. The literature, however, evidences a limited amount of information regarding essential functional characteristics, e.g., sensitivity, selectivity, and humidity interference, that allow for a more realistic appraisal of II-VI semiconductor's gas sensing performance. Overall, future research on gas-sensitive II-VI semiconducting films needs to deepen into the stability of these materials under thermal operation. Further research on the advantages of photoactivation, given the promising prospects of II-VI semiconductors in photosensitive devices, is also essential. The surface modification of II-VI semiconductors and the availability of methods that allow for their integration in multisensory is another topic that deserves attention. Thus, the response of these systems may be part of multivariable analysis and pattern recognition algorithms that are eventually essential to boost selectivity in chemical sensors.

## References

1. Hontañón E, Vallejos S. One-dimensional metal oxide nanostructures for chemical sensors. In: Nanostructured materials - classification, growth, simulation, characterization, and devices, IntechOpen; 2021.
2. Šetka M, Claros M, Chmela O, Vallejos S. Photoactivated materials and sensors for NO<sub>2</sub> monitoring. *J Mater Chem C*. 2021;9(47):16804–27.
3. Li HY, Yoon JW, Lee CS, Lim K, Yoon JW, Lee JH. Visible light assisted NO<sub>2</sub> sensing at room temperature by CdS nanoflake array. *Sens Actuator B*. 2018;255:2963–70.
4. Chakraborty S, Pal M. Improved ethanol sensing behaviour of cadmium sulphide nanoflakes: beneficial effect of morphology. *Sensors Actuators B Chem*. 2017;242:1155–64.
5. Gaiardo A, Fabbri B, Guidi V, Bellutti P, Giberti A, Gherardi S, et al. Metal sulfides as sensing materials for chemoresistive gas sensors. *Sensors*. 2016;16(3):296.
6. Long G, Guo Y, Li W, Tang Q, Zu X, Ma J, et al. Surface acoustic wave ammonia sensor based on ZnS mucosal-like nanostructures. *Microelectron Eng*. 2020;222:111201.
7. Shinde MS, Swapna Samanta S, Sonawane MS, Ahirrao PB, Patil RS. Gas sensing properties of nanostructured ZnS thin films. *J Nano Adv Mater*. 2015;3(2):99.
8. Maticiuc N, Kukk M, Spalatu N, Potlog T, Krunks M, Valdna V, et al. Comparative study of CdS films annealed in neutral, oxidizing and reducing atmospheres. *Energy Procedia*. 2014;44:77–84.
9. Navale ST, Mane AT, Chougule MA, Shinde NM, Kim J, Patil VB. Highly selective and sensitive CdS thin film sensors for detection of NO<sub>2</sub> gas. *RSC Adv*. 2014;4(84):44547–54.

10. Nemade KR, Waghuley SA. Ultra-violet C absorption and LPG sensing study of zinc sulphide nanoparticles deposited by a flame-assisted spray pyrolysis method. *J Taibah Univ Sci.* 2016;10(3):437–41.
11. Liu X-H, Yin P-F, Kulinich SA, Zhou Y-Z, Mao J, Ling T, et al. Arrays of ultrathin CdS Nanoflakes with high-energy surface for efficient gas detection. *ACS Appl Mater Interfaces.* 2016;9(1):602–9.
12. Saxena N, Kumar P, Gupta V. CdS nanodroplets over silica microballs for efficient room-temperature LPG detection. *Nanoscale Adv.* 2019;1(6):2382–91.
13. Dzhurkov V, Levi Z, Nesheva D, Hristova-Vasileva T. Room temperature sensitivity of ZnSe nanolayers to ethanol vapours. *J Phys Conf Ser.* 2019;1186(1):012023.
14. Al-Hilli BA. The effect of cadmium selenide thin film thickness on carbon monoxide gas sensing properties prepared by plasma DC-sputtering technique. *Iraqi J Sci.* 2018;59:2234–41.
15. Fabbri B, Gaiardo A, Guidi V, Malagù C, Giberti A. Photo-activation of cadmium sulfide films for gas sensing. *Procedia Eng.* 2014;87:140–3.
16. Xing R, Xue Y, Liu X, Liu B, Miao B, Kang W, et al. Mesoporous ZnS hierarchical nanostructures: facile synthesis, growth mechanism and application in gas sensing. *CrystEngComm.* 2012;14(23):8044–8.
17. Xiao J, Song C, Song M, Dong W, Li C, Yin Y. Preparation and gas sensing properties of hollow ZnS microspheres. *J Nanosci Nanotechnol.* 2016;16(3):3026–9.
18. Hu P, Gong G, Zhan F, Zhang Y, Li R, Cao Y. The hydrothermal evolution of the phase and shape of ZnS nanostructures and their gas-sensing properties. *Dalton Trans.* 2016;45(6):2409–16.
19. Zhang N, Ma X, Han J, Ruan S, Chen Y, Zhang H, et al. Synthesis of sea urchin-like microsphere of CdS and its gas sensing properties. *Mater Sci Eng B.* 2019;243:206–13.
20. Guo W, Ma J, Pang G, Wei C, Zheng W. Synergistic effect of the reducing ability and hydrogen bonds of tested gases: highly orientational CdS dendrite sensors. *J Mater Chem A.* 2013;2(4):1032–8.
21. Fu X, Liu J, Wan Y, Zhang X, Meng F, Liu J. Preparation of a leaf-like CdS micro-/nanosstructure and its enhanced gas-sensing properties for detecting volatile organic compounds. *J Mater Chem.* 2012;22(34):17782–91.
22. Sonker RK, Yadav BC, Gupta V, Tomar M. Synthesis of CdS nanoparticle by sol-gel method as low temperature NO<sub>2</sub> sensor. *Mater Chem Phys.* 2020;239:121975.
23. Korotcenkov G. Metal oxides for solid-state gas sensors: what determines our choice? *Mater Sci Eng B.* 2007;139(1):1–23.
24. Kurtin S, McGill TC, Mead CA. Fundamental transition in the electronic nature of solids. *Phys Rev Lett.* 1969;22(26):1433.
25. Giberti A, Casotti D, Cruciani G, Fabbri B, Gaiardo A, Guidi V, et al. Electrical conductivity of CdS films for gas sensing: selectivity properties to alcoholic chains. *Sens Actuators B.* 2015;207(PartA):504–10.
26. Zhang L, Wang H, Guo W, Ma J. Sensitive NO sensor based CdS microparticles assembled by nanoparticles. *RSC Adv.* 2016;6(51):45386–91.
27. Yamazoe N. New approaches for improving semiconductor gas sensors. *Sens Actuator B.* 1991;5(1–4):7–19.
28. Gurlo A. Nanosensors: towards morphological control of gas sensing activity. SnO<sub>2</sub>, In<sub>2</sub>O<sub>3</sub>, ZnO and WO<sub>3</sub> case studies. *Nanoscale.* 2011;3(1):154–65.
29. Smytyna VA, Gerasutenko V, Kashulis S, Mattogno G, Reghini S. The causes of thickness dependence of CdSe and CdS gas-sensor sensitivity to oxygen. *Sens Actuators B.* 1994;19(1–3):464–5.
30. Smytyna V, Gerasutenko V, Golovanov V, Kačiulis S, Mattogno G, Viticoli S. Surface spectroscopy study of CdSe and CdS thin-film oxygen sensors. *Sens Actuators B.* 1994;22(3):189–94.
31. Yamazoe N, Sakai G, Shimanoe K. Oxide Semiconductor Gas Sensors. *Catal Surv from Asia.* 2003;7(1):63–75.

32. Miller DR, Akbar SA, Morris PA. Nanoscale metal oxide-based heterojunctions for gas sensing: a review. *Sens Actuators B*. 2014;204: Elsevier:250–72.
33. Degler D, Weimar U, Barsan N. Current understanding of the fundamental mechanisms of doped and loaded semiconducting metal-oxide-based gas sensing materials. *ACS Sensors*. 2019;4(9):2228–49.
34. Li Z, Yao ZJ, Haidry AA, Plecenik T, Xie LJ, Sun LC, et al. Resistive-type hydrogen gas sensor based on TiO<sub>2</sub>: a review. *Int J Hydrog Energy*. 2018;43(45):21114–32.
35. Huang Z, Wei D, Wang T, Jiang W, Liu F, Chuai X, et al. Excellent gas sensing of hierarchical urchin-shaped Zn doped cadmium sulfide. *J Alloys Compd*. 2019;773:299–304.
36. Kim HJ, Il Choi K, Kim KM, Na CW, Lee JH. Highly sensitive C<sub>2</sub>H<sub>5</sub>OH sensors using Fe-doped NiO hollow spheres. *Sens Actuators B*. 2012;171–172:1029–37.
37. Mondal S. LPG sensing property of nickel doped CdS thin film synthesised by silar method. *Adv Mater Process Technol*. 2020;8:344. <https://doi.org/10.1080/2374068X.2020.1809234>.
38. Zhong F, Wu Z, Guo J, Jia D. Ni-doped ZnS nanospheres decorated with Au nanoparticles for highly improved gas sensor performance. *Sensors*. 2018;18(9):2882.
39. Lin F, Lai Z, Zhang L, Huang Y, Li F, Chen P, et al. Fluorometric sensing of oxygen using manganese(II)-doped zinc sulfide nanocrystals. *Microchim Acta*. 2020;187(1):1–9.
40. Park S, An S, Ko H, Lee S, Lee C. Synthesis, structure, and UV-enhanced gas sensing properties of au-functionalized ZnS nanowires. *Sens Actuators B*. 2013;188:1270–6.
41. Park S, An S, Mun Y, Lee C. UV-activated gas sensing properties of ZnS nanorods functionalized with Pd. *Curr Appl Phys*. 2014;14(SUPPL. 1):S57–62.
42. Prokopenko SL, Gunya GM, Makhno SM, Gorbyk PP. Room-temperature gas sensor based on semiconductor nanoscale heterostructures ZnS/CdS. *Him Fiz ta Tehnol Poverhni*. 2017;8(4):432–8.
43. Chizhov AS, Rummyantseva MN, Vasiliev RB, Filatova DG, Drozdov KA, Krylov IV, et al. Visible light activation of room temperature NO<sub>2</sub> gas sensors based on ZnO, SnO<sub>2</sub> and In<sub>2</sub>O<sub>3</sub> sensitized with CdSe quantum dots. *Thin Solid Films*. 2016;618:253–62.
44. Ding P, Xu D, Dong N, Chen Y, Xu P, Zheng D, et al. A high-sensitivity H<sub>2</sub>S gas sensor based on optimized ZnO-ZnS nano-heterojunction sensing material. *Chinese Chem Lett*. 2020;31(8):2050–4.
45. Hieu NM, Van Lam D, Hien TT, Chinh ND, Quang ND, Hung NM, et al. ZnTe-coated ZnO nanorods: hydrogen sulfide nano-sensor purely controlled by pn junction. *Mater Des*. 2020;191:108628.
46. Zhang H, Jin Z, Da Xu M, Zhang Y, Huang J, Cheng H, et al. Enhanced isopropanol sensing performance of the CdS nanoparticle decorated ZnO porous nanosheets-based gas sensors. *IEEE Sensors J*. 2021;21(12):13041–7.
47. Liu W, Gu D, Li X. Ultrasensitive NO<sub>2</sub> detection utilizing mesoporous ZnSe/ZnO heterojunction-based chemiresistive-type sensors. *ACS Appl Mater Interfaces*. 2019;11(32):29029–40.
48. Tsai YS, Chou TW, Xu CY, Chang Huang W, Lin CF, Wu YCS, et al. ZnO/ZnS core-shell nanostructures for hydrogen gas sensing performances. *Ceram Int*. 2019;45(14):17751–7.
49. Arunraja L, Thirumoorthy P, Karthik A, Subramanian R, Rajendran V. Investigation and characterization of ZnO/CdS nanocomposites using chemical precipitation method for gas sensing applications. *J Mater Sci Mater Electron*. 2017;28(23):18113–20.
50. Šetka M, Bahos FA, Chmela O, Matatagui D, Gràcia I, Drbohlavová J, et al. Cadmium telluride/polypyrrole nanocomposite based love wave sensors highly sensitive to acetone at room temperature. *Sens Actuators B*. 2020;321:128573.
51. Kim D, Park KM, Shanmugam R, Yoo B. Electrochemically decorated ZnTe nanodots on single-walled carbon nanotubes for room-temperature NO<sub>2</sub> sensor application. *J Nanosci Nanotechnol*. 2014;14(11):8248–52.
52. Qin N, Xiang Q, Zhao H, Zhang J, Xu J. Evolution of ZnO microstructures from hexagonal disk to prismoid, prism and pyramid and their crystal facet-dependent gas sensing properties. *CrystEngComm*. 2014;16(30):7062–73.

53. Patel NG, Panchal CJ, Makhija KK. Use of cadmium selenide thin films as a carbon dioxide gas sensor. *Cryst Res Technol*. 1994;29(7):1013–20.
54. Maserati L, Moreels I, Prato M, Krahne R, Manna L, Zhang Y. Oxygen sensitivity of atomically passivated CdS nanocrystal films. *ACS Appl Mater Interfaces*. 2014;6(12):9517–23.
55. Nesheva D, Aneva Z, Reynolds S, Main C, Fitzgerald AG. Preparation of micro -and nanocrystalline CdSe and CdS thin films suitable for sensor applications. *J Optoelectron Adv Mater*. 2006;8(6):2120–5.
56. Laatar F, Harizi A, Zarroug A, Ghrib M, Hassen M, Gaidi M, et al. Novel CdSe nanorods/porous anodic alumina nanocomposite-based ethanol sensor: sensitivity enhancement by visible light illumination. *J Mater Sci Mater Electron*. 2017;28(16):12259–67.
57. Podgorny SO, Demeshko IP, Podgornaya OT, Lukoyanova OV, Skutin ED, Fedotova KI. Cadmium telluride nanofilms application in carbon monoxide detection. In: *Proceedings of Dyn Syst Mech Mach Dyn*, 15–17 November 2016, Omsk, p. 16602519.
58. Giberti A, Fabbri B, Gaiardo A, Guidi V, Malagù C. Resonant photoactivation of cadmium sulfide and its effect on the surface chemical activity. *Appl Phys Lett*. 2014;104(22):222102.
59. Bube RH. Surface photoconductivity in cadmium sulfide crystals. *J Chem Phys*. 2004;21(8):1409.
60. Miremadi BK, Colbow K, Harima Y. A CdS photoconductivity gas sensor as an analytical tool for detection and analysis of hazardous gases in the environment. *Rev Sci Instrum*. 1998;68(10):3898.
61. Park S, Kim S, Ko H, Lee C. Light-enhanced gas sensing of ZnS-core/ZnO-shell nanowires at room temperature. *J Electroceram*. 2014;33(1–2):75–81.
62. Yang Z, Guo L, Zu B, Guo Y, Xu T, Dou X, et al. CdS/ZnO core/shell nanowire-built films for enhanced photodetecting and optoelectronic gas-sensing applications. *Adv Opt Mater*. 2014;2(8):738–45.
63. Chizhov AS, Rummyantseva MN, Vasiliev RB, Filatova DG, Drozdov KA, Krylov IV, et al. Visible light activated room temperature gas sensors based on nanocrystalline ZnO sensitized with CdSe quantum dots. *Sens Actuators B*. 2014;205:305–12.
64. Geng X, Zhang C, Debliquy M. Cadmium sulfide activated zinc oxide coatings deposited by liquid plasma spray for room temperature nitrogen dioxide detection under visible light illumination. *Ceram Int*. 2016;42(4):4845–52.
65. Park S, Kim S, Ko H, Lee C. Light assisted room temperature ethanol gas sensing of ZnO-ZnS nanowires. *J Nanosci Nanotechnol*. 2014;14(12):9025–8.
66. Wu B, Lin Z, Sheng M, Hou S, Xu J. Visible-light activated ZnO/CdSe heterostructure-based gas sensors with low operating temperature. *Appl Surf Sci*. 2016;360:652–7.
67. Dengo N, De Fazio AF, Weiss M, Marschall R, Dolcet P, Fanetti M, et al. Thermal evolution of ZnS nanostructures: effect of oxidation phenomena on structural features and photocatalytic performances. *Inorg Chem*. 2018;57(21):13104–14.
68. Shanmugam N, Cholan S, Kannadasan N, Sathishkumar K, Viruthagiri G. Effect of annealing on the ZnS nanocrystals prepared by chemical precipitation method. *J Nanomater*. 2013;2013:351798.
69. Schultze D, Steinike U, Kussin J, Kretzschmar U. Thermal oxidation of ZnS modifications sphalerite and wurtzite. *Cryst Res Technol*. 1995;30(4):553–8.
70. Murugadoss G. Synthesis, optical, structural and thermal characterization of Mn<sup>2+</sup> doped ZnS nanoparticles using reverse micelle method. *J Lumin*. 2011;131(10):2216–23.
71. Trenczek-Zajac A. Thermally oxidized CdS as a photoactive material. *New J Chem*. 2019;43(23):8892–902.
72. Eom NSA, Kim TS, Choa YH, Kim WB, Kim BS. Surface oxidation behaviors of Cd-rich CdSe quantum dot phosphors at high temperature. *J Nanosci Nanotechnol*. 2014;14(10):8024–7.

# Chapter 8

## Nanocomposite and Hybrid-Based Electric and Electronic Gas Sensors



Roman B. Vasiliev, Artem S. Chizhov, and Marina N. Rumyantseva

### 8.1 Introduction

Resistive semiconductor gas sensors are used in various fields, including air quality monitoring, medical diagnostics, detection of toxic, flammable and explosive gases, control in the food industry, monitoring of technological processes, etc. The advantages of resistive semiconductor gas sensors include low cost, high sensitivity, a wide range of detectable components, miniaturization, and the ability to integrate into information networks. The physical principles of operation of semiconductor gas sensors are based on the high sensitivity of the semiconductor surface to the composition of the surrounding atmosphere. Chemisorption of molecules from the gas phase and chemical reactions on the surface lead to significant changes in the band structure in a narrow near-surface layer, the formation of energy barriers at the solid–gas interface, which affects the values of the work function and surface conductivity of semiconductor materials.

By analogy with the Schottky barrier at the metal–semiconductor interface, the value of the barrier on the semiconductor surface can be represented as

$$V_s = X \cdot (\varphi_s - \varphi), \quad (8.1)$$

where  $\varphi_s$  represents the electron work function for surface state,  $\varphi$  the thermoelectric work function of semiconductor, and  $X$  the chemical parameter depending on the nature of the semiconductor. Parameter  $X$  is defined as the coefficient of the linear dependence connecting  $V_s$  and  $\varphi_s$ , and can be interpreted as a manifestation of the sensitivity of the electrophysical properties of a semiconductor to the state of its surface. The dependence of the parameter  $X$  on the difference of Pauling

---

R. B. Vasiliev · A. S. Chizhov · M. N. Rumyantseva (✉)  
Chemistry Department, Moscow State University, Moscow, Russia  
e-mail: [roum@inorg.chem.msu.ru](mailto:roum@inorg.chem.msu.ru)

electronegativity  $\Delta\chi$  of anion and cation forming a semiconductor has an *S*-shaped form [1]. The observed increase of parameter *X* at  $\Delta\chi = 0.8$  corresponds to the transition from more covalent (Si, Ge, GaAs) to more ionic (ZnO, SnO<sub>2</sub>) compounds. Thus, materials with a predominantly ionic bond type have the greatest sensitivity to changes in the concentration of molecules adsorbed on the surface and, consequently, to changes in the composition of the gas phase. This determines the most frequent use of semiconductor metal oxides as materials for gas sensors. Group of II-VI semiconductors, including cadmium and zinc chalcogenides, is inferior in value of parameter *X* compared to semiconductor metal oxides; however, due to the smaller band gap and lower work function, it is characterized by higher electrical conductivity and optical absorption in the visible range, which can provide additional advantages when creating gas sensors.

The modern approach in the field of semiconductor materials to meet the current requirements for resistive sensors is based on hybrids or composites that combine two or more separate components at the nanometer or molecular level to achieve new and/or improved sensor properties [2]. The improved sensitivity characteristics of such materials are due to many factors, including electronic effects (band bending due to Fermi level equilibration, charge carrier separation, depletion layer manipulation, increased interfacial potential barrier energy), chemical effects (reduced activation energy, specific catalytic activity, synergistic surface reactions), and geometric effects (grain refinement, increase in specific surface area, increase in gas accessibility) [3]. This chapter will consider the methods for the synthesis of II-VI semiconductors in the nanocrystalline state, methods for the formation of nanocomposites containing II-VI semiconductors, and also analyze the sensor properties of these composites depending on the type of their components.

## 8.2 Recent Approaches to the Synthesis of Nanoparticles of II-VI Semiconductors

Synthesis in colloidal systems allows not only to obtain a wide range of II-VI semiconductors nanoparticles with controlled sizes and shapes but also to minimize their particle size distribution. In general, the methods of nanoparticles synthesis in colloidal systems follow the idea of the sol formation by the rapid interaction of reagents at high temperatures in an organic medium. The “hot injection” method was developed on the basis of first works [4–10] on the synthesis of CdS nanoparticles in tributylphosphine and tributylphosphine oxide at high temperatures up to 300 °C. Subsequently, the method was further modified for the synthesis of all cadmium chalcogenides [11].

Typical hot injection protocols involve rapid injection of anionic and cationic precursors into a non-polar solvent containing a nanoparticle stabilizer heated to high temperatures [12]. For colloidal synthesis of II-VI semiconductor nanoparticles, alkyl derivatives of cadmium or zinc, oxides of these elements and their organic

salts can be used as cationic precursors. Cadmium oxide CdO [13–21], cadmium acetate Cd(Ac)<sub>2</sub> [22, 23], dimethyl cadmium (CH<sub>3</sub>)<sub>2</sub>Cd [24–29], etc., have been described as cadmium precursors. Phosphine chalcogenides [17–29] or trimethylsilyl chalcogenides [11] are usually used as anionic precursors. Another convenient and highly effective variant of anionic chalcogen precursors are solutions of elemental chalcogens (sulfur or selenium) in octadecene [30–35]. The activation by primary amines of the interaction of anionic precursors with zinc carboxylates or diethyl zinc in the preparation of ZnSe nanoparticles is shown in Refs. [36–39], which made it possible to obtain high-quality nanoparticles at temperatures of 300–320 °C.

Non-injection methods, which exclude the stage of rapid injection and, as a rule, consist in heating a solution containing both anionic and cationic precursors, also have been proposed [40]. After the first publication [41], high-quality CdS, CdSe, and CdTe nanoparticles [42–45], as well as ZnS, ZnSe, and ZnTe [46–48] were obtained by this method. Cadmium carboxylates are used as a cationic precursor, and solutions of elementary chalcogens in octadecene are used as an anionic precursor. Thiols are also used as an anionic precursor for the synthesis of sulfides [49, 50]. A number of high-quality cadmium chalcogenide nanoparticles in the form of anisotropic nanorods and their derivatives were obtained using specific ligands – alkylphosphonic acids, which change the growth rate of various facets as a result of specific adsorption [51].

The synthesis of nanoparticles consisting of domains of dissimilar materials is associated with the formation of an interface between materials differing in chemical nature and crystal structure. The growth of such nanoparticles requires heterogeneous nucleation of a new phase that differs from the homogeneous nucleation discussed above. The synthesis strategy using heterogeneous nucleation consists in the growth of the second component on the preformed nuclei of the first material [34, 52–56]. Formation of the shell by sequential adsorption and reaction of cationic and anionic layers (Successive Ionic Layer Adsorption and Reaction, SILAR) is another variant of the strategy for the synthesis of multicomponent nanoparticles of the “core/shell” type [57–60].

Another common approach for the synthesis of II–VI semiconductor nanoparticles is the use of hydrothermal or solvothermal synthesis. Under conditions of high temperature and high pressure, the role of the liquid phase increases significantly since it simultaneously performs various functions: a medium that transmits kinetic and thermal energy, pressure, and so on; an adsorbate characterized by specific adsorption/desorption parameters on various crystallographic faces of the forming solid phase; a solvent that determines the dissolution/precipitation of reagents and the resulting products; and a reagent participating in a chemical reaction that results in the formation of the target product [61]. By this reason hydrothermal/solvothermal techniques are ideal for the processing of very fine particles characterized by high purity, controlled stoichiometry, high quality, narrow particle size distribution, controlled morphology, uniformity, high crystallinity, excellent reproducibility, controlled microstructure, high reactivity/sinterability, and so on [61].



CdS nanoparticles [62, 63], ZnS and ZnSe microspheres [64, 65], CdSe nanorods [66], and CdS nanowires [67–69] were obtained using hydrothermal/solvothermal synthesis. Soluble salts are used as metal precursors – chlorides, acetates, zinc and cadmium nitrates, thiourea  $\text{SC}(\text{NH}_2)_2$ , or thiourea dioxide  $\text{O}_2\text{SC}(\text{NH}_2)_2$  act as a source of sulfur. To obtain selenides, Se(IV) in the form of  $\text{SeO}_2$  or  $\text{Na}_2\text{SeO}_2$  and ethylenediamine or triethylenetetramine, simultaneously acting as a reducing agent and a complexing agent, are introduced into the reaction mixture. To obtain ZnTe layers on the surface of ZnO nanorods [70], Te layers were obtained on the surface of ZnO nanorods during the reduction of  $\text{Na}_2\text{TeO}_3$  by  $\text{NaBH}_4$  under hydrothermal conditions, and the subsequent formation of ZnTe layers occurred during annealing of the obtained structures in an inert Ar atmosphere at 350 °C. Y.-C. Liang et al. [71] applied the method of sacrificial template sulfidation under hydrothermal conditions to form ZnS nanorods using ZnO as sacrificial layer.

The synthesis methods of II–VI semiconductor nanoparticles from the liquid phase without the use of high temperatures and pressures are chemical precipitation in aqueous media, chemical bath deposition, and sonochemical synthesis. These methods are applicable for the synthesis of CdS and ZnS nanoparticles [72–79]. Soluble zinc and cadmium salts are used as metal precursors. Thiourea  $\text{SC}(\text{NH}_2)_2$ , thioacetamide  $\text{CH}_3\text{CSNH}_2$ , or soluble thiosulfates commonly serve as sources of  $\text{S}^{2-}$  ions [80]. The amount of chalcogenide precursor added to the solution will primarily determine the concentration of the free chalcogenide ion. So, one of the ways to slow down (and therefore to control) the rate of solid phase formation is to reduce the starting concentration of the chalcogenide source. In cases of chemical precipitation in aqueous media and chemical bath deposition, a complexing agent often is added (triethanolamine, for example), as an additional tool of controlling the rate of formation of the solid. Typically, these complexants supply ligands for the metal, and the greater their affinity for the metal relative to that of the chalcogenide, the more the complexant helps slow down the reactions that lead to formation of the solid phase [80]. It was demonstrated that generally the particle size distribution for nanoparticles is narrower for sonocrystallization than for other comparable synthesis methods [77]. In the sonochemical synthesis, heating by cavitation and bubble implosion provides a potential route to high-temperature reactions from a liquid phase. Moreover, cavitation is responsible for the mixed phase reactions, emulsification, and extraction in a liquid–liquid heterogeneous system and it increases the surface area and the mass transfer between two phases. This behavior leads to the enhancement of diffusion coefficient on the interface mixing better than conventional agitation [78]. Variation of chalcogen precursors in combination with ultrasonic treatment allowed to obtain CdS nanoparticles in the form of nanospheres (thiourea precursor) and in the form of nanorods (thioacetamide precursor). The formation mechanism of these nanocrystals is connected with the sonochemical effect of ultrasonic irradiation [76].

When creating gas-sensitive nanocomposites, especially when synthesizing directly on substrates that provide sensor response reading, methods of synthesis from the gas phase have certain advantages. As examples, one can consider

formation of CdTe quantum dots on the surface of MoS<sub>2</sub> nanowires [81] using RF magnetron sputtering, as well as CdTe nanoparticles on ZnO coated porous Si substrates [82]. In both cases, targets compressed from CdTe powders were used.

A common method of synthesizing II-VI semiconductor nanowires from the gas phase is thermal evaporation inside a horizontal tube furnace. In this case, Au assisted nanowires growth occurs by vapor-liquid-solid (VLS) mechanism. In this way CdS, ZnS, CdSe, ZnSe nanowires were obtained [83–90].

### 8.3 Synthesis of II-VI Semiconductor-Based Nanocomposites

Let us consider the main techniques that allow obtaining II-VI semiconductor nanoparticles directly on the surface of a metal oxide matrix. In the SILAR method, a metal oxide substrate is immersed sequentially in a solution containing a source of metal ions and in a solution containing a source of chalcogenide ions. Between dives, the substrate is washed with a solvent to remove excess precursors from the surface and leave a monolayer of adsorbed ions. Thus, the formation of metal chalcogenide occurs in a layer of adsorbed ions and after several cycles of immersion, island particles of several nanometers appear on the surface of the metal oxide [60, 79, 91, 92]. In the chemical bath deposition method, metal precursors and chalcogenide ions present in the same solution, in which a metal oxide substrate is also placed. When maintaining a low supersaturation, the formation of II-VI semiconductor nanoparticles occurs by the mechanism of heterogeneous nucleation on the surface of a metal oxide substrate [74, 93, 94]. The formation of chalcogenide nanoparticles from the liquid phase on the surface of pre-synthesized oxides can be realized under ultrasonic irradiation [75] or by impregnation with a solution of a suitable precursor followed by its thermal decomposition in an inert atmosphere [95].

Nanocomposites containing different oxides CeO<sub>2</sub> [67], CuO [68], ZnO [69, 70], SnO<sub>2</sub> [64], In<sub>2</sub>O<sub>3</sub> [65], chalcogenides CdS [67–69], ZnS [65], ZnSe [64], and ZnTe [70] were obtained by solvothermal/hydrothermal synthesis. Basically, these methods are used for the formation of oxide nanoparticles on the surface of pre-synthesized chalcogenides; however, N.-M. Hieu et al. [70] formed ZnTe layer on the ZnO surface through the deposition of Te layer under reduction in hydrothermal conditions followed by annealing in an inert atmosphere.

Synthesis of nanocomposites formed by oxide and chalcogenide of the same metal CdS/CdO, ZnSe/ZnO, and ZnS/ZnO can be effectuated by thermal oxidation of chalcogenides in an oxygen-containing atmosphere [62, 96] or, conversely, through gas-phase (using hydrogen sulfide) or liquid-phase (using thioacetamide CH<sub>3</sub>CSNH<sub>2</sub> [97] or Na<sub>2</sub>S [98] in solvothermal conditions) sulfidation. The authors of [90] synthesized ZnS-core/ZnO-shell nanowires in which ZnS nanowires were obtained by VLS method, and the ZnO shell was formed by atomic layer deposition (ALD) using diethylzinc and H<sub>2</sub>O as reagents.

Immobilization of preformed II-VI semiconductor nanoparticles on the surface of metal oxides can be carried out by various methods. In the direct adsorption method, the metal oxide matrix is immersed in II-VI semiconductor nanoparticles sols and kept for some time. In this case, the adsorption of II-VI semiconductor nanoparticles occurs on the surface of metal oxide [34, 35, 99]. The kinetics of this process was investigated in [6]. Two processes occur in parallel on the metal surface: the formation of a submonolayer of nanoparticles (the kinetics of this process is described by the pseudo-first order Langmuir equation) and the formation of aggregates of nanoparticles.

Another way is to “sew” II-VI semiconductor nanoparticles to the metal oxide surface using bifunctional molecules (linkers), one functional group of which has a pronounced affinity for the  $A^{\text{II}}B^{\text{VI}}$  material and the other to the metal oxide surface. Such linker molecules can be different mercaptocarboxylic acids: 2- or 3-mercaptopropionic acid (MPA), 6-mercaptohexanoic acid (MHA), and 11-mercaptoundecanoic acid (MUA) [33, 100]. The thiol group (SH) of mercaptocarboxylic acids passivates the surface of II-VI semiconductor nanoparticles and ensure their binding to linker molecules. The carboxyl group (COOH) of mercaptocarboxylic acids provides sol stability in water, avoids nanoparticles aggregation, and binds to the metal ions at the metal oxide surfaces. When using this method of immobilization, it is possible to achieve a stronger bond of II-VI semiconductor nanoparticles with the oxide surface and their higher surface concentration compared with the method of direct adsorption.

Spin coating method was used to immobilize metal oxide nanoparticles on the surface of II-VI semiconductors. Thus, preformed suspensions of CuO and  $\text{In}_2\text{O}_3$  nanoparticles were deposited on substrates with ZnS nanowires arrays synthesized by VLS method [84, 85].

Finally, heterostructures, including metal oxides and II-VI semiconductor layers, can be obtained using sputtering techniques. In this case, metal oxide layers are synthesized by reactive magnetron sputtering of metals, and chalcogenide layers are formed by RF sputtering from targets of the corresponding metal chalcogenide [82].

Similar approaches can be applied to obtain nanocomposites based on II-VI semiconductors and carbon compounds or layered chalcogenides. Thus, CdS/rGO nanocomposites were synthesized by photochemical reduction of suspensions containing colloidal CdS and GO nanoparticles [72] and rGO/MoS<sub>2</sub>/CdS nanocomposites were obtained as a result of solvothermal synthesis of CdS nanoparticles on the surface of rGO/MoS<sub>2</sub> composites [63]. The SILAR method made it possible to obtain ZnS nanoparticles on the surface of WS<sub>2</sub> nanosheets [73]. CdTe/MoS<sub>2</sub> heterostructures have been synthesized by a combination of various sputtering techniques [81].

## 8.4 Gas Sensors Based on II-VI Semiconductors/Metal Oxide Nanocomposites

The creation of nanocomposites is one of the approaches that can significantly improve the sensor characteristics (primarily sensitivity and selectivity, but in some cases also power consumption) of a combined sensitive material compared to its constituent individual components. This can be realized by one or a combination of typical methods, which are classified as follows [2]: (i) catalytic reactions between the target gas and catalyst nanoparticles (usually platinum group metal, Au, Ag) deposited on the matrix of a semiconductor material (sensor characteristics are determined by processes occurring on the surface of the sensitive material); (ii) fast charge transfer between materials forming a nanocomposite (implemented on the interface with the participation of carbon-based materials); (iii) regulation of charge carrier transfer in conductive/semiconductive materials when interacting with the target gas (sensor characteristics are determined by processes at the interface and structural characteristics of components); (iv) creation of  $n-n$ ,  $p-n$ ,  $p-p$ , and  $p-n-p$  heterojunctions between different semiconductor materials (sensor characteristics are determined by processes on the interface); and (v) filtration/concentration of the target gas by creating molecular sieving/binding layers for selective gas detection (sensor characteristics are determined by the processes on the surface and structural characteristics of components).

The advantages of the gas sensors based on nanocomposites with heterojunctions, including II-VI semiconductors, can be summarized as follows: (i) higher sensitivity due to manipulation of the energy barrier formed due to band bending of contacting semiconductors; (ii) specific sensitivity to certain gases; (iii) reduced sensitivity to interfering gases, e.g., humidity; and (iv) shifting the optical sensitivity of wide-band gap semiconductor metal oxides to the long-wavelength region to create sensors operating at room temperature under visible light activation.

### 8.4.1 *Sensor Properties of II-VI Semiconductors/Metal Oxide Nanocomposites Under Thermal Activation*

Manipulation of the energy barrier formed at interface between different semiconductors is the main factor determining the increased sensitivity of II-VI semiconductors/metal oxide nanocomposites under thermal activation. In the contact area of different semiconductors, the band bending occurs along with the formation of electron depleted region due to various work functions. Accordingly, an internal electric field is formed at the interface, which is determined by the difference in work functions of contacting materials. Due to the exponential dependence of the electrical conductivity on the height of the formed potential barrier, even a small change in the latter causes a significant change in conductivity, which leads to a high sensitivity of nanocomposites when detecting various gases (Table 8.1). Jaiswal et al. [82] have

**Table 8.1** Summary of gas sensor properties of II–VI semiconductors/metal oxide nanocomposites under thermal activation

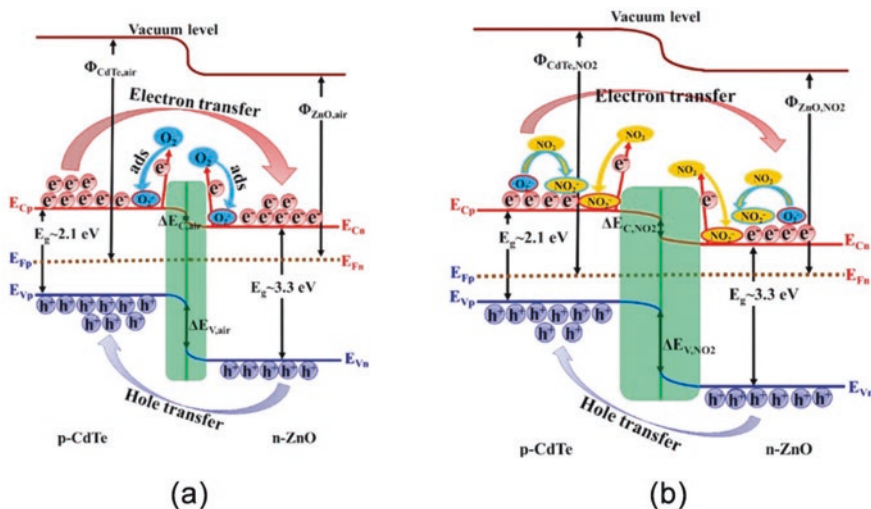
Composite	Morphology	Synthesis method	Gas	Concentration, ppm	T, °C	RH, %	Sensor response, %	Response/recovery time, s	Ref.
CdTe/ZnO/PSi	Thin film heterostructure	MS	NO <sub>2</sub>	1	90	n/a	20	13/54	[82]
NiO@ZnSe	Powder	HT	NO <sub>2</sub>	8	140	n/a	96	n/a	[101]
CdO@CdS	NPs	ST + TO	NO <sub>2</sub>	2	150	25	27	76/82	[62]
SnO <sub>2</sub> @ZnSe	CS microspheres	HT	NO <sub>2</sub>	2.4	160	10	6.94	64/52	[64]
ZnO@ZnSe	Nanoflakes	TO	NO <sub>2</sub>	8	200	n/a	10.2	98/141	[96]
ZnS@TiO <sub>2</sub>	Films	IM + thermolysis	NO <sub>2</sub>	1	300	n/a	32.5	4/1000	[95]
In <sub>2</sub> O <sub>3</sub> @ZnS	NWs decorated NPs	TE; HT	Ethanol	500	300	n/a	300	25/210	[85]
ZnS@ZnO	CS hollow nanocages	HT + etching and sulfidation	Ethanol	20	210	n/a	4.2	5/ n/a	[97]
ZnS@TiO <sub>2</sub>	CS NRs	HT	Ethanol	100	100	n/a	5.62	12/30	[71]
CeO <sub>2</sub> @CdS	NWs decorated NPs	ST	Ethanol	100	160	n/a	52	12/3	[67]
CuO@CdS	NWs decorated NPs	ST	Ethanol	100	180	n/a	120	1/2	[68]
In <sub>2</sub> O <sub>3</sub> @ZnS	Microspheres	HT	Ethanol	100	200	n/a	11	21/34	[65]
ZnS@In <sub>2</sub> O <sub>3</sub>	CS hollow spheres	HT	n-Butanol	100	260	25	8.6	n/a	[102]
ZnS@In <sub>2</sub> O <sub>3</sub>	Hollow spheres	HT	n-Butylamine	100	300	25	5.8	n/a	[102]
CdS@Co <sub>3</sub> O <sub>4</sub>	QDs + NSs assembled into hollowed microspheres	SV;SILAR	H <sub>2</sub> S	100	25	25	12.7	0.6/1	[60]
p-CdTe@n-ZnO	CS NRs	HT	H <sub>2</sub> S	100	200	Dry air	70	<60	[70]

CS core–shell; HT hydrothermal; IM impregnation; MS magnetron sputtering; NPs nanoparticles; NR nanorods; NS nanosheets; RH related humidity; ST solvothermal; QDs quantum dots; TE thermal evaporation; TO thermal oxidation

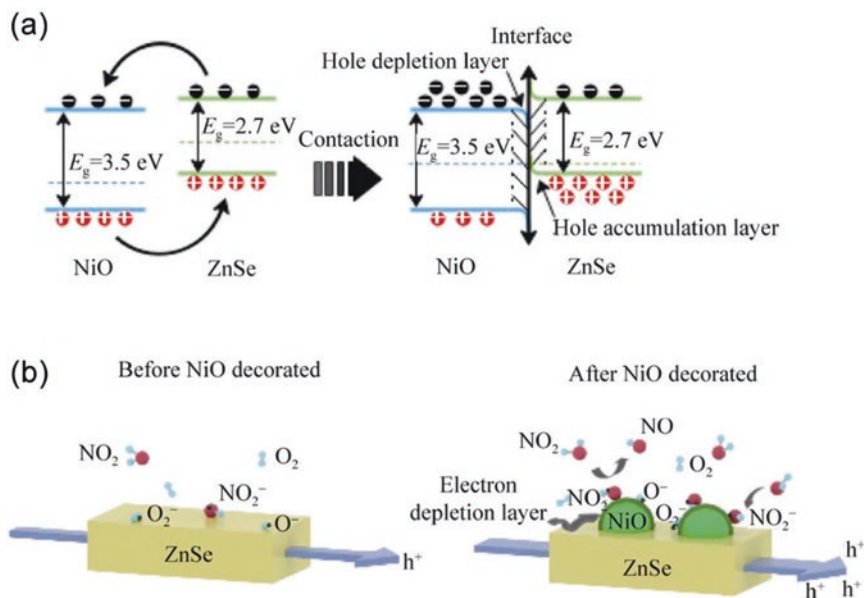
grown *p*-CdTe and *n*-ZnO nanostructured thin films on the porous silicon (PSi) substrates using a scalable magnetron sputtering technique. The work function difference ( $\sim 1.0$  eV) between *p*-CdTe (5.5 eV) and *n*-ZnO (4.5 eV) provided a high specific sensitivity to  $\text{NO}_2$  (Fig. 8.1) compared to reducing gases  $\text{NH}_3$ ,  $\text{H}_2$ ,  $\text{CO}$ ,  $\text{H}_2\text{S}$ , and ethanol  $\text{C}_2\text{H}_5\text{OH}$  at  $90^\circ\text{C}$  and signal independence from humidity changes in a wide range of relative humidity (5% to 90%).

Similarly, the enhanced sensing performance of the *p*-CuO decorated *n*-ZnS nanowires in  $\text{NO}_2$  detection was explained by electronic sensitization mechanism [84]. The change in the height of the potential barrier at the *p*-CuO/*n*-ZnS interface makes an additional contribution to the change in the resistance of the sensitive material when interacting with the electron acceptor gas that provides increased sensitivity to  $\text{NO}_2$  compared to reducing gases  $\text{H}_2$ ,  $\text{NH}_3$ ,  $\text{H}_2\text{S}$ ,  $\text{CH}_4$ , and  $\text{CO}$ .

A selective increase in sensitivity to  $\text{NO}_2$  compared with reducing gases methanol, ethanol, acetone, benzene,  $\text{NH}_3$ , and formaldehyde at measurement temperature of  $140^\circ\text{C}$  was demonstrated for *p*-NiO@*p*-ZnSe nanocomposites obtained by W. Liu et al. as a result of hydrothermal synthesis of NiO nanoparticles on the surface of commercial ZnSe [101]. During the formation of a *p*–*p* heterocontact between NiO nanoparticles and ZnSe flakes, electrons are transferred from the ZnSe conduction band to NiO, while holes are transferred in the opposite direction from the NiO valence band to ZnSe (Fig. 8.2). This leads to the formation of a hole accumulation layer on the ZnSe surface and a hole depletion layer in the NiO. Since the resistance of the sensor is mainly determined by ZnSe, and its hole concentration turns out to be increased, the resistance of *p*-NiO@*p*-ZnSe nanocomposites turns out to be less than the resistance of ZnSe. When the nanocomposite interacts with



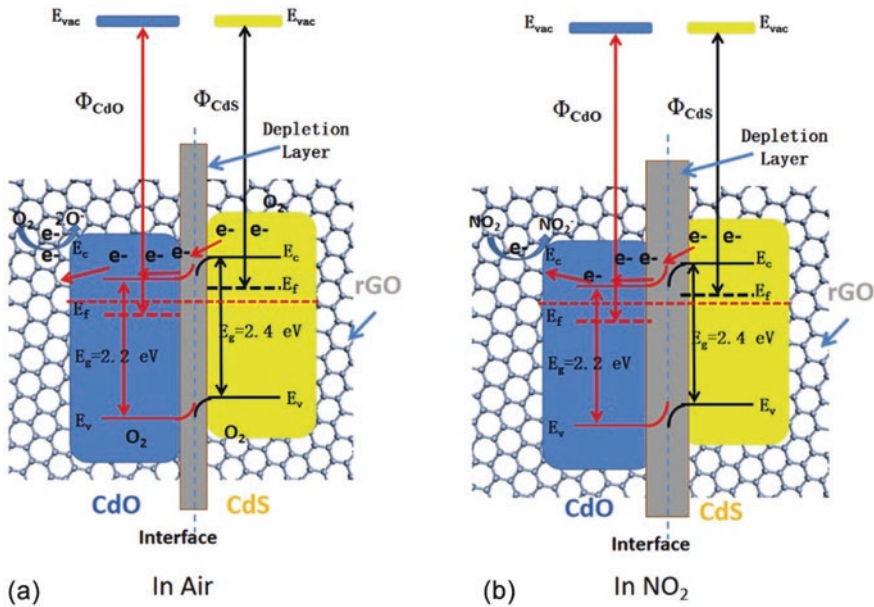
**Fig. 8.1** The schematic diagram of the  $\text{NO}_2$  gas sensing mechanism of the CdTe/ZnO@PSi nanostructured thin film sensor in dry air (a) and in the presence of  $\text{NO}_2$  (b). (Reprinted with permission from [82]. Copyright 2021: Elsevier)



**Fig. 8.2** Schematic view of energy band diagram and charge transfer (a); gas adsorption model (b). (Reprinted with permission from [101]. Copyright 2021: Elsevier)

nitrogen dioxide,  $\text{NO}_2$  molecules are adsorbed on the surface with electron capture to form  $\text{NO}_2^-$ . This results in the increase in the length of the hole accumulation layer in ZnSe and causes a change in the height of the barrier at the  $p$ - $p$  interface, which provides an increase in the sensitivity of  $p$ -NiO@ $p$ -ZnSe nanocomposites compared to pristine ZnSe.

Sun et al. [62] obtained CdO@CdS nanocomposites by solvothermal synthesis of CdS nanoparticles followed by the formation of a CdO layer by thermal oxidation. Additionally, the resulting composite was decorated with rGO nanoparticles. The authors explain the increased sensitivity of the obtained material to  $\text{NO}_2$  at 125 °C by two reasons: the formation of an  $n$ - $n$  heterojunction and the decoration of rGO (Fig. 8.3). During the formation of the  $n$ -CdO/ $n$ -CdS heterocontact, electrons flow from semiconductor with smaller work function (CdS) to semiconductor with larger work function (CdO) until the Fermi level is equalized. Consequently, a layer of electron depletion and electron accumulation, respectively, are formed at the interface between CdS and CdO. Considering that the CdO layer is in direct contact with the target  $\text{NO}_2$  gas, which is an electron acceptor, the formation of the accumulation layer stimulates the adsorption of  $\text{NO}_2$  and provides a more significant increase in the resistance of the composite compared to pristine CdS. Additional decoration of the CdO@CdS composite with rGO nanoparticles gives the material with a larger specific surface area and forms additional defects that can act as adsorption sites, and also accelerates electron transfer during the reaction on the



**Fig. 8.3** The structures of energy band and change of depletion layer in gas sensing process for CdS/CdO/rGO composite in air (a) and in  $NO_2$  (b). (Reprinted with permission from [62]. Copyright 2019: Elsevier)

nanocomposite surface, which favorably affects the adsorption/desorption of  $NO_2$  resulting in higher sensitivity.

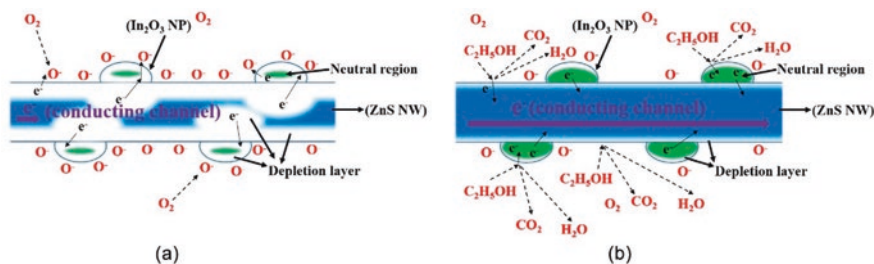
The same situation is realized in nanocomposites ZnSe-core/ $SnO_2$ -shell microspheres [64] and ZnO@ZnSe nanoflakes [96]. ZnSe-core/ $SnO_2$ -shell microspheres were obtained as a result of two-step hydrothermal synthesis, and ZnO@ZnSe nanoflakes were formed as a result of thermal oxidation of commercial ZnSe nanoflakes. In both cases, the increased sensitivity of these materials to  $NO_2$  in comparison with reducing gases was demonstrated. Since ZnSe work function ( $\sim 4.09 \text{ eV}$ ) is less than ZnO or  $SnO_2$  work function ( $\sim 4.7\text{--}4.9 \text{ eV}$ ), the electrons would transfer from ZnSe to the metal oxide. Due to formation of the electron accumulation layer in ZnO or  $SnO_2$  nanocrystals, they can attract more  $NO_2$ , resulting in the enhanced sensor response.

As for reducing gases, the detection of which is based on a change in the resistance of the sensitive material as a result of the oxidation of target gases with chemisorbed oxygen, the formation of a heterocontact increases sensitivity, but does not increase selectivity if none of the components of the composite enters into a specific interaction with a certain gas. Thus, K.-K. Kim et al. [85] studied the sensor properties of ZnS nanowires obtained by VLS method and decorated with  $In_2O_3$  nanoparticles formed by hydrothermal route when detecting various volatile organic compounds (VOCs): methanol, ethanol, acetone, formaldehyde, and benzene. Nanocomposites  $In_2O_3$ @ZnS demonstrated the maximum response at  $300 \text{ }^\circ\text{C}$  when

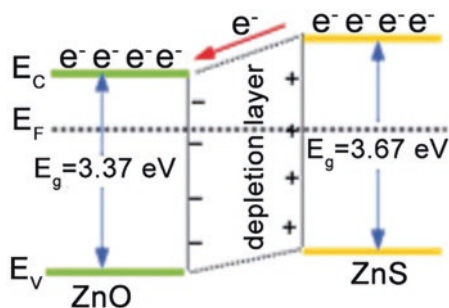


detecting ethanol; however, decoration with  $\text{In}_2\text{O}_3$  particles increases the response of ZnS to all the VOCs considered approximately equally. This is consistent with the mechanism proposed by the authors for the sensor response formation based on a change in the width of the conducting channel in ZnS nanowires (Fig. 8.4). At the same time, the overall increase in sensitivity to reducing gases is due to the increased concentration of chemisorbed oxygen on the surface of  $\text{In}_2\text{O}_3$  nanoparticles. Electron transfer from ZnS with a smaller work function to  $\text{In}_2\text{O}_3$  with a larger work function stimulates the chemisorption of oxygen, which acts as an oxidant in VOCs conversion reactions on the surface of semiconductors. Nanocomposites containing  $\text{In}_2\text{O}_3$  and ZnS also have been studied in Refs. [65, 102]. Q. Chen et al. [65] synthesized  $\text{In}_2\text{O}_3@\text{ZnS}$  composite microspheres by two-step hydrothermal process, and P. He et al. [102] obtained  $\text{ZnS}@\text{In}_2\text{O}_3$  nanocomposites as ZnS modified hollow  $\text{In}_2\text{O}_3$  microspheres and ZnS-shell/ $\text{In}_2\text{O}_3$ -core structures in one-step hydrothermal synthesis. A large proportion of ZnS in ZnS/ $\text{In}_2\text{O}_3$  nanocomposites provides high sensitivity to alcohols – ethanol [65] and *n*-butanol [102]. On the contrary, in the case when the predominant component is  $\text{In}_2\text{O}_3$ , a specific sensitivity to *n*-butylamine at 300 °C was observed. The authors of [102] do not discuss the reason for the anti-bate character of the change in the sensitivity of ZnS/ $\text{In}_2\text{O}_3$  nanocomposites depending on the ZnS: $\text{In}_2\text{O}_3$  molar ratio. It can be assumed that since  $\text{In}^{3+}$  is a stronger Lewis acid than  $\text{Zn}^{2+}$ , ZnS/ $\text{In}_2\text{O}_3$  nanocomposites, in which the electron percolation way is realized through  $\text{In}_2\text{O}_3$  phase, have a greater response to *n*-butylamine having pronounced basic properties. An increase in the surface coating with ZnS nanoparticles leads to the formation of an electron percolation way through ZnS phase that leads to a decrease in the sensor response to *n*-butylamine.

An increase in the response to different VOCs (*n*-butanol, ethanol, acetone, methanol, and ether) after sonochemical formation of ZnS shell on the surface of ZnO microrods obtained under hydrothermal conditions was observed by W. Zhang et al. [98]. Electron transfer from ZnS to ZnO in combination (Fig. 8.5) with the porous structure of ZnS shell provides an increased concentration of chemisorbed oxygen on the surface of ZnO that causes an increased sensitivity of ZnO-core/ZnS-shell nanocomposites to reducing gases. At the same time, the authors note that compared to pure ZnO, the response is increased as 4.1 times to *n*-butanol, 3.1 times to ethanol, 1.9 times to acetone, 2.4 times to methanol, and 1.4 times to ether,



**Fig. 8.4** Schematic images of ZnS nanowire decorated with  $\text{In}_2\text{O}_3$  nanoparticles when it is exposed to (a) air and (b) ethanol. (Reprinted with permission from [85]. Copyright 2017: Elsevier)



**Fig. 8.5** Energy band structure ZnO-core/ZnS-shell nanocomposites. (Reprinted with permission from [98]. Copyright 2015: RSC)

respectively, but do not offer any explanation for the observed specific increase in response to alcohols. High sensitivity to ethanol has been also demonstrated by X.-L. Yu et al. [97] for ZnO-core/ZnS-shell hollow nanocages synthesized via hydrothermal route combined with subsequent etching treatment and liquid phase sulfidation.

Nanocomposites containing  $\text{TiO}_2$  should be discussed separately. Y.-C. Liang et al. [71] synthesized  $\text{TiO}_2$ -core/ZnS-shell composite nanorods using ZnO as a sacrificial shell layer in a hydrothermal reaction. A.M. Laera et al. [95] obtained ZnS@ $\text{TiO}_2$  nanocomposite films via impregnation of porous titania with unimolecular zinc bis(benzyl)thiol precursor with subsequent thermolysis. In both cases, it was shown that nanocomposites exhibit increased sensitivity to oxidizing ( $\text{NO}_2$  [71]) and reducing (ethanol [95]) gases compared to unmodified  $\text{TiO}_2$ . The authors do not discuss the formation of a heterocontact and the transfer of electrons between semiconductors forming a composite. But considering that  $\text{TiO}_2$  is characterized by exceptionally high resistance, it can be assumed that its modification with ZnS nanoparticles is accompanied by electron transfer from ZnS to  $\text{TiO}_2$  that increases the concentration of charge carriers in titanium dioxide and stimulates the adsorption of electron acceptor gases  $\text{NO}_2$  and oxygen. An increase in the concentration of chemisorbed oxygen, in turn, leads to an increase in sensor sensitivity when detecting reducing gases.

An increase in selectivity of II-VI semiconductors/metal oxide nanocomposites was demonstrated toward ethanol and hydrogen sulfide. M. Li et al. [67] observed a selective increase in sensitivity to ethanol compared to acetone, toluene, formaldehyde, acetylene, and methane after hydrothermal decoration of CdS nanowires with  $\text{CeO}_2$  nanoparticles. Similarly, N. Zhang et al. [68] found a selective increase in response to ethanol compared to ammonium, acetylene, acetone, xylene, methylbenzene, and carbon monoxide for CuO decorated CdS nanowires synthesized by two-step solvothermal method. Such a change in the sensor properties of  $\text{CeO}_2$ @CdS and CuO@CdS composites compared to unmodified CdS nanowires is due to  $\text{CeO}_2$  and CuO catalytic activity in the oxidative dehydrogenation of alcohols, which is favorable route of incomplete alcohol oxidation resulting in strong response of semiconductor gas sensors [103].

M. Dun et al. [60] synthesized CdS quantum dots supported by ultra-thin porous  $\text{Co}_3\text{O}_4$  nanosheets assembled into hollowed-out microspheres, which showed selectivity in detecting  $\text{H}_2\text{S}$  compared to ethanol, toluene, acetone, propanol, and hydrogen. The authors consider  $\text{Co}_3\text{O}_4$  only as a support for localization and stabilization of CdS, but the possibility of the formation of  $n\text{-CdS}/p\text{-Co}_3\text{O}_4$  heterojunction and the participation of  $\text{Co}_3\text{O}_4$  in the formation of sensor response could not be excluded. It is known [104] that  $\text{H}_2\text{S}$  reduces  $p\text{-Co}_3\text{O}_4$  to cobalt (II) sulfides with metallic conductivity. Even if this process takes place in a thin near-surface layer of  $\text{Co}_3\text{O}_4$  microspheres, it can result in the removal of the  $n\text{-CdS}/p\text{-Co}_3\text{O}_4$  junction and in significant increase in the nanocomposites conductivity. Such removal of the barriers is only possible in the presence of sulfur containing reducing gases providing high selectivity of  $n\text{-CdS}/p\text{-Co}_3\text{O}_4$  nanocomposites.

N.M. Dieu et al. [70] found out that applying a thin layer of  $p\text{-CdTe}$  to the surface of  $n\text{-ZnO}$  nanorods leads to a significant increase in the sensor response when detecting  $\text{H}_2\text{S}$  with a simultaneous decrease in the temperature corresponding to the maximum response from 350 to 200 °C. At the same time, no similar effect was observed when detecting  $\text{CO}$ ,  $\text{CH}_4$ ,  $\text{H}_2$ ,  $\text{NH}_3$ , acetone, and methanol. The authors did not propose any explanation for the increase in selectivity to hydrogen sulfide of  $p\text{-CdTe}/n\text{-ZnO}$  compared to  $\text{ZnO}$ . On the contrary, it is suggested that the role of  $\text{ZnTe}$  layer is only to control the resistance of the  $\text{ZnO}$  receptor and transducer by forming a  $p-n$  junction. According to the authors,  $\text{ZnTe}$  played neither of a role of a receptor nor that of a catalyst to aid in the adsorption and/or interaction of  $\text{H}_2\text{S}$  on  $\text{ZnO}$ .

#### **8.4.2 Sensor Properties of II-VI Semiconductors/Metal Oxide Nanocomposites Under Photoactivation**

A known disadvantage of metal oxide-based gas sensors is high operating temperature 200–500 °C, which is necessary to activate surface chemical reactions, desorb the products of these reactions, as well as achieve suitable electrical conductivity. At the same time high operating temperature causes a number of problems: (i) high power consumption, which imposes restrictions on the use of such sensors in portable and mobile devices; (ii) degradation of the sensor material because of grain sintering and diffusion processes, resulting in the drift of sensor characteristics; (iii) mechanical deformation of the sensor layer because of different thermal expansion coefficients of the sensor layer and the substrate; and (iv) explosion or fire risk [105].

So, there was a need to search for sensor materials that do not require additional heating. The use of light activation instead of heating, i.e., irradiation of the sensitive layer with UV or visible light, as a more gentle and less power-consuming activation method, has become widespread (Table 8.2). The phenomenon of light activation of sensor sensitivity is inextricably linked with the appearance of photoconductivity due to the processes of light absorption and generation of photoexcited charge

**Table 8.2** Summary of gas sensor properties of II-VI semiconductors/metal oxide nanocomposites under light activation

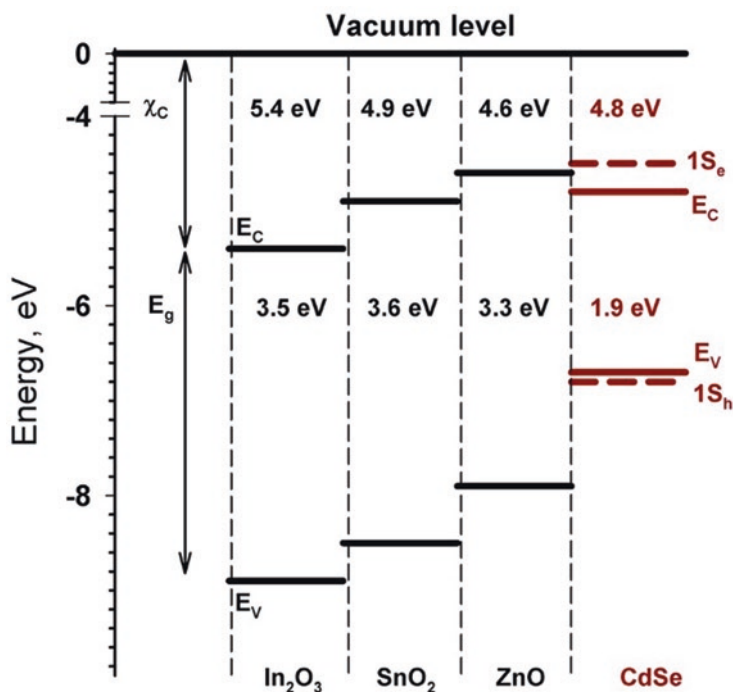
Composite	Morphology	Synthesis method	Gas (Concentration, ppm)	T, °C	Light wavelength, nm	RH, %	Sensor response, %	Response/recovery time, s	Ref.
ZnO@ZnS	CS NWs	TE ALD	NO <sub>2</sub> (5)	RT	365	n/a	12	n/a	[90]
<i>p</i> -CuO@ <i>n</i> -ZnS	NW <sub>s</sub> decorated NPs	TE; ST	NO <sub>2</sub> (5)	RT	365	40	10.55	40/150	[84]
CdSe@ZnO	Powder decorated QDs	WCS; CS	NO <sub>2</sub> (1.6)	RT	535	Dry air	30	n/a	[33]
CdSe@SnO <sub>2</sub>	Powder decorated QDs	WCS; CS	NO <sub>2</sub> (1.6)	RT	535	Dry air	100	n/a	[35]
CdSe@In <sub>2</sub> O <sub>3</sub>	Powder decorated QDs	WCS; CS	NO <sub>2</sub> (1.6)	RT	535	Dry air	8900	n/a	[35]
(ZnSe@CdS)@ZnO	Powder decorated CS QDs	WCS; CS	NO <sub>2</sub> (2)	RT	535	25	80	n/a	[34]
(CdS@CdSe)@ZnO	Powder decorated CS QDs	WCS; CS	NO <sub>2</sub> (2)	RT	535	25	30	n/a	[34]
CdS@ZnO	NRs decorated NPs	SC	HCHO (110)	RT	> 450	n/a	126	n/a	[75]
ZnO@CdS	NW <sub>s</sub> decorated NPs	SC	HCHO (10)	RT	450	n/a	120	n/a	[69]

CS colloidal synthesis; SC sonochemical synthesis; WCS wet chemical synthesis

carriers. S. Park et al. [90] revealed a synergistic effect of a combination of UV irradiation and core–shell nanostructures formation on the sensing properties of ZnS-core/ZnO-shell nanowires in room-temperature NO<sub>2</sub> detection. Under UV light with a photon energy larger than the ZnO band gap, electron–hole pairs are generated in the ZnO shell. The decrease in the height of the potential barrier at the ZnS-core/ZnO-shell interface by thermionic emission of the trapped electrons from the interface states leads to the easier transfer of carriers across the interface. According to the authors, under UV illumination chemisorbed oxygen in O<sub>2</sub><sup>-</sup> form can be desorbed at room temperature, facilitating the interaction of the semiconductor surface with NO<sub>2</sub> that leads to an increase in the sensor response. The response of ZnS nanowires in room-temperature NO<sub>2</sub> detection was also enhanced significantly by a combination of CuO decoration and UV illumination [84]. The authors supposed that the increase in the response of the *p*-CuO decorated *n*-ZnS nanowires under UV illumination is caused by the increased number of carriers participating in the reactions with NO<sub>2</sub> molecules as a result of the photogenerated electron–hole pairs and modulation of the potential barrier height and the modulation of conduction channel width.

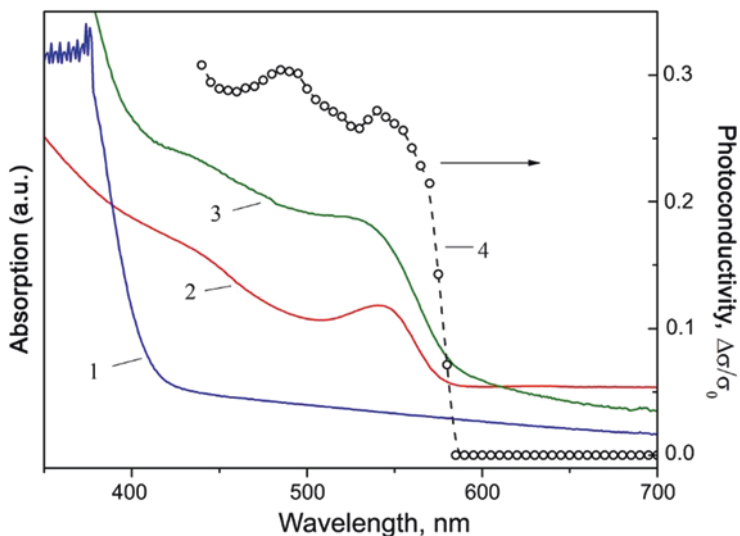
Further reduction of power consumption by replacing thermal heating with photoactivation becomes possible when using visible light. Visible range radiation sources have a lower cost and are characterized by lower own power consumption. In addition, it is the visible range that accounts for the maximum intensity of solar radiation that can be additionally used as an illumination source. Metal oxides, most commonly used as materials for resistive gas sensors, are wide-band gap semiconductors that determines their optical absorption, mainly in the UV range. The shift of the optical sensitivity of semiconductor oxides toward longer wavelengths becomes possible when creating composite materials containing a sensitizer that meets the following conditions: (i) high absorption coefficient of visible light; (ii) the ability to transfer photoexcitation energy to the oxide matrix due to the mutual arrangement of the energy levels of the sensitizer and the matrix. The transfer of photoinduced electrons from the sensitizer to the metal oxide becomes possible if the excited level of the sensitizer lies higher in energy than the bottom of the conduction band  $E_C$  of the semiconductor oxide (Fig. 8.6), while photoexcited holes remain in the sensitizer particle. Such a scenario is realized in the sensitization of *n*-type semiconductor oxides by nanoparticles of II-VI semiconductors that was confirmed by the study of the optical properties and the photoconductivity spectral dependence of CdSe@ZnO nanocomposites, in which CdSe quantum dots acted as sensitizers (Fig. 8.7) [33]. The CdSe quantum dots absorb visible light with a sharp maximum corresponding to the excitonic transition at  $\lambda = 535$  nm. The maximum of photoresponse curve for CdSe@ZnO nanocomposite matches well the maximum in absorption spectrum of the CdSe nanocrystals. The onset of the absorption edge coincides with the appearance of the photoresponse of CdSe@ZnO composites. Zinc oxide does not absorb visible light with  $\lambda > 425$  nm. Photoconductivity of pure ZnO samples without CdSe sensitizer was negligibly small.

Articles by J. Zhai et al. describing nanocomposites CdS (nanoparticles)@ZnO (nanorods) [75] and ZnO (nanospheres)@CdS (nanowires) [69], should probably be considered as the earliest works devoted to the sensor properties of II-VI semiconductors/metal oxide nanocomposites under visible light activation. Nanocomposites

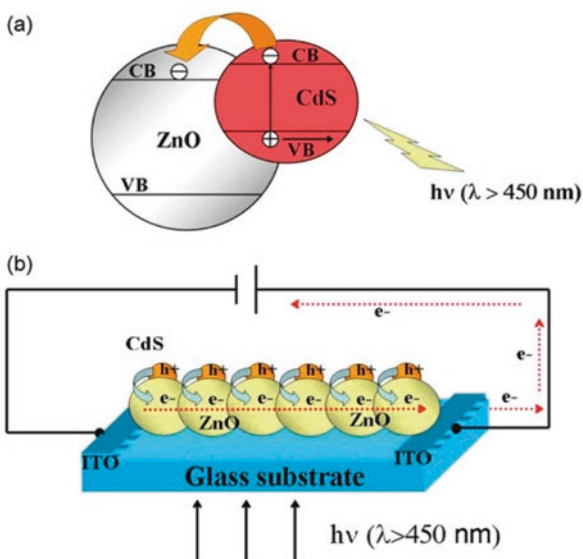


**Fig. 8.6** Scheme of the mutual arrangement of the energy levels for bulk  $\text{In}_2\text{O}_3$ ,  $\text{SnO}_2$ ,  $\text{ZnO}$ , and  $\text{CdSe}$ : conduction band  $E_C$ , valence band  $E_V$ , band gap  $E_g$ , electron affinity  $\chi_c$ , level of photoexcited electron  $1S_e$ , level of photoexcited hole  $1S_h$ . (Reprinted with permission from [35]. Copyright 2016: Elsevier)

$\text{CdS}$  (nanoparticles)@ $\text{ZnO}$  (nanorods) obtained via sonochemical synthesis demonstrate a visible-light-induced photoelectric gas sensitivity to formaldehyde at room temperature. Under photoactivation  $\text{CdS}$  nanoparticles work as visible light harvesters and photogenerated electron's donors (Fig. 8.8), while  $\text{ZnO}$  works as the gas sensing units, photogenerated electron's acceptors, and pathways of electrons transfer [75]. In the "inverted" structure of  $\text{ZnO}$  (nanospheres)@ $\text{CdS}$  (nanowires) obtained in hydrothermal/solvothermal synthesis,  $\text{ZnO}$  nanospheres modulate electron transport through  $\text{CdS}$  nanowires [69]. The enhanced sensing properties of the  $\text{ZnO}$  (nanospheres)@ $\text{CdS}$  (nanowires) nanocomposites in formaldehyde detection can be attributed to an additional depletion layer at the interface between  $\text{ZnO}$  nanospheres and  $\text{CdS}$  nanowires. Compared with bare  $\text{CdS}$  nanowires, the decoration with  $\text{ZnO}$  nanospheres induces more active sites for the adsorption of oxygen molecules. In addition, spatial separation of photogenerated electrons and holes between  $\text{ZnO}$  and  $\text{CdS}$  retards the recombination probability of the excess carriers. This synergistic effect results in the enhancement of sensing properties attributed to the interfacial transport of photogenerated carriers. A.E. Gad et al. [74] synthesized  $\text{CdS}@n\text{-ZnO}/p\text{-Si}$  nanowires heterojunctions through a combination of wet chemical etching (Si NWs) and atomic layer deposition ( $\text{ZnO}$ ) techniques followed by chemical bath deposition ( $\text{CdS}$ ). The device showed diode I-V characteristics in dark conditions



**Fig. 8.7** Absorption spectra of ZnO powder (1), CdSe quantum dot sol (2), CdSe@ZnO nanocomposite (3), and dependence of photoconductivity of CdSe@ZnO nanocomposite on the excitation wavelength (4). (Reprinted with permission from [33]. Copyright 2014: Elsevier)

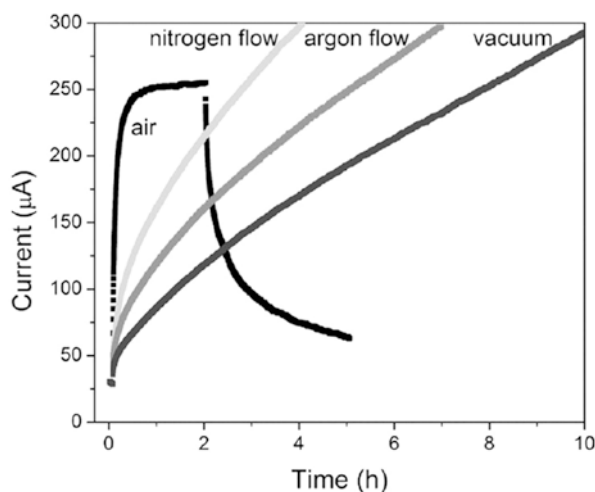


**Fig. 8.8** (a) The scheme of interfacial charge carriers' generation, transfer, and separation between ZnO and CdS in a CdS NPs/ZnO heterostructure. (b) Process of the photocurrent generation of the CdS NPs/ZnO heterostructure on the electrode surface. (Reprinted with permission from [75]. Copyright 2010: Elsevier)

and a photovoltaic response under solar illumination. The authors noted that the presence of CdS is indispensable in the sensing system not only to harvest the solar light but also to activate the interaction between target gas (oxygen) and metal oxide since *n*-ZnO/*p*-Si nanowires did not show the observed solar diode effect. The device showed promising sensing properties at room temperature by using only solar light to drive the sensor without any external power sources.

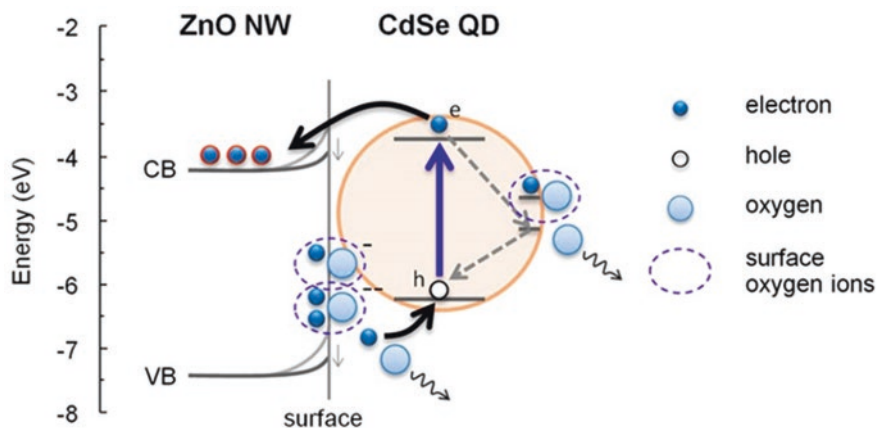
One of the first papers demonstrating the gas-sensitive properties of the CdSe@ZnO nanocomposite, in which quantum dots were used as a sensitizer, was published in 2012 [106]. CdSe quantum dots were synthesized in an aqueous medium using mercaptopropionic acid as a stabilizer, while ZnO nanowires were grown under hydrothermal conditions. Under blue light  $\lambda = 458$  nm CdSe@ZnO nanocomposite obtained by direct adsorption showed a photoresponse an order of magnitude greater compared to unsensitized ZnO nanowires. It was found that the photoconductivity of the CdSe@ZnO nanocomposite, as well as its kinetic parameters, depend on the composition of the atmosphere, and the presence of oxygen is critical (Fig. 8.9). In a vacuum and an inert atmosphere, photoconductivity behaves in a similar way, continuously increasing during illumination; in air and oxygen atmosphere a stationary value of photoconductivity is quickly achieved. This behavior is associated with the participation of oxygen in interaction with photoexcited charge carriers, causing the processes of photoadsorption and photodesorption; thus, the stationary level of photoconductivity is controlled by the ratio of the rates of these processes. The dependence of the room-temperature photoconductivity of CdSe@ZnO nanocomposites on the oxygen partial pressure was also confirmed in the case of periodic illumination with green light ( $\lambda = 535$  nm) [16, 33].

The processes of oxygen adsorption/desorption under visible light photoactivation are investigated by S. Bley et al. [100] for ZnO nanowires decorated with CdSe quantum dots stabilized with different ligands (3-mercaptopropionic acid,



**Fig. 8.9** Photoconductivity dynamics of the CdSe@ZnO nanocomposite measured in four different gas environments under the same excitation conditions. (Reprinted with permission from [106]. Copyright 2012: American Chemical Society)





**Fig. 8.10** Schematic energy diagram of the oxygen-controlled electron transfer between the CdSe quantum dot and ZnO nanowire. (Reprinted with permission from [100]. Copyright 2015 American Chemical Society)

6-mercaptohexanoic acid, 11-mercaptoundecanoic acid). Schematic energy diagram of the oxygen-controlled electron transfer between the CdSe quantum dot and ZnO nanowire is shown in Fig. 8.10. When CdSe quantum dots are selectively excited using a wavelength of 460 nm in air, oxygen adsorption occurs on the CdSe and ZnO surface. Saturation of the photocurrent is reached through a dynamic equilibrium between oxygen desorption and readsorption from and on both the ZnO and CdSe surfaces. The results reveal that for shorter linker molecules the growth of CdSe@ZnO photoconductivity is faster due to smaller diffusion barriers for oxygen molecules, but the overall increase in photocurrent will be smaller because of higher probability of oxygen readsorption.

The sensor properties of nanocomposites based on metal oxides ZnO,  $\text{In}_2\text{O}_3$ ,  $\text{SnO}_2$ , and CdSe quantum dots in visible light ( $\lambda = 535 \text{ nm}$ ) activated room-temperature  $\text{NO}_2$  detection were investigated by A. Chizhov et al. [33, 35]. CdSe quantum dots were synthesized by high-temperature colloidal synthesis using oleic acid as a stabilizer. Nanocomposites were obtained by depositing CdSe sol in hexane on the surface of preformed layers of nanocrystalline ZnO,  $\text{SnO}_2$ ,  $\text{In}_2\text{O}_3$ . Nanocomposites demonstrated a reversible sensor response to  $\text{NO}_2$ . It is supposed [33, 35] that the role of illumination in the formation of sensor response toward  $\text{NO}_2$  is the same as in the case of oxygen-controlled photoconductivity. Under visible light the electron-hole pair is generated not in the wide-gap semiconductor oxide but in the CdSe quantum dot. Then photoexcited electron transfers to the conduction band of the semiconductor matrix, while photoexcited hole can recombine with the electrons trapped by the chemisorbed  $\text{NO}_2^-$ , which loses its charge and becomes physically adsorbed and weakly coupled. Thermal fluctuations can cause  $\text{NO}_2$  desorption. So, the stationary level of photoconductivity in the  $\text{NO}_2$  containing atmosphere is controlled by the ratio of the rates of the adsorption and desorption of nitrogen dioxide.

A significant change in the electronic and optical properties of II-VI semiconductor quantum dots can be achieved by creating core-shell heterostructures. The formation of a type I heterojunction occurs when the shell of a wider-band semiconductor, such as CdS or ZnS, builds up on the surface of CdSe nuclei. This approach leads to passivation of surface defects of quantum dots, and, as a consequence, a significant increase in the quantum yield of luminescence. The passivation of surface defects should also enhance the efficiency of electron transfer from quantum dots into oxide matrix that was confirmed by K. Drozdov et al. [107] for the nanocomposites based on SnO<sub>2</sub> and CdSe quantum dots coated with CdS shell of various thicknesses. Another type of heterostructures (type II) makes it possible to separate photoexcited electrons and holes between the nucleus and the shell due to the suitable mutual position of energy levels in the selected materials. Localization of a hole in the shell of quantum dot can facilitate its interaction with chemisorbed gas molecules, which, for example, is a critical process in the NO<sub>2</sub> detection. An example of such heterostructures are ZnSe-core/CdS-shell quantum dots, which were used as a ZnO sensitizer when detecting NO<sub>2</sub> in air at room temperature under visible light ( $\lambda = 535$  nm) [34]. The resulting ZnO/CdS@ZnSe nanocomposite actually showed an order of magnitude higher sensor response compared to the similar ZnO/CdSe nanocomposite. The ZnO/CdS@CdSe nanocomposite used in the same work showed a higher photoresponse compared to ZnO/CdSe due to passivation of surface defects and an increase in the efficiency of electron injection; however, its sensor sensitivity was comparable to the ZnO/CdSe nanocomposite. Thus, the possibility of increasing the efficiency of phodesorption processes by using type II heterostructures as sensitizers was shown.

## 8.5 Gas Sensors Based on II-VI Semiconductors/ Non-oxide Materials

In addition to nanocomposites with semiconductor metal oxides, II-VI semiconductors are used in combination with layered metal chalcogenides and 2D carbon-based materials to create new gas sensors with enhanced characteristics (Table 8.3). In all cases, the resulting heterocontact plays a major role in the sensor response formation. S. Shao et al. [63] have grown CdS nanocones on the 2D layered RGO-MoS<sub>2</sub> substrate by solvothermal synthesis. The obtained nanocomposites demonstrated at 75 °C selective sensitivity to NO<sub>2</sub> compared to reducing gases H<sub>2</sub>S, NH<sub>3</sub>, formaldehyde, methanol and ethanol. The authors attribute the observed effect to the formation of *n*-MoS<sub>2</sub>/*n*-CdS heterojunction, weak interaction of NO<sub>2</sub> with RGO, and formation of continuous conducting channel through CdS hexagonal nanocones.

Jaiswal et al. [81] described the sensor properties of heterostructures formed by layers of MoS<sub>2</sub> nanowires and CdTe quantum dots on *p*-type Si substrates by magnetron sputtering. According to the authors, the work function values determine the transfer of electrons from MoS<sub>2</sub> to CdTe. Since CdTe is located on the top of

**Table 8.3** Summary of gas sensor properties of II-VI semiconductors/non-oxide materials

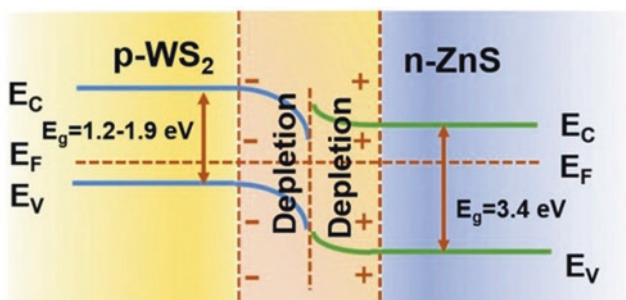
Composite	Morphology	Synthesis method	Gas (Concentration, ppm)	T, °C	RH, %	Sensor response, %	Response/recovery time, s	Ref.
CdS@MoS <sub>2</sub> /rGO	Nanocoines on the 2D layered substrate	ST	NO <sub>2</sub> (10)	75	90	130	n/a	[63]
CdTe@MoS <sub>2</sub>	NW's decorated QDs	MS	NO <sub>2</sub> (10)	RT	Dry air	40	16/114	[81]
ZnS@WS <sub>2</sub>	NS decorated QDs	LPE; SILAR	NO <sub>2</sub> (5)	RT	n/a	32.5	4/1000	[73]
Pr-SnS <sub>2</sub> /ZnS	NFs	HT	NH <sub>3</sub> (50)	160	n/a	14.03	6/13	[108]

*LPE* Liquid-phase exfoliation; *NFs* nanoflowers

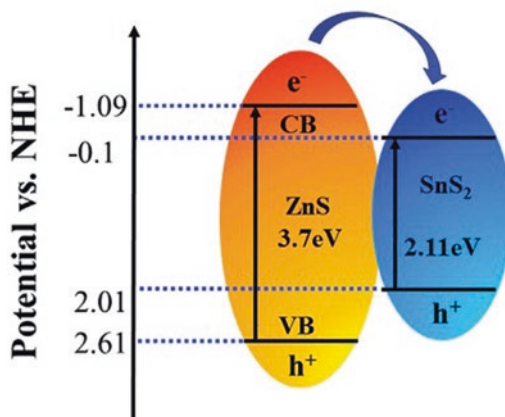
heterostructure and is in direct contact with the gas phase, an increase in the electron concentration in this semiconductor stimulates the  $\text{NO}_2$  absorption. In general, the sensor response toward  $\text{NO}_2$  is small, but reversible without additional thermal or photoactivation that is typical for systems based on layered chalcogenides as  $\text{MoS}_2$ . However, it should be noted that in their discussions about the mechanism of sensor response formation, the authors did not take into account the presence of a layer containing Mo (VI) and oxygen, which was detected by the XPS method.

2D/0D  $\text{WS}_2/\text{ZnS}$  heterostructures obtained by Y. Han et al. by  $\text{WS}_2$  liquid-phase exfoliation with subsequent chemical deposition of  $\text{ZnS}$  [73] demonstrated selective response to  $\text{NO}_2$  (compared with reducing gases  $\text{NH}_3$ , methanol, ethanol, acetone, toluene) at room temperature 25 °C. Exfoliated  $\text{WS}_2$  nanosheets shows a  $p$ -type character and  $\text{ZnS}$  is an intrinsic  $n$ -type semiconductor. The electrons in  $n$ -type  $\text{ZnS}$  move to  $p$ -type  $\text{WS}_2$  that results in the formation of both an electron depletion layer and a positively charged area on the surface of  $\text{ZnS}$ . Simultaneously, the holes of  $p$ -type  $\text{WS}_2$  near the  $p$ - $n$  interface have a tendency to diffuse into  $n$ -type  $\text{ZnS}$ , building a hole depletion layer and a negatively charged region on the surface of  $\text{WS}_2$  (Fig. 8.11). The built-in electric field (acting as potential barrier) restricts the further diffusion of charges, which can be modulated by  $\text{NO}_2$  adsorption and desorption processes. The built-in electric field also promotes the transport efficiency of charge carriers, which enhances the electron transfer between  $\text{NO}_2$  molecules and heterostructure at room temperature. Furthermore, the formed depletion region at the heterojunction can act as a passivation layer to prevent the interaction between atmospheric oxygen and  $\text{WS}_2$  and result in the reliable long-term stability of the heterostructure.

Quite sensitive ammonia gas sensor based on  $\text{Pr-SnS}_2/\text{ZnS}$  nanoflowers was created by Q. Zhang et al. [108] in hydrothermal conditions. The energy band structures of  $\text{SnS}_2$  and  $\text{ZnS}$  are shown in Fig. 8.12. The conduction band of  $\text{ZnS}$  is higher than that of  $\text{SnS}_2$ , so the electrons of  $\text{ZnS}$  can transfer toward  $\text{SnS}_2$ . The  $\text{SnS}_2/\text{ZnS}$   $n$ - $n$  heterojunction could reduce the recombination probability of electron-hole



**Fig. 8.11** Energy band structure of  $p$ - $\text{WS}_2/n$ - $\text{ZnS}$  heterostructure in air. (Reprinted with permission from [73]. Copyright 2019: Elsevier)



**Fig. 8.12.** Energy band structure of  $\text{SnS}_2/\text{ZnS}$  heterocontact. (Reprinted with permission from [108]. Copyright 2019: Elsevier)

pairs and improve the electrons transmission efficiency. Therefore, the  $\text{SnS}_2/\text{ZnS}$  heterojunction plays an important modulating role in electrical conductivity for Pr- $\text{SnS}_2/\text{ZnS}$  sensor.

## 8.6 Summary

II-VI semiconductors (zinc and cadmium chalcogenides) are important components of nanocomposites and heterostructures containing wide-band metal oxides or layered transition metal chalcogenides. II-VI semiconductors in these materials form a heterojunction, which leads to increased gas sensitivity under thermal activation, or provide the formation of photogenerated charge carriers under visible light that shifts the optical sensitivity of semiconductor oxides to the visible region and allows the detection of gases at room temperature without the use of UV radiation.

Further improvement of the sensor characteristics requires understanding which processes are responsible for the formation of the sensor response to the target gas. There are numerous articles devoted to the study of the mechanism of gas sensitivity of materials based on semiconductor oxides, for example, using in situ spectroscopy methods, or involving DFT calculations, while there is no similar information for materials based on II-VI semiconductors. Such experimental and theoretical studies would contribute to the development of new sensor materials specially designed to solve specific problems in various fields in which resistive gas sensors are required.

**Acknowledgements** This work was supported by RFBR grant 21-53-53018.

## References

1. Kurtin S, McGill TC, Mead CA. Fundamental transition in the electronic nature of solids. *Phys Rev Lett.* 1969;22:1433–6. <https://doi.org/10.1103/PhysRevLett.22.1433>.
2. Jian Y, Hu W, Zhao Z, Cheng P, Haick H, Yao M, Wu W. Gas sensors based on chemi-resistive hybrid functional nanomaterials. *Nano-Micro Lett.* 2020;12:71. <https://doi.org/10.1007/s40820-020-0407-5>.
3. Miller DR, Akbar SA, Morris PA. Nanoscale metal oxide-based heterojunctions for gas sensing: a review. *Sensors Actuators B Chem.* 2014;204:250–72. <https://doi.org/10.1016/j.snb.2014.07.074>.
4. Henglein A. Photochemistry of colloidal cadmium sulfide. 2. Effects of adsorbed methyl viologen and of colloidal platinum. *J Phys Chem.* 1982;86:2291–3. <https://doi.org/10.1021/j100210a010>.
5. Spanhel L, Haase M, Weller H, Henglein A. Photochemistry of colloidal semiconductors. 20. Surface modification and stability of strong luminescing CdS particles. *J Am Chem Soc.* 1987;109:5649–55. <https://doi.org/10.1021/ja00253a015>.
6. Spanhel L, Weller H, Fojtik A, Henglein A. Photochemistry of semiconductor colloids. 17. Strong luminescing CdS and CdS-Ag<sub>2</sub>S particles. *Ber Bunsenges Phys Chem.* 1987;91:88–94. <https://doi.org/10.1002/bbpc.19870910204>.
7. Haase M, Weller H, Henglein A. Photochemistry of colloidal semiconductors. 26. Photoelectron emission from cadmium sulfide particles and related chemical effects. *J Phys Chem.* 1988;92:4706–12. <https://doi.org/10.1021/j100327a030>.
8. Rossetti R, Brus LJ. Electron-hole recombination emission as a probe of surface chemistry in aqueous cadmium sulfide colloids. *Phys Chem.* 1982;86:4470–2. <https://doi.org/10.1021/j100220a003>.
9. Rossetti R, Ellison JL, Gibson JM, Brus LE. Size effects in the excited electronic states of small colloidal CdS crystallites. *J Chem Phys.* 1984;80:4464–9. <https://doi.org/10.1063/1.447228>.
10. Rossetti R, Nakahara S, Brus LE. Quantum size effects in the redox potentials, resonance Raman spectra, and electronic spectra of CdS crystallites in aqueous solution. *J Chem Phys.* 1983;79:1086–8. <https://doi.org/10.1063/1.445834>.
11. Murray CB, Norris DJ, Bawendi MG. Synthesis and characterization of nearly monodisperse CdE (E = sulfur, selenium, tellurium) semiconductor nanocrystallites. *J Am Chem Soc.* 1993;115:8706–15. <https://doi.org/10.1021/ja00072a025>.
12. Hühn J, Carrillo-Carrion C, Soliman MG, Pfeiffer C, Valdeperez D, Masood A, Chakraborty I, Zhu L, Gallego M, Yue Z, Carril M, Feliu N, Escudero A, Alkilany AM, Pelaz B, del Pino OP, Parak WJ. Selected standard protocols for the synthesis, phase transfer, and characterization of inorganic colloidal nanoparticles. *Chem Mater.* 2017;29:399–461. <https://doi.org/10.1021/acs.chemmater.6b04738>.
13. Jones M, Kumar S, Lo SS, Scholes GD. Exciton trapping and recombination in type II CdSe/CdTe nanorod heterostructures. *J Phys Chem C.* 2008;112:5423–31. <https://doi.org/10.1021/jp711009h>.
14. Dooley CJ, Dimitrov SD, Fiebig T. Ultrafast electron transfer dynamics in CdSe/CdTe donor–acceptor nanorods. *J Phys Chem.* 2008;112:12074–6. <https://doi.org/10.1021/jp804040r>.
15. Shieh F, Saunders AE, Korgel BA. General shape control of colloidal CdS, CdSe, CdTe quantum rods and quantum rod heterostructures. *J Phys Chem B.* 2005;109:8538–42. <https://doi.org/10.1021/jp0509008>.
16. Sun ZH, Oyanagi H, Uehara M, Nakamura H, Yamashita K, Fukano A, Maeda H. Study on initial kinetics of CdSe nanocrystals by a combination of in situ X-ray absorption fine structure and microfluidic reactor. *J Phys Chem C.* 2009;113:18608–13. <https://doi.org/10.1021/jp907481q>.
17. Park J, Lee KH, Galloway JF, Searson PC. Synthesis of cadmium selenide quantum dots from a non-coordinating solvent: growth kinetics and particle size distribution. *J Phys Chem C.* 2008;112:17849–54. <https://doi.org/10.1021/jp803746b>.

18. Crouch DJ, O'Brien P, Malik MA, Skabara PJ, Wright SP. A one-step synthesis of cadmium selenide quantum dots from a novel single source precursor. *Chem Commun.* 2003;12:1454–5. <https://doi.org/10.1039/B301096A>.
19. Milliron DJ, Hughes SM, Cui Y, Manna L, Li J, Wang LW, Alivisatos AP. Colloidal nanocrystal heterostructures with linear and branched topology. *Nature.* 2004;430:190–5. <https://doi.org/10.1038/nature02695>.
20. Manna L, Milliron DJ, Meisel A, Scher EC, Alivisatos AP. Controlled growth of tetrapod-branched inorganic nanocrystals. *Nature Mater.* 2003;2:382–5. <https://doi.org/10.1038/nmat902>.
21. Talapin DV, Nelson JH, Shevchenko EV, Aloni S, Sadtler B, Alivisatos AP. Seeded growth of highly luminescent CdSe/CdS nanoheterostructures with rod and tetrapod morphologies. *Nano Lett.* 2007;7:2951–9. <https://doi.org/10.1021/nl072003g>.
22. Oron D, Kazes M, Banin U. Multiexcitons in type-II colloidal semiconductor quantum dots. *Phys Rev B.* 2007;75:035330. <https://doi.org/10.1103/PhysRevB.75.035330>.
23. Qu LH, Peng ZA, Peng XG. Alternative routes toward high quality CdSe nanocrystals. *Nano Lett.* 2001;1:333–7. <https://doi.org/10.1021/nl0155532>.
24. Talapin DV, Koeppel R, Gotzinger S, Kornowski A, Lupton JM, Rogach AL, Benson O, Feldman J, Weller H. Highly emissive colloidal CdSe/CdS heterostructures of mixed dimensionality. *Nano Lett.* 2003;3:1677–81. <https://doi.org/10.1021/nl034815s>.
25. Peng ZA, Peng X. Formation of high-quality CdTe, CdSe, and CdS nanocrystals using CdO as precursor. *J Am Chem Soc.* 2001;123:183–4. <https://doi.org/10.1021/ja003633m>.
26. Manna L, Scher EC, Alivisatos AP. Synthesis of soluble and processable rod-, arrow-, tear-drop-, and tetrapod-shaped CdSe nanocrystals. *J Am Chem Soc.* 2000;122:12700–6. <https://doi.org/10.1021/ja003055+>.
27. Talapin DV, Haubold S, Rogach AL, Kornowski A, Haase M, Weller H. A novel organometallic synthesis of highly luminescent CdTe nanocrystals. *J Phys Chem B.* 2001;105:2260–3. <https://doi.org/10.1021/jp003177o>.
28. Manna L, Scher EC, Li LS, Alivisatos AP. Epitaxial growth and photochemical annealing of graded CdS/ZnS shells on colloidal CdSe nanorods. *J Am Chem Soc.* 2002;124:7136–45. <https://doi.org/10.1021/ja025946i>.
29. Brennan JG, Siegrist T, Carroll PJ, Stuczynski SM, Reynders P, Brus LE, Steigerwald ML. Bulk and nanostructure Group II-VI compounds from molecular organometallic precursors. *Chem Mater.* 1990;2:403–9. <https://doi.org/10.1021/cm00010a017>.
30. Li Z, Ji Y, Xie R, Grisham SY, Peng X. Correlation of CdS nanocrystal formation with elemental sulfur activation and its implication in synthetic development. *J Am Chem Soc.* 2011;133:17248–56. <https://doi.org/10.1021/ja204538f>.
31. Bullen C, van Embden J, Jasieniak J, Cosgriff JE, Mulder RJ, Rizzardo E, Gu M, Raston CL. High activity phosphine-free selenium precursor solution for semiconductor nanocrystal growth. *Chem Mater.* 2010;22:4135–43. <https://doi.org/10.1021/cm903813r>.
32. Sung TW, Lo YL. Ammonia vapor sensor based on CdSe/SiO<sub>2</sub> core-shell nanoparticles embedded in sol-gel matrix. *Sensors Actuators B Chem.* 2013;188:702–8. <https://doi.org/10.1016/j.snb.2013.07.040>.
33. Chizhov AS, Rumyantseva MN, Vasiliev RB, Filatov DG, Drozdov KA, Krylov IV, Abakumov AM, Gaskov AM. Visible light activated room temperature gas sensors based on nanocrystalline ZnO sensitized with CdSe quantum dots. *Sensors Actuators B Chem.* 2014;205:305–12. <https://doi.org/10.1016/j.snb.2014.08.091>.
34. Chizhov A, Vasiliev R, Rumyantseva M, Krylov I, Drozdov K, Batuk M, Hadermann J, Abakumov A, Gaskov A. Light-activated sub-ppm NO<sub>2</sub> detection by hybrid ZnO/QD nanomaterials vs. charge localization in core-shell QD. *Front Mater.* 2019;6:231. <https://doi.org/10.3389/fmats.2019.00231>.
35. Chizhov A, Rumyantseva M, Vasiliev R, Filatova D, Drozdov K, Krylov I, Marchevsky A, Karakulina O, Abakumov A, Gaskov A. Visible light activation of room temperature NO<sub>2</sub>

- gas sensors based on ZnO, SnO<sub>2</sub> and In<sub>2</sub>O<sub>3</sub> sensitized with CdSe quantum dots. *Thin Solid Films*. 2016;618:253–62. <https://doi.org/10.1016/j.tsf.2016.09.029>.
36. Li LS, Pradhan N, Wang Y, Peng X. High quality ZnSe and ZnS nanocrystals formed by activating zinc carboxylate precursors. *Nano Lett*. 2004;4:2261–4. <https://doi.org/10.1021/nl048650e>.
  37. Pradhan N, Peng X. Efficient and color-tunable Mn-doped ZnSe nanocrystal emitters: control of optical performance via greener synthetic chemistry. *J Am Chem Soc*. 2007;129:3339–47. <https://doi.org/10.1021/ja068360v>.
  38. Pradhan N, Goorskey D, Thessing J, Peng X. An alternative of CdSe nanocrystal emitters: pure and tunable impurity emissions in ZnSe nanocrystals. *J Am Chem Soc*. 2005;127:17586–7. <https://doi.org/10.1021/ja055557z>.
  39. Hines MA, Guyot-Sionnest P. Bright UV-blue luminescent colloidal ZnSe Nanocrystals. *J Phys Chem B*. 1998;102:3655–7. <https://doi.org/10.1021/jp9810217>.
  40. van Embden J, Chesman ASR, Jasieniak JJ. The heat-up synthesis of colloidal nanocrystals. *Chem Mater*. 2015;27:2246–85. <https://doi.org/10.1021/cm5028964>.
  41. Yang YA, Wu H, Williams KR, Cao YC. Synthesis of CdSe and CdTe nanocrystals without precursor injection. *Angew Chem Int Ed*. 2005;44:6712–5. <https://doi.org/10.1002/anie.200502279>.
  42. Ouyang J, Vincent M, Kingston D, Descours P, Boivineau T, Zaman MB, Wu X, Yu K. Noninjection, one-pot synthesis of photoluminescent colloidal homogeneously alloyed CdSeS quantum dots. *J Phys Chem C*. 2009;113:5193–200. <https://doi.org/10.1021/jp8110138>.
  43. Jia J, Tian J, Mi W, Tian W, Liu X, Dai J, Wang X. Growth kinetics of CdSe nanocrystals synthesized in liquid paraffin via one-pot method. *J Nanopart Res*. 2013;15:1724. <https://doi.org/10.1007/s11051-013-1724-0>.
  44. Park E, Ryu J, Choi Y, Hwang KJ, Song R. Photochemical properties and shape evolution of CdSe QDs in a non-injection reaction. *Nanotechnology*. 2013;24:145601. <https://doi.org/10.1088/0957-4484/24/14/145601>.
  45. Zhu CQ, Wang P, Wang X, Li Y. Facile phosphine-free synthesis of CdSe/ZnS Core/Shell nanocrystals without precursor injection. *Nanoscale Res Lett*. 2008;3:213. <https://doi.org/10.1007/s11671-008-9139-z>.
  46. Zhuang Z, Lu X, Peng Q, Li Y. A facile “dispersion–decomposition” route to metal sulfide nanocrystals. *Chem Eur J*. 2011;17:10445–52. <https://doi.org/10.1002/chem.201101145>.
  47. Liu Y, Tang Y, Ning Y, Li M, Zhang H, Yanga B. “One-pot” synthesis and shape control of ZnSe semiconductor nanocrystals in liquid paraffin. *J Mater Chem*. 2010;20:4451–8. <https://doi.org/10.1039/C0JM00115E>.
  48. Zhang J, Sun K, Kumbhar A, Fang J. Shape-control of ZnTe nanocrystal growth in organic solution. *J Phys Chem C*. 2008;112:5454–8. <https://doi.org/10.1021/jp711778u>.
  49. Zhong H, Zhou Y, Ye M, He Y, Ye J, He C, Yang C, Li Y. Controlled synthesis and optical properties of colloidal ternary chalcogenide CuInS<sub>2</sub> nanocrystals. *Chem Mater*. 2008;20:6434–43. <https://doi.org/10.1021/cm8006827>.
  50. Liao HC, Jao MH, Shyue JJ, Chen YF, Su WF. Facile synthesis of wurtzite copper–zinc–tin sulfide nanocrystals from plasmonic djurleite nuclei. *J Mater Chem A*. 2013;1:337–41. <https://doi.org/10.1039/C2TA00151A>.
  51. Choi CL, Alivisatos AP. From artificial atoms to nanocrystal molecules: preparation and properties of more complex nanostructures. *Annu Rev Phys Chem*. 2010;61:369–89. <https://doi.org/10.1146/annurev.physchem.012809.103311>.
  52. Carbone L, Cozzoli PD. Colloidal heterostructured nanocrystals: synthesis and growth mechanisms. *Nano Today*. 2010;5:449–93. <https://doi.org/10.1016/j.nantod.2010.08.006>.
  53. Oh MH, Cho MG, Chung DY, Park I, Kwon YP, Ophus C, Kim D, Kim MG, Jeong B, Gu XW, Jo J, Yoo JM, Hong J, McMains S, Kang K, Sung YE, Alivisatos AP, Hyeon T. Design and synthesis of multigrain nanocrystals via geometric misfit strain. *Nature*. 2020;577:359–63. <https://doi.org/10.1038/s41586-019-1899-3>.



54. Costi R, Saunders AE, Banin U. Colloidal hybrid nanostructures: a new type of functional materials. *Angew Chem Int Ed*. 2010;49:4878–97. <https://doi.org/10.1002/anie.200906010>.
55. Schartl W. Current directions in core–shell nanoparticle design. *Nanoscale*. 2010;2:829–43. <https://doi.org/10.1039/C0NR00028K>.
56. Reiss P, Protière M, Li L. Core/shell semiconductor nanocrystals. *Small*. 2009;5:154–68. <https://doi.org/10.1002/smll.200800841>.
57. Li JJ, Tsay JM, Michalet X, Weiss S. Wavefunction engineering: from quantum wells to near-infrared type-II colloidal quantum dots synthesized by layer-by-layer colloidal epitaxy. *Chem Phys*. 2005;318:82–90. <https://doi.org/10.1016/j.chemphys.2005.04.029>.
58. Blackman B, Battaglia DM, Mishima TD, Johnson MB, Peng X. Control of the morphology of complex semiconductor nanocrystals with a type II heterojunction, dots vs peanuts, by thermal cycling. *Chem Mater*. 2007;19:3815–21. <https://doi.org/10.1021/cm0704682>.
59. Li JJ, Wang YA, Guo W, Keay JC, Mishima TD, Johnson MB, Peng X. Large-scale synthesis of nearly monodisperse CdSe/CdS core/shell nanocrystals using air-stable reagents via successive ion layer adsorption and reaction. *J Am Chem Soc*. 2003;125:12567–75. <https://doi.org/10.1021/ja0363563>.
60. Dun M, Tan J, Tan W, Tang M, Huang X. CdS quantum dots supported by ultrathin porous nanosheets assembled into hollowed-out Co<sub>3</sub>O<sub>4</sub> microspheres: a room-temperature H<sub>2</sub>S gas sensor with ultra-fast response and recovery. *Sensors Actuators B Chem*. 2019;298:126839. <https://doi.org/10.1016/j.snb.2019.126839>.
61. Yoshimura M, Byrappa K. Hydrothermal processing of materials: past, present and future. *J Mater Sci*. 2008;43:2085–103. <https://doi.org/10.1007/s10853-007-1853-x>.
62. Sun J, Sun L, Han N, Chu H, Bai H, Shu X, Luo R, Chen A. rGO decorated CdS/CdO composite for detection of low concentration NO<sub>2</sub>. *Sensors Actuators B Chem*. 2019;299:126832. <https://doi.org/10.1016/j.snb.2019.126832>.
63. Shao S, Che L, Chen Y, Lai M, Huang S, Koehn R. A novel RGO-MoS<sub>2</sub>-CdS nanocomposite film for application in the ultrasensitive NO<sub>2</sub> detection. *J Alloys Compd*. 2019;774:1–10. <https://doi.org/10.1016/j.jallcom.2018.09.271>.
64. Liu W, Gu D, Li X. Detection of ppb-level NO<sub>2</sub> using mesoporous ZnSe/SnO<sub>2</sub> core-shell microspheres based chemical sensors. *Sensors Actuators B Chem*. 2020;320:128365. <https://doi.org/10.1016/j.snb.2020.128365>.
65. Chen Q, Ma SY, Xu XL, Jiao HY, Zhang GH, Liu LW, Wang PY, Gengzang DJ, Yao HH. Optimization ethanol detection performance manifested by gas sensor based on In<sub>2</sub>O<sub>3</sub>/ZnS rough microspheres. *Sensors Actuators B Chem*. 2018;264:263–78. <https://doi.org/10.1016/j.snb.2018.02.172>.
66. Laatar F. Synthesis of the PS/CdSeNRs composite for room temperature NO<sub>2</sub> gas sensing. *SILICON*. 2021;13:4155–62. <https://doi.org/10.1007/s12633-020-00646-4>.
67. Li M, Ren W, Wu R, Zhang M. CeO<sub>2</sub> enhanced ethanol sensing performance in a CdS gas sensor. *Sensors*. 2017;17:1577. <https://doi.org/10.3390/s17071577>.
68. Zhang N, Ma X, Yin Y, Chen Y, Li C, Yin J, Ruan S. Synthesis of CuO–CdS composite nanowires and their ultrasensitive ethanol sensing properties. *Inorg Chem Front*. 2019;6:238–47. <https://doi.org/10.1039/c8qi00951a>.
69. Zhai J, Wang L, Wang D, Li H, Zhang Y, He D, Xie T. Enhancement of gas sensing properties of CdS nanowire/ZnO nanosphere composite materials at room temperature by visible-light activation. *ACS Appl Mater Interfaces*. 2011;3:2253–8. <https://doi.org/10.1021/am200008y>.
70. Hieu NM, Lam DV, Hien TT, Chinh ND, Quang ND, Hung NM, Phuoc CV, Lee SM, Jeong JR, Kim C, Kim D. ZnTe-coated ZnO nanorods: hydrogen sulfide nano-sensor purely controlled by pn junction. *Mater Design*. 2020;191:108628. <https://doi.org/10.1016/j.matdes.2020.108628>.
71. Liang YC, Xu NC. Synthesis of TiO<sub>2</sub>-ZnS nanocomposites via sacrificial template sulfidation and their ethanol gas-sensing performance. *RSC Adv*. 2018;8:22437. <https://doi.org/10.1039/c8ra04157a>.

72. Hasani A, Dehsari HS, Zarandi AA, Salehi A, Taromi FA, Kazeroni H. Visible light-assisted photoreduction of graphene oxide using CdS nanoparticles and gas sensing properties. *J Nanomater.* 2015;2015:930306. <https://doi.org/10.1155/2015/930306>.
73. Han Y, Liu Y, Su C, Wang S, Li H, Zeng M, Hu N, Su Y, Zhou Z, Wei H, Yang Z. Interface engineered WS<sub>2</sub>/ZnS heterostructures for sensitive and reversible NO<sub>2</sub> room temperature sensing. *Sensors Actuators B Chem.* 2019;296:126666. <https://doi.org/10.1016/j.snb.2019.126666>.
74. Gad AE, Hoffmann M, Leuning T, Prades JD, Hernandez-Ramirez F, Shen H, Mathur S. Solar Driven Zinc Oxide Based Heterojunctions for Gas Sensing Applications. In: Proceedings of 14th Meeting on Chemical Sensors-IMCS 2012, 1312–1315, 20–23.05.2012, Nürnberg, Germany; 2012. <https://doi.org/10.5162/IMCS2012/P2.0.16>.
75. Zhai J, Wang D, Peng L, Lin Y, Li X, Xie T. Visible-light-induced photoelectric gas sensing to formaldehyde based on CdS nanoparticles/ZnO heterostructures. *Sensors Actuators B Chem.* 2010;147:234–40. <https://doi.org/10.1016/j.snb.2010.03.003>.
76. Geng J, Jia XD, Zhu JJ. Sonochemical selective synthesis of ZnO/CdS core/shell nanostructures and their optical properties. *CrystEngComm.* 2011;13:193–8. <https://doi.org/10.1039/c0ce00180e>.
77. Palanisamy B, Paul B, Chang C. The synthesis of cadmium sulfide nanoplatelets using a novel continuous flow sonochemical reactor. *Ultrason Sonochem.* 2015;26:452–60. <https://doi.org/10.1016/j.ultrasonch.2015.01.004>.
78. Ghows N, Entezari MH. A novel method for the synthesis of CdS nanoparticles without surfactant. *Ultrason Sonochem.* 2011;18:269–75. <https://doi.org/10.1016/j.ultrasonch.2010.06.008>.
79. Villani M, Calestani D, Lazzarini L, Zanotti L, Mosca R, Zappettini A. Extended functionality of ZnO nanotetrapods by solution-based coupling with CdS nanoparticles. *J Mater Chem.* 2012;22:5694–9. <https://doi.org/10.1039/c2jm16164h>.
80. De Guire MR, Bauermann LP, Parikh H, Bill J. Chapter 14: Chemical bath deposition. In: Schneller T, Waser R, Kosec M, Payne D, editors. Chemical solution deposition of functional oxide thin films. Vienna: Springer; 2013. p. 319–39. [https://doi.org/10.1007/978-3-211-99311-8\\_14](https://doi.org/10.1007/978-3-211-99311-8_14).
81. Jaiswal J, Sanger A, Tiwari P, Chandra R. MoS<sub>2</sub> hybrid heterostructure thin film decorated with CdTe quantum dots for room temperature NO<sub>2</sub> gas sensor. *Sensors Actuators B Chem.* 2020;305:127437. <https://doi.org/10.1016/j.snb.2019.127437>.
82. Jaiswal J, Singh P, Chandra R. Low-temperature highly selective and sensitive NO<sub>2</sub> gas sensors using CdTe-functionalized ZnO filled porous Si hybrid hierarchical nanostructured thin films. *Sensors Actuators B Chem.* 2021;327:128862. <https://doi.org/10.1016/j.snb.2020.128862>.
83. Kar S, Chaudhuri S. Shape selective growth of CdS one-dimensional nanostructures by a thermal evaporation process. *J Phys Chem B.* 2006;110:4542–7. <https://doi.org/10.1021/jp056058n>.
84. Park S, Sun GJ, Kheel H, Ko T, Kim HW, Lee C. Light-activated NO<sub>2</sub> gas sensing of the networked CuO-decorated ZnS nanowire gas sensor. *Appl Phys A Mater Sci Process.* 2016;122:504. <https://doi.org/10.1007/s00339-016-0042-7>.
85. Kim KK, Kim D, Kang SH, Park S. Detection of ethanol gas using In<sub>2</sub>O<sub>3</sub> nanoparticle-decorated ZnS nanowires. *Sensors Actuators B Chem.* 2017;248:43–9. <https://doi.org/10.1016/j.snb.2017.03.120>.
86. Zhang Q, Li H, Ma Y, Zhai T. ZnSe nanostructures: synthesis, properties and applications. *Prog Mater Sci.* 2016;83:472–535. <https://doi.org/10.1016/j.pmatsci.2016.07.005>.
87. Yoon YJ, Park KS, Heo JH, Park JG, Nahm S, Choi KJ. Synthesis of Zn<sub>x</sub>Cd<sub>1-x</sub>Se (0 ≤ x ≤ 1) alloyed nanowires for variable-wavelength photodetectors. *J Mater Chem.* 2010;20:2386–90. <https://doi.org/10.1039/b917531h>.
88. Park S, Kim S, Lee WI, Kim KK, Lee C. Room temperature, ppb-level NO<sub>2</sub> gas sensing of multiple networked ZnSe nanowire sensors under UV illumination. *Beilstein J Nanotechnol.* 2014;5:1836–41. <https://doi.org/10.3762/bjnano.5.194>.

89. Wang X, Xie Z, Huang H, Liu Z, Chen D, Shen G. Gas sensors, thermistor and photodetector based on ZnS nanowires. *J Mater Chem*. 2012;22:6845–50. <https://doi.org/10.1039/c2jm16523f>.
90. Park S, Kim S, Ko H, Lee C. Light-enhanced gas sensing of ZnS-core/ZnO-shell nanowires at room temperature. *J Electroceram*. 33:75–81. <https://doi.org/10.1007/s10832-014-9923-3>.
91. Larramona G, Choné C, Jacob A, Sakakura D, Delatouche B, Péré D, Cieren X, Nagino M, Bayón R. Nanostructured photovoltaic cell of the type titanium dioxide, cadmium sulfide thin coating, and copper thiocyanate showing high quantum efficiency. *Chem Mater*. 2006;18:1688–96. <https://doi.org/10.1021/cm052819n>.
92. Guijarro N, Lana-Villarreal T, Shen Q, Toyoda T, Gómez R. Sensitization of titanium dioxide photoanodes with cadmium selenide quantum dots prepared by SILAR: Photoelectrochemical and carrier dynamics studies. *J Phys Chem C*. 2010;114:21928–37. <https://doi.org/10.1021/jp105890x>.
93. Lee W, Min SK, Dhas V, Ogale SB, Han SH. Chemical bath deposition of CdS quantum dots on vertically aligned ZnO nanorods for quantum dots-sensitized solar cells. *Electrochem Commun*. 2009;11:103–6. <https://doi.org/10.1016/j.elecom.2008.10.042>.
94. Gad A, Hoffmann MWG, Prades JD, Hernandez-Ramirez F, Fiz R, Shen H, Mathur S, Waag A. Self-Powered Solar Diode Gas Sensors. Extended Abstracts of the 2014 International Conference on Solid State Devices and Materials, Tsukuba; 2014, pp. 572–573. <https://doi.org/10.7567/SSDM.2014.D-1-4>
95. Laera AM, Mirengi L, Cassano G, Capodici L, Ferrara MC, Mazzarelli S, Schioppa M, Dimiao D, Rizzo A, Penza M, Tapfer L. Synthesis of nanocrystalline ZnS/TiO<sub>2</sub> films for enhanced NO<sub>2</sub> gas sensing. *Thin Solid Films*. 2020;709:138190. <https://doi.org/10.1016/j.tsf.2020.138190>.
96. Liu W, Gu D, Li X. Ultrasensitive NO<sub>2</sub> detection utilizing mesoporous ZnSe/ZnO heterojunction-based chemiresistive-type sensors. *ACS Appl Mater Interfaces*. 2019;11:29029–40. <https://doi.org/10.1021/acsami.9b07263>.
97. Yu XL, Ji HM, Wang HL, Sun J, Du XW. Synthesis and sensing properties of ZnO/ZnS nanocages. *Nanoscale Res Lett*. 2010;5:644–8. <https://doi.org/10.1007/s11671-010-9528-y>.
98. Zhang W, Wang S, Wang Y, Zhu Z, Gao X, Yang J, Zhang H. ZnO@ZnS core/shell microrods with enhanced gas sensing properties. *RSC Adv*. 2015;5:2620–9. <https://doi.org/10.1039/c4ra12803f>.
99. Vasiliev R, Babynina A, Maslova O, Rumyantseva M, Ryabova L, Dobrovolsky A, Drozdov K, Khokhlov D, Abakumov A, Gaskov A. Photoconductivity of nanocrystalline SnO<sub>2</sub> sensitized with colloidal CdSe quantum dots. *J Mater Chem C*. 2013;1:1005–10. <https://doi.org/10.1039/c2tc00236a>.
100. Bley S, Diez M, Albrecht F, Resch S, Waldvogel SR, Menzel A, Zacharias M, Gutowski J, Voss T. Electron tunneling from colloidal CdSe quantum dots to ZnO Nanowires studied by time-resolved luminescence and photoconductivity experiments. *J Phys Chem C*. 2015;119:15627–35. <https://doi.org/10.1021/acs.jpcc.5b01392>.
101. Liu W, Gu D, Zhang JW, Li XG, Rumyantseva MN, Gaskov AM. ZnSe/NiO heterostructure-based chemiresistive-type sensors for low-concentration NO<sub>2</sub> detection. *Rare Metals*. 2021;40:1632–41. <https://doi.org/10.1007/s12598-020-01564-5>.
102. He P, Fu H, Yang X, Xiong S, Han D, An X. Variable gas sensing performance towards different volatile organic compounds caused by integration types of ZnS on In<sub>2</sub>O<sub>3</sub> hollow spheres. *Sensors Actuators B Chem*. 2021;345:130316. <https://doi.org/10.1016/j.snb.2021.130316>.
103. Rumyantseva M, Kovalenko V, Gaskov A, Makshina E, Yuschenko V, Ivanova I, Ponzoni A, Faglia G, Comini E. Nanocomposites SnO<sub>2</sub>/Fe<sub>2</sub>O<sub>3</sub>: sensor and catalytic properties. *Sensors Actuators B Chem*. 2006;118:208–14. <https://doi.org/10.1016/j.snb.2006.04.024>.
104. Vladimirova SA, Rumyantseva MN, Filatova DG, Chizhov AS, Khmelevsky NO, Konstantinova EA, Kozlovsky VF, Marchevsky AV, Karakulina OM, Hadermann J, Gaskov AM. Cobalt location in p-CoO<sub>x</sub>/n-SnO<sub>2</sub> nanocomposites: correlation with gas sensor performances. *J Alloys Compd*. 2017;721:249–60. <https://doi.org/10.1016/j.jallcom.2017.05.332>.

105. Chizhov A, Rumyantseva M, Gaskov A. Light activation of nanocrystalline metal oxides for gas sensing: principles, achievements, challenges. *Nanomaterials*. 2021;11:892. <https://doi.org/10.3390/nano11040892>.
106. Hou D, Dev A, Frank K, Rosenauer A, Voss T. Oxygen-controlled photoconductivity in ZnO nanowires functionalized with colloidal CdSe quantum dots. *J Phys Chem C*. 2012;116:19604–10. <https://doi.org/10.1021/jp307235u>.
107. Drozdov KA, Kochnev VI, Dobrovolsky AA, Popelo AV, Rumyantseva MN, Gaskov AM, Ryabova LI, Khokhlov DR, Vasiliev RB. Photoconductivity of structures based on the SnO<sub>2</sub> porous matrix coupled with core-shell CdSe/CdS quantum dots. *Appl Phys Lett*. 2013;103:133115. <https://doi.org/10.1063/1.4823549>.
108. Zhang Q, Ma S, Zhang R, Zhu K, Tie Y, Pei S. Optimization NH<sub>3</sub> sensing performance manifested by gas sensor based on Pr-SnS<sub>2</sub>/ZnS hierarchical nanoflowers. *J Alloys Compd*. 2019;807:151650. <https://doi.org/10.1016/j.jallcom.2019.151650>.

# Chapter 9

## II–VI Semiconductor-Polymer Nanocomposites and Their Gas-Sensing Properties



Chandan Kumar, Satyabrata Jit, Sumit Saxena, and Shobha Shukla

### 9.1 Introduction

Nanostructured materials have much attracted for electronic and sensing applications due to their tunable properties [1–5]. They are used in the fabrication of electronic devices depending on their conductivity. The nanostructures of conductors, semiconductors and non-conductors (insulators) materials are achieved by either top-down or bottom-up approaches. Top-down approaches are relatively expensive to bottom-up approaches. Semiconductors-based nanostructured materials have been researched mostly due to their tunable conductivity for electronic device applications [6–8]. Further, nanostructured materials are of three types, namely zero-dimensional (0D), one-dimensional (1D) and two-dimensional (2D) structures based on their dimension. These structures have some specific advantages, and accordingly, they are used in electronic devices and sensors. The most important features of semiconductor nanostructures are increased surface-to-volume ratio, bandgap modulation and catalytic behaviour [6, 8]. These features of nanostructure are also advantageous for II–VI compound semiconductors. II–VI compound semiconductors have a structure of MD where M is Cd, Zn and D is S, Se, Te. Other elements of the II–VI group are either not suitable for gas sensors or grouped as metal oxides. Furthermore, the gas-sensing performances of nanostructured II–VI compound semiconductor-based devices are improved through composite with polymers [6, 8–12]. The most preferred uses of pristine polymers are for

---

C. Kumar (✉) · S. Saxena · S. Shukla

Nanostructures Engineering and Modeling Laboratory, Department of Metallurgical Engineering and Materials Science, Indian Institute of Technology Bombay, Mumbai, India  
e-mail: [chandank@iitb.ac.in](mailto:chandank@iitb.ac.in)

S. Jit

Department of Electronics Engineering, Indian Institute of Technology (BHU), Varanasi, India

high-performance flexible electronic devices and sensors [13–17]. The polymers have the advantage of low-temperature processing and are sensitive to low concentrations of hazardous gases. The conducting polymer has the additional advantage of reducing any void in the thin film of nanostructured II–VI semiconductors. In this chapter, various II–VI semiconductor-polymer nanocomposites and their gas-sensing performance are discussed.

## 9.2 Gas Sensors Based on II–VI Compound-Polymer Composites: General Consideration

Gas sensors are used to detect any leakage of hazardous or flammable gases. The gases typically become dangerous after crossing certain concentrations. The danger limit for different gases is shown in Table 9.1. Therefore, it is important to detect the presence of these hazardous gases before the permissible concentration. Gas sensors are designed accordingly for the highest sensitivity towards the target gas. Different types of gases are reported in the literature to detect before the danger limit; however, semiconductor materials-based gas sensors have better controllability and are compatible with electronic circuits. Electronic gas sensors are primarily fabricated using a gas-sensitive semiconductor layer as the main active component. The gas sensors are fabricated using both inorganic and organic semiconductor materials. Among inorganic materials, II–VI semiconductors and oxides are widely used for the fabrication of gas sensors. In organic materials, polymers have shown excellent sensitivity towards various hazardous gases. The polymer-based gas sensor has the advantage of room temperature sensitivity [13–15, 18–20]. Some II–VI semiconductor nanomaterials have shown room temperature sensitivity to various gases but are very poor. Nanocomposite has the additional advantage of the

**Table 9.1** Different toxic gases and their danger limit

Gases	Permissible exposure limit	Immediate danger to life limit
Ammonia	50 ppm	500 ppm
Nitrogen dioxide	5 ppm	20 ppm
Hydrogen sulphide	10 ppm	100 ppm
Sulphur dioxide	5 ppm	100 ppm
Carbon dioxide	5000 ppm	40,000 ppm
Carbon monoxide	25 ppm	1200 ppm
Hydrogen selenide	0.05 ppm	1 ppm
Nitric oxide	25 ppm	100 ppm
Nitrous oxide	50 ppm	–
Phosphine	0.3 ppm	50 ppm
Propane	1000 ppm	–
Silane	5 ppm	–

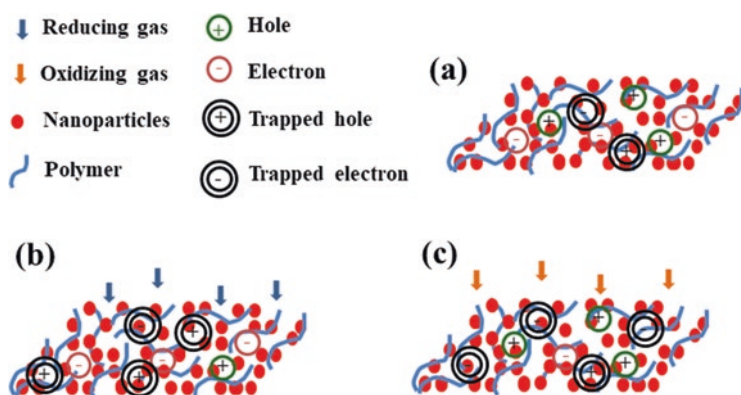
Source: Data extracted from [23]

controllability and selectivity for target gases through variation in the amount of II–VI compounds/polymer and size of nanomaterials. Nanocomposite-based gas sensors have improved sensitivity and selectivity towards hazardous gases [4, 16, 17, 21, 22]. The general characteristics of II–VI compound-polymer composites-based gas sensors are discussed in the following subsections:

### 9.2.1 Gas-Sensing Mechanism and Measurement Parameters

In an electronic device-based gas sensor, the target gas is adsorbed in the semiconducting layer and a change in physical or/and chemical properties is observed in the semiconducting layer. When gas is exposed to the II–VI compound-polymer composite, the composite interacts with gases and results in physisorption or chemisorption. The gas-sensing mechanism of II–VI semiconductor-polymer nanocomposites-based sensors is illustrated in Fig. 9.1.

The surface of the composite layer is an assembly of II–VI compounds and polymers. The surface of the nanocomposite responds differently to reducing and oxidising gases, as illustrated in Fig. 9.1b, c. If the nanocomposite exhibits dominant p-type conductivity, the reducing gas increase resistivity, whereas oxidising gas reduces resistivity. On the other hand, n-type conductivity dominancy in nanocomposite results in a decrease in resistivity when reducing gas is exposed, whereas resistivity increases with interaction with oxidising gases. Under the exposure of gases, the device parameters of the sensor get changed. The gas sensor performance parameters are evaluated from the change in the device parameters. The interaction process and time taken for a change in the device parameters are crucial for sensor performance. Different gas-sensing parameters and effects of nanocomposite are discussed below:



**Fig. 9.1** Nanomaterial-polymer nanocomposite layers (a) without gas exposure, (b) with exposure to reducing gas and (c) with exposure to oxidising gas. (Adapted with permission from [14]. Copyright 2018: Elsevier)

**Gas Response** The gas response ( $R_G$ ) is the ratio of change in the device parameter (device parameter can be current, voltage, resistance, etc.) to the initial value. The gas response is generally expressed in percentage. The ratio of the device parameter under gas exposure to the initial value is also commonly defined as the gas response. The gas response is mathematically expressed as

$$R_G (\%) = \frac{|I_G - I_0|}{I_0} \times 100\% \approx \frac{|V_G - V_0|}{V_0} \times 100\% \approx \frac{|R_G - R_0|}{R_0} \times 100\% \quad (9.1)$$

Here,  $I_0$ ,  $V_0$  and  $R_0$  are initial (unexposed) current, voltage and resistance, respectively. After interaction with gases, current, voltage and resistance are changed to  $I_G$ ,  $V_G$  and  $R_G$ , respectively. The II–VI semiconductor-polymer nanocomposites have the advantage of higher conductivity and enhanced surface-to-volume ratio. Thus, the change in the sensor current after gas exposure is relatively higher, and so is the gas response.

**Sensitivity** The sensitivity ( $S$ ) of a gas sensor is defined as the ratio of gas response to the concentration of gas exposed. It is the slope of the calibration curve of gas response over the gas concentration. It is expressed in per ppm (or ppb) of the target gas. The amount of II–VI compound/polymer and size of nanomaterials are generally optimised for the improvement in the gas sensitivity. The sensitivity increases with an increase in the gas response.

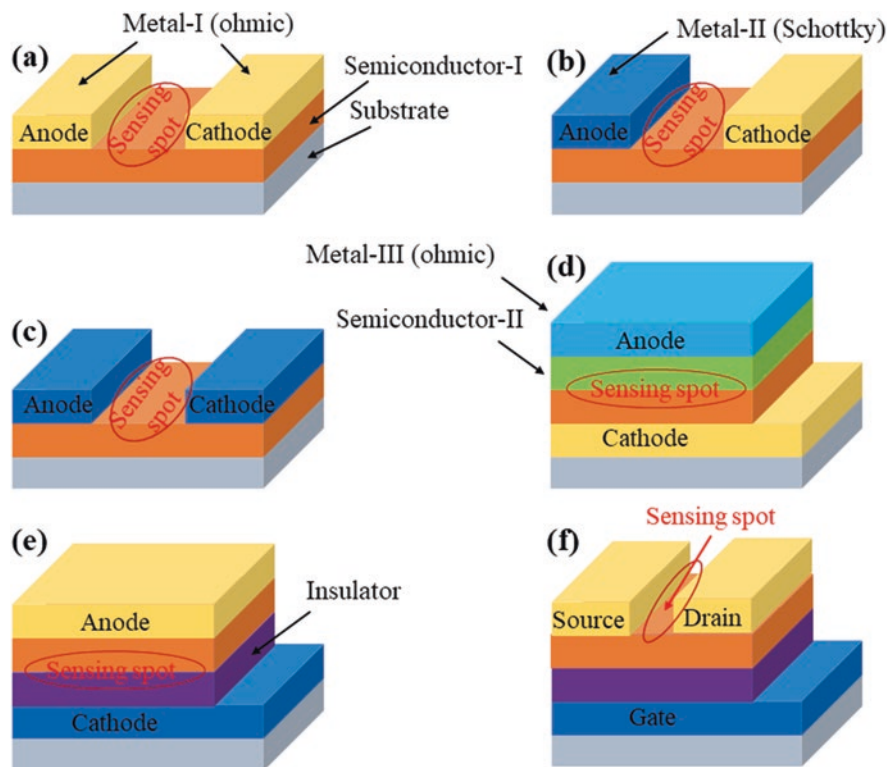
**Selectivity** The selectivity ( $S_L$ ) tells about the sensitivity towards the target gas over other interference gases. The selectivity is expressed as the ratio of gas response towards the target gas to the interference gases. It should be much higher (typically more than 5) for better gas-sensing performance. It is observed that the selectivity towards specific gas can be improved by varying the II–VI compounds/polymer ratio, size of the nanomaterials and distribution of nanomaterials.

**Response and Recovery Time** The response time is the time taken by the sensor to reach 90% of the gas response from the unexposed condition, whereas the recovery time is the time taken by the sensor to reach 10% of gas response from 100% of the gas response. The response and recovery should be as low as possible for the fast sensor. II–VI semiconductor-polymer nanocomposites provide a better site for fast gas adsorption and de-adsorption, which result in fast response and recovery.

**Detection Limit** Detection limit or limit of detection (LOD) specify the minimum concentration of target gas detectable by the sensor. It is either experimentally measured by exposing the smallest possible concentration or calculated from the calibration curve of gas response over the gas concentration. The enhanced gas sensitivity in II–VI semiconductor-polymer nanocomposites has also resulted in the improvement in detection limit.



The performance parameters of the gas sensors are improved through various device structures of the gas sensors. Commonly, metal (ohmic)-semiconductor-(ohmic) metal, metal (Schottky)-semiconductor-(ohmic) metal, metal (Schottky)-semiconductor-(Schottky) metal, hetero/homo structure, capacitor (metal-insulator-semiconductor-metal) and transistor are used for the gas sensors. The device structures for the gas sensor are shown in Fig. 9.2. Figure 9.2a–e illustrate two-terminal devices (with anode and cathode), and Fig. 9.2f illustrates a three-terminal device (with gate, source and drain). Devices in Fig. 9.2a–c, f are called horizontal structures, whereas devices in Fig. 9.2d, e are called vertical devices. The exposed gases interact with the sensor devices at the sensing spot marked in Fig. 9.2a–f, and the adsorption of gases results in the change in an electrical parameter of the devices. The internal gain in two-terminal devices (Schottky and hetero/homo structure) is relatively lower, whereas field-effect gain in a three-terminal device (transistor structure) is higher, provides much improvement in the gas response.



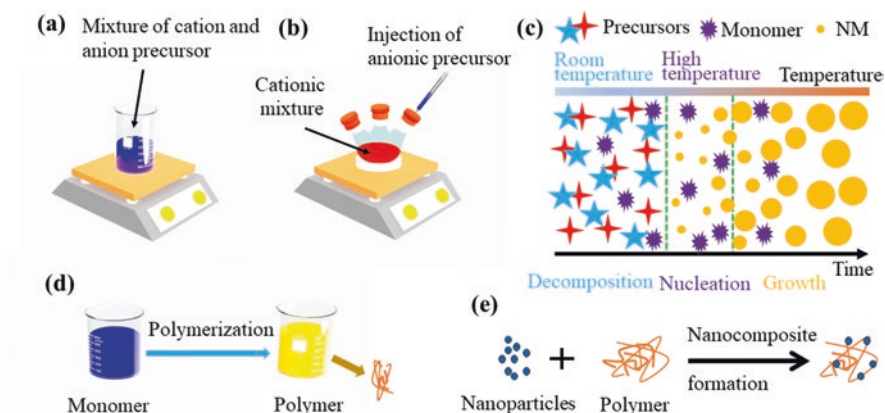
**Fig. 9.2** Different device structures for gas sensor: (a) metal (ohmic)-semiconductor- (ohmic) metal, (b) metal (Schottky)-semiconductor- (ohmic) metal, (c) metal (Schottky)-semiconductor-(Schottky) metal, (d) hetero/homo structure, (e) capacitor (metal-insulator-semiconductor) and (f) transistor

### ***9.2.2 Role of II–VI Semiconductor Nanoparticle and Polymer Concentration in Composite***

Various II–VI compound semiconductor nanomaterials and polymers are considered for the fabrication of gas sensors. II–VI semiconductors have higher atmospheric stability and sensitivity towards hazardous gases. After blending with the polymer, the II–VI compound semiconductor-polymer nanocomposites exhibit improved selectivity and sensitivity at room temperature operation. The size and structure of nanomaterials in the composites play a crucial role in the determination of their characteristics [16]. It is observed that the distribution of CdSe nanoparticles over the P3HT polymer results in increased current density in the nanocomposite-based electronic devices [24]. The improvement in current density is possible due to the development of the internal electric field and reduction in trap density. Similarly, the charge carrier transport in the PVK polymer is also improved by the incorporation of CdSe nanoparticles [25]. At a certain concentration of CdSe nanoparticles, the nanocomposites of CdSe and PVK exhibit a strong current increase due to charge capturing in the CdSe and degraded charge carrier transport if the excess concentration of CdSe nanoparticles is mixed. For performance improvement, binanoparticles are also used for the realisation of nanocomposites. The incorporation of CdSe nanoparticles and CdTe nanoparticles in the polymer matrix of polyaniline (PANI) resulted in PL quenching and improved optoelectronic properties [26]. The nanocomposites of CdS and PVA exhibit negative differential resistance in the current-voltage characteristics due to the formation of junction-like CdS/PVA nanocomposites [27]. Biswas et al. have also found similar behaviour in the nanocomposite made of CdS and MEH-PPV polymer [28]. The tailorable performance in the nanocomposites is possible due to the size-dependent quantum confinement offered by quantum dots (QDs) [29, 30]. The amount of the polymer also modifies the surface behaviour of the nanocomposites.

### ***9.2.3 Methods for the Formation of II–VI Compounds-Polymer Nanocomposite***

Various techniques are developed by researchers for the synthesis of II–VI semiconductor-polymer nanocomposites. Some techniques include in-situ synthesis, whereas some are based on the mixing or blending of II–VI semiconductors and polymers [31]. The general process for the synthesis of II–VI semiconductor-polymer nanocomposite is illustrated in Fig. 9.3. In the first step, II–VI semiconductor nanomaterials and polymers are synthesised separately, as illustrated in Fig. 9.3a, b, d. The II–VI semiconductor nanomaterials are commonly synthesised either at room temperature or at elevated temperature. Room temperature synthesis is based



**Fig. 9.3** (a) Room-temperature synthesis of nanomaterials, (b) Hot injection-based synthesis of nanomaterials, (c) Effect of temperature on the size of nanomaterials, (d) Synthesis process of polymer from monomer and (e) Synthesis of nanomaterial-polymer nanocomposites. Figure 3c is adapted from [32]. Published 2017 by Korea Science as open access.

on chemical reactions at room temperature, and the process is depicted in Fig. 9.3a. In the elevated temperature process, the chemical reaction is controlled at a higher temperature and called as hot injection method. The precursor is added in steps, and the growth of the nanomaterial is controlled by temperature and reaction time, as illustrated in Fig. 9.3b. The effect of synthesis temperature on the size of nanomaterials is shown in Fig. 9.3c. In the second step, an optimised quantity of II–VI semiconductor nanomaterials and polymers are mixed to form a blend (composite) solution, as illustrated in Fig. 9.3e. Depending on the coverage/morphology, nanocomposites are finally obtained. The nanocomposites possess the advantage of both the II–VI semiconductor nanomaterials and polymers.

### 9.3 Gas Sensors Based on II–VI Semiconductor-Polymer Nanocomposites

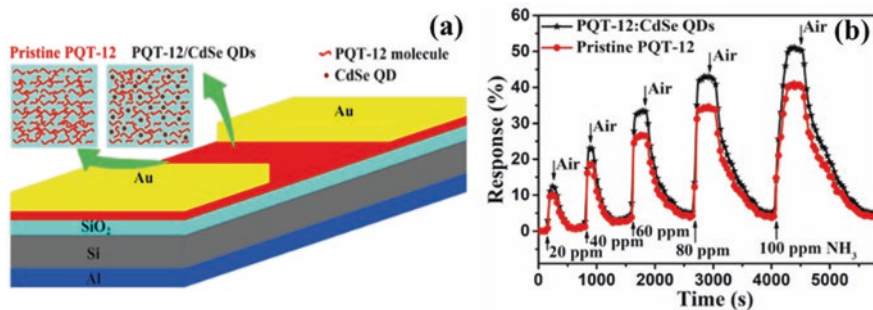
The II–VI semiconductor-polymer nanocomposites provide improvement in the gas-sensing capability. Based on the film formation ability and the sensing performance, various combinations of II–VI semiconductors and polymers are used in the sensor devices. Different types of II–VI semiconductor-polymer nanocomposites-based gas sensors are discussed in the following sub-sections.

### 9.3.1 CdSe-Polymer Nanocomposite

CdSe has shown attractive electronic and sensing characteristics. The nanostructures of CdSe are commonly used for the fabrication of LED, solar cells, photodetectors, tunable gas sensors, etc. The n-CdSe/p-polyaniline heterojunction resulted in the formation of liquefied petroleum gas (LPG) sensor [33]. The sensor has a maximum response of 70% for an LPG concentration of 0.08 vol% at room temperature. In this heterojunction-type sensor, the performance improvement is due to the modified charge transfer characteristics at the junction. The gas-sensing performance is further improved by composting with different materials [33–36]. The nanocomposite of multisized CdSe nanocrystals and PMMA is explored by Potyrailoa and Leach [35]. The sensor device made of nanocomposite is photoactivated and exposed to methanol and toluene. The nanocomposite has shown gas-sensitive optical characteristics. The exposed gas modulates the photoluminescence behaviour of the nanocomposite. The performance is improved further by the formation of bulk heterojunction between n-type CdSe and p-type polymer in the nanocomposites. A multi-material-based nanocomposite made of CdSe/ZnS, polystyrene and polystyrene-*co*-maleic anhydride is also explored for the gas-sensing application [36]. The nanocomposite-based gas sensor has shown sensitivity towards chloroform, DMF and THF. The sensing of gases takes place through the diffusion of gases in the composite, which is commonly explained by the electrical percolation theory [37]. The polymer matrix with nanomaterial is swelled when the reducing gas molecules are diffused in the matrix. As a result, electrical conductivity is reduced because of an increase in the intermolecular distance between nanomaterials in the nanocomposite due to the expansion of the matrix.

CdSe and P3HT-based nanocomposites have shown excellent room temperature sensitivity towards chloroform vapour [38]. The improved sensing of chloroform happens due to the chemical modulation at the bulk-heterojunction surface interface. Here, chloroform is a strong reducing agent, so after interaction with the nanocomposite of CdSe and P3HT, it reduces the sensor current. It is also found that the sensor current is increased with increasing the loading of the CdSe; however, higher loading of CdSe reduces the sensing performance. Weak electron acceptor gases like toluene, acetone, propanol, etc., generally have a low effect on the conductivity of the CdSe/P3HT nanocomposites.

Nanocomposite made of PQT-12 and CdSe QDs has also shown improvement in the ammonia gas response compared to pristine PQT-12-based sensors [39]. The incorporation of CdSe QDs in the PQT-12 polymer framework improved the charge transport capability due to a decrease in the trap density. Additionally, the HOMO/LUMO level mismatch between PQT-12 and CdSe QDs provides an internal electric field to drive the charge carrier for improvement in the overall conductivity. The exposed ammonia gas donates lone pair to the pristine PQT-12 and CdSe QD/PQT-12 nanocomposite sensing layer in an organic thin-film transistor (OTFT), as shown in Fig. 9.4a. The lone pair of electrons disturb the PQT-12 chain and charge carrier density. As a result, the hole concentration in the nanocomposite is reduced,

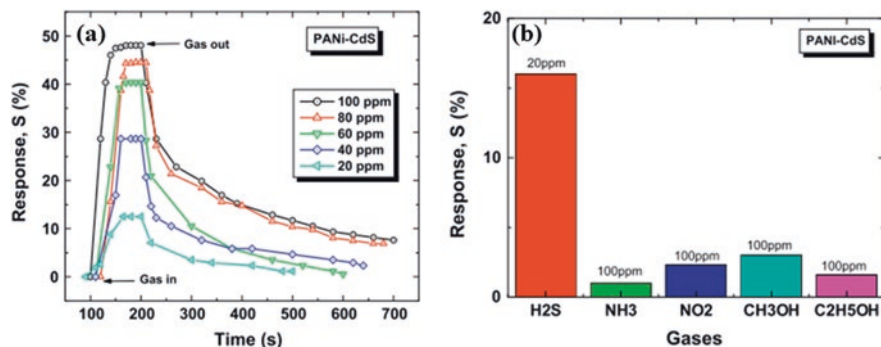


**Fig. 9.4** (a) Device structure of OTFT sensor using pristine PQT-12 and PQT-12-CdSe QDs nanocomposite; (b) Gas response of pristine PQT-12 and PQT-12-CdSe QDs nanocomposite sensor for different concentrations of NH<sub>3</sub> gas. (Reprinted with permission from [39]. Copyright 2018: IEEE)

and so is the drain current in the OTFT sensor. The loading of the CdSe in composite increases the surface area to volume ratio for the interaction with ammonia gas. The loading of 50% CdSe QDs in the PQT-12 polymer framework results in enhanced electrical and ammonia gas-sensing characteristics. The ammonia gas response was about 25% more in PQT-12 and CdSe nanocomposite than the pristine PQT-12. The comparative gas response in pristine PQT-12 and CdSe QDs/PQT-12 nanocomposite-based OTFT sensor is shown in Fig. 9.4b.

### 9.3.2 CdS-Polymer Nanocomposite

The bulk CdS is slightly sensitive to the gases like SO<sub>2</sub>, H<sub>2</sub>S and NH<sub>3</sub>, at room temperature. The gas sensitivity is commonly improved in the CdS nanostructures [40]. The sensitivity towards the target gases is further increased by making nanocomposites with polymers. The gas response enhancement is also achieved in the bilayer heterojunction of polyaniline/CdS [41]. The polyaniline/CdS heterojunction results in a higher LPG gas response compared to only polyaniline or only CdS film. The CdS-polyaniline nanocomposite provides a porous surface for increased gas adsorption in the resistive sensor. Raut et al. have fabricated the CdS-polyaniline nanocomposite-based sensor for H<sub>2</sub>S gas operated at room temperature [42]. Different concentrations of H<sub>2</sub>S gas are exposed at the sensing spot consisting of CdS-polyaniline nanocomposite and the corresponding gas response is measured. The obtained gas response is shown in Fig. 9.5a, and the selectivity of the sensor is shown in Fig. 9.5b. In this work, excellent gas selectivity and sensitivity towards H<sub>2</sub>S gas under room temperature conditions are achieved. The H<sub>2</sub>S gas sensing is also improved by using polymer nanocomposite with bi-nanoparticles. In this design, CdSe/CdS quantum dots are successfully embedded into PDMS film, and H<sub>2</sub>S gas sensing was performed based on the change in fluorescence [43]. Under the exposure of H<sub>2</sub>S gas, significant quenching in fluorescence spectra was observed.

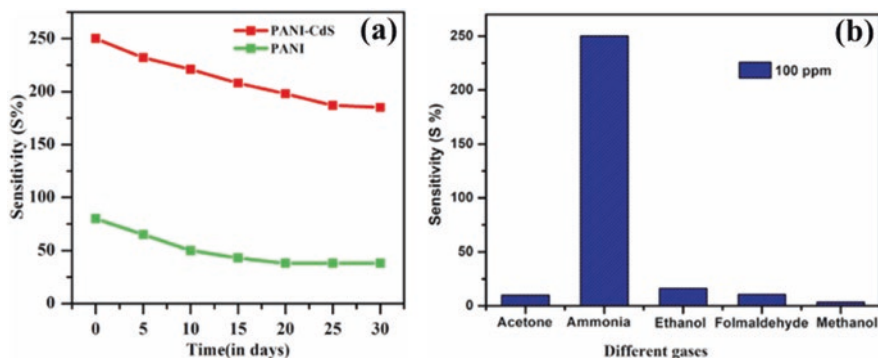


**Fig. 9.5** (a) Gas response of CdS-polyaniline nanocomposite sensor for different concentrations of H<sub>2</sub>S gas. (b) Selectivity characteristics of CdS-polyaniline nanocomposite-based H<sub>2</sub>S sensor. (Reprinted with permission from [42]. Copyright 2012: Elsevier)

The fluorescence quenching increases with the increasing concentration of exposed H<sub>2</sub>S gas. The H<sub>2</sub>S gas adsorption is very fast in this nanocomposite, and the recovery is also fast in the sensor.

PEDOT:PSS polymer over the CdS form nanocomposite, which has enhanced sensitivity towards LPG gas [44]. After exposure to LPG gas, it forms a layer around the nanocomposite and modulates the conductivity of the nanocomposite. The CdS-PEDOT:PSS nanocomposite-based gas sensor exhibits a gas response of 58.9% for 900 ppm of LPG gas when operated at room temperature. Further, CdS is used to make a composite with polypyrrole for the fabrication of an ammonia sensor [45]. CdS-polypyrrole nanocomposite interacted with the reducing ammonia gas and adsorbed the gas. The adsorption of ammonia gas results in a change in the conductivity of the CdS-polypyrrole nanocomposite. A maximum gas response of 4.1 is obtained for 250 ppm of ammonia gas when 3% CdS is used in the nanocomposite [45]. The selective gas response towards ammonia and LPG is tailored by using silver sulphide in the nanocomposite of CdS and polypyrrole [46]. By varying the amount of silver sulphide, CdS and polypyrrole, a maximum selective ammonia gas response is obtained for silver sulphide and CdS of 1:1 ratio.

The gas response and selectivity towards any gas in the CdS-based nanocomposites depend on many factors, including particle size of CdS, the morphology of the nanocomposites, surface defects, film thickness of nanocomposites, ratio of CdS and polymer, rate of chemical reaction at the surface, the diffusion rate of gases, etc. [47, 48]. Therefore, the optimised gas response and the selectivity towards any gas are achieved by tailoring these factors. CdS nanoparticles are decorated over the surface of polyaniline nanorods to achieve a selective high gas response for ammonia gas [47]. The gas response is extremely high in the CdS-polyaniline nanocomposite compared to a pristine polyaniline-based sensor, as shown in Fig. 9.6a. The selectivity is also high towards ammonia, as shown in Fig. 9.6b. The sensing mechanism in pristine polyaniline and CdS-polyaniline nanocomposite is different due to the presence of CdS. The gas sensing in polyaniline is mainly through protonation and



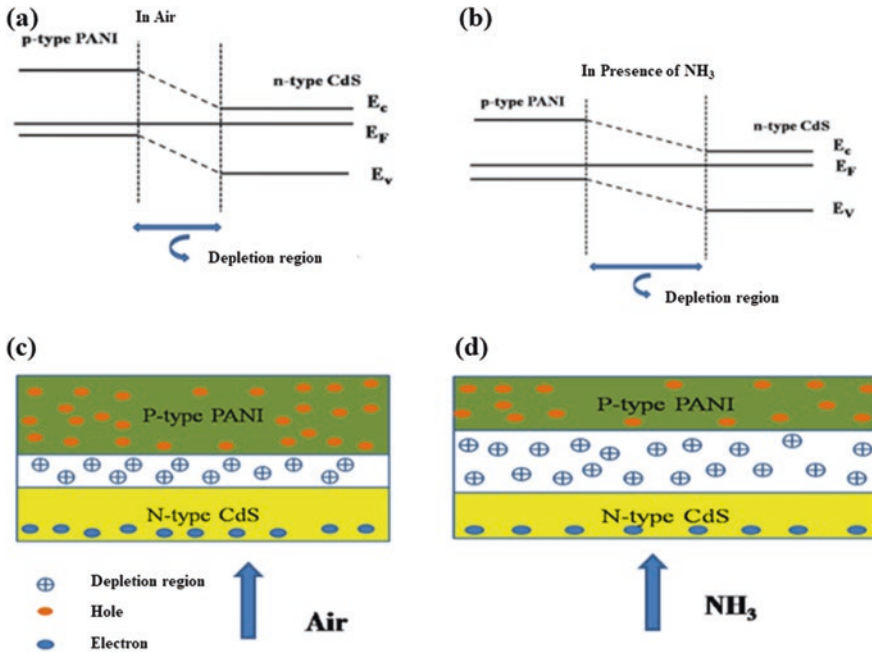
**Fig. 9.6** (a) Time-dependent ammonia gas sensitivity of Polyaniline-CdS nanocomposite sensor, and (b) Selectivity of the Polyaniline-CdS nanocomposite sensor towards ammonia gas. (Reprinted with permission from [47]. Copyright 2020: Elsevier)

deprotonation, which occurs due to the adsorption and desorption of ammonia gas. The reducing ammonia gas reacts with polyaniline and reduces to a non-conductive emeraldine base (from conductive emeraldine salt). The interaction with ammonia results in increased resistance and lower charge carrier density. In the case of the CdS-polyaniline nanocomposite, ammonia gas molecules are trapped and change the surface resistance of the CdS-polyaniline nanocomposite. The n-type CdS and p-type polyaniline form the bulk heterojunction and create a depletion region, as shown in Fig. 9.7 [47]. The depletion region is generally thin (in Fig. 9.7a, c) before ammonia exposure (in the air), but the depletion layer increases (in Fig. 9.7b, d) when ammonia gas is exposed. The ammonia gas increases the electron density and reduces the hole density, which results in an increased barrier at the interface and thus resistance.

Additionally, CdS-polyaniline nanocomposite-based sensor shows enhanced gas response for nitrogen dioxide compared to pristine polyaniline or CdS [49]. The interaction mechanism in the CdS-polyaniline nanocomposite for nitrogen dioxide gas is similar to ammonia gas, but nitrogen dioxide acts as an oxidising agent and reduces resistance. CdS-polyaniline nanocomposite-based sensor is also responsive to the formaldehyde gas [50]. CdS nanorods are grown over the polyaniline nanoparticles using a hydrothermal method in a hexagonal wurtzite structure. CdS-polyaniline nanocomposite-based sensor exhibits a maximum gas response of 4.8 for 5 ppm of formaldehyde gas.

### 9.3.3 CdTe-Polymer Nanocomposite

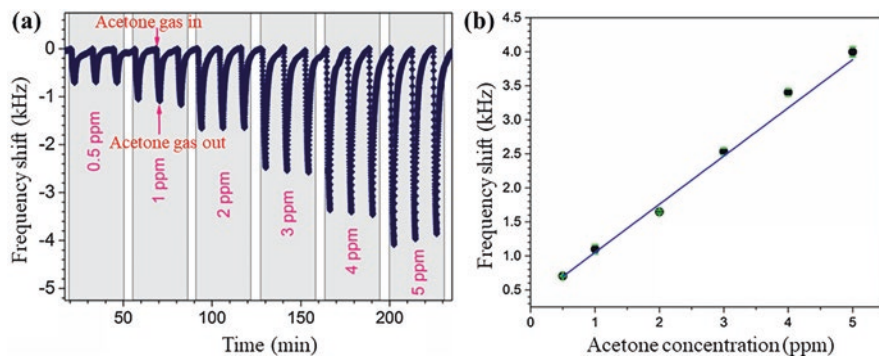
Like other II–VI semiconductors, CdTe is also used for the preparation of nanocomposite with polymers. CdTe-polymer nanocomposite improves the electronic and sensing performance over the pristine polymer or CdTe. It is observed that the



**Fig. 9.7** (a) Band diagram for polyaniline and CdS in air, (b) band diagram for polyaniline and CdS in the presence of ammonia, (c) charge carriers (electron and hole) and ion in depletion region for polyaniline and CdS in air, (d) charge carriers (electron and hole) and ion in depletion region for polyaniline and CdS in the presence of ammonia. (Reprinted with permission from [47]. Copyright 2020: Elsevier)

CdTe-polypyrrole-based nanocomposite improves the sensitivity of the gas sensor towards acetone at room temperature [51]. The acetone sensing by the CdTe-polypyrrole nanocomposite is primarily due to the catalytic behaviour of CdTe QDs and adsorption in polypyrrole, which results in dipole-dipole interaction. The change in frequency for the different concentrations of acetone is shown in Fig. 9.8a. Here, frequency shift increases with an increase in the acetone concentration. The sensitivity and the detection limit of the CdTe-polypyrrole nanocomposite-based sensor are calculated using the calibration curve shown in Fig. 9.8b. Improved sensitivity of 771 Hz/ppm for acetone is achieved in nanocomposite with a detection limit of 5 ppb and the lowest interference from ethanol and toluene. The agglomeration of CdTe QDs on the surface of polypyrrole generally affects the sensing performance of the nanocomposite-based sensor. Similar to the formation of bulk heterojunction between CdTe and polypyrrole in CdTe-polypyrrole nanocomposite, heterojunction of n-type CdTe and p-type polyaniline exhibits high-performance LPG gas-sensing characteristics [52]. The gas performance can be further improved by the formation of bulk heterojunction between CdTe and polyaniline in the CdTe-polyaniline nanocomposite.





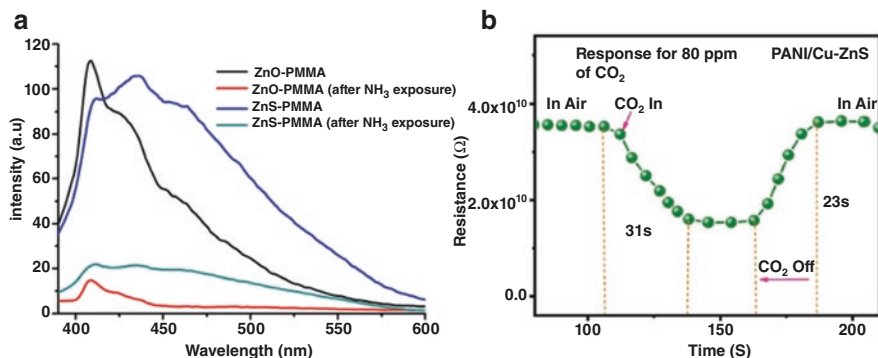
**Fig. 9.8** (a) Frequency shift in CdTe-polypyrrole nanocomposite-based sensor under exposure of different acetone gas concentrations, and (b) calibration curve for CdTe-polypyrrole nanocomposite sensor. (Reprinted with permission from [51]. Copyright 2020: Elsevier)

### 9.3.4 ZnSe-Polymer Nanocomposite

ZnSe has potential use in various electronic and sensing applications. It has a characteristic property to enhance fluorescence when embedded in a P3HT thin film [53]. This improvement in optical properties in the ZnSe-P3HT nanocomposite will enhance the optical sensing of hazardous gases. ZnSe (i.e., ZnSe-NiO heterostructure) has exhibited NO<sub>2</sub> sensing through chemiresistor structure and detected a low concentration of NO<sub>2</sub> at a temperature of 140 °C [54]. ZnSe-polymer nanocomposites have adsorption characteristics appropriate for gas-sensing applications. ZnSe QDs-starch-g-PAA nanocomposites have also shown improvement in dye adsorption and photocatalytic degradation [55]. In literature, the gas sensing performance of ZnSe-polymer nanocomposites is not explored, but these nanocomposites have the potential to be used in the future gas sensor with improved performance and capability.

### 9.3.5 ZnS-Polymer Nanocomposite

ZnS is excellent gas sensor material that is supported by its chemical structure suitable for the adsorption of various gases. The incorporation of ZnS nanoparticles in the P3HT polymers also improves the electrical conductivity of the nanocomposites [56]. The conductivity improvement in the nanocomposite is possible by a reduction in trap sites and internal electrical field to HOMO/LUMO levels of ZnS and P3HT. ZnS is widely used for the fabrication of electronic sensors for different gases and organic vapours [57]. However, the ZnS-based gas sensors have limitations for low gas sensitivity and poor selectivity. ZnS composites are used for further improvement in gas sensitivity and selectivity. The gas response of 293% for 1 ppm NO<sub>2</sub> gas, when operated at 300 °C, is achieved with an inorganic composite of ZnS [58]. The nanocomposite of ZnS enhances the gas response two-fold as



**Fig. 9.9** (a) Ammonia gas response of ZnS-PS and ZnS-PMMA. (Reprinted with permission from [12]. Copyright 2016: Springer). (b) Resistive response for carbon dioxide gas in Cu doped ZnS-PANI nanocomposite sensor. (Reprinted with permission from [60]. Published 2020 by Royal Society of Chemistry as open access)

compared to pristine ZnS. To reduce the operating temperature of the gas sensor, nanocomposites of ZnS with organic materials (polymers) are considered in the gas sensor fabrication. ZnS-PS and ZnS-PMMA nanocomposites have exhibited improvement in the fluorescence peak and significant quenching in the fluorescence under exposure to ammonia vapour [12]. The quenching in the fluorescence after exposure to ammonia gas is shown in Fig. 9.9a. Here, ZnS nanoparticle acts as catalytic sites, and PS (and PMMA) provides better adsorption sites for ammonia gas. Further, PS/PMMA-CdSe/ZnS nanocomposite-based resistive sensor has shown improvement in the sensing of volatile organic compounds [59]. Gas sensing primarily depends on coverage by the presence of polyethylene oxide and the concentration of QDs. The highest sensitivity is achieved in the presence of polyethylene oxide and the maximum concentration of QDs. Furthermore, the PANI-Cu-doped ZnS nanocomposite has shown excellent sensitivity to carbon dioxide gas [60]. The porous microstructure of the Cu-ZnS-PANI nanocomposite is responsible for the enhanced sensing properties. The exposed carbon dioxide gas diffuses on the surface of the nanocomposite. Moreover, the enhancement is also attributed due to surface defects in the nanocomposite. Similar to other nanocomposites, Cu-ZnS-PANI nanocomposite also has the advantage of the formation of bulk heterojunction for the enhanced gas response. The change in resistance to underexposure to carbon dioxide is shown in Fig. 9.9b. A maximum gas response of ~57% is obtained in a Cu-ZnS-PANI nanocomposite-based sensor for 80 ppm of carbon dioxide gas.

### 9.3.6 ZnTe-Polymer Nanocomposite

ZnTe-based nanomaterials such as quantum dots and nanorods are commonly used for electronic device fabrication. The ZnTe nanomaterials-based electronic devices exhibit improvement in optical and sensing performance. Further, the exciting

**Table 9.2** Different types of II–VI semiconductor-polymer nanocomposites-based gas sensors

Nanocomposite materials (ratio)	Target gas/vapour	Sensor response	Reference
CdSe:PQT-12 (1:2)	100 ppm NH <sub>3</sub>	51%	[39]
CdS:polyaniline (1:2)	100 ppm H <sub>2</sub> S	48%	[42]
CdS:Polyaniline:CSA (1:2:1.2)	100 ppm H <sub>2</sub> S	76%	[48]
CdS-polypyrrole (0.03:1)	250 ppm NH <sub>3</sub>	4.2	[45]
CdS-polyaniline (1:2)	46 ppm NO <sub>2</sub>	847%	[49]
CdTe-polypyrrole (1:10)	5 ppm acetone	4 kHz frequency shift	[51]
ZnS:Cu:polyaniline (1:0.01)	80 ppm CO <sub>2</sub>	~57%	[60]

feature of the ZnTe-polymer nanocomposite has shown possibility in electronic and optical detection applications [61]. It is found that the ZnTe nanocomposites have improved electro-oxidation characteristics for ethanol [62]. This affinity for ethanol can be further explored for the sensing of different alcohol and other gases. Nonenzymatic determination of catechol is also done by using ZnTe nanocomposites [63]. At present, ZnTe-polymer nanocomposites are not explored for gas-sensing applications, but their attractive structural features and affinities for adsorption can result in improved gas-sensing performance. The comparisons among major II–VI semiconductor-polymer nanocomposites-based gas sensors are listed in Table 9.2.

## 9.4 Conclusion

In this chapter, the II–VI semiconductor-polymer nanocomposites are briefly discussed. These nanocomposites have attractive features for improved electrical and sensing performance. Generally, Cd and Zn-based nanomaterials are utilised for the synthesis of nanocomposites for gas-sensing applications. It is also outlined that some of the II–VI semiconductor-polymer nanocomposites are less explored for possible applications in gas sensing. Further modification in the nanostructures of II–VI semiconductors is also possible for the preparation of high-performance nanocomposites. CdSe-polymer and CdS-polymer nanocomposites have been used largely for the fabrication of gas sensors. CdS-polyaniline nanocomposite has shown the highest gas response of 847% for 46 ppm nitrogen dioxide gas. On the other hand, a maximum gas response of 51% is obtained for 100 ppm ammonia gas in CdSe-PQT-12 nanocomposite-based sensor. In summary, II–VI semiconductor-polymer nanocomposites have shown improvement in gas-sensing performance. Additional advantages include tailored selectivity, mechanical flexibility, improved long-term stability, etc. The major drawback in II–VI semiconductor-polymer nanocomposites is the presence of less stable polymers. Highly stable polymers have a low response towards the target gases. The surface modification and selective window for the sensing can improve the lifetime of the nanocomposite-based gas sensors.

## References

1. Saleh TA, Shetti NP, Shanbhag MM, Raghava Reddy K, Aminabhavi TM. Recent trends in functionalized nanoparticles loaded polymeric composites: an energy application. *Mater Sci Energy Technol.* 2020;3:515–25. <https://doi.org/10.1016/j.mset.2020.05.005>.
2. Liu W, Gu D, Li X. Detection of Ppb-level NO<sub>2</sub> using mesoporous ZnSe/SnO<sub>2</sub> core-shell microspheres based chemical sensors. *Sensors Actuators B Chem.* 2020;320(2):128365. <https://doi.org/10.1016/j.snb.2020.128365>.
3. Kumar C, Kushwaha BK, Kumar A, Jarwal DK, Upadhyay RK, Singh AP, Jit S. Fibrous al-doped zno thin film ultraviolet photodetectors with improved responsivity and speed. *IEEE Photon Technol Lett.* 2020;32(6):337–40. <https://doi.org/10.1109/LPT.2020.2974780>.
4. Said RAM, Hasan MA, Abdelzaher AM, Abdel-Raouf AM. Review—Insights into the developments of nanocomposites for its processing and application as sensing materials. *J Electrochem Soc.* 2020;167(3):037549. <https://doi.org/10.1149/1945-7111/ab697b>.
5. Concina I, Natile MM, Tondello E, Sberveglieri G. Growth kinetics of CdSe quantum dots generated in polar polymers. *Dalton Trans.* 2012;41(47):14354–9. <https://doi.org/10.1039/c2dt31364b>.
6. Lin Y, Yuan G, Liu R, Zhou S, Sheehan SW, Wang D. Semiconductor nanostructure-based photoelectrochemical water splitting: a brief review. *Chem Phys Lett.* 2011;507(4–6):209–15. <https://doi.org/10.1016/j.cplett.2011.03.074>.
7. Sang L, Liao M, Sumiya M. A comprehensive review of semiconductor ultraviolet photodetectors: from thin film to one-dimensional nanostructures. *Sensors.* 2013;13(8):10482–518. <https://doi.org/10.3390/s130810482>.
8. Ayodhya D, Veerabhadram G. A review on recent advances in photodegradation of dyes using doped and heterojunction based semiconductor metal sulfide nanostructures for environmental protection. *Mater Today Energy.* 2018;9:83–113. <https://doi.org/10.1016/j.mtener.2018.05.007>.
9. García-Carvajal S, Hernández-Martínez D, Linzaga-Elizalde I, Maldonado JL, Altuzar-Coello P, Nicho ME. Effect of the functionalization of CdS nanoparticles in the in-situ synthesis of P3HT/CdS composites. *Eur Polym J.* 2019;116(April):471–9. <https://doi.org/10.1016/j.eurpolymj.2019.04.034>.
10. Paulraj R, Shankar P, Mani GK, Nallathambi L, Rayappan JBB. PANI–CdO nanocomposite thin films as a room temperature methanol sensor. *J Electron Mater.* 2018;47(10):6000–6. <https://doi.org/10.1007/s11664-018-6485-1>.
11. Jain S, Karmakar N, Shah A, Shimpi NG. Development of Ni doped ZnO/polyaniline nanocomposites as high response room temperature NO<sub>2</sub> sensor. *Mater Sci Eng B Solid-State Mater Adv Technol.* 2019;247(May):114381. <https://doi.org/10.1016/j.mseb.2019.114381>.
12. Hariharan PS, Subhashini N, Vasanthalakshmi J, Anthony SP. A facile method for the synthesis fluorescent zinc chalcogenide (ZnO, ZnS and ZnSe) nanoparticles in PS and PMMA polymer matrix. *J Fluoresc.* 2016;26(2):703–7. <https://doi.org/10.1007/s10895-015-1757-0>.
13. Kumar C, Rawat G, Kumar H, Kumar Y, Prakash R, Jit S. Electrical and ammonia gas sensing properties of poly (3, 3'-dialkylquaterthiophene) based organic thin film transistors fabricated by floating- film transfer method. *Org Electron.* 2017;48:53–60. <https://doi.org/10.1016/j.orgel.2017.05.040>.
14. Kumar C, Rawat G, Kumar H, Kumar Y, Prakash R, Jit S. Flexible poly (3, 3'-dialkylquaterthiophene) based interdigitated metal-semiconductor-metal ammonia gas sensor. *Sensors Actuators B Chem.* 2018;255:203–9. <https://doi.org/10.1016/j.snb.2017.08.014>.
15. Kumar C, Rawat G, Kumar H, Kumar Y, Ratan S, Prakash R, Jit S. Poly (3, 3'-dialkylquaterthiophene) based flexible nitrogen dioxide gas sensor. *IEEE Sensors Lett.* 2018;2(1):1–4. <https://doi.org/10.1109/lsens.2018.2799851>.
16. Zhang L, Du W, Nautiyal A, Liu Z, Zhang X. Recent progress on nanostructured conducting polymers and composites: synthesis, application and future aspects. *Sci China Mater.* 2018;61(3):303–52. <https://doi.org/10.1007/s40843-017-9206-4>.

17. Yan Y, Yang G, Xu JL, Zhang M, Kuo CC, Wang SD. Conducting polymer-inorganic nanocomposite-based gas sensors: a review. *Sci Technol Adv Mater.* 2020;21(1):768–86. <https://doi.org/10.1080/14686996.2020.1820845>.
18. Sahu PK, Pandey M, Kumar C, Pandey SS, Takashima W, Mishra VN, Prakash R. Air-stable vapor phase sensing of ammonia in sub-threshold regime of poly(2,5-bis(3-tetradecylthiophen-2yl)thieno(3,2-b)thiophene) based polymer thin-film transistor. *Sensors Actuators B Chem.* 2017;246:243–51. <https://doi.org/10.1016/j.snb.2017.02.063>.
19. Duc C, Boukhenane ML, Wojkiewicz JL, Redon N. Hydrogen sulfide detection by sensors based on conductive polymers: a review. *Front Mater.* 2020;7(September):215. <https://doi.org/10.3389/fmats.2020.00215>.
20. Majumdar S, Sarmah K, Mahanta D. A simple route to prepare polypyrrole-coated filter papers via vapor phase polymerization and their gas sensing application. *ACS Appl Polym Mater.* 2020;2(5):1933–42. <https://doi.org/10.1021/acsapm.0c00147>.
21. Pandey S. Highly sensitive and selective chemiresistor gas/vapor sensors based on polyaniline nanocomposite: a comprehensive review. *J Sci Adv Mater Devices.* 2016;1(4):431–53. <https://doi.org/10.1016/j.jsamd.2016.10.005>.
22. Wang Y, Liu A, Han Y, Li T. Sensors based on conductive polymers and their composites: a review. *Polym Int.* 2020;69(1):7–17. <https://doi.org/10.1002/pi.5907>.
23. Compressed Gas: Toxic and Hazardous Gas Classifications. <https://blink.ucsd.edu/safety/research-lab/chemical/gas/toxic.html> (accessed 01 March 2022).
24. Kumari K, Chand S, Vankar VD, Kumar V. Enhancement in hole current density on polarization in poly(3-hexylthiophene):cadmium selenide quantum dot nanocomposite thin films. *Appl Phys Lett.* 2009;94(21):213503. <https://doi.org/10.1063/1.3142393>.
25. Li F, Cha HM, Seo SM, Son DI, Kim HJ, Kim TW. Investigation of carrier transport mechanism in CdSe/PVK hybrid nanocomposites. *J Korean Phys Soc.* 2008;53(1):376–9. <https://doi.org/10.3938/jkps.53.376>.
26. Verma D, Dutta V. Bi-nanoparticle (CdTe and CdSe) mixed polyaniline hybrid thin films prepared using spin coating technique. *J Appl Phys.* 2009;105(3):034904. <https://doi.org/10.1063/1.3072627>.
27. Mondal SP, Dhar A, Ray SK, Chakraborty AK. Bonding, vibrational, and electrical characteristics of CdS nanostructures embedded in polyvinyl alcohol matrix. *J Appl Phys.* 2009;105(8):084309. <https://doi.org/10.1063/1.3111971>.
28. Biswas S, Dutta M, Strocio MA. Negative differential resistance in conductive polymer and semiconducting quantum dot nanocomposite systems. *Appl Phys Lett.* 2009;95(18):6–9. <https://doi.org/10.1063/1.3258350>.
29. Kumar H, Kumar Y, Mukherjee B, Rawat G, Kumar C, Pal BN, Jit S. Electrical and optical characteristics of self-powered colloidal CdSe quantum dot-based photodiode. *IEEE J Quantum Electron.* 2017;53(3):4400108.
30. Kumar H, Kumar Y, Rawat G, Kumar C, Mukherjee B, Pal BN, Jit S. Colloidal CdSe Quantum Dots and PQT-12-Based Low-Temperature Self-Powered Hybrid Photodetector. *IEEE Photon Technol Lett.* 2017;29(20):1715–8. <https://doi.org/10.1109/LPT.2017.2746664>.
31. Kisslinger R, Hua W, Shankar K. Bulk heterojunction solar cells based on blends of conjugated polymers with ii-vi and iv-vi inorganic semiconductor quantum dots. *Polymers (Basel).* 2017;9(2):1–29. <https://doi.org/10.3390/polym9020035>.
32. Han CY, Yang H. Development of colloidal quantum dots for electrically driven light-emitting devices. *J Korean Ceram Soc.* 2017;54(6):449–69. <https://doi.org/10.4191/kcers.2017.54.6.03>.
33. Joshi SS, Lokhande CD, Han SH. A room temperature liquefied petroleum gas sensor based on all-electrodeposited n-CdSe/p-polyaniline junction. *Sensors Actuators B Chem.* 2007;123(1):240–5. <https://doi.org/10.1016/j.snb.2006.08.023>.
34. Laatar F. Synthesis of the PS/CdSeNRs composite for room temperature NO<sub>2</sub> gas sensing. *SILICON.* 2021;13:4155. <https://doi.org/10.1007/s12633-020-00646-4>.

35. Potyrailo RA, Leach AM. Selective gas nanosensors with multisize CdSe nanocrystal/polymer composite films and dynamic pattern recognition. *Appl Phys Lett*. 2006;88(13):1–4. <https://doi.org/10.1063/1.2190272>.
36. Tatavarty R, Hwang ET, Park JW, Kwak JH, Lee JO, Gu MB. Conductive quantum dot-encapsulated electrospun nanofibers from polystyrene and polystyrene-co-maleic anhydride copolymer blend as gas sensors. *React Funct Polym*. 2011;71(2):104–8. <https://doi.org/10.1016/j.reactfunctpolym.2010.11.029>.
37. Zhang B, Fu R, Zhang M, Dong X, Wang L, Pittman CU. Gas sensitive vapor grown carbon nanofiber/polystyrene sensors. *Mater Res Bull*. 2006;41(3):553–62. <https://doi.org/10.1016/j.materresbull.2005.09.009>.
38. Mondal SP, Bera S, Narender G, Ray SK. CdSe quantum dots-poly(3-hexylthiophene) nanocomposite sensors for selective chloroform vapor detection at room temperature. *Appl Phys Lett*. 2012;101:173108.
39. Kumar C, Rawat G, Kumar H, Kumar Y, Kumar A, Prakash R, Jit S. Electrical and ammonia gas sensing properties of PQT-12/CdSe quantum dots composite-based organic thin film transistors. *IEEE Sensors J*. 2018;18(15):6085–91.
40. Fu T. Sensing behavior of CdS nanoparticles to SO<sub>2</sub>, H<sub>2</sub>S and NH<sub>3</sub> at room temperature. *Mater Res Bull*. 2013;48(5):1784–90. <https://doi.org/10.1016/j.materresbull.2013.01.037>.
41. Dhawale DS, Dubal DP, Jamadade VS, Salunkhe RR, Joshi SS, Lokhande CD. Room temperature LPG sensor based on n-CdS/p-polyaniline heterojunction. *Sensors Actuators B Chem*. 2010;145(1):205–10. <https://doi.org/10.1016/j.snb.2009.11.063>.
42. Raut BT, Godse PR, Pawar SG, Chougule MA, Bandgar DK, Patil VB. Novel method for fabrication of polyaniline-CdS sensor for H<sub>2</sub>S gas detection. *Measurement*. 2012;45(1):94–100. <https://doi.org/10.1016/j.measurement.2011.09.015>.
43. Xu H, Wu J, Chen CH, Zhang L, Yang KL. Detecting hydrogen sulfide by using transparent polymer with embedded CdSe/CdS quantum dots. *Sensors Actuators B Chem*. 2010;143(2):535–8. <https://doi.org/10.1016/j.snb.2009.09.049>.
44. Sonawane NB, Ahire RR, Gurav KV, Kim JH, Sankapal BR. PEDOT:PSS shell on CdS nanowires: room temperature LPG sensor. *J Alloys Compd*. 2014;592:1–5. <https://doi.org/10.1016/j.jallcom.2013.12.090>.
45. Yeole B, Sen T, Hansora DP, Mishra S. Effect of electrical properties on gas sensitivity of polypyrrole/cds nanocomposites. *J Appl Polym Sci*. 2015;132(32):1–9. <https://doi.org/10.1002/app.42379>.
46. Yeole B, Sen T, Hansora D, Mishra S. Polypyrrole/metal sulphide hybrid nanocomposites: synthesis, characterization and room temperature gas sensing properties. *Mater Res*. 2016;19(5):999–1007. <https://doi.org/10.1590/1980-5373-MR-2015-0502>.
47. Akbar A, Das M, Sarkar D. Room temperature ammonia sensing by CdS nanoparticle decorated polyaniline (PANI) nanorods. *Sensors Actuators A Phys*. 2020;310:112071. <https://doi.org/10.1016/j.sna.2020.112071>.
48. Raut BT, Chougule MA, Nalage SR, Dalavi DS, Mali S, Patil PS, Patil VB. CSA doped polyaniline/CdS organic-inorganic nanohybrid: physical and gas sensing properties. *Ceram Int*. 2012;38(7):5501–6. <https://doi.org/10.1016/j.ceramint.2012.03.064>.
49. Al-Jawad SMH, Rafic SN, Muhsen MM. Preparation and characterization of polyaniline-cadmium sulfide nanocomposite for gas sensor application. *Mod Phys Lett B*. 2017;31(26):1–15. <https://doi.org/10.1142/S0217984917502347>.
50. Zhang L, Li X, Mu Z, Miao J, Wang K, Zhang R, Chen S. A novel composite of CdS nanorods growing on a polyaniline-Cd<sup>2+</sup> particles surface with excellent formaldehyde gas sensing properties at low temperature. *RSC Adv*. 2018;8(54):30747–54. <https://doi.org/10.1039/c8ra05082a>.
51. Šetka M, Bahos FA, Chmela O, Matatagui D, Gràcia I, Drbohlavová J, Vallejos S. Cadmium telluride/polypyrrole nanocomposite based Love wave sensors highly sensitive to acetone at room temperature. *Sensors Actuators B Chem*. 2020;321(July):128573. <https://doi.org/10.1016/j.snb.2020.128573>.

52. Joshi SS, Gujar TP, Shinde VR, Lokhande CD. Fabrication of n-CdTe/p-polyaniline heterojunction-based room temperature LPG sensor. *Sensors Actuators B Chem.* 2008;132(1):349–55. <https://doi.org/10.1016/j.snb.2008.01.059>.
53. Mastour N, Ben Hamed Z, Benchaabane A, Sanhoury MA, Kouki F. Effect of ZnSe quantum dot concentration on the fluorescence enhancement of polymer P3HT film. *Org Electron.* 2013;14(8):2093–100. <https://doi.org/10.1016/j.orgel.2013.05.005>.
54. Liu W, Gu D, Zhang JW, Li XG, Rummyantseva MN, Gaskov AM. ZnSe/NiO heterostructure-based chemiresistive-type sensors for low-concentration NO<sub>2</sub> detection. *Rare Metals.* 2021;40(6):1632–41. <https://doi.org/10.1007/s12598-020-01564-5>.
55. Abdolahi G, Dargahi M, Ghasemzadeh H. Synthesis of starch-g-poly (acrylic acid)/ZnSe quantum dot nanocomposite hydrogel, for effective dye adsorption and photocatalytic degradation: thermodynamic and kinetic studies. *Cellulose.* 2020;27(11):6467–83. <https://doi.org/10.1007/s10570-020-03198-3>.
56. Singh B, Kaur A. Enhanced photoelectrical conductivity of poly (3-hexylthiophene) by incorporation of ZnS nanoparticles. *Synth Met.* 2014;195:306–11. <https://doi.org/10.1016/j.synthmet.2014.06.016>.
57. Wang X, Xie Z, Huang H, Liu Z, Chen D, Shen G. Gas sensors, thermistor and photodetector based on ZnS nanowires. *J Mater Chem.* 2012;22(14):6845–50. <https://doi.org/10.1039/c2jm16523f>.
58. Mun Y, Park S, Ko H, Lee C, Lee S. NO<sub>2</sub> gas sensing properties of ZnO/ZnS core-shell nanowires. *J Korean Phys Soc.* 2013;63(8):1595–600. <https://doi.org/10.3938/jkps.63.1595>.
59. De San Luis A, Aguirreurreta Z, Pardo LM, Perez-Marquez A, Maudes J, Murillo N, Paulis M, Leiza JR. PS/PMMA-CdSe/ZnS quantum dots hybrid nanofibers for VOCs sensors. *Isr J Chem.* 2018;58(12):1347–55. <https://doi.org/10.1002/ijch.201800038>.
60. Parangusan H, Bhadra J, Ahmad Z, Mallick S, Touati F, Al-Thani N. Investigation of the structural, optical and gas sensing properties of PANI coated Cu-ZnS microsphere composite. *RSC Adv.* 2020;10(45):26604–12. <https://doi.org/10.1039/d0ra04991c>.
61. El-Hachemi B, Miloud S, Sabah M, Souad T, Zineddine O, Boubekeur B, Toufik SM, Ouahiba H. Structural, electrical and optical properties of PVC/ZnTe nanocomposite thin films. *J Inorg Organomet Polym Mater.* 2021;31(9):3637–48. <https://doi.org/10.1007/s10904-021-01994-3>.
62. Mollarasouli F, Majidi MR, Asadpour-Zeynali K. Facile synthesis of ZnTe/Quinhydrone nanocomposite as a promising catalyst for electro-oxidation of ethanol in alkaline medium. *Int J Hydrog Energy.* 2019;44(39):22085–97. <https://doi.org/10.1016/j.ijhydene.2019.06.071>.
63. Mollarasouli F, Kurbanoglu S, Asadpour-Zeynali K, Ozkan SA. Preparation of porous Cu metal organic framework/ZnTe nanorods/Au nanoparticles hybrid platform for nonenzymatic determination of catechol. *J Electroanal Chem.* 2020;856:113672. <https://doi.org/10.1016/j.jelechem.2019.113672>.

# Chapter 10

## Nanomaterial-Based Electric and Electronic Gas Sensors



Andrea Gaiardo, Barbara Fabbri, and Matteo Valt

### 10.1 Introduction

Chemical gas sensors are measuring devices that – based on certain fundamentals, which combine detection principles, material science and processing technology – convert a chemical or physical property of a specific analyte into a measurable signal, whose magnitude is normally proportional to the type and the concentration of the gaseous compounds [1]. Nowadays, materials and devices for chemical gas sensor production must be progressively downsized, eco-friendly, energetically efficient, reliable, multifunctional and low-cost in order to meet market needs. Then, in order to meet these expectations, material and technology sciences research has advanced dramatically. In particular, materials have to feature effective functionality and stability, while the final device must operate at low/room temperature (RT) and be simple to integrate into technological platforms [2–6].

Due to their high specific area, large number of active sites, controlled morphology, change of unique physicochemical properties on exposure to gases, and high photoconduction abilities, nanomaterials (NMs) have found numerous uses in gas sensing [7, 8]. Furthermore, using improved nanosensing technologies to detect low gas concentrations in complex gas mixtures is a promising strategy [6]. Many potential definitions for NMs have been presented in recent years, including the one recommended by the European Union [9]. The properties of NMs are heavily influenced by the type and nature of nanostructures (NSs). In other words,

---

A. Gaiardo (✉) · M. Valt  
MNF-Micro Nano Facility, Sensors and Devices Center, Bruno Kessler Foundation,  
Trento, Italy  
e-mail: [gaiardo@fbk.eu](mailto:gaiardo@fbk.eu)

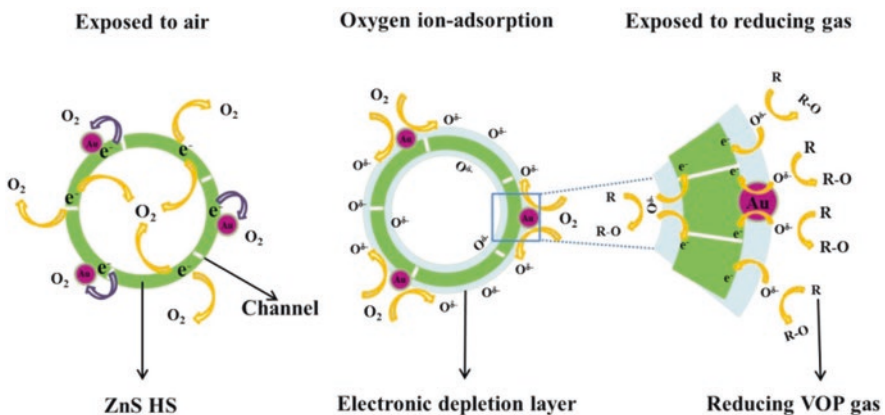
B. Fabbri  
Department of Physics and Earth Sciences, University of Ferrara, Ferrara, Italy



depending on the NSs, the same NMs may have different properties and be suited for different applications.

NMs are composed of submicron or nanoscale building blocks that exhibit size effects in at least one direction. Due to the enormous number of structures that have been produced in recent years, classification is required. Gleiter [10] proposed a first classification scheme. This NMs classification is based on crystalline forms and chemical composition, in particular, intercrystallite grain boundaries parallel with crystallites were regarded as building blocks. However, due to the lack of consideration of zero- and one-dimensional (0D, 1D) structures like fullerenes and nanotubes, this method was incomplete. Later, V.V. Pokropivny et al. [11] proposed that NSs be categorised accurately based on dimensionality (Fig. 10.1), which they defined as a broad natural attribute combining size and form.

In fact, all NSs are made up of low-dimensional elementary units: zero-dimensional (0D structure), one-dimensional (1D structure) and two-dimensional structure (2D structure). Besides, three-dimensional structures (3D structures) are composed of one or more low-dimensional structures [1]. Then, the 3D units are excluded from the classification since they cannot be used to build low-dimensional NSs except the 3D matrix. 3D structures, on the other hand, can be deemed NMs if they contain 0D, 1D and 2D NSs. The  $kDlmn$  notation was established in the categorisation proposed by V.V. Pokropivny et al. [11], where  $k$  is a dimensionality of the nanostructure as a whole, while the integers  $l, m, n$  denote the dimensionality of the NSs building units. Because each of the numerals  $l, m, n$  represents a distinct type of unit, the total number of these integers must equal the total number of constituent units. The requirement leads to  $k \geq l, m, n$ , and  $k, l, m, n = 0, 1, 2, 3$ . It follows that a restricted number of NSs classes exists and they are summarised in Table 10.1 [11]. All kinds of known NSs in the literature belong to one of these classes. On these bases, the combined classification can be further developed taking into account the nature and composition of materials such as, in this chapter, II–VI TMC semiconductors.



**Fig. 10.1** Schematic illustration for the sensing mechanism of the Au NPs-ZnS hollow spheres-based sensor. (Reproduced with permission from Zhang et al. [23]. Copyright 2017: Elsevier)

**Table 10.1** The classification of NSs and typical morphology

Structure	Dimensions in the nanoscale	Morphology
0D	3	Nanoparticle, quantum dot, nanocluster
1D	2	Nanowire, nanofibre, nanorod, nanotube
2D	1	Nanosheet, nanobelt, superlattice
3D	Assembled by one or more kinds of NSs	3D hierarchical structures (nanoflower, etc.), hollow sphere, nano-mesoporous material
Core–shells	0, 1, 2 or 3	Mesoporous, nanorod, quantum dot, etc.

Source: Adapted from Yuan et al. [1]. Published 2019 by MDPI as open access

**Table 10.2** The types and characteristics of preparation methods of NMs

Method	Advantaged	Disadvantages	Examples
Solid phase	Simple synthesis process, high yield, low pollution	Not homogeneous particle size distribution, high agglomeration	Ball milling, shear milling
Liquid phase	Simple synthesis process, controllable particle size	Low distribution, low uniformity	Sol–gel, hydrothermal, micro-emulsion, chemical bath deposition
Vapour phase	High purity powder, small particle size, low agglomeration	High cost, high requirements for instruments	Molecular beam epitaxy, chemical vapour deposition, sputtering

Source: Reprinted with permission from Yuan et al. [1]. Published 2019 by MDPI as open access

Their properties are determined by the atomic structure, composition, microstructure, defects and interfaces, all influenced by the thermodynamics and kinetics of synthesis. Advanced fabrication technology allows the microstructure and morphology of NMs to be manipulated, paving a world of possibilities for NM-based functional devices and applications. In general, the various NM synthesis methods can be listed into three main categories: solid-phase method, vapour-phase method and liquid-phase method, based on the state of the reagents, as shown in Table 10.2.

So far, several techniques have been explored to fabricate NMs of desired size, shape and orientation. Top-down and bottom-up approaches are two types of technological techniques that play an important role in the device business as well as in nanoproducts.

Top-down techniques are naturally easier since they rely on either removing or breaking down the bulk material into nanosized structures or particles, or on miniaturising bulk production procedures to obtain the necessary structure with the needed attributes. Examples of such techniques are mechanical methods, such as cutting, etching, grinding, high-energy wet ball milling, atomic force manipulation, gas-phase condensation, aerosol spray, etc., and lithographic methods, for example, photo-lithography, electron beam lithography. Top-down synthesis techniques are variations upon those previously utilised to make micron-sized particles. Despite top-down approaches allowing a large-scale production avoiding chemical

purification, they feature a broad size distribution (10–1000 nm) and a wide variety in shape or geometry of the particles. Additionally, it is challenging to control deposition settings, and the methods are expensive. The primary drawback of the top-down strategy, however, is the flaws in the surface structure. Indeed, these flaws would significantly affect the chemical and physical characteristics of NSs and nanomaterials. For instance, lithographically produced nanowires (NWs) may not have a smooth surface and have several impurities and structural flaws.

The bottom-up strategy (physical and chemical processing methods) is an alternative that may result in less waste and is therefore more cost-effective. It describes the process of building up a substance atom by atom, molecule by molecule or cluster by cluster. Two approaches can be used to categorise the reported bottom-up methods for the preparation of nanoparticles (NPs): physical processing, which is directed at a thermodynamic equilibrium (creation of supersaturation, nucleation and subsequent growth), and chemical processing, which is directed at a kinetic approach (limiting the number of precursors for the growth confining in a limited space). Physical techniques include physical vapour deposition (PVD), evaporation, sputtering, plasma arcing and laser ablation. Chemical techniques include chemical vapour deposition (CVD), the reverse micelle route, sol-gel synthesis, colloidal precipitation, hydrothermal synthesis, template-assisted sol-gel and electrodeposition. For the commercial manufacture of nanopowders, several of these techniques are still in development or are only now being started.

Although large-scale production is challenging and chemical NPs purification is necessary, bottom-up technique is low cost and offers a narrow size distribution (1–20 nm) of the NSs and better control of deposition settings.

In conclusion, the bottom-up technique is preferred for the synthesis of NPs over the top-down approach due to various advantages including fewer flaws, a more homogeneous chemical composition and better ordering [12].

### ***10.1.1 Performance Parameters and Influence Factors for Nanomaterial-Based Electrical and Electronic Gas Sensors***

High sensitivity, outstanding selectivity, quick reaction and recovery times and good long-term stability are anticipated of a top-notch gas sensor.

Four crucial factors, or the so-called ‘4S’, must be considered in order to assess the detecting abilities of gas sensors: sensitivity, selectivity to target gases, speed of sensor response/recovery and signal stability [13].

*Sensitivity* is the slope of the calibration curve, i.e., the ratio between the variation of a suitable physical quantity (such as resistance, conductance, circulating current, etc.) and the variation of analyte concentration. The variation of the sensor signal output, related to such physical quantity, during the exposure to the analyte is

known as response ( $R$ ) (i.e. tested gas). The reaction can be described by the following formula, denoting this physical quantity as  $X$ :

$$R = \left| \frac{(X_{\text{air}} - X)}{X_{\text{air}}} \right| \quad (10.1)$$

where  $X$  and  $X_{\text{air}}$  are the values of the selected quantity when the sensor is exposed or not to the analyte, respectively. Usually, resistance is used to calculate the response of the sensing film since it depends on the type and concentration of the gas [14]. For the calculation of the sensing response of electrical and electronic gas sensor it is important to consider the type of the sensing NM used (e.g. n- or p-type semiconductor) and the physico-chemical properties of the target gas (e.g. oxidising/reducing molecule).

*Selectivity* is studied by comparing the cross-sensitivity to some different gases at given concentrations, which denotes the ability to identify the target gas.

*Speed* of gas sensors can be quantified using response and recovery time.

*Stability* refers to the capacity of reproducing results and outputting stable signals for gas sensors even after a long-term operation, which is always influenced by material components, humidity, working temperature and other factors.

Based on the dominance of size confinement, distribution and morphology, interfacial processes and quantum effects, the most ideal gas sensing qualities can be attained at the nanoscale. Table 10.3 shows a comparison of NMs from 0D to 3D features in the field of electrically-transduced sensing materials, starting from the aforementioned essential critical aspects to be taken into account in the assessment of NMs-based gas sensors performance.

### ***10.1.2 Influence Factors: Advantages on Using II–VI Semiconductor Nanomaterials in Electric and Electronic Gas Sensors***

The principle of gas sensing are complex and some important performance challenges have to be addressed:

- Humidity affects the interaction between the gas and the sensor. For real applications, the presence of humidity cannot be overlooked, since it provides a decrease of gas sensor sensitivity.
- When detecting a mixture of similar gases, the cross-sensitivity of gas sensors would be impacted by interfering gases that have the same chemical properties as the target gas.
- Long-term stability, or signal drift, is a relatively complex and unavoidable phenomenon, which is produced by different surrounding conditions, including

**Table 10.3** Types and characteristics of preparation methods of NMs [15]

	Advantages	Disadvantages
0D	Atomic control of structure–property relationship Large surface-to-volume ratio Single-molecular electronic-based sensing Tunable size and shape	Low conductivity Difficulty with device integration Limited stability of devices
1D	High surface-to volume ratio Excellent stability of the devices High density of reactive sites Good thermal stability Compatible with device miniaturisation	Required chemical modification to enhance selectivity Difficulty in establishing reliable electrical contacts Difficult purification Limited structure and precision control
2D	Wide tunability of conductivity Large surface-to-volume ratio Thickness-dependent electronic properties Excellent mechanical flexibility Good functionalisation ability Compatible with ultra-thin silicon channel technology	Lack of mass production of materials with large area, high and uniform quality Lack of facile, effective and reliable strategies for device integration Limited stability of some forms at ambient conditions
3D	Strong analyte adsorption/binding Good mechanical strength Good thermal stability Easy to interface with solid-state devices Good design ability to improve selectivity	Low surface area (for non-porous materials) Difficulty to miniaturisation Slow dynamics of analyte transport

Source: Adapted with permission from Meng et al. [15]. Copyright 2019: ACS Publications

device aging and poisoning, environmental temperature and humidity and transmission delay.

- RT operation has a significant disadvantage in terms of power consumption, application in hazardous settings and desire for affordable and portable devices due to the high operating temperature (200–500 °C) required to trigger chemical reactions on the active sensing material.

II–VI semiconductor compounds can be used as sensing materials in all types of gas sensors, including chemiresistors, surface acoustic wave (SAW) and heterojunction-based gas sensors. This versatility is provided by diverse significant properties:

- (i) In II–VI TMC semiconductors, the surface Fermi-level position or the band bending, can vary over a large range, which helps to obtain high sensor responsiveness through exposition to the surrounding gases. Then, II–VI compounds are frequently used in gas sensing applications due to their special ability to behave as either wide-bandgap (1.5–3.5 eV) or narrow-bandgap (0–1.5 eV) materials. Additionally, because they are ‘ionic’ materials, II–VI semiconductor

- compounds lack surface Fermi-level pinning. This means that they show little or no Fermi-level stabilisation at the interface [16].
- (ii) II–VI TMC semiconductors hold a favorable position among the diverse range of sensing materials just by virtue of their elemental composition. In fact, compared to semiconductors based on oxides, the absence of oxygen in the crystal lattice results in a distinct catalytic mechanism on the surface reaction. The consistent signal drift experienced by the last and attributed to the in/out diffusion of oxygen vacancies, which modifies the doping level, may also be resolved by this absence [2, 17].
  - (iii) These materials work as functional semiconductors for chemical sensors primarily by altering their resistance, photoconductivity, optical absorption and fluorescence as a result of adsorbate-induced modifications. Indeed, the properties of interest for chemical sensing with II–VI TMC NMs include strong resistance change or high quantum yields in combination with broad absorption spectra, narrow size-tunable photoluminescence and exceptional resistance to both photobleaching and chemical degradation [18].
  - (iv) II–VI TMC NMs can be used for surface functionalisation and composite formation, giving the option to fine-tune the nanostructure morphology and crystal structure using quick, low-cost techniques.

### ***10.1.3 Approaches to Optimise Chemical Gas Sensing Devices***

The current generation of sensing materials has progressed from MOSs, which are still the industry standard for gas sensors [19], to new two-dimensional (2D) materials like graphene and other ones [20, 21], as well as a variety of nanocomposites [22]. Despite the remarkable advancements of MOS-based gas sensors, including high sensitivity and quick reaction and recovery times, these NMs have revealed disadvantages, such as low selectivity and high operating temperatures, that limit their exploitation in many applications [19].

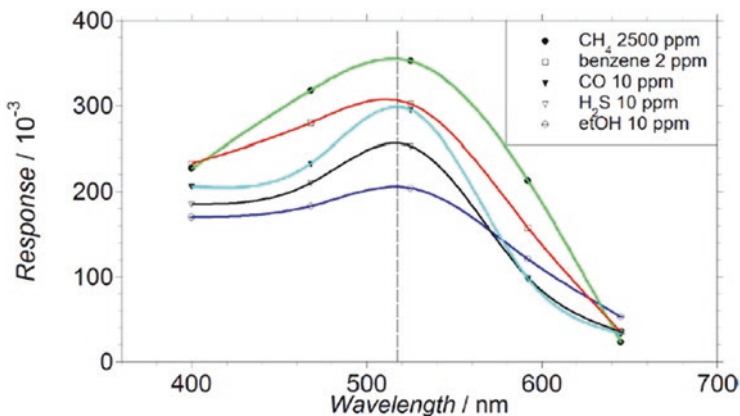
The investigation of semiconductors with tunable or narrow bandgap, high charge carrier's mobility, high surface reactivity and low/room-temperature sensing performance has resulted from the hunt for materials that would overcome the constraints of MOS-based gas sensors. According to this viewpoint, some of the advantageous features of II–VI TMC compounds would enable them to meet these requirements. Although gas sensors based on II–VI TMC compounds are sensitive to the same gases and vapours as MOS gas sensors, they do so with lower sensitivity, which makes it hard to replace MOS gas sensors despite the results of research on gas sensors to date. Illumination and temperature have a significant impact on the characteristics of II–VI semiconductor compounds. Indeed, despite high melting temperatures, sublimation and particularly irreversible oxidation occur at significantly lower temperatures. As a result, for the most stable ZnS and CdS compounds, working temperatures of II–VI-based gas sensors cannot exceed 300–350 °C. This suggests that more research and development are necessary since II–VI

semiconductor compounds, at the current state-of-art, are still unable to address issues with selectivity and instability of gas sensors over the time [16].

II–VI TMC compounds should have pores with small grain sizes and nanostructures with small diameters for improved detection capabilities. Additionally, the thinner films have demonstrated greater sensitivity and faster response times. Response and recovery times often decrease as operating temperature rises. Surface modification, such as decorating with noble metal particles, enhances the sensing performance of II–VI semiconductor compounds, including improved sensitivity and selectivity, shorter response/recovery time, etc. In this regard, ZnS is extensively researched by both decoration with metal nanoclusters and doping [23, 24]. For instance, Au NPs-ZnS hollow spheres (Au NPs-ZnS HSs) have recently shown outstanding gas sensing capabilities, including high response, quick response–recovery times and strong repeatability, as well as increased responsiveness to a number of volatile organic pollutants (Fig. 10.1).

Utilising UV-visible radiation and taking advantage of the photoconductivity and photocatalytic capabilities of II–VI TMCs, the aforementioned issues concerning temperature dependence might be overcome. In general, the regulation of conductance by adsorbed oxygen is enhanced by illumination with the appropriate energy. The creation and recombination of electron-hole pairs in the semiconductor determines the response and recovery speed. The highest overlap between the emission spectra of the radiation source and the absorption of the sensing material is recommended to maximise the energy efficiency of light-activated sensors.

Although it was already noted that nanocrystalline wide-gap MOSs are able to exhibit a photo-response when exposed to visible light [25], this effect is usually quite weak, due to the small absorption coefficient in the visible light range, leading to a limited absorption of the emitted photons. Semiconducting gas sensors with improved photo- and gas sensitivity in the visible region can be made essentially by using two different methods. The first approach is to employ a semiconductor, such as certain halides, sulphides and other compounds, as the sensing layer. This semiconductor must have a lower bandgap than an oxide and be able to absorb photons in the visible spectrum. CdS, one of the II–VI TMCs, has demonstrated strong photoconductivity, making it a possible solution for the manufacturing of RT working devices, avoiding temperature effects on the sensing materials. It has been shown that a bandgap-resonant excitation (Fig. 10.2) maximises surface chemical activity as well as photoconductivity [26]. However, the photostability of sulfides may not be sufficient in the long term. In this regard, even though the number of scientific papers pertaining to such systems is rapidly rising [27], other semiconducting materials of the II–VI group with an energy bandgap in the visible range, such as ZnSe (2.70 eV) and ZnTe (2.26 eV), are more promising and underexplored in the gas sensing field. The second approach for increasing gas sensitivity is to sensitise wide-gap semiconductors to the visible radiation by doping, spectral sensitisation with dyes or particles of narrow-band semiconductors and with plasmon metal particles. However, so far, the literature does not provide data on the long-term stability of these sensitisation strategies [25].



**Fig. 10.2** Electrical response of CdS film to the tested gases vs. wavelength of the exciting radiation. The vertical line corresponds to the bandgap energy. (Reproduced with permission from Giberti et al. [26], with the permission of AIP Publishing)

## 10.2 II–VI Semiconductor Nanomaterials for Chemical Gas Sensors

### 10.2.1 0D Nanomaterials

0D materials are sized at nanoscale level in all three dimensions. For example, in the system of quantum dots (QDs), all the electrons are confined within an ‘infinitely deep potential well’ and they cannot exit from this delimited region. Therefore, electron delocalisation is not observed. 0D NMs can be amorphous or single and polycrystalline, exhibiting diverse shapes and forms. Within 0D materials their length equals the width.

According to the quantum confinement theory, when an electron is promoted from the valence to the conduction band, an exciton is generated in the bulk lattice. The physical separation distance between electron and hole is defined as the exciton Bohr radius ( $r_b$ ). Within 0D materials (such QDs), the  $r_b$  is of the same order of magnitude as nanocrystal diameter, giving rise to quantum confinement of the exciton. Subsequently, if nanostructured materials possess sufficiently small dimensions, the exciton quantum confinement results in discrete energy levels. Therefore, any modification of the atomic structure will result in a significant change of the nanocrystal dimensions and bandgap. Due to confinement of electrons and holes, the lowest energy optical transition from the valence to conduction band will increase in energy, subsequently increasing the bandgap. The discrete energy ( $E_n$ ) for different NMs can be described by Eq. (10.2):

$$E_n = \left[ \frac{\pi^2 \hbar^2}{mL^2} \right] (n_x^2 + n_y^2 + n_z^2) \quad (10.2)$$



where  $\hbar$  is the Planck's constant in J·s,  $m$  is the electron mass in amu,  $L$  is the orbital perimeter in nm and  $n$  dimensional coordinates, which are dimensionless units.

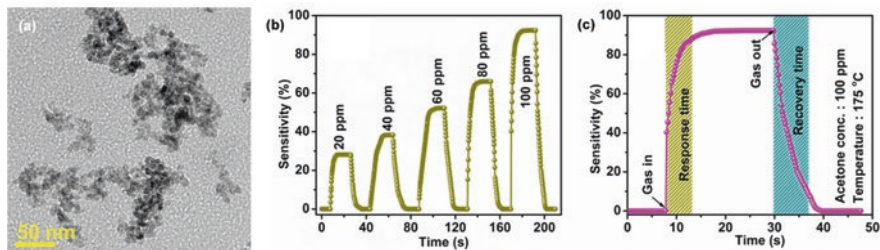
From the above equation, one can observe that the bandgap value may be easily fine-tuned by changing the diameter of the QD, if the dimensions are controlled at the size smaller than  $r_b$ . This characteristic is one of the main advantages of QDs as their electrical and optical properties can be engineered by precise control of the nanoparticle size exhibiting great potential for applications in functional devices. The variation of these parameters can affect the rate of adsorption and desorption processes of gaseous molecules on the semiconductor surface playing a major role in the detection of different gases in the atmosphere. QD-containing devices offer several advantages over conventional thick-film-based sensors in terms of enhanced charge transport and surface area, opening new pathways for the development of next-generation portable and flexible sensing systems.

QDs are generally prepared by colloidal synthesis techniques or epitaxial growth. The last, provides an ordered growth of QDs, where the temperature, structure and crystallographic orientation of the substrate should be considered and controlled in detail. The colloidal synthesis method has been intensively developed to fabricate different QDs semiconductors. Colloidal synthesis is a liquid-phase condensation, wherein the chemical reactions supersaturate the precursors and cause nucleation of QDs. In this context, the precursor solutions and the environmental conditions of the chemical reactions are the key factors for the quality of the produced QDs [28].

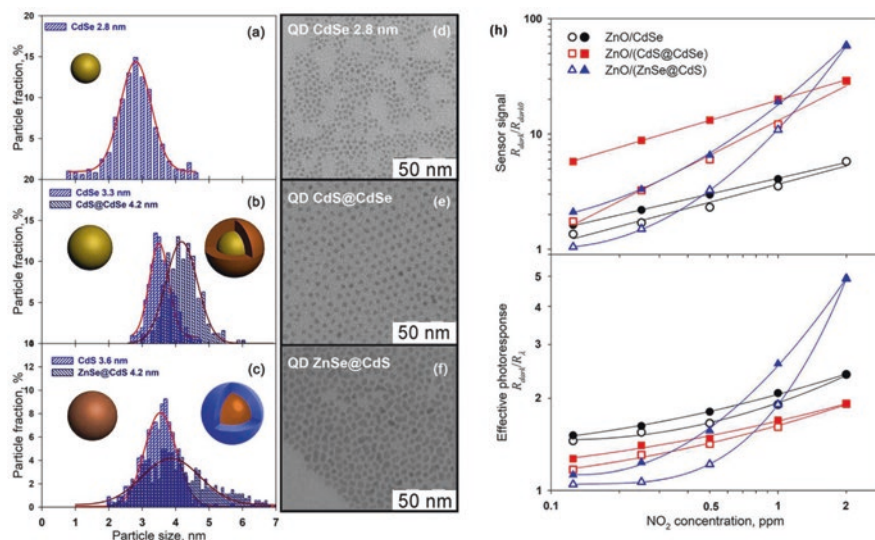
The selection of suitable material is essential for enhancing the sensing properties of the final device. For example, ZnS has been extensively studied due to its excellent electrical, optical and catalytic properties. It has useful interstitial sulphur lattice defects, sulphur vacancies and trapped surface states, enhancing possible surface oxygen adsorption, which can further facilitate adsorbed  $O^-$  ion species on the surface. These adsorbates can enhance interactions between the sensing materials and gas molecules leading to the high gas sensing performance of the ZnS sensor (Fig. 10.3) [29].

II–VI group QDs nanocrystals are characterised by peculiar optical properties, such as broad absorption and sharp emission bands as well as size-dependent photoluminescence in the visible spectral range. These characteristics can foster the use of QDs as photosensitisers to increase sensitivity to the visible light of semiconductors that are transparent in this region of the spectrum. For example, CdSe/CdS QDs resulted to be quite popular due to their bright emission with a wide excitation spectra and narrow emission bandwidths have been used as sensitisers for large bandgap semiconductors, such as  $TiO_2$  or ZnO (Fig. 10.4). These kinds of semiconductors heterostructures can exploit visible light and a high surface-to-volume ratio. Thus, they are an attractive option for visible-light-activated sensors [30].

CdS QDs with their large specific surface area and good charge transport properties resulted in the sensitisation of  $Co_3O_4$  microspheres towards  $H_2S$  [31]. The CdS/ $Co_3O_4$  composites showed high sensing response as well as very short response and recovery times at RT. However, CdS QDs can be easily oxidised and transformed into CdO at temperatures higher than 25 °C. Therefore, chemical stability of CdS QDs still needs to be enhanced in order to reduce possible oxidation phenomena.



**Fig. 10.3** Transmission electron microscopy (TEM) images of ZnS QDs at different magnifications: (a) Agglomerated and overlapped QDs, (b) transient characteristics at 175 °C and (c) response and recovery time calculation of ZnS QDs-based acetone sensor. (Reproduced with permission from Mishra et al. [29]. Published 2021 by MDPI as open access)



**Fig. 10.4** Distribution of the particle size of (a) CdSe, (b) CdS@CdSe and (c) ZnSe@CdS nanocrystals. The size distribution for the CdSe and CdS core in CdS@CdSe and ZnSe@CdS heterostructures is also presented. Low magnification TEM images of (d) CdSe, (e) CdS@CdSe and (f) ZnSe@CdS. (g) Sensor signal  $S = R_{dark}/R_{dark0}$  and (h) effective photoresponse  $P_{eff} = R_{dark}/R$  of ZnO/CdSe, ZnO/(CdS@CdSe) and ZnO/(ZnSe@CdS) nanocomposites under periodic green light illumination ( $\lambda_{max} = 535$  nm) with increasing (open symbols) and decreasing (filled symbols)  $NO_2$  concentration in the gas phase. (Reproduced with permission from Chizhov et al. [30]. Published 2019 by Frontiers as open access)

Results from other studies on composite structures based on CdSe and MOSs ( $ZnO$ ,  $SnO_2$  and  $In_2O_3$ ) indicated that their sensing properties can be improved by the irradiation with green light with good results towards  $NO_2$ . Under this condition, the electron-hole pairs will be generated in the CdSe QDs and not in the wide bandgap oxide materials, where UV activation is needed.

Hence, the photoactivated electrons in the CdSe will move to the conduction band of the MOS, here, the holes can recombine with electrons trapped by the chemisorbed  $\text{NO}_2$  at surface. The composite materials based on CdSe QDs and MOS exhibited reproducible sensing characteristics in dark and under green light activation. Furthermore, the CdSe QDs– $\text{In}_2\text{O}_3$  structure showed a better sensing response towards  $\text{NO}_2$  compared to other compositions, which was attributed to the maximum band offset between the  $\text{In}_2\text{O}_3$  and CdSe QDs. Nevertheless, the effects of environmental conditions on the sensing performance of II–VI semiconductor QDs, especially in stability, need to be further investigated [32, 33]. Table 10.4 summarises some examples of sensors produced employing QDs.

### 10.2.2 1D Nanomaterials

1D semiconductor NSs are sized at nanoscale level in two dimensions. This family of materials include nanotubes (NTs), nanofibres (NFs), NWs, nanorods (NRs) and nanofilaments (NFLs). In these systems, electrons are confined within two dimensions. 1D NMs can be amorphous or crystalline, single or polycrystalline, ceramic, metallic or polymeric like 0D materials. In addition, these materials can be employed as stand-alone or embedded within another medium. Within this class of material, their length is larger than the width. Following the quantum confinement theory, one can obtain that  $E_n$  for 1D NMs can be described by Eq. (10.3):

**Table 10.4** Summary of the sensing performance of 0D NSs of II–VI TMCs

Material	Synthesis route/ morphology	Gas	$C_g$ (ppm)	$T_{\text{oper}}$ (°C)	$S$	$\tau_{\text{res}}/\tau_{\text{rec}}$ (s)	References
ZnS	Hot-injection method/ QDs	$(\text{CH}_3)_2\text{CO}$	20	175	20	5.5/6.7	[29]
ZnO/ZnSe@ CdS	Solvothermal/ZnO decorated QDs core-shell	$\text{NO}_2$	0.12	RT	#	#	[30]
ZnO/ CdS@CdSe	Solvothermal/ZnO decorated QDs core-shell	$\text{NO}_2$	0.12	RT	#	#	[30]
$\text{Co}_3\text{O}_4/\text{CdS}$ QDs	Solvothermal/ $\text{Co}_3\text{O}_4$ decorated QDs	$\text{H}_2\text{S}$	100	RT	12.7	0.6/1.0	[31]
CdS	Solvothermal/NPs	ButOH	5	250	20	>500 />500	[33]
CdS	Solvothermal/NPs	CO	10	RT+ VIS	20	>500/ >500	[26]
ZnO/CdSe	Solvothermal/ZnO decorated QDs	$\text{NO}_2$	0.12	RT	#	#	[30]

$C_g$  concentration of target gas,  $(\text{CH}_3)_2\text{CO}$  acetone, *ButOH* butanol,  $\tau_{\text{res}}$ ,  $\tau_{\text{rec}}$  response and recovery times,  $S$  sensor response,  $T_{\text{oper}}$  operating temperature

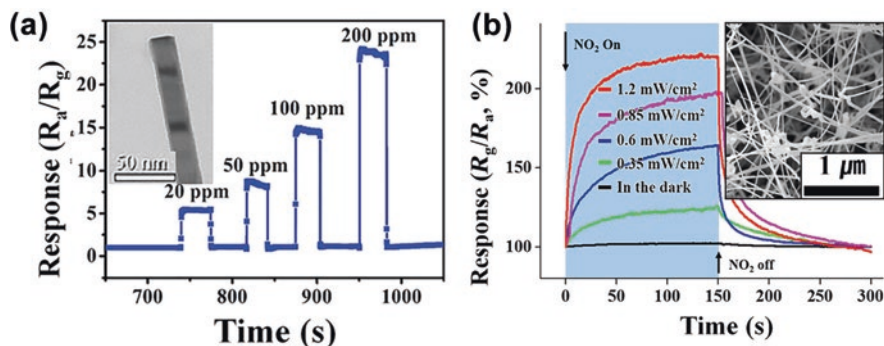
$$E_n = \left[ \frac{\pi^2 \hbar^2}{mL^2} \right] (n_x^2 + n_y^2) \quad (10.3)$$

Therefore, an appropriate comparison that explores the transition from QDs to 2D confinement can be found on rods. This transition is revealed in the bandgaps and their diameter dependencies, both of which are larger in 3D-confined dots than in 2D-confined rods. In addition, rods should exhibit 3D confinement in the short limit and 2D confinement in the long limit. As an example, Li et al. have experimentally estimated the minimum length at which presently known CdSe quantum rods have achieved the 2D confinement of a quantum wire [34].

Size dependencies of the bandgaps in CdSe dots, rods and wires should all scale linearly with  $1/d^2$ , on a first approximation. This assertion is based on overly simple particle-in-a-box calculations of the kinetic confinement energies of electrons and holes but can serve as a rule-of-thumb to provide a convenient common basis for comparing quantum confinement energies in corresponding sets of dots, rods and wires [35].

Most processes employed to synthesise one-dimensional structures are incompatible with the electrical characterisation of individual NSs. For this scope, an additional processing is necessary to remove the NWs, NRs or NTs from their growth substrate and then transfer them onto a suitable platform that allows the characterisation of single wires using them as a sensing element. Thus, one of the major problems to overcome in the manufacturing of 1D structure-based sensors is their integration with electrodes. Single 1D structures device is often realised using a 'pick and place' approach. 1D structures are, at first, dispersed into an adequate solvent such as methanol, ethanol, isopropanol or water in very low concentrations. Then, a drop of dilute suspension of 1D structures is placed on the substrate and evaporated under heating or low vacuum. Finally, NWs with manipulator tips can be moved from a template substrate [36]. Otherwise, for example, Zhu et al. [37] have utilised a solvothermal method to prepare 1D single-crystalline CdS NWs, which have shown interesting gas sensing performance towards ethanol. The inset of Fig. 10.5a shows that the CdS NWs possess a smooth surface with uniform width. However, diameters and lengths of NWs are in the generally in the range of 30–110 nm and several micrometers, respectively.

Jiang et al. [38], have utilised a thermal co-evaporation method to prepare aluminium-doped n-type ZnS NWs. Park et al. [39], had prepared Au-functionalised ZnS NWs using a combination of thermal evaporation, sputtering and thermal annealing for the preparation of gas sensing devices for the detection of NO<sub>2</sub>. The dynamic responses of the materials to different concentrations of NO<sub>2</sub> at a working temperature of 300 °C in dark and under UV illumination conditions were investigated. The same research group [40] had thermally evaporated ZnSe nanopowders to prepare multiple-networked ZnSe NWs for the detection of NO<sub>2</sub> at RT under UV illumination. The dynamic response toward 5 ppm NO<sub>2</sub> gas at RT showed a direct correlation between the ZnSe NWs responses and the UV illumination intensity. The SEM image in Fig. 10.5b shows a fibre-like morphology with widths and



**Fig. 10.5** (a) Response–recovery curves of CdS NWs gas sensor toward 20, 50, 100 and 200 ppm ethanol, respectively, (inset) High-resolution transmission electron microscopy (HRTEM) image of a CdS NW. (Adapted with permission from Zhu et al. [37]. Copyright 2014: AIP Publishing). (b) Electrical response of ZnSe NW gas sensors under UV (365 nm) illumination for different UV illumination intensities, (inset) scanning electron microscopy (SEM) image of ZnSe NWs. (Reproduced with permission from Park et al. [40]. Published 2014 by Beilstein as open access)

**Table 10.5** Summary of the sensing performance of 1D NSs of II–VI TMCs

Material	Synthesis route/ morphology	Gas	$C_g$ (ppm)	$T_{oper}$ (°C)	$S$	$\tau_{res}/\tau_{rec}$ (s)	References
CdS	Solvothermal/NWs	EtOH	100	206	14.9	0.4/0.2	[37]
Au/CdS	Solvothermal/NWs	EtOH	100	230	110	15/5	[41]
CdSe	Thermal evaporation/ nanoribbons	EtOH	50	200 + VIS	1	#	[42]
Au/ZnS	Thermal evaporation/ NWs	NO <sub>2</sub>	5	300	313 (%)	#	[39]
ZnO/ ZnS	Hydrothermal/ core–shell	ButOH	100	300	28	4/2	[43]
In <sub>2</sub> O <sub>3</sub> / ZnS	Hydrothermal + spinning/NWs	EtOH	500	300	28	28/225	[44]
ZnSe	Chemical synthesis/ NWs	NO <sub>2</sub>	0.05	RT	101 (%)	#	[40]

$C_g$  concentration of target gas, *EtOH* ethanol, *ButOH* butanol,  $\tau_{res}$ ,  $\tau_{rec}$  response and recovery times,  $S$  sensor response,  $T_{oper}$  operating temperature

lengths varying in the range of 30–100 nm and 300 nm, respectively. A summary of the sensing performance of devices based on 1D structure can be found in Table 10.5.

### 10.2.3 2D Nanomaterials

2D materials are sized at the nanoscale in one dimension. Some examples include ultrathin films and multilayer material. 2D NMs can exist as amorphous or crystalline and can be used as single or multilayer structures and are normally deposited on

a substrate and/or integrated into surrounding matrix material. Like in 1D structures, electrons in 2D materials are subject to confinement and delocalisation. Therefore, the quantum confinement theory indicates that  $E_n$  for 2D NMs can be described by the following equation:

$$E_n = \left[ \frac{\pi^2 \hbar^2}{mL^2} \right] (n_x^2) \quad (10.4)$$

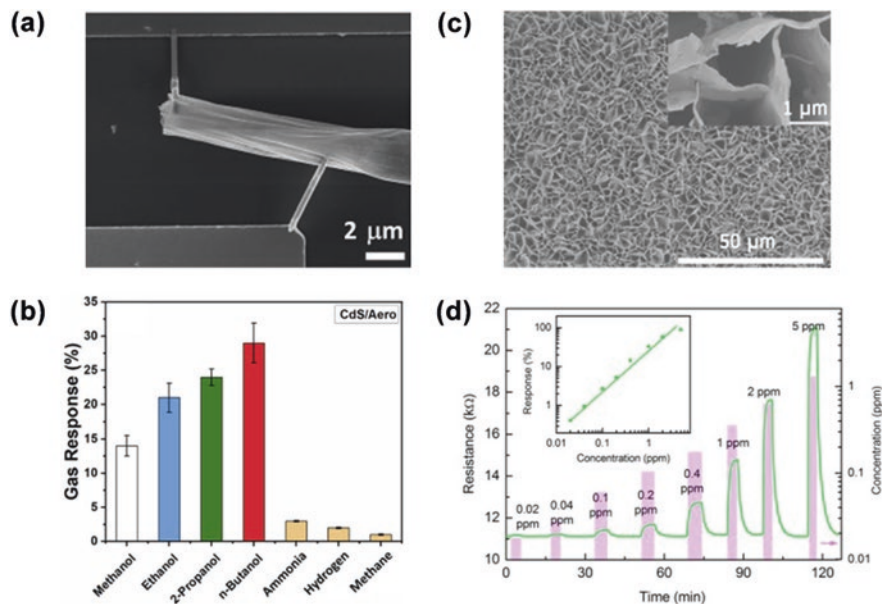
Electrons in this class are confined within one quantised dimension and still free to move in directions parallel to the layers. Hence, in this model, the optical absorption can be seen as a series of steps, with one step for each quantum number. Thus, as we imagine increasing the number of layers, we will make a smooth transition to the bulk behaviour. These latter characteristics greatly impact on the final device experimental sensing performance having a pivotal role in the surface kinetics [45].

Development of synthetic methods that allows the deposition of the 2D NSs directly onto the device can promote and improve signal reproducibility in analytical measurements [15]. As an example, Ghimpu et al. [46] uses radio frequency magnetron sputtering to obtain a thin layer of CdS that is deposited onto tubular graphitic/aerographite microstructures capable to detect ethanol at RT (Fig. 10.6a, b). In addition, the group of Li et al. [47] presented a highly ordered CdS nanoflake array, fabricated by CVD, grown directly on the substrate.

The sensing performance of the as-prepared material shows that the sensor exhibited high response to 5 ppm of NO<sub>2</sub> under green LED illumination with good selectivity and small humidity interference (Fig. 10.6c, d). However, some technological difficulties need to be addressed for the fabrication of 2D NMs-based devices. For example, if 2D NMs are composed of large nanosheets, with the use of thick-film technology employed for the deposition of the sensing layer, the possible formation of strongly agglomerated 2D nanosheets exists [36]. A summary of the sensing performance of devices based on 2D structure can be found in Table 10.6.

### 10.2.4 3D Nanomaterials

0D, 1D and 2D NMs show great potential for gas sensing applications. However, due to the lack of dispersibility control and structure liability, they also have some shortcomings in terms of sensitivity, repeatability and response speed [3]. Furthermore, the deposition of films composed of low-dimensional NMs usually leads to the stacking of NPs and to a strong decrease in available active sites, which are physically covered by the neighbouring NPs [48]. In order to overcome these problems, 3D NSs incorporate low dimensional particles for the optimisations of the gas sensing performances [48–50]. Generally, the most common 3D NSs can be divided in two macro-categories: (1) 3D NSs assembled from low-dimensional 0D, 1D and 2D building sub-units, commonly leading to 3D hierarchical structures or



**Fig. 10.6** (a) SEM image of a device based on an individual tubular microstructure of aerographite covered with a thin layer of CdS (NPs). (b) Gas response at RT of an individual CdS/aerographite microtube to 100 ppm of different vapours and gases. (Reprinted with permission from Ghimpu et al. [46]. Copyright 2019: Elsevier). (c) SEM images of CdS nanoflake arrays (NFAs) gas sensor. (d) Response–recovery curve of the sensor to different NO<sub>2</sub> concentrations. The inset in (d) shows the response of the sensor to various gas concentrations. (Reprinted with permission from Li et al. [47]. Copyright 2018: Elsevier)

**Table 10.6** Summary of the sensing performance of 2D NSs of II–VI TMCs

Material	Synthesis route/morphology	Gas	$C_g$ (ppm)	$T_{oper}$ (°C)	$S$	$\tau_{res}/\tau_{rec}$ (s)	References
CdS	Individual microtube/ Aerographite	EtOH	100	RT	22(%)	9/>500	[46]
CdS	CVD/nanoflake array	NO <sub>2</sub>	5	RT	89(%)	44/113	[47]

$C_g$  concentration of target gas, *EtOH* ethanol,  $\tau_{res}$ ,  $\tau_{rec}$  response and recovery times,  $S$  sensor response,  $T_{oper}$  operating temperature

hollow spheres; (2) 3D nano- and mesoporous structures [51, 52]. These 3D architectures result in great gas permeability and a very high specific area, providing the opportunity to tune the sensing behaviour by modifying the dimension and shape of the structure. Furthermore, the development of 3D NMs with specific designs leads to an increase of the carriers mobility, involving an improvement of the electrical properties as well as the enhancement of the reaction kinetics on the material surface [51]. 3D NSs can be developed by using either bottom-up or top-down approaches, enabling the integration of these materials into processes for manufacturing advanced devices [12].

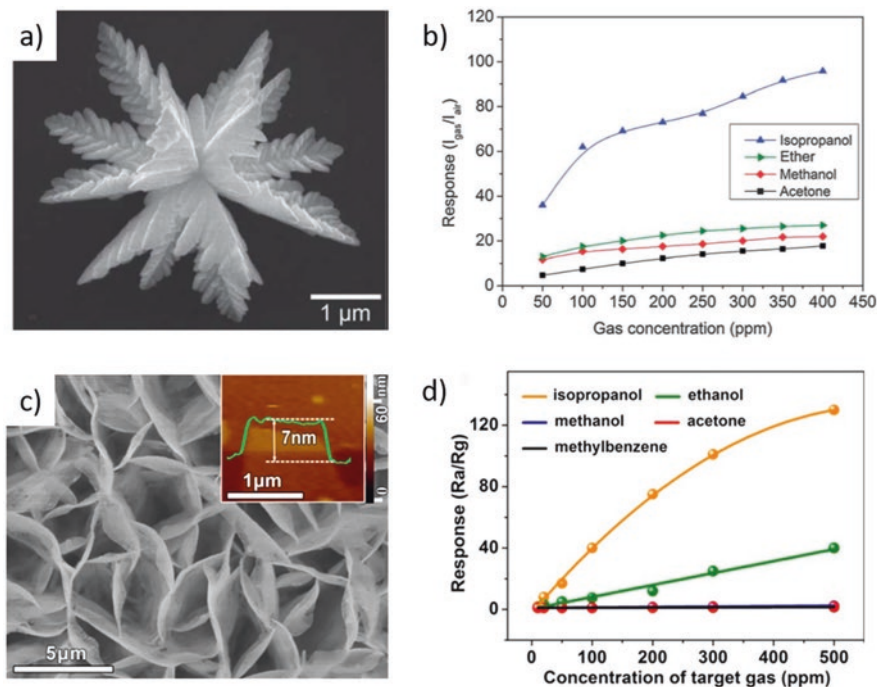
### 10.2.4.1 3D Spatial Ensembles of 0D, 1D and 2D NSs

The imitation of the natural world is one of the most widely used approaches for the development of spatial ensembled 3D NSs, this results in synthesis of the so-called bio-inspired NMs that exhibit remarkably improved chemical and physical properties [52–55]. The peculiar characteristics of these structures have enabled the investigation of 3D bio-inspired NMs for many applications, including catalysis, electronic devices, self-cleaning structures and many others [52–54]. Concerning the gas sensing field, both pure and composite bio-inspired NSs have been investigated, highlighting very interesting sensing performance. For this specific application, the bottom-up approach has been preferentially used for the development of the II–VI NSs [24, 48, 56–58], and in particular the hydrothermal synthesis paving the way for an optimal NS size and morphology control by modified synthesis parameters. For instance, Fu et al. [48] used a facile hydrothermal method for the synthesis of a novel leaf-inspired CdS micro-/nanosstructure, designed for gas-sensing application (Fig. 10.7a). The so-obtained hierarchical structures showed fascinating sensing performance including high sensitivity, low detection limit and short response/recovery times towards typical volatile organic compounds (VOC), including ether, methanol, acetone and isopropanol (Fig. 10.7b). The comparison with the sensing performance of conventional CdS spherical NPs revealed an enhancement of the leaf-like 3D NSs ability for the diffusion and adsorption/desorption of gases, resulting in a strong improvement of the sensing performance at a working temperature of 210 °C.

In order to avoid the above-mentioned problem of stacking, Liu et al. [56] grew on interdigital electrodes a CdS ultrathin NFA via CVD, maintaining, at the same time, the peculiar advantages of low dimensional NSs (Fig. 10.7c). The development of CdS NFA led to multiple advantages from the gas sensing viewpoint, including: (i) development of nanoflakes with an ultrathin thickness, which can be tune by modifying the grow parameters; (ii) exposition of the high energy {0001} CdS facets, providing a high number of active sites. The CdS NFAs layer showed a high selectivity towards isopropanol at 225 °C (Fig. 10.7d), with better sensing performance than the typical CdS NPs-based sensing films. Alongside the 3D hierarchical structures, hollow micro- and nanospheres have strongly attracted the research interests for the development of electronic and electrical gas sensors, due to their unique physical and chemical properties such as high surface-to-volume ratio, high concentration of active sites and good surface permeability allowing rapid diffusion of gas molecules [23, 58].

ZnS has been the most investigated II–VI TMC semiconductor for the development of gas sensors based on HSs, thanks to its crystal structure that enables simple and low-cost syntheses of this particular 3D structure. Brunauer-Emmett-Teller (BET) analysis highlighted a very high surface area of 26.98 m<sup>2</sup>/g for the so-prepared microsphere. The sensing characterisation revealed a good selectivity of the ZnS sensor towards ethanol, with a very fast response of 1–2 s at a lower working temperature (160 °C) than other ZnS NSs investigated so far. Zhang et al. [23], from their side, increased the carrier density and enhanced the surface reactivity of



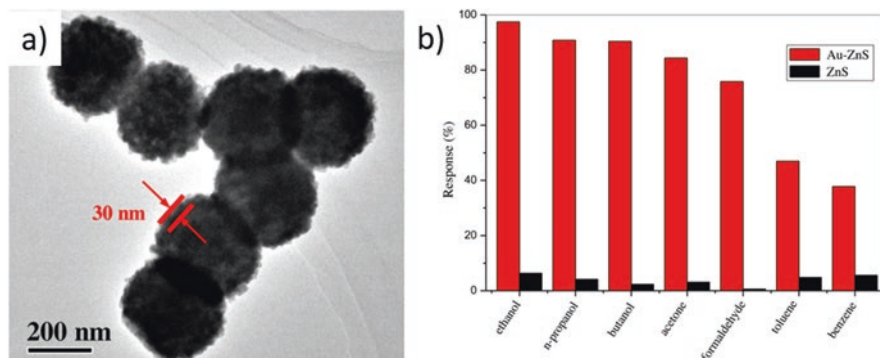


**Fig. 10.7** (a) Field emission SEM image of a leaf-like CdS micro-/nanosstructure and (b) calibration curves of CdS sensing responses vs. VOCs. (Reproduced with permission from Fu et al. [48]. Copyright 2012: Royal Society of Chemistry). (c) SEM image of CdS NFAs (inset is an atomic force microscopy image of a nanoflake thickness) and (d) dependence between CdS nanoflake thickness and sensitivity towards isopropanol. (Reproduced with permission from Liu et al. [56]. Copyright 2017: ACS Publications)

the ZnS HSs (Fig. 10.8a) by functionalisation with Au NPs. The significant improvement of the sensing performance for the VOCs detection, compared to pristine ZnS HSs (Fig. 10.8b), can be attributed to the spillover and catalytic effect of Au NPs. A summary of the sensing performance of devices based on 3D spatial ensembles of 0D, 1D and 2D NSs can be found in Table 10.7.

#### 10.2.4.2 3D Nano- and Mesoporous Structures

The classification of these NSs is based on the size of pores, which should be smaller than 100 nm and 50 nm for nano- and mesoporous materials, respectively. The morphology of nano-/mesoporous semiconductors is particularly beneficial for the development of electrical and electronic gas sensors with optimised sensing performance, owing to the possibility to tune the grain size, surface area and surface chemical properties of the materials by controlling the pore sizes [59, 60]. Basically, nanostructured nano-/mesoporous materials with nanometer-sized crystals lead to



**Fig. 10.8** (a) TEM image of ZnS HSs. (b) Sensing responses of Au NPS-ZnS HSs and ZnS HSs-based sensors vs. 100 ppm of different VOCs. (Reproduced with permission from Zhang et al. [23]. Copyright 2017; Elsevier)

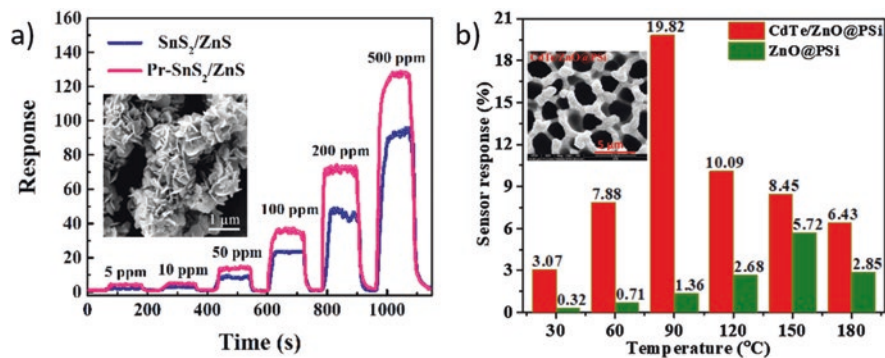
**Table 10.7** Summary of the sensing performance of 3D spatial ensembles of 0D, 1D and 2D NSs of II–VI TMCs

Material	Synthesis route/morphology	Gas	$C_g$ (ppm)	$T_{oper}$ ( $^{\circ}C$ )	$S$	$\tau_{res}/\tau_{rec}$ (s)	References
CdS	Hydrothermal/leaf-like	IPOH	100	210	63	6/15	[48]
CdS	Chemical vapour deposition/ultrathin nanoflake array	IPOH	100	225	40	12/#	[56]
PPy/ Ag <sub>2</sub> S:CdS	Sonochemical/hybrid nanocomposite	NH <sub>3</sub>	100	RT	0.65	20/#	[57]
ZnS	Hydrothermal/hollow microspheres	EtOH	100	160	4.5	1/21	[58]
Au/ZnS	Hydrothermal/hollow spheres	EtOH	100	260	34.4	6/8	[23]

$C_g$  concentration of target gas, *EtOH* ethanol, *IPOH* isopropanol,  $\tau_{res}$ ,  $\tau_{rec}$  response and recovery times,  $S$  sensor response,  $T_{oper}$  operating temperature

fast adsorption/desorption processes during gas measurements, due to the total exposures of sensing sites to target gases [61]. Furthermore, these 3D NSs exhibit unusual dynamics of charge carriers photo- and/or thermo-activated, giving rise to a superior efficiency on the receptor/transduction mechanism [62, 63].

Although nano-/mesoporous structures of II–VI TMCs have been sporadically investigated for gas sensing applications so far, and the few published studies have highlighted interesting sensing features. For instance, Xing et al. [64] used a bottom-up approach to synthesise mesoporous ZnS hierarchical NSs through a low-cost hydrothermal method (inset Fig. 10.9a). The characterisation highlighted that polyvinylpyrrolidone (PVP) plays a significant role in the formation of the mesoporous NSs. The obtained nanostructured materials showed a surface area of about 58 m<sup>2</sup>/g and an average pore size of 5–30 nm. The mesoporous ZnS active layer highlighted a high sensitivity vs. gasoline among the different gases analysed, at the



**Fig. 10.9** (a) Dynamic response of Pr-SnS<sub>2</sub>/ZnS sensing material vs. different concentrations of NH<sub>3</sub> at 160 °C (inset is the high-magnification SEM image of Pr-SnS<sub>2</sub>/ZnS hierarchical NSs). (Adapted with permission from Zhang et al. [65]. Copyright 2019: Elsevier). (b) Sensing responses of CdTe/ZnO@PSi-based sensors vs. 1 ppm of NO<sub>2</sub> at different working temperatures (inset is the field emission SEM image of the porous CdTe/ZnO@PSi structure). (Adapted with permission from Jaiswal et al. [66]. Copyright 2019: Elsevier)

optimal working temperature of 290 °C. The better sensing performance of mesoporous ZnS than ZnS solid nanospheres was attributed to the higher amount of exposed active sites of the porous structure.

The investigation of Zhang et al. [65] demonstrated that the hydrothermal method can be used also for the development of advanced 3D mesoporous morphologies based on II–VI and IV–VI heterojunction. In that study, pristine SnS<sub>2</sub>/ZnS and Pr-doped SnS<sub>2</sub>/ZnS hierarchical nanoflowers (inset Fig. 10.9a), with a very high specific surface area and small pore sizes, were successfully synthesised and deposited as active materials on tube-shaped ceramic substrates. The gas sensing characterisation proved that the Pr-SnS<sub>2</sub>/ZnS active layer showed higher response and faster response/recovery time than pristine SnS<sub>2</sub>/ZnS (Fig. 10.9a), due to the synergistic effect of the SnS<sub>2</sub>/ZnS heterojunction and Pr<sup>3+</sup>/Pr<sup>4+</sup> doping [65].

Concerning the top-down approaches, Jaiswal et al. [66] produced a CdTe-functionalised ZnO hierarchical nanostructure via magnetron sputtering deposition on a silicon substrate previously porousified through electrochemical anodisation (inset Fig. 10.9b). The so-obtained CdTe/ZnO@PSi layer was investigated as an active material for conductometric gas sensors, highlighting better sensing performance than pristine ZnO@PSi vs. NO<sub>2</sub> at a relatively low working temperature (90 °C) (Fig. 10.9b). The improvement of the sensing performance is due to the CdTe functionalisation, which led to multiple advantages including: (i) high sensitivity of CdTe to NO<sub>2</sub> even at RT; (ii) the increase of active sites due to the CdTe spillover effect; (iii) electron sensitisation effect of the nanostructured material; (iv) creation of the p-n heterojunction between CdTe and ZnO. A summary of the sensing performance of devices based on 3D nano- and mesoporous structures can be found in Table 10.8.

**Table 10.8** Summary of the sensing performance of 3D nano- and mesoporous structures of II–VI TMCs

Material	Synthesis route/ morphology	Gas	$C_g$ (ppm)	$T_{oper}$ (°C)	$S$	$\tau_{res}/\tau_{rec}$ (s)	References
ZnS	Hydrothermal/ mesoporous hierarchical NSs	Gasoline	100	290	25	7/5	[64]
Pr-SnS <sub>2</sub> / ZnS	Hydrothermal/ mesoporous hierarchical nanoflowers	NH <sub>3</sub>	50	160	14.03	6/13	[65]
ZnSe/ ZnO	Thermal oxidation/ mesoporous heterojunction	NO <sub>2</sub>	8	200	10.42	98/141	[67]
CdS/PbS/ SnO <sub>2</sub>	Hydrothermal/ mesoporous composite	H <sub>2</sub>	100	200	1125%	10.6/36.9	[68]
CdTe/ ZnO@ PSi	Electrochemical anodisation + sputtering/ hybrid hierarchical NS	NO <sub>2</sub>	1	90	19.8%	13/54	[66]

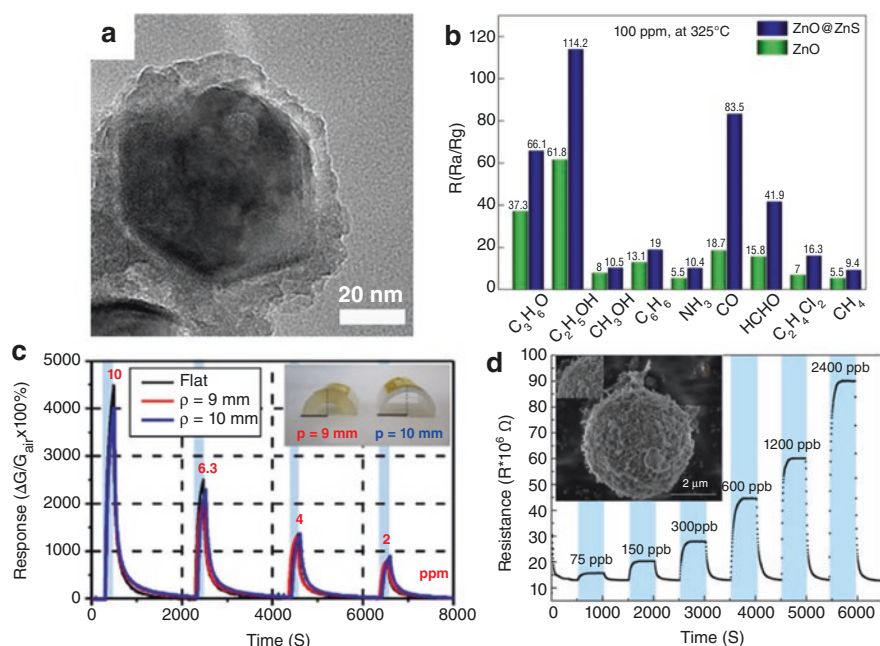
$C_g$  concentration of target gas, *EtOH* ethanol,  $\tau_{res}$ ,  $\tau_{rec}$  response and recovery times,  $S$  sensor response,  $T_{oper}$  operating temperature

### 10.2.5 Core/Shell Nanostructures

Core-shell (C-S) nanostructure is a particular type of nanocomposite material, whose special features are particularly beneficial for gas sensing applications. In particular, C-S structure allows to maximise the interfacial area between two or more materials, characteristic missing in other composite materials [69]. This is particularly advantageous for electrical and electronic gas sensors based on semiconductors, allowing to optimise the formation of the p-p, p-n or n-n heterojunction. In addition, the peculiar structure of the C-S can be used to protect the core nanomaterial from the surrounding environment, stabilising its physical and chemical properties over time [70]. A very important role in the sensing properties of a C-S is played by: (i) type of materials involved in the C-S; (ii) thickness of the shell, in which a thickness close to the Debye length of the shell material results in the optimisation of the sensing response; (iii) size and morphology of the nanostructure [71]. Concerning the latter, it should be pointed out that C-S can be applied to all types of low-dimensional materials, i.e., 0D, 1D, 2D and 3D NMs [69].

With regards to the use of II–VI TMC semiconductors in C-S for gas sensing applications, the use of hybrids of TMCs and MOSs resulted to be a promising strategy in improving the sensing performance of TMCs-based gas sensors. So far, the most investigated nanocomposite is the one composed by ZnO core and ZnS shell, due to the stability of the hybrid material and the bandgap offset between ZnO and ZnS. Furthermore, ZnO@ZnS core-shell can be synthesised in a simple way through several methods, including solution-based chemical synthesis, sulfurisation, hydrothermal method and thermal evaporation [72–75]. Y. Li et al. [72], proposed the synthesis of ZnO NPs through hydrothermal method, followed by the

formation of the ZnS shell by adding thioacetamide to the solution containing the ZnO NPs (Fig. 10.10a). In their investigations, the authors highlighted that the sensitivity and selectivity of the prepared ZnO@ZnS C-S can be tuned by modifying the thickness of the ZnS shell and the sensor operating temperature. On the one hand, a good selectivity and high sensitivity was observed vs.  $\text{NO}_2$  at 130 °C using a thin shelled structure of about a few nm, due to the presence of the Schottky junction between ZnO and ZnS, and the wide electron depletion layer (Fig. 10.10b) [72]. On the other hand, the increase of the working temperature (325 °C) and the thickening of the ZnS shell led to an increase of the sensing response towards the reducing gases, especially to ethanol (Fig. 10.10c) [76]. The sulfurisation of ZnO nanorods directly grown on substrates has been investigated to tune the ZnS shell thickness for gas sensing applications [74, 75]. For example, Yang et al. [74] exploited gaseous  $\text{H}_2\text{S}$  to sulfurise the surface of ZnO nanorods grown on a polyimide substrate. Pd nanoclusters were synthesised on the NWs to further improve the surface area and reactivity of ZnO@ZnS C-S. The Pd-ZnO@ZnSe nanocomposite showed good stability, sensitivity and selectivity on the detection of  $\text{H}_2\text{S}$ ,



**Fig. 10.10** (a) TEM image of ZnO@ZnS C-S. (Reproduced with permission from Li et al. [72]. Copyright 2021; Elsevier). (b) Selectivity diagram of ZnO@ZnS core-shell to 100 ppm of different gases at 325 °C. (Reproduced with permission from Li et al. [76]. Copyright 2021; Elsevier). (c) Comparison of dynamic sensing responses of the Pd-ZnO@ZnSe vs.  $\text{H}_2\text{S}$  concentrations at three different bending conditions. (Reproduced with permission from Yang et al. [74]. Copyright 2019; ACS Publications). (d) Dynamic response of the Zn/Sn-I-based sensor to different concentrations of  $\text{NO}_2$  at 160 °C (inset is the SEM image of Zn/Sn-I C-S). (Adapted with permission from Liu et al. [77]. Copyright 2020; Elsevier)

with a sensing response of 4491% vs. 10 ppm at 200 °C (Fig. 10.10d). Pd nanoclusters were synthesised on the NWs to further improve the surface area and reactivity of ZnO@ZnS C-S. The Pd-ZnO@ZnSe nanocomposite showed good stability, sensitivity and selectivity on the detection of H<sub>2</sub>S, with a sensing response of 4491% vs. 10 ppm at 200 °C (Fig. 10.10d).

II–VI tellurides have also been investigated as potential materials to be used as cores for C-S-based gas sensors [77]. Aiming to exploit the difference in the work function between ZnSe and SnO<sub>2</sub>, which usually causes an increase in the electron content on the surface of the sensing layer, Liu et al. [77] synthesised mesoporous ZnSe@SnO<sub>2</sub> C-S using a two-step hydrothermal process. The characterisations highlighted that the Zn:Sn ratio during the step of the SnO<sub>2</sub> shells formation strongly influenced the porosity and surface area of the final C-S. The mesoporous material obtained with a 1:1 ratio of Zn:Sn (Zn/Sn-1) showed the highest surface area, resulting in the active material for conductometric gas sensor with the best sensing performance among others developed and tested in that work. The electrical characterisation highlighted a great selectivity and sensitivity of (Zn/Sn-1) vs. NO<sub>2</sub>, with a sensing response of 6.94 to 2.4 ppm at 160 °C. A summary of the sensing performance of devices based on C-S NSs can be found in Table 10.9.

**Table 10.9** Summary of the sensing performance of core/shell NSs of II–VI TMCs

Material	Synthesis route/ morphology	Gas	C <sub>g</sub> (ppm)	T <sub>oper</sub> (°C)	S	τ <sub>res</sub> /τ <sub>rec</sub> (s)	References
ZnO/ZnS	Hydrothermal + sulfurisation in solution/ mesoporous C-S NPs	NO <sub>2</sub>	1	130	41.12	#	[72]
ZnO/ZnS	Thermal evaporation/C-S NWs	NO <sub>2</sub>	1	300	239%	#	[73]
Pd-ZnO/ ZnS	Hydrothermal + sulfurisation in gas/C-S NWs	H <sub>2</sub> S	10	200	4491%	61/62	[74]
ZnO/ZnS	Hydrothermal + sulfurisation in solution/C-S NWs	H <sub>2</sub>	1000	300	20%	#	[75]
Zn/ZnS	Hydrothermal + sulfurisation in solution/ mesoporous C-S NPs	EtOH	100	325	118.3	3/8	[76]
ZnS/ In <sub>2</sub> O <sub>3</sub>	Hydrothermal/rough C-S microspheres	EtOH	100	260	11.7	21/34	[78]
ZnSe/ SnO <sub>2</sub>	Hydrothermal/mesoporous C-S microspheres	NO <sub>2</sub>	2.4	160	6.94	64/52	[77]
WS <sub>2</sub> - CdSe/ ZnS	CVD-r + commercial QDs C-S/ nanowalls + QDs C-S	NO <sub>2</sub>	1	RT + UV	95.7%	26.8/#	[79]

C<sub>g</sub> concentration of target gas, EtOH ethanol, τ<sub>res</sub>, τ<sub>rec</sub> response and recovery times, S sensor response, T<sub>oper</sub> operating temperature

### 10.3 Summary and Outlook

This chapter proposes a critical analysis of the state of the art concerning the development and use of II–VI TMC semiconducting NMs, from 0D to 3D, for the development of electric and electronic gas sensors. Although poorly investigated in the gas sensing field so far, preliminary studies published over the last 10 years have shown peculiar sensing properties of II–VI TMCs, which are particularly suitable for the development of conductimetric and Schottky diode-based gas sensors. The possibility to easily control the morphology and crystal structure of TMC NMs allows for tailoring sensing behaviour for the detection of specific target gases. The great gas adsorption capacity of TMCs, together with the high surface-to-volume ratio of the low dimensional morphologies, provide a multitude of reactive sites leading to high sensitivity of TMC gas sensors. Due to their peculiar catalytic and optoelectronic properties, the sensing properties of II–VI TMCs can be enabled either in thermo- or photo-activation. The latter leads to the detection of gases at RT, particularly sought after for the development of gas sensors with low-power consumption. In most cases, the best sensing performance arises from the combination of different NMs, allowing the exploitation of multiple factors influencing the reception and transduction phenomena underlying gas sensing mechanisms. By heterojunction constructing, defect state controlling, doping/loading, functionalisation, etc., the composites and hybrid structures allow for tailoring sensing behaviour. Despite the obvious progress, the effective applicability of these devices for in-field applications has not been demonstrated yet. Furthermore, there are still some key issues towards the development of more practical gas sensor devices:

- (i) An appropriate selectivity towards specific gas targets has not been achieved yet, especially for low concentrations. A strong signal with low cross-sensitivity is necessary for several gas sensing applications, including air quality monitoring.
- (ii) The sensitivity of TMC gas sensors is strongly affected by the presence of humidity, leading to unreliable sensing responses especially for high concentrations of water vapour.
- (iii) The effective lifetime and stability over the time of TMC gas sensors has not been investigated in detail. However, the oxidation occurring on the surface of TMC NMs especially at high working temperatures could lead to drift of the baseline resistance and to a decrease of sensing responses over the time.
- (iv) The gas sensing mechanism commonly proposed for II–VI TMC gas sensors is inspired by the MOS sensing model, due to a lack of in-depth knowledge concerning the receptor-transducer mechanism of TMCs. Qualitative and quantitative analyses on a physical and chemical level, including operando measurements, are necessary to investigate the dominant influencing factors of the mechanism. Furthermore, the combination of experimental analysis and computer simulation are necessary to provide theoretical guidance on the adsorption between target gases and sensing layers.

Bearing in mind that many of the above-mentioned problems are common to all gas sensing materials developed to date, excellent active materials for electrical and electronic gas sensors are still in high demand. Some of the peculiar sensing performance shown by TMCs are noteworthy and could open up for a future integration of these materials into commercial devices. However, since not enough information has been gathered so far, it will be necessary a thorough investigation.

In brief, we hope that this chapter will provide a comprehensive understanding of the current state of the art on II–VI TMC gas sensing materials and their applications. With the advent of innovative nanotechnologies relevant to sensing materials and devices, there is no doubt that II–VI TMC will play a role in the future development of high-performing gas sensors.

## References

1. Yuan Z, Li R, Meng F, Zhang J, Zuo K, Han E. Approaches to enhancing gas sensing properties: a review. *Sensors (Basel)*. 2019;19(7):1495.
2. Gaiardo A, Fabbri B, Guidi V, Bellutti P, Giberti A, Gherardi S, Vanzetti L, Malagù C, Zonta G. Metal sulfides as sensing materials for chemoresistive gas sensors. *Sensors (Basel)*. 2016;16(3):296.
3. Fabbri B, Bonoldi L, Guidi V, Cruciani G, Casotti D, Malagù C, et al. Crystalline microporous organosilicates with reversed functionalities of organic and inorganic components for room-temperature gas sensing. *ACS Appl Mater Interfaces*. 2017;9(29):24812–20.
4. Liu L, Li X, Dutta PK, Wang J. Room temperature impedance spectroscopy-based sensing of formaldehyde with porous TiO<sub>2</sub> under UV illumination. *Sens Actuators B Chem*. 2013;185:1–9.
5. Zhang C, Boudiba A, De Marco P, Snyders R, Olivier M-G, Debliquy M. Room temperature responses of visible-light illuminated WO<sub>3</sub> sensors to NO<sub>2</sub> in sub-ppm range. *Sens Actuators B Chem*. 2013;181:395–401.
6. Ossai CI, Raghavan N. Nanostructure and nanomaterial characterization, growth mechanisms, and applications. *Nanotechnol Rev*. 2018;7(2):209–31.
7. Chen X, Leishman M, Bagnall D, Nasiri N. Nanostructured gas sensors: from air quality and environmental monitoring to healthcare and medical applications. *Nano*. 2021;11(8):1927.
8. Zhou X, Xue Z, Chen X, Huang C, Bai W, Lu Z, Wang T. Nanomaterial-based gas sensors used for breath diagnosis. *J Mater Chem B*. 2020;8(16):3231–48.
9. Recommendation on the definition of a nanomaterial (2011/696/EU). <https://eur-lex.europa.eu/legal-content/EN/TXT/?uri=CELEX:32011H0696>
10. Gleiter H. Nanostructured materials: basic concepts and microstructure. *Acta Mater*. 2000;48(1):1–29.
11. Pokropivny VV, Skorokhod VV. New dimensionality classifications of nanostructures. *Physica E Low Dimens Syst Nanostruct*. 2008;40(7):2521–5.
12. Nasrollahzadeh M, Sajadi SM, Sajjadi M, Issaabadi Z. An introduction to nanotechnology. *Interface Sci Technol*. 2019;28:1–27.
13. Zhou T, Zhang T. Recent progress of nanostructured sensing materials from 0D to 3D: overview of structure–property–application relationship for gas sensors. *Small Methods*. 2021;5(9):2100515.
14. Della Ciana M, Valt M, Fabbri B, Bernardoni P, Guidi V, Morandi V. Development of a dedicated instrumentation for electrical and thermal characterization of chemiresistive gas sensors. *Rev Sci Instrum*. 2021;92(7):074702.



15. Meng Z, Stolz RM, Mendecki L, Mirica KA. Electrically-transduced chemical sensors based on two-dimensional nanomaterials. *Chem Rev.* 2019;119(1):478–598.
16. Korotcenkov G. *Handbook of gas sensor materials.* New York: Springer; 2013. p. 167–95.
17. Malagú C, Giberti A, Morandi S, Aldao CM. Electrical and spectroscopic analysis in nanostructured SnO<sub>2</sub>: “long-term” resistance drift is due to in-diffusion. *Int J Appl Phys.* 2011;110(9):093711.
18. Nesheva D. Nanosized and nanostructured II-VI semiconductors: chemical sensor applications. In: Vaseashta A, Braman E, Susmann P, editors. *Technological innovations in sensing and detection of chemical, biological, radiological, nuclear threats and ecological terrorism, NATO science for peace and security series a: chemistry and biology.* Dordrecht: Springer; 2012. p. 159–64.
19. Neri G. First fifty years of chemoresistive gas sensors. *Chemosensors.* 2015;3(1):1–20.
20. Valt M, Fabbri B, Gaiardo A, Gherardi S, Casotti D, Cruciani G, et al. Aza-crown-ether functionalized graphene oxide for gas sensing and cation trapping applications. *Mater Res Express.* 2019;6(7):075603.
21. Valt M, Caporali M, Fabbri B, Gaiardo A, Krik S, Iacob E, et al. Air stable nickel-decorated black phosphorus and its room-temperature chemiresistive gas sensor capabilities. *ACS Appl Mater Interfaces.* 2021;13(37):44711–22.
22. Gaiardo A, Fabbri B, Giberti A, Valt M, Gherardi S, Guidi V, et al. Tunable formation of nanostructured SiC/SiOC core-shell for selective detection of SO<sub>2</sub>. *Sens Actuators B Chem.* 2020;305:127485.
23. Zhang L, Dong R, Zhu Z, Wang S. Au nanoparticles decorated ZnS hollow spheres for highly improved gas sensor performances. *Sens Actuators B Chem.* 2017;245:112–21.
24. Shakil MA, Das S, Rahman MA, Akther US, Majumdar MKH, Rahman MK. A review on zinc sulphide thin film fabrication for various applications based on doping elements. *Mater Sci Appl.* 2018;9(9):751–78.
25. Chizhov A, Rummyantseva M, Gaskov A. Light activation of nanocrystalline metal oxides for gas sensing: principles, achievements, challenges. *Nano.* 2021;11(4):892.
26. Giberti A, Fabbri B, Gaiardo A, Guidi V, Malagú C. Resonant photoactivation of cadmium sulfide and its effect on the surface chemical activity. *Appl Phys Lett.* 2014;104(22):222102.
27. Zhang Q, Li H, Ma Y, Zhai T. ZnSe nanostructures: synthesis, properties and applications. *Prog Mater Sci.* 2016;83:472–535.
28. Galstyan V. “Quantum dots: perspectives in next-generation chemical gas sensors” – a review. *Anal Chim Acta.* 2021;1152:238192.
29. Mishra RK, Choi G-J, Choi H-J, Gwag J-S. ZnS quantum dot based acetone sensor for monitoring health-hazardous gases in indoor/outdoor environment. *Micromachines.* 2021;12(6):598.
30. Chizhov A, Vasiliev R, Rummyantseva M, Krylov I, Drozdov K, Batuk M, et al. Light-activated sub-ppm NO<sub>2</sub> detection by hybrid ZnO/QD nanomaterials vs. charge localization in core-shell QD. *Front Mater.* 2019;6:231.
31. Dun M, Tan J, Tan W, Tang M, Huang X. CdS quantum dots supported by ultrathin porous nanosheets assembled into hollowed-out Co<sub>3</sub>O<sub>4</sub> microspheres: a room-temperature H<sub>2</sub>S gas sensor with ultra-fast response and recovery. *Sens Actuators B Chem.* 2019;298:126839.
32. Chizhov AS, Rummyantseva MN, Vasiliev RB, Filatova DG, Drozdov KA, Krylov IV, et al. Visible light activation of room temperature NO<sub>2</sub> gas sensors based on ZnO, SnO<sub>2</sub> and In<sub>2</sub>O<sub>3</sub> sensitized with CdSe quantum dots. *Thin Solid Films.* 2016;618:253–62.
33. Giberti A, Casotti D, Cruciani G, Fabbri B, Gaiardo A, Guidi V, et al. Electrical conductivity of CdS films for gas sensing: selectivity properties to alcoholic chains. *Sens Actuators B Chem.* 2015;207:504–10.
34. Li L-S, Hu J, Yang W, Alivisatos AP. Band gap variation of size- and shape-controlled colloidal CdSe quantum rods. *Nano Lett.* 2001;1(7):349–51.
35. Li J, Wang L-W. Comparison between quantum confinement effects of quantum wires and dots. *Chem Mater.* 2004;16(21):4012–5.
36. Korotcenkov G. Current trends in nanomaterials for metal oxide-based conductometric gas sensors: advantages and limitations. Part 1: 1D and 2D nanostructures. *Nano.* 2020;10(7):1392.

37. Zhu L, Feng C, Li F, Zhang D, Li C, Wang Y, et al. Excellent gas sensing and optical properties of single-crystalline cadmium sulfide nanowires. *RSC Adv.* 2014;4(106):61691–7.
38. Jiang P, Jie J, Yu Y, Wang Z, Xie C, Zhang X, et al. Aluminium-doped n-type ZnS nanowires as high-performance UV and humidity sensors. *J Mater Chem.* 2012;22(14):6856–61.
39. Park S, An S, Ko H, Lee S, Lee C. Synthesis, structure, and UV-enhanced gas sensing properties of Au-functionalized ZnS nanowires. *Sens Actuators B Chem.* 2013;188:1270–6.
40. Park S, Kim S, Lee WI, Kim K-K, Lee C. Room temperature, ppb-level NO<sub>2</sub> gas sensing of multiplexed ZnSe nanowire sensors under UV illumination. *Beilstein J Nanotechnol.* 2014;5(1):1836–41.
41. Ma X, Guo S, Shen J, Chen Y, Chen C, Sun L, et al. Synthesis and enhanced gas sensing properties of Au-nanoparticle decorated CdS nanowires. *RSC Adv.* 2016;6(75):70907–12.
42. Lin Z, Liao F, Zhu L, Lu S, Sheng M, Gao S, et al. Visible light enhanced gas sensing of CdSe nanoribbons of ethanol. *CrystEngComm.* 2014;16(20):4231–5.
43. Zhang W, Wang S, Wang Y, Zhu Z, Gao X, Yang J, et al. ZnO@ZnS core/shell microrods with enhanced gas sensing properties. *RSC Adv.* 2015;5(4):2620–9.
44. Kim K-K, Kim D, Kang S-H, Park S. Detection of ethanol gas using In<sub>2</sub>O<sub>3</sub> nanoparticle-decorated ZnS nanowires. *Sens Actuators B Chem.* 2017;248:43–9.
45. Gaponenko SV, Hilmi VD. *Applied nanophotonics.* Cambridge: Cambridge University Press; 2018.
46. Ghimpu L, Lupan O, Postica V, Strobel J, Kienle L, Terasa M-I, et al. Individual CdS-covered aerographite microtubes for room temperature VOC sensing with high selectivity. *Mater Sci Semicond Process.* 2019;100:275–82.
47. Li H-Y, Yoon J-W, Lee C-S, Lim K, Yoon J-W, Lee J-H. Visible light assisted NO<sub>2</sub> sensing at room temperature by CdS nanoflake array. *Sens Actuators B Chem.* 2018;255:2963–70.
48. Fu X, Liu J, Wan Y, Zhang X, Meng F, Liu J. Preparation of a leaf-like CdS micro-/nanosstructure and its enhanced gas-sensing properties for detecting volatile organic compounds. *J Mater Chem.* 2012;22(34):17782–91.
49. Wang G, Qin J, Zhou X, Deng Y, Wang H, Zhao Y, et al. Self-template synthesis of mesoporous metal oxide spheres with metal-mediated inner architectures and superior sensing performance. *Adv Funct Mater.* 2018;28(51):1806144.
50. Tao Z, Li Y, Zhang B, Sun G, Xiao M, Bala H, et al. Synthesis of urchin-like In<sub>2</sub>O<sub>3</sub> hollow spheres for selective and quantitative detection of formaldehyde. *Sens Actuators B Chem.* 2019;298:126889.
51. Zhao H, Lei Y. 3D nanostructures for the next generation of high-performance nanodevices for electrochemical energy conversion and storage. *Adv Energy Mater.* 2020;10(28):2001460.
52. Wulff G, Liu J. Design of biomimetic catalysts by molecular imprinting in synthetic polymers: the role of transition state stabilization. *Acc Chem Res.* 2012;45(2):239–47.
53. Ruiz-Hitzky E, Darder M, Aranda P, Ariga K. Advances in biomimetic and nanostructured biohybrid materials. *Adv Mater.* 2010;22(3):323–36.
54. Yuan J-J, Jin R-H. Temporally and spatially controlled silicification for self-generating polymer@silica hybrid nanotube on substrates with tunable film nanostructure. *J Mater Chem.* 2012;22(11):5080–8.
55. Rao W, Wang D, Kups T, Baradács E, Parditka B, Erdélyi Z, et al. Nanoporous gold nanoparticles and Au/Al<sub>2</sub>O<sub>3</sub> hybrid nanoparticles with large tunability of plasmonic properties. *ACS Appl Mater Interfaces.* 2017;9(7):6273–81.
56. Liu X-H, Yin P-F, Kulinich SA, Zhou Y-Z, Mao J, Ling T, Du X-W. Arrays of ultrathin CdS nanoflakes with high-energy surface for efficient gas detection. *ACS Appl Mater Interfaces.* 2017;9(1):602–9.
57. Yeole B, Sen T, Hansora D, Mishra S. Polypyrrole/metal sulphide hybrid nanocomposites: synthesis, characterization and room temperature gas sensing properties. *Mater Res.* 2016;19(5):999–1007.
58. Xiao J, Song C, Song M, Dong W, Li C, Yin Y. Preparation and gas sensing properties of hollow ZnS microspheres. *Nanosci Nanotechnol.* 2016;16(3):3026–9.

59. Hoa ND, Duy NV, Hieu NV. Crystalline mesoporous tungsten oxide nanoplate monoliths synthesized by directed soft template method for highly sensitive NO<sub>2</sub> gas sensor applications. *Mater Res Bull.* 2013;48(2):440–8.
60. Wang X, Qiu S, Liu J, He C, Lu G, Liu W. Synthesis of mesoporous SnO<sub>2</sub> spheres and application in gas sensors. *Eur J Inorg Chem.* 2014;5:863–9.
61. Teoh LG, Hung IM, Shieh J, Lai WH, Hon MH. High sensitivity semiconductor NO<sub>2</sub> gas sensor based on mesoporous WO<sub>3</sub> thin film. *Electrochem Solid-State Lett.* 2003;6(8):G108–11.
62. Hoa ND, Duy NV, El-Safty SA, Hieu NV. Meso-/nanoporous semiconducting metal oxides for gas sensor applications. *J Nanomater.* 2015;2015:972025.
63. Nandhakumar I, Gabriel T, Li X, Attard G, Markham M, Smith D, et al. Optical properties of mesoporous II-VI semiconductor compound films. *Chem Commun (Camb).* 2004;4(12):1374–5.
64. Xing R, Xue Y, Liu X, Liu B, Miao B, Kang W, et al. Mesoporous ZnS hierarchical nanostructures: facile synthesis, growth mechanism and application in gas sensing. *CrystEngComm.* 2012;14(23):8044–8.
65. Zhang Q, Ma S, Zhang R, Zhu K, Tie Y, Pei S. Optimization NH<sub>3</sub> sensing performance manifested by gas sensor based on Pr-SnS<sub>2</sub>/ZnS hierarchical nanoflowers. *J Alloys Compd.* 2019;807:151650.
66. Jaiswal J, Singh P, Chandra R. Low-temperature highly selective and sensitive NO<sub>2</sub> gas sensors using CdTe-functionalized ZnO filled porous Si hybrid hierarchical nanostructured thin films. *Sens Actuators B Chem.* 2021;327:128862.
67. Liu W, Gu D, Li X. Ultrasensitive NO<sub>2</sub> detection utilizing mesoporous ZnSe/ZnO heterojunction-based chemiresistive-type sensors. *ACS Appl Mater Interfaces.* 2019;11(32):29029–40.
68. Bai H, Guo H, Tan Y, Wang J, Dong Y, Liu B, et al. Facile synthesis of mesoporous CdS/PbS/SnO<sub>2</sub> composites for high-selectivity H<sub>2</sub> gas sensor. *Sens Actuators B Chem.* 2021;340:129924.
69. Xue S, Cao S, Huang Z, Yang D, Zhang G. Improving gas-sensing performance based on MOS nanomaterials: a review. *Materials.* 2021;14(15):4263.
70. Ghosh Chaudhuri R, Paria S. Core/shell nanoparticles: classes, properties, synthesis mechanisms, characterization, and applications. *Chem Rev.* 2012;112(4):2373–433.
71. Kim J-H, Mirzaei A, Kim HW, Kim SS. Variation of shell thickness in ZnO-SnO<sub>2</sub> core-shell nanowires for optimizing sensing behaviors to CO, C<sub>6</sub>H<sub>6</sub>, and C<sub>7</sub>H<sub>8</sub> gases. *Sens Actuators B Chem.* 2020;302:127150.
72. Li Y, Shan L-X, Lian X-X, Zhou Q-J, An D-M. Enhanced NO<sub>2</sub> sensing performance of ZnO@ZnS core-shell structure fabricated using a solution chemical method. *Ceram Int.* 2021;47(19):27411–9.
73. Mun Y, Park S, Ko H, Lee C, Lee S. NO<sub>2</sub> gas sensing properties of ZnO/ZnS core-shell nanowires. *J Korean Phys Soc.* 2013;63(8):1595–600.
74. Yang D, Cho I, Kim D, Lim MA, Li Z, Ok JG, Lee M, Park I. Gas sensor by direct growth and functionalization of metal oxide/metal sulfide core-shell nanowires on flexible substrates. *ACS Appl Mater Interfaces.* 2019;11(27):24298–307.
75. Tsai Y-S, Chou T-W, Xu CY, Chang Huang W, Lin CF, Wu YS, et al. ZnO/ZnS core-shell nanostructures for hydrogen gas sensing performances. *Ceram Int.* 2019;45(14):17751–7.
76. Li Y, Song S, Zhang L-B, Lian X-X, Shan L-X, Zhou Q-J. Fabrication of hollow porous ZnO@ZnS heterostructures via hydrothermal method and enhanced gas-sensing performance for ethanol. *J Alloys Compd.* 2021;855:157430.
77. Liu W, Gu D, Li X. Detection of Ppb-level NO<sub>2</sub> using mesoporous ZnSe/SnO<sub>2</sub> core-shell microspheres based chemical sensors. *Sens Actuators B Chem.* 2020;320:128365.
78. Chen Q, Ma SY, Xu XL, Jiao HY, Zhang GH, Liu LW, et al. Optimization ethanol detection performance manifested by gas sensor based on In<sub>2</sub>O<sub>3</sub>/ZnS rough microspheres. *Sens Actuators B Chem.* 2018;264:263–78.
79. Chueh Y-L, Tang S-Y, Yang C-C, Su T-Y, Yang T-Y, Wu S-C, et al. Design of core-shell quantum dots-3D WS<sub>2</sub> nanowall hybrid nanostructures with high-performance bifunctional sensing applications. *ACS Nano.* 2020;14(10):12668–78.

# Chapter 11

## II–VI Semiconductor-Based Humidity Sensors



Ghenadii Korotcenkov, Michail Ivanov, and Vladimir Brinzari

### 11.1 Introduction in Humidity Measurements

Due to the unique properties of water, humidity strongly affects living organisms, including humans, and materials [30]. Water molecules in the air change the length of organic materials, the conductivity and weight of hygroscopic materials and chemical absorbents, and the overall resistance of virtually any material. It changes the color of chemicals, the refractive index of air and liquids, the speed of sound in air or electromagnetic radiation in solids, and the thermal conductivity of gases as well as liquids and solids [58]. The efficiency and safety of many manufacturing processes, including the production, drying and storage of paint, paper, matches, furs, leather, wood products, foodstuffs, pharmaceuticals, ceramics, printing materials and semiconductor devices, are also highly dependent on the level of humidity in the surrounding atmosphere. Moreover, the industries mentioned above are just a few of the industries that need to control humidity. The amount of water vapor in the air also affects our safety, human comfort and quality of life, health, and living conditions of all living organisms, including microorganisms. In agriculture, the measurement of humidity is important for the plant protection (dew prevention), the soil moisture monitoring, etc. In the medical field, a humidity control should be used in respiratory equipment, sterilizers, incubators, pharmaceutical processing, and biological products.

Humidity measurements at the Earth's surface are also required for meteorological analysis and forecasting, climate studies, and for many special applications in hydrology, aeronautical services, and environmental studies, because water vapor is key agent in both weather and climate. As is known, water vapor is the most abundant greenhouse gas. Along with other greenhouse gases, water vapor is transparent

---

G. Korotcenkov (✉) · M. Ivanov · V. Brinzari  
Department of Physics and Engineering, Moldova State University, Chisinau, Moldova

to most solar energy. However, at the same time water vapor absorbs the infrared energy emitted upward by the earth's surface, preventing the earth from cooling at night. However, it should be borne in mind that air humidity is not constant. Changes in the water vapor content in the atmosphere not only varies with the time of day and latitude but also is affected by seasonal changes. The amount of water vapor in the air also depends on the air temperature, and this change can occur in a very wide range. Therefore, to predict changes caused by humidity, humidity control becomes mandatory in all areas of our activities, from meteorological observations and industrial control to create comfortable conditions for our lives and understand the nature of changes in the climate [16, 31, 46, 50, 53, 54, 59].

People began to realize the importance of the process of measuring humidity many years ago. Back in the fifteenth century, Leonardo da Vinci built the first device to measure air humidity. According to other sources, the German Nicolaus de Cusa invented the first hydrometer in the same fifteenth century. It was wool gravimetric *hygrometer*. There is also evidence that accurate measurement of relative humidity was very important even in ancient China and Japan [22].

Currently, many different devices, using different principles, have been developed to measure the level of relative humidity (RH) [31, 32]. For example, there is a variety of optical hygrometers, fiber-optic and planar optical humidity sensors [31]. However, in this chapter we will only consider solid-state II–VI semiconductor-based sensors operating on the basis of electrical and electronic principles [32, 46, 50, 54]. These devices, first of all, include capacitance-, conductometric-, and mass-sensitive humidity sensors. It is important to note that for the development of humidity sensors based on II–VI semiconductors, the most stable ZnS, ZnSe, and CdS compounds were mainly used. Goodell et al. [19] have shown that even ZnS nanoparticles (~3 nm) in humid atmosphere are stable at low temperatures. At a high humidity level close to 100% RH, structural changes become noticeable only after prolonged treatments (18 h) at temperatures ~50 °C. Goodell et al. [19] believe that at these temperatures, increased surface coverage with water allows the nanoparticles to rearrange within the aggregate, creating more contacts between the particles. These additional contacts provide an additional mechanism to reduce surface energy and stabilize the more crystalline structure.

## 11.2 General View on the Mechanisms of Humidity Sensing

Unfortunately, the interface of water and the II–VI compounds is not well understood yet, which makes it difficult to understand the processes occurring on the surface of these compounds when interacting with water vapor. We found only a few direct experimental reports on water adsorption on II–VI semiconductor surfaces [20, 24, 26, 62, 63]. We also found several publications presenting the results of theoretical modeling of the processes of interaction of water molecules with the ZnS surface [5, 39, 63] and CdS [21]. However, given that the principles of operation of gas sensors based on metal oxides and II–VI semiconductors are identical, it

can be assumed that the mechanisms of humidity sensing for these materials will also be identical. Other developers of II–VI semiconductor-based humidity sensors [7, 61] share the same opinion. This is quite understandable, since metal oxides formally refer to II–VI compounds in terms of their electronic and chemical properties.

According to existing concepts, the sensor response to water vapor is due to three processes, which are chemisorption, physisorption, and capillary condensation of water vapor [14, 32–34]. The chemisorption effect dominates at low humidity levels, and is manifested in the formation of OH groups on the surface of solids with a corresponding electronic exchange between chemisorbed particles and the bulk of the semiconductor. As in metal oxides, the OH group on the stoichiometric surface of chalcogenides is bonded to the metal atom, and a hydrogen, as a proton, is bonded to the surface chalcogen atom [60]. FTIR measurements performed by Goswami and Sen [20], experimentally supported this statement. They believe that S–H and Zn–O bonds are dominated on the surface of ZnS after water interaction with ZnS. With a further increase in the level of humidity and the formation of a continuous layer of OH groups, physisorption begins to dominate, which manifests itself in the formation of a multilayer of water, where both H<sup>+</sup> and H<sub>3</sub>O<sup>+</sup> act as charge carriers [42, 43]. At the stage of chemisorption, a change in conductivity can be associated with both a change in the surface potential of crystallites and the height of the intercrystalline potential barrier, which limits the flow of current in polycrystalline materials, and surface migration of protons, carried out by hopping from site to site across the surface. When the surface is covered by water, proton transport is predominant. The results of research carried out by Choudhari et al. [7] are direct confirmation of the ongoing changes in the mechanism of conductivity with a change in humidity. By studying the impedance of ZnSe films in the range of 20–100% RH, they found that at low levels of relative humidity, the impedance is purely resistive, while at high levels of relative humidity, the impedance is purely capacitive. According to Choudhari et al. [7], at high humidity, water molecules condense in intergrain space, and therefore, ZnSe films behave like an electric two-layer capacitor.

As for the capillary condensation of water vapor, the role of this process in changing the properties of the material increases sharply in the presence of pores in these materials, especially in the nanometer range [1]. It was found that in the presence of narrow capillaries, vapor condensation occurs at pressures below the normal saturated vapor pressure. The Kelvin radius characterizes the critical size of pores for a capillary condensation effect. In the case of water, the condensation of vapor into the pores can be expressed by a simplified Kelvin equation [49]:

$$r_k = \frac{2\gamma V_M \cos\theta}{\rho RT \ln(\%RH / 100)}, \quad (11.1)$$

where  $\gamma$  is the surface tension of vapor in the liquid phase,  $V_M$  is molecular volume,  $\theta$  is contact angle, and  $\rho$  is the density of vapor in the liquid phase. In this

equation, the thickness of the adsorbed layer was ignored. It is seen that the Kelvin radius increases with the relative humidity, and the rate of change (the slope) increases with relative humidity as well. This means that the pores with smaller diameter are filled first, while bigger pores are filled later. At that the larger the  $\theta$ , the larger the Kelvin radius.

## 11.3 II–VI-Based Humidity Sensors

### 11.3.1 Conductometric RH Sensors

Conductometric or resistive RH sensors in their design and principles of operation are almost identical to conductometric gas sensors, discussed in previous Chapters. The only difference is the operating temperature. Conductometric RH sensors generally operate at room temperature. The main results related to the study of conductometric RH sensors developed on the basis of II–VI compounds are shown in Table 11.1.

Analyzing the results presented in Table 11.1, we can conclude that in the development of humidity sensors based on II–VI compounds, all approaches used in the development of sensors based on metal oxides were used. As can be seen from Table 11.1, sensors based on films formed by thick-film technology [7, 9, 25, 37, 61], individual nanowires (NWs) [12, 28], NWs array [25, 36, 40, 47, 56, 64], and composites [6] were tested. There have been also attempts to develop paper-based sensors [3, 23].

#### 11.3.1.1 Thin Film RH Sensors

Naturally, the simplest way to manufacture humidity sensors is to form a sensitive layer on a dielectric substrate using the thick-film technology. The experiment has shown that for the synthesis of nanoparticles used for preparing humidity-sensitive layer, a variety of methods can be used, from hydrothermal synthesis [7, 37] to chemical bath deposition [9, 25] and co-precipitation [3, 6]. Sensors manufactured using this approach, regardless of the synthesis technology of II–VI semiconductor nanoparticles (NPs) used, have demonstrated high sensitivity. For most sensors, when the humidity changes in the range of 20–95% RH, the resistance changes up to  $3 \cdot 10^3$  times (see, for example, Fig. 11.1a). The best sensor samples also demonstrated fast response and recovery after contact with water vapor (Table 11.1). Further testing after additional measurement cycles demonstrated good reproducibility of the sensor response (Fig. 11.1b). These are good parameters for conductometric-type humidity sensors [31, 32], which testify that the electrical response of II–VI semiconductor nanoparticles is very sensitive to changes in humidity, and these materials can indeed be used to develop humidity sensors.

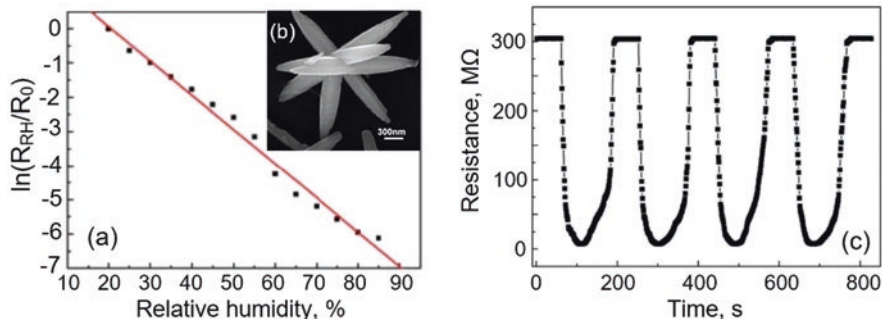
**Table 11.1** Parameters of conductometric humidity sensors based on II–VI semiconductor compounds

Material	Method	Structure	RH, %	$R_0$ , Ohm	$S$ , $R_0/R_{RH}$	$\tau_{rec}/\tau_{rec}$ , s	References
ZnS: Au, sphere ( $D \sim 200$ nm; $t \sim 10\text{--}20$ nm)	HT	Film	11–95	N/A	45	$\sim 18/30$	[37]
ZnS NPs ( $t \sim 50$ nm)	CBD	Film	30–95	$8 \cdot 10^9$	$\sim 10^2$	N/A	[25]
ZnSe NR ( $d \sim 200$ nm; $l \sim 1\text{--}2$ $\mu\text{m}$ )	SSCR	Film	20–85	$3 \cdot 10^9$	$\sim 4 \cdot 10^2$	50/80	[61]
ZnSe NPs ( $t \sim 7\text{--}21$ nm)	HT	Film	20–100	$\sim 10^9$	$\sim 10^3$	8/13	[7]
CdS NPs	CBD	Film	15–85	$\sim 10^{11}$	$\sim 5 \cdot 10^2$	60/30	[9]
CdSNPs ( $t \sim 3$ nm)	CP	Film, composite CdS-PANI	11–95	$\sim 10^5$	$\sim 10^4$	8/–	[6]
ZnS:Cu (1%) NPs	Pur.	Film, ZnS:Cu/paper	30–90	N/A	$\sim 1.3$	180/150	[23]
CdS NPs ( $t \sim 3$ nm)	CP	Film, CdS/ paper	5–99	N/A	$\sim 1.5$	55/–	[3]
ZnS NWs ( $d \sim 120\text{--}160$ nm)	VLS	NWs array	33–84	$3 \cdot 10^3$	$\sim 10^3$	14/8	[56]
ZnS NWs ( $d \sim 60\text{--}120$ nm)	VLS	NWs array	30–97	N/A	$3 \cdot 10^3$	N/A	[47]
ZnSe NWs	TcE	NWs array	10–95	$2 \cdot 10^9$	$\sim 10^3$	$< 10/10$	[36]
CdSSe NWs	CVD	NWs array	25–80	$\sim 10^6$	$\sim 2$	N/A	[40]
CdSSe NWs	CVD	NWs array	25–80	$2 \cdot 10^7$	$\sim 4$	N/A	[64]
ZnS:Al NWs ( $d \sim 60\text{--}120$ nm)	TcE	Ind-NW	50–90	$2 \cdot 10^6$	$2 \cdot 10^2$	N/A	[28]
CdS NW ( $d \sim 50\text{--}150$ nm)	CVD	Ind-NW	30–90	$\sim 5 \cdot 10^6$	$\sim 10^2$	1.5/2.5	[12]

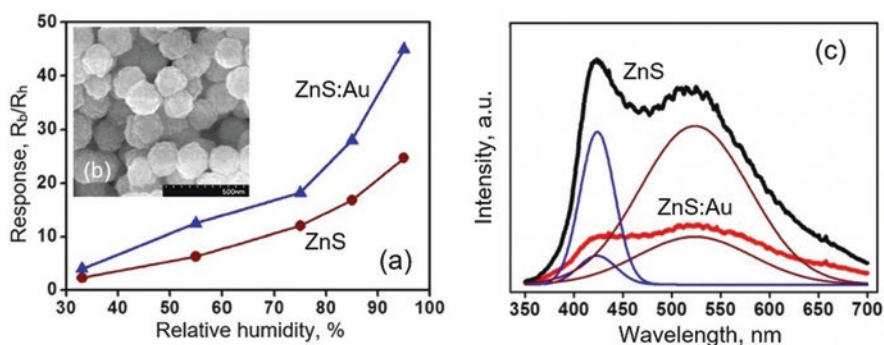
*CBD* chemical bath deposition, *CP* chemical precipitation technique, *CVD* chemical vapor deposition,  $d$  diameter of the nanowires,  $D$  diameter of the spheres, *HT* hydrothermal, *Ind-NW* individual NW,  $l$  length, *N/A* not available, *NR* nanorod, *NW* nanowire, *PANI* polyaniline, *Pur.* Purchased, *SSCR* solid-state chemical reaction,  $t$  crystallite size, *TcE* thermal co-evaporation method, *VLS* vapor–liquid–solid

Only sensors based on ZnS spheres synthesized by the hydrothermal method, despite the small size of the crystallites that form the spheres, had a noticeably lower sensitivity to humidity. Based on the analysis of TEM images of the ZnS spheres, which are an agglomeration of densely packed crystallites, it can be assumed that exactly this specific structure of nanospheres is the reason for such behavior of humidity sensors. Due to the dense structure of the sphere walls, “dead” zones are formed inside them, which do not participate in interaction with water vapor. In this regard, only crystallites from the outer layer participate in the gas-sensing effect. This means that the sensitive layer is too thin to make a significant





**Fig. 11.1** (a) Static and (c) dynamic conductometric responses of ZnSe nanorod-based films to humidity, (b) SEM image of ZnSe nanorod. (Reprinted with permission from Yan et al. [61]. Copyright 2009; Elsevier)

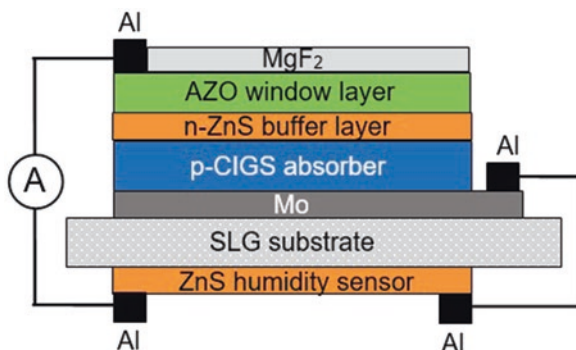


**Fig. 11.2** (a) Humidity-sensing responses of the ZnS and ZnS-Au sphere-based sensors, (b) SEM image of ZnS nanospheres with diameter  $\sim 200$  nm. (b, c) PL spectra of the ZnS and ZnS-Au spheres. Each PL spectrum was divided by two Gaussian deconvolution curves, which were centered at approximately 425 nm (blue line) and 525 nm (brown line). (Reprinted from Liang and Liu [37]. Published 2014 by Springer as open access)

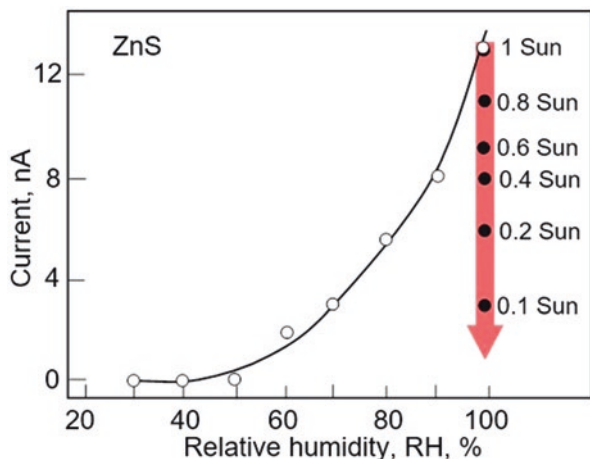
contribution to the change in the conductivity of the sensitive layer formed by the nanospheres. Surface modification by noble metals can improve the sensitivity of these sensors (Fig. 11.2a). In particular, Liang and Liu [37] established that the ZnS:Au sensors exhibited twofold increase in sensitivity compared with sensors based on a pure ZnS nanocrystalline spheres. Unfortunately, the authors did not offer an acceptable description of the mechanism of the observed sensing of sensors. The studies carried out do not answer the question – how do gold clusters on the ZnS surface affect the proton conductivity of the surface layer? There is only an assumption that the observed changes are associated not with the appearance of gold clusters, but with the peculiarity of the used process of its deposition. It is possible that it is the process of plasma sputtering used to deposit gold can damage the ZnS surface to a certain extent, and thus alter the surface characteristics of the ZnS, involved in interaction with water vapor. This assumption is confirmed by the change in the photoluminescence spectrum after the deposition of gold (Fig. 11.2b).

Thin film humidity sensors also include sensors developed by Hsueh et al. [25]. They have integrated ZnS thin film humidity sensors with  $\text{MgF}_2/\text{ZnS}/\text{CuIn}_{1-x}\text{Ga}_x\text{Se}_2$  (CIGS)/Mo photovoltaic cell to create the so-called self-powered device. Its structure and connections between elements of the sensor are shown in Fig. 11.3. Soda-lime glass (SLG) was used as a substrate. Both ZnS layers of this double-sided device were deposited simultaneously by chemical bath deposition method at 80 °C. All interdigitated electrodes were deposited on the back of the ZnS film by sputtering. 100-nm-thick  $\text{MgF}_2$  was also deposited on the top of the photovoltaic (PV) cell as the anti-reflection layer by thermal evaporation.

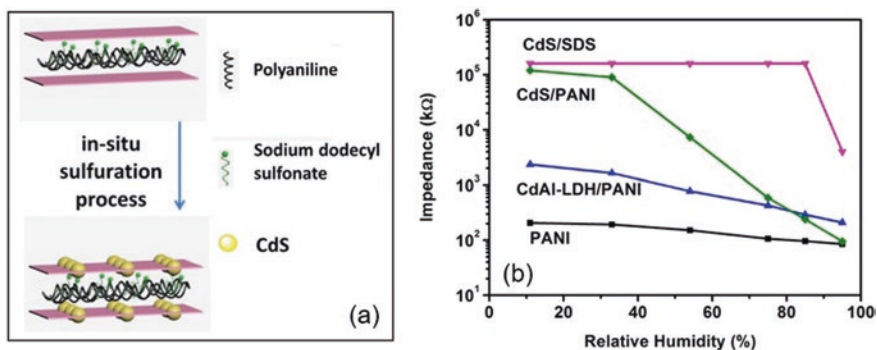
Testing of the developed devices has shown that the backside ZnS humidity sensor can function using power from the front CIGS *photovoltaic (PV)* cell. The curve in Fig. 11.4 reflects the effect of humidity on the sensor readings under illumination corresponding to 1 sun. Repeated measurements showed good reproducibility of the sensor response. The measured currents were very stable with negligible fluctuation. This suggests that the developed device is indeed a self-powered humidity sensor. However, when the illumination changes in the range of 1–0.1 of sun illumination, the signal decreases almost threefold (Fig. 11.4). It was found that the observed change is a consequence of the change in the open-circuit voltage ( $V_{oc}$ ). When changing solar illumination from 1 sun to 0.8, 0.6, 0.4, 0.2, and 0.1 sun,  $V_{oc}$  varied from 0.6 to 0.59, 0.58, 0.57, 0.55, and 0.52 V, respectively. Since, due to the high resistance of the ZnS film ( $10^7$ – $10^9$  Ohm), the PV cell operates in open-circuit mode, the sensor supply voltage corresponds to  $V_{oc}$ . Therefore, due to the change in  $V_{oc}$ , the measured currents also changed. True, the change in sensor signal significantly exceeds the change in open-circuit voltage. In all likelihood, in the course of measurements, illumination of the humidity sensor also occurs, contributing to the change in the resistance of the ZnS film. It follows that for correct humidity measurements, it is necessary not only to control the sensor resistance and the open-circuit voltage of the PV cell but also to use some calibration curves that take into account the effect of lighting on the sensor readings. This creates certain difficulties for the use of such sensors.



**Fig. 11.3** Schematic diagram of the bifacial self-powered device with an integrated CIGS PV cell and ZnS humidity sensor. (Idea from Hsueh et al. [25])

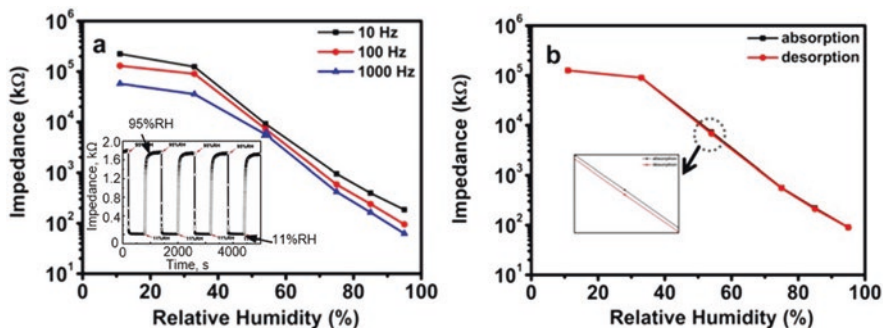


**Fig. 11.4** The current measured at RH 95% with varied illumination. (Data extracted from Hsueh et al. [25])



**Fig. 11.5** (a) Schematic illustration of the transformation from the CdAl-LDH to the CdS. (b) Response of the sensors of CdS/PANI, CdS/SDS, CdAl-LDH/PANI, and PANI to humidity: SDS sodium dodecyl sulfonate, CdAl-LDH co-intercalated Cd, Al layered double hydroxides. (Reprinted with permission from Chen et al. [6]. Copyright 2018; Elsevier)

As for the most sensitive humidity sensors based on 2–6 compounds and fabricated as the thin films, such sensors are devices developed by Chen et al. [6]. The main element of these sensors is the layers of CdS/PANI composite with sandwich structure (Fig. 11.5a). CdS/PANI composite was synthesized by in situ sulfuration process of polyaniline (PANI) and sodium dodecyl sulfonate (SDS) co-intercalated Cd, Al layered double hydroxides (CdAl-LDH/PANI). Sensors based on CdS/PANI composite showed good sensitivity to humidity, low hysteresis (0.5% under 54% RH) (Fig. 11.6b), and fast response/recovery processes compared with PANI-based sensors. When the relative humidity increased from 11% to 95%, the impedance quickly decreased by four orders of magnitude after just 8 s and response improved by three orders of magnitude compared to pure PANI (see Fig. 11.6b). It is also



**Fig. 11.6** (a) The impedances of sensor based on CdS/PANI varied with a humidity series at different frequencies and the insert plots the repeated response and recovery characteristics of CdS/PANI composite; (b) Humidity hysteresis of CdS/PANI sensor at the working frequency of 100 Hz. (Reprinted with permission from Chen et al. [6]. Copyright 2018; Elsevier)

important to note that the logarithmic impedance of the CdS-PANI layer formed on the Ag-Pd interdigitated electrodes was linear with respect to relative humidity and had a weak frequency dependence, as well as good repeatability in cyclic tests (Fig. 11.6a).

According to Chen et al. [6], reported characteristics of CdS/PANI-based humidity sensors are attributed to the unique construction of CdS/PANI composite, which can form orderly interwoven network structure between CdS and PANI. At that sensor response of such a structure mainly arises from the interaction of water vapor with PANI. Polyaniline (PANI) is conjugated conducting polymer that exhibits good conductivity and electrochemical reversibility. It was confirmed that the change in the conductivity of PANI under influence of humidity is associated with the “proton effect.” Water is well known for its protonation, and the released proton interacts with universally conjugated C=C double bonds in polyaniline. The electrical conductivity of PANI under the influence of water vapor can be viewed as a jump of electrons, which is facilitated by the exchange of protons. Chen et al. [6] believe that sandwich construction of composite is favorable for enhanced mobility of the anion or the charge transfer across the polymer chains. In addition, the sandwich structure provides polymer molecules with a confined and stable environment, which improves humidity and thermal stability [6].

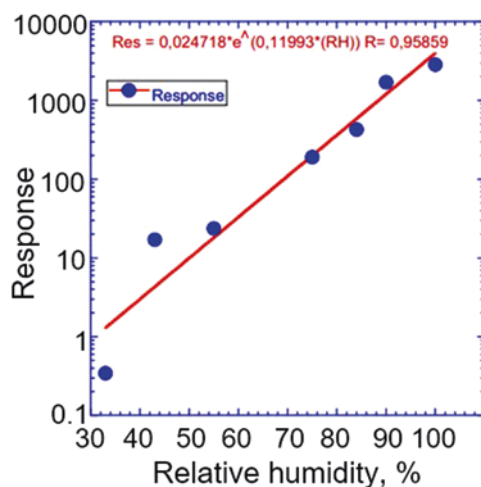
### 11.3.1.2 Nanowire-Based Sensors

Currently, the use of 1D nanostructures in the development of various devices is a very popular direction. As can be seen from the results presented in Table 11.1, 1D nanostructures are also used in the development of II–VI semiconductor-based RH sensors. The main result of these studies is confirmation of the fact that the use of both individual nanowires (NWs) and an array of NWs helps reduce response and recovery times, as well as hysteresis. For example, Du et al. [12] reported that their humidity sensors based on individual CdS nanowires had response and recovery times ~1.3 and 2.4 s, correspondingly. It should be noted that the same situation was

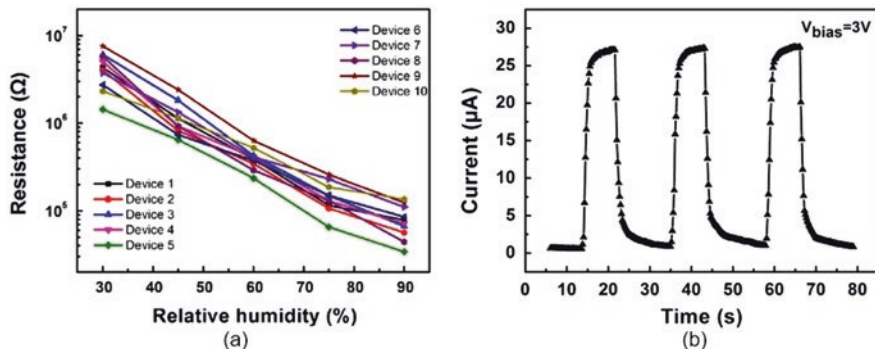
observed for humidity sensors based on the metal oxide 1D nanostructures [17]. High gas permeability in the absence of nanopores is the main explanation for the observed effect. Fast response is an important advantage of NW-based RH sensors. The absence of pores in 1D structures also excludes the possibility of capillarity condensation of water vapor, which allows such sensors to operate at very high humidity levels. However, the absence of intercrystalline barriers and nanopores in such structures leads to the fact that the noticeable sensitivity to humidity in these devices is shifted toward higher humidity levels in comparison with traditional sensors based on nanocrystalline materials. These statements are clearly visible in Fig. 11.7, where the results, obtained by Okur et al. [47], are presented for ZnS nanowire-based humidity sensors. The sensors are capable of operating up to 97% RH, but an acceptable sensor response is only observed above 30% RH.

Nanowire-based sensors also show good repeatability (Fig. 11.8b). However, as noted in Korotcenkov [34], with the existing technology for growing 1D structures, one cannot expect good reproducibility of the sensor parameters. This is confirmed by the results given in Fig. 11.8a. It can be seen that the resistance of individual nanowires varies within a fairly wide range. This variation in parameters creates additional difficulties when replacing sensors in real devices used in different applications.

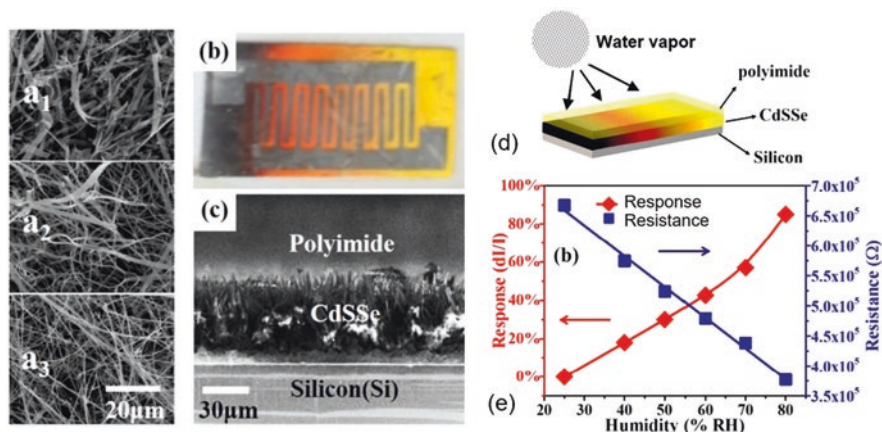
Zhang et al. [64] and Lu et al. [40] tried to optimize the structure of nanowire-based humidity sensors (Fig. 11.9a). However, their attempts were not successful. Given the specific properties of polyimide (PI), such as high temperature resistance, good mechanical and adhesive properties, good chemical resistance, low dielectric constant, long-term stability in the presence of moisture, and insulation, Zhang et al. [64] and Lu et al. [40] proposed to apply polyimide to the surface of the CdSSe nanowire array (Fig. 11.9c). As a result, they obtained the structure shown in Fig. 11.9d. The humidity-sensing response of these sensors is shown Fig. 11.9e. The manufactured sensors showed a linear dependence of resistance on humidity and a



**Fig. 11.7** Variation in sensor values of ZnS nanowires versus 22%, 33%, 43%, 55%, 75%, 84%, and 97% RH. (Reprinted with permission from Okur et al. [47]. Copyright 2012: Elsevier)



**Fig. 11.8** (a) Relative humidity influence on the resistances of sensors based on the individual CdS nanowire for ten devices; (b) Current response of a CdS NW sensor to dynamic switches between dry air (5%) and moist air of 75% RH at  $V_{bias} = 3$  V. The CdS NWs were synthesized via a CVD method in a Cd-enriched atmosphere. The CdS NWs had the diameter in the range of 50–150 nm and the length of typically tens of micrometers. (Reprinted with permission from Du et al. [12]. Copyright 2014: Elsevier)



**Fig. 11.9** (a) ( $a_1$ – $a_3$ ) the SEM images of CdSSe nanowire array chips. Scale bar: 20  $\mu\text{m}$ . (b) The image of the humidity sensor with interdigital electrodes. (c) Cross-sectional SEM image of PI coated CdSSe nanowire chip. Scale bar: 30  $\mu\text{m}$ . (d) Schematic diagram of the sensor; (e) The humidity-sensing response and sensor resistance at different relative humidity values. (Reprinted from Lu et al. [40]. Published 2019 by IOP as open access)

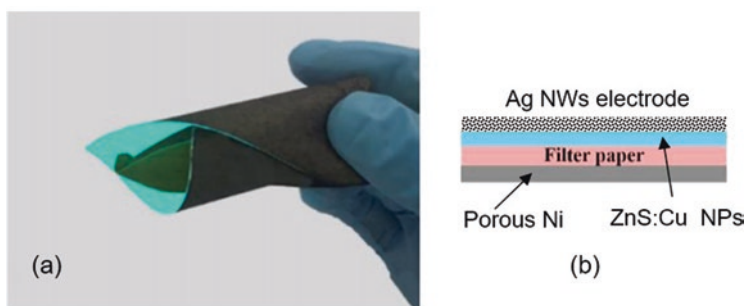
fairly good stability of characteristics. The resistance of the sensors, regardless of the humidity level, was stable for 1000 s. However, the magnitude of the sensor response was significantly less than that of sensors with an open surface of the CdSSe nanowire array (see Table 11.1). Sensor response appears to have been very slow too.

According to the authors of these articles, the functional layer for humidity monitoring is PI, which, due to the expansion caused by humidity in the PI layer, puts

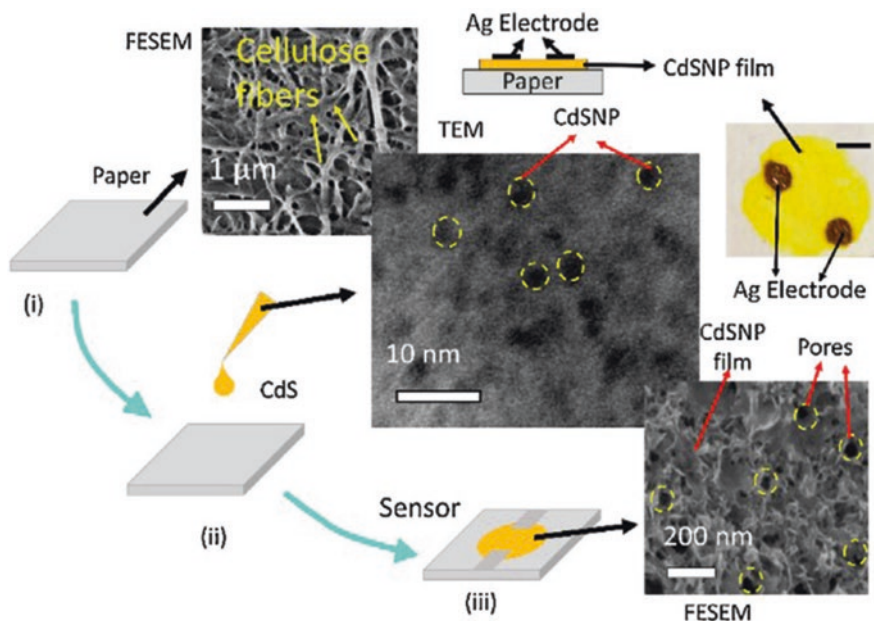
pressure on the conductive layer of the nanowire, causing a change in its conductivity and thus provides humidity measurement. In principle, this mechanism of sensitivity to humidity is realistic, since swelling of the PI occurs in a humid atmosphere [51]. According to Sager et al. [51], a humidity extension coefficient is only 60–80 ppm/%RH. However, it is not known if this expansion is sufficient for the observed effect to occur, since it is not clear how this expansion will affect the underlying layer of NWs array. Besides, experiments carried out by [2] showed that only an amount of 1.5–6% water (by mass) can be absorbed by the polymer material in 100% RH air. That is, the change in PI film weight is also not significant. It should also not be forgotten that polyimide, depending on the manufacturing technology, can have good permeability for gases and water vapors. Therefore, the very effect of the sensitivity to humidity of sensors developed by Zhang et al. [64] and Lu et al. [40] may be a simple consequence of the permeability of the polyimide. In this case its small value only indicates that the polyimide coating, due to its low permeability, significantly limits the penetration of water vapor to the CdSSe nanowire array.

### 11.3.1.3 Paper-Based RH Sensors

He et al. [23] and Bhattacharjee et al. [3] suggested an interesting approach to developing flexible humidity sensors. For the manufacture of sensors, they used filter paper on which CdS [3] or ZnS:Cu [23] nanoparticles were applied by drop casting or spin coating. Previously, this approach has already been used in the development of gas and humidity sensors [18, 29, 41, 45]. He et al. [23] have shown that paper-based sensors have excellent flexibility and can operate under different bending conditions (see Fig. 11.10). However, such sensors, regardless of their design features and the material used, had low sensitivity and long response and recovery times. The reasons for the low sensitivity even when using CdS NPs with a size of ~3 nm are not explained by the authors. It can only be assumed that this behavior is associated with the influence of the paper used as a substrate, or with design flaws



**Fig. 11.10** (a) Schematic image of the paper-based sensor, (b) Image of изогнутого сенсора fabricated on the paper. (Reprinted from [23]. Published 2019 by MDPI as open access)



**Fig. 11.11** Image (a) of this figure shows the fabrication steps (i–iii) of the sensor along with the FESEM image of the paper surface, TEM image of the CdSNPs, a cross-sectional schematic diagram along with a photographic image of the sensor, and a FESEM image of the paper embedded with CdSNPs. The scale bar in the sensor image is of 1.5 mm. (Reprinted with permission from Bhattacharjeea et al. [3]. Copyright 2019: Elsevier)

in the manufactured sensors. In one case (see Fig. 11.10a), the resistance of the paper makes a significant contribution to the total resistance of the sensor, sharply limiting the change in resistance of the sensor in a humid atmosphere. In another case (Fig. 11.11), due to the special structure of the paper, CdS nanoparticles do not form a continuous layer necessary to create a channel for the flow of charge carriers, which is controlled by the properties of only CdS nanoparticles. It should not be forgotten that the paper itself is involved in the processes of adsorption and desorption of water vapor and can significantly affect the response kinetics of sensors developed using layers of II–VI semiconductor compounds formed on its surface.

### 11.3.2 Capacitance RH Sensors

In the simplest case, a capacitance-type sensor is made of two parallel plates. In such structure the capacitance between the two electrodes is given by equation

$$C = \epsilon_r \epsilon_0 \frac{A}{d}, \quad (11.2)$$



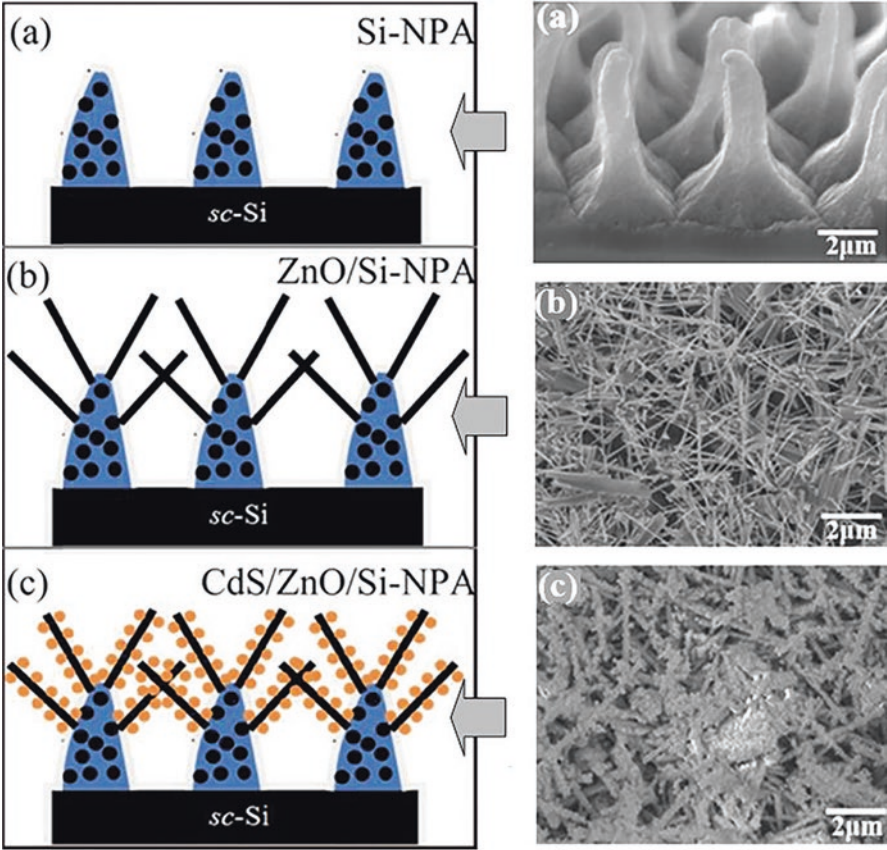
where  $\varepsilon_r$  and  $\varepsilon_0$  are the relative and vacuum permittivity constants, respectively,  $A$  is the plate surface area, and  $d$  is the plate distance. From this equation, it is evident that only three ways exist to effect a change in the capacitance of that device: (1) alter the distance  $d$  between the two plates, (2) alter the overlapping area  $A$  between the two plates, and (3) change the dielectric permittivity between the plates [27]. This means that capacitive sensors can detect only those gases and vapors that affect these parameters. In principle, water vapor when interacting with various materials can exert such influence. In particular, the filling of pores in sensing material with water during its condensation can give rise to a multiple increase in the dielectric constant at the corresponding porosity of the material. As is known, the dielectric constant of air is 1 and that of water is 81. The dielectric constants of CdS and ZnS are  $\sim 9$ – $10$ . That is why, by measuring the change in capacitance, it is possible to determine the presence of water vapor in the air. The principles of operation and a more detailed description of the design of capacitive gas and humidity sensors can be found in Ref. [4, 27].

Parameters of capacitance RH sensors based on II–VI compounds are listed in Table 11.2. It is seen that all these sensors were developed using metal oxide-based composites [15, 44, 48]. Their testing showed that the highest capacitance response ( $C_{RH}/C_0$ ) was possessed by sensors based on CdS–ZnO heterostructures with a specific structure formed on the basis of silicon nanoporous pillar array (NPA) (see Fig. 11.12). ZnO nanorods were formed using chemical vapor deposition (CVD) method, and CdS nanoparticles with average diameter of  $\sim 70$  nm were synthesized using successive ion layer adsorption reaction (SILAR) method. With a change in humidity in the range of 3–95%, the capacity of such sensors changed by more than  $2 \cdot 10^3$  times (Fig. 11.13a). The results also show that the response of the sensor prototypes decreases with increasing frequency. It may be due to the comparability of the relaxation time of the related processes with the period of applied measuring AC voltage. According to Feng et al. [15], fast response/recovery times and low hysteresis of CdS/ZnO/Si-NPA-based sensors were attributed to the combined effect of the channel network created by Si-NPA (see Fig. 11.12a), which provided an efficient path for the penetration and removal of water vapor from the sensitive layer, and the physical and chemical properties of CdS, which facilitate adsorption/desorption processes.

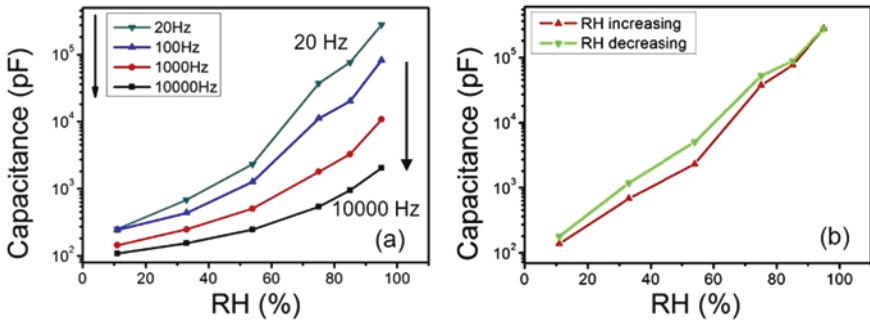
**Table 11.2** Parameters of capacitance humidity sensors based on II–VI semiconductor compounds

Material	Method	RH, %	$S (C_{\max}/C_{\min})$	$\tau_{\text{res}}/\tau_{\text{rec}}$ , s	References
CdS–ZnO	ZnO-CVD CdS-SILAR	3–95	$\sim 2000$ (20 Hz)	110/32	[15]
CdSe–F8	CdSe (QDs)-chemical	10–95	$\sim 8$ (120 Hz)	9/7	[44]
ZnS:Cu(1%)-PANI	ZnS:Cu - HT	30–90	$\sim 1.5$ (N/A Hz)	42/24	[48]
ZnS:Cu(0.1%)-paper	ZnS:Cu – purchased	20–90	30 (10 kHz)	180/140	[23]

F8 polymeric semiconductor poly-(9,9-di-n-octylfluorenyl-2,7-diyl), HT hydrothermal method, PANI polyaniline



**Fig. 11.12** The structural schematic diagrams and SEM images of (a) Si-NPA, (b) ZnO/Si-NPA, and (c) CdS/ZnO/Si-NPA. (Reprinted with permission from Feng et al. [15]. Copyright 2017: Elsevier)



**Fig. 11.13** (a) The capacitance variation of CdS/ZnO/Si-NPA with RH level measured with different frequencies. (b) The hysteresis of CdS/ZnO/Si-NPA between RH increasing and decreasing processes. (Reprinted with permission from Feng et al. [15]. Copyright 2017: Elsevier)

**Table 11.3** Comparison of various parameters of capacitive humidity sensor based on polymer II–VI semiconductor composites

Material	C, pF		Sensitivity, $\Delta C/\Delta RH$ (pF/RH), %	Res./ Rec. time (s)	Hysteresis(%)	References
	30%RH	90%RH				
PANI	16	23.2	12	53/30	17.8	[48]
PANI/1% Cu-ZnS	18	25.1	12	42/24	1.5	
PANI/3% Cu-ZnS	22.1	24	3.2	47/29	2.7	
PANI/5% Cu-ZnS	21.6	23.2	2.5	55/30	2.9	
Ag/F8/Ag	16	65 (75%RH)	110	15/7	N/A	[44]
Ag/F8-CdSe/ Ag	12.1	89	116	9/7	~5	

As for the sensors based on polymer-based composites, their sensitivity to humidity was significantly lower. Moreover, given the concentration of CdSe and ZnS in the composite, at which some optimizing effect was achieved (see Table 11.3), II–VI compounds apparently do not determine the capacitive properties of the formed structures, but only affect the porosity of humidity-sensitive matrix. In this case, the polymer is the sensitive element in this matrix and its properties mainly determine the characteristics of humidity sensors. In particular, PANI is conducting/semiconducting stable polymer, the conductivity of which is largely dependent on its oxidation state. The increase in the capacity of capacitive moisture sensors based on PANI is mainly explained by an increase in the dielectric constant due to the absorption of water molecules, as well as by doping of PANI with water molecules. This doping, in addition to increasing the concentration of charges, also increases the polarizability of PANI.

### 11.3.3 QCM-Based RH Sensors

Quartz crystal microbalance (QCM) is a piezoelectric device based on the piezoelectric effect of materials. Typically, piezoelectric sensors are a quartz crystal disc coated on both sides with gold electrodes that serve as sensing surfaces. Quartz is the most commonly used piezoelectric material because of its low cost and stability against thermal, chemical, and mechanical stress. It was found that the quartz crystal microbalance technique is very sensitive to mass changes on the nanogram scale ( $\sim 1 \text{ ng/cm}^2$ ) by measuring the change in the resonance frequency (Eq. 11.3). It responds to a given increase of mass simultaneously, regardless of the species adsorbed. Based on this, it can be concluded that these sensors are not selective. However, water in the range of commonly measured humidity levels (30–90% RH) can be adsorbed in much larger quantities than gases. Therefore, we can assume that QCM-based humidity sensors have some selectivity. The change in resonant

**Table 11.4** Parameters of QCM-based humidity sensors developed using II–VI semiconductor compounds

Material	Method	Thickness	$f_0$ , MHz	RH, %	$\Delta f$ , Hz	$\tau_{res}/\tau_{rec}$	References
CdS NPs (30–40 nm)	CBD	200 nm	8	17–85	~1000	<6 min	[8]
ZnCdSSe NWs	CVD	NWs array	10	10–95	~1300	21/8 s	[55]
ZnS NWs (120–160 nm)	VLS	NWs array	8	30–100	~200	14/18 s	[56]
ZnS NWs (60–120 nm)	VLS	NWs array (100 nm)	8	22–97	~900	<50 s	[47]

CBD chemical bath deposition, NPs nanoparticles, NWs nanowires, VLS vapor–liquid–solid method

frequency depends on the change in mass of the sensitive layer ( $\Delta m$ ) on the surface of the quartz crystal and can be calculated using the Sauerbrey linear frequency change relation [52]:

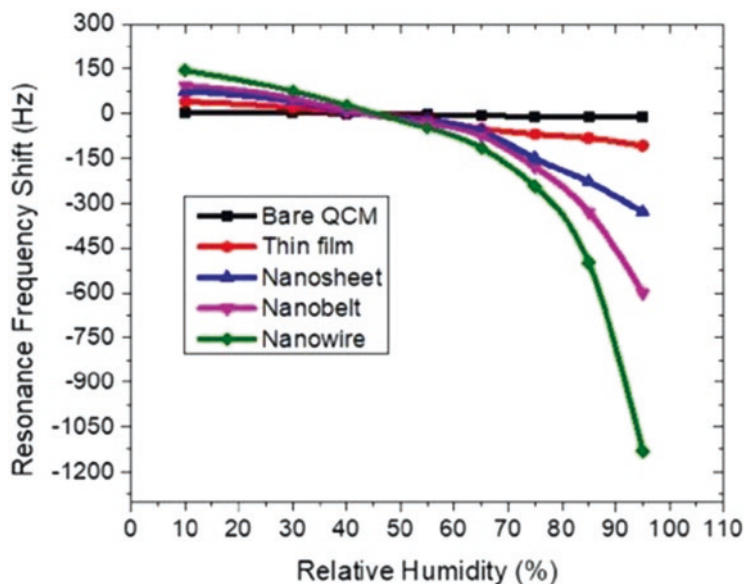
$$\Delta f = \frac{2f_0^2 \Delta m}{A\sqrt{\mu\rho}}, \quad (11.3)$$

where  $f_0$  is the resonant frequency of the fundamental mode of the QCM crystal,  $A$  is the area of the gold coated electrodes on the quartz crystal,  $\rho$  is the density, and  $\mu$  is the shear modulus of the quartz substrate. Hence, it follows that the sensitivity of the sensors is determined by the adsorption properties of the material applied to the surface of the quartz crystal.

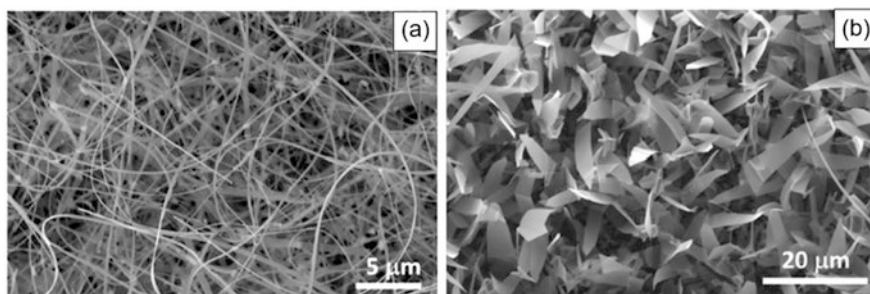
Quartz crystal microbalance (QCM)-based sensors are the most common type of mass-sensitive sensors used for both gas sensor [57] and biosensor applications [38]. The same situation is observed in the development of humidity sensors. Only QCM-based mass-sensitive sensors using II–VI compounds as sensitive layer have been tested as humidity sensors. The main parameters of these sensors are given in Table 11.4.

The results given in Table 11.4 indicate that QCM-based humidity sensors based on II–VI compounds have parameters suitable for practical use. It is seen that the change in the resonant frequency with a change in humidity in the range of 10–90% RH can exceed 1000 Hz. This means that the change in humidity in the specified range can be controlled with high accuracy.

An important result of these studies is also the confirmation of the significant role of the size effect in humidity sensing by QCM devices [55]. As is seen in Fig. 11.14, the sensor coated with ZnCdSSe NWs shows greater frequency shift than the others coated with thin film, nanosheets (NSs) and nanobelts (NBs). This is expected because the size of the NWs significantly less than the size of NSs and NBs (see, for example, Fig. 11.15). This means that such structures with the same weight of the sensitive layer have more of the specific and total surface, which creates the basis for greater water adsorption. The increase in sensor response with decreasing crystallite size or diameter of NWs, NSs, and NBs formed by the sensitive layer also correlates well with the conclusions drawn by Zhang et al. [63] in the process of analyzing the results of molecular dynamics (MD) simulations of the

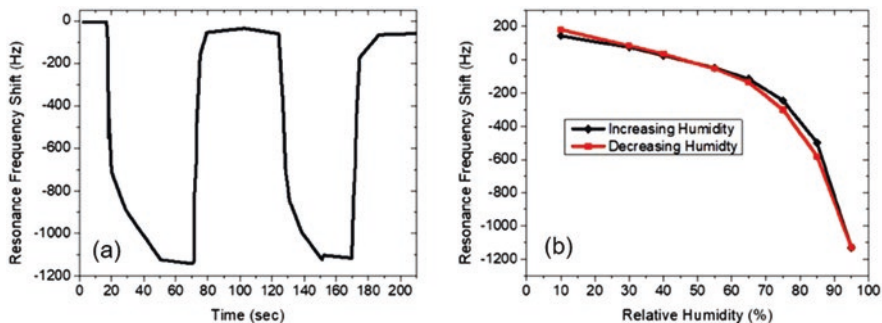


**Fig. 11.14** Frequency shift response of different sensors fabricated with materials in different morphology respect to relative humidity of the environment. (Reprinted with permission from Turkdogan [55]. Copyright 2019: Springer)



**Fig. 11.15** SEM images of ZnCdSSe (a) nanowires and (b) nanosheets. (Reprinted with permission from Turkdogan [55]. Copyright 2019: Springer)

interaction between water molecules and zinc sulfide nanoparticles (3–5 nm). They concluded the followings. First, ZnS nanoparticles can adsorb more water molecules per unit of surface area because of the significantly increased curvature and more open surface configuration. Second, the water binding energy is higher in nanoparticles than in bulk crystals (although compared with isolated nanoparticles, aggregation can reduce the binding energy) because the intermolecular interaction of water on the curved nanoparticle surfaces is not as strong as in flat bulk surfaces. This means that a larger number of water molecules can be adsorbed by ZnS nanoparticles with a higher bond strength on the nanoparticle surface compared to bulk ZnS.



**Fig. 11.16** (a) Repeatabable sensing curve of the NW coated QCM gathered between  $\sim 95\%$  RH and  $\sim 40\%$  RH. (b) Hysteresis characteristic of NW coated QCM sensor. (Reprinted with permission from Turkdogan [55]. Copyright 2019: Springer)

Testing of sensors based on nanowires revealed another advantage of such sensors, which we noted when considering conductometric gas and humidity sensors. This advantage is high-speed performance. Figure 11.16b shows the response curve of the ZnCdSSe NW-based sensor as a function of time under the humidity levels of 40% RH and 95% RH. It was found that average response time of the sensor was around 21 s, while the recovery time was around 8 s in average. Such rates of response/recovery are very promising for practical application. They are not inferior to the best results described in the literature, or even surpass them (see Table 11.3). Okur et al. [47] also reported that their NW-based sensors were characterized by fast response and recovery.

Another promising characteristic of NW-based sensor is the small hysteresis. As shown in Fig. 11.16b, a hysteresis loop under increasing and decreasing humidity is only  $\sim 3\%$  under 85% RH. This favorably distinguishes NW-based sensors from conventional capacitive humidity sensors based on porous materials, in which hysteresis is mainly associated with the processes of adsorption and desorption of water vapor from nanosized pores. As is known, there are no nanoscale pores in the NWs array.

In the manufacture of QCM-based humidity sensors based on II–VI compounds for the deposition of a sensitive layer on a quartz crystal, thick-film technology methods were usually used, such as immersion of gold coated QCM in the reaction solution [8], and drop casting method [47, 55, 56]. As a rule, after the deposition of a sensitive layer and its drying at room temperature, the formed layers were not further subjected to additional heat treatment to improve their adhesion to the metalized quartz substrate. This can be considered as a significant drawback of this technology, since in the absence of good adhesion, the sensitive layer may peel off during operation. Unfortunately, there are no data in the literature confirming the long-term stability of such sensors and thus refuting our statement.

## 11.4 Outlooks

If we compare humidity sensors based on II–VI semiconductor compounds with sensors developed on the basis of other materials [31–33], then we can state that their parameters do not differ much from the best samples. However, based on this, we have no right to assert that humidity sensors based on semiconductors II–VI will certainly appear on the humidity sensor market. Firstly, they cannot replace sensors already on the market, in particular metal oxide sensors, since the use of II–VI semiconductors does not improve performance and does not contribute to an increase in sensor selectivity compared to metal oxide sensors. Secondly, the parameters of II–VI semiconductor compounds are highly dependent on lighting and temperature, which complicates their operation. In addition, despite the high melting points, sublimation and especially irreversible oxidation occur at significantly lower temperatures [10, 11]. As a result, when operating such sensors, we cannot use heat treatment to restore the original characteristics of sensors after long-term operation, as can be done for metal oxide sensors [35]. The available information also does not provide grounds for asserting the long-term stability of the parameters of the sensors, especially when they are used in high humidity conditions. There is simply no such research. In most works, testing was limited to a time of no more than 20 minutes [64]. As a result, we do not know what processes can occur in II–VI semiconductor-based humidity sensors during operation, and how the aging effect will affect the parameters of the sensors. Too high resistance of ZnS and CdS can also create difficulties when using conductometric humidity sensors [13]. For example, sensors developed by Choudhari et al. [7] had resistance more than  $10^9$  Ohm.

**Acknowledgments** G.K., M.I., and V.B. are grateful to the State Program of the Republic of Moldova, project 20.80009.5007.02, for supporting their research.

## References

1. Adamson AW, Gast AP. Physical chemistry of surface. New York: Wiley; 1997.
2. Bereir GA, Kline DE. Dynamic mechanical behaviour of polyimide. *J Appl Polym Sci.* 1968;12:593–604.
3. Bhattacharjeea M, Bandyopadhyay D. Mechanisms of humidity sensing on a CdS nanoparticle coated paper sensor. *Sens Actuators A Phys.* 2019;285:241–7.
4. Chatzandroulis S, Tserapi A, Goustouridis D, Normand P, Tsoukalas D. Fabrication of single crystal Si cantilevers using a dry release process and application in a capacitive-type humidity sensor. *Microelectron Eng.* 2002;61–62:955–61.
5. Chen H, Shi D, Qi J, Wang B. Electronic and mechanical properties of ZnS nanowires with different surface adsorptions. *Phys E.* 2009;42:32–7.
6. Chen Q, Nie M, Guo Y. Controlled synthesis and humidity sensing properties of CdS/polyaniline composite based on CdAl layered double hydroxide. *Sensors Actuators B Chem.* 2018;254:30–5.
7. Choudhari U, Jagtap S. Hydrothermally synthesized ZnSe nanoparticles for relative humidity sensing application. *J Electron Mater.* 2020;49:5903–16.

8. Demir R, Okur S, Seker M, Zor M. Humidity sensing properties of CdS nanoparticles synthesized by chemical bath deposition method. *Ind Eng Chem Res.* 2011;50:5606–10.
9. Demir R, Okur S, Seker M. Electrical characterization of CdS nanoparticles for humidity sensing applications. *Ind Eng Chem Res.* 2012;51:3309–13.
10. Dimitrov RI, Boyanov BS. Oxidation of metal sulphides and determination of characteristic temperatures by DTA and TG. *J Therm Anal Calorim.* 2000;61:181–9.
11. Dimitrov RI, Moldovanska N, Bonev IK. Cadmium sulphide oxidation. *Thermochim Acta.* 2002;385:41–9.
12. Du L, Zhang Y, Lei Y, Zhao H. Synthesis of high-quality CdS nanowires and their application as humidity sensors. *Mater Lett.* 2014;129:46–9.
13. Fang X, Zhai T, Gautam UK, Li L, Wua L, Bando Y, Golberg D. ZnS nanostructures: from synthesis to applications. *Prog Mater Sci.* 2011;56:175–287.
14. Farahani H, Wagiran R, Hamidon MN. Humidity sensors principle, mechanism, and fabrication technologies: a comprehensive review. *Sensors.* 2014;14:7881–939.
15. Feng MH, Wang WC, Li XJ. Capacitive humidity sensing properties of CdS/ZnO sesame-seed-candy structure grown on silicon nanoporous pillar array. *J Alloys Compd.* 2017;698:94–8.
16. Fleming WJ. A physical understanding of solid state humidity sensors. *Soc Automot Eng Trans.* 1981;90(2):1656–67.
17. Fu XQ, Wang C, Yu HC, Wang YG, Wang TH. Fast humidity sensors based on CeO<sub>2</sub> nanowires. *Nanotechnology.* 2007;18:145503.
18. Gimenez AJ, Luna-Barcenas G, Sanchez IC, Yanez-Limon JM. Paper-based ZnO oxygen sensor. *IEEE Sensors J.* 2015;15:1246–51.
19. Goodell CM, Gilbert B, Weigand SJ, Banfield JF. Kinetics of the water adsorption driven structural transformation of ZnS nanoparticles. *J Phys Chem C.* 2008;112(13):4791–6.
20. Goswami N, Sen P. Water-induced stabilization of ZnS nanoparticles. *Solid State Commun.* 2004;132:791–4.
21. Gupta SS, van Huis MA. Adsorption study of a water molecule on vacancy-defected on polar CdS surfaces. *J Phys Chem C.* 2017;121(18):9815–24.
22. Hattingh J. The importance of relative humidity measurements in the improvement of product quality. In: *Proceedings of 2001 NCSL International Workshop & Symposium.* 2001. [http://www.ncsli.org/i/c/TransactionLib/C01\\_R7.pdf](http://www.ncsli.org/i/c/TransactionLib/C01_R7.pdf)
23. He Y, Zhang M, Zhang N, Zhu D, Huang C, Kang L, et al. Paper-based ZnS:Cu alternating current electroluminescent devices for current humidity sensors with high-linearity and flexibility. *Sensors.* 2019;19:4607.
24. Hertl W. Surface chemical properties of zinc sulfide. *Langmuir.* 1988;4:594–8.
25. Hsueh H-T, Hsiao Y-J, Lin Y-D, Wu C-L. Bifacial structures of ZnS humidity sensor and Cd-free CIGS photovoltaic cell as a self-powered device. *IEEE Electron Dev Lett.* 2014;35(12):1272–4.
26. Huang F, Gilbert B, Zhang H, Banfield JF. Reversible, surface-controlled structure transformation in nanoparticles induced by an aggregation state. *Phys Rev Lett.* 2004;92:155501.
27. Ishihara T, Matsubara S. Capacitive type gas sensors. *J Electroceram.* 1998;2(4):215–28.
28. Jiang P, Jie J, Yu Y, Wang Z, Xie C, Zhang X, et al. Aluminium-doped n-type ZnS nanowires as high-performance UV and humidity sensors. *J Mater Chem.* 2012;22:6856.
29. Kannan PK, Saraswathi R, Rayappan JBB. CO<sub>2</sub> gas sensing properties of DC reactive magnetron sputtered ZnO thin film. *Ceram Int.* 2014;40:13115–22.
30. Korotcenkov G. Why do we need to control humidity? In: Korotcenkov G, editor. *Handbook of humidity measurements, vol. 1: Spectroscopic methods of humidity measurement.* Boca Raton: CRC Press; 2018. p. 17–45.
31. Korotcenkov G. *Handbook of humidity measurement: methods, materials and technologies, vol. 1: Spectroscopic methods of humidity measurement.* Boca Raton: CRC Press; 2018.
32. Korotcenkov G. *Handbook of humidity measurement: methods, materials and technologies, vol. 2: Electronic and electrical humidity sensors.* Boca Raton: CRC Press; 2019.



33. Korotcenkov G. Handbook of humidity measurement: methods, materials and technologies, vol. 3: Sensing materials and technologies. Boca Raton: CRC Press; 2020.
34. Korotcenkov G. Current trends in nanomaterials for metal oxide-based conductometric gas sensors: advantages and limitations. Part 1: 1D and 2D nanostructures. *Nanomaterials*. 2020;10:1392.
35. Kulwick BM. (1991) Humidity sensors. *J Am Ceram Soc*. 1991;74(4):697–708.
36. Leung YP, Choy WCH, Yuk TI. Linearly resistive humidity sensor based on quasi one-dimensional ZnSe nanostructures. *Chem Phys Lett*. 2008;457:198–201.
37. Liang Y-C, Liu S-L. Synthesis and enhanced humidity detection response of nanoscale Au-particle-decorated ZnS spheres. *Nanoscale Res Lett*. 2014;9:647.
38. Lim HJ, Saha T, Tey BT, Tan WS, Ooi CW. Quartz crystal microbalance-based biosensors as rapid diagnostic devices for infectious diseases. *Biosens Bioelectron*. 2020;168(15):112513.
39. Long X, Chen J, Chen Y. Adsorption of ethyl xanthate on ZnS(110) surface in the presence of water molecules: a DFT study. *Appl Surf Sci*. 2016;370:11–8.
40. Lu T, Zhang M, Guo S, Liu R. Humidity and salt sensor based on CdSSe nanowire chip. *IOP Conf Series: Mater Sci Eng*. 2019;569:022006.
41. Luo M, Shao K, Long Z, Wang L, Peng C, Ouyang J, Na N. A paper-based plasma-assisted cataluminescence sensor for ethylene detection. *Sens Actuators B Chem*. 2017;240:132–41.
42. McCafferty E, Zettlemoyer AC. Adsorption of water vapour on  $\alpha$ -Fe<sub>2</sub>O<sub>3</sub>. *Faraday Discuss*. 1971;52:239–54.
43. Morimoto T, Nagao M, Tokuda F. Relation between the amounts of chemisorbed and physisorbed water on metal oxides. *J Phys Chem*. 1969;73:243–8.
44. Muhammad F, Tahir M, Zeb M, Wahab F, Kalasad MN, Khan DN, Karimov KS. Cadmium selenide quantum dots: synthesis, characterization and their humidity and temperature sensing properties with poly-(diocetylfluorene). *Sens Actuators B Chem*. 2019;285:504–12.
45. Niarchos G, Dubourg G, Afroudakis G, Georgopoulos M, Tsouti V, Makarona E, Crnojevic-Bengin V, Tsamis C. Humidity sensing properties of paper substrates and their passivation with ZnO nanoparticles for sensor applications. *Sensors*. 2017;17:516.
46. Nitta T. Ceramic humidity sensor. *Ind Eng Chem Prod Res Dev*. 1981;20:669–74.
47. Okur S, Uzar N, Tekguzel N, Erol A, Arkan MC. Synthesis and humidity sensing analysis of ZnS nanowires. *Phys E*. 2012;44:1103–7.
48. Parangusan H, Bhadra J, Ahmad Z, Mallick S, Touati F, Al-Than N. Capacitive type humidity sensor based on PANI decorated Cu-ZnS porous microspheres. *Talanta*. 2020;219:121361.
49. Ponec V, Knor Z, Cerný S. Adsorption on solids. London: Butterworth; 1974. p. 405.
50. Rittersma ZM. Recent achievements in miniaturised humidity sensors—a review of transduction techniques. *Sens Actuators A Phys*. 2002;96:196–210.
51. Sager K, Schroth A, Nakladal A, Gerlach G. Humidity-dependent mechanical properties of polyimide films and their use for IC-compatible humidity sensors. *Sensors Actuators A Phys*. 1996;53:330–4.
52. Sauerbrey G. The use of quartz oscillators for weighing thin layers and for microweighing. *Z Phys*. 1959;155:206–22.
53. Spomer LA, Tibbitts TW. Humidity. In: Langhans RW, Tibbitts TW, editors. *Plant growth chamber handbook*. Ames: Iowa State University; 1997. p. 43–64.
54. Srivastava R. Humidity sensor: an overview. *Int J Green Nanotechnol*. 2012;4:302–9.
55. Turkdogan S. Bandgap engineered II–VI quaternary alloys and their humidity sensing performance analyzed by QCM. *J Mater Sci Mater Electron*. 2019;30:10427–34.
56. Uzar N, Okur S, Arikana MC. Investigation of humidity sensing properties of ZnS nanowires synthesized by vapor liquid solid (VLS) technique. *Sens. Actuators A*. 2011;167:188–93.
57. Vashist SK, Vashist P. Recent advances in quartz crystal microbalance-based sensors. *J Sensors*. 2011;2011:571405.
58. Visscher GJW. Chapter 72: Humidity and moisture measurement. In: Webster JG, editor. *The measurement, instrumentation, and sensors: handbook*. Boca Raton: CRC; 1999.

59. Wiederhold PR. *Water vapor measurement: methods and instrumentation*. New York: CRC Press; 1997.
60. Wang M, Zhang Q, Hao W, Sun Z-X. Surface stoichiometry of zinc sulfide and its effect on the adsorption behaviors of xanthate. *Chem Cent J*. 2011;5:73.
61. Yan W, Hu C, Xi Y, Wan B, He X, Zhang M, Zhang Y. ZnSe nanorods prepared in hydroxide-melts and their application as a humidity sensor. *Mater Res Bull*. 2009;44:1205–8.
62. Zhang H, Gilbert B, Huang F, Banfield JF. Water-driven structure transformation in nanoparticles at room temperature. *Nature*. 2003;424:1025–9.
63. Zhang H, Rustad JR, Banfield JF. Interaction between water molecules and zinc sulfide nanoparticles studied by temperature-programmed desorption and molecular dynamics simulations. *J Phys Chem A*. 2007;111:5008–14.
64. Zhang M, Guo S, Weller D, Hao Y, Wang X, Ding C, et al. CdSSe nanowire-chip based wearable sweat sensor. *J Nanobiotechnology*. 2019;17:42.

**Part III**  
**Optical Sensors**

# Chapter 12

## II–VI Semiconductor-Based Optical Gas Sensors



Savita Sharma, Ayushi Paliwal, Pragati Kumar, and Nupur Saxena

### 12.1 Introduction

The increasing world population has put an unbound challenge on technology developers to meet the basic requirements of mankind. In fact, with the development of civilization, the basic requirements have been changed from just food, clothes and shelter to numerous aspects like plenty of energy, transportation, quality education, information and communication systems and many more. This modernization of society and various technologies developed are increasing pollution day by day and are responsible for the weakening of the ecosystem of the earth. The dissolving of various harmful gases and volatile organic compounds (VOCs) from industries, power stations, automobiles, constructions, households, etc., into the environment, is actually devastating the eco-balance and is a serious concern for health, our soil and water, lives of different species, our heritage and as a whole our “Green Planet”. According to various agencies like Intergovernmental Panel on Climate Change (IPCC), United States Environmental Protection Agency (EPA) and Union of Concerned Scientists (UCS), USA, etc., the major source of climate

---

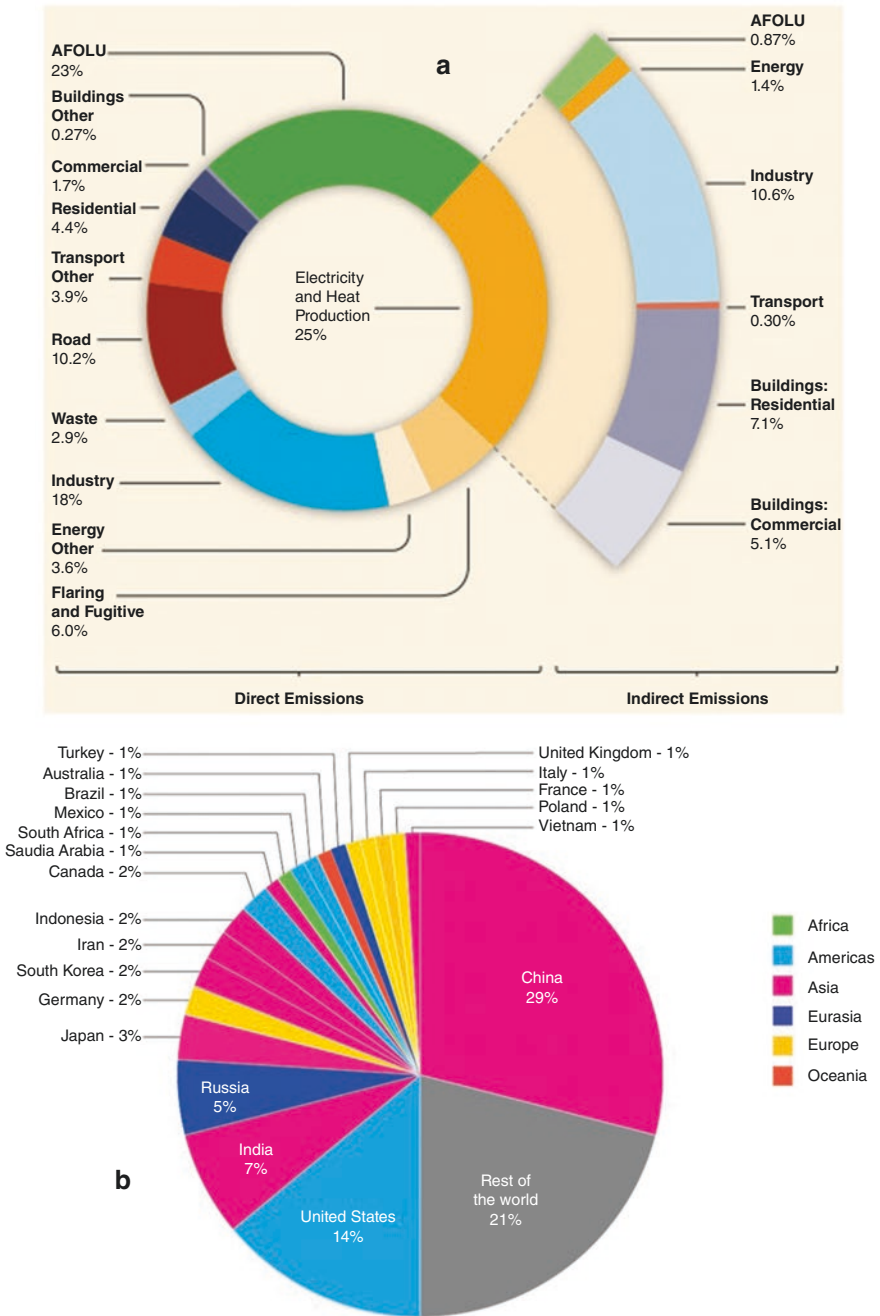
S. Sharma  
Department of Physics, Kalindi College, University of Delhi, Delhi, India

A. Paliwal  
Department of Physics and Astrophysics, University of Delhi, Delhi, India

P. Kumar  
Department of Nanoscience and Materials, Central University of Jammu,  
Samba, Jammu, J & K, India

Nanomaterials and Device Lab, Department of Nanoscience and Materials,  
Central University of Jammu, Jammu, India

N. Saxena (✉)  
Organisation of Science Innovations and Research, Bah, India



**Fig. 12.1** Human-caused greenhouse gas emission (a) Sector-wise emitters. (Adapted with permission from Zhou et al. [1]. Copyright 2014: Intergovernmental Panel on Climate Change), and (b) Country-wise share of CO<sub>2</sub> emission. (Adapted with permission from Each Country’s Share of CO<sub>2</sub> Emissions [2]. Copyright 2021: Union of Concerned Scientists)

change is the emission of human-caused greenhouse gases as shown in Fig. 12.1. Of course, energy sector is the prime emitter (~ three-fourths of total emissions) followed by agriculture. Among all energy sectors, the most-emitter is power generation, second is transportation followed by manufacturing (Fig. 12.1a) [1]. It is not surprising that more than 60% of entire greenhouse gas emission comes from only 10 countries whereas just less than 3% is caused by over 100 least emitting countries (Fig. 12.1b) [2].

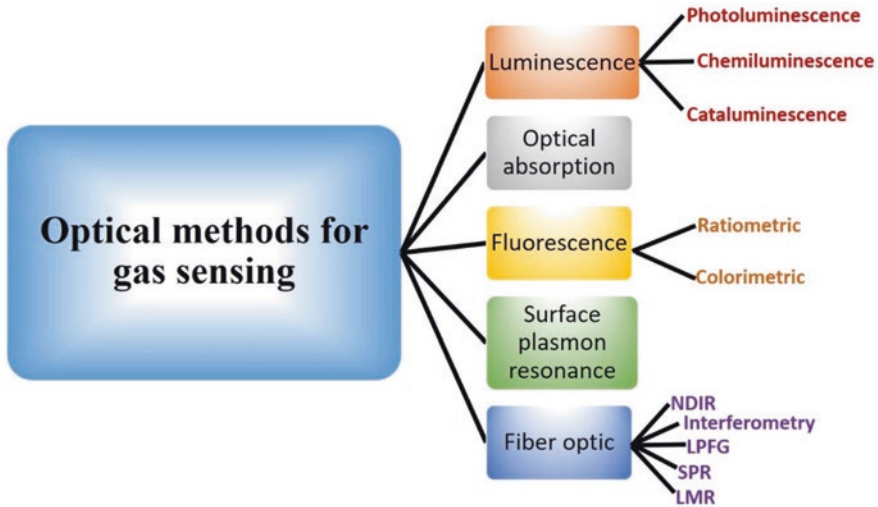
The monitoring of the human caused greenhouse gases and other harmful gases is utmost required for the sustainable environment and a number of sensors based on different methods and materials are available in the market viz. MEMS pellistors, infrared gas sensors, catalytic pellistors, thermal conductivity gas sensors, metal oxide gas sensors, electrochemical gas sensors, evaluation kits, indoor air quality sensors, etc. Moreover, optical methods of gas sensing are equally popular and important because of their room temperature operation, no power consumption, etc., and owing to very interesting optical properties of the materials depending on their shape, size, morphology and sensor architectures.

### 12.1.1 *Optical Methods for Gas Sensing*

Most of the gas sensors available are of mainly the electrical type, that is, based on either chemiresistance or electrochemical methods and it is not an exaggeration that chemiresistive property dominates hugely covering more than 85% of all the gas sensors [3, 4]. The optical sensors are enviable to present an efficient alternative to the conventional gas sensors owing to various advantages over the electrical ones, viz. high sensitivity, room temperature operation, low power consumption, etc. Besides, they offer remote sensing; contact-less detection, that is, without the requirement of any leads or probes for excitation or measurement; reversibility, that is, the same sensor can be used for number of times; selectivity of gas species, etc.

To realize optical gas sensors, a number of optical methods have been employed in which the response of different optical signals is observed with respect to “ON” and “OFF” of gases of definite concentration. The optical wavelength usually spans from visible to infrared for II–VI compound semiconductors, if only bulk is considered. With time, there has been lots of developments in synthesis and characterization methods of semiconductors particularly and hence a variety of materials, their size, shape, structure and morphology has been emerged that resulted in tunable optical properties. In particular, the optical methods for gas sensing may be categorized as presented in Fig. 12.2.

In luminescence-based gas sensors, the emission from the material is recorded in the absence and presence of gas or volatile organic compound (VOC). Further, the emission may be of different types: photoluminescence (PL), chemiluminescence, cataluminescence (CTL), etc. The observed response may be in terms of intensity, FWHM, or peak position.



**Fig. 12.2** Various types of optical methods for gas sensing

Whereas the general technique for the sensing mechanism of a little bit amount of gas using SPR phenomenon is that there is a discrepancy in refractive indices occurring at the faces of the metallic medium. The variation in refractive indices can be because of the given factors:

- (i) Conversion of the refractive indices from air of the bulky medium to a greater refractive index gaseous medium
- (ii) Conversion of the refractive indices of the gaseous medium because of the twist in solid-state chemistry over the metal by adsorbed gas molecules

In every case, the performance parameters of the sensor vary accordingly.

### ***12.1.2 Performance Parameters and Figures of Merit***

There are various parameters viz. response, sensitivity, figure of merit (FOM), detection accuracy (DA), and response time to analyse the sensor characteristics. Certain parameters are common in all methods of sensing, however, the definition may differ from method to method.

The sensor response in PL and fluorescence is generally defined as [5].

$$\text{Response} = \frac{S_{\text{gas}} - S_{\text{air}}}{S_{\text{air}}} \times 100\% \quad (12.1)$$

where  $S_{\text{gas}}$  and  $S_{\text{air}}$  are the integrated area or intensity under the PL/fluorescence peak in gas and air, respectively, if the sensing is done by negative or positive luminescence/fluorescence quenching.

In case of ratiometric fluorescent sensors, the ratio of the intensity of two fluorescence peaks or emission wavelengths  $R$  is obtained and then divided by  $R_{\text{max}}$  to get the normalized response of the sensor [6].

The limit of detection (LOD) is defined as the minimum quantity or concentration of the analyte which can be measured by the sensor. It is usually obtained by finding a linear relationship between the concentration of the analyte and the response of the sensor [7].

The SPR sensors use two separate interrogation techniques: angular interrogation and wavelength interrogation. The resonance angle ( $\theta_{\text{res}}$ )/wavelength ( $\lambda_{\text{res}}$ ) corresponding to the refractive index of the sensing medium  $n_s$  is found in the case of angular/wavelength interrogation. The sensor's sensitivity is defined as the change in  $\theta_{\text{res}}/\lambda_{\text{res}}$  per unit change in the detecting medium's refractive index. The sensor's sensitivity is defined as follows: If the resonance angle/wavelength is altered by  $\Delta\theta_{\text{res}}/\Delta\lambda_{\text{res}}$  for a change of  $\Delta n_s$  in refractive index of sensing medium, the sensor's sensitivity is defined as follows [8]:

$$\text{For angular interrogation : } S_{\theta} = \frac{\Delta\theta_{\text{res}}}{\Delta n_s} \quad (12.2)$$

$$\text{For wavelength interrogation } S_{\lambda} = \frac{\Delta\lambda_{\text{res}}}{\Delta n_s} \quad (12.3)$$

The sensitivity of a functionalized SPR sensor is determined by the change in resonance wavelength or resonance angle caused by a constant change in the sensing medium's refractive index. The sensor's sensitivity increases as the shift increases. The sensitivity of surface-functionalized SPR chemical and biosensors is determined by the difference between the effective and surface refractive index changes generated by surface interaction/binding.

The detection accuracy (DA) of a system is defined as the precision with which it can detect a sensing sample; in this case, the SPR sensor, resonance angle/wavelength, and thus the sensing sample's refractive index. The characteristic parameter of the SPR-based sensor is the resonance angle/wavelength. The spectral breadth of the SPR response curve determines the precision with which a characteristic parameter can be detected. The detection accuracy is proportional to the breadth of the SPR curve. As a result, the sensor's detection accuracy can be expressed as an inverse function of the breadth (FWHM) of the SPR curve corresponding to 50% reflectivity or normalized output power. For instance, in spectral interrogation, if the FWHM of the surface Plasmon curve is  $\Delta\lambda_{0.5}$ , the sensor's detection accuracy can be represented as



$$DA = \frac{1}{\Delta\lambda_{0.5}} \quad (12.4)$$

The ratio of the sensitivity ( $S$ ) and the width (FWHM) of the SPR curve is defined as the figure of merit (FOM) of the SPR [9]. Consequently,

$$FOM = \frac{S}{FWHM} \quad (12.5)$$

Response time is the time it takes for a sensor to reach its real output after being exposed to its input. The sensor is excellent if the response time is short. The response time of an SPR sensor is defined by how quickly the SPR dip changes location to a stable point in response to changes in sensing samples in the proximity of the sensing surface.

Aside from this, there are a number of other factors to consider when it comes to commercialization. Shelf life, reusability, microscopic size, cost, and so on are all factors to consider.

### ***12.1.3 Suitability of II–VI Materials for Optical Gas Sensors***

II–VI compound semiconductor materials are very well explored for their gas sensing characteristics owing to the peculiar optical and electrical properties in bulk as well as in nanodimensions. In particular, the nanostructures of these materials dominate optical gas sensing applications as they exhibit size-dependent emission, absorption and other optical properties, that is, they can emit different colours with the same excitation wavelength. Besides, their shape can also be tailored to a great extent and hence the optical properties can be tuned.

The easy and economic synthesis methods for bulk production of these materials is one of the major factors for the dominance of II–VI materials in the field of optical gas sensing. Besides, II–VI materials can be synthesized in colloidal form suitable for thin film deposition via spin coating/drop casting, etc.

The most important factor for the suitability of II–VI materials is their direct band gap, that is, the existence of direct electronic transition between the conduction band and the valence band. This significantly reduces the lifetime of the decay to ns thereby swiftly absorbing and emitting light falling on it. When the intensity of excitation light is more as in case of laser-based optical gas sensing setups, this swift action prevents the saturation of emission, and a bright PL can be obtained, especially from quantum dots (QDs). This bright PL enables us to fabricate better optical sensors as it is too vulnerable to any slight change in its environment. Besides, QDs have excellent photostability as compared to organic dyes, that is, they can resist prolonged excitation of even UV light with very less degradation of emission intensity.

## 12.2 Photoluminescence-Based Gas Sensors

Enhanced luminescence is the most cited property of the II–VI compound semiconductor nanostructures and hence it opens multichannels for vast range of applications. Luminescence is a very responsive kind of signal, that is, it can be affected by very small changes in the environment of the material and hence it has a tremendous range of applications. Many types of sensors have been devised using the luminescence property of II–VI materials and their composites viz. temperature sensor, pH sensor, ion sensor, gas sensor, bio-sensor, humidity sensor, etc. [10–15]. In all, luminescence-based sensing is one of those major areas that has been harnessed effectively and it is still an interesting topic of research.

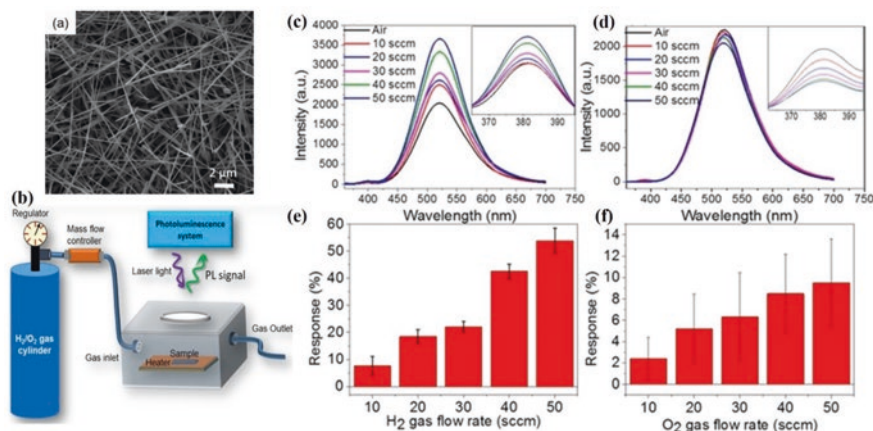
There have been great efforts for obtaining enhanced and sustained emission from II to VI materials. Various morphologies have been explored and their luminescence properties have been studied. Different morphology have their own pros and cons, some are better for emission but not so good for sensing and vice versa. Here, we present a morphology-based classification of II–VI materials for their application as a luminescence-based gas sensor. II–VI materials are easy to synthesize in various dimensions viz. 1D nanowires, nanorods; single or core-shell (CSH) QDs; embedded 1D, QDs, CSHs in matrix; composites, etc. These all morphologies are designed and studied for a high surface-to-volume ratio so as to achieve more area to adsorb the gas and enhanced emission so as to achieve efficient signals for sensing.

### 12.2.1 1D Nanostructures as Luminescence-Based Gas Sensor

The morphologies with quantum confinement exhibit enhanced, sharp, and stable emission due to the confinement of electrons, and this property can be utilized for realizing sensors. One-dimensionally confined nanostructures such as nanowires and nanorods offer a very high surface-to-volume ratio as their entire surface can be directly exposed to gas, and hence many researchers have approached to utilize their properties for luminescence-based gas sensing [5, 16–18].

The H<sub>2</sub>/O<sub>2</sub> sensing based on PL was reported by Yadav et al. [5] using thermal chemical vapour deposited (CVD) 50–100 nm ZnO NWs. A special vacuum chamber of dimensions 5 × 6 × 2 cm<sup>3</sup> was designed with heater to control the sample temperature during the measurements. The concentration of the gas in the chamber was adjusted using a mass flow controller attached to the chamber.

ZnO NWs exhibited two major peaks in the PL spectrum: a dominating oxygen vacancy defect (OVD) emission at ~2.39 eV and a weak NBE emission in the UV range at ~3.27 eV and both the peaks responded in the presence of H<sub>2</sub>/O<sub>2</sub>. However, the intensity of only the prominent green emission is considered for sensing studies. They reported a high sensor response of 54% and 9% towards H<sub>2</sub> and O<sub>2</sub>,

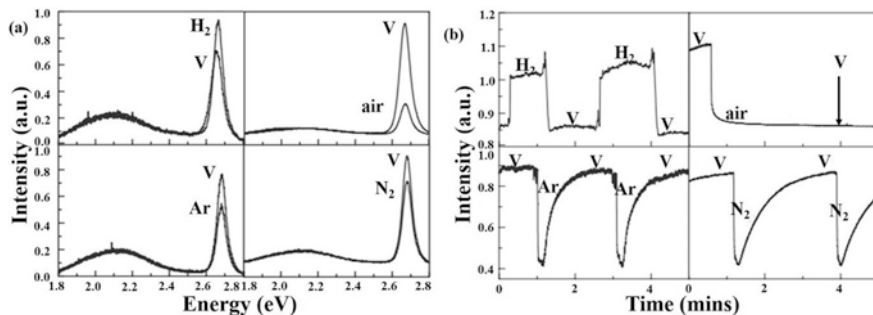


**Fig. 12.3** (a) SEM image of ZnO nanowires. (b) Schematic design of photoluminescence-based contact-less gas sensing setup. Room temperature photoluminescence spectra obtained from ZnO nanowires in (c) hydrogen and (d) oxygen gas environment. The insets show variations in UV peak intensity. Variation of sensing response for a different flow rate of (e) H<sub>2</sub> and (f) O<sub>2</sub> gases measured at room temperature. (Adapted with permission from Yadav et al. [5]. Copyright 2016: American Institute of Physics)

respectively, for 50 sccm gas which increases significantly with the rise in sample temperature as shown in Fig. 12.3.

Ip et al. [18] investigated the effects of the adsorption of different gases H<sub>2</sub>, O<sub>2</sub>, N<sub>2</sub> and Ar on the photoluminescence (PL) property of ZnSe nanowires (NWs). These nanowires were synthesized by metal-organic chemical vapour phase deposition (MOCVD) on Au spin-coated over Si(001) wafer. The nanowires were passivated in order to study the effect of surface treatment. For this purpose, the deposited NWs were first etched in a solution of H<sub>2</sub>SO<sub>4</sub>:H<sub>2</sub>O<sub>2</sub>:H<sub>2</sub>O in 1:20:1 ratio at 5 °C for 6 s to eliminate surface oxides followed by dipping in a 20% (NH<sub>4</sub>)<sub>2</sub>S solution at room temperature for various time. The PL intensity was found to be increased more than six times for 3 hours of immersion time, and then it decreases for longer dipping. For this particular study, samples with 60 min passivation time were used for further investigations. A special vacuum chamber was designed with a sample mount to allow optical access to 325 nm or 442 nm line of He-Cd laser as well as IN and OUT of gas. No qualitative difference was observed in the PL spectrum with the two lines of the He-Cd laser.

Two major peaks were observed in the PL spectrum of ZnSe NWs; the prominent near band edge (NBE) emission at ~2.67 eV and a broad deep level emission (DLE) at ~2.1 eV. It was observed that the passivation as well as the gas ambience (H<sub>2</sub>, N<sub>2</sub>, O<sub>2</sub>, Ar) of ZnSe NWs affects the NBE peak enormously while DLE remains unchanged. The gas response to H<sub>2</sub> gas was positive with respect to measurements in vacuum, whereas other gases responded negatively. No significant peak broadening or shifting was observed in any ambience. The authors reported the response of the NWs qualitatively in the transient studies and found that the NWs responded



**Fig. 12.4** (a) Comparisons of the PL spectra of ZnSe nanowires in vacuum and in different gases at 760 Torr (H<sub>2</sub>, Ar, N<sub>2</sub> and air, anti-clockwise from upper left). The intensities have been normalized to facilitate a clearer comparison. The variations in the intensities of spectra of nanowires in vacuum reflect the inhomogeneous nature of the sample. (b) Response of the intensity of the NBE emissions to the cyclic changes of pressure in different ambient gases. Periods of vacuum (~ 10 mTorr) and of gas-filled (760 Torr) conditions are labelled by V and by the species of gas used. (Adapted with permission from Ip et al. [18]. Copyright 2005: Institute of Physics)

almost instantly to the increase and decrease of H<sub>2</sub> pressure. However, in case of Ar and N<sub>2</sub>, the rise time was almost the same as for H<sub>2</sub>, whereas the fall time was considerably higher as depicted in Fig. 12.4.

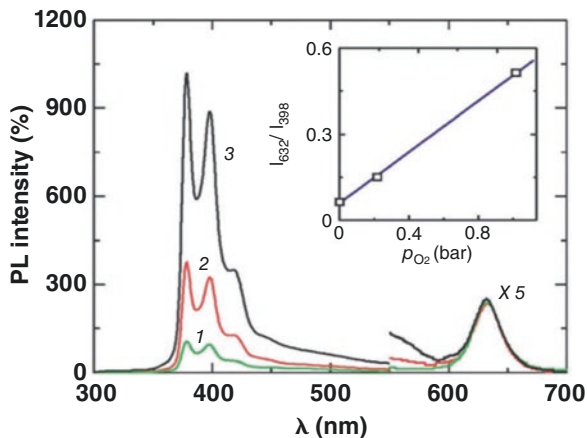
### 12.2.2 Surface-Modified Single and Core-Shell (CSh) QDs for Luminescence-Based Gas Sensor

Morphologies like single or CSh QDs are highly preferred for luminescence-based gas sensing owing to sharp emission peaks vulnerable to any ambient [19]. This property of QDs has been desperately harnessed by various researchers to develop ultra-sensitive optical gas sensors; for example, Sergeev et al. [20] studied the luminescence properties of glutathione-modified Mn:ZnS QDs in presence of various toxic compounds like phenol, methylamine, isopropanol, methane and benzene and found that fluorescence quenching efficiency for the methane (mixture of 10% CH<sub>4</sub> and 90% Ar) was relatively very high than in the other toxic compounds, indicates good selectivity and specificity of Mn:ZnS QDs for methane. They observed a gradual reduction in peak intensity centred at 590 nm assigned to Mn ion as a function of increasing concentration of CH<sub>4</sub>, whereas the peak centred at 410 nm and originated from ZnS QDs shows the opposite trend. In another work [21], they have investigated that in the mixture of 10% CH<sub>4</sub> and 90% Ar, it is CH<sub>4</sub>, that is responsible for major changes in fluorescence intensity. Further, they have deconvoluted emission spectra by fitting of Gaussian peaks and found that the major contribution to emission intensity change is of Zn vacancies and interstitials. In subsequent work [22], they have studied the sensor as a function of CH<sub>4</sub> concentration at various thermostanding times and found that the

degree of changes in the sensory response depends on the nature of the emission centre and thermostanding time up to 6 hours significantly affects the emission response. Mn:ZnS QDs capped with L-cysteine were also used for acetone sensing. They observed quenching in phosphorescence emission of QDs with addition of acetone (varying from 0.5 up to 600 mgL<sup>-1</sup>). The Stern–Volmer equation represents linear fit in the variation of emission intensity with acetone concentration up to a maximum concentration of 600 mgL<sup>-1</sup> [23]. The statistical and dynamic luminescence measurements were carried out to study the nitrogen (N<sub>2</sub>) and N<sub>2</sub>+oxygen (O<sub>2</sub>) sensing behaviour of Mn-doped ZnS with varying concentration of Mn [24]. They observed in statistical luminance measurement that with the excitation of 355 nm all the samples except pure ZnS and 10% Mn-doped ZnS show emission whose intensity decreases with an excitation wavelength of 280 nm. The dynamic measurements showed sensing behaviour only for 280 nm excitation. They observed that the average decay time (calculated from number of luminescence decay curves) reduces as an increasing function of both dopant concentration and excitation intensity under exposure of two gasses.

PL of bare QDs suffered a setback due to surface defects on the QDs as well as agglomeration of QDs with ageing due to which PL observed was weak and temporal photostability was less. To overcome these problems, different methods were developed to synthesize high-quality, uniform sized, monodispersed and smoother-surfaced QDs. Among all developed methods, two techniques were the most important and applied to date. One of them was to encapsulate the semiconductor core with another semiconductor shell with larger energy gap. This was called core/shell (CSh) structure and was very effective in suppressing the electron leakage from the core semiconductor thereby increasing the PL intensity significantly and improving the temporal stability of QDs.

Thin films of CdSe/CdZnS, CdSe/ZnS and CdSeTe/ZnS core/shell QDs deposited on glass substrate were used to detect the O<sub>3</sub> up to concentrations 0.1 ppm and a reversible PL feature were observed, that is, PL intensity diminishes rapidly under the exposure to O<sub>3</sub> in air, and it reversibly recovered when gases are exhausted. Contrary, PL intensity remained unaffected under all components of natural air like O<sub>2</sub>, N<sub>2</sub>, Ar, carbon dioxide (CO<sub>2</sub>), hydrogen (H<sub>2</sub>), etc. The maximum change in PL intensity was observed for the green emitting QDs of smallest size [25]. In a subsequent study, same group tested CdSe/ZnS and CdSeTe/ZnS QDs film for the gaseous alkylamines sensing and observed reversibility in PL spectra similar to a previous study [26]. The ratiometric O<sub>2</sub> sensing was carried out using pyrenyl functionalized CdSe/ZnS QDs. It was observed that the emission spectrum of both pyrene ( $\lambda_{em} = 378$  nm) and QD ( $\lambda_{em} = 632$  nm) are fully independent of each other and strongly influenced (particularly functional ligand assist) by O<sub>2</sub> concentration. Further, the optical output of the nanosensor is evaluated from the ratio of two peaks ( $I_{632}/I_{378}$ ), plotted as a function of O<sub>2</sub> pressure (Fig. 12.5) and the quenching rate constant is calculated as  $k_q = 1.1 \times 10^{10} \text{ M}^{-1} \text{ s}^{-1}$  [27].



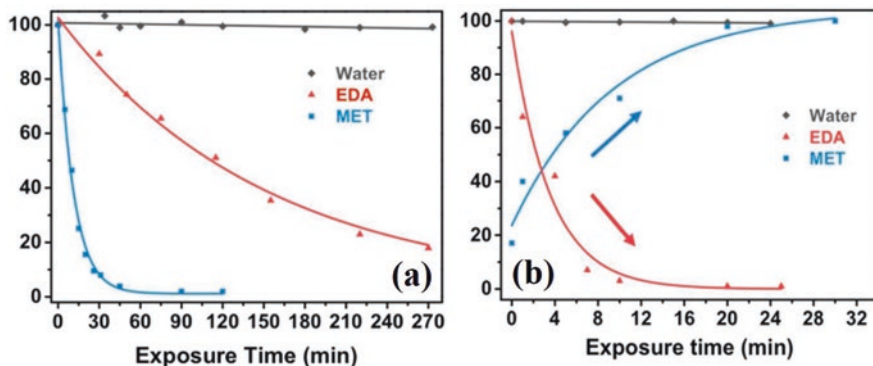
**Fig. 12.5** Emission spectra ( $\lambda_{exc} = 275$  nm) of CdSe/ZnS QD-pyrene in  $CH_3Cl$  in the presence of: 0 (1), 0.213 (2) and 1.013 (3) bar  $O_2$ . The inset shows the linear correlation between the ratiometric PL responses. (Adapted with the permission Amelia et al. [27], Copyright 2011: The Royal Society of Chemistry)

### 12.2.3 Embedded 1Ds and QDs, Composites, CSh in Matrix, and Other Special Forms

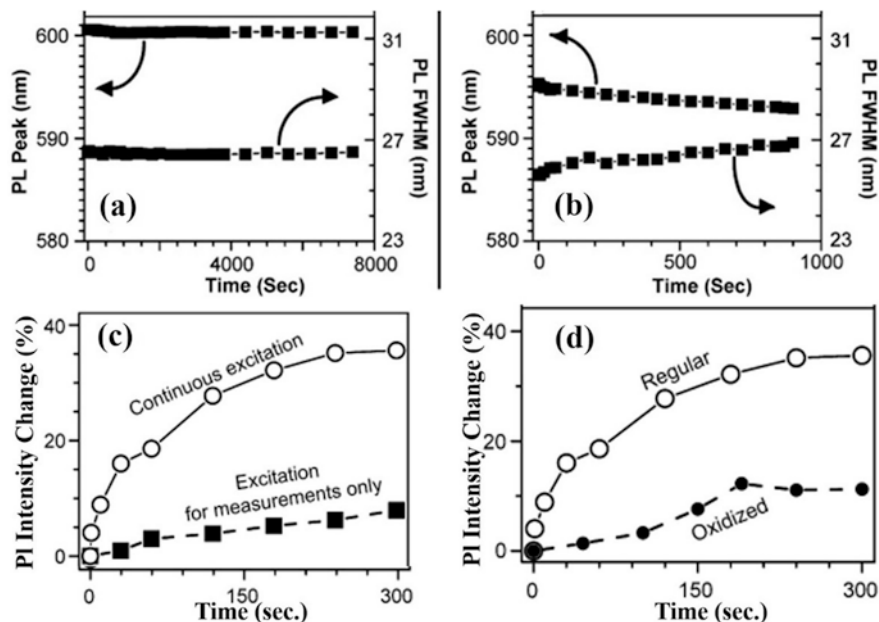
In order to overcome the problem of surface defects of bare and CSh QDs, another method was developed at the same time when CSh was established. This method was to cap the QDs or CShs with some appropriate material to deactivate the unsaturated surface bonds. This resulted in enormous enhancement in PL intensity and brightness along with a reduction in the possibility of agglomeration. Embedding 1Ds, QDs and CShs in some matrices is a very powerful tool to enhance mechanical strength, dispersion, photostability and temporal stability.

A novel multifunctional hybrid nanocomposite is formulated for photolithography using either luminescent CdSe or PbS colloidal QDs embedded in a polyisoprene-based photoresist (PIP) was developed for the fabrication and testing of 2-mercaptoethanol (MET) and ethylenediamine (EDA) in gaseous form. The fabricated sensor response to the analyte-QD interactions was significantly short and sensitive due to the high diffusion of analysed through the polymer matrix. Both the nanocomposites showed the similar feature of luminescence quenching behaviour as a function of time for EDA sensing whereas for MET sensing they showed an opposite trend in luminescence behaviour. It was luminescence quenching for CdSe-based nanocomposites and luminescence stimulation for PbS-based nanocomposites (Fig. 12.6a, b) [28].

The sensing properties of CdSe NCs incorporated into polymer thin were tested for oxygen, triethylamine (TEA), benzylamine (BZA), butylamine (BTA), etc. [29]. They observed huge degradation in PL of NCs thin film with respect to NCs solution, however, PL stability can be recovered by photo-irradiation of films for 5 to 10 min in both air and Ar. Additionally, they have not noticed any signification



**Fig. 12.6** Real-time response upon the exposure to a  $10^{-4}$  M aqueous solution of MET and EDA (and the corresponding fitting curves) and water (a) CdSe-PIP and (b) PbS-PIP nanocomposite sensor. (Adopted with permission from Rodríguez-Cantó et al. [28]. Copyright 2015: The Royal Society of Chemistry)



**Fig. 12.7** PL properties of CdSe NCs as a function of photo-irradiation time under (a) Ar and (b) TEA. Change PL intensity of CdSe NCs exposed in TEA under (c) either continuous or short and (d) with and without the existence of a monolayer of oxides on the surface of the NCs. (Adapted with permission from Nazzal et al. [29]. Copyright 2003: American Chemical Society)

variation in the shape, size, and position of emission spectra even the continuous and long exposure of photo irradiation of 2 h (Fig. 12.7a). Under the exposure of different gases, the PL properties of activated NCs are species-specific as no and maximum (Fig. 12.7b) changes were noticed for BTA and TEA, respectively.

Further, they noticed that the percentile change in PL intensity depends on photo-irradiation time and type along with the oxidation status (Fig. 12.7c, d).

CdSe/SiO<sub>2</sub>NPs embedded in a borosilicate porous glass matrix were also tested for gas sensing application and found good sensitivity in the form of luminescence quenching for NH<sub>3</sub> relative to other gaseous species. Further, they studied the effect of relative humidity on the sensing properties for NH<sub>3</sub> and observed that relative humidity of >80% only slightly affect the emission intensity [30]. The gas sensing properties of CdSe/ZnS QDs embedded in a borosilicate porous glass matrix were investigated and observed a reversible PL quenching and shortening in luminescence decay time under the exposure of ammonia (NH<sub>3</sub>) gas [31].

A special form of highly porous material CdSe aerogel was investigated for TEA sensing using –ve PL quenching. The study was compared with a previous study on CdSe QDs and found that the PL intensity enhancement is dependent on the concentration of analyte and is linear in the range  $4.7 \times 10^3$ – $75 \times 10^3$  ppm with reversible nature [32]. An intensified PL was achieved by integrating CdSe QDs and anodic aluminium oxide (AAO) nanopore arrays by Zhao et al. They studied the application of this optically active element for sensing of different hydrocarbons like benzene, xylene and toluene. The investigation revealed the enhanced and selective sensing of xylene within the limit of 10–9400 ppm [33].

Table 12.1 summarizes the luminescence-based optical gas sensors fabricated using II–VI compound semiconductors with different morphologies.

From Table 12.1, it may be concluded that ZnO, ZnS and CdSe are the most preferred II–VI semiconductors in luminescence-based optical gas sensing owing to their high emission properties in QDs state. Besides, chemical route is more suitable for synthesis as it provides various parameters to play with for the desired morphology, size, shape and thereby the desired emission properties. However, some physical routes are also explored, for example, thermal evaporation and PLD, etc. But these are massive techniques that enhance the cost of the device. Colloidal QDs, CShs, embedded in the matrix can be easily synthesized though much economic chemical routes and morphologies can be varied as well. Hence, different chemical methods have been explored for the synthesis of various II–VI nanostructures for optical gas sensing applications.

As far as the mechanism of luminescence-based optical gas sensors is concerned, in general, two peaks are observed in the PL spectra of II–VI semiconductors. Out of which, one belongs to band edge emission and the other belongs to both bulk and surface-related defects. The peak parameters, that is, intensity, peak position, and peak width, of either of these peaks can be influenced by the adsorption/desorption of gas. When the gas interacts with the surface of material, it either traps or releases electrons which expands or reduces the electron depletion layer via charge transfer and affects the emission peak. A few observations can be summarized as a factor affecting the sensor performance:

- (a) The surface-to-volume ratio: the higher the ratio, the better the sensitivity as more gas molecules can be adsorbed on the surface.
- (b) The packing density: the lower the density, the better the sensitivity as porosity becomes better with lower packing density and gas adsorption can take place at a larger surface area. However, this factor should be optimized for intense PL and porosity.



**Table 12.1** Summary of luminescence-based optical gas sensors fabricated using II–VI compound semiconductors

Material and morphology	Synthesis method	Sensing gas/chemical	Sensing method	Parameter (s)	References
ZnO NWs	Thermal CVD	H <sub>2</sub>	–ve PL quenching	R. ~ 54%	[5]
		O <sub>2</sub>	PL quenching	R. ~ 9% for 50 sccm	
ZnO nanobelts	Thermal CVD	NO <sub>2</sub>	PL quenching	R. ~ 66%	[16]
ZnO NRs	PLD	O <sub>2</sub>	PL quenching	R. ~ 35% at 150 °C	[17]
ZnSe NWs	MOCVD	H <sub>2</sub>	–ve PL quenching	R. ~ 15% (+ve)	[18]
		O <sub>2</sub>	PL quenching	R. ~ 20% (–ve)	
		N <sub>2</sub>	PL quenching	R. ~ 50% (–ve)	
		Ar	PL quenching	R. ~ 40% (–ve)	
Mn-doped ZnS QDs	Chemical precipitation	Methane	PL quenching	R. ~ 35%	[20]
Mn-doped ZnS QDs	Chemical precipitation	Methane in aqueous media	–ve PL quenching	R. ~ 76% for 100 ppm CH <sub>4</sub>	[21]
Mn-doped ZnS QDs	Chemical precipitation	Methane	PL quenching and decay time	S. R. ~ 1.8 for 100 ppm	[22]
Min-doped ZnS QDs	Chemical precipitation	Acetone	Phosphorescence quenching	LOD ~ 0.2 mgL <sup>–1</sup>	[23]
Mn-doped ZnS QDs	Chemical precipitation	N <sub>2</sub>	PL decay	$\tau_{\text{max.}} = 1259.6 \mu\text{s}$	[24]
		N <sub>2</sub> + 20% O <sub>2</sub>		$\tau_{\text{max.}} = 1208.8 \mu\text{s}$	
CdSe/ZnS CSh	Drop casting	O <sub>3</sub>	PL quenching	R. ~ 43% for 1 ppm	[25]
		HA, DEA, TEA, HA	PL quenching	R. ~ 22% (1.0 vol.%) R. ~ 10% (25.0 vol.%) R. ~ 3.9% (6.8 vol.%) R. ~ 15% (1.0 vol.%)	
CdSe/ZnS CSh	One-pot synthesis and SILAR	O <sub>2</sub>	Ratio of 2 PL peaks	R. ~ (0.061 ± 0.004) + (0.445 ± 0.007) × pO <sub>2</sub>	[27]

CdSe QDs in PIP	Hot injection and spin coating	MET EDA	PL quenching	LOD = $10^{-3}$ ng/L LOD = 270 ng/L	[28]
CdSe QDs in PMMA	Spin casting	TEA BZA	-ve PL quenching	R. ~ 120% (+ve) R. ~ 80% (-ve)	[29]
			PL quenching		
CdSe/SiO <sub>2</sub> core/shell NPs	Micro-emulsion	NH <sub>3</sub>	PL quenching	LOD = 1.2 ppm, $\tau$ = 6.1 s	[30]
CdSe/ZnS QDs in porous glass	Chemical route	NH <sub>3</sub>	PL quenching and decay time	$I \sim -25\%$ , $\tau = -10\%$ for 5 min. with $1.7 \times 10^{-3}$ Mol l <sup>-1</sup> conc.	[31]

*CVD* chemical vapour deposition, *PLD* pulsed laser deposition, *MOCVD* metal organic chemical vapour phase deposition, *SILAR* successive ionic layer adsorption and reaction, *HA* hexylamine, *DEA* diethylamine, *TEA* triethylamine, *PIP* polyisoprene-based-photoresist, *MET* 2-mercaptoethanol, *EDA* ethylenediamine, *PMMA* polymethylmethacrylate, *BZA* benzylamine

- (c) The size of nanostructure: the size lower than Bohr's radius is preferable so as to achieve strong confinement with a better surface-to-volume ratio and sharp, reproducible and sustainable emission. The size of the nanostructure affects the emission properties of the material directly and thereby the gas sensing characteristics.
- (d) Surface defects: surface defects like defects due to oxygen vacancies, dangling bonds, etc., play a decisive role in some materials for gas sensing. Hence, the more the defects, the more chances for the adsorption of analyte gas.

## 12.3 Fluorescence-Based Gas Sensors

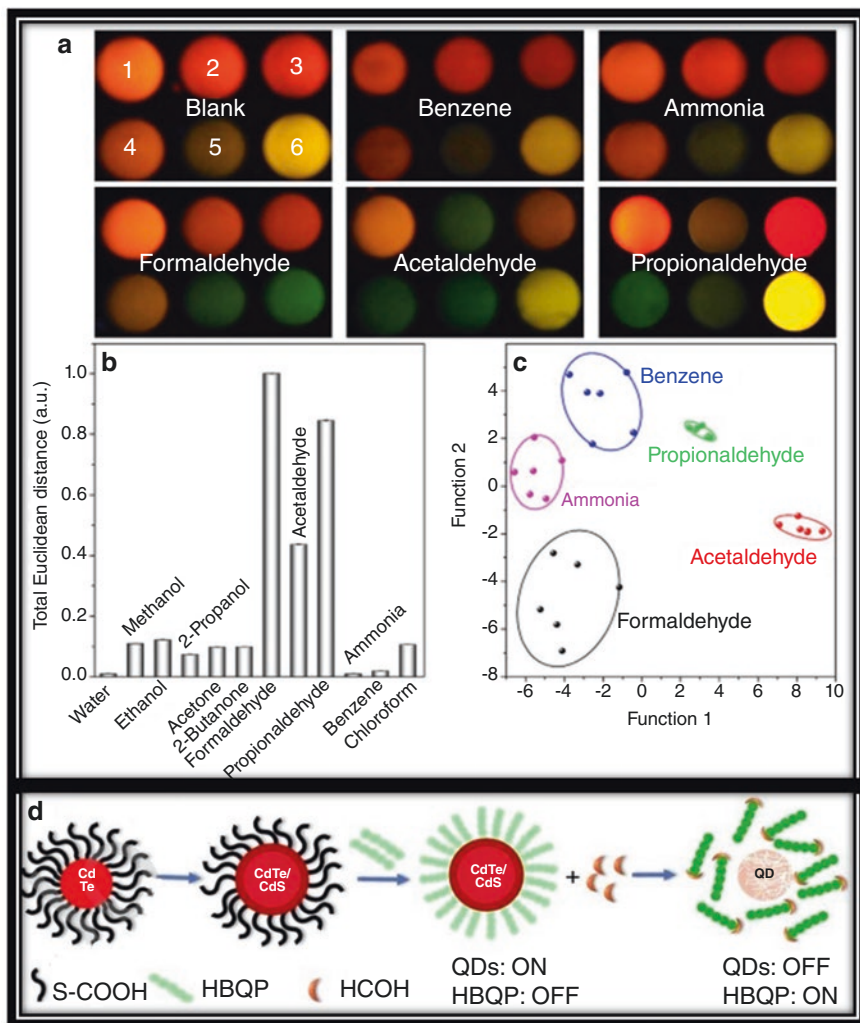
Fluorimetry is a non-conventional method that can allow us to sense any analyte by the naked eye. Fluorescence-based gas sensors typically work in four ways: quenching, ratiometric, colourimetric or a combination of these [34]. In this section, these sensors will be discussed in detail.

A ZnS-supramolecular organogel (composed of cholesterol derivative-based low-molecular-mass gelators (LMMGs)) hybrid film with surface morphology of uniform cross-linked nanofibres was synthesized for accurate and rapid detection of organic amines in the vapour phase and found that the developed sensor exhibiting good sensitive for organic monoamine and diamine vapours, particularly for EDA. The sensitivity improved with the increased quantities of ZnS loading. The fluorescence lifetimes suggested that the involvement of both mainly static and dynamic quenching with dominating sensing mechanism of static quenching [35].

Self-assembled CdTe QDs/poly(diallyldimethylammonium chloride) (PDDA) multilayer films (QDMF) were synthesized by layer-by-layer (LBL) technique to study the gas sensing properties. The developed sensor was suitable for sensing VOCs based on fluorescence quenching and was highly sensitive and selective for formaldehyde (FA) [7].

### 12.3.1 Ratiometric and Colourimetric

Xia et al. [36] designed a simple and sensitive colourimetric sensor array-based red-emitting CdTe QDs and green-coloured fluorescein that exhibited RGB-type colour change for visual detection of trace VOCs. They used six different common thiol-capped CdTe QDs as quenching units and fluorescein as the colour reference, the proposed method could discriminate FA with high selectivity and identified the existence of potential interference from acetaldehyde as illustrated in Fig. 12.8a–c [36]. The colourimetric and ratiometric fluorescence sensor was introduced based on the surface ligand crafting of CdTe/CdS quantum dots (QDs) by 3-(6-hydrazinyl-1,3-dioxo-benzoisoquinoliny) propanoic acid (HBQP) as illustrated in Fig.8d for determination of VOCs. It was noted that the fluorescence intensity of QDs



**Fig. 12.8** Selectivity of CdTe QDs array for FA detection: (a) colour change patterns of main co-existing indoor gases (1–6: mercaptosuccinic acid (MSA), N-acetyl-cysteine (N-A-cys), 3-mercaptopropionic acid (MPA), glutathione (GSH), L-cysteine (L-Cys) and thioglycolic acid (TGA)-capped CdTe QDs, respectively); (b) interference with FA (5 ppm) determination at 50 ppm of interference reagents, the total Euclidean distance was evaluated by the method shown in supplementary and (c) LDA cluster analysis for distinguishing main co-existing indoor gases. (Adopted with permission from Xia et al. [36] © 2016 Nature publishing group) (d) The schematic of the QDs preparation, crafting by HBQP and the sensing mechanism. (Adopted with permission from Ahmad et al. [37]. Copyright 2020: Elsevier)

diminishes steadily, while it increases for HBQP. The developed sensor was found the highly sensitive and selective for FA [37].

## 12.4 Other Optical Methods of Gas Sensing

As an alternate method of sensing, chemiluminescent CdSe/ZnS QDs were employed to study the O<sub>3</sub> gas-induced luminescence in QDs by Saren et al. [38]. In their investigation, they compared the chemiluminescence with PL and found that both are analogous and a significant wavelength shift occurs in the PL spectrum with O<sub>3</sub> treatment cycles.

A novel and highly sensitive gas sensor was proposed based on a special kind of chemiluminescence, that is, cataluminescence (CTL) from cetrimonium bromide (CTAB) templated nano-CdS. The sensor so developed was found highly selective and sensitive for alcohols in particular methanol. They studied the effect of working temperature and airflow rate on CTL and observed that both CTL intensity and signal-to-noise (S/N) ratio increases with an increase in temperature up to 330 °C at a constant airflow rate of 300 mL/min, whereas both CTL intensity and S/N ratio increase up to air flow rate of 250 mL/min and beyond that decreases at contact temperature of 330 °C [39]. Xia et al. [40] utilized CTL from nano/micro CuO/ZnO composite to sense VOCs. The sensor so developed was highly selective for acetic acid with satisfactory stability, better sensitivity and linearity.

Alternatively, an optical absorption-based gas sensor harnessing In-doped ZnO NRs for the detection of carbon monoxide (CO) was demonstrated by Tan et al. [41]. They obtained a highly responsive and RT working sensor with an optical absorbance change of 0.067 a.u. for a low concentration of CO of 10 ppm at the sensing wavelength of 373 nm. Besides, the sensor exhibited the fastest response and recovery time of  $70.3 \pm 1.9$  s and  $6.3 \pm 0.5$  s, respectively [41].

## 12.5 Surface Plasmon Resonance-Based Gas Sensors

Surface plasmon resonance (SPR) is one of the most important optical techniques that find various applications in a variety of domains. The first use of the SPR technique was reported in 1983. SPR was first detected by Wood to describe narrow dark bands in the light spectrum. Metals show a surface plasmon effect because they have high concentrations of free electrons. Recently, SPR has become a very important technique in describing a relationship between different molecules.

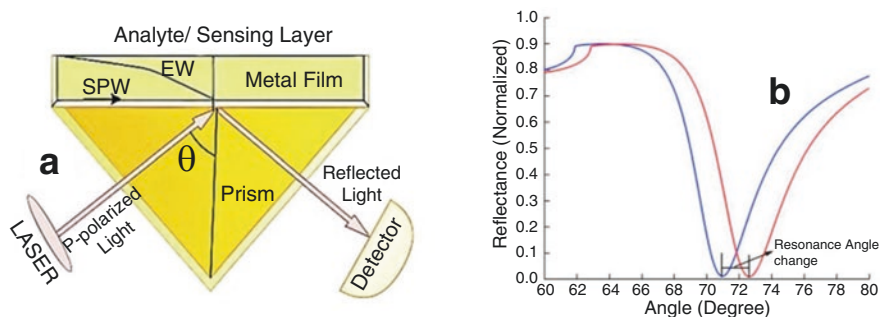
In this technique, a light source passes through a prism reflected from the back-side of the sensors' surface and is collected into a detector. At a certain incident angle, light that is coming from the source is absorbed by electrons of the metal surface, this angle is known as resonance angle and causes the electrons to resonate. These resonating electrons are called as the surface plasmon, this results in a loss of

intensity of the reflected beam. This loss of intensity can be seen as a dark band in the detector and a dip can be seen in the SPR reflection intensity curve. The loss of the reflected light intensity becomes maximum at a particular angle is known as the SPR angle.

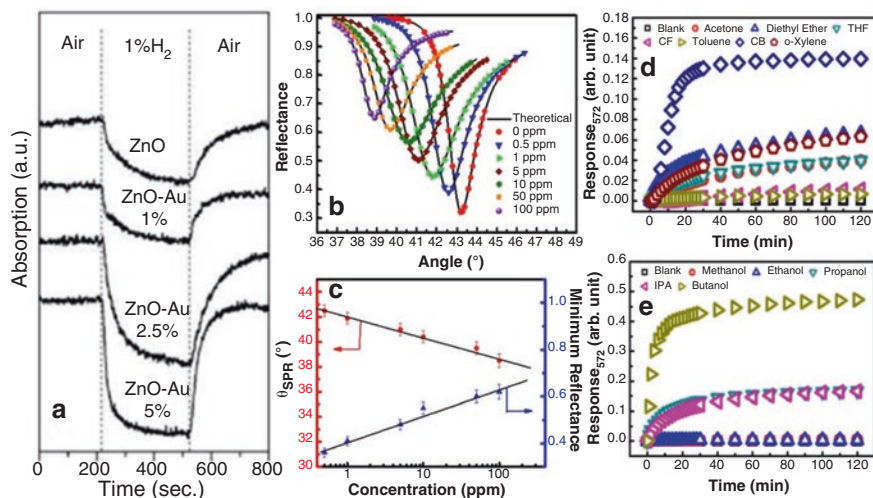
SPR is a useful technique to see the changes in the refractive index on the surface of the metal. Whenever there is a change in the refractive index of the metal surface, the angle at which the intensity of light becomes minimum will change and shift to another position. This principle of angle shift can be used in a variety of applications, like detection of chemical, physical and biological specimens, both in gaseous or liquid phase as shown in Fig. 12.9.

SPR-based gas sensors fabricated using II–VI compound semiconductors are not very much studied. Among all II–VI compounds ZnO finds many applications in SPR-based physical, chemical and biological sensors. A few gas sensors utilizing the SPR method on II–VI compounds are discussed here.

The thin film of Au NPs embedded in ZnO with varying concentrations of Au NPs was used to detect the pollutant gases. The SPR peak shift in absorption spectra was used to sense the gases and found that film sensors were detected H<sub>2</sub>, CO and NO<sub>2</sub> gases. The dynamic response of sensor under the exposure to H<sub>2</sub> gas is shown in Fig. 12.10a [42]. The prism/Au/ZnO/air system was used to detect various gases based on the shifting in a dip of SPR resonance angle ( $\theta_{\text{SPR}}$ ). The sensor was tested by measuring the gas sensing response for target gases like NO<sub>2</sub>, CO, CO<sub>2</sub>, NH<sub>3</sub>, H<sub>2</sub> and LPG and found that the system was highly selective and sensitive (0.091 °/ppm) with very fast response of 1 s towards a wide concentration range (0.5–100 ppm) of CO gas at room temperature. The reflectance spectra illustrate (Fig. 12.10b) the concentration-dependent shift in  $\theta_{\text{SPR}}$  under the exposure of CO gas, which follows linear variation as illustrated in Fig. 12.10c [43]. The photoelectrochemical charging effect of the Au-NPs in the Au-CdS NP array was employed to fabricate an SPR sensor for acetylcholinesterase (AChE) inhibitors. The sensitivity limit of detection for inhibitor was found to be  $1 \times 10^{-6}$  M [44]. The electrospinning process and UV-ozone etching treatment were carried out to test CdSe-CdS/Ag/PMMA



**Fig. 12.9** (a) Simplified diagram of SPR optical gas sensors. (b) The resonance shift ( $\nabla\theta_{\text{res}}$ ) with respect to the RI change ( $\nabla n$ ). (Blue curve represents the SPR curve at sensing refractive index ( $n_s$ ), and the red curve represents the SPR curve after sensing refractive index change ( $\nabla n_s$ )). (Adopted with permission from Yesudasu et al. [8]. Copyright 2021: Elsevier)



**Fig. 12.10** (a) Comparison of the dynamic response at 400 nm for Au embedded ZnO-based sensor during one air–1% H<sub>2</sub>–air cycle at 300 °C. (Adapted with permission from Gaspera et al. [42]. Copyright 2012: Elsevier). (b) SPR reflectance data obtained for the prism/Au/ZnO structure on exposure of different concentrations of CO gas and (c) Variation of SPR dip angle ( $\theta_{SPR}$ ) and  $R_{min}$  for the SPR sensing system with different concentrations of CO gas (calibration curve). (Adapted with permission from Paliwal et al. [43]. Copyright 2017: Elsevier). The response plots of the CdSe–CdS/Ag/PMMA composite scaffold under the exposure of 10,000 ppm of (d) typical VOCs and (e) alcoholic solvents. (Adapted with permission from Wu et al. [45]. Copyright 2020: Elsevier)

composite scaffolds for the detection of typical VOCs and alcoholic solvents. It was noticed that the composite scaffolds achieved a spectacular non-selective detection limit of 100 ppm for butanol and 500 ppm for chlorobenzene within a minute. The response plots and response time of the composite scaffold under the exposure of VOCs and alcoholic solvents are shown in Fig. 12.10d and 12.10e, respectively [45].

## 12.6 Fibre Optic-Based Gas Sensors

Fibre optic-based gas sensors are becoming increasingly important in many industrial areas due to remote sensing power, internal explosion safety, high sensitivity of electrical fields and compliance with harsh environments. Gas sensor applications are extensive and vivid. Gases such as NO<sub>x</sub> in coal-fired power plants, H<sub>2</sub>S in wastewater treatment plants and ethanol for making wine in industrial processes are measured. The fibre optic-based gas sensors are usually demonstrated using thin nanofilms or nanostructures embedded in a cylindrical waveguide, coating over an optical fibre and recording emission, resonance-based such as surface plasmon resonance, lossy mode resonance, etc. [46–55]. A number of optical fibre configurations have been employed to device II–VI compounds-based optical gas sensors such as:

- (a) Single-mode fibre (SMF) [56]
- (b) Multimode fibre (MMF) [57]
- (c) D-shaped fibre [58]

Along with utilizing various investigating techniques like

- (i) Non-dispersive infrared sensors (NDIR) [59]
- (ii) Interferometry [60]
- (iii) Longer periods of fibre gratings LPFG [61, 62]
- (iv) Surface plasmon resonance [63, 64]
- (v) Lossy mode resonances [65].

As far as resonance-based sensors are concerned, these are achieved by the coating of thin films or nanostructures onto the optical fibres. In 1993, the first-ever optical sensor was discovered based on the surface plasmon resonance (SPR) method and these sensors have been set up as a gold standard. In these sensors, the gas molecules interacted with thin film then the resonance wavelength was converted, which can be straightway lined up with gas concentration. On the other hand, lossy mode resonance (LMR)-based sensors are obtained when the optical fibre optical mode detects the change in the shape of a thin film. Conversion gives rise to a high-frequency band of a certain wavelength which is known as a resonance wavelength. One more resonance wavelength is acquired when the second mode is directed at a thin film and can be continued in other ways, leading to the emergence of high-pitched sounds. However, there are certain similarities and differences between these two resonance-type sensors (Fig. 12.11).

Among II–VI compound semiconductors, ZnO is the most promising candidate for all types of fibre optic-based sensors. A few of these sensors are discussed here:

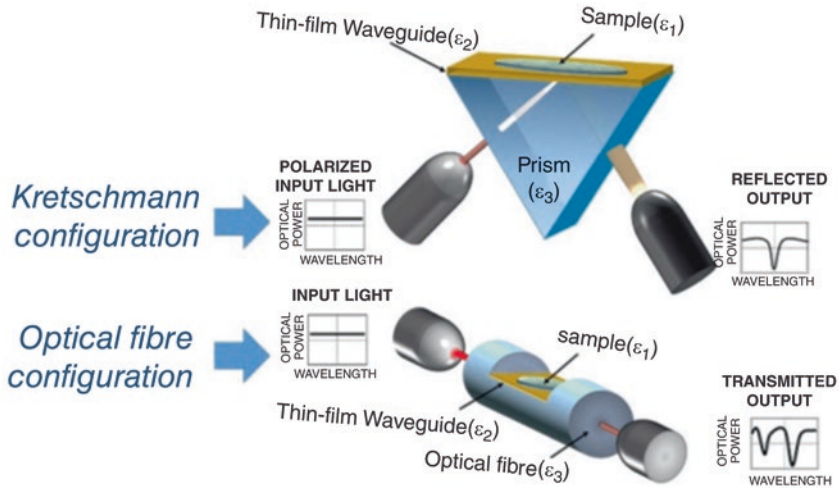
The surface of ZnO NSs was passivated with chalcogenide (CdS and CdSe) NPs and deposited on the cladding-modified optical fibre to sense the gas vapours. The CdS NPs decorated ZnO demonstrate a high vapour sensing behaviour for NH<sub>3</sub> and the sensing of it was enhanced nearly thrice than the core/shell-like ZnO/CdSe NSs. It was attributed to the effective interaction of the incident light and the sensing media, the change in the refractive index of the modified cladding regime, the rate of vapour adsorption and the effective charge-carrier transport between the so-formed hetero-junction interfaces [67].

The sensing properties of cadmium telluride (CdTe) QDs film were examined under exposure to volatile organic compounds (VOCs); ethanol, 2-propanol and acetone and noted the quenching of fluorescence under VOCs. The rate and amount of fluorescence quenching depend on the type of VOCs [68].

An optical fibre sensor was developed using CuInS<sub>2</sub>/ZnS QDs for CO<sub>2</sub> sensing. It was noted that emission wavelength shift due to changes in the absorption of a pH indicator ( $\alpha$ -naphtholphthalein) with a changing CO<sub>2</sub> concentration and the associated wavelength shift was found to be 630 pm/%CO<sub>2</sub> [69]. The gas sensing properties of CdTe/CdS core/shell QDs coated core fibre on the basis of the fluorescence quenching mechanism of QDs were studied and noticed that this fibre was highly selective and sensitive for Nitric oxide (NO) with a detection limit of 10<sup>-11</sup> M [70].

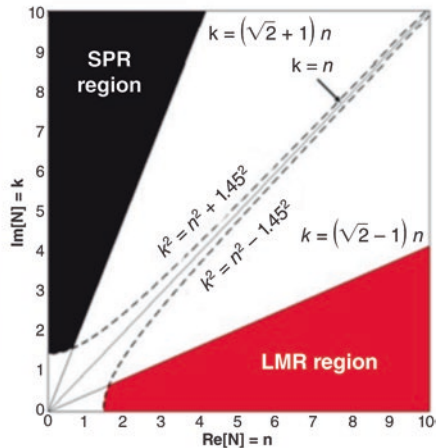


**(a) Setups for LMR and SPR generation**



**(b) LMR and SPR generation conditions**

TYPE OF RESONANCE	$\epsilon$ CONDITIONS	n,k CONDITIONS $\forall n > 0, k > 0$
<b>SPR</b> surface plasmon Resonance	$\epsilon_2' < 0$ $ \epsilon_2'  >  \epsilon_2'' $ $ \epsilon_2'  >  \epsilon_3' $	$k_2 > (\sqrt{2} + 1)n_2$ $k_2^2 - n_2^2 > 1.45^2$
<b>LMR</b> Lossy Mode Resonance	$\epsilon_2' > 0$ $ \epsilon_2'  >  \epsilon_2'' $ $ \epsilon_2'  >  \epsilon_3' $	$k_2 > (\sqrt{2} - 1)n_2$ $n_2^2 - k_2^2 > 1.45^2$



**Fig. 12.11** (a) Generation of LMR and SPR with a nanostructured optical prism (Kretschmann configuration) and a nanostructured D-shaped optical fibre. (b) Conditions for LMR and SPR generation in both configurations. (Adopted with permission from Del Villar et al. [66]. Copyright 2017: Elsevier)

CdS-coated clad-modified fibre optics were tested for the detection of toxic gases like  $\text{NO}_2$ ,  $\text{SO}_2$  and  $\text{CO}_2$ -based of luminescence quenching mechanism and found high sensitivity and selective for  $\text{NO}_2$  gas [57]. Optical fibre in conjunction with ZnTe QDs was investigated for sensing application of VOCs and found that the sensitivity of the sensor increases with the use of QDs for both alcohol and ammonia [71].

## 12.7 Conclusion

In summary, this chapter discussed about the importance and need for optical gas sensors based on II–VI compound semiconductors. The optical sensors are preferred over other kinds of gas sensors owing to their various advantages like high sensitivity on the analyte gas, fast response and insensitivity to any change in environmental conditions, etc. There are a number of optical methods that can be harnessed to realize gas sensors and some of these methods are very particular for II–VI semiconductors like luminescence and fluorescence spectroscopies owing to the band gap and colour tunable properties of these semiconductors. Besides, a number of optical methods like emission, absorption, and surface plasmon resonance can also be realized for gas sensing using fibre optics along with the traditional interferometry, waveguides, cladding and clad modification techniques. The optical gas sensors based on these different methods were elaborated in view of morphologies, forms and complexity of II–VI compounds.

At the same point, apart from the multifold advantages of II–VI compound semiconductor-based optical gas sensors, these sensors possess few drawbacks like incompatibility with existing technologies, complexity in miniaturization along with high cost due to their processing, maintenance and instability issues. Moreover, the temporal stability of IDs, QDs, CShs and their thin films is badly affected if exposed to harsh conditions. For example, photoactivation, photooxidation and photo corrosion are the synergetic effects of light, moisture and oxygen on the characteristic emission of the most preferred Cd-based QDs and are irreversible. In photoactivation, the PL intensity of CdSe QDs is observed to be enhanced under illumination in presence of moisture. The combined effect of oxygen and light is photooxidation where the surface of QDs gets oxidized resulting in trap states. The third one affects most badly by causing reduction in the size of QDs core, PL quenching, spectrum broadening and blue-shifting of band edge emission when exposed to oxygen and light for a long time. In order to overcome these issues, if the shell of another semiconductor or matrix-like  $\text{SiO}_2$  is used, then it is an additional requirement and also the sensing mechanism changes that affect the sensitivity of the sensor. Besides, the toxic nature of Cd ions makes these semiconductors vulnerable to green environment and applications as the handling of Cd ions can cause multiple diseases like itai-itai, lung damage, flu-like sickness (chilling, fever and muscular pains), etc.

Nevertheless, optical gas sensors are the high-end market product in this business and find applications in remote air quality and environment monitoring, NO<sub>x</sub> sensing in coal-fired thermal power plants, H<sub>2</sub>S sensing in wastewater management plants and ethanol sensing in wine manufacturing industries. These sensors are also used in accurate and safe detection of gas leakage in industries, stores, etc. Moreover, there are still many areas like rigorous synthesis process, cost, response time and tedious instrumentation in view of the optical gas sensors based on II–VI compounds that need to be addressed through further research and development in this important field.

## References

1. Zhou D, Victor DG, Ahmed EHM, Dadhich PK, Olivier JGJ, Rogner H-H, Sheikho K, Yamaguchi M. Introductory chapter. In: Edenhofer O, Pichs-Madruga R, Sokona Y, Farahani ESK, Seyboth K, Adler A, et al., editors. Climate change 2014: mitigation of climate change. Contribution of Working Group III to the Fifth Assessment Report of the Intergovernmental Panel on Climate Change. Cambridge, UK; New York: Cambridge University Press; 2014. p. 111–68.
2. Each Country's Share of CO<sub>2</sub> Emissions. 2008. <https://www.ucsusa.org/resources/each-country-share-co2-emissions>. Accessed 25 Apr 2022.
3. Korotcenkov G, Cho BK. Metal oxide composites in conductometric gas sensors: achievements and challenges. *Sensors Actuators B Chem.* 2017;244:182–210.
4. Korotcenkov G, Han SD, Stetter JR. Review of electrochemical hydrogen sensors. *Chem Rev.* 2009;109:1402–33.
5. Yadav K, Gahlaut SK, Mehta BR, Singh JP. Photoluminescence based H<sub>2</sub> and O<sub>2</sub> gas sensing by ZnO nanowires. *Appl Phys Lett.* 2016;108(7):071602.
6. Duong HD, Rhee JI. Development of ratiometric fluorescence sensors based on CdSe/ZnS quantum dots for the detection of hydrogen peroxide. *Sensors (Basel).* 2019;19(22):4977.
7. Xu S, Dong K, Wen J, Jiang N, Wang J, Zheng C, Zhao S, Zhang J. CdTe quantum dots/poly (diallyl dimethyl ammonium chloride) multilayer films: preparation and application for gaseous sensors. *Int J Environ Agric Res (IJOEAR).* 2017;3(3):7–14.
8. Yesudasu V, Pradhan HS, Pandya RJ. Recent progress in surface plasmon resonance based sensors: a comprehensive review. *Heliyon.* 2021;7(3):e06321.
9. Szunerits S, Shalabney A, Boukherroub R, Abdulhalim I. Dielectric coated plasmonic interfaces: their interest for sensitive sensing of analyte-ligand interactions. *Rev Anal Chem.* 2012;31(1):15–28.
10. Saxena N, Kumar P, Gupta V. CdS: SiO<sub>2</sub> nanocomposite as a luminescence-based wide range temperature sensor. *RSC Adv.* 2015;5(90):73545–51.
11. Paek K, Chung S, Cho CH, Kim BJ. Fluorescent and pH-responsive diblock copolymer-coated core-shell CdSe/ZnS particles for a color-displaying, ratiometric pH sensor. *Chem Commun (Camb).* 2011;47(37):10272–4.
12. Chu C-S, Chuang C-Y. Optical fiber sensor for dual sensing of dissolved oxygen and Cu<sup>2+</sup> ions based on PdTFPP/CdSe embedded in sol–gel matrix. *Sensors Actuators B Chem.* 2015;209:94–9.
13. Xue S, Jiang XF, Zhang G, Wang H, Li Z, Hu X, Chen M, Wang T, Luo A, Ho HP, He S, Xing X. Surface plasmon-enhanced optical formaldehyde sensor based on CdSe@ZnS quantum dots. *ACS Sens.* 2020;5(4):1002–9.
14. Buiculescu R, Hatzimarinaki M, Chaniotakis NA. Biosilicated CdSe/ZnS quantum dots as photoluminescent transducers for acetylcholinesterase-based biosensors. *Anal Bioanal Chem.* 2010;398(7–8):3015–21.

15. Hu J, Wu P, Deng D, Jiang X, Hou X, Lv Y. An optical humidity sensor based on CdTe nanocrystals modified porous silicon. *Microchem J.* 2013;108:100–5.
16. Bismuto A, Lettieri S, Maddalena P, Baratto C, Comini E, Faglia G, Sberveglieri G, Zanotti L. Room-temperature gas sensing based on visible photoluminescence properties of metal oxide nanobelts. *J Opt A Pure Appl Opt.* 2006;8(7):S585–8.
17. Liu X, Sun Y, Yu M, Yin Y, Yang B, Cao W, Ashfold MNR. Incident fluence dependent morphologies, photoluminescence and optical oxygen sensing properties of ZnO nanorods grown by pulsed laser deposition. *J Mater Chem C.* 2015;3(11):2557–62.
18. Ip KM, Liu Z, Ng CM, Hark SK. Effects of passivation and ambient gases on the photoluminescence of ZnSe nanowires. *Nanotechnology.* 2005;16(8):1144–7.
19. Ganesan M, Nagaraaj P. Quantum dots as nanosensors for detection of toxics: a literature review. *Anal Methods.* 2020;12(35):4254–75.
20. Proceedings of International Conference on Metamaterials and Nanophotonics (METANANO-2017) AIP Conf. Proc. 1874, 030032-1–030032-4.
21. Sergeev AA, Sergeeva KA, Leonov AA, Postnova IV, Voznesenskiy SS, Kulchin YN. Manganese-doped zinc sulfide quantum dots for methane detection in aqueous media. *Defect Diffus Forum.* 2018;386:229–35.
22. Sergeev AA, Leonov AA, Galkina AN, Voznesenskiy SS. Application of zinc sulfide quantum dots for optical sensing. *Key Engin Mater.* 2019;806:186–91.
23. Sotelo-Gonzalez E, Fernandez-Arguelles MT, Costa-Fernandez JM, Sanz-Medel A. Mn-doped ZnS quantum dots for the determination of acetone by phosphorescence attenuation. *Anal Chim Acta.* 2012;712:120–6.
24. Poeplau M, Ester S, Henning B, Wagner T. Recombination mechanisms of luminescence type gas sensors. *Phys Chem Chem Phys.* 2020;22(35):19948–56.
25. Ando M, Kamimura T, Uegaki K, Biju V, Shigeri Y. Sensing of ozone based on its quenching effect on the photoluminescence of CdSe-based core-shell quantum dots. *Microchim Acta.* 2016;183(11):3019–24.
26. Ando M, Kamimura T, Uegaki K, Biju V, Damasco Ty JT, Shigeri Y. Reversible photoluminescence sensing of gaseous alkylamines using CdSe-based quantum dots. *Sensors Actuators B Chem.* 2017;246:1074–9.
27. Amelia M, Lavie-Cambot A, McClenaghan ND, Credi A. A ratiometric luminescent oxygen sensor based on a chemically functionalized quantum dot. *Chem Commun (Camb).* 2011;47(1):325–7.
28. Rodríguez-Cantó PJ, Abargues R, Gordillo H, Suarez I, Chirvony V, Albert S, Martínez-Pastor J. UV-patternable nanocomposite containing CdSe and PbS quantum dots as miniaturized luminescent chemo-sensors. *RSC Adv.* 2015;5:19874–83.
29. Nazzal AY, Qu L, Peng X, Xiao M. Photoactivated CdSe nanocrystals as nanosensors for gases. *Nano Lett.* 2003;3(6):819–22.
30. Sung T-W, Lo Y-L. Ammonia vapor sensor based on CdSe/SiO<sub>2</sub> core/shell nanoparticles embedded in sol–gel matrix. *Sensors Actuators B Chem.* 2013;188:702–8.
31. Orlova AO, Gromova YA, Maslov VG, Andreeva OV, Baranov AV, Fedorov AV, Prudnikau AV, Artemyev MV, Berwick K. Reversible photoluminescence quenching of CdSe/ZnS quantum dots embedded in porous glass by ammonia vapor. *Nanotechnology.* 2013;24(33):335701.
32. Yao Q, Brock SL. Optical sensing of triethylamine using CdSe aerogels. *Nanotechnology.* 2010;21(11):115502.
33. Zhao Z, Dansereau TM, Petrukhina MA, Carpenter MA. Nanopore-array-dispersed semiconductor quantum dots as nanosensors for gas detection. *Appl Phys Lett.* 2010;97(11):113105.
34. Wu D, Sedgwick AC, Gunnlaugsson T, Akkaya EU, Yoon J, James TD. Fluorescent chemosensors: the past, present and future. *Chem Soc Rev.* 2017;46(23):7105–23.
35. Xia H, Geng T, Zhao X, Li F, Wang F, Gao L. Preparation and sensing properties of organic gel fluorescence films based on ZnS nanoparticles. *Acta Phys -Chim Sin.* 2019;35(3):337–44.
36. Xia H, Hu J, Tang J, Xu K, Hou X, Wu P. A RGB-type quantum dot-based sensor Array for sensitive visual detection of trace formaldehyde in air. *Sci Rep.* 2016;6:36794.

37. Ahmad I, Zhou Z, Li H-Y, Zang S-Q. Crafting CdTe/CdS QDs surface for the selective recognition of formaldehyde gas via ratiometric contrivance. *Sensors Actuators B Chem.* 2020;304:127379.
38. Saren AA, Kuznetsov SN, Kuznetsov AS, Gurtov VA. Excitonic chemiluminescence in Si and CdSe nanocrystals induced by their interaction with ozone. *ChemPhysChem.* 2011;12(4):846–53.
39. Jiao X, Zhang L, Lv Y, Su Y. A new alcohols sensor based on cataluminescence on nano-CdS. *Sensors Actuators B Chem.* 2013;186:750–4.
40. Xia H, Zhou R, Zheng C, Wu P, Tian Y, Hou X. Solution-free, in situ preparation of nano/micro CuO/ZnO in dielectric barrier discharge for sensitive cataluminescence sensing of acetic acid. *Analyst.* 2013;138(13):3687–91.
41. Tan CH, Tan ST, Lee HB, Ginting RT, Oleiwi HF, Yap CC, Jumali MHH, Yahaya M. Automated room temperature optical absorbance CO sensor based on in-doped ZnO nanorod. *Sensors Actuators B Chem.* 2017;248:140–52.
42. Gaspera ED, Guglielmi M, Martucci A, Giancaterini L, Cantalini C. Enhanced optical and electrical gas sensing response of sol-gel based NiO–Au and ZnO–Au nanostructured thin films. *Sensors Actuators B Chem.* 2012;164:54–63.
43. Paliwal A, Sharma A, Tomar M, Gupta V. Carbon monoxide (CO) optical gas sensor based on ZnO thin films. *Sensors Actuators B Chem.* 2017;250:679–85.
44. Zayats M, Kharitonov AB, Pogorelova SP, Lioubashevski O, Katz E, Willner I. Probing photoelectrochemical processes in Au–CdS nanoparticle arrays by surface plasmon resonance: application for the detection of acetylcholine esterase inhibitors. *J Am Chem Soc.* 2003;125:16006–14.
45. Wu M-C, Kao C-K, Lin T-F, Chan S-H, Chen S-H, Lin C-H, Huang Y-C, Zhou Z, Wang K, Lai C-S. Surface plasmon resonance amplified efficient polarization-selective volatile organic compounds CdSe–CdS/Ag/PMMA sensing material. *Sensors Actuators B Chem.* 2020;309:127760.
46. Mariammal RN, Stella C, Ramachandran K. Chunk-shaped ZnO nanoparticles for ethanol sensing. *AIP Conf Proc.* 2013;1512:368–9.
47. Narasimman S, Balakrishnan L, Alex ZC. Fiber-optic ammonia sensor based on amine functionalized ZnO nanoflakes. *IEEE Sensors J.* 2018;18(1):201–8.
48. Narasimman S, Balakrishnan L, Alex ZC. ZnO nanorods based fiber optic hexane sensor. *AIP Conf Proc.* 2019;2162:020105.
49. Narasimman S, Balakrishnan L, Meher SR, Sivacoumar R, Alex ZC. ZnO nanoparticles based fiber optic gas sensor. *AIP Conf Proc.* 2016;1731:050052.
50. Narasimman S, Balakrishnan L, Meher SR, Sivacoumar R, Alex ZC. Influence of surface functionalization on the gas sensing characteristics of ZnO nanorhombuses. *J Alloys Compd.* 2017;706:186–97.
51. Renganathan B, Ganesan AR. Fiber optic gas sensor with nanocrystalline ZnO. *Opt Fiber Technol.* 2014;20(1):48–52.
52. Renganathan B, Sastikumar D, Gobi G, Rajeswari Yogamalar N, Chandra Bose A. Nanocrystalline ZnO coated fiber optic sensor for ammonia gas detection. *Opt Laser Technol.* 2011;43(8):1398–404.
53. Devendiran S, Sastikumar D. Gas sensing based on detection of light radiation from a region of modified cladding (nanocrystalline ZnO) of an optical fiber. *Opt Laser Technol.* 2017;89:186–91.
54. Dikovska AO, Atanasova GB, Nedyalkov NN, Stefanov PK, Atanasov PA, Karakoleva EI, Andreev AT. Optical sensing of ammonia using ZnO nanostructure grown on a side-polished optical-fiber. *Sensors Actuators B Chem.* 2010;146(1):331–6.
55. Noel JL, Udayabhaskar R, Renganathan B, Muthu Mariappan S, Sastikumar D, Karthikeyan B. Spectroscopic and fiber optic ethanol sensing properties Gd doped ZnO nanoparticles. *Spectrochim Acta A Mol Biomol Spectrosc.* 2014;132:634–8.
56. Saidin N, Idris NF, Yaacob MH, Harun SW, Ralib AAM, Hasbullah NF. Single-mode fiber coated with zinc oxide (ZnO) nanorods for H<sub>2</sub> gas sensor applications. In: *Proceedings of IEEE*

- international conference on sensors and nanotechnology, 24–25 July 2019, Penang, Malaysia, 19258786.
57. Cameron Theoderaj AK, Inbaraj DJ, Mangalaraj C. CdS coated clad-modified fiber optic sensor for detection of NO<sub>2</sub> gas. *Mater Res Express*. 2019;6(10):1050c8.
  58. de Oliveira HJB, Filho JFM, do Nascimento JF. Computational modeling of H<sub>2</sub>S gas sensor using surface plasmon resonance in a D-shaped optical fiber. In: Proceedings of SBFoton international optics and photonics conference (SBFoton IOPC), 08–10 October 2018, Campinas, Brazil, 18403526.
  59. Charlton C, de Melas F, Inberg A, Croitoru N, Mizaikoff B. Hollow-waveguide gas sensing with room-temperature quantum cascade lasers. *IEE Proc Optoelectron*. 2003;150(4):306–9.
  60. Fu H, Jiang Y, Ding J, Zhang J, Zhang M, Zhu Y, Li H. Zinc oxide nanoparticle incorporated graphene oxide as sensing coating for interferometric optical microfiber for ammonia gas detection. *Sensors Actuators B Chem*. 2018;254:239–47.
  61. Coelho L, Viegas D, Santos JL, de Almeida JMMM. Characterization of zinc oxide coated optical fiber long period gratings with improved refractive index sensing properties. *Sensors Actuators B Chem*. 2016;223:45–51.
  62. Konstantaki M, Klini A, Anglos D, Pissadakis S. An ethanol vapor detection probe based on a ZnO nanorod coated optical fiber long period grating. *Opt Express*. 2012;20:8472–84.
  63. Tabassum R, Mishra SK, Gupta BD. Surface plasmon resonance-based fiber optic hydrogen sulfide gas sensor utilizing Cu-ZnO thin films. *Phys Chem Chem Phys*. 2013;15(28):11868–74.
  64. Usha S, Mishra S, Gupta B. Fabrication and characterization of a SPR based fiber optic sensor for the detection of chlorine gas using silver and zinc oxide. *Materials*. 2015;8(5):2204–16.
  65. Usha SP, Mishra SK, Gupta BD. Fiber optic hydrogen sulfide gas sensors utilizing ZnO thin film/ZnO nanoparticles: a comparison of surface plasmon resonance and lossy mode resonance. *Sensors Actuators B Chem*. 2015;218:196–204.
  66. Del Villar I, Arregui FJ, Zamarreño CR, Corres JM, Barriain C, Goicoechea J, et al. Optical sensors based on lossy-mode resonances. *Sensors Actuators B Chem*. 2017;240:174–85.
  67. Rajeswari Yogamalar N, Sadhanandham K, Chandra Bose A, Jayavel R. Band alignment and depletion zone at ZnO/CdS and ZnO/CdSe hetero-structures for temperature independent ammonia vapor sensing. *Phys Chem Chem Phys*. 2016;18(47):32057–71.
  68. Bakar NA, Rahmi A, Umar AA, Salleh MM, Yahaya M. Fluorescence gas sensor using CdTe quantum dots film to detect volatile organic compounds. *Mater Sci Forum*. 2010;663–665:276–9.
  69. Chu C-S, Hsieh M-W. Optical fiber carbon dioxide sensor based on colorimetric change of  $\alpha$ -naphtholphthalein and CIS/ZnS quantum dots incorporated with a polymer matrix. *Opt Mater Express*. 2019;9(7):2937–45.
  70. Ding L, Ruan Y, Li T, Huang J, Warren-Smith SC, Eborndorff-Heidepriem H, Monro TM. Nitric oxide optical fiber sensor based on exposed core fibers and CdTe/CdS quantum dots. *Sensors Actuators B Chem*. 2018;273:9–17.
  71. Sundaray M, Das C, Tripathy SK. Sensing application of an optical fiber dip coated with L-Cystein ethyl ester hydrochloride capped ZnTe quantum dots. *Mater Sci-Pol*. 2016;34(3):665–8.

# Chapter 13

## Spectroscopic Gas Sensing Systems



Zhenhui Du and Jinyi Li

### 13.1 Introduction

Spectroscopic gas sensing, namely gas detection by analysis of the characteristic spectra of molecules, is becoming more popular in wide variety of areas including urban and industrial emission [1], environmental monitoring [2], chemical and industrial process control [3], medical diagnostics [4], homeland security [5] and scientific research [6]. Traditional approaches of spectroscopic gas sensing based on incoherent light sources are non-dispersive infrared (NDIR), differential optical absorption spectroscopy (DOAS), Fourier transform infrared spectroscopy (FTIR), photometry, etc.

NDIR is a technique to determine gas concentration by detecting a few absorption lines across a restricted wavelength range with fixed narrow-band filters in the infrared spectral region. A typical NDIR instrument uses a double-beam methodology and consists of a light source (e.g. halogen lamp, LED, etc.), filters, gas cells and infrared detectors. The sensing wavelength is carefully selected by the existing output range of infrared sources and within the ‘atmospheric windows’ to reduce spectral interferences. NDIR gas analysers have the merits of real-time response for easy algorithms, low-cost, compact, robust, in situ and stable and long-term operation needs minimum recalibration, which allow for measurement of a variety of components including CO<sub>2</sub>, CO, CH<sub>4</sub>, NO, SO<sub>2</sub>, etc. However, NDIR gas analysers

---

Z. Du (✉)

State Key Laboratory of Precision Measuring Technology and Instruments, Tianjin University, Tianjin, China

e-mail: [duzhenhui@tju.edu.cn](mailto:duzhenhui@tju.edu.cn)

J. Li

Key Laboratory of Intelligent Control of Electrical Equipment, Tiangong University, Tianjin, China

e-mail: [lijinyi@tiangong.edu.cn](mailto:lijinyi@tiangong.edu.cn)

are suffered from low sensitivity and selectivity, and susceptible to ambient humidity and fluctuation of temperature and pressure.

DOAS, pioneered by Noxon [7], is a method to determine concentrations of trace gases by measuring their specific narrow-band absorption structures in the UV and visible spectral regions. DOAS can simultaneously detect multiple gases in an open optical path or in sampling mode. A typical DOAS instrument consists of a continuous light source (e.g. a Xe-arc lamp, a deuterium lamp, sunlight, etc.) and an optical setup to send and receive the light through the objective gases. The received light is sent to a grating spectrometer and converted to spectrum data. The narrow part of the absorption spectrum is separated and used to calculate the concentrations of the multiple species. By means of a typical length of the light path in the atmosphere ranges from several hundred metres to many kilometres, DOAS can measure concentrations of many different trace gases, including photochemical smog formation;  $O_3$ ,  $NO_2$ , HCHO, HONO,  $H_2O$ ,  $NO_3$ ,  $SO_2$ , BrO, IO, OIO; and several aromatic hydrocarbons.

FTIR is an analytical technique used to measure the absorption of infrared radiation by the samples versus wavelength, in which both open optical path measurement and sampling sensing are available. The infrared absorption bands identify molecular components and structures. A typical FTIR spectrometer uses an interferometer to modulate the wavelength from a broadband infrared source. The signal obtained from the detector is an interferogram and is analysed with a computer using Fourier transforms to obtain a single-beam infrared spectrum. FTIR-based gas analyser is capable of low detection limits of ppb to ppm for multiple gas species in many gas analysis applications, such as toxic gas detection, monitoring industrial facilities, accidental releases and hazardous waste site emissions.

Practically, spectroscopic gas sensing with coherent light sources, for example, tunable lasers, ushered in a new era for their advantages of non-contact, fast response time, high-sensitivity and -selectivity, potential calibration-free, low maintenance requirements and long-life cycle. While, laser absorption spectroscopy (LAS) in the mid-infrared region (MIR, 2.5–25  $\mu\text{m}$ ) is attractive due to the strong fundamental ro-vibrational bands and the highly specific molecular signature, which allows both identification and quantification of the molecular species [2, 8]. Thanks to newly developed MIR devices, including quantum cascade lasers (QCLs) [9], interband cascade lasers (ICLs) [10] and II–VI semiconductor lasers [11], LAS technology progressed rapidly and developed high-performance, compact and rugged gas sensors.

In this chapter, we introduce primarily on LAS for trace gas detection. After a brief overview of the principle in Sect. 13.2, we discuss the spectroscopic gas sensing system configurations, including pump suction system, open path sensing system, gas diffusion sensors and spectroscopic imaging system. We discuss spectroscopic applications with II–VI lasers in Sect. 13.4. Section 13.5 is the conclusion and prospects.



## 13.2 Principle

At its most basic, the interaction of light with matter, for example, gaseous molecule, two physical processes happen, absorption and scattering. Absorption is a basis of spectral analysis, quantitatively based on the Beer–Lambert law, which gives the relationship between the incident and the transmitted radiation through a gas cell or an open pathway filled with molecular gas sample:

$$I(\nu) = I_0(\nu) \times \exp\{-\sigma(\nu) \times L \times C\} \quad (13.1)$$

where  $I_0$  and  $I$  are the incident and transmitted radiant powers, respectively;  $\sigma$  is the absorption cross-section of the molecule in  $\text{cm}^2/\text{molecule}$ ;  $L$  is the absorption path length in  $\text{cm}$ ;  $C$  is the density of the molecule in  $\text{molecule}/\text{cm}^3$ . Usually, the absorption cross-section  $\sigma$  is also used to describe the absorption intensity. The line strength is retrieved by spectrally integrating the absorption line shape and applying the ideal gas law,

$$S(T) = \frac{K_B T A}{X_i L P r_{\text{iso}}} \quad (13.2)$$

where  $K_B$ ,  $T$  ( $K$ ) and  $P$  ( $\text{Pa}$ ) are the Boltzmann constant, gas temperature and total pressure of the gas sample, respectively;  $X_i$  is the amount fraction of  $i$  species;  $A$  ( $\text{cm}^{-1}$ ) is integral absorbance;  $r_{\text{iso}}$  is a correction factor for isotopic fractionation of the gas sample.

### 13.2.1 Direct Absorption Spectroscopy

Direct absorption spectroscopy (DAS) is that a tunable narrow linewidth laser is tuned across the objective spectral line, and the light absorption in a sample is measured as a function of the wavelength. With the measured incident and transmitted laser powers, one could deduce the absorption intensity or gas concentration, and further the state parameters of the gas, for example, temperature or pressure.

DAS is the most common technique for simple-optical configuration, –signal processing and potential absolute measurement. However, DAS often suffers from low sensitivity (absorbance  $\sim 10^{-3}$ – $10^{-4}$ ) for the interference from low-frequency noise (i.e.  $1/f$  noise) in the system and laser power fluctuation.

There are basically two ways to improve the spectroscopic sensitivity: (1) to reduce the noise in the signal, (2) to increase the absorption. The former can be achieved by using modulation techniques, for example, wavelength modulation spectroscopy (WMS) and frequency modulation spectroscopy (FMS), with a typical sensitivity of absorbance  $\sim 10^{-5}$ – $10^{-6}$ . Whereas the latter can be obtained by placing the gas inside a cavity in which the light passes through multiple times to increase

the interaction length, for example, multiple-pass and cavity-enhanced absorption spectroscopy (CEAS) [12]. Both ways of reducing noise and increasing absorption can be further applied in the same system, for example, cavity-enhanced wavelength modulation spectrometry and noise-immune cavity-enhanced optical heterodyne molecular spectroscopy (NICE-OHMS) [13].

The absorbed energy during interaction of light with matter may possibly be converted to acoustic waves, that is, photoacoustic (PA) effect. By recording a photoacoustic spectrum, the amplitude of the acoustic wave is measured with the aid of a microphone as a function of the wavelength of the incident radiation, that is, photoacoustic spectroscopy. Photoacoustic spectroscopy is one of the most powerful techniques for gas sensing that covers a broad range of applications. The detection scheme photoacoustic spectroscopy can be excited by the absorption of modulated or pulsed radiation with very high sensitivity and selectivity.

### 13.2.2 Wavelength Modulation Spectroscopy

WMS is that a periodic sawtooth ramp ridden by a high-frequency sinusoidal is applied to the laser injection current, thus the laser wavenumber,  $\nu(t) = \nu_c + \nu_a \cos \omega t$ , is scanned across the transition of gas to be detected, where  $\nu_c$  and  $\nu_a$ , are the laser centre wavenumber and modulation depth, respectively;  $\omega$  is the radian frequency. In case of ideal conditions, ignoring all kinds of interferences, the modulated absorption signal is detected by a photodiode and then processed using a lock-in amplifier (LIA) to demodulate the signal at the harmonics ( $1f$ ,  $2f$ ,  $3f$ , etc.). The second harmonic component (WMS- $2f$ ) is commonly used for calculating the concentration of target gas. In case of optically thin, that is,  $(\nu)L \cdot C \leq 0.05$ , the ideal  $2f$  signal is modelled as:

$$A_{\text{ideal } 2f} = \frac{2I_0CL}{\pi} \int_0^\pi -\alpha(\nu_c + \nu_a \cos \theta) \cos 2\theta d\theta \propto I_0CL \quad (13.3)$$

where  $\alpha$  is the absorption coefficient and  $\theta = \omega t$  is the phase angle. When incident laser intensity  $I_0$  and optical path  $L$  are constant, the amplitude of WMS- $2f$  signal is proportional to the gas concentration.

Traditionally, tunable diode laser absorption spectroscopy (TDLAS) analyses a discrete narrow absorption line of small molecule for the detection of a single gas. The modulation index of the laser plays a pivotal role in WMS. A modulation index of 2.2 is recognized as the optimum to achieve the maximum SNR for WMS with an isolated spectrum line with Lorentzian, Gaussian or Voigt profile.

However, for larger molecules, for example, volatile organic compounds (VOCs), there are so many lines overlapping each other that results in the spectral features being broad and smooth except for occasional spikes [8, 14]. These spectral features are distinct from that of the discrete narrow absorption lines. Since the WMS- $2f$  signal profile of broadband absorption with a modulation index of 2.2 is absolutely

improper and may lead to broadening and overlapping by the adjacent spectrum, interference and optical fringes as well, detection of trace gas with broadband absorption is much more difficult. The overlapping may deteriorate and even disable the WMS measurement, especially for broadband spectra. So, the modulation index determination should balance the spectral discrimination and the SNR in WMS for a broadband spectrum.

Reference [14] provides a parameter of spectral discrimination (SD) and a criterion for optimizing the modulation index for broadband spectrum. Thanks to the recently developed broadband modulation absorption spectroscopy, one could detect some larger molecules (e.g. VOCs) or multiple gases with a simple system configuration by using a single semiconductor laser [14]. Further requirements of multi-gas sensing could be benefited from the broad tunable coverage of laser with II–VI semiconductors.

Practically, apart from the WMS- $2f$  signal described in Eq. (13.3), the detected signal consists of random noises and the derivation of optical fringes. The optical fringes appear as unpleasant spectral features which are usually mixed with the target absorption and constitute one of the major obstacles in trace gas detection. In a well-designed and well-fabricated spectroscopic system, the optical fringes should be well reduced, and only small residual fringes remain with sinusoidal waveforms [15]. While, random noise is little time-varying wiggles superimposed on the true underlying signal, with a small standard deviation. Thus, the detected signal could be described as:

$$A_{\text{detected } 2f} = e_n + \sum a_j(t) \times \cos(\omega_j(t) \times t) + A_{\text{ideal } 2f} \quad (13.4)$$

where  $\alpha_j(t)$  and  $\omega_j(t)$  are the instantaneous amplitude and frequency of  $j^{\text{th}}$  fringe component, respectively;  $A_{\text{ideal } 2f}$  is the WMS- $2f$  signal modelled by Eq. (13.3).

The profiles of second harmonic of absorption, fringes and noise will inherit the features of their origination. These profile differences among WMS- $2f$ , harmonic of optical fringes and noise will be novel breakthrough point to distinguish and eliminate the interference from the signal [14].

### 13.2.3 Frequency Modulation Spectroscopy

FMS is a method of optical heterodyne spectroscopy capable of rapid measurement of the absorption or dispersion associated with narrow spectral features. The absorption or dispersion is measured by detecting the heterodyne beat signal that occurs when the FMS optical spectrum of the probe wave is distorted by the spectral feature of interest. Recently, dispersion spectroscopy, namely chirped laser dispersion spectroscopy or heterodyne phase-sensitive dispersion spectroscopy attracts the attention of both immunities to optical intensity changes and superb linearity in the measurement of concentration.

### 13.3 System Configurations

A typical LAS consists of a laser, a photodetector and an optical configuration for light interaction with gas. For modulation-based LAS, there are additionally a modulator and a demodulator, the latter usually by a lock-in amplifier (LIA).

The laser is the key component of LAS, which usually needs to be continuously tunable, mode-hop-free, reliable, low-intensity noise and single-frequency with narrow linewidth (typically <1 MHz). The spectral resolution of a TDLAS system is largely depended on the dynamic spectral characteristics during the laser tuning [16], and then determines the selectivity of gas sensing for a gas mixture. Recently developed single-frequency tunable lasers, for example, distributed feedback (DFB) QCL, DFB ICL and single-frequency II–VI semiconductor lasers are all excellent candidates for MIR spectroscopic gas sensing systems.

High-sensitive and low-noise detectors are essential for trace gas detection. Mercury–cadmium–telluride (MCT, or HgCdTe) semiconductor-based detector is popular for its higher speed and wide MIR spectral response. The limitation of the MCT detector is the need for cooling to reduce noise due to dark current. Alternatively, newly developed quantum heterostructure detectors could take a vital part in future infrared detection.

The optical configuration provides interaction between light and gas samples, and the interaction length directly relates to the detection sensitivity. Thus, a long interaction length is desired to achieve high sensitivity. Long path absorption cell and open long path are commonly used in LAS to measure low-concentration components or to observe weak spectra in gas. Traditional multipass cells (MPCs), such as White or Herriott cell, are still widely used, but the requirements of compact, small sample volume and fast response time have stimulated the development of new type of gas cells. Recently, modified MPCs, circular multi-reflection (CMR) cells and hollow waveguides (HWGs)-based gas cells hint at the glorious perspective of compact integrated sensors. On the other hand, the need for open-path gas detection, for example, leak detection, aroused the development of standoff remote sensing with or without a retroreflector. Here in this section, the laser spectroscopic gas sensing systems are classified and reviewed according to the optical configuration that they utilize.

#### 13.3.1 Pump Suction System (Sampling Sensing System)

Gas cells have been introduced for path length enhancement to achieve high sensitivity in spectroscopic analysis systems. In actual applications, a gas cell based-system usually requires a pump for sampling gas, namely pump suction sampling system.

### 13.3.1.1 Multipass Cell-Based System

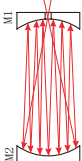
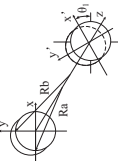
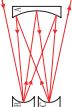
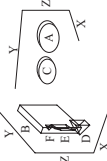
MPCs are commonly used in laboratories or in industrial process applications for more than 70 years, where the simplest designs are the two-mirror Herriott design or the three-mirror White cell. Conventional MPCs commonly have disadvantages in high requirement of alignment stability, long gas exchange time, high cost and large physical size. Recent publications present also more sophisticated designs, such as modified MPC, circular multi-reflection (CMR) cell and quasi-chaotic cell designs. MPC technology has evolved rapidly in the aspects of compactness, small sample volume and fast response time. Herein modelling on C. Robert's classification [17], the MPC optical systems are summarized and classified into six categories as shown in Table 13.1.


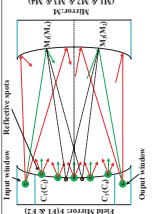
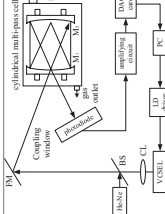
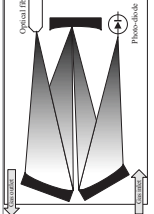
### 13.3.1.2 Hollow Waveguide-Based Sensor

HWGs, capillary tubes with metal/dielectric internal coatings, are promising for transmitting laser beams owing to the advantages of flexibility, high power threshold, low transmission loss, absence of end reflections and broadband ranging from X-ray to ultraviolet, visible, infrared and terahertz. They are ideal candidates for gas cells in spectroscopic system, which could be classified to three categories: ① Ag/AgI-coated HWGs (Ag/AgI-HWG); ② photonic bandgaps HWGs (PBG-HWG); ③ substrate-integrated HWGs (iHWG), respectively [2, 30, 31], as shown in Fig. 13.1. Compared with modified MPCs and CMR cells, HWGs have advantages of easy configurations, compact structure and higher path-to-volume ratio. Hence, HWGs can easily be integrated into the spectroscopic gas sensing system, as shown in Fig. 13.2, for environmental monitoring [32, 33] and breath analysis [4, 34].

In spectroscopic gas sensor, an HWG is exploited as both light waveguide and gas transmission cell. However, the capillary structure of HWG makes it necessary to pay extra attention to the following issues when used for accurate gas measurement, including transmission characteristics of laser beam propagating in HWG, effective optical path [35], influence of adsorption effect of polar molecules on gas measurement [36, 37] and non-uniform distribution of pressure during gas flowing in HWG [38]. Additionally, it is worth noting that filling PBG-HWG with analyte gas for sensing is difficult owing to considerable back-pressure building up in the hollow structure. However, techniques to improve the sample filling time have been proposed, which include increasing the pressure difference across the fibre to drive the gas through and introducing holes to allow gas flow or diffusion along the waveguide's length.

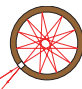
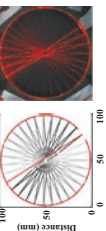
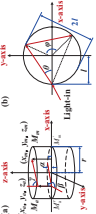
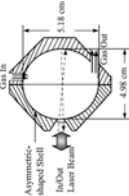
**Table 13.1** Summary of the various types of multipass cells up to now

Type	Subtype	Structure	Performance	Advantages	Disadvantages	Ref.
Herriott cells with two mirrors	Herriott Cell	Two spherical mirrors of radii $R_1$ and $R_2$ face to face and separated by the distance $d$ . 	Pathlength/m: 30 Number of passes/: 74 Volume/L: 1	Optomechanically stable; Simple path length changes.	Hard to align; Spot diffusion introduced by aberrations	[18]
	Herriott Cell with Astigmatic Mirrors	A multipass cell, based on an astigmatic variant of the off-axis resonator (Herriott) configuration. 	Number of passes: 182 100 m in 3.6 L; 36 m in 0.27 L	More efficient utilization of mirror area ; Accepts high NA beams.	Extreme precision in the manufacture of the mirrors; A re-entrant condition must be established for two axes simultaneously	[19]
White cells with three mirrors	White Cell	This cell includes three spherical mirrors of equal curvature radius. Two mirrors are put side by side. On the other end of the cell, a third mirror is put at a distance equal to the radius of curvature. 	Pathlength/m: 7.5 Number of passes/: 12 Volume/L: 10	Accepts high NA beams.	Short optical path.	[20]
	White Cell with Recirculation	Left, field mirror B and three retroreflectors D, E and F; right, two objective mirrors A and C. 	144-pass configuration.	High NA beams acceptable; Long pathlength	Multiplication of the number of optical elements.	[21]

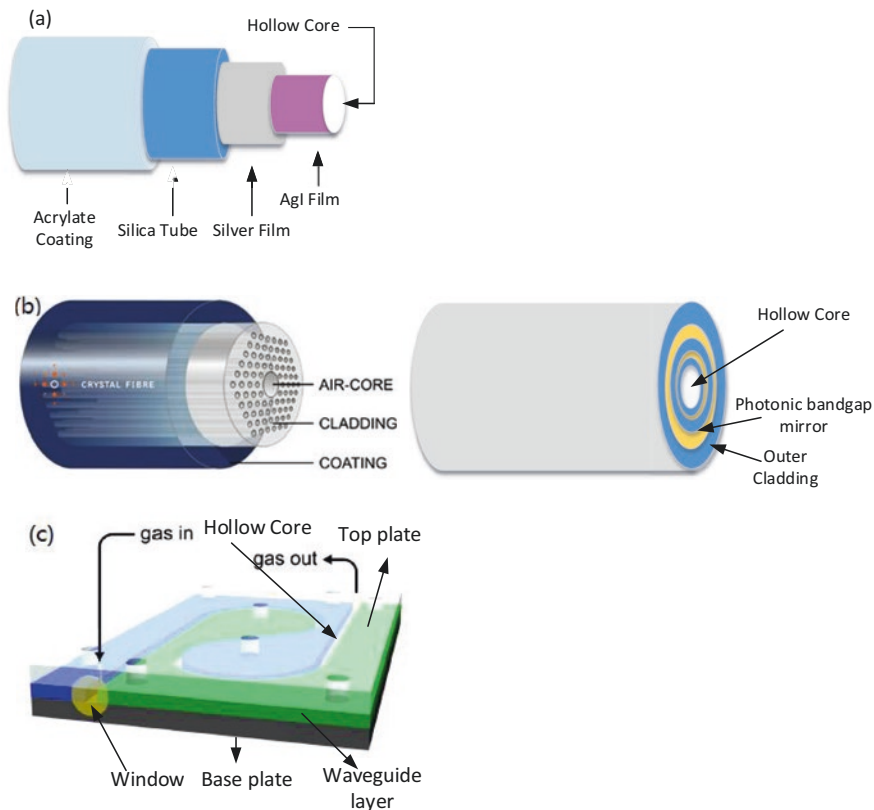
<p>Multi-mirrors cells of Chernin type</p>	<p>These cells contain from five to six mirrors of equal radii of curvature.</p> 	<p>The reflections on these mirrors are arranged in the shape of a focused dot matrix.</p>	<p>Compact structure; High number of possible paths; Corrected aberration; Variable pathlength.</p>	<p>High assembly accuracy of two mirrors. [22]</p>
<p>Modified MPCs</p>	<p>Modified MPC with 6 mirrors</p> 	<p>Base length: 300 mm OPL 32.4 m; Volume 0.48 L; PVR 67.5 m/L;</p>	<p>keeping focal properties, low-aberrations; High PVR; compact structure; suitable for MIR.</p>	<p>Multiple components and requiring adjustment; slow gas exchanging; Spherical mirror has aberration distortion. [23]</p>
<p>Modified MPC with 2 mirrors</p> 	<p>Base length: 121 mm OPL: 22 m Volume: 0.55 L PVR: 40 m/L</p>	<p>Keeping focal properties, low aberrations; compact structure; low fringes and high thermal stability.</p>	<p>Large volume; slow gas exchanging [24]</p>	
<p>Modified MPC with 3 mirrors</p> 	<p>Base length: 120 mm OPL 1.46 m; Volume 0.33 L; PVR 4.4 m/L;</p>	<p>Keeping focal properties, low aberrations; suitable for MIR; Suited for field operation.</p>	<p>Multiple components and requiring adjustment; Interference of light; Long gas exchange time. [25]</p>	

(continued)

Table 13.1 (continued)

Type	Subtype	Structure	Performance	Advantages	Disadvantages	Ref.
Circular multi-reflection (CMR) cells	CMR cell with a confocal, parabolic mirror arrangement	Such cells rely on a circular arrangement of spherical mirrors 	Pathlength/m: 12.24 Number of passes/:89	Robustness toward mechanical stress.	Surface shape bending; High machining accuracy.	[26]
	CMR cell with six spherical, gold-coated mirrors	Six spherical mirrors form a nearly continuous ring with ~100-mm inner diameter. A 12.6 mm space between two of the mirrors is reserved for coupling optics. 	Basic length/m: 0.1 OPL/m: 3.1 Volume/cm <sup>3</sup> : 236	Easily modification of the optical path length; Strong applicability; flexibility of optical path selection		[27]
Other cells	CMR cell with multi-layer patterns		2-layer pattern: 8.3 m, 71 mL; 3-layer pattern: 10 m, 110 mL	Inner surface of the toroidal multi-pass cell is utilized efficiently (increase path length); easy to fabricate.	The etalon effect; High accuracy of incident angle of light.	[28]
	Chaotic multipass cell		15.5 m orbit with a mean cavity radius of 2.54 cm.	Long path lengths; Reduced beam overlap; Small beam divergence; Re-entrant conditions.	Coherence evolution of laser beams in the chaotic multipass cavity.	[29]



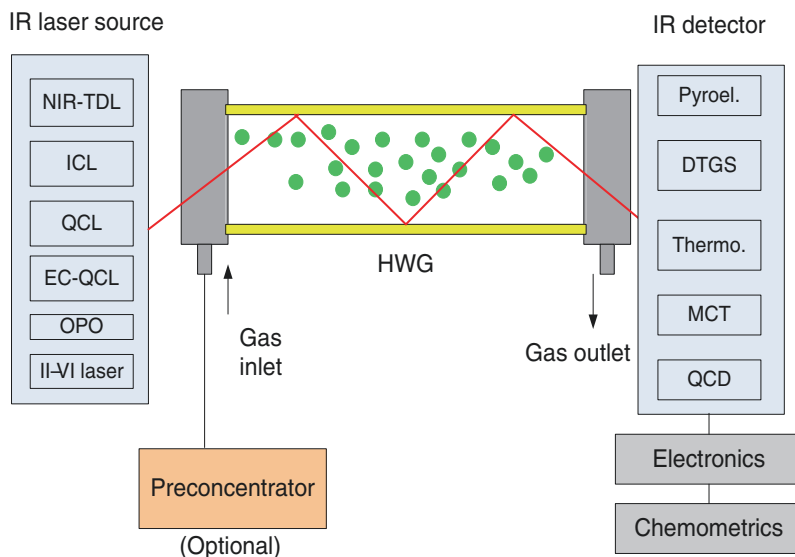


**Fig. 13.1** Schematic structure (a) Ag/AgI-coated hollow waveguide; (b) photonic bandgap hollow waveguide (PBG -HWG); (c) substrate-integrated hollow waveguide (iHWG). (Reprinted with permission from Ref. [18]. Copyright 2017: Peking University Press)

### 13.3.2 Diffusion Sensors

Different from pump suction sampling system, diffusion-type gas sensor can avoid the need for a gas valve and pump. A diffusion-type gas sensor can be obtained by reforming the system via removing the sealing cover of the gas cell or replacing it with an air-permeable shell. These kinds of sensors are widely used to monitor the target gas in the atmospheric environment, or loaded on an unmanned aerial vehicle or a mobile vehicle to perform highly sensitive detection of the target gas in the area of interest. However, the open-path-cell optical system is very easy to cause contamination of the multi-reflective lens and requires frequent maintenance.

On the other hand, an alternative diffusion-type laser gas sensor has been developed for point measurement, which is similar to a semiconducting metal oxide gas sensor or catalytic sensor in shape and size but better in selectivity and sensitivity. Most recently, a novel compact intrinsic safety full range methane ( $\text{CH}_4$ )



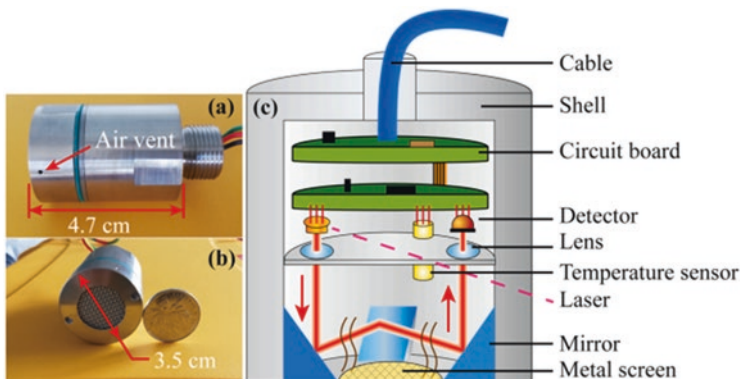
**Fig. 13.2** Overview of the most prevalent hollow waveguide-based laser gas sensing principles. The laser source includes the following: NIR-TDL near-infrared tunable diode laser, ICL interband cascade laser, QCL quantum cascade laser, EC-QCL external cavity coupled QCL, OPO optical parametric oscillator. The detector includes the following: pyroel pyroelectric detector, DTGS deuterated triglycine sulphate detector, thermo thermopile detector, MCT mercury cadmium telluride semiconductor detector, QCD quantum cascade detector. (Reprinted with permission from Ref. [18]. Copyright 2017: Peking University Press)

microprobe sensor based on the TDLAS technique has been proposed for leaking detection in explosion risk environment, such as natural gas industries, petrochemical enterprises and coal mines. A minimized diffused laser  $\text{CH}_4$  probe sensor with sensitivity of ppm is shown in Fig. 13.3 [39].

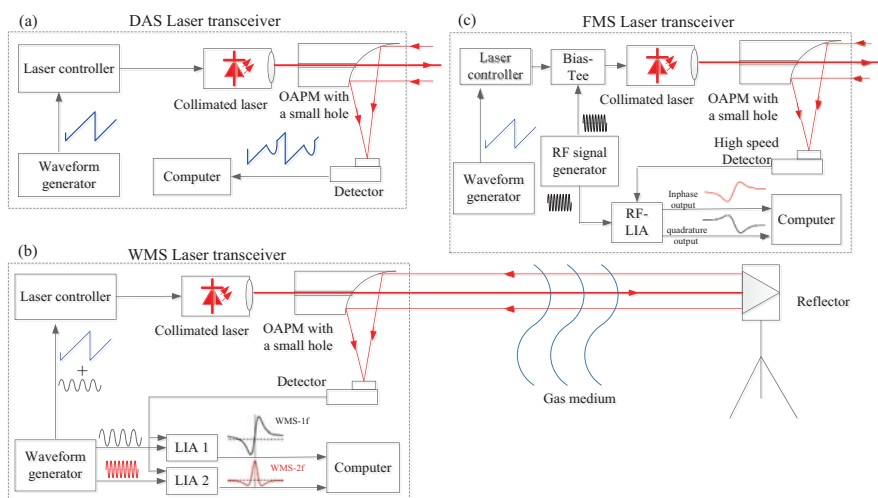
### 13.3.3 Open Path Sensing

#### 13.3.3.1 Open Path Detection with Retroreflectors

A simple standoff open-path TDLAS can be realized by means of a transceiver coupled with a retroreflector, which retrieves path-averaged gas concentrations by a long-path transmission measurement. A schematic diagram is shown in Fig. 13.4 to describe typical TDLAS systems with three different modes of operation, that is, DAS, WMS and FMS. The optical signal is directly collected through the photodetector and then processed by the computer, as shown in Fig. 13.4a. DAS relies on a measurement of a small change of a signal on top of a large background. Any noise introduced by the light source or the optical system will deteriorate the detectability of the technique. Since DAS is vulnerable to the effects of background noise, it is seldom used for standoff detection applications.



**Fig. 13.3** Photograph of CH<sub>4</sub> probe sensor. Length (a), (b) diameter and (c) structure of the probe. (Reprinted with permission from Ref. [39]. Copyright 2021: Elsevier)



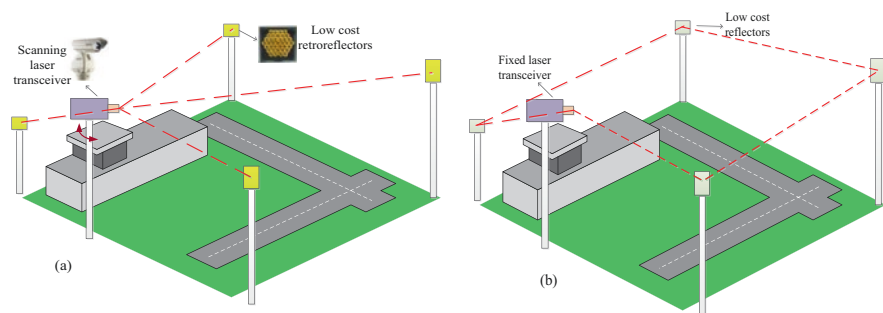
**Fig. 13.4** Schemes of open-path spectroscopic gas systems with an optical reflector and direct absorption spectroscopy (DAS) (a), wavelength modulation spectroscopy (WMS) (b) and frequency modulation spectroscopy (FMS) (c). RF radio frequency, LIA lock-in amplifier, OAPM off-axis parabolic mirror. (Reprinted from Ref. [42]. Published 2020 by MDPI as open access)

Alternatively, modulation spectroscopy is widely used to improve SNR. As shown in Fig. 13.4b, WMS is characterized by the use of a large modulation depth generating a large number of sidebands, and a modulation frequency is much smaller than the linewidth of the target gas ( $f < 1$  MHz). The modulated laser is then collimated and passes through a gaseous medium through an off-axis parabolic mirror (OAPM) with a small hole and then illuminates onto an opposite optical reflector. The reflected laser propagates back to the gaseous medium and is concentrated by the OAPM onto a photodetector. The detector signal is demodulated in two LIAs,

respectively, with reference-in signals of one- and two-times modulation frequency. The first ( $1f$ ) and second harmonic ( $2f$ ) signals are obtained simultaneously and then processed in a computer or an embedded processor for WMS- $2f/1f$  calibration-free measurement to avoid the influence of light intensity fluctuations in open-path detection. While in the case of FMS, the modulation depth is small, but the frequency is very high ( $f > 100$  MHz), which is the same magnitude as the line width of the target gas. Therefore, a radio frequency (RF) signal generator is usually utilized to generate such a high modulation signal, and a bias tee is used to superimpose the RF signal with the scanning signal to drive the laser, as shown in Fig. 13.4c. The frequency-modulated laser reflected by the mirror at a far end carries both absorption and dispersion information of the target gas, which is detected by a high-speed detector. The detector signal is sent to a radio frequency lock-in amplifier (RF-LIA). The absorption component and dispersion component are obtained by in-phase and quadrature-phase demodulation in the RF-LIA, respectively, to retrieve gas concentration [40]. Although FMS has lower  $1/f$  noise, it has a higher cost of LIA and other optoelectronic devices than WMS as a result of the requirement for higher modulation frequency. Therefore, WMS techniques are most widely used in TDLAS for standoff gas detection [41, 42].

Obviously, the scheme is like the TDLAS with a gas cell system, except that the open path is used to replace the multipath gas absorption cell. Moreover, there is almost no extra loss in detection capability compared with the latter, due to the use of optical reflectors. A broadly tunable laser, for example, ECQCL or II-IV laser, could be used for standoff gas-phase chemical detection over hundred-metre distances using a corner-cube retroreflector, from which multiple gases could be monitored in real time.

With open-path spectroscopic gas sensing, a safeguard concept of an optical fence is developed for the protection of outdoor facilities, such as for leakage detection and warning in the oil depot [43], as shown in Fig. 13.5. The transceiver of the system is directed in sequence to inexpensive retroreflectors placed at opposite ends of the facility and measures the transmittance along each of the optical paths, as shown in Fig. 13.5. If a threat cloud crosses the ‘optical fence’, the sensing system



**Fig. 13.5** Optical fence system for threat cloud detection and facilities protection by constructing an ‘optical fence’ with (a) laser transceiver scanning mode and (b) laser transceiver fixed mode. (Reprinted from Ref. [42]. Published 2020 by MDPI as open access)

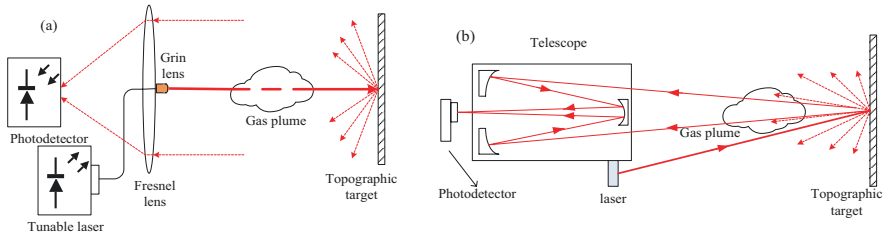
will detect its presence. In addition to sequentially interrogating multiple-beam paths, it is also practicable to configure a system of mirrors such that the laser beam crosses the facility in such a way that the transceiver does not require to move. Moreover, the system is suitable for the protection of large indoor areas, such as airports. Advantages of this method include the capability of detecting a diversity of gases with high sensitivity over large distances (several kilometres). Furthermore, the system needs no consumables and leads to low maintenance compared to a network of point sensors.

Note that the WMS signal is intensity-dependent and requires normalization for the received light power, which might be a major source of significant measurement errors in particular at low-light conditions. In order to mitigate this limitation of WMS, Wysocki and Weidman introduced a novel technique, named chirped laser dispersion spectroscopy (CLaDS) [44], for quantitative trace gas detection based on molecular dispersion measurements. Rather than measuring absorption, CLaDS detects refractive index changes that occur in the vicinity of a molecular transition. The essence of phase detection makes it highly immune to amplitude noise and transmission fluctuations, which means CLaDS is particularly suitable for open-path remote or standoff sensing.

### 13.3.3.2 Standoff Sensing Without Retroreflectors

Although the TDLAS systems can achieve highly sensitive detection in open-path with the help of retroreflectors or other cooperative targets, they are not feasible for mobile or multidirectional measurements. This is because the direction of the beam is defined by the system layout and has to be realigned when the system is moved. In the last decade, special attention has been devoted to the research and development of a real standoff sensing with backscattered light with non-co-operators, called backscatter-TDLAS. Here in this section, we focus on this kind of standoff open-path system that retrieves path-averaged gas concentrations by collecting the backscattered light from a distant non-cooperative topographic target.

In backscatter-TDLAS, a transceiver projects the laser beam onto a remote non-cooperative surface instead of an optical reflector and only receives a small fraction of the passively scattered laser light returned from the surface. The biggest challenge of this technique is the collection of weak backscattered light to ensure adequate detection of SNR. The commonly used optical structure for backscatter-TDLAS can be generally divided into two categories. The first approach uses a large-diameter Fresnel lens [45], as shown in Fig. 13.6a. The simple structure is conducive to integrating a compact, lightweight and low-cost handheld system for short-path standoff detection. A 5 cm diameter receiver is adequate to collect sufficient scattered light for ~10 m distance standoff detection [45]. The second approach, which utilizes a large-aperture telescope [46], as shown in Fig. 13.6b, can be used for long-range standoff detection. On the other hand, the overall performance of the instrument greatly depends on the optical properties of the backscattering target. Most recently, backscattering properties and hemispherical reflectance of some



**Fig. 13.6** Typical transceiver units of the TDLAS system with the non-cooperative target (a) with a single Fresnel lens and (b) with a large-aperture telescope. (Reprinted from Ref. [42]. Published 2020 by MDPI as open access)

common topographic targets have been measured in the visible, NIR and MIR spectral ranges [47], which is useful for optimizing active standoff TDLAS detection and DIAL with hard-target, as well as for increasing their overall efficiency.

The typical application of backscatter-TDLAS is to detect hazardous chemicals leakage in the field of pipelines, for example,  $\text{CH}_4$ ,  $\text{H}_2\text{S}$ , etc. The characteristic absorption of  $\text{CH}_4$  at  $1.65 \mu\text{m}$  band is a superior choice for commercial sensors, because of the rugged and easy-to-align fibre-coupled DFB laser diode, the low-cost optical components commercially available in optical communication and the field-tested durability. A handheld remote methane leak detector employs a 10 mW scale laser and is capable of detecting a few ppm-m methane at about 30 m range [48]. By inserting an erbium-doped fibre amplifier that boosts the laser output power  $\sim 500\times$  to the 5 W scale, and increasing the telescope diameter, they have extended the standoff distance to 3000 m (increased the standoff range by approximately two orders of magnitude) [49]. Then, they provided relatively low-cost lightweight and battery-powered aerial leak sensors. A miniaturized ultra-lightweight TDLAS sensor flies aboard a small quad-rotor uncrewed aerial vehicle (UAV) for landfill methane monitoring less than 1 W of electrical power [49]. Additionally, they presented measured range limits from a variety of common tomographic targets (as many as 22 different surfaces). The latest progress is that a miniaturized, downward-facing remote methane leak detector mounted on a small UAV has been developed to investigate natural gas fugitive leaks and further to localize the leakage, as well as quantify the emission rate. Recently, benefit from the broad tuning range and high power, DFB QCL has become a reliable MIR light source for a variety of trace gas sensing applications either in pulsed or continuous mode. DFB QCLs can work at room temperature with a high output optical power, are relatively compact and can address mid- to long-wave infrared spectral range applications where many trace gases exhibit significant absorption features. Consequently, DFB QCLs have been successfully used for many standoff detection applications with sub-ppm levels, for example,  $\text{CH}_4$ ,  $\text{N}_2\text{O}$ ,  $\text{CO}$ ,  $\text{CO}_2$ , peroxide-based explosives, etc.

TDLAS standoff detection, based on MIR DFB QCLs with a non-cooperative target, is not only employed to detect chemicals in the gas phase but is also used as a powerful method to identify bulk materials and trace contaminants on surfaces. Most recently, a TDLAS system with three MIR QCLs has been reported for

detection and quantification of explosives in soils at a distance of tens of centimetres. Using multivariate analysis and artificial intelligence techniques, the system is capable of distinguishing between soils contaminated with DNT, TNT or RDX and uncontaminated soils with high accuracy.

The concept, based on TDLAS standoff detection with non-cooperative targets, has also been employed for in situ measurement of combustion diagnosis. A single-ended laser-absorption-spectroscopy (SE-LAS) sensor has been developed to the anal size of the return scattering light from native surfaces, such as the piston of an automotive engine, which benefits of ease of installation and mitigates the invasive drawbacks [50]. The SE-LAS sensor can collect 10  $\mu\text{W}$  backscatters through a 2-mm-diameter aperture in the case of a 20 mW DFB laser as the light source. Afterwards, the authors demonstrated the feasibility of spatially resolved measurements of gas properties using a SE-LAS sensor in conjunction with two-line thermometry. A 1-D distribution of  $\text{H}_2\text{O}$  mole fraction and temperature with a spatial resolution of 5 mm were obtained. The method can be extended to measurements for other species' distribution and 2-D scanning. SE-LAS MIR sensors based on QCLs have also been developed for simultaneous in situ measurements of  $\text{H}_2\text{O}$ ,  $\text{CO}_2$ , CO and temperature in combustion flows [50]. Most recently, C. S. Goldenstein has designed and demonstrated a compact SE-LAS sensor for measuring temperature and  $\text{H}_2\text{O}$  in high-temperature combustion gases by collecting laser light back-scattered off native surfaces [51]. The SE-LAS sensor achieved an optical collection efficiency and provided a measurement accuracy and precision that is similar to or better than the conventional line-of-sight-based LAS sensor.

In practical remote detection by standoff WMS with a non-cooperative target, the received light energy varies, due to the variation of the scattering surface characteristics, as well as the change of the distance between the sensor and the tomographic surface. Therefore, measures should be taken to eliminate the fluctuation of the light intensity detected, among which the most commonly used effective method is using the first harmonic WMS-1f to normalize the second harmonic WMS-2f, namely WMS-2f/1f technique. Indeed, there are several methods to realize the calibration-free measurement [52]. Ding et al. [53] put forward a scheme called 'Baselineoffset' WMS, which means the zero response of the detector has been offset by a reference cell inserted into the measuring optical path. This scheme inherits the merits of WMS and can achieve high SNR, especially in a low-concentration environment.

This type of standoff detection has great potential in applications of atmospheric environmental monitoring, leak detection and security early warning, benefiting from great robustness and flexibility. The current performance of this technique is summarized in. However, as we can see, the detection distance of TDLAS with non-cooperative target ranges only from a few metres to tens of metres. Although it can be extended by approximately two orders of magnitude via utilizing a fibre-amplified source and increasing the telescope diameter, standoff range improvement needs to be compromised with human eye safety in practical applications. Another research direction is to develop chip-scale low-power integrated-optic gas-phase chemical sensors based on TDLAS, which are beneficial towards robot-assisted gas remote sensing and leak rate quantification and localization with small UAVs.

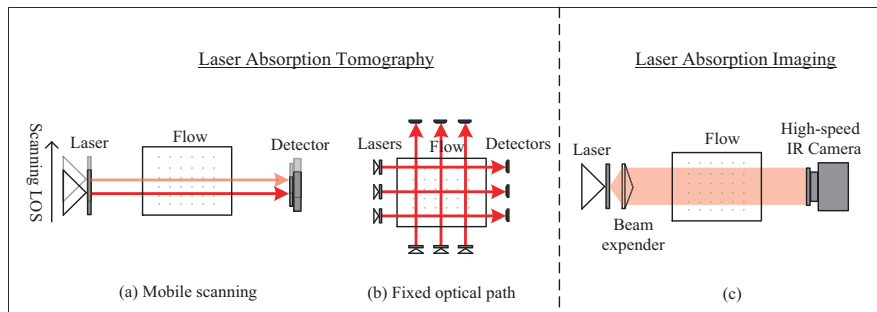
### 13.3.4 Spectroscopic Imaging

Two-dimensional (2D) or even three-dimensional (3D) measurement of gas flow field has attracted more and more attention, since the actual flow field is usually non-uniform distribution. For example, in the combustion flow field, there will be obvious gradients in gas concentration and temperature due to factors such as gas flow, mixing, chemical reaction and heat conduction. The two-dimensional spatial imaging of gas flow field is helpful to analyse the reaction mechanism of combustion, so as to verify the theoretical model and numerical model of the combustion flow field. Moreover, in the application of leakage detection, high spatial resolution imaging of leakage gas is helpful to locate the leakage point accurately. Imaging the gas flow field can make people more intuitive to observe and study the flow field state. Therefore, various laser imaging methods for gas flow fields have been developed in recent years.

By means of the interaction of emission, scattering, refraction and absorption, several non-invasive optical measurement techniques have been used to image the gas flow field. Some representative active laser gas imaging techniques mainly include laser-induced fluorescence (LIF), Rayleigh Scattering, Raman Scattering, LAS, etc. LIF is a promising optical measurement technique to characterize concentration fields with high spatial and temporal resolution; however, the high optical complexity and high cost hinder its practical applications. Rayleigh scattering is a simple way to detect the molecular number density and temperature of the flow field, but it is not selective. Raman scattering provides a detection method for gases with no inherent dipole moment. The system is simple in structure, but the scattering signal is very weak, usually requiring a very high-power light source. LAS employs laser as the light source and measures the flow field information by detecting the change in the intensity of the laser after transmission through the gas flow field. LAS is the most widely used technology for 2D measurement in the actual flow field due to its stability and robustness.

There are mainly two ways for LAS to realize 2D gas flow measurement, that is, laser absorption tomography (LAT) and laser absorption imaging (LAI). LAT technology is a combination of TDLAS and computer tomography (CT) technology. In order to cover the entire gas flow field to be measured, a typical LAT system is by using motion machinery to control a single transceiver to scan and measure from different angles and positions (Fig. 13.7a) or arrange multiple laser transceivers at different angles (Fig. 13.7b). The absorbance of multiple light beams in different directions, that is, the projections, is used to reconstruct the two-dimensional distribution of the gas concentration or temperature field by means of a tomographic algorithm. LAT with mobile scanning method can obtain many projections, but its time resolution is low and cannot meet the needs of combustion diagnosis due to the use of scanning components. Therefore, LAT with a fixed optical path method is more preferable in practical applications. Reasonable beam arrangements and reconstruction algorithms are helpful to improve the quality of reconstructed images, which makes LAT competitive for online and in situ combustion diagnosis.

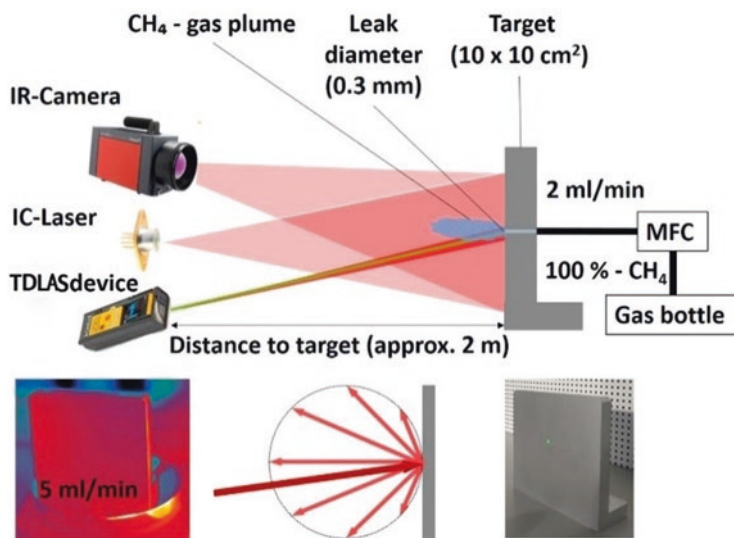




**Fig. 13.7** Comparison of three imaging methods. (a) Moving Line-of-Sight LAS; (b) Multi-projection TDLAT technology; (c) LAI method

LAI technology is developed based on LAT technology, which utilizes high-speed infrared cameras instead of traditional photodetectors to achieve projection acquisition as shown in Fig. 13.7c. The system is relatively simple and has an extremely high spatial resolution. The optical arrangement for the LAI system involves one or more high-speed infrared cameras that image a flow-field backlit with tunable infrared laser radiation. Using MIR LAI technology, Wei et al. [54] characterize the thermochemical structure of a laboratory Bunsen style  $C_2H_6$ -air flame by 2D measuring  $C_2H_6$  (@3.34  $\mu m$ ), CO (@4.97  $\mu m$ ) and  $CO_2$  (@4.19  $\mu m$ ), respectively, in the axisymmetric laminar flame, with an effective spatial resolution for LOS absorbance of  $\sim 50 \mu m$  in the horizontal direction and  $\sim 125 \mu m$  in the vertical direction. Subsequently, the research group used Tikhonov regularized linear tomography method to extend the mid-infrared LAI to 3D measurement of flame temperature and species concentration. Most recently, the team developed a deep learning method for laser absorption tomography to effectively integrate physical prior information related to flow field thermochemistry and transmission. Compared with LAT technology, the advantage of LAI technology is that it increases the spatial resolution to an order of micrometres. This is of great significance to the combustion field with steep gradients. However, limited by the frame rate of the camera, LAI is usually based on DAS technology, which is impeded to further improve the measurement sensitivity with the help of the anti-noise advantage of WMS technology.

In addition, mid-infrared LAI is a powerful tool for a sensitive and quantitative visualization of gas leaks [55]. A standoff methane leak detection system has been developed recently within 2 m by a 3270 nm ICL and an infrared camera, which is demonstrated visualization of methane leakage rates down to 2 ml/min by images and sequences at frame rates up to 125 Hz. The gas plume and leak can be localized and quantified within a single image by DAS with pixel-wise sensitivities around 1 ppm-m. This method improves the efficiency of leakage detection and localization and provides a new solution for safety monitoring of the petroleum industry and other industrial applications (Fig. 13.8).

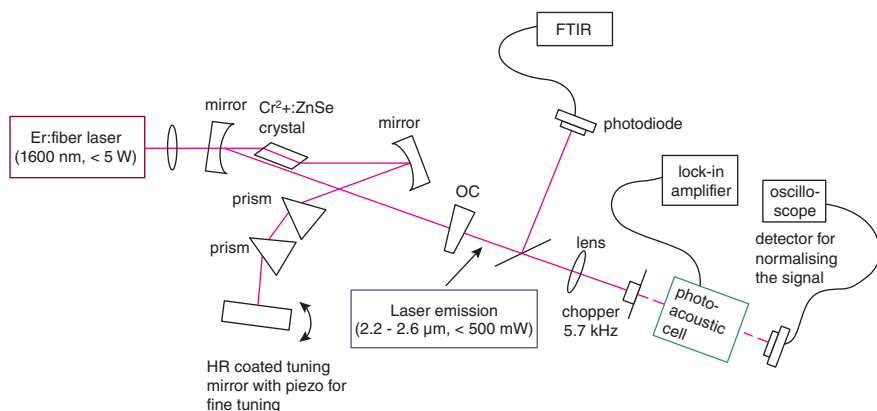


**Fig. 13.8** Diagram of the standoff MIR LAI experiment system built by the Fraunhofer Institute of Physical Measurement Technology in Germany. (Reprinted from Ref. [55]. Published 2021 by the Optical Society as open access)

### 13.4 II–VI Laser Application in Spectroscopic Gas Sensing

II–VI semiconductors, comprising elements of Groups II and VI of the *Periodic Table*, include materials ME (M = Cd, Zn, Hg; E S, Se and Te), such as cadmium selenide (CdSe), cadmium sulphide (CdS), cadmium telluride (CdTe), zinc selenide (ZnSe), zinc sulphide (ZnS) and zinc telluride (ZnTe). II–VI semiconductors feature broad infrared transparency, low phonon frequency and low optical losses. When doped with transition metal ions, these media exhibit a four-level energy structure, the absence of excited state absorption and broad absorption and emission bands. Significant results have been achieved in the development of II–VI semiconductor-based MIR tunable lasers, for example, Cr:ZnSe, Cr:ZnS and Fe:ZnSe. These results include access to a broad spectral range of 1.8–8.4  $\mu\text{m}$  with high quantum efficiency, tunability exceeding thousands of nanometres, output powers exceeding hundred-Watt in continuous-wave operation, multi-Joule output energies in free-running and gain-switched regimes [56, 57].

The II–VI semiconductors-based lasers are still in developing stages and rarely commercialized. Applications with the state of art of lasers are still not very common. Even though, a few pioneer reports show exciting and glorious prospects. Cr:ZnSe lasers are the pioneers in the applications of gas sensing for their broad tuning ranges and high output power in the 2–3.5  $\mu\text{m}$  wavelength region. Fischer et al. [58] presented the first photoacoustic spectroscopic measurements of trace gas using Cr<sup>2+</sup>:ZnSe laser emitting at wavelengths between 2.2 and 2.8  $\mu\text{m}$ . Their experimental setup, shown in Fig. 13.9, consists of an continuous wave (cw)



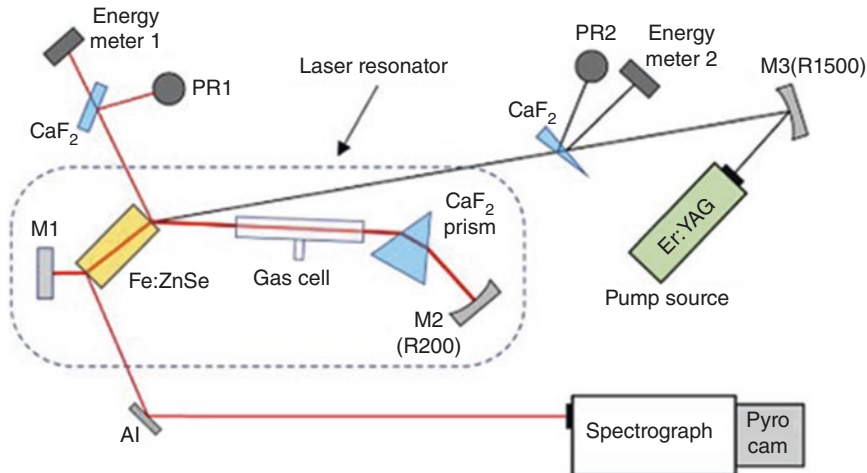
**Fig. 13.9** Experimental set-up consisting of the Er<sup>3+</sup>:fibre laser pumped Cr<sup>2+</sup>:ZnSe laser source, a chopper operated at 5.7 kHz, the PA gas cell and a detector for power normalizing the measured PA signal. OC output coupler, HR high reflectivity mirror. (Reprinted with permission from Ref. [58]. Copyright 2005: Elsevier)

Cr<sup>2+</sup>:ZnSe laser source, a chopper, a PA cell and a detector employed as power reference in order to power-normalize the detected PA signal. An FTIR spectrometer is used to monitor and to coarse-tune the wavelength.

The average output power of the Cr<sup>2+</sup>:ZnSe laser is up to 500 mW across the entire tuning range of 2.2–2.8 μm. The wavelength selection of the laser is provided by a tandem of fused silica prisms. Wavelength tuning is performed by rotating the end mirror. The coarse wavelength tuning was obtained by a micrometre screw, while fine-tuning and spectrum scanning was achieved additionally via a piezo actuator. The gas measurement cell is a single-pass in-house built PA cell equipped with four microphones. The measured data is compared with the calculated data taken from the HITRAN database which results in a conversion coefficient from the measured normalized PA signal. They presented measurements on methane, nitrous oxide, and ambient air and deduced detection limits of 0.2 ppm for carbon dioxide, 0.8 ppm for methane and 2.7 ppm for carbon monoxide.

Fjodorow et al. [59] demonstrated an intracavity absorption spectroscopy (ICLAS) system by using a single-crystal pulsed Fe:ZnSe laser continuously tunable from 3.76 to 5.29 μm at room temperature. The experimental setup consists of a laser resonator formed by two aluminium mirrors M1 and M2, an Fe:ZnSe crystal placed close to M1 under an angle of  $\theta = 51^\circ$  to the normal of M1. A gas cell is installed in the resonator for ICAS measurements in human breath and in gas flows of N<sub>2</sub>O (diluted in N<sub>2</sub>), as shown in Fig. 13.10.

The system was applied for measurements of ① CO<sub>2</sub> isotopes in the atmosphere and in human breath, ② CO in breath (after cigarette smoking) and in the smoke of a smouldering paper and ③ N<sub>2</sub>O in a gas flow. They achieved detection limits: 0.1 ppm for <sup>12</sup>CO<sub>2</sub> and <sup>13</sup>CO<sub>2</sub>, 3 ppm for CO and 1 ppm for N<sub>2</sub>O. The authors believe that the low sensitivity is primarily limited by the short pump-pulse duration of 40 ns. Possibilities for sensitivity enhancement by up to a factor of 10<sup>7</sup> are discussed.



**Fig. 13.10** Intracavity laser absorption spectroscopic sensing system. (Reprinted from Ref. [59]. Published 2021 by the Optical Society as open access)

Compared to conventional spectroscopy techniques, ICLAS offers several key advantages. In contrast to the conventional scheme of light source  $\rightarrow$  sample  $\rightarrow$  detector, with ICAS the sample is placed inside the laser resonator. The successive interaction of laser photons with the broadband gain and the narrow-band absorption determines the laser emission spectrum. The laser light passes through the sample many times, resulting in large effective absorption path lengths of up to  $7 \times 10^7$  m [59]. The most important advantage of ICAS compared to conventional absorption spectroscopy techniques is the ability to compensate broadband losses (e.g. light scattering and absorption by particles or by dirty windows of a technical apparatus, as well as beam steering) by the broadband gain medium. This mechanism makes ICAS unique and ideally suitable for measurements in challenging environments.

Wang et al. [60] reported a single-frequency continuous wave (cw) Cr:ZnSe laser with tuning range of 427 nm from 2164 to 2591 nm potentially competitive for trace gas sensing applications. Bernhardt et al. [61] presented a proof-of-principle experiment of frequency-comb Fourier-transform spectroscopy with two Cr<sup>2+</sup>:ZnSe femtosecond oscillators directly emitting in the 2.4  $\mu$ m mid-infrared region. The acetylene absorption spectrum in the region of the  $\nu_1 + \nu_{51}$  band, extending from 2370 to 2525 nm, could be recorded within a 10  $\mu$ s acquisition time without averaging with 12 GHz resolution. Voronina et al. [62] presented a differential absorption LIDAR for atmospheric constituents and pollutants measurements using a Cr<sup>2+</sup>:ZnSe laser with spectral wavelength tunability range on a line-by-line basis. Frolov et al. [63] developed single-crystal Fe:ZnSe lasers, which could operate in 77 K and room temperature pumped by 40-ns pulses from a Q-switched Er:YAG laser at 2.94  $\mu$ m or a Fe:ZnSe laser at 4.1  $\mu$ m. Furthermore, a record 2300-nm smooth and continuous wavelength tunability over 4.5–6.8  $\mu$ m is achieved. They used the Fe:ZnSe laser for intracavity absorption spectroscopy of atmospheric H<sub>2</sub>O sensing.

### 13.5 Prospects for II–VI Laser in Spectroscopic Gas Sensing

MIR spectral trace gas sensing is particularly attractive for the unique and strong fingerprint absorption of the molecule. A higher sensitivity has been achieved by solving all the challenges of the spectral feature, that is, broad, serried crowded and even overlapped, in the MIR region. Benefiting from the progress of high-power and broad tuning of MIR lasers and also the spectroscopic technologies of multi-component simultaneous detection is an expected achievement.

The development of high-performance MIR lasers in the aspects of compact, output power of hundreds of milliwatts, low emission linewidth of  $\sim 100$  kHz and broad tuning range will promote the development and application of MIR tunable laser-based trace gas sensors, especially in multiple gas sensing, large molecules or organic molecules and remote sensing applications. Though more than one hundred types of gas have been detected by tunable laser-based sensors, there are huge demands for higher detection sensitivity, or in extreme conditions, or scientific exploration, or more other types of gas need to be detected. Thus, we believe greater progress will be performed in the next decade, which may include the following:

1. *Multicomponent and VOCs Sensing System.* Multicomponent sensors will achieve a more progress benefiting from the wider wavelength coverage by II–VI semiconductors-based laser, integrated laser arrays, OFC or EC-QCL. More species could be detected simultaneously by a particular devised broadband laser, which could expand their applications in scientific research, including combustion diagnosis, chemical reaction process dynamics, exhaled breath analysis and metabolomics.
2. *Standoff Remote Sensing.* The techniques of open-path standoff detection by backscatter MIR light provide a promising way for prompt and flexible assessment of atmospheric environmental, leaks, explosive and security by handheld devices or equipped with UAV. The detection sensitivity could be substantially improved by newly developed high-performance MIR detectors and the progress of high-power DFB-QCL.
3. *Ultra-sensitive Sensing.* With the development of a mid-infrared laser source and high-performance detector, combined with cavity enhancement technology and noise immunity technology, ultra-high detection sensitivity becomes possible.

### References

1. Jane H, Ralph PT. Optical gas sensing: a review. Meas Sci Technol. 2013;24:012004. <https://doi.org/10.1088/0957-0233/24/1/012004>.
2. Du ZH, Zhang S, Li JY, Gao N, Tong KB. Mid-infrared tunable laser-based broadband fingerprint absorption spectroscopy for trace gas sensing: a review. Appl Sci. 2019;9:338. <https://doi.org/10.3390/app9020338>.
3. Haas J, Mizaikoff B. Advances in mid-infrared spectroscopy for chemical analysis. Ann Rev Anal Chem. 2016;9:45–68. <https://doi.org/10.1146/annurev-anchem-071015-041507>.

4. Liu L, Xiong B, Yan Y, Li JY, Du ZH. Hollow waveguide-enhanced mid-infrared sensor for real-time exhaled methane detection. *IEEE Photon Technol Lett*. 2016;28:1613–6. <https://doi.org/10.1109/pt.2016.2559528>.
5. Bauer C, Sharma AK, Willer U, Burgmeier J, Braunschweig B, Schade W, et al. Potentials and limits of mid-infrared laser spectroscopy for the detection of explosives. *Appl Phys B-Lasers Opt*. 2008;92:327–33. <https://doi.org/10.1007/s00340-008-3134-z>.
6. Bolshov MA, Kuritsyn YA, Romanovskii YV. Tunable diode laser spectroscopy as a technique for combustion diagnostics. *Spectroc Acta Pt B-Atom Spectr*. 2015;106:45–66. <https://doi.org/10.1016/j.sab.2015.01.010>.
7. Noxon J. Nitrogen dioxide in the stratosphere and troposphere measured by ground based absorption spectroscopy. *Science*. 1975;189:547.
8. Sigrist MW. Air monitoring by spectroscopic techniques. New York: Wiley; 1994. p. 335–8.
9. Wu D, Razeghi M, Lu QY, McClintock R, Slivken S, Zhou W. Recent progress of quantum cascade laser research from 3 to 12  $\mu\text{m}$  at the Center for Quantum Devices. *Appl Opt*. 2017;56:H30–44. <https://doi.org/10.1364/AO.56.000H30>.
10. Vurgaftman I, Weih R, Kamp M, Meyer JR, Canedy CL, Kim CS, et al. Interband cascade lasers. *J Phys D-Appl Phys*. 2015;48:123001. <https://doi.org/10.1088/0022-3727/48/12/123001>.
11. Xu F, Pan QK, Fei C, Zhang K, Yu DY, He Y, et al. Development progress of  $\text{Fe}^{2+}$ :ZnSe lasers. *Chin Opt*. 2021;14(3):458–69. <https://doi.org/10.37188/CO.2020-0180>.
12. O'Keefe A, Deacon DAG. Cavity ring-down optical spectrometer for absorption measurements using pulsed laser sources. *Rev Sci Instrum*. 1988;59:2544–51. <https://doi.org/10.1063/1.1139895>.
13. Foltynowicz A, Schmidt FM, Ma W, Axner O. Noise-immune cavity-enhanced optical heterodyne molecular spectroscopy: current status and future potential. *Appl Phys B Lasers Opt*. 2008;92:313. <https://doi.org/10.1007/s00340-008-3126-z>.
14. Du ZH, Li JY, Cao XH, Gao H, Ma YW. High-sensitive carbon disulfide sensor using wavelength modulation spectroscopy in the mid-infrared fingerprint region. *Sens Actuator B-Chem*. 2017;247:384–91. <https://doi.org/10.1016/j.snb.2017.03.040>.
15. Xiong B, Du ZH, Li JY. Modulation index optimization for optical fringe suppression in wavelength modulation spectroscopy. *Rev Sci Instrum*. 2015;86:113104. <https://doi.org/10.1063/1.4935920>.
16. Du ZH, Luo G, An Y, Li JY. Dynamic spectral characteristics measurement of DFB interband cascade laser under injection current tuning. *Appl Phys Lett*. 2016;109:011903. <https://doi.org/10.1063/1.4955411>.
17. Robert C. Simple, stable, and compact multiple-reflection optical cell for very long optical paths. *Appl Opt*. 2007;46(22):5408–18.
18. Toptica 2009 Product specification. Compact Herriott cell for absorption spectroscopy: CMP-30 Toptica Photonics AG, Munchen, Germany. [www.toptica.com](http://www.toptica.com).
19. Mcmanus JB, Kebabian PL, Zahniser MS. Astigmatic mirror multipass absorption cells for long-path-length spectroscopy. *Appl Opt*. 1995;34(18):3336–48.
20. White JU. Long optical paths of large aperture. *J Opt Soc Am B* (1917–1983). 1942;32(5):285.
21. Grassi L, Guzzi R. Theoretical and practical consideration of the construction of a zero-geometric-loss multiple-pass cell based on the use of monolithic multiple-face retroreflectors. *Appl Opt*. 2001;40(33):6062.
22. Steyert DW, Sirota JM, Mickelson ME, Reuter DC. Two new long-pass cells for infrared and visible spectroscopy. *Rev Sci Instrum*. 2001;72(12):4337–43.
23. Guo Y, Sun L. Compact optical multipass matrix system design based on slicer mirrors. *Appl Opt*. 2018;57:1174–81.
24. Shen C, Zhang Y, Ni J. Compact cylindrical multipass cell for laser absorption spectroscopy. *Chin Opt Lett*. 2013;11:091201.
25. Kühnreich B, Höh M, Wagner S, Ebert V. Direct single-mode fibre-coupled miniature White cell for laser absorption spectroscopy. *Rev Sci Instrum*. 2016;87:023111.

26. Mangold M, Tuzson B, Hundt M, Jágerská J, Looser H, Emmenegger L. Circular paraboloid reflection cell for laser spectroscopic trace gas analysis. *J Opt Soc Am.* 2016;33(5):913.
27. Manninen A, Tuzson B, Looser H, Bonetti Y, Emmenegger L. Versatile multipass cell for laser spectroscopic trace gas analysis. *Appl Phys B Lasers Opt.* 2012;109(3):461–6.
28. Chang H, Feng S, Qiu X, Meng H, Guo G, He X, et al. Implementation of the toroidal absorption cell with multi-layer patterns by a single ring surface. *Opt Lett.* 2020;45(21):5897–900.
29. Qu D, Gmachl C. Quasichotic optical multipass cell. *Phy Rev A.* 2008;78(3):4061.
30. Li JY, Du ZH, Wang RX, Yang X, Song LM, Guo QH. Applications of hollow waveguide in spectroscopic gas sensing. *Spectrosc Spectr Anal.* 2017;37(7):2259–66.
31. Jaworski P. A review of antiresonant hollow-core fiber-assisted spectroscopy of gases. *Sensors.* 2021;21(16):5640.
32. Li JY, Luo G, Du ZH, Ma YW. Hollow waveguide enhanced dimethyl sulfide sensor based on a 3.3  $\mu\text{m}$  interband cascade laser. *Sens Actuator B-Chem.* 2018;255:3550–7.
33. Li JY, Du ZH, Zhang ZY, Song LM, Guo QH. Hollow waveguide-enhanced mid-infrared sensor for fast and sensitive ethylene detection. *Sens Rev.* 2017;37:82–7.
34. Xiong B, Du ZH, Liu L, Zhang ZY, Li JY, Cai QL. Hollow-waveguide-based carbon dioxide sensor for capnography. *Chin Opt Lett.* 2015;13(11):111201.
35. Liu L, Du ZH, Li JY. Calibration of effective optical path length for hollow-waveguide based gas cell using absorption spectroscopy. In: *Proc. SPIE 10157, Infrared Technology and Applications, and Robot Sensing and Advanced Control, 101572K*; 2016. <https://doi.org/10.1117/12.2246928>.
36. Li JY, Yang S, Du ZH, Wang RX, Yuan LM, Wang HY, et al. Quantitative analysis of ammonia adsorption in Ag/AgI-coated hollow waveguide by mid-infrared laser absorption spectroscopy. *Opt Lasers Eng.* 2019;121:80–6.
37. Du ZH, Wang RX, Li JY. Preliminary investigation of the capillary adsorption for a hollow waveguide-based laser ammonia analyzer. In: *Proc. SPIE 10157, Infrared Technology and Applications, and Robot Sensing and Advanced Control, 101572T*; 2016. <https://doi.org/10.1117/12.2247057>.
38. Du ZH, Wang SK, Li JY, Meng S, Wang JH. Towards high-precision hollow waveguide-based gas sensors adapting nonuniform pressure and immune to flow fluctuation. *Sens Actuator B-Chem.* 2020;308:127703.
39. Zhang L, Pang T, Zhang Z, Sun P, Xia H, Wu B, et al. A novel compact intrinsic safety full range Methane microprobe sensor using “trans-world” processing method based on near-infrared spectroscopy. *Sens Actuator B-Chem.* 2021;334:129680. [10.1016/j.snb.2021.129680](https://doi.org/10.1016/j.snb.2021.129680)
40. Chen J, Du ZH, Sun T, Li JY, Ma YW. Self-corrected frequency modulation spectroscopy immune to phase random and light intensity fluctuation. *Opt Express.* 2019;27:30700–9. <https://doi.org/10.1364/oe.27.030700>.
41. Wang F, Jia S, Wang Y, Tang ZAS. Recent developments in modulation spectroscopy for methane detection based on tunable diode laser. *Appl Sci.* 2019;9:2816. <https://doi.org/10.3390/app9142816>.
42. Li JY, Yu ZW, Du ZH, Ji Y, Liu C. Standoff chemical detection using laser absorption spectroscopy: a review. *Remote Sens.* 2020;12(17):2771.
43. Deutsch ER, Kotidis P, Zhu N, Goyal AK, Ye J, Mazurenko A, et al. Active and passive infrared spectroscopy for the detection of environmental threats. In: *Proceedings of the Advanced Environmental, Chemical, and Biological Sensing Technologies XI*. Baltimore, MD; 2014. p. 91060A.
44. Wysocki G, Weidmann D. Molecular dispersion spectroscopy for chemical sensing using chirped mid-infrared quantum cascade laser. *Opt Express.* 2010;18:26123–40. <https://doi.org/10.1364/oe.18.026123>.
45. Wainner RT, Green BD, Allen MG, White MA, Stafford-Evans J, Naper R. Handheld, battery-powered near-IR TDL sensor for stand-off detection of gas and vapor plumes. *Appl Phys B Lasers Opt.* 2002;75:249–54. <https://doi.org/10.1007/s00340-002-0984-7>.

46. Wang T, Zhou T, Jia X. Remote sensing with laser spectrum radar. In: Proceedings of the Hyperspectral Remote Sensing Applications and Environmental Monitoring and Safety Testing Technology. Beijing; 2016. p. 101560C.
47. Basistyy R, Genoud A, Thomas B. Backscattering properties of topographic targets in the visible, shortwave infrared, and mid-infrared spectral ranges for hard-target lidars. *Appl Opt*. 2018;57:6990–7. <https://doi.org/10.1364/AO.57.006990>.
48. Frish MB, Wainner RT, Laderer MC, Green BD, Allen MG. Standoff and miniature chemical vapor detectors based on tunable diode laser absorption spectroscopy. *IEEE Sensors J*. 2010;10:639–46. <https://doi.org/10.1109/Jsen.2009.2038536>.
49. Frish MB, Wainner RT, Laderer MC, Allen MG, Rutherford J, Wehnert P, et al. Low-cost light-weight airborne laser-based sensors for pipeline leak detection and reporting. In: Proceedings of the Next-Generation Spectroscopic Technologies VI. Baltimore, MD; 2013. p. 87260C.
50. Wang Z, Sanders ST. Toward single-ended absorption spectroscopy probes based on backscattering from rough surfaces: H<sub>2</sub>O vapor measurements near 1350 nm. *Appl Phys B Lasers Opt*. 2015;121:187–92. <https://doi.org/10.1007/s00340-015-6216-8>.
51. Zhou Y, Mathews GC, Goldenstein CS. Compact, fiber-coupled, single-ended laser-absorption- spectroscopy sensors for high-temperature environments. *Appl Opt*. 2018;57:7117–26. <https://doi.org/10.1364/AO.57.007117>.
52. Wang ZH, Fu PF, Chao X. Laser absorption sensing systems: challenges, modeling, and design optimization. *Appl Sci*. 2019;9:2723. <https://doi.org/10.3390/app9132723>.
53. Ding W, Sun L, Yi L, Zhang E. ‘Baseline-offset’ scheme for a methane remote sensor based on wavelength modulation spectroscopy. *Meas Sci Technol*. 2016;27:085202. <https://doi.org/10.1088/0957-0233/27/8/085202>.
54. Wei CY, Pineda DI, Goldenstein CS, Spearrin RM. Tomographic laser absorption imaging of combustion species and temperature in the mid-wave infrared. *Opt Express*. 2018;26(16):20944–51.
55. Strahl T, Herbst J, Lambrecht A, Maier E, Steinebrunner J, Wöllenstein J. Methane leak detection by tunable laser spectroscopy and mid-infrared imaging. *Appl Opt*. 2021;60(15):C68–75.
56. Moskalev I, Mirov S, Mirov M, Vasilyev S, Smolski V, Zakrevskiy A, et al. 140 W Cr:ZnSe laser system. *Opt Express*. 2016;24:21090–104.
57. Mirov SB, Moskalev IS, Vasilyev S, Smolski V, Fedorov VV, Martyshkin D, et al. Frontiers of mid-IR lasers based on transition metal doped chalcogenides. *IEEE J Sel Top Quantum Electron*. 2018;24(5):1–29. <https://doi.org/10.1109/JSTQE.2018.2808284>.
58. Fischer C, Sorokin E, Sorokina IT, Sigris MW. Photoacoustic monitoring of gases using a novel laser source tunable around 2.5  $\mu\text{m}$ . *Opt Laser Eng*. 2005;43:573–82. <https://doi.org/10.1016/j.optlaseng.2004.03.015>.
59. Fjodorow P, Frolov MP, Korostelin YV, Kozlovsky VI, Schulz C, Leonov SO, et al. Room-temperature Fe:ZnSe laser tunable in the spectral range of 3.7–5.3  $\mu\text{m}$  applied for intracavity absorption spectroscopy of CO<sub>2</sub> isotopes, CO and N<sub>2</sub>O. *Opt Express*. 2021;29:12033–48.
60. Wang Z, Wei Y, Li Y, Zhang TC, Wang Y, Zhao W, et al. Trace gas sensing based on min-IR CW broadly tunable Cr:ZnSe laser, ICOCN 2017. In: Proceeding of the 16th International Conference on Optical Communications and Networks, 2017, January, 1–3; 2017. <https://doi.org/10.1109/ICOCN.2017.8121276>
61. Bernhardt B, Sorokin E, Jacquet P, Thon R, Becker T, Sorokina IT, et al. Mid-infrared dual-comb spectroscopy with 2.4  $\mu\text{m}$  Cr<sup>2+</sup>: ZnSe femtosecond lasers. *Appl Phy B*. 2010;100(1):3–8.
62. Voronina YV, Ponomarev YN, Balabanov SS. Cr<sup>2+</sup>:ZnSe laser for mid-IR remote sensing of atmospheric gases. In: Proc. SPIE 9680, 21st International Symposium Atmospheric and Ocean Optics: Atmospheric Physics, 96803F; 2015.
63. Frolov MP, Korostelin FY, Kozlovsky VI, Leonov SO, Fjodorow P, Skasyrsky YK. Recent progress in single-crystal Fe:CdTe lasers. In: Proc. SPIE 11777, High Power Lasers and Applications, 117770H; 2021.



# Chapter 14

## Luminescence and Fluorescence Ion Sensing



Faheem Amin, Yasir Iqbal, and Ghenadii Korotcenkov

### 14.1 Introduction

Environmental pollution with heavy metals such as  $\text{Hg}^{2+}$ ,  $\text{Pb}^{2+}$ ,  $\text{Cr}^{2+}$ ,  $\text{Cu}^{2+}$  and  $\text{Zn}^{2+}$  is a serious problem worldwide due to their toxicity, non-degradability and long-term accumulation in the environment [2, 10, 124]. This may be partly due to human activities such as mining, metallurgy, chemical, leather and medical industries, batteries and energy storage devices, agriculture or natural phenomena such as soil erosion and volcanic eruptions [72]. Heavy metal ions in water pose a threat to general health, causing memory loss, anaemia and other neurological problems [49]. The metals mentioned earlier, as well as arsenic, cadmium and nickel, are used on a large scale and are classified by the International Agency for Research on Cancer as group 1 carcinogens. They can alter cell organelles and damage DNA. Exposure to these metals has been reported to disrupt the expression of tumour-suppressor genes, provoking the development of cancers [8]. Thus, repeated long-term interaction with some heavy metals or their compounds can damage nucleic acids, cause mutation and mimic hormones, thereby disrupting the endocrine and reproductive systems and ultimately leading to cancer [50]. In the human body, they can also enter tissues and cells, where they bind to macromolecules such as proteins and amino acids and alter their cellular functions. They can also affect the functioning of the central nervous system, leading to psychiatric disorders, damaging blood components and can even damage the lungs, liver, kidneys and other vital organs, causing a range of disorders [6]. In addition, their long-term

---

F. Amin (✉) · Y. Iqbal

Department of Physics, School of Natural Sciences, National University of Sciences and Technology, Islamabad, Pakistan

e-mail: [faheemamin@sns.nust.edu.pk](mailto:faheemamin@sns.nust.edu.pk)

G. Korotcenkov

Department of Physics and Engineering, Moldova State University, Chisinau, Moldova

**Table 14.1** Heavy metals and their source and health effect

Major items	As	Pb	Hg	Cd
Main sources	Metal smelters, fungicides and pesticides	Burning of coal, paint, automobile emission, pesticides, mining and smoking	Batteries, pesticides, paper and the dental industry	Electroplating, smoking, welding, fertilizer, pesticides
Health effect	Dermatitis, bronchitis and cardiovascular disorders	Liver and renal failure, development delay, mental retardation, fatal neonatal encephalopathy, acute and chronic damage to nervous system	Gingivitis, tremors, protoplasm poisoning, spontaneous abortion and nervous system disorder	Pneumonitis and lung cancer, renal dysfunction, bone defects, bone marrow and kidney damage

Source: Reprinted from Maghsoudi et al. [71]. Published by Dove Press as open access

accumulation in the body can lead to a slowdown in physical, muscle and neurological regenerative processes that can trigger diseases such as Parkinson's disease and Alzheimer's disease. The main sources of heavy metals and diseases caused by some heavy metals are shown in Table 14.1.

Thus, determining the concentration of heavy metals in surface, ground and drinking waters, as well as in the human body, is very important for maintaining the health of people using these water resources. Maximum levels of heavy metal ions in the environment have been recommended by several environmental agencies, including the World Health Organization (WHO), the US Environmental Protection Agency (EPA) and the European Health Agency (EMA) [103, 121–123]. In general, most of these allowable limits are in the ppt to ppm range [57]. This means that to monitor the content of metal ions in water, sensors are required that have a sensitivity that makes it possible to organize such control. Given the level of environmental pollution, the development of fast, inexpensive and sensitive sensors for the detection of heavy metals for the early detection of pollution in living systems and the environment becomes highly desirable.

From a simplified point of view, a sensor is a device that, when interacting with an analyte, generates a measurable signal, the magnitude of which is proportional to the concentration of this analyte. Depending on the mechanism of interaction of the analyte with the sensor, the resulting signal can be measured using optical, electrical, thermal, chemical, gravimetric or magnetic methods. In this review, we considered only optical sensors, since the luminescent properties of II–VI compounds can be used with maximum efficiency precisely in the development of such sensors.

In addition, quantum dots will be considered as the main material for these sensors. Due to their unique optical properties, semiconductor QDs are widely used in various applications, including biological labelling, water purification, solar cells and optoelectronic and photovoltaic devices [119]. Starting with the pioneering work of Clark et al. [24], it was shown that quantum dots are also of great interest for the development of optical sensors. Due to the small size, high surface activity

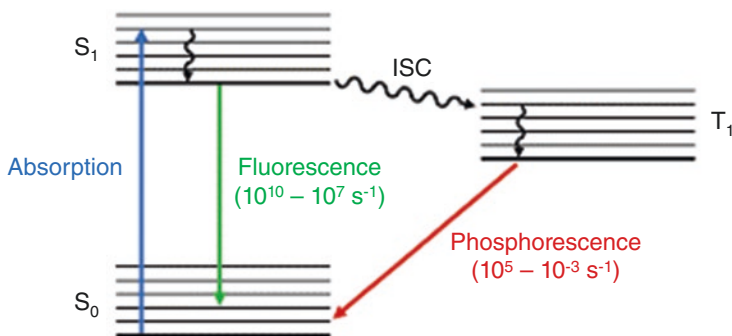
and large surface-to-volume ratio, even weak interaction of the analyte with the QD surface leads to significant changes in the QD fluorescence. For example, numerous scientific groups have observed that the photoluminescence (PL) of QDs can change significantly in the presence of ions, making QDs themselves ion sensors, often with specific properties [20, 93, 126, 134]. For example, Chen and Rosenzweig [20] observed that the photoluminescence of CdS quantum dots is quenched in the presence of  $\text{Cu}^{2+}$  but does not respond to other cations such as  $\text{Na}^+$ ,  $\text{Ca}^{2+}$  and  $\text{Mg}^{2+}$ . This is a typical effect of metal ions on the photoluminescence intensity. However, the appearance of metal ions in solution can also cause both an increase in the PL intensity and a shift in the position of the PL peak. In particular, Lai et al. [60] observed simultaneous fluorescence enhancement and redshift of the PL peak of bismuthiol II modified CdS quantum dots when detecting silver ions from 0.01 to 5.0  $\mu\text{mol}\cdot\text{L}^{-1}$ . Another advantage of quantum dots is the ability to tune the absorption and emission spectra by adjusting the size and band gap of quantum dots. This makes it possible to excite several coloured quantum dots with a single excitation source, thereby reducing the cost of complex optical systems being developed for the detection of metal ions.

## 14.2 Optical QDs-Based Ion Sensors

Optical sensors offer numerous attractive features due to their ease of integration into microfluidic platforms and the ability to monitor hazardous environments. Among optical sensors, fluorescent and phosphorescence sensors have gained popularity in recent years because they provide high specificity, as well as low limits of detection, fast response time, low cost and technical simplicity. As a result, in recent years, fluorescence spectroscopy has become a powerful tool for detecting transition and heavy metal ions [42, 77].

Fluorescence spectroscopy is a sensitive technique in which sample molecules are first excited by a light source. Those molecules are excited and then relaxed by radiative emission, a phenomenon known as luminescence. Fluorescence or luminescence is absorption of energy by atoms or molecules followed by instant emission of light or electromagnetic radiation (Fig. 14.1). In fluorescence, the excited atom has comparatively short time prior to its return to lower energy states. In the fluorescence process, the time interval between absorption and emission is very short. The fluorescence emission takes place from a singlet excited state in  $10^{-10}$  to  $10^{-7}$  s.

Phosphorescence, on the other hand, is a type of luminescence in which energy of light absorbed by a substance is released relatively slow in the form of light as compared to fluorescence. This is caused by intermediate metastable states causing delayed emission of electromagnetic radiation. The emitted photon has lower energy than the absorbed photon and emission occurs at a longer wavelength than fluorescence. The phosphorescence emission takes place from a triplet excited state in an average time  $10^{-5}$  to  $10^3$  s. Nevertheless, both fluorescence and phosphorescence



**Fig. 14.1** Schematic illustration of fluorescence and phosphorescence

occur when molecule or atom-bounded electrons absorb photon or light energy which makes them to excite and transit to a higher energy state. An excited electron then relaxes and loses energy. This results in return to the ground state and the emission of photon takes place known as photoluminescence.

There is currently a large group of organic phosphors and fluorophores, or organic dyes, that can be used to develop ion sensors. Organic dyes are molecules that absorb light at one wavelength and emit light at a different wavelength. Fluorescent dyes have a narrow excitation spectrum and fast decay. However, they are characterized by a low quantum yield. In addition, the use of organic dyes is severely limited by the poor optical stability of the reporter molecules and their dependence on the local environment. It was found that inorganic optical materials such as semiconductor quantum dots (QDs) can solve these problems.

The experiment showed that QDs, especially II–VI QDs, have such advantageous characteristics as narrow emission bands, high brightness and increased photostability compared to organic fluorophores. QDs also have high stability in the aqueous phase. Colloidally stable QDs can be obtained in two ways: (1) by directly obtaining QDs in an aqueous phase or (2) by transferring already synthesized QDs from organic solvents to an aqueous phase. These technologies are discussed in detail in Chaps. 12 and 13 (Volume 1). However, despite the progress in the development of technologies for the synthesis of colloidal QDs, the problems of increasing the quantum yield remain. QDs can have defect states that cause non-radiative decay of an exciton electron-hole pair. There is also a problem of biocompatibility, especially QDs based on cadmium compounds. Numerous studies have been devoted to eliminating these problems over the past decade. For example, it was found that highly luminescent and colloidally stable quantum dots can be prepared in coordinating organic solvents. However, such quantum dots are not biocompatible due to the presence of organic ligands on the surface. Therefore, different strategies, including ligand exchange, ligand modification and polymer coating, are adopted to render these molecules water-soluble. Capping reagents can also remove the impurities from the surface of QD and prevent agglomeration [37, 92]. Normally, organic capped QDs are widely used for sensing different water-dissolved metal

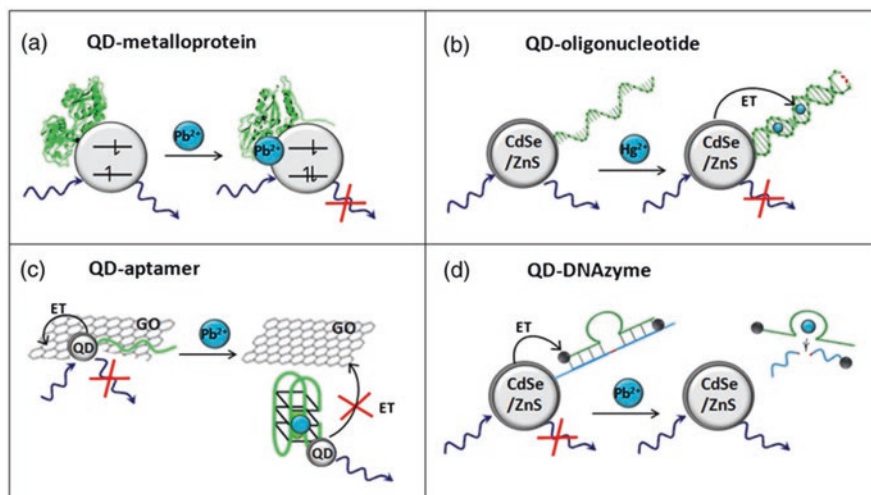
ions and also detoxifying heavy metal ions by binding with them through polymerization [37, 90].

Many papers have been reported on CdSe, CdS and CdSeS/ZnS QDs with various capping organic reagents [4, 86]. But capping reagents have some disadvantages. In many cases, a decrease in the photoluminescence (PL) efficiency of QDs has been observed [89] due to the long chain structure of the capping reagents. Thus, in order to improve the efficiency of CdTe photoluminescence, a small-size blocking reagent such as a carboxyl ( $\geq\text{C} = \text{O}$ ), amino ( $\geq\text{N}-\text{H}$ ) or aldehyde ( $\geq\text{C}-\text{O}-\text{H}$ ) functional group [39], etc., have been tested. It has been found that the presence of a carboxyl (-COOH) group can make CdTe QDs ionized, less toxic [69] and water-soluble. The carboxyl end also promoted a negative charge on the outer layer, which prevents QD aggregation [12], and increased the photoluminescence efficiency.

However, the experiment showed that the most effective approach to solving the above problems, such as toxicity, stability, aggregation, and quantum yield of CdSe QDs, is the formation of core-shell structures, such as CdSe/ZnS (read Chap. 12, Vol. 1). It was established that, due to surface passivation of QDs, it is possible to achieve a significant increase in the quantum yield and reduce the toxicity of cadmium-based compounds.

It is important to note that capping agents can perform other functions in addition to stabilizing the properties of colloidal particles. For example, the use of organic compounds such as thioglycolic acid (TGA) or L-cysteine as capping agents has been found to significantly improve the selectivity of ion sensors [20]. It was found that the same quantum CdS QDs capped with thioglycerol showed specificity towards copper and iron ions, while L-cysteine was found to be sensitive towards zinc ion [20]. In case of thioglycolic acid (TGA) capped CdTe QDs, an electron transfer process occurs between the functional groups of TGA and  $\text{Hg}^{2+}$  ions, which quenches the luminescent intensity of the CdTe QDs [25]. In case of L-cysteine capped CdTe QDs, the interaction of QDs with  $\text{Hg}^{2+}$  ions depends on the concentration of the metal ion: for lower concentrations of  $\text{Hg}^{2+}$ , these ions interact with the carboxylate moiety of the L-cysteine on the surface of CdTe QDs by electrostatic forces while at higher concentrations of  $\text{Hg}^{2+}$ , there is an electron transfer between the  $\text{Hg}^{2+}$  ions and the L-cysteine capped CdTe QDs which induces not only a quenching of the luminescence but also a red shift in the luminescence peak.

The functionalization of quantum dots surface with biomolecules for detecting heavy metal ions is also one of the promising approaches to the development of sensors selective to metal ions. These are the so-called bioinspired quantum dot-based sensors [45]. Many examples of 'bio-inspired' QD-based systems for the analysis of heavy metal ions are emerging during the last decade [106]. Figure 14.2 shows some analytical strategies combining QDs with different functional biomolecules and different interaction mechanisms.

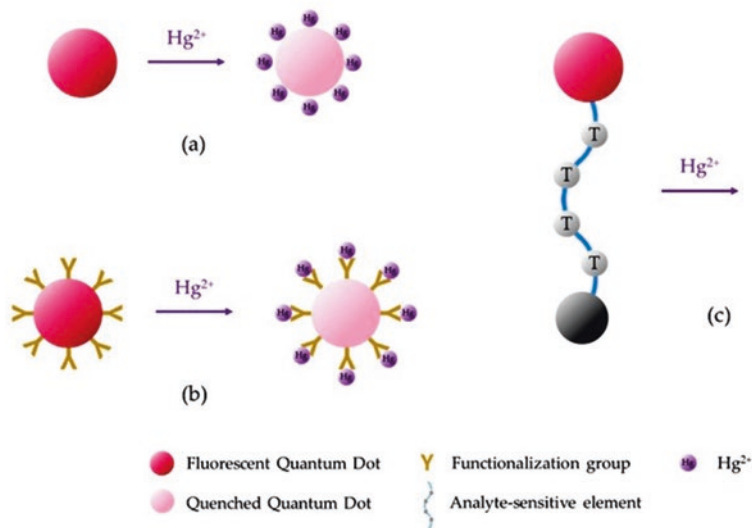


**Fig. 14.2** Scheme of several analytical strategies using QD-biomolecule ensembles for the detection of heavy metal ions: (a) QD-metalloprotein, (b) QD-oligonucleotide, (c) QD-aptamer and (d) QD-DNAzyme. (Reprinted from Vázquez-González and Carrillo-Carrion [106]. Published by SPIE as open access)

### 14.3 Mechanisms of Operation of Ion Sensors Based on QDs

As it was shown before, semiconductor quantum dots are fascinating materials due to their remarkable optical properties which lead to their preferable use as ion sensors. This can be done primarily in three different ways (i) direct interaction between analyte and QDs, (ii) functionalization of QDs with molecules and (iii) integration of QDs with other sensing materials. These approaches are described in Fig. 14.3.

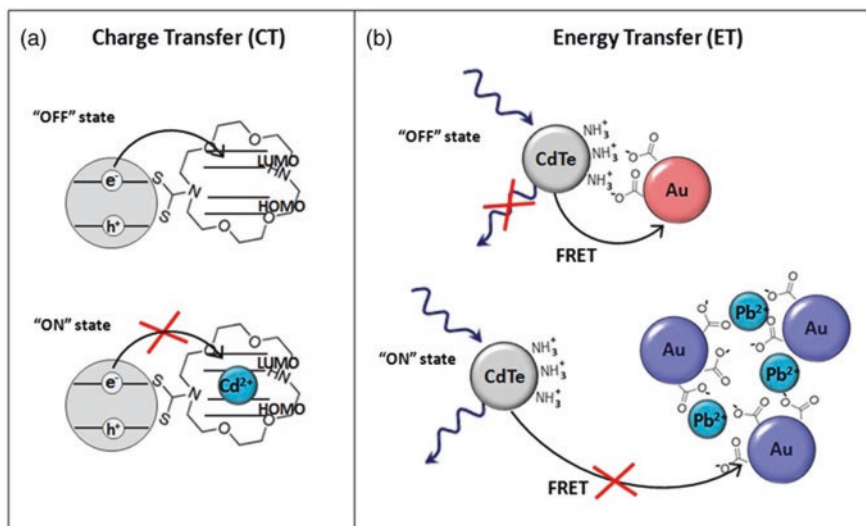
The lowering/raising of the PL peak is associated with the surface defect states, the concentration of which increases or decreases during the interaction of the analyte with the surface of the QDs. For example, in Luo et al. [70] an increase in photoluminescence was observed and in [75] a decrease in PL intensity was observed during the interaction of QDs with metal ions. It has been found that emission is enhanced by ions that passivate surface defects [70]. As regards PL quenching, this effect can have a different nature. For example, Pei et al. [84] believe that the mechanism of fluorescence quenching of cysteamine-coated CdTe QDs during  $Hg^{2+}$  detection can be associated with the following three processes. First, due to the strong affinity of  $Hg^{2+}$  for the N atom [73],  $Hg^{2+}$  is adsorbed on the surface of QDs through functional amide groups in cysteamine, which facilitates electron transfer from QDs to  $Hg^{2+}$ . Second, the solubility of HgTe is approximately 20 times lower than that of CdTe [101], which leads to the substitution of  $Cd^{2+}$  in CdTe QDs by  $Hg^{2+}$  and the formation of doped  $Cd_xHg_{1-x}Te$ . These ultrasmall particles promote non-radiative recombination of excited electrons ( $e^-$ ) in the conduction band and holes ( $h^+$ ) in the valence band [13], thus quenching the recombination luminescence



**Fig. 14.3** Sensing mechanisms based on fluorescent quantum dots: (a) direct interaction between the analyte and the QDs, (b) interaction of the analyte with the functionalized QDs and (c) integration of the QD with another sensory material. (Adapted from Acha et al. [2]. Published by MDPI as open access)

of CdTe nanoparticles. Such a quenching process is similar to the effect of Cu<sup>2+</sup> on CdS QDs, studied by Isarov and Chrysohoos [40]. Thirdly, in accordance with the theory proposed by Pendyala et al. [82], according to which the alignment of bands between the central and surface regions of structures is one of the reasons for the enhancement or quenching of PL, the smaller band gap of HgTe (−0.41 eV) than that of CdTe (1.47 eV) contributes to this quenching mechanism.

To describe the quenching effect of fluorescence, processes such as collisional (dynamic) quenching, complex formation (static) quenching, fluorescence resonance energy (FRET) and photoinduced electron (PET) transfer-based quenching are also used. FRET and PET are two mechanisms that lead to a variation of fluorescence emission by distance-dependent fluorescence quenching between a fluorophore and a quenching moiety. A schematic diagram illustrating the charge and energy transfer mechanisms is shown in Fig. 14.4. FRET is an electrodynamic phenomenon resulting from a non-radiative process in which an excited state donor *D* (usually a fluorophore) transfers energy to a ground state acceptor *A* via long-range dipole–dipole interactions [94]. The acceptor must absorb energy for the wavelength of emission from the donor, but need not itself emit energy fluorescently. The rate of energy transfer depends on a number of factors, including the fluorescence quantum yield of the donor in the absence of an acceptor, the refractive index of the solution and the angular orientation of the dipole of each molecule. PET-quenching can occur transiently through molecular collisions, a process called ‘dynamic quenching’, or in molecular complexes that are stable for multiple excitation-emission [30]. Depending on the oxidation and reduction potentials, an electron can be



**Fig. 14.4** Possible flow transfer processes between a QD (donor) and an acceptor: (a) charge transfer (CT) or photoinduced electron transfer (PET) and (b) energy transfer (FRET). (Reprinted from Vázquez-González and Carrillo-Carrion [106]. Published by SPIE as open access)

transferred from the chromophore, which is a donor  $D$ , to its interaction partner, acceptor  $A$ , or vice versa, which leads to non-radiative dissipation of the energy of the excited state. In a dynamic collision, an excited fluorophore experiences contact with an atom (or molecule) that can facilitate non-radiative relaxation of the excited molecule to the ground state. Such collisional events follow the Stern–Volmer relation which relates the fractional decrease in fluorescence intensity to the concentration of quencher  $[Q]$  through the quenching rate  $K_{SV}$  ( $K_{SV} = k_q\tau_0$ ) as follows:

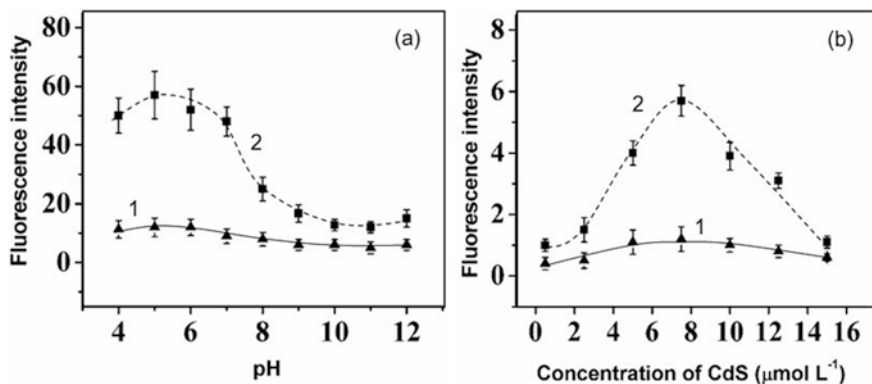
$$F_0 / F = 1 + K_{SV} [Q] \quad (14.1)$$

where  $k_q$  is the molecular quenching rate constant and  $\tau_0$  is the lifetime of fluorophore in the excited state in the absence of a quencher.

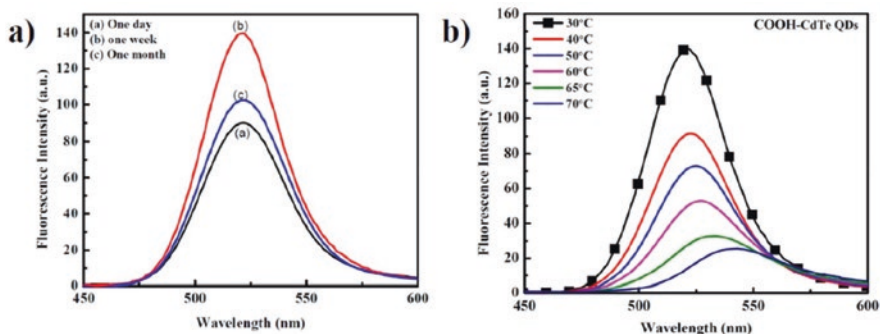
## 14.4 Ratiometric Ion Sensors

One of the most significant limitations of sensors based on fluorescence is the dependence of the emission intensity not only on the concentration of the analyte in the solution but also on such factors as the pH of the solution, the excitation intensity, the temperature and the concentration of the QDs themselves (see Figs. 14.5 and 14.6), which may change as a result of aggregation. Therefore, chemosensors that have only one signal to detect, that is, fluorescence intensity, can be easily perturbed by environmental conditions and instruments [29].





**Fig. 14.5** (a) Effect of pH value and (b) concentration of CdS QDs modified by bismuthiol II on the enhancement of the fluorescence before (1) and after (2) in addition of silver ions. The concentration: CdS QDs,  $7.5 \mu\text{mol}\cdot\text{L}^{-1}$ ; silver ion,  $0.10 \mu\text{mol}\cdot\text{L}^{-1}$ ; the volume of PBS, 2.0 mL; incubation temperature,  $25^\circ\text{C}$ ; incubation time, 25 min. (Reprinted from Lai et al. [60]. Published by Wiley as open access)



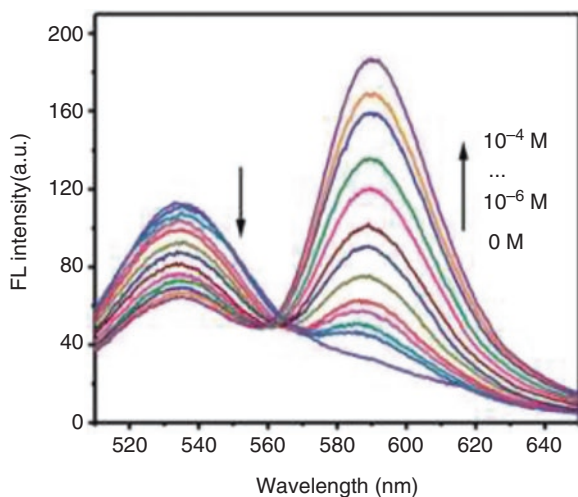
**Fig. 14.6** Effect of (a) time and (b) temperature on the fluorescence intensity of COOH-CdTeQDs in hydroxylic medium. (Reprinted with permission from Pooja and Chowdhury [86]. Copyright 2021: Elsevier)

The experiment showed that these problems can be solved with the help of ratiometric sensing. Unlike single signal sensors, ratiometric sensors containing two different fluorophores emitted at two different wavelengths use the ratio of the two fluorescence intensities to quantitatively detect analytes. The ratiometric sensors can eliminate or reduce the effects of abovementioned factors by the self-calibration of the two emission bands [56, 148]. The external factors, such as excitation source fluctuations and QDs concentration, will not affect the ratio between the two fluorescence intensities [16]. Dual colour sensors can exhibit uncoupled or coupled emission, whereby the second colour acts either as a constant emitter for normalization of the variable emission or exhibits variable emission with inversely proportional changes in emission intensity to the first emitter, respectively [21]. In the

former case, the consistent emission intensity of the secondary colour is used as a control in the system, whereas in the latter case, the secondary colour intensity enhances the effective change in signal in response to the stimulus.

The design of ratiometric sensors can be done by two methods based on (i) PET and (ii) FRET (electron and Fluorescence Resonance Energy Transfer) processes, discussed before. For many PET-based ion sensors, it is difficult to determine the ratio between two relatively broad signal emissions. The advantage of FRET- over PET-based sensors is that the ratio between two fluorescence intensities is independent of these external factors such as fluctuation of excitation source and sensor concentration, that is, the concentration of QDs. FRET-based sensors observe the changes in the intensity ratio of absorption and emission which is favourable in increasing the signal selectivity. A significant advantage of FRET-based sensing is that it simplifies the design of the fluorophore. Recently, FRET-based sensing has become the most effective method for the detection of metal ions in the environment [19, 45, 93, 148].

There are few criteria that must be satisfied in order for FRET to occur. These are [46]: (i) The donor must be a fluorophore and has a reasonably large quantum yield. (ii) The fluorescence emission spectrum of the donor molecule must overlap the absorption or excitation spectrum of the acceptor chromophore (see Fig. 14.7). Figure 14.7 (left) shows the absorption and emission spectra of QDs and dye. The green region shows the overlap between the emission profile of QD and the absorption spectrum of the dye. It is evident that the transfer energy efficiency is directly



**Fig. 14.7** *Left:* Absorption (solid line) and emission spectra (dotted line) of dye ATTO-590 (black) and CdSe/ZnS QDs (red). The overlap (green region) determines the efficiency of energy transfer from donor (QDs) to acceptor (dye) molecule. *Right:* Normalized PL transients of CdSe/ZnS QDs (squares), of the ATTO dye bound to the Au NPs (dots) and of the ATTO dye bound to the CdSe/ZnS QDs (triangles). The decay time has clearly increased for the dye in close proximity to QDs. (Reprinted with permission from Kaiser et al. [51]. Copyright 2014: AIP)

linked to the overlap between the emission and absorption of donor and acceptor, respectively. The degree of overlap is referred to as spectral overlap integral (J). (iii) The two fluorophores (donor and acceptor) must be in close proximity to one another (typically 1–10 nanometres). The FRET can be achieved by anchoring the acceptor molecule on the outer surface of QDs. (iv) The transition dipole orientations of the donor and acceptor must be approximately parallel to each other. (v) The fluorescence lifetime of the donor molecule must be of sufficient duration to allow the FRET to occur. Figure 14.7 (right) shows the time-resolved PL intensity of polymer-coated CdSe/ZnS QDs (black), dye incorporated polymer-coated CdSe/ZnS QDs (blue) and dye-incorporated polymer-coated Au NPs. It is quite clear that the decay dynamics of dye-incorporated polymer-coated QDs are much slower than the comparable system with Au NPs as core material. Therefore, it can be expected that QDs act as an efficient donor to the dye, when the latter is located in close vicinity of QDs. More details on the role of II–VI quantum dots in designing FRET-based sensors can be found in [22, 93].

The decay kinetics of a mixture of QD and dye molecules are given as [76]:

$$\frac{dn_{QD}}{dt} = -\frac{n_{QD}}{\tau_{QD}} + w_c \cdot n_t \quad (14.2)$$

$$\frac{dn_{dye}}{dt} = -\frac{n_{dye}}{\tau_{dye}} + w_{reab} \cdot n_{QD} \quad (14.3)$$

Here,  $n_t$  is the number of feeding (trap states) for QDs.  $w_c$  is the transfer probability to bright QD state while  $w_{reab}$  is the probability that the emitted photon will be captured by the dye molecule. The solution to Eqs. (14.2) and (14.3) are biexponential and three exponential functions, including all the possible transitions from the excited state, respectively. The anchoring of dye molecules in the vicinity of QD can trigger an additional non-radiative decay path known as resonance energy transfer mechanism. The decay kinetics in the presence of this non-radiative path is given by

$$\frac{dn_{QD}}{dt} = -\frac{n_{QD}}{\tau_{QD}^{eff}} + w_c \cdot n_t \quad (14.4)$$

$$\text{where } \frac{1}{\tau_{QD}^{eff}} = -\frac{1}{\tau_{QD}} + w_{FRET} \quad (14.5)$$

The decay rate of different species can be determined by curve fitting of the experimental data. The energy transfer also depends upon the size of QDs. The Förster transfer rate from a donor to  $N$  surrounding acceptors can be determined as

$$w_{FRET} = \frac{1}{\tau_{QD}} \cdot \sum_{i=1}^N \left( \frac{R_0}{r_i} \right)^6 \quad (14.6)$$

$r_i$  is the distance of  $i^{\text{th}}$  acceptor from donor.  $R_0$  is the so-called Förster radius.

Another approach to develop ratiometric ion sensors is to use two QD emitters [22, 113, 114]. An example of this approach is  $\text{Hg}^{2+}$  ion sensors developed on the basis of CdTe/CdS QDs, which simultaneously emit red light (CdTe core) and green light (CdS shell). Due to the fact that only the shell is exposed to the environment [75], the green PL was quenched in the presence of  $\text{Hg}^{2+}$  ions, while the red one was not, which leads to a change in the ratio of red and green luminescence intensities. By measuring the lifetime of green fluorescence, the authors found that the lifetime decreased from 25.5 to 6.5 ns, while the lifetime of red fluorescence remained unchanged. A decrease in the lifetime of green PL indicated that  $\text{Hg}^{2+}$  ions were indeed adsorbed on the surface of the CdS shell, initiating charge transfer [52]. Although quenching of green fluorescence was observed in the presence of other divalent cations, none of them showed such a significant change in PL intensity and colour as  $\text{Hg}^{2+}$ . Dual-emission quantum dot nanohybrid has also been used for selective fluorescence turn-on and ratiometric detection of cadmium ions [114]. The nanohybrid probe was composed of green-emitting CdSe QDs covalently linked onto the surface of silica nanoparticles embedded with red-emitting CdTe QDs. Upon exposure to different amounts of  $\text{Cd}^{2+}$ , the green fluorescence was gradually restored, whereas the inner red fluorescence remained constant.

## 14.5 Implementation of Luminescence and Fluorescence II–VI Semiconductor QDs-Based Ion Sensors

### 14.5.1 Cu Ions Sensing

Copper is an essential nutrient involved in the electron transport chain in plants and animals. It is vital for the functioning of various enzymes such as cytochrome oxidase and superoxide dismutase. It also shows good antibacterial and antimicrobial properties. At the same time, however, copper exposure has been associated with several diseases such as Alzheimer's disease, Parkinson's disease and familial amyotrophic lateral sclerosis. Copper is also thought to cause amyloid precipitation. Therefore, the determination of  $\text{Cu}^{2+}$  ions is very important from an ecological and biological point of view due to their potential toxicological effects on the ecosystem and human health. Several spectroscopic detection methods, including inductively coupled plasma mass spectrometry (ICP-MS), atomic absorption spectroscopy (AAS) and UV-visible spectroscopy, are used to efficiently detect  $\text{Cu}^{2+}$  ions. Easy and reliable detection of  $\text{Cu}^{2+}$  can be performed using spectrophotometric methods using chromogenic reagents such as sodium diethyldithiocarbamate trihydrate, N-ethyl-2-naphthylamine [74], di-2-pyridylketone benzoylhydrazone [85], thiomichler ketone [35] and fluorescent reagents, mainly europiumpyridine polyaminopoly-carboxylate chelate [54] and 5-(3-fluoro-4-chlorophenylazo)-8-aminoquinoline [15] due to their excellent sensitivity.

However, the experiment showed that QD-based fluorescent sensors are also an effective tool for detecting copper ions. A detailed computational study on the possible interaction mechanism of different divalent metal ions with L-cysteine has been reported by Belcastro et al. [9]. Biranje et al. [10] have reviewed the techniques and methodologies to improve QD nanosensor performance by capping the surface with nanoparticles, polymers and biological moieties. Chen et al. [18] reported the role of  $Mn^{2+}$  doping on the sensing efficiency of L-cysteine-capped ZnS QDs for several analytes. The prepared sensors were found to be sensitive towards both Cu(II) and Hg(II) ions. However, since the concentration of copper is quite high in industrial waste solutions so the interference can be ignored. Furthermore, they found that pH can also be tuned to enhance the specificity. Similarly, Qin et al. [87] used silica coated ZnS:Mn QDs to detect  $Cu^{2+}$  ions in seawater. They found that the detection of  $Cu^{2+}$  concentrations in seawater can be achieved over a linear range from  $8.2 \times 10^{-8}$  to  $5.0 \times 10^{-4}$  mol·L<sup>-1</sup>.

Bo and Ping [11] discovered that extremely low concentrations of  $Cu^{2+}$  ions can quench the fluorescence of water-soluble CdTe nanocrystals prepared and modified by using 3-mercaptopropionic acid. The fluorescence of nanocrystal was found to quench as well as redshift significantly in the concentration range of 0–384 ng/mL. They reported an extraordinary limit of detection of 0.19 ng/mL. Cao et al. [14] used polymer-modified CdSe/CdS core-shell QDs for selective detection of  $Cu^{2+}$  ions in water. Sung and Lo [100] immobilized silica-encapsulated CdSe/ZnS QDs via polyvinyl alcohol on the tip of fibre optic for selective and sensitive detection of  $Cu^{2+}$  ions. The fluorescence of CdSe/ZnS@SiO<sub>2</sub> was found to be immensely reduced upon interaction with  $Cu^{2+}$  ions. The sensitivity test was carried out in a concentration range of 0–10 μM with a limit of detection found to be 0.9 μM. Lai et al. [59] worked with chitosan-modified CdS QDs to achieve a LOD of 2.0 nmol·L<sup>-1</sup> in a concentration range of 8.0 nmol·L<sup>-1</sup> to 3.0 μmol·L<sup>-1</sup>. The adopted mechanism showed good selectivity towards  $Cu^{2+}$  ions.

Wang et al. [115] used N-acetyl-L-cysteine capped CdHgSe QDs for selective determination of  $Cu^{2+}$  ions. Their results suggest that incorporation of Hg improves the Limit of Detection by two orders of magnitude as compared to undoped CdSe-rGO nanocomposites [38], citric acid capped CdS QDs [112] or polymer-modified CdSe/CdS core/shell QDs [14, 131]. The selectivity studies were carried out in the presence of interfering ions  $Ag^+$ ,  $Zn^{2+}$ ,  $Co^{2+}$  and  $Ni^{2+}$ . The fluorescence intensity was found to be linearly proportional to the concentration of copper ions in the range of  $1.0 \times 10^{-9}$ – $4.0 \times 10^{-7}$  mol·L<sup>-1</sup>, with a detection limit as low as  $2.0 \times 10^{-10}$  mol·L<sup>-1</sup>. The ‘fluorescence turn-on’ can also be utilized for efficient detection of  $Cu^{2+}$  ions. Ding et al. [27] have used this phenomenon to irreversibly cleave the ds-DNA, which was used as spacer between GO and CdTe nanocrystals.

Table 14.2 summarizes different works carried out for the detection of  $Cu^{2+}$  ions using II–VI QDs. For most sensors, the limit of detection is in the nmol·L<sup>-1</sup> region, with the exception of a few developments.

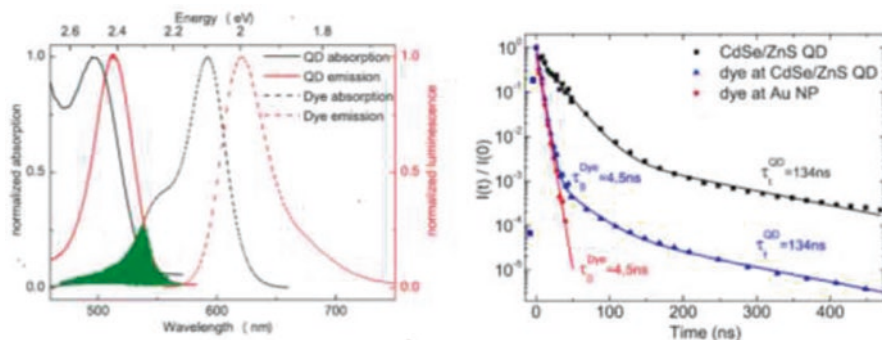
**Table 14.2** Comparison of analytical characteristics of II–VI QDs-based sensors to  $\text{Cu}^{2+}$ 

Materials	Coating/modification	Linear range $\times 10^{-6}(\text{mol}\cdot\text{L}^{-1})$	LOD $\times 10^{-9}(\text{mol}\cdot\text{L}^{-1})$	References
CdHgSe	N-acetyl-L-cysteine	0.001–0.40	0.2	[115]
CdS QDs	Thioglycerol		100	[20]
CdSe/CdS QDs	Diethyldithiocarbamate	0–1.56	4.53	[116]
CdSe QDs	2-Mercaptoethane sulphonic acid	<0.469	3.13	[34]
CdSe-ZnS QDs	Bovine serum albumin	0.01–2	10	[133]
CdTe	Gold nanoclusters	0.001–1250	0.3	[67]
CdTe/CdS QDs	Glyphosate	0.375–437.5	20.3	[65]
CdTe QDs	L-cysteine	0.313–4.69	145.3	[117]
CdSe/ZnS	Silica	0–10	900	[100]
CdSe/CdS QDs	L-cysteine	10–200	3	[141]
CdTe	G-quadruplex	0.008–2	3.0	[137]

### 14.5.2 Hg Ion Detection

Another important water-borne ionic pollutant is mercury due to its severe ecological and health risks. It is carcinogenic and may cause malfunctioning of nervous, urinary and reproductive systems in humans. It is reported that  $\text{Hg}^{2+}$  can easily pass through skin, digestive tract and respiratory tract, leading to DNA damage, mitosis impairment and permanent damage to the central nervous system. The maximum allowed concentration of  $\text{Hg}^{2+}$  in drinking water is 10 nM according to the United States Environment Protection Agency (USEPA). Therefore, many research studies have been carried out over the past few years to develop an ultrasensitive detection system for  $\text{Hg}^{2+}$  ions.

Various detection methods based on fluorescence, electrochemistry, colourimetry, photoelectrochemistry, surface resonance Raman scattering and surface plasmon resonance have been established [66, 78, 110, 149]. Among these fluorescence-based sensing is one of the most popular methods due to its high sensitivity and flexibility. Fan et al. [33] studied the role of hyperbranched graft copolymer-capped CdS in the selective sensing of mercury ions. They reported an excellent LOD of 15 nM. Cai et al. [13] studied the effect of pH on the selective detection of  $\text{Hg}(\text{II})$  ions in solution. They reported a LOD of  $20 \text{ nmol}\cdot\text{L}^{-1}$  for a linear range of  $16\text{--}112 \text{ nmol}\cdot\text{L}^{-1}$ . Zhou et al. [147] have utilized Mn-doped ZnSe QDs to detect  $\text{Hg}^{2+}$  efficiently and selectively. Their results suggest  $\text{Hg}^{2+} + \text{Mn}^{2+}$  replacement mechanism for the detection of  $\text{Hg}^{2+}$ . The replacement results in fluorescence ‘turn-on’ of an unreplaced sample. Wang et al. [112] used a nanohybrid of CdSe



**Fig 14.8** (a) Fluorescence responses of the sensor to various concentrations of  $\text{Hg}^{2+}$  ions in 2.5 mL of phosphate-buffered saline (PBS) (10 mM, pH 7.4). (b) Calibration plot of fluorescence intensity vs  $\text{Hg}^{2+}$  ion concentration between 0.25 and 100 nM. Inset: calibration plot of fluorescence intensity vs  $\text{Hg}^{2+}$  ion concentration between 0.1 and 1 nM. The vertical bars designate the standard deviation for the mean of three replicate tests. (Reprinted with permission from Zhang et al. [136]. Copyright 2020: ACS. Fig. 5)

QDs and g- $\text{C}_3\text{N}_4$  nanosheets to successfully determine the presence of as low as 5.3 nM  $\text{Hg}^{2+}$ . Zhang et al. [136] prepared CdSe/CdS QD labelled lipid lysosomes to enhance the selectivity and sensitivity of the probe for  $\text{Hg}^{2+}$  detection to a sublime level of 0.01 nM, which met the requirements of environmental sample detection. The sensor also exhibited high selectivity for  $\text{Hg}^{2+}$  detection in the presence of other high-level metal ions, such as  $\text{Fe}^{3+}$ ,  $\text{Al}^{3+}$ ,  $\text{Zn}^{2+}$ ,  $\text{Pb}^{2+}$ ,  $\text{Ni}^{2+}$ ,  $\text{Mn}^{2+}$ ,  $\text{Mg}^{2+}$ ,  $\text{Cu}^{2+}$ ,  $\text{Cr}^{2+}$ ,  $\text{Co}^{2+}$ ,  $\text{Cd}^{2+}$ ,  $\text{Ca}^{2+}$ ,  $\text{Ba}^{2+}$  and  $\text{K}^+$ . As it is seen in Fig. 14.8, the fluorescence signals increased sensitively in response to the increasing  $\text{Hg}^{2+}$  concentration (Fig. 14.8a). The peak current was linearly related to the  $\text{Hg}^{2+}$  concentration in the range from 0.25 to 100 nM (Fig. 14.8b).

Kini et al. [55] used MPA-coated CdTe/CdS core/shell QDs for the selective detection of mercury in an aqueous solution. The authors elucidated that efficient energy transfer between QDs and rhodamine 6G molecule happens in the presence of cetyl trimethyl ammonium bromide (CTAB). They found that the system exhibits Stern–Volmer behaviour in the concentration range of 0.1 nM to 2.0  $\mu\text{M}$  with a detection limit of 3.8 nM. Labeb et al. [58] reported that the sensitivity of CdTe QDs can be enhanced by orders of magnitude from nmol range to pmol range by changing the surface ligand from TGA to L-cysteine. Table 14.3 summarizes a comparison of detection range and limit of detection (LOD) of  $\text{Hg}^{2+}$  for various other materials used.

### 14.5.3 $\text{Pb}^{2+}$ Ion Sensing

Lead has no known natural biological role. The primary cause of lead-contaminated soils, air and water systems are anthropogenic activities such as burning leaded gasoline, use of lead solder, lead piping and lead-based paints. The natural

**Table 14.3** Comparison of the reported methods for Hg<sup>2+</sup> detection using II–VI QDs

Materials	Coating/Modification	Linear range × 10 <sup>-6</sup> (mol·L <sup>-1</sup> )	LOD × 10 <sup>-9</sup> (mol·L <sup>-1</sup> )	References
ZnSe	MPA	0.0–7.0	0.2	[147]
ZnS	ZnS:Ce	10–100	820	[23]
CdTe	BSA	<0.469	4	[150]
CdTe	Glutathione and cysteine	0.6–20	100 and 600	[43]
CdTe	GSH capped and BSA coated Au NCs conjugated	0.131–0.710	9	[80]
CdTe	2-Mercaptoethane-sulphonate (MES)	0. – 0.5	9.5	[79]
CdTe	Thioglycolic acid	0.012–1.5	4	[132]
CdTe	Cysteamine	0.005–0.3	1	[17]
CdTe/ CdS	Unmodified	0.0–6.0	5.6	[98]
CdTe/ CdS	Oligonucleotides	0.00025–0.1	0.01	[136]
CdSe/ ZnS	G-quadruplex	0.001–0.5	1.0	[137]
CdTe	Cysteamine	0.006–0.45	4.0	[28]
CdTe	Thiourea	1–300 µg·L <sup>-1</sup>	0.56 µg·L <sup>-1</sup>	[130]

levels of lead in surface and underground waters are <5 ppb, but it may get higher than 1000 ppb in some regions. Even at extremely low levels, lead has been linked with a range of health effects including behavioural problems and learning disabilities especially in young children through toys and candies. Lead acid batteries have been widely used as energy devices and therefore are a major source of lead in air, water and soil. Weidenhamer and Clement [120] examined 39 jewellery items and found they contain 90% or more lead by weight. More specifically Pb<sup>2+</sup> affects a wide variety of targets in the living body causing lead poisoning. According to WHO guidelines, the admissible range of Pb<sup>2+</sup> ions within our body is 48 nM. In India, this concentration is 480 nM which is a real health menace. Hence, sensitive, selective and simple methods of lead detection are crucial in not only preventing contamination but also for a better understanding of the biological pathways of lead.

Ren et al. [91] used luminescent L-cysteine-modified CdSe QDs for sensitive detection of lead ions in Kolthoff buffer solution. They found that fluorescence intensity of CdSe QDs varies linearly in the range 0.0–1.0 × 10<sup>-6</sup> M with a limit of detection to be 8.39 × 10<sup>-8</sup> M. Based on thermodynamics studies, the quenching mechanism was attributed to surface adsorption of ions followed by cation displacement. Zhong et al. [145] used thioglycolic acid-stabilized CdTe QDs of varying sizes for efficient detection of lead ions. Zhao et al. [143] utilized the fluorescence



**Table 14.4** Comparison of the reported systems for Pb<sup>2+</sup> detection based upon II–VI QDs

Materials	Coating/modification	Linear range × 10 <sup>-6</sup> (mol·L <sup>-1</sup> )	LOD × 10 <sup>-9</sup> (mol·L <sup>-1</sup> )	References
CdSe/CdS QDs	Xylenol orange	0.05–6.00	20	[142]
Au QDs	Covalently linked Au NCs embedded in SiO <sub>2</sub>	0.025–0.250	3.5	[151]
ZnS QDs	Silica	0.001–260	–	[88]
CdTe QDs	–	0.02–3.60	80	[135]
PbS	In situ QD formation	0.0–25.0	452	[62]
CdSe/ZnS	Siloxane shell with covalently coupled DNAzymes	–	0.2	[127]
CdTe QDs	TGA	2·10 <sup>-6</sup> –1·10 <sup>-4</sup>	2.7·10 <sup>-7</sup>	[128]

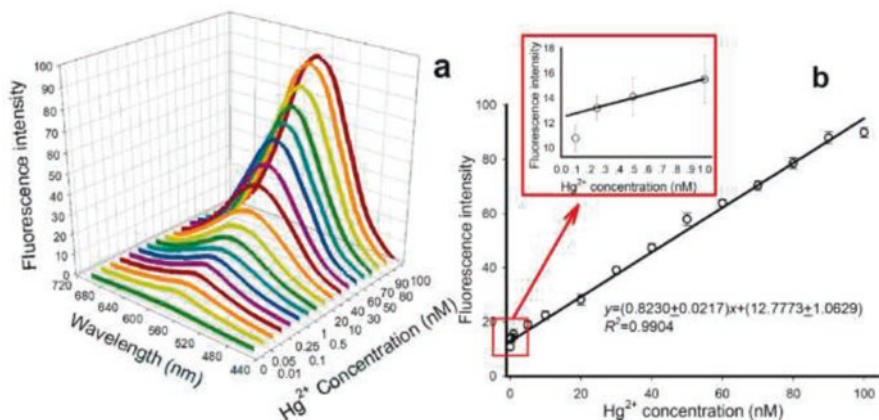
‘turn-on’ mechanism from dithizone-capped CdSe/CdS QDs. The fluorescence turn-on was concerted due to the complex formation between Pb<sup>2+</sup> and dithizone. This results in the blockage of FRET mechanism established between dithizone and QD. Bach et al. [7] used Glutathione capped CdSe QDs for the detection of Pb<sup>2+</sup> ions in solution. They found that the relative luminescence of GSH-functionalized CdSe QDs increases linearly with Pb<sup>2+</sup> ion concentration in a range between 2.0 × 10<sup>-8</sup> and 2.0 × 10<sup>-6</sup> M. Wang et al. [111] used chiral CdSe nanoplatelets for ultrasensitive detection of Pb<sup>2+</sup> with limit of detection as low as 4.9 nM. They have taken the advantage of chiroptical activity of these ultrathin platelets for sensitive and selective determination of trace level Pb<sup>2+</sup> ion concentration in water. Wu et al. [128] used thiol-capped CdTe QDs for the detection of Pb<sup>2+</sup> ions in solution. They reported a LOD of 270 nM in the concentration range of 2.0–100.0 μM.

Jacob et al. [48] used biologically synthesized ZnS for the detection of Pb<sup>2+</sup> in the concentration range of 5–200 μM. They have reported a detection limit of 2.46 μM. Li et al. [63] used aptamer functionalized CdSe/ZnS QDs and their composite with graphene oxide (GO) sheets to determine Pb<sup>2+</sup> concentration in solution. The nanoensemble enables energy transfer from QDs to GO quenching the fluorescence of QDs. The GO/aptamer–QD ensemble assay acts as a “turn-on” fluorescent sensor for Pb<sup>2+</sup> detection. When Pb<sup>2+</sup> ions are present in the assay, the interaction of Pb<sup>2+</sup> with the aptamer induces a conformational change in the aptamer, leading to the formation of a G-quadruplex/Pb<sup>2+</sup> complex and therefore “turns on” the fluorescence of the QDs. This sensor exhibits a limit of detection of 90 pM and excellent selectivity toward Pb<sup>2+</sup> over a wide range of metal ions between 0.1 and 10.0 nM. The excellent detection limit is attributed to the nano-metal surface energy transfer (NSET) mechanism rather than the conventional Förster resonance energy transfer (FRET) process. Table 14.4 summarizes further works for selective determination of Pb<sup>2+</sup> ions in solution.

### 14.5.4 Cr Ion Sensing

Another notable hazardous heavy metal is chromium. Although it is known to be a micronutrient, it is also one of the most important toxicants that exist in different valence states. Among these states Cr(III) and Cr(VI) states exist in the natural environment. Although the toxicity of Cr(VI) is a proven fact, Cr(III) is a controversial element with mixed advantages and disadvantages [140]. The dietary sources of Cr(III) include vegetables including broccoli and green beans, fruits including grapes and oranges and meat including beef, poultry and milk dairies. Interestingly, a distinction can be made between Cr(III) and Cr(VI) by tailoring the surface functional groups of CdTe QDs. The basic effect is the difference in electrostatic interaction between the multivalent ion and the QD surface [41]. The essentiality of chromium has been demonstrated by Schwarz and Mertz [95] through the existence of a dietary factor which was absent in the diet of rats fed with *Torula* yeast as a sole protein source. Such rats were found to develop an inability to remove efficiently glucose from their bloodstream. This inability was reversed when these mice were fed with foods rich in chromium or by adding chromium(III) complexes to the diet. Wada et al. [109] and Yamamoto et al. [129] reported the isolation and characterization of a unique chromium-binding oligopeptide named low-molecular weight chromium-binding substance (LMWCr) or chromodulin. The oligopeptide possesses a molecular weight of ~1500 Da and is comprised of only four types of amino acid residues, that is, glycine, cysteine, glutamate and aspartate. Despite its small molecular weight, it binds four equivalents of chromic ions, apparently in a tetranuclear assembly, as necessitated by charge balance arguments. The most important attribute of chromodulin is its ability to potentiate the effects of insulin on the conversion of glucose into carbon dioxide or lipid by isolated rat adipocytes. No other naturally occurring chromium-containing species potentiates insulin action in this manner [107].

Studies have shown that, like other heavy metal ions, chromium ions can be detected using QD-based fluorescent sensors. Elmizadeh et al. [32] reported a cyclic ligand-coated CdTe for the detection of Cr(III) ions in water samples. They found highly sensitive and selective detection of Cr ions in a range of  $6.8 \times 10^{-8}$ – $3.7 \times 10^{-6}$  mol·L<sup>-1</sup> with a detection limit of  $20.3 \times 10^{-9}$  mol·L<sup>-1</sup>. Parani and Oluwafemi [81] used Cd-free green synthesized glutathione (GSH) capped AgInS<sub>2</sub>-ZnS QDs for selective and sensitive detection of Cr(III) with a detection limit of 0.51 nM. Cu(III) influence on the PL spectra of AgInS<sub>2</sub>-ZnS QDs is shown in Fig. 14.9. It has been established that AIS-ZnS QD fluorescent nanoprobe demonstrate selective detection of Cr(III) ions in a mixture of interfering divalent metal ions, such as Cu(II), Pb(II), Hg(II), Ni(II). The detection mechanism of Cr(III), studied using a high-resolution transmission electron microscope (HRTEM) and Fourier transform infrared spectroscopy (FTIR), showed that the binding of Cr(III) ions to the GSH capping agent leads to QD aggregation followed by fluorescence quenching.



**Fig. 14.9** Effect of different Cr(III) ion concentrations on the fluorescence spectra of AIS-ZnS QDs. (Reprinted with permission from Parani and Oluwafemi [81]. Copyright 2020: IOP. Fig. 4)

**Table 14.5** Comparison of several literature reports on fluorescent sensing of Cr (III) ions using II–VI QDs

Materials	Coating/modification	Linear range $\times 10^{-6}$ (mol·L <sup>-1</sup> )	LOD $\times 10^{-9}$ (mol·L <sup>-1</sup> )	References
ZnO QDs	–	0.01–0.30	2	[53]
Mn-doped ZnS QDs	Protein-functionalized	0.01–0.30	3	[144]
CdS QDs	Thioglycolic acid	58.0–770.0	20	[1]
CdSe QDs	Silane	0.1–20.0	30	[99]
CdS QDs	Pectin	0.016–0.266	16	[3]
Capped-CdSe QDs	Thioglycolic acid	0.48–6.25	0.1	[26]
CdTe QDs	Heterocyclic ligand	0.067–3.700	20	[32]
CdTe QDs	GSH	0.0–2.0	3	[83]
AgInS <sub>2</sub> -ZnS QDs	GSH	0.025–10.00	0.51	[81]

Source: Reprinted with permission from Parani and Oluwafemi [81]. Copyright 2020: IOP

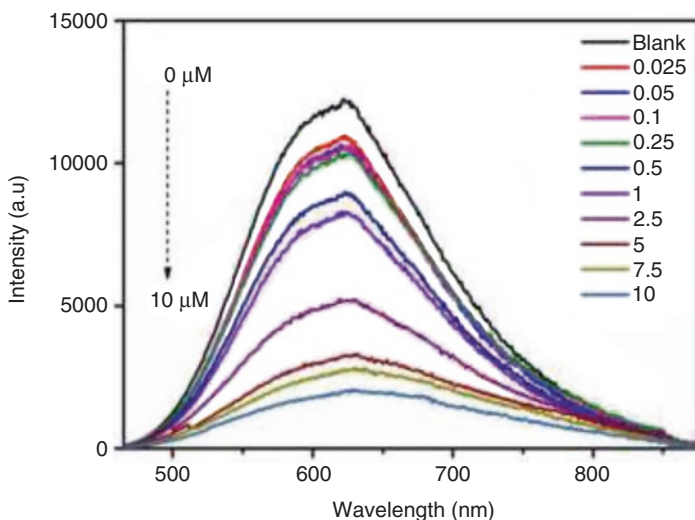
Abolhasani et al. [1] reported TGA-capped CdS QDs with a low limit of detection of 0.2–1.3 ng·mL<sup>-1</sup>. The QDs were sensitive to both Cr<sup>3+</sup> and Pb<sup>2+</sup> in different conditions while the interference from iron, sodium, calcium, potassium and magnesium was found to be absent. Peng et al. [83] used GSH-capped CdTe QDs for selective and sensitive detection of Cr<sup>3+</sup> and Cr(III) picolinate, a Cr-containing vitamin. The quenching of QDs was found to vary linearly in a concentration range of 0–2  $\mu$ M while the limit of detection was reported to be 3.0 nM. Some parameters of sensors developed for fluorescent sensing of Cr (III) are listed in Table 14.5.

### 14.5.5 Other Metal Ions

Using previously described approaches, other ions, including Ag (see Fig. 14.10) [60, 102], As [105], Au [31], Cd [114, 146], Co [64], Ni [108] and Zn [125], cyanide [96] can also be detected in solution with high selectivity and sensitivity. For example, Chen and Rosenzweig [20] have shown that the selectivity of CdS QDs for different ions can be tuned by controlling the surface of QDs. For example, by replacing the phosphate ions with L-cysteine results in the selectivity towards the Zn ion. This has been attributed to the complexation of Zn with L-cysteine. A brief summary of the characteristics of these sensors is given in Table 14.6.

### 14.5.6 QD-Based pH Sensing

Intracellular pH control is crucial for the proper functioning of cells. Cells maintain their pH by controlling membrane proton pumps and transporters often at the expense of acidifying the extracellular pH. In turn, extracellular acidification impacts cells via specific acid-sensing ion channels (ASICs) and proton-sensing G-protein coupled receptors (GPCRs). Active transporters or ion pumps in transmembrane also transport energy from various sources such as ATP, sunlight and other redox reactions. The microenvironment of a tumour is a complex interplay of poor vascular perfusion, local hypoxia and increased flux of carbons through



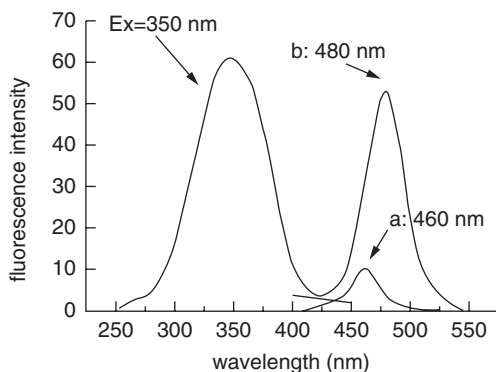
**Fig. 14.10** Excitation and emission spectrum of functional CdS QDs before (a) and after (b) adding silver ion. CdS QDs:  $7.5 \mu\text{mol}\cdot\text{L}^{-1}$ ; silver ion:  $0.1 \mu\text{mol}\cdot\text{L}^{-1}$ ; pH, 5.0. (Reprinted from Lai et al. [60]. Published by Wiley as open access)

**Table 14.6** Summary of characteristics of various ion sensors

Materials	Coating/modification	Analyte	Linear range $\times 10^{-6}$ (mol·L <sup>-1</sup> )	LOD $\times 10^{-9}$ (mol·L <sup>-1</sup> )	References
CdS	Bismuthiol II	Ag <sup>+</sup>	0.01–5.00	1.6	[60]
CdTe	L-cysteine	As <sup>2+</sup>	0.002–0.500	2.0	[105]
Cu <sub>2</sub> S	N-acetyl-L-cysteine	Au <sup>3+</sup>	1.62–60.80	162	[31]
Mn:ZnSe	Mercaptopropionic acid	Cd <sup>2+</sup>	0.0–90.0	18	[146]
ZnS	–	Co <sup>2+</sup>	10–1000 mg/L	10 mg/L	[64]
Gd:ZnS	<i>Aspergillus falvus</i>	Ni <sup>2+</sup>	–	–	[108]
ZnS	–	Cyanide	2.44–25.90	170 at pH 11	[96]
ZnS	–	Nitrite	20.0–1.35 $\times 10^6$	8.5	[5]

fermentative glycolysis. This leads to extracellular acidosis in solid tumours with pH values as low as 6.5. Most cancer cells produce energy predominantly not through the ‘usual’ citric acid cycle (Kerb cycle) and oxidative phosphorylation in the mitochondria as observed in normal cells but through a less efficient process of ‘aerobic glycolysis’ consisting of a high level of glucose uptake and glycolysis followed by lactic acid fermentation taking place in the cytosol, not the mitochondria, even in the presence of abundant oxygen. This effect is called the Warburg effect. The quantity of ATP produced through lactic acid fermentation is less as compared to kerb cycle-derived ATP. The glycolytic by-products, lactate and H<sup>+</sup>, challenge the mechanisms to maintain intracellular pH homeostasis. Intracellular acidification has been shown to be cytotoxic through the induction of apoptosis. To overcome low pH due to elevated rates of glycolysis, cancer cells employ a large redundancy of mechanisms to remove acids in order to maintain physiological pH. In response to glycolytic acidosis, pH can be maintained via lactate and H<sup>+</sup> efflux by monocarboxylate transporters and Na-driven proton extrusion, respectively. Consequently, the pH of the extracellular space of tumours becomes acidic and thus forming a reversed pH gradient (pH<sub>e</sub> < pH<sub>i</sub>) in comparison to normal physiological conditions (pH<sub>e</sub> > pH<sub>i</sub>). Therefore, the determination of pH is important for early diagnosis of diseases as this is envisaged to be associated with some chemical changes at the cellular level that are observable before tissue-level changes become evident. Hence, detection of malfunctioning at the prognosis level can help in better treatment strategy and recovery chances.

Apropos to above, intracellular and extracellular pH determination is vital for cancer diagnosis of carcinogenesis. The detection of tumour growth at the avascular pre-invasive stage is critical in the choice of treatment modalities. Fluorescence-based sensing of regional pH may serve as a litmus test in this case. Fluorescent nanoprobes have been extensively used for analyte sensing in cells. This is due to the excellent quantum yield of these organic molecules and a variety of emission wavelengths available for specific sensing of various molecules. However, major drawback of these wonderful molecules is their ability to get rapid photobleaching



**Fig. 14.11** Fluorescence intensity for CdTe QDs prepared with mercaptoethylamine (MEA) stabilizing agent as a function of wavelength at different pH values. (Reprinted with permission from Gao et al. [36]. Copyright 2018: IOP)

**Table 14.7** QDs-based sensors for pH determination

Marker	Sensing platform	Coating/modification	Transduction type	References
pH	CdSe/ZnS	Methacrylic acid	FRET	[68]
pH: 3–11	CdSe/ZnS	Oxazine	Intensity change	[104]
pH	CdSe/ZnS	Phosphine oxide	FRET	[97]
pH: 4–6	CdTe	Thioglycolic acid	Intensity change	[101]
pH	CdTe	–	Intensity change	[118]
Urea	CdSe/ZnS	Mercaptosuccinic acid	Intensity change	[47]

Source: Reprinted from Lesiak et al. [61]. Published by MDPI as open access

and their narrow absorption region. Inorganic semiconductor QDs have better photostability and narrow emission and therefore suffer less from photobleaching and cross-talk problems.

A number of reports exist on sensing of extracellular and intracellular pH. How strong the effect of pH on the luminescent properties of quantum dots can be seen from the results shown in Fig. 14.11. This is the property of quantum dots to change their luminescent properties under the influence of the pH of the solution has a promising application in the design of a variety of luminescence sensors, examples of which are shown in Table 14.7. For example, Tomasulo et al. [104] studied the effect of pH on the luminescent properties of CdSe/ZnS QDs capped with an organic compound incorporating a dithiolane anchoring group, an electron-rich indole, a 4-nitrophenylazophenoxy chromophore and a 1,3-oxazine ring in their skeleton. The pH sensing was based on the 1,3-oxazine ring opening upon the addition of base or acid. The bifunctional system works based on both energy (FRET) and electron (PET) transfer from QD to nearby molecules. CdSe/ZnS QDs encapsulated in pH-sensitive squaraine conjugated amphiphilic polymer was used to determine the pH reversibly in the solution. The ratiometric sensing mechanism is based on the pH dependence of the dye absorption spectrum. The spectral overlap between dye absorption and NC emission increases as the pH is lowered [97].

Alternatively, ratiometric sensing can be accomplished by using dual-emission fluorescent probes. Zhang et al. [139] used dual emission seminaphtharhodafluor (SNARF) for ratiometric detection of pH of local environment. In order to fully comply with experimental complexities, different control experiments were conducted. The fluorophore was linked to the backbone of an amphiphilic polymer through ester bond. The dye-conjugated polymer was then used to cap hydrophobic gold nanoparticles. PEG separators of different molecular weights (lengths) were used to control the spacing between the negatively charged nanoparticle surface and the fluorophore. The binding equilibrium of the fluorophore was found to shift to higher bulk pH values when in close proximity to the surface. The counter-ion distribution around the negatively charged surface of the polymer was found to follow Stern double-layer model rather than Debye-Hückel or Gouy-Chapman model. This is attributed to the roughness of the polymer-electrolyte interface and the fact that  $H^+$  ions can access the negatively charged  $COO^-$  ions directly at the surface, particularly below  $pK_a$ . Harimech et al. [44] used the same ratiometric fluorophore to follow the reversible conversion of oxaloacetic acid into L-malic acid through an enzyme malate dehydrogenase. The conversion occurs in the presence of nicotinamide adenine dinucleotide. Multilayer polyelectrolyte (PAH/PSS) microcapsules were used as a carrier system and all the ingredients were loaded in the cavity of the capsules. Zhang et al. [138] used the pH-sensitive fluorophore OG-488-cadaverine and the reference fluorophore amine-ATTO-590, which have been linked to the polymer surface by means of EDC chemistry. ATTO-590 is a pH-insensitive molecule and has an emission at 610 nm which is quite far from the absorbance/emission range of OG-488. The prepared system was used as a ratiometric sensor for pH sensing.

## 14.6 Summary

The detection and quantification of heavy metal ions is of paramount importance in environmental and biological contexts. Among various ions copper, mercury and lead ions have attracted more attention due to their high toxicity and relevance to health. The development of novel methods to use nanoparticles, especially QDs, has seen enormous growth during the last decade. It was established that ions can be detected based on the adsorption of ions on the QD surface. This results in either enhancement or quenching of the fluorescence signal. The fluorescence quenching is typically used as opposed to enhancement. The mechanism of quenching depends upon the concentration of ions according to Stern–Volmer equation. On the other hand, FRET-based sensing provides an enhanced LOD for ions and hence provides a very sensitive method for the detection of heavy metal ions in solution. It has been found that appropriate modification of surface may result in preferential detection of one kind of cation in the presence of other ions in a certain concentration range. However, the interference has remained a major challenge in the accurate determination of these ions. Different strategies can be adapted for resolving these problems. For example, introduction of small chelating molecules, supramolecular chemistry, place exchange mechanism and metal-mediated DNA duplexes can be applied.

**Acknowledgements** G.K. is grateful to the State Program of the Republic of Moldova, project 20.80009.5007.02, for supporting his research.

## References

1. Abolhasani J, Hassanzadeh J, Jalali ES. Ultrasensitive determination of lead and chromium contamination in well and dam water based on fluorescence quenching of CdS quantum dots. *Int Nano Lett.* 2014;4:65–72.
2. Acha ND, Elosúa C, Corres JM, Arregui FJ. Fluorescent sensors for the detection of heavy metal ions in aqueous media. *Sensors.* 2019;19:599.
3. Ahmed KBA, Pichikannu A, Veerappan A. Fluorescence cadmium sulfide nanosensor for selective recognition of chromium ions in aqueous solution at wide pH range. *Sens Actuators B Chem.* 2015;221:1055–61.
4. Ali EM, Zheng Y, Yu H, Ying JY. Ultrasensitive Pb<sup>2+</sup> detection by glutathione-capped quantum dots. *Anal Chem.* 2007;79(24):9452–8.
5. Annalakshmi M, Kumaravel S, Chen SM, Balasubramanian P, Balamurugan TST. A straight-forward ultrasonic-assisted synthesis of zinc sulfide for supersensitive detection of carcinogenic nitrite ions in water samples. *Sens Actuators B Chem.* 2020;305:127387.
6. Anyanwu BO, Ezejiofor AN, Igweze ZN, Orisakwe OE. Heavy metal mixture exposure and effects in developing nations: an update. *Toxics.* 2018;6(4):1–32.
7. Bach LG, Nguyen TD, Thuong NT, Van HTT, Lim KT. Glutathione capped CdSe quantum dots: synthesis, characterization, morphology, and application as a sensor for toxic metal ions. *J Nanosci Nanotechnol.* 2019;19(2):1192–5.
8. Bánfalvi G. Heavy metals, trace elements and their cellular effects. In: Bánfalvi G, editor. *Cellular effects of heavy metals.* New York: Springer; 2011. p. 3–28.
9. Belcastro M, Marino T, Russo N, Toscano M. Interaction of cysteine with Cu<sup>2+</sup> and group IIb (Zn<sup>2+</sup>, Cd<sup>2+</sup>, Hg<sup>2+</sup>) metal cations: a theoretical study. *J Mass Spectrom.* 2005;40(3):300–6.
10. Biranje A, Azmi N, Tiwari A, Chaskar A. Quantum dots based fluorescent probe for the selective detection of heavy metal ions. *J Fluoresc.* 2021;31:1241–50.
11. Bo C, Ping Z. A new determining method of copper(II) ions at ng-mL<sup>-1</sup> levels based on quenching of the water-soluble nanocrystals fluorescence. *Anal Bioanal Chem.* 2005;381:986–92.
12. Brahim NB, Mohamed NBH, Echabaane M, Haouari M, Chaabane RB, Negrerie M, H.B. Ouada H.B. Thioglycerol-functionalized CdSe quantum dots detecting cadmium ions. *Sens Actuators B Chem.* 2015;220:1346–53.
13. Cai ZX, Yang H, Zhang Y, Yan XP. Preparation, characterization and evaluation of water-soluble L-cysteine-capped-CdS nanoparticles as fluorescence probe for detection of Hg(II) in aqueous solution. *Anal Chim Acta.* 2005;559(2):234–9.
14. Cao Z, Gu Z, Zeng JL, Liu JH, Deng Q, Fan JB, Xiang JN. A novel fluorescent probe for copper ions based on polymer-modified CdSe/CdS core/shell quantum dots. *Anal Sci.* 2011;27:643–7.
15. Cao Q-E, Wang K, Hu Z, Xu Q. Syntheses of three new derivatives of 8-aminoquinoline and its applications for fluorimetric determination of copper(II). *Talanta.* 1998;47:921–7.
16. Chan YH, Wu C, Ye F, Jin Y, Smith PB, Chiu DT. Development of ultrabright semiconducting polymer dots for ratiometric pH sensing. *Anal Chem.* 2011;83:1448–55.
17. Chen B, Ma J, Yang T, Chen L, Gao PF, Huang CZ. A portable RGB sensing gadget for sensitive detection of Hg<sup>2+</sup>, using cysteamine-capped QDs as fluorescence probe. *Biosens Bioelectron.* 2017;98:36–40.
18. Chen GF, Tsai HP, Lai PS, Liao MY. Functionalized Mn<sup>2+</sup>-doped zinc sulfide quantum dots as a metal ion sensor for industrial wastes. *Sens Mater.* 2013;25:437–42.



19. Chen G, Jin Y, Wang L, Deng J, Zhang C. Gold nanorods-based FRET assay for ultrasensitive detection of Hg<sup>2+</sup>. *Chem Commun.* 2011;47:12500–2.
20. Chen Y, Rosenzweig Z. Luminescent CdS quantum dots as selective ion probes. *Anal Chem.* 2002;74:5132–8.
21. Chern M, Kays JC, Bhuckory S, Dennis AM. Sensing with photoluminescent semiconductor quantum dots. *Methods Appl Fluoresc.* 2019;7:012005.
22. Chou KF, Dennis AM. Förster resonance energy transfer between quantum dot donors and quantum dot acceptors. *Sensors.* 2015;15:13288–325.
23. Chu H, Yao D, Chen J, Yu M, Su L. Double-emission ratiometric fluorescent sensors composed of rare-earth-doped ZnS quantum dots for Hg<sup>2+</sup> detection. *ACS Omega.* 2020;5:9558–65.
24. Clark HA, Barker SLR, Brasuel M, Miller MT, Monson E, Parus S, et al. Subcellular optochemical nanobiosensors: probes encapsulated by biologically localised embedding (PEBBLEs). *Sens Actuators B Chem.* 1998;51:12–6.
25. De Acha N, Elosúa C, Corres JM, Arregui FJ. Fluorescent sensors for the detection of heavy metal ions in aqueous media. *Sensors.* 2019;19:599.
26. De Souza GC, de Santana ÉE, da Silva PA, Freitas DV, Navarro M, Paim APS, Lavorante AF. Employment of electrochemically synthesized TGA–CdSe quantum dots for Cr<sup>3+</sup> determination in vitamin supplements. *Talanta.* 2015;144:986–91.
27. Ding L, Xu B, Li T, Huang J, Bai W. A “turn-on” fluorescence copper biosensor based on DNA cleavage-dependent graphene oxide-dsDNA–CdTe quantum dots complex. *Sensors.* 2018;18:2605.
28. Ding X, Qu L, Yang R, Zhou Y, Li J. A highly selective and simple fluorescent sensor for mercury (II) ion detection based on cysteamine-capped CdTe quantum dots synthesized by the reflux method. *Luminescence.* 2015;30:465–71.
29. Dodani SC, He Q, Chang CJ. A turn-on fluorescent sensor for detecting nickel in living cells. *J Am Chem Soc.* 2009;131:18020–1.
30. Doose S, Neuweiler H, Sauer M. Fluorescence quenching by photoinduced electron transfer: a reporter for conformational dynamics of macromolecules. *ChemPhysChem.* 2009;10:1389–98.
31. Du W, Liao L, Yang L, Qin A, Liang A. Aqueous synthesis of functionalized copper sulfide quantum dots as near-infrared luminescent probes for detection of Hg<sup>2+</sup>, Ag<sup>+</sup> and Au<sup>3+</sup>. *Sci Rep.* 2017;7:11451–62.
32. Elmizadeh H, Soleimani M, Faridbod F, Bardajee GR. A sensitive nano-sensor based on synthetic ligand-coated CdTe quantum dots for rapid detection of Cr(III) ions in water and wastewater samples. *Colloid Polymer Sci.* 2018;296:1581–90.
33. Fan Y, Cai Y, Liu H, et al. CdS quantum dots capped with hyperbranched graft copolymers: role of hyperbranched shell in fluorescence and selective mercury-sensing. *Sens Actuators B Chem.* 2017;251:171–9.
34. Fernández-Argüelles MT, Jin WJ, Costa-Fernández JM, Pereira R, Sanz-Medel A. Surface-modified CdSe quantum dots for the sensitive and selective determination of Cu(II) in aqueous solutions by luminescent measurements. *Anal Chim Acta.* 2005;549:20–5.
35. Fu D, Yuan D. Spectrophotometric determination of trace copper in water samples with thiomichlerketone. *Spectrochim Acta A.* 2007;66:434–7.
36. Gao J, Fei X, Li G, Jiang Y, Li S. The effects of QD stabilizer structures on pH dependence, fluorescence characteristics, and QD sizes. *J Phys D Appl Phys.* 2018;51:285101.
37. Gao M, Kirstein S, Mohwald H, Rogach AL, Kornowski A, Eychmüller A, Weller H. Strongly photo luminescent CdTe nanocrystals by proper surface modification. *J Phys Chem B.* 1998;102:8360–3.
38. Ibrahim I, Lim HN, Huang NM, Pandikumar A. Cadmium Sulphide-reduced graphene oxide-modified photoelectrode-based photoelectrochemical sensing platform for copper(II) ions. *PLoS One.* 2016;11(5):e0154557.

39. Iyer G, Pinaud F, Xu J, Ebenstein Y, Li J, Chang J, et al. Aromatic aldehyde and hydrazine activated peptide coated quantum dots for easy bioconjugation and live cell imaging. *Bioconjug Chem.* 2011;22:1006–11.
40. Isarov AV, Chrysochoos J. Optical and photochemical properties of nonstoichiometric cadmium sulfide nanoparticles: surface modification with Copper(II) ions. *Langmuir.* 1997;13:3142–9.
41. Han J, Bu X, Zhou D, Zhang H, Yang B. Discriminating Cr(III) and Cr(VI) using aqueous CdTe quantum dots with various surface ligands. *RSC Adv.* 2014;4:32946–52.
42. Han J, Burgess K. Fluorescent indicators for intracellular pH. *Chem Rev.* 2010;110(2010):2709–28.
43. Han B, Yuan J, Wang E. Sensitive and selective sensor for biothiols in the cell based on the recovered fluorescence of the CdTe quantum dots-Hg(II) system. *Anal Chem.* 2009;81:5569–73.
44. Harimech PK, Hartmann R, Rejman J, del Pino P, Rivera-Gil P, Parak WJ. Encapsulated enzymes with integrated fluorescence-control of enzymatic activity. *J Mater Chem B.* 2015;3:2801–7.
45. Hildebrandt N, Spillmann CM, Algar WR, Pons T, Stewart MH, Oh E, et al. Energy transfer with semiconductor quantum dot bioconjugates: a versatile platform for biosensing, energy harvesting, and other developing applications. *Chem Rev.* 2017;117(2):537–711.
46. Hildebrandt N, Medintz I. FRET – Förster resonance energy transfer. Weinheim: WileyVCH Verlag GmbH and Co. KGaA; 2013.
47. Huang CP, Li YL, Chen TM. A highly sensitive system for urea detection by using CdSe/ZnS core-shell quantum dots. *Biosens Bioelectron.* 2007;22:1835–8.
48. Jacob JM, Rajan R, Kurup GG. Biologically synthesized ZnS quantum dots as fluorescent probes for lead (II) sensing. *Luminescence.* 2020;35(8):1328–37.
49. Jaishankar M, Tseten T, Anbalagan N, Mathew BB, Beeregowda KN. Toxicity, mechanism and health effects of some heavy metals. *Interdiscip Toxicol.* 2014;7:60–72.
50. Jiwan S, Ajay K. Effects of heavy metals on soil, plants, human health and aquatic life. *Int J Res Chem Environ.* 2011;1:15–21.
51. Kaiser U, Jimenez de Aberasturi D, Malinowski R, Amin F, Parak WJ, Heimbrodt W. Multiplexed measurements by time resolved spectroscopy using colloidal CdSe/ZnS quantum dots. *Appl Phys Lett.* 2014;104:041901.
52. Kamat PV. Photochemistry on nonreactive and reactive (semiconductor) surfaces. *Chem Rev.* 1993;93:267–300.
53. Kaviya S, Kabila S, Jayasree KV. Room temperature biosynthesis of greatly stable fluorescent ZnO quantum dots for the selective detection of Cr<sup>3+</sup> ions. *Mater Res Bull.* 2017;95:163–8.
54. Kessler MA. Determination of copper at ng·mL<sup>-1</sup>-levels based on quenching of the europium chelate luminescence. *Anal Chim Acta.* 1998;364:125.
55. Kini S, Ganiga V, Kulkarni SD, Chidangil S, George SD. Sensitive detection of mercury using the fluorescence resonance energy transfer between CdTe/CdS quantum dots and Rhodamine 6G. *J Nanopart Res.* 2018;20:232–44.
56. Kubo Y, Yamamoto M, Ikeda M, Takeuchi M, Shinkai S, Yamaguchi S, Tamao K. A colorimetric and ratiometric fluorescent chemosensor with three emission changes: fluoride ion sensing by a Triarylborane– porphyrin conjugate. *Angew Chem.* 2003;42(2003):2036.
57. Kumar P, Kim K-H, Bansal V, Lazarides T, Kumar N. Progress in the sensing techniques for heavy metal ions using nanomaterials. *J Ind Eng Chem.* 2017;54:30–43.
58. Labe M, Sakr A-H, Soliman M, Abdel-Fettah TM, Ebrahim S. Effect of capping agent on selectivity and sensitivity of CdTe quantum dots optical sensor for detection of mercury ions. *Opt Mater.* 2018;79:331–5.
59. Lai SJ, Chang XJ, Fu C. Cadmium sulfide quantum dots modified by chitosan as fluorescence probe for copper (II) ion determination. *Microchim Acta.* 2009;165:39–44.

60. Lai S, Mao X CJ, Zhai Y, Lian N, Zheng H. Determination of silver ion with cadmium sulfide quantum dots modified by bismuthiol II as fluorescence probe. *Ann Chim.* 2007;97(1–2):109–21.
61. Lesiak A, Drzozga K, Cabaj J, Banski M, Malecha K, Podhorodecki A. Optical sensors based on II–VI quantum dots. *Nano.* 2019;9:192.
62. Li YJ, Huang TT, Liu J, Xie YQ, Shi B, Zhang YM, et al. Detection of Lead(II) in living cells by inducing the transformation of a supramolecular system into quantum dots. *ACS Sustain Chem Eng.* 2022;10(24):7907–15.
63. Li M, Zhou X, Guo S, Wu N. Detection of lead(II) with a “turn-on” fluorescent biosensor based on energy transfer from CdSe/ZnS quantum dots to graphene oxide. *Biosens Bioelectron.* 2013;43:69–74.
64. Liu X, Yang Y, Li Q, Wang Z, Xing X, Wang Y. Portably colorimetric paper sensor based on ZnS quantum dots for semi-quantitative detection of Co<sup>2+</sup> through the measurement of grey level. *Sens Actuators B Chem.* 2018;260:1068–75.
65. Liu Z, Liu S, Yin P, He Y. Fluorescence enhancement of CdTe/CdS quantum dots by coupling of glyphosate and its application for sensitive detection of copper ion. *Anal Chim Acta.* 2012;745:78–84.
66. Liu B, Zeng F, Wu G, Wu S. Nanoparticles as scaffolds for FRET-based ratiometric detection of mercury ions in water with QDs as donors. *Analyst.* 2012;137:3717.
67. Liu H, Zhang X, Wu X, Jiang L, Burda C, Zhu J. Rapid sonochemical synthesis of highly luminescent non-toxic AuNCs and Au@AgNCs and Cu(II) sensing. *Chem Commun.* 2011;47:4237–9.
68. Liu YS, Sun Y, Vernier PT, Liang CH, Chong SYC, Gundersen MA. pH-sensitive photoluminescence of CdSe/ZnSe/ZnS quantum dots in human ovarian cancer cells. *J Phys Chem C.* 2007;111:2872–8.
69. Lopez AR, Agarwal V, Esparza JR, Fragoso LR. Cellular localization and toxicity assessment of CdTe-COOH quantum dots in hela cells. *Int J Nanomed Nanosurg.* 2017;3(2) <https://doi.org/10.16966/2470-3206.122>.
70. Luo XB, Guo B, Wang LC, Deng F, Qi RX, Luo SL, Au CT. Synthesis of magnetic ion-imprinted fluorescent CdTe quantum dots by chemical etching and their visualization application for selective removal of Cd(II) from water. *Colloids Surf A Physicochem Eng Asp.* 2014;462:186–93.
71. Maghsoudi AS, Hassani S, Mirnia K, Abdollahi M. Recent advances in nanotechnology-based biosensors development for detection of Arsenic, Lead, Mercury, and Cadmium. *Int J Nanomedicine.* 2021;16:803–32.
72. Men C, Liu R, Xu F, Wang Q, Guo L, Shen Z. Pollution characteristics, risk assessment, and source apportionment of heavy metals in road dust in Beijing, China. *Sci Total Environ.* 2018;612:138–47.
73. Miyake Y, Togashi H, Tashiro M, Yamaguchi H, Oda SJ, Kudo M, et al. Mercury<sup>II</sup>-mediated formation of Thymine–Hg<sup>II</sup>–Thymine base pairs in DNA duplexes. *J Am Chem Soc.* 2006;128(2006):2172–3.
74. Mori I, Fujimoto T, Fujita Y, Matsuo T. Selective and sensitive spectrophotometric determination of copper(II) and benzoylperoxide with N-ethyl-2-naphthylamine. *Talanta.* 1995;42:77–81.
75. Mu Q, Li Y, Xu H, Ma Y, Zhu W, Zhong X. Quantum dots-based ratiometric fluorescence probe for mercuric ions in biological fluids. *Talanta.* 2014;119:564–71.
76. Niebling T, Zhang F, Ali Z, Parak WJ, Heimbrod W. Excitation dynamics in polymer-coated semiconductor quantum dots with integrated dye molecules: the role of reabsorption. *J Appl Phys.* 2009;106:104701.
77. Nolan EM, Lippard SJ. Tools and tactics for the optical detection of mercuric ion. *Chem Rev.* 2008;108:3443–80.
78. Ono A, Togashi H. Highly selective oligonucleotide-based sensor for Mercury(II) in aqueous solutions. *Angew Chem Int Ed Engl.* 2004;43(33):4300–2.

79. Paim APS, Rodrigues SSM, et al. Fluorescence probe for mercury(II) based on the aqueous synthesis of CdTe quantum dots stabilized with 2-mercaptoethanesulfonate. *New J Chem.* 2017;41:3265–72.
80. Paramanik B, Bhattacharyya S, Patra A. Detection of Hg<sup>2+</sup> and F<sup>-</sup> ions by using fluorescence switching of quantum dots in an Au-cluster-CdTe QDs nanocomposite. *Chem Eur J.* 2013;19:5980–7.
81. Parani S, Oluwafemi OS. Selective and sensitive fluorescent nanoprobe based on AgInS<sub>2</sub>-ZnS quantum dots for the rapid detection of Cr (III) ions in the midst of interfering ions. *Nanotechnology.* 2020;31(39):395501.
82. Pandyal NB, Koteswara Rao KSR. Efficient Hg and Ag ion detection with luminescent PbS quantum dots grown in poly vinyl alcohol and capped with mercaptoethanol. *Colloids Surf.* 2009;339:43–7.
83. Peng CF, Zhang YY, Qian ZJ, Xie ZJ. Fluorescence sensor based on glutathione capped CdTe QDs for detection of Cr<sup>3+</sup> ions in vitamins. *Food Sci Human Wellness.* 2018;7:71–6.
84. Pei J, Zhu H, Wang X, Zhang H, Yang X. Synthesis of cysteamine-coated CdTe quantum dots and its application in mercury (II) detection. *Anal Chim Acta* 2012;757:63–8.
85. Pinto JJ, Moreno C, García-Vargas M. A simple and very sensitive spectrophotometric method for the direct determination of copper ions. *Anal Bioanal Chem.* 2002;373:844–8.
86. Pooja CP. Functionalized CdTe fluorescence nanosensor for the sensitive detection of water borne environmentally hazardous metal ions. *Opt Mater.* 2021;111:110584.
87. Qin J, Dong B, Gao R, Su G, Han J, Li X, et al. Water-soluble silica-coated ZnS:Mn nanoparticles as fluorescent sensors for the detection of ultra-trace copper(II) ions in seawater. *Anal Methods.* 2017;9:322–8.
88. Qu H, Cao L, Su G, Liu W, Gao R, Xia C, Qin J. Silica-coated ZnS quantum dots as fluorescent probes for the sensitive detection of Pb<sup>2+</sup> ions. *J Nanopart Res.* 2014;16:2762.
89. Rana M, Chowdhury P. L-glutathione capped CdSeS/ZnS quantum dot sensor for the detection of environmentally hazardous metal ions. *J Lumin.* 2019;206(2019):105–12.
90. Reiss P, Bleuse J, Pron A. Highly luminescent CdSe/ZnSe core/shell nanocrystals of low size dispersion. *Nano Lett.* 2002;2:781–4.
91. Ren J, Chen HL, Ren CL, Sun JF, Liu Q, Wang M, Chen XG. L-cysteine capped CdSe as sensitive sensor for detection of trace lead ion in aqueous solution. *Mater Res Innov.* 2010;14(2):133–7.
92. Ribeiro DSM, Castro RC, Pascoa RNMJ, Soares JX, Rodrigues SSM, Santos JLM. Tuning CdTe quantum dots reactivity for multipoint detection of mercury(II), silver(I) and copper(II). *J Lumin.* 2019;207:386–96.
93. Saha J, Datta RA, Dey D, Bhattacharjee D, Hussain SA. Role of quantum dot in designing FRET based sensors. *Mater Today: Proc.* 2018;5:2306–13.
94. Sapsford KE, Berti L, Medintz IL. Materials for fluorescence resonance energy transfer analysis: beyond traditional donor–acceptor combinations. *Angew Chem.* 2006;45:4562–89.
95. Schwarz K, Mertz W. Chromium(III) and glucose tolerance factor. *Arch Biochem Biophys.* 1959;85:292–5.
96. Shamsipur M, Rajabi HR. Pure zinc sulfide quantum dot as highly selective luminescent probe for determination of hazardous cyanide ion. *Mater Sci Eng C.* 2014;36:139–45.
97. Snee PT, Somers RC, Nair G, Zimmer JP, Bawendi MG, Nocera DG. A ratiometric CdSe/ZnS nanocrystal pH sensor. *J Am Chem Soc.* 2006;128:13320–1.
98. Sun X, Liu B, Xu Y. Dual-emission quantum dots nanocomposites bearing an internal standard and visual detection for Hg<sup>2+</sup>. *Analyst.* 2012;137:1125–9.
99. Sung TW, Lo YL, Chang IL. Highly sensitive and selective fluorescence probe for Cr<sup>3+</sup> ion detection using watersoluble CdSe QDs. *Sens Actuators B Chem.* 2014;202:1349–56.
100. Sung TW, Lo YL. Highly sensitive and selective sensor based on silica-coated CdSe/ZnS nanoparticles for Cu<sup>2+</sup> ion detection. *Sens Actuators B Chem.* 2012;165:119–25.
101. Susa AS, Javier AM, Parak WJ, Rogach AL. Luminescent CdTe nanocrystals as ion probes and pH sensors in aqueous solutions. *Colloids Surf A Physicochem Eng Asp.* 2006;281:40–3.

102. Tang G, Wang J, Lia Y, Su X. Determination of arsenic(III) based on the fluorescence resonance energy transfer between CdTe QDs and rhodamine 6G. *RSC Adv.* 2015;5(2015):17519–25.
103. Terra IAA, Mercante LA, Andre RS, Correa DS. Fluorescent and colorimetric electrospun nanofibers for heavy-metal sensing. *Biosensors.* 2017;7:61.
104. Tomasulo M, Yildiz I, Kaanumalle SL, Raymo FM. pH-sensitive ligand for luminescent quantum dots. *Langmuir.* 2006;22:10284–90.
105. Vaishnav SK, Korram J, Pradhan P, Chandraker K, Nagwanshi R, Ghosh KK, et al. Green luminescent CdTe quantum dot based fluorescence nano-sensor for sensitive detection of arsenic (III). *J Fluoresc.* 2017;27(3):781–9.
106. Vázquez-González M, Carrillo-Carrion C. Analytical strategies based on quantum dots for heavy metal ions detection. *J Biomed Opt.* 2014;19(10):101503.
107. Vincent JB. Quest for the molecular mechanism of chromium action and its relationship to diabetes. *Nutr Rev.* 2000;58(3):67–72.
108. Uddandaro P, Balakrishnan RJ, Ashok A, Swarup S, Sinha P. Bioinspired ZnS:Gd nanoparticles synthesized from an Endophytic Fungi *Aspergillus flavus* for fluorescence-based metal detection. *Biomimetics.* 2019;4:11–20.
109. Wada O, Wu GY, Yamamoto A, Manabe S, Ono T. Purification and chromium-excretory function of low-molecular-weight, chromium-binding substances from dog liver. *Environ Res.* 1983;32:228–39.
110. Wang W, Liu T, Yi D. Detection of mercury ion based on quantum dots using miniaturised optical fibre sensor. *J Eng.* 2019;23:8595–8.
111. Wang X, Hao J, Cheng J, Li J, Miao J, Li R, et al. Chiral CdSe nanoplatelets as an ultrasensitive probe for lead ion sensing. *Nanoscale.* 2019;11(19):9327–34.
112. Wang Z, Xiao X, Zou T, Yang Y, Xing X, Zhao R, et al. Citric acid capped CdS quantum dots for fluorescence detection of copper ions (II) in aqueous solution. *Nano.* 2018;9:32.
113. Wang J, Jiang CX, Yang F, Chen AM, Wang LG, Hu J. Controlled synthesis of a dual-emission hierarchical quantum dot hybrid nanostructure as a robust ratiometric fluorescent sensor. *RSC Adv.* 2016;6:15716–23.
114. Wang J, Jiang C, Wang X, Wang L, Chen A, Hu J, Luo Z. Fabrication of an ‘ion-imprinting’ dual-emission quantum dot nanohybrid for selective fluorescence turn-on and ratiometric detection of cadmium ions. *Analyst.* 2016;141:5886–92.
115. Wang Q, Yu X, Zhan G, Li C. Fluorescent sensor for selective determination of copper ion based on N-acetyl-L-cysteine capped CdHgSe quantum dots. *Biosens Bioelectron.* 2014;54:311–6.
116. Wang J, Zhou X, Ma H, Tao G. Diethyldithiocarbamate functionalized CdSe/CdS quantum dots as a fluorescent probe for copper ion detection. *Spectrochim Acta A.* 2011;81:178–83.
117. Wang Y, Lu J, Tong Z, Huang H. A fluorescence quenching method for determination of copper ions with CdTe quantum dots. *J Chil Chem Soc.* 2009;54:274–7.
118. Wang Y, Ye C, Zhu ZH, Hu YZ. Cadmium telluride quantum dots as pH-sensitive probes for tiopronin determination. *Anal Chim Acta.* 2008;610:50–6.
119. Wegner KD, Hildebrandt N. Quantum dots: bright and versatile in vitro and in vivo fluorescence imaging biosensors. *Chem Soc Rev.* 2015;44:4792–834.
120. Weidenhamer JD, Clement ML. Evidence of recycling of lead battery waste into highly leaded. *Chemosphere.* 2007;67:961–5.
121. WHO. Lead in drinking-water. World Health Organization, Geneva: Background Document for Development of WHO Guidelines for Drinking-Water Quality; 2011.
122. WHO. Copper in Drinking-Water. World Health Organization, Geneva: Background Document for Development of WHO Guidelines for Drinking-Water Quality; 2004.
123. WHO. Chromium in drinking-water, background document for development of WHO guidelines for drinking-water quality. Geneva: World Health Organization; 2003.
124. Wijayawardena MAA, Megharaj M, Naidu R. Bioaccumulation and toxicity of lead, influenced by edaphic factors: using earthworms to study the effect of Pb on ecological health. *J Soils Sediments.* 2017;17:1064–72.

125. Wu L, Guo Q-S, Liu Y-Q, Sun Q-J. Fluorescence resonance energy transfer-based ratiometric fluorescent probe for detection of  $Zn^{2+}$  using a dual-emission silica-coated quantum dots mixture. *Anal Chem.* 2015;87(2015):5318–23.
126. Wu DD, Chen Z, Huang GB, Liu XG. ZnSe quantum dots based fluorescence sensors for  $Cu^{2+}$  ions. *Sens Actuators A Phys.* 2014;205:72–8.
127. Wu CS, Khaing Oo MK, Fan XD. Highly sensitive multiplexed heavy metal detection using quantum-dot-labeled DNazymes. *ACS Nano.* 2010;4:5897–904.
128. Wu HM, Liang JG, Han H. A novel method for the determination of  $Pb^{2+}$  based on the quenching of the fluorescence of CdTe quantum dots. *Microchim Acta.* 2008;161:81–6.
129. Yamamoto A, Wada O, Ono T. Isolation of a biologically active low-molecular-mass chromium compound from rabbit liver. *Eur J Biochem.* 1987;165:627–31.
130. Xi LL, Ma H-B, Tao GH. Thiourea functionalized CdSe/CdS quantum dots as a fluorescent sensor for mercury ion detection. *Chin Chem Lett.* 2016;27:1531–6.
131. Xie T, Zhong X, Liu Z, Xie C. Silica-anchored cadmium sulfide nanocrystals for the optical detection of copper(II). *Microchim Acta.* 2020;187:323.
132. Xia Y-S, Zhu C-Q. Use of surface-modified CdTe quantum dots as fluorescent probes in sensing mercury (II). *Talanta.* 2008;75:215–21.
133. Xie HY, Liang J, Zhang ZL, Liu Y, He ZK, Pang DW. Luminescent CdSe-ZnS quantum dots as selective  $Cu^{2+}$  probe. *Spectrochim Acta A.* 2004;60:2527–30.
134. Xing XW, Wang DM, Chen Z, Zheng BD, Li BH, Wu DD. ZnTe quantum dots as fluorescence sensors for the detection of iron ions. *J Mater Sci-Mater Electron.* 2018;29:14192–9.
135. Xu S, Xu S, Zhu Y, Xu W, Zhou P, Zhou C, et al. A novel upconversion, fluorescence resonance energy transfer biosensor (FRET) for sensitive detection of lead ions in human serum. *Nanoscale.* 2014;6:12573–9.
136. Zhang Y, Xiao J-Y, Zhu Y, Tian L-J, Wang W-K, Zhu T, et al. Fluorescence sensor based on biosynthetic CdSe/CdS quantum dots and liposome carrier signal amplification for mercury detection. *Anal Chem.* 2020;92:3990–7.
137. Zhang L, Zhu J, Ai J, Zhou Z, Jia X, Wang E. Label-free G-quadruplex-specific fluorescent probe for sensitive detection of copper(II) ion. *Biosens Bioelectron.* 2013;39:268–73.
138. Zhang F, Lees E, Amin F, Gil PR, Yang F, Mulvaney P, Parak WJ. Polymer-coated nanoparticles: a universal tool for biolabelling experiments. *Small.* 2011;7(22):3113–27.
139. Zhang F, Ali Z, Amin F, Riedinger A, Parak WJ. In vitro and intracellular sensing by using the photoluminescence of quantum dots. *Anal Bioanal Chem.* 2010;397:935–42.
140. Zhang L, Xu C, Li B. Simple and sensitive detection method for chromium (VI) in water using glutathione-capped CdTe quantum dots as fluorescent probes. *Microchim Acta.* 2009;166:61–8.
141. Zhang Y, Zhang H, Guo X, Wang H. L-cysteine-coated CdSe/CdS core-shell quantum dots as selective fluorescence probe for copper(II) determination. *Microchem J.* 2008;89:142–7.
142. Zhao Q, Rong X, Chen L, Ma H, Tao G. Layer-by-layer self-assembly xylenol orange functionalized CdSe/CdS quantum dots as a turn-on fluorescence lead ion sensor. *Talanta.* 2013;114:110–6.
143. Zhao Q, Rong X, Ma H, Tao G. Dithizone functionalized CdSe/CdS quantum dots as turn-on fluorescent probe for ultrasensitive detection of lead ion. *J Hazard Mat.* 2013;250-251:45–52.
144. Zhao T, Hou X, Xie YN, Wu L, Wu P. Phosphorescent sensing of  $Cr^{3+}$  with protein-functionalized Mn-doped ZnS quantum dots. *Analyst.* 2013;138:6589–94.
145. Zhong W, Zhang C, Gao Q, Li H. Highly sensitive detection of lead(II) ion using multicolor CdTe quantum dots. *Microchim Acta.* 2012;176:101–7.
146. Zhou ZQ, Yang LY, Liao YP, Wu HY, Zhou XH, Huang S, et al. Mn:ZnSe quantum dots-based turn-on fluorescent sensor for highly selective and sensitive detection of  $Cd^{2+}$ . *Anal Methods.* 2020;12:552–6.
147. Zhou ZQ, Yan R, Zhao J, Yang LY, Chen JL, Hu YJ, Jiang FL, Liu Y. Highly selective and sensitive detection of  $Hg^{2+}$  based on fluorescence enhancement of Mn-doped ZnSe QDs by  $Hg^{2+}$ -Mn<sup>2+</sup> replacement. *Sens Actuators B Chem.* 2018;254:8–15.

148. Zhou Y, Zhu CY, Gao XS, You X-Y, Yao C. Hg<sup>2+</sup>-selective ratiometric and “off–on” chemosensor based on the Azadiene–pyrene derivative. *Org Lett.* 2010;12(2010):2566–9.
149. Zhu J, Chang H, Li J-J, Li X, Zhao J-W. Using silicon-coated gold nanoparticles to enhance the fluorescence of CdTe quantum dot and improve the sensing ability of mercury (II). *Spectrochim Acta A.* 2018;188:170–8.
150. Zhu J, Zhao Z-J, Li J-J, Zhao J-W. CdTe quantum dot based fluorescent probes for selective detection of Hg(II): the effect of particle size. *Spectrochim Acta A.* 2017;177:140–6.
151. Zhu H, Yu T, Xu H, Zhang K, Jiang H, Zhang Z, et al. Fluorescent nanohybrid of gold nano-clusters and quantum dots for visual determination of lead ions. *ACS Appl Mater Interfaces.* 2014;6:21461–7.

# Chapter 15

## Photoelectrochemical Ion Sensors



Alka Pareek and Pramod H. Borse

### 15.1 Introduction

Recent decades have witnessed a tremendous increase in the environmental pollution due to the fast urbanisation and unstoppable industrial development. The progress of mankind has thus led to an unwanted discharge of various pollutants into the environment in the form of pesticides, heavy metal-ions, phenolics and different toxins, etc. [83]. The timely detection and sensing of these environmental pollutants is crucial, as they are fatal to the living-being's health and their effects on the whole ecosystem. It is important to recall specifically, that such pollutants are dangerous owing to their refractory behaviour, toxic nature and because of the threat of their entry in the food chain [81].

#### 15.1.1 Photoelectrochemical Sensors

Sensors are generally separated into two classes: chemical sensors and biosensors. A chemical sensor is defined as a device that transforms the chemical interactions between the active species and analyte into a useful electrical (readable) signal [31]. On the contrary, biosensors employ biomolecules such as enzymes, nucleic acids, antibodies, or oligonucleotides; as the biological recognition elements for analysis [105]. Various traditional sensing methods are prevalent nowadays including fluorescence spectroscopy, absorption/emission spectrometry, mass spectrometry, liquid chromatography and gas spectrometry [87, 116]. These advanced methods offer

---

A. Pareek · P. H. Borse (✉)  
International Advanced Research Centre for Powder Metallurgy and New Materials (ARCI),  
Hyderabad, Telangana, India  
e-mail: [phborse@arci.res.in](mailto:phborse@arci.res.in)

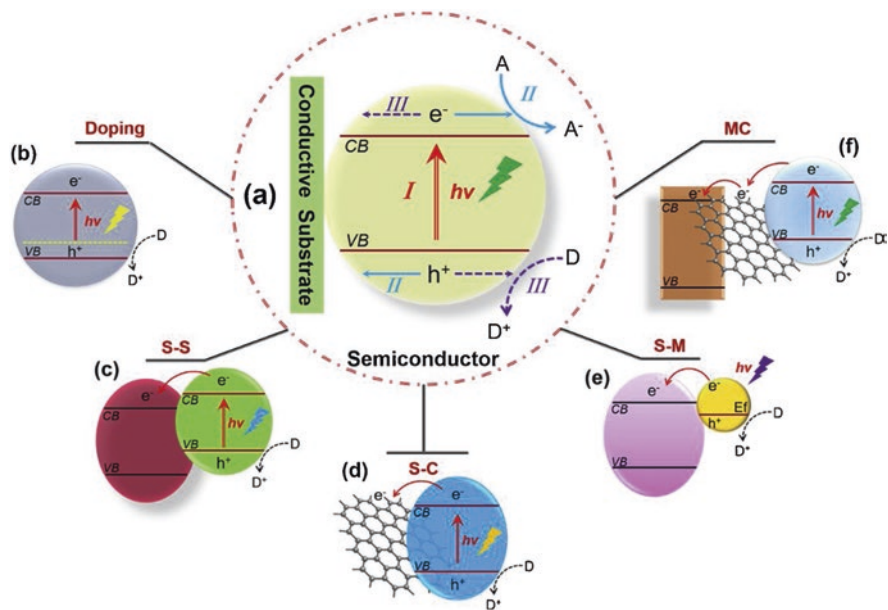


highly accurate and reliable outcome, but they require costly and sophisticated instrumentation, those are linked to the high maintenance and their operation by the skilled experts. With the discovery of photoelectric effect in 1839 by Becquerel, photoelectrochemistry has predominantly influenced various technical fields like photovoltaics, photocatalysis, fuel cell, and sensors [40, 71, 72]. Recently, photoelectrochemical (PEC) sensor has emerged as a promising sensing strategy owing to its low cost and remarkable sensitivity for the analyses of the chemical and biological species [115]. There are numerous reports on the PEC sensing research, and the interest among the research community is increasing day-by-day, indicating its importance in the field of analytical chemistry [27]. Photoelectrochemical (PEC) technique combines the light sensitivity of the semiconductors with their electrochemical response towards the species, that in turn validates the detection of the chemical species [131]. Background noise in the PEC sensors can be dramatically reduced to achieve higher sensitivity as compared to the sophisticated sensors, because PEC sensors employ light-photons as a source, and the photocurrent as detected signal. Moreover, it offers a fast sensor response, and an ease of miniaturisation along with the cost-effective module. Further, the associated charge transfer processes in the PEC device are dependent on two main components [78]: (1) photoactive electrode and (2) the kinetics of the redox-species at electrode/electrolyte interface of the sensor. These parameters basically control the output photoelectric signal, while analysing the targeted species thus rendering it a wide detection range [132]. The main component of these devices is the photoactive material which decides the sensitivity of sensor for specific analyte, magnitude of signal depending on the efficient charge separation. Thus, PEC sensors which exhibit high potential for analyses of chemical and biological species, display a very efficient detection mechanism. Such detection is concluded from the variation in the photocurrent/photopotential. Specifically, the photocurrent variation is induced by chemical interactions between analyte and the photoactive material. The kinetics of the charge transfer involved in such chemical interactions, result in yielding a measurable output signal (photocurrent) between photoactive material and counter electrode. In principle, engineering of the photoactive sensor material is very important as it controls the electron-hole separation and charge transfer processes those in turn yield an efficient PEC sensor. Specifically, the “photon-to-electricity” conversion efficiency of PEC the sensor [125] is detrimental in design of efficient sensor. As discussed above, the species to be detected, induce photoexcitation process affecting the optical and electrochemical signals in PEC sensor.

In recent years, there have been numerous published reports, and a rapid growth of PEC sensing research is evident. There have been several reviews on the photoactive materials, type of analysis (like PEC DNA biosensors, PEC immunoassays and PEC enzymatic biosensors), the modes of sensing and their application for quantitative detection [128]. This book chapter highlights a general overview of the PEC sensors including its basic principle, current status, recent development in the photoactive materials and the application of PEC sensors for metal detection.

### 15.1.2 Principle of Photoelectrochemical Sensor

PEC sensor is comprised of a set of electrodes in the vicinity of electrolyte. Among these electrodes, the photosensitive semiconductor working electrode (WE) has a capacity to absorb photons of wavelength corresponding to semiconductor bandgap. After illumination of photoelectrode, electrons and holes are generated at the interface of electrode and analyte [1]. The photogenerated electrons are transferred from the semiconductor WE surface to the counter electrode (CE) through an external circuit that generates a photocurrent as output signal. On the other hand, the holes participate in the oxidation process thereby completing the total reaction. Further, there are four significant steps involved in the working of a typical PEC sensor: (1) photon absorption by the material; (2) photo-induced charge generation, that is, electron-hole (e-h) pairs, in the photoactive material (Fig. 15.1a(I)); (3) charge separation, that is, transfer of the excited electrons to counter electrode (see Fig. 15.1a(II,III)), while holes, combined with the electron donors; and (4) photocurrent generation, *via.* electron transfer to the counter electrode (current) this results as sensor output [83]. Accordingly, PEC sensing involves a redox mechanism [7].



**Fig. 15.1** Schematic of (a) basic principle of charge-generation and charge-separation in the semiconductor-based PEC sensor; (b) doped semiconductor; (c) semiconductor-semiconductor heterojunction; (d) semiconductor-carbon heterojunction; (e) semiconductor-metal heterojunction; (f) multicomponent heterojunction. (Reproduced with permission from Shi et al. [83]. Copyright 2019:Elsevier Publishing)

## 15.2 Progress in Photoactive Sensing Materials

Photoactive material plays an important role in the field of PEC sensing as it absorbs light and converts chemical or biological information into electrical signals. Various materials like metal-chalcogenides, metal-oxides and organic molecules and polymers have been used as photoactive materials. This section includes a discussion of PEC photoactive materials that can be prepared by various strategies, like doping (Fig. 15.1b), semiconductor–semiconductor (Fig. 15.1c), semiconductor–carbon (Fig. 15.1d), semiconductor–metal (Fig. 15.1e), multicomponent heterojunctions (Fig. 15.1f).

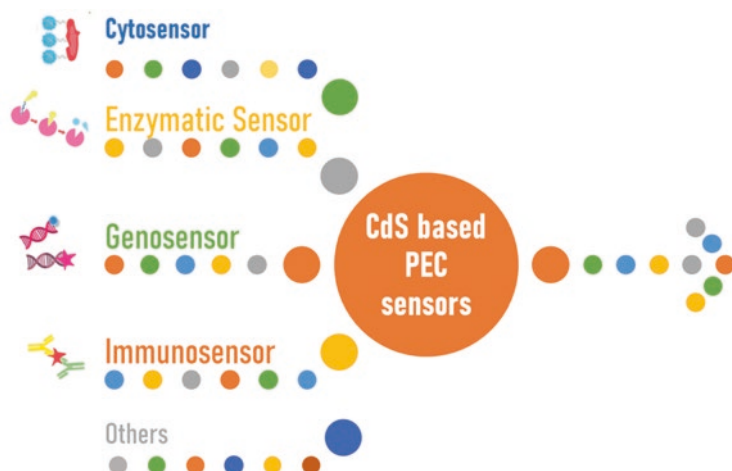
### 15.2.1 Metal Chalcogenides

Chalcogenides are a prominent class of materials, owing to their exceptional optoelectronic properties. They find potential applications in various fields – viz. thin-film photovoltaics, nano-photodetectors, lasers, phosphors, sensors, and other optoelectronic devices. Typically, they exhibit suited wide-range of bandgap that encompasses both, wide-bandgap (1.5–3.5 eV) and narrow-bandgap (0–1.5 eV) materials. Thus, they are very useful as photoconductors, ultrasonic transducers, and Hall effect devices [39]. Especially, Cd chalcogenides have been implemented in the field of optics, electronics, optoelectronics, photovoltaics, photoelectrochemistry and sensors [18]. These optical materials, are also very useful as they display (i) optical transparency in IR region, (ii) high linear and non-linear index of refraction, and (iii) very significant intensive luminescence properties [66], required in diverse applications.

#### 15.2.1.1 CdS

Cd chalcogenides, like CdS, are the most studied material for photovoltaics, solar cell absorber layer, PEC cell and sensor applications. It exhibits a low band gap of 2.54 eV, as well as displays a very favourable photoconductivity. Interestingly, it can be easily synthesised [22]. Figure 15.2 shows the schematic illustration of various applications of CdS-based PEC sensors [34], in reference to chemical and biological detection.

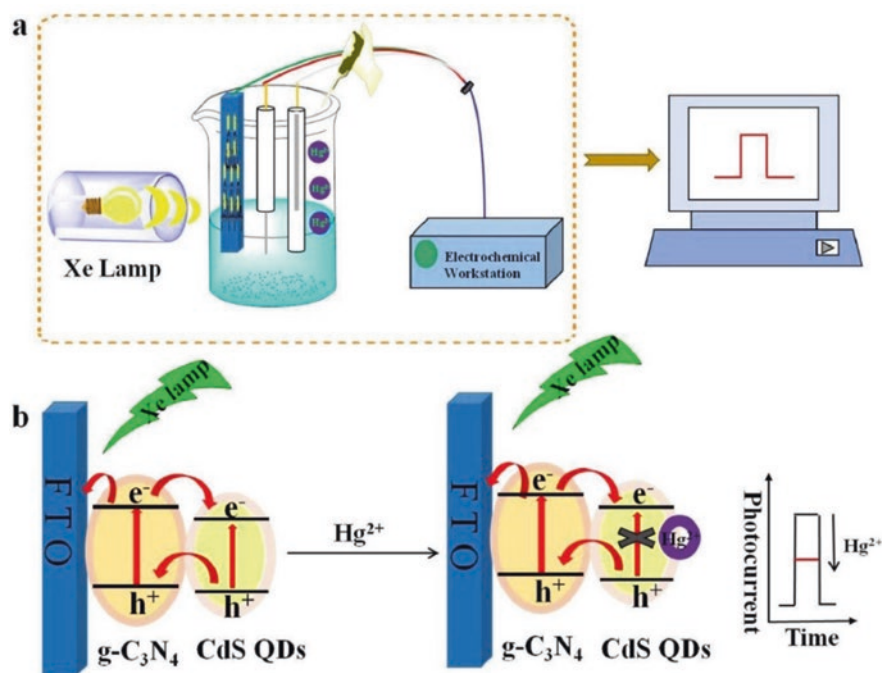
There have been several studies on property improvement of this chalcogenide *via*. its property modulation by (i) surface modifications [53]; (ii) heterostructure formation with semiconductors [25]; (iii) heterostructure formation with metals; (iv) heterostructure formation with carbon-based materials [36]; and (v) heterostructure formation with noble metals [11]. Apart from the above reports, some reports on the superior performance of hexagonal CdS as compared to the Cubic phase of CdS [49] are also known. They attributed the superior performance to the



**Fig. 15.2** Schematic illustration of various applications of CdS-based PEC sensors for chemical and biological detection

high crystallinity of the hexagonal phase (with low defects density), which in turn reduced the unwanted charge recombination process. Li et al. [53] proved this fact by synthesis of hexagonal three-dimensional CdS nanostructures and compared its performance with cubic CdS nanoparticles. Additionally, this has also yielded a high absorption of light, large surface area and efficient charge transfer in hexagonal CdS. Further, Bao et al. [6] fabricated CdS nanorods those displayed wide range of light absorption and output photocurrent. Wang et al. [97] synthesised novel nanocomposite of CdS decorated ZnO-graphene oxide for  $\text{Cu}^{2+}$  detection. The study reported a low detection limit of  $0.03 \mu\text{M}$  and wide linear concentration range from  $0.2 \mu\text{M}$  to  $1 \text{mM}$  with high selectivity and stability. Cao et al. [9] reported the CdSe quantum dots co-sensitised ZnO-CdS nanostructure for  $\text{Pb}^{2+}$  ions detection. The novel structure displayed a linear relation between ‘photocurrent variation’, versus the ‘logarithm of  $\text{Pb}^{2+}$  concentration’ yielding a detection limit of  $3.4 \times 10^{-10} \text{M}$ . Yu et al. [117] studied the dual Z-scheme CdS/ $\text{Bi}_2\text{S}_3$ / $\text{BiOCl}$  composites for highly sensitive detection of alkaline phosphate, that has exhibited detection limit of  $0.06 \text{U L}^{-1}$ . Mao et al. [62] reported a heterojunction of polymer dots and CdS quantum dots to form a molecularly imprinted polymer photoelectrochemical (MIP-PEC) sensor. The MIP-PEC sensor showed a linear range from  $0.01$  to  $1000 \text{ng mL}^{-1}$  with a detection limit of  $6.5 \text{pgmL}^{-1}$  for  $\alpha$ -Solanine. CdS sensitised  $\text{BiVO}_4/\text{GaON}$  composite was prepared to constitute a sensitive sensor for the photoelectrochemical immunoassay of procalcitonin, establishing a linear relationship in range of  $0.1 \text{pgmL}^{-1}$ – $50 \text{nM L}^{-1}$ , and the detection limitation of  $0.03 \text{pgmL}^{-1}$  [45]. Wu et al. [107] demonstrated a highly sensitive photoelectrochemical sensing of copper (II) ions by pulsed electrodeposition of CdS on ZnO nanorods for detection of  $\text{Cu}^{2+}$  ions. Wang et al. [103] fabricated a visible-light active photoelectrochemical sensor based on CdS quantum dots, graphene and molecularly imprinted polypyrrole (MIP) on an

FTO electrode. The heterostructure sensor was used for sensing of 4-aminophenol and exhibited a detection limit ( $3S/N$ ) of  $2.3 \times 10^{-8} \text{ molL}^{-1}$ . Wu et al. [106] synthesised a CdS/Bi<sub>2</sub>O<sub>2.33</sub> direct Z-scheme heterojunction for photoelectrochemical sensing of Hg<sup>2+</sup> ions. Similarly, heterojunction of CdS with ZnO, TiO<sub>2</sub>, WO<sub>3</sub> and Fe<sub>2</sub>O<sub>3</sub> were fabricated and showed remarkable sensing capabilities for the detection of various entities [20, 82, 92, 99]. Carbon nitride (g-C<sub>3</sub>N<sub>4</sub>) sensitised with CdS QDs was developed as an efficient photoactive material for PEC tetracycline (TET) determination [56]. Similarly, the band-gap alignment of the CdS/RGO/ZnO heterostructure in the PEC bioanalysis of glutathione (GSH) demonstrated excellent performance and enhanced the mobility of electron–holes [129]. Moreover, Zhang et al. [122] exploited a dual operation of PEC sensing for Cd<sup>2+</sup> and Cu<sup>2+</sup> ions using Zn-doped CdS-photoactive materials. Au-decorated CdS nanoparticles were explored for detection of Cu<sup>2+</sup> ions, which shows improved performance due to the plasmonic effect [35]. Li et al. fabricated C<sub>3</sub>N<sub>4</sub>@CdS QDs for sensitive detection of Hg<sup>2+</sup> ions and demonstrated good linear range of 20–550 nM, with a detection limit of 12 nM [48]. The group elaborated on the charge transfer process involved in the heterostructure-based sensor and explained that internal electric field formed between the g-C<sub>3</sub>N<sub>4</sub> and CdS monolayers suppresses the e-h recombination and thus improves the photocurrent (as shown in Fig. 15.3). Wang et al. studied the



**Fig. 15.3** Schematic diagram showing (a) working of PEC sensor and (b) charge-transfer process involved in g-C<sub>3</sub>N<sub>4</sub>@CdS based PEC sensor. (Reprinted with permission from Li et al. [48]. Copyright 2020: Elsevier Publishing)

CdS-sensitised hydrogenated TiO<sub>2</sub> nanorod arrays and demonstrated its linear detection range from 0.8 nM to 82.0 μM, with the detection limit of 0.3 nM for copper ions detection [100]. Liu et al. [55] constructed a novel CuS/CdS *p-n* junction for the detection of copper ions. The sensor demonstrated a low detection limit of 0.1 nM, and a detection range from 0.2 nM to 60 μM, owing to the formation of *p-n* junction between CuS and CdS and the component transformation of CdS to Cu<sub>x</sub>. Ibrahim et al. [33] reported the CdS nanorods modified with Au and graphene quantum-dots-based PEC sensor for the detection of copper-ions and observed a detection limit of 2.27 nM. In a similar kind of work, TiO<sub>2</sub> nanotube arrays decorated RGO/CdS electrodes showed a linear detection range from 0.1 μM to 10 mM, and a detection limit of 0.002 μM [47]. Li et al. [51] explored the Au-CdS composite thin films for PEC sensing of Hg<sup>2+</sup> ions that exhibited a low limit of detection of 2.5 μM.

### 15.2.1.2 CdSe

The next important semiconductor material under the present category is CdSe. It possesses a bandgap of 1.7 eV. Its conduction band minimum is higher than that of CdS whereas valance band maximum is also higher than CdS. Li et al. [52] fabricated CdS/CdSe core/shell nano-wall arrays where the morphology was controlled via precursor solution concentration. Such core-shell nanostructures showed extended light absorption throughout visible range, and an improved photocurrent that increased from original 3.78 to of 8.3 mA/cm<sup>2</sup>. Similarly, He et al. [26] synthesised CdSe QDs decorated ZnIn<sub>2</sub>S<sub>4</sub> nanosheets for PEC sensing of adenosine triphosphate. The heterojunction triggered “OFF-ON” signalling strategy and demonstrated broad linear range of detection from 0.2 pM to 1 μM, with a detection limit of 0.1 pM. Zhong et al. [135] studied the dual photocurrent signal-based PEC immunosensor fabricated by MIL-101(Cr) and CdSe QDs-based composite electrode. The electrode depicted the limit of detection of 0.082 and 0.054 ng mL<sup>-1</sup>, when it is used as an anode and cathode, respectively. Dashiton et al. [12] reported polydopamine-coated CdS/CdSe/Zn heterojunction for the detection of L-phenylalanine. The interface between the Zn marigold flower layer and CdS/CdSe heterojunction as well as n-type characteristics of polydopamine improved the light trapping and absorption in the visible range and reduced the charge carrier recombination that boosted the performance of PEC sensor. The heterostructure exhibited wide linear range of 0.005–2.5 μM and 2.5–130 μM and a low detection limit of 0.9 nM. Li et al. [46] employed CdSe QDs and TiO<sub>2</sub> complex for thrombin detection, which depicted exceptional performance with a wide linear range from 1.0 to 100.0 nM and detection limit of 0.331 fM. Meng et al. [65] reported DNA-linked CdSe quantum dots/amino-functionalised graphene quantum dots for DNA assay. The “Z-scheme” system has shown a linear range of 1 aM–100 pM with detectable limit of 0.1 aM. CdSe quantum dots sensitised Ho<sup>3+</sup>/Yb<sup>3+</sup>-TiO<sub>2</sub> system was explored by Hao et al. [25] to construct a novel label-free PEC immune sensor for detection of *Vibrio parahaemolyticus*. These immune sensors demonstrated not only high

stability but also a short detection time over a wide detection range of 102–108 CFU/mL. Cao et al. [9] studied CdSe/CdS/ZnO system for detection of  $\text{Pb}^{+2}$  ions and reported a wide linear range, good selectivity, and high sensitivity with a detection limit of  $3.4 \times 10^{-10}$  Mb. Xie et al. [109] reported CdSe@BiVO<sub>4</sub> co-sensitised TiO<sub>2</sub> nanorods for detection of Carcinoembryonic Antigen, that demonstrated linear detection range from 0.01 to 50 ng mL<sup>-1</sup> with detection limit of 0.5 pg mL<sup>-1</sup>. The modification of electrode extended the absorption range of TiO<sub>2</sub> from ultraviolet to visible light region. Further, the suitable alignment of energy levels among TiO<sub>2</sub>, CdSe and BiVO<sub>4</sub> accelerates the charge-separation and transfer of the photogenerated ions. Fan et al. explored CdSe nanoparticles sensitised La-doped TiO<sub>2</sub> composites for the quantitative detection of the prostate-specific antigen (PSA). These composite-based sensors demonstrated the detection of PSA in the range of 0.05–100 pg mL<sup>-1</sup> with a detection limit of 17 fg mL<sup>-1</sup> [15]. Leng et al. [44] reported MoSe<sub>2</sub>/CdSe heterojunction exhibiting improved visible light absorption and a low recombination of photogenerated carriers. Such electrodes were used in PEC immunoassay for clinical diagnosis and found to exhibit a linear detection range, from 0.0001 to 100 ng/mL with a detection limit of 28 fg/mL. Qin et al. [75] synthesised CdSe/TiO<sub>2</sub> nanotube array microsensor for ultrasensitive in situ detection of dopamine with a detection limit of 16.7 μM. There are many other multicomponent systems made by using CdSe QDs- like CdSe/CdS/Pt/TiO<sub>2</sub> nanotube array, CdSe quantum dot-functionalised TiO<sub>2</sub>nanohybrids, Mn:CdSe/Bi<sub>2</sub>WO<sub>6</sub>/CdS, TiO<sub>2</sub>/CdS/CdSe, DNA–CdSe/TiO<sub>2</sub>, for the efficient PEC sensors with high sensitivity [16, 68, 70, 110, 113].

### 15.2.1.3 CdTe

One-dimensional or nanostructured CdTe is a promising candidate for biosensing and optical applications due to its narrow band gap of 1.5 eV. Additionally, it also exhibits significant stability, suitable electrical conductivity, and shows an ease of forming the high surface area nanostructures [61]. Qin et al. [76] reported CdTe/rGO/ITO photoelectrode to detect trace catechol that exhibited a wide linear range, low detection limit, and high sensitivity. Roushani et al. [80] utilised CdTe quantum dots (QDs) for selective detection of dopamine in the presence of ascorbic acid and uric acid. In a potential window of 0–350 mV, which corresponds to an electroactivity of only dopamine. This showed a detection limit of  $8.27 \times 10^{-9}$  M and  $1.30 \times 10^{-9}$  M by using square wave voltammetry and amperometry, respectively. Pang et al. [69] explored aligned ZnO@CdTe core-shell nanocable arrays/carboxylated g-C<sub>3</sub>N<sub>4</sub> to detect proprotein convertase subtilisin/kexin type 6. The photoelectrode demonstrated a linear detection range from 10 pg/mL to 20.0 ng/mL with a detection limit of 2 pg/mL. Cai et al. [8] constructed CdTe/CdS co-sensitised TiO<sub>2</sub> nanotube array structure for the operation of label-free PEC immunosensor to detect octachlorostyrene. The PEC immunosensor has shown high sensitivity with a limit of detection of 2.58 pM, and a linear range from 5 pM to 50 nM. Some groups studied Ag nanoparticles coupled with CdTe quantum dots and reported high specificity

and sensitivity for PEC sensor [90, 127]. Shi et al. [37] studied ultrasensitive PEC apta-sensor by designing CdTe QDs on MoS<sub>2</sub>-CdS:Mn nanocomposites for Pb<sup>2+</sup> detection. The fabricated PEC sensor demonstrated a low detection limit of 16.7 fM owing to the formation of *G-quadruplex* structure. Guo et al. [22] prepared a CdTe-BiOBr heterostructure that followed Z-scheme electron transfer and exhibited a linear range from 10 to 1500 pM with a low detection limit of 9.25 pM. Peng et al. [74] reported CdTe and nickel tetra-aminophthalocyanine covalently linked with graphene oxide for the detection of curcumin. The PEC sensor with composite electrode has recorded linear detection range from 0.25 to 100 μM with a detection limit of 12.50 nM.

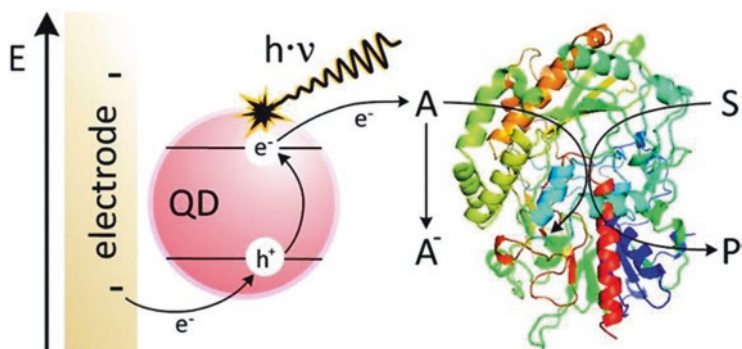
#### 15.2.1.4 Other Chalcogenides

Zinc chalcogenides systems were also studied for the fabrication of PEC sensors, owing to their varied band gaps that renders them light absorption under ultraviolet and visible light region. Wang et al. [101] studied the effect of ITO/ZnS-HgS electrodes for detection of Hg<sup>2+</sup> ions that demonstrated a linear detection range from  $1 \times 10^{-11}$  to  $1 \times 10^{-6}$  M, with a detection limit of 2 pM. Hollow photoelectrodes of ZnS-CdS nanocage were synthesised and utilised in a PEC sensor for sensitive detection of oxytetracycline (OTC). The PEC sensor has shown linear relationship with OTC concentration from 1 nmol L<sup>-1</sup> to 3 μmol L<sup>-1</sup> with detection limit of 0.10 nmol L<sup>-1</sup> [3]. Zhang et al. [120] fabricated bead chain-like Ag<sub>2</sub>S integrated with ZnS coated onto the ITO for the analysis of mercury. The electrodes depicted efficient performance with concentrations ranging from 0.010 to 1000 nM and a detection limit of about 1.0 pM. Xu et al. [111] employed the assembly of Au/ZnS nanoparticles as electrode for detection of copper-ions. The PEC sensor exhibited linear detection in range from 1 nM to 1 μM with detection limit of 0.5 nM. Similarly, some researchers have explored ZnSe hybrid nanostructured electrodes for application in PEC sensors. For example, Au/ZnSe/ZnO heterojunction and ZnSe-CdSe/SiO<sub>2</sub> core-shell electrodes were used for the detection of ascorbic acid and copper ions [5, 98]. ZnSe-sensitised ZnO heterostructures were reported by Sunaina et al. [91] for photo-detector applications. The ZnO-ZnSe heterostructures-based photo-detector generated fast rise and decay time of 23 and 80 ms, respectively, and a high photo-responsivity of 91.25 mA W<sup>-1</sup>.

#### 15.2.1.5 II-VI Semiconductor-Based Quantum Dots

Quantum dots (QDs) of II-VI semiconductors like CdS, CdSe, HgS, ZnS and ZnSe [14, 67] have been extensively explored for numerous decades owing to their unique physical and chemical properties. When light is incident on the semiconductor QDs, it produces electrons and holes in their conduction band and valence band, respectively [104]. The size-dependent bandgap tuning, large surface area, fluorescence emission, quantum confinement effect and unique surface chemistry make QDs





**Fig. 15.4** Schematic illustration showing charge transfer process involved after illuminating a QD electrode. (Reprinted with permission from Tanne et al. [93]. Copyright 2011: American Chemical Society)

very suitable for biological labelling [64]. The steps involved in the charge-transfer process of QDs are shown in Fig. 15.4. In this context, CdSQDs were explored in PEC sensors by Grinyte et al. [21] for  $\text{Cu}^{2+}$  ions detection, but it demonstrated poor performance due to higher rate of recombination of charge carriers. Soon after that many efforts were made to enhance the performance of QDs by surface modification or other material integration. Wang et al. [102] developed a visible PEC sensor by using CdS QDs decorated B-TiO<sub>2</sub> NR arrays for sensitive detection of cellular H<sub>2</sub>S. There are few reports suggesting the construction of graphene-assembled CdS QDs, that improved the efficiency of PEC sensors dramatically [86, 124]. In a similar work, graphene-like g-C<sub>3</sub>N<sub>4</sub>/CdS QD were synthesised to be used as a photoactive material to enhance the output photocurrent [133]. Mn-doped CdS (CdS:Mn) QDs were fabricated by Wu et al. [108] for cytosensing that increased the performance of sensors as compared to the undoped counterparts, owing to introduction of d-bands with Mn<sup>2+</sup> ions. There were few new ideas devised to further improve the performance of QDs as sensor material like “adding metal ions to QDs” and “coupling CdS:Mn QDs with g-C<sub>3</sub>N<sub>4</sub>” [121]. There are many studies focused on different combination of QDs with metal and semiconductor materials, yielding very potential for various sensing opportunities [127, 131].

## 15.2.2 Other Materials

### 15.2.2.1 Metal Oxides

Metal oxides are very important class of materials for various sensing and solar applications due to their favourable band-gap alignment, ease of synthesis, stability, eco-friendliness, optoelectronic nature, and chemical properties [118]. Moreover, these properties can be easily regulated by synthesis condition that can be controlled by size, surface [89] features, morphology, roughness etc. Among metal oxides,

TiO<sub>2</sub> and ZnO have received enormous interest in the construction of PEC sensors. TiO<sub>2</sub> is one of the most studied materials in various fields since the pioneering work of Fujishima in 1972 [19]. Due to its remarkable properties like low density, higher surface area, large strength-to-weight ratio, biocompatibility, excellent catalytic efficiency, higher stability and corrosion resistance; TiO<sub>2</sub> is used in wide sectors including photocatalysis, solar cells [57, 88, 89], PEC hydrogen generation [79], batteries [23], sensors [4], biological and chemical coatings and drug delivery [32]. But due to wide band gap of these metal-oxides, their absorbance edge lies in the UV region and photosensitivity is limited to 5% of solar spectrum. Moreover, biological systems are sensitive to exposure of UV light. The holes generated by the illumination of these semiconductors have strong oxidising power, that can cause undesired damage to biomolecules [13]. Therefore, various strategies like nanostructuring, doping and formation of heterostructure, have been adopted to improve the visible activity and safety of biological system [77].

ZnO is another most studied metal oxide, that is more preferred in bioanalysis owing to higher electron mobility, large exciton temperature, biocompatibility and photocatalytic nature [41]. Various ZnO nanostructures like nanorods, nanotubes, nanowires, nanoflowers, hollow nanospheres, etc., have been studied [27].

Recently, many other metal-oxides are also being studied like SnO<sub>2</sub>, WO<sub>3</sub>, PbO, CuO, Fe<sub>2</sub>O<sub>3</sub>, Co<sub>3</sub>O<sub>4</sub>, BiVO<sub>4</sub>, etc. [13]. Especially, SnO<sub>2</sub>-employed PEC sensors are gathering special attention due to its high electron mobility, low cost, eco-friendliness, high thermal and chemical stability [114].

### 15.2.2.2 Carbon-Based Materials

Semiconductor material usage in the PEC sensors is limited by their conductivity, hole mobility, strong oxidation capacity (harmful for biomolecules), wide band-gaps, and instability due to photocorrosion [58]. Carbon-based nanomaterials like graphene, fullerenes (C60), graphene oxide, etc., have been studied extensively in the field of photovoltaics, fuel cells, water splitting, and sensors owing to their absorption band covering whole UV-Vis spectrum, strong electron-accepting capacity, long-lived triplet excited state, high photon-electron conversion efficiency, and tunable photocurrent responses controlled with various functional materials [33, 48]. Hu et al. [29] demonstrated carboxylated multiwalled carbon nanotube (MWNT)-Congo red-C60 material for detection of carcinoembryonic antigen. Recently, graphene quantum dots (GQDs) were synthesised by reducing graphite layer into a mono-atomic layer (lattice distance of 0.23 nm) planar sheet of graphite [134] and used as fluorophores in bioimaging showing their light reception ability. In a similar work, GQDs/Si NWs were used to detect microcystin-LR in a PEC immunosensor [94]. The study revealed that GQD/SiNW electrode exhibited better PEC performance than SiNWs in the linear range from 0.1 to 10 μM, with a limit of detection of 0.055 μM. Among carbon-based materials, g-C<sub>3</sub>N<sub>4</sub>, has appeared as a significant polymeric semiconductor material in PEC sensors. It has a band gap of 2.7 eV and shows some remarkable qualities like desirable electronic structure, outstanding biocompatibility and low toxicity.

### 15.2.2.3 Dichalcogenides

Among various materials, transition metal dichalcogenides ( $\text{MoS}_2$ ,  $\text{WS}_2$ ) play significant role as photocatalytic material owing to their electrical conductivity, high catalytic activity, tunable bandgap, high surface area and favourable crystal structure [38].  $\text{MoS}_2$  possesses a highly desirable lamellar structure, high carrier mobility of  $>30,000 \text{ cm}^2 \text{ V}^{-1} \text{ s}^{-1}$  with small bandgap of 1.2–1.9 eV, which makes it suitable for its application in PEC sensors [38]. On the other hand,  $\text{WS}_2$  possessing a bandgap of 1.35–2.05 eV, in the form of composites, are also studied extensively in PEC sensors [60].

### 15.2.2.4 Hybrid Materials

Dual-sensitised materials are also proved to be more beneficial as compared to single-sensitised structures owing to their maximum light absorption, fast charge transfer and higher photocurrent generation [54]. For example,  $\text{TiO}_2/\text{CdS}$  and  $\text{TiO}_2/\text{CdSe}$  electrodes demonstrated power conversion efficiency of 1.15% and 1.24%, respectively, whereas co-sensitisation of CdS and CdSe, both exhibited 2.90% [42, 43, 89] of efficiency. Metal nanoparticles also known as plasmonic particles, when combined with metal oxide systems, introduces new functionalities thereby imparting enhanced physical and chemical properties to the hybrid structure [13]. The higher performance of the metal-modified materials could be attributed to their enhanced absorption due to surface plasmon resonance, the formation of Schottky barrier that facilitates suited charge separation, the increase in the conductivity by virtue of metal nanoparticles, and exciton-plasmon interaction, which is favourable for PEC sensing.

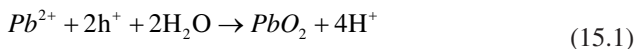
## 15.3 Applications of PEC Sensors-Detection of Heavy Metal Ions

Metal-ions are known to be beneficial as well as dangerous for the human body and ecosystem, depending on their concentration [126]. Generally, metal-ions in trace levels are indispensable for cellular functions and natural systems, but existence above certain limit, causes dysfunctional cytological/physiological effects [130]. Heavy metals, having atomic weights between 63.5 and 200.6  $\text{g mol}^{-1}$  and a specific gravity of more than 5  $\text{g cm}^{-3}$ , are regarded as highly toxic. For example, Cu, Fe, Mn, Co and Zn [95] are essential for basic biological activities in low concentrations, whereas causes toxicity in excess, on the other hand- Pb, Hg, Cr, Cd and As [73] are dangerous even at low concentrations. These categories of heavy metals are non-biodegradable, and their accumulation poses threat to the biosphere. So, their detection and removal from the natural system is a significant task [63]. In this

section, some of the heavy metals, their properties and side effects are discussed, with specific emphasis on PEC-based detection.

### 15.3.1 Lead (Pb) Ions

Lead (Pb) is known to be the most plentiful poisonous heavy metal that is harmful to all the organs of human body, especially nervous system. It can enter any system through inhalation, digestion, or direct contact. In the human body, during nerve conduction, lower levels of Pb interferes with ion channels that can affect cognition. Moreover, Pb has the ability to decrease the heme production, and stimulate the generation of reactive oxygen species, which may damage the lipids and DNA constituents. Li et al. synthesised TiO<sub>2</sub>nanorod arrays on FTO substrates by a hydrothermal method for PEC sensing of Pb<sup>2+</sup>-ions [50]. Due to direct oxidation process on electrode surface, as shown in the reaction (15.1), Pb<sup>2+</sup> ions could be detected at nano-molar level. Luo et al. studied PbS nanoparticles (NPs) decorated TiO<sub>2</sub> nanotubes [59]. The fabricated PEC sensor displayed a high selectivity for metal-ion detection within a broad linear range from 10<sup>-8</sup> to 10<sup>-5</sup> M, and low detection limit of 0.39 nM:



Chen et al. [10] studied Bi<sub>2</sub>WO<sub>6</sub>-reduced graphene oxide nanocomposites GO, which displayed an enhanced photocurrent density approximately 2.7 times as compared to that of pure Bi<sub>2</sub>WO<sub>6</sub>. It could be attributed to the efficient charge separation and an improved visible light absorption. The PEC sensor exhibited a linear relationship between the photocurrent density, and the logarithm of the Pb<sup>2+</sup>-ion in the broad range from 0.01 to 50 μM, and with a detection limit of 3.3 nM. Zang et al. [119] devised a “signal-on” PEC sensing strategy for selective detection of Pb<sup>2+</sup>-ions using reduced graphene oxide and resonance energy transfer between CdS QDs and gold NPs. The PEC sensor displayed a linear relationship between photocurrent and the logarithm of Pb<sup>2+</sup> concentration in the broad range of 0.1–50 nM with detection limit of 0.05 nM. Zhang et al. [123] designed a flower-like ZnO nanostructure for detection of Pb<sup>2+</sup>-ions that depicted a linear relationship between photocurrent and Pb<sup>2+</sup> concentration over the broad range from 0.5 to 20 nM, with a detection limit of 0.1 nM.

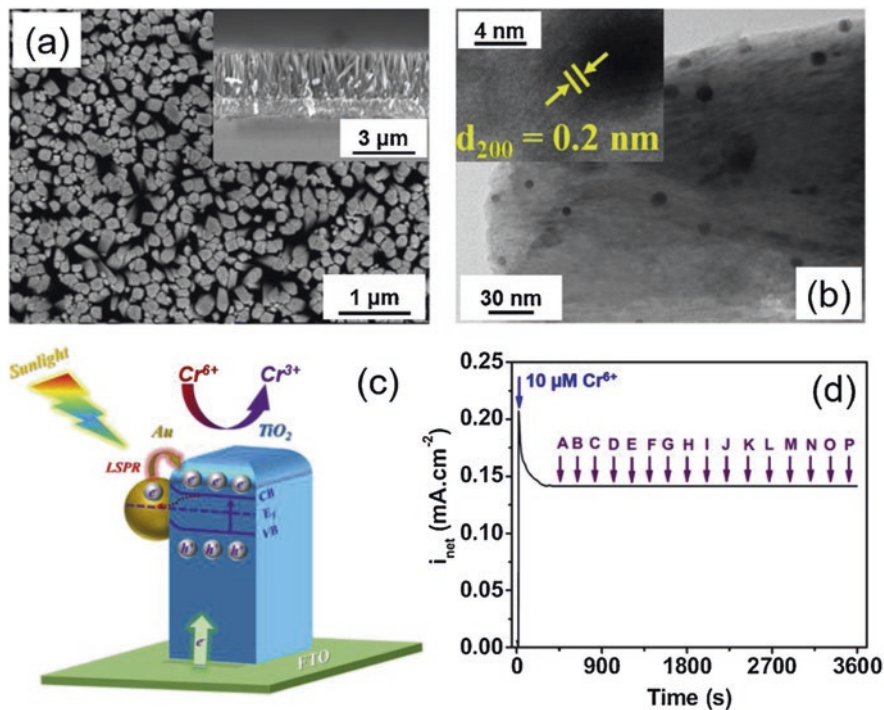
### 15.3.2 Mercury (Hg) Ions

Among other known heavy metals, mercury (Hg) is highly toxic to the human body and biosystem, which is commonly found in nature through ‘stationary and waste disposal combustion’, gold and non-ferrous metal production and cement

production. Hg exposure through inhalation, digestion leads to disorder related to brain, central nervous system, immune system, cognitive and motion. The PEC sensors displayed an outstanding outcome with a 6-order wide linear range of  $1.0 \times 10^{-9} - 1.0 \times 10^{-3}$  M, and a detection limit of  $0.3 \times 10^{-9}$  M. Wang et al. [103] synthesised Cysteine-capped ZnS QDs/ FTO that formed *p-n* junction-based PEC sensor by in situ formation of HgS, for detection of Hg<sup>2+</sup> ions. The formation of *p-n* junction promoted the charge transport and lead to an efficient electron-hole separation. The PEC sensor displayed a linear relationship between photocurrent and Pb<sup>2+</sup> ion concentration in the broad range of 0.01–10.0  $\mu$ M with a detection limit of  $4.6 \times 10^{-9}$  mol/L. Zhang et al. [121] reported GO-ZnO-CdS hybrid electrode-based PEC sensor by simple hydrothermal method that displayed a linear relationship in the range of 5 pM–500 pM with the detection limit of 1:5 pM. A novel PEC sensor was constructed using CdS QDs and Au NPs by Han et al. [24]. The photocurrent was enhanced and sensor has shown remarkable performance with linear relationship in the range from  $3.0 \times 10^{-9}$  to  $1.0 \times 10^{-7}$  M, with the detection limit of  $6.0 \times 10^{-10}$  M [24]. Zhao et al. [131] synthesised TiO<sub>2</sub>/CdS hybrid structure by depositing CdS QDs on TiO<sub>2</sub> thin films. The hybrid structure enhances the absorption of electrode in visible range and improves the charge transfer process. The PEC sensor recorded linear relationship between photocurrent variation and logarithm of Hg<sup>2+</sup> ions in the wide range 10 fM to 200 nM, with a detection limit of 3.3 fM. Bagheri Hariri et al. [2] synthesised Au–Pt NPs on indium tin oxide by electrodeposition method for the detection of Hg<sup>2+</sup> heavy ions in water samples with high sensitivity of 2.08  $\mu$ A nM<sup>-1</sup>.

### 15.3.3 Chromium (Cr) Ions

Chromium (Cr) compounds are found in various oxidation states like Cr(III) and Cr(VI), which are most stable states, while Cr(I), (II), (V) and (IV) are rare. They are usually contained in daily usage products like dyes, paints, and leather tanning, etc. Though Cr(III) is essential for human health, exposure to Cr(VI) may hinder enzymes, change metabolic pathway and cause lipid peroxidation. Li et al. [53] constructed TiO<sub>2</sub> photoanode-based indirect PEC sensing system where quercetin acted as both the electron donor and photosensitizer. The PEC sensor worked efficiently for sub-nanomole level detection of Cr(VI) ions with a detection limit of 0.24 nmolL<sup>-1</sup>. Siavash Moakhar et al. [84] fabricated single crystal TiO<sub>2</sub> nanorods decorated with Au nanoparticles that displayed the highest sensitivity of 13.94  $\mu$ A  $\mu$ M<sup>-1</sup> for Cr(VI) detection with a wide linear concentration range from 0.01 to 50  $\mu$ M and low detection limit of 0.006  $\mu$ M. Figure 15.5 shows the morphology and mechanism of chromium detection using Au/TiO<sub>2</sub> nanorods. When the electrode is illuminated, due to localised surface plasmon resonance (LSPR) effect hot electrons generated in Au NPs are transferred into the CB of TiO<sub>2</sub>. In addition, photogenerated electrons are produced in the CB of TiO<sub>2</sub>. This generation of electrons was used for the reduction of Cr<sup>6+</sup> to Cr<sup>3+</sup>. The same group also studied



**Fig. 15.5** (a) Morphology of Au NPs/TiO<sub>2</sub> nano rod arrays (NRAs); (b) TEM and HRTEM images of Au NPs on TiO<sub>2</sub>; (c) Schematic mechanism for PEC sensing of Cr<sup>6+</sup>; (d) Selectivity test of PEC sensor (from A to P: 10 mM Cr<sup>3+</sup>, 4 mM Fe<sup>3+</sup>, K<sup>+</sup>, Mg<sup>2+</sup>, Ca<sup>2+</sup>, Zn<sup>2+</sup>, Pb<sup>2+</sup>, Hg<sup>2+</sup>, Cd<sup>2+</sup>, NO<sub>3</sub><sup>-</sup>, Cl<sup>-</sup>, S<sub>2</sub>O<sub>3</sub><sup>2-</sup>, VO<sub>3</sub><sup>-</sup>, MnO<sup>+</sup>, MoO<sub>4</sub><sup>2-</sup> and WO<sub>4</sub><sup>2-</sup>). (Reprinted with permission from Shi et al. [83]. Copyright 2019: Elsevier Publishing)

screen-printed TiO<sub>2</sub> electrodes for direct determination and reduction of hexavalent chromium, which exhibited a linear concentration range from 0.01 to 100 μM with a very low detection limit of 0.004 μM and high sensitivity of 11.88 μA.μM<sup>-1</sup> [85]. The PEC sensor displayed linear relationship over the range from 0.01 to 100.00 ppb with a detection limit of 0.006 ppb.

### 15.3.4 Cadmium (Cd) Ions

Cd (II) is another exceptionally toxic and carcinogenic metal that inhibits important enzymes and can cause damage to liver and kidney. It is also known to increase the risk of cardiovascular diseases and cancer mortality. In a similar kind of study, Wang et al. studied the in situ electrodeposition of CdS on ZnO nanorods on ITO substrate [96]. Analysis of CdS/ZnO electrode revealed that the thickness of CdS could be varied by changing the concentration of Cd<sup>2+</sup> ions which thereby affected

the output photocurrent of the sensor. A linear relationship between the photocurrent variation and  $\text{Cd}^{2+}$  concentration was obtained in the range from 0.01 to 5 mM with a detection limit of 3.3  $\mu\text{M}$ . Zhang et al. [122] carried out an in situ electrodeposition of Zn-doped CdS-based film for PEC detection of two different metal ions ( $\text{Cd}^{2+}$  and  $\text{Cu}^{2+}$ ) on the common platform. The PEC sensor displayed a linear range of  $10^{-9}$ – $10^{-2}$  M and  $10^{-8}$ – $10^{-4}$  M, with a detection limit of 0.35 and 3 nM for detection of  $\text{Cd}^{2+}$  and  $\text{Cu}^{2+}$ , respectively.

### 15.3.5 Copper (Cu) Ions

Cu is considered as third most abundant element which is essential for all creatures in trace amount as a dietary mineral in the human system. It catalyses various biological processes such as heme synthesis/iron absorption and is useful in regulation of several proteins and enzymes. However, ingestion of large amount of Cu can be highly toxic to affect the cellular processes thus leading to neurodegenerative diseases, vital organ (like liver/kidney) failure and DNA damage. Huang et al. prepared  $\text{SnO}_2/\text{CdS}$  heterostructure films on fluorine-doped tin oxide for its application in selective PEC sensing of  $\text{Cu}^{2+}$  ions, where the films were deposited by SILAR method [30]. The  $\text{Cu}^{2+}$  ions sensing was dependent on the interaction between copper ions and CdS, where the film was immersed in the solution containing  $\text{Cu}^{2+}$  ions for 5 min. The linking of  $\text{Cu}^{2+}$  and  $\text{S}^{2-}$  on the electrode surface resulted in decrease of the photocurrent and the extent of decay in the photocurrent could be correlated to concentration of  $\text{Cu}^{2+}$  in the sample solution. The above designed PEC sensor displayed considerable selectivity with the detection limit of 0.55  $\mu\text{M}$ , and detection range from 1.00 to 38.0  $\mu\text{M}$ . Yan et al. fabricated various  $\text{Cd}_x\text{Zn}_{1-x}\text{S}$ -reduced graphene-oxide nanocomposites by one-pot reaction.  $\text{Cd}_{0.5}\text{Zn}_{0.5}\text{S}$ -rGO nanocomposite showed the best performance, where the photocurrent was found linearly proportional to the logarithm of the concentration of  $\text{Cu}^{2+}$  ions in a wide linear range of 0.02–20  $\mu\text{M}$ , and with a low detection limit of  $6.7 \times 10^{-9}$  M [112]. Shen et al. [82] designed ZnO/CdS hierarchical nanospheres for PEC sensing of  $\text{Cu}^{2+}$  ions. The enhanced light scattering phenomenon was observed due to ZnO nanospheres, and the heterojunction between CdS and ZnO improved light absorption and charge-separation of electrodes, which in turn provided high sensitivity. Tang et al. [92] synthesised  $\text{Fe}_2\text{O}_3$ -CdS nanopyramid heterostructures for PEC sensing of  $\text{Cu}^{2+}$  ions. The performance of the PEC sensor was improved owing to its excellent flexibility, high surface area of 87  $\text{m}^2/\text{g}$ , and large pore size of 20 nm that resulted in an efficient charge transport and provided an increased population of active electrochemical sites. Foo et al. [17] fabricated reduced graphene oxide/cadmium sulphide-modified carbon cloth through aerosol-assisted chemical vapour deposition (AACVD) method. The PEC sensor depicted photocurrent response linearly dependent on concentration of  $\text{Cu}^{2+}$  ion over wide range from 0.1 to 1.0  $\mu\text{M}$  and 1.0 to 40.0  $\mu\text{M}$  with a detection limit of 0.05  $\mu\text{M}$ .

## 15.4 Conclusions

In this chapter on the PEC sensor, we have conspicuously and briefly elaborated on principles, mechanisms, material advances and application-related aspects. It is presented that the PEC sensors category possess a very high potential to show significant performance improvement for detection of much-desired chemical and biological species. Nonetheless, further there is a lot of scope for improvement in PEC sensor performance in terms of amplification, stability of signal, reduce toxicity, enhanced selectivity and sensitivity and miniaturisation. CdS-based PEC sensors play a significant role in the detection of multiple contaminants but offer toxicity problem and possible release of metal ions. The problem of material toxicity can be reduced by introducing less-toxic materials, such as fluorescent metal nanoparticles, carbon- or Zn-based materials in combination with CdS. Rigorous efforts are required to design CdS nanocomposites and heterostructures those could enhance the electronic properties of sensor material, and improve the magnitude of overall output signal of PEC sensor. Moreover, research on suitable photocatalytic materials is required which would result in high external quantum efficiency and sensitivity-based PEC sensors. In addition, there is a requirement of in-depth investigation of nanostructures-biomolecule interfaces so that simpler biomolecular immobilisation strategies could be designed. This would lead to industry-scale implementation of high-efficiency and sustained stability PEC sensors. Accordingly, the future objectives should be designed not just to improve the sensitivity of PEC sensors, but also adopting integrated detection devices and the steps that would inherit the scope of developing the multidisciplinary technologies involving reusable sensing components, substitutable electronics, micro-nano processing, and additive manufacturing/production. Commercial viability of the PEC sensors can further be increased by imbuing dual functionality to them, such as ability of simultaneous detection and removal of targeted metal ions. There is wide scope for further research and development of strategies to detect various metal ions viz. arsenic, zinc, iron, manganese, tin, etc., and also the simultaneous detection of multiple metal ions. Metals with various oxidation states show distinct physiochemical properties hence a selective differentiation of these metal-ion species can be a valuable asset for PEC sensors. Highly robust PEC sensors with reusability and mass production capability are thus highly required. This could tackle important problems associated with real-time applications like monitoring of water bodies, or detection of metal ions in biological samples like living systems, saliva, urine, blood, etc.

## References

1. Aruchamy A, Aravamudan G, Subba Rao GVS. Semiconductor based photoelectrochemical cells for solar energy based conversion- an overview. *Bull Mater Sci.* 1982;4:483–526.
2. Bagheri Hariri M, Siavash Moakhar R, Sharifi Abdar P, et al. Facile and ultra-sensitive voltammetric electroreduction of  $\text{Hg}^{2+}$  in aqueous media using electrodeposited AuPtNPs/ITO. *Anal Methods.* 2021;13:2688–700.



3. Bai X, Zhang Y, Gao W, et al. Hollow ZnS–CdS nanocage based photoelectrochemical sensor combined with molecularly imprinting technology for sensitive detection of oxytetracycline. *Biosens Bioelectron.* 2020;168:112522.
4. Bai J, Zhou B. Titanium dioxide nanomaterials for sensor applications. *Chem Rev.* 2014;114:10131–76.
5. Bakhsh EM, Khan SB, Marwani HM, et al. Efficient electrochemical detection and extraction of copper ions using ZnSe–CdSe/SiO<sub>2</sub> core–shell nanomaterial. *J Ind Eng Chem.* 2019;73:118–27.
6. Bao C, Zhu G, Yang J, et al. Small molecular amine mediated synthesis of hydrophilic CdS nanorods and their photoelectrochemical water splitting performance. *Dalt Trans.* 2014;44:1465–72.
7. Cai Y, Kozhummal R, Kübel C, et al. Spatial separation of photogenerated electron–hole pairs in solution-grown ZnO tandem n–p core–shell nanowire arrays toward highly sensitive photoelectrochemical detection of hydrogen peroxide. *J Mater Chem A.* 2017;5:14397–405.
8. Cai J, Sheng P, Zhou L, et al. Label-free photoelectrochemical immunosensor based on CdTe/CdS co-sensitized TiO<sub>2</sub> nanotube array structure for octachlorostyrene detection. *Biosens Bioelectron.* 2013;50:66–71.
9. Cao JT, Liao XJ, Wang YL, Liu YM. A novel photoelectrochemical strategy for lead ion detection based on CdSe quantum dots co-sensitized ZnO–CdS nanostructure. *J Electroanal Chem.* 2021;880:114828.
10. Chen S, Nan H, Zhang X, et al. One-step hydrothermal treatment to fabricate Bi<sub>2</sub>WO<sub>6</sub>-reduced graphene oxide nanocomposites for enhanced visible light photoelectrochemical performance. *J Mater Chem B.* 2017;5:3718–27.
11. Dana J, Debnath T, Maity P, Ghosh HN. Enhanced charge separation in an epitaxial metal–semiconductor nanohybrid material anchored with an organic molecule. *J Phys Chem C.* 2015;119:22181–9.
12. Dashtian K, Hajati S, Ghaedi M. L-phenylalanine-imprinted polydopamine-coated CdS/CdSe n-n type II heterojunction as an ultrasensitive photoelectrochemical biosensor for the PKU monitoring. *Biosens Bioelectron.* 2020;165:112346.
13. Devadoss A, Sudhagar P, Terashima C, et al. Photoelectrochemical biosensors: new insights into promising photoelectrodes and signal amplification strategies. *J Photochem Photobiol C: Photochem Rev.* 2015;24:43–63.
14. Esteves ACC, Trindade T. Synthetic studies on II/VI semiconductor quantum dots. *Curr Opin Solid State Mater Sci.* 2002;6:347–53.
15. Fan D, Ren X, Wang H, et al. Ultrasensitive sandwich-type photoelectrochemical immunosensor based on CdSe sensitized La–TiO<sub>2</sub> matrix and signal amplification of polystyrene@Ab<sub>2</sub> composites. *Biosens Bioelectron.* 2017;87:593–9.
16. Fan GC, Ren XL, Zhu C, et al. A new signal amplification strategy of photoelectrochemical immunoassay for highly sensitive interleukin-6 detection based on TiO<sub>2</sub>/CdS/CdSe dual co-sensitized structure. *Biosens Bioelectron.* 2014;59:45–53.
17. Foo CY, Lim HN, Pandikumar A, et al. Utilization of reduced graphene oxide/cadmium sulfide-modified carbon cloth for visible-light-prompt photoelectrochemical sensor for copper (II) ions. *J Hazard Mater.* 2016;304:400–8.
18. Frumar M, Frumarova B, Nemeč P, et al. Thin chalcogenide films prepared by pulsed laser deposition – new amorphous materials applicable in optoelectronics and chemical sensors. *J Non-Cryst Solids.* 2006;352:544–61.
19. Fujishima A, Honda K. Electrochemical photolysis of water at a semiconductor electrode. *Nature.* 1972;238:37–8.
20. Gao B, Zhao X, Liang Z, et al. CdS/TiO<sub>2</sub> nanocomposite-based photoelectrochemical sensor for a sensitive determination of nitrite in principle of etching reaction. *Anal Chem.* 2020;93:820–7.
21. Grinyte R, Barroso J, Díez-Buitrago B, et al. Photoelectrochemical detection of copper ions by modulating the growth of CdS quantum dots. *Anal Chim Acta.* 2017;986:42–7.

22. Guo Z, Jiang K, Jiang H, et al. Photoelectrochemical aptasensor for sensitive detection of tetracycline in soil based on CdTe-BiOBr heterojunction: improved photoactivity enabled by Z-scheme electron transfer pathway. *J Hazard Mater.* 2022;424:127498.
23. Han H, Song T, Lee E-K, et al. Dominant factors governing the rate capability of a TiO<sub>2</sub> nanotube anode for high power lithium ion batteries. *ACS Nano.* 2012;6:8308–15.
24. Han D-M, Jiang L-Y, Tang W-Y, et al. Photoelectrochemical determination of inorganic mercury ions based on energy transfer between CdS quantum dots and Au nanoparticles. *Electrochem Commun* 2015;5172–75. <https://doi.org/10.1016/j.elecom.2014.12.002>
25. Hao H, Hao S, Hou H, et al. A novel label-free photoelectrochemical immunosensor based on CdSe quantum dots sensitized Ho<sup>3+</sup>/Yb<sup>3+</sup>-TiO<sub>2</sub> for the detection of *Vibrio parahaemolyticus*. *Methods.* 2019;168:94–101.
26. He X, Zhao X, Deng W, et al. CdSe quantum dots-decorated ZnIn<sub>2</sub>S<sub>4</sub> nanosheets for “signal-on” photoelectrochemical aptasensing of ATP by integrating exciton energy transfer with exciton-plasmon coupling. *Sensors Actuators B Chem.* 2021;348:130686.
27. He X, Yoo JE, Lee MH, Bae J. Morphology engineering of ZnO nanostructures for high performance supercapacitors: enhanced electrochemistry of ZnO nanocones compared to ZnO nanowires. *Nanotechnology.* 2017;28:245402.
28. Hou T, Zhang L, Sun X, Li F. Biphasic photoelectrochemical sensing strategy based on in situ formation of CdS quantum dots for highly sensitive detection of acetylcholinesterase activity and inhibition. *Biosens Bioelectron.* 2016;75:359–64.
29. Hu C, Zheng J, Su X, et al. Ultrasensitive all-carbon photoelectrochemical bioprobes for zeptomole immunosensing of tumor markers by an inexpensive visible laser light. *Anal Chem.* 2013;85:10612–9.
30. Huang F, Pu F, Lu X, et al. Photoelectrochemical sensing of Cu<sup>2+</sup> ions with SnO<sub>2</sub>/CdS heterostructural films. *Sens Actuators B* 2013;183:601–607. <https://doi.org/10.1016/j.snb.2013.04.047>
31. Hulanicki A, Glab S, Ingman F. Chemical sensors: definitions and classification. *Pure Appl Chem.* 1991;63:1247–50.
32. Huo K, Gao B, Fu J, et al. Fabrication, modification, and biomedical applications of anodized TiO<sub>2</sub> nanotube arrays. *RSC Adv.* 2014;4:17300–24.
33. Ibrahim I, Lim HN, Huang NM, et al. Selective and sensitive visible-light-prompt photoelectrochemical sensor of Cu<sup>2+</sup> based on CdS nanorods modified with Au and graphene quantum dots. *J Hazard Mater.* 2020;391:122248.
34. Ibrahim I, Lim HN, Zawawi RM, et al. A review on visible-light induced photoelectrochemical sensors based on CdS nanoparticles. *J Mater Chem B.* 2018;6:4551–68.
35. Ibrahim I, Lim HN, Abou-Zied OK, et al. Cadmium sulfide nanoparticles decorated with Au quantum dots as ultrasensitive photoelectrochemical sensor for selective detection of copper(II) ions. *J Phys Chem C.* 2016;120:22202–14.
36. Ibrahim I, Lim HN, Huang NM, Pandikumar A. Cadmium sulphide-reduced graphene oxide-modified photoelectrode-based photoelectrochemical sensing platform for copper(II) ions. *PLoS One.* 2016;11:e0154557.
37. Shi J-J, Zhu J-C, Zhao M, et al. Ultrasensitive photoelectrochemical aptasensor for lead ion detection based on sensitization effect of CdTe QDs on MoS<sub>2</sub>-CdS:Mn nanocomposites by the formation of G-quadruplex structure. *Talanta.* 2018;183:237–44.
38. Kim SS, Lee JW, Yun JM, Na SI. 2-Dimensional MoS<sub>2</sub> nanosheets as transparent and highly electrocatalytic counter electrode in dye-sensitized solar cells: effect of thermal treatments. *J Ind Eng Chem.* 2015;29:71–7.
39. Krishnan B, Shaji S, Acosta-Enríquez MC, et al. Group II–VI semiconductors. In: Pech-Canul M, Ravindra N, editors. *Semiconductors*. Cham: Springer; 2019. p. 397–464.
40. van de Krol R. Principles of photoelectrochemical cells. In: van de Krol R, Grätzel M, editors. *Photoelectrochemical hydrogen production, Electronic materials: science & technology*, vol. 102. Boston, MA: Springer; 2012. p. 13–67.

41. Le S, Jiang T, Li Y, et al. Highly efficient visible-light-driven mesoporous graphitic carbon nitride/ZnO nanocomposite photocatalysts. *Appl Catal B Environ.* 2017;200:601–10.
42. Lee Y-L, Lo Y-S. Highly efficient quantum-dot-sensitized solar cell based on co-sensitization of CdS/CdSe. *Adv Funct Mater.* 2009;19:604–9.
43. Lee Y-L, Chi C-F, Liau S-Y. CdS/CdSe co-sensitized TiO<sub>2</sub> photoelectrode for efficient hydrogen generation in a photoelectrochemical cell. *Chem Mater.* 2009;22:922–7.
44. Leng D, Zhao J, Ren X, et al. MoSe<sub>2</sub>/CdSe heterojunction destruction by cation exchange for photoelectrochemical immunoassays with a controlled-release strategy. *Anal Chem.* 2021;93:10712–8.
45. Li S, Xing Z, Feng J, et al. A sensitive biosensor of CdS sensitized BiVO<sub>4</sub>/GaON composite for the photoelectrochemical immunoassay of procalcitonin. *Sensors Actuators B Chem.* 2021;329:129244.
46. Li H, Zhao Y, Yue M-e, Jie G. Signal-off photoelectrochemical biosensing platform based on hybridization chain-doped manganese porphyrin quenching on CdSe signal coupling with cyclic amplification for thrombin detection. *J Electroanal Chem.* 2020;879:114803.
47. Li L, Li B, Liu H, et al. Photoelectrochemical sensing of hydrogen peroxide using TiO<sub>2</sub> nanotube arrays decorated with RGO/CdS. *J Alloys Compd.* 2020;815:152241.
48. Li Z, Dong W, Du X, et al. A novel photoelectrochemical sensor based on g-C<sub>3</sub>N<sub>4</sub>@CdS QDs for sensitive detection of Hg<sup>2+</sup>. *Microchem J.* 2020;152:104259.
49. Li K, Han M, Chen R, et al. Hexagonal@cubic CdS Core@Shell nanorod photocatalyst for highly active production of H<sub>2</sub> with unprecedented stability. *Adv Mater.* 2016;28:8906–11.
50. Li S, Gu X, Zhao Y, et al. Photoelectrochemical determination of Pb<sup>2+</sup> ions by using TiO<sub>2</sub> nanorod arrays grown on FTO substrates via a facile two-stage hydrothermal route. *J Mater Sci Mater Electron.* 2016;278(27):8455–63.
51. Li P, Huang S, Pan HC. Synthesis and characterization of Au-CdS composite thin films for photoelectrochemical sensing of Hg<sup>2+</sup> ions. *Adv Mater Res.* 2015;1088:91–5.
52. Li X, Yang Q, Hua H, et al. CdS/CdSe core/shell nanowall arrays for high sensitive photoelectrochemical sensors. *J Alloys Compd.* 2015;630:94–9.
53. Li X, Hu C, Zhao Z, et al. Three-dimensional CdS nanostructure for photoelectrochemical sensor. *Sensors Actuators B Chem.* 2013;182:461–6.
54. Li Y-J, Ma M-J, Zhu J-J. Dual-signal amplification strategy for ultrasensitive photoelectrochemical immunosensing of  $\alpha$ -fetoprotein. *Anal Chem.* 2012;84:10492–9.
55. Liu J, Liu Y, Wang W, et al. Component reconstitution-driven photoelectrochemical sensor for sensitive detection of Cu<sup>2+</sup> based on advanced CuS/CdS p-n junction. *Sci China Chem.* 2019;6212(62):1725–31.
56. Liu Y, Yan K, Zhang J. Graphitic carbon nitride sensitized with CdS quantum dots for visible-light-driven photoelectrochemical aptasensing of tetracycline. *ACS Appl Mater Interfaces.* 2016;8(42):28255–64.
57. Liu J, Xu S, Liu L, Sun DD. The size and dispersion effect of modified graphene oxide sheets on the photocatalytic H<sub>2</sub> generation activity of TiO<sub>2</sub> nanorods. *Carbon NY.* 2013;60:445–52.
58. Fagiolari L, Bella F. Carbon-based materials for stable, cheaper and large-scale processable perovskite solar cells. *Energy Environ Sci.* 2019;12:3437–72.
59. Luo Y, Dong C, Li X, Tian Y. A photoelectrochemical sensor for lead ion through electro-deposition of PbS nanoparticles onto TiO<sub>2</sub> nanotubes. *J Electroanal Chem.* 2015;759:51–4.
60. Ma W, Wang L, Zhang N, et al. Biomolecule-free, selective detection of o-diphenol and its derivatives with WS<sub>2</sub>/TiO<sub>2</sub>-based photoelectrochemical platform. *Anal Chem.* 2015;87:4844–50.
61. Manikandan M, Revathi C, Senthilkumar P, et al. CdTe nanorods for nonenzymatic hydrogen peroxide biosensor and optical limiting applications. *Ionics.* 2019;264(26):2003–10.
62. Mao L, Gao M, Xue X, et al. Organic-inorganic nanoparticles molecularly imprinted photoelectrochemical sensor for  $\alpha$ -solanine based on p-type polymer dots and n-CdS heterojunction. *Anal Chim Acta.* 2019;1059:94–102.

63. Maria da Costa Silva L, Farias Melo A, Medeiros Salgado A. Biosensors for environmental applications. In: Somerset V, editor. Environmental biosensors. InTech.; 2011. p. 3–16.
64. Medintz IL, Uyeda HT, Goldman ER, Mattoussi H. Quantum dot bioconjugates for imaging, labelling and sensing. *Nat Mater*. 2005;4(4):435–46.
65. Meng L, Xiao K, Zhang X, et al. DNA-linked CdSe QDs/AGQDs “Z-scheme” system: ultra-sensitive and highly selective photoelectrochemical sensing platform with negative background signal. *Sensors Actuators B Chem*. 2020;305:127480.
66. Mourzina YG, Schubert J, Zander W, et al. Development of multisensor systems based on chalcogenide thin film chemical sensors for the simultaneous multicomponent analysis of metal ions in complex solutions. *Electrochim Acta*. 2001;47:251–8.
67. Murray CB, Norris DJ, Bawendi MG. Synthesis and characterization of nearly monodisperse CdE (E = sulfur, selenium, tellurium) semiconductor nanocrystallites. *J Am Chem Soc*. 2002;115:8706–15.
68. Nguyen Van M, Li W, Sheng P, et al. Photoelectrochemical label-free immunoassay of octachlorostyrene based on heterogeneous CdSe/CdS/Pt/TiO<sub>2</sub> nanotube array. *J Electroanal Chem*. 2015;736:69–75.
69. Pang X, Pan J, Gao P, et al. A visible light induced photoelectrochemical aptsensor constructed by aligned ZnO@CdTe core shell nanocable arrays/carboxylated g-C<sub>3</sub>N<sub>4</sub> for the detection of Proprotein convertase subtilisin/kexin type 6 gene. *Biosens Bioelectron*. 2015;74:49–58.
70. Pang X, Pan J, Wang L, et al. CdSe quantum dot-functionalized TiO<sub>2</sub> nanohybrids as a visible light induced photoelectrochemical platform for the detection of proprotein convertase subtilisin/kexin type 6. *Biosens Bioelectron*. 2015;71:88–97.
71. Pareek A, Paik P, Borse PH. Stable hydrogen generation from Ni- and Co-based co-catalysts in supported CdS PEC cell. *Dalt Trans*. 2016;45:11120–8.
72. Pareek A, Paik P, Borse PH. Nanoniobia modification of CdS photoanode for an efficient and stable photoelectrochemical cell. *Langmuir*. 2014;30:15540.
73. Patrick L. Lead toxicity part II: the role of free radical damage and the use of antioxidants in the pathology and treatment of lead toxicity. *Altern Med Rev*. 2006;11:114–28.
74. Peng J, Huang Q, Liu Y, et al. Photoelectrochemical sensor based on composite of CdTe and nickel tetra-aminated phthalocyanine covalently linked with graphene oxide for ultrasensitive detection of curcumin. *Sensors Actuators B Chem*. 2019;294:157–65.
75. Qin C, Bai X, Zhang Y, Gao K. Photoelectrochemical CdSe/TiO<sub>2</sub> nanotube array microsensor for high-resolution in-situ detection of dopamine. *Microchim Acta*. 2018;185(5):2278.
76. Qin Q, Bai X, Hua Z. Electrochemical synthesis of well-dispersed CdTe nanoparticles on reduced graphene oxide and its photoelectrochemical sensing of catechol. *J Electrochem Soc*. 2017;164:H241–9.
77. Qiu Z, Tang D. Nanostructure-based photoelectrochemical sensing platforms for biomedical applications. *J Mater Chem B*. 2020;8:2541–61.
78. Rajeshwar K. Fundamentals of semiconductor electrochemistry and photoelectrochemistry. In: Encyclopedia of electrochemistry: online. Wiley Online Library; 2007. <https://doi.org/10.1002/9783527610426.bard060001>.
79. Rodenas P, Song T, Sudhagar P, et al. Quantum dot based heterostructures for unassisted photoelectrochemical hydrogen generation. *Adv Energy Mater*. 2013;3:176–82.
80. Roushani M, Shamsipur M, Rajabi HR. Highly selective detection of dopamine in the presence of ascorbic acid and uric acid using thioglycolic acid capped CdTe quantum dots modified electrode. *J Electroanal Chem*. 2014;712:19–24.
81. Schwarzenbach RP, Egli T, Hofstetter TB, et al. Global water pollution and human health. *Annu Rev Environ Resour*. 2010;35:109–36.
82. Shen Q, Zhao X, Zhou S, et al. ZnO/CdS hierarchical nanospheres for photoelectrochemical sensing of Cu<sup>2+</sup>. *J Phys Chem C*. 2011;115:17958–64.
83. Shi L, Yin Y, Zhang LC, et al. Design and engineering heterojunctions for the photoelectrochemical monitoring of environmental pollutants: a review. *Appl Catal B Environ*. 2019;248:405–22.

84. Siavash Moakhar R, Goh GKL, Dolati A, Ghorbani M. Sunlight-driven photoelectrochemical sensor for direct determination of hexavalent chromium based on Au decorated rutile TiO<sub>2</sub> nanorods. *Appl Catal B Environ*. 2017;201:411–8.
85. Siavash Moakhar R, Goh GKL, Dolati A, Ghorbani M. A novel screen-printed TiO<sub>2</sub> photoelectrochemical sensor for direct determination and reduction of hexavalent chromium. *Electrochem Commun*. 2015;61:110–3.
86. Song J, Wang J, Wang X, et al. Using silver nanocluster/graphene nanocomposite to enhance photoelectrochemical activity of CdS:Mn/TiO<sub>2</sub> for highly sensitive signal-on immunoassay. *Biosens Bioelectron*. 2016;80:614–20.
87. Stradiotto NR, Yamanaka H, Zanoni MVB. Electrochemical sensors: a powerful tool in analytical chemistry. *J Braz Chem Soc*. 2003;14:159–73.
88. Sudhagar P, González-Pedro V, Mora-Seró I, et al. Interfacial engineering of quantum dot-sensitized TiO<sub>2</sub> fibrous electrodes for futuristic photoanodes in photovoltaic applications. *J Mater Chem*. 2012;22:14228–35.
89. Sudhagar P, Jung JH, Park S, et al. The performance of coupled (CdS:CdSe) quantum dot-sensitized TiO<sub>2</sub> nanofibrous solar cells. *Electrochem Commun*. 2009;11:2220–4.
90. Sun B, Dong J, Cui L, et al. A dual signal-on photoelectrochemical immunosensor for sensitively detecting target avian viruses based on AuNPs/g-C<sub>3</sub>N<sub>4</sub> coupling with CdTe quantum dots and in situ enzymatic generation of electron donor. *Biosens Bioelectron*. 2019;124–125:1–7.
91. Sunaina, Ganguli AK, Mehta SK. High performance ZnSe sensitized ZnO heterostructures for photo-detection applications. *J Alloys Compd*. 2022;894:162263.
92. Tang J, Li J, Zhang Y, et al. Mesoporous Fe<sub>2</sub>O<sub>3</sub>–CdS heterostructures for real-time photoelectrochemical dynamic probing of Cu<sup>2+</sup>. *Anal Chem*. 2015;87:6703–8.
93. Tanne J, Schäfer D, Khalid W, et al. Light-controlled bioelectrochemical sensor based on CdSe/ZnS quantum dots. *Anal Chem*. 2011;83:7778–85.
94. Tian J, Zhao H, Quan X, et al. Fabrication of graphene quantum dots/silicon nanowires nano-hybrids for photoelectrochemical detection of microcystin-LR. *Sensors Actuators B Chem*. 2014;196:532–8.
95. Valko M, Morris H, Cronin M. Metals, toxicity and oxidative stress. *Curr Med Chem*. 2005;12:1161–208.
96. Wang R, Pang X, Zhang H, et al. *Anal Methods* 2015;7(13):5406–5411. <https://doi.org/10.1039/C5AY01012H>
97. Wang C, Dai J, Guo S, et al. Efficient photoelectrochemical sensor of Cu<sup>2+</sup> based on ZnO-graphene nanocomposite sensitized with hexagonal CdS by calcination method. *J Electroanal Chem*. 2021;893:115330.
98. Wang X, Li G, Peng J, et al. The Au/ZnSe/ZnO heterojunction improves the electron transfer behavior to enhance the detection performance of ascorbic acid. *J Alloys Compd*. 2021;873:159721.
99. Wang J, Pan Y, Jiang L, et al. Photoelectrochemical determination of Cu<sup>2+</sup> using a WO<sub>3</sub>/CdS heterojunction photoanode. *ACS Appl Mater Interfaces*. 2019;11:37541–9.
100. Wang R, Zu M, Yang S, et al. Visible-light-driven photoelectrochemical determination of Cu<sup>2+</sup> based on CdS sensitized hydrogenated TiO<sub>2</sub> nanorod arrays. *Sensors Actuators B Chem*. 2018;270:270–6.
101. Wang Y, Wang P, Wu Y, Di J. A cathodic “signal-on” photoelectrochemical sensor for Hg<sup>2+</sup> detection based on ion-exchange with ZnS quantum dots. *Sensors Actuators B Chem*. 2018;254:910–5.
102. Wang Y, Ge S, Zhang L, et al. Visible photoelectrochemical sensing platform by in situ generated CdS quantum dots decorated branched-TiO<sub>2</sub> nanorods equipped with Prussian blue electrochromic display. *Biosens Bioelectron*. 2017;89:859–65.
103. Wang R, Yan K, Wang F, Zhang J. A highly sensitive photoelectrochemical sensor for 4-aminophenol based on CdS-graphene nanocomposites and molecularly imprinted polypyrrole. *Electrochim Acta*. 2014;121:102–8.

104. Wannier GH. The structure of electronic excitation levels in insulating crystals. *Phys Rev.* 1937;52:191.
105. Wilson GS, Gifford R. Biosensors for real-time in vivo measurements. *Biosens Bioelectron.* 2005;20:2388–403.
106. Wu S, Zhao Y, Deng X, et al. Oxygen defects engineered CdS/Bi<sub>2</sub>O<sub>2.33</sub> direct Z-Scheme heterojunction for highly sensitive photoelectrochemical assay of Hg<sup>2+</sup>. *Talanta.* 2020;217:121090.
107. Wu H, Zheng Z, Tang Y, et al. Pulsed electrodeposition of CdS on ZnO nanorods for highly sensitive photoelectrochemical sensing of copper (II) ions. *Sustain Mater Technol.* 2018;18:e00075.
108. Wu P, Pan J-B, Li X-L, et al. Long-lived charge carriers in Mn-doped CdS quantum dots for photoelectrochemical cytosensing. *Chem A Eur J.* 2015;21:5129–35.
109. Xie Y, Zhang M, Bin Q, et al. Photoelectrochemical immunosensor based on CdSe@BiVO<sub>4</sub> Co-sensitized TiO<sub>2</sub> for carcinoembryonic antigen. *Biosens Bioelectron.* 2020;150:111949.
110. Xu R, Wei D, Du B, et al. A photoelectrochemical sensor for highly sensitive detection of amyloid beta based on sensitization of Mn:CdSe to Bi<sub>2</sub>WO<sub>6</sub>/CdS. *Biosens Bioelectron.* 2018;122:37–42.
111. Xu H, Huang D, Wu Y, Di J. Photoelectrochemical determination of Cu<sup>2+</sup> ions based on assembly of Au/ZnS nanoparticles. *Sensors Actuators B Chem.* 2016;235:432–8.
112. Yan J, Wang K, Liu Q, et al. One-pot synthesis of CdxZn1-xS-reduced graphene oxide nanocomposites with improved photoelectrochemical performance for selective determination of Cu<sup>2+</sup>. *RSC Adv* 2013;3:14451–14457. <https://doi.org/10.1039/c3ra41118d>
113. Yan K, Wang R, Zhang J. A photoelectrochemical biosensor for o-aminophenol based on assembling of CdSe and DNA on TiO<sub>2</sub> film electrode. *Biosens Bioelectron.* 2014;53:301–4.
114. Yanagimoto T, Yu Y-T, Kaneko K. Microstructure and CO gas sensing property of Au/SnO<sub>2</sub> core-shell structure nanoparticles synthesized by precipitation method and microwave-assisted hydrothermal synthesis method. *Sens Actuators B* 2012;166–167:31–35. <https://doi.org/10.1016/j.snb.2011.11.047>
115. Ye X, Wang X, Kong Y, et al. FRET modulated signaling: a versatile strategy to construct photoelectrochemical microsensors for in vivo analysis. *Angew Chemie Int Ed.* 2021;60:11774–8.
116. Yogeswaran U, Chen S-M. A review on the electrochemical sensors and biosensors composed of nanowires as sensing material. *Sensors.* 2008;8:290–313.
117. Yu LD, Wang YN, Zhang XY, et al. A novel signal-on photoelectrochemical platform for highly sensitive detection of alkaline phosphatase based on dual Z-scheme CdS/Bi<sub>2</sub>S<sub>3</sub>/BiOCl composites. *Sensors Actuators B Chem.* 2021;340:129988.
118. Zang Y, Fan J, Ju Y, et al. Current advances in semiconductor nanomaterial-based photoelectrochemical biosensing. *Chem A Eur J.* 2018;24:14010–27.
119. Zang Y, Lei J, Hao Q, Ju H. “Signal-on” photoelectrochemical sensing strategy based on target-dependent aptamer conformational conversion for selective detection of lead(II) ion. *ACS Appl Mater Interfaces.* 2014;6:15991–7.
120. Zhang L, Li P, Feng L, et al. Synergetic Ag<sub>2</sub>S and ZnS quantum dots as the sensitizer and recognition probe: a visible light-driven photoelectrochemical sensor for the “signal-on” analysis of mercury (II). *J Hazard Mater.* 2020;387:121715.
121. Zhang K, Lv S, Lin Z, Tang D. CdS:Mn quantum dot-functionalized g-C<sub>3</sub>N<sub>4</sub> nano hybrids as signal-generation tags for photoelectrochemical immunoassay of prostate specific antigen coupling DNAzyme concatamer with enzymatic biocatalytic precipitation. *Biosens Bioelectron.* 2017;95:34–40.
122. Zhang Y, Ma H, Wu D, et al. A generalized in situ electrodeposition of Zn doped CdS-based photoelectrochemical strategy for the detection of two metal ions on the same sensing platform. *Biosens Bioelectron.* 2016;77:936–41.
123. Zhang B, Lu L, Hu Q, et al. ZnO nanoflower-based photoelectrochemical DNAzyme sensor for the detection of Pb<sup>2+</sup>. *Biosens Bioelectron.* 2014;56:243–9.

124. Zhang X, Xu F, Zhao B, et al. Synthesis of CdS quantum dots decorated graphene nanosheets and non-enzymatic photoelectrochemical detection of glucose. *Electrochim Acta*. 2014;133:615–22.
125. Zhang L, Mohamed HH, Dillert R, Bahnemann D. Kinetics and mechanisms of charge transfer processes in photocatalytic systems: a review. *J Photochem Photobiol C: Photochem Rev*. 2012;13:263–76.
126. Zhang X-B, Kong R-M, Lu Y. Metal ion sensors based on DNAszymes and related DNA molecules. *Annu Rev Anal Chem*. 2011;4(1):105–28.
127. Zhao Y, Tan L, Gao X, et al. Silver nanoclusters-assisted ion-exchange reaction with CdTe quantum dots for photoelectrochemical detection of adenosine by target-triggering multiple-cycle amplification strategy. *Biosens Bioelectron*. 2018;110:239–45.
128. Zhao WW, Xu JJ, Chen HY. Photoelectrochemical enzymatic biosensors. *Biosens Bioelectron*. 2017;92:294–304.
129. Zhao K, Yan X, Gu Y, et al. Self-powered photoelectrochemical biosensor based on CdS/RGO/ZnO nanowire array heterostructure. *Small*. 2016;12:245–51.
130. Zhao W-W, Xu J-J, Chen H-Y. Photoelectrochemical detection of metal ions. *Analyst*. 2016;141:4262–71.
131. Zhao W-W, Xu J-J, Chen H-Y. Photoelectrochemical bioanalysis: the state of the art. *Chem Soc Rev*. 2015;44:729–41.
132. Zhao W-W, Xu J-J, Chen H-Y. Photoelectrochemical DNA biosensors. *Chem Rev*. 2014;114:7421–41.
133. Zhao X, Zhou S, Shen Q, et al. Fabrication of glutathione photoelectrochemical biosensor using graphene–CdS nanocomposites. *Analyst*. 2012;137:3697–703.
134. Zheng XT, Than A, Ananthanaraya A, et al. Graphene quantum dots as universal fluorophores and their use in revealing regulated trafficking of insulin receptors in adipocytes. *ACS Nano*. 2013;7:6278–86.
135. Zhong X, Zhang M, Guo L, et al. A dual-signal self-checking photoelectrochemical immunosensor based on the sole composite of MIL-101(Cr) and CdSe quantum dots for the detection of  $\alpha$ -fetoprotein. *Biosens Bioelectron*. 2021;189:113389.

# Chapter 16

## II–VI Semiconductor-Based Optical Temperature Sensors



Nupur Saxena and Pragati Kumar

### 16.1 Introduction

Temperature is a fundamental quantity which comes across us here and there in everyday life. Recently, during the crucial situations of the COVID-19 pandemic, thermal scanners were the most reliable devices to detect body temperatures of affected people in mass gatherings like at airports, malls, railway stations, etc. [1]. Thanks to our ancestor's scientists that they had identified this important physical quantity and devised many thermometers, sensors, detectors, scanners, etc., that can work in different range of temperatures, measure it and save human lives. Their hard work is paid off in various aspects of life whether it is medical, household, engineering, industries or any other. However, the thirst never ends and with the inception of new technologies, the modes of temperature sensing also advance [2].

Optical sensing of temperature is one of the fields that facilitates non-contact thermometry. It has its own advantages like faster operation, immunity to electrical fluctuations and noises, reliability, high sensitivity, etc. This chapter deals with the application of II–VI compound semiconductors with different morphologies in optical temperature sensing. There are a number of optical methods that offer easy and effective temperature detection through a wide range. The following subsection will detail the principles of methods for optical thermometry.

---

N. Saxena (✉)  
Organisation of Science Innovations and Research, Bah, Uttar Pradesh, India

P. Kumar  
Nanomaterials and Device Lab, Department of Nanoscience and Materials,  
Central University of Jammu, Jammu, Jammu and Kashmir, India

© The Author(s), under exclusive license to Springer Nature  
Switzerland AG 2023

G. Korotcenkov (ed.), *Handbook of II-VI Semiconductor-Based Sensors and Radiation Detectors*, [https://doi.org/10.1007/978-3-031-24000-3\\_16](https://doi.org/10.1007/978-3-031-24000-3_16)



### 16.1.1 Principles (Methods) of Operation and Figures of Merit

The optical temperature sensors (OTP) have been devised using a number of methods in which different optical properties were measured with respect to changes in temperature. Besides, a number of measured quantities can be altered with temperature in one method and a temperature sensor (TS) can be realised using one or more parameters. For clarity, let us start with luminescence-based TS, further methods will be taken one by one.

Luminescence thermometry is a versatile technique for the measurement of temperature. The first indication of using luminescent materials for thermal sensing was reported in the early twentieth century by Nuebert [3]. Luminescence temperature probe is used to diagnose the temperature of a material by incorporating it into the material. Luminescence thermometry is based on the particular parameter of luminescence, that is, intensity, bandwidth and lifetime from which the thermal reading can be extracted. Based on these parameters, luminescence thermometry is divided into sub-classes:

**Intensity:** The temperature of the material can be determined by examining the temperature-dependent luminescence from that material. The number of photons emitted per second from the material varies with the change in temperature and thus causes a more or less intense spectrum. This variation in the luminescent intensity generally causes by the thermal activation of luminescence quenching mechanism and non-radiative decay probabilities. At elevated temperatures, the excitation of electrons within the excited state occurs which promotes non-radiative transitions to ground states and vice-versa. The figures of merit (FOMs) in this case are deduced as follows [4].

A linear function  $\ln P = -\frac{\varepsilon}{kT} + \ln A$  can be derived by the variation of integrated intensity with temperature as per the equation:  $I_T = \frac{B}{Ae^{-\varepsilon/kT} + 1}$ , where  $A$  and  $B$  are constants,  $\varepsilon$  is the activation energy,  $k$  is the Boltzmann constant and  $P = (B/I_T) - 1$ . These constants can be determined by fitting the experimental data and a linear fit is obtained. The sensitivity of the sensor can be obtained by this linear fit as the rate of change of intensity with respect to change in temperature.

The sensitivity of intensity-based TS is deduced from the slope of the linear fit and described as the rate of change of intensity with respect to the change in temperature whereas the average sensitivity can be obtained by the relation  $\Delta I/\Delta T$ , where  $\Delta I$  is the change in  $\ln P$ , with respect to the change in temperature  $\Delta T$ . The resolution of the TS is obtained using the resolution of the detector and the computed sensitivity.

**Peak wavelength shift and full width at half maxima (FWHM):** The peak wavelength is directly related to the band gap of the material that varies with temperature through Varshni relation [5]:

$$E_g(T) = E_{g0} - \alpha \frac{T^2}{T + \beta} \quad (16.1)$$

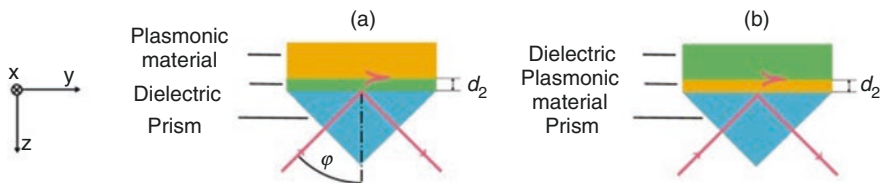
where  $E_{g0}$  is the energy gap at absolute zero, while  $\alpha$  and  $\beta$  are material constants termed as Varshni coefficients that define the sensitivity, that is, temperature dependent linear shift in the bandgap and the Debye temperature,  $\theta_D$ , respectively. The experimental data are fitted with the equation and the parameters can be obtained [6].

In case of FWHM, line broadening is considered which is due to two reasons: (1) inhomogeneous and (2) homogenous. The complex Voigt or a simple Lorentz fitting of PL spectra gives the homogenous part at higher temperatures. The electron–phonon processes viz. exciton scattering with acoustic and longitudinal optical (LO) phonons which cause the broadening in the FWHM,  $\Gamma$ , with rising temperature is given by [7]:

$$\Gamma(T) = \Gamma_{inh} + \gamma_{AC}T + \Gamma_{LO} \left[ \exp\left(\frac{E_{LO}}{k_B T}\right) - 1 \right]^{-1} \quad (16.2)$$

where  $\Gamma_{inh}$  is term for inhomogeneous broadening,  $\gamma_{AC}$  is the exciton–acoustic phonon scattering coefficient,  $\Gamma_{LO}$  stands for the exciton–LO phonon coupling strength,  $E_{LO}$  is the LO-phonon energy = 25 meV for CdSe QDs, and  $k_B$  is the Boltzmann constant. The term for inhomogeneous broadening in (16.2) is responsible for the morphology and composition of the QD. The other two terms belong to exciton–phonon interactions.

In order to use *surface plasmon resonance (SPR) technique* in temperature sensing, the sensing layer of a large thermo-optic coefficient should be used. The surface plasmons are excited by the evanescent field produced from the reflection of light from the interface between two dielectric mediums. Two basic configurations for the photon surface plasmon coupling are: the Otto and Kretschmann–Raether (KR) configurations [8, 9] and are shown in Fig. 16.1a, b. In the Otto configuration, the sensing target is limited by metal and prism air gap and the wave propagation constant corresponding to the incident angle  $\theta$  for this configuration is given as:  $K = \frac{\omega}{c} \sqrt{e_p} \sin \theta$ , where  $e_p$  represents the dielectric constant of the prism,  $\omega$  and  $c$  represents the frequency and velocity of incident light, respectively. Kretschmann modified the Otto configuration for the excitation of surface plasmons While in

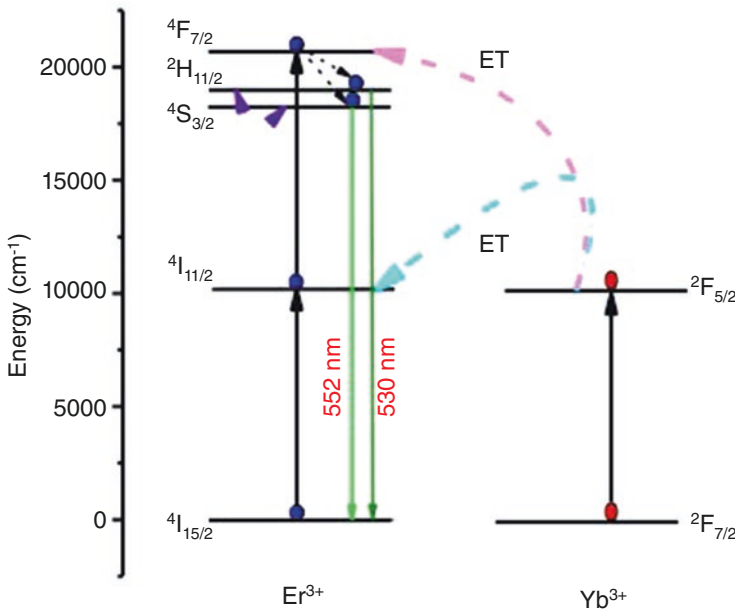


**Fig. 16.1** (a) Otto configuration and (b) Kretschmann configuration for phonon surface coupling. (Adapted with permission from Ref. [11]. Copyright 2017: Nature Portfolio)

Kreschmann configuration, the sensing layer is located between the metal layer and layer and the angle of incidence for the wave propagation is replaced by  $\theta_{res}$  and thus is given by:  $K = \frac{\omega}{c} \sqrt{\epsilon_p} \sin \theta_{res}$  (Fig. 16.1a, b). The sensitivity of a SPR sensor depends on the shifting of the resonance angle with a change in refractive index of the sensing layer. Bruce et al. [10] demonstrated an SPR-based TS in which the change in the refractive index of dielectric coating with temperature produces TS.

*Fluorescent Intensity Ratio (FIR)* is a simple and straightforward technique to analyse the luminescence intensity data. In this technique, the fluorescence from the two closely spaced levels to a common lower level is governed by the appropriate wavelengths. The use of thermally coupled levels in the FIR method is that the population of the individually coupled levels is directly proportional to the total population and it is easy to detect the peak behaviour. The use of relatively closely spaced energy levels helps to reduce the effects due to the wavelength dependent that arises during the measurement. For an illustration, Fig. 16.2 predicts the two thermally couple levels of  $\text{Er}^{3+}\text{-Tm}^{3+}\text{-Yb}^{3+}$  codoped  $\text{CaMoO}_4$  phosphor in which two green bands do not overlap with each other but an increase in temperature results increase in the intensity ratio of the  ${}^2\text{H}_{11/2} \rightarrow {}^4\text{I}_{15/2}$  to  ${}^4\text{S}_{3/2} \rightarrow {}^4\text{I}_{15/2}$  transition. This signifies larger increment in the population of the  ${}^2\text{H}_{11/2}$  level at elevated temperatures than that of the  ${}^4\text{S}_{3/2}$  level [12].

Typically, high signal-to-noise ratio is achieved by amalgamation of a periodic excitation with a phase-sensitive detector due to smaller intensity from the upper level at lower temperatures. An increase in temperature thermally excites the



**Fig. 16.2** Thermally coupled levels of  $\text{Er}^{3+}\text{-Tm}^{3+}\text{-Yb}^{3+}$  codoped  $\text{CaMoO}_4$  phosphor. (Adapted with permission from Ref. [12]. Copyright 2017: Institute of Physics Publishing)

lower-state ions which increases the number of ions in the excited state  $N_2$ . The temperature-dependent variation of the ratio of the two thermally coupled states  $R$  is described by Boltzmann distribution and is given as:

$$R = \frac{N_2}{N_1} = C e^{\frac{-\diamond E}{kT}} \quad (16.3)$$

where  $E$  is the energy gap between the two states,  $k$  is the Boltzmann constant, and  $T$  is the absolute temperature and  $C = \frac{\omega_{20}\sigma_{20g_2}}{\omega_{10}\sigma_{10g_1}}$ , and  $\sigma_{i0}$ ,  $\omega_{i0}$  and  $g_i$  are emission cross-sections, angular frequency of the radiation and degeneracies, respectively.

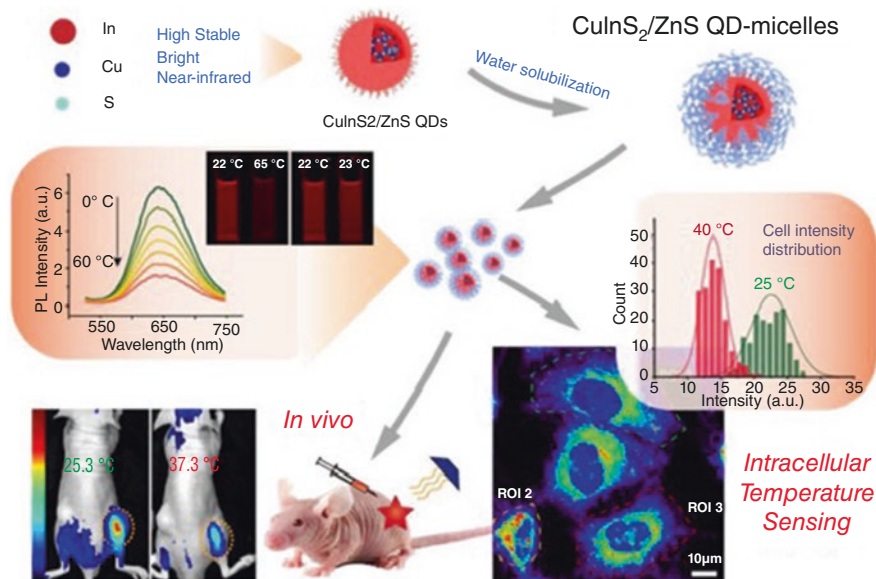
Here the number of ions in the lowered and excited state is governed by measuring the fluorescence intensity originating from these two thermally linked states. The fluorescence intensity from particular energy levels of the impurity ion doped into the host matrix dependent upon several factors such as the dimension of the dopant added to the host matrix, method used for the excitation and the particular level of interest. The sensitivity of the TS can be calculated by using this FIR and is given by:

$$S = \frac{1}{R} \frac{dR}{dT} = \frac{\diamond E}{KT^2} \quad (16.4)$$

### 16.1.2 Applications of Particularly Optical TS

Temperature is a non-additive quantity and had exceptional implications for its measurement and the creation of temperature scale. The exact measurement of temperature is vital for the study of cellular processes like reaction metabolisms, cancer therapy and research in science and technology. Recent advances in nanoscaled thermometers make accurate measurements of temperature distributions at a nanoscale regime where conventional methods are unable to make measurements. Non-invasive accurate thermometers with high resolution at nanoscale are provoking since from the last few years. TSs are the devices used to measure the temperature in various fields including medicines [13], electronics industry [14], petrochemical [15], textile [16], etc.

OTs are suitable for use in sensitive industrial locations like boiler units, HVAC systems, energy and power stations, etc. Generally, in industries, there are many locations where humans cannot reach like boiler vessels. A surface-mounted, probe type TS is a best option for monitoring the temperature conditions there. Certain industries like mining restrict human movements due to unhealthy environment, release of toxic gases, extremely high temperatures, etc. In such cases, TS probes are inserted into the complex locations and temperature monitoring is possible. Besides, material processing industries like forging, casting, metallurgy, etc., require very high temperatures and hence OTs can be useful due to their



**Fig. 16.3** Schematic illustration of the preparation of the CuInS<sub>2</sub>/ZnS QD-micelles and their intracellular and in vivo temperature sensing. (Adapted with permission from Ref. [18]. Copyright 2019: Royal Society of Chemistry)

non-contact probe method. Moreover, applications like automobile, aircraft and aerospace engineering utilise TS probes in non-human locations.

In the medical field, OTSs are frequently used for diagnosing infected cells and their thermal therapies by analysing the dynamic behaviour of cells, that is, the emission behaviour of fluorescent materials as a function of temperature. Jiang et al. [17] measured the heat generation in human umbilical vein endothelial cells (HUVEC cells) using CdTe/CdS/ZnS QDs with a sensitivity of 0.16 nm/°C and demonstrated the biocompatibility of these QDs. In another report, Zhang et al. [18] employed CuInS<sub>2</sub>/ZnS QDs encapsulated by amphiphilic micelles for accurate measurement of the intracellular temperature of HeLa and human prostate cancer cell line (PC-3) with a high thermal sensitivity of 2% °C<sup>-1</sup> at near room temperature (Fig. 16.3). Similarly, CdSe/ZnS CSHs QDs were used for thermal therapy of PC-3 cells by Han et al. [19].

## 16.2 II–VI Materials for Luminescence-Based TS

Luminescence-based TSs are in particular realised with II–VI materials owing to their peculiar emission properties. The sharp and stable emission from II to VI compound semiconductor QDs is highly desirable for such sensors. Moreover, the temperature is an important factor that significantly alters the emission properties of

these materials. The detailed discussion on the peculiar emission properties of II–VI materials and the fabrication of luminescence-based TSs are presented in the subsequent sub-sections:

### ***16.2.1 Importance and Suitability of II–VI Semiconductors for Luminescence-Based TS***

II–VI materials are mostly direct band gap materials with energy band gap from 0.02 to >4.0 eV, that is, the emission range is covered from ultraviolet to infrared spectrum. The confinement in II–VI nanostructures (NSs) such as nanoparticles, nanowires, nanorods, nanosheets, and nanocomposites leads to an increase in its band gap that lies well in the visible region and can be extensively used for emission-based devices. Tunability of optical properties of these NSs results in tuning the band gap or by selecting the size of the particles due to exhibiting of quantum confinement effect with dimensions below Bohr exciton radius, which leads to interesting luminescence properties. II–VI NSs are extensively used in diverse applications ranging from optoelectronic devices and gas sensors to optical sensors [4, 20–25]. These materials are easy to synthesise using the chemical as well as the physical routes, stable under ageing and photo exposure and can be a host to wide range of dopants due to their affinity towards activators and magnetic elements.

The widely used approach to tune the emission range and improve the efficiency of sensing devices further is the incorporation of impurity atoms in host materials. The introduction of various activators as an impurity results in the emission of various visible bands depending on the type and concentration of the impurity. The radiative efficiency of the impurity-induced emission increases significantly, which is essential for highly sensitive fluorescent sensors. As the dominating process in NSs-based sensors is emission quenching at high temperatures therefore initial high emission is must for highly sensitive and accurate sensing. Furthermore, doped NSs as well as their core-shell (CSh) structure provide a larger Stokes shift than conventional ones, which are interesting from the perspective of their application as a luminescence-based TS [25, 26].

### ***16.2.2 Single QDs and Core-Shell (CSh) QDs for Luminescence-Based TS***

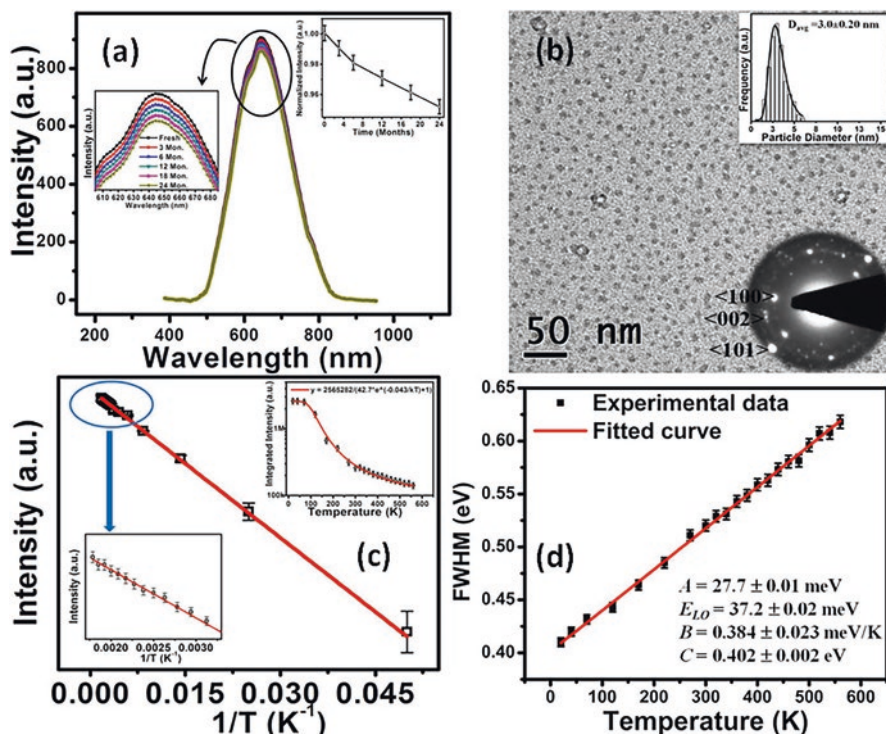
The concept of nanothermometry using QDs was established by Wang et al. [27]. They employed semiconductor nanoparticles of CdTe and doped nanoparticles of ZnS:Mn<sup>2+</sup> that exhibited a reversible linear temperature response over the physiological temperature range 30–50 °C and have potential for biomedical thermometry. The sensing resolution achieved was up to 0.02 °C. They have also studied

double-doped QDs of ZnS:Mn<sup>2+</sup>, Eu<sup>3+</sup> that displayed different temperature response for each dopant, due to the difference in transition properties of these dopants.

In order to improve the stability and tunability of single QDs, CShs are proposed and explored. Jaschinski and Wehner [28] reported a non-invasive technique for thermometry using CdSe-ZnS CShs dissolved in bovine serum albumin (BSA). Temperature-dependent photoluminescence revealed a linear peak wavelength shift of 653 nm peak with varying temperatures in the range from 30 to 70 °C. The observed sensitivity was 0.153 nm °C<sup>-1</sup> on heating. A step further was taken by Park et al. [29] by doping Mn in CdS-ZnS CShs and achieved a ratiometric luminescence-based TS with sensitivity ( $\Delta I_R/I_R = 0.5\%/K$  at 293 K,  $I_R$  = intensity ratio at two different wavelengths) linear in the temperature range from 77 to 380 K. In a successful intracellular thermal measurement for the biological study of cells and tissues, Zhang et al. [18] utilised the temperature dependence of luminescence intensity of CuInS<sub>2</sub>/ZnS CShs. They studied the intracellular and in vivo temperature sensing after encapsulation of these CShs by amphiphilic micelles (QD-micelles). Approximately 10.1 ± 2.5 nm QD-micelles exhibited an intense emission band at nearly 650 nm. A high thermal sensitivity of 2% °C<sup>-1</sup> at near room temperature is achieved and found insensitive to the pH of the solution, ionic strength and concentration of protein. Their QD-micelles exhibited an intracellular thermal sensitivity of 2.0% °C<sup>-1</sup> and 2.1% °C<sup>-1</sup> in tumour tissue, as well as good linearity in the physiological temperature range of 0–60 °C. A new non-toxic nanoparticles of ZnS–AgInS<sub>2</sub> (ZAIS) with two different compositions, that is, ZAIS<sub>x=0.4</sub> and ZAIS<sub>x=0.9</sub> were investigated for potential application as luminescence-based TS by Matsuda et al. [30] and a temperature sensitivity of ca. 1%/K was achieved in the temperature range 293–353 K.

### 16.3 Embedded QDs Composites in CSh Matrix for Luminescence-Based TS

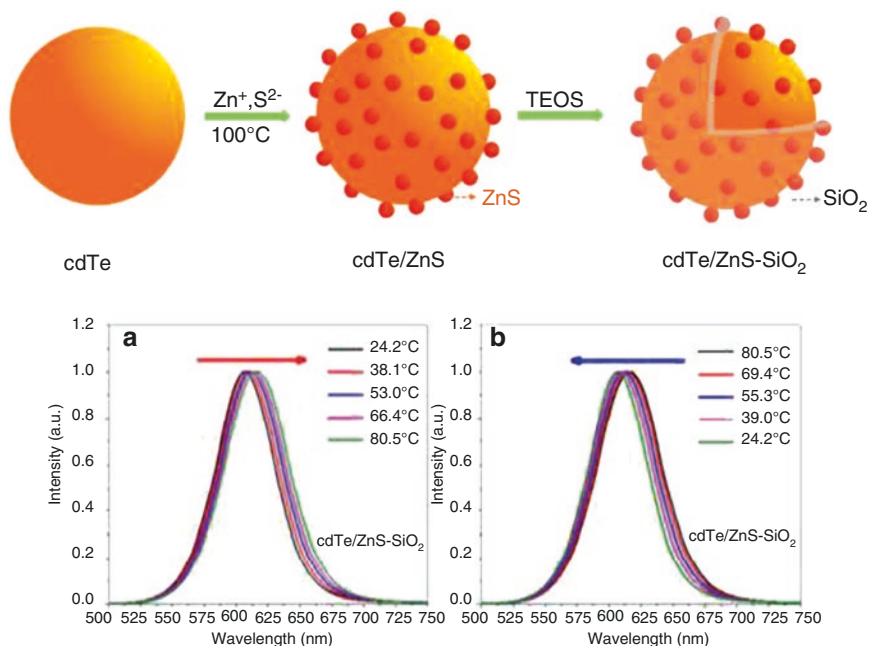
In order to further improve the stability of QDs and CShs, a matrix is very important to provide them mechanical robustness, better photostability, saturation on surface states and resistance against oxidation and moisture as well as decreasing toxicity for biomedical applications. CdS QDs were ablated with SiO<sub>2</sub> and deposited on silicon substrate to form CdS:SiO<sub>2</sub> nanocomposite thin films to realise a wide range (20–560 K) luminescence-based TS by Saxena et al. [4]. The sensor was based on the intensity and FWHM of the emission peak. This TS was reported with the highest average sensitivity of 10<sup>-2</sup> K<sup>-1</sup> and a resolution of 10<sup>-4</sup> K, respectively, and a maximum relative sensitivity of ~8.4% K<sup>-1</sup> at 120 K using intensity as the sensing method. Whereas, the FWHM sensing method yields an analytic sensitivity of ~0.388 meV K<sup>-1</sup> for this sensor. Figure 16.4a–d represents this vital TS ever reported to date.



**Fig. 16.4** (a) Room temperature PL of the CdS:SiO<sub>2</sub> nanocomposite TS recorded at definite intervals. Inset: Variation of PL intensity as a function of ageing time. (b) TEM image of CdS:SiO<sub>2</sub> nanocomposite. Inset: particle size histogram and SAED pattern. (c) Linear fitting to intensity as a function of inverse temperature. Inset: Variation of integrated intensity with temperature. The linear fit to the experimental data is represented by the red line. (d) FWHM variation with temperature. The solid curve represents fitting to the experimental data

In another attempt, CdSe(ZnS) CShs were suspended in a SiO<sub>2</sub> dielectric matrix to form a nanocomposite by Pugh-Thomas et al. [6]. The variation of emission peak wavelength and FWHM with temperature in a range 295–525 K with a sensitivity of  $\sim 0.11$  nm °C<sup>-1</sup>. CdTe/ZnS-SiO<sub>2</sub> nanocomposites were investigated for temperature-dependent luminescence properties by Zhang et al. [31] in the range from room temperature to 80 °C. Figure 16.5 depicts a schematic representation of the preparation of CdTe/ZnS-SiO<sub>2</sub> nanocomposites, while temperature-dependent PL is presented in heating and cooling cycle in Fig. 16.5a, b, respectively. Table 16.1 summarises different types of morphologies employed for luminescence-based TSs using II–VI materials.





**Fig. 16.5** Schematic of the synthesis process of CdTe/ZnS-SiO<sub>2</sub> nanocomposite. Temperature-dependent PL in (a) heating and (b) cooling process. (Adapted with permission from Ref. [31]. Copyright 2021: Elsevier)

**Table 16.1** Luminescence-based TS utilising II–VI QDs, CSHs, Embedded QDs/CSHs, nanocomposites, etc

II–VI materials and morphology	Sensing method	Sensitivity	Temperature range	References
CdSe in aqueous solution	Lifetime decay	-0.08%	20–50 °C	[32]
CdTe in aqueous solution		-0.17%		
CdS-Zn: Mn <sup>2+</sup> in solution	Intensity ratiometric	0.5%	77–380 K	[29]
ZnS:Mn <sup>2+</sup> in solution	Intensity	-0.25%	303–423	[27]
ZnS:Mn <sup>2+</sup> , Eu <sup>2+</sup> in solution		-0.55		
ZnS-AgInS <sub>2</sub> in dried state	Intensity	-1%	293–353	[30]
CdSe-ZnS CSHs thin films on SiO <sub>2</sub>	Peak shift	~0.1 nm/°C	30–180	[33]
	Intensity FWHM	0.076 nm/°C		
CdSe-ZnS CSHs on AA-TSP	Intensity	-0.7 to -1.5%/K	100–315 K	[26]
CdSe QDs in (toluene, PMMA, PDMS and epoxy)	Intensity and wavelength		30~75 °C	[34]
CdSe:SiO <sub>2</sub>	Peak shift	-0.095 nm	303–373	[35]
CdSe-ZnS:SiO <sub>2</sub>	Peak shift	0.11 nm	295–525	[6]

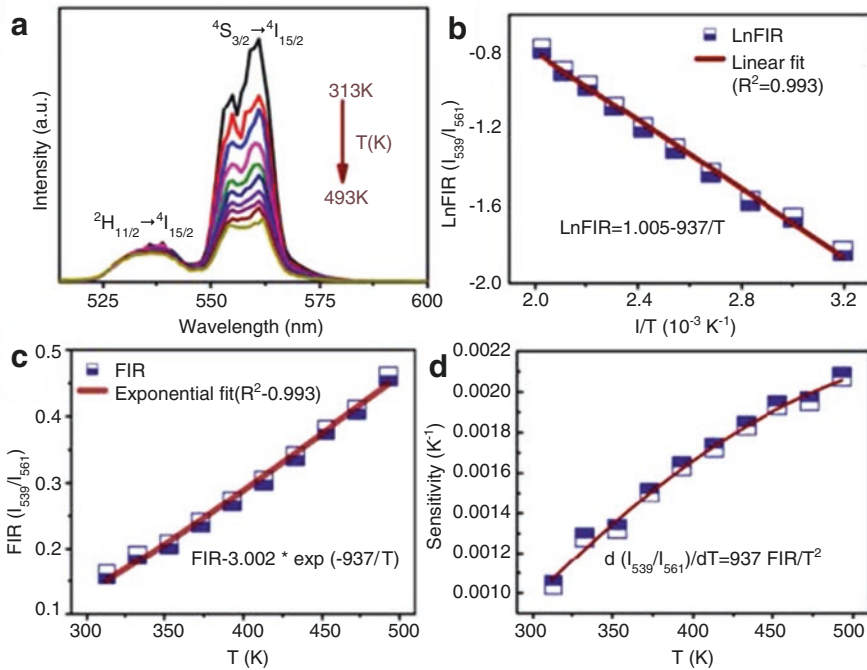
AA-TSP Anodised Aluminium-Temperature Sensitive Paint, PMMA Poly methyl methacrylate, PDMS Polydimethylsiloxane

## 16.4 Ratiometric, Colorimetric and Lifetime Fluorescence-Based Optical TS

The first application of the FIR technique in temperature sensing was reported by Kusama et al. in 1976 in  $\text{Eu}^{3+}:\text{Y}_2\text{O}_3$  phosphor where the measurements were made in the temperature range  $-173 + -27^\circ\text{C}$  [36].  $\text{Er}^{3+}:\text{BaTiO}_3$  TS reported by Marcio et al. [37] is based upon the FIR method to measure the sensitivity. González et al. [32] studied the response of the CdTe-QDs fluorescence lifetime in the temperature range of  $20\text{--}50^\circ\text{C}$  which is a biological range. They reported a systematic study on the dependence of lifetime-based temperature sensing response on size of CdSe and CdTe QDs as fluid samples. The sensitivity achieved by them was  $0.0008$  and  $0.017^\circ\text{C}^{-1}$  for  $4\text{ nm}$  CdSe QDs and  $1\text{ nm}$  CdTe QDs, respectively.

CdTe/ZnS QDs mediated fluorescence TS was developed and characterised in a temperature range relevant to hyperthermic therapies. Further, a temperature-intensity relationship was established to demonstrate the feasibility of spatiotemporal monitoring of thermal lesions [19]. TS was fabricated using CdTe/CdS/ZnS core/shell/shell QDs to measure the intracellular temperature variation. The biocompatibility of QDs for cells was confirmed by cytotoxicity evaluation and thermal sensibility of the QDs was calibrated which showed a linear correlation of  $0.16\text{ nm}/^\circ\text{C}$  with the temperature variation. The PL spectral shift of QDs uptake in cell indicated a thermogenesis of  $3.125^\circ\text{Ct}$  [17]. A multi-colour (orange–yellow–green) and multi-mode (upconversion/down-shifting/energy transfer) luminescence material ( $\text{Er}^{3+}$  doped ZnS) has been developed for anti-counterfeiting and TS. TS was carried out on the basis of the intensity ratio of the two thermally coupled emission peaks over  $300\text{--}500\text{ K}$  and found that absolute sensitivity ( $S_a$ ) increases with increasing temperature with the maximum sensitivity  $0.0021\text{ K}^{-1}$  [38]. Figure 16.6a–d depicts ratiometric temperature sensing using  $\text{Er}^{3+}$  doped ZnS under  $980\text{ nm}$  wavelength excitation.

Vlaskin and co-workers observed intrinsic high-temperature dual emission from  $\text{Zn}_{1-x}\text{Mn}_x\text{Se}/\text{ZnCdSe}$  core/shell QDs and fabricated TS that showed a high sensitivity over a temperature range  $223$  and  $403\text{ K}$  with a maximum sensitivity of  $9 \times 10^{-3}\text{ K}^{-1}$  [39]. In subsequent work, they developed TS based on  $\text{Zn}_{1-x}\text{Mn}_x\text{Se}/\text{ZnS}/\text{CdS}/\text{ZnS}$  core/shell/shell QDs that displayed display a maximum sensitivity of  $8.3 \times 10^{-3}\text{ K}^{-1}$  [40]. Whereas Jethi et al. [41] succeeded to generate dual emission from CdSe QDs itself and developed TS, which, worked well in the range  $82\text{--}280\text{ K}$  with a sensitivity range, is  $\sim 0.69\text{--}0.32\%\text{ K}^{-1}$  and a maximum slope of  $0.44\%\text{ K}^{-1}$ . Zhao et al. [42] discussed recent progress perspectives for future work on dual-emitting QD-based nanothermometers.

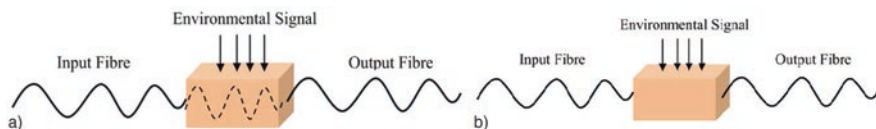


**Fig. 16.6 (a–d)** Fluorescence intensity ratio-based temperature sensing using  $\text{Er}^{3+}$  doped ZnS. (Adapted with permission from Ref. [38]. Copyright 2020: Elsevier)

## 16.5 Fibre Optic and Surface Plasmon Resonance-Based TS

### 16.5.1 Fibre Optic-Based TS

Small size, high and better selectivity, large bandwidth, low cost, immune to electromagnetic interference and ease in signal light transmission are the characteristics of optical fibre (OF)-based temperature sensors which make them an important optical sensor. The sensor of this category works on the principle of temperature dependence change in band gap of semiconductor materials/crystals. The semiconductor is placed on the tip of the fibre and will be transparent at/above a certain wavelength. The position of the band edge is temperature dependent and is shifted about few  $\text{\AA}/\text{K}$  to few  $\text{nm}/\text{K}$ . The light is directed via the optical fibre to the semiconductor, where it is absorbed and partially reflected back into the fibre. The temperature can be calculated from a miniature spectrometer which gives a spectrum with the peak position of the band edge. On the basis of techniques, different types of fibre-optic sensors have been developed. The optical signal is transmitted to optic-electronic detection systems via optic fibre. A temperature-sensitive material undergoes changes with respect to temperature, for example, absorption, reflection, interference and scattering. A light source, optical fibre, a sensing element and a



**Fig. 16.7** (a) Extrinsic FOS (b) Intrinsic FOS. (Adapted with permission from Ref. [43]. Published 2013 by MDPI as open access)

detector are the main components of an OF sensing system. An optical fibre structure contains a core encapsulated by some cladding which is a material of a lower refractive index and both are transparent dielectrics and cylindrical in shape. The basic requirement of fibre optic system (FOS) is to have its minimum optical and mechanical attenuation without any performance degradation. FOS are of two types: intrinsic and extrinsic. Figure 16.7a, b shows the basic designing of extrinsic and intrinsic FOS, respectively. The intrinsic devices are based on a light beam transmitting through the fibre and an interaction takes place between the environmental signal and the optical fibre itself while in extrinsic fibre, the optical fibre is utilised to collate the light. The light beam transmits and comes out of fibre after exposing to the environment signal. The light becomes doubled and returns to the fibre again [43].

To date, there is a wide range of TS based upon optical fibres have been commercialised. The first ever optic sensor was silica-based optical fibre that uses Raman backscattered light to measure the distribution of temperature [44]. In the past few decades, Fibre Bragg Grating (FBG) is most extensively used for the sensor heads due to their susceptibility to minute changes in refractive index. The basic concept for operation of an FBG sensor system is to study the shift in the wavelength of the reflected Bragg signal [45]. This characteristic of FBG-based sensor systems is used to sense temperature due to their ability to operate over a broad spectral range. A simple formula for grating is represented by

$$\lambda_B = 2 \cdot n_{\text{eff}} \cdot \Lambda \quad (16.5)$$

where  $\lambda_B$  is the Bragg wavelength.  $n_{\text{eff}}$  is the effective refractive index of the material and  $\Lambda$  is the grating pitch.

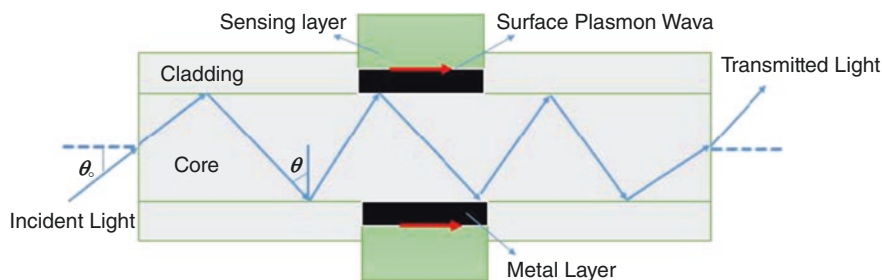
But they suffer from limited temperature-induced spectral displacements ( $\sim 0.01 \text{ nm}/^\circ\text{C}$ ) and need isolators to prevent back reflections and also cannot operate at high temperature due to its tendency of being erased.

The length and the refractive index of an optical fibre will alter if it is exposed to an environmental disturbance. Interferometry techniques are used to record these changes with a high level of sensitivity and better resolution. Different types of fibre optic with two-beam interferometer sensors such as the Mach-Zehnder [46], Michelson [47], multi-beam interferometer sensors such as Sagnac [48] and Fabry-Perot [49], can be used to sense the temperature. Generally, interferometry sensors are good enough to enhance the performance parameters.

Out of various fluorescent materials, II–VI group compound semiconductor QDs are widely employed for the development of OFTS because of their easy synthesis procedures, high absorption and emission tunability and high-temperature sensitivity. An OFTS based on CdSe-nanocrystallite-doped phosphate glass with a simple intensity detection scheme showed a reversible temperature-induced absorption edge shift at temperatures less than the annealing temperature of the glass (370 °C). TS exhibited a linear shift of the absorption edge with temperature in the range from –20 to 120 °C and a reversible temperature-induced absorption-edge shift of 0.12 nm/K has been measured for 6-nm particles [50]. A reflective OFTS was proposed using ZnO thin film over sapphire prism surface that showed a temperature resolution of  $\sim 1$  °C in the temperature region of 300–773 K. However, a measurement range from 10 to 1800 K is predicted theoretically by integrating low (minus) temperature and high-temperature testing functions [51]. The nanocomposites of CdSe and CdTe QDs embedded in a PMMA matrix were employed to develop PL quenching-based OFTS that showed sensing in a temperature range from 25 to 50 °C with a temperature resolution of 0.05 °C and blue shift of 0.25 nm/°C and  $\sim 0$  nm/°C for CdTe-PMMA and CdSe-PMMA-based OFTS, respectively [52]. Temperature-dependent linear relation PL intensity degradation was observed in the temperature range of 25 and 135 °C for OFTS fabricated using carboxylated capped CdSe/ZnS core/shell QDs [53]. Whereas, a reflective OFTS was designed by deposition of CdSe/ZnS core/shell QDs on the SiO<sub>2</sub> glass substrates that showed a linear red shift in PL peak with increasing temperature 30–200 °C and exponential relationship of peak intensity and FWHM as a function of temperature according to the specific physical law with the average resolution of 0.12 nm/°C and 0.056 nm/°C according to the shift and FWHM of PL spectrum, respectively [54]. In his another work, a similarly linear red shift in PL peak with temperature was recorded through TS based on the hollow-core photonic bandgap fibre filled with the CdSe/ZnS QDs in the temperature range from 40 to 140 °C, with a correlation factor of 0.99263 and a sensitivity of 0.05744 nm/°C. The peak intensity was also exponentially temperature dependent and a linear temperature-dependence result with a correlation factor of 0.99917 and a slope of  $2.04 \times 10^{-3}$  °C<sup>-1</sup> was obtained with a self-reference spectral intensity method [55]. While the CdSe/ZnS core/shell QDs doped in PMMA matrix-based OFTS showed a linear red shift PL peak variation with temperature over the range 25–48 °C [56].

### 16.5.2 Surface Plasmon Resonance-Based TS

SPR is a phenomenon that takes place when a polarised light incidents on a metal film having an interface with media of different refractive indices under specific resonance conditions [57]. This resonance condition is extremely sensitive to the refractive index and thickness of the dielectric medium in contact with the metal surface. In the last 20 years, SPR has been extensively studied for the measurement of temperature [10]. The first sensing application of SPR was reported in 1983 [58]



**Fig. 16.8** A typical probe of an SPR-based fibre optic sensor. (Adapted with permission from Ref. [65]. Published 2019 by Hindawi, as open access)

in the field of chemical sensing. The SPR technique can be employed to sense the temperature of a medium due to the dependence of the refractive index of the material on its temperature. SPR-based TS was proposed by Xiaoke et al. [59] using a coupling prism and angle interrogation mode of operation.

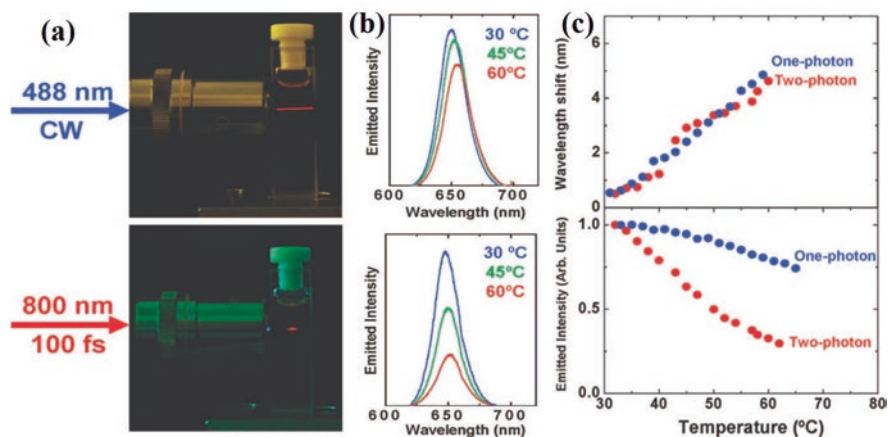
The coupling prism used in SPR sensing system can be replaced by the core of an OF. Simplicity, Flexibility, small size and remote sensing capability are some of the advantages of using OF over prism. For the fabrication of an SPR-based fibre optic sensor, a small portion of the silicon cladding is removed and the unclad core is coated with another metal layer which is surrounded by a dielectric sensing layer as shown in Fig. 16.8. The polychromatic light is then launched into one end of the optical fibre and causes the surface plasmons to excite at the metal-dielectric sensing layer interface and the intensity of the light transmitted after passing through the SPR. Therefore, it is more suitable for sensing applications. SPR enables the construction of optical sensors for the measurement of the concentration of chemical, pressure and temperature [60–62]. The first report on the fibre-optic SPR-based TS was given by Villuendas and Pelayo in 1990 [63].  $\text{TiO}_2$  was reported as a prominent material for temperature sensing if deposited onto the tip of an OF owing to its high  $\frac{dn}{dt} \sim -1.49 \times 10^{-4} \text{ K}^{-1}$  [64].

## 16.6 Thermal Imaging with II–VI Materials

Since the end of twentieth century, intra-cellular incorporation of fluorescent nanothermometers (NThMs) is the widely used approach for intracellular thermal sensing. Typically, any fluorescent QDs whose emission properties (intensity, spectral position, spectral shape or decay time) are strongly dependent on the local temperature of the environment surrounding of QDs are potential aspirants for fluorescent NThMs [66, 67]. The thermal sensing in NThMs usually relies upon one of the temperature-dependent parameters that results in high-resolution thermal imaging techniques, like scanning thermal and molecular fluorescence polarisation microscopies. In addition, several features like monodispersity in aqueous media, high

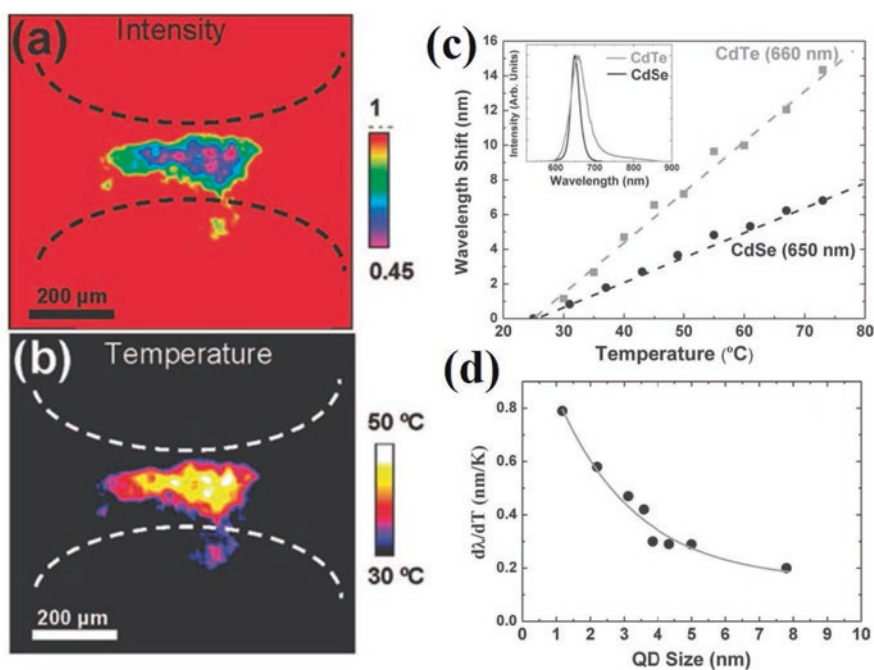
quantum efficiency, long-term thermal stability, minimal interaction capability with the investigated medium, and excitation wavelength in NIR region via multiphoton (MP) processes are the basic requirements of luminescence NThMs in the real-world application for both intracellular and small animal levels thermal sensing and imaging [66]. The large two-photon absorption cross-section offered by QDs enables to produce significant visible emission under near-infrared (NIR) two-photon excitation which is not possible with organic probes [68]. In particular, the use of NIR radiation is essential for real 3D thermal sensing and imaging of living cells as NIR radiation matches the biological windows (BW-I: 700–950 nm, BW-II: 1000–1350 nm and BW-III: 1500–1800 nm) and thus minimise the absorption and scattering of light by tissues that turn into larger penetration depths, minimum energy deposition and reduced nonselective light-induced damage [66, 67, 69]. Besides, NIR radiation (multiphoton excitation) offers high spatial resolution, even below the diffraction limit and overcomes the limiting factor in the resolution of conventional fluorescence microscopes [70].

Maestro et al. [68] have assessed the ability of CdSe QDs in fluorescent NThMs to realise thermal imaging by means of modern multiphoton fluorescence imaging microscopes. They have initially recorded emission spectra of CdSe QDs as a function of temperature in the physiological temperature range under both single-photon and two-photon excitation to test their thermal detection capability and noticed diverse thermal behaviours of QDs under two excitation that were used for thermal sensing and calibration (Fig. 16.9a–c). Further, they determined the thermal gradients induced in a liquid by a focused laser beam and finally demonstrated the prospective of these two-photon excited NThMs in biomedical imaging by measuring



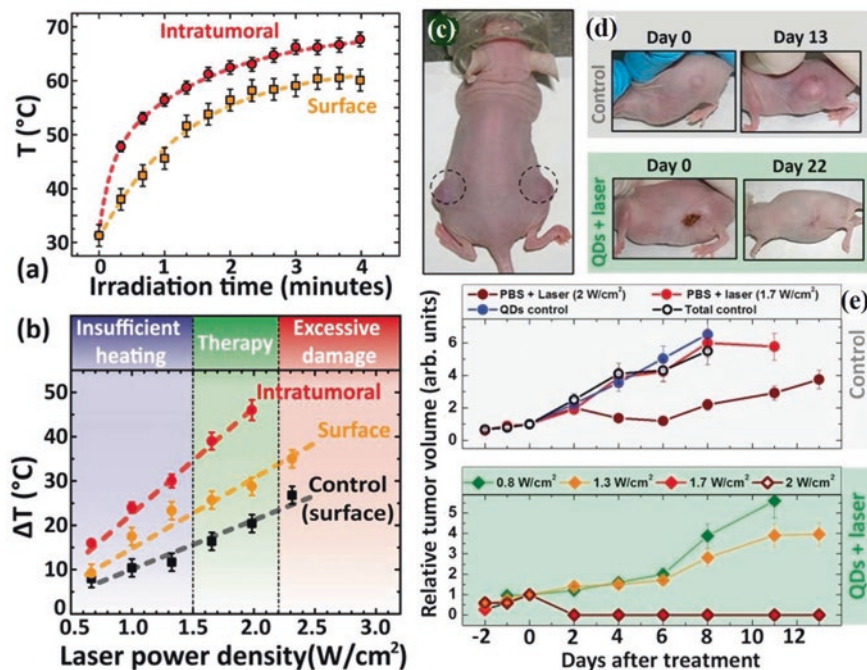
**Fig. 16.9** (a) Digital images of the CdSe-QDs/PBS solution obtained at room temperature, (b) Emission spectra of the CdSe-QDs/PBS solution at three different temperatures (30, 45 and 60 °C) obtained with one-photon (top) and two-photon (bottom) excitation, respectively, and (c) Variation of the emission peak wavelength (top) and integrated emitted intensity (bottom) with temperature as obtained from the CdSe-QDs/PBS solution under one and two-photon excitation. (Adapted with permission from Ref. [68]. Copyright 2010: American Chemical Society)

the temperature evolution of a single HeLa cancer cell (Fig. 16.10a–b). In their subsequent work, they have systematically investigated the temperature dependence (25–70 °C) of the two-photon emission of CdTe QDs of different sizes (from  $\approx 1$  to 8 nm) and found that temperature sensitivity of emission from the CdTe QDs is higher than that of the previously explored CdSe QDs (Fig. 16.10c). Further, the spectral shift coefficient of CdTe QDs as a function of QDs size was systematically analysed and results are summarised in Fig. 16.10d. It was observed that spectral shift coefficient is remarkably increased when the QDs size is less than  $\approx 4$  nm and reaches a maximum of 0.8 nm/K for the smallest QDs analysed in that work (1.2 nm) which was more than five times larger than that of the CdSe QD in their previous work [66]. In their other work, they have reported that large (8 nm) CdTe QDs are the most prominent optical probes for deep tissue biological imaging. This is due to the fact that both excitation (900 nm) and emission (800 nm) wavelengths lie within



**Fig. 16.10** (a) Spatial variation of the two-photon excited emission intensity as obtained from a CdSe-QDs/PBS solution in the presence of a focused 980 nm heating laser beam (the profile is schematically shown with the dashed lines). (b) Thermal image of the CdSe-QDs/PBS solution denoting the local temperature increment at the 980 nm beam focus. (c) Temperature-induced peak wavelength shift as obtained from CdSe and CdTe QDs, demonstrating the superior thermal sensitivity of CdTe. Inset: room-temperature emission spectra of CdSe and CdTe QDs with a peak emission wavelength at approximately 650 nm and (d) Spectral thermal sensitivity of CdTe QDs as a function of the peak emission wavelength and of QD size. Circles are experimental data, solid line is a guide for the eyes. (Adapted with permission from Ref. [68]. Copyright 2010: American Chemical Society)





**Fig. 16.11** Temperature increment during treatment. (a) Intra-tumour temperature and skin surface temperature measured during PTT treatment of a tumour under irradiation at  $1.7\text{ W cm}^{-2}$  with an 808 nm laser. The data were collected using QDs and a thermographic camera, respectively. The dashed lines represent guides for the eyes. (b) Temperature increment for different irradiation power densities measured at the tumour site and at the skin surface. The black dots represent the temperature increments at the tumour skin surface for control mice, which were injected with PBS. Three different ranges are indicated in the graph, which corresponds to the different effects (no significant tumour damage, successful PTT, and extensive damage to the tissues adjacent to the tumour) observed in the treated mice depending on the irradiation power density. Evolution of the tumours after the treatment. (c) Representative mouse with one tumour in each flank (dashed circles), anaesthetised and ready for the treatment. (d) Top: evolution of a total control tumour. Bottom: after the QDs + laser ( $1.7\text{ W cm}^{-2}$ ) treatment. (e) Top: size evolution of the tumours under different control conditions: total control, QDs only and PBS + 808 nm laser at 1.7 and  $2\text{ W cm}^{-2}$ . The dashed line indicates the day of the treatment. Bottom: size evolution of the tumours as a function of irradiation power densities and days. Error bars correspond to the experimental determination of the tumour size ( $\pm 15\%$ ). (Adapted with permission from Ref. [67]. Copyright 2016: WILEY-VCH Verlag GmbH & Co. KGaA)

the ‘biological window’ allowing for high resolution fluorescence imaging at depths close to 2 mm which can be used to obtain the ‘deep tissue’ imaging [71].

Choudhury et al. have used CdTe QDs within an optofluidic device consisting of a microchannel locally illuminated by an adjacent buried waveguide and demonstrated the importance of the microchannel optical local heating that cannot be disregarded within the context of on-chip optical cell manipulation. They

presented thermal imaging of locally illuminated microchannels when filled with nano-heating particles such as carbon nanotubes [72]. Temperature self-monitored PbS/CdS/ZnS QDs that emit light in BW-II were used in photothermal therapy (PTT) of cancer cells. These QDs can be used as both photothermal agents (heaters) and high-resolution fluorescent thermal sensors simultaneously that make it possible to achieve full control over the intratumoral temperature increment during PTT. The need for real-time control of the intratumoral temperature is highlighted through the comprehensive investigation of the differences observed between intratumoral and surface temperatures under different irradiation conditions (Fig. 16.11a, b). Their study allows a dynamic adjustment of the treatment conditions in order to maximise the efficacy of the therapy (Fig. 16.11c–e) [67].

## 16.7 Conclusion and Future Prospective

This chapter outlines the optical thermometry based on II–VI compound semiconductors. A systematic approach is presented here to look into every aspect of OTS. A lot of methods have been approached to realise these OTSs and a variety of materials have been explored owing to their peculiar size-dependent optical properties. There are many reports on very advanced OTSs which can be used to measure the intracellular temperature and detection of tumours in the body. However, certain challenges are there to be overcome in near future.

The very important and foremost concern with II–VI semiconductors is their stability against moisture, oxygen, light and temperature. Single QDs suffer a lot of drawbacks if exposed to these conditions. A right approach is to coat the single QDs with some other II–VI material or any other material in the form of CShs. This approach reduced the drawbacks to some extent but unsaturated surface states were still affecting the emission properties significantly. An insulating, robust and transparent matrix was proven to be one solution to this problem. Hence, encapsulation of single QDs and CShs in a matrix preferably  $\text{SiO}_2$  was well studied and proven to be the best matrix so far. The emission is conserved for prolonged exposure and so is the sensor. The temperature sensor devised using this technique are reusable, economic, robust and durable.

From a future prospective, it is imperative to be selective for a particular application. Moreover, many other applications require measurement of local temperatures, so a lot of scope is there to study the temperature-dependent response of various materials which are dominating in one or other applications. It works like if in a particular device made of a particular material, the data of variation of its different properties with temperature should be available, so that the local temperature of that device could be measured in case of any wear or tear due to high temperature.

## References

1. Fan S, Wu M, Ma S, Zhao S. A preventive and control strategy for COVID-19 infection: an experience from a third-tier Chinese City. *Front Public Health*. 2020;8:562024.
2. Seshadri DR, Davies EV, Harlow ER, Hsu JJ, Knighton SC, Walker TA, Voos JE, Drummond CK. Wearable sensors for COVID-19: a call to action to harness our digital infrastructure for remote patient monitoring and virtual assessments. *Front Dig Health*. 2020;2:8.
3. Neibert P. Device for indicating the temperature distribution of hot bodies, U.S. patent, US2071471A, 23 February 1933.
4. Saxena N, Kumar P, Gupta V. CdS: SiO<sub>2</sub> nanocomposite as a luminescence-based wide range temperature sensor. *RSC Adv*. 2015;5(90):73545–51.
5. Varshni YP. Temperature dependence of the energy gap in semiconductors. *Physica*. 1967;34:149–54.
6. Pugh-Thomas D, Walsh BM, Gupta MC. CdSe(ZnS) nanocomposite luminescent high temperature sensor. *Nanotechnology*. 2011;22(18):185503.
7. Zhang L-G, Fan X-W, Lu S-Z. Exciton-phonon scattering in CdSe<sub>x</sub>ZnSe<sub>1-x</sub> quantum dots. *Chin Phys Lett*. 2002;19:578–80.
8. Otto A. Excitation of nonradiative surface plasma waves in silver by the method of frustrated total reflection. *Z Physik*. 1968;216(4):398–410.
9. Kretschmann E, Raether H. Radiative decay of non radiative surface plasmons excited by light. *Zeitschrift für Naturforschung A*. 1968;23(a):2135–6.
10. Chadwick B, Gal M. An optical temperature sensor using surface plasmons. *Jpn J Appl Phys*. 1993;32:2716–7.
11. Chochol J, Postava K, Cada M, Pistora J. Experimental demonstration of magnetoplasmon polariton at InSb(InAs)/dielectric interface for terahertz sensor application. *Sci Rep*. 2017;7(1):13117.
12. Dey R, Kumar Rai V. Er<sup>3+</sup>-Tm<sup>3+</sup>-Yb<sup>3+</sup>:CaMoO<sub>4</sub> phosphor as an outstanding upconversion-based optical temperature sensor and optical heater. *Methods Appl Fluoresc*. 2017;5(1):015006.
13. Yamamoto Y, Yamamoto D, Takada M, Naito H, Arie T, Akita S, Takei K. Efficient skin temperature sensor and stable gel-less sticky ECG sensor for a wearable flexible healthcare patch. *Adv Healthc Mater*. 2017;6(17)
14. Lee CY, Lee SJ, Tang MS, Chen PC. In situ monitoring of temperature inside lithium-ion batteries by flexible micro temperature sensors. *Sensors (Basel)*. 2011;11(10):9942–50.
15. Wang Q, Zhang L, Sun C, Yu Q. Multiplexed fiber-optic pressure and temperature sensor system for down-hole measurement. *IEEE Sensors J*. 2008;8(11):1879–83.
16. Sibinski M, Jakubowska M, Sloma M. Flexible temperature sensors on fibers. *Sensors (Basel)*. 2010;10(9):7934–46.
17. Jiang X, Li BQ, Qu X, Yang H, Liu H. Thermal sensing with CdTe/CdS/ZnS quantum dots in human umbilical vein endothelial cells. *J Mater Chem B*. 2017;5(45):8983–90.
18. Zhang H, Wu Y, Gan Z, Yang Y, Liu Y, Tang P, Wu D. Accurate intracellular and in vivo temperature sensing based on CuInS<sub>2</sub>/ZnS QD micelles. *J Mater Chem B*. 2019;7(17):2835–44.
19. Han B, Hanson WL, Bensalah K, Tuncel A, Stern JM, Caddeu JA. Development of quantum dot-mediated fluorescence thermometry for thermal therapies. *Ann Biomed Eng*. 2009;37(6):1230–9.
20. Kumar P, Saxena N, Dewan S, Singh F, Gupta V. Giant UV-sensitivity of ion beam irradiated nanocrystalline CdS thin films. *RSC Adv*. 2016;6(5):3642–9.
21. Kumar P, Saxena N, Singh F, Gupta V. Ion beam assisted fortification of photoconduction and photosensitivity. *Sens Actuator A Phys*. 2018;279:343–50.
22. Saxena N, Kumar P, Gupta V. CdS nanodroplets over silica microballs for efficient room-temperature LPG detection. *Nanoscale Adv*. 2019;1(6):2382–91.
23. Kalsi T, Kumar P. Cd<sub>1-x</sub>Mg<sub>x</sub>S CQD thin films for high performance and highly selective NIR photodetection. *Dalton Trans*. 2021;50(36):12708–15.
24. Singh S, Khan ZH, Khan MB, Kumar P, Kumar P. Quantum dots-sensitized solar cells: a review on strategic developments. *Bull Mater Sci*. 2022;45(2)

25. Lesiak A, Drzozga K, Cabaj J, Banski M, Malecha K, Podhorodecki A. Optical sensors based on II–VI quantum dots. *Nanomaterials* (Basel). 2019;9(2)
26. Claucherty S, Sakaue H. Temperature characterization of an optical-chemical tunable-peak sensor using CdSe/ZnS quantum-dots applied on anodized-aluminum for surface temperature measurement. *Sensors Actuators B Chem.* 2017;251:958–62.
27. Wang S, Westcott S, Chen W. Nanoparticle luminescence thermometry. *J Phys Chem B.* 2002;106:11203–9.
28. Jaschinski E, Wehner M. CdSe–ZnS quantum dots as temperature sensors during thermal coagulation of bovine serum albumin (BSA) solder. *Appl Phys A.* 2012;107(3):691–6.
29. Park Y, Koo C, Chen HY, Han A, Son DH. Ratiometric temperature imaging using environment-insensitive luminescence of Mn-doped core-shell nanocrystals. *Nanoscale.* 2013;5(11):4944–50.
30. Matsuda Y, Torimoto T, Kameya T, Kameyama T, Kuwabata S, Yamaguchi H, Niimi T. ZnS–AgInS<sub>2</sub> nanoparticles as a temperature sensor. *Sensors Actuators B Chem.* 2013;176:505–8.
31. Zhang P, Pan A, Yan K, Zhu Y, Hong J, Liang P. High-efficient and reversible temperature sensor fabricated from highly luminescent CdTe/ZnS–SiO<sub>2</sub> nanocomposites for rolling bearings. *Sensors Actuators A Phys.* 2021;328:112758.
32. Haro-Gonzalez P, Martinez-Maestro L, Martin IR, Garcia-Sole J, Jaque D. High-sensitivity fluorescence lifetime thermal sensing based on CdTe quantum dots. *Small.* 2012;8(17):2652–8.
33. Wang H-L, Yang A-J, Sui C-H. Luminescent high temperature sensor based on the CdSe/ZnS quantum dot thin film. *Optoelectron Lett.* 2013;9(6):421–4.
34. Ke T-T, Lo Y-L, Sung T-W, Liao C-C. CdSe quantum dots embedded in matrices: characterization and application for low-pressure and temperature sensors. *IEEE Sensors J.* 2016;16(8):2404–10.
35. Sung T-W, Lo Y-L. Dual sensing of temperature and oxygen using PtTFPP-doped CdSe/SiO<sub>2</sub> core–shell nanoparticles. *Sensors Actuators B Chem.* 2012;173:406–13.
36. Kusama H, Sovers OJ, Yoshioka T. Line shift method for phosphor temperature measurements. *Jpn J Appl Phys.* 1976;15:2349–58.
37. Alencar M, Maciel GS, de Araújo CB, Patra A. Er<sup>3+</sup>-doped BaTiO<sub>3</sub> nanocrystals for thermometry: influence of nanoenvironment on the sensitivity of a fluorescence based temperature sensor. *Appl Phys Lett.* 2004;84(23):4753–5.
38. Yan W, Bai G, Ye R, Yang X, Xie H, Xu S. Dual-mode luminescence tuning of Er<sup>3+</sup> doped Zinc Sulfide piezoelectric microcrystals for multi-dimensional anti-counterfeiting and temperature sensing. *Opt Commun.* 2020;475:126262.
39. Vlaskin VA, Janssen N, van Rijssel J, Beaulac R, Gamelin DR. Tunable dual emission in doped semiconductor nanocrystals. *Nano Lett.* 2010;10(9):3670–4.
40. McLaurin EJ, Bradshaw LR, Gamelin DR. Dual-Emitting Nanoscale Temperature Sensors. *Chem Mater.* 2013;25(8):1283–92.
41. Jethi L, Krause MM, Kambhampati P. Toward ratiometric nanothermometry via intrinsic dual emission from semiconductor nanocrystals. *J Phys Chem Lett.* 2015;6(4):718–21.
42. Zhao H, Vomiero A, Rosei F. Tailoring the heterostructure of colloidal quantum dots for ratiometric optical nanothermometry. *Small.* 2020;16(28):e2000804.
43. Chong SS, Aziz AR, Harun SW. Fibre optic sensors for selected wastewater characteristics. *Sensors* (Basel). 2013;13(7):8640–68.
44. Dakin JP, Pratt DJ, Bibby GW, Ross JN. Distributed optical fibre Raman temperature sensor using a semiconductor light source and detector. *Electron Lett.* 1985;21:569–70.
45. Rao Y-J. In-fibre Bragg grating sensors. *Meas Sci Technol.* 1997;8:355–75.
46. Hu X, Shen X, Wu J, Peng J, Yang L, Li J, Li H, Dai N. All fiber M-Z interferometer for high temperature sensing based on a hetero-structured cladding solid-core photonic bandgap fiber. *Opt Express.* 2016;24(19):21693–9.
47. Yuan L, Wei T, Han Q, Wang H, Huang J, Jiang L, Xiao H. Fiber inline Michelson interferometer fabricated by afemtosecond laser. *Opt Lett.* 2012;37:4489.
48. Cui Y, Shum PP, Hu DJJ, Wang G, Humbert G, Dinh XQ. Sagnac interferometer based temperature sensor by using selectively filled photonic crystal fiber. In: *Proceedings of IEEE Photonics Conference*, 23–27 September 2012, Burlingame, CA. p. 743–4.

49. Tsai WH, Lin CJ. A novel structure for the intrinsic fabry–perot fiber-optic temperature sensor. *J Light Technol.* 2001;19:682–6.
50. Sifuentes C, Starodumov AN, Filippov VN, Lipovskii AA. Application of CdSe-nanocrystallite-doped glass for temperature measurements in fiber sensors. *Opt Eng.* 2000;39:2182–6.
51. Sui C, Xia J, Wang H, Xu T, Yan B, Liu Y. Optical temperature sensor based on ZnO thin film's temperature-dependent optical properties. *Rev Sci Instrum.* 2011;82(8):084901.
52. Bueno A, Suarez I, Abargues R, Sales S, Pastor JPM. Temperature sensor based on colloidal quantum dots–PMMA nanocomposite waveguides. *IEEE Sensors J.* 2012;12(10):3069–74.
53. Chun J, Yang W, Kim JS. Thermal stability of CdSe/ZnS quantum dot-based optical fiber temperature sensor. *Mol Cryst Liq Cryst.* 2011;538(1):333–40.
54. Wang H, Yang A, Chen Z, Geng Y. Reflective photoluminescence fiber temperature probe based on the CdSe/ZnS quantum dot thin film. *Opt Spectrosc.* 2014;117(2):235–9.
55. Wang H, Yang A. Temperature sensing property of hollow-core photonic bandgap fiber filled with CdSe/ZnS quantum dots in an UV curing adhesive. *Opt Fiber Technol.* 2017;38:104–7.
56. Irawati N, Harun SW, Rahman HA, Chong SS, Hamizi NA, Ahmad H. Temperature sensing using CdSe quantum dot doped poly(methyl methacrylate) microfiber. *Appl Opt.* 2017;56(16):4675–9.
57. Pockrand I. Surface plasma oscillations at silver surfaces with thin transparent and absorbing coatings. *Surf Sci.* 1978;72(3):577–88.
58. Liedberg B, Nylander C, Lunström I. Surface plasmon resonance for gas detection and biosensing. *Sensors Actuators.* 1983;4:299–304.
59. Wan X, Taylor HF. Intrinsic fiber Fabry–Perot temperature sensor with fiber Bragg grating mirrors. *Opt Lett.* 2002;27:1388–90.
60. Matsubara K, Kawata S, Minami S. Optical chemical sensor based on surface plasmon measurement. *Appl Opt.* 1988;27(6):1160–3.
61. Schilling A, Yavas O, Bischof J, Boneberg J, Leiderer P. Absolute pressure measurements on a nanosecond time scale using surface plasmons. *Appl Phys Lett.* 1996;69:4159.
62. Peng Y, Huang Z, Lu Q. Temperature sensor based on surface plasmon resonance within selectively coated photonic crystal fiber. *Appl Opt.* 2012;51(26):6361–7.
63. F, Villuendas, J. Pelayo optical fibre device for chemical sensing based on surface plasmon excitridon. *Sens Actuator A Phys.* 1990;23(1–3):1142–5.
64. Fischer LH, Harms GS, Wolfbeis OS. Upconverting nanoparticles for nanoscale thermometry. *Angew Chem Int Ed Engl.* 2011;50(20):4546–51.
65. Kashyap R, Nemova G. Surface plasmon resonance-based fiber and planar waveguide sensors. *J Sensors.* 2009;2009:1–9.
66. Maestro LM, Jacinto C, Silva UR, Vetrone F, Capobianco JA, Jaque D, Sole JG. CdTe quantum dots as nanothermometers: towards highly sensitive thermal imaging. *Small.* 2011;7(13):1774–8.
67. del Rosal B, Carrasco E, Ren F, Benayas A, Vetrone F, Sanz-Rodríguez F, Ma D, Juarranz Á, Jaque D. Infrared-emitting QDs for thermal therapy with real-time subcutaneous temperature feedback. *Adv Funct Mater.* 2016;26(33):6060–8.
68. Maestro LM, Rodríguez EM, Rodríguez FS, la Cruz MC, Juarranz A, Naccache R, Vetrone F, Jaque D, Capobianco JA, Sole JG. CdSe quantum dots for two-photon fluorescence thermal imaging. *Nano Lett.* 2010;10(12):5109–15.
69. Xu CT, Axelsson J, Andersson-Engels S. Fluorescence diffuse optical tomography using upconverting nanoparticles. *Appl Phys Lett.* 2009;94(25):251107.
70. Xu C, Zipfel W, Shear JB, Williams RM, Webb WW. Multiphoton fluorescence excitation: new spectral windows for biological nonlinear microscopy. *Proc Natl Acad Sci.* 1996;93:10763–8.
71. Maestro LM, Ramirez-Hernandez JE, Bogdan N, Capobianco JA, Vetrone F, Sole JG, Jaque D. Deep tissue bio-imaging using two-photon excited CdTe fluorescent quantum dots working within the biological window. *Nanoscale.* 2012;4(1):298–302.
72. Choudhury D, Jaque D, Rodenas A, Ramsay WT, Paterson L, Kar AK. Quantum dot enabled thermal imaging of optofluidic devices. *Lab Chip.* 2012;12(13):2414–20.

**Part IV**  
**Biosensors**

# Chapter 17

## Introduction to Biosensing



**Ghenadii Korotcenkov, Rabi Garba Ahmad, Praveen Guleria,  
and Vineet Kumar**

### 17.1 Introduction

Various analytical methods are used as detection methods for routine analysis in medicine, agriculture, pharmaceuticals, food production, etc. However, most of these methods are time consuming, expensive, require well-trained experts, and often suffer from false-positive or false-negative results [146, 149]. Many experts believe that the advent of biosensors can solve these problems. Biosensors can become alternative analytical tools with high efficiency, high sensitivity, and selectivity. In this chapter, we consider various approaches and materials that are used to develop biosensors, as well as evaluate the prospects for their application in various fields.

---

G. Korotcenkov

Department of Physics and Engineering, Moldova State University, Chisinau, Moldova

R. G. Ahmad

Department of Biotechnology, School of Bioengineering and Biosciences, Lovely Professional University, Phagwara, Punjab, India

Department of Biology, School of Science Education, Sa'adatu Rimi College of Education, Kumbotso Kano, Nigeria

P. Guleria

Department of Biotechnology, DAV University, Jalandhar, Punjab, India

V. Kumar (✉)

Department of Biotechnology, School of Bioengineering and Biosciences, Lovely Professional University, Phagwara, Punjab, India

## 17.2 Biosensors. What Is It?

The first biosensor was invented in the 1950s by the American biochemist L.L. Clark [38]. This biosensor is used to measure the oxygen content in the blood and the electrode used in this sensor is called Clark electrode or oxygen electrode. Then, in 1962, Clark and Lyons [37] applied a gel with an enzyme that oxidizes glucose to an oxygen electrode, which led to the development of the first glucose meter to measure blood sugar levels. It is from this time that the era of biosensors begins [53].

Currently, a biosensor is understood as an analytical device that combines a physicochemical transducer with a biomolecule or biological active element such as proteins, enzymes, nucleic acids, and microorganisms to generate a signal proportional to the analyte concentration [4, 105, 154, 155, 160]. Thus, a biosensor can be represented as a device shown in Fig. 17.1.

In the first segment, the sensor is a bio-receptor with recognition elements for selective binding of target analytes contained in biological fluids such as whole blood, serum, plasma, urine, saliva, sweat, tissue, and cell culture extracts [149]. The second segment is the detector part, a transducer that converts interaction with a biological object into an electrical or optical signal. The biological component identifies and also interacts with the analyte to generate a signal that can be measured. These receptor biomolecules at concentrations of 1–5  $\mu\text{g}/\text{mm}^2$  are properly immobilized on the transducer surface using different physical and chemical methods, which depend on the choice of the measurement method used and the type of biosensor. Schematically, the main methods of immobilization are presented in Fig. 17.2. The last section is an electronic device that measures this signal, amplifies it, converts it, and displays it in an accessible form. It includes an amplifier, which is known as a signal conditioning circuit, a display unit, and a processor. The main characteristics of biosensors are stability, cost, sensitivity, and reproducibility of parameters. Linearity, selectivity, and response time are also important biosensor parameters.

As our knowledge about the operation of biosensors improves, the requirements for sensor systems based on them become more complex. Currently, scientists identify three requirements for the sensory system of the next generation [126]: (1) a change in the system caused by interaction with the analyte must lead to a visible result; (2) the change in the system should not depend on the target molecule, so that the system as a whole can be used for the detection of various substances; and

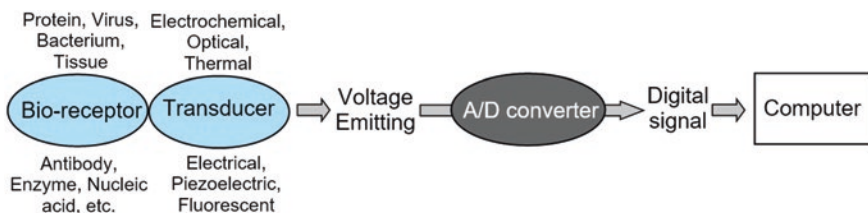
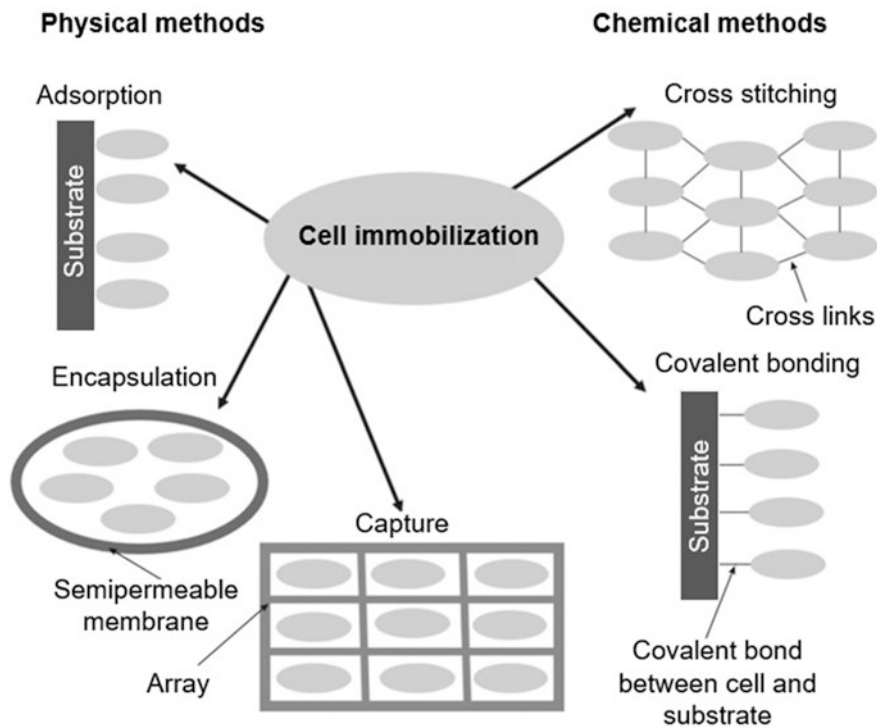


Fig. 17.1 Typical configuration of biosensor. (Idea from Yoon [177])





**Fig. 17.2** Schematic representation of the main methods of cell immobilization. (Idea from Plekhanova and Reshetilov [122])

finally (3) the system must be easily configurable so that substances with different energy binding characteristics to the sensor can be detected, and so that the minimum detectable concentration can be adjusted.

### 17.3 Types of Biosensors

As mentioned earlier, all types of biological elements such as enzymes, antibodies, receptors, and living cells, can be used as a bio-selective element. Various transducers can also be used: electrochemical, optical, gravitational, calorimetric, and resonant systems. Theoretically, any bio-selective element can be combined with any of the possible transducers. As a result, there is a wide variety of different types of possible biosensors, which are classified depending on the transducer type, the materials used, as well as the biological element immobilized in the biosensor.

Biosensors that can quickly and reproducibly recover are reusable. Using reusable biosensors, direct monitoring of an increase or decrease in the concentration of the biological agent being determined is carried out. Biosensors that cannot be

reproducibly and quickly restored are called disposable, and these include bioassays and bio-indicators. The potential use of disposable biosensors, especially in environmental monitoring, is more focused on warning and signalling systems that do not require accurate determination of the concentration of the analyte.

### 17.3.1 *Electrochemical Biosensors*

This type of biosensor produces an electrical signal proportional to the analyte concentration when it reacts with it [35, 66]. Such biosensors typically have three separate electrodes: a working electrode (WE), a counter electrode (CE), and a reference electrode (RE). One of these electrodes (WE), on the surface of which a layer of biomaterial is deposited via the immobilization method, generates a potential, while others generate an electric current resulting from the reaction of the biomaterial with the analyte. As a rule, the operation of an electrochemical biosensor is based on an enzymatic catalysis reaction that occurs on the surface of the active electrode and consumes or generates electrons, forming a signal that corresponds to the concentration of the investigating analyte [28, 127]. The enzymes involved in this reaction are called redox enzymes.

Electrochemical biosensors are classified into four types:

- Amperometric biosensors
- Potentiometric biosensors
- Impedimetric biosensors
- Voltammetric biosensors
  - An *amperometric biosensor* is a device that measures the magnitude of the current produced due to the oxidation-reduction reaction occurring on the surface of the working electrode [18, 23, 81, 121]. Typically, these biosensors have a response time, energy range, and sensitivity comparable to potentiometric biosensors. The Clark oxygen electrode is a simple amperometric biosensor. More complex biosensors also exist. For example, Singh et al. [141] have developed a DNA-based amperometric sensor for one of the most common human pathogens—*Streptococcus pyogenes*.
  - The main types of *potentiometric biosensors* are membrane-based ion-selective electrodes (ISE) and ion-selective field-effect transistors (ISFET). These biosensors are often equipped with electrodes coated with a polymer to which an enzyme is bound. Enzyme-analyte interactions result in a change in potential. Therefore, the transducer used here measures the variations that exist between the potential of reference electrode and working electrode [102]. This type of biosensor provides a logarithmic response.
  - *Conductometric* or *impedimetric biosensors*: In a sensor of this type, due to biocatalytic reactions, the ionic composition of the solution varies, as a result of which a change in the conductivity of the solution in the sensor is observed [54]. This effect is used in various biosensors for the detection of urea [158], *Escherichia coli* [69], microbes [81], and many other biological analytes.

Despite some advantages, such as low-cost thin-film applications [135], real-time direct monitoring [19], no need for a reference electrode, and the possibility of miniaturization, this method gives less sensitive responses than other electrochemical methods [79].

- *Voltammetry* is a widely adaptable method of electrochemical analysis, and there are a large number of reports on this type of biosensor [44, 124]. During the measurement process, current and voltage are simultaneously monitored. Voltammetric methods can be divided into: cyclic voltammetry (CV), differential pulse voltammetry (DPV), stripping voltammetry, AC voltammetry, polarography, linear sweep voltammetry (LSV), etc. However, CV, DPV, and LSV are most commonly used. The difference lies in the way the potential is changed at the electrodes [79]. The simplest is LSV, where at WE the applied potential increases linearly with time. The position of the current peak is related to the nature of the detected analyte, and the magnitude of the peak is related to its concentration. One of the main advantages of this type of sensor is that this system has a low noise level, which makes it possible to create a biosensor with high sensitivity. Moreover, many compounds with different characteristic potentials can be found in one measurement [81].

The use of electrochemical sensing offers significant advantages that include high sensitivity, high accuracy when the surface of electrodes is well modified with for examples biomarker this could also be used for rapid detection as well as suitability for field applications. The advantages of these devices also include simple measuring equipment and the possibility of developing portable devices. In addition to their cost-effectiveness, high sensitivity, and large range of detection linearity, electrochemical sensors are capable of handling small sample volumes. In addition, the measurement result is not affected by the turbidity of the samples, unlike optical methods based on spectroscopic transduction [17, 142].

### 17.3.2 *Physical Biosensors*

Any biosensor that uses a response to a change in the physical properties of the medium has been called a physical biosensor. Physical biosensors are the most fundamental, widely used sensors. Physical biosensors are divided into three types: piezoelectric biosensors, thermometric, and magnetic biosensors.

- *Thermometric biosensors* are type of biosensor in which the heat is released as a result of various biological reactions [2]. A heat-sensitive enzyme sensor known as “thermistor” was developed by Mosbach and Danielsson in [111]. This type of biosensor measures changes in the temperature of a solution containing an analyte resulting from enzymatic reactions. The thermometric biosensor is also used to measure or evaluate serum cholesterol levels. When cholesterol is oxidized by the enzyme cholesterol oxidase, heat is released that can be calculated. Similarly, glucose, urea, uric acid, and penicillin G levels can be assessed using these biosensors [2].

- *Piezoelectric biosensors* work on a principle affinity by interaction of recording [123, 156]. Piezoelectric biosensors typically have a surface modified with an antigen or antibody. When an analyte molecule is attached to a membrane, cantilever, or surface of a piezoelectric crystal, their mass changes, resulting in a change in the resonant frequency of the oscillation. This change in frequency, proportional to the change in mass of the adsorbed analyte, can be measured. Piezoelectric biosensors are also known as acoustic biosensors. These sensors offer many advantages [103]. Based on acoustic biosensors, immunosensors have been developed for the detection of *Salmonella typhimurium*, the herpes virus [45]. Using specific immunoglobulins and *Francisella tularensis* antigens, piezoelectric biosensors have been developed to detect the causative agent of tularemia in water and milk [125].
- The *magnetic biosensor* is another type of biosensor. This type of sensor is used to detect changes in magnetic effects or magnetic properties caused by the interaction of a bio-receptor with an analyte [114]. Recently, with the development of magnetic nanoparticles and their use in biosensors, new diagnostic methods at the nanolevel have appeared that allow diagnosing diseases at an early stage [173, 176]. For example, Yang et al. [176] developed a core-shell aptasensor containing a magnetic core, an aptamer, and gold nanoparticles. After the addition of the target molecule, an interaction occurs between the target molecule and the aptamer thrombin, which leads to the release of gold nanoparticles from the magnetic ball. The amount of thrombin can be calculated based on the amount of released gold nanoparticles. The resulting limit of detection was 2.54 fM.

### 17.3.3 Optical Biosensors

An optical biosensor is another type of biosensors most commonly used for bio-recognition [11, 24, 33, 63, 72]. Optical detection is usually based on the measurement of luminescent, fluorescent, colorimetric, or other optical signals arising from the interaction of microorganisms with analytes and correlating with their concentration. Optical biosensors typically use a light source, a light detector, and a sensitive material that allow interaction with the analyte in the gas and liquid phases [1]. Antibodies and enzymes are mainly used as bio-receptors in these sensors.

- *Fluorescent biosensors*: The basic principle of operation of this biosensor is based on the change in the absorption/emission of light when a detectable analyte is added. Fluorescence can be defined as an optical phenomenon in which shorter wavelength photons are absorbed, resulting in longer wavelength emission. Due to its high performance in terms of selectivity, sensitivity, and low detection limit, the luminescent sensors are most applicable for both chemical and biological analyses [91, 92]. Fluorescent microbial biosensors can be divided into two categories: *in vivo* and *in vitro* [63]. The *in vivo* fluorescent microbial biosensor uses genetically modified microorganisms with a transcriptional fusion between an inducible promoter and a reporter gene encoding a fluorescent pro-

tein. The green fluorescent protein (GFP), encoded by the *gfp* gene, is one of the most popular tools due to its attractive stability and sensitivity, and the fluorescence emitted by GFP can be conveniently detected by modern optical equipment with little or no damage to the host system.

- *Biosensors based on bioluminescence*: Bioluminescence is associated with the emission of light by living microorganisms and plays a very important role in real-time monitoring of the process. The bacterial luminescence *lux* gene is widely used as a reporter, either in an inducible or constitutive manner. In the inducible manner, the reporter *lux* gene is fused to a promoter controlled by the concentration of the analyte of interest. As a result, the concentration of the analyte can be quantitatively analyzed by determining the intensity of the bioluminescence [58].
- The operation of a *colorimetric biosensor* is based on the formation of a colored compound during the interaction of a bio-receptor with an analyte, the color of which can be assessed and correlated with the concentration of analyte [39]. For example, a whole cell colorimetric biosensor has recently been designed to detect arsenite with high sensitivity. His work is based on the following; the photosynthetic bacterium, *Rhodovulum sulfidophilum*, synthesizes carotenoids via the spheroiden (SE) pathway, where yellowish SE is catalyzed by SE mono-oxygenase (CrtA) to form reddish spheroidenone, which is the predominant carotenoid under semi-aerobic conditions. In this biosensor, a genetically engineered photosynthetic bacterium, crtA-deleted *R. sulfidophilum*, was used as the host strain, which accumulated SE and therefore displayed yellow color [63].
- *Surface Plasmon biosensors*: Among the family of optical label-free biosensors, surface plasmon resonance (SPR) is one of the most accessible, developed, and most successfully used technologies for medical diagnostic applications in recent years. This is due to the high sensitivity and versatility of this type of sensors. In addition, they allow real-time detection and direct measurement of the kinetics of molecular ligand-receptor interaction [113, 118]. The principle of operation of such biosensors is based on the effect of surface Plasmon resonance. If gold (or silver) is deposited onto a hydrogel plate, then a phenomenon arises associated with the presence of free electrons in this metal, which, when illuminated, begin to be affected by an alternating electric field. These electrons are able to collectively oscillate and resonate, adjusting to the frequency of the incident light. Such electron oscillations in noble metal nanoparticles are called plasmonic oscillations [65, 115]. In addition, the unique properties of gold and silver nanoparticles that can be used instead of a continuous film increase the sensitivity and selectivity of biosensors [118, 179]. For example, in recent years, a SPR-based biosensor has been proposed for the detection and monitoring in urine of biomolecules of *M. tuberculosis* and nontuberculous mycobacteria, such as CFP10 and MPT64 [36, 51, 65]. Based on the principle of surface Plasmon resonance, biosensors have also been developed to detect anthrax spores [168] and serogroup O1 *Vibrio cholerae* [78].
- *Chemiluminescent-based biosensors*: Chemiluminescent is the process in which emission of light takes place due to chemical reaction. Either the emission can be

produced/generated by direct oxidation of the chemiluminescent reagent, resulting in the formation of emitting substances, or indirectly through the enhancing/inhibiting effects of certain phosphor compounds. Recently, chemiluminescence research has been extended to nanomaterials to improve intrinsic sensitivity and extended to new detection applications [49]. For example, Luo et al. [93] developed a chemiluminescence-based biosensor to detect DNA using graphene oxide, which exhibited high sensitivity and selectivity with a limit of detection of 34 pM.

Optical biosensors can be label-free or label-based depending on the choice of detection method as well as the analyte of the biosensor. In label-free detection method, there is no need for any probe mediator and the interaction of analyte with bio-receptor in the sensor is converted either directly into electric signal that is measurable or combined intrinsically with another transduction for the production of signal for detection of the analyte [139].

Optical-based biosensors offer advantages of compactness, flexibility, resistance to electrical noise, and a small probe size [169]. Optical biosensors allow for safe nonelectrical noncontact sensing. An additional advantage is that they often do not need reference sensors, since a reference signal can be obtained using a light source. However, one of the big problems with an optical sensor is the sensitivity to humidity, which can vary widely. Another disadvantage of label-free optical biosensors using the effects of prismatic light refraction and SPR is their relatively large size, which is incompatible with mobile use in point-of-care mode [113, 164]. Therefore, a modern promising alternative to this type of optical biosensors are fiber-optic biosensors, which are excellent for creating miniature portable devices, which have a low cost and have successfully proven themselves for clinical diagnostics [113]. For example, fiber-optic-based immunosensors have been developed to detect the capsular antigen “fraction 1” of the plague microbe [10] and antibodies to it [9].

Various approaches can be used for immobilization in fiber optic biosensors. But in recent years, the use of hydrogels for these purposes has become most widespread. Hydrogels (polyacrylamide) are hydrophilic cross-linked polymers that can be molded into a variety of shapes for immobilization, ranging from thin films to nanoparticles. Hydrogels are considered to be a simple substrate for DNA immobilization, with a number of advantages, such as the ability to retain molecules, their controlled release, enrichment of analytes, and protection of DNA. These characteristics are unique for hydrogels compared to other materials suitable for biomolecular immobilization. Compared to other materials, immobilization in a hydrogel occurs in three dimensions, which ensures the loading of a large number of sensitive molecules. Moreover, the good optical transparency of hydrogels allows for a convenient visual detection strategy. Methods for immobilizing DNA biosensors in monolithic polyacrylamide gels and gel microparticles are often regarded as a technical achievement in the field of biosensor technologies.

At the end of the consideration of biosensors using various transducers, we will give a comparative description of several biosensors and test systems for enzyme immunoassay (Table 17.1) and biosensors for the detection of influenza virus (Table 17.2).

**Table 17.1** Comparative characteristics of biosensors and test systems for enzyme immunoassay

Sensor group	Analysis time, min	Advantages	Limitations
Potentiometric biosensors	30–45	Simplicity, reliability	Slow response, sensitive to electrical noise
Amperometric biosensors	55	Low cost, small size, stable response	Low sensitivity, low selectivity
Piezoelectric biosensors	5–10	Speed, stability of response	Low sensitivity, nonspecific binding error
Biosensors based on SPR	40	High sensitivity, noncontact measurement	Optical interference, the need for photodetectors
Fiber-optic biosensors	1–3	Fast response, little influence of electrical interference	The need to use photodetectors
Immunoenzymatic test systems	180–240	Specificity	Duration of analysis, the need to use labels, chromogen

Source: Data extracted from Utkin et al. [162]

**Table 17.2** Comparison of the sensitivity of the developed biosensors for the detection of influenza virus

Sensor	Probe	Virus	Sensitivity or affinity	Remark
SPR	Glycan-ligands	H1N1	$K_d$ 1.5 $\mu$ M (10 $\mu$ g/mL, $\sim$ 17 $\mu$ M)	Low affinity and nonspecific interaction
	RNA aptamer	H1N1	$K_d$ 67 fM	High affinity.
	Glycan	H5N1	$K_d$ 1.6 nM	High affinity; specific substrate (Biacore chip) required
	DNA aptamer	H5N1	$K_d$ 4.65 nM	Good affinity.
	RNA aptamer	H3N2	$K_d$ 120 pM	High affinity; unstable RNA aptamer probe
QCM	Glycan	H5N3	$K_d$ 14.4 nM	Good affinity
WG	Antibody	H1N1, H5N1	1 nM	Dissociation of dye from antibody may decrease sensitivity.
IF	RNA aptamer	H3N2	10 nM	Relative low sensitivity
EC	Immunoliposome-Ru	H1N1	$3 \times 10^{-14}$ g/mL (12 fM)	Very high sensitivity; complex probe preparation step
FET	Glycan	H5N1, H1N1	50 aM	Very high sensitivity

Source: Reprinted from Chen and Neethirajan [32]. Published by MDPI as open access. Table 1 EC Electrochemical, FET Field Effect Transistor, IF Interferometry, QCM quartz crystal microbalance, WG Waveguide

### ***17.3.4 Sensors Based on Specific Biological Material***

#### **17.3.4.1 Enzyme Biosensor**

An enzyme biosensor is a sensor on the surface of which an enzyme is immobilized [95]. Enzymes are biological catalysts that have a pronounced ability to selectively catalyze many chemical transformations both in a living cell and outside the body. When enzymes are adsorbed on solid surfaces (metals, ceramics, polymers, semiconductors), they usually retain their structure and catalytic activity. The conjugation of enzymatic catalytic and electrochemical reactions occurring on electrically conductive materials immersed in an electrolyte solution has made it possible to develop many modern biosensors. The simplest case in the design of an enzyme biosensor is realized under the condition that either the substrate or the product of the enzymatic reaction is electrochemically active, that is, they are able to quickly and preferably reversibly oxidize or reduce on the electrode when an appropriate voltage is applied to it. It is most convenient to carry out measurements on enzyme electrodes in the amperometric mode. The best known enzyme biosensor is the glucose biosensor discussed earlier. They use the enzymes glucose oxidase or glucose dehydrogenase as a bio-recognizing component, which are immobilized on the electrode surface and break down glucose. The products of enzymatic reactions are transformed into a physicochemical signal [55]. It is important to note that, when designing an enzyme biosensor, the main task is to increase the duration of the enzyme action. The fact is that the native enzyme retains its properties only for a relatively short time. Therefore, the operation of the so-called immobilization of enzymes was developed (see Fig. 17.2). In the process of immobilization with the help of special reagents, the enzyme is “fixed” either on the surface of adsorbents, such as silica gel, coal, or cellulose, or is introduced into a porous polymer film, or is “attached” covalently through chemical bonds to some substrate. Upon fixation, the enzyme ceases to be mobile, is not washed out of the bio-layer, and its catalytic activity lasts much longer.

#### **17.3.4.2 DNA Biosensors or Aptasensors**

An aptasensor is a special class of biosensors in which the element of biological recognition is a DNA or RNA aptamer. In the aptasensor, the aptamer recognizes the molecular target against which it was previously selected in vitro. The development of DNA biosensors has been based on nucleic acid identification techniques for simple, rapid, and cost-effective testing of genetic and infectious diseases. In addition, the accurate detection of a DNA series is important in several fields such as food quality analysis, clinical analysis, environmental monitoring, etc. It is believed that aptasensors are very promising analytical devices due to the high specificity and stability of nucleic receptors, their low cost, and the potential for creating various sensor platforms [161, 180]. For example, SAM [16] and SELEX [40] technologies, which were developed to more efficiently recognize DNA biosensors, can



be used to improve detection methods. Self-assembled monolayer (SAM) is the method for DNA surface immobilization and a paradigm for the attachment of unmodified DNA of any length or sequence. Systematic evolution of ligands by exponential enrichment (SELEX) is a well-established and efficient technology for the generation of oligonucleotides with a high target affinity. These SELEX-derived single-stranded DNA and RNA molecules, called aptamers, were selected against various targets, such as proteins, cells, microorganisms, and chemical compounds.

#### 17.3.4.3 Immunosensors or Antibody-Based Biosensors

Immunosensors were created based on the fact that antibodies have a high affinity for their specific antigens. For example, antibodies specifically bind to toxins or pathogens or interact with toxins or pathogens through components of the host's immune system. Antibodies, antibody fragments, or antigens are used for the monitoring of bioelectrochemical reactions in immunosensors [66]. Immunosensors are widely used, in particular, to detect *Soybean* rust [106], hepatitis B antigen [60], and virus [92].

#### 17.3.4.4 Protein Biosensors

Protein biosensors are created on the basis of naturally occurring proteins. To do this, a protein domain is selected that can bind to the target molecule and connect to a reporter domain that produces a readable signal. In particular, biologists have created a class of proteins that glow in the presence of a given pathogen or disease marker [84]. The main drawback of this approach is laboriousness, because a lot of bioengineering transformations are required to obtain an effective biosensor from these two domains. Therefore, researchers are looking for a universal platform on the basis of which it will be possible to easily create biosensors for various pathogens or disease markers using protein molecules, simply by replacing the necessary “details” in it. Studies performed by Baek and Baker [15] have shown that in order to create biosensors for new target molecules, it is enough to carry out computer analysis and replace one of the protein domains. Quijano-Rubio et al. [126] tested this approach when developing sensors for botulinum toxin, coronavirus, a marker of myocardial infarction, and other clinically significant targets. In fundamental research, protein sensors are used to study the processes occurring in cells, and in medicine, for example, they are used to predict the effectiveness of therapy for patients with cancer.

#### 17.3.4.5 Cell-Based Biosensors

One of the achievements of biotechnology and bioengineering is associated with the development of methods for incorporating living cells into polymers and solid carriers of various nature and the use of such materials for the development of

biosensors for various purposes [41, 129, 163, 174]. Several surprising properties of immobilized cells can be noted. First, cells are available biological material. Cells of plants, animals, and humans are used, but the cells of microorganisms that are cultivated, easily reproduced, and maintained in pure culture have found the greatest use. Second, unlike enzymes, the use of cells does not require expensive purification steps. Third, the available methods of immobilization make it possible to obtain cells that retain about 100% of enzyme activity and are able to function for sufficiently long periods of time. Features of cell metabolism make it possible to create biosensors both for individual molecules and for very wide classes of compounds. To create cell-based biosensors, as well as for enzyme sensors and aptasensors, a wide variety of physical transducers can be used: from electrochemical to optical and acoustic.

Currently, cell-based biosensors have been created for the determination of phenols, glutamine, tyrazine, and lactic acids. There are also cell-based biosensors for water and wastewater quality analysis. An amperometric sensor for ammonia (in wastewater) based on immobilized nitrifying bacteria and a Clark oxygen electrode can be mentioned as an example of such devices. The advantages and disadvantages of microbial biosensors compared to enzymatic biosensors are presented in Table 17.3. The main advantage of cell-based biosensors is that the cell is the most comfortable environment for enzymes, since they are in their natural state and therefore have the highest stability when functioning in a biosensor. Significant

**Table 17.3** Advantages and disadvantages of cell-based biosensors compared to enzymatic ones

Advantages	Limitations
Broad substrate specificity of microorganisms Lack of labor-intensive techniques such as isolation, purification, and immobilization of pure enzymes At several stages of substrate oxidation, the electrochemical signal when using whole cells is higher than in the case of an isolated enzyme Some enzymes lose their activity upon isolation or immobilization, if these processes lead to damage to the active center or to the disintegration of the enzyme complex. By using whole cells, this danger is minimized Enzymes in cells are in their natural environment, so many biosensors based on microorganism cells are characterized by high stability The cells contain coenzymes and activators of biochemical processes, so there is no need to add them to the measurement medium Many microorganisms have been genetically characterized in detail The use of mutations makes it possible to further increase the activity, selectivity, and specificity of the cell-based biosensor For a biosensor based on microbial cells, it is possible to create conditions under which the receptor element is regenerated due to their growth; this technique can be used to restore the sensitivity of the biosensor	Low speed of analytical signal generation Low selectivity High adaptability and variability of properties The problem of maintaining the activity of microorganisms unchanged for a long time

Source: Data extracted from Plekhanova and Reshetilov [122]

disadvantages of such biosensors include the low selectivity of determination due to the fact that the cells of living organisms are in fact a source of a wide variety of enzymes. In addition, the response time of biosensors based on tissues and microorganisms can be quite long, which also reduces their practical value.

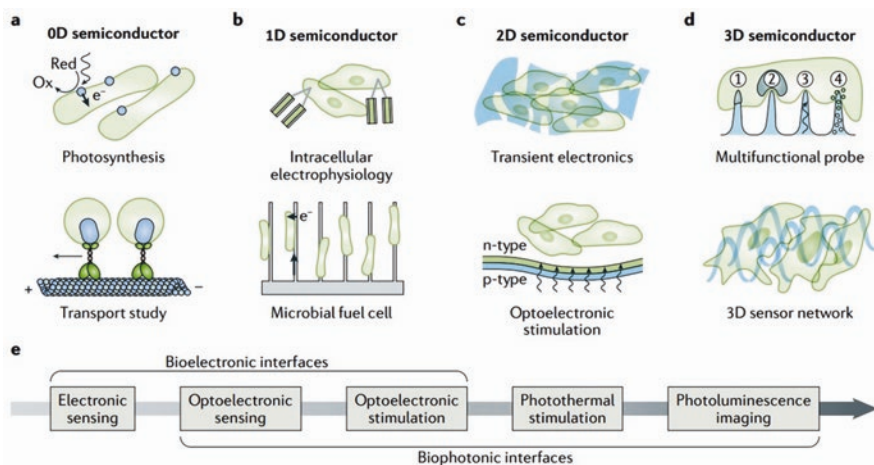
## 17.4 Features of Biosensor Design

### 17.4.1 *Bio-Interfaces*

As follows from the previous sections, a biosensor is a kind of composite formed by transducer materials and a biomolecule or cell. At the same time, the materials that form the transducer can have a very different shape from 0D to 3D, which introduces its own specifics into the formation of the interface between the transducer and biomolecule or cell used for the biofunctionalization of the transducer surface. Figure 17.3 shows how different this interface can be. First, the processes occurring at bio-interfaces depend on the function of semiconductors during their interaction with the cell (Fig. 17.3e). Second, the semiconductor-cell interface can be both extracellular and intracellular bio-interface. In particular, nanosized semiconductors can enter the cell and thus form intracellular bio-interfaces for either perception or stimulation [75, 153]. Intracellular semiconductors are in direct contact with the organelles and/or cytosol, allowing for highly accurate studies of subcellular activity [75]. Unfortunately, a clear understanding of semiconductor internalization mechanisms is still difficult to achieve.

When designing highly sensitive biosensors, the correct choice of not only the matrix, but also the conditions for bio-receptor immobilization is of key importance [27]. When using noncovalent binding, the receptor is held on the sensor substrate of the transducer by electrostatic, van der Waals, or ionic interactions. The main advantage of this type of immobilization is that the matrix does not affect the biological properties of the receptor [55, 133]. However, noncovalent binding does not always provide strong retention of the biomolecule. For example, biosensors with adsorbed enzymes have low stability during operation and storage. Therefore, adsorption in combination with crosslinking is very often used for enzyme immobilization [87].

Modification of electrode surfaces by covalent bonding is advantageous because it produces a more stable biosensitive material. Covalent bonding results in irreversible bonding and high surface coverage [80]. In this case, receptor biomolecules in a sensor are firmly held, which prevents them from being washed out of the sensor matrix, and this is of key importance in the development of a reusable biosensor [129, 161, 174]. But covalent bonding requires a large amount of bioreagent and is generally poorly reproducible [87], as such bonding can potentially adversely affect the active site. Covalent bonding is carried out due to the functional groups of the exposed amino acids of the enzyme, such as amino, carboxyl, imidazole, thiol, and



**Fig. 17.3** Semiconductor geometries and possible modes for bio-interfaces. **(a)** 0D semiconductors can be used to mimic photosynthesis, for example, by using CdS nanoparticles that are precipitated on the cell wall of a bacterium to sensitize non-photosynthetic bacteria through photoinduced electron transfer pathways. Photoluminescent quantum dots can be coupled to motor proteins to enable the tracking of intracellular transport mechanisms. **(b)** 1D semiconductors, for example, nanoscale kinked Si nanowire field-effect transistors, allow intracellular recordings of single cell action potentials. Nanowire–bacteria hybrids can photoelectrochemically fix carbon dioxide and produce value-added chemicals. **(c)** 2D semiconductors, for example, biodegradable Si, provide a physically transient form of electronic devices. The photovoltaic effect of thin-film Si diode junctions can be used for the optical control of biological activities. **(d)** 3D semiconductors, for example, semiconductor micropillar or nanopillar arrays, can detect cellular electrophysiological signals, potentially probe nucleus mechanics, deliver optical stimuli for photo-stimulation, and release drugs. Strain-engineered 3D mesostructures of Si can serve as electronic scaffolds for neural networks. **(e)** Typical signal transduction mechanisms of semiconductor devices involve electrical or optical inputs and outputs. Ox - oxidation; Red - reduction. (Reprinted with permission from Jiang and Tian [74]. Copyright 2018: Springer Nature)

hydroxyl groups, which do not significantly affect its catalytic activity. These groups create a covalent bond with the functional groups present on the surface of the solid substrate, or which can be obtained by chemical or electrochemical processing. Many procedures for covalently binding an enzyme to a solid substrate have been reported [80, 132].

### 17.4.2 Nanomaterial-Based Biosensors

Nanomaterials [104, 131], whose unique catalytic activity, high surface-to-volume ratio, and excellent adsorption properties provide optimal physicochemical characteristics of the sensor substrate surface, are increasingly being used in the development of new generation biosensors [55, 83, 107, 119]. Nanomaterials are considered important components of bioanalytical devices due to their ability to increase

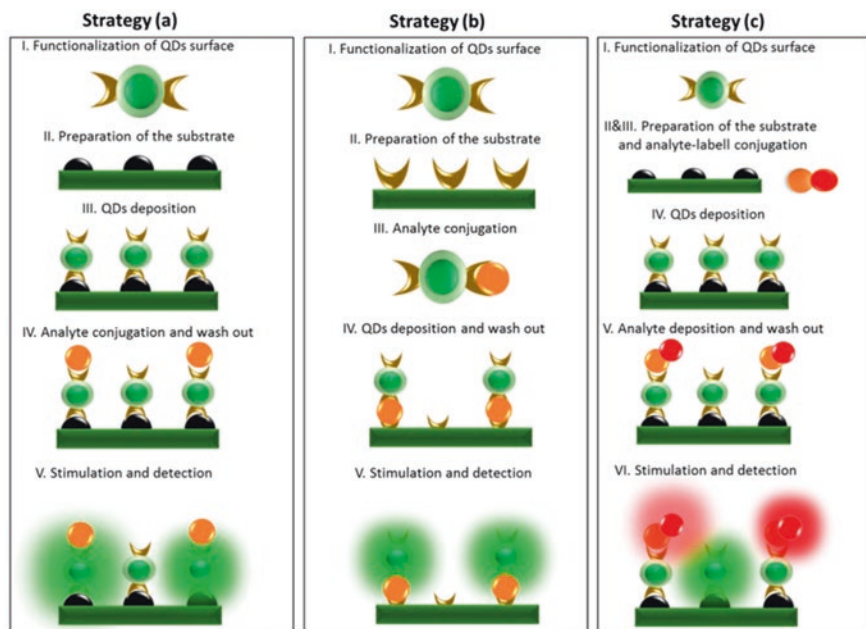
sensitivity and detection thresholds, which is important for single molecule detection. Nanomaterials ultimately provide efficient ligand-receptor interaction, which is transmitted as a specific equivalent enhanced signal [55, 83, 131]. It is important to note that in this case, neither bio-receptors nor analytes undergo conformational changes and loss of biological activity.

#### 17.4.2.1 Biosensors Using Semiconductor QDs

Quantum dots (QDs) are semiconductors, which are crystalline nanostructures ranging in size from 2 to 10 nm. They play a significant role in modern biosensor technologies, especially in medical and biological applications [97]. QDs play an important role in the creation of biosensors due to the amazing properties they possess [5]. They have fluorescent superior behavior. Semiconductor QDs have the higher fluorescence efficiency compared to other traditional fluorophores. Due to size-dependent properties of QDs [59, 70, 97, 134], emission can be controlled over a very wide spectral range from IR to blue fluorescence by changing the size of the QDs. QDs also have a strong biological probe and are more photostable compared to other common traditional organic dyes [5, 172]. All these properties of QDs make it possible to develop on their basis various approaches to biosensing, immunoassays, mapping, and visualization, including those in multicolor mode. QDs can be synthesized based on various semiconductors. However, II-VI compounds are of the greatest interest. These compounds have a particularly high quantum yield, which contributes to an increase in the efficiency of biosensors being developed [140].

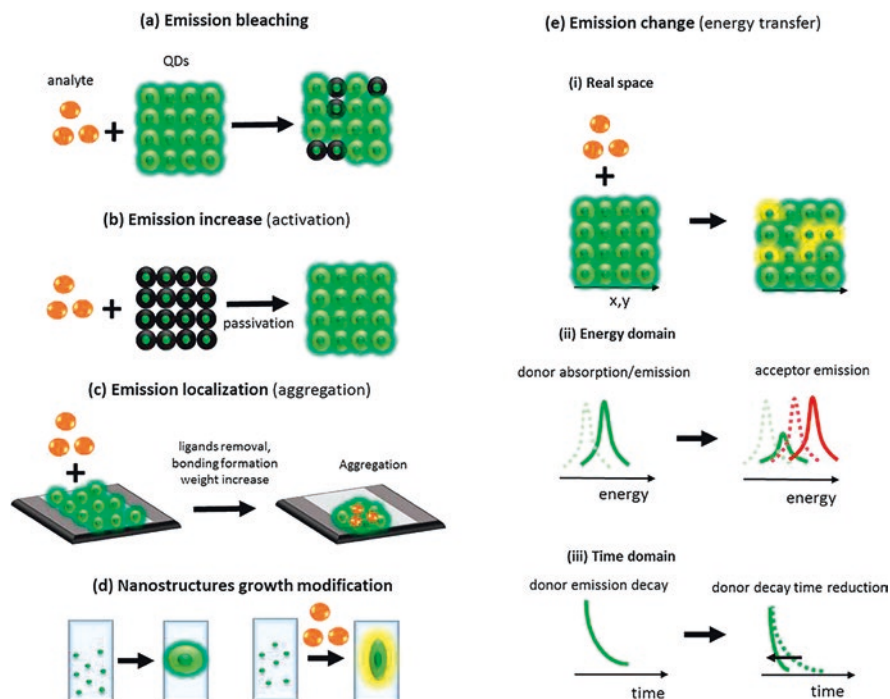
QD-based biosensors can be designed in several ways, depending on the requirements for their sensitivity and the type of analyte being detected [90]. Figure 17.4 shows examples of preparation protocols used in the fabrication of QD-based optical sensors. In all cases, the protocol begins with the appropriate modification of the QD surface to achieve the desired selectivity for a particular analyte. An important aspect is also the preparation of substrates that can be used during measurements. Strategies (a) and (b) differ in steps III and IV, which occur in reverse order. Whereas in strategy (a), step III is the deposit of QDs, in strategy (b) it is step IV. This step can be performed by methods such as layer-by-layer [42], sol-gel [165], or the electrochemical method [73]. Step IV in strategy (a) and step III in strategy (b) represent the conjugation of the analyte, which may be possible due to the pre-prepared and targeted substrate. Jie et al. [76] proposed the binding of an analyte to a pre-prepared substrate based on CdSe nanocomposite QDs using antibodies selective for an antigen called human IgG. The last step in all strategies is QD stimulation, which is used to detect the analyte. As a result, both qualitative and quantitative assessment of the presence of the analyte is possible. As seen in Fig. 17.4, the strategies presented differ in the number of steps and require specific preparation of both the QD and the substrates used, which significantly complicates the measurements and imposes increased requirements on the measurement specialists.

As for the mechanisms of analyte detection by QD-based sensors [90], the most popular mechanism is QD emission quenching. In this mechanism, due to the



**Fig. 17.4** Three examples of the strategy of QDs-based optical sensors (strategy a—modification of substrate with QDs directed to detection of analyte, strategy b—modification of substrate for detection of analyte-QDs complex, strategy c—using the analyte labeled with appropriate fluorophore). (Reprinted from Lesiak et al. [90]. Published by MDPI as open access)

interaction of the QD surface with the analyte, the QD emission intensity decreases (Fig. 17.5a) [144]. For example, Weng and Neethirajan [172] developed a QD-based biosensor for sensitive and rapid detection of food allergens. In this probing method, QDs-Aptamer-GO acts as a probe in which interaction with food allergens results in fluorescence quenching. Another mechanism is based on an increase in the emission of QDs due to passivation of the QD surface with an analyte (Fig. 17.5b). For example, addition of bovine serum albumin or nucleic acids resulted in increased emission of mercaptoacetic acid-coated CdS QDs [170]. The third mechanism that can be used to detect an analyte is stimulated aggregation of QDs (Fig. 17.5c). In this mechanism, due to the interaction of the analyte with the QD surface, surface ligands are cleaved and QDs are aggregated. Aggregation can also be caused by analyte-stimulated bonding between functionalized QDs [82]. There is also a very rarely used analyte detection mechanism based on the modification of the nanostructure growth process by introducing an analyte during the nanostructure growth process. Because of this perturbation, nanostructures can have different emission or other detectable properties (Fig. 17.5d). There is also a fifth detection mechanism based on the transfer of excitation energy from the QD to another optical center (QD or dye). As a result, the color of the emission or the decay time of the donor radiation changes (Fig. 17.5e) [12, 157].



**Fig. 17.5** Examples of physicochemical mechanisms used for analyte optical detection—emission bleaching (a), increase of emission (b), emission localization (c), nanostructures growth's modification (d), emission change (e). (Reprinted from Lesiak et al. [90]. Published by MDPI as open access)

### 17.4.3 Biosensor Using Metallic Nanoparticles

Metallic nanoparticles (NPs) are another example of nanoparticles widely used in biosensor development [167]. Lower toxicity and the possibility of fairly simple surface modification make noble metals such as gold and silver nanoparticles with excellent biocompatibility ideal for use in biological analysis [62]. At the same time, the experiment showed that their size and shape are of great importance for achieving high bio-recognition efficiency. For example, a biosensor based on a tilted fiber Bragg grating (TFBG) coated with noble metal nanoparticles showed improved analyte (protein) selectivity and a low detection limit compared to other biosensors that do not contain gold NPs [89]. It has also been reported that many metal nanoparticles are effectively used for immobilization in order to increase the sensitivity of electrochemical biosensors. This is due to the fact that they are able to stimulate direct electron transfer after capture by biomolecules, thereby maintaining the biological activity of the biosensor for a long period [31, 181, 120].

It is important to note that localized surface Plasmon resonance (SPR) is of great importance for the use of metal nanoparticles in biosensors. Particularly effective is the use of metal nanoparticles in SPR-based biosensors developed on the basis of

metal-enhanced fluorescence (MEF) and surface-enhanced Raman scattering (SERS). MEF and SERS remain the most sensitive detection methods for many analytes such as biomolecules, ions, macromolecules, and microorganisms, respectively. In particular, anisotropic metal nanoparticles, which have a good improved electric field with a large number of excitation wavelengths, are very suitable for developing biosensors with ultrasensitive Plasmon amplification capability [120].

#### ***17.4.4 Biosensor Using Polymers and Polymeric Nanoparticles***

To develop biosensors, various categories of polymeric materials, both bulk and in the form of nanoparticles, are used. It is noted that the modification of electrodes with conductive polymeric materials in electrochemical sensors provides good stability, high sensitivity, low applied potential, low detection limit, as well as fast electron transfer. The use of polymers also promotes the immobilization of enzymes on the electrode surface [112]. Conductive polymers have been found to be an excellent matrix for the functionalization of many biological molecules. Various methods have been used for these purposes. This can be either direct adsorption, covalent bonding, cross-linking with glutaraldehyde, or simple mixing of enzymes with polymers.

The field of application of polymer nanoparticles is growing rapidly and plays a significant role in areas such as biosensors and nanomedicine. Recently, biomedical applications such as bioimaging, diagnostics, and drug delivery using polymer nanoparticles have been developed. The unique chemical and physical properties of polymer-based nanoparticles can become the basis for the development of new nanomaterials for biosensors [98]. In particular, the integration of biocompatible polymers into a biosensor using nanoparticle-based nanotechnologies as well as nanoengineered smart polymers can lead to composites with new and desirable characteristics that provide high sensitivity and stable immobilization of biomolecules. The integration of conductive polymers with metals, metal oxides, or semiconductors such as II-VI compounds also increases the sensitivity and stability of the biosensor [56, 94]. Together, this can form the basis for the development of advanced analytical devices for various applications [152].

#### ***17.4.5 Biosensor Using Core-Shell Materials***

Core-shell nanoparticles can be considered as a kind of QD containing two or more materials, one of which forms the core, and the second - the shell. Core-shell nanostructures are very important [86, 117], since the creation of core-shell structures can significantly increase the reactivity, chemical and thermal stability, solubility, and reduce the toxicity of II-VI compounds. In addition, the formation of core-shell structures gives such structures many new properties suitable for use in biosensors.



The nanostructure of core-shell nanoparticles can have a different shape and size of the core with different surface morphology and shell thickness. Their shapes can be centric, eccentric, spherical, star-shaped, and tubular [30, 64, 86]. Metals, semiconductors, and polymers can be used to form core-shell structures. In biosensors, polymers are especially often used to form shell in core-shell structures. To obtain a homogeneous core-shell structure, as well as to improve the properties of the material, the synthesis technology of core-shell nanoparticles is of great importance. The synthesis of these nanostructures can be organized in various ways. Possible technologies for the formation of core-shell structures based on II-VI compounds are described in the Chap. 12 (Volume 1).

### **17.4.6 Biochips**

Biosensors can be designed using a variety of approaches. For example, electrochemical biosensors can be manufactured using the so-called bulk technology, in which the individual components listed in the diagram (Fig. 17.1) are assembled into a single physical ensemble as they are manufactured. Such biosensors are currently dominant and are used in practice. But they have disadvantages associated with difficulties in organizing their mass production and microminiaturization. Advances in the development of microelectronic technologies have pushed the developers of electrochemical biosensors to new solutions.

In particular, it turned out that planar and printing technologies offer great opportunities for microminiaturization of electrochemical biosensors. Screen-printed three-mini-electrodes are deposited or printed onto polymer substrate forming ultrasmall measuring system. Taking advantage of these opportunities, laboratory-on-a-chip (LOC) devices were developed in which the three-electrode system was miniaturized to a platform of several square centimeters with many laboratory functions. Such devices can handle very small volumes of liquid (picoliter level) [19]. Currently, LOC devices are mass-produced with high reproducibility and low cost. This kit makes it easy to modify the WE surface [79, 175]. With the help of this technology, it has also become possible to manufacture a so-called biochip that combines a sensor system, a converter, an analog-to-digital converter, and a micro-processor for measuring an analytical signal and calculating analysis results. This approach has allowed the development of a large number of portable and wearable biosensors that analyze the biochemical composition of body fluids, such as sweat from the skin surface or tears. Such devices have been created by directly transferring sensors to the skin (using E-skin or temporary printed tattoos), embedding sensors in bracelets, patches, or textiles to ensure close contact with the skin. Such portable biosensor platforms provide insight into the dynamic processes in biological fluids, providing continuous real-time monitoring, which, in turn, is of great importance for maintaining the health of the user. Evaluation of indicators in real time allows you to monitor the state of health and the course of treatment and warns the patient and the attending physician about sudden violations. Although such

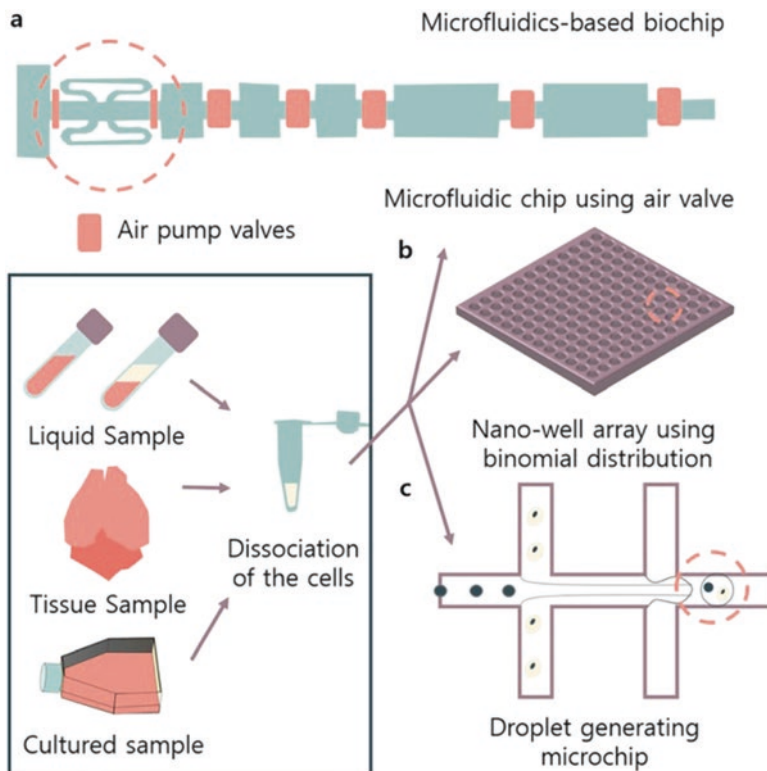
biochips can be replicated, the main problem in this case will be the reproducibility of the microstructure of the surface with the deposited layer of biologically active enzyme.

There is another approach to the development of biochips, which has recently become very widespread. In this case, a biochip is understood as a set of diminished microarrays placed on a solid substrate, which allows many experiments to be carried out simultaneously to obtain a high performance in less time. This device contains a set of sensor elements or biosensors. Unlike microchips, these are not electronic devices. Each biochip can be considered as a microreactor that can detect a specific analyte like an enzyme, protein, DNA, biological molecule, or antibody. The main function of this chip is to perform hundreds of biological reactions in a few seconds like decoding genes (a sequence of DNA).

Three types of biochips are currently available, namely DNA biochip, protein microarray, and microfluidic chip. The first DNA biochip or DNA microarray was developed by the American company Affymetrix, and the product of this company is the GeneChip. A DNA biochip is a set of tiny DNA spots fixed on a solid surface with an array of nano-wells (see Fig. 17.6b). For example, the SMARTer ICeLL8 multisample nanodispenser from Takara (<https://www.takarabio.com>) uses a biochip with isolated 5184 nano-wells for specific DNA labels. Each DNA tag contains picomoles of specific genes called probes. This may be a short segment of genetic material under conditions of high rigidity. Typically, probe-target hybridization is noticed and counted by recognition of fluorophore-labeled or chemiluminescent targets to determine the relative number of nucleic acid series in the target [68, 108].

Protein microarray or protein chips are used to track the actions and relationships of proteins and to elucidate their functions in large scale studies [77, 171]. The main advantage of protein microarrays is that we can track a large number of proteins in parallel. Protein chips are automated, fast, economical, very sensitive, and require fewer samples. The first protein array methodology was presented in scientific publications on antibody microarrays in 1983. Subsequently, protein chip technology has been fairly easily adapted to DNA microarrays, which have now become the most widely used biomicroarrays. Despite the large number of successful examples of the use of protein biochips in biomedical and biotechnological research, many problems remain to be solved. Most protein biochips are currently made using traditional strategies that result in the random orientation of proteins on the surface of the chip. This random arrangement can adversely affect protein activity or ligand binding due to steric hindrance and thus can lead to reduced assay performance or even falsified assay results [147]. The problem can be solved by introducing more advanced methods for preparing protein biochips. Many such methods have been developed over the past few years [77].

Microfluidic biochips or “laboratory on a chip” are an alternative to traditional biochemical laboratories. Microfluidic biochips combine various biochemical analysis functions (e.g., dispensers, filters, mixers, separators, detectors) on a chip, miniaturizing the macroscopic chemical and biological processes that are often handled by laboratory robots to the submillimeter scale. There are several types of microfluidic biochips, each with its own advantages and limitations [88]. In flow biochips



**Fig. 17.6** Representative microfluidics-based biochips and representative references. Microfluidics-based biochips can be categorized into three major platforms: (a) microfluidic channel-based, (b) well-array-based, and (c) droplet-based. After biological samples are dissociated into solution, the samples are processed through these biochips and can be applied to various fields in biology and medicine. (Adapted from Lee et al. [88]. Published by AIP as open access)

(Fig. 17.6a), the on-chip microfluidic channel circuit is equipped with microvalves built into the chip, which are used to control the flow of fluid on the chip. By combining multiple microvalves, it is possible to create more complex devices such as mixers, micropumps, multiplexers, etc., with thousands of devices on a single chip. In droplet-based biochips, liquid is treated as individual drops on an array of electrodes (Fig. 17.6c).

Microfluidic biochips have a number of advantages over conventional chemical analyzers. These include reduced sample and reagent volumes, faster biochemical reactions, ultra-sensitive detection, and higher system throughput allowing multiple analyzes to be performed simultaneously on a single chip. Microfluidic biochips have great potential in many applications such as clinical diagnostics, advanced sequencing, drug discovery, and environmental monitoring. The use of microfluidic biochips also facilitates tasks such as DNA analysis, protein studies, and disease diagnosis (clinical pathology) [34, 57, 61, 100].

Of course, biochips are expensive. But the positive effect of their application is obvious. Biochips have helped to significantly accelerate the identification of approximately 80,000 genes in human DNA as part of the international Human Genome Project. In addition to genetic applications, the biochip is suitable for toxicological, protein, and biochemical research. Biochips can also be used to quickly detect chemical agents used in biological warfare so that protective measures can be taken.

## 17.5 Applications of Biosensors

Currently, biosensors have a very wide field of applications (see Fig. 17.7). Environmental monitoring and pollution control using biosensors is also of great importance [7, 130], since human activities and industry create many environmental hazards that worsen the quality of human life. Agriculture and veterinary medicine, military affairs, drug development and quality improvement, disease diagnosis, treatment, and clinical research are also areas where biosensors should be widely used [11]. Several examples of the use of the biosensors are shown in Table 17.4. According to the experts' forecasts, in 10–15 years the market for these analytical devices will exceed \$ 70 billion [55]. Companies such as Roche Diagnostics,

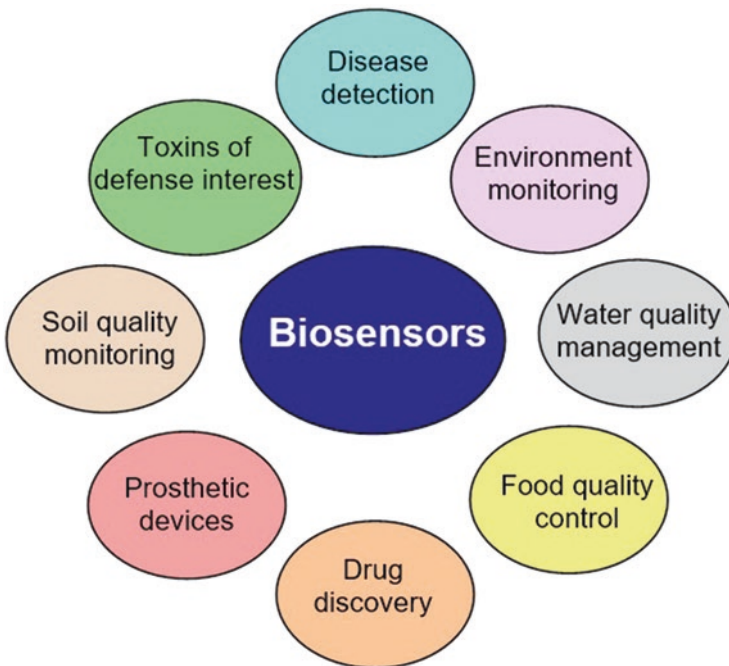


Fig. 17.7 Major areas of applications for biosensors. (Data extracted from Bhalla et al. [22])

**Table 17.4** Various approaches to the detection of biological objects

Approach	Target bio-analyte	Detection limit	References
Electrochemical	Protein	10 pM	[96]
	Carcinoembryonic antigen (CEA)	3.3 fg/mL	[166]
	Xanthine,	0.25 mM	[46]
	Antipsychotic clozapine	24 nM	[138]
	<i>Salmonella</i>	10 <sup>1</sup> CFU mL <sup>-1</sup>	[48]
Amperometric	Aromatic hydrocarbons	0.5 μm	[28]
	Baeyer–Villiger (BV)	–	[137]
Electrical	Hepatitis B-antigen	20 aM	[29]
Voltammetric	Fluvoxamine	3.5 × 10 <sup>-9</sup> Mol L <sup>-1</sup>	[21]
Potentiometric	Lead	8.5 pM	[151]
	Zinc	510 <sup>-4</sup> M	[41]
Conductometric	Diazinon	60 μg/L	[182]
Impedometric	Bacterial endotoxin	2 μg mL <sup>-1</sup>	[26]
	<i>Escherichia coli</i> 0157:H7	10 <sup>2</sup> CFU mL <sup>-1</sup>	[25]
Piezoelectric	Pesticide residue	–	[143]
Optical	Bacterial endotoxin	0.4 ng/mL	[101]
Electrical/Fluorescent	Bacteria	1 CFU/mL	[71]

Johnson and Johnson Innovative Biosensors Inc., Cranfield Biotechnology Centre, EG and IC Sensors, Inc., Biosensor BV, QTL Biosystem, Molecular Devices Corporation, AZUR Environmental, Pharmacia Biosensor AB, Strategic Diagnostics, Affinity Sensor, Pinnacle Technologies Inc., DuPont Biosensor Materials, and others work in the field of biosensors and biochips development.

### 17.5.1 Biosensor Detection of Diseases

Biosensors are of great importance for monitoring and detection/diagnosis of diseases and subsequent treatment [11, 109, 136, 159]. This is because the biosensor approach is easy to use, has high sensitivity, fast detection time, real-time analysis and miniaturization, as well as low cost. The use of biosensors, which make it possible to detect diseases at an early stage, dramatically increases the effectiveness of therapy. In addition, rapid and accurate laboratory diagnosis of infectious diseases can reduce the incidence and prevent the formation and spread of dangerous epidemics. Therefore, biosensors designed for these purposes can serve as an alternative tool for the development of diagnostics of epidemic diseases [3, 50, 146]. For example, a disposable electrochemical immunosensor using a screen electrode with functionalized gold nanoparticles was developed by Rama and colleagues [128] to detect amyloid beta 1–42 in situ. This identification is significant because Alzheimer’s disease is one of the most common forms of dementia. Testing showed

that these immunosensors had detection limits of 0.1 ng/mL. Biosensors can also be used for early detection of heart disease, cancer, diabetes, and many other infectious diseases. QD-based biosensors make it possible to detect viral, bacterial, and fungal diseases in human. Some other examples of such applications of biosensors are listed in Table 17.5. All these indicate that biosensor technologies that have appeared in recent years and are actively developing are innovative platforms for the analysis of infectious process biomarkers. They have a high potential to become affordable, fast and reliable, highly specific and sensitive tools for timely and reliable diagnosis and monitoring of bacterial and viral diseases [85, 178].

### 17.5.2 *Biosensor for Detection of Toxins and Pathogens*

In the last decade, more and more attention has been paid to the use of biosensors for monitoring toxins and pathogens. Microbial pathogens such as bacteria, fungi, viruses and protozoa can have a major impact on public safety and human health [110]. Therefore, the detection of microorganisms as well as microbial toxins is of great importance for security and public health care systems [150]. In these applications, sensitivity, accuracy, and speed of detection are important. The developed biosensors solve this problem. For example, Sheng et al. [145] developed a label-free biosensor with an RNA aptamer that allows for rapid quantitative recognition of foodborne pathogens. In the proposed aptosensor, the RNA aptamer acts as “anti-nucleic acid antibodies” of target microorganisms. The oligonucleotide nature of aptamers makes it possible to amplify or chemically synthesize the desired pool rather quickly and in any quantities, which makes it possible to create highly specific homogeneous sensors that perform accurate quantitative detection of pathogen nucleic chains [47, 113].

**Table 17.5** Use of biosensors in disease diagnosis

Biosensor	Disease diagnosis or medical applications
Glucose oxidase electrode-based biosensor and HbA1c biosensor	Diabetes
Uric acid biosensor	Cardiovascular and general disease diagnosis
Microfabricated biosensor	Optical corrections
Hydrogel (polyacrylamide)-based biosensor	Regenerative medicine
Silicon biosensor	Cancer biomarker development and applications
Nanomaterials-based biosensors	For therapeutic applications

Source: Reprinted from Vigneshvar et al. [160]. Published by Frontiers as open access

### 17.5.3 *Biosensor for Environmental Monitoring*

Biosensors play an important role in environmental monitoring, in particular in the control of water, air, and soil pollution [7, 28, 52, 112]. For example, Bidmanova et al. [20] have developed a portable biosensor to detect halogenated pollutants (halogenated aliphatic hydrocarbons). The developed optical biosensor with a fluorescent indicator makes it possible to detect pollutants with halogen-containing compounds in water samples in the pH range of 4–10 and the temperature range of 5–60 °C. In addition, the biosensor with detection limits of 2.4, 1.4, and 12.1 mg/l had a short measurement response time (1 min) and small dimensions (60 × 30 × 190 mm<sup>3</sup>), which is an additional advantage of the developed sensor. The functionalized nanopolymer immunosensor developed by Deep et al. [43] had high sensitivity specificity for atrazine and gave a detection limit of 0.01 ng/mL. A biosensor based on the Au@Ag core-shell for SERS detection of arsenic (III) was successfully developed [148]. This biosensor had high efficiency in the range of arsenic III concentrations from 0.5 to 10 ppb and a detection limit of 0.1 ppb. This detection limit is below the maximum value established by the US Environmental Protection Agency (EPA) and the World Health Organization (WHO), respectively. In addition, the results showed that the detection of As(III) did not interfere with other ions present in the water sample.

### 17.5.4 *Biosensor for Food Quality Control and Agriculture*

Biosensors are of great importance in food quality control and agriculture [6, 8, 13, 14, 67, 110, 116], etc. The agricultural sector plays an important role in the sustainable economic development of the country and the world community, in connection with which it is of great importance to develop methods that allow early detection of plant diseases and prevent their spread over large areas. To achieve regional and global food security goals, there is also an urgent need for food control at all stages of their production and storage. The experiment showed that biosensors have such an opportunity. For example, it has been reported that biosensors can be used to detect plant pathogens [70, 99]. Wang et al. [163] showed that a biosensor can be used to monitor plant health. Fang et al. [58] developed electrochemical biosensors to detect *p-ethylguaiacol*, a fungus that infects fruit plants with *Phytophthora cactorum* pathogens and causes root rot during growth. To do this, they investigated the effect of various treatments on specific plant stress. In the field of quality control in the food industry, the importance of express methods for assessing shelf life, spoilage, and contamination of products is studied. Advances in biotechnology are stimulating the development of methods for monitoring fermentation processes, which also expands the possibilities of continuous monitoring of these processes.

## 17.6 Conclusion

Many approaches can be used to detect analytes. However, traditional methods are labor-intensive, expensive, and require well-trained staff and personnel. This chapter shows that biosensors are ideal for this task. Biosensors can provide real-time detection of various analytes with high efficiency, sensitivity, low detection limits, and good linearity. Therefore, biosensors can become a promising analytical tool for routine analysis and monitoring in various fields such as medicine, environmental monitoring, food quality assurance, the agricultural sector, etc. Unfortunately, most biosensors are disposable or have a short lifespan. Therefore, the goal of the next level of development should be to create more stable regenerative biosensors for long-term use.

**Acknowledgments** V.K. sincerely thanks everyone who contributed to the creation of this chapter. R.G.A. and P.G. are also thankful to Assistant Prof. Vineet Kumar for the tirelessness guidance and encouragement. G.K. is grateful to the State Program of the Republic of Moldova, project 20.80009.5007.02, for supporting his research.

## References

1. Abd-Elsalam AK. Nanoplatforms for plant pathogenic fungi management. *Fungal Genom Biol.* 2013;2(2):1000e107.
2. Adlerberth J, Meng Q, Mecklenburg M, Tian Z, Zhou Y, Bülow L, Xie B. Thermometric analysis of blood metabolites in ICU patients. *J Therm Anal Calorim.* 2020;140:763–71.
3. Akolpoglu MB, Bozuyuk U, Erkoç P, Kizilel S. Biosensing—drug delivery systems for in vivo applications. *Adv Biosens Health Care Appl.* 2019;2019:249–62.
4. Alhadrami HA. Biosensors: classifications, medical applications, and future prospective. *Biotechnol Appl Biochem.* 2017;65(3):497–508.
5. Altintas Z, Davis F, Scheller FW. Applications of quantum dots in biosensors and diagnostics. In: Altintas Z, editor. *Biosensors and nanotechnology: applications in health care diagnostics.* Wiley; 2017. p. 183–99.
6. Alves RC, Barroso MF, González-García MB, Beatriz M, Oliveira PP, Matos CD. New trends in food allergens detection: toward biosensing strategies. *Crit Rev Food Sci Nutr.* 2016;56(14):2304–19.
7. Amine A, Mohammadi H, Bourais I, Palleschi G. Enzyme inhibition-based biosensors for food safety and environmental monitoring. *Biosens Bioelectron.* 2006;21(8):1405–23.
8. Anand TP, Chellaram C, Murugaboopathi G, Parthasarathy V, Vinurajkumar S. Applications of biosensors in food industry. *Biosci Biotechnol Res Asia.* 2013;10(2):711–4.
9. Anderson GP, King KD, Cao LK, Jacoby M, Ligler FS, Ezzell J. Quantifying serum anti-plague antibody with a fiber-optic biosensor. *Clin Diagn Lab Immunol.* 1998;5(5):609–12.
10. Anderson GP, Breslin KA, Ligler FS. Assay development for a portable fiberoptic biosensor. *ASAIO J.* 1996;42(6):942–6.
11. Andryukov BG, Lyapun IN, Matosova EV, Somova LM. Biosensor technologies in medicine: from detection of biochemical markers to research into molecular targets (review). *Sovrem Tekhnologii Med.* 2021;12(6):70–83. (in Russian)
12. Anikeeva PO, Madigan CF, Halpert JE, Bawendi MG, Bulovic V. Electronic and excitonic processes in light-emitting devices based on organic materials and colloidal quantum dots. *Phys Rev B.* 2008;78:085434.



13. Arora K. Advances in nano based biosensors for food and agriculture. In: Gothandam KM, Ranjan S, Dasgupta N, Ramalingam C, Lichtfouse E, editors. Nanotechnology, food security and water treatment. Springer; 2018. p. 1–52.
14. Arora K, Chand S, Malhotra BD. Recent developments in bio-molecular electronics techniques for food pathogens. *Anal Chim Acta*. 2006;568(1–2):259–74.
15. Baek M, Baker D. Deep learning and protein structure modeling. *Nat Methods*. 2021;19:11–26.
16. Bamdad C. A DNA self-assembled monolayer for the specific attachment of unmodified double- or single-stranded DNA. *Biophys J*. 1998;75(4):1197–2003.
17. Barreiros dos Santos M, Aguil JP, Prieto-Simón B, Sporer C, Teixeira V, Samitier J. Highly sensitive detection of pathogen *Escherichia coli* O157:H7 by electrochemical impedance spectroscopy. *Biosens Bioelectron*. 2013;45:174–80.
18. Belluzo M, Ribone M, Lagier C. Assembling amperometric biosensors for clinical diagnostics. *Sensors*. 2008;8(3):1366–99.
19. Bettazzi F, Marraza G, Minunni M. Biosensors and related bioanalytical tools. *Compr Anal Chem*. 2017;77:1–33.
20. Bidmanova S, Kotlanova M, Rataj T, Damborsky J, Trtilek M, Prokop Z. Fluorescence-based biosensor for monitoring of environmental pollutants: from concept to field application. *Biosens Bioelectron*. 2016;84:97–105.
21. Bishnoi S, Sharma A, Singhal R, Goyal RN. Edge plane pyrolytic graphite as a sensing surface for the determination of fluvoxamine in urine samples of obsessive-compulsive disorder patients. *Biosens Bioelectron*. 2020;168:112489.
22. Bhalla N, Jolly P, Formisano N, Estrela P. Introduction to biosensors. *Essays Biochem*. 2016;60(1):1–8.
23. Bollella P, Gorton L. Enzyme based amperometric biosensors. *Curr Opin Electrochem*. 2018;10:157–73.
24. Borisov SM, Wolfbeis OS. Optical biosensors. *Chem Rev*. 2008;108(2):423–61.
25. Brose-Oliu S, Ferreira R, Uria N, Abramova N, Gargallo R, Muñoz-Pascual F-X, Bratov A. Novel impedimetric aptasensor for label-free detection of *Escherichia coli* O157:H7. *Sensors Actuators B Chem*. 2018;255:2988–95.
26. Brose-Oliu S, Galyamin D, Abramova N, Muñoz-Pascual F-X, Bratov A. Impedimetric label-free sensor for specific bacteria endotoxin detection by surface charge registration. *Electrochim Acta*. 2017;243:142–51.
27. Carrara S, Ghoreishizadeh S, Olivo J, Taurino I, Baj-Rossi C, Cavallini A, et al. Fully integrated biochip platforms for advanced healthcare. *Sensors*. 2012;12:11013–60.
28. Çevik E, Dervisevic M, Gavba AR, Yanik-Yildirim KC, Abasiyanik MF, Vardar-Schara G. Amperometric monoxygenase biosensor for the detection of aromatic hydrocarbons. *Sens Lett*. 2016;14(3):234–40.
29. Chakraborty B, Ghosh S, Das N, RoyChaudhuri C. Liquid gated ZnO nanorod FET sensor for ultrasensitive detection of hepatitis B surface antigen with vertical electrode configuration. *Biosens Bioelectron*. 2018;122:58–67.
30. Chatterjee K, Sarkar S, Jagajjanani RK, Paria S. Core/shell nanoparticles in biomedical applications. *Adv Colloid Interf Sci*. 2014;209:8–39.
31. Chen A, Chatterjee S. Nanomaterials based electrochemical sensors for biomedical applications. *Chem Soc Rev*. 2013;42(12):5425–38.
32. Chen L, Neethirajan S. A homogenous fluorescence quenching based assay for specific and sensitive detection of influenza virus A *Hemagglutinin* antigen. *Sensors*. 2015;15:8852–65.
33. Chen C, Wang J. Optical biosensors: an exhaustive and comprehensive review. *Analyst*. 2020;145:1605–28.
34. Chin CD, Linder V, Sia SK. Lab-on-a-chip devices for global health: past studies and future opportunities. *Lab Chip*. 2007;7:41–57.
35. Cho I, Kim DH, Park S. Electrochemical biosensors: perspective on functional nanomaterials for on-site analysis. *Biomater Res*. 2020;24:6.

36. Chuensirikulchai K, Laopajon W, Phunpae P, Apiratmateekul N, Surinkaew S, Tayapiwatana C, et al. Sandwich antibody-based biosensor system for identification of mycobacterium tuberculosis complex and nontuberculous mycobacteria. *J Immunoassay Immunochem.* 2019;40(6):590–604.
37. Clark LC Jr, Lyons C. Electrode systems for continuous monitoring in cardiovascular surgery. *Ann N Y Acad Sci.* 1962;102(29):29–45.
38. Clark LC Jr, Wolf R, Granger D, Taylor Z. Continuous recording of blood oxygen tensions by polarography. *J Appl Physiol.* 1953;6(3):189–93.
39. Cui S, Ling P, Zhu H, Keener H. Plant pest detection using an artificial nose system: a review. *Sensors.* 2018;18(2):378.
40. Darmostuk M, Rimpelova S, Gbelcova H, Ruml T. Current approaches in SELEX: an update to aptamer selection technology. *Biotechnol Adv.* 2015;33:1141–61.
41. Datta M, Mittal S, Goyal D. Potentiometric Zn<sup>2+</sup> biosensor based on bacterial cells. *Asian J Biotechnol.* 2009;1:67–73.
42. De Bastida G, Arregui FJ, Javier Goicoechea J, Matias IR. Quantum dots-based optical fiber temperature sensors fabricated by layer-by-layer. *IEEE Sensors J.* 2006;6:1378–9.
43. Deep A, Saraf M, Neha BSK, Sharma AL. Styrene Sulphonic acid doped polyaniline based immunosensor for highly sensitive impedimetric sensing of atrazine. *Electrochim Acta.* 2014;146:301–6.
44. De Fátima Giarola J, Mano V, Pereira AC. Development and application of a voltammetric biosensor based on polypyrrole/uricase/graphene for uric acid determination. *Electroanalysis.* 2017;30(1):119–27.
45. Deisingh A. Biosensors for microbial detection. *Microbiologist.* 2003;2:30–3.
46. Dervisevic M, Dervisevic E, Cevik E, Senel M. Novel electrochemical xanthine biosensor based on chitosan-polypyrrole-gold nanoparticles hybrid bio-nanocomposite platform. *J Food Drug Anal.* 2017;25(3):510–9.
47. Dietrich JA, McKee AE, Keasling JD. High-throughput metabolic engineering: advances in small-molecule screening and selection. *Annu Rev Biochem.* 2010;79:563–90.
48. Dinshaw IJ, Muniandy S, Teh SJ, Ibrahim F, Leo BF, Thong KL. Development of an aptasensor using reduced graphene oxide chitosan complex to detect salmonella. *J Electroanal Chem.* 2017;806:88–96.
49. Dippel AB, Anderson WA, Evans RS, Deutsch S, Hammond MC. Chemiluminescent biosensors for detection of second messenger cyclic di-GMP. *ACS Chem Biol.* 2018;13:1872–9.
50. Du X, Zhou J. Application of biosensors to detection of epidemic diseases in animals. *Res Vet Sci.* 2018;118:444–8.
51. Dudak FC, Boyaci IH. Rapid and label-free bacteria detection by surface plasmon resonance (SPR) biosensors. *Biotechnol J.* 2009;4(7):1003–11.
52. Durrieu C, Lagarde F, Jaffrezic-Renault N. Nanotechnology assets in biosensors design for environmental monitoring. In: Brayner R, Fiévet F, Coradin T, editors. *Nanomaterials: a danger or a promise?* London: Springer; 2013. p. 189–229.
53. Działowska K, Czaczyk E, Nidzworski D. Application of electrochemical methods in biosensing technologies. In: Rinken T, Kivirand K, editors. *Biosensing technologies for the detection of pathogens – a prospective way for rapid analysis.* Intechopen; 2018. p. 151–71.
54. Dzyadevych S, Jaffrezic-Renault N. Conductometric biosensors. In: Schaudies RP, editor. *Biological Identification.* Elsevier; 2014. p. 153–93.
55. Ebara M, editor. *Biomaterials Nanoarchitectonics.* Elsevier; 2016.
56. El-Said WA, Abdelshakour M, Choi J-H, Choi J-W. Application of conducting polymer nanostructures to electrochemical biosensors. *Molecules.* 2020;25(2):307.
57. Emaminejad S, Javanmard M, Dutton RW, Davis RW. Microfluidic diagnostic tool for the developing world: contactless impedance flow cytometry. *Lab Chip.* 2012;12:4499–507.
58. Fang Y, Umasankar Y, Ramasamy RP. Electrochemical detection of p-ethylguaiaicol, a fungi infected fruit volatile using metal oxide nanoparticles. *Analyst.* 2014;139(15):3804–10.

59. Frasco MF, Chantiotakas N. Semiconductor quantum dots in chemical sensors and biosensors. *Sensors*. 2009;9:7266–86.
60. Gao Z, Li Y, Zhang X, Feng J, Kong L, Wang P, et al. Ultrasensitive electrochemical immunosensor for quantitative detection of HBeAg using Au@Pd/MoS<sub>2</sub>@MWCNTs nanocomposite as enzyme-mimetic labels. *Biosens Bioelectron*. 2018;102:189–95.
61. Gardeniers JG, van den Berg A. Lab-on-a-chip systems for biomedical and environmental monitoring. *Anal Bioanal Chem*. 2004;378:1700–3.
62. Gayda G, Demkiv O, Stasyuk N, Serkiz R, Lootsik M, Errachid A, et al. Metallic nanoparticles obtained via “green” synthesis as a platform for biosensor construction. *Appl Sci*. 2019;9(4):720.
63. Ghica M, Pauliukaite R, Fatibello-Filho O, Brett MAC. Application of functionalized carbon nanotubes immobilized into chitosan films in amperometric enzymes biosensors. *Sensors Actuators B Chem*. 2009;142:308–12.
64. Ghosh Chaudhuri R, Paria S. Core/shell nanoparticles: classes, properties, synthesis mechanisms, characterization, and applications. *Chem Rev*. 2011;112(4):2373–433.
65. Golichenari B, Velonia K, Nosrati R, Nezami A, Farokhi-Fard A, Abnous K, et al. Label-free nano-biosensing on the road to tuberculosis detection. *Biosens Bioelectron*. 2018;113:124–35.
66. Grieshaber D, MacKenzie R, Vörös J, Reimhult E. Electrochemical biosensors - sensor principles and architectures. *Sensors*. 2008;8(3):1400–58.
67. Griesche C, Baeumner AJ. Biosensors to support sustainable agriculture and food safety. *TrAC Trends Anal Chem*. 2020;128:115906.
68. Heller MJ. DNA microarray technology: devices, systems, and applications. *Annu Rev Biomed Eng*. 2002;4:129–53.
69. Hnaiein M, Hassen WM, Abdelghani A. A conductometric immunosensor based on functionalized magnetite nanoparticles for E. coli detection. *Electrochem Commun*. 2008;10:1152–4.
70. Hong S, Lee C. The current status and future outlook of quantum dot-based biosensors for plant virus detection. *Plant Pathol J*. 2018;34(2):85–92.
71. Huang J, Zhong Y, Li W, Wang W, Li C, s, et al. Fluorescent and opt-electric recording bacterial identification device for ultrasensitive and specific detection of microbials. *ACS Sens*. 2021;6:443–9.
72. Huertas CS, Calvo-Lozano O, Mitchell A, Lechuga LM. Advanced evanescent-wave optical biosensors for the detection of nucleic acids: an analytic perspective. *Front Chem*. 2019;7:724.
73. Jiang H, Ju H. Electrochemiluminescence sensors for scavengers of hydroxyl radical based on its annihilation in CdSe quantum dots film/peroxide system. *Anal Chem*. 2007;79:6690–6.
74. Jiang Y, Tian B. Inorganic semiconductor biointerfaces. *Nat Rev Mater*. 2018;3:473–90.
75. Jiang YW, Li X, Liu B, Yi J, Fang Y, Shi F, et al. Rational design of silicon structures for optically controlled multiscale biointerfaces. *Nat Biomed Eng*. 2018;2:508–21.
76. Jie G, Zhang J, Wang D, Cheng C, Chen H-Y, Zhu J-J. Electrochemiluminescence immunosensor based on CdSe nanocomposites. *Anal Chem*. 2008;80:4033–9.
77. Jonkheijm P, Weinrich D, Schroeder H, Niemeyer CM, Waldmann H. Chemical strategies for generating protein biochips. *Angew Chem Int Ed*. 2008;47:9618–47.
78. Jyoung JY, Hong S, Lee W, Choi JW. Immunosensor for the detection of vibrio cholerae O1 using surface plasmon resonance. *Biosens Bioelectron*. 2006;21(12):2315–9.
79. Karunakaran C, Bhargava K, Benjamin R, editors. *Biosensors and bioelectronics*. Netherlands: Elsevier; 2015.
80. Katz E, Willner B. Integration of layered redox proteins and conductive supports for bioelectronic applications. *Angew Chem Int Edn*. 2000;39:1180–218.
81. Kavousi F, Goodarzi M, Ghanbari D, Hedayati K. Synthesis and characterization of a magnetic polymer nanocomposite for the release of metoprolol and aspirin. *J Mol Struct*. 2019;1183:324–30.
82. Kavosia B, Navaei A, Salimi A. Amplified fluorescence resonance energy transfer sensing of prostate specific antigen based on aggregation of CdTe QDs/antibody and aptamer decorated AuNPs-PAMAM dendrimer. *Luminescence*. 2018;204:368–74.

83. Khan T, Civas M, Cetinkaya O, Abbasi NA, Akan OB. Nanosensor networks for smart health care. In: Han B, Tomer VK, Nguyen TA, Singh PK, editors. *Nanosensors for smart cities*. Elsevier; 2020. p. 387–403.
84. Klima JC, Doyle LA, Lee JD, Rappleye M, Gagnon LA, Lee MY, et al. Incorporation of sensing modalities into de novo designed fluorescence-activating proteins. *Nat Commun*. 2021;12:856.
85. Kozel TR, Burnham-Marusch AR. Point-of-care testing for infectious diseases: past, present, and future. *J Clin Microbiol*. 2017;55(8):2313–20.
86. Kumar KS, Kumar VB, Paik P. Recent advancement in functional core-shell nanoparticles of polymers: synthesis, physical properties, and applications in medical biotechnology. *J Nanopart*. 2014;2014:1–24.
87. Leca-Bouvier D, Blum LJ. Enzyme for biosensing applications. In: Zourob M, editor. *Recognition receptors in biosensors*. New York: Springer; 2010. p. 177–220.
88. Lee AC, Lee Y, Lee D, Kwon S. Divide and conquer: a perspective on biochips for single-cell and rare-molecule analysis by next-generation sequencing. *APL Bioeng*. 2019;3:020901.
89. Lepinay S, Staff A, Ianoul A, Albert J. Improved detection limits of protein optical fiber biosensors coated with gold nanoparticles. *Biosens Bioelectron*. 2014;52:337–44.
90. Lesiak A, Drzozga K, Cabaj J, Banski M, Malecha K, Podhorodecki A. Optical sensors based on II–VI quantum dots. *Nano*. 2019;9:192.
91. Li Y, Wang H, Tang H. Chemo/bionanosensors for medical applications. In: Han B, Tomer VK, Nguyen TA, Singh PK, editors. *Nanosensors for smart cities*. Elsevier; 2020a. p. 483–500.
92. Li Z, Liu Y, Chen X, Cao H, Shen H, Mou L, et al. Surface-modified mesoporous nanofibers for microfluidic immunosensor with an ultra-sensitivity and high signal-to-noise ratio. *Biosens Bioelectron*. 2020b;166:112444.
93. Luo M, Chen X, Zhou G, Xiang X, Chen L, Jia X, He Z. Chemiluminescence biosensors for DNA detection using graphene oxide and a horseradish peroxidase-mimicking DNzyme. *Chem Commun*. 2012;48:1126–8.
94. Luong JHT, Narayan T, Solanki S, Malhotra BD. Recent advances of conducting polymers and their composites for electrochemical biosensing applications. *J Funct Biomater*. 2020;11(4):71.
95. Lyagin IV, Efremenko EN, Varfolomeev SD. Enzymatic biosensors for determination of pesticides. *Russ Chem Rev*. 2017;86(4):339.
96. Ma S, Li X, Lee Y-K, Zhang A. Direct label-free protein detection in high ionic strength solution and human plasma using dual-gate nanoribbon-based ion-sensitive field-effect transistor biosensor. *Biosens Bioelectron*. 2018a;117:276–82.
97. Ma F, Li C, Zhang C. Development of quantum dot-based biosensors: principles and applications. *J Mater Chem B*. 2018b;6:6173–90.
98. Mallakpour S, Behranvand V. Polymeric nanoparticles: recent development in synthesis and application. *eXPRESS Polym Lett*. 2016;10(11):895–913.
99. Makiola A, Dickie IA, Holdaway RJ, Wood JR, Orwin KH, Glare TR. Land use is a determinant of plant pathogen alpha- but not beta-diversity. *Mol Ecol*. 2019;28(16):3786–98.
100. Malic L, Brassard D, Veres T, Tabrizian M. Integration and detection of biochemical assays in digital microfluidic LOC devices. *Lab Chip*. 2010;10:418–31.
101. Manoharan H, Kalita P, Gupta S, Sai VVR. Plasmonic biosensors for bacterial endotoxin detection on biomimetic C-18 supported fiber optic probes. *Biosens Bioelectron*. 2019;129:79–86.
102. Marchenko SV, Kucherenko IS, Hereshko AN, Panasiuk IV, Soldatkin OO, El'skaya A V., Soldatkin A.P. Application of potentiometric biosensor based on recombinant urease for urea determination in blood serum and hemodialyzate. *Sensors Actuators B Chem*. 2015;207:981–6.
103. Marrazza G. Piezoelectric biosensors for organophosphate and carbamate pesticides: a review. *Biosensors*. 2014;4(3):301–17.

104. Matea CT, Mocan T, Tabaran F, Pop T, Mosteanu O, Puia C, et al. Quantum dots in imaging, drug delivery and sensor applications. *Int J Nanomedicine*. 2017;12:5421–31.
105. Mehrotra P. Biosensors and their applications – A review. *J Oral Biol Craniofac Res*. 2016;6(2):153–9.
106. Mendes RK, Laschi S, Stach-Machado DR, Kubota LT, Marrazza G. A disposable voltammetric immunosensor based on magnetic beads for early diagnosis of soybean rust. *Sensors Actuators B Chem*. 2012;166-167:135–40.
107. Mercante LA, Scagion VP, Migliorini FL, Mattoso LHC, Correa DS. Electrospinning-based (bio)sensors for food and agricultural applications: a review. *TrAC Trends Anal Chem*. 2017;91:91–103.
108. Mischel PS, Cloughesy TF, Nelson SF. DNA-microarray analysis of brain cancer: molecular classification for therapy. *Nat Rev Neurosci*. 2004;5:782–92.
109. Moharana M, Pattanayak SK. Biosensors: a better biomarker for diseases diagnosis. In: Chaki J, Dey N, De D, editors. *Smart biosensors in medical care*. Elsevier; 2020. p. 49–64.
110. Moran KLM, Fitzgerald J, McPartlin DA, Loftus JH, O’Kennedy R. Biosensor-based technologies for the detection of pathogens and toxins. *Compr Anal Chem*. 2016;93:120. <https://doi.org/10.1016/bs.coac.2016.04.002>
111. Mosbach K, Danielsson B. An enzyme thermistor. *Biochim Biophys Acta*. 1974;364:140–5.
112. Moyo M, Okonkwo JO, Agyei NM. An amperometric biosensor based on horseradish peroxidase immobilized onto maize tassel-multi-walled carbon nanotubes modified glassy carbon electrode for determination of heavy metal ions in aqueous solution. *Enzyme Microb Technol*. 2014;56:28–34.
113. Muniandy S, Teh SJ, Appaturi JN, Thong KL, Lai CW, Ibrahim F, Leo BF. A reduced graphene oxide-titanium dioxide nanocomposite based electrochemical aptasensor for rapid and sensitive detection of *Salmonella enterica*. *Bioelectrochemistry*. 2019;127:136–44.
114. Nabaei V, Chandrawati R, Heidari H. Magnetic biosensors: modelling and simulation. *Biosens Bioelectron*. 2018;103:69–86.
115. Nasrin F, Chowdhury AD, Takemura K, Lee J, Adegoke O, Deo VK, Abe F, Suzuki T, Park EY. Single-step detection of norovirus tuning localized surface Plasmon resonance-induced optical signal between gold nanoparticles and quantum dots. *Biosens Bioelectron*. 2018;122:16–24.
116. Nikoleli G-P, Nikolelis DP, Siontorou CG, Karapetis S, Varzakas T. Novel biosensors for the rapid detection of toxicants in foods. *Adv Food Nutr Res*. 2018;84:57–102.
117. Nomoev AV, Bardakhanov SP, Schreiber M, Bazarova DG, Romanov NA, Baldanov BB, et al. Structure and mechanism of the formation of core–shell nanoparticles obtained through a one-step gas-phase synthesis by electron beam evaporation. *Beilstein J Nanotechnol*. 2015;6:874–80.
118. Nquyet NT, Yen LTH, Doan VY, Hoang NL, Van Thu V, Lan H, et al. A label-free and highly sensitive DNA biosensor based on the core-shell structured CeO<sub>2</sub>-NR@Ppy nanocomposite for *Salmonella* detection. *Mater Sci Eng C*. 2019;96:790–7.
119. Park M, Tsai SL, Chen W. Microbial biosensors: engineered microorganisms as the sensing machinery. *Sensors (Basel)*. 2013;13(5):5777–95.
120. Parnianchi F, Nazari M, Maleki J, Mohebi M. Combination of graphene and graphene oxide with metal and metal oxide nanoparticles in fabrication of electrochemical enzymatic biosensors. *Int Nano Lett*. 2018;8:229–39.
121. Pilo M, Farre R, Lachowicz JJ, Masolo E, Panzanelli A, Sanna G, et al. Design of amperometric biosensors for the detection of glucose prepared by immobilization of glucose oxidase on conducting (Poly)Thiophene films. *J Anal Methods Chem*. 2018;2018:1849439.
122. Plekhanova YV, Reshetilov AN. Microbial biosensors for the determination of pesticides. *J Anal Chem*. 2019;74(12):883–901. (in Russian)
123. Pohanka M. Overview of piezoelectric biosensors, immunosensors and DNA sensors and their applications. *Materials*. 2018;11(3):448.

124. Pohanka M, Drobik O, Krenkova Z, Zdarova-Karasova J, Pikula J, Cabal J, Kuca K. Voltammetric biosensor based on acetylcholinesterase and different immobilization protocols: a simple tool for toxic organophosphate assay. *Anal Lett.* 2011;44(7):1254–64.
125. Pohanka M, Skládal P. Piezoelectric immunosensor for the direct and rapid detection of *Francisella tularensis*. *Folia Microbiol (Praha).* 2007;52(4):325–30.
126. Quijano-Rubio A, Yeh H-W, Park J, Lee H, Langan RA, Boyken SE, et al. De novo design of modular and tunable protein biosensors. *Nature.* 2021;591:482–7.
127. Rabiou GA, Kumar V. Microorganisms based biosensors to detect soil pollutants. *Plant Arch.* 2020;20(Suppl 2):2509–16.
128. Rama EC, González-García MB, Costa-García A. Competitive electrochemical immunosensor for amyloid-beta 1-42 detection based on gold nanostructured screen-printed carbon electrodes. *Sensors Actuators B Chem.* 2014;201:567–71.
129. Renella G, Giagnoni L. Light dazzles from the black box: whole-cell biosensors are ready to inform on fundamental soil biological processes. *Chem Biol Technol Agric.* 2016;3:8.
130. Rodriguezmozaz-Mozaz S, Alda M, Marco M, Barcelo D. Biosensors for environmental monitoring: a global perspective. *Talanta.* 2005;65(2):291–7.
131. Ronkainen N, Okon S. Nanomaterial-based electrochemical immunosensors for clinically significant biomarkers. *Materials (Basel).* 2014;7(6):4669–709.
132. Rusmini F, Zhong Z, Feijen J. Protein immobilization strategies for protein biochips. *Biomacromolecules.* 2007;8:1775–89.
133. Sadasivuni KK, Ponnamma D, Kim J, Cabibihan J-J, AlMaadeed MA, editors. *Biopolymer composites in electronics.* Elsevier; 2017.
134. Safarpour H, Safarnejad MR, Tabatabaei M, Mohsenifar A, Rad F, Basirat M, Hasanzadeh F. Development of a quantum dots FRET-based biosensor for efficient detection of *Polymyxa betae*. *Can J Plant Pathol.* 2012;34(4):507–15.
135. Salek-Maghsoudi A, Vakhshiteh F, Torabi R. Recent advances in biosensor technology in assessment of early diabetes biomarkers. *Biosens Bioelectron.* 2018;99:122–35.
136. Saylan Y, Erdem Ö, Ünal S, Denizli A. An alternative medical diagnosis method: biosensors for virus detection. *Biosensors.* 2019;9(2):65.
137. Schenk Mayerová A, Bučko M, Gemeiner P, Katrlík J. Microbial monooxygenase amperometric biosensor for monitoring of Baeyer–Villiger biotransformation. *Biosens Bioelectron.* 2013;50:235–8.
138. Senel M, Alachkar A. Lab-in-a-pencil graphite: a 3D-printed microfluidic sensing platform for real-time measurement of antipsychotic clozapine level. *Lab Chip.* 2021;21:405–11.
139. Singh P, Yadava RDS. Nanosensors for health care. In: Han B, Tomer VK, Kumar P, editors. *Nanosensors for smart cities.* Elsevier; 2020. p. 433–50.
140. Singh RD, Shandilya R, Bhargava A, Kumar R, Tiwari R, Chaudhury K, et al. Quantum dot based nano-biosensors for detection of circulating cell free miRNAs in lung carcinogenesis: from biology to clinical translation. *Front Genet.* 2018;9:616.
141. Singh S, Kaushal A, Khare S. DNA chip based sensor for amperometric detection of infectious pathogens. *Int J Biol Macromol.* 2017;103:355–9.
142. Singh R, Mukherjee MD, Sumana G, Gupta RK, Sood S, Malhotra BD. Biosensors for pathogen detection: a smart approach towards clinical diagnosis. *Sensors Actuators B Chem.* 2014;197:385–404.
143. Shang Z, Xu Y, Gu Y, Wang Y, Wei D, Zhan L. A rapid detection of pesticide residue based on piezoelectric biosensor. *Procedia Eng.* 2011;15:4480–5.
144. Shang L, Zhang L, Dong S. Turn-on fluorescent cyanide sensor based on copper ion-modified CdTe quantum dots. *Analyst.* 2009;134:107–13.
145. Sheng L, Lu Y, Deng S, Liao X, Zhang K, Ding T, et al. A transcription aptasensor: amplified, label-free and culture-independent detection of foodborne pathogens via light-up RNA aptamers. *Chem Commun (Camb).* 2019;55(68):10096–9.
146. Sin ML, Mach KE, Wong PK, Liao JC. Advances and challenges in biosensor-based diagnosis of infectious diseases. *Expert Rev Mol Diagn.* 2014;14(2):225–44.

147. Sleno L, Emili A. Proteomic methods for drug target discovery. *Curr Opin Chem Biol.* 2008;12:46–54.
148. Song L, Mao K, Zhou X, Hu J. A novel biosensor based on Au@Ag core-shell nanoparticles for SERS detection of arsenic (III). *Talanta.* 2016;146:285–90.
149. Su L, Jia W, Hou C, Lei Y. Microbial biosensors: a review. *Biosens Bioelectron.* 2011;26(5):1788–99.
150. Sutarlie L, Ow SY, Su X. Nanomaterials-based biosensors for detection of microorganisms and microbial toxins. *Biotechnol J.* 2016;12(4):1–25.
151. Tang W, Yu J, Wang Z, Jeerapan I, Yin L, Zhang F, He P. Label-free potentiometric aptasensing platform for the detection of Pb<sup>2+</sup> based on guanine quadruplex structure. *Anal Chim Acta.* 2019;1078:53–9.
152. Teles FRR, Fonseca LP. Applications of polymers for biomolecule immobilization in electrochemical biosensors. *Mater Sci Eng C.* 2008;28(8):1530–43.
153. Tian BZ, Cohen-Karni T, Qing Q, Duan X, Xie P, Lieber CM. Three-dimensional, flexible nanoscale field-effect transistors as localized bioprobes. *Science.* 2010;329:830–4.
154. Thevenot DR, Toth K, Durst RA, Wilson GS. Electrochemical biosensors: recommended definitions and classification. *Anal Lett.* 2001;34:635–59.
155. Thevenot DR, Toth K, Durst RA, Wilson GS. Electrochemical biosensors: recommended definitions and classification. *Pure Appl Chem.* 1999;71:2333–48.
156. Tombelli S. Piezoelectric biosensors for medical applications. In: Higson S, editor. *Biosensors for medical applications.* Elsevier; 2012. p. 41–64.
157. Wilfried GJ, Van Sark HM, Frederix PLTM, Bol AA, Gerritsen HC, Meijerink A. Bleaching, and blinking of single CdSe/ZnS quantum dots. *ChemPhysChem.* 2002;3:871–9.
158. Velychko TP, Soldatkin OO, Melnyk VG, Marchenko SV, Kirdeciler SK, Akata B, Dzyadevych SV. A novel conductometric urea biosensor with improved analytical characteristic based on recombinant urease adsorbed on nanoparticle of silicalite. *Nanoscale Res Lett.* 2016;11(1):106.
159. Vidic J, Manzano M, Chang C-M, Jaffrezic-Renault N. Advanced biosensors for detection of pathogens related to livestock and poultry. *Vet Res.* 2017;48(1):11.
160. Vigneshvar S, Sudhakumari CC, Senthilkumaran B, Prakash H. Recent advances in biosensor technology for potential applications – an overview. *Front Bioeng Biotechnol.* 2016;4:11.
161. Urmann K, Reich P, Walter JG, Beckmann D, Segal E, Scheper T. Rapid and label-free detection of protein a by aptamer-tethered porous silicon nanostructures. *J Biotechnol.* 2017;257:171–7.
162. Utkin DV, Ossina NA, Kouklev VE, Erokhin PS, Scherbakova SA, Kutuyev VV. Biosensors: current state and prospects of applying in laboratory diagnostics of particularly dangerous infectious diseases. *Problems of particularly dangerous infections.* 2009;102:11–4. (in Russian).
163. Wang X, Cheng M, Yang Q, Wei H, Xia A, Wang L, et al. A living plant cell-based biosensor for real-time monitoring invisible damage of plant cells under heavy metal stress. *Sci Total Environ.* 2019a;697:134097.
164. Wang Z, Yao X, Wang R, Ji Y, Yue T, Sun J, Li T, Wang J, Zhang D. Label-free strip sensor based on surface positively charged nitrogen-rich carbon nanoparticles for rapid detection of *Salmonella enteritidis*. *Biosens Bioelectron.* 2019b;132:360–7.
165. Wang Z, Zhang Y, Zhang B, Lu X. Mn<sup>2+</sup> doped ZnS QDs modified fluorescence sensor based on molecularly imprinted polymer/sol-gel chemistry for detection of Serotonin. *Talanta.* 2018;190:1–8.
166. Wang Y, Li X, Cao W, Li Y, Li H, Du B, Wei Q. Ultrasensitive sandwich-type electrochemical immunosensor based on a novel signal amplification strategy using highly loaded toluidine blue/gold nanoparticles decorated KIT-6/carboxymethyl chitosan/ionic liquids as signal labels. *Biosens Bioelectron.* 2014;61:618–24.
167. Wang J. Electrochemical biosensing based on noble metal nanoparticles. *Microchim Acta.* 2012;177:245–70.

168. Wang DB, Bi LJ, Zhang ZP, Chen YY, Yang RF, Wei HP, et al. Label-free detection of *B. anthracis* spores using a surface plasmon resonance biosensor. *Analyst*. 2009;134(4):738–42.
169. Wang S, Yumei TY, Zhao D, Liu G. Amperometric tyrosinase biosensor based on Fe<sub>3</sub>O<sub>4</sub> nanoparticles-chitosan nanocomposites. *Biosens Bioelectron*. 2008;23:1781–7.
170. Wang LY, Wang L, Gao F, Yu ZY, Wu ZM. Application of functionalized CdS nanoparticles as fluorescence probe in the determination of nucleic acid. *Analyst*. 2002;127:977–80.
171. Weinrich D, Jonkheijm P, Niemeyer CM, Waldmann H. Applications of protein biochips in biomedical and biotechnological research. *Angew Chem Int Ed*. 2009;48:7744–51.
172. Weng X, Neethirajan S. A microfluidic biosensor using graphene oxide and aptamer-functionalized quantum dots for peanut allergen detection. *Biosens Bioelectron*. 2016;85:649–56.
173. Wu K, Saha R, Su D, Krishna VD, Liu J, Cheeran MC-J, Wang J-P. Magnetic nanosensor-based virus and pathogen detection strategies before and during COVID-19. *ACS Appl Nano Mater*. 2020;3(10):9560–80.
174. Yagi K. Applications of whole-cell bacterial sensors in biotechnology and environmental science. *Appl Microbiol Biotechnol*. 2007;73(6):1251–8.
175. Yamanaka K, Vestergaard MC, Tamiya E. Printable electrochemical biosensors: a focus on screen-printed electrodes and their application. *Sensors*. 2016;16(10):1761.
176. Yang R, Liu S, Wu Z, Tan Y, Sun S. Core-shell assay based aptasensor for sensitive and selective thrombin detection using dark-field microscopy. *Talanta*. 2018;182:348–53.
177. Yoon JY. Introduction. In: Yoon JY, editor. *Introduction to biosensors*. Cham: Springer; 2016.
178. Zarei M. Infectious pathogens meet point-of-care diagnostics. *Biosens Bioelectron*. 2018;106:193–203.
179. Zarei SS, Soleimani-Zad S, Ensafi AA. An impedimetric aptasensor for *Shigella dysenteriae* using a gold nanoparticle-modified glassy carbon electrode. *Mikrochim Acta*. 2018;185(12):538.
180. Zhang S, Ma L, Ma K, Xu B, Liu L, Tian W. Label-free aptamer-based biosensor for specific detection of chloramphenicol using AIE probe and graphene oxide. *ACS Omega*. 2018;3(10):12886–92.
181. Zhu C, Yang G, Li H, Du D, Lin Y. Electrochemical sensors and biosensors based on nanomaterials and nanostructures. *Anal Chem*. 2014;87(1):230–49.
182. Zehani N, Kherrat R, Dzyadevych SV, Jaffrezic-Renault N. A microconductometric biosensor based on lipase extracted from *Candida rugosa* for direct and rapid detection of organophosphate pesticides. *Int J Environ Anal Chem*. 2015;95(5):466–79.



# Chapter 18

## Fluorescent Biosensors Based on II–VI Quantum Dots



Nguyen Thu Loan, Ung Thi Dieu Thuy, and Nguyen Quang Liem

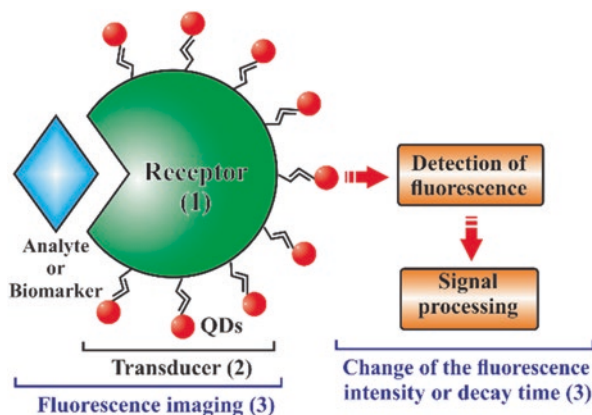
### 18.1 Fundamentals of Biosensors and Fluorescence Biosensors

Biosensors are sensors to detect biological analytes, and then transduce the detected responses into measurable and/or processable signals. Depending on the kind of analytes, concentrations and objective applications, the difficulty and sophistication in designing biosensors are different. The general structure of a biosensor is just composed of three main parts as shown in Fig. 18.1. For matching to analyte, receptor (1) must be appropriately designed to catch the analyte selectively and sensitively. Transducer (2) must respond sensitively, selectively/specifically and reproducibly to any change got by the receptor. Eventually, responses from the transducer would be measurable, displayed, monitored and/or further processed in (3). All three main parts of a biosensor are equally important and have to well match together to demonstrate the most effective and selective responses from the receptor. The biosensing event can be qualitatively detected (to know if the analyte is there or not) or quantitatively analysed (to know how much analyte is in the sample). An FBS uses fluorescence materials to detect/recognise bio-analytes and then the fluorescence signals are analysed by measuring the fluorescence intensity as a function of change of the analyte or by imaging the fluorescence-bound analytes. There have been good reviews on different kinds of biosensors using QDs as fluorescence monitors [1–5].

A good biosensor must exhibit (i) high selectivity, (ii) high sensitivity or low limit of detection, (iii) reasonable range of detection, (iv) signal readability and (v) reproducibility/reliability. Also, biosensors should demonstrate rapid detection/fast

---

N. T. Loan · U. T. D. Thuy · N. Q. Liem (✉)  
Institute of Materials Science (IMS), Vietnam Academy of Science and Technology (VAST),  
Cau Giay, Hanoi, Vietnam  
e-mail: [loannt@ims.vast.ac.vn](mailto:loannt@ims.vast.ac.vn); [dieuthuy@ims.vast.vn](mailto:dieuthuy@ims.vast.vn); [liemnq@vast.vn](mailto:liemnq@vast.vn)



**Fig. 18.1** General structure of a biosensor that is composed of (1) receptor, (2) transducer (fluorescence QDs or NCs) and (3) signal reader/processor

response, to be easy to operate and process the detected signals, and to be low-cost. In many cases, it must be compromised between the features mentioned above or made the priority for some of them.

- (i) Regarding the selectivity, it can be achieved on the basis of specific biochemical reactions or selective match between analyte and receptor. In a FBS, the selectivity or elimination of wrong detection of analyte can be accomplished by appropriate functionalisation of the fluorescence material (FM) for directly and selectively combining to the analyte; or to a specific biomarker which is representative for the analyte; or to a specific biomarker which is representative for the analyte. In the latter, the biomarker must be prepared to specifically combine with the analyte. The FMs used in FBSs can be organic dyes, luminescence complexes or semiconductor QDs. These fluorescence entities have sizes smaller than those of most analytes. Using each kind of the mentioned FMs, people have tried to exploit the advantage and avoid the drawback. Recently, QDs have been intensively considered because of their remarkable optical characteristics suitable for FBSs, such as emitting strong and narrow luminescence at certain wavelengths in the visible spectral range dependent on their sizes or compositions, while absorption in a wide spectral range due to the semiconductor nature. This is practically efficient for simultaneously detecting different analytes at the same time, by using the same excitation. In addition, the QDs can be functionalised with different molecules/complexes to selectively couple to different analytes/biomarkers. Compared to traditional fluorescent proteins or organic dyes, QDs emit stable brightness, and almost no bleaching during the measurement which is a big advantage in applications. Most FBS based on QDs exhibits the fluorescence signal dependent on the energy transfer between the QDs and analytes/biomarkers via dipole-dipole interactions (Förster Resonance Energy Transfer, FRET). This non-radiative energy transfer process is strongly dependent on the distance between the QDs and analytes/biomarkers, and the spectral overlap of the QDs emission and

analytes/biomarkers absorption. QDs based on II–VI compounds (CdSe, CdTe,... and their core/shell structures with the shell made from ZnS and/or ZnSe) are easily synthesised by chemical method in organic solvents or in water to achieve very high quality, emit narrow fluorescence peaking in the whole spectral range from UV to IR with the high quantum efficiency [6, 7]. In order to achieve high selectivity of a QDs-based FBS, QDs need to be appropriately functionalised for well coupling to various vectors specific to the analyte or biomarker. After being functionalised, the fluorescence entity is ready to selectively couple on the target analyte or biomarker via covalent coupling to and/or specific recognition of antibodies, enzymes, proteins, supramolecules, etc. QDs-functionalised antibodies are very suitable proteins responsible for foreign antigens such as virus particles, drugs, toxins, etc. Also, aptamers (oligonucleotide or peptide), which are less expensive, more stable and easy synthesise, and capable of binding to different target proteins with high affinities and specificities, are alternatives to antibodies in designing flexible sensing platforms [8]. Appropriate fluorophores could be used to label the analytes to enhance the selectivity. In some cases, immobilisation of the complexes of functionalised fluorescence entity and analyte/biomarker/label on a substrate is needed for fluorescence measurement or imaging/display. In other cases, the fluorescence-analyte/biomarker combinations in colloidal solutions are good and convenient enough for signalling or imaging. To avoid interference from the self-fluorescence of the studied specimens in imaging, type-II quantum structured QDs are good because they show strong luminescence with a very long decay time so that one can get the image after a certain delay time from the excitation when the self-fluorescence is already most decayed.

- (ii) About the signal detection limit, it depends on both the absolute fluorescence intensity from the complexes of functionalised fluorophore and analyte/biomarker/label and the readability by eyes or by certain instruments. In other words, both the absolute fluorescence intensity and the readability play equally important roles in the final result. This is because if the fluorescence is strong but the reading device is bad to read or the device reads well but has no fluorescence, neither the analyte signal could be detected. The harmony and match between the two is a mandatory requirement when designing an FBS. Nowadays, it is easy to use a UV- or blue-LED as the excitation source for QDs to fluoresce, then their fluorescence can be recorded and analysed using a compact, portable spectrometer. Of course, the ideal limit should be as low as possible, even to the single-molecule level. This is of particular significance when using FBS for diagnosing the disease at a very early stage or detecting extremely toxic substances in very low concentrations. However, striving for a low detection limit/high sensitivity often comes with complexity and high cost. Therefore, practically, the detection limit is often harmonised to the specific use for certain analyte detection, for example, it must be better than the requirement for the analyte concentration which is under the safe level. For safety reasons, many countries/organisations determine and announce the safe concentrations of pesticides, herbicides, and antibiotic residuals in food products and the environment. In some cases, to increase the sensitivity, one can collect the analytes/

- biomarkers which were bound to magnetic nanoparticles by using an external magnetic field to concentrate them in a small space to increase their density.
- (iii) The range of detection is dependent on the low limit of detection and the saturated measure. Usually, a sensor with high sensitivity is soon saturated by a strong enough signal to limit the operating range. In practice, in order for an FBS works in the large signal response range, people can divide the whole range into smaller intervals, in which the appropriate filters are put to avoid the saturation; the known attenuation factors of the filters are used for normalising the final data after measurement. Another characteristic that is practically useful is the linear range of the measured signal. The more linear the device, the easier it is to use so that the user can extrapolate the measured concentration more easily.
  - (iv) Any fluorescence signal from the analyte/biomarker/label must be finally readable or displayed, imaged with high repeatability and reproducibility. The simpler the reading and the more linear the better. It is important and applicable for an FBS is that it must give repeatedly or reproducibly the response from the analyte. This show the reliability of a measure. For single-use biosensors, it is simpler because it only needs to manufacture the same sensors and perform measurements in the same manner under the same conditions. However, with a multi-use biosensor, cleaning the sensor to remove any interference from the previous measurement as well as correcting the degraded sensitivity after multiple measurements are essential to ensure the accuracy. For imaging biological objects, as already mentioned above, it is very important that the fluorescence decay time of QDs, especially in type II quantum structure or transition metal-doped QDs, is much longer compared to that of self-fluorescence from the biological objects, so that one can do the temporal discrimination of the signal from cellular self-fluorescence and scattered excitation light.

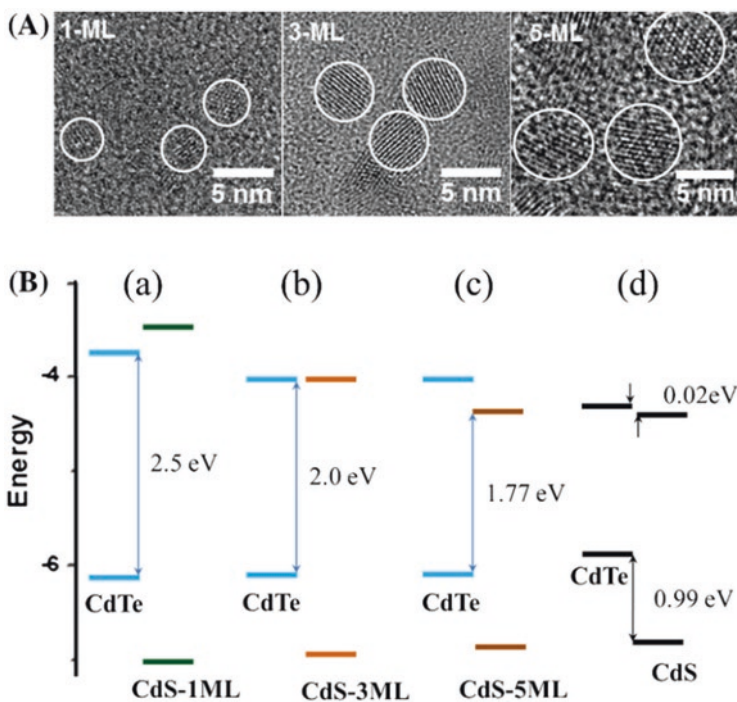
## **18.2 Fluorescent Biosensor for Clinical Diagnostics, Treatment of Diseases, and Health Care**

After the success of synthesising high-quality CdSe QDs in 1993 by Murray et al., attempts to use QDs in FBSs had bloomed [1–5, 9]. The first FBS and imaging system based on QDs were developed by Alivisatos and Nie in 1998 [10, 11]. The most important applications of FBS are for detecting viruses, mycotoxins, pathogens, specific proteins, enzymes, nucleic acids, cellular, reactive oxygen species and *in vivo* targeting/imaging that serve clinical diagnostics, disease treatment and health care. For the mentioned issues, it is extremely important to detect correctly and as early as possible the cause of the disease. FBSs of different types are investigated and manufactured for this purpose, namely to detect antigens (viruses, cancer cells, bacteria, etc.) at low concentrations but they are signs of the early stage of diseases. In the living body, the normal body's immune system can produce

antibodies when antigens are present. At the early stage of infection, the concentration of antigens or pathogens, in general, is very low and the body does not sense enough unusual, but it is a dangerous stage for developing the disease because the concentration of antigens would quickly increase to take over the body's immune system function, making the body really sick. Therefore, detecting the antigens or pathogens at very low concentrations at the early stage of the disease is very important for not only diagnostics but also for the treatment of the diseases and health care. In the approaches of FBS, there are two types of signal that can be readable or displayed: (i) the change of the luminescence intensity from QDs-bound analyte (antigens or pathogens or biomarkers) or (ii) fluorescence imaging. QDs can be functionalised to bind directly to the analyte or can also target the analyte via another analyte-specific marker. Because QDs are synthesised in organic solvents or in water depending on the chemical reaction nature, the final QDs usually exist with different ligands on the surface, consequently, appropriate functionalisation is needed. One more thing should be noted is that the functionalisation of QDs surfaces must ensure the QDs are in association with the living analyte, not with the dead one, to avoid the misinterpretation of QDs fluorescence efficiency as well as false signal analysis. For imaging, suitable light is used to excite the QDs-bound analytes to have luminescence, then people can take images of the objects under the microscope. In other cases, measurement of the luminescence spectra as a function of the analyte concentration or even the on-off luminescence is applied. Because human tissues are made up of organic molecules which absorb UV-Vis light and luminesce under ultraviolet light excitation, it is more convenient to use near-infrared (NIR) light to excite QDs for imaging to avoid absorption and autofluorescence from the tissues. Practically it is good for FBSs to work with light in the two biological windows of 750–940 nm and 1200–1700 nm because that light is able to penetrate deep into the human body with low absorption and is not excitable to give the autofluorescence from the tissues.

Among the II–VI QDs, CdTe and CdSe are probably the most studied and synthesised to emit strong and narrow excitonic luminescence in the whole visible range [6, 7, 12]. However, because CdTe is efficiently and easily prepared in aqueous media, it is easily used for biomedical applications without the need for ligand exchanges. As a result, there have been more publications on the use of CdTe QDs in FBSs. Moreover, by varying the shell (CdS, CdSe and ZnSe) thickness, one can form type I or type II quantum structure to emit efficiently luminescence peaking at different wavelengths (Fig. 18.2). For type-II CdTe/CdS core/shell structure, which has a very long fluorescence lifetime of up to several hundred ns, it is very convenient for application in time-gated fluorescence imaging to eliminate the autoemission from the organic analyte [13].

Analytes including viruses, biomarkers, specific proteins, enzymes, and pathogens, in general, have the size of several tens nm to micrometres (SARS-CoV-2 have differently reported diameters ranging between 50 nm and 140 nm). In contrast, the QDs used for labelling or attaching to analytes are several nm in size, therefore many QDs may bind to one analyte to improve the fluorescence intensity at the target. Though the designs and structures of FBSs are different for detection

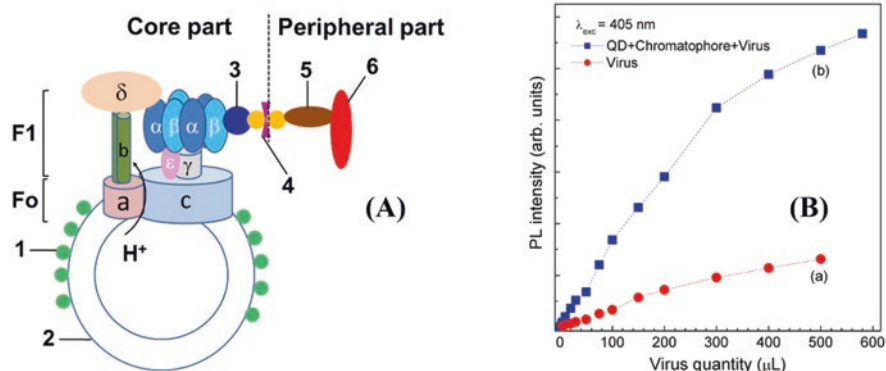


**Fig. 18.2** (a) HR-TEM images of CdTe/CdS QDs with the different CdS shell thicknesses and (b) the sketch of their energy diagram showing the transition from (a) type I to (b and c) type II quantum structure along with thickening the CdS shell, (d) the energy diagram of bulk CdTe/CdS for comparison. (Reproduced with permission from Ref. [13]. Copyright 2016: Elsevier B.V)

of various analytes, the reading signals are based on (i) the change in the fluorescence intensity or (ii) the image of the fluorescence QDs-bound analytes. The change in the fluorescence intensity may be caused by the change of pH in the vicinity of QDs, the charge state at the surface of QDs or by fluorescence resonance energy transfer (FRET) from QDs to analytes. In the following, examples of the two kinds of FBS mentioned above are presented.

### 18.2.1 Reading Signals by Measuring the Fluorescence Intensity

Figure 18.3 illustrates a typical design of the FBS for the detection of H5N1 influenza virus using CdTe/CdS QDs bound to chromatophores with  $F_0 F_1$ -ATPase [14]. In this design, it is practically nice and convenient for the detection of various analytes (by replacing accordingly in the peripheral part) with the same core part. The core is kept with the working principle that any change in the peripheral part would



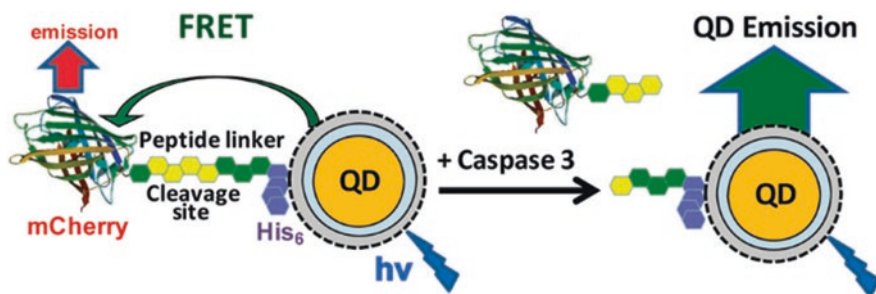
**Fig. 18.3** (a) A typical fluorescence biosensor for virus detection. The core part consisted of (1) CdTe/CdS QDs, (2) chromatophores with *FoF1*-ATPase and (3) the antibody of  $\beta$ -subunit. (4) the biotin–streptavidin–biotin bridge linked the core part with the peripheral part consisting of (5) the antibody of the H5N1 avian influenza virus and (6) the H5N1 avian influenza virus. (b) the PL intensities of (a) H5N1 viruses and (b) biosensor composed of all the CdTe/CdS QDs, chromatophore and H5N1 virus under detection as a function of the H5N1 virus concentrations. (Reproduced from Ref. [14]. Published 2012 by IOP Publishing as open access)

make change the  $H^+$  flux in the chromatophore, correspondingly changing pH of the local environment, causing the change of the fluorescence intensity from the bound QDs. The biotin–streptavidin–biotin bridge (4) is a good biolink to bind the core part with the peripheral part of this FBS. The selectivity is determined by using the right antibody (5) to match antigen (6) in the peripheral part and it can be flexible depending on the antibody–antigen couple. For this design, it is possible to detect the H5N1 avian influenza virus at a concentration as low as 3 ng/ $\mu$ L [14]. This kind of FBS demonstrates really higher sensitivity and selectivity, and flexibility as well. Other kinds of biosensors for the detection of the H5N1 avian influenza virus were also developed, for example the one used isothermal amplification method for the sensitive detection of the H5N1 influenza virus in the concentration range from 10 fM to 0.25 pM, with a detection limit of 9 fM at a signal/noise ratio of 3 [15]; or a sensitive quantitative lateral flow immunoassay (LFIA) to detect influenza viruses H5 and H9 simultaneously showing the accuracy is as high as that of real-time PCR [16]; or recently the label-free one based on three-segment branched DNA-templated fluorescent silver nanoclusters to detect the H5N1 gene sequence with the wide linear range of 500 pM–2  $\mu$ M and a low-limit of detection (LOD) of 500 pM [17].

Another example is the use of highly luminescent CdTe/CdS QDs covalently attached to the polyamidoamine (PAMAM) dendrimer to make the ultrasensitive solid surface fluorescence immunosensor for determination of HBsAg (hepatitis B virus surface antigen), the earliest definite serologic marker of hepatitis B [18]. Therefore, this FBS has great potential in early diagnostics of hepatitis B, an immune disease that causes cirrhosis and liver cancer. The study shows a good analysis with the excellent linearity of HBsAg concentration from 5 fg/mL to 0.15 ng/mL with the LOD of 0.6 fg/mL. The sensitivity and LOD of this FBS are

thousands times better than that obtained by using other kinds of sensors (namely based on the differential pulse voltammetry, electrochemical detection and normal fluorescence) reported in the literature (Table 1A in Ref [18]). The selectivity of this FBS is responsible for the right antibody of hepatitis B virus.

Proteins are the main constituent of viruses, cells, and any live entity. In the structure of FBSs using QDs to detect/analyse proteins, molecules that efficiently conjugate the proteins (or peptides, DNA) with the QDs surface are indispensable. Upon the presence of proteins, the fluorescence of the QDs donor is quenched via FRET. Note that the energy transfer, in this case, is via electrical dipole-dipole interaction, it is therefore inversely proportional to the distance to the power of 6 [ $E = nR^6/(nR^6 + r^6)$ ]. Dihydrolipoic acid (DHLLA)-functionalized CdSe/ZnS QDs emitting at 550 nm were selected for assembly with mCherry because of the favourable spectral overlap (Forster distance  $R_0 = 4.9$  nm). Polyhistidine(His<sub>6</sub>) could be a good one to append proteins, peptides and even DNA to CdSe/ZnS QDs via metal-affinity coordination [19]. Figure 18.4 illustrates a sensitive and specific FRET-based protease sensor to detect caspase 3, an important downstream protease in apoptosis. Once activated by upstream initiator caspases, this cysteine protease specifically cleaves substrate proteins as part of the apoptotic cascade. Detection of caspase 3 is necessary and of particular interest in cancer research, as its activity is a prognostic indicator of chemosensitivity in breast and ovarian tumours. In this FBS, mCherry, a monomeric red fluorescent protein, with an N-terminal linker expressing the caspase 3 cleavage site and a His<sub>6</sub> sequence is chosen to be the FRET acceptor that is self-assembled on the surface of CdSe/ZnS QDs, resulting in FRET quenching of the QD fluorescence. The FRET also sensitizes emission from the mCherry acceptor. When adding caspase 3 to this complex, it cleaves the linker to reduce the FRET efficiency to recover the fluorescence from the QD [19]. The change in FRET efficiency depends on the ratio of mCherry to QD emissions. The recovered fluorescence from the CdSe/ZnS QDs is proportional to the caspase 3



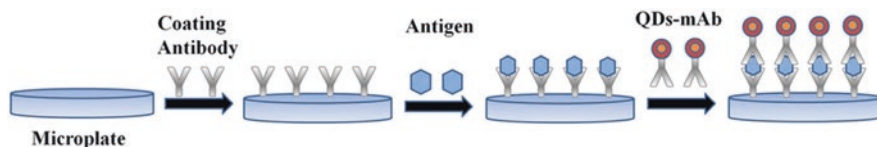
**Fig. 18.4** A sensitive and specific FRET-based protease sensor to detect caspase 3. mCherry with an N-terminal linker expressing the caspase 3 cleavage site and a His<sub>6</sub> sequence were self-assembled to the surface of CdSe/ZnS QDs, resulting in FRET quenching of the QD and sensitized emission from the mCherry acceptor. Caspase 3 cleaves the linker, reducing the FRET efficiency to recover the fluorescence from the QD. (Reproduced with permission from Ref. [19]. Copyright 2009: American Chemical Society)



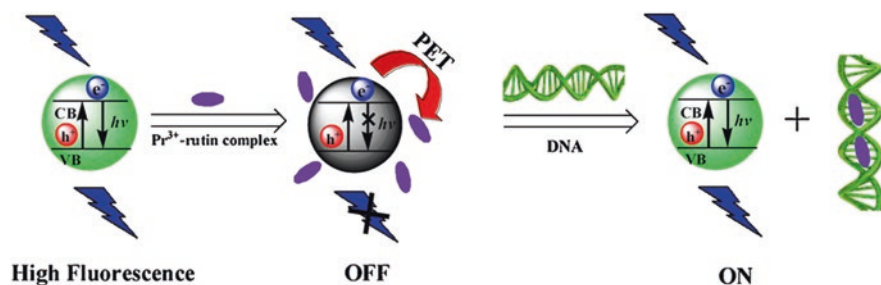
concentration, with the ability to detect enzymatic activity for caspase 3 concentrations as low as 20 pM.

In human body, C-reactive protein (CRP) is a measure for inflammation. Doctors might order a CRP test to check for inflammation due to an infection, for diagnosing a chronic inflammatory disease, and for determining a risk of heart disease or risk of a second heart attack. A high-sensitivity C-reactive protein (hs-CRP) test has been developed to detect slight increases within the normal range of standard CRP levels. This is a novel fluorescence-linked immunosorbent assay (FLISA) for rapid detection of C-reactive protein using QDs as a fluorescence label (Fig. 18.5) [20]. The selectivity for the antigen (CRP in this case) is determined by the monoclonal antibody (mAb) labelled on CdSe/ZnS QDs. First, CRP antigens (Ag) are captured by the CRP mAb coating on the microplate. Then, the QDs-labelled antibodies are combined with antigens to form a mAb-Ag-mAb sandwich structure after sufficient incubation time. Fluorescence intensity from QDs is first increased by increasing the incubating time of QDs-mAb probe after the CRP antigen was incubated, then stable after 20–30 min, namely the optimal incubation time. The fluorescence intensity is increased with increasing the concentration of the CRP antigens. The FLISA showed a good linear correlation with the concentration range from 1.56 ng/mL to 400 ng/mL, with the limit of detection (LOD) of 0.46 ng/mL. The accuracy of the assay meets the requirements with recoveries of 95.4–105.7%. This *in vitro* QDs-based detection method offers a lower LOD and a wide linear detection range than ELISA. And, the total reaction time is only 50 min, much shorter than the commercialisation ELISA (about 120 min). All of the results show that FLISA is a fast, convenient, sensitive, selective and accurate method for the detection of CRP samples, and can be a rapid, selective and cost-effective *in vitro* diagnostic kit.

Deoxyribonucleic acid (DNA) plays a very important role in biochemical processes occurring in the cellular system including gene expression, gene transcription, mutagenesis, carcinogenesis, etc. [21]. The binding of small molecule drugs to DNA has been an active area of research to better understand the mechanism of antiviral activity, as well as the advanced design of new drugs. A QDs-based FBS using  $\text{Pr}^{3+}$ -rutin complex is presented in Fig. 18.6. Rutin is a well-established chelating agent reactable with rare earth elements to form complexes.  $\text{Pr}^{3+}$ -rutin complex is the one efficiently quenches the fluorescence of glutathione (GSH)-capped CdTe QDs due to the ultrafast photoinduced electron transfer (PET). The ensemble



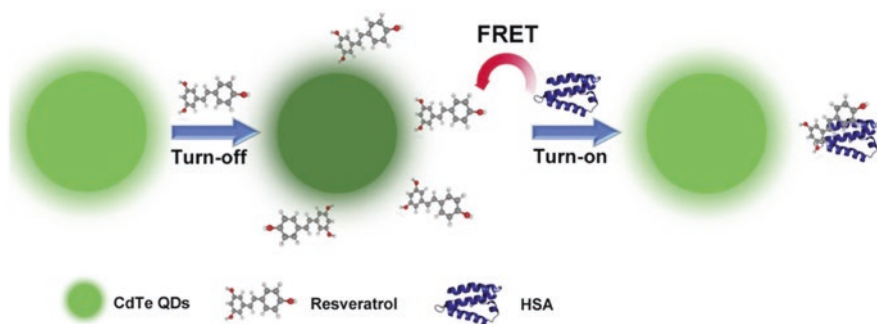
**Fig. 18.5** Schematic illustration of FLISA procedure. Antibodies are immobilised on the microplate to selectively catch antigens; while the QDs-labelled antibodies are also combined with antigens to form a mAb-Ag-mAb sandwich labelled with QDs. The measured fluorescence intensity from these QDs is the monitor for the antigen concentration. (Reproduced from Ref. [20]. Published in 2017 by Springer Nature as open access)



**Fig. 18.6** Schematic diagram of the mechanism to detect hsDNA. 'OFF-state' of FBS is due to Pr<sup>3+</sup>-rutin complex that efficiently quenches the fluorescence of GSH-capped CdTe QDs. Then, 'ON-state' is recovered by adding hsDNA into ensemble of GSH-capped CdTe QDs-Pr<sup>3+</sup>-rutin complex to release GSH-capped QDs free for their fluorescence. (Reproduced with permission from Ref. [21]. Copyright 2012: Elsevier B.V)

of GSH-capped CdTe QDs-Pr<sup>3+</sup>-rutin complex is therefore able to display a desirable 'off-state' of the biosensor. On the other hand, the Pr<sup>3+</sup>-rutin complex also serves as the receptor to bind specifically with herring sperm (hs) DNA. When the hsDNA is added, because of its strong binding affinity with the Pr<sup>3+</sup>-rutin complex, hsDNA can break up and remove the Pr<sup>3+</sup>-rutin complex from the surface of CdTe QDs to restore the fluorescence of QDs. Concentrations of rutin and Pr<sup>3+</sup> are 50 nM/L, and the total volume of rutin and Pr<sup>3+</sup> is 5.0 mL in the Job's method; the solutions of rutin and Pr<sup>3+</sup> are mixed and diluted with water to the mark of the 10 mL calibrated flask, and then are shaken thoroughly. The relative recovered fluorescence intensity is directly proportional to the concentration of hsDNA between 0.0874 μg/mL and 20 μg/mL, and the detection limit is 0.0262 μg/mL. More than the FBSs described above, CdTe/ZnSe QDs were also successfully applied to detect easily any change in the sequence (mutation) of DNA. The QDs also showed their ability to detect DNAs directly from the extracts of human cancer (PC3) and normal (PNT1A) cells (detection limit of 500 pM of DNA) [22].

Human serum albumin (HSA) is an endogenous protein abundant in human blood and is a hot object in research in clinical medicine. The development of albumin drug carriers is gaining increasing importance in the targeted delivery of cancer therapy. Therefore, the detection of HSA is of great significance in clinical diagnosis. In recent years, to satisfy the clinical requirements, many detection methods for HSA have been developed, such as high-performance liquid chromatography, electrochemical, resonance light scattering, spectrofluorimetric, etc. However, due to the complexity, low sensitivity and selectivity, and high cost of sample preparation, the application of most aforementioned methods is limited. Therefore, a highly sensitive and selective FBS for the detection of HSA based on the 'turn-off-on' fluorescence of QDs has been developed [23]. Because of the facile synthesis in water to produce highly luminescent CdTe QDs, these QDs have been again efficiently used for the fabrication of FBSs. The principle of such an FBS is shown in Fig. 18.7. The fluorescence of CdTe QDs is first quenched due to resveratrol, a polyphenol, because of the collision between excited CdTe QDs and resveratrol. Then, when adding



**Fig. 18.7** Schematic diagram of the proposed “turn-off-on” mode of the QDs-resveratrol-HSA system. “OFF-state” is due to the interaction between excited CdTe QDs and resveratrol. Then, “ON-state” is established by adding HSA into the system to form resveratrol-HSA binding complexes to release QDs free to fluoresce. (Reproduced with permission from Ref. [23]. Copyright 2020: Elsevier B.V)

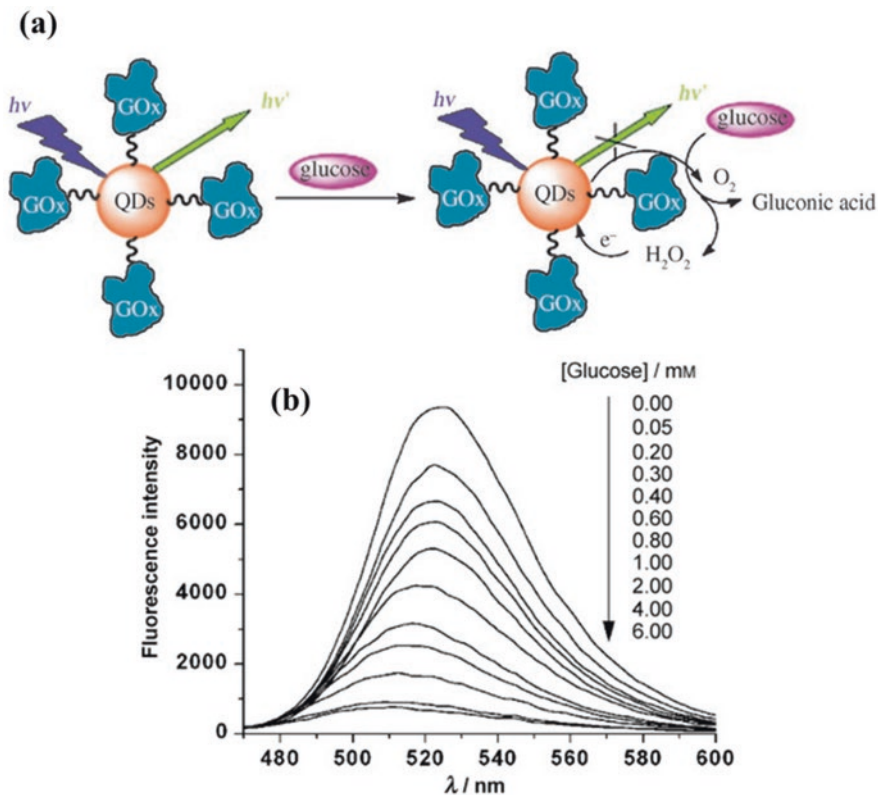
HSA to the system, the resveratrol-HSA binding complexes is formed resulting in the resveratrol to move away from the QDs, leading to the recovered fluorescence of CdTe QDs. This fluorescent “turn-off-on” biosensor can selectively and rapidly detect HSA in a wide concentration range of 0.0237–100  $\mu\text{g/mL}$ , with very low detection limit of 6.898  $\text{ng/mL}$ . This QDs-based FBS is successfully applicable to determine HSA; the method is accurate, rapid and sensitive enough for determining HSA at low ppb levels.

Along with viruses, proteins, DNA that cause diseases and affect human health, bacteria are also the important source to cause different diseases. Therefore, how to efficiently detect the bacteria by using BFSs is attracting the attention of many researchers. This is important and necessary for clinical diagnostics, treatment of diseases and health care. Bacteria are usually very large compared to QDs, which is advantageous and convenient to bind many QDs on bacteria for the good fluorescence signal. In an FBS, to detect directly bacteria or just its representative biomarker, in many cases, QDs need certain molecules to work as matchmakers to conjugate to both the QD and bacteria/biomarker. Among bacteria, *Serratia marcescens* is the one most commonly isolated from human infections including bacteraemia, pneumonia, etc. *S. marcescens* is the Gram-negative bacillus found ubiquitously in soil, water, plants, insects, animals, food and the gastrointestinal tract. Lipopolysaccharide (LPS) is a major component of the outer membrane of Gram-negative bacteria that induces a strong immune response upon its internalisation into the mammalian cells. Detection of LPS from *S. marcescens* is therefore very important in healthcare and public biodefense. The design and working principle of an FBS using CdTe QDs is based on the conjugation of fluorescence QDs with Concanavalin A (Con A), a lectin from jack bean, to detect selectively and specifically LPS. Upon the presence of LPS, the fluorescence of CdTe QDs is quenched. A good linear relationship between the relative fluorescence intensity and the cell population of *S. marcescens* in the range from 10 to  $10^6$  CFU/mL at pH 7 was

established. The fluorescence of CdTe QDs-Con A is linearly decreased with increasing the LPS concentration from 10 to 90 fg/mL [24].

Another kind of analytes, which is blood glucose that must be importantly determined because it is the most common and very necessary indicator for the human health. Blood glucose comes from the food and is the main source of energy for keeping all body cells alive. Blood glucose level refers to the total amount of glucose circulating in the blood that is between 4 and 7 mmol/L (mM) or 0.72–1.26 mg/mL for normal non-diabetics. Recently there is a comprehensive review of commercial and scientific solutions for blood glucose monitoring by using different methods [25]. Commercial products for blood glucose measurement are mainly based on the microwave and electrochemical principle. However, due to the high sensitivity and the ability to measure many other blood parameters at the same time, many studies on blood glucose measurement using fluorescent biosensors have been conducted. Blood glucose content can be determined through measurements of plasma, body secretions or of tears [25–29]. The principle of these measurements is based on the change of fluorescence intensity from QDs due to redox chemiluminescent reactions. Figure 18.8 shows a typical FBS to detect H<sub>2</sub>O<sub>2</sub>-bioprecursors (glucose) in the presence of glucose oxidase (GOx). Many important biomolecules in body fluids, including glucose, sarcosine, uric acid, cholesterol, etc., can be defined as “H<sub>2</sub>O<sub>2</sub>-bioprecursors” because they release H<sub>2</sub>O<sub>2</sub> by the catalytic action of their oxidases. This H<sub>2</sub>O<sub>2</sub>-bioprecursors belong to the reactive oxygen species (ROS) which have been found in living bodies including mammals and plants. In other words, in the reaction, GOx catalyses the oxidation process to change glucose into gluconic acid and produces H<sub>2</sub>O<sub>2</sub> simultaneously. H<sub>2</sub>O<sub>2</sub> then provides the electrons at the surface of the CdTe QDs to quench fluorescence or produce nonfluorescent CdTe QDs anion. The working principle of such an FBS to detect glucose is based on the change in the fluorescence intensity of QDs in conjugation with GOx [29]. Using CdTe QDs, the FBS demonstrated good linearity in the glucose concentration range of 1–20 µg/mL (0.6–11.1 mM) [27] and could determine glucose in the wide concentration range from micro- to milli-molar with the LOD of 0.1 µM [29]. The calibration and appropriate protocol (sample preparation including GOx-QDs and glucose, excitation light and fluorescence detection) are needed for real applications of FBS to detect glucose from different sources (blood, urine, saliva and tears) of human body [28].

Very similar to the FBS that used CdTe QDs mentioned above, FBS used TGA-capped CdSe/ZnS QDs (of the mean particle size of 10–12 nm to emit luminescence peaking at 620 nm) conjugated with GOx and horseradish peroxidase (HRP) enzymes was developed for the detection of glucose in aqueous samples. Here, glucose was determined depending on the enzymatic reaction of glucose that releases H<sub>2</sub>O<sub>2</sub> to change the fluorescence intensity from CdSe/ZnSQDs. In more detail, the process is explained by the exchange of the electron at the outer surface of the core-shell QDs, whereby H<sub>2</sub>O<sub>2</sub> is reduced to oxygen and H<sub>2</sub>O, which traps the electron holes at the surface of the QDs, further causing the decrease of the fluorescence intensity. The higher glucose concentrations used, the more H<sub>2</sub>O<sub>2</sub> produced



**Fig. 18.8** (a) a typical FBS based on CdTe QDs conjugated with GOx for the detection of glucose. The oxidation catalysed by GOx changes glucose into gluconic acid and produces  $H_2O_2$  simultaneously to quench the fluorescence of CdTe QDs and (b) the changes in fluorescence intensity from CdTe QDs-GOx as a function of glucose concentration. (Reproduced with permission from Ref. [29]. Copyright 2008: Wiley-VCH Verlag GmbH & Co.)

and thus the greater the fluorescence quenching effect on the QDs. The bioconjugated GOx:HRP/QDs capped with TGA shows a good linearity for the glucose determination in the range of 0–10 mM, with the LOD to be 0.045 mM [30].

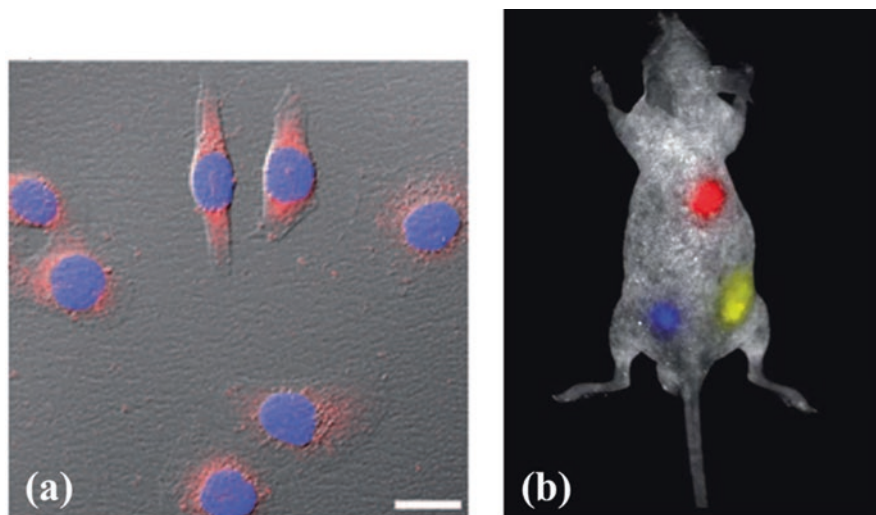
Other kinds of II–VI QDs such as ZnO [31] and Mn-doped ZnS [32] were used to fabricate FBSs for the detection of blood glucose that shows high sensitivity and good selectivity. The fluorescence sensing of several monosaccharides using boronic acid-substituted viologen quenchers/sugar receptors in combination with the fluorescent Mn-ZnS QDs as signals that are capable of identifying six sugars (D-fructose, D-glucose, D-galactose, D-mannose, L-sorbose and sucrose) and discriminating different sugar concentrations [32]. For all these FBSs,  $H_2O_2$  must be borne by the enzyme (mainly GOx)-assisted oxidation of glucose to quench fluorescence of QDs [26–34].

### ***18.2.2 Reading Signals by Imaging the Fluorescence QDs-Bound Analytes***

Imaging is an effective way to monitor tumours or tissues or cells. The first important requirement for imaging is how the QDs can be targeted and linked to the object to be imaged. This means that in order to image the analytes by fluorescence QDs, the QDs must be prepared to selectively bind to the analytes via functionalisation with antibodies or any suitable binder on the surface so that QDs are target-oriented with analytes, ignoring other objects around. Then, the second important issue is the manner in which the QDs are delivered for in vitro or in vivo imaging. For in vitro, it is simple but in case in vivo is needed the direct injection of functionalised QDs into the living body is the best way for this purpose. Finally, good fluorescence images could be taken to observe with the suitable excitation light and camera. If QDs could give fluorescence by the near-infrared (NIR) excitation (two-photon excitation process) it would be advantageous because the near-infrared light can penetrate deep into the living organism, excite QDs-bound tumours or tissue deep inside the body and NIR is usually could not excite living protein to have luminescence which interferes to that from QDs. In fact, because it is possible to target the cancer cells or pathogens, tumours, then checking by imaging them under microscope would help very much to determine the cancer cells or pathogens or tissues/tumours for necessary clinic actions. There have been comprehensive reviews and original articles on the use of CdTe, CdSe QDs for imaging cells and tumours or biomarkers [35–40]. Some examples of multi-colour in vivo imaging by using different QDs are presented in Fig. 18.9.

### **18.3 Fluorescent Biosensors for Detection of Pesticides and Growth-Promoting Hormone in Agricultural Productions**

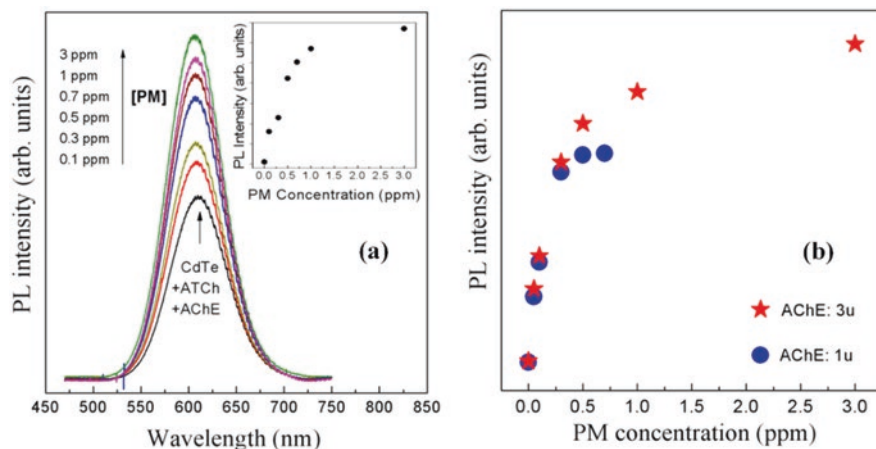
Along with the agricultural production, people have used various kinds of pesticides, herbicides, growth-promoting hormones, etc., that more or less remain in the products and soil, and environment. These residuals are toxic in contaminated products and also make the environment harmful after a long-term accumulation. Therefore, detection of the toxic residuals in agricultural products or environmental samples is mandatory to confirm the cleanness of products and safe production. FBSs seem to be effective and practically applicable from the viewpoints of cost, time-consuming and sensitivity to ensuring constant control of the concentration of pesticides in agricultural productions. There have been a number of articles devoted to the studies of biosensors for the detection of pesticides and antibiotics, growth-promoting hormones, etc., using QDs showing the potential of QDs in practical applications [41–45]. In the following are demonstrated two examples of detecting



**Fig. 18.9** (a) Dual-colour immunofluorescence cellular imaging with QDs (scale bar: 20 mm). The HeLa cells are labelled by the QDs/protein conjugates (red) and Hoechst (blue). Reproduced with permission from Ref. [38]. Copyright 2011: Wiley-VCH Verlag GmbH & Co. (b) multiplex imaging capability of CdTe/CdSe QDs in a live athymic nude mouse. Reproduced with permission from Ref. [39]. Copyright 2011: RSC Publishing

pesticides and growth-promoting hormones. The working principles of these two can be applicable to other kinds of analytes with some modifications.

Pesticides are chemical compounds commonly used in agricultural production to ensure high outcomes. Among them, organophosphorus (OP) compounds have been widely used because of their high efficiency for insect killing, easy synthesis and low cost. The good selectivity of biosensors for the detection of OPs is based on the selective interaction potential of OPs with acetylcholinesterase (AChE) enzyme. These selective biosensors are a promising alternative to conventional techniques for field sensing [42]. Figure 18.10 represents an example of FBSs to detect parathion methyl (PM), a kind of organophosphate insecticide, possessing an organothiophosphate group. This FBS is actually constructed from the complex of CdTe QDs, acetylcholinesterase (AChE) and acetylthiocholine (ATCh). The biosensor activity is based on the change of luminescence from CdTe QDs with pH, while the pH is changed with the hydrolysis rate of ATCh catalysed by the enzyme AChE, whose activity is specifically inhibited by pesticides. The inhibition of the AChE enzyme would lead to many health issues in the living system by affecting the functionalities of important organs. CdTe QDs could be efficiently synthesised in water in the presence of thioglycolic acid (TGA) or mercaptoacetic acid (MAA) or 3-mercaptopropionic acid (MPA) or mercaptosuccinic acid (MSA) as surfactants/stabiliser. By using the fabricated FBSs, normal checks show the detection of PM at very low concentrations of ppm with the LOD as low as 0.05 ppm. The dynamic range from 0.05 ppm to 1 ppm for the pesticide detection could be expandable by



**Fig. 18.10** (a) PL spectra (under the 405 nm laser light excitation) of CdTe-AChE-ATCh as a biosensor to detect different PM contents. The inset shows the relationship between the PL intensity and the PM contents; (b) extending the dynamics of PM concentration by increasing the AChE enzyme. (Reproduced from Ref [43]. Published 2012 by IOP Publishing as open access)

increasing the AChE amount in the biosensor [43]. Another FBS without AChE enzyme has been performed for TGA-capped CdTe QDs to detect malathion, a kind of OPs [44]. CdTe QDs functionalised by TGA give the carboxyl heads which mimic the AChE enzyme binding sites. The OPs pesticides specifically bind to the active sites (carboxyl and hydroxyl moieties of amino acids) of AChE and lead to the phosphorylation of the enzyme. Here, pesticides interact with the carboxyl functionalities on the CdTe QDs. The high coordination ability of TGA-capped CdTe QDs with malathion enables the electron transfer rate between QDs and malathion of  $2 \times 10^8 \text{ s}^{-1}$ . The fluorescence quenching of CdTe QDs as a function of the concentration of malathion is evaluated and presented, showing the LOD and limit of quantification (LOQ) as low as 0.68 nM and 2.26 nM, respectively. These results were considered as an arsenal tool to deliberate selective sensing approach among the pool of OPs that have the same mechanism of interaction with acetylcholine enzyme inhibition.

Chlorothalonil (CHL, 2,4,5,6-tetrachloroisophthalonitrile) has also been widely used in agricultural productions because of its broad spectrum effect, a nonsystemic fungicide. To detect effectively and selectively CHL, a new FBS has been realised based on the inner-filter effect (IFE) between AuNPs and ratiometric fluorescent QDs (RF-QDs), which are designed by two different colour CdTe QDs. Concretely, one kind of RF-QDs is designed to emit green luminescence in resonance with the plasmonic absorption of AuNPs, at around 540 nm; while the other emits red luminescence at around 640 nm. The zeta potentials of the RF-QDs and AuNPs were  $-13.4$  and  $-27.8$  mV, respectively, meaning that they both have negative charges to electrostatically repel each other to keep their distance far. Due to IFE, the AuNPs quench the fluorescence of the green RF-QDs; but then, because of the electrostatic



attraction between protamine (PRO, a basic protein having high-density positive charges) and AuNPs, the PRO makes restoration of the green fluorescence effectively. With increasing the amount of PRO added, the IFE is decreased to release more the green fluorescence. The red luminescence is kept unchanged as a reference in the ratiometric fluorescent measurement. Papain (PAP), a cysteine protease enzyme, is used to easily hydrolyse PRO to keep quenching the green fluorescence; while its activity is inhibited by CHL. Therefore, to determine CHL, just add CHL into the [RF-QDs + AuNPs+PRO+PAP]complex and measure the restored fluorescent signal. The ability of CHL to inhibit PAP activity is evaluated by measuring the fluorescence of the green RF-QDs in reference to that of the red one. Under the optimal conditions, this FBS shows the good selective detection of CHL in the range of 0.34–2320 ng/mL with the LOD of 0.0017 ng/mL. The practical application of the proposed FBS was demonstrated by detecting CHL in food and environmental samples with satisfying results [45].

Clenbuterol is a chemical used in farming to increase meat for pigs and cows. This is a growth-promoting hormone often used by the breeder in a short period of time (21 days) before selling farmed animals. The big problem is that clenbuterol in pork meat cannot be decomposed by cooking at high temperatures. The clenbuterol residuals in meats could affect human health, causing cancers, poisoning, heart failure, hypertension and even death. To detect these residuals in meats, the key points for designing this FBS are based on the fluorescence resonance energy transfer (FRET). First, CdTe QDs are coated with naphthol, the clenbuterol-recognisable agent. Because CdTe QDs synthesised in water with MPA molecules on the surface that contain carboxyl group (-COOH), which can be further modified with carbodiimide, then can react with the amino group from 2-amino 8-naphthol-6-sulphonic acid to form stable amide coupling. Also, clenbuterol is diazotised by a chemical reaction in the presence of  $\text{NaNO}_2$  in HCl. This reaction forms the specific orange-yellow colour of the azo compound and occurs with the diazo group only. Then, the naphthol-complexed QDs can recognise the diazotized clenbuterol [46], changing the fluorescence intensity from CdTe QDs. Thus, this reaction can be used as a specific reaction to recognise clenbuterol in solution. In the practical case, there are also some amine groups in protein and urea from a test sample obtained from urine or internal organs of animals but this amine group cannot form diazo coupling with QDs. The change in fluorescence intensities of the FBS is utilized to determine the clenbuterol concentrations. Without CdTe QDs in the FBS, the quantitative clenbuterol concentration in a solution cannot be determined because of lack of the FRET. Without clenbuterol, the fluorescence intensity from CdTe QDs is maximum. The fluorescence intensity detected from FBS is found to decrease with increasing clenbuterol concentrations, following a linear correlation in the range of 0–40 pg/mL, with a sensitivity up to 10 pg/mL. Another kind of growth promoter used in animal foods is doxycycline. A rapid, simple and inexpensive spectrofluorimetric biosensor for the determination of doxycycline has been developed based on the quenching of fluorescence of TGA/CdTe QDs in the presence of doxycycline due to electron transfer from the QDs to doxycycline. This FBS exhibited to be fast (the response time of <10 s) and could determine the doxycycline in a concentration

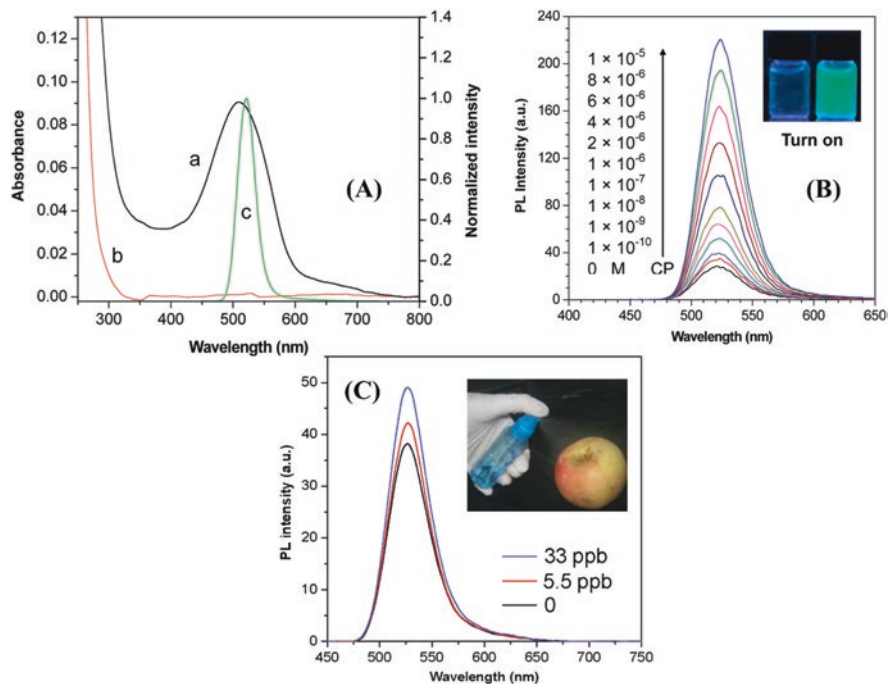
range of  $1.9 \times 10^{-6}$ – $6.1 \times 10^{-5}$  mol/L with a LOD of  $1.1 \times 10^{-7}$  mol/L. The sensor was applied for the determination of doxycycline in honey and human serum samples [47].

## 18.4 Fluorescent Biosensors for Food Safety

The food safety is very serious for human healthcare. Daily used foods are made from agricultural products in which various kinds of harm or toxicity are possibly reduced. Also, during food processing, some additives have been introduced accidentally or intentionally, potentially causing harm to consumers' health. To detect these toxic residuals in fruits, vegetables, drinking water, processed foods and other agricultural products, FBSs seem to be effective and practically applicable from the viewpoints of cost, time-consuming and sensitivity. Especially how to select and on-site detection of pesticide residues with rapid, simple operation and low cost is still a hot topic. In the following, as examples, some types of FBSs for the detection of pesticides in fruits, some toxins in milk and bacteria contaminated in foods are presented.

As mentioned in the previous section, for many years, millions of tons of OP-based pesticides have been used in agricultural productions worldwide that have consequently contaminated the air, water, soil and many kinds of agricultural products, ultimately long-term accumulation in ecosystems, including humans. Therefore, there is a great demand for fast, sensitive, high-accuracy detection of OP pesticide residues to improve food safety and to protect the environment. OP pesticides are composed of two main types of derivative compounds, organophosphorus esters (containing P=O bonds) and organophosphorus thioates (containing P=S bonds). Of the organophosphorothioate pesticides, chlorpyrifos (CP) has received the most attention because they are widely used and environmentally sustainable, making them easier to accumulate and long-lasting in agricultural products and the environment. CdTe QDs again are good materials for the fabrication of an FBS to detect residues of the above pesticides [48]. The working principle of this FBS is based on the change of the fluorescence intensity from QDs due to fluorescence resonance energy transfer (FRET). The general design of the fabricated FBS is the "turning on" fluorescence when detecting pesticides by changing the ligands, which can be described as follows:

- Dithizone has the ability to combine with  $\text{Cd}^{2+}$  ion in CdTe QD to form the dithizone–Cd (DZ–Cd) complex. This complex has an absorption peak at 510 nm, which can completely overlap the fluorescence spectrum of CdTe QDs, as shown in Fig. 18.11A. Thus, when the DZ–Cd complex adheres to the surface of the CdTe QDs, the FRET process will occur, which quenches the fluorescence of CdTe QDs. Therefore, when combined with dithizone to form the DZ–Cd complex, the CdTe QDs do not fluoresce and is called a DZ–QD detector.



**Fig. 18.11** (A) Absorption spectra of (a) the DZ-Cd complex, (b) the DEP-Cd complex and (c) the PL spectrum of CdTe QDs; (B) PL of CdTe QDs is minimum in the presence of DZ-Cd complex, then recovered as the DZ-Cd complex on the surface of CdTe QD is replaced by DEP-Cd complex. The inset shows the fluorescence “on” when CP is detected; (C) example for detection of CP insecticide residues on the apple peels in that the fluorescence intensity from the DZ-Cd complex-quenched CdTe QDs is increased due to the replacement of the DZ-Cd complex by DEP-Cd complex. (Reproduced with permission from Ref. [48]. Copyright 2010: American Chemical Society)

CP insecticide molecules are easily hydrolysed in water to form diethyl phosphorothioate (DEP) and trichloro-2-pyridinol (TCP); in which DEP also has the ability to form complexes with  $\text{Cd}^{2+}$  ions like dithizone (the bond between DEP and  $\text{Cd}^{2+}$  is stronger than that of dithizone and  $\text{Cd}^{2+}$ ). When the DZ-QD detection material encounters the CP insecticide, because the complexing bond between DEP and  $\text{Cd}^{2+}$  is stronger, DEP replaces DZ, forming a DEP-Cd complex. Since there is no longer a DZ-Cd complex, so there is no longer a FRET, the fluorescence of the CdTe QDs is restored (the new DEP-Cd complex does not quench the 520 nm fluorescence of the CdTe QDs) as seen in Fig. 18.11B. Figure 18.11C presents a fascinating example of the detection of CP insecticide residue on apple peels. The allowable CP residue limit of apples is the lowest (10 ppb) in agricultural products because apples possess many nutritional components including cellulose, sugar, vitamins, organic acids, minerals substances, polyphenols and flavones. The experiment was conducted as follows: dilute CP in methanol and spray on apples with a spray bottle. After 2 days at room temperature, take about 20 g of apple flesh and mix it with

50 ml of acetonitrile, shake for 20 minutes, then filter out the insoluble fraction. Then, take 30  $\mu\text{L}$  of filtered apple juice, and add to 1 mL of DZ-QD detection solution. In the figure, it is clearly seen the two samples with different amounts of CP give different fluorescence intensities; from which CP residues of 5.5 and 33 ppb were calculated, respectively [48]. These values are very small, close to those analysed by chromatography, indicating the high sensitivity of the fluorescent labelling method, with the advantage of simplicity and convenience.

The immunosorbent assay is an alternative method widely used for the detection of OPs, with high sensitivity and efficiency. However, the antibodies have low stability and short lifetime and high cost. Attempts have been made to design and synthesise artificial antibodies as replacements for natural antibodies. The molecularly imprinted polymers as antibodies possess good rigidity and stability, and high specific recognition ability is used to detect trichlorfon, a phosphonic ester belonging to the OPs family, with CdSe/ZnS QDs as the marker. The hydrophilic imprinted film was synthesised directly on the surface of a 96-well plate. The method exhibits high stability, selectivity and sensitivity showing the LOD and sensitivity of the biomimetic immunosorbent assay of 9.0  $\mu\text{g/L}$  and 5.0 mg/L (0.1 mg/kg and 62.5 mg/kg for vegetable samples), respectively. The method was applied for the detection of trichlorfon residues in leek and cucumber samples, and results correlated well with those obtained using standard gas chromatography [49].

Another kind of pesticide is thiram a type of sulphur fungicide which has drawn considerable attention in agriculture, environment and food safety in recent years. An effective method for the detection of thiram is proposed using Mn-doped ZnS QDs (ZnS:Mn<sup>2+</sup> QDs) combined by an affinity reaction between thiram and Ag<sup>+</sup> ions. As-prepared ZnS:Mn<sup>2+</sup> QDs fluoresce strongly at 590 nm characteristic of the electronic transitions in Mn<sup>2+</sup> ions. A commercial UV-LED can be effectively used as an excitation light. The Mn-originated fluorescence can be effectively quenched by Ag<sup>+</sup> ions due to the direct cation-exchange reaction at the surface of QDs. In the presence of thiram, the formation of a stable Ag-thiram complex can inhibit fluorescence quenching, resulting in a recovery of the 590-nm emission intensity. This relationship is used to determine the amount of thiram. In buffer condition, thiram could be detected within the concentration range of 50 nM to 2.5  $\mu\text{M}$  with the LOD of 25 nM. Moreover, the proposed method has been successfully applied to thiram residue identification at fresh fruit peels, providing an instant and visual detection of surface residues using QDs [50].

Recently, in some markets, melamine was added into milk, infant formulas and animal feed to give a false measure of the milk's high protein due to its 66% nitrogen content. This of course makes troubles the consumers' health and distorts the market for milk production and consumption. Melamine (1,3,5-triazine-2,4,6-triamine), a trimer of cyanamide (CH<sub>2</sub>N<sub>2</sub>), is toxic with a safety limit of 2.5 ppm in the United States and European Union, 1 ppm for infant formula in China. Therefore, the detection of melamine in milk products and animal feeds has become very important to public health. An efficient and enhanced fluorescence energy transfer system between CdTe QDs entrapped into the mesoporous silica shell (CdTe@SiO<sub>2</sub>) as donors and AuNPs as acceptors have been proposed to detect melamine

[51]. At pH 6.50, CdTe@SiO<sub>2</sub> and AuNPs coalesce together to form larger clusters, giving rise to the fluorescence quenching of CdTe@SiO<sub>2</sub> as a result of energy transfer, provides an “off-state” of the sensitive “turn-on” assay. Upon addition of melamine, because of the strong interactions between the amino group of melamine and the AuNPs via covalent bond that release AuNPs from the surfaces of CdTe@SiO<sub>2</sub> to turn on the fluorescence of CdTe@SiO<sub>2</sub> QDs. Under the optimal conditions, the fluorescence enhanced efficiency shows a linear function against the melamine concentrations ranging from  $7.5 \times 10^{-9}$  to  $3.5 \times 10^{-7}$  M (i.e. 1.0<sup>-44</sup> ppb). Moreover, the proposed method was successfully applied to the determination of melamine in real samples with excellent recoveries in the range from 97.4 to 104.1% [51]. Similarly, another study has reported the use of TGA-capped CdTe QDs of different sizes to determine melamine by the quenching of the fluorescence of TGA-CdTe QDs in an aqueous solution. Under optimum conditions, the fluorescence intensity of TGA-CdTe QDs versus melamine concentrations shows a linear response according to the Stern–Volmer equation. The proposed method has been successfully used to detect melamine in liquid milk with the LOD of 0.04 mg/L for the whole process including sample pre-treatment within 30 min. The obvious merits provided by this method, such as simplicity, rapidity, low cost and high sensitivity would make it promising for on-site screening of melamine adulterants in milk products [52].

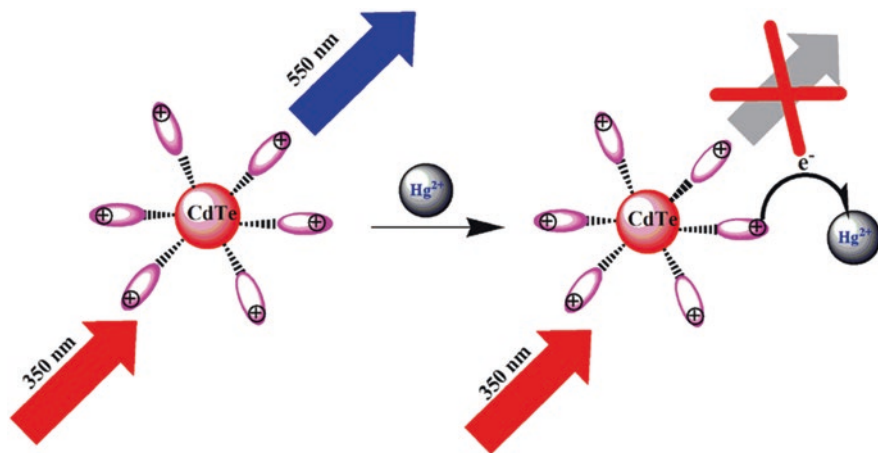
Foods contaminated with different bacteria may cause different diseases to affect differently to human health. The traditional methods for detecting foodborne pathogens are time-consuming (on the order of days). Rapid screening of bacteria-contaminated foods is therefore the key to preventing and controlling the outbreaks of foodborne diseases. It is also needed to develop a portable and low-cost technology to make on-site detection of pathogenic species. Among common foodborne pathogenic bacteria, *E. coli* O157:H7 is well known to be an important opportunistic pathogen to human, and often causes a variety of intestinal infections. Li Xue et al. have developed a novel FBS for ultrasensitive and rapid detection of *E. coli* O157:H7 [53]. The specificity of this proposed FBS is mainly dependent on the monoclonal antibody (MAb) and the polyclonal antibodies (PAb) against the *E. coli* O157:H7 cells that make the FBS selective. The proposed FBS uses the double-layer channel with the immune magnetic nanoparticles (MNPs) for specific separation and efficient concentration of the target bacteria, the immune CdSe/ZnS QDs, and a portable spectrometer for quantitative detection of the bacteria. First, the bacteria are captured by the immune MNPs in the channel in the presence of the high gradient magnetic fields to form the MNP-bacteria complexes to contribute to the increase of the sensitivity. Then, the immune QDs are used to react with the target bacteria to form the MNP-bacteria-QDs complexes in the channel. Finally, the enriched complexes are collected and detected using the portable spectrometer to take the fluorescence spectra relative to the *E. coli* O157:H7 cells in the sample. In a real measurement, 20  $\mu$ L of the streptavidin-modified red-emitting CdSe/ZnS QDs (used as fluorescent indicator) were mixed with 20  $\mu$ L of biotinylated PABs (0.4 ~ 0.5 mg/mL) against *E. coli* O157:H7 and 160  $\mu$ L of phosphate-buffered saline (PBS, pH 7.4) solution and incubated using a rotating mixer at 15 rpm for 30 min at room temperature to form the immune QDs. The proposed biosensor could detect as

low as 14 cells of *E. coli* O157:H7 within 2 h. To evaluate the applicability of this FBS for real sample, different concentrations of *E. coli* O157:H7 cells ranging from  $10^1$  CFU/mL to  $10^5$  CFU/mL were artificially added into the diluted milk to prepare the spiked milk sample. The recovery of *E. coli* in the spiked milk samples ranged from 95.92% to 108.15%, indicating that it can detect *E. coli* in real samples. The proposed FBS might be extended for the detection of other foodborne pathogens or biological targets by changing the antibodies and could be further studied for multiplex detection and high-throughput detection. Another convenient and useful FBS was designed using MPA-capped ZnSe/ZnS QDs and established a rapid fluorescence method to detect *E. coli* cells. Fluorescence microscopy was used to obtain fluorescence microscope images of MPA-capped ZnSe/ZnS QDs that bind to bacteria. The fluorescence peak intensity increases with increasing cells to detect total *E. coli* in the range of  $10^1$ – $10^8$  CFU/mL, with a LOD of 10 CFU/mL [54].

## 18.5 Fluorescent Sensors for Detecting Heavy Metals in Environmental Samples

Heavy metal ions are among environmental pollutants that are long-term toxic for health if accumulated enough in the human body. Suitable FBSs are needed to detect such heavy metal ions in environmental samples. For this kind of work, it is still mainly based on the analyte with ligands that are selective for the metal ion to be recognized, but the selectivity mechanism is unknown, so it is often tested with many different types of metal ions to confirm the selectivity. However, it must be seen that the test is not exhaustive anyway with all metals and other agents that can decrease/increase the fluorescence of QDs, so substantive selectivity remains unconfirmed. Among heavy metals, Hg is highly harmful even at low content. In the following, typical FBSs for the detection of Hg ions in the environmental samples are presented to demonstrate the applicable analytical methods. The working principle is based on the change of the fluorescence intensity from QDs in FBSs in correlation with the presence of  $\text{Hg}^{2+}$  ions. As having many advantages, CdTe QDs synthesised in water again exhibit to be very good materials for designing such FBSs.

Cysteamine-capped CdTe QDs (CA–CdTe QDs) are used to fabricate the FBS to detect  $\text{Hg}^{2+}$  ions. The working principle of this FBS is based on the selective quenching of the fluorescence from CA–CdTe QDs by  $\text{Hg}^{2+}$  ions that originate from the photogenerated electron attraction of  $\text{Hg}^{2+}$  ions. This implies that the fluorescence quenching mechanism may happen by effective electron transfer from the amide groups of CA to the  $\text{Hg}^{2+}$  ion due to strong affinity of mercury for nitrogen atoms as illustrated in Fig. 18.12. The fluorescence measurement is performed in the acetic–acetate buffer solution at pH 5.0.60  $\mu\text{L}$  of 0.01 mol/L CA–CdTe QDs, 70  $\mu\text{L}$  of 10.0 mmol/L acetic–acetate buffer and an appropriate amount of  $\text{Hg}^{2+}$  stock solution are sequentially added to give the desired concentrations. The mixture was diluted with pure deionized water to a final volume of 3.00 mL and then incubated at room temperature for 5 min to get a sufficient reaction between  $\text{Hg}^{2+}$  ions and CA–CdTe



**Fig. 18.12** Schematic illustration for an FBS based on cysteamine-capped CdTe QDs (CA–CdTe QDs) for detection of  $\text{Hg}^{2+}$  ions. Fluorescence from CA–CdTe QDs is selectively quenched by  $\text{Hg}^{2+}$  ions due to the electron attraction of  $\text{Hg}^{2+}$  ions which have a strong affinity for nitrogen atoms of cysteamine. (Adapted with permission from Ref. [55]. Copyright 2014: Wiley-VCH Verlag GmbH & Co.)

QDs to reaching equilibrium. The fluorescence spectra of CA–CdTe QDs are narrow, peaking at about 550 nm under the 350 nm light excitation. The fluorescence quenching effect of CA–CdTe QDs is linear at the  $\text{Hg}^{2+}$  concentrations in the range of 6.0–450 nmol/L, with the LOD of 4.0 nmol/L. To estimate the selectivity to the detection of  $\text{Hg}^{2+}$  ions, the fluorescence of CA–CdTe QDs in 80 nmol/L  $\text{Hg}^{2+}$  and 10-fold concentrations of other metal ions (Pb, Cu, Ag, Co, Ni, Mn, Fe, Mg, Zn, Al, Ca and Na) are measured showing that even with a 10-fold addition of other metal ions, the quenching effect on the fluorescence from CA–CdTe QDs caused by them is just less than 7%, much smaller than that caused by  $\text{Hg}^{2+}$  ions [55]. Similar work has been reported on the TGA or L-cysteine capped CdTe QDs emitting at about 550 nm that are used to fabricate FBSs for detecting  $\text{Hg}^{2+}$  ions in very low concentration in the range of nM or pM depending on the type of capping agents. These concentrations are calibrated based on the quenching of fluorescence intensity from CdTe QDs in FBSs. For quenching the fluorescence in FBSs, different possible mechanisms are proposed including cation exchange, competition of ligands, electron transfer, binding with surface ligands and inner filter effect. In the case of TGA-capped CdTe QDs, the fluorescence is sensitive to the surface states via surface charges. Thus,  $\text{Hg}^{2+}$  ions make quenching the fluorescence of the CdTe QDs through the release of photogenerated electrons from the surface of the TGA-capped CdTe QDs due to interacting with  $\text{Hg}^{2+}$  ions. For fluorescence measurement, typically 2 mL of CdTe QDs solution is prepared in a 5-mL flask, and then various amounts of freshly prepared  $\text{Hg}^{2+}$  ions solution are sequentially added. The mixture is diluted with ultrapure water and is incubated under darkness for 20 min at room temperature. The fluorescence spectra of the mixture are taken in the range from 470 to 700 nm with the 450-nm excitation using a spectrometer. For estimating the

selectivity, the  $\text{Hg}^{2+}$  solution is replaced by solutions containing different ions  $\text{Zn}^{2+}$ ,  $\text{Se}^{2+}$ ,  $\text{Cu}^{2+}$ ,  $\text{Cd}^{2+}$ ,  $\text{Al}^{3+}$ ,  $\text{Fe}^{3+}$  or  $\text{Pb}^{2+}$  with the same concentration. For FBS using TGA-capped CdTe QDs,  $\text{Hg}^{2+}$  ions quench the QDs' fluorescence linearly with the  $\text{Hg}^{2+}$  concentrations in the range from 1.25 to 10 nM. While for the one using L-cysteine-capped CdTe QDs, it shows the linearity and sensitivity of  $6 \times 10^9 \text{ M}^{-1}$  with the LOD of 2.7 pM in the range from 5 to 25 pM. There are two possible interaction modes between L-cysteine capped CdTe QDs and  $\text{Hg}^{2+}$  ions: at relatively low  $\text{Hg}^{2+}$  ions concentration, the  $\text{Hg}^{2+}$  ions interact with the carboxylate moiety of L-cysteine on the surface of CdTe QDs by electrostatic forces; however, at high  $\text{Hg}^{2+}$  ions concentration,  $\text{Hg}^{2+}$  ions interact with CdTe QDs by forming an alloy of  $\text{Cd}_x\text{Hg}_{1-x}\text{Te}$  QDs. A weak signal response was noted upon the addition of other metal ions indicating the good selectivity of these CdTe QDs-based FBSs for detection of  $\text{Hg}^{2+}$  ions [56].

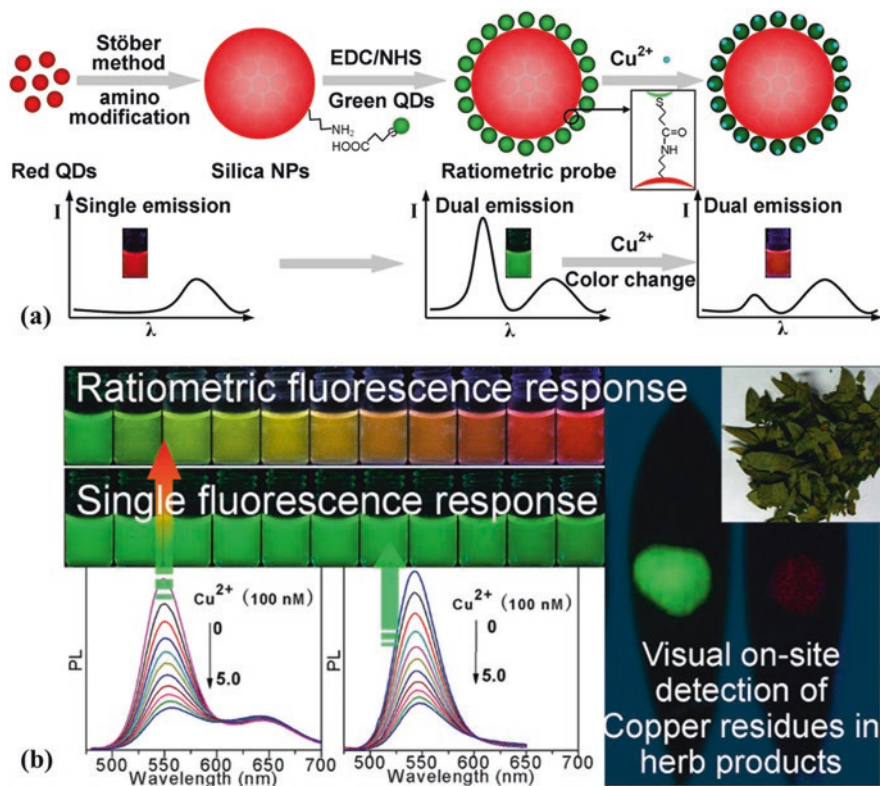
Using biocompatible CdSe/CdS core/shell QDs, one can design and fabricate FBSs highly sensitive FBS for detecting  $\text{Hg}^{2+}$  ions. This FBS is integrated into the use of QDs and liposome carrier signal amplification to boost the signal response and improve the detection capability. To construct this FBS, three single-stranded DNA probes are designed based on the thymine– $\text{Hg}^{2+}$ –thymine (T– $\text{Hg}^{2+}$ –T) coordination chemical principles that adequately reduce the ambient interference to avoid the false results, and take advantage of the biocompatibility of the biosynthetic QDs.  $\text{Hg}^{2+}$  could be determined in the range from 0.25 to 100 nM with a LOD of 0.01 nM, which met the requirements of environmental sample detection. This FBS also exhibits the high selectivity for  $\text{Hg}^{2+}$  detection in the presence of other high-level metal ions, as tested by using samples containing  $\text{Fe}^{3+}$ ,  $\text{Al}^{3+}$ ,  $\text{Zn}^{2+}$ ,  $\text{Pb}^{2+}$ ,  $\text{Ni}^{2+}$ ,  $\text{Mn}^{2+}$ ,  $\text{Mg}^{2+}$ ,  $\text{Cu}^{2+}$ ,  $\text{Cr}^{2+}$ ,  $\text{Co}^{2+}$ ,  $\text{Cd}^{2+}$ ,  $\text{Ca}^{2+}$ ,  $\text{Ba}^{2+}$  and  $\text{K}^+$  at a concentration of 500 nM [57].

Another strategy to determine  $\text{Hg}^{2+}$  ions is the ratiometric fluorescence measurement, in which red-emitting CdTe QDs embedded in  $\text{SiO}_2$  nanoparticles are used as the fluorescence reference, while blue-emitting carbon dots (CDs) distributed on the surface of the  $\text{SiO}_2$  nanoparticles play the role of fluorescence probes. Both CdTe QDs and CDs strongly luminesce under the 365-nm light excitation. The CdTe QDs are fully wrapped by the silica shell which can improve the optical stability and also prevents direct contact of QDs with external  $\text{Hg}^{2+}$  ions to be the reliable reference signal in the ratiometric measurement. While the blue-emitting CDs are very sensitive to  $\text{Hg}^{2+}$  exhibiting continuous colour change from light purple to red with increasing concentrations of  $\text{Hg}^{2+}$  ions. This ratiometric FBS demonstrates the high sensitivity to  $\text{Hg}^{2+}$  ions with an LOD of 0.47 nM, much lower than the allowable level of mercury (10 nM,  $\sim 10$  ppb) in drinking water set by the US Environmental Protection Agency. To examine the selectivity of the ratiometric FBS for  $\text{Hg}^{2+}$  ions, the effects of different metal ions including  $\text{Na}^+$ ,  $\text{K}^+$ ,  $\text{Li}^+$ ,  $\text{Ag}^+$ ,  $\text{Cd}^{2+}$ ,  $\text{Mg}^{2+}$ ,  $\text{Ni}^{2+}$ ,  $\text{Ca}^{2+}$ ,  $\text{Co}^{2+}$ ,  $\text{Cu}^{2+}$ ,  $\text{Ba}^{2+}$ ,  $\text{Al}^{3+}$ ,  $\text{Mn}^{2+}$ ,  $\text{Pb}^{2+}$ ,  $\text{Zn}^{2+}$  and  $\text{Fe}^{3+}$  on the fluorescence intensity ratios are recorded, showing that except  $\text{Fe}^{3+}$  caused slight change of the CDs fluorescence intensity ratio, other 10-fold metal ions do not give tremendous quenching of the ratiometric probe, and same for even 1000-fold concentrations of  $\text{K}^+$ ,  $\text{Na}^+$ ,  $\text{Ca}^{2+}$  and  $\text{Mg}^{2+}$ . This kind of ratiometric FBS can be prepared in filter paper-based assays for



point-of-care pollution control, showing potential applications for rapid and low-cost visual identification of  $\text{Hg}^{2+}$  ions [58].

The ratiometric fluorescence probe using two different coloured fluorescences is advantageous to increase the sensitivity, built-in correction for ambient noises, and to visualising the colour change when detecting analytes by the naked eyes. Therefore, this kind of FBS is attractive for practical applications, especially for on-site analysis. In the ratiometric fluorescence measurement, the red-emitting CdTe QDs (to emit strong luminescence peaking at 650 nm) embedded in  $\text{SiO}_2$  nanoparticles are used as the fluorescence reference, while green-emitting CdTe QDs (550 nm) covalently distributed onto the surface of the  $\text{SiO}_2$  nanoparticles play the role of fluorescence probes. These CdTe QDs are capped with MPA ligands to facilitate the fabrication of the ratiometric FBS, in which MPA ligands act as reaction sites for  $\text{Cu}^{2+}$  ions. MPA-capped green-emitting CdTe QDs are linked on the surface of  $\text{SiO}_2$  nanoparticles via functional 3-aminopropyltriethoxysilane by reacting the end amino groups with the surface carboxylic groups of the MPA. By hybridising dual-emission CdTe QDs on-site visual determination of  $\text{Cu}^{2+}$  ions can be performed. In fact, Cu is an element that is small, very mobile, is one of the important elements for human health, and ranks third in abundance among the essential transition metals in the human body. The working principle of the ratiometric FBSs based on the dual-emission CdTe QDs is shown in Fig. 18.13a, in which the red fluorescence of the embedded CdTe QDs is insensitive to the presence of Cu, meanwhile, the green-emitting QDs on the surface of  $\text{SiO}_2$  nanoparticles are functionalized to be selectively quenched by the  $\text{Cu}^{2+}$  ions. Upon exposure to different amounts of  $\text{Cu}^{2+}$  ions, the variations of the dual emission intensity ratios display continuous colour changes from green to red clearly visible to the naked eye (see Fig. 18.13b). The ratiometric FBS was tested showing a good response to detect  $\text{Cu}^{2+}$  ions in the range 0–500 nM with the LOD for Cu is estimated to be 1.1 nM, much lower than the allowable level of Cu ( $\sim 20 \mu\text{M}$ ) in drinking water set by US Environmental Protection Agency. This ratiometric FBS is simple, easy to use, fully self-contained and thus potentially attractive for visual identification without the need for elaborate equipment. It is quite applicable to determining  $\text{Cu}^{2+}$  ions in lake water and mineral water samples. A special example is the use of this ratiometric FBS in the on-site visual determination of  $\text{Cu}^{2+}$  ions on herb leaves: 10  $\mu\text{L}$  of the ratiometric probe solution is dripped on the surface of a diarrhoea leaf sprayed with  $\text{CuSO}_4$  solution, then observing the fluorescence under a 365-nm light excitation. Note that UV-LEDs are available commercially, cheap and easy to use as a pointer to excite QDs for the fluorescence in this kind of application. The observation of the “off” fluorescence (the last part of Fig. 18.13b) with a leaf treated with  $\text{Cu}^{2+}$  ions shows the nice potential for visual on-site application of this ratiometric FBS. The quantitative amount of  $\text{Cu}^{2+}$  ions on the surface of diarrhoea leaves can be calibrated by using the inductively coupled plasma emission analysis. To evaluate the sensitivity and selectivity of this ratiometric FBS to various metal ions other than Cu, 50  $\mu\text{L}$  of the as-synthesised ratiometric probe solution and a series of selected metal ions ( $\text{Cd}^{2+}$ ,  $\text{Mg}^{2+}$ ,  $\text{Ni}^{2+}$ ,  $\text{K}^+$ ,  $\text{Ca}^{2+}$ ,  $\text{Co}^{2+}$ ,  $\text{Ba}^{2+}$ ,  $\text{Na}^+$ ,  $\text{Pb}^{2+}$  and  $\text{Fe}^{3+}$ ) of the concentration of 0.5  $\mu\text{mol/L}$  are mixed in 2.0 mL of a HEPES buffer (pH 7.4, 10 mM) solution,



**Fig. 18.13** (a) Schematic illustration of the ratiometric probe structure, in which the red fluorescence CdTe QDs embedded in SiO<sub>2</sub> NPs are insensitive to the presence of Cu, meanwhile, the green-emitting QDs on the surface of SiO<sub>2</sub> NPs are functionalized to be selectively quenched by the Cu<sup>2+</sup> ions; (b) the colour change for visual detection of Cu<sup>2+</sup> ions and their corresponding PL spectra in sensing Cu<sup>2+</sup> ions at different concentrations in comparison between single- and ratiometric-fluorescence response. The right half of (b) shows an example of visual on-site detection of Cu<sup>2+</sup> residues on diarrhoea leaves using CdTe QDs-based ratiometric FBS to observe the “off” fluorescence with the leaf treated with Cu<sup>2+</sup> ions. (Reproduced with permission from Ref. [59]. Copyright 2013: American Chemical Society)

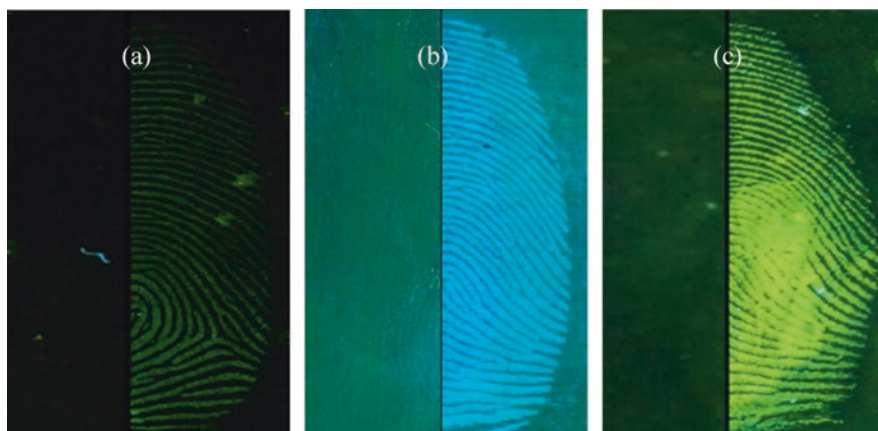
respectively; then observe then change of fluorescence from the mixtures. The results show that 500 nM of the mentioned metals do not quench significantly the green fluorescence for the obvious colour change while adding 250 nM of Cu<sup>2+</sup> ions make quenching the fluorescence of the green-emitting CdTe QDs to change the colour in the ratiometric FBS. This presents the good selectivity of the fabricated ratiometric FBS for visual identification of Cu<sup>2+</sup> ions over other metals [59].

Other heavy metals such as Fe, Pb, Cd, Ag, etc., are detectable by using FBSs fabricated from QDs capped with appropriate ligands [50, 60–62]. The working principles for such FBSs are similar to those presented above. Once FBSs are used, it is clearly advanced that the sample preparation is simple and the detection time is fast, and in most cases can be implemented on-site.

## 18.6 Fluorescent Imaging for Forensic Science and Criminal Investigation

In addition to the FBSs for different applications mentioned in the previous sections, in the following, we present two other applications of QDs in forensic science and criminal investigation, namely the fluorescence enhancement of fingerprint imaging and the detection of TNT explosive traces. Highly luminescence QDs can be easily used for onsite applications with simple protocols that are necessary and convenient for these kinds of applications.

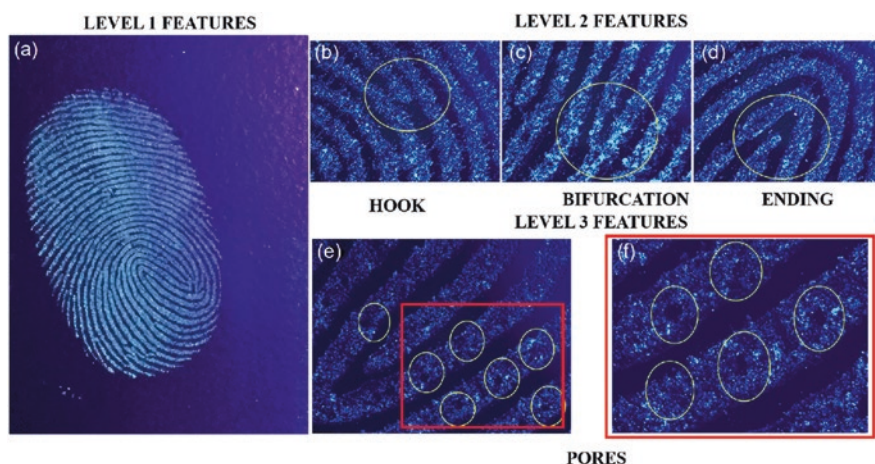
For fluorescence imaging of the fingerprint, the following elements are equally important that needs to be well done. First, QDs have to efficiently bind to the fingerprint using methods that the fluorescence of QDs must be retained as much as possible; second, appropriate photoexcitation is required to make QDs fluorescent only while other materials of the substrate, on which is the fingerprint remains, do not fluoresce to cause any interference to the fluorescence image; third, a sensitive photoapparatus is needed to take the final good images. There have been commonly two main kinds of fingerprint images which are processed with solutions or powders. For the former, Fig. 18.14 illustrates the super-fast detection of latent fingerprints on different surfaces (transparent tape, aluminium and stainless steel) with highly fluorescent water-soluble CdTe QDs and comparisons to those without QDs [63]. The results show very clear that without QDs to give fluorescence one could not take images of the fingerprints in these cases. CdTe synthesised in water are usually capped with TGA or MAA or MPA or MSA to have a carboxyl ( $-\text{COOH}$ ) group on the surface as the binding sites of fingerprint residues. It needs very short time (1–3 s) to immerse the latent fingerprints into the QDs solution to get excellent



**Fig. 18.14** Fluorescent images of fingerprints developed by CdTe QDs on different surfaces: (a) transparent tape, (b) aluminium and (c) stainless steel. In each one, the right half of the fingerprint was processed by fluorescence QDs, while the left half was unprocessed. (Reproduced with permission from Ref. [63]. Copyright 2013: Elsevier Ireland Ltd.)

fingerprint images. Moreover, compared to methyl violet and rhodamine 6G, which are commonly used to develop the latent fingerprints remained on non-porous surfaces, especially on non-porous surfaces with light colours, CdTe QDs have demonstrated the much higher sensitivity and image quality with great details of latent fingerprints. Clear images then can be maintained for months by extending the exposure time of the CCD camera and storing fingerprints in a low-temperature condition, and the digital images can be used for further processing and development.

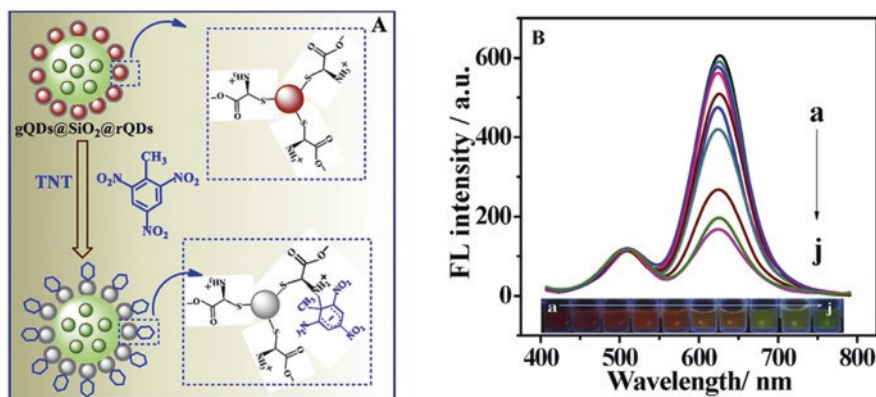
For the latter, as an example using powder brushing technology,  $\text{Fe}_3\text{O}_4@\text{SiO}_2\text{-NH-CO-CdTe-QDs}$  nanoparticles for the visualisation of latent fingerprints are presented in Fig. 18.15. As mentioned above, the powder technique is one of the two most common and widely used methods for identifying latent fingerprints. The basic principle of the powder technique is based on the fact that the inorganic salts and organic grease substances in latent fingerprints have strong adhesion or electrostatic interaction with the powders used for latent fingerprint detection. Currently, the most widely used powders are ninhydrin, aluminium and bronze, which show strong adhesion interaction with fingerprints. However, these powders have an irregular shape and large particle sizes and are easily dispersed in the air when brushing, they, therefore, affect the detection details of latent fingerprint ridges.  $\text{Fe}_3\text{O}_4@\text{SiO}_2\text{-NH}_2$  NPs of 30 nm in size then functionalized with GSH-modified CdTe QDs (of the mean size of about 3 nm) to have the bifunctional  $\text{Fe}_3\text{O}_4@\text{SiO}_2\text{-NH-CO-CdTe-QDs}$  NPs could be easily fabricated in spherical shapes to facilitate the brushing. In most cases, the fingerprint ridge details on the selected object surfaces could be well defined with high fluorescence and low background interference [64], showing much better resolution and less background interference than using



**Fig. 18.15** Fluorescence visualisation of a latent fingerprint on a glass slide using  $\text{Fe}_3\text{O}_4@\text{SiO}_2\text{-NH-CO-CdTe-QDs}$  NPs powder: (a) level 1 features and magnified images of (a) under a fluorescence microscope to detail at (b–d) level 2 and (e, f) level 3 features. (Reproduced with permission from Ref. [64]. Copyright 2019: Springer Science Business Media B.V)

commercial fluorescent powder and brushing silver powder. High resolution for both level 2 and level 3 details would be really useful in forensic applications.

For the detection of trace explosives for homeland security and environmental concerns, some important factors need to pay attention. First, how to conjugate or to make complex of QDs with 2,4,6-trinitrotoluene TNT explosives; second, using a suitable spectrometer to detect the signal and do further processing. Amino ligand-modified  $Mn^{2+}$ -doped ZnS QDs have been used to detect TNT with a LOD of 50 nM [65]. Figure 18.16 demonstrates the detection of trace explosives [66]. A new strategy for increasing the detection sensitivity is based on the ratiometric fluorescence measurement using two kinds of CdTe QDs. One is MPA-capped green-emitting CdTe QDs (gQDs) embedded into the  $SiO_2$  sphere and the other is L-cysteine (Lcys)-capped red-emitting CdTe QDs (rQDs) conjugated onto  $SiO_2$  surface. The surface Lcys is used as the stabilizer of the rQDs and also the primary amine provider which can react with TNT to form Meisenheimer complexes. The fluorescence of rQDs capped with Lcys is selectively quenched by TNT because electrons of the rQDs are transferred to TNT molecules due to the formation of Meisenheimer complexes. Meanwhile, the fluorescence from embedded gQDs always remained constant and is used as a reference. With increasing the TNT amounts, the fluorescence from rQDs is quenched correspondingly and is compared to that from the gQDs. The dual emission intensity ratios exhibited a good linear correlation with the TNT concentration over the range of 10 nM–8  $\mu$ M with a LOD of 3.3 nM. Because



**Fig. 18.16** (a) Detection of trace TNT explosive using ratiometric fluorescence from MPA-capped green-emitting CdTe QDs (gQDs) embedded into  $SiO_2$  nanosphere and from L-cysteine-capped red-emitting CdTe QDs (rQDs) conjugated onto the  $SiO_2$  nanosphere surface. The gQDs give the reference red fluorescence that is not influenced by TNT explosive, meanwhile, the rQDs having L-cysteine to react with TNT to form Meisenheimer complexes which selectively quench the red fluorescence from rQDs; (b) normalised to the gQDs fluorescence intensity, the rQDs fluorescence intensity is decreased with increasing concentrations of TNT (the bottom inset for a to j: 0, 10, 50, 100, 500, 1200, 2100, 5000, 8000 and 16,000 nM, respectively). As the TNT concentration increased, the red fluorescence is correspondingly quenched to make the ratio of green-to-red fluorescence increase to show more green colour that enables to perform on-site visual determination of TNT. (Reproduced with permission from Ref. [66]. Copyright 2016: Elsevier B.V)

of the ratiometric fluorescence in the two colours, the system can obviously change the fluorescence colour enabling to perform onsite visual determination of TNT with high resolution. This sensing strategy has been already integrated into a filter paper-based assay to successfully apply in real samples showing potential applications with featuring easy handling and cost-effectiveness [66].

## 18.7 Conclusions

In conclusion, we have remarked that the FBSs based on II–VI QDs possess unique advantages such as easy fabrication, high fluorescence efficiency in the whole visible-IR spectral region and large Stokes shift, particularly when they are in the type II quantum structure that has long fluorescence lifetime for fluorescence imaging out from the autofluorescence noise. Among the II–VI QDs, CdTe-based ones have appeared to have more promising applications because of their advantageous characteristics such as being easily synthesised in water or in organic solvent, not needing any ligand exchange for most applications, being of high quality suitable for many orientably designed applications. II–VI QDs should be intensively used in FBSs, especially in applications that do not put directly them inside the human body in case such QDs are based on Cd to avoid toxicity. Numerous examples from literature have been cited to provide the overview of applications of FBSs in different fields, for the detection of: (i) viruses, mycotoxins, pathogens, specific proteins, enzymes, nucleic acids, cellular, in vivo targeting imaging for diagnostics, disease treatments and health care; (ii) residues of pesticides/herbicides, the growth-promoting hormone in agricultural productions; (iii) banned/toxic residuals, bacteria-contaminated in foods, drinking water, agricultural products for food safety; (iv) heavy metals in environmental samples and (v) latent fingerprints and TNT explosive trace for criminal, forensic and security investigations. It is important to note that with the development of technologies in the fourth industrial revolution, particularly the internet of things in human life and production, FBSs would play an integral role in many future technologies. It is also noted that there is potential for further investigations of QDs in multiplex detection, particularly via continued miniaturisation and integration into lab-on-chip platforms.

**Acknowledgement** The authors would like to express their sincere gratitude to Academician Nguyen Van Hieu for his continuous encouragement on the topic and kindly acknowledge the supports from Vietnam Academy of Science and Technology (codes NVCC04.01/22-23 and CSCL04.01/22-23).

## References

1. Sapsford KE, Pons T, Medintz IL, Mattoussi H. Biosensing with luminescent semiconductor quantum dots. *Sensors*. 2006;6:925–53. <https://doi.org/10.3390/s6080925>.

2. Lia J, Zhu J-J. Quantum dots for fluorescent biosensing and bio-imaging applications. *Analyst*. 2013;138:2506–15. <https://doi.org/10.1039/c3an36705c>.
3. Ma F, Li C-c, Zhang C-y. Development of quantum dot-based biosensors: principles and applications. *J Mater Chem B*. 2018;6:6173–90. <https://doi.org/10.1039/C8TB01869C>.
4. Lesiak A, Drzozga K, Cabaj J, Bański M, Malecha K, Podhorodecki A. Optical sensors based on II-VI quantum dots. *Nanomaterials*. 2019;9:192. (24 pages). <https://doi.org/10.3390/nano9020192>.
5. Şahin S, Ünlü C, Trabzon L. Affinity biosensors developed with quantum dots in microfluidic systems. *Emerg Mater*. 2021;4:187–209. <https://doi.org/10.1007/s42247-021-00195-5>.
6. Rogatch A. Semiconductor nanocrystal quantum dots. Springer-Verlag/Wien; 2008, ISBN: 978-3-211-75235-7.
7. Liem NQ. CdSe, CdTe, InP and CuInS<sub>2</sub> semiconductor quantum dots: synthesis, optical properties and applications. Publishing House for Science and Technology, VAST; ISBN: 978-604-913-029-8 (in Vietnamese).
8. McConnell EM, Nguyen J, Li Y. Aptamer-based biosensors for environmental monitoring. *Front Chem*. 2020;8:434. <https://doi.org/10.3389/fchem.2020.00434>.
9. Bea Murray C, Norris DJ, Bawendi MG. Synthesis and characterization of nearly monodisperse CdE (E = sulfur, selenium, tellurium) semiconductor nanocrystallites. *J Am Chem Soc*. 1993;115:8706–15. <https://doi.org/10.1021/ja00072a025>.
10. Bruchez M Jr, Moronne M, Gin P, Shimon W, Alivisatos AP. Semiconductor nanocrystals as fluorescent biological labels. *Science*. 1998;281:2013–6. <https://doi.org/10.1126/science.281.5385.2013>.
11. Chan WC, Nie S. Quantum dot bBioconjugates for ultrasensitive nonisotopic detection. *Science*. 1998;281:2016–8. <https://doi.org/10.1126/science.281.5385.2016>.
12. Gaponik N, Talapin DV, Rogach AL, Hoppe K, Shevchenko EV, Kornowski A, Eychmüller A, Weller H. Thiol-capping of CdTe nanocrystals: an alternative to organometallic synthetic routes. *J Phys Chem B*. 2002;106:7177–85. <https://doi.org/10.1021/jp025541k>.
13. Thuy UTD, Tu LA, Loan NT, Chi TTK, Liem NQ. Comparative photoluminescence properties of type-I and type-II CdTe/CdS core/shell quantum dots. *Opt Mater*. 2016;53:34–8. <https://doi.org/10.1016/j.optmat.2016.01.022>.
14. Nguyen TH, Ung TDT, Vu TH, Tran TKC, Dong VQ, Dinh DK, Nguyen QL. Fluorescence biosensor based on CdTe quantum dots for specific detection of H5N1 avian influenza virus. *Adv Nat Sci*. 2012;3:035014. (5pp). <https://doi.org/10.1088/2043-6262/3/3/035014>.
15. Hamidi SV, Ghourchian H, Tavoosidana G. Real-time detection of H5N1 influenza virus through hyperbranched rolling circle amplification. *Analyst*. 2015;140:1502–9. <https://doi.org/10.1039/C4AN01954G>.
16. Wu F, Yuan H, Zhou CH, Mao M, Liu Q, Shen HB, Cen Y, Qin ZF, Ma L, Li LS. Multiplexed detection of influenza A virus subtype H5 and H9 via quantum dot-based immunoassay. *Biosens Bioelectron*. 2016;77:464–70. <https://doi.org/10.1016/j.bios.2015.10.002>.
17. Zhang Y, Fei M, Duan Y, Li Q, Pan Y, Hongfang D, He P, Shen X, Luo Z, Zhu C, Wang L. Label-free analysis of H5N1 virus based on three-segment branched DNA-templated fluorescent silver nanoclusters. *ACS Appl Mater Interfaces*. 2020;12(43):48357–62. <https://doi.org/10.1021/acsami.0c14509>.
18. Babamiri B, Hallaj R, Salimi A. Solid surface fluorescence immunosensor for ultrasensitive detection of hepatitis B virus surface antigen using PAMAM/CdTe@CdS QDs nanoclusters. *Methods Appl Fluoresc*. 2018;6:035013. <https://doi.org/10.1088/2050-6120/aac8f7>.
19. Boeneman K, Mei BC, Dennis AM, Bao G, Deschamps JR, Mattooussi H, Medintz IL. Sensing Caspase 3 activity with quantum dot-fluorescent protein assemblies. *J Am Chem Soc*. 2009;131:3828–9. <https://doi.org/10.1021/ja809721j>.
20. Lv Y, Wu R, Feng K, Li J, Mao Q, Yuan H, Shen H, Chai X, Li LS. Highly sensitive and accurate detection of C-reactive protein by CdSe/ZnS quantum dot-based fluorescence-linked immunosorbent assay. *J Nanobiotechnol*. 2017;15:35. <https://doi.org/10.1186/s12951-017-0267-4>.

21. Liu Z, Liu S, Wang X, Li P, He Y. A novel quantum dots-based OFF–ON fluorescent biosensor for highly selective and sensitive detection of double-strand DNA. *Sens Actuators B*. 2013;176:1147–53. <https://doi.org/10.1016/j.snb.2012.10.085>.
22. Moullick A, Milosavljevic V, Vlachova J, Podgajny R, Hynek D, Kopel P, Adam V. Using CdTe/ZnSe core/shell quantum dots to detect DNA and damage to DNA. *Int J Nanomed*. 2017;12:1277–91. <https://doi.org/10.2147/IJN.S121840>.
23. Wang X, Liu Z, Gao P, Li Y, Qu X. Quantum dots mediated fluorescent “turn-off-on” sensor for highly sensitive and selective sensing of protein. *Colloids Surfaces B*. 2020;185:110599. <https://doi.org/10.1016/j.colsurfb.2019.110599>.
24. Ebrahim S, Reda M, Hussien A, Zayed D. CdTe quantum dots as a novel biosensor for *Serratia marcescens* and Lipopolysaccharide. *Biomol Spectrosc*. 2015;150:212–9. <https://doi.org/10.1016/j.saa.2015.05.042>.
25. Xue Y, Thalmayer AS, Zeising S, Fischer G, Lübke M. Commercial and scientific solutions for blood glucose monitoring—a review. *Sensors*. 2022;22:425. <https://doi.org/10.3390/s22020425>.
26. Duong HD, Sohn O-J, Rhee JI. Development of a ratiometric fluorescent glucose sensor using an oxygen-sensing membrane immobilized with glucose oxidase for the detection of glucose in tears. *Biosensors*. 2020;10:86. <https://doi.org/10.3390/bios10080086>.
27. Chen G, Hu Q, Shu H, Lu W, Cui X, Han J, Bashir K, Luo Z, Chang C, Fu Q. Fluorescent biosensor based on magnetic cross-linking enzyme aggregates/CdTe quantum dots for the detection of H<sub>2</sub>O<sub>2</sub>-bioprecursors. *New J Chem*. 2020;44:17984–92. <https://doi.org/10.1039/d0nj03761c>.
28. Hu M, Tian J, Lu H-T, Weng L-X, Wang L-H. H<sub>2</sub>O<sub>2</sub>-sensitive quantum dots for the label-free detection of glucose. *Talanta*. 2010;82:997–1002. <https://doi.org/10.1016/j.talanta.2010.06.005>.
29. Cao L, Ye J, Tong L, Tang B. A new route to the considerable enhancement of glucose oxidase (GOx) activity: the simple assembly of a complex from CdTe quantum dots and GOx and its glucose sensing. *Chem Eur J*. 2008;14:9633–40. <https://doi.org/10.1002/chem.200800681>.
30. Rahman SA, Ariffin N, Yusof NA, Abdullah J, Mohammad F, Zubir ZA, Aziz NMANA. Thiolate-Capped CdSe/ZnS core-shell quantum dots for the sensitive detection of glucose. *Sensors*. 2017;17(7):1537. <https://doi.org/10.3390/s17071537>.
31. Mai HH, Pham VT, Nguyen VT, Sai CD, Hoang CH, Nguyen TB. Non-enzymatic fluorescent biosensor for glucose sensing based on ZnO nanorods. *J Electron Mater*. 2017;46:3714–9. <https://doi.org/10.1007/s11664-017-5300-8>.
32. Miao Y-m, Yang Q, Lv J-z, Yan G-q. A two-dimensional sensing device based on manganese doped zinc sulfide quantum dots for discrimination and identification of common sugars. *New J Chem*. 2017;41:14882–9. <https://doi.org/10.1039/c7nj02169k>.
33. Saran AD, Sadawana MM, Srivastava R, Bellare JR. An optimized quantum dot-ligand system for biosensing applications: Evaluation as a glucose biosensor. *Colloids Surf A*. 2011;384:393–400. <https://doi.org/10.1016/j.colsurfa.2011.04.022>.
34. Yu M, Zhao K, Zhu X, Tang S, Nie Z, Huang Y, Zhao P, Yao S. Development of near-infrared ratiometric fluorescent probe based on cationic conjugated polymer and CdTe/CdS QDs for label-free determination of glucose in human body fluids. *Biosens Bioelectron*. 2017;95:41–7. <https://doi.org/10.1016/j.bios.2017.03.065>.
35. Eleonora P, Russ Algar W, Medintz IL. Quantum dots in bioanalysis: a review of applications across various platforms for fluorescence spectroscopy and imaging. *Appl Spectrosc*. 2013;67:215–52. <https://doi.org/10.1366/12-06948>.
36. Chinnathambi S, Shirahata N. Recent advances on fluorescent biomarkers of near-infrared quantum dots for in vitro and in vivo imaging. *Sci Technol Adv Mater*. 2019;20:337–55. <https://doi.org/10.1080/14686996.2019.1590731>.
37. Xing Y, Chaudry Q, Shen C, Kong KY, Zhau HE, Chung LW, Petros JA, O'Regan RM, Yezhelyev MV, Simons JW, Wang MD, Nie S. Bioconjugated quantum dots for multiplexed and quantitative immunohistochemistry. *Nat Protoc*. 2007;2(5):1152–65. <https://doi.org/10.1038/nprot.2007.107>.



38. He Y, Zhong Y, Yuanyuan S, Lu Y, Jiang Z, Peng F, Xu T, Shao S, Huang Q, Fan C, Lee S-T. Water-dispersed near-infrared-emitting quantum dots of ultra small sizes for in vitro and in vivo imaging. *Angew Chem Int Ed*. 2011;50:5695–8. <https://doi.org/10.1002/anie.2011004398>.
39. Hu D, Zhang P, Gong P, Lian S, Lu Y, Gao D, Cai L. A fast synthesis of near-infrared emitting CdTe/CdSe quantum dots with small hydrodynamic diameter for in vivo imaging probes. *Nanoscale*. 2011;3:4724–32. <https://doi.org/10.1039/C1NR10933B>.
40. Sun X, Huang X, Guo J, Zhu W, Ding Y, Niu G, Wang A, Kiesewetter DO, Wang ZL, Sun S, Chen X. Self-illuminating 64Cu-doped CdSe/ZnS nanocrystals for in vivo tumor imaging. *J Am Chem Soc*. 2014;136:1706–9. <https://doi.org/10.1021/ja410438n>.
41. Nsiband SA, Forbes PBC. Fluorescence detection of pesticides using quantum dot materials – a review. *Anal Chim Acta*. 2016;945:9–22. <https://doi.org/10.1016/j.aca.2016.10.002>.
42. Chauhan N, Narang J, Jain U. Amperometric acetylcholinesterase biosensor for pesticides monitoring utilising iron oxide nanoparticles and poly(indole-5-carboxylic acid). *J Exp Nanosci*. 2016;11:111–22. <https://doi.org/10.1080/17458080.2015.1030712>.
43. Tran TKC, Vu DC, Ung TDT, Nguyen HY, Nguyen NH, Dao TC, Pham TN, Nguyen QL. Fabrication of fluorescence-based biosensors from functionalized CdSe and CdTe quantum dots for pesticide detection. *Adv Nat Sci*. 2012;3:035008. (4pp). <https://doi.org/10.1088/2043-6262/3/3/035008>.
44. Kanagasubbulakshmi S, Kathiresan R, Kadirvelu K. Structure and physiochemical properties based interaction patterns of organophosphorous pesticides with quantum dots: Experimental and theoretical studies. *Eng Aspects*. 2018;549:155–63. <https://doi.org/10.1016/j.colsurfa.2018.04.007>.
45. Sheng E, Lu Y, Tan Y, Xiao Y, Li Z, Dai Z. A ratiometric fluorescent quantum dot-based biosensor for chlorothalonil detection via an inner-filter effect. *Anal Chem*. 2020;92:4364–70. <https://doi.org/10.1021/acs.analchem.9b05199>.
46. Nguyen DN, Ngo TT, Nguyen QL. Highly sensitive fluorescence resonance energy transfer (FRET)-based nanosensor for rapid detection of clenbuterol. *Adv Nat Sci*. 2012;3:035011. (6pp). <https://doi.org/10.1088/2043-6262/3/3/035011>.
47. Tashkhourian J, Absalan G, Jafari M, Zare S. A rapid and sensitive assay for determination of doxycycline using thioglycolic acid-capped cadmium telluride quantum dots. *Spectrochim Acta Part A*. 2016;152:119–25. <https://doi.org/10.1016/j.saa.2015.07.063>.
48. Zhang K, Mei Q, Guan G, Liu B, Wang S, Zhang Z. Ligand replacement-induced fluorescence switches of quantum dots for ultrasensitive detection of organophosphorothioate pesticides. *Anal Chem*. 2010;82:9579–86. <https://doi.org/10.1021/ac102531z>.
49. Liu Q, Jiang M, Zeliang J, Qiao X, Xu Z. Development of direct competitive biomimetic immunosorbent assay based on quantum dot label for determination of trichlorfon residues in vegetables. *Food Chem*. 2018;250:134–9. <https://doi.org/10.1016/j.foodchem.2017.12.079>.
50. Cheng Z, Zhang K, Zhao T, Liu B, Wang Z, Zhang Z. Selective phosphorescence sensing of pesticide based on the inhibition of silver(I) quenched ZnS:Mn<sup>2+</sup> quantum dots. *Sens Actuators B*. 2017;252:1083–8. <https://doi.org/10.1016/j.snb.2017.06.087>.
51. Gao F, Ye Q, Cui P, Zhang L. Efficient fluorescence energy transfer system between CdTe-Doped silica nanoparticles and gold nanoparticles for turn-on fluorescence detection of melamine. *J Agric Food Chem*. 2012;60:4550–8. <https://doi.org/10.1021/jf300386y>.
52. Zhang M, Ping H, Cao X, Li H, Guan F, Sun C, Liu J. Rapid determination of melamine in milk using watersoluble CdTe quantum dots as fluorescence probes. *Food Addit Contam*. 2012;29:333–44. <https://doi.org/10.1080/19440049.2011.643459>.
53. Xue L, Zheng L, Zhang H, Jin X, Lin J. An ultrasensitive fluorescent biosensor using high gradient magnetic separation and quantum dots for fast detection of foodborne pathogenic bacteria. *Sens Actuators B*. 2018;265:318–25. <https://doi.org/10.1016/j.snb.2018.03.014>.
54. Wu P, Huang R, Li G, He Y, Chen C, Xiao W, Ding P. Optimization of synthesis and modification of ZnSe/ZnS quantum dots for fluorescence detection of *Escherichia coli*. *J Nanosci Nanotechnol*. 2018;18:3654–9. <https://doi.org/10.1166/jnn.2018.14673>.

55. Ding X, Lingbo Q, Yang R, Zhou Y, Li J. A highly selective and simple fluorescent sensor for mercury (II) ion detection based on cysteamine-capped CdTe quantum dots synthesized by the reflux method. *Luminescence*. 2015;30(4):465–71. <https://doi.org/10.1002/bio.2761>.
56. Labeb M, Sakr A-H, Soliman M, Abdel-Fettah TM, Ebrahim S. Effect of capping agent on selectivity and sensitivity of CdTe quantum dots optical sensor for detection of mercury ions. *Opt Mater*. 2018;79:331–5. <https://doi.org/10.1016/j.optmat.2018.03.060>.
57. Zhang Y, Xiao J-Y, Zhu Y, Tian L-J, Wang W-K, Zhu T-T, Li W-W, Han-Qing Y. Fluorescence sensor based on biosynthetic CdSe/CdS quantum dots and liposome carrier signal amplification for mercury detection. *Anal Chem*. 2020;92:3990–7. <https://doi.org/10.1021/acs.analchem.9b05508>.
58. Xu H, Zhang K, Liu Q, Liu Y, Xie M. Visual and fluorescent detection of mercury ions by using a dually emissive ratiometric nanohybrid containing carbon dots and CdTe quantum dots. *Microchim Acta*. 2017;184:1199–206. <https://doi.org/10.1007/s00604-017-2099-1>.
59. Yao J, Zhang K, Zhu H, Ma F, Sun M, Yu H, Sun J, Wang S. Efficient ratiometric fluorescence probe based on dual-emission quantum dots hybrid for on-site determination of copper ions. *Anal Chem*. 2013;85:6461–8. <https://doi.org/10.1021/ac401011r>.
60. Zhou M, Guo J, Yang C. Ratiometric fluorescence sensor for Fe<sup>3+</sup> ions detection based on quantum dot-doped hydrogel optical fiber. *Sensors Actuators B Chem*. 2018;264:52–8. <https://doi.org/10.1016/j.snb.2018.02.119>.
61. Zhou J, Li B, Qi A, Shi Y, Qi J, Xu H, Chen L. ZnSe quantum dot based ion imprinting technology for fluorescence detecting cadmium and lead ions on a three-dimensional rotary paper-based microfluidic chip. *Sens Actuators B*. 2020;305:127462. <https://doi.org/10.1016/j.snb.2019.127462>.
62. Li M, Zhou X, Guo S, Wu N. Detection of lead(II) with a “turn-on” fluorescent biosensor based on energy transfer from CdSe/ZnS quantum dots to graphene oxide. *Biosens Bioelectron*. 2013;43:69–74. <https://doi.org/10.1016/j.bios.2012.11.039>.
63. Cai K, Yang R, Wang Y, Yu X, Liu J. Super fast detection of latent fingerprints with water soluble CdTe quantum dots. *Forensic Sci Int*. 2013;226:240–3. <https://doi.org/10.1016/j.forsciint.2013.01.035>.
64. Wang Z, Xue J, Liu W, Lu G, Huang X. A rapid and operator-safe powder approach for latent fingerprint detection using hydrophilic Fe<sub>3</sub>O<sub>4</sub>@SiO<sub>2</sub>-CdTe nanoparticles. *Sci China Chem*. 2019;62:889–96. <https://doi.org/10.1007/s11426-019-9460-0>.
65. Wang Y, Zou W. 3-Aminopropyltriethoxysilane-functionalized manganese doped ZnS quantum dots for room-temperature phosphorescence sensing ultratrace 2,4,6-trinitrotoluene in aqueous solution. *Talanta*. 2011;85:469–75. <https://doi.org/10.1016/j.talanta.2011.04.014>.
66. Qian J, Hua M, Wang C, Wang K, Liu Q, Hao N, Wang K. Fabrication of l-cysteine-capped CdTe quantum dots based ratiometric fluorescence nanosensor for onsite visual determination of trace TNT explosive. *Anal Chim Acta*. 2016;946:80–7. <https://doi.org/10.1016/j.aca.2016.10.007>.

# Chapter 19

## QDs-Based Chemiluminescence Biosensors



Fahimeh Ghavamipour and Reza H. Sajedi

### 19.1 Introduction

Chemiluminescence (CL) generates light through a chemical reaction that induces the transition of an electron from the ground state to an excited electronic state, and the decay of the excited molecules to the electronic ground state emits photons ranging from ultraviolet and visible to infrared radiation [1]. In the aqueous phase system, CL is mainly produced by reactions with suitable redox conditions and CL reagents. Unstable products generated by intermediate radicals in the CL reaction process decompose to form electronically excited molecules that are inactivated by CL emission [2]. The CL can take place by direct oxidation of the target compound to generate emitting species or by indirect enhancing or inhibitory effects of certain luminescence compounds [3]. The CL generated from the reactions of inorganic molecules is relatively weak due to low quantum yield, therefore, increasing the CL intensity is necessary for analytical applications. Compounds or reaction strategies, including nanomaterials, catalytic process, transition elements, and energy transfer process, have been proposed for an enhanced CL. In this regard, quantum dots [QDs] have attracted a great deal of attention as CL emitters or as a new alternative to catalyse CL redox reactions due to their reactivity, brightness, and continuous bandgap tunability, enhancing the CL emission under proper conditions [4–7]. Because of their good optical and electrical properties, large Stokes shifts, broad excitation spectra, high quantum yield, size-dependent and tunable luminescence, and long-term photostability, QDs have been used in the CL reactions either as a catalyst or as light emitters [8, 9]. High-quality semiconductor nanocrystals exhibit strong luminescence from ultraviolet to near-infrared light with precisely adjustable

---

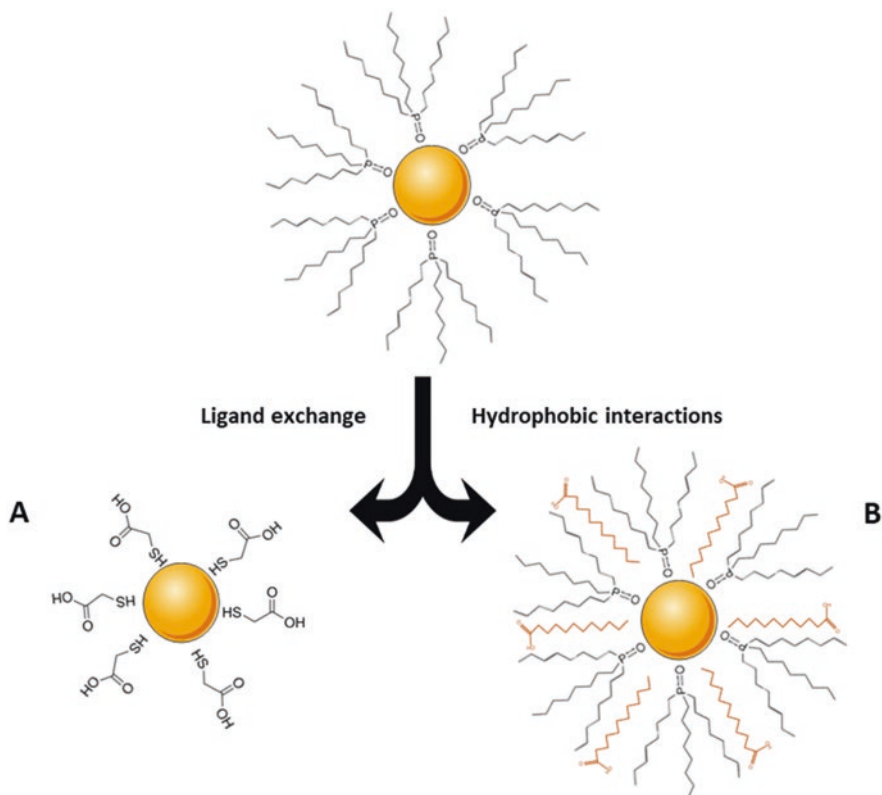
F. Ghavamipour · R. Sajedi (✉)  
Department of Biochemistry, Faculty of Biological Sciences, Tarbiat Modares University,  
Tehran, Iran  
e-mail: [fahimeh.ghavami@modares.ac.ir](mailto:fahimeh.ghavami@modares.ac.ir); [sajedi\\_r@modares.ac.ir](mailto:sajedi_r@modares.ac.ir)

emission bands. These superior emission properties in QDs have attracted much attention for the development of QDs-based nanoprobe for CL analysis [10]. The nanocrystal chemiluminescence can be substantially improved by optimising the nanocrystal composition, capping ligands, and the chemical “fuel” which provides energy for the generation of the excited state. In addition to the academic interest in this phenomenon that is novel for QDs, nanocrystal chemiluminescence might find use in analytical and biomedical applications. Thus, CL analysis, for example, CL labelling and detection of immunoassays, is the most sensitive of any nonradioactive method, allowing attomolar amounts of the target to be detected [11]. In this chapter, an overview of CL of QDs was provided including mechanisms of principle, covering characteristics, advantages and disadvantages, and the applications in biosensors in which they have been put to use.

## 19.2 QDs and Core/Shell QDs

QDs of groups II–VI elements such as CdTe, CdSe, CdS [12], ZnSe [13], CdSe/ZnS [14], etc., are semiconductor crystals at the nanometre scale and are defined as particles with physical dimensions smaller than the exciton Bohr radius. Core/shell QDs are a special class of nanoparticles with unique optical properties including wide absorption, narrow emission, and photo-stability. The specific structure of core/shell QDs elevates their optical properties. Bare QDs are commonly thought to be impractical for biological applications for a variety of reasons. Because QDs are water-insoluble in most synthesis strategies. Therefore, to use their optical properties in the biological system, the surface must be modified by a hydrophilic coating. On the other hand, due to the large surface area to volume ratio, the QDs core is highly reactive and suffers from very strong unspecific interactions with macromolecules, leading to particle aggregation and emission variation. In addition, the surface modification method can greatly reduce the toxicity of QDs. QDs also attract a great deal of attention for the toxicity and biocompatibility during biomedical applications due to their heavy metal composition, small size, and active surface. It has been reported that QDs could induce biological toxicity mainly in the following two ways [15]. One is that the slow oxidation process occurs for bare QDs exposed to UV light and free cadmium ions are released into the environment, causing toxicity to labelled living organisms. Other cases include the formation of reactive oxygen species [ROS] such as free radicals (hydroxyl radical:  $\text{OH}^\bullet$  and superoxide:  $\text{O}_2^{\bullet-}$ ) and singlet oxygen ( $^1\text{O}_2$ ), which are known to cause irreversible damage to nucleic acids, proteins, and cellular components such as mitochondria and both plasma and nuclear membranes. After surface modification, the impermeable coating shell effectively prevents the release of heavy metal ions and detects interaction between the producing ROS and the functional molecules in the biological system, thus, reducing the toxicity of QDs.

Among the various surface modification techniques, two general methods are shown in Fig. 19.1: A surface exchange of hydrophobic surfactants for bifunctional



**Fig. 19.1** An overview of two common strategies used to disperse hydrophobic QDs in an aqueous solution. (a) Ligands surrounding tri-n-octyl phosphine oxide (TOPO)-coated QDs may be replaced with heterobifunctional ligands, like mercaptoacetic acid. (b) Native TOPO ligands on the QDs surface may be retained and used to interact with an amphiphilic polymer. (Adapted with permission from Ref. [16]. Copyright 2004: Elsevier)

linker molecules [17], and B phase-transfer methods using amphiphilic molecules that act as detergents for solubilising the QDs coated with hydrophobic groups [18, 19]. Both methods use a wide variety of molecules that act in similar ways to solubilise QDs and provide functional groups [carboxylic acid, amine, etc.] which are conjugated to biomolecules through well-established protocols.

The synthesis of QDs can be adjusted according to specific requirements, with core, shell, and coating properties that all affect photochemical characteristics. QDs may be made with diameters ranging from a few nanometres to a few micrometres, and size distribution can be controlled within 2% using precise growth techniques, which include high annealing temperatures [20, 21]. The choice of shell and coating is of particular importance, as the shell stabilises the nanocrystal and alters the photophysical properties to some extent, while the coating confers properties to the QDs that allow its integration into the desired applications [21].

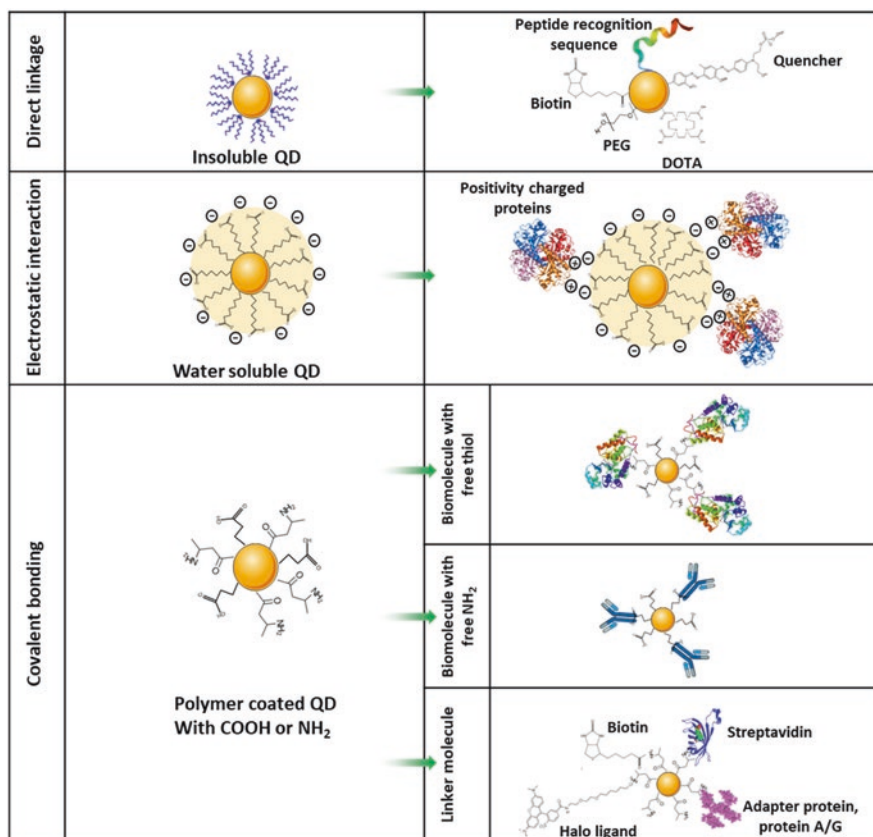
So far, various surface stabilising and coating materials and protocols have been used to obtain monodispersed, bioinert, and highly stable QDs. Among the various surface modification strategies, the ligand exchange method has been extensively studied. One of the simplest ways is the binding of thiolated poly (ethylene glycol) polymers, which produces water solubility and decreases unspecific cellular uptake of QDs [22–24]. Other polymers with different chain lengths and the number of binding dentates, such as dendrimers [25], PEGylated dihydrolipoic acid [26, 27], and multidentate phosphine polymers [28], are also applied to stabilise QDs in an aqueous solution. An alternative method for solubilisation and stabilisation is ligand capping by various amphiphilic polymers such as triblock copolymer and alkyl-modified poly (acrylic acid) [29, 30] and poly (maleic anhydride alt-1-tetradecene) [31] to form highly stable polymeric link or micelle-like structures [19, 32]. Depending on the coating of QDs with polymers, the overall size of the assemblies may increase to 5–10 nm. However, the main advantage of the hydrophobic interaction technique is that ligand exchange reactions are avoidable. Also, the second method has been particularly advantageous in that it allows for the preservation of the native surfactant molecules, which appear to increase stability and efficiency in samples that have been separated from the native layer and replaced with a bifunctional linker molecule. It is worth noting that this approach has already been investigated via small organic molecules instead of polymers. The QDs are in that case coated with cyclodextrins [33, 34] or amphiphilic phospholipids [35, 36], to achieve the same goal. In addition, the silica coating method has been used to adapt QDs to obtain solubilisation and functionalisation to conjugate with bifunctional molecules [37, 38]. By microemulsion or reverse microemulsion strategies, the silica-coated QDs of uniform sizes have been synthesised. The core/shell QDs show good photostability and low cytotoxicity requisite for biological use.

Recently, various methods have been introduced to produce biocompatible QDs with long-term stability including the use of engineered recombinant proteins electrostatically bound to a surface of QDs modified with dihydrolipoic acid, the use of hydrophilic organic dendron ligands to form hydrophilic shells around the QDs, and the use of a micellar encapsulation method in which phospholipid molecules surround the TOPO-coated QDs surface [39–41]. In the latter method, the phospholipid hydrocarbon tails interdigitate with the alkyl chains extending from the particle surface, and the polar phosphate head groups extend out into the solution to form a water-stable micelle [19]. In addition, QDs conjugated to streptavidin via an amphiphilic polymer coating are now commercially available [18].

### 19.3 The Functionalisation of Quantum Dots

To make more useful for biological applications, QDs must be conjugated into biological molecules without interfering with the biological function. Biomolecules including peptides, proteins, and oligonucleotides have been successfully linked to QDs. Several successful methods have been used for the binding of biological molecules to QDs,

including non-specific adsorption, electrostatic interaction, mercapto [-SH] exchange, and covalent bonding (Fig. 19.2) [43]. First, biological molecules containing thiol groups can be conjugated to the surface of QDs through a mercapto exchange process [44]. Unfortunately, since the bond between Zn and thiol is not very strong and is dynamic, biomolecules attached to QDs in this way can be easily separated from the nanoparticle surface and cause QDs to precipitate from the solution. It has also been reported that simple small molecules such as oligonucleotides [45] and serum albumin [46, 47] are readily adsorbed to the surface of water-soluble QDs. This nonspecific adsorption depends on pH, temperature, ionic strength, and surface charge of the molecule. However, due to the complexity of the biological environment, electrostatic interactions are generally not sufficiently specific. Therefore, conjugates made in this way are not suitable for in vivo or ex vivo cell labelling due to the potential interference of positively charged proteins. Covalent bonding of biomolecules to functional groups on QDs surfaces results in more stable bonding using cross-linker molecules (Fig. 19.2)



**Fig. 19.2** General methods used for the biofunctionalisation of QDs, including direct linkage, electrostatic interaction, and covalent bonding. (Data extracted from Ref. [42])

[17, 48, 49]. Most water solubilisation methods cause the QDs to be covered with carboxylic acid, amino, or thiol groups. Under these conditions, it is easy to bind QDs to biological molecules that also have these functional groups. For example, the cross-linker 1-ethyl-3-[3-dimethylaminopropyl] carbodiimide (EDC) is commonly used for cross-linking of  $-\text{NH}_2$  and  $-\text{COOH}$  groups, while 4-[N-maleimidomethyl]-cyclohexane carboxylic acid N-hydroxysuccinimideester (SMCC) can be used for cross-linking of  $-\text{SH}$  and  $-\text{NH}_2$  groups. Using these methods, there have been several reports of conjugating QDs with various biological molecules, including oligonucleotides [50], biotin [48], peptides [51], and proteins such as albumin [46, 52], avidin/streptavidin [18], antibodies, and adaptor proteins [e.g. protein A and protein G] [18, 49]. In addition, native functional groups ( $-\text{COOH}$ ,  $-\text{NH}_2$  or  $-\text{SH}$ ) on the surface of water-soluble QDs can be further converted to other functional groups to allow more versatile conjugation of QDs with biomolecules (site-specific conjugation, molecules that are sensitive to EDC or SMCC modification) (Fig. 19.2). For example, the carboxylic acids on QDs have been converted to hydrazides, which allow the binding of biomolecules containing sugar groups [49]. To date, various affinity reagents for modifying QDs, such as peptides, aptamers, and small molecules, which specifically detect certain biomarkers on cancer cells, have been reported to produce cancer diagnosis probes and target drug delivery vesicles [53, 54].

## 19.4 Chemiluminescence Mechanisms of QDs

Three possible mechanisms can be used to describe the involvement of QDs in a CL reaction: (a) QDs as emitter species after direct oxidation; (b) QDs as reaction catalysts containing other luminophores; and (c) QDs as emitter species after chemiluminescence resonance energy transfer (CRET). The identification of the QDs role in a CL emission could be a challenging task. Indeed, when for example the QDs are the final emitters, it is particularly difficult to determine if the CL generation mechanism is related to the direct QDs oxidation or if a CRET phenomenon has occurred. Sometimes, these two mechanisms may occur simultaneously. Nevertheless, in a broad perspective when QDs are the only luminescent compound in a CL system, it can definitely be presumed as a direct oxidation. However, if an additional luminophore is also included in the reaction scheme, the mechanism can be either CRET, if the final emitters are QDs, or CL catalysed by the QDs, when the final emitter is the luminophore [55, 56].

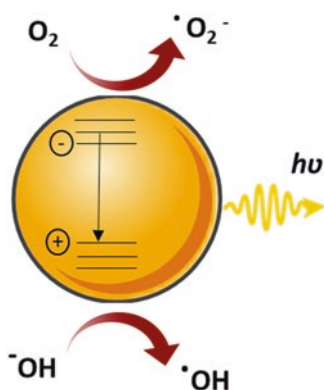
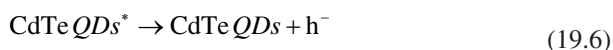
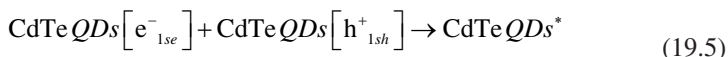
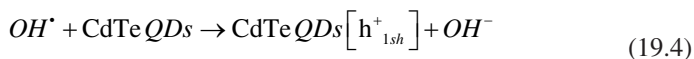
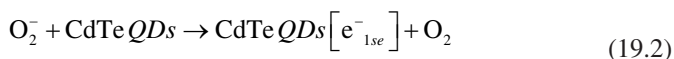
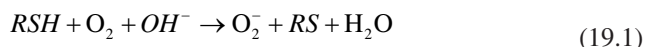
### 19.4.1 Direct Chemiluminescence

This mechanism involves the direct excitation of the QDs which leads to the production of the electron in the conduction band and hole in the valence band due to chemical reaction. Excitons are produced by the recombination of the injected



electrons and holes. Direct QDs CL occurs when chemically produced excitons relax by radiant energy emitting. The intensity of CL depends on the redox reactions that regulate electron-hole transfer as well as on the efficient coupling of these reactions and the QDs. The transition of injected electrons from a higher energy state to a lower energy state leads to CL as shown in Fig. 19.3 [57].

Wang et al. were the first to directly oxidise CdTe TGA-capped nanocrystals in a solution with a corresponding CL emission. They found thioglycolic acid (TGA) coated CdTe QDs could be directly oxidised by oxidants, especially hydrogen peroxide and potassium permanganate. In this work, the evaluation of the effect of the oxidants used in the reaction exhibited that the intensity of the CL produced depends on the nature of the oxidant, as  $\text{H}_2\text{O}_2 > \text{KMnO}_4 > \text{KIO}_4 > \text{Ce}^{4+} > \text{K}_3\text{Fe}[\text{CN}]_6 > [\text{NH}_4]_2\text{S}_2\text{O}_8$  [58]. The proposed mechanism for the CdTe QDs– $\text{H}_2\text{O}_2$  system is presented in Reactions (19.1)–(19.6):



**Fig. 19.3** Schematic representation of the electron-hole transition leading to direct chemiluminescence. (Adapted with permission from Ref. [55]. Copyright 2012: Elsevier)

### 19.4.2 Chemiluminescence Catalysts

QDs can also be utilised as a catalyst in CL systems, due to the redox properties of both the conduction and valence bands. A hole can be injected into the valence band by a strong oxidiser and an electron can be injected into the conduction band by a reducer. During the injection process, short-lived radical species, such as  $O_2^{\cdot-}$  and hydroxyl radicals  $[OH^{\cdot}]$  are produced that can oxidise CL organic dyes, such as luminol, resulting in a CL emission, or act individually as radical. In addition, in the production of oxidising species by photoirradiation of QDs solutions [10], these can be considered as catalysts because they formed exciton itself acts as a redox system, producing radical species (Fig. 19.4). Wang et al. confirmed that the combined utilisation of TAG capped CdTe QDs and luminol in the presence of  $KMnO_4$  has a significant sensitising effect on the CL emission [59]. The enhanced signals are the result of the accelerated luminol CL induced by the oxidised species of CdTe. Qu et al. reported soluble glutathione-capped ZnSe QDs can increase the CL emission from the luminol- $K_3Fe[CN]_6$  system in an alkaline medium, and phenols can inhibit the CL [60]. The enhanced CL originated from the catalysis of ZnSe QDs in the radical generation and electron-transfer process of the luminol CL reaction. Zhao et al. added CdTe QDs into the running buffer of capillary electrophoresis to catalyse the post-column CL reaction between luminol and hydrogen peroxide [61]. CdTe QDs accelerate the electron-transfer process and facilitate the CL radical generation in luminol CL reaction, achieving higher CL emission. Kanwal et al. found that mercaptosuccinic acid-capped CdTe QDs with a diameter of 3.8 nm can significantly increase the CL of the pyrogallol- $H_2O_2$  system [62]. In this system, the exciting product of pyrogallol (purpurogallin) was the main CL emitter. There was no energy transfer from purpurogallin to CdTe QDs, and CdTe QDs only acted as an enhancer in the enhanced CL reaction.

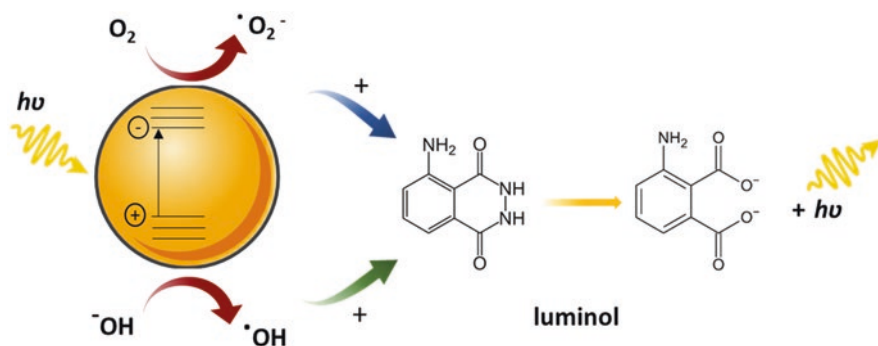


Fig. 19.4 Emission with quantum dots as chemiluminescence catalysts. (Adapted with permission from [55]. Copyright 2012: Elsevier)

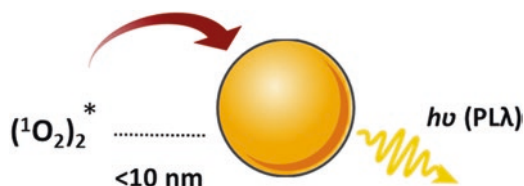
### 19.4.3 Chemiluminescent Energy Acceptor

CRET is the nonradiative process in which energy transfer takes place from a chemiluminescent donor to a fluorophore acceptor, provided that the CL emission spectrum must overlap with the absorption spectrum of fluorescent acceptor. Due to the wide-spectrum range of QDs, they act as excellent the fluorescent acceptors in CRET processes [57] (Fig. 19.5). In CRET, contrary to what was mentioned in the previous section, QDs are the final emitters and not the sensitizers as this evidence is clearly understood when monitoring the emitted spectra. Also, with CRET it is difficult to understand if the QDs excited species are generated by a resonance energy transmission process or by a redox process because there are different reducing and oxidising species in all reactions. Another important point is that in various conditions QDs play a double role in the reaction: acting initially as sensitizers and after that as final emitter, sometimes even co-emitting with a CL organic dye [55].

In CRET, QDs are the final emitters, which can be verified by the emitted spectra. Ren et al. first demonstrated an efficient CRET between luminol and CdTe QDs based on the HRP-QDs conjugates and the immuno-interaction of the QDs-BSA and anti-BSA-HRP in the hydrogen peroxide–luminol CL system (Fig. 19.5) [63]. The luminol CL can efficiently excite the CdTe QDs acceptor, which means the performing of the CRET between the luminol donor and QDs acceptor. Li et al. examined the resonance energy transfer between CL donor (luminol–H<sub>2</sub>O<sub>2</sub> system) and TGA-capped CdTe QDs (with different emission peaks) acceptors [64]. Zhao et al. [65] observed the resonance energy transfer from CL donor (luminol–H<sub>2</sub>O<sub>2</sub> system) to CdSe/ZnS QDs (emission at 593 nm) acceptors.

## 19.5 Advantages and Disadvantages of QD-Based Chemiluminescence Sensors

Chemiluminescence assays of a wide range of compounds (immunoassays, drugs, biotechnology, food technology, biosensing, clinical, etc.) are a well-known luminescent technique and have grown exponentially in the last decade [66]. CL-based sensors are better than optical sensors due to the very low background signal



**Fig. 19.5** Chemiluminescence emission in CRET system. (Adapted with permission from Ref. [55]. Copyright 2012: Elsevier)

compared to the absorbance and fluorescence emitted by a light source [67]. CL is often defined as a dark-field technique. The absence of a strong background light level, as in absorption spectroscopy, decreases the background signal, improving detection limits. Small changes in a small signal are more easily observed than small changes in the presence of a large signal. The most common advantages of CL reactions include the relatively simple instrumentation required, low detection limits and wide dynamic ranges, reproducible, rapid, sensitive, and selective method has contributed to the interest in CL detection in HPLC and flow injection analysis (FIA). They have unique size-dependent properties (optical and electronic) and have excellent analytical potential [68]. As a principle, CL measurement in a fluorometer is possible by turning off the excitation source. What is needed, is a photomultiplier tube, sufficiently sensitive in the spectral region of interest [69].

Most CL-based reactions have low quantum efficiencies and therefore produce a weak luminescence. Semiconductor quantum dots can be employed as sensitizers due to their size-dependent and optical properties and consequently can have a significant increase in weak emission. CL sensors were widely discovered and developed based on the CL behaviour of these nanoparticles. These nanoparticles have great properties as CL emitters such as large molar extinction coefficients, easy multicolour labelling for visible and NIR spectral regions, surface trap-control luminescence, low photobleaching/photodegradation, high quantum efficiency, and are chemically resistant [70]. Due to their high fluorescence quantum yield, wide excitation range, and good optical stability, QDs have been adopted as suitable energy acceptors for traditional CL luminophore donors for CRET design. The advances of QDs-based CL not only open a new field for the development of novel CL-emitting species but also extend the conventional optical application of QDs. Nanosized materials-based diagnostics can be a great alternative to expensive techniques such as liquid chromatography-mass spectrometry (LC-MS). These nanomaterials-based CL assays will serve as an inexpensive, more efficient system in the future for the detection of toxins, antibiotics, chemical contaminants, and so on in food materials [57].

However, some disadvantages must also be considered. A CL reagent may yield significant emissions not just for one unique analyte, that is, a lack of selectivity may happen. Furthermore, the intensities of CL emission are sensitive to a variety of environmental factors such as solvent, temperature, pH, ionic strength, and other species present in the system. As a result, the separation conditions (HPLC, CE, etc.) may not always correspond to the optimum CL emission conditions. Because the emission intensity of a CL reaction changes with time (light flash consists of a signal increase after mixing of the reagent, passing through a maximum, then decreasing back to the baseline), the CL emission versus time profile differs broadly from one compound to another and care must be taken to detect the signal in the flowing stream during strictly defined periods. For many CL systems, there is a low background level of emission in the absence of an analyte. Hence, CL signals in flow systems, which increase in proportion to the analyte concentration, appear as sharp peaks superimposed on a low constant blank signal, measured as viewed by the time window when the mixture of analyte and reagent[s] pass through the

detector cell. Due to the small portion of CL emission that can only be measured from this time profile, reactions with complex kinetics can provide nonlinear plots of response to analyte concentration [69, 71].

In addition, conventional semiconductor QDs contain heavy metals that are hazardous and therefore have toxicity concerns in the living system, so there is a need to discover more environmentally friendly and biocompatible QDs. The optical and electronic properties of QDs may be used to design sensitive multiplexed biosensors. As far as bioconjugation of nanomaterials is concerned certain issues such as stabilisation due to pH, agglomeration, toxicity, and the large size of the biomolecules are still prevalent. Besides, the integration of QDs in real-life clinical applications is a major challenge especially in the production of reproducible nanoparticle bioconjugates [57]. Some of the challenges that still need to be overcome are economic factors.

QDs are more expensive than organic dyes, and early investment is needed for researchers and instrument suppliers to produce systems optimised for use with QDs. Also, the size of the probe and steric hindrance should be considered when evaluating the suitability of a QD-based approach to labelling molecules [16]. Because labelling various biomolecules with QDs of different sizes can lead to varying degrees of perturbation due to the large differences in the QDs sizes. Recently, however, it has been demonstrated that the size differences of multicolour QDs can be addressed using alloyed semiconductor QDs in which tuning of the emission wavelength is achieved through nanocrystal composition rather than size [72–74].

## 19.6 Applications of QDs-Based Chemiluminescence

The use of metal nanoparticles in CL reactions has provided new paths to increase the inherent sensitivity and develop novel applications of this detection mode [75]. Nowadays, CL has been extensively employed in various fields including bioengineering, pharmacy, molecular biology, clinical diagnosis, and food and environmental analysis [76–78]. So far, certain small molecules or macromolecules like proteins and DNAs, metal ions, and enzyme activity have been successfully detected through QDs-based CL as follows.

### 19.6.1 Detection of Small Biological Molecules

Many CL analytical methods are well-established based on the amplification (enhanced CL signal) or inhibition (reduced CL signal) of various analytes in QDs-based CL systems [75, 79]. Phenolic compounds have been shown to inhibit CL emission from the CdTe–H<sub>2</sub>O<sub>2</sub>–Tween 20 system and could be detected using CL with this proposed system. CL emission from L-cysteine-capped CdS QDs in the

presence of acidic  $\text{KMnO}_4$  was reported by Khataee and coworkers [80].  $\text{Na}_2\text{S}_2\text{O}_3$  could markedly amplify CL emission from the L-cysteine-capped CdS QDs– $\text{KMnO}_4$  system. The CL signal was strongly inhibited by baclofen, therefore a flow-injection CL method was developed to test baclofen. In addition, this group further designed a CL method to detect vancomycin with L-cysteine-modified CdS QDs as the nanoprobe in the morin– $\text{KMnO}_4$  system [81]. Due to the excellent separation capacity of aimed analytes using molecularly imprinted polymers (MIPs), the molecule imprinting technique is a promising tool to improve the selectivity of QDs-based CL nanoprobe for extensive applications [82, 83]. Combining the high sensitivity of CL with the good selectivity of MIP, Lin and colleagues [84] synthesised Mn-doped ZnS QDs capped with MIPs and applied these to CL detection of 4-nitrophenol in tap water. A CL sensor was designed by Ge and colleagues to determine deltamethrin (DM) using CdTe QDs and MIP [82]. QDs system was utilised by Chen et al. [56, 85] as a chemiluminescence probe to determine L-ascorbic acid in human serum. The results showed that CL intensity and the concentration of L-ascorbic acid had a good linear relationship and detection limit. Zhou et al. [86] found that CL intensity of the luminol-KIO<sub>4</sub> system was catalytically enhanced by thioglycolic acid-capped CdTe quantum dots in alkaline media. The effect of KIO<sub>4</sub> on the CL intensity suggested that at optimum concentration KIO<sub>4</sub> decomposes to produce some radical intermediates [such as  $\text{O}_2^{\cdot-}$  and  $\text{OH}^{\cdot}$ ] that accelerated the oxidation of luminol. The system was utilised to determine methionine in commercial pharmaceutical formulations [86]. Azizi et al. [87] developed a CL analysis system based on L-cysteine-capped ZnS-Mn QDs and used for the chemiluminometric determination of folic acid in the pharmaceutical formulation. So that when the ionic liquid 1,3-dipropylimidazolium bromide/copper complex was exposed to the system, an increase in intense light emission was observed due to the strong interaction between  $\text{Cu}^{2+}$  and the imidazolium ring. Khataee et al. [88] observed that the CL intensity of the  $\text{KMnO}_4$ –carminic acid system catalysed by CdS QDs was quenched in the presence of a trace level of cloxacillin. The results recommended that the decreased CL intensity had a good linear relation with the concentration of cloxacillin. A CL system based on the reaction between  $\text{KMnO}_4$ –CdS QDs reaction catalysed by cetyltrimethylammonium bromide (CTAB) in an acidic medium was developed as a CL probe for the sensitive determination of atenolol by Khataee et al. [89]. The method provided suitable results in detection of atenolol in spiked environmental water samples and commercial pharmaceutical formulation. Hosseini et al. [90] found that amino acids histidine and tryptophan catalysed the CL reaction of the CdSe QDs– $\text{H}_2\text{O}_2$  system due to the reaction of QDs with hydrogen peroxide. In another work, Hosseini et al. utilised the CdSe QDs– $\text{H}_2\text{O}_2$  system for the determination of dysprosium ions in water samples. The results showed that QDs optimum concentration should be preserved as the CL intensity quenches with increasing concentration of QDs. The limited energy produced due to reaction between  $\text{H}_2\text{O}_2$  and  $\text{OH}^-$  cannot excite all QDs and therefore affect CL efficiency [91]. Dong et al. [92] very recently found that weak CL of lucigenin obtained in alkaline solution (in the absence of  $\text{H}_2\text{O}_2$ ) could be significantly enhanced by CdS, CdSe, and CdTe QDs (CdS QDs produced the most intense CL). The enhancement in the intensity was

attributed to CRET that could occur due to overlapping of the lucigenin CL spectrum and the UV–vis absorption spectrum of CdS QDs. This method was satisfactorily applied to determine ascorbic acid in juice samples. Kang et al. reported a CL energy transfer process in  $K_3Fe(CN)_6$ –calcein system in alkaline medium catalysed by CdTe. The process involved CdTe QDs as an energy donor and the calcein as an acceptor. It was found that a good linear relationship existed between the quenched CL intensity and the concentration of polyphenols hence the method was applied for the determination of the polyphenols like chlorogenic acid, quercetin, hyperin, catechin, and kaempferol. The CdTe/calcein/ $K_3Fe(CN)_6$  CL system was applied for determining hyperin in the seed of *Cuscuta chinensis* Lam. with satisfactory results [93]. TGA-capped CdTe QDs were applied in a CL Ce[IV]– $SO_3$ –FIA system by Sun et al. [94] for the determination of various reducing organic compounds. Fortes et al. [95] implemented an automated multi-pumping flow system combining Ce[IV]– $SO_3$ –QDs CL system, using MPA capped CdTe QDs for the determination of two anti-diabetic drugs in pharmaceutical formulations. Both glipizide and gliclazide quenched the CL emission, probably due to radical scavenging activity. Zhao et al. found an efficient CRET occurred between a luminol donor and a CdTe QDs acceptor in the luminol–NaBrO–QDs system. The CL emission was sensitively inhibited by certain organic compounds of biological interest, such as biogenic amines and thiols, amino acids, organic acids, and steroids [96]. Based on these findings, they developed sensitive microchip electrophoresis [MCE]–CL method for the detection of the above compounds. Willner et al. [97] modified glucose oxidase with hemin/G-quadruplex units and conjugated the hybrid to CdSe/ZnS QDs for the CL detection of glucose. The glucose oxidase catalysed the oxidation of glucose to produce gluconic acid and  $H_2O_2$ . The latter in the presence of luminol catalysed by hemin/G-quadruplex produced strong CL, which originated a CRET process to the CdSe/ZnS QDs.

### 19.6.2 Detection of Proteins

In the CdTe QDs-based CRET reported by Ren's group, the energy donor was luminol, which was not directly attached to CdTe QDs, and the catalyst as HRP was linked to the CdTe QDs. CRET was activated when HRP continuously catalysed the CL reaction between luminol and  $H_2O_2$  [63]. They applied CRET to immunoassay based on the antigen (BSA)–antibody (anti-BSA IgG) interaction. CRET was stimulated when anti-BSA–HRP bounded to the BSA–CdTe QDs. Also, Ghavamipour et al. [98] developed a novel convenient CL-sensing protocol to detect vascular endothelial growth factor (VEGF) using catalase-mediated chemiluminescence immunoassay based on the CdTe QD/ $H_2O_2$  system.

In another work, a CRET aptasensor was proposed based on the VEGF-induced assembly of a CdSe/ZnS QDs–hemin/G-quadruplex. The amine-modified anti-VEGF aptamer was covalently conjugated to CdSe/ZnS QDs. The hemin/G--quadruplex–VEGF complex was formed when VEGF and hemin were added, which

catalysed the CL from luminol–H<sub>2</sub>O<sub>2</sub> system. The CL proceeded in the vicinity of the CdSe/ZnS QDs and led to the CRET process and the luminescence of the CdSe/ZnS QDs. The system was used to determine VEGF in human serum samples [99].

Li et al. [94] synthesised TGA-capped CdTe QDs which could enhance the CL of Ce[IV]–SO<sub>3</sub><sup>2-</sup> system from an efficient CRET [111]. The mechanism was explained as follows: in acid environment, HSO<sub>3</sub><sup>-</sup> was oxidised by Ce[IV] and HSO<sub>3</sub><sup>•</sup> radical was generated. Then, the combination of two HSO<sub>3</sub><sup>•</sup> radicals produced S<sub>2</sub>O<sub>6</sub><sup>2-</sup>, which further converted to the excited intermediate SO<sub>2</sub><sup>•</sup>. Finally, CdTe QDs were excited by the CL energy transfer from SO<sub>2</sub><sup>•</sup>. When the excited CdTe QDs returned to its ground state, the CL emission was produced. Organic compounds containing –SH, –NH<sub>2</sub>, or –OH groups, and some electron transfer proteins such as haemoglobin, myoglobin and cytochrome c, can quench the emission of this CL system by interacting with CdTe QDs. In combination with the flow injection technique, this CL system has been used to detect the above compounds and proteins [94].

### 19.6.3 Detection of DNA

Willner et al. [100] also developed aptamer sensing and DNA-sensing platforms using DNAzyme to stimulate CRET with luminol as donors and CdSe/ZnS QDs as acceptors. CdSe/ZnS QDs were attached to one of the aptamer subunits in the self-assembled ATP-aptamer subunits/hemin-G-quadruplex DNAzyme. The QDs-conjugated hairpin nucleic acid included the G-quadruplex sequence in a “caged” configuration, that was used to analyse DNA. The CRET process was stimulated when the target DNA opened the hairpin structure and assembled the hemin-G-quadruplex DNAzyme. Zhou et al. [101] developed a CRET-based aptasensor for the detection of ATP using CdTe QDs. The CL reaction of luminol–H<sub>2</sub>O<sub>2</sub> catalysed by HRP was used as the light source. Two pieces of ssDNA cut from an adenosine aptamer were conjugated to CdTe QDs and HRP, respectively. The CRET occurred when the two fragments reassemble into specific structures in the presence of ATP, which decreased the distance of HRP and CdTe QDs. ATP can be selectively determined according to this mechanism.

### 19.6.4 Detection of Metal Ions

Zhang and colleagues [102] investigated the influence of metal ions on the CdTe–H<sub>2</sub>O<sub>2</sub> CL system and showed that Fe<sup>2+</sup>, Ca<sup>2+</sup>, Ba<sup>2+</sup>, Pb<sup>2+</sup>, and Cu<sup>2+</sup> enhanced CL intensity, while Ni<sup>2+</sup>, Zn<sup>2+</sup>, Cr<sup>3+</sup>, and Ag<sup>+</sup>, inhibited CL intensity. Similarly, Cu<sup>2+</sup>, Ag<sup>+</sup>, and Hg<sup>2+</sup> reduced CL emission from the reaction between TGA-modified CdTe QDs and H<sub>2</sub>O<sub>2</sub>, based on which Han and colleagues developed a CL method to test for Cu<sup>2+</sup>, Ag<sup>+</sup> and Hg<sup>2+</sup> [103]. K<sub>3</sub>Fe(CN)<sub>6</sub>–CdTe–GSH system was successfully



applied to detect nine different ions ( $\text{Ca}^{2+}$ ,  $\text{Co}^{2+}$ ,  $\text{Mn}^{2+}$ ,  $\text{Hg}^{2+}$ ,  $\text{Mg}^{2+}$ ,  $\text{Cu}^{2+}$ ,  $\text{Ni}^{2+}$ ,  $\text{Cr}^{3+}$  and  $\text{Fe}^{3+}$ ). An interesting example of CRET is the system studied by Kanwal et al. [104] MSA-capped CdTe QDs conjugated with IgG were used to successfully enhance the CL emission of luminol– $\text{H}_2\text{O}_2$  and to determine some reducing compounds and metal ions.

### 19.6.5 Determination of Enzyme Activity

Li's group [105] found that horseradish peroxidase [HRP]-mimicking DNAzyme amplified greatly CL emission in the CdTe QDs –  $\text{H}_2\text{O}_2$  system, although HRP did not enhance CL intensity that could be used to detect targets labelled with HRP-mimicking DNAzyme. Ghavamipour et al. [75] reported that the CL emission from the CdTe– $\text{H}_2\text{O}_2$  system decreased due to consumption of  $\text{H}_2\text{O}_2$  via the catalytic action of catalase (CAT), therefore a rapid and convenient determination method for CAT was proposed. In another work, Ghavamipour et al. [106] proposed a chemiluminescence assay for HRP activity using QDs/ $\text{H}_2\text{O}_2$  system and developed an improved chemiluminescence method for HRP-based ELISA.

## 19.7 Conclusion

In a nutshell, the quantum dots of nanoparticles are extremely promising with great potential for application in very distinct fields of analytical chemistry, combining great functionalisation simplicity with a good chemiluminescence property. In this chapter, we describe the mechanism of QDs in CL reactions, and their summaries and applications. These wide applications show that the combination of QDs with CL is a good platform for the development of analytical methods and the design of new optical sensors. QDs with excellent optical properties provide powerful tools for designing the ideal CL with signal amplification, which is an efficient analytical technique with high sensitivity, wide linear range and, simple instrumentation. Since QDs have a wide absorption spectrum and a narrow symmetrical emission, QDs luminescent at multiple wavelengths can be excited by the light produced by the same CL system, making it possible to perform multiplex analysis. The QDs-based CRET mode is defined by no interference of autofluorescence and photobleaching. It has great potential applications in intracellular sensing and in vivo imaging, as well as providing excellent platforms for the easy monitoring of changes in protein structure and the sensitive detection of molecular binding events in complex samples without isolation. The development of CRET probes with low toxicity and environmentally friendly QDs is an important direction in the future to realise the application of CRET in biological systems. Further efforts are needed to find some new QDs with high quantum yields or to search for novel and efficient CL systems to improve the sensitive detection of QDs-enhanced CL and to expand the promising potential applications. Although continuous advancements and

increasing applications of QDs-enhanced CL are already known, new developments and challenges are continuously appearing, and the research of QDs-enhanced CL remains an active subject.

## References

1. Meng L, Zi-Yue W, C-Y ZHANG. Recent advance in chemiluminescence assay and its biochemical applications. *Chin J Anal Chem.* 2016;44(12):1934–41.
2. Giokas DL, Vlessidis AG, Tsogas GZ, Evmiridis NP. Nanoparticle-assisted chemiluminescence and its applications in analytical chemistry. *TrAC Trends Anal Chem.* 2010;29(10):1113–26.
3. Yari A, Karami M. Peroxyoxalate chemiluminescence of 1, 4-dihydroxy-3-methylthioxanthone and quenching effect of  $\beta$ -cyclodextrin. *J Incl Phenom Macrocycl Chem.* 2012;73(1):287–93.
4. Yang L, Guan G, Wang S, Zhang Z. Nano-anatase-enhanced peroxyoxalate chemiluminescence and its sensing application. *J Phys Chem C.* 2012;116(5):3356–62.
5. Zhao S, Liu J, Huang Y, Liu Y-M. Introducing chemiluminescence resonance energy transfer into immunoassay in a microfluidic format for an improved assay sensitivity. *Chem Commun.* 2012;48(5):699–701.
6. Bi S, Zhao T, Luo B. A graphene oxide platform for the assay of biomolecules based on chemiluminescence resonance energy transfer. *Chem Commun.* 2012;48(1):106–8.
7. Zhang L, Zhang Z, Lu C, Lin J-M. Improved chemiluminescence in Fenton-like reaction via dodecylbenzene-sulfonate-intercalated layered double hydroxides. *J Phys Chem C.* 2012;116(27):14711–6.
8. Zhou W, Cao Y, Sui D, Lu C. Radical pair-driven luminescence of quantum dots for specific detection of peroxynitrite in living cells. *Anal Chem.* 2016;88(5):2659–65.
9. Zhou W, Cao Y, Sui D, Lu C. Turn-on luminescent probes for the real-time monitoring of endogenous hydroxyl radicals in living cells. *Angew Chem.* 2016;128(13):4308–13.
10. Song H, Su Y, Zhang L, Lv Y. Quantum dots-based chemiluminescence probes: an overview. *Luminescence.* 2019;34(6):530–43.
11. Dodeigne C, Thunus L, Lejeune R. Chemiluminescence as diagnostic tool. *Rev Talanta.* 2000;51(3):415–39.
12. Murray CB, Norris DJ, Bawendi MG. Synthesis and characterization of nearly monodisperse CdE (E= sulfur, selenium, tellurium) semiconductor nanocrystallites. *J Am Chem Soc.* 1993;115(19):8706–15.
13. Hines MA, Guyot-Sionnest P. Bright UV-blue luminescent colloidal ZnSe nanocrystals. *J Phys Chem B.* 1998;102(19):3655–7.
14. Hines MA, Guyot-Sionnest P. Synthesis and characterization of strongly luminescing ZnS-capped CdSe nanocrystals. *J Phys Chem.* 1996;100(2):468–71.
15. Tsay JM, Michalet X. New light on quantum dot cytotoxicity. *Chem Biol.* 2005;12(11):1159–61.
16. Bailey RE, Smith AM, Nie S. Quantum dots in biology and medicine. *Physica E.* 2004;25(1):1–12.
17. Chan WCW, Nie S. Quantum dot bioconjugates for ultrasensitive nonisotopic detection. *Science.* 1998;281(5385):2016–8.
18. Wu X, Liu H, Liu J, Haley KN, Treadway JA, Larson JP, et al. Immunofluorescent labeling of cancer marker Her2 and other cellular targets with semiconductor quantum dots. *Nat Biotechnol.* 2003;21(1):41–6.
19. Dubertret B, Skourides P, Norris DJ, Noireaux V, Brivanlou AH, Libchaber A. *In vivo* imaging of quantum dots encapsulated in phospholipid micelles. *Science.* 2002;298(5599):1759–62.

20. Santra S, Wang K, Tapeç R, Tan W. Development of novel dye-doped silica nanoparticles for biomarker application. *J Biomed Opt.* 2001;6(2):160–6.
21. Raab RM, Stephanopoulos G. Dynamics of gene silencing by RNA interference. *Biotechnol Bioeng.* 2004;88(1):121–32.
22. Mei BC, Susumu K, Medintz IL, Mattoussi H. Polyethylene glycol-based bidentate ligands to enhance quantum dot and gold nanoparticle stability in biological media. *Nat Protoc.* 2009;4(3):412–23.
23. Stewart MH, Susumu K, Mei BC, Medintz IL, Delehanty JB, Blanco-Canosa JB, et al. Multidentate poly (ethylene glycol) ligands provide colloidal stability to semiconductor and metallic nanocrystals in extreme conditions. *J Am Chem Soc.* 2010;132(28):9804–13.
24. Schipper ML, Iyer G, Koh AL, Cheng Z, Ebenstein Y, Aharoni A, et al. Particle size, surface coating, and PEGylation influence the biodistribution of quantum dots in living mice. *Small.* 2009;5(1):126–34.
25. Liu J, Li H, Wang W, Xu H, Yang X, Liang J, et al. Use of ester-terminated polyamidoamine dendrimers for stabilizing quantum dots in aqueous solutions. *Small.* 2006;2(8–9):999–1002.
26. Susumu K, Mei BC, Mattoussi H. Multifunctional ligands based on dihydroliipoic acid and polyethylene glycol to promote biocompatibility of quantum dots. *Nat Protoc.* 2009;4(3):424–36.
27. Tan SJ, Jana NR, Gao S, Patra PK, Ying JY. Surface-ligand-dependent cellular interaction, subcellular localization, and cytotoxicity of polymer-coated quantum dots. *Chem Mater.* 2010;22(7):2239–47.
28. Kim S-W, Kim S, Tracy JB, Jasanoff A, Bawendi MG. Phosphine oxide polymer for water-soluble nanoparticles. *J Am Chem Soc.* 2005;127(13):4556–7.
29. Luccardini C, Tribet C, Vial F, Marchi-Artzner V, Dahan M. Size, charge, and interactions with giant lipid vesicles of quantum dots coated with an amphiphilic macromolecule. *Langmuir.* 2006;22(5):2304–10.
30. Yu WW, Chang E, Falkner JC, Zhang J, Al-Somali AM, Sayes CM, et al. Forming biocompatible and nonaggregated nanocrystals in water using amphiphilic polymers. *J Am Chem Soc.* 2007;129(10):2871–9.
31. Pellegrino T, Manna L, Kudera S, Liedl T, Koktysh D, Rogach AL, et al. Hydrophobic nanocrystals coated with an amphiphilic polymer shell: a general route to water soluble nanocrystals. *Nano Lett.* 2004;4(4):703–7.
32. Wu Y, Chakraborty S, Gropeanu RA, Wilhelmi J, Xu Y, Er KS, et al. pH-responsive quantum dots via an albumin polymer surface coating. *J Am Chem Soc.* 2010;132(14):5012–4.
33. Rakshit S, Vasudevan S. Resonance energy transfer from  $\beta$ -cyclodextrin-capped ZnO: MgO nanocrystals to included Nile red guest molecules in aqueous media. *ACS Nano.* 2008;2(7):1473–9.
34. Freeman R, Finder T, Bahshi L, Willner I.  $\beta$ -cyclodextrin-modified CdSe/ZnS quantum dots for sensing and chiroselective analysis. *Nano Lett.* 2009;9(5):2073–6.
35. Jin T, Fujii F, Sakata H, Tamura M, Kinjo M. Amphiphilic p-sulfonatocalix (4) arene-coated CdSe/ZnS quantum dots for the optical detection of the neurotransmitter acetylcholine. *Chem Commun.* 2005;34:4300–2.
36. Jin T, Fujii F, Yamada E, Nodasaka Y, Kinjo M. Control of the optical properties of quantum dots by surface coating with calix (n) arene carboxylic acids. *J Am Chem Soc.* 2006;128(29):9288–9.
37. Koole R, Van Schooneveld MM, Hilhorst J, de Mello DC, 't Hart DC, Van Blaaderen A, et al. On the incorporation mechanism of hydrophobic quantum dots in silica spheres by a reverse microemulsion method. *Chem Mater.* 2008;20(7):2503–12.
38. Han R, Yu M, Zheng Q, Wang L, Hong Y, Sha Y. A facile synthesis of small-sized, highly photoluminescent, and monodisperse CdSeS QD/SiO<sub>2</sub> for live cell imaging. *Langmuir.* 2009;25(20):12250–5.
39. Goldman ER, Anderson GP, Tran PT, Mattoussi H, Charles PT, Mauro JM. Conjugation of luminescent quantum dots with antibodies using an engineered adaptor protein to provide new reagents for fluoroimmunoassays. *Anal Chem.* 2002;74(4):841–7.

40. Goldman ER, Balighian ED, Mattoussi H, Kuno MK, Mauro JM, Tran PT, et al. Avidin: a natural bridge for quantum dot-antibody conjugates. *J Am Chem Soc.* 2002;124(22):6378–82.
41. Wang YA, Li JJ, Chen H, Peng X. Stabilization of inorganic nanocrystals by organic dendrons. *J Am Chem Soc.* 2002;124(10):2293–8.
42. Xing Y, Rao J. Quantum dot bioconjugates for *in vitro* diagnostics & *in vivo* imaging. *Cancer Biomark.* 2008;4(6):307–19.
43. Alivisatos AP, Gu W, Larabell C. Quantum dots as cellular probes. *Annu Rev Biomed Eng.* 2005;7:55–76.
44. Patolsky F, Gill R, Weizmann Y, Mokari T, Banin U, Willner I. Lighting-up the dynamics of telomerization and DNA replication by CdSe–ZnS quantum dots. *J Am Chem Soc.* 2003;125(46):13918–9.
45. Mahtab R, Harden HH, Murphy CJ. Temperature- and salt-dependent binding of long DNA to protein-sized quantum dots: thermodynamics of “inorganic protein”–DNA interactions. *J Am Chem Soc.* 2000;122(1):14–7.
46. Motevalian M, Ghavamipour F, Maroufi B, Mirshahi M, Sajedi RH. Mutual effects of protein corona formation on CdTe quantum dots. *Anal Biochem.* 2020;610:113983.
47. Hanaki K, Momo A, Oku T, Komoto A, Maenosono S, Yamaguchi Y, et al. Semiconductor quantum dot/albumin complex is a long-life and highly photostable endosome marker. *Biochem Biophys Res Commun.* 2003;302(3):496–501.
48. Bruchez M, Moronne M, Gin P, Weiss S, Alivisatos AP. Semiconductor nanocrystals as fluorescent biological labels. *Science.* 1998;281(5385):2013–6.
49. Xing Y, Chaudry Q, Shen C, Kong KY, Zhau HE, Chung LW, et al. Bioconjugated quantum dots for multiplexed and quantitative immunohistochemistry. *Nat Protoc.* 2007;2(5):1152–65.
50. Xiao Y, Barker PE. Semiconductor nanocrystal probes for human metaphase chromosomes. *Nucleic Acids Res.* 2004;32(3):e28.
51. Pinaud F, King D, Moore H-P, Weiss S. Bioactivation and cell targeting of semiconductor CdSe/ZnS nanocrystals with phytochelatin-related peptides. *J Am Chem Soc.* 2004;126(19):6115–23.
52. Gao X, Chan WCW, Nie S. Quantum-dot nanocrystals for ultrasensitive biological labeling and multicolor optical encoding. *J Biomed Opt.* 2002;7(4):532–7.
53. Zhang T, Stilwell JL, Gerion D, Ding L, Elboudwarej O, Cooke PA, et al. Cellular effect of high doses of silica-coated quantum dot profiled with high throughput gene expression analysis and high content cellomics measurements. *Nano Lett.* 2006;6(4):800–8.
54. Bottini M, D’Annibale F, Magrini A, Cerignoli F, Arimura Y, Dawson MI, et al. Quantum dot-doped silica nanoparticles as probes for targeting of T-lymphocytes. *Int J Nanomedicine.* 2007;2(2):227.
55. Frigerio C, Ribeiro DSM, Rodrigues SSM, Abreu VLRG, Barbosa JAC, Prior JAV, et al. Application of quantum dots as analytical tools in automated chemical analysis: a review. *Anal Chim Acta.* 2012;735:9–22.
56. Chen H, Lin L, Li H, Lin J-M. Quantum dots-enhanced chemiluminescence: mechanism and application. *Coord Chem Rev.* 2014;263:86–100.
57. Tiwari A, Dhoble SJ. Recent advances and developments on integrating nanotechnology with chemiluminescence assays. *Talanta.* 2018;180:1–11.
58. Wang Z, Li J, Liu B, Hu J, Yao X, Li J. Chemiluminescence of CdTe nanocrystals induced by direct chemical oxidation and its size-dependent and surfactant-sensitized effect. *J Phys Chem B.* 2005;109(49):23304–11.
59. Wang Z, Li J, Liu B, Li J. CdTe nanocrystals sensitized chemiluminescence and the analytical application. *Talanta.* 2009;77(3):1050–6.
60. Guo C, Zeng H, Ding X, He D, Li J, Yang R, et al. Enhanced chemiluminescence of the luminol-K<sub>3</sub>Fe(CN)<sub>6</sub> system by ZnSe quantum dots and its application. *J Lumin.* 2013;134:888–92.
61. Zhao Y, Zhao S, Huang J, Ye F. Quantum dot-enhanced chemiluminescence detection for simultaneous determination of dopamine and epinephrine by capillary electrophoresis. *Talanta.* 2011;85(5):2650–4.

62. Kanwal S, Fu X, Su X. Size dependent active effect of CdTe quantum dots on pyrogallol- $H_2O_2$  chemiluminescence system for chromium (III) detection. *Microchim Acta*. 2010;169(1–2):167–72.
63. Huang X, Li L, Qian H, Dong C, Ren J. A resonance energy transfer between chemiluminescent donors and luminescent quantum-dots as acceptors (CRET). *Angew Chem Int Ed*. 2006;45(31):5140–3.
64. Li Z, Wang Y, Zhang G, Xu W, Han Y. Chemiluminescence resonance energy transfer in the luminol–CdTe quantum dots conjugates. *J Lumin*. 2010;130(6):995–9.
65. Wang H-Q, Li Y-Q, Wang J-H, Xu Q, Li X-Q, Zhao Y-D. Influence of quantum dot's quantum yield to chemiluminescence resonance energy transfer. *Anal Chim Acta*. 2008;610(1):68–73.
66. Gámiz-Gracia L, García-Campaña AM, Huertas-Pérez JF, Lara FJ. Chemiluminescence detection in liquid chromatography: applications to clinical, pharmaceutical, environmental and food analysis—a review. *Anal Chim Acta*. 2009;640(1–2):7–28.
67. Coulet PR, Blum LJ. Bioluminescence/chemiluminescence based sensors. *TrAC Trends Anal Chem*. 1992;11(2):57–61.
68. Medintz IL, Uyeda HT, Goldman ER, Mattoussi H. Quantum dot bioconjugates for imaging, labelling and sensing. *Nat Mater*. 2005;4(6):435.
69. Baeyens WRG, Schulman SG, Calokerinos AC, Zhao Y, Campana AMG, Nakashima K, et al. Chemiluminescence-based detection: principles and analytical applications in flowing streams and in immunoassays. *J Pharm Biomed Anal*. 1998;17(6–7):941–53.
70. Lei J, Ju H. Fundamentals and bioanalytical applications of functional quantum dots as electrogenerated emitters of chemiluminescence. *TrAC Trends Anal Chem*. 2011;30(8):1351–9.
71. Baeyens W, Bruggeman J, Lin B. Enhanced chemiluminescence detection of some dansyl amino acids in liquid chromatography. *Chromatographia*. 1989;27(5–6):191–3.
72. Bailey RE, Nie S. Alloyed semiconductor quantum dots: tuning the optical properties without changing the particle size. *J Am Chem Soc*. 2003;125(23):7100–6.
73. Kim S, Fisher B, Eisler H-J, Bawendi M. Type-II quantum dots: CdTe/CdSe (core/shell) and CdSe/ZnTe (core/shell) heterostructures. *J Am Chem Soc*. 2003;125(38):11466–7.
74. Zhong X, Han M, Dong Z, White TJ, Knoll W. Composition-tunable  $Zn_xCd_{1-x}Se$  nanocrystals with high luminescence and stability. *J Am Chem Soc*. 2003;125(28):8589–94.
75. Ghavamipour F, Sajedi RH, Khajeh K. A chemiluminescence-based catalase assay using  $H_2O_2$ -sensitive CdTe quantum dots. *Microchim Acta*. 2018;185(8):376.
76. Orooji Y, Irani-Nezhad MH, Hassandoost R, Khataee A, Pouran SR, Joo SW. Cerium doped magnetite nanoparticles for highly sensitive detection of metronidazole via chemiluminescence assay. *Spectrochim Acta A Mol Biomol Spectrosc*. 2020;234:118272.
77. Qi Y, He J, Xiu F-R, Yu X, Gao X, Li Y, et al. A convenient chemiluminescence detection for bisphenol A in E-waste dismantling site based on surface charge change of cationic gold nanoparticles. *Microchem J*. 2019;147:789–96.
78. Li F, Guo L, Hu Y, Li Z, Liu J, He J, et al. Multiplexed chemiluminescence determination of three acute myocardial infarction biomarkers based on microfluidic paper-based immunodevice dual amplified by multifunctionalized gold nanoparticles. *Talanta*. 2020;207:120346.
79. Hosseini M, Ganjali MR, Vaezi Z, Arabsorkhi B, Dadmehr M, Faridbod F, et al. Selective recognition histidine and tryptophan by enhanced chemiluminescence ZnSe quantum dots. *Sensors Actuators B Chem*. 2015;210:349–54.
80. Khataee A, Hasanzadeh A, Iranifam M, Joo SW. A novel flow-injection chemiluminescence method for determination of baclofen using l-cysteine capped CdS quantum dots. *Sensors Actuators B Chem*. 2015;215:272–82.
81. Su Y, Deng D, Zhang L, Song H, Lv Y. Strategies in liquid-phase chemiluminescence and their applications in bioassay. *TrAC Trends Anal Chem*. 2016;82:394–411.
82. Ge S, Zhang C, Yu F, Yan M, Yu J. Layer-by-layer self-assembly CdTe quantum dots and molecularly imprinted polymers modified chemiluminescence sensor for deltamethrin detection. *Sensors Actuators B Chem*. 2011;156(1):222–7.

83. Duan H, Li L, Wang X, Wang Y, Li J, Luo C. CdTe quantum dots- luminol for trace-level chemiluminescence sensing of phenacetin based on biological recognition materials. *New J Chem*. 2016;40(1):458–63.
84. Liu J, Chen H, Lin Z, Lin J-M. Preparation of surface imprinting polymer capped Mn-doped ZnS quantum dots and their application for chemiluminescence detection of 4-nitrophenol in tap water. *Anal Chem*. 2010;82(17):7380–6.
85. Chen H, Li R, Lin L, Guo G, Lin J-M. Determination of l-ascorbic acid in human serum by chemiluminescence based on hydrogen peroxide–sodium hydrogen carbonate–CdSe/CdS quantum dots system. *Talanta*. 2010;81(4–5):1688–96.
86. Zhou M, Wang A, Li C, Luo X, Ma Y. Flow-based determination of methionine in pharmaceutical formulations exploiting TGA-capped CdTe quantum dots for enhancing the luminol-KIO<sub>4</sub> chemiluminescence. *J Lumin*. 2017;183:206–11.
87. Azizi SN, Shakeri P, Chaichi MJ, Bekhradnia A, Taghavi M, Ghaemy M. The use of imidazolium ionic liquid/copper complex as novel and green catalyst for chemiluminescent detection of folic acid by Mn-doped ZnS nanocrystals. *Spectrochim Acta A Mol Biomol Spectrosc*. 2014;122:482–8.
88. Khataee A, Hasanzadeh A, Lotfi R, Joo SW. Enhanced chemiluminescence of carminic acid-permanganate by CdS quantum dots and its application for sensitive quenchometric flow injection assays of cloxacillin. *Talanta*. 2016;152:171–8.
89. Chowdhury ZZ, Ali AE, Khalid K, Ikram R, Rahman M, Sagadevan S, et al. Science and technology roadmap for photocatalytic membrane separation: a potential route for environmental remediation and fouling mitigation. In: *Green photocatalytic semiconductors*. Cham: Springer; 2022. p. 513–50.
90. Hosseini M, Ganjali MR, Jarrahi A, Vaezi Z, Mizani F, Faridbod F. Enhanced chemiluminescence CdSe quantum dots by histidine and tryptophan. *Spectrochim Acta A Mol Biomol Spectrosc*. 2014;132:629–33.
91. Hosseini M, Ganjali MR, Vaezi Z, Faridbod F, Arabsorkhi B, Sheikhha MH. Selective recognition of dysprosium (III) ions by enhanced chemiluminescence CdSe quantum dots. *Spectrochim Acta A Mol Biomol Spectrosc*. 2014;121:116–20.
92. Dong Y, Wang J, Peng Y, Chu X, Wang S. Chemiluminescence resonance energy transfer between CdS quantum dots and lucigenin and its sensing application. *J Lumin*. 2017;181:433–8.
93. Kang J, Li X, Geng J, Han L, Tang J, Jin Y, et al. Determination of hyperin in seed of *Cuscuta chinensis* Lam. by enhanced chemiluminescence of CdTe quantum dots on calcein/K<sub>3</sub>Fe(CN)<sub>6</sub> system. *Food Chem*. 2012;134(4):2383–8.
94. Sun C, Liu B, Li J. Sensitized chemiluminescence of CdTe quantum-dots on Ce (IV)-sulfite and its analytical applications. *Talanta*. 2008;75(2):447–54.
95. Fortes PR, Frigerio C, Silvestre CIC, Santos JLM, Lima JLFC, Zagatto EAG. Cadmium telluride nanocrystals as luminescent sensitizers in flow analysis. *Talanta*. 2011;84(5):1314–7.
96. Zhao S, Huang Y, Shi M, Liu R, Liu Y-M. Chemiluminescence resonance energy transfer-based detection for microchip electrophoresis. *Anal Chem*. 2010;82(5):2036–41.
97. Niazov A, Freeman R, Girsh J, Willner I. Following glucose oxidase activity by chemiluminescence and chemiluminescence resonance energy transfer (CRET) processes involving enzyme-DNAzyme conjugates. *Sensors*. 2011;11(11):10388–97.
98. Ghavamipour F, Rahmani H, Shanehsaz M, Khajeh K, Mirshahi M, Sajedi R. Enhanced sensitivity of VEGF detection using catalase-mediated chemiluminescence immunoassay based on CdTe QD/H<sub>2</sub>O<sub>2</sub> system. *J Nanobiotechnol*. 2020;18:1–10.
99. Freeman R, Girsh J, Fang-ju Jou A, Ho JA, Hug T, Dervede J, et al. Optical aptasensors for the analysis of the vascular endothelial growth factor (VEGF). *Anal Chem*. 2012;84(14):6192–8.
100. Freeman R, Liu X, Willner I. Chemiluminescent and chemiluminescence resonance energy transfer (CRET) detection of DNA, metal ions, and aptamer–substrate complexes using hemin/G-quadruplexes and CdSe/ZnS quantum dots. *J Am Chem Soc*. 2011;133(30):11597–604.

101. Zhou Z-M, Yu Y, Zhao Y-D. A new strategy for the detection of adenosine triphosphate by aptamer/quantum dot biosensor based on chemiluminescence resonance energy transfer. *Analyst*. 2012;137(18):4262–6.
102. Li X, Li J, Tang J, Kang J, Zhang Y. Study of influence of metal ions on CdTe/H<sub>2</sub>O<sub>2</sub> chemiluminescence. *J Lumin*. 2008;128(7):1229–34.
103. Sheng Z, Han H, Liang J. The behaviors of metal ions in the CdTe quantum dots–H<sub>2</sub>O<sub>2</sub> chemiluminescence reaction and its sensing application. *Lumin J Biol Chem Lumin*. 2009;24(5):271–5.
104. Kanwal S, Traore Z, Zhao C, Su X. Enhancement effect of CdTe quantum dots–IgG bioconjugates on chemiluminescence of luminol–H<sub>2</sub>O<sub>2</sub> system. *J Lumin*. 2010;130(10):1901–6.
105. Zhang J, Li B. Enhanced chemiluminescence of CdTe quantum dots–H<sub>2</sub>O<sub>2</sub> by horseradish peroxidase-mimicking DNzyme. *Spectrochim Acta A Mol Biomol Spectrosc*. 2014;125:228–33.
106. Ghavamipour F, Khajeh K, Sajedi RH. The application of the QDs/H<sub>2</sub>O<sub>2</sub> chemiluminescence system in HRP assay and HRP-based immunoassay. *Colloids Surf B Biointerfaces*. 2021;206:111942.

# Chapter 20

## Electrochemiluminescent Biosensors Based on II–VI Quantum Dots



Xiao-Yan Wang, Zhi-Yuan Che, and Shou-Nian Ding

### 20.1 Introduction

Electrochemiluminescence (ECL) refers to the light emitted when the excited state formed by the high-energy electron transfer reaction on the electrode returns to its fundamental state [1–3]. In other words, ECL is chemiluminescence excited by electrochemistry. Therefore, ECL not only has the advantages of electrochemistry, such as simple operation, simple instrument, and fast response, but also possesses the advantages of traditional chemiluminescence with wide dynamic range and high sensitivity [4–6]. According to the source of free radicals, the ECL mechanism can be divided into annihilation ECL and co-reactant ECL [7]. In the application of biological analysis, water is often used as the main medium. However, it is difficult for luminescent species to be simultaneously oxidized and reduced due to the electrochemical splitting of water itself. Thus, although the annihilation pathway is the origin of early ECL studies, the co-reactant pathway is more prevalent in basic research and practical applications.

In recent decades, the rapid development of biosensors with high sensitivity and specificity has brought great breakthroughs for early clinical diagnosis [8–10]. It is well known that biosensor includes biometrics and physicochemical signal transduction. The former is responsible for selectivity of biosensors and the latter corresponds to sensitivity of biosensors. Biosensor should be stable, rapid, of high sensitivity, and low cost to realize commercial application. Therefore, various energy conversion pathways are used in signal transduction, including photoluminescence [11–13], chemiluminescence [14, 15], fluorescence [16], and electrochemiluminescence [17–19]. Among them, ECL biosensors have many unique

---

X.-Y. Wang · Z.-Y. Che · S.-N. Ding (✉)

Jiangsu Province Hi-Tech Key Laboratory for Bio-medical Research, School of Chemistry and Chemical Engineering, Southeast University, Nanjing, China  
e-mail: [snding@seu.edu.cn](mailto:snding@seu.edu.cn)



advantages. First, ECL does not require excited light, which reduces the background noise of scattered light and unnecessary luminescence. Second, ECL is activated and regulated by potential, which provides excellent controllability and reproducibility. Third, the diversity of ECL luminescent materials make ECL widely used in different biosensors. In addition, ECL also has the advantages of fast response, simple operation process, and low equipment cost [20–22]. ECL biosensor, as a powerful analytical method, has been successfully applied in clinical diagnosis.

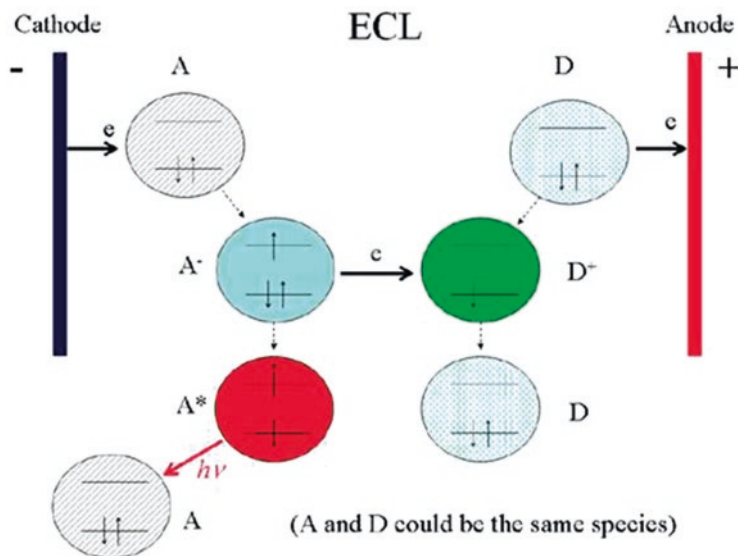
Luminophores are the most important part of ECL biosensor system. The early molecular luminophores such as tris(bipyridine)-ruthenium ( $\text{Ru}(\text{bpy})_3^{2+}$ ) and luminol have some disadvantages such as poor modifiability, monotonous, and wide emission wavelength. Therefore, researchers have been developing new ECL luminophores for several years. In 2002, Bard's group reported the electrochemiluminescence of silicon quantum dots (QDs), which triggered a boom in the research of quantum dots in the ECL field [23, 24]. Quantum dots (QDs) are a class of semiconductor nanocrystals whose size is smaller than the Bohr radius of excitons [25]. QDs, especially II–VI compound semiconductor QDs, have wideband absorption, narrowband emission, and continuous tunable wavelength of size under the influence of quantum limiting effect [26]. With the development of synthesis chemistry and spectroscopy of quantum dots, the luminescence properties of QDs have been continuously improved [27]. High-quality QDs possess perfect fluorescence properties, such as 100% fluorescence quantum yield, single exponential decay of fluorescence lifetime, and stable non-scintillation of light [28, 29]. Thus, QDs have the potential to replace the traditional ECL luminescent molecules due to their excellent optical properties and flexible structural composition.

This chapter mainly summarizes the ECL signal transmission strategy and ECL mechanism of II–VI semiconductor quantum dots as ECL. Furthermore, the practical application of ECL biosensor based on II–VI semiconductor quantum dots will also be discussed. Finally, we describe some critical issues and some perspectives for the future development of ECL sensors.

## 20.2 ECL Mechanism of II–VI Quantum Dots

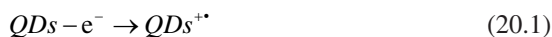
The basic principle of ECL consists of two parts: one is redox generation of excited states and the other is light radiation. By applying a scanning voltage, the ECL luminescent material undergoes a redox reaction and high-energy electron transfer on the electrode surface to generate an unstable excited state, which produces ECL emission after relaxation [2] (Fig. 20.1).

ECL mechanisms of quantum dots mainly include two types; the first type is an annihilation-type mechanism, and the second type is a co-reactant-type mechanism. In the annihilation pathway, a reductant and an oxide are simultaneously generated on the electrode surface by applying an alternating pulse potential. The reaction between these two substances produces an excited state, which emits photons



**Fig. 20.1** Schematic diagrams showing the general principles of electrogenerated chemiluminescence. (Reprinted with permission from Miao [2]. Copyright 2008: American Chemical Society)

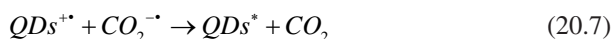
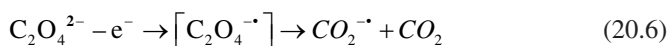
during the relaxation process to the ground state [30, 31]. The corresponding luminescence mechanism is as follows:



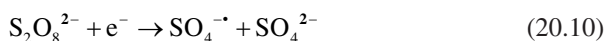
In the co-reactant pathway, the co-reactant is reduced or oxidized on the electrode surface through a single potential step to form a very active intermediate, which can react with the luminophores in the system to generate excited state. Subsequently, the excited state returns to the ground state accompanied by the phenomenon of luminescence. The introduction of co-reactants can overcome the problems of limited solvent potential or poor stability of radical ions. The co-reaction ECL mechanism of QDs can be divided into “oxidation–reduction” type and “reduction–oxidation” type. Oxidation–reduction ECL refers to the simultaneous oxidation reaction of the co-reactant and the ECL luminescent material, and the co-reactant forms a strong reduction radical and reacts with the oxidative ECL luminescent material to form an unstable excited state, which generates ECL emission after relaxation. Redox co-reactants, also known as anode co-reactants, mainly include  $\text{Na}_2\text{C}_2\text{O}_4$  and TPrA. Reduction–oxidation ECL means that the co-reactant and the

ECL luminescent material undergo a reduction reaction at the same time, and the co-reactant forms a strong oxidative radical and reacts with the reducing ECL luminescent material to form an unstable excited state, and the ECL is generated after relaxation. The co-reactants of the reduction–oxidation ECL are called cathode co-reactants and mainly include  $K_2S_2O_8$  and  $H_2O_2$ . The two types of reaction mechanisms are shown below [32, 33]:

Oxidation–reduction:



Reduction–oxidation:



### 20.3 ECL Signal Transduction Strategy

Clinical diagnosis requires accurate detection of microtargets, so it is urgent to design more effective ECL sensors. The signal strategy of ECL sensor is the key step of biosensor construction. In order to meet the sensitivity requirements of early disease detection, a variety of sensing mechanisms to convert biological information into detectable signals were explored. At present, the effective conversion of sensitive signals mainly includes three modes: signal-on, signal-off, and ratiometric effect.

Signal-on is the signal processing from weak to strong before and after target recognition, which has the advantages of wide detection range and low background signal. Signal-on is a very popular ECL signal output mode and has become an effective method in the field of analysis and detection. The methods of signal-on can be divided into four types: (i) Signal-on induced by luminophores enrichment: the ECL signal of quantum dots is easily disturbed and weak in the detection environment due to the instability and easy agglomeration of quantum dots. At present,

materials with high specific surface area, excellent biocompatibility, easy functionalization, and low cost have been widely used as the carrier of quantum dots. Compared with single quantum dots, the quantum dots gathered in the nanocarrier have stronger ECL emission, which can effectively improve the sensitivity of the sensor. So far, quantum dot carriers commonly used in various ultrasensitive biosensors mainly include silica nanoparticles [34], carbon nanomaterials [35], metal-organic frameworks (MOFs) [36], and transition metal oxides [37]. (ii) Signal-on regulated by ECL co-reaction: in order to further improve the sensitivity of the quantum dot ECL sensor, a co-reaction accelerator can be introduced in addition to the introduction of nanocarriers into a single ECL luminescent group [38]. The co-reaction accelerator can interact with the co-reactant, thereby increasing the ECL reaction rate of the luminophore and the co-reactant. (iii) Signal-on induced by nucleic acid amplified strategy: isothermal nucleic acid amplification technology converts trace nucleic acid target into a large number of nucleic acid molecules for export. The introduction of nucleic acid amplification amplifies detectable signals and improves detection sensitivity, which has been widely used in biological detection [39].

Signal-off refers to the process of signal transition in which the ECL emission of the luminophore decreases with increasing analyte concentration. Over the past few years, there has been a huge effort to build traditional “signal-off” sensors. The key to the structure of the “signal-off” biosensor is that the stronger the initial signal, the greater the quenching rate of the “signal-off” state and the lower the background signal. At present, there are two common causes of signal-off: (i) Signal-off regulated by steric hindrance effect: the steric hindrance effect is the simplest and most effective signal-off mechanism. Steric hindrance suppresses not only the mass transfer diffusion on the electrode, but also the electron transfer, thereby reducing the current [40]. (ii) Signal-off induced by ECL-RET: ECL-RET usually occurs between an efficient energy donor and a suitable acceptor, an attractive technique for sensitive detection of analytes due to the absence of interference from scattered light [41].

Both signal-on and signal-off modes are based on changes in single emission intensity, but instrument errors or some environmental changes may cause false-positive/false-negative results during the detection process. In order to effectively suppress these interference factors, a measurement method of ratiometric ECL was proposed. Ratiometric ECL relies on the ratio change of the two ECL intensities and can provide more precise results by normalizing to the most ambiguous data. There are three main types of ratiometric ECL biosensors. (i) Dual-potential: dual-potential ratiometric sensor refers to a sensor that quantitatively analyzes the ratio of ECL intensities produced by two ECL emitters at different potentials. At present, the main strategies to realize bipotential ratiometric ECL sensing analysis include resonance energy transfer and regulation of co-reactant concentration [42]. (ii) Dual-wavelength: dual-wavelength ratiometric ECL biosensors require appropriate spectral overlap between the donor’s ECL spectrum and the acceptor’s absorption spectrum. When the donor/acceptor pair energies completely overlap, the light emitted by the donor can be transferred to the closed acceptor, thereby exciting its

optical signal [43]. (iii) Bipolar electrode (BPE): bipolar electrode (BPE) is a conductor immersed in an electrolyte. When a sufficient voltage is applied, the conductor can undergo electrochemical reactions at its ends without any ohmic contact. The two ECL emitters of the BPE-ECL ratiometric ECL biosensor need to satisfy the three conditions of high emission intensity, significantly different emission potentials, and microwaveable lengths to produce compelling changes [44].

## 20.4 Applications in ECL Biosensor

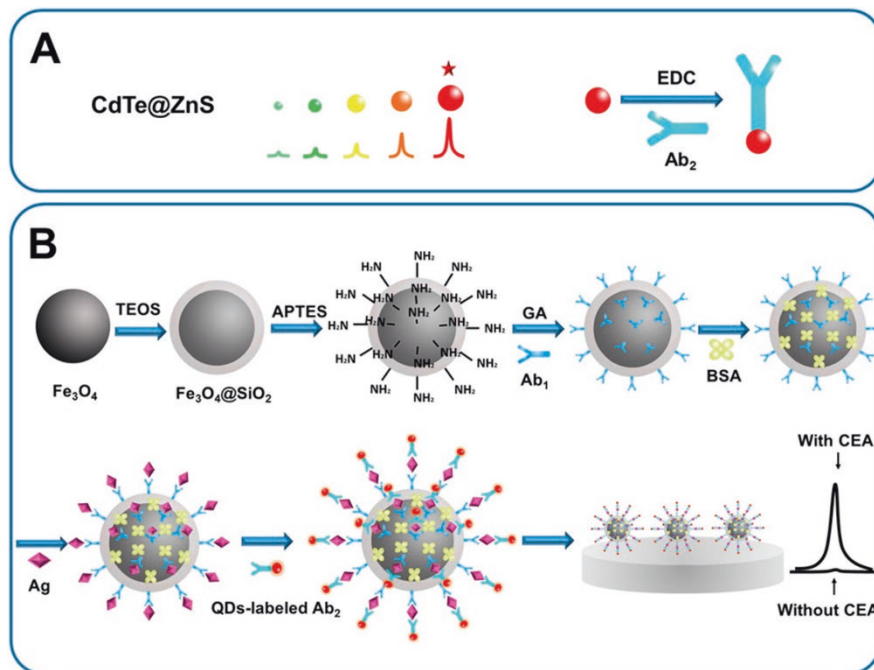
### 20.4.1 Immunosenors

ECL immunosensor is a clinical diagnosis method with high sensitivity and specificity developed based on the specific recognition properties of antigen–antibody and electrochemiluminescence technology. At this stage, immunoassay methods mainly include direct immunization, competitive immunization, and sandwich immunization.

The most widely used method for detecting cancer biomarker is sandwich immunization, which consists of coated antibodies, target antigens, and target antibodies labeled with ECL luminescence. As shown in Fig. 20.2, Dong's group has designed several ECL biosensors for the detection of carcinoembryonic antigen. One of them used magnetically separable  $\text{Fe}_3\text{O}_4@\text{SiO}_2$  as the nanocarrier and  $\text{CdTe}@\text{ZnS}$  QDs as the ECL luminophore to construct a carcinoembryonic antigen sandwich ECL immunosensor with a detection limit as low as 3.0 pg/mL [45]. Subsequently, two sandwich ECL immunosensors were constructed using  $\text{CdTe}$  QDs as ECL emitters, and  $\text{Fe}_3\text{O}_4@\text{SiO}_2\text{-Pt}$  complex with catalytic and magnetically separable properties and  $\text{Fe}_3\text{O}_4@\text{SiO}_2@\text{PS}$  complex as nanocarrier with the detection limit of 0.2 pg/mL and 0.3 pg/mL, respectively [45, 46].

In addition to cancer biomarkers, ECL immunosensor is also one of the common tools for clinical diagnosis of viruses. Babamiri et al. [47] used PAMAM dendrimers to immobilize  $\text{CdTe}@\text{CdS}$  QDs to construct a signal-amplified ECL immunosensor for detecting hepatitis B virus with a wide linear range from 3 fg/mL to 0.3 ng/mL. Zhang et al. [48] reported that 1-(3-dimethylaminopropyl)-3-ethylcarbodiimine (EDC)-activated  $\text{CdS}$  QDs could enhance the ECL strength of  $\text{CdS}$  QDs and constructed the ECL immunosensor of Zika virus with the detection limit of 0.3 fg/mL.

ECL immunosensors are also popular in the field of environmental monitoring due to their excellent sensitivity and specificity. However, competitive immune ECL sensors are often constructed to detect environmental pollution targets, because the environmental targets are mostly small molecules. Zhang et al. [49] used the  $\text{MoS}_2\text{-Au}$  hybrid nanocomposite with a large number of active sites as the matrix and graphene nanosheet/ $\text{CdSe}$  QDs composite as the ECL probe to construct an electrochemiluminescence immunosensor based on dual signal amplification for detection trace microcystin in water. Chen et al. [50] constructed a signal-enhanced



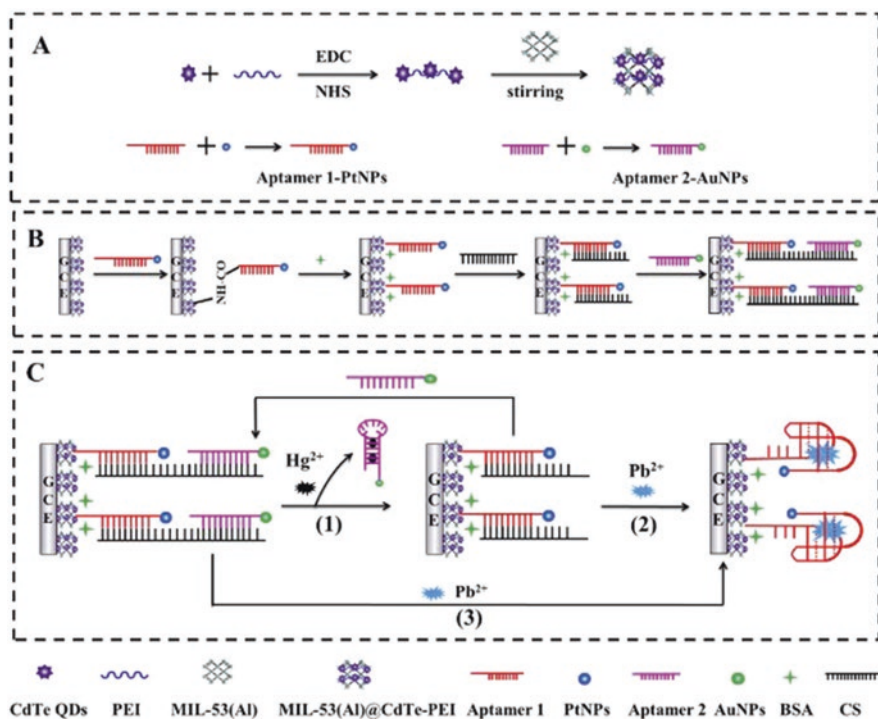
**Fig. 20.2** Schematic illustration of the preparation process of QDs-labeled Ab<sub>2</sub> and fabrication process of the proposed ECL nano-immunosensor. (Reprinted with permission from Dong et al. [45]. Copyright 2017: Elsevier)

ECL biosensor to detect diclofenac in environmental samples, using Pd NPs/PEI-GO-CdSe@CdS QDs composite material as the enhanced ECL luminary and Ce:ZnO as the substrate to improve the electron transfer rate. Chen et al. [51] constructed an ECL immunosensor with the detection limit of 0.33 pg/mL based on enrofloxacin antibiotics based on flower-like Au@BSA nanoparticles enriched with a large number of ECL luminescent CdSe QDs and Au/C<sub>60</sub>, which accelerated the electron transfer on the electrode surface.

### 20.4.2 Aptasensor

Aptamers are single-stranded DNA or RNA fragments screened by ligand index enrichment phylogeny [52]. Compared with traditional molecular recognition elements, aptamers have the advantages of simple synthesis, good stability, easy storage, high affinity, easy curing, and good specificity. Aptasensors are of great research significance in the field of gene expression analysis, forensic analysis, and clinical diagnosis, because aptamer has the ability to recognize molecular targets including ionic, small molecule, proteins, and cell.

Metal ion analysis is a fundamental and important area of ECL sensing because of the adverse effects of some metal ions on human health and environmental protection. To date, many ECL aptasensors have been manufactured for the determination of a range of metal ions. Wang et al. [53] prepared lanthanum-doped CdS QDs (CdS:La QDs) with significantly enhanced ECL intensity and constructed a mercury ion ( $\text{Hg}^{2+}$ ) aptasensor based on surface plasmon resonance and energy resonance transfer between CdS:La QDs and metal ions. Au NPs-based surface plasmonic resonance enhanced the ECL strength of CdS:La QDs (signal-on) when GCE/CdS:La QD-ssDNA 1 hybridized with Au NPs-ssDNA 2. In the presence of  $\text{Hg}^{2+}$ , the conformation of oligonucleotide changed from linear chain to hairpin due to the base pair of T-Hg<sup>2+</sup>-T. The ECL intensity of CdS:La QDs reduced (signal-off) on account of the forceful energy resonance transfer between CdS:La QDs and Au NPs. The difference of ECL intensity in the absence and presence of  $\text{Hg}^{2+}$  can be used to detect  $\text{Hg}^{2+}$  with the detection range of  $1 \times 10^{-12}$  to  $1 \times 10^{-5}$  mol/L and the detection limit of  $3 \times 10^{-13}$  mol/L. Similarly, Babamiri et al. [54] used CdTe@CdS QDs as the ECL emitter to build a  $\text{Hg}^{2+}$  ECL aptasensor based on the energy resonance transfer effect between CdTe@CdS QDs and Au NPs and the interaction of T-Hg<sup>2+</sup>-T base pair. Feng et al. [55] constructed an ECL aptasensor based on MIL-53(Al)@CdTe QDs luminescence, which can be used for multiple detection of mercury ions ( $\text{Hg}^{2+}$ ) and lead ions ( $\text{Pb}^{2+}$ ). As shown in Fig. 20.3, Aptamer 2-Au NPs



**Fig. 20.3** Schematic illustration of MIL-53(Al)@CdTe-PEI aptasensor fabrication and detection of  $\text{Hg}^{2+}$  and  $\text{Pb}^{2+}$ . (Reprinted with permission from Feng et al. [55]. Copyright 2020: Elsevier)

formed a hairpin structure and disengaged from the electrode, after GCE/MIL-53(Al)@CdTe QDs/aptamer 1-Pt NPs/aptamer 2-Au NPs recognizes  $\text{Hg}^{2+}$ . In the presence of  $\text{Pb}^{2+}$ , aptamer 1-Pt NPs captured  $\text{Pb}^{2+}$  to form G-quadruplexes, making the Pt NPs carried on aptamer1 close enough to CdTe QDs to generate ECL energy resonance transfer. The interaction of aptamers with  $\text{Hg}^{2+}$  and  $\text{Pb}^{2+}$  enhanced the energy resonance transfer between CdTe QDs and metal ions, resulting in the continuous decrease of ECL intensity. Therefore, ECL strength difference can be used for multiple detection of heavy metal ions with detection limits of  $4.1 \times 10^{-12}$  mol/L (path 1,  $\text{Hg}^{2+}$ ),  $3.7 \times 10^{-11}$  mol/L (path 2,  $\text{Pb}^{2+}$ ), and  $2.4 \times 10^{-11}$  mol/L (path 3,  $\text{Pb}^{2+}$ ), respectively.

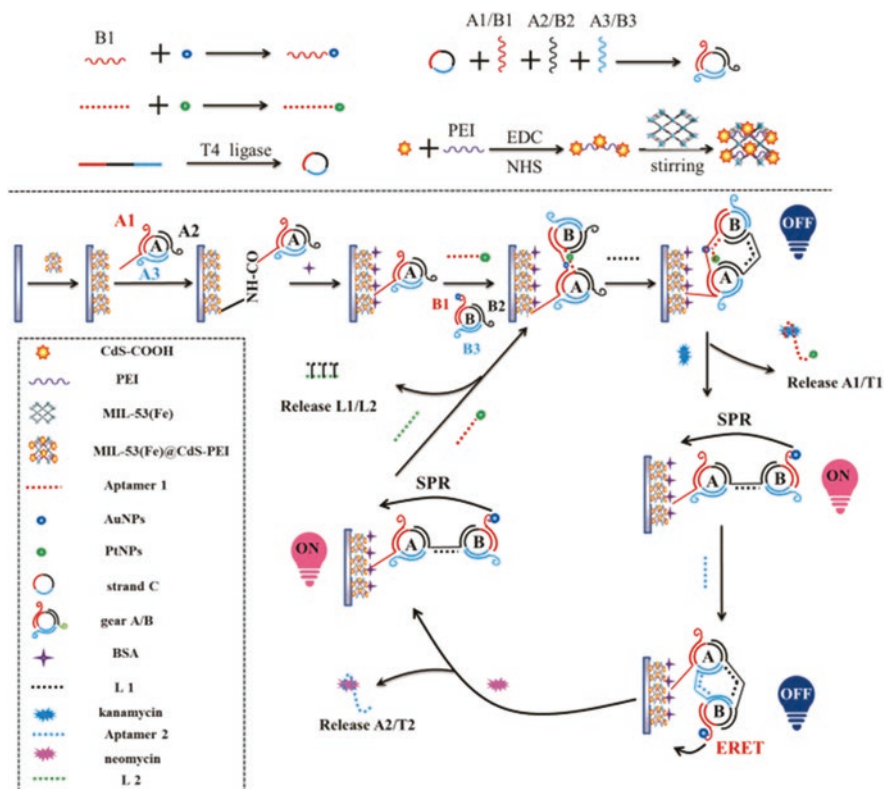
Quantitative detection of small molecules is very important in food safety, environmental problems, and disease diagnosis. Therefore, it is very necessary to develop a series of ECL sensors with high sensitivity and low cost. Liu et al. [56] developed a “signaloff-on” aptasensor for detection of chlorpyrifos using a high-efficiency electrochemiluminescence resonance energy transfer strategy between  $\text{MoS}_2/\text{CdS}$  nanospheres and silver/carbon quantum dots (Ag/CDs). Analogously, Gao et al. [57] and Wei et al. [58] used CdTe QDs and CdS QDs as donors and cyanine dyes as acceptors to construct aptasensors for Ochratoxin A with the detection limits of 0.17 pg/mL and 0.012 nmol/L, respectively. Feng et al. [59] designed a double-gear ECL aptasensor for the multiple detection of kanamycin and neomycin. As Fig. 20.4 shows, the GCE/MIL-53(Fe)@CdS-PEI electrode was assembled with gears and aptamers modified with metal materials, and the ECL signal was turned off due to the influence of the energy resonance transfer between Au NPs and CdS QDs. In the presence of kanamycin, ECL strength was enhanced because the surface plasmonic resonance between Au NPs and CdS QDs was dominant. The double gear was “closed” again and the energy resonance transfer between Au NPs and CdS QDs plays a leading role when the aptamer 2 was attached to the modified electrode. Subsequently, the introduced neomycin was completely hybridized with aptamer 2 to form a gear and detached from the electrode, resulting in enhanced ECL. The ingenious double-gear aptamer sensing mode realizes the multiple ECL detection of kanamycin and neomycin by a single luminant with low detection limit of  $1.7 \times 10^{-11}$  M and  $3.5 \times 10^{-10}$  M, respectively.

ECL aptasensors are suitable not only for the detection of ions and small molecules, but also for protein and cell detection. The ECL aptasensors for detection of carcinoembryonic antigen [60] and prostate-specific antigen [37] were constructed using CdS QDs as the donor and Au NPs or Pt NPs as receptors in the energy resonance transfer system. Ding et al. [61] constructed a ratiometric ECL cell aptasensor using CdTe QDs-labeled cancer cells aptamer as detection signal and luminol as internal standard.

### 20.4.3 Genosensor

Since the discovery of DNA molecule by Friedrich et al. in 1869, this biological molecule containing genetic information has become a research hotspot of biologists all over the world. Gene fragments are widely developed and used in



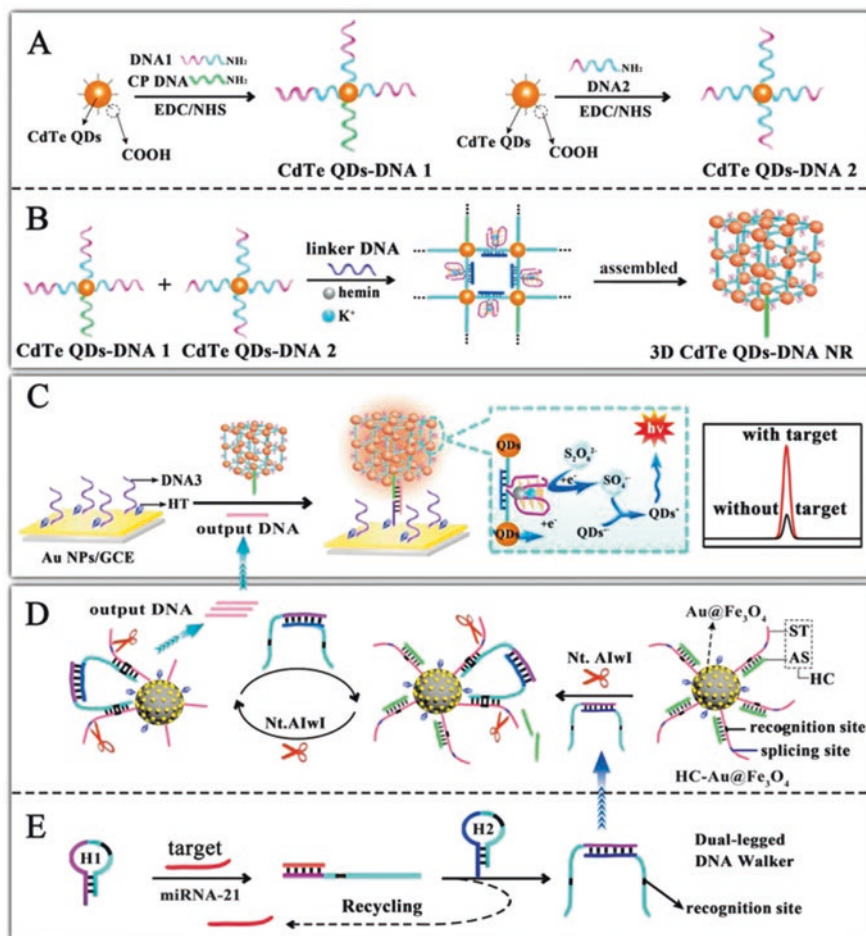


**Fig. 20.4** Schematic representation of an ECL aptasensor for kanamycin and neomycin detection. (Reprinted with permission from Feng et al. [59]. Copyright 2019: Elsevier)

biosensors, because the stable and specific molecular structure of genes is interacted by the base pairs of complementary sequences. ECL genosensor is a kind of sensor which takes the single-chain polynucleotides of known sequence as the sensitive element and transforms the biological signal formed by hybridization of complementary sequence to double-chain molecule into detectable light signal for expression through the transducer. In the beginning, genosensors were mainly used to explore the origin of life, study the evolution of species, and diagnose genetic diseases. With the continuous deepening of the intersection of interdisciplinary research, the application of genosensors in genetic diagnosis, drug research, environmental monitoring, and other fields has received increasing attention. Tan et al. [62] devised a brilliant enzyme-assisted multiple amplification strategy to construct a sensitive DNA biosensor using amplified PAMAM-Au-CdSe QDs ECL signal probes. The authors have designed a powerful hairpin template that contains an overhang nucleic acid segment (wathet) complementary to the target DNA, a specific sequence (yellow) for the recognition site of the nicking endonuclease, and a stem structure formed by two complementary sequences linked by 18-carbon spacer

(pink). When the target DNA was present, three phenomena were triggered in the hairpin template: (1) the target DNA hybridized with the overhanging region of the hairpin template, initiating the first polymerization and stopping at the site of the 18-carbon spacer block; (2) a double-stranded DNA with a recognition site for the nicking endonuclease was generated; and (3) the hairpin template was opened. Subsequently, the separated arm (blue) of the hairpin template anchored to a complementary sequence of the hairpin modified on the graphene-modified electrode, and the PAMAM-Au-CdSe QDs probe hybridized with the exposed stem of the hairpin and triggered the second polymerization reaction. With the extension of the ECL probe as the primer, the detached arm of the hairpin template was peeled off and hybridized with the new hairpin for a new cycle. At the same time, the first switch keeps producing a lot of DNA triggers (red). The DNA trigger can be hybridized directly with the hairpin template to produce the separation arm (blue), which then turns on the modified hairpin on the electrode to guide the second switch. A large number of ECL probes are fixed on the electrode based on cascade amplification technology to achieve ECL signal amplification and sensitive detection of target DNA. Dong et al. [63] constructed a signal-off biosensor for quantitative detection of DNA based on the anodic electrochemiluminescence of  $\text{Ru}(\text{bpy})_3^{2+}$  with CdSe QDs as co-reactants and the fact that  $\text{Ru}(\text{bpy})_3^{2+}$  can be inserted into the loop of hairpin DNA through electrostatic interaction to generate strong ECL signals. In addition, ECL energy resonance transfer and cyclic amplification techniques are also commonly used in DNA ECL biosensors [64, 65].

MicroRNAs (miRNAs) are a class of non-coding RNA molecules containing approximately 19–23 nucleotides that play an important regulatory role in physiological processes by regulating the expression of target genes. More and more reports have shown that abnormal expression of miRNAs is closely related to many cancer diseases. Therefore, the quantitative detection of highly sensitive miRNAs is of great research significance for cancer classification and early disease diagnosis. Yuan and colleagues have made great efforts to achieve the ultrasensitive detection of microRNAs. For example, Sun et al. [66] used a novel three-dimensional CdTe quantum dots–DNA nanorectification (3D CdTe QDs–DNA-NR) as a signal probe to construct an ultrasensitive microRNA-21 ECL biosensor based on the target-induced dual-legged DNA walker circular amplification strategy. As presented in Fig. 20.5, DNA 1 and DNA 2 were modified on the surface of CdTe QDs to form CdTe QDs–DNA 1 and CdTe QDs–DNA 2, respectively. Subsequently, a novel 3D CdTe QDs–DNA-NR, which demonstrated an excellent capacity of CdTe QDs and hemin/G-quadruplex for intense ECL emission in the CdTe QDs/ $\text{S}_2\text{O}_8^{2-}$ /hemin/G--quadruplex system, was hybridized from CdTe QDs–DNA 1, CdTe QDs–DNA 2 and Linker DNA. Au NPs were electrodeposited at the GCE electrode interface to immobilize DNA 3 by the Au–S bond. Then, 3D CdTe QDs–DNA-NR was attached to the surface of the electrode based on the ligation of CP DNA to DNA 3 with the help of output DNA from the target-induced double-legged DNA walker cyclic amplification strategy. When the target miRNA-21 was present, it was hybridized with Hairpin 1 and Hairpin 2 to form a dual-legged DNA walker. Then, with the participation of Nt. A1wI, the support of  $\text{Au}@\text{Fe}_3\text{O}_4$  modified with Substrate DNA



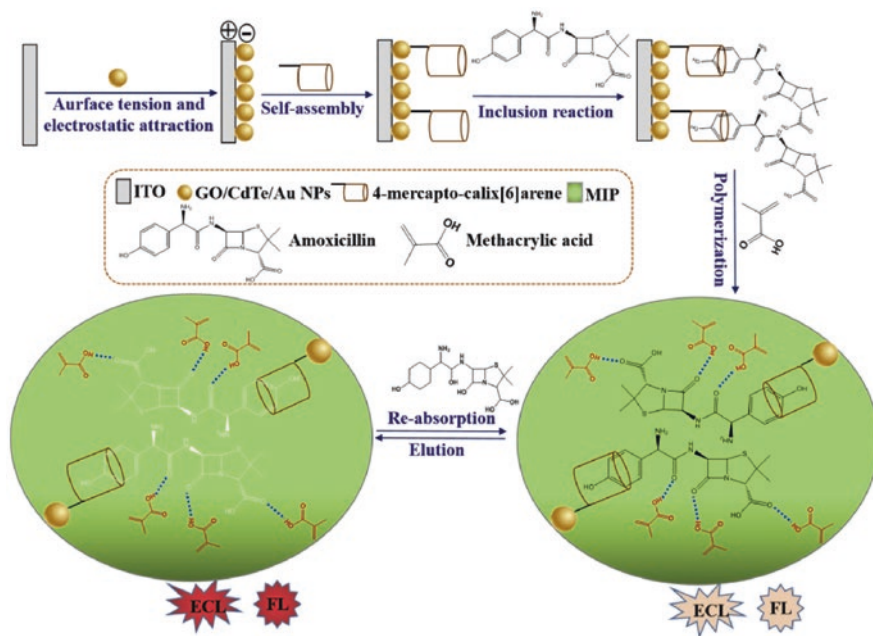
**Fig. 20.5** Schematic illustration of the biosensor. (a and b) Preparation of the 3D CdTe QDs–DNA–NR; (c) operating principle of the biosensor for miRNA-21 detection and the reaction mechanism of the ECL biosensor; (d and e) synthesis and working principle of target-induced dual-legged DNA walker circular amplification. (Reprinted with permission from Sun et al. [66]. Copyright 2019: American Chemical Society)

(ST) and Assistant DNA (AS), the dual-legged DNA walker free-walked on the HC–Au@Fe<sub>3</sub>O<sub>4</sub> to operate the target-induced circular amplification strategy for the generation of numerous output DNA, and the target miRNA-21 was successfully detected with a low detection limit of 34 amol/L. Similarly, an “on–off–super on” ECL biosensor for the ultrasensitive detection of miRNA-141 was constructed by combining the structure of the earlier 3D walking machine with the unique ECL performance of the range-based energy transfer between CdS:Mn QDs and Au NPs [67]. Then, Yuan’s team improved the 3D DNA walking machine to build a remarkable bidirectional DNA walking machine that can detect two miRNAs

simultaneously, by designing a DNA walking machine which could move along the track and then move back to the original position following the previous steps [68].

#### 20.4.4 MIP Sensor

Molecular imprinting technology (MIT) is a molecular recognition technology that can specifically recognize a given analyte or a specific group in an analyte from a multicomponent system. The core research content of MIT is molecularly imprinted polymer (MIP), which has the advantages of good stability, reproducibility, strong specificity and adsorption capacity. MIP-ECL sensor combines the advantages of the high sensitivity of ECL and high selectivity of MIP and is widely used in clinical diagnosis, environmental monitoring, and food safety. Amoxicillin, as a commonly used antibiotic, does great harm to human health due to excessive abuse of residues in the environment and animal and plant products. As displayed in Fig. 20.6, Li et al. [69] manufactured a MIP-based sensor with dual recognition and dual detection modes (fluorescence and electrochemiluminescence) based on graphene oxide loaded with CdTe quantum dots/gold nanoparticles (GO/CdTe/Au NPs) and MIP prepared using amoxicillin as the template molecule. Diethylstilbestrol, as a typical synthetic exogenous estrogen, is often used as an animal growth promoter and



**Fig. 20.6** Fabrication of the sensor for amoxicillin detection. (Reprinted with permission from Li et al. [69]. Copyright 2020: Elsevier)

widely used in aquaculture and animal husbandry. Diethylstilbestrol residue in human body is associated with potential teratogenicity and carcinogenicity, which can cause other reproductive and endocrine diseases. Zhao et al. [70] and Wang et al. [71] constructed ECL biosensor with the limit of detection of 0.25 pmol/L and 0.1 pg/mL based on diethylstilbestrol MIP using CdTe@ZnS/r-GO and CdS QDs as luminescent probe, respectively. MIP-ECL sensors are not only used in the environment and food fields, but also often used in disease diagnosis. Cao et al. [72] constructed creatinine sensor and sialic acid sensor, respectively, based on the phenomenon that PEI-CdS QDs significantly promoted the ECL emission of Ru(bpy)<sub>3</sub><sup>2+</sup> and MIT technology.

## 20.5 Conclusions and Perspectives

ECL biosensor is a commercially successful analysis platform with excellent specificity, outstanding sensitivity, satisfactory selectivity, simple construction, low cost, fast response, and simple operation. Moreover, ECL is widely used for the detection of a wide range of analytes, such as biomarkers, toxins, metal ions, viruses, and cells. The uniqueness of ECL technology and the popularity of commercial ECL instruments not only provide more possibilities for new disease diagnosis, but also pave the way for the application of ECL analysis strategies in drug screening, biological defense, environmental monitoring, and food testing. This chapter introduced the basic mechanism and common detection strategies of ECL biosensors based on II–VI semiconductor quantum dots and reviewed the applications of ECL biosensing systems, such as ECL immunosensors, aptasensor, genosensor, and MIP sensor.

Although many examples of ECL sensors are cited in this article, the ECL method based on II–VI quantum dots is still an underestimated and underutilized analysis technique. Improving the sensitivity of ECL biosensors and reducing their construction cost should continue to be done. The future development trend of ECL biosensing based on II–VI quantum dots may include the following: (1) Improve the participation of quantum dots in ECL sensors. Further development of high-quantum yield aqueous quantum dots and high-performance nanocarriers is crucial. It is necessary to continuously improve the synthesis methods and modification schemes of II–VI quantum dots to obtain satisfactory ECL emitters, because the perfect quantum dots are the basis of ECL sensors. In addition, high-performance nanocarriers can not only enrich quantum dots but also improve the efficiency of the ECL reaction, so finding new and efficient nanocarriers is a sustainable research field. (2) Construct a low-potential ECL sensing strategy. The ECL reaction starts under the excitation of voltage, so the voltage level is the key to ECL generation. High potentials may interfere with the stability of biomolecules. Therefore, it is very necessary to construct an ECL system with low excitation potential. Selection of low oxidation luminescence groups, matching of low potential co-reaction, and designing of ingenious electrode structure will help achieve low excitation potential ECL. (3)

Develop the ECL of a single entity [73]. Single-entity ECL analysis includes intensity- and imaging-based ECL. The study of a single-entity analysis has great potential in elucidating new natural truths, which are averaged out in the overall analysis or hidden in complex systems. Currently, the development of single-entity analysis based on II–VI quantum dots is still very scarce. Therefore, it is meaningful to construct more single-entity analysis of II–VI quantum dots to gain a deeper understanding of science and nature.

Additionally, we found that not many ECL sensors have been truly commercialized, although the development of ECL sensors has grown exponentially in recent years. The portability of the sensor and the accuracy of the analysis are necessary steps to commercialize the ECL biosensor. Therefore, how to improve the portability and result accuracy of ECL biosensors is the common direction of all future biosensors.

## References

1. Ma XG, Gao WY, Du FX, Yuan F, Yu J, Guan YR, et al. Rational design of electrochemiluminescent devices. *Acc Chem Res.* 2021;54(14):2936–45.
2. Miao WJ. Electrogenated chemiluminescence and its biorelated applications. *Chem Rev.* 2008;108(7):2506–53.
3. Peng H, Huang Z, Sheng Y, Zhang X, Liu J. Pre-oxidation of gold nanoclusters results in a 66% anodic electrochemiluminescence yield and drives mechanistic insights. *Angew Chem Int Ed.* 2019;58(34):11691–4.
4. Chen MY, Ning ZQ, Chen KY, Zhang YJ, Shen YF. Recent advances of electrochemiluminescent system in bioassay. *J Anal Test.* 2020;4(2):57–75.
5. Lu HJ, Xu JJ, Zhou H, Chen HY. Recent advances in electrochemiluminescence resonance energy transfer for bioanalysis: fundamentals and applications. *Trac-Trends Analyt Chem.* 2020;122:115746.
6. Wang FF, Liu YQ, Fu CP, Li N, Du M, Zhang LN, et al. Paper-based bipolar electrode electrochemiluminescence platform for detection of multiple miRNAs. *Anal Chem.* 2021;93(3):1702–8.
7. Liu ZY, Qi WJ, Xu GB. Recent advances in electrochemiluminescence. *Chem Soc Rev.* 2015;44:3117–42.
8. Zhou Y, Chen SH, Luo XL, et al. Ternary electrochemiluminescence nanostructure of Au nanoclusters as a highly efficient signal label for ultrasensitive detection of cancer biomarkers. *Anal Chem.* 2018;90(16), 10:024–30.
9. Habtamu HB, Sentic M, Silvestrini M, De Leo L, Not T, Arbault S, Manojlovic D, Sojic N, et al. A sensitive electrochemiluminescence immunosensor for celiac disease diagnosis based on nanoelectrode ensembles. *Anal Chem.* 2015;87(24):12080–7.
10. Rusling JF, Forster RJ. Biosensors designed for clinical applications. *Biomedicines.* 2021;9(7):702.
11. Zhao CQ, Zhou J, Wu K-W, Ding SN, Xu JJ, Chen HY. Plasmonic enhanced gold nanoclusters-based photoelectrochemical biosensor for sensitive alkaline phosphatase activity analysis. *Anal Chem.* 2020;92(10):6886–92.
12. Zhao CQ, Ding SN, Xu JJ, Chen HY. ZnAgInS quantum dot-decorated BiOI heterostructure for cathodic photoelectrochemical bioanalysis of glucose oxidase. *Acs Appl Nano Mater.* 2020;3(11):11489–96.
13. Zhao CQ, Ding SN. Perspective on signal amplification strategies and sensing protocols in photoelectrochemical immunoassay. *Coord Chem Rev.* 2019;391:1–14.

14. Liu JX, Liang XL, Chen F, Ding SN. Ultrasensitive amperometric cytosensor for drug evaluation with monitoring early cell apoptosis based on  $\text{Cu}_2\text{O@PtPd}$  nanocomposite as signal amplified label. *Sensors Actuators B Chem.* 2019;300:127046.
15. Liu JX, Bao N, Luo X, Ding SN. Nonenzymatic amperometric aptamer cytosensor for ultrasensitive detection of circulating tumor cells and dynamic evaluation of cell surface N-glycan expression. *Acs Omega.* 2018;3(8):8595–604.
16. Zuo JY, Jiao YJ, Zhu J, Ding SN. Rapid detection of severe fever with Thrombocytopenia syndrome virus via colloidal gold immunochromatography assay. *Acs Omega.* 2018;3(11):15399–406.
17. Wang XY, Zhu KD, Zhu J, Ding SN. Photonic crystal of polystyrene nanomembrane: signal amplification and low triggered potential electrochemiluminescence for tetracycline detection. *Anal Chem.* 2021;93(5):2959–67.
18. Wang XY, Wu MX, Ding SN. Anodic electrochemiluminescence from  $\text{CsPbBr}_3$  perovskite quantum dots for an alkaline phosphatase assay. *Chem Commun.* 2020;56(58):8099–102.
19. Li ZZ, Wu MX, Ding SN. Anodic near-infrared electrochemiluminescence from Cu-doped CdTe quantum dots for tetracycline detection. *Anal Methods.* 2021;13(20):2297–304.
20. Zhang S, Liu Y. Recent progress of novel electrochemiluminescence nanoprobe and their analytical applications. *Front Chem.* 2021;8:626243.
21. Rahn KL, Anand RK. Recent advancements in bipolar electrochemical methods of analysis. *Anal Chem.* 2021;93(1):103–23.
22. Du F, Chen Y, Meng C, Lou B, Zhang W, Xu G. Recent advances in electrochemiluminescence immunoassay based on multiple-signal strategy. *Curr Opin Electrochem.* 2021;28:100725.
23. Ding ZF, Quinn BM, Haram SK, Pell LE, Korgel BA, Bard AJ. Electrochemistry and electrogenerated chemiluminescence from silicon nanocrystal quantum dots. *Science.* 2002;296(5571):1293–7.
24. Abdussalam A, Xu G. Recent advances in electrochemiluminescence luminophores. *Anal Bioanal Chem.* 2022;414(1):131–46.
25. Brus LE. Electron-electron and electron-hole interactions in small semiconductor crystallites: the size dependence of the lowest excited electronic state. *J Chem Phys.* 1984;80(9):4403–9.
26. Qi H, Wang S, Jiang X, Fang Y, Wang A, Shen H, et al. Research progress and challenges of blue light-emitting diodes based on II-VI semiconductor quantum dots. *J Mater Chem C.* 2020;8(30):10160–73.
27. Peng X. An essay on synthetic chemistry of colloidal nanocrystals. *Nano Res.* 2009;2(6):425–47.
28. Zhou J, Zhu M, Meng R, Qin H, Peng X. Ideal CdSe/CdS core/shell nanocrystals enabled by entropic ligands and their core size-, shell thickness-, and ligand-dependent photoluminescence properties. *J Am Chem Soc.* 2017;139(46):16556.
29. Chen O, Zhao J, Chauhan VP, Jian C, Wong C, Harris DK, et al. Compact high-quality CdSe-CdS core-shell nanocrystals with narrow emission linewidths and suppressed blinking. *Nat Mater.* 2013;12(5):445–51.
30. Martinez-Perinan E, Gutierrez-Sanchez C, Garcia-Mendiola T, Lorenzo E. Electrochemiluminescence biosensors using screen-printed electrodes. *Bios.* 2020;10(9):118.
31. Zhang Q, Zhang X, Ma Q. Recent advances in visual electrochemiluminescence analysis. *Anal Test.* 2020;4(2):92–106.
32. Feng L, Hua C, Lin X. Potential-resolved electrochemiluminescence of  $\text{Ru}(\text{bpy})_3^{2+}/\text{C}_2\text{O}_4^{2-}$  system on gold electrode. *Luminescence.* 2002;17(2):117–22.
33. Liang XL, Bao N, Luo X, Ding SN. CdZnTeS quantum dots based electrochemiluminescent image immunoanalysis. *Biosens Bioelectron.* 2018;117:145–52.
34. Zhu HY, Ding SN. Dual-signal-amplified electrochemiluminescence biosensor for microRNA detection by coupling cyclic enzyme with CdTe QDs aggregate as luminophore. *Biosens Bioelectron.* 2019;134:109–16.
35. Shan Y, Zhang HL, Zhu Y, Wang Y, Song HJ, Shi CG. Electrochemiluminescent CdTe nanocrystal/reduced graphene oxide composite films for the detection of diethylstilbestrol. *ACS Appl Nano Mater.* 2020;3(5):4670–80.

36. Du DX, Shu JN, Guo MQ, Haghghatbin MA, Yang D, Bian ZP, et al. Potential-resolved differential electrochemiluminescence immunosensor for cardiac troponin I based on MOF-5-wrapped CdS quantum dot nanoluminophores. *Anal Chem.* 2020;92(20):14113–21.
37. Dai PP, Liu C, Xie CG, Ke JJ, He Y, Wei LY, et al. TiO<sub>2</sub> nanotubes loaded with CdS nanocrystals as enhanced emitters of electrochemiluminescence: application to an assay for prostate-specific antigen. *Anal Bioanal Chem.* 2020;412(6):1375–84.
38. Hu L, Wu Y, Xu M, Gu W, Zhu C. Recent advances in co-reaction accelerators for sensitive electrochemiluminescence analysis. *Chem Commun.* 2020;56(75):10989–99.
39. Craw P, Balachandran W. Isothermal nucleic acid amplification technologies for point-of-care diagnostics: a critical review. *Lab Chip.* 2012;12(14):2469–86.
40. Liu Q, Xie XL, Mao CJ, Chen JS, Niu HL, Song JM. Electrochemiluminescent biosensor with DNA link for selective detection of human IgG based on steric hindrance. *Talanta.* 2019;194:745–51.
41. Achermann M, Petruska MA, et al. Energy-transfer pumping of semiconductor nanocrystals using an epitaxial quantum well. *Nature.* 2004;429(6992):642–6.
42. Zhang H, Zhang C, Liu D, Zuo FM, Chen SH, Yuan R, et al. A ratiometric electrochemiluminescent biosensor for Con A detecting based on competition of dissolved oxygen. *Biosens Bioelectron.* 2018;120:40–6.
43. Feng QM, Shen YZ, Li MX, Zhang ZL, Zhao W, Xu JJ, et al. Dual-wavelength electrochemiluminescence ratiometry based on resonance energy transfer between Au nanoparticles functionalized g-C<sub>3</sub>N<sub>4</sub> nanosheet and Ru(bpy)<sub>3</sub><sup>2+</sup> for microRNA detection. *Anal Chem.* 2016;88(1):937–44.
44. Lu HJ, Zhao W, Xu JJ, Chen HY. Visual electrochemiluminescence ratiometry on bipolar electrode for bioanalysis. *Biosens Bioelectron.* 2018;102:624–30.
45. Dong H, Han TT, Ren LL, Ding SN. Novel sandwich-structured electrochemiluminescence immunosensing platform via CdTe quantum dots-embedded mesoporous silica nanospheres as enhanced signal labels and Fe<sub>3</sub>O<sub>4</sub>@SiO<sub>2</sub>@PS nanocomposites as magnetic separable carriers. *J Electroanal Chem.* 2017;806:32–40.
46. Ren LL, Dong H, Han TT, Chen Y, Ding SN. Enhanced anodic electrochemiluminescence of CdTe quantum dots based on electrocatalytic oxidation of a co-reactant by dendrimer-encapsulated Pt nanoparticles and its application for sandwiched immunoassays. *Analyst.* 2017;142(20):3934–41.
47. Babamiri B, Hallaj R, Salimi A. Ultrasensitive electrochemiluminescence immunosensor for determination of hepatitis B virus surface antigen using CdTe@CdS-PAMAM dendrimer as luminescent labels and Fe<sub>3</sub>O<sub>4</sub> nanoparticles as magnetic beads. *Sensors Actuators B Chem.* 2018;254:551–60.
48. Zhang HJ, Zhu J, Bao N, Ding SN. Enhanced electrochemiluminescence of CdS quantum dots capped with mercaptopropionic acid activated by EDC for Zika virus detection dagger. *Analyst.* 2021;246(9):2928–35.
49. Zhang JJ, Liu WJ, Gong W, Liu N, Jia YT, Ding D, et al. Ultrasensitive determination of Microcystin-Leucine-Arginine (MCLR) by an Electrochemiluminescence (ECL) immunosensor with graphene nanosheets as a scaffold for cadmium-selenide quantum dots (QDs). *Anal Lett.* 2021;54(16):2523–36.
50. Chen WL, Zhu Q, Tang QH, Zhao K, Deng AP, Li JG. Ultrasensitive detection of diclofenac based on electrochemiluminescent immunosensor with multiple signal amplification strategy of palladium attached graphene oxide as bioprobes and ceria doped zinc oxide as substrates. *Sensors Actuators B Chem.* 2018;268:411–20.
51. Chen WL, Zhou R, Yao X, Zhao K, Deng AP, Li JG. Sensitive detection of enrofloxacin using an electrochemiluminescence immunosensor based on gold-functionalized C-60 and Au@BSA nanoflowers. *New J Chem.* 2018;42(17):14142–8.
52. Shi ZX, Li GK, Hu YF. Progress on the application of electrochemiluminescence biosensor based on nanomaterials. *Chin Chem Lett.* 2019;30(9):1600–6.



53. Wang C, Chen M, Wu JL, Mo FJ, Fu YZ. Multi-functional electrochemiluminescence aptasensor based on resonance energy transfer between Au nanoparticles and lanthanum ion-doped cadmium sulfide quantum dots. *Anal Chim Acta*. 2019;1086:66–74.
54. Babamiri B, Salimi A, Hallaj R. Switchable electrochemiluminescence aptasensor coupled with resonance energy transfer for selective attomolar detection of Hg<sup>2+</sup> via CdTe@CdS/dendrimer probe and Au nanoparticle quencher. *Biosens Bioelectron*. 2018;102:328–35.
55. Feng DF, Li PH, Tan XC, Yeyu W, Wei FC, Du FK, et al. Electrochemiluminescence aptasensor for multiple determination of Hg<sup>2+</sup> and Pb<sup>2+</sup> ions by using the MIL-53(Al)@CdTe-PEI modified electrode. *Anal Chim Acta*. 2020;1100:232–9.
56. Liu JH, Chen PP, Xia FQ, Liu Z, Liu HB, Yi JL, et al. Sensitive electrochemiluminescence aptasensor for chlorpyrifos detection based on resonance energy transfer between MoS<sub>2</sub>/CdS nanospheres and Ag/CQDs. *Sensors Actuators B Chem*. 2020;315:128098.
57. Gao JW, Chen ZY, Mao LB, Zhang W, Wen W, Zhang XH, et al. Electrochemiluminescent aptasensor based on resonance energy transfer system between CdTe quantum dots and cyanine dyes for the sensitive detection of Ochratoxin A. *Talanta*. 2019;199:178–83.
58. Wei M, Wang CL, Xu ES, Chen J, Xu XL, Wei W, et al. A simple and sensitive electrochemiluminescence aptasensor for determination of ochratoxin A based on a nicking endonuclease-powered DNA walking machine. *Food Chem*. 2019;282:141–6.
59. Feng DF, Tan XC, Wu YY, Ai CH, Luo YN, Chen QY, et al. Electrochemiluminescence nanogears aptasensor based on MIL-53(Fe)@CdS for multiplexed detection of kanamycin and neomycin. *Biosens Bioelectron*. 2019;129:100–6.
60. Cao JT, Wang YL, Wang JB, Zhou QM, Ma SH, Liu YM. An electrochemiluminescence ratiometric self-calibrated biosensor for carcinoembryonic antigen detection. *J Electroanal Chem*. 2018;814:111–7.
61. Ding CF, Li YX, Wang L, Luo XL. Ratiometric electrogenerated chemiluminescence cytosensor based on conducting polymer hydrogel loaded with internal standard molecules. *Anal Chem*. 2019;91(1):983–9.
62. Tan L, Ge JJ, Jiao M, Jie GF, Niu SY. Amplified electrochemiluminescence detection of DNA based on novel quantum dots signal probe by multiple cycling amplification strategy. *Talanta*. 2018;183:108–13.
63. Dong YP, Gao TT, Zhou Y, Jiang LP, Zhu JJ. Anodic electrogenerated chemiluminescence of Ru(bpy)<sub>3</sub><sup>2+</sup> with CdSe quantum dots as coreactant and its application in quantitative detection of DNA. *Sci Rep*. 2015;5:15392.
64. Lu LP, Wu J, Li M, Kang TF, Cheng SY. Detection of DNA damage by exploiting the distance dependence of the electrochemiluminescence energy transfer between quantum dots and gold nanoparticles. *Microchim Acta*. 2015;182(1–2):233–9.
65. Jie GF, Qin YQ, Meng QM, Wang JL. Autocatalytic amplified detection of DNA based on a CdSe quantum dot/folic acid electrochemiluminescence energy transfer system. *Analyst*. 2015;140(1):79–82.
66. Sun MF, Liu JL, Chai YQ, Zhang J, Tang Y, Yuan R. Three-dimensional cadmium telluride quantum dots-DNA nanoreticulation as a highly efficient electrochemiluminescent emitter for ultrasensitive detection of microRNA from cancer cells. *Anal Chem*. 2019;91(12):7765–73.
67. Xu ZQ, Liao LL, Chai YQ, Wang HJ, Yuan R. Ultrasensitive electrochemiluminescence biosensor for microRNA detection by 3D DNA walking machine based target conversion and distance-controllable signal quenching and enhancing. *Anal Chem*. 2017;89(16):8282–7.
68. Peng LC, Zhang P, Chai YQ, Yuan R. Bi-directional DNA walking machine and its application in an enzyme-free electrochemiluminescence biosensor for sensitive detection of microRNAs. *Anal Chem*. 2017;89(9):5036–42.
69. Li SH, Ma XH, Pang CH, Li HB, Liu CH, Xu Z, et al. Novel molecularly imprinted amoxicillin sensor based on a dual recognition and dual detection strategy. *Anal Chim Acta*. 2020;1127:69–78.
70. Zhao WR, Kang TF, Xu YH, Zhang X, Liu H, Ming AJ, et al. Electrochemiluminescence solid-state imprinted sensor based on graphene/CdTe@ZnS quantum dots as luminescent probes for low-cost ultrasensing of diethylstilbestrol. *Sensors Actuators B Chem*. 2020;306:127563.

71. Wang ZH, Qian YX, Wei XL, Zhang YF, Wu GF, Lu XQ. An “on-off” electrochemiluminescence biosensor based on molecularly imprinted polymer and recycling amplifications for determination of dopamine. *Electrochim Acta*. 2017;250:309–19.
72. Cao N, Zhao FQ, Zeng BZ. A novel self-enhanced electrochemiluminescence sensor based on PEI-CdS/Au@SiO<sub>2</sub>@RuDS and molecularly imprinted polymer for the highly sensitive detection of creatinine. *Sensors Actuators B Chem*. 2020;306:127591.
73. Zhao W, Chen HY, Xu JJ. Electrogenerated chemiluminescence detection of single entities. *Chem Sci*. 2021;12(16):5720–36.

# Chapter 21

## Electrochemical Biosensors



Mayank Garg, Arushi Gupta, Amit L. Sharma, and Suman Singh

### 21.1 Introduction

Electrochemical biosensors are the most reported and sought-after biosensors for almost all the molecules of interest. By definition, these are the analytical devices which help in the detection of analytes of interest by recording the electrochemical changes taking place in the system. These have been developed for monitoring environmental health, personal health, food quality and so on [15]. By virtue of its simple construction, low sample volumes, high throughput, miniaturization, portability, and cost-effectiveness, many of the electrochemical biosensors have been commercialized, for instance glucometers. The integration of the electrochemical biosensors with smartphones makes them future proof and enables the IoT platform for personalized healthcare [37].

Abundant literature is available for the detailed analysis of the electrochemical biosensors, which can be of interest to the readers. However, this chapter focuses only on the construction of the electrochemical biosensors made from core-shell nanostructures. The most essential part of an electrochemical biosensor is an immobilization matrix. This largely provides a surface for the electrochemical reactions to take place. Generally, nanomaterials are employed as immobilization matrices

---

Contributed equally for the first authorship.

---

M. Garg  
Texas A&M University, College Station, TX, USA

A. Gupta · A. L. Sharma · S. Singh (✉)  
CSIR- Central Scientific Instruments Organisation, Chandigarh, Uttar Pradesh, India

Academy of Scientific and Innovative Research (AcSIR), Ghaziabad, Uttar Pradesh, India  
e-mail: [ssingh@csio.res.in](mailto:ssingh@csio.res.in)

because of high surface-to-volume ratio, ease of synthesis, low toxicity, and biocompatibility. For chemo-sensors, these nanomaterials act as catalysts for the oxidation or reduction of the analytes, thereby generating a signature electrochemical signal. In case of biosensors, these nanomaterials provide a functional surface for the immobilization of the bio-recognition elements such as antibodies, aptamers, or peptides as well as provide electrochemical signals.

A comprehensive knowledge is required prior to fabricating an electrochemical biosensor. In this regard, this chapter gives an overview of various electrochemical techniques, sensing platforms, importance of nanomaterials, especially core-shell nanostructures for developing electrochemical biosensors.

## 21.2 Electrochemical Techniques Used in Biosensors

Based on the electrochemical changes taking place in the reaction, the choice of the suitable electrochemical technique varies. While recording electrochemical signals from a biosensor, a researcher can choose amongst the following broad techniques.

### 21.2.1 Voltammetry

Voltammetry involves the study of current generated as a result of application of variable potential to a system under observation [3]. There are multiple variations of voltammetry such as cyclic voltammetry (CV), differential pulse voltammetry (DPV), and linear sweep voltammetry (LSV). In a CV measurement, the current is constantly recorded from the system while the potentiostat is applying varying potential. This technique is helpful in understanding the redox behavior of the analytes [5]. This is the simplest electrochemical technique, which is often favored while understanding the electrochemical nature of the electrodes and materials. For DPV, the potential is applied in a linear ramp-like fashion and the current is recorded [6]. DPV is highly sensitive as compared to a CV scan because in DPV only the Faradaic current is measured as opposed to both Faradaic and non-Faradaic current in a CV. As a result, a lot of publications report the use of DPV for the electrochemical biosensors over CV. Garg et al. [12] compared the electrochemical sensitivity of CV and DPV against the electrochemical detection of ferritin. The work reported the use of biosurfactant-functionalized tungsten disulfide quantum dots for the modification of the screen-printed electrode, which was further modified with anti-ferritin antibodies. The modified electrode was then tested against varying ferritin concentrations using both DPV and CV. It was observed that a better limit of detection (LOD) was obtained with DPV as compared to CV.

### 21.2.2 *Amperometry*

Amperometry is the most used electrochemical technique for bioanalysis. In amperometry, a constant potential (usually the oxidation or reduction potential of the analyte) is applied to the system and the generated current is recorded. More often, the generated current is reported as a function of time. This helps in the analysis of redox behavior of the analytes at the interface of the electrode surface and electrolyte [22]. It is the most used method for the systems, wherein current is generated due to biochemical reactions between the biomolecules such as enzymes and their substrates. This is the oldest known technique for the analysis of glucose concentrations, and is still being employed. The oxidation of glucose into gluconic acid by glucose oxidase generates electrons, signaling an increase in the systems current. This current is monitored over time to analyze the kinetics of glucose oxidation [7]. In similar fashion, catechol can also be detected using biosensors. In a work by Singh et al., the authors demonstrated the use of gold nanoparticle-coated surface with immobilized tyrosinase enzyme for the amperometric detection of catechol [34].

### 21.2.3 *Impedimetry*

Impedimetry or the measurement of impedance is one of the most popular electrochemical techniques for biosensing applications. In this technique, a sinusoidal voltage is applied to the system under observation and the impedance generated is then reported as a Nyquist plot [16]. A Nyquist plot is made from two components, i.e., real and imaginary impedance. For a typical Nyquist plot, often a semicircle is obtained. The diameter of the semicircle is directly proportional to the resistance on the surface. The larger the diameter, the larger is the resistance. In some cases, a linear curve is also obtained along with the semicircle, indicating Warburg resistance, representing a diffusion-controlled process. Nyquist plots are useful for the calculation of charge transfer resistance. Usually, charge transfer resistance is a sum of solution resistance and polarization resistance. As a thumb rule, larger the resistance on the surface, higher will be its charge transfer resistance. In biosensing context, the increase in the resistance on the surface can help in the determination of analytes of interest. Garg et al. [13] reported the use of electrochemical impedance spectroscopy for the electrochemical detection of ferritin. The work reported the use of a screen-printed electrode modified with white graphene quantum dots, which were used for the immobilization of anti-ferritin antibodies. These antibodies were able to capture ferritin. Since antibodies and antigen are biomolecules, they hinder the flow of electrons to the electrode surface, thus creating resistance. Hence, higher the antigen concentration, more is the antigen-antibody interactions and higher will be the charge transfer resistance.

## 21.3 Electrochemical Sensing Platforms

Having discussed the various electrochemical techniques in the previous section, it is important to discuss the different configurations of the electrochemical sensing platforms. These can be broadly classified into two major classifications:

### 21.3.1 Non-portable Platforms

As the name indicates, the non-portable platforms use non-portable potentiostats. These are conventional and bulky instrumentation which cannot be moved around limiting their applicability for on-site usage. Figure 21.1a shows a conventional potentiostat with (i) potentiostat, (ii) three-cell electrode system, (iii) working pencil electrode, (iv) reference electrode, and (v) counter electrode. Despite the limitation of their bulkiness, these have various advantages over the portable ones. The most noticeable advantage is their high sensitivity and ability to upgrade (multiplexing or bi-potentiostats). These instruments are compatible with almost all types of electrodes such as pencil electrodes, interdigitated electrodes, and screen-printed electrodes. The pencil electrodes can be used multiple times after cleaning.

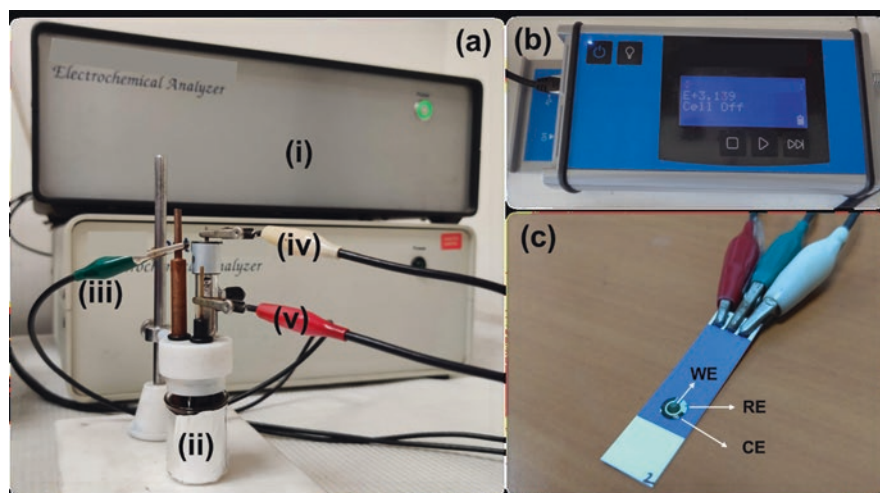


Fig. 21.1 (a) Non-portable platform; (b) portable platform; (c) screen-printed electrode

### 21.3.2 *Portable Platforms*

The use of portable platforms enables fabrication of on-site detection platforms. These portable systems can even be worn directly over the body to allow for continuous and real-time monitoring of bodily functions. These portable systems can be controlled wirelessly giving huge advantage over the conventional non-portable systems. Figure 21.1b shows one such portable potentiostat. Generally, screen-printed electrodes are used in the portable platforms because of their small size, compactness, and low cost. These electrodes are intended for one-time use and are made from plastic or ceramic materials. Figure 21.1c shows a screen-printed electrode having WE: working electrode, RE: reference electrode, and CE: counter electrode.

### 21.3.3 *Steps for Fabrication of an Electrochemical Biosensor*

The following is a broad sequence that is generally employed for the fabrication of a biosensor:

- *Electrode preparation:* Prior to using an electrode for any application, it should be cleaned thoroughly. For most of the pencil electrodes, they are first polished with coarse and smooth alumina powder to remove any contamination from the electrode surface. The polished electrode is then sonicated in water and ethanol to remove any trace chemicals from the previous usage. The electrodes are then air-dried and used for any modification steps [30].
- *Electrode modification:* Since this chapter is discussing the use of nanomaterials for biosensor fabrication, this section will focus entirely on electrode modification using nanomaterials. Suspensions or solutions of nanomaterials are used for electrode modification. The simplest method of electrode modification is using the drop-casting method, wherein a small quantity of the sample is placed over the electrode surface and allowed to air-dry. Another approach of electrode modification is the use of electrodeposition, wherein the working electrode is subjected to a seed solution of the material (for instance, chloroauric acid for gold nanoparticles) while subjecting the electrode to an oxidation or reduction potential. This causes the growth and electrodeposition of the nanomaterial directly over the working electrode [31]. This nanomaterial-modified surface is then modified further with bio-recognition elements such as antibodies, aptamers, or nucleic acids. This final prepared electrode is then used for the detection of the analyte using one or a combination of the electrochemical techniques mentioned in the previous section.

## 21.4 Role of Nanomaterials in Electrochemical Biosensors

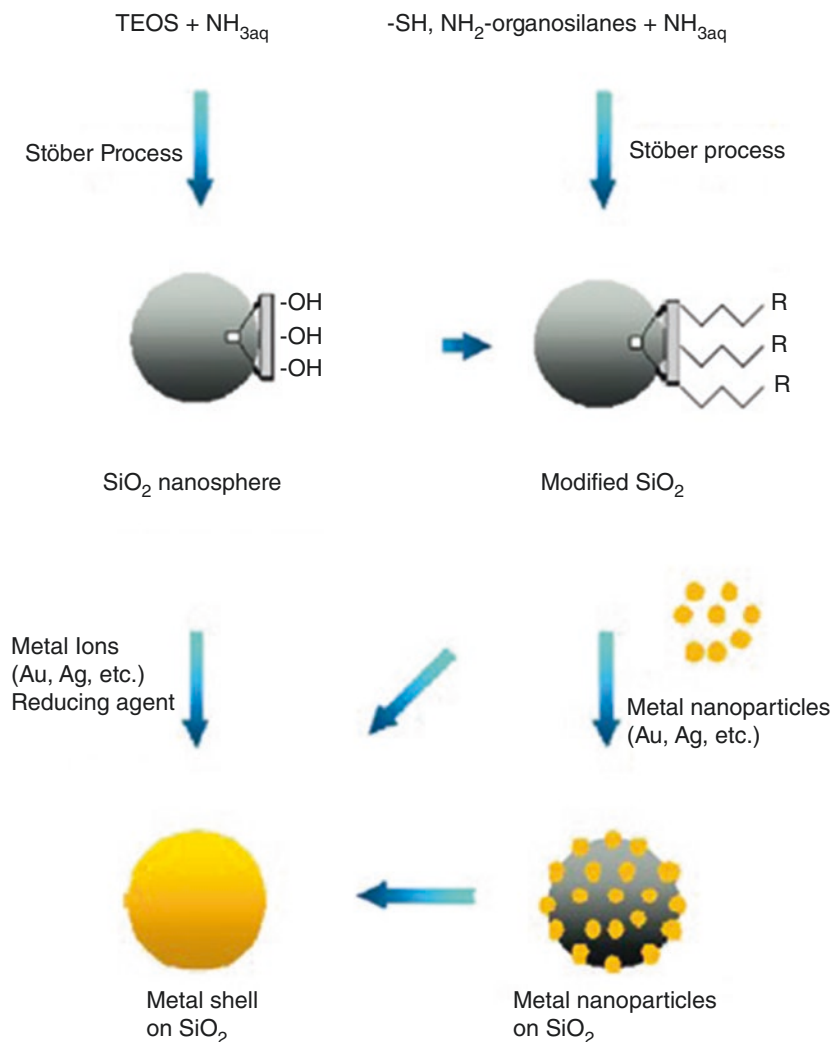
Nanomaterials have garnered great interest in recent years and have emerged as a promising material for the construction of biosensors [27]. They can be defined as materials having dimensions less than 100 nm. They possess unique properties such as high surface area and improved electrical properties with ease of functionalization. These features offer advanced improvements in speed, sensitivity, and selectivity in comparison to other conventional methods. As a result, they have a wide range of applications in the field of nanoelectronics, catalysis, data storage, and biosensors. One of the desired properties of a biosensor is its portable nature capable of on-site detection [18, 32].

Due to manipulation at the nanoscale level, they can detect the minute concentration of an analyte. In addition, electrochemical biosensors incorporating nanomaterials hold the potential to improve speed, sensitivity, and selectivity. They also endow device miniaturization and high sensitivity giving them great potential to assess an analyte on-site. Also, they have higher electrical conductivity and are compatible with biological molecules like enzyme, antibodies, DNA, and cell. The sensitivity of the biosensor is also increased by the use of nanomaterials. Immobilization of bioreceptor at a transducer surface is an important step for the construction of biosensor. Various parameters of the sensor can be improved by determining the effective method for immobilization. Adsorption, covalent interactions, and entrapment are important methods for conjugation of nanomaterials [4]. Despite its use for the construction of various types of biosensors, electrochemical biosensors present an interesting class that can be employed for the analysis of a variety of samples. Nanostructures such as core-shell (CS), quantum dots, metal-organic frameworks (MOF), graphene oxide (GO), and nanoparticles offer wide range of advantages and can be used for various applications [17, 20, 25].

Core-shell nanostructures can exist in different sizes and shapes (spherical, centric, tubular, star-like) and are basically composed of metals and metal oxides as either core or shell [24]. Ever since their discovery, they have garnered huge interest because of their tunable structure and unique morphology. This is because the combination of core and shell possesses advanced properties in comparison to individual counterparts. The use of stabilizers is widespread and is utilized to control different shapes and sizes. For example, Au coated with magnetic core-shell nanostructure helps in drug loading [9]. The core part can be either solid, liquid, or gas but the shell is usually solid in nature and can also vary with the type of application targeted. The core material can be either metal or magnetic silica nanoparticles, whereas shells are generally metals, metal oxides, proteins, and polysaccharides. They can also be classified into various categories depending upon the physico-chemical properties such as core-shell magnetic nanoparticles, core-shell metallic nanoparticles, and core-shell up-conversion nanoparticles.

Core-shell nanostructures can be synthesized using various methods like sol-gel, reduction, coprecipitation, hydrolysis, polyol synthesis, and cation exchange [35]. The fabrication of C-S nanostructure requires accurate precision at each step so as





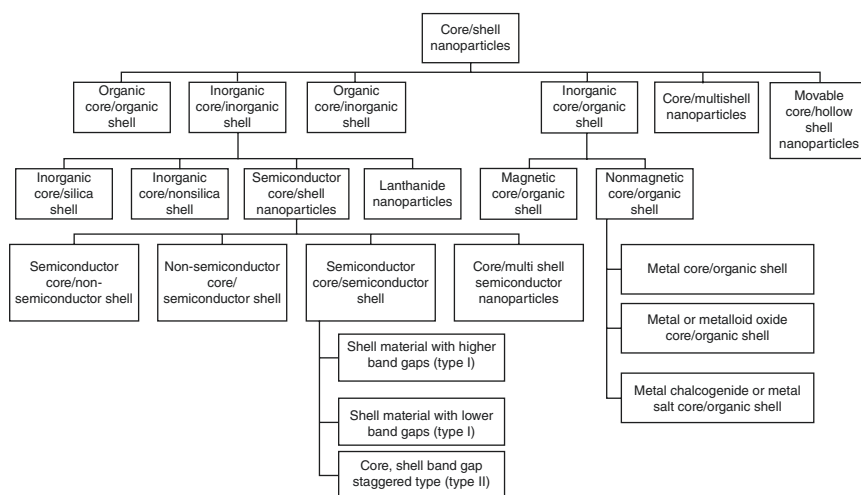
**Fig. 21.2** Synthesis procedure of C-S nanostructures by core surface modification and metal nanoparticles deposition. (Reprinted with permission from Choma et al. [8]. Copyright 2011: Elsevier)

to obtain structure with application-oriented properties. The major problem in fabrication lies with the control in thickness and homogeneity. The general overview for synthesis of C-S nanostructures is shown in Fig. 21.2.

Multiple pathways can be adopted for the synthesis of C-S nanostructure. For example, in one of the pathways, silica core is modified with Au nanoparticles (AuNPs) and organosilanes. The AuNPs act as seed and help in further growth of the nanoshell. The sol-gel synthesis can be achieved via Stöber route and

microemulsion route. The first method is employed for the synthesis of silica-coated composites whereas microemulsion route is used for the preparation of thermodynamically stable dispersion. This approach was used by Abbas et al. [1] for the synthesis of  $\text{Fe}_3\text{O}_4/\text{SiO}_2$  C-S nanostructure with stability of 4 months and having magnetization value of 50.7 emu/g. As the name implies, reduction method employs the use of reducing agents in the presence of a surfactant. Using this method, gold–silver C-S nanostructures were synthesized using tyrosine as a reducing agent and octadecyl amine as a surfactant [33]. Thus, because of its distinctive structure, popularity of C-S nanostructures in diverse fields such as electronics, pharmaceuticals, and biomedical has increased manifold times [19]. The unique merits such as protection from high temperature and pressure by shell structure are commendable. Also, the cost of material synthesis can be cut down by coating with a cost-effective material. The properties of C-S nanostructures can be tuned by changing the ratio between the core and shell particles. The shell molecule over the core molecule offers significant improvements such as thermal stability, reactivity, and dispersibility. It can also help in sustained release of analyte or to improve the optical properties. The wide range of classification of C-S nanostructures makes them a much more sought-after nanostructure for various applications. Figure 21.3 classifies different types of C-S nanostructures.

Due to their unique properties, C-S nanostructures open a diverse field of research in multiple sectors such as medical science, healthcare sector, and diagnostic sector [11, 29]. They offer unique features such as biocompatibility and efficiency and play a crucial role in wide range of applications.

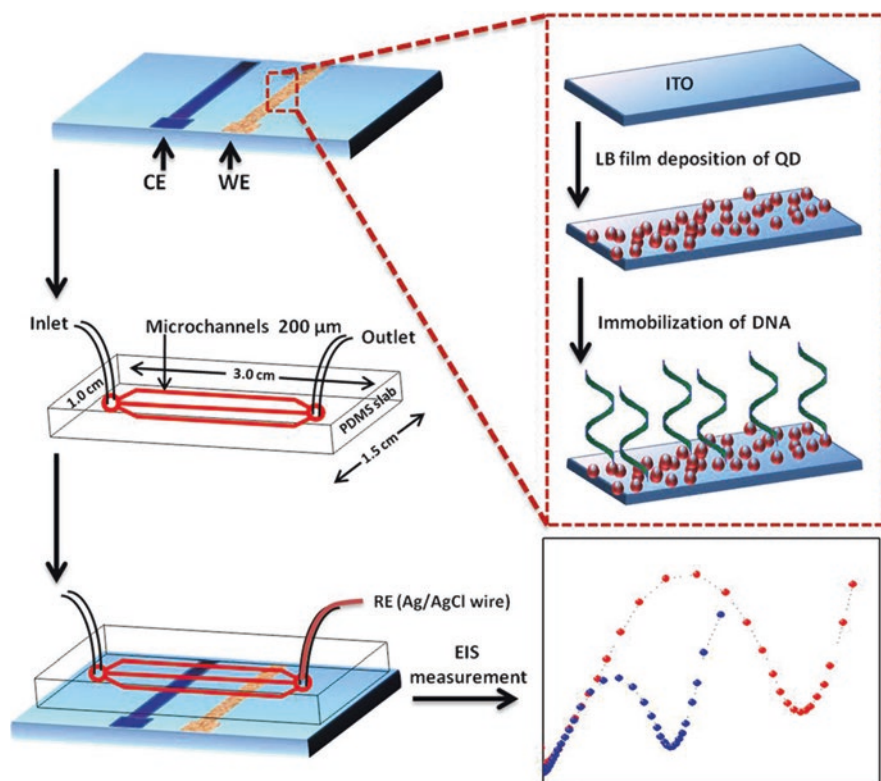


**Fig. 21.3** Classification of C-S nanostructures. (Reprinted with permission from Dhas et al. [10]. Copyright 2018; Elsevier)

## 21.5 Biosensing Applications of II–VI Semiconductor-Based Electrochemical Sensors

Majority of the semiconductor-based quantum dots have very high optical activity due to the quantum coupling effect. This means that almost all the research related to these materials have been limited to fluorescence- or chemiluminescence-based biosensors. However, the focus of the current chapter is the electrochemical biosensors based on these materials. Cadmium-based quantum dots have been the most famous choice while developing a biosensor, whether optical or electrochemical. In this regard, cadmium-based chalcogens such as cadmium sulphide-, cadmium selenide-, and cadmium telluride-based electrochemical biosensors have been widely reported, which shall be discussed now.

Malhotra and co-workers [14] developed a microfluidic electrochemical sensor for the determination of DNA sequence responsible for chronic myelogenous leukemia. The electrode surface was prepared by depositing CdSe QDs on an ITO-coated glass plate using Langmuir–Blodgett technique. The surface was functionalized

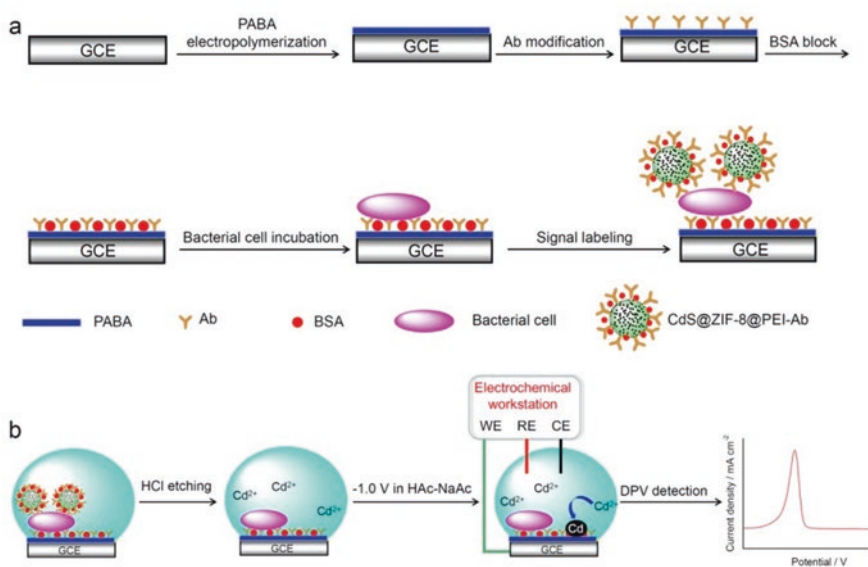


**Fig. 21.4** Fabrication of a microfluidic-based electrochemical sensor for cancer biomarker. (Reprinted with permission from Gherra et al. [14]. Copyright 2015: American Institute of Physics)

with DNA sequences, complementary to the target DNA sequence. The biosensor setup also consisted of a PDMS-based microfluidic channels for the fluid flow over the electrodes (Fig. 21.4). The binding of the target DNA sequence to the probe on the electrode surface created a charge barrier for the redox probe ions, leading to an increase in the impedance signal. The sensor's linear range was  $10^{-15}$  to  $10^{-11}$  M [14].

For the sensitive detection of rifampicin, which is an antibiotic, core-shell material such as polyvinyl pyrrolidone-capped  $\text{CoFe}_2\text{O}_4$ @CdSe core-shell has been reported. The developed material was found to be highly porous and hence the square wave adsorptive stripping voltammetry was employed for the electrochemical measurements. The prepared material had a high electrocatalytic activity toward the analyte and thus could enable sensitive estimation of the analyte, with detection limit of  $4.55 \times 10^{-17}$  M. The biosensor was rigorously tested against biological and pharmaceutical samples to claim for selectivity [2]. A CdSe/ZnS quantum dots-based core-shell electrochemical biosensor was fabricated for the detection of 3-chlorophenol [28]. The quantum dots were drop-casted on a glassy carbon electrode followed by the addition of Nafion (a binding agent). The cured electrode was used as a working electrode with platinum electrode as the counter electrode. The linear detectable concentration range for the analyte was found to be from 0.1 nM to 0.1 mM.

Cadmium sulfide (CdS) is another commonly used photoactive nanomaterial. The low band gap allows this material to be employed for various catalytic and sensing applications. The optical and electrochemical property of CdS was employed to form a conjugate with copper oxide inverse opal photonic crystal for the

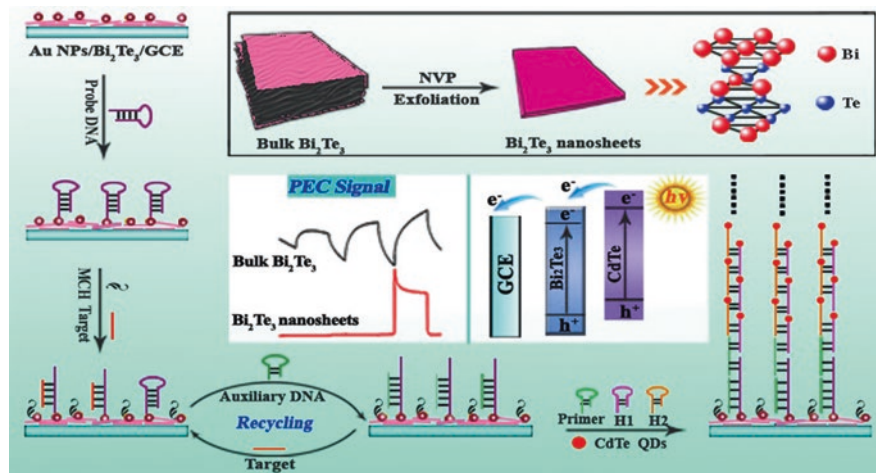


**Fig. 21.5** (a) Biosensor fabrication steps and (b) principle of the biosensor operation. (Reprinted with permission from Zhong et al. [40]. Copyright 2019: Elsevier)

photoelectrochemical non-enzymatic detection of glucose. The QDs were deposited on the crystal using successive ionic layer adsorption and reaction. This material was coated on an FTO. The amperometric detection of glucose using this fabricated sensor gave a limit of detection of  $0.15 \mu\text{M}$  [36]. Yao and co-workers [40] employed the use of cadmium sulfide-encapsulated ZIF-8 MOF for the detection of pathogen, i.e., *Escherichia coli*. The biosensor fabrication and principle can be understood from Fig. 21.5.

Briefly, PABA was first electropolymerized on a glassy carbon electrode to generate a conductive surface which was used as a platform for the immobilization of primary antibodies against the analyte. This modified electrode was then incubated against fixed concentrations of the bacteria followed by the addition of secondary antibodies tagged with CdS@ZIF-8 nanomaterial. On addition of HCl on the electrode, cadmium ions are released into the electrolyte, which are then recorded using differential pulse voltammetry. The amount of cadmium released is directly proportional to the concentration of the bacteria present in the sample [40]. The electrooxidation of the analytes is of high advantage while designing a biosensor as the use of external redox probes can be easily avoided. In this regard, cholesterol and hydrogen peroxide can be detected because of their unique oxidation signature. Khaliq et al. [21] developed a non-enzymatic platform for the detection of these mentioned molecules using nanomaterials of titanium and cadmium sulfide. The titanium oxide nanotubes grown on titanium electrode were first modified with cadmium sulfide quantum dots. These were further modified with gold nanoparticles using sputtering. The prepared electrode was used for the non-enzymatic detection of cholesterol and hydrogen peroxide. The redox peaks were observed at  $-1.2$  and  $-0.55$  V for cholesterol and hydrogen peroxide, respectively. The role of gold and CdS was to channelize the transport of electrons from the oxidation of the analyte to the electrode surface [21].

Cadmium telluride is yet another highly explored optically active material, which has not been explored for its electrochemical potential. Yu et al. [38] explored the use of this material for the electrochemical determination of dopamine, which is of neurological importance. A glassy carbon electrode was modified with the prepared CdTe QDs followed by dopamine exposure. The hydroxyl groups on the surface of CdTe QDs can bind to the amine functional group of dopamine, thereby enabling their detection. Differential pulse voltammetry was employed as the electrochemical technique for this work. The limit of detection was calculated to be in micromolar range [38]. A similar approach was used by Kus and co-workers [23] for the detection of ascorbic acid, which is an important antioxidant. The authors used a composite of graphene oxide and CdTe QDs for the detection of the said molecule. Graphene oxide provides a high surface area for the electrocatalytic processes to take place, whereas the CdTe QDs provide electrochemical activity. This composite was used for the modification of glassy carbon electrode. The detection limit for this work was  $6.1 \mu\text{M}$  [23]. High optical activity of CdTe QDs has been utilized for the fabrication of a



**Fig. 21.6** A photoelectrochemical biosensor for the detection of miRNA-21 based on CdTe QDs. (Reprinted with permission from Yuan et al. [39]. Copyright 2020: American Chemical Society)

photoelectrochemical biosensor. The work by Yuan and co-workers [39] is a nice demonstration for this. The research work used bismuth telluride nanosheets as a platform onto which gold nanoparticles and CdTe QDs were added to make the base material more sensitive to light. The final material was used for the modification of a glassy carbon electrode, which was further immobilized with a probe DNA. The fabricated biosensor (Fig. 21.6) was highly sensitive to the target, which can be seen from the ultra-low detection limit of 3.3 fM [39].

A similar photoelectrochemical biosensor was prepared by Zhu et al. [41] for the detection of *Listeria monocytogenes*. The work used tungsten trioxide as the photosensitive material onto which gold nanoparticles were added for the immobilization of complementary DNA. Sensitization of the biosensor was done using CdTe QDs. The photoelectrochemical biosensor thus developed was able to detect the bacteria in the concentration range of  $1.3 \times 10^1$ – $1.3 \times 10^7$  CFU/mL.

Zinc-based quantum dots have also been reported to some extent. Zinc sulfide is one such semiconducting material which is biocompatible and non-toxic in nature. Shekhari and co-workers [26] developed a simple biosensor for miR-200a, which is an ovarian cancer biomarker based on ZnS QDs. The QDs were functionalized with L-cysteine which acted as an immobilization platform for DNA probe. The L-cysteine-functionalized ZnS QDs were electrodeposited on the surface of glassy carbon electrode using cyclic voltammetry in the range of  $-0.8$  to  $+2.0$  V. The modified surface was then subjected to EDC/NHS chemistry to enable probe immobilization. The prepared surface was then exposed to miR-200a for its impedimetric determination. Higher the concentration of the analyte, more is the impedance. This sensor was capable of ultrasensitive detection of the analyte leading to femtomolar detection limit [26].

## 21.6 Conclusion and Future Outlook

This chapter discusses the various properties, advantages, and disadvantages associated with core-shell nanostructures with emphasis on their application toward electrochemical biosensors. Electrochemical biosensors are capable of offering high sensitivity, selectivity, compactness with ease of fabrication, and involvement of clean process in sample preparation and its analysis. However, the scope for future research is highly exponential with wide chances of improvements in various dimensions. The core-shell nanostructure-based sensors can be explored for smart electrochemical devices such as wearables or flexible electronics.

**Acknowledgments** The authors acknowledge the financial support from the Council of Scientific and Industrial Research (CSIR), India New Delhi, for project HCP 31 (Advancing Technological Leads for Assuring Safety of Food (ATLAS)).

**Conflict of Interest** The authors do not have any conflict of interest to declare.

## References

1. Abbas M, Torati S, Lee C, Rinaldi C, Kim C. Fe<sub>3</sub>O<sub>4</sub>/SiO<sub>2</sub> core/shell nanocubes: novel coating approach with tunable silica thickness and enhancement in stability and biocompatibility. *J Nanomed Nanotechnol.* 2014;5(6):1–8.
2. Asadpour-Zeynali K, Mollarasouli F. Novel electrochemical biosensor based on PVP capped CoFe<sub>2</sub>O<sub>4</sub>@CdSe core-shell nanoparticles modified electrode for ultra-trace level determination of rifampicin by square wave adsorptive stripping voltammetry. *Biosens Bioelectron.* 2017;92:509–16.
3. Avelino KYPS, Silva RR, da Silva Junior AG, Oliveira MDL, Andrade CAS. Smart applications of bionanosensors for BCR/ABL fusion gene detection in leukemia. *J King Saud Univ Sci.* 2017;29(4):413–23.
4. Azandaryani AH, Kashanian S, Jamshidnejad-Tosaramandani T. Recent insights into effective nanomaterials and biomacromolecules conjugation in advanced drug targeting. *Curr Pharm Biotechnol.* 2019;20(7):526–41.
5. Bałczewski P, Kudelska W, Bodzioch A. 4.12 – 1,3-dithioles. In: Katritzky AR, Ramsden CA, Scriven EFV, Taylor RJK, editors. *Comprehensive heterocyclic chemistry III.* Oxford: Elsevier; 2008. p. 955–1090.
6. Batista Deroco P, Giarola JDF, Wachholz Júnior D, Arantes Lorga G, Tatsuo Kubota L. Chapter four – Paper-based electrochemical sensing devices. In: Merkoçi A, editor. *Comprehensive analytical chemistry.*, vol. 89. Elsevier; 2020. p. 91–137.
7. Castle JR, Ward WK. Amperometric glucose sensors: sources of error and potential benefit of redundancy. *J Diabetes Sci Technol.* 2010;4(1):211–5.
8. Choma J, Dziura A, Jamiola D, Nyga P, Jaroniec M. Preparation and properties of silica-gold core-shell particles. *Colloids Surf A Physicochem Eng Asp.* 2011;373(1–3):167–71.
9. Deshpande S, Sharma S, Koul V, Singh N. Core-shell nanoparticles as an efficient, sustained, and triggered drug-delivery system. *ACS Omega.* 2017;2(10):6455–63.
10. Dhas NL, Raval NJ, Kudarha RR, Acharya NS, Acharya SR. Core-shell nanoparticles as a drug delivery platform for tumor targeting. *Inorganic frameworks as smart nanomedicines:* Elsevier; 2018. p. 387–448.

11. Feng H-P, Tang L, Zeng G-M, Zhou Y, Deng Y-C, Ren X, Song B, Liang C, Wei M-Y, Yu J-F. Core-shell nanomaterials: applications in energy storage and conversion. *Adv Colloid Interface Sci.* 2019;267:26–46.
12. Garg M, Chatterjee M, Sharma AL, Singh S. Label-free approach for electrochemical ferritin sensing using biosurfactant stabilized tungsten disulfide quantum dots. *Biosens Bioelectron.* 2020;151:111979.
13. Garg M, Rani R, Sharma AL, Singh S. White graphene quantum dots as electrochemical sensing platform for ferritin. *Faraday Discuss.* 2021;217:204–12.
14. Ghrera AS, Pandey CM, Ali MA, Malhotra BD. Quantum dot-based microfluidic biosensor for cancer detection. *Appl Phys Lett.* 2015;106(19):193703.
15. Grieshaber D, MacKenzie R, Vörös J, Reimhult E. Electrochemical biosensors – sensor principles and architectures. *Sensors (Basel).* 2008;8(3):1400–58.
16. Guan J-G, Miao Y-Q, Zhang Q-J. Impedimetric biosensors. *J Biosci Bioeng.* 2004;97(4):219–6.
17. Gupta A, Bhardwaj SK, Sharma AL, Kim K-H, Deep A. Development of an advanced electrochemical biosensing platform for *E. coli* using hybrid metal-organic framework/polyaniline composite. *Environ Res.* 2019;171:395–402.
18. Holzinger M, Le Goff A, Cosnier S. Nanomaterials for biosensing applications: a review. *Front Chem.* 2014;2:63.
19. Jankiewicz B, Jamiola D, Choma J, Jaroniec M. Silica–metal core–shell nanostructures. *Adv Colloid Interf Sci.* 2012;170(1–2):28–47.
20. Kalambate PK, Huang Z, Li Y, Shen Y, Xie M, Huang Y, Srivastava AK. Core@ shell nanomaterials based sensing devices: a review. *TrAC Trends Anal Chem.* 2019;115:147–61.
21. Khaliq N, Rasheed MA, Khan M, Maqbool M, Ahmad M, Karim S, Nisar A, Schmuki P, Cho SO, Ali G. Voltage-switchable biosensor with gold nanoparticles on TiO<sub>2</sub> nanotubes decorated with CdS quantum dots for the detection of cholesterol and H<sub>2</sub>O<sub>2</sub>. *ACS Appl Mater Interfaces.* 2021;13(3):3653–68.
22. Kotanen CN, Moussy FG, Carrara S, Guiseppi-Elie A. Implantable enzyme amperometric biosensors. *Biosens Bioelectron.* 2012;35(1):14–26.
23. Kucukkolbasi S, Erdogan ZO, Baslak C, Sogut D, Kus M. A highly sensitive ascorbic acid sensor based on graphene oxide/CdTe quantum dots-modified glassy carbon electrode. *Russ J Electrochem.* 2019;55(2):107–14.
24. Kumar R, Mondal K, Panda PK, Kaushik A, Abolhassani R, Ahuja R, Rubahn H-G, Mishra YK. Core–shell nanostructures: perspectives towards drug delivery applications. *J Mater Chem B.* 2020;8(39):8992–9027.
25. Marín S, Merkoçi A. Nanomaterials based electrochemical sensing applications for safety and security. *Electroanalysis.* 2012;24(3):459–69.
26. Moazampour M, Zare HR, Shekari Z. Femtomolar determination of an ovarian cancer biomarker (miR-200a) in blood plasma using a label free electrochemical biosensor based on l-cysteine functionalized ZnS quantum dots. *Anal Methods.* 2021;13(17):2021–9.
27. Pandey P, Datta M, Malhotra B. Prospects of nanomaterials in biosensors. *Anal Lett.* 2008;41(2):159–209.
28. Rahman MM, Karim MR, Alam MM, Zaman MB, Alharthi N, Alharbi H, Asiri AM. Facile and efficient 3-chlorophenol sensor development based on photoluminescent core-shell CdSe/ZnS quantum dots. *Sci Rep.* 2020;10(1):557.
29. Ramli RA, Laftah WA, Hashim S. Core–shell polymers: a review. *RSC Adv.* 2013;3(36):15543–65.
30. Rani R, Deep A, Mizaikoff B, Singh S. Copper based organic framework modified electrosensor for selective and sensitive detection of ciprofloxacin. *Electroanalysis.* 2020;32(11):2442–51.
31. Rani R, Deep A, Mizaikoff B, Singh S. Zirconium metal organic framework based opto-electrochemical sensor for nitrofurazone detection. *J Electroanal Chem.* 2022;909:116124.
32. Rowland CE, Brown CW III, Delehanty JB, Medintz IL. Nanomaterial-based sensors for the detection of biological threat agents. *Mater Today.* 2016;19(8):464–77.



33. Shankar SS, Rai A, Ahmad A, Sastry M. Rapid synthesis of Au, Ag, and bimetallic Au core–Ag shell nanoparticles using Neem (*Azadirachta indica*) leaf broth. *J Colloid Interface Sci.* 2004;275(2):496–502.
34. Singh S, Jain DVS, Singla ML. Sol–gel based composite of gold nanoparticles as matrix for tyrosinase for amperometric catechol biosensor. *Sensors Actuators B Chem.* 2013;182:161–9.
35. Singh S, Kaur V, Kumar N. Core–shell nanostructures: an insight into their synthetic approaches. In: *Metal semiconductor core-shell nanostructures for energy and environmental applications.* Elsevier; 2017. p. 35–50.
36. Xia L, Xu L, Song J, Xu R, Liu D, Dong B, Song H. CdS quantum dots modified CuO inverse opal electrodes for ultrasensitive electrochemical and photoelectrochemical biosensor. *Sci Rep.* 2015;5(1):10838.
37. Yoon J, Cho H-Y, Shin M, Choi HK, Lee T, Choi J-W. Flexible electrochemical biosensors for healthcare monitoring. *J Mater Chem B.* 2020;8(33):7303–18.
38. Yu H-W, Zhang Z, Jiang J-H, Pan H-Z, Chang D. Simple strategy for sensitive detection of dopamine using CdTe QDs modified glassy carbon electrode. *J Clin Lab Anal.* 2018;32(3):e21320.
39. Yuan Y, Hu T, Zhong X, Zhu M, Chai Y, Yuan R. Highly sensitive photoelectrochemical biosensor based on quantum dots sensitizing Bi<sub>2</sub>Te<sub>3</sub> nanosheets and DNA-amplifying strategies. *ACS Appl Mater Interfaces.* 2020;12(20):21624–9.
40. Zhong M, Yang L, Yang H, Cheng C, Deng W, Tan Y, Xie Q, Yao S. An electrochemical immunobiosensor for ultrasensitive detection of *Escherichia coli* O157:H7 using CdS quantum dots-encapsulated metal-organic frameworks as signal-amplifying tags. *Biosens Bioelectron.* 2019;126:493–500.
41. Zhu L, Hao H, Ding C, Gan H, Jiang S, Zhang G, Bi J, Yan S, Hou H. A novel photoelectrochemical aptamer sensor based on cdte quantum dots enhancement and exonuclease i-assisted signal amplification for listeria monocytogenes detection. *Foods.* 2021;10(12):2896.

# Chapter 22

## Photoelectrochemical Biosensors



Sirlon F. Blaskievicz, Byanca S. Salvati, Alessandra Alves Correa,  
and Lucia Helena Mascaro

### 22.1 Introduction

Light is fundamental in many photochemical processes in biology and chemistry. Due to this, solar energy harvesting technologies represent a sustainable approach, as photoelectrochemical processes involve photo-induced chemical phenomena, for example, charge generation/separation and charge transport/transfer. These kinds of mechanisms can be exploited in areas such as analytical detection, as observed in classic techniques such as electroanalytical stripping voltammetry being enhanced by light-mediated strategies [1]. An example to highlight is the generation of anodic photocurrent at an n-type semiconductor, the photo-generated holes at the electrode surface can oxidise an analytical target in the solution. The electrons are then collected by a conductor into the external circuit as a current response (signal from the analyte). Among the materials that can be useful for photoelectroanalysis are semiconductor oxides, as nanoparticles or as quantum dots (QDs) but also carbon-based nanomaterials like graphene, carbon nanotubes and fullerenes. These carbon-based nanomaterials often show better conductivity in comparison to semiconductor oxides, being an alternative to conventional photoactive materials [2, 3]. Besides the electrical conductivity, the usually large surface area leads to enhanced photocurrents and enhanced analytical sensitivity, which makes materials such as carbon-derived nanomaterials suitable for strategies based on signal amplification [4].

---

S. F. Blaskievicz · B. S. Salvati · L. H. Mascaro (✉)  
Department of Chemistry, Federal University of São Carlos (UFSCar), São Carlos, SP, Brazil  
e-mail: [lmascaro@ufscar.br](mailto:lmascaro@ufscar.br)

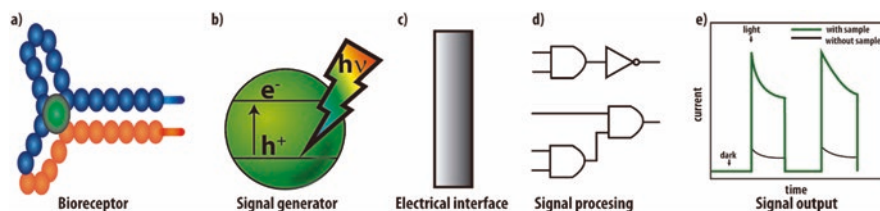
A. A. Correa  
PPCEM, Department of Materials Engineering, Center for Exact Sciences and Technology,  
Federal University of São Carlos (UFSCar), São Carlos, SP, Brazil

Nanotechnology National Laboratory for Agriculture, Embrapa Instrumentação,  
São Carlos, SP, Brazil

Other approaches for photocurrent response amplification include the coupling with organic molecules that act as electron-relay units [5], or with materials that present strong light scattering/absorption such as plasmonic nanoparticles [6]. Furthermore, combining small and large bandgap semiconductors with a favourable band alignment leads to sensitised heterostructures, with stepwise band-edge levels. It improves charge separation and mainly leads to better solar spectra utilisation [7]. Not only ways to improve the sensitivity and the photoresponse of the process must be discussed, but selectivity is a key factor for correct analytical employ. The sensitivity level of the sensing process depends mainly on the surface interaction between the analyte and the photoelectrode. Stronger and selectivity interactions lead to a better sensing process. Then, the critical task is to aim at the materials engineering and strategies that improve the interactions between the sensor and the analyte, such as combination with biomaterials (e.g. enzymes and aptamers) that can act as a receptor for the analyte. The advantages that made photoelectrochemical biosensors attract great interest are their rapid response and potential for simple on-site measurement, but with the condition that an embedded light source or solar activation is tolerable. Otherwise, the operational conditions required change in each material studied, but generally are a light radiation energy enough to excite the semiconducting species and mild conditions of pH and temperature, aiming to maintain the biorecognition element (enzyme, DNA, aptamer, etc.) activity. Figure 22.1 represents the main components and steps of PEC bioanalysis, the interactions between the target analyte and the bioreceptor (a), through a redox reaction lead to a change in the measured PEC current or voltage response from the semiconductor (b). This photoelectrochemical response is transported through the electrical interface (c) to the signal processing circuit (d), then shown as the current or voltage signal (e).

In a review del Barrio et al. [8] have summarised many of the benefits of adding a light stimulus to biosensing devices. The combination of inorganic semiconductors with biomaterials, however, brings another question. How are the mechanisms of charge generation, separation and transport at the complex inorganic-biological interfaces? These mechanisms are not well predictable and can currently be developed and identified only with extensive research for each sample, not allowing general behaviour description.

In Fig. 22.2, different photo(bio)electroanalytical sensors approaches that will further be discussed in the present chapter are represented. In Fig. 22.2a, a



**Fig. 22.1** Illustration of photoelectrochemical biosensing components: (a) Biorecognition element, (b) PEC signal transducer, (c) electrical interface, (d) signal processing and (e) signal output

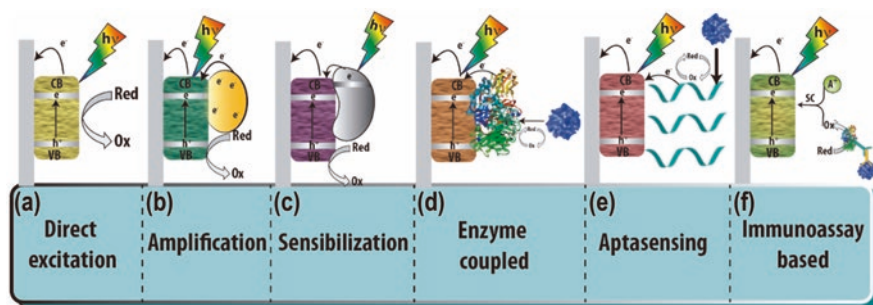


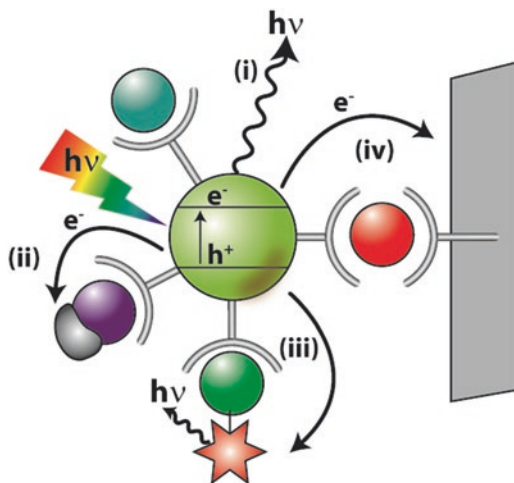
Fig. 22.2 Illustration of the typical photo(bio)electroanalytical sensors

semiconductor electrode is directly photo-excited and the oxidation of the analyte reacting with holes leads to the measured signal. As the monitored reactions involve charge transfer, the combination with metallic nanoparticles (illustrated in Fig. 22.2b) that corroborate with charge injection, plasmonic mechanism, or even hot electrons is very welcome [9]. An alternative approach (illustrated in Fig. 22.2c) is the sensitisation of the semiconductor with a photo absorber to use lower energy than the bandgap for the photoexcitation. There are several variations of possible mechanisms, as there are benefits from the coupling of biological receptor systems with photoactive semiconductor components, as an enhanced selectivity of the sensor. Approaches of integration between photoelectrochemistry and bioanalysis aim for a good signal with the selective recognition of a specific analyte [10, 11]. It can be exemplified in ways of using biological receptors such as an enzyme (Fig. 22.2d) or an aptamer (Fig. 22.2e) directly reacting with the analyte, or by a biochemical route as used in immunoassay tests, where the product obtained is an intermediate for generating or reacting a semiconductor, being indirectly detected (illustrated in Fig. 22.2f).

The use of biological compounds (e.g. enzymes and oligonucleotides) for sensing, however, may introduce intrinsic instabilities depending on the system conditions [12]. It is challenging to maintain the enzyme activity, and it can be overcome by the correct architecture of photo(bio)electroanalytical devices. Usually, a biosensor requires a sensing agent, which can be an oligonucleotide or a transducer. The transducer must convert the chemical signal obtained by the sensing agent, into an electrical signal for the external circuit. Many photoelectroactive materials are suitable for the function of the transducer. The electrical signal comes from the photocurrent response. As there are separate sources for excitation and detection, photo(bio)electroanalytical methods are potentially more sensitive compared to traditional sensors.

Hence, photo(bio)electroanalysis is a fast-emerging methodology. Quite different openings arising from self-powered photoelectroanalytical sensors had been reported [13–15]. Among other examples, light-activated bioelectroanalytical sensors also can be used for the parallel detection of multiple analytes with a single device based on an array of sensors with light activation [16]. If a semiconductor is

**Fig. 22.3** Representation of semiconductor quantum dot process, suitable for sensing applications: (i) CRET; (ii) electron transfer for an adsorbed substrate; (iii) FRET; and (iv) photocurrent response



employed as a quantum dot (QD) in the photo(bio)electroanalysis, unique photo-physical properties are added to the sensor. Besides the electron transfer mechanism, due to size-controlled luminescence properties of QDs, chemiluminescence resonance energy transfer (CRET) and fluorescence resonance energy transfer (FRET) can be achieved [17] (see Fig. 22.3).

FRET is a useful tool to investigate the formation of recognition complexes. As it involves interactions between a donor–acceptor pair, it can be employed in a broad range of substrate detection challenges. This includes DNA, aptamer–substrate complex, or even mixtures of ions [18]. The emitted luminescence from QD enables a secondary chromophore excitation. It can lead to an electron transfer in the recognition process. The fluorescence ratio of a QD may change according to the wavelength excitation and before and after the addition of an analyte. It opens the possibility of using the material as a ratiometric sensor, as reported by Zhang and coworkers [19]. Dopamine dithiocarbamate proved to be a selective energy transfer quencher for the  $\text{Mn}^{2+}$  and easily displaced by diethylphosphorothioate. Due to differences in transition pathways and, consequently emission wavelengths, selective modulation of these two bands enables ratiometric sensing.

## 22.2 Cd-Based Semiconductors in Photoelectrochemical Bioanalysis

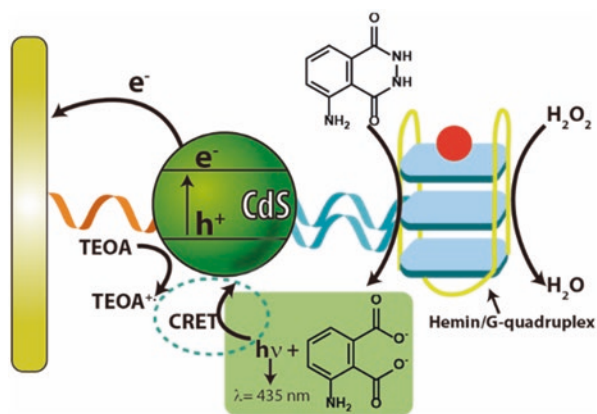
### 22.2.1 Cd-Based Sensors for Nucleic Acids and Other Biological Samples

As an alternative to FRET, CRET may allow for achieving photocurrent without external illumination. The CRET-driven photocurrent was applied by Golub et al. [20], for DNA sensing by an architecture of hemin/G-quadruplex immobilised on

CdS QDs. In the presence of luminol and  $\text{H}_2\text{O}_2$ , the hemin/G-quadruplex catalyses the chemiluminescence reaction. The CRET results in the photogeneration of electron-hole pair in the CdS QD, and the photogenerated electrons are transferred to the electrode while the holes are quenched by triethanolamine (TEOA), resulting in a photocurrent (Fig. 22.4).

Semiconductors QD sensitizers are well employed to enhance the response of sensors in a wide range of targets [21], such as nucleic acids [22], viruses [23], environmental potential contaminants [24, 25], glucose [26, 27], among others. Wang et al. [28] developed a glucose sensor by CdS QD combined with three-dimensional (3D) nanoporous NiO (3D NiO/CdS) and glucose oxidase. Due to the enzyme selectivity, commonly encountered interferents like dopamine, cysteine and ascorbic acid showed negligible effect for the cathodic photocurrent. This sensor gave satisfactory results in real samples with glucose injections. Similarly, Zheng et al. detected glucose with a nanocomposite of  $\text{TiO}_2/\text{CdSe}@/\text{CdS}$  [29].  $\text{TiO}_2/\text{CdSe}@/\text{CdS}$  was obtained by depositing water-soluble CdSe@CdS, with a mixture of [cobalt(o-phen) $_3$ ] $^{2+/3+}$  and poly(ethyleneimine) over  $\text{TiO}_2$  films. The electrode showed good stability and presented a linear relationship between the photocurrent with the glucose concentration. Zhao and co-workers employed an interesting strategy for adenosine ultrasensitive detection, based on cascade multiple DNA amplification cycle assay protocols combined with silver ion-exchange reaction with CdTe QD [22]. The DNA cycle started in the presence of the target (adenosine), with complementary DNA s1 being released from adenosine aptamer and hybridising with hairpin DNA (HP1). HP1 is further cleaved, leading to DNA b and c products, the DNA b then acts as the “DNA trigger”, generating many DNA s1, thus returning to the beginning of the cycle. This cycling reaction releases large amounts of DNA c, which is captured by carboxylic-modified magnetic beads (MB), generating silver nanoclusters. In the end, Ag nanoclusters react with CdTe QD through ion exchange (forming CdTe/Ag $_2$ Te), resulting in significant photocurrent change proportional to the adenosine concentration (with the detection limit of 0.5 fM), an

**Fig. 22.4** CRET-driven detection of DNA by of in an architecture containing CdS QDs associated with a hemin/G-quadruplex. (Adapted with permission from ref. [20]. Copyright 2012 American Chemical Society)



approach with great potential for trace analysis and that provides insights for different biomolecules detection.

The heterojunction is a strategy employed to overcome some drawbacks in semiconductors such as limited light-harvesting and high-rate recombination of electron-hole pairs [30]. The nature of the semiconductor (n or p-type) deeply modulates the properties of the final material in a heterojunction. In a p-n junction (an isotype junction), there is a depletion region and an electric field that naturally favours electrons and holes in the opposite direction. For a sufficiently thick junction, this phenomenon will occur to some extent except where the doping levels and electron affinities result in Fermi levels in both materials with similar energies before being brought into contact.

For junctions of equal natures (isotype), for example, n-n junction, the charge transport occurs via the band offsets. For any heterojunction of sufficient thickness, it must be considered the band alignment of the different materials, aiming for a staggered band structure (type II heterojunction) and p-n equilibration effects [32]. An n-n heterojunction between two chalcogenides (CdS/CdSe) can be used to exemplify the positive effects of a type-II heterojunction. This material was synthesised by the ion-exchange method and decorated over a flower-like Zn layer [32]. This hierarchical structure was coated with molecularly imprinted polydopamine (MIP); however, the electropolymerisation of dopamine was carried in the presence of L-phenylalanine (L-Phe), to obtain a film of polydopamine containing L-Phe as a biomarker (bio-MIP). Due to the interface between the Zn layer with a low work function, support with the dichalcogenide CdS/CdSe heterojunction, as well as n-type characteristics of bio-MIP sharply increase the light-harvesting in the visible range, which dramatically hinders the charge carrier recombination, which is crucial for boosting the material performance. Besides that, the presence of the biomarker increased the selectivity of the sensor, allowing the PEC detection of a polynucleotide kinase with a detection limit in the order of nanomolar.

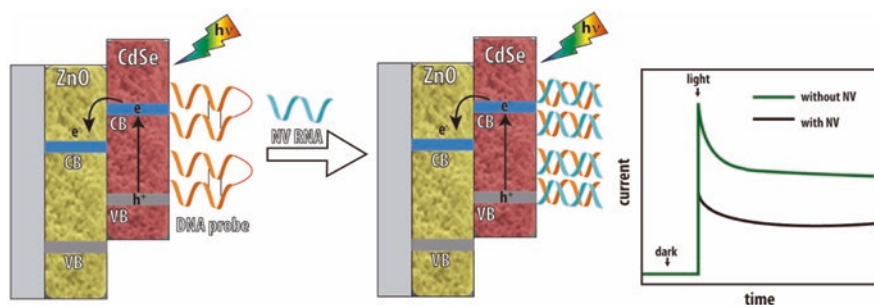
A co-sensitisation strategy was explored by Li et al. [31], using CdSe QD, which has a narrow bandgap, in combination TiO<sub>2</sub> and g-C<sub>3</sub>N<sub>4</sub> (TiO<sub>2</sub>/g-C<sub>3</sub>N<sub>4</sub>/CdS) for ultrasensitive evaluation of T4 polynucleotide kinase (T4 PNK). This ternary junction presented a cascade energy level arrangement, being a suitable matrix to build a PEC sensing platform, as it was further confirmed. After functionalisation with a DNA probe with 5-hydroxyl termini, it was specifically phosphorylated by T4 PNK. This biorecognition route was conducted to an increased photocurrent response, and also a wide linear range for T4 PNK, from 0.0001 to 0.02 U mL<sup>-1</sup>.

### ***22.2.2 Cd-Based PEC Immunosensors and Combination with Immunoassay Tests***

Heterojunctions and Z-scheme brings a series of advantages to the system that leads to a better photoelectrocatalytic performance, such as wide spectra absorption, increase in the separation of the photogenerated charges, increasing the lifetime of

the charge carriers. In the work of Li and co-workers [31], a  $g\text{-C}_3\text{N}_4/\text{MoS}_2$  heterojunction sensitised with CdSe QD and immobilised with a DNA probe was used as a PEC biosensor. Both materials ( $g\text{-C}_3\text{N}_4$  and  $\text{MoS}_2$ ) are bi-dimensional, so the obtained heterojunction had unique properties associated with the 2D structure, such as better separation of photogenerated electron-hole pairs, and an enhanced photocurrent. In the presence of target DNA, CdSe QDs worked as a transducer and, due to the better charge separation from heterostructure and sensitisation effect, the signal (photocurrent) was sharply increased. On the contrary, Han et al. [32] prepared a CdSe–ZnO flower-rod heterostructure (CSZFRs) and immobilised a DNA probe on the surface of CSZFRs. When the probe reaches the target norovirus (NV), due to complementary base pairing, occurs combination between the probe and target, leading to a decrease in the photocurrent (Fig. 22.5). This “antiphotocurrent” is a remarkable way to interpret the signal response from the analyte and is probably due to two factors: (i) A steric hindrance and insulation of DNA and RNA and (ii) charge transfer inhibited after the DNA probe hybridisation.

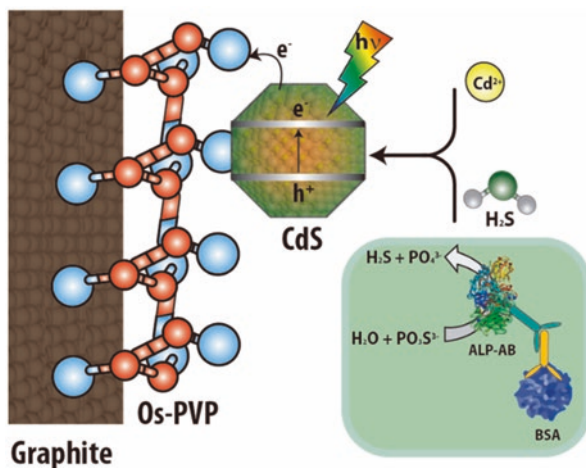
A great challenge found for sensing in real biological media is to avoid some aggressive metabolites products.  $\text{H}_2\text{S}$  for example is often not desired, because sulphide is quite aggressive to most materials used as sensors compromising its performance. However, it is possible to take advantage of  $\text{H}_2\text{S}$  in the system, for in situ generations of sulphide-based semiconductors, such as the CdS QD. Enzyme-linked immunosorbent assay (ELISA), opens the possibility to use a subproduct from the immunoassay test, to generate semiconductors and then, provide unique architectures capable of sensing in the nanogram order. In the work of Barroso et al. [33], a photoelectroanalytical immunoassay method for bovine serum albumin antibody (BSA) detection was reported. The system operated based on the in situ generations of CdS QDs by the reaction of  $\text{Cd}^{2+}$  with an enzymatic product. Alkaline phosphatase (ALP) was added to the system to catalyse the hydrolysis of sodium thiophosphate. The product (hydrogen sulphide) then reacts with  $\text{Cd}^{2+}$  ions generating CdS QD that is deposited in polyvinyl pyridine osmium complex (Os–PVP) (see Fig. 22.6) and used as a signal transducer. Then, 365 nm irradiation of the CdS QD results in photoelectrooxidation of 1-thioglycerol, mediated by the Os–PVP



**Fig. 22.5** Norovirus PEC biosensor, with an “antiphotocurrent” as the response from the target. (Adapted from ref. [32]. Published 2018 by MDPI as open access)



**Fig. 22.6** Representation of a PEC-enhanced immunoassay method for BSA detection based on in situ CdS QD generation. (Adapted with permission from ref. [33]. Copyright 2016: Elsevier)



complex. This synergistic combination of a photoelectron(bio)analytical methodology with an ELISA procedure, leads to a photo-enhanced immunoassay method detection, with a detection limit as low as  $2 \text{ ng mL}^{-1}$ .

Due to its capacity to combine with immunoassay tests, PEC biosensors are a promising platform for clinical diagnostics. Sun et al. combined CdTe QD with gold nanoparticles and graphitic carbon nitrides (CdTe QD/AuNPs/g- $C_3N_4$ ) for sensitive detection of J avian leukosis viruses (ALV-J) [23]. By immobilising the primary antibody of the virus in the electrode for biorecognition, and due to the matched energy levels between AuNPs/g- $C_3N_4$  and CdTe QDs. The obtained material showed to be a PEC immunosensor with specificity and stability for ALV-J, in a wide linear range, and with a very low detection limit (85 tissue culture infectious dose-TCID 50  $\text{mL}^{-1}$ ).

Amyloid beta ( $A\beta$ ) is a compound with a progressive neurotoxic effect on Alzheimer's disease (AD).  $A\beta$  was detected with high sensitivity with an architecture containing  $Bi_2WO_6$ , CdS and  $Mn^{2+}$  doped CdSe (Mn:CdSe) [34]. While  $Bi_2WO_6$ /CdS heterojunction was used aiming for better charge separation, and, consequently an improved photocurrent, Mn:CdSe function in the system was to label  $A\beta$  to lead to Mn:CdSe- $A\beta$  bioconjugate, detecting  $A\beta$  by an immunoreaction photoassisted. The idea of doping CdSe nanoparticles with  $Mn^{2+}$  was to induce intermediary energy levels, mitigate the recombination of photo-generated charge carriers and further enhance the PEC response for ultrasensitive detection of  $A\beta$ . This showed, besides a low detection limit ( $0.068 \text{ pg mL}^{-1}$ ), high selectivity and good stability. PEC immunosensors can also be useful for the detection of environmental contaminants such as the pesticide octachlorostyrene (OCS) [24]. CdTe/CdS QD-sensitised  $TiO_2$  nanotube arrays (NTAs) were cross-linked with the OCS

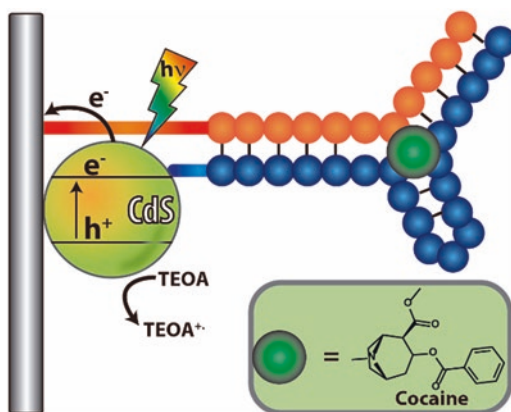
antibody (anti-OCS). To obtain the anti-OCS, the antibody was formed through immunisation with BSA–OCS in rabbits. The combination between CdTe/CdS/TiO<sub>2</sub> NTAs was very beneficial for light-harvesting, due to an ideal stepwise band edge structure. The obtained PEC immunosensor was able to analyse OCS in real samples from river water.

### 22.2.3 Cd-Based Aptasensors

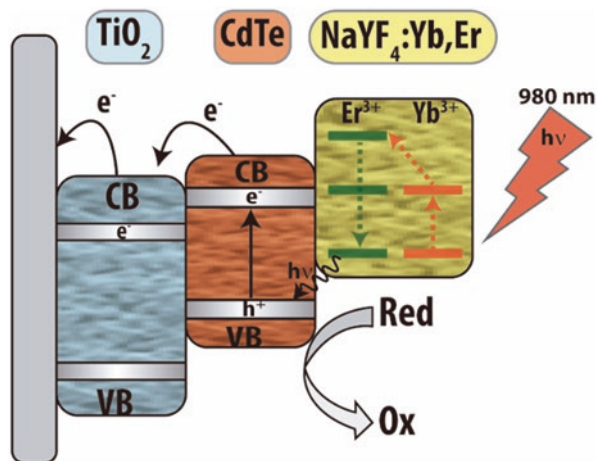
Aptamers configure a class of biological compounds that also can be a valuable tool for photoelectrochemical sensors with enhanced selectivity. Amongst the aptasensors found on literature, must be mentioned the thrombin sensor developed by Zhang et al. [35] based on chemical functionalised graphene and CdSe nanoparticles, and also the work of Liu and co-workers on tetracycline (TET) detection [36]. In this work, CdS QDs grafted onto graphitic carbon nitride (g-C<sub>3</sub>N<sub>4</sub>), aiming an enhanced light absorption for g-C<sub>3</sub>N<sub>4</sub>. The obtained nanocomposite (g-C<sub>3</sub>N<sub>4</sub>–CdS) was the transducer of the immobilised TET-binding aptamer, thus, giving a PEC aptasensing platform for TET determination. The response was linear in the range of 10 to 250 nM, with a detection limit of 5.3 nM. Another quite interesting example of the sensor was built by labelling the anticocaine aptamer subunit with CdS nanoparticles. In contact with cocaine, the NP-labelled aptamer subunits lead to the formation of a supramolecular complex. This supramolecular complex modulates the photocurrent with the addition of a hole scavenger (TEOA), allowing the quantitative photoelectrochemical detection of cocaine (Fig. 22.7) [37].

Usually, PEC biosensors work based on a single photocurrent change, which is due to biorecognition events among the probe and the analyte. Anyway, some interferences may give a photoresponse besides target analytes, thus, bringing a false result. Hao and co-workers showed an approach for improving the reliability and

**Fig. 22.7** Supramolecular complex formation between cocaine and CdS-functionalised aptamer, giving a sensing method for cocaine. (Adapted with permission from ref. [38]. Copyright 2009: American Chemical Society)



**Fig. 22.8** Illustration of UCNPs ( $\text{NaYF}_4:\text{Yb,Er}$ ) converting near-infrared radiation into visible radiation leading to photoexcitation of CdTe/ $\text{TiO}_2$ . (Adapted with permission from ref. [40]. Copyright 2016 American Chemical Society)



precision of PEC biosensing, a dual-channel self-reference PEC biosensor [38]. The authors employed pure CdTe and a composite of CdTe and graphene oxide (CdTe-GO) as the photoactive anodic and cathodic materials respectively, then functionalising both with aflatoxin B1 (AFB1) aptamer. The cathodic and anodic photocurrent could be well distinguished through the applied bias voltage, and, by applying an on/off signal, it makes it possible to attain dual concentration information in one detection. By comparing both results, the signal change from AFB1 can be clearly distinguished from any interference factor.

In the topic of biosensing, must be highlighted the use of upconverting nanoparticles (UCNPs). Usually, UCNPs contain in their composition, rare-earth-like lanthanides or actinides and exhibit anti-Stokes luminescent (photon upconversion). In other words, two or more incident photons of relatively low energy (such as infrared) are absorbed by the particle, and then emitted as one photon with higher energy (visible or ultraviolet) [39]. Due to the chemical stability of UCNPs, it is widely employed as fluorescence probes, facilitating bioassay tests. A near-infrared-driven PEC aptasensor for the detection of the MCF-7 cells, a kind of cell directly related to breast cancer was reported by Wang et al. [40]. The UCNPs ( $\text{NaYF}_4:\text{Yb,Er}$ ) were combined with a  $\text{TiO}_2/\text{CdTe}$  heterostructure, and the aptamer AS1411 was conjugated to the electrode for the recognition of the MCF-7 cell. Besides the heterojunction being photoexcited from visible radiation, the system was able to operate under near-infrared radiation. The UCNPs converted the near-infrared light to visible light, thus exciting the  $\text{TiO}_2/\text{CdTe}$  (see Fig. 22.8). As a result, the obtained PEC aptasensor was able to detect specifically MCF-7 cells in a range from  $1 \times 10^3$  to  $1 \times 10^5$  cells/mL.

## 22.3 Zn-Based Photoelectrochemical Biosensors

### 22.3.1 *Zn Sulphides and Selenides for Biological Samples Sensing*

Core-shell QDs have attracted a lot of attention in scientific research due to their chemical and physical properties [41, 42]. These materials are nanocrystals composed of a core of a semiconductor material enclosed within a shell of another semiconductor, and the second semiconductor has a larger spectral bandgap. QDs have small sizes (1–10 nm), then these materials display unique properties, unlike the bulk material. Due to the quantum-size confinement effects, QDs have important optical properties such as luminescence and photostability [43, 44]. CdE (E = S, Se, Te) have been widely used due to their luminescent properties. However, CdE is carcinogenic to humans, and inhalation of dust of the CdE can have harmful effects on the kidneys (impairment) and bone (bone weakness) [45, 46].

ZnS is considered a good substitute for CdE because is nontoxic to the human body, and is very cheap and abundant. This material is an n-type II-VI compound with a bandgap of 3.7 eV at room temperature and has high transparency. ZnS is a promising material for many applications: window layers of solar cells, data storage, data transfer and coatings that are sensitive to UV light [46, 47]. Zhang et al. [48] developed the first biosensor based on zinc sulphide (ZnS) QDs to detect a reagentless amperometric uric acid (UA). UA is a waste product found in the blood, and it is created when the body breaks down chemicals called purines. Most UA dissolves in the blood, passes through the kidneys and leaves the body in urine. High concentrations of UA in the human body can lead to gout or other cardiovascular diseases. ZnS QDs with free carboxyl groups on their surface were synthesised to prepare a uricase/ZnS QDs/L-cysteamine biosensor. Amperometric response for the uricase/ZnS QDs/L-cysteamine biosensor was performed using differential pulse voltammetry (DPV) measurements in uric acid solution. The obtained sensor was reproducible and the stabilisation of the sensor was tested in the presence of UA and stored at 4 °C for 20 days, maintaining 80.5% of its original activity. ZnS QDs presented good biocompatibility and conductivity and acts as an effective conjugate to provide a sufficient amount of the sites for binding of uricase and L-cysteamine. The ZnS QDs-derived uric acid biosensor exhibited high sensitivity, excellent thermal stability and anti-interference.

Some authors studied ZnS-based nanostructures as electrochemical and photoelectrochemical biosensors for UA detection [49]. ZnS nanomaterials were deposited on indium tin oxide (ITO) conducting glass and then coated with uricase by physical absorption. ZnS nanomaterials with different morphologies were prepared by a hydrothermal method and the fabrication of the UA sensor was carried out using the spin coating method. Uricase was immobilised to ZnS nanomaterials via the entrapment method and the effect of nanostructured material morphology on uric acid detection was compared. Different ZnS morphologies were obtained with different molar ratios of ethylenediamine and water in the hydrothermal process.

When the ratio (ethylenediamine and water) is 0:1 were obtained ZnS nanoparticles. Otherwise, when the ratio is changed to 1:1, the observed ZnS nanocrystal was urchin-like spherical structures assembled into bunches of nanorods. Finally, for the ratio is 3:1, the product obtained was nanoflakes. The ZnS urchin-like nanostructures electrode shows better sensitivity compared with those made of nanoparticles and nanoflakes because of its high surface-area-to-volume ratio. The photoelectrochemical method for the detection of UA showed that the sensitivity was increased 5 times after irradiation of 300 nm UV light.

Using ZnSe-COOH nanoflakes (NFs) decorated with gold nanoparticles, [50] developed a dual signal amplification PEC biosensing approach for microRNA (miRNA)-122a detection. Due to localised surface plasmon resonance of the Au NPs, the UV-Vis absorption spectrum of the Au NPs superimposed with ZnSe-COOH NFs emission spectrum, leading to an efficient FRET, that further improved PEC response. By combining this FRET process, with p19 protein specificity and affinity for miRNA-122a, the obtained PEC biosensor was ultrasensitive in a range from 350 fm to 5 nm. The authors also reported successful analysis of miRNA-122a in HeLa cells, which can be a valuable tool for early tumour diagnosis.

Some authors reported the combination of CdTe/CdSe/ZnSe QDs as a platform for enzyme-based electrochemical cholesterol biosensor [51]. The mercaptopropionic acid (MPA)-capped CdTe/CdSe/ZnSe QDs were synthesised in an aqueous phase and attached on a poly(propylene imine) (PPI)-coated glassy carbon electrode. Last, the biosensor was obtained by incubating the PPI/QDs-modified electrode into a cholesterol oxidase (ChOx) solution for 6 h. Since an efficient electron transfer process between the ChO<sub>x</sub> and the PPI/QDs-modified electrode was reached, the obtained biosensor was, besides being stable, able to detect cholesterol from 0.1 to 10 mM with a detection limit of 0.075 mM.

Glucose oxidase (GOD) is a homodimer flavoprotein and catalyses the oxidation of glucose to gluconic acid by utilising oxygen as an electron acceptor with simultaneous production of hydrogen peroxide. There is a study that makes a comparison of the electrochemical and photoelectrochemical behaviours of three biosensors, based on the use of Au, CdS and ZnS nanoparticles-GOD systems [52]. The three nanoparticles were electrodeposited onto an indium tin oxide (ITO) electrode. The immobilisation of GOD on the surface of electrodes modified with nanoparticles was performed using the sol-gel technique. The three systems generated outstanding photocurrents upon illumination. The electrochemical and photoelectrochemical biosensors based on ZnS nanostructures presented higher sensitivity than that of Au or CdS nanostructures.

Du et al. [46] did a more in-depth study of biosensors based on GOD and ZnS nanoparticles. The electrochemical and photoelectrochemical biosensors were investigated. ZnS nanoparticles were directly electrodeposited on the surface of an ITO electrode without using any link molecules and organic solvents. GOD was immobilised on the ZnS nanoparticles surface by the sol-gel method. The obtained biosensor can catalyse the reduction of oxygen and determine the concentration of glucose. The photocatalytic property of ZnS nanoparticles was investigated and the

glucose sensitivity of the biosensor under illumination was higher than that without illumination.

Suganthi et al. [53] prepared a glucose biosensor using ZnS nanoparticle-substituted graphene nanosheets. In this work, graphene was functionalised with ZnS nanoparticles by a simple chemical reduction method. The electrode used in the biosensor was carbon paper and it was modified by a simple drop-casting method, followed by the deposition of GOD (obtaining graphene/ZnS/GOD). The incorporation of graphene into the electrode increases the surface area and serves as excellent support for ZnS nanoparticles that effectively catalyse redox reactions involving  $H_2O_2$ , while ZnS nanoparticles allow for a lower potential amperometric detection of glucose. This biosensor presented good reproducibility and stability. The same research group [54] also prepared a cholesterol biosensor based on cholesterol oxidase (ChOx) using chitosan (CHI)-capped ZnS nanoparticles (ZnS/CHI). The biosensor was also prepared on a carbon paper electrode and modified by a simple drop-casting method. Initially, the deposition of the ZnS/CHI nanocomposite was performed. Next, the addition of nafion and enzyme was made and the methodology scheme is shown in Fig. 22.9. This work showed that the ZnS nanoparticles and CHI acted as an effective mediator between the enzyme ChOx and a carbon paper electrode. Nafion was added into a carbon paper electrode with immobilised ChOx and worked as a protective layer against electroactive interferences.

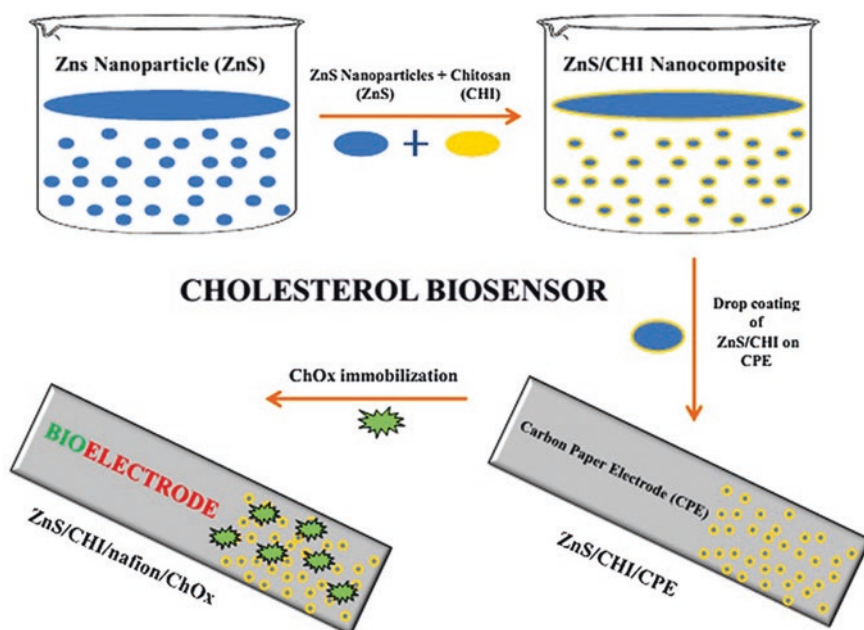


Fig. 22.9 Schematic diagram showing the fabrication procedure of ZnS/CHI/ChOx/NA/CPE biosensor. (Adapted with permission from ref. [56]. Copyright 2016; Elsevier)

Wang et al. [55] developed a new vapour deposition method, which was used to immobilise the horseradish peroxidase (HRP) with lipophilic CdSe/ZnS QDs on glassy carbon (GC) electrode surface and then, it was fabricated a hydrogen peroxide ( $H_2O_2$ ) biosensor. The authors concluded that lipophilic QDs could promote the electron transfer between proteins and electrodes and this electrochemical behaviour depends on the way that QDs modify the surface of the electrode. In this work, several methods for incorporation of HRP and lipophilic QDs were tested, but the best way was through vapour deposition.

A recent work prepared a biosensor for the detection of  $H_2O_2$  [56]. The bioelectrode was fabricated over the carbon paper electrode by the drop-casting method. The materials used in the biosensor preparation were ZnS, graphene (G), chitosan (CHI), horseradish peroxidase (HRP) and Nafion (NA). In this way were prepared two kinds of electrodes: ZnS/G/HRP/NA/CPE and ZnS/G/CHI/HRP/NA/CPE. The electrochemical activity of the fabricated nanocomposites was studied by recording cyclic voltammograms. With the addition of 0.3 mM  $H_2O_2$ , in electrochemical measurements, the reduction peak of the immobilised HRP increased, indicating a typical electro-catalytic behaviour to the reduction of  $H_2O_2$ . The cathodic current of ZnS/G/CHI/HRP/NA/CPE was higher than that for the ZnS/G/HRP/NA/CPE. Thus, it was possible to conclude that the existence of amino groups in CHI acting as a stabilising mediator is due to its excellent biocompatibility, film-forming ability and self-renewability. Moreover, the combination of ZnS/G nanocomposite and CHI increased the electroactive surface area of the electrode. The biosensor presented a performance for the detection of  $H_2O_2$  and good reproducibility, high sensitivity, rapid response and longtime stability.

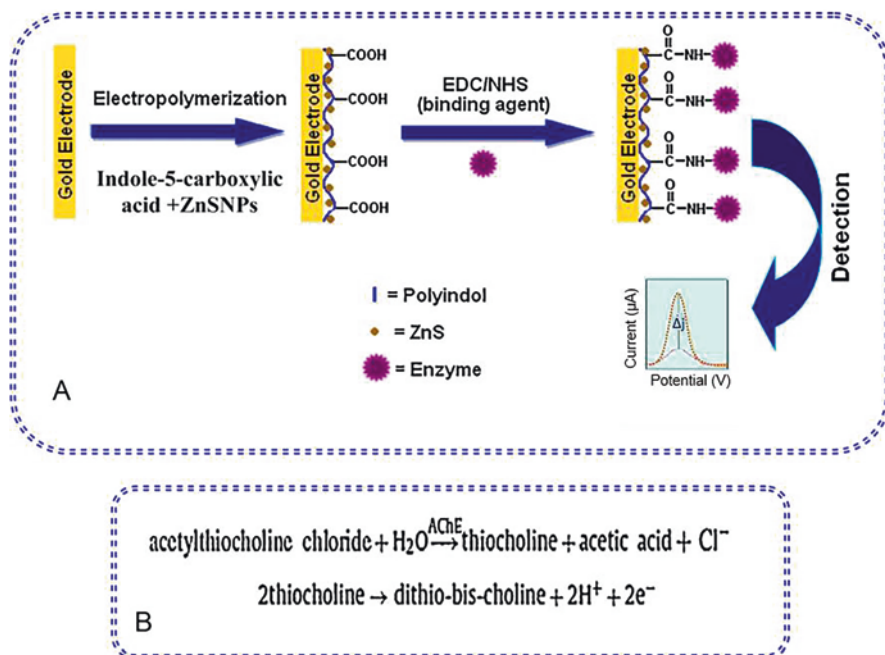
### 22.3.2 Zn-Based PEC Biosensors Designed for Pollutants

The detection of pollutant traces in public water supplies and aquifers is essential for the safety of the population. Catechol is considered a target pollutant due to its high toxicity and low degradability in the environment. Then, some authors [57] studied the catechol biosensor based on ZnS:Ni/ZnS QDs and laccase-modified glassy carbon electrode. The electrochemical method developed for the detection of catechol used cyclic voltammetry measurements. The biosensor showed excellent repeatability, stability and selectivity and was applied for real water samples determination.

Acetylcholinesterase (AChE) has drawn the attention of researchers because it is inhibited by organophosphorus (OP) compounds. Some authors prepared a highly sensitive amperometric biosensor for the detection of organophosphorus (OP) compounds [58]. The biosensor was synthesised based on rat brain acetylcholinesterase (AChE) immobilised onto nanocomposite of ZnS-nanoparticles (ZnSNPs) and poly(indole-5-carboxylic acid) (Pin5COOH) electrodeposited on Au electrode. Construction of nanocomposites modified Au electrode was made by electropolymerisation of ZnSNPs/Pin5COOH nanocomposite. On the prepared nanocomposite

surface were added few drops of enzyme solution followed by a mixture of N-ethyl-N'-(3-dimethylaminopropyl) carbodiimide (EDC) and N-hydroxysuccinimide (NHS). This biosensor determined malathion and chlorpyrifos in spiked tap water samples with high accuracy (95–100%). The biosensor could be used for the direct determination of pesticides in real samples as soils extract, vegetables, milk and water (see Fig. 22.10).

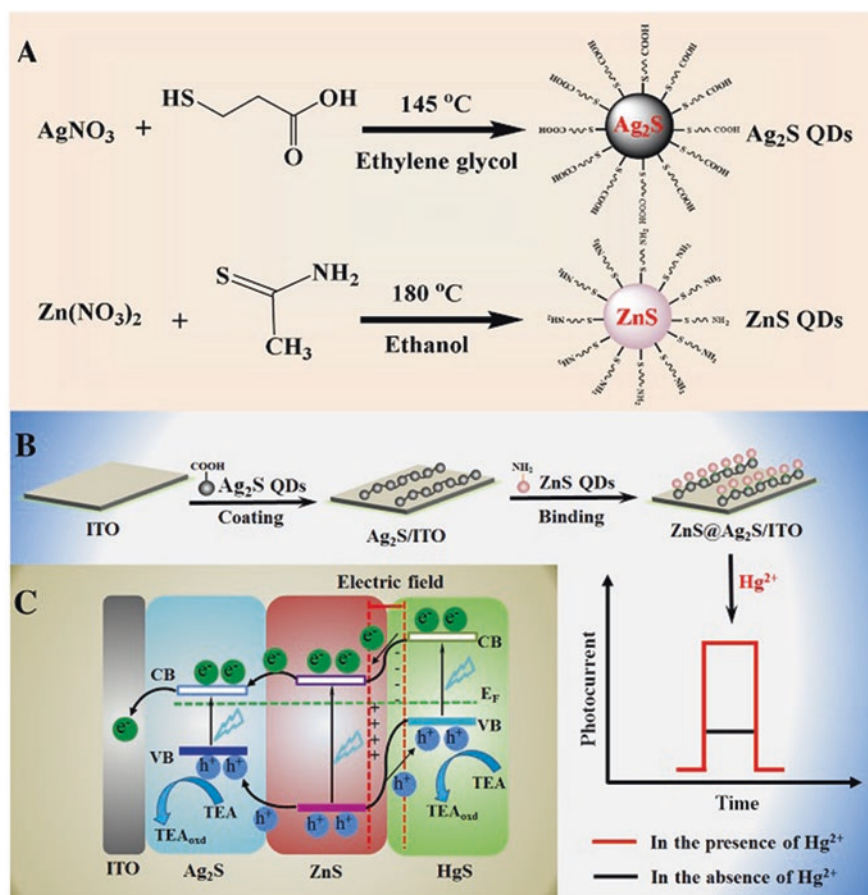
Li et al. [59] prepared a sensitive photoelectrochemical biosensor for the detection of OPs pesticides. The biosensor was prepared by nanocomposite of CdSe@ZnS QDs and graphene deposited on the ITO-coated glass electrode. The graphene/CdSe@ZnS nanostructures were modified with acetylcholine esterase (AChE). The increased photocurrent was observed by the formation of thiocholine, which acts as an electron donor for the photogenerated holes in the valence band of the CdSe@ZnS QDs. Thiocholine was generated because the AChE in assemblies catalyses the hydrolysis of acetylthiocholine. The AChE–CdSe@ZnS/graphene nanocomposite can generate photocurrent that was inversely dependent on the concentration of OPs. The organophosphorus pesticides tested in this work were paraoxon and dichlorvos. The photoelectrochemical biosensor showed good sensitivity, reproducibility and stability.



**Fig. 22.10** (a) Schematic illustration of the stepwise amperometric biosensor fabrication process and immobilisation of enzyme. (b) Measurement of electrochemical response. (Adapted with permission from ref. [60]. Copyright 2011: Elsevier)



Mercury is a heavy metal and its excessive accumulation in the human body may cause serious diseases such as pneumonia, enteritis and bronchitis. Zhang et al. [60] developed a visible-light-driven photoelectrochemical sensor for the “signal-on” analysis of  $\text{Hg}^{2+}$  by the synergetic combination of low-bandgap  $\text{Ag}_2\text{S}$  and wide-bandgap  $\text{ZnS}$  QDs.  $\text{Ag}_2\text{S}$  QDs were synthesised by the self-assembly route and further covalently coated with  $\text{ZnS}$  QDs (obtaining  $\text{ZnS}@Ag_2\text{S}$ ) onto the ITO electrodes. The synthetic route employed by the authors is shown in Fig. 22.11a. The manufacturing procedure of the  $\text{ZnS}@Ag_2\text{S}$ -modified electrode is disclosed in Fig. 22.11b. The schematic diagram of the main sensing principle is illustrated in



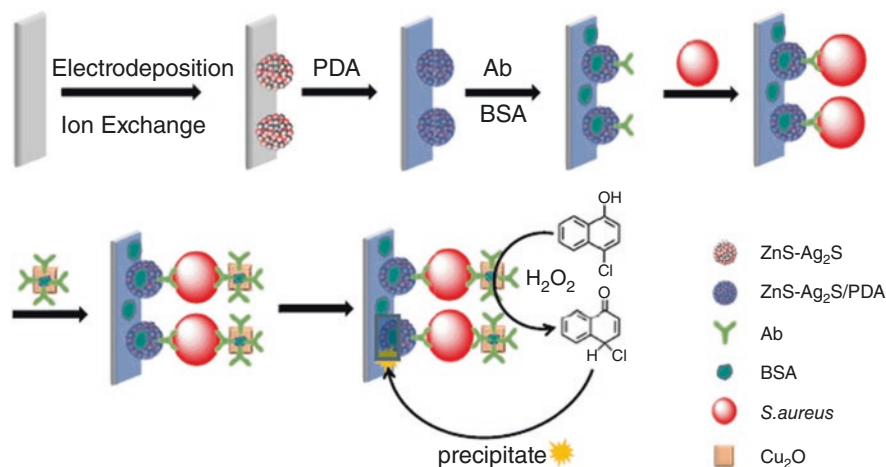
**Fig. 22.11** Schematic illustration of (a) the synthetic process of carboxyl-derivatized  $\text{Ag}_2\text{S}$  and amine-derivatized  $\text{ZnS}$  QDs using 3-MPA and TAA, respectively; (b) the immobilisation procedure of  $\text{Ag}_2\text{S}$  and  $\text{ZnS}$  QDs onto the ITO electrodes ( $\text{ZnS}@Ag_2\text{S}$ -modified electrodes) for the photoelectroanalysis of  $\text{Hg}^{2+}$ ; and (c) the mechanism of photocurrent responses of  $\text{ZnS}@Ag_2\text{S}$ -modified electrodes, showing the band structures of  $\text{HgS}/\text{ZnS}@Ag_2\text{S}$  heterojunction and charge separation under the visible-light illumination. (Adapted with permission from ref. [62]. Copyright 2020: Elsevier)

Fig. 22.11c. Band edges of  $\text{Ag}_2\text{S}$  QDs and ZnS QDs could be excited to generate the photoinduced carriers under visible light illumination. ZnS QDs, which otherwise are hard to be excited to generate photocurrents under visible light, displaying the improved photocurrent responses once coupled with  $\text{Ag}_2\text{S}$  QDs, which could act as the photoelectrochemical sensitiser to endow ZnS QDs with the enhanced light absorption and separation of photogenerated electrons and holes. The photocurrent responses of the modified  $\text{ZnS@Ag}_2\text{S}$  electrodes obtained were activated in the presence of  $\text{Hg}^{2+}$  under visible light illumination. This activation occurred due to the selective exchange of Zn to Hg in ZnS QDs that could act as the  $\text{Hg}^{2+}$  recognition probe. The formation of  $\text{HgS/ZnS@Ag}_2\text{S}$  heterojunction could be triggered to expect the enhanced charge separation towards the improved photoelectrochemical performance of  $\text{ZnS@Ag}_2\text{S}$  nanocomposites. A visible-light-activated photoelectrochemical sensor was developed for the determination of “signalling” of the  $\text{Hg}^{2+}$  trace, with levels below 1.0 pM.

### 22.3.3 Zn-Based PEC Immunosensors

Contamination of fish caused by bacteria can cause large-scale deaths. One type of bacteria that can contaminate fish is the *Aeromonas hydrophila*. Some authors studied a new molecular method for its detection [61]. In this used electrochemical techniques work was in preparation of a DNA biosensor. A screen-printed electrode was modified with ZnS nanospheres through electrodeposition. The obtained biosensor was able to detect the DNA of *Aeromonas hydrophila* in the range  $1.0 \times 10^{-4}$  to  $1.0 \times 10^{-9}$  mol  $\text{L}^{-1}$  and the limit of detection in this study was  $1 \times 10^{-13}$  mol  $\text{L}^{-1}$ . The biosensor presented high sensitivity and specificity in low concentrations and with little amounts of analyte.

Some authors noted the photoelectrochemical immunosensing of *Staphylococcus aureus* using ZnS- $\text{Ag}_2\text{S}$ /polydopamine (PDA) as novel photoelectric material and  $\text{Cu}_2\text{O}$  for peroxidase mimic tag [62]. ZnS- $\text{Ag}_2\text{S}$  heterojunctions were prepared by potentiostatic electrodeposition of ZnS nanoparticles on ITO, followed by silver ion exchange. The scheme of photoelectrochemical immunosensing preparation is presented in Fig. 22.12. ZnS nanoparticles were prepared on the ITO electrode by potentiostatic electrodeposition. The ZnS/ITO was subjected to ultrasonic-assisted ion exchange in an aqueous solution containing  $\text{AgNO}_3$ . The ZnS-PDA/ZnS- $\text{Ag}_2\text{S}$ /ITO was prepared by soaking the ZnS- $\text{Ag}_2\text{S}$ /ITO electrode in a Tris-HCl buffer containing dopamine. Subsequently, the deposition of  $\text{CuO}_2$  nanocubes was performed. Due to the excellent photoelectric performance and the great signal amplification of  $\text{Cu}_2\text{O}$  labelling, the photoelectrochemical immunosensor showed high sensitivity and a low detection limit.



**Fig. 22.12** Illustration of modification steps of the photoelectrochemical immunosensor. (Adapted with permission from ref. [62]. Copyright 2020: Elsevier)

## 22.4 Concluding Remarks

Usually, the use of a light source and biological compounds in the sensor is challenging in terms of commercialisation, in part due to requirements for long-term stability and the need to combine a light source within the sensor, requiring genuine advantages from both photo and bio responses to justify the development. Self-powered photoelectroanalytical devices offer an interesting alternative, but also chemical selectivity based on the interaction of the photoexcited electrode and the analyte can be beneficial. Despite being remarkably interesting from an academic perspective, it remains to be seen where the real application benefits of the photo(bio) electroanalytical tools lie.

Semiconductors suitable for photoelectro(bio)analysis lie in an area under constant development. The different materials morphologies and structures often trigger new concepts for sensor architectures. However, more detailed studies nearby the nano-bio interface are required aiming to achieve simpler and more effective biomolecular immobilisation routes. New biomolecule encapsulation and stabilisation methods, then, aim to enable large-scale production of simple semiconductor-based sensors to embed in complex surface designs.

The synergic effects from multifunctional materials combined with biological materials like enzymes or aptamers conduce to a device with enhanced sensibility, selectivity and reproducibility. The use of biological compounds can provide the specificity of enzymatic reactions (instead of observed in most bare photo-active films), the biorecognition of aptamers and DNA probes that combined with photo-electrochemistry offers a path to take advantage of natural selectivity merging good performance with low cost.

**Acknowledgements** This study was financed in part by the Coordenação de Aperfeiçoamento de Pessoal de Nível Superior – Brazil (CAPES) – Finance Code 001(Proc. 88887.362974/2019-00), CNPq, FAPESP (#grant 2013/07296-2, # grant 2017/11986-5).

## References

1. Xin YM, Zhang ZH. Photoelectrochemical stripping analysis. *Anal Chem.* 2018;90:1068–71. <https://doi.org/10.1021/acs.analchem.7b04381>.
2. Bonifazi D, Eger O, Diederich F. Supramolecular [60] fullerene chemistry on surfaces. *Chem Soc Rev.* 2007;36:390–414. <https://doi.org/10.1039/b604308a>.
3. Hu C, Zheng J, Su X, Wang J, Wu W, Hu S. Ultrasensitive all-carbon photoelectrochemical bioprobes for zeptomole immunosensing of tumor markers by an inexpensive visible laser light. *Anal Chem.* 2013;85:10612–9. <https://doi.org/10.1021/ac4028005>.
4. Lightcap IV, Kamat PV. Graphitic design: prospects of graphene-based nanocomposites for solar energy conversion, storage, and sensing. *Acc Chem Res.* 2013;46:2235–43. <https://doi.org/10.1021/ar300248f>.
5. Sheeney-Haj-Idria L, Willner I. Enhanced photoelectrochemistry in supramolecular CdS-nanoparticle-stoppered pseudorotaxane monolayers assembled on electrodes. *J Phys Chem B.* 2002;106:13094–7. <https://doi.org/10.1021/jp022102c>.
6. Da P, Li W, Lin X, Wang Y, Tang J, Zheng G. Surface Plasmon resonance enhanced real-time photoelectrochemical protein sensing by gold nanoparticle-decorated TiO<sub>2</sub> nanowires. *Anal Chem.* 2014;86:6633–9. <https://doi.org/10.1021/ac501406x>.
7. Lee YL, Chi CF, Liao SY. CdS/CdSe Co-sensitized TiO<sub>2</sub> photoelectrode for efficient hydrogen generation in a photoelectrochemical cell. *Chem Mater.* 2010;22:922–7. <https://doi.org/10.1021/cm901762h>.
8. del Barrio M, Luna-Lopez G, Pita M. Enhancement of biosensors by implementing Photoelectrochemical processes. *Sensors.* 2020;20:3281. <https://doi.org/10.3390/s20113281>.
9. Wang Y, Shen L, Wang Y, Hou B, Gibson GN, Poudel N, Chen J. Hot electron-driven photocatalysis and transient absorption spectroscopy in plasmon resonant grating structures. *Faraday Discuss.* 2019;214:325–39. <https://doi.org/10.1039/C8FD00141C>.
10. Zhao WW, Xu JJ, Chen HY. Photoelectrochemical enzymatic biosensors. *Biosens Bioelectron.* 2017;92:294–304. <https://doi.org/10.1016/j.bios.2016.11.009>.
11. Zhao W-W, Xiong M, Li X-R, Xu J-J, Chen H-Y. Photoelectrochemical bioanalysis: a mini review. *Electrochem Commun.* 2014;38:40–3. <https://doi.org/10.1016/j.elecom.2013.10.035>.
12. Voccia D, Palchetti I, J. Photoelectrochemical biosensors for nucleic acid detection. *Nanosci Nanotechnol.* 2015;15:3320–32. <https://doi.org/10.1166/jnn.2015.10039>.
13. He LH, Zhang QS, Gong CL, Liu H, Hu FQ, Zhong F, Wang GJ, Su HH, Wen S, Xiang SC, Zhang BQ. The dual-function of hematite-based photoelectrochemical sensor for solar-to-electricity conversion and self-powered glucose detection. *Sens Actuators B.* 2020;310:127842. <https://doi.org/10.1016/j.snb.2020.127842>.
14. Cakiroglu B, Ozacar M. A self-powered photoelectrochemical glucose biosensor based on supercapacitor Co3O4-CNT hybrid on TiO<sub>2</sub>. *Biosens Bioelectron.* 2018;119:34–41. <https://doi.org/10.1016/j.bios.2018.07.049>.
15. Zhao K, Yan XQ, Gu YS, Kang Z, Bai ZM, Cao SY, Liu YC, Zhang XH, Zhang Y. Self-powered photoelectrochemical biosensor based on CdS/RGO/ZnO nanowire array heterostructure. *Small.* 2016;12:245–51. <https://doi.org/10.1002/smll.201502042>.
16. Zhao S, Volkner J, Riedel M, Witte G, Yue Z, Lisdat F, Parak WJ. Multiplexed readout of enzymatic reactions by means of laterally resolved illumination of quantum dot electrodes. *ACS Appl Mater Interfaces.* 2019;11:21830–9. <https://doi.org/10.1021/acsami.9b03990>.

17. Freeman R, Girsh J, Willner B, Willner I. Sensing and biosensing with semiconductor quantum dots. *Israel J Chem.* 2012;52:1125–36. <https://doi.org/10.1002/ijch.201200079>.
18. Freeman R, Girsh J, Willner I. Nucleic acid/quantum dots (QDs) hybrid systems for optical and photoelectrochemical sensing. *ACS Appl Mater Interfaces.* 2013;5:2815–34. <https://doi.org/10.1021/am303189h>.
19. Zhang K, Yu T, Liu F, Sun MT, Yu H, Liu BH, Zhang ZP, Jiang H, Wang SH. Selective fluorescence turn-on and ratiometric detection of organophosphate using dual-emitting Mn-doped ZnS nanocrystal probe. *Anal Chem.* 2014;86:11727–33. <https://doi.org/10.1021/ac503134r>.
20. Golub E, Niazov A, Freeman R, Zatsepin M, Willner I. Photoelectrochemical biosensors without external irradiation: probing enzyme activities and DNA sensing using Hemin/G-Quadruplex-stimulated Chemiluminescence Resonance Energy Transfer (CRET) generation of photocurrents. *J Phys Chem C.* 2012;116:13827–34. <https://doi.org/10.1021/jp303741x>.
21. Sudip S, Chan Y, Soleymani L. Enhancing the photoelectrochemical response of DNA biosensors using wrinkled interfaces. *ACS Appl Mater Interfaces.* 2018;10:31178–85. <https://doi.org/10.1021/acsami.8b12286>.
22. Zhao Y, Tan L, Gao X, Jie G, Huang T. Silver nanoclusters-assisted ion-exchange reaction with CdTe quantum dots for photoelectrochemical detection of adenosine by target-triggering multiple-cycle amplification strategy. *Biosens Bioelectron.* 2018;110:239–45. <https://doi.org/10.1016/j.bios.2018.03.069>.
23. Sun B, Dong J, Cui L, Feng T, Zhu J, Liu X, Ai S. A dual signal-on photoelectrochemical immunosensor for sensitively detecting target avian viruses based on AuNPs/g-C<sub>3</sub>N<sub>4</sub> coupling with CdTe quantum dots and in situ enzymatic generation of electron donor. *Biosens Bioelectron.* 2019;124:1–7. <https://doi.org/10.1016/j.bios.2018.09.100>.
24. Cai J, Sheng P, Zhou L, Shi L, Wang N, Cai Q. Label-free photoelectrochemical immunosensor based on CdTe/CdS co-sensitized TiO<sub>2</sub> nanotube array structure for octachlorostyrene detection. *Biosens Bioelectron.* 2013;50:66–71. <https://doi.org/10.1016/j.bios.2013.05.040>.
25. Yan K, Wang R, Zhang J. A photoelectrochemical biosensor for o-aminophenol based on assembling of CdSe and DNA on TiO<sub>2</sub> film electrode. *Biosens Bioelectron.* 2013;53:301–4. <https://doi.org/10.1016/j.bios.2013.09.073>.
26. Wang W, Bao L, Lei J, Tu W, Ju H. Visible light induced photoelectrochemical biosensing based on oxygen-sensitive quantum dots. *Anal Chim Acta.* 2012;744:33–8. <https://doi.org/10.1016/j.aca.2012.07.025>.
27. Sun J, Zhu Y, Yang X, Li C. Photoelectrochemical glucose biosensor incorporating CdS nanoparticles. *Particuology.* 2009;7:347–52. <https://doi.org/10.1016/j.partic.2009.04.009>.
28. Wang GL, Liu KL, Dong YM, Wu XM, Li ZJ, Zhang C. A new approach to light up the application of semiconductor nanomaterials for photoelectrochemical biosensors: using self-operating photocathode as a highly selective enzyme sensor. *Biosens Bioelectron.* 2014;62:66–72. <https://doi.org/10.1016/j.bios.2014.06.033>.
29. Zheng M, Cui Y, Li X, Liu S, Tang Z. Photoelectrochemical sensing of glucose based on quantum dot and enzyme nanocomposites. *Electroanal Chem.* 2011;656:167–73. <https://doi.org/10.1016/j.jelechem.2010.11.036>.
30. Huanli W, Zhang L, Chen Z, Hu J, Li S, Wang Z, Liu J, Wang X. Semiconductor heterojunction photocatalysts: design, construction, and photocatalytic performances. *Chem Soc Rev.* 2014;43:5234. <https://doi.org/10.1039/C4CS00126E>.
31. Li PP, Cao Y, Mao CJ, Jin BK, Zhu JJ. TiO<sub>2</sub>/g-C<sub>3</sub>N<sub>4</sub>/CdS nanocomposite-based photoelectrochemical biosensor for ultrasensitive evaluation of T4 polynucleotide kinase activity. *Anal Chem.* 2018;91:1563–70. <https://doi.org/10.1021/acs.analchem.8b04823>.
32. Han Z, Weng Q, Lin C, Yi J, Kang J. Development of CdSe–ZnO flower-rod Core-Shell structure based photoelectrochemical biosensor for detection of norovirus RNA. *Sensors.* 2018;18:2980–8. <https://doi.org/10.3390/s18092980>.
33. Barroso J, Saa L, Grinyte R, Pavlov V. Photoelectrochemical detection of enzymatically generated CdS nanoparticles: application to development of immunoassay. *Biosens Bioelectron.* 2016;77:323–9. <https://doi.org/10.1016/j.bios.2015.09.043>.

34. Xu R, Wei D, Du B, Cao W, Fan D, Zhang Y, Ju H. A photoelectrochemical sensor for highly sensitive detection of amyloid beta based on sensitization of Mn: CdSe to Bi<sub>2</sub>WO<sub>6</sub>/CdS. *Biosens Bioelectron.* 2018;122:37–42. <https://doi.org/10.1016/j.bios.2018.09.030>.
35. Zhang X, Li S, Jin X, Zhang S. A new photoelectrochemical aptasensor for the detection of thrombin based on functionalized graphene and CdSe nanoparticles multilayers. *Chem Commun.* 2011;47:4929–31. <https://doi.org/10.1039/C1CC10830A>.
36. Liu Y, Yan K, Zhang J. Electrochemical, photoelectrochemical, and surface plasmon resonance detection of cocaine using supramolecular aptamer complexes and metallic or semiconductor nanoparticles. *ACS Appl Mater Interfaces.* 2016;8:28255–64. <https://doi.org/10.1021/ac901551q>.
37. Golub E, Pelosoff G, Freeman R, Zhang H, Willner I. Electrochemical, photoelectrochemical, and surface plasmon resonance detection of cocaine using supramolecular aptamer complexes and metallic or semiconductor nanoparticles. *Anal Chem.* 2009;81:9291–8. <https://doi.org/10.1021/ac901551q>.
38. Hao N, Zhang Y, Zhong H, Zhou Z, Hua R, Qian J, Liu Q, Li H, Wang K. Design of a dual channel self-reference photoelectrochemical biosensor. *Anal Chem.* 2017;89:10133–6. <https://doi.org/10.1021/acs.analchem.7b03132>.
39. Loo JFC, Chien YH, Yin F, Kong SK, Ho HP, Yong KT. Upconversion and downconversion nanoparticles for biophotonics and nanomedicine. *Coord Chem Rev.* 2019;400:213042–82. <https://doi.org/10.1016/j.ccr.2019.213042>.
40. Wang K, Zhang R, Sun N, Li X, Wang J, Cao Y, Pei R. Near-infrared light-driven photoelectrochemical aptasensor based on the upconversion nanoparticles and TiO<sub>2</sub>/CdTe heterostructure for detection of cancer cells. *Appl Mater Interfaces.* 2016;8:25834–9. <https://doi.org/10.1021/acsami.6b09614>.
41. Halliday DP, Eggleston JM, Durose K. A study of the depth dependence of photoluminescence from thin film CdS/CdTe solar cells using bevel etched samples. *Thin Solid Films.* 1998;322:314–8. [https://doi.org/10.1016/S0040-6090\(97\)00917-6](https://doi.org/10.1016/S0040-6090(97)00917-6).
42. Azzazy HME, Mansour MMH, Kazmierczak SC. From diagnostics to therapy: prospects of quantum dots. *Clin Biochem.* 2007;40:917–27. <https://doi.org/10.1016/j.clinbiochem.2007.05.018>.
43. Jin WJ, Costa-Fernandez JM, Pereira R, Sanz-Medel A. Surface-modified CdSe quantum dots as luminescent probes for cyanide determination. *Anal Chim Acta.* 2004;522:1–8. <https://doi.org/10.1016/j.aca.2004.06.057>.
44. Huang CP, Liu SW, Chen TM, Li YK. A new approach for quantitative determination of glucose by using CdSe/ZnS quantum dots. *Sensors Actuators B Chem.* 2008;130:338–42. <https://doi.org/10.1016/j.snb.2007.08.021>.
45. Miyawaki T, Ichimura M. Fabrication of ZnS thin films by an improved photochemical deposition method and application to ZnS/SnS heterojunction cells. *Mater Lett.* 2007;61:4683–6. <https://doi.org/10.1016/j.matlet.2007.03.006>.
46. Du J, Yu X, Wu Y, Di J. ZnS nanoparticles electrodeposited onto ITO electrode as a platform for fabrication of enzyme-based biosensors of glucose. *Mater Sci Eng C.* 2013;33:2031–6. <https://doi.org/10.1016/j.msec.2013.01.019>.
47. Fathy N, Ichimura M. Photoelectrical properties of ZnS thin films deposited from aqueous solution using pulsed electrochemical deposition. *Solar Energy Mater.* 2005;87:747–56. <https://doi.org/10.1016/j.solmat.2004.07.048>.
48. Zhang F, Li C, Li X, Wang X, Wan Q, Xian Y, Jin L, Yamamoto K. ZnS quantum dots derived a reagentless uric acid biosensor. *Talanta.* 2006;68:1353–8. <https://doi.org/10.1016/j.talanta.2005.07.051>.
49. Zhao Y, Wei X, Peng N, Wang J, Jiang Z. Study of ZnS nanostructures based electrochemical and photoelectrochemical biosensors for uric acid detection. *Sensors.* 2017;17:1235–45. <https://doi.org/10.3390/s17061235>.
50. Tu W, Cao H, Zhang L, Bao J, Liu X, Dai Z. Dual signal amplification using gold nanoparticles-enhanced Zinc Selenide nanoflakes and P19 protein for ultrasensitive photoelectrochemical biosensing of MicroRNA in cell. *Anal. Chem.*, 2016;88(21), 10459–10465. <https://doi.org/10.1021/acs.analchem.6b02381>.

51. Mokwebo KV, Oluwafemi OS, Arotiba OA. An electrochemical cholesterol biosensor based on a CdTe/CdSe/ZnSe quantum dots—poly (propylene imine) dendrimer nanocomposite immobilisation layer. *Sensors*. 2018;18(10):3368. <https://doi.org/10.3390/s18103368>.
52. Du J, Yu X, Di J. Comparison of the direct electrochemistry of glucose oxidase immobilized on the surface of Au, CdS and ZnS nanostructures. *Biosens Bioelectron*. 2012;37:88–93. <https://doi.org/10.1016/j.bios.2012.04.044>.
53. Suganthi G, Arockiadoss T, Uma TS. ZnS nanoparticles decorated graphene nanoplatelets as immobilisation matrix for glucose biosensor. *Nanosyst Phys Chem Math*. 2016;7:637–42. <https://doi.org/10.17586/2220-8054-2016-7-4-637-642>.
54. Suganthi G, Ramanathan G, Arockiadoss T, Sivagnanama UT. Facile synthesis of chitosan-capped ZnS nanoparticles as a soft biomimetic material in biosensing applications. *Process Biochem*. 2016;51:845–53. <https://doi.org/10.1016/j.procbio.2016.04.001>.
55. Wang Z, Xu Q, Wang HQ, Yang Q, Yu JH, Zhao YD. Hydrogen peroxide biosensor based on direct electron transfer of horseradish peroxidase with vapor deposited quantum dots. *Sensors Actuators B Chem*. 2009;138:278–82. <https://doi.org/10.1016/j.snb.2008.12.040>.
56. Suganthi G, Ramanathan G, Arockiadoss T, Sivagnanam UT. H<sub>2</sub>O<sub>2</sub> biosensor based on horseradish peroxidase immobilized onto the zinc sulphide–graphene–chitosan modified carbon paper electrode. *Bull Mater Sci*. 2021;44:70–5. <https://doi.org/10.1007/s12034-021-02358-w>.
57. Wang Y, Qu J, Li S, Qu J. Catechol biosensor based on ZnS:Ni/ZnS quantum dots and laccase modified glassy carbon electrode. *J Nanosci Nanotechnol*. 2016;16:8302–7. <https://doi.org/10.1166/jnn.2016.11649>.
58. Chauhan N, Narang J, Pundir CS. Immobilization of rat brain acetylcholinesterase on ZnS and poly(indole-5-carboxylic acid) modified Au electrode for detection of organophosphorus insecticides. *Biosens Bioelectron*. 2011;29:82–8. <https://doi.org/10.1016/j.bios.2011.07.070>.
59. Li X, Zheng Z, Liu X, Zhao S, Liu S. Nanostructured photoelectrochemical biosensor for highly sensitive detection of organophosphorus pesticides. *Biosens Bioelectron*. 2015;64:1–5. <https://doi.org/10.1016/j.bios.2014.08.006>.
60. Zhang L, Li P, Feng L, Chen X, Jiang J, Zhang S, Zhang C, Zhang A, Chen G, Wang H. Synergetic Ag<sub>2</sub>S and ZnS quantum dots as the sensitizer and recognition probe: a visible light-driven photoelectrochemical sensor for the “signal-on” analysis of mercury (II). *J Hazard Mater*. 2020;387:121715–25. <https://doi.org/10.1016/j.jhazmat.2019.121715>.
61. Negahdary M, Jafarzadeh M, Rahimzadeh R, Rahimi G, Dehghani H. A DNA biosensor for molecular diagnosis of *Aeromonas hydrophila* using zinc sulfide nanospheres. *J Sens Sens Syst*. 2017;6:259–67. <https://doi.org/10.5194/jsss-6-259-2017>.
62. Yang H, Chen H, Cao L, Wang H, Deng W, Tan Y, Xie Q. An immunosensor for sensitive photoelectrochemical detection of *Staphylococcus aureus* using ZnS–Ag<sub>2</sub>S/polydopamine as photoelectric material and Cu<sub>2</sub>O as peroxidase mimic tag. *Talanta*. 2020;212:120797–804. <https://doi.org/10.1016/j.talanta.2020.120797>.

# Chapter 23

## II–VI Semiconductor QDs in Surface Plasmon Resonance Sensors



Hina F. Badgajar and Anuj K. Sharma

### 23.1 Introduction: Principles of Surface Plasmon Resonance (SPR)

Surface plasmon resonance (SPR) sensor platform works on optical theory to measure the refractive index (RI) variation within the range of the surface plasmon field, which extends up to ~300 nm away from the sensor surface (x- and y-axis direction) and is equivalent to an evanescent wave (EW). The penetration depth of EW depends on the wavelength of incident light and it decays exponentially in the direction of the z-axis with the distance from the interface. In order to generate a plasmonic field at the metal-dielectric interface, the momentum of the incoming light must match with the momentum of the conduction band electrons. When the coupling condition is satisfied at a particular angle and wavelength, the light is converted very effectively into surface plasmon waves (SPW). This phase matching is achieved through the phenomenon of attenuated total reflection (ATR) at smooth flat surfaces. It generally requires a higher RI material (Fig. 23.1a). The matching condition may be interpreted according to the dispersion relation given by Raether et al. [59]:

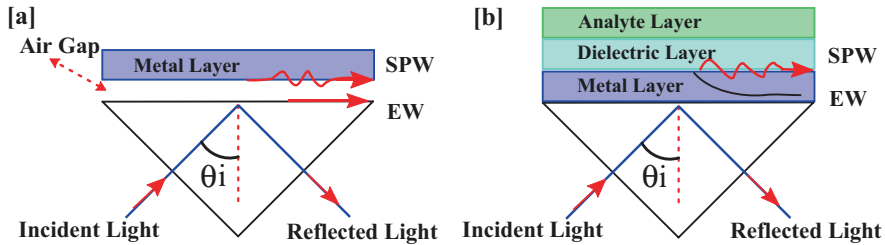
$$K_{\text{spp}} = \frac{2\pi}{\lambda_0} \sqrt{\frac{\epsilon_m \epsilon_d}{\epsilon_m + \epsilon_d}} = \frac{2\pi}{\lambda_0} n_p \sin \theta_i \quad (23.1)$$

---

H. F. Badgajar  
Central University of Gujarat, Gandhinagar, India

A. K. Sharma (✉)  
National Institute of Technology Delhi, Delhi, India  
e-mail: [anujsharma@nitdelhi.ac.in](mailto:anujsharma@nitdelhi.ac.in)





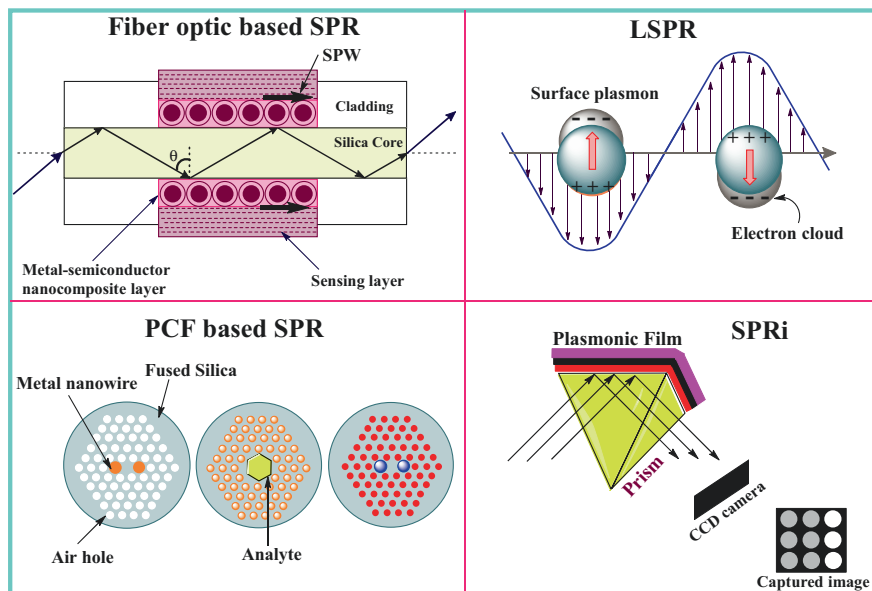
**Fig. 23.1** Otto (a) and Kretschmann (b) configuration. EW stands for Evanescent Wave and SPW refers to the surface plasmon wave

where  $n_p$  is the RI of the coupling prism,  $\theta_i$  is the incident angle of light,  $\epsilon_m$  is the dielectric constant of metal,  $\epsilon_d$  is the dielectric constant of dielectric and  $K_{spp}$  is the wave vector of surface plasmon. The biosensing mechanism takes place by detecting the analytes layer adjacent to the metal-dielectric layer with the EW through the interaction of light (Fig. 23.1b). In the plasmon resonance condition, any minute changes in RI can be monitored in terms of variations in intensity, wavelength, or angular shift for sensing purposes. Here  $\epsilon_m$  depends on the wavelength of the incident light, and  $\epsilon_d$  depends on the RI of the dielectric environment.

Further, in order to generate localised surface plasmon resonance (LSPR), particularly around the nanoparticle vertices, the external electric field can be applied to “nano-islands” of NPs. These islands induce very strong surface plasmon field gradients that could potentially lead to a phenomenon of light entrapment. When this occurs, the electron clouds of nano-islands encounter combined harmonic oscillations and are smaller than the light wavelength, typically in the Mie scattering region. NPs of gold (Au) and silver (Ag) are generally used to produce the strongly localised electromagnetic field with very high intensity.

SPR biosensing platform can be designed using different transducer configurations, such as the conventional Kretschmann configuration, including ATR, fibre-optic configuration, lossy mode resonances (LMRs) and SPR imaging (SPRi). Recently, it has been observed that the optical sensor design based on LSPR, long-range SPR (LRSPR), optical waveguide, optical resonator and photonic crystal (PC) are capable of providing enhanced sensing performance in comparison to the conventional SPR configuration (Fig. 23.2).

For SPRi, the phase or reflectivity is measured by a collimated beam of light passing through a prism and is rendered incident on a deposited plasmonic film. The reflected light is then detected with a CCD camera after crossing a narrow band interference filter, and an SPR image of the surface is thus obtained [30]. Among others, semiconducting NPs embedded transducer systems are of great importance in medical diagnostics and therapeutics. These solid-state SPR sensors provide new insights and information for understanding the effects of monitoring molecular interactions by RI increment on signal changes. These NPs are assumed to have the freedom to oscillate under the influence of the EW created by surface electrons. Collective oscillations of such surface electrons are highly sensitive to the RI



**Fig. 23.2** Design of SPR biosensor-based quantitative platforms for biomolecular detection

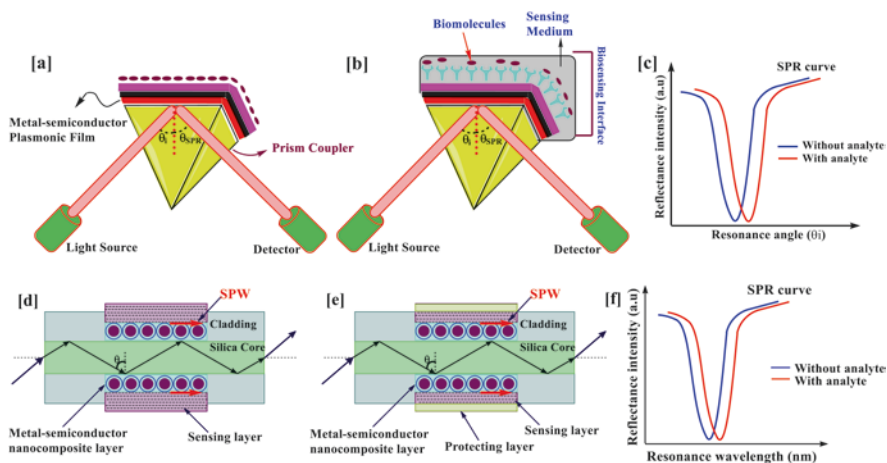
changes, which can be directly correlated with the mass density changes on a sensor surface, and can be used to measure real-time biomolecular interactions and quantification events [24, 53]. Classical models offer a qualitative approximation for understanding the biomolecule interaction. In this way, several approximations and models have been applied to transform a biomolecular binding event or biological reaction into a physically measurable signal [43].

Semiconductor plasmonicbiointerfaces are often designed with regenerative surface chemistry, allowing multiple interactions without loss of reactivity. The biointerface design typically consists of three essential components integrated into a single system: the optical setup, the fluid handling chamber and the sensing surface. The sensor configuration offers a physical barrier between the optical setup (dry portion) and the measurement chamber (wet portion). The characteristic of the biosensor has a major impact on the measurement of biological interaction. The importance of light interaction in a biophysical interface is an important area of research in the scientific community. However, the toughest task is to indulge the clinicians and clinical chemists in the functioning principles and assure them about its benefits. The non-invasive and label-free technology may be advantageous to exploit its acceptance by the healthcare industry in the near future biopsy technique. The following are the main components to fabricate the biosensor for biomedical applications and clinical prospects:

- Plane polarised incident wave that should be operated in the red and infrared region
- The thin film formation of plasmonic material (Au/Ag nanoarray)
- Coupling prism with a higher RI

Some components may vary according to the requirement of the applications. Many researchers have investigated nanostructure semiconductors for various biotechnological and optical sensing applications, and in this regard, the quantum dots (QDs) induce a dominant tunable LSPR. Over the last decades, the exploitation of QDs in a biosensor has been very prominent for probing biological processes and the associated biological surroundings effect in real-time measurement. Owing to its careful monitoring of biomolecules and high selectivity with a label-free approach, it has been extensively used to analyse the kinetics of biomolecular interactions such as lipid membrane-protein interactions [3], virus detection [71], hybridisation of DNA [24] and protein/polymer adsorption [11].

While fabricating SPR sensors, there are a few crucial parameters such as sensitivity, signal-to-noise ratio, accuracy, precision and response time that need to be taken into account and, to be calibrated with standard methods. The plasmon depth must be short enough to allow the molecular binding event to fill most of the plasmon field. However, it is not too short for the binding event to occur outside the plasmonic field. Therefore, the penetration depth must be optimal in the range of 10 to 20 nm. These parameters are strongly dependent on the measurement method, the preferred optical platform and selection of the deposited layer (as NPs, thin-films and pores nanomaterials) and even on the operational parameters (excitation wavelength, detector efficacy, etc.). Moreover, sensing ability such as cross-sensitivity or selectivity relies on the affinity between the bio-marker and the bio-receptor, as well as the environmental conditions (e.g. in vivo or in vitro) in which the sensor is being



**Fig. 23.3** Schematic representation of the Kretschmann configuration-based SPR biosensor. Prism-based SPR sensor consists of a prism (a), biomolecules and analyte layers (b) and its SPR curve when RI changes in the presence of analyte (c); and fibre optic SPR sensor with core-shell metal-semiconductor nanocomposite layer (d) sensing region coated with protecting layer (e) and its SPR curve when RI changes in the presence of analyte (f). Here, SPW stands for surface plasmon wave, which exists at the interface of the metal-semiconductor nanocomposite layer and the adjacent sensing layer

operated. For instance, experiments can be done under controlled buffer (PBS) conditions (Fig. 23.3), or in more complex matrices such as blood serum, plasma or blood itself [21]. Metal films corrode into biological solutions, thus, reducing the quality factor and the darkness of plasmon resonances and sensitivity. The use of semiconductor layer on the metallic film extends the range of metals that can be used for plasmon biosensing and increases sensitivity by higher orders of magnitude [96]. It promises the stability of metal in a liquid and preserves plasmonic resonance under biofunctionalisation [90]. Essential parameters, for example, regeneration, repeatability, or reproducibility, are highly dependent on the testing chip and, consequently, introducing external bio-agents, like enzymes, that can disturb the already functionalised bioreceptors or biomarker connection to start the detection process again.

As the complexity of the experimental medium increases, it is necessary to handle the potential number of difficulties, since many other biomolecules can trigger the reaction by interfering with the detection of analyte solution [6].

The planar geometry of SPR lends itself well to multilayer structures to enrich the biological sensitivity. Accordingly, multilayer approaches have generally been demonstrated in prism-coupled systems and adapted for boosting the SPR biosensor performance [58]. However, the difficulty lies in incorporating the biofunctionalised sensing layer without disturbing the optical properties of the multilayer. The semiconductor NPs layers between the metal coating and the bio-receptors determine the biomolecules immobilisation and provide new avenues for achieving bio-detection selectivity [67]. The performance is commonly measured in terms of RI sensitivity, RI resolution and figure of merit (FOM). An optimal biosensor would have enormous RI sensitivity (leading to an extremely fine RI resolution) with a narrow plasmon resonance for high FOM defined as:

$$\text{FOM} = \frac{\text{Sensitivity}}{\text{FWHM}} \quad (23.2)$$

In the above expression, FWHM is the full width of the plasmon band at half maximum. The improvement in sensor design is the most exciting research field in biomedical application and clinical chemistry, especially for LSPR sensors. Regardless of these, the plasmon resonance should ideally be tuned into the biological window in the near-infrared (NIR) region to avoid spectral interference to detect LSPR resonance in biofluids. Many strategies to enhance biological interaction have been demonstrated. Here, a fibre optic SPR probe with metal (core) semiconductor (shell) nanocomposite design based on wavelength and angular mode is shown (see Fig. 23.3d, e) [65]. The effect of NP diameter, thickness of the sensing layer and their surrounding curvature on sensor's performance were studied in this work [65]. Four types of spherical shape semiconductor materials, namely, cadmium sulphide (CdS), cadmium selenide (CdSe), lead sulphide (PbS) and zinc oxide (ZnO) are taken into account for the plasmonic resonance. In further work, different values of RI for different sensing layers are also considered for the core-shell NPs. However, a more practical difficulty is their stability while performing an

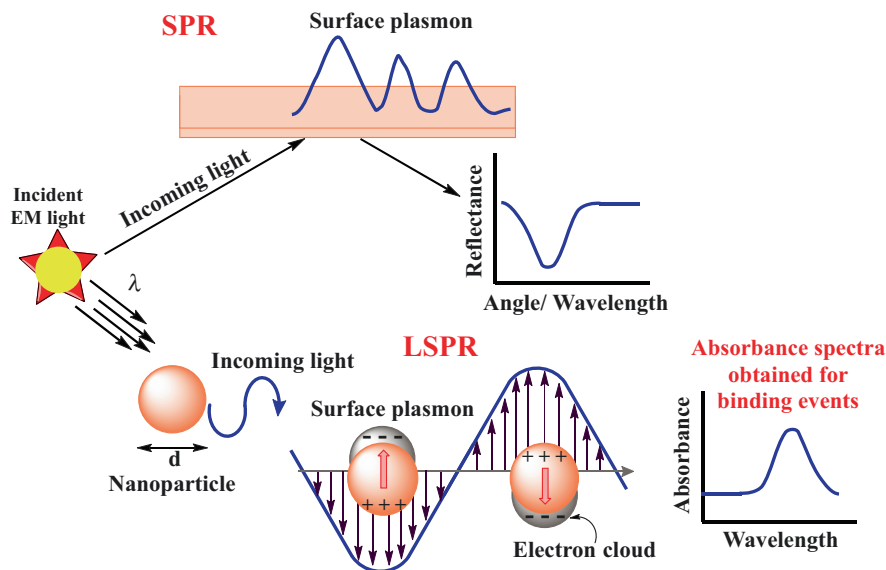
in vivo test. As a result, the signal does not suffer from light scattering through the very dense matrix. To achieve this objective, measurements in undiluted biological fluids, long-term stability in complex matrices and integration into the body are vital.

To access the biological window, semiconducting NPs are currently considered to achieve higher sensitivity and resonances in the infrared region [5, 41]. It is important to note that in vivo biosensors may be used to continuously monitor therapeutic concentrations of drugs with a narrow therapeutic range. Therefore, more advanced spectroscopic techniques needed to be applied for accurate determination of particles size, concentration and deformations at biointerfaces [60]. Conceivably, semiconductor nanostructures could provide unperturbed light intensities at different measurement angles or wavelengths, thereby reducing signal drift arising from biointerferences at the sensor design level.

## 23.2 SPR-Based Biosensors

The basic functionality of an SPR biosensor is to analyse the kinetics of biomolecular events in the presence of biochemical target analytes for performing the wide ranges of clinical tasks such as imaging, detection, recognition and monitoring of different tissues and organs. SPR sensors facilitate noninvasive, label-free and rapid biological response during the biomolecular binding events in real-time analysis. For label-free real-time detection, the physicochemical transduction method is utilised to convert the biological signal into an accurate electronic signal based on the bio-signalling of the analytes. These signals carry helpful information (i.e. quantitative analysis of targeted analyte or group of analytes) in understanding the physiological mechanisms of a specific event or biological system. The application of SPR biosensing can be helpful in real-time medical diagnosis using portable point-of-care devices.

In order to acquire basic knowledge about the SPR operation, a fundamental understanding of the optics is sufficient, as we have discussed in an earlier section. The result for the sensor chip based on the metal interface is broadly achievable in all aspects, but the metal-semiconductor nanoplasmonic interface offers good performance owing to recent chip progression [1, 45, 66, 94]. The semiconductor medium leads to a rapid injection of the charge carriers into the metal to produce an enormous plasmonic response and quantum efficiency [65]. The coupling of the SPW and the electromagnetic behaviour of the background medium could be expected to produce a tunable optical response with a dominant LSPR. Thus, the collective and coherent oscillation of electrons across the NPs upon the interaction with light at a specific resonant wavelength causes LSPR phenomena (Fig. 23.4). The plasmonic resonance can be influenced by the diameter and doping concentration and the nature of the composition, including the inter-particle distance [80]. To manifest a resonance effect, an appropriate selection of NP is significant for achieving excellent sensing performance.



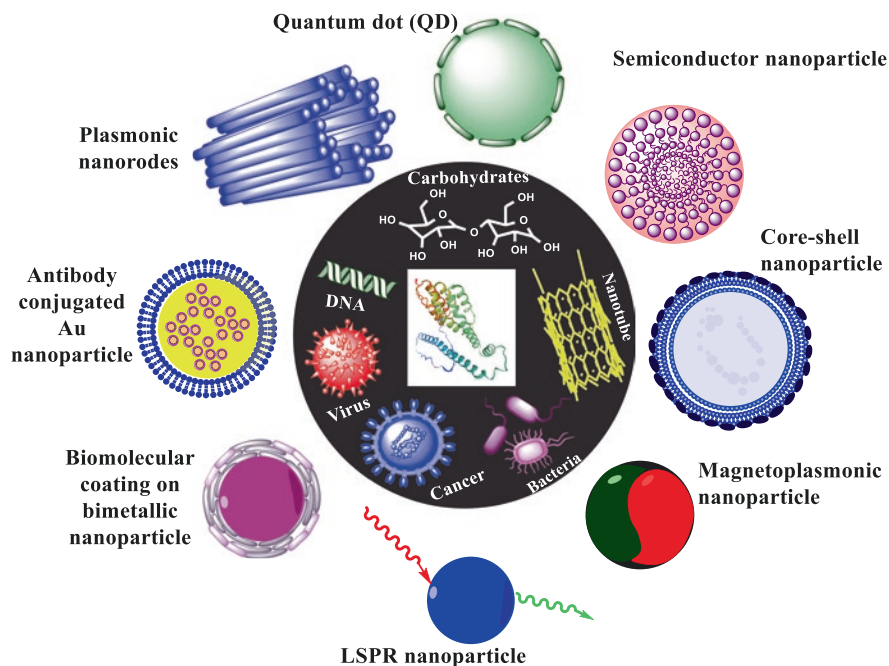
**Fig. 23.4** Schematic of surface plasmon oscillations in prism coupling configuration and localised surface plasmon on NP. Incoming light impinges on a thin metallic film deposited on a prism surface where the p-polarised light absorbed by the surface plasmon is seen from a minimum in the reflection spectra. In LSPR, a confined oscillation of the surface plasmon in the NP surface is generated corresponding absorbance spectra for binding events on NPs

NP-based optical platforms have received considerable interest due to their higher sensitivity and selectivity. Interesting developments have been carried out concerning the application in metallic semiconductor NP-based biosensors. The use of various metal-semiconductor nanostructures has resulted in faster detection, low-cost manufacturing, reproducibility, flexibility and adequate sensitivity. In this context, near-field enhancement and high LSPR characteristics of metal-semiconductor NPs were studied theoretically and experimentally for plasmon-related applications [1, 17, 19, 65, 72]. The enhanced plasmonic behaviour of NPs depends on geometric morphology (i.e. sphere, cubic, tubular, tetrahedron and octahedron), matrix structure (i.e. rigid sphere, hollow core and core-shell) and composition of NPs, excitation wavelength, as well as the local dielectric environment [63, 89, 95].

The concept of light interaction and plasmonic oscillations in metal-semiconductor-based nanosystem has received much attention in the fabrication of SPR biosensors [57]. Also, the coupling of plasmonic and semiconducting features could lead to tunable photoluminescence (PL), large resonance Raman scattering and ultimate linear/non-linear optical characteristics. Plasmonic properties of semiconductors are suitable for NIR and mid-infrared (MIR) wavelength sensing applications [9]. Quantum effects gain importance for NPs, when electron tunnelling across the dielectric barrier occurs in the minimal gap. Electronic tunnelling reduces the magnitude of total mode splitting with an additional narrowing of the gap and field improvement compared to conventional predictions. Metal NPs can be

incorporated into a semiconductor matrix using experimental methods, resulting in higher extinction, more scattering quantum efficiency and more remarkable field improvement than metallic NPs [98]. In particular, LSPR peak shifts caused by RI changes have been found useful in detecting various biochemical changes occurring at the cellular scale [16, 81]. Here, the important and excellent photonics characteristics of nanocrystalline semiconductor materials have been explained in detail. These electron-hole carrier nanomaterials provide the perspective of additional exotic properties such as CdSe, CdTe, CdS, ZnS and QDs, and in enhancing the local electromagnetic field with longer plasmon wavelength, superior polarities and high curvatures.

The leading sensory components are biological machines like whole cells, tissues, enzymes, antibodies, antigens, receptors, nucleic acids, microorganisms and organelles (Fig. 23.5). They generate biosignals in the specific interaction between the target analytes and biological system. Thus, the biological signal has passed through the physiological system's proximity and is immensely important for medical diagnosis. Potential bimolecular interactions include affinity, kinetics, thermodynamics and analysis of the specificity and concentration of interacting molecules. In general, biological and biochemical interactions occur when the analyte RI ranges from 1.33 to 1.36 [28]. Higher detection accuracy and sensitive



**Fig. 23.5** Nanoscale materials that have been explored to design SPR biosensors, and their performance play leading role in profiling biomolecules binding or cellular events, such as, carbohydrates, protein, DNA/miRNA, bacteria viruses and tumour cells

functioning of sensors emerged as ideal devices for clinical monitoring biomolecules in a series of medical conditions (i.e. Alzheimer's disease, tumour, diabetes, hepatitis, leukaemia, etc.). A different class of bio-analytes has been extensively studied on SPR-based biosensor platforms [14, 22, 31].

Accordingly, it has been explored to detect tumour biomarkers [55], including proteins/enzymatic interaction [27], antigen-antibody binding [81], therapeutic drug sensing [87], monitoring metabolite pathway [13], hormones, miRNA, DNA [70] and among other active biomarkers detection [2, 36, 47]. Still, the active researches on the detection of such biomarkers are very broad, and the contemporary sensor design yet needs to be improved. As per one such work, nearly 64% of the money involved in the market is due to activities related to medicine: home healthcare and point-of-care testing [68]. Core-shell nanostructure paves significant interest due to the geometric parameters (core diameter and shell thickness) and hence, used in many modern medical diagnostic devices in recent years. The effects of the thickness of the internal core, the outer diameter of the shell layer, and the superior quantum efficiency have essentially shown tunable plasmonic bands based on Mie's theory. Thus, varying geometrical parameters of core-shell structure can render the shift with an increment in scattering intensity [13]. Higher-order plasmonic excitation can be achieved by forming large NPs, and by exploiting short and long-range interactions, the latter spectra become more complicated than pure/single NPs [25, 83]. In most cases, SPR of core-shell NPs is red-shifted over a broad spectrum range from the visible to infrared by merely increasing core diameter or shell thickness.

### 23.3 SPR in II–VI Semiconductor QDs

Conventional plasmonic NPs are used for biosensing applications and perform well in the visible and near-infrared region but they demonstrate limitations especially at higher wavelengths due to intrinsic losses [93]. The research of tunable and suitable materials is an essential requirement for creating biosensors for the IR environment. A number of the proposal have been made for alternative plasmonic materials, such as Group IV materials and II–VI semiconductors, where, in particular, InAs have excellent properties [5, 39, 41]. NPs with a CdS and CdSe core in particular, which are readily available with a wide range of emissions are a major class of NPs used in biological detection due to their favourable photophysical properties [4]. InSb was also designed for mid-infrared plasmonics [40]. In practice, the proximity of the excitation energy of semiconductor NPs and the plasmon exciton energy for metal NPs offers the opportunity to produce nanocomposite materials in which excitation of the semiconductor leads to rapid charge injection into the metal. In a metal-semiconductor thin film diode experiment, the large enhancement in electromagnetic field was observed due to surface plasmon resonance of NPs [37]. The plasmonic effect of the metal-semiconductor nanocomposites interface provided



light trapping effect to allow more plasmon generation. As a result, it enhanced the resonance angle shift and thus the SPR sensing.

### 23.3.1 Theory for Optical Properties of Core–Shell NP System

The optical properties of core–shell metal–semiconductor nanocomposite are governed by Maxwell Garnett’s (MG) theory when a metal NP embedded in a host matrix is subjected to an average polarisation field due to both the matrix as well as the surrounding NPs [23]. According to Drude model, the frequency-dependent complex dielectric function may be written as:

$$\varepsilon(\omega) = \varepsilon^\infty - \frac{\omega_p^2}{\omega(\omega + i\omega_d)} \quad (23.3)$$

where  $\varepsilon^\infty$  is the high-frequency dielectric function, while  $\omega_p$  and  $\omega_d$  are the bulk plasma frequency and damping frequency, respectively. These are given by

$$\omega_p^2 = \frac{Ne^2}{m\varepsilon_0} \quad (23.4)$$

and,

$$\omega_d = \frac{v_f}{R_{\text{bulk}}} \quad (23.5)$$

where  $N$  represents the concentration of free electrons;  $m$  and  $e$  represent the effective mass and the charge of the electron.  $R_{\text{bulk}}$  represents the mean free path of the conduction electrons, and  $v_f$  represents the velocity of the electrons at the Fermi energy.

When the particle size,  $R$ , is smaller than the mean free path in the bulk metal, conduction electrons are additionally scattered by the surface, and the mean free path,  $R_{\text{eff}}$ , becomes size-dependent with

$$\frac{1}{R_{\text{eff}}} = \frac{1}{R} + \frac{1}{R_{\text{bulk}}} \quad (23.6)$$

Hence, the size dependence of damping frequency is given by

$$\omega_d(R) = \omega_d(\text{bulk}) + \frac{v_f}{R} \quad (23.7)$$

Thus, Eq. (23.3) together with Eqs. (23.4)–(23.7) completely represents the size-dependent dielectric function of a metal particle even down to a size of 2 nm. According to MG theory, the effective dielectric function ( $\epsilon_{av}$ ) of a composite consisting of high-volume-fraction metal NPs isotropically dispersed in a medium is given by the expression

$$\epsilon_{av} = \epsilon_m \left( 1 + \frac{3\phi\beta}{1-\phi\beta} \right), \text{ where} \quad (23.8)$$

$$\beta = \frac{\epsilon - \epsilon_m}{\epsilon + 2\epsilon_m} \quad (23.9)$$

and  $\phi$  is the volume fraction of the embedded particles and  $\epsilon_m$  is the dielectric function of the host semiconductor material in which the metal particles are embedded. Some of the compound semiconductor materials, which are commonly used in core–shell nanostructures with different semiconductor materials, are CdS, CdSe, PbS and ZnO. The dispersion relation (i.e. the variation of dielectric constant  $\epsilon_m$  with wavelength) for all the four semiconductor materials CdS [74], CdSe [7], PbS [97] and ZnO [10] are available in the related literature.

Usually, MG theory is most appropriate for small spherical NPs (e.g. gold or silver) isotropically distributed within a continuous matrix. The net effect is the creation of a dense matrix of the host material containing mono-disperse metal NPs with known dielectric properties, embedded at a constant, uniform distance from one another. Further, the MG equations deal with the metal volume fraction, so one is still required to specify how the NPs pack within the films. If one assumes that the metal NPs are closely packed, and there is a geometric fcc lattice packing, the volume fraction of the spheres is 0.74 of the total film volume, and the volume fraction of metal particles may be given by Ung et al. [77]

$$\phi = \frac{0.74R^3}{(R + R_{\text{host}})^3} \quad (23.10)$$

where  $R_{\text{host}}$ , in the present case, represents the semiconductor shell thickness.

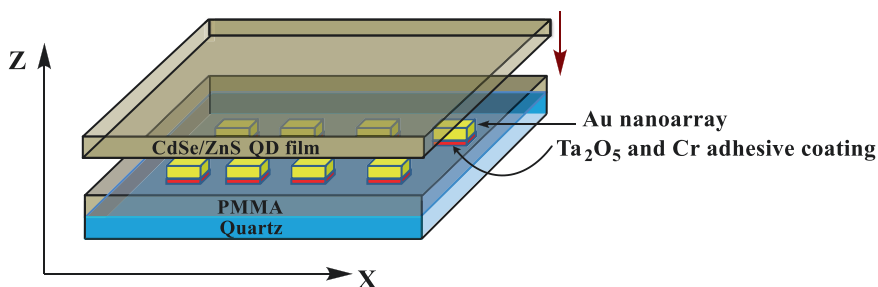
Semiconductor QDs have emerged as fluorescence signal amplifiers to enhance plasmonic biosensors' luminescence signals. QDs-based SPR biosensors can be applied in faster, real-time detection and identification of microbial toxins and to study the interaction of microorganisms with different pathogenic microflora or other molecular species. The inherent ultrahigh RI sensitivity of semiconductor plasmonic materials has been widely explored to detect a quantifiable optical signal corresponding to the RI change of the bio-analytes in which the biological recognition events occurred.

SPR biosensor showed promising results to detect foodborne pathogens related to the processing of poultry, milk and leafy vegetables [8, 38, 48, 75]. A sensitivity as high as  $1 \times 10^6$  CFU/mL for *Salmonella typhimurium* detection was achieved.

Initial results show that applying NPs mixture with a secondary antibody or a gold-conjugated antibody increased the detection limit. Also, for its application in pathogenic bacteria monitoring, it has the potential to differentiate the pathogens, such as human pathogens *Pseudomonas aeruginosa*, *Brucella* spp. and *Serratia* spp.; and some animal pathogens such as *Photobacterium damsela* and *Aeromonas salmonicida* [48]. The recent study visualised rapid detection and characteristic-specific binding kinetics of full-length tail protein by transmission electron microscopy (TEM). A protein was functionalised on SPR biosensor and then employed for bacterial capture using microagglutination assays [32]. In another study, the plasmonic effect of gold triangular nanoprisms (AuTNPs) enhanced the existing LSPR properties for sensing performances. Hati et al. [29] and his co-workers have designed a nanoplasmonic biosensor design for ultrasensitive, precise and programmable detection of microRNAs and proteins at attomolar concentrations in standard human plasma and urine samples femtomolar concentrations from bladder cancer patient plasma and urine. The solid-state structure comprises the light-induced reversible conformational change of spiropyran (SP)-merocyanine (MC) covalently attached to Au TNPs via alkylthiolate self-assembled monolayers (SAM) to produce a large LSPR response ( $\sim 24$  nm).

Monitoring the change of a biomarker in real-time allows for identifying the susceptibility to different therapies and interactive optimisation of medical treatments with reduced time and costs compared to clinical validation of therapies. Different protein biomarkers are correlated with the presence of pathogenic processes and diseases. Usually, the performance of a new optical fibre biosensor is evaluated by direct binding model assays. According to the literature, the most standardised biological measurements involving the detection of bioreceptors-analyte complexes are IgG/anti-IgG, streptavidin/biotin and BSA/anti-BSA. They are normally chosen because of their low price, ease of handling, availability and widely-studied binding and immobilisation process. Once the adequate performance of the biosensor is proved, the biomarkers associated with specific pathologies are employed to identify a specific use for the biosensor.

Another important application domain of biosensors is the detection of nucleic acids, which are employed as biomarkers with diverse applications, including diagnosis, prognosis and selection of targeted therapies. Currently, publications on the wavelength-based optical fibre biosensors for nucleic acids are limited, but some research evidences the scientific community's interest in the topic. The most sensitive optical structure among the different fibre gratings optical platforms used to detect specific sequences of DNA was DTP-LPFG (1359 nm/RIU), which reported the lowest LOD: 4 nM ( $\sim 18.4$  ng/mL) of DNA [15]. The selection of appropriate plasmonic material is crucial for good sensing performance from PCF-SPR sensors. Recent researches show that some alloys can also be potential candidates as plasmonic materials for their remarkable plasmonic characteristics. To investigate the sensing performance of the SPR sensor, gold, silver and copper as noble plasmonic materials and gold-silver, gold-silver and copper-zinc as alloys have been selected. The obtained results reported that the sensor shows maximum amplitude sensitivity (AS) of  $9759.00$  RIU $^{-1}$  and figure of merit (FOM) of  $923.07$  RIU $^{-1}$  when the silver



**Fig. 23.6** 3D diagram to illustrate the CdSe/ZnS quantum dots-based biosensing device on the coupling of exciton and LSPR on the surface of plasmonic nanoarrays coated with a spacer layer of PMMA

coating is used. Moreover, the reported sensor shows maximum spectral sensitivity (SS) of  $26,000 \text{ nmRIU}^{-1}$  and a resolution of  $3.84 \times 10^{-6}$  with copper-zinc alloy. Such sensor probe can be an impressive appliance for the identification of organic substances, biological fluids and samples [64].

Wang et al. [84] have reported LSPR-induced emission enhancement from CdSe/ZnS QDs near well-engineered Au TNPs through a high-performance exciton LSPR coupling system with a versatile  $\text{Ta}_2\text{O}_5$  layer (Fig. 23.6).

By the combination of the matching conditions and a low extinction coefficient with minimal damping absorption of the  $\text{Ta}_2\text{O}_5$  layer in the system, stronger LSPR is induced by the efficient coupling between QDs and Au TNPs and efficiently scattering into the far-field without damping. The plasmon-enhanced emission from QDs with a high PL enhancement factor was achieved by the coupling of excitons and LSPRs. It can be observed that the proposed design concept and method with greatly enhanced light-matter interactions will open up avenues toward actual applications of LSPR-based fluorescence enhancement in biomedicine and optoelectronic devices.

### 23.4 SPR-Enhanced Optical Gas Sensors Based on II–VI Semiconductor QDs

Certain gas molecules and volatile organic compounds (VOCs) are considered to be highly harmful and toxic to human health as well as the natural ecosystem [88]. Formaldehyde and benzene are well-known carcinogenic substances that have a high potential for adverse effects on the human respiratory and immune systems [62, 92]. Furthermore, organic compounds such as dioxins, acetone, nitrogen, ethyl alcohol, n-hexane, chlorobenzene, o-xylene and toluene have a prolonged effect on human health and showed high responsivity when exposed to the environment [50]. Concerning the potential hazards of VOCs and even their small leakage in hostile environments may cause serious respiratory disorders and chronic skin diseases.

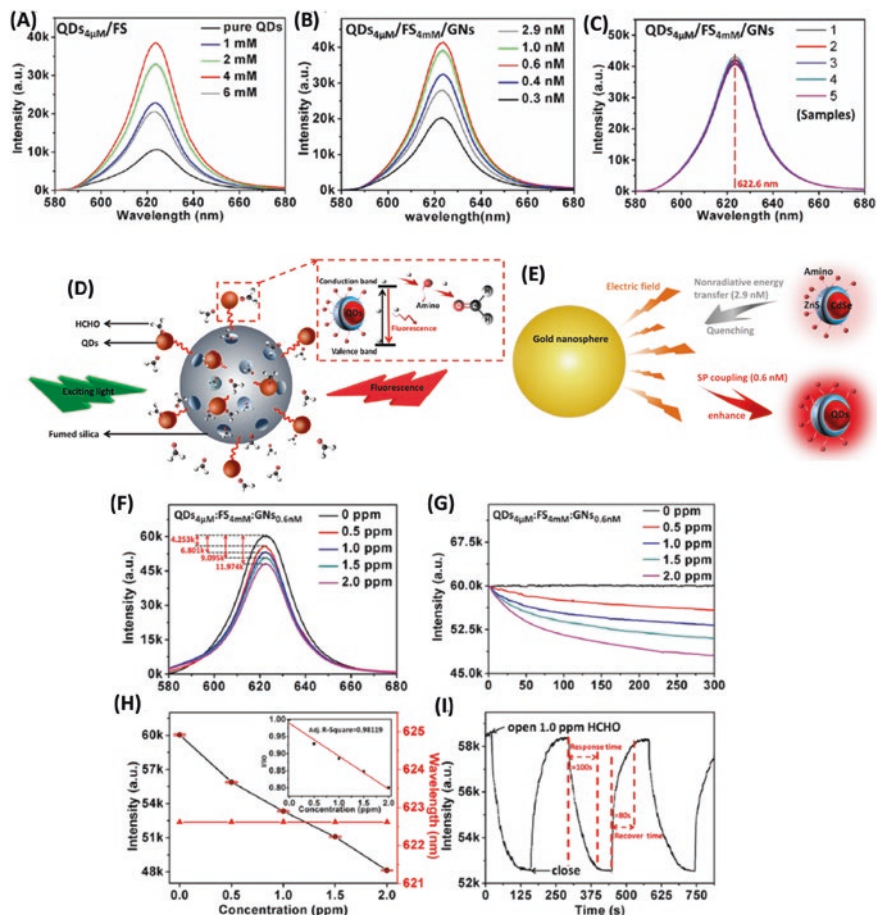
Therefore, effective VOCs monitoring methods are greatly in demand for measuring and monitoring the atmospheric environment and human well-being and health surveillance. Present high-sensitive analytical methods, such as high-performance liquid chromatography (HPLC) [26], gas chromatography (GC) [61] and spectrophotometry [76] have been used to detect the ultra-low concentrations of VOCs, which are based on expensive set-up and rigorous experimental conditions [20, 79].

Carbon-based fluorescent nanomaterials (e.g. graphene QDs) have been studied empathetically to detect toxic gas leakages that can be used as intelligent functionalised photonic materials in the field of gas sensing and biosensing [42, 44]. However, the surface functionalisation of graphene QDs needed further improvement in order to enhance their fluorescence performance in an aqueous environment. Furthermore, their potential use in the detection of gas molecules is still largely untapped due to chemical and electrochemical stability in a small potential window. As a consequence, their low stability remains the biggest challenge for practical gas detection applications [81, 82]. These disadvantages have shifted the focus of the scientific community to synthesise semiconductor-based photonic NPs with the smallest size.

It is known that conductometric devices based on nanostructured semiconductor materials, such as metal oxides and II–VI compounds, make it possible to control the appearance and determine the concentration of toxic gases and VOCs in the atmosphere. The choice of semiconductor materials for the detection of a specific gas is determined by the influence of the interaction of its superficial active surface sides created by chemisorbed  $O^-$ ,  $O^{2-}$ ,  $H^+$  and  $OH^-$  ions with molecules of detected gas on their electrical conductivity [49]. The choice of nanostructured semiconductors for gas sensing is due to the reversibility of the processes of interaction with the detected gases and high sensitivity. At the same time, it was shown that as gas molecules are absorbed onto the metal oxide NP surface, changes in the dielectric constant occur that cause changes in the RI. This means that surface plasmon structures based on nanostructured semiconductors can also be used to detect toxic gases and VOCs in the atmosphere. The experiment confirmed this assumption.

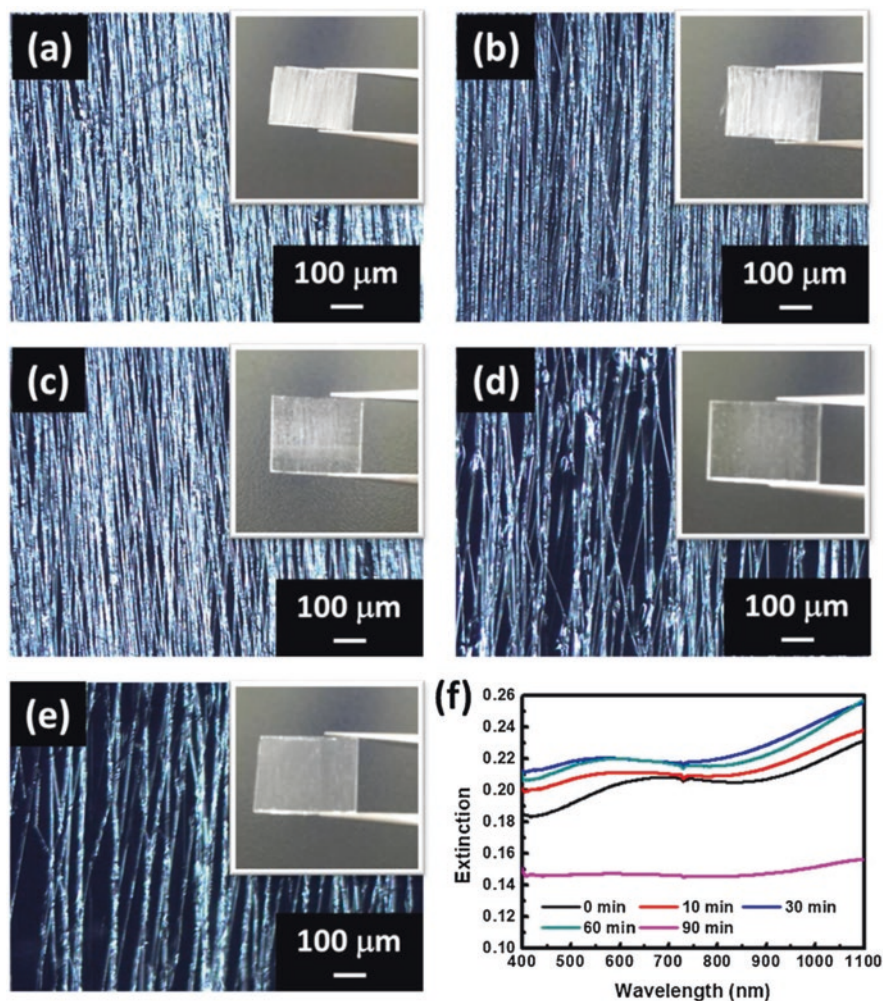
Recently, a research group has proposed SPR-based formaldehyde sensor with very low ( $\sim 0.5$  ppm) detection range by depositing the mixture of amino-modified CdSe@ZnS QDs, fumed silica and gold NPs on the surface of the silica sphere. Under the optimisation conditions, the fluorescence intensity showed significant quenching to gaseous formaldehyde ( $\sim 1.0$  ppm) with a short response time, as seen in Fig. 23.7 [92]. SPR-based gas sensor emerged as an excellent and precautionary sensory technique for the identification and qualitative determination of VOCs concentration. It is worth mentioning that the SPR gas sensor showed accurate sensitivity, high stability and reproducibility with good recoverability in a short response.

Wu et al. [91] also embedded semiconductor QDs in the SPR configuration and found that this device can be considered as rapid, sensitive and convenient gas sensor. The nanocomposite scaffold consists of CdSe–CdS core–shell semiconductor quantum rods, Ag NPs and poly(methyl methacrylate) (PMMA) nanofibres (Fig. 23.8).



**Fig. 23.7** (a) Fluorescence intensities of sensing films with different concentrations of fumed silica (FS) solutions together with that of pure QDs. (b) Fluorescence intensities of sensing films with different concentrations of gold NP (GN) solutions based on  $\text{QDs}_{4\mu\text{M}}/\text{FS}_{4\text{mM}}$ . (c) Fluorescence intensities and wavelengths of different samples fabricated under the same conditions. (d) Fluorescence quenching mechanism (e) The mechanism of influence of gold nanoparticle on the quenching and enhancement of fluorescence (f) Sensing performance of quantum dot-based PEF sensors under optimization conditions ( $\text{QDs}_{4\mu\text{M}}/\text{FS}_{4\text{mM}}/\text{GN}_{0.6\text{nM}}$ ). (g) Fluorescence intensities of sensing films after injecting different concentrations of gaseous formaldehyde for 500 s. (h) Variation of fluorescence intensities in different concentrations of gaseous formaldehyde within 500 s. The relationship between the fluorescence intensity and the formaldehyde concentration. The inset shows a calibration plot of the presented sensor for formaldehyde over the range of 0.5–2.0 ppm ( $n = 5$ , Adj.  $R^2$ :0.98119). (i) Response-recovery properties of sensing devices at 1.0 ppm concentration of formaldehyde. (Reprinted with permission from Xue et al. [92]. Copyright 2020: American Chemical Society)

CdSe-CdS/Ag/PMMA-based sensors showed versatile sensitivity below the lowest explosion limits. In fact, it reached a non-selective detection threshold of 500 ppm for chlorobenzene and 100 ppm for butanol [91]. Mishra et al. [51] employed an LMR-based hydrogen gas sensor by coating an ITO ( $\text{In}_2\text{O}_3 + \text{SnO}_2$ )

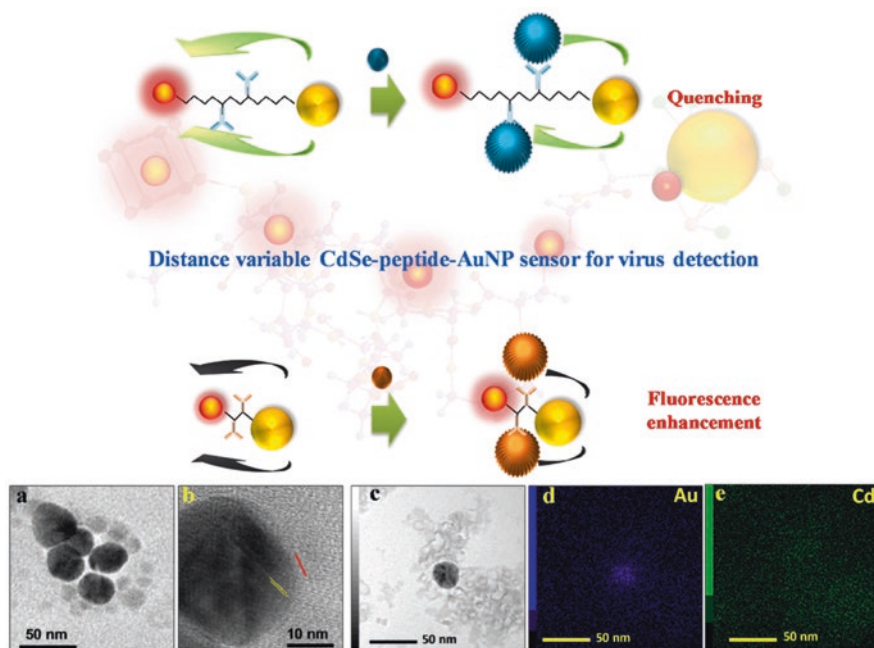


**Fig. 23.8** The optical images of CdSe-CdS/Ag/PMMA composite scaffolds treated with UV-ozone etching after (a) 0 min, (b) 10 min, (c) 30 min, (d) 60 min and (e) 90 min. The insets are the photographs of each sensing chip. (f) The extinction spectra of CdSe-CdS/Ag/PMMA composite scaffolds with various etching time. (Reprinted with permission from Wu et al. [91]. Copyright 2020: Elsevier)

thin film on the core of an optical fibre [52]. The same researcher later reposted a highly sensitive SPR-based ammonia gas sensor designed using ITO and polyaniline thin film. Further, an LSPR gas detection system has been developed, in which evaporated gold island films have been coated with polymer polystyrene sulphuric acid and polystyrene. These polymers swell and/or shrink when exposed to the various gases used (chloroform, water vapour, etc.), which affects the local RI and causes an intense peak of LSPR [35].

### 23.5 SPR-Based Biosensors Functionalised with II–VI Semiconductor QDs

The direct band-gap plasmonic semiconductor nanomaterials (II–VI: CdS, CdSe, CdTe, etc.; III–V: InP, InAs, etc.; IV–VI: PbSe, etc.) are widely classified for changes to RI variations at the sensor surface. The changes in RI practically offer the potential of measuring low levels of biological signals adjacent to the metallic NP boundaries. Such NPs and their combination with plasmonic semiconductors have been extensively modified with the linker molecules to couple with biomolecules for developing plasmonic biosensors (Fig. 23.9). Interestingly, gold NP islands have shown exceptional LSPR properties, which make them unique colorimetric biosensors [18]. Their high optical excitation coefficient, broad absorption spectrum, fluorescence quenching and catalytic efficacy showed a non-radiative energy transfer process, called the fluorescence resonance energy transfer (FRET) phenomenon. FRET is another method to identify the proteins or histone modifications associated with a specific DNA sequence [69].



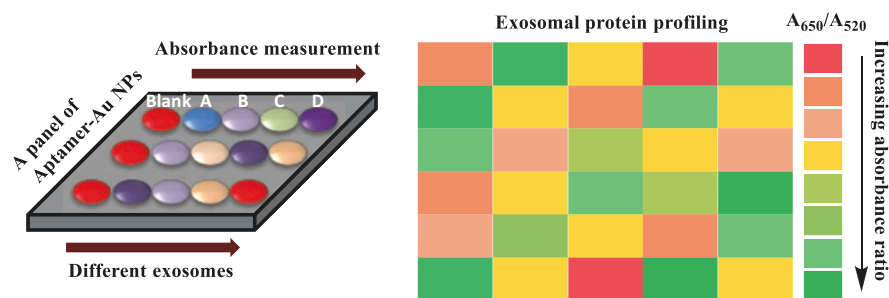
**Fig. 23.9** Virus detection with the sensor probe varying the peptide length: schematic illustration for the virus sensing using CdSe QD-peptide-AuNP system for two modes of detection and characterisations of CdSe QD-peptide-AuNP nanoconjugate: (a) TEM image (b) HRTEM image of CdSe QD-peptide-AuNP, showing their own fringes, (c–e) STEM mapping of CdSe QD-peptide-AuNP with Cd and Au. (Reprinted with permission from Chowdhury et al. [18]. Copyright 2020: Elsevier)



Early-stage diagnosis and appropriate treatment are vital challenges in the fight against cancer. As an alternative tool for conventional options, SPR-based label-free detection of cancer biomarkers in real-time with high sensitivity (picomolar level) is comparable to that of single-colour and dual-colour labelling approaches. The plasmon resonance characteristics of QD NPs and their associated electromagnetic field enhancement produced by LSPR excitation have made feasible the design of biosensors for the exosome quantification in liquid biopsies for cancer diagnosis. The considerably enhanced response and visual detection of protein binding may demonstrate using gold NPs stabilised with the linker-modified molecules. LSPR colorimetric sensors based on the aggregation of NPs may provide high sensitivities and functional designs.

The stability of plasmonic NP assemblies can be modulated through covalent or non-covalent interactions (i.e. electrostatic interactions, hydrophobic forces, hydrogen linkage and specific biological linkage) and depend greatly on external conditions such as temperature, pH and buffer. Au NPs are functionalised by the non-covalent bio-conjugated system with a panel of DNA aptamers, which are able to bind the exosome surface proteins with high specificity and affinity. Their individual appearance reflected in distinctive colours as a consequence of NP aggregation (from red to blue) following the specific binding between the aptamers and cell-surface proteins (Fig. 23.10). These colorimetric changes are responsible for generating patterns to identify the multiple proteins on the exosome surface, which can be further implemented for cancer diagnosis [34].

LSPR biosensors can be designed for solution-phase or surface-bound sensors and can result in a spectral change in absorption/extinction or scattering and even colour variation of plasmonic NP solutions. Solution-based biosensors are much more attractive due to the less complexity of the measurement and of the assay analysis [85]. Strong emphasis has been given to the colloidal NPs in complex liquid medium because of the formation of a protein corona and ionic potency of the



**Fig. 23.10** A coat of many colours: A gold NP/aptamer biosensor (AuNP/AptX) provides a colorimetric platform for rapid and multiplexed protein analysis of exosomes. (Adapted with permission from Jiang et al. [34]. Copyright 2017: Wiley)

biofluids. In combination with a unique set of plasmonic properties of LSPR nano-materials, the hydrophobic interactions can be potentially used in both biosensing and nanomedicine. The impact of complex liquid media on LSPR sensors can be condensed by functionalising the layers, biological scaffolds and particle diameter, but yet remains an issue to believe. Dilution of the media can also be an option to minimise the impacts related to the biofluid, as shown for sensing real samples. Solution-based LSPR can also serve to conquer the response of an ELISA assay for real samples.

On the other side, surface-bound LSPR sensors are fabricated by immobilisation of NPs on a solid substrate to alleviate the concerns of the colloidal stability of NPs in liquid media solution. This configuration is also simpler to multiplex on-chip and to integrate with microfluidics. The field of integrated plasmonic devices is gaining a lot of attention recently. Typical bioreceptors include, in general, antibodies, enzymes, proteins, aptamers, cells, or microorganisms. They are specially designed to detect other target molecules, also known as “analytes” or “biomarkers”. Once deposited on the transducer substrate, these biological interactions transform into measurable variables and simulate them into optical, electrical, mechanical, or acoustic signals that can be further treated [73]. Finally, the bio-functionalised interface is the middle layer. It consists of one or more layer-by-layer (LbL) that binds the bioreceptors to the substrate using nanotechnology-based manufacturing techniques.

Many materials other than pure metals (typical of SPRs) can induce LMRs. Thus, significant progress has been reported on LMRs with metal oxides, polymer coatings; LbL-coated structures and considered an almost unavoidable component in the majority of combining plasmonic materials or even immunosensors consisting of multilayer of polymers and antibodies [68]. Furthermore, SPR biosensing surfaces can be functionalised by thin polymer films to which antibodies are coupled through amino groups [54]. Protein contact printing was considered for spatially controlled binding of bovine serum albumin (BSA) and dinitrophenylated BSA to adjacent reference and signal channels of a dual-channel SPR sensor [46]. Nano-range biomolecules can be immobilised on the surfaces of gold SPR sensors by forming a streptavidine layer on a gold surface followed by biotinylated DNA attachment [86]. A multi-step surface modification based on alkanethiol SAM was also used to attach DNA to gold surfaces [12]. Then, later, biomimetic materials made from micro-contact imprinting techniques for the detection of urinary tract pathogens have been exploited in SPR biosensors [56].

Novel semiconductor nanostructures for LSPR sensing are frequently reported for optimising the sensitivity of sensors. The advantage of a colloidal NP-based LSPR sensor is the possibility of naked-eye detection from aggregation assays, NP etching, or growth mechanism, such as for the detection of glucose [33]. These possibilities are highly promising and the use of gold NPs in microfluidic-based biosensing for point-of-care applications has attracted a lot of attention. LSPR biosensors can be designed for solution-phase or surface-bound sensors. Solution-based biosensors are interesting due to the simplicity of the measurement and of the

assay. Biomolecule-attached metal NPs are the most popular probes for easy separation by centrifugation and can be readily assembled with thiolated molecules. The single-crystalline Au islands furnished the possibility of effective separation of the surface-plasmon bands of the islands and the bound NPs. LSPR provides a plasmon resonance in a broader optical window, enhances sensitivity, facilitates integration into a simple device, comprises easy surface chemistry, and is relatively economical to fabricate.

Plasmonic nanostructures are either prepared from colloidal synthesis or with nanofabrication techniques. Nanofabricated plasmonic structures can reach high FOM, and, thus, their performance can exceed other SPR sensing platforms but may be very costly and complex to fabricate. Hence, the fabrication of LSPR NPs on a solid substrate is widely employed to alleviate some of the issues, such as stability and ease of integration with microfluidic. Placing an NP on a colloidal substrate affects the optical properties and sensitivity. But, when it comes to the RI sensitivity, FOM and RI resolution are bulk properties; the penetration depth is directly associated with the sensitivity of the device to a binding event, which straightly influences the RI shift from the detection of a molecule.

Generally, the penetration depth is expected to be relatively small but even greater than the molecules to be detected to ensure that the binding events result in a significant change in the wavelength or resonance angle of the plasmon. A drawback of the SPR is the requirement of sufficient quantities of ligand which is successfully connected to the surface of the sensor chip. Moreover, this ligand must be sufficiently robust to withstand several regeneration cycles. There is currently a large heterogeneity in nanostructures used for SPR sensing, and therefore focus needed to be placed on identifying the best anisotropic or pronged colloidal nanostructures and optimising their synthesis to achieve highly reproducible fabrication, as well as identifying 2D nanofabricated surfaces that are relatively simple to fabricate and of high sensitivity. This constitutes the major challenge of plasmonic nanomaterials, as methods for classical SPR sensing should be translated with relatively few obstacles [78]. The scope of QDs synthesis is very broad and cannot be fully explored from a specific application perspective, so only colloidal stability is the main concern. Colloidal synthesis facilitates the advantage of simplicity and cost-effective fabrication, but colloidal-based sensors often suffer from reproducibility in synthesis and usually have a lower FOM.

## 23.6 Conclusions and Future Directions

Semiconducting nanostructure-based SPR sensor is a promising approach for making a progression in advanced biosensing applications. Their specificity and active surface feature advantageously for light entrapment within a smaller region. Quantum dot and metal oxide-based gas sensing devices are expanding their infrared bandwidth utilisation. The discussion projected on the metal-semiconductor nanocomposites provides deep insights into the important aspects, such as surface

features, fabrication, sensitivity, label-free detection and in-vivo adaptation. The sensitivity to the detection of biomolecules and target molecules in the complex fluids described in the chapter required increased miniaturisation and user-friendly interface design. In the forthcoming era of printable devices, semiconductor materials will gain significant foresight in lithographic research. The flexibility of semiconductor film can result in portable devices with great potential for health monitoring and toxic gas leakages. Thus, the futuristic sensory device would be reusable, easy to operate, simple to functionalised with the recognition element and replace in terms of hardware and software.

**Acknowledgements** Anuj K. Sharma gratefully acknowledges the sponsored research project grants “03(1441)/18/EMR-II” and “CRG/2019/002636” funded by the Council of Scientific & Industrial Research (India) and the Science & Engineering Research Board (India), respectively.

## References

1. Agrawal A, Cho SH, Zandi O, Ghosh S, Johns RW, Milliron DJ. Localized surface Plasmon resonance in semiconductor nanocrystals. *Chem Rev.* 2018;118(6):3121–207. <https://doi.org/10.1021/acs.chemrev.7b00613>.
2. Akgönüllü S, Yavuz H, Denizli A. SPR nanosensor based on molecularly imprinted polymer film with gold NPs for sensitive detection of aflatoxin B1. *Talanta.* 2020;219:121219. <https://doi.org/10.1016/j.talanta.2020.121219>.
3. Ali MA, Srivastava S, Pandey MK, Agrawal VV, John R, Malhotra BD. Protein-conjugated quantum dots interface: binding kinetics and label-free lipid detection. *Anal Chem.* 2014;86(3):1710–8. <https://doi.org/10.1021/ac403543g>.
4. Aubret A, Pillonnet A, Houel J, Dujardin C, Kulzer F. CdSe/ZnS quantum dots as sensors for the local RI. *Nanoscale.* 2016;8(4):2317–25. <https://doi.org/10.1039/c5nr06998j>.
5. Barho FB, Gonzalez-Posada F, Milla-Rodrigo M-J, Bomers M, Cerutti L, Taliercio T. All-semiconductor plasmonic gratings for biosensing applications in the mid-infrared spectral range. *Opt Express.* 2016;24(14):16175. <https://doi.org/10.1364/oe.24.016175>.
6. Bhalla N, Pan Y, Yang Z, Payam AF. Opportunities and challenges for biosensors and nanoscale analytical tools for pandemics: COVID-19. *ACS Nano.* 2020;14(7):7783–807. <https://doi.org/10.1021/acsnano.0c04421>.
7. Bhar GC. RI interpolation in phase-matching. *Appl Opt.* 1976;15(2):305\_1. [https://doi.org/10.1364/ao.15.0305\\_1](https://doi.org/10.1364/ao.15.0305_1).
8. Bokken GCAM, Corbee RJ, Van Knapen F, Bergwerff AA. Immunochemical detection of Salmonella group B, D and E using an optical surface plasmon resonance biosensor. *FEMS Microbiol Lett.* 2003;222(1):75–82. [https://doi.org/10.1016/S0378-1097\(03\)00250-7](https://doi.org/10.1016/S0378-1097(03)00250-7).
9. Boltasseva A, Atwater HA. Low-loss plasmonic metamaterials. *Science.* 2011;331(6015):290–1. <https://doi.org/10.1126/science.1198258>.
10. Bond WL. Measurement of the refractive indices of several crystals. *J Appl Phys.* 1965;36(5):1674–7. <https://doi.org/10.1063/1.1703106>.
11. Breault-Turcot J, Chaurand P, Masson JF. Unravelling nonspecific adsorption of complex protein mixture on surfaces with SPR and MS. *Anal Chem.* 2014;86(19):9612–9. <https://doi.org/10.1021/ac502077b>.
12. Brockman JM, Frutos AG, Corn RM. A multistep chemical modification procedure to create dna arrays on gold surfaces for the study of protein-DNA interactions with surface plasmon resonance imaging. *J Am Chem Soc.* 1999;121(35):8044–51. <https://doi.org/10.1021/ja991608e>.

13. Cao Y, Griffith B, Bhomkar P, Wishart DS, McDermott MT. Functionalized gold NP-enhanced competitive assay for sensitive small-molecule metabolite detection using surface plasmon resonance. *Analyst*. 2018;143(1):289–96. <https://doi.org/10.1039/c7an01680h>.
14. Chang CC. Recent advancements in aptamer-based surface plasmon resonance biosensing strategies. *Biosensors*. 2021;11(7). <https://doi.org/10.3390/bios11070233>.
15. Chen Liu XC. EDC-mediated oligonucleotide immobilization on a long period grating optical biosensor. *J Biosens Bioelectron*. 2015;6(2):1000173. <https://doi.org/10.4172/2155-6210.1000173>.
16. Cheng XR, Hau BYH, Endo T, Kerman K. Au NP-modified DNA sensor based on simultaneous electrochemical impedance spectroscopy and localized surface plasmon resonance. *Biosens Bioelectron*. 2014;53:513–8. <https://doi.org/10.1016/j.bios.2013.10.003>.
17. Chiang HP, Chen CW, Wu JJ, Li HL, Lin TY, Sánchez EJ, Leung PT. Effects of temperature on the surface plasmon resonance at a metal-semiconductor interface. *Thin Solid Films*. 2007;515(17):6953–61. <https://doi.org/10.1016/j.tsf.2007.02.034>.
18. Chowdhury AD, Nasrin F, Gangopadhyay R, Ganganboina AB, Takemura K, Kozaki I, et al. Controlling distance, size and concentration of nanoconjugates for optimized LSPR based biosensors. *Biosens Bioelectron*. 2020;170:112657. <https://doi.org/10.1016/j.bios.2020.112657>.
19. Dahlman CJ, Agrawal A, Staller CM, Adair J, Milliron DJ. Anisotropic origins of localized surface plasmon resonance in n-type Anatase TiO<sub>2</sub> nanocrystals. *Chem Mater*. 2019;31(2):502–11. <https://doi.org/10.1021/acs.chemmater.8b04519>.
20. Descamps MN, Bordy T, Hue J, Mariano S, Nonglaton G, Schultz E, et al. Real-time detection of formaldehyde by a fluorescence-based sensor. *Procedia Eng*. 2010;5:1009–12. <https://doi.org/10.1016/j.proeng.2010.09.280>.
21. Ermini ML, Song XC, Špringer T, Homola J. Peptide functionalization of gold NPs for the detection of carcinoembryonic antigen in blood plasma via SPR-based biosensor. *Front Chem*. 2019;7:40. <https://doi.org/10.3389/fchem.2019.00040>.
22. Fasoli JB, Corn RM. Surface enzyme chemistries for ultrasensitive microarray biosensing with SPR imaging. *Langmuir*. 2015;31(35):9527–36. <https://doi.org/10.1021/la504797z>.
23. Garnett JCM. XII. Colours in metal glasses and in metallic films. *Philos Trans R Soc London, Series A*. 1904;203(359–371):385–420. <https://doi.org/10.1098/rsta.1904.0024>.
24. Ghrera AS, Pandey MK, Malhotra BD. Quantum dot monolayer for surface plasmon resonance signal enhancement and DNA hybridization detection. *Biosens Bioelectron*. 2016;80:477–82. <https://doi.org/10.1016/j.bios.2016.02.013>.
25. Giannini V, Vecchi G, Gómez Rivas J. Lighting up multipolar surface plasmon polaritons by collective resonances in arrays of nanoantennas. *Phys Rev Lett*. 2010;105(26):266801. <https://doi.org/10.1103/PhysRevLett.105.266801>.
26. Gil RL, Amorim CG, Montenegro MCBSM, Araújo AN. HPLC-potentiometric method for determination of biogenic amines in alcoholic beverages: a reliable approach for food quality control. *Food Chem*. 2022;372:131288. <https://doi.org/10.1016/j.foodchem.2021.131288>.
27. Haes AJ, Van Duyne RP. A nanoscale optical biosensor: sensitivity and selectivity of an approach based on the localized surface plasmon resonance spectroscopy of triangular silver NPs. *J Am Chem Soc*. 2002;124(35):10596–604. <https://doi.org/10.1021/ja020393x>.
28. Hasan MR, Akter S, Rifat AA, Rana S, Ahmed K, Ahmed R, Subbaraman H, Abbott D. Spiral photonic crystal fiber-based dual-polarized surface plasmon resonance biosensor. *IEEE Sensors J*. 2018;18(1):133–40. <https://doi.org/10.1109/JSEN.2017.2769720>.
29. Hati S, Langlais SR, Masterson AN, Liyanage T, Muhoberac BB, Kaimakliotis H, Johnson M, Sardar R. Photoswitchable machine-engineered plasmonic nanosystem with high optical response for ultrasensitive detection of microRNAs and proteins adaptively. *Anal Chem*. 2021;93(41):13935–44. <https://doi.org/10.1021/acs.analchem.1c02990>.
30. Hinman SS, McKeating KS, Cheng Q. Surface plasmon resonance: material and interface design for universal accessibility. *Anal Chem*. 2018;90(1):19–39. <https://doi.org/10.1021/acs.analchem.7b04251>.

31. Huang Y, Zhang L, Zhang H, Li Y, Liu L, Chen Y, Qiu X, Yu D. Development of a portable SPR sensor for nucleic acid detection. *Micromachines*. 2020;11(5). <https://doi.org/10.3390/mi11050526>.
32. Hyeon SH, Lim WK, Shin HJ. Novel surface plasmon resonance biosensor that uses full-length Det7 phage tail protein for rapid and selective detection of *Salmonella enterica* serovar Typhimurium. *Biotechnol Appl Biochem*. 2021;68(1):5–12. <https://doi.org/10.1002/bab.1883>.
33. Jiang Y, Zhao H, Lin Y, Zhu N, Ma Y, Mao L. Colorimetric detection of glucose in rat brain using gold NPs. *Angew Chem Int Ed*. 2010;49(28):4800–4. <https://doi.org/10.1002/anie.201001057>.
34. Jiang Y, Shi M, Liu Y, Wan S, Cui C, Zhang L, Tan W. Aptamer/AuNP biosensor for colorimetric profiling of exosomal proteins. *Angew Chem*. 2017;129(39):12078–82. <https://doi.org/10.1002/ange.201703807>.
35. Karakouz T, Vaskevich A, Rubinstein I. Polymer-coated gold island films as localized plasmon transducers for gas sensing. *J Phys Chem B*. 2008;112(46):14530–8. <https://doi.org/10.1021/jp804829t>.
36. Kluková L, Bertok T, Kasák P, Tkáč J. Nanoscale-controlled architecture for the development of ultrasensitive lectin biosensors applicable in glycomics. *Anal Methods*. 2014;6(14):4922–31. <https://doi.org/10.1039/c4ay00495g>.
37. Konda RB, Mundle R, Mustafa H, Bamiduro O, Pradhan AK, Roy UN, et al. Surface plasmon excitation via Au NPs in n-CdSe/p-Si heterojunction diodes. *Appl Phys Lett*. 2007;91(19):191111. <https://doi.org/10.1063/1.2807277>.
38. Lan YB, Wang SZ, Yin YG, Hoffmann WC, Zheng XZ. Using a surface plasmon resonance biosensor for rapid detection of salmonella typhimurium in chicken carcass. *J Bionic Eng*. 2008;5(3):239–46. [https://doi.org/10.1016/S1672-6529\(08\)60030-X](https://doi.org/10.1016/S1672-6529(08)60030-X).
39. Law S, Yu L, Wasserman D. Epitaxial growth of engineered metals for mid-infrared plasmonics. *J Vac Sci Technol B, Nanotechnol Microelectron*. 2013;31(3):03C121. <https://doi.org/10.1116/1.4797487>.
40. Law S, Liu R, Wasserman D. Doped semiconductors with band-edge plasma frequencies. *J Vac Sci Technol B, Nanotechnol Microelectron*. 2014;32(5):052601. <https://doi.org/10.1116/1.4891170>.
41. Li D, Ning CZ. All-semiconductor active plasmonic system in mid-infrared wavelengths. *Opt Express*. 2011;19(15):14594. <https://doi.org/10.1364/oe.19.014594>.
42. Li Y, Zhao Y, Cheng H, Hu Y, Shi G, Dai L, Qu L. Nitrogen-doped graphene quantum dots with oxygen-rich functional groups. *J Am Chem Soc*. 2012;134(1):15–8. <https://doi.org/10.1021/ja206030c>.
43. Li X, Wang M, Zhang B. Equivalent medium theory of layered sphere particle with anisotropic shells. *J Quant Spectrosc Radiat Transfer*. 2016;179:165–9. <https://doi.org/10.1016/j.jqsrt.2016.03.008>.
44. Li HJ, Sun X, Xue F, Ou N, Sun BW, Qian DJ, et al. Redox induced fluorescence on-off switching based on nitrogen enriched graphene quantum dots for formaldehyde detection and bioimaging. *ACS Sustain Chem Eng*. 2018;6(2):1708–16. <https://doi.org/10.1021/acsschemeng.7b02941>.
45. Liu G, Qi S, Chen J, Lou Y, Zhao Y, Burda C. Cu-Sb-S ternary semiconductor NP plasmonics. *Nano Lett*. 2021;21(6):2610–7. <https://doi.org/10.1021/acs.nanolett.1c00006>.
46. Lu HB, Homola J, Campbell CT, Nenninger GG, Yee SS, Ratner BD. Protein contact printing for a surface plasmon resonance biosensor with on-chip referencing. *Sensors Actuators B Chem*. 2001;74(1–3):91–9. [https://doi.org/10.1016/S0925-4005\(00\)00716-4](https://doi.org/10.1016/S0925-4005(00)00716-4).
47. Mauriz E. Recent progress in plasmonic biosensing schemes for virus detection. *Sensors (Switzerland)*. 2020;20(17):1–27. <https://doi.org/10.3390/s20174745>.
48. Mazumdar SD, Hartmann M, Kämpfer P, Keusgen M. Rapid method for detection of *Salmonella* in milk by surface plasmon resonance (SPR). *Biosens Bioelectron*. 2007;22(9–10):2040–6. <https://doi.org/10.1016/j.bios.2006.09.004>.

49. Mei GS, Susthitha Menon P, Hegde G. ZnO for performance enhancement of surface plasmon resonance biosensor: a review. *Mater Res Express*. 2020;7(1) <https://doi.org/10.1088/2053-1591/ab66a7>.
50. Mirzaei A, Leonardi SG, Neri G. Detection of hazardous volatile organic compounds (VOCs) by metal oxide nanostructures-based gas sensors: a review. *Ceram Int*. 2016;42(14):15119–41. <https://doi.org/10.1016/j.ceramint.2016.06.145>.
51. Mishra SK, Kumari D, Gupta BD. Surface plasmon resonance based fiber optic ammonia gas sensor using ITO and polyaniline. *Sensors Actuators B Chem*. 2012;171–172:976–83. <https://doi.org/10.1016/j.snb.2012.06.013>.
52. Mishra SK, Usha SP, Gupta BD. A lossy mode resonance-based fiber optic hydrogen gas sensor for room temperature using coatings of ITO thin film and NPs. *Meas Sci Technol*. 2016;27(4):045103. <https://doi.org/10.1088/0957-0233/27/4/045103>.
53. Naik GV, Shalaev VM, Boltasseva A. Alternative plasmonic materials: beyond gold and silver. *Adv Mater*. 2013;25(24):3264–94. <https://doi.org/10.1002/adma.201205076>.
54. Oliverio M, Perotto S, Messina GC, Lovato L, De Angelis F. Chemical functionalization of plasmonic surface biosensors: a tutorial review on issues, strategies, and costs. *ACS Appl Mater Interfaces*. 2017;9(35):29394–411. <https://doi.org/10.1021/acsami.7b01583>.
55. Ou H, Cheng T, Zhang Y, Liu J, Ding Y, Zhen J, et al. Surface-adaptive zwitterionic NPs for prolonged blood circulation time and enhanced cellular uptake in tumor cells. *Acta Biomater*. 2018;65:339–48. <https://doi.org/10.1016/j.actbio.2017.10.034>.
56. Özgür E, Topçu AA, Yılmaz E, Denizli A. Surface plasmon resonance based biomimetic sensor for urinary tract infections. *Talanta*. 2020;212:120778. <https://doi.org/10.1016/j.talanta.2020.120778>.
57. Pereira RMS, Borges J, Smirnov GV, Vaz F, Vasilevskiy MI. Surface plasmon resonance in a metallic NP embedded in a semiconductor matrix: exciton-plasmon coupling. *ACS Photon*. 2019;6(1):204–10. <https://doi.org/10.1021/acsphotonics.8b01430>.
58. Qu JH, Dillen A, Saeys W, Lammertyn J, Spasic D. Advancements in SPR biosensing technology: an overview of recent trends in smart layers design, multiplexing concepts, continuous monitoring and in vivo sensing. *Anal Chim Acta*. 2020;1104:10–27. <https://doi.org/10.1016/j.aca.2019.12.067>.
59. Raether H, Hohler G, Niekisch EA. Surface plasmons on smooth and rough surfaces and on gratings. In: Raether H, editor. *Springer tracts in modern physics*, vol. 111. Berlin: Springer; 1988. p. 136. <https://doi.org/10.1007/BFb0048317>.
60. Saleviter S, Fen YW, Sheh Omar NA, Mustaqim Mohd Daniyal WME, Abdullah J, Mat Zaid MH. Structural and optical studies of cadmium sulfide quantum dot-graphene oxide-chitosan nanocomposite thin film as a novel SPR spectroscopy active layer. *J Nanomater*. 2018;2018:4324072. <https://doi.org/10.1155/2018/4324072>.
61. Santos FJ, Galceran MT. Modern developments in gas chromatography-mass spectrometry-based environmental analysis. *J Chromatogr A*. 2003;1000(1–2):125–51. [https://doi.org/10.1016/S0021-9673\(03\)00305-4](https://doi.org/10.1016/S0021-9673(03)00305-4).
62. Scharf P, Broering MF, da Rocha GHO, Farsky SHP. Cellular and molecular mechanisms of environmental pollutants on hematopoiesis. *Int J Mol Sci*. 2020;21(19):1–30. <https://doi.org/10.3390/ijms21196996>.
63. Shabaninezhad M, Kayani A, Ramakrishna G. Theoretical investigation of optical properties of embedded plasmonic NPs. *Chem Phys*. 2021;541:111044. <https://doi.org/10.1016/j.chemphys.2020.111044>.
64. Shafkat A, Reja MI, Miah MJ, Fatema S, Absar R, Akhtar J. Numerical exploration of external sensing scheme based photonic crystal fiber surface plasmonic sensor with different noble plasmonic materials and their alloys. *Optik*. 2021;231:166418. <https://doi.org/10.1016/j.ijleo.2021.166418>.
65. Sharma AK, Gupta BD. Metal-semiconductor nanocomposite layer based optical fibre surface plasmon resonance sensor. *J Opt A Pure Appl Opt*. 2007;9(2):180–5. <https://doi.org/10.1088/1464-4258/9/2/011>.

66. Sharma AK, Pandey AK, Kaur B. Simulation study on comprehensive sensing enhancement of BlueP/MoS<sub>2</sub> - and BlueP/WS<sub>2</sub> -based fluoride fiber surface plasmon resonance sensors: analysis founded on damping, field, and optical power. *Appl Opt.* 2019;58(16):4518. <https://doi.org/10.1364/ao.58.004518>.
67. Singh S, Prajapati YK. TiO<sub>2</sub>/gold-graphene hybrid solid core SPR based PCF RI sensor for sensitivity enhancement. *Optik.* 2020;224:165525. <https://doi.org/10.1016/j.ijleo.2020.165525>.
68. Socorro-Lerános AB, Santano D, Del Villar I, Matias IR. Trends in the design of wavelength-based optical fibre biosensors (2008–2018). *Biosens Bioelectron.* 2019;1:100015. <https://doi.org/10.1016/j.biosx.2019.100015>.
69. Stryer L. Fluorescence energy transfer as a spectroscopic ruler. *Annu Rev Biochem.* 1978;47(5):819–46. <https://doi.org/10.1146/annurev.bi.47.070178.004131>.
70. Tadimety A, Wu Z, Molinski JH, Beckerman R, Jin C, Zhang L, et al. Rational design of on-chip gold plasmonic NPs towards ctDNA screening. *Sci Rep.* 2021;11(1):1–10. <https://doi.org/10.1038/s41598-021-93207-7>.
71. Takemura K, Adegoke O, Suzuki T, Park EY. A localized surface plasmon resonance-amplified immunofluorescence biosensor for ultrasensitive and rapid detection of nonstructural protein 1 of Zika virus. *PLoS One.* 2019;14(1):1–14. <https://doi.org/10.1371/journal.pone.0211517>.
72. Tandon B, Ghosh S, Milliron DJ. Dopant selection strategy for high-quality factor localized surface plasmon resonance from doped metal oxide nanocrystals. *Chem Mater.* 2019;31(18):7752–60. <https://doi.org/10.1021/acs.chemmater.9b02917>.
73. Tang L, Li J. Plasmon-based colorimetric nanosensors for ultrasensitive molecular diagnostics. *ACS Sensors.* 2017;2(7):857–75. <https://doi.org/10.1021/acssensors.7b00282>.
74. Tatian B. Fitting refractive-index data with the Sellmeier dispersion formula. *Appl Opt.* 1984;23(24):4477. <https://doi.org/10.1364/ao.23.004477>.
75. Taylor AD, Ladd J, Yu Q, Chen S, Homola J, Jiang S. Quantitative and simultaneous detection of four foodborne bacterial pathogens with a multi-channel SPR sensor. *Biosens Bioelectron.* 2006;22(5):752–8. <https://doi.org/10.1016/j.bios.2006.03.012>.
76. Teixeira LSG, Leão ES, Dantas AF, Pinheiro HLC, Costa ACS, De Andrade JB. Determination of formaldehyde in Brazilian alcohol fuels by flow-injection solid phase spectrophotometry. *Talanta.* 2004;64(3):711–5. <https://doi.org/10.1016/j.talanta.2004.03.047>.
77. Ung T, Liz-Marzán LM, Mulvaney P. Optical properties of thin films of AuO/SiO<sub>2</sub> particles. *J Phys Chem B.* 2001;105(17):3441–52. <https://doi.org/10.1021/jp003500n>.
78. Wang Q, Wang JF, Geil PH, Padua GW. Zein adsorption to hydrophilic and hydrophobic surfaces investigated by surface plasmon resonance. *Biomacromolecules.* 2004;5(4):1356–61. <https://doi.org/10.1021/bm049965r>.
79. Wang X, Si Y, Wang J, Ding B, Yu J, Al-Deyab SS. A facile and highly sensitive colorimetric sensor for the detection of formaldehyde based on electro-spinning/netting nano-fiber/nets. *Sensors Actuators B Chem.* 2012;163(1):186–93. <https://doi.org/10.1016/j.snb.2012.01.033>.
80. Wang Y, Ou JZ, Chrimes AF, Carey BJ, Daeneke T, Alsaif MMYA, et al. Plasmon resonances of highly doped two-dimensional MoS<sub>2</sub>. *Nano Lett.* 2015;15(2):883–90. <https://doi.org/10.1021/nl503563g>.
81. Wang J, Zhang HZ, Li RS, Huang CZ. Localized surface plasmon resonance of gold nanorods and assemblies in the view of biomedical analysis. *TrAC.* 2016a;80:429–43. <https://doi.org/10.1016/j.trac.2016.03.015>.
82. Wang X, Sun G, Li N, Chen P. Quantum dots derived from two-dimensional materials and their applications for catalysis and energy. *Chem Soc Rev.* 2016b;45(8):2239–62. <https://doi.org/10.1039/c5cs00811e>.
83. Wang W, Ramezani M, Väkeväinen AI, Törmä P, Rivas JG, Odom TW. The rich photonic world of plasmonic NP arrays. *Mater Today.* 2018;21(3):303–14. <https://doi.org/10.1016/j.mattod.2017.09.002>.
84. Wang Y, Jin Y, Zhang T, Huang Z, Yang H, Wang J, Jiang K, Fan S, Li Q. Emission enhancement from CdSe/ZnS quantum dots induced by strong localized surface plasmonic resonances without damping. *J Phys Chem Lett.* 2019a;10(9):2113–20. <https://doi.org/10.1021/acs.jpcclett.9b00818>.



85. Wang H, Rao H, Luo M, Xue X, Xue Z, Lu X. Noble metal NPs growth-based colorimetric strategies: from monocolorimetric to multicolorimetric sensors. *Coord Chem Rev.* 2019b;398:113003. <https://doi.org/10.1016/j.ccr.2019.06.020>.
86. Watts HJ, Partes H, Yeung D. Real-time detection and quantification of DNA hybridization by an optical biosensor. *Anal Chem.* 1995;67(23):4283–9. <https://doi.org/10.1021/ac00119a013>.
87. Wätzig H, Oltmann-Norden I, Steinicke F, Alhazmi HA, Nachbar M, El-Hady DA, et al. Data quality in drug discovery: the role of analytical performance in ligand binding assays. *J Comput Aided Mol Des.* 2015;29(9):847–65. <https://doi.org/10.1007/s10822-015-9851-6>.
88. Wetchakun K, Samerjai T, Tamaekong N, Liewhiran C, Siriwong C, Kruefu V, Wisitsoraat A, Tuantranont A, Phanichphant S. Semiconducting metal oxides as sensors for environmentally hazardous gases. *Sensors Actuators B Chem.* 2011;160(1):580–91. <https://doi.org/10.1016/j.snb.2011.08.032>.
89. Wiley BJ, Im SH, Li ZY, McLellan J, Siekkinen A, Xia Y. Maneuvering the surface plasmon resonance of silver nanostructures through shape-controlled synthesis. *J Phys Chem B.* 2006;110(32):15666–75. <https://doi.org/10.1021/jp0608628>.
90. Wu F, Thomas PA, Kravets VG, Arola HO, Soikkeli M, Iljin K, et al. Layered material platform for surface plasmon resonance biosensing. *Sci Rep.* 2019;9(1):20286. <https://doi.org/10.1038/s41598-019-56105-7>.
91. Wu MC, Kao CK, Lin TF, Chan SH, Chen SH, Lin CH, et al. Surface plasmon resonance amplified efficient polarization-selective volatile organic compounds CdSe–CdS/Ag/PMMA sensing material. *Sensors Actuators B Chem.* 2020;309:127760. <https://doi.org/10.1016/j.snb.2020.127760>.
92. Xue S, Jiang XF, Zhang G, Wang H, Li Z, Hu X, et al. Surface plasmon-enhanced optical formaldehyde sensor based on CdSe@ZnS quantum dots. *ACS Sensors.* 2020;5(4):1002–9. <https://doi.org/10.1021/acssensors.9b02462>.
93. Yang Y, Miller OD, Christensen T, Joannopoulos JD, Soljačić M. Low-loss plasmonic dielectric nanoresonators. *Nano Lett.* 2017;17(5):3238–45. <https://doi.org/10.1021/acs.nanolett.7b00852>.
94. Yang W, Liu Y, McBride JR, Lian T. Ultrafast and long-lived transient heating of surface adsorbates on plasmonic semiconductor nanocrystals. *Nano Lett.* 2021;21(1):453–61. <https://doi.org/10.1021/acs.nanolett.0c03911>.
95. Yu H, Peng Y, Yang Y, Li ZY. Plasmon-enhanced light–matter interactions and applications. *Npj Comput Mater.* 2019;5(1):1–14. <https://doi.org/10.1038/s41524-019-0184-1>.
96. Zdanowicz M, Mroczynski R, Szczepanski P. Strong second-harmonic response from semiconductor–dielectric interfaces. *Appl Opt.* 2021;60(5):1132. <https://doi.org/10.1364/ao.414255>.
97. Zemel JN, Jensen JD, Schoolar RB. Electrical and optical properties of epitaxial films of PbS, PbSe, PbTe, and SnTe. *Phys Rev.* 1965;140(1A):A330. <https://doi.org/10.1103/PhysRev.140.A330>.
98. Zhang H, Cao P, Dou J, Cheng L, Niu T, Zhang G. Double-exponential RI sensitivity of metal–semiconductor core-shell NPs: the effects of dual-plasmon resonances and red-shift. *RSC Adv.* 2018;8(3):1700–5. <https://doi.org/10.1039/c7ra11981j>.

# Chapter 24

## Biomarkers and Bioimaging and Their Applications



Suchismita Ghosh and Kaustab Ghosh

### 24.1 Introduction

Advancement in nanoscience and nanotechnology facilitate present-day researches with a wealth of metallic and semiconducting nanoparticles for a wide range of applications in novel electronic devices, photonics to biomedical imaging technology [1–10]. The nanoparticles confining electrons in all three dimensions are also referred to as 0D nanoparticles or quantum dots. The highly tunable electronic and optical properties of these 0D nanoparticles with variation of size are due to its three-dimensional carrier confinement with ‘delta-like’ density of states. These unique properties are exhibited in the form of broader excitation spectra with narrow and sharply defined emission peaks. Important to mention the properties of quantum dots belonging to II–VI groups, such as CdS, CdSe or ZnO, exhibit intense luminescence in the visible region of the electromagnetic spectrum [11–13]. Conjugation of these nanoparticles to target molecules thus imparts bright fluorescence to cells and tissues and is widely used as fluorescent probes for live cell imaging and medical diagnosis [14, 15]. Clinical procedure thus involved in this aspect involves both in vitro and in vivo testing with these nanoparticles so as to validate it for human use. The in vivo studies are conducted on animal models such as mice and rat to extrapolate these findings to human populations. The results are validated with other more standard clinical chemistry markers and ultrastructural/histopathological evaluations of the clinical manifestations of disease. In vitro testing serves

---

S. Ghosh

Engineering and R&D Services (ERS), HCL Technologies, Elcot Economic Zone,  
Chennai, India

K. Ghosh (✉)

Centre for Nanoelectronics and VLSI Design, Vellore Institute of Technology, Chennai, India

School of Electronics Engineering, Vellore Institute of Technology, Chennai, India

e-mail: [kaustab@vit.ac.in](mailto:kaustab@vit.ac.in)

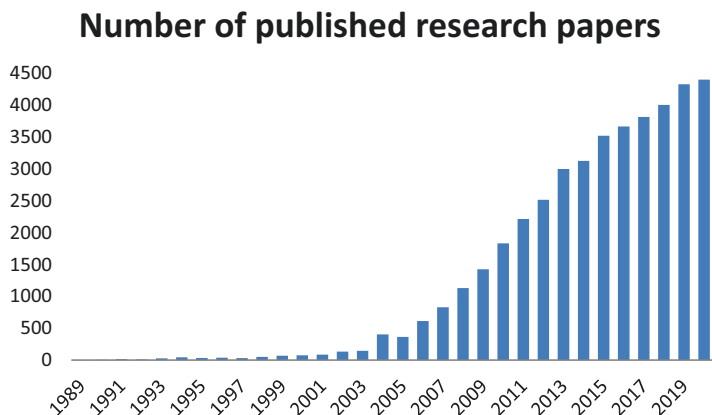
as an alternative to animal testing, with the study conducted on tissue from a living organism. One of the most crucial challenges this test aims at is to control cell toxicity of the synthesised nanoparticle, in a way to avoid adverse effects, while preserving the option of targeted cell death for direct tumour destruction. While these hurdles have restricted pre-clinical tests for years, they are now mature and are likely to reach the routine clinic in the near future.

The type of radiation which is used for biomedical imaging is also an important parameter as well. The optical transmission of the biological tissues in near-infrared (NIR) range (750–1000 nm) allows higher light penetration, resulting in lower autofluorescence and reduced light scattering, which gives clear image contrast. Therefore, probes which are excitable in NIR range are preferable for both in vitro and in vivo imaging. Near-infrared radiation (NIR) (within the range of 700–1100 nm wavelength) having high penetration depth in tissues is favourable for this type of imaging. Hence, it is essential to choose suitable nanoparticles in which the electrons can be excited by NIR wavelength. However, highly luminescent QDs such as CdS and ZnO have larger band gaps (2.49 to 2.78 eV for CdS QDs and 3.5 to 4 eV for ZnO QDs [16, 17]). Thus, electrons in these nanoparticles can be excited by radiation near to the ultraviolet (UV) region, which causes severe photodamage to the living cells and tissues. To circumvent this effect, the nanoparticles are doped by lanthanides which act as sensitizers and activators. The sensitizer (mostly  $\text{Yb}^{3+}$  ion) is used to absorb the incoming photon in the NIR range and the absorbed energy is transferred to the activators (which are mostly  $\text{Ho}^{3+}$ ,  $\text{Er}^{3+}$  or  $\text{Tm}^{3+}$  ions). This process of energy transfer promotes the electrons to the higher energy excited states of the activators, which eventually relax to the lower energy states. The difference in energy between the states is given up in the form of photons with energies in the UV, visible or in the NIR range. This process is known as upconversion (UC) and the nanoparticle doped with these optically active ions is referred to as upconversion nanophosphors (UCNs). The same concept also applies to the down conversion (DC) except that the electron relaxation in the activator occurs between the states with lesser energy difference leading to higher wavelength infrared (IR) emission. Figures 24.1 and 24.2 show the upconversion and downconversion processes occurring in nanophosphors.

Nanophosphors thus play an important role in medical imaging technology for early detection and diagnosis of various diseases, which in turn have resulted in decrease in mortality rate. Survey has shown significant data to prove that this development coincides with the decrease in the mortality rate due to cancer (total decline of 31% from 1991 to 2018) [19]. The development of nanophosphors in clinical practice has also led to enormous research over the last two decades and the number of published papers is found to increase exponentially as depicted in Fig. 24.3.

This paper thus provides a detailed review on the synthesis and characterisation of the highly luminescent II–VI semiconductor nanoparticles and the techniques involved towards the development of efficient biomarkers for medical imaging applications. Main focus of our discussion is on stability of these nanoparticles, functionalisation of molecules, toxicity effect and the overall clinical trials and





**Fig. 24.3** Exponential increase in the number of published research papers on nanoparticles and bioimaging over the last three decades (Source: Clarivate Analytics's Web of Science (WoS) (version 5.32) scientific citation search platform)

procedures involved in this process. Finally, we have given a guideline towards future research, anticipation of different challenges involved along with strategies to overcome the effects.

## 24.2 Research in Upconversion and Downconversion with II–VI Semiconductor Nanophosphors

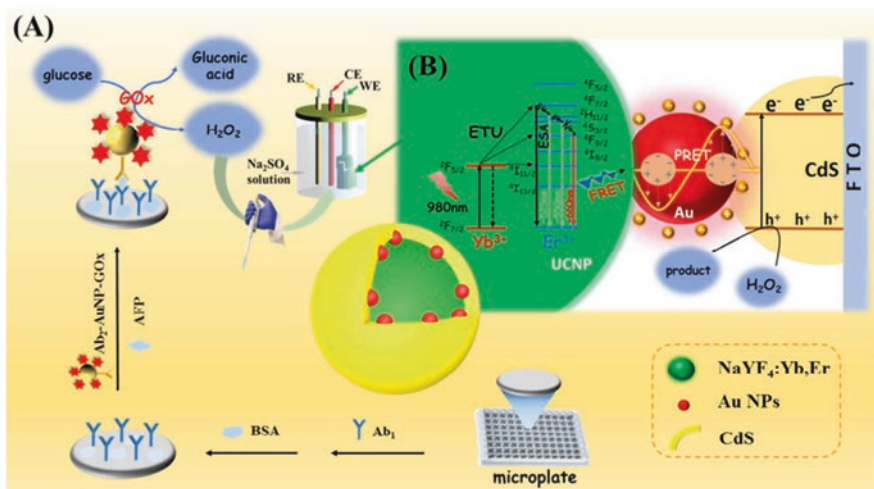
In the lanthanide-doped upconverting QD system, the QDs act as energy acceptors and the lanthanide act as energy donors. Here the absorption band of the QDs overlaps with the fluorescence emission band of lanthanides. If the distance between the lanthanide dopant atom and the QD is less than 10 nm, then the emission energy is transferred to the QDs by a process known as Förster resonance energy transfer. Otherwise, re-absorption takes place which transfer energy as photons. This process finds enormous applications in the photodynamic therapy of cancer cells. Here the upconverting nanoparticle is conjugated with photosensitiser molecule and carried it to the targeted cancer cells. Under near-infrared excitation, the visible light emitted by the nanoparticle sensitises the photosensitisers to generate photocatalytic activity for destroying the cancer cells. After the therapy, the nanoparticles can also be used to monitor and detect the presence of any cancer cells through the detection of cancer protein biomarkers that are overexpressed in these cells.

Several researches thus reported the synthesis of upconversion in II–VI QDs for photocatalytic activity which can be applied in the aforementioned domain of research. Tou et al. [20] synthesised carbon layer-modified  $\text{NaYF}_4:\text{Yb},\text{Tm}$  nanocrystals which served as a good substrate for CdS deposition. The product exhibited good photocatalytic activity under visible light and enhanced performance in

Vis-NIR region. Through upconversion luminescence analysis, Balaji et al. [21] exhibited the processes of energy transfer routes between  $\text{NaYF}_4:\text{Yb}/\text{Er}$  and  $\text{CdS}$  which is an important factor responsible for the photocatalytic activity in materials. A photoelectrochemical enzyme immunoassay is also designed by Luo et al. [22] with plasmonic gold sandwiched between upconversion  $\text{NaYF}_4:\text{Yb}^{3+}, \text{Er}^{3+}$  to semiconductor  $\text{CdS}$  as shown in Fig. 24.4.

Several works also reported the process of enhancing the upconversion luminescence which finds important applications in biological sensing and magnetic imaging such as in  $\text{ZnO}:\text{Yb}^{3+}/\text{Tm}^{3+}$  nanoparticles and  $\text{ZnO}:\text{Er}^{3+}, \text{Yb}^{3+}$  on  $\text{Mo}^{6+}$  co-doping [23, 24]. Apart from the lanthanum-based materials, upconversion nanoparticles like mesoporous  $\text{SiO}_2$  decorated with  $\text{CdS}$  nanoparticles also exhibited excellent photocatalytic activity under irradiation of infrared light, and Li et al. [25] and Slejko et al. [26] demonstrated upconversion photoluminescence in  $\text{CdSe}/\text{CdS}$  nanocrystal-based solid films.

Light emission in the visible region requires downconversion of nanoparticles. In this domain, Kung et al. [27] fabricated silver nanoparticles on the surface of  $\text{ZnO}$  nanorods for sensitising downconversion luminescence. Kundu et al. [28] exhibited stable down conversion in  $\text{CdSe}/\text{CdS}$  nanophosphors which showed larger Stokes shift greater than 100 nm or 0.39 eV along with the efficient colour-pure conversion from blue to red light and Chu et al. [29] reported yellow-orange emitting  $\text{ZnO}-\text{Lu}_3\text{Al}_{5-x}\text{SixO}_{12-x}\text{N}_x:\text{Ce}^{3+}$  down-conversion phosphors with enhanced visible light photocatalytic activity.



**Fig. 24.4** A schematic representation of near-infrared light triggered photoelectrochemical immunoassay (a) Immunoreaction process in the assay, and (b) energy transfer mechanism among lanthanide ion, Au and CdS with  $\text{H}_2\text{O}_2$  under near-infrared irradiation (980 nm). (Reprinted with permission from Ref. [22]. Copyright 2018: American Chemical Society)

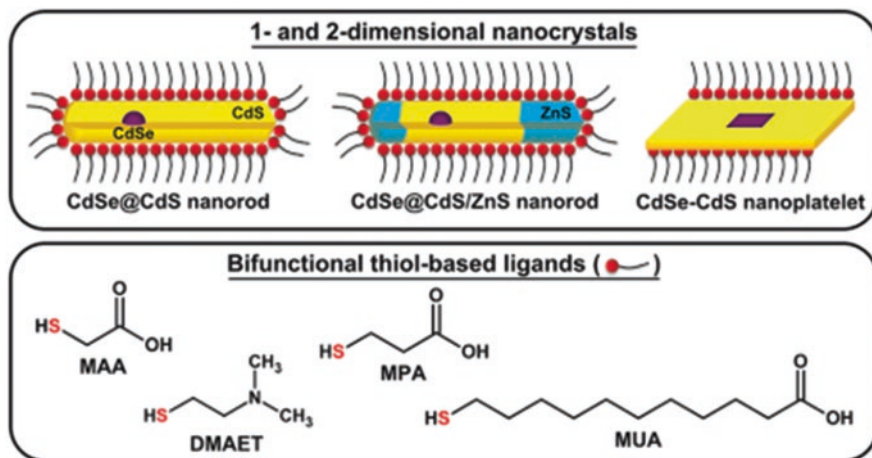
### 24.3 Surface Modification of Luminescent Nanoparticles

Surface modification is one of the important prerequisite for rendering the aqueous solubility of the II–VI nanoparticles. Several strategies have been developed to circumvent this problem, which is summarised as follows. The first one is to synthesise QDs in aqueous solution directly, which has been depicted in this review [30]. The second is to obtain QDs in organic solvents and then transfer them to aqueous solutions. As these nanoparticles are prepared in nonpolar organic media, the surface of the particles gets covered with hydrophobic ligand that provides stability and prevents aggregation of the particle core. For example, trioctylphosphine (TOP) capped synthesised CdSe/ZnS quantum dots by Vo et al. [31] exhibited strong repulsive force between the particles and better durability from zeta potential measurements. It is also essential for the QDs to have a good water solubility. Nie and Weiss groups [32, 33] pioneered the preparation of water-dispersed QDs by ligand exchange method. In addition, polymer and lipid coating is another efficient way to render QDs with good water solubility [34, 35].

However, for compatibility in the biological media, phase transfer process becomes essential which converts the hydrophobic surface into hydrophilic. In this process, the nanoparticles are coated with amphiphilic polymers for phase transferring from non-polar to polar environment. Amphiphilic polymers or amphiphiles have both hydrophilic and hydrophobic components. Generally, the hydrophobic component consists of long saturated or unsaturated hydrocarbon chain which connects to the hydrophobic ligand of the nanoparticle by the process called hydrophobic interaction. The other hydrophilic part which is thus free imparts solubility of the nanoparticle in the polar medium. Example again includes the aforesaid work of Vo et al. [31], who used mercaptopropionic and mercaptosuccinic acid containing thiol and carboxylic group as ligands which exhibits good dispersion of QD in water and biological media. Kodanek et al. [36] also used these types of thiol-based ligands for aqueous phase transfer of CdSe/CdS/ZnS nanorods and CdS core crown nanoplatelets as depicted in Fig. 24.5. They found that short-chained thiols are the best choice to obtain high quantum yields for samples with better inorganic passivation. However, long-chained ligands are suitable towards enhancing the quantum yield of samples with poorer inorganic passivation.

### 24.4 Biorecognition and Bioimaging for Cell Therapy with Nanophosphors

Biorecognition and bioimaging have been intensely used for the advance clinical practices for the diagnosis and detection by medical imaging, invasive tissue biopsy, bio-analytical evaluation of body fluids and optical imaging to visualise the 3D structure of specimens and its biological activity. For these bio-recognition events and cell tracking, the biomolecules are required to be conjugated with the



**Fig. 24.5** Phase transfer mechanism of the nanocrystals and the bifunctional thiol-based ligands. (Reproduced from Ref. [36] with permission from the Royal Society of Chemistry)

nanoparticle which is also known as functionalisation. This process includes the coupling of the biomolecules to the surface of the nanoparticles via covalent interactions. A wide variety of targeted molecules such as biotin, folic acid, receptor binding elements like aptamers, antibodies and peptides are known to be linked to the surface of the nanoparticles through functionalisation. For example, some essential cofactors like biotin, lipoic acid and pantothenic acid are overexpressed in cancer cells and sodium-dependent multivitamin transporter (SMVT) is an important transmembrane protein which is responsible for translocations of these vitamins. Hence, to target SMVT in cancer cell, biotin can be chosen as an affinity ligand after modifying the QD surface with streptavidin. Vijayabharathi et al. [37] prepared such biotin streptavidin CdSe QD which is found to be stable and compatible in biological medium with reduced level of toxicity in both cancer and normal cells.

Recently many efforts are being made on the functionalisation of QDs to various in vitro and in vivo imaging sensitivity and specificity. In this session, we will review the recent development of conjugated QDs for in vitro and in vivo imaging.

#### 24.4.1 *In Vitro Bioimaging for Cell Therapy with Nanophosphors*

Uptake of nanophosphors for cellular imaging occurs through endocytic or phagocytic mechanism. For example, during in vitro imaging, the biomolecular cells can endocytose the capped nanoparticles when injected into an animal. The labelled cells can be tracked in vivo and follow their biodistribution for various diagnosis applications and cell therapy research. Jaiswal et al. demonstrated the potential

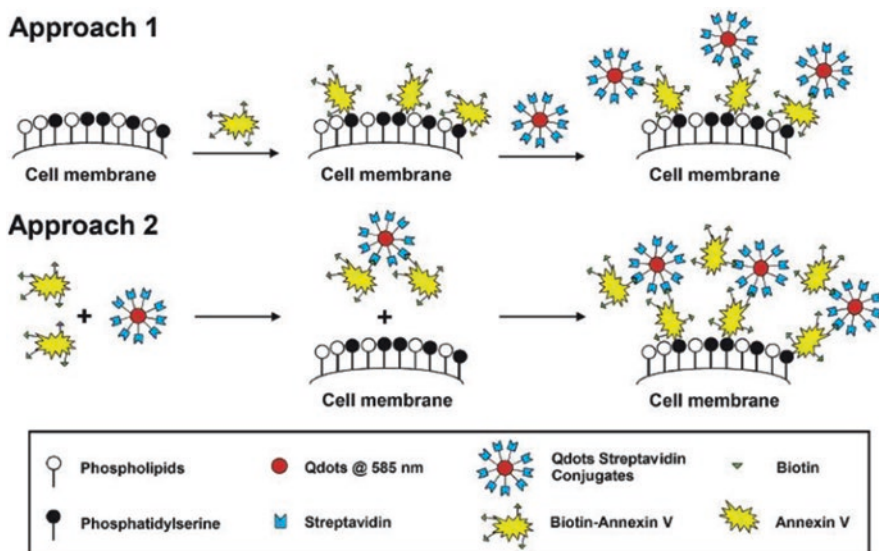


application of QDs in cell tracking by reporting that the cells can store capped CdSe/ZnS QDs in vesicles through endocytosis after washing away the excess QDs [38]. Tracking of targeted cells has also been made possible by functionalised QDs binding to specific moieties present on the membrane of apoptotic cells but not on healthy or necrotic cells. For example, Gac et al. [39] have successfully detected apoptotic cells by conjugating QDs with biotinylated Annexin V, a 35-kDa protein, using two approaches as illustrated in Fig. 24.6. This enabled detection and imaging of apoptotic cells to monitor specific photostable apoptosis.

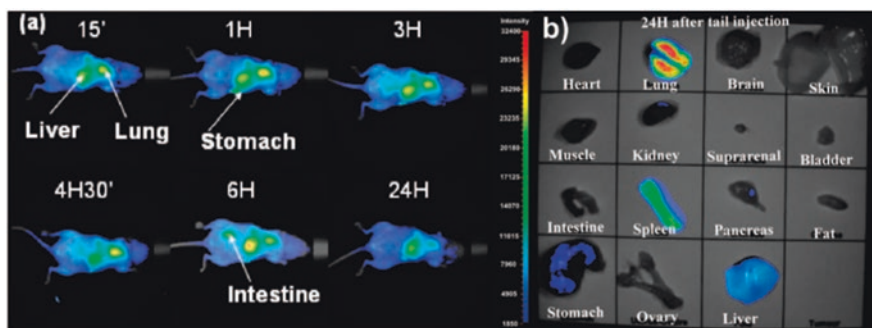
#### 24.4.2 *In Vivo Bioimaging for Cell Therapy with Nanophosphors*

Nanophosphors is not only the most popular biomarker for *in vitro* imaging but also have been widely used as *in vivo* imaging agents. Using CuInS<sub>2</sub>/ZnS QDs as *in vivo* agent, Li et al. [40] demonstrated high contrast fluorescence imaging as well as the temporal evolution of the distribution of injected QDs in live mice, shown in Fig. 24.7.

However, cytotoxicity and the potential interference of QDs labelling with cellular processes are primary issues in any live-cell or animal experiment. The *in vivo* application of QDs requires them to be low in toxicity, have high contrast, high



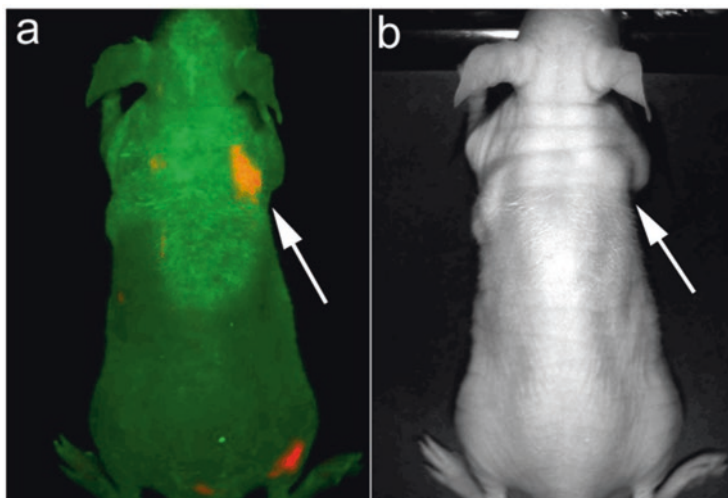
**Fig. 24.6** Schematic sketch of two approaches for detecting apoptotic cells by conjugating QDs with biotinylated Annexin V. (Reprinted with permission from Ref. [39] Copyright 2006: American Chemical Society)



**Fig. 24.7** (a) Fluorescence images exhibiting the temporal evolution of the distribution of intravenously injected  $\text{CuInS}_2/\text{ZnS}$  QDs into the tail of a healthy nude mouse (b) Fluorescence images of different parts of the mouse after dissection. (Reprinted in a modified form with permission from Ref. [40]. Copyright 2009: American Chemical Society)

sensitivity and photostability. The functionalised molecules also need to be assessed for longer time storage due to higher stability and resistant to extreme conditions of the chemical environment. Aptamers are found to possess these qualities and thus can potentially be an alternative or replace antibodies with short shelf life and batch-to-batch variation. Highly specific binding of oligonucleotides to the aptamer molecules can thus be used to detect pathogens like SARS-CoV-2 virus [41] and bacteria such as *Salmonella typhimurium* within the concentration range from 3.3 to  $3.3 \times 10^6$  CFU/ml [42]. Another molecule such as phospholipid block-copolymer micelles also demonstrates the same type of characteristics. Important to mention the work of Dubertret et al. [43], who fabricated  $\text{CdSe}/\text{ZnS}$  QDs encapsulated individually in phospholipid block-copolymer micelles, which were found not only to be highly stable and nontoxic after injection into embryo but also concluded that these could be followed during embryogenesis.

We have discussed earlier the use of PEG for increasing cell penetration. For in vivo imaging, Ballou et al. [44] showed long-term imaging of live mice revealing the importance of coating QDs with high molecular weight PEG molecules to reduce their toxicity and accumulation in the liver and bone marrow. Some studies also pointed out that the increase in the length of PEG coating polymer on the surface of QDs was able to slow down their extraction toward the liver. So coating polymer on the surfaces was another factor worthy of considering when QDs are employed for in vivo imaging. However, this can be overcome by peptide-conjugated QDs as Yong et al. [45] demonstrated encapsulated hydrophobic  $\text{CdSe}/\text{CdS}/\text{ZnS}$  quantum rods (QRs) coated with PEGylated phospholipids and conjugated with cyclic RGD peptide to be a bright, photostable, and biocompatible luminescent probe for the early diagnosis of cancer. This is illustrated in Fig. 24.8. Yang et al. [46] also showed cell-penetrating peptides to conjugate near-infrared quantum dots and labelled oral squamous carcinoma cells with quantum dot conjugates by endocytosis for visual in vivo imaging. With this deep tissue penetration power,

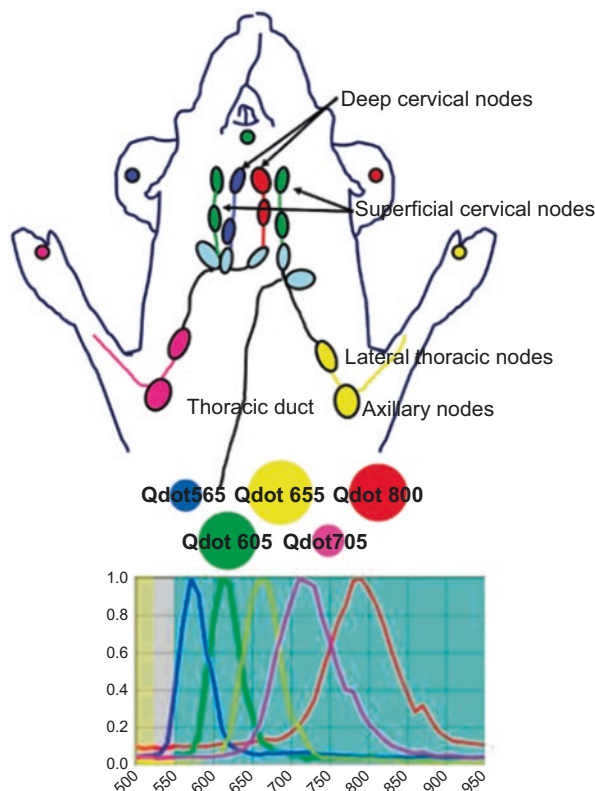


**Fig. 24.8** Strong luminescence signal towards in vivo imaging of mice at 2 weeks post-inoculation of Panc-1 cancer cells (pointed by white arrows) and injected with  $\sim 0.5$  mg of cRGD peptide conjugated quantum rods (QRs). The autofluorescence is coded with green colour from tumour-bearing mice and red colour with the unmixed QR signal. The transmission image in (b) corresponds to the luminescence image in (a). (Reprinted with permission from Ref. [45]. Copyright 2009: American Chemical Society)

near-infrared quantum dot technology has efficiently increased the sensitivity of early diagnosis, visual observation and individualised treatment of cancer cells.

In the recent years, the potential of the QDs has been further explored to demonstrate simultaneous imaging of trafficking lymph nodes which helps in predicting the route of cancer metastasis into the lymph nodes. Kobayashi et al. were the first to use the different emission spectra of the QDs to report fluorescence lymphangiography. He injected five QDs with similar physical sizes but different emission spectra simultaneously into five different sites of the mouse body, that is, in the middle of phalanges, the upper extremity, the ears, and the chin. Different parts of the mouse body can be identified by certain fluorescence colours. Figure 24.9 is the schematic illustration of the five-colour spectral fluorescence imaging of the lymphatic system in the upper body of the mouse. The coloured lymph nodes are the draining nodes visualised in the body. This is the first demonstration of simultaneous imaging of trafficking lymph nodes with QDs having different emission spectra [47].

The type of radiation which is used for biomedical imaging is also an important parameter. The optical transmission of the biological tissues in near-infrared (NIR) range (750–1000 nm) allows higher light penetration, results in lower autofluorescence and reduced light scattering, which gives clear image contrast. Therefore, probes which are excitable in the NIR range are preferable for both in vitro and in vivo imaging. As mentioned above the nanoparticles can be optically excited under ultraviolet light before their injection into small animals to emit a NIR persistent



**Fig. 24.9** Anatomic representation of the five-colour spectral fluorescence imaging of the lymphatic system in the upper body of the mouse with a graph of the emission spectra of each of the five QDs used. (Reprinted with permission from Ref. [47]. Copyright 2007: American Chemical Society)

luminescence, which can be monitored *in vivo* for up to 1 h after their systemic injection. This short span has been the limitation of the first-generation persistent luminescence nanoparticles (PLNPs), as the long-term imaging *in vivo* needs permeability and retention effect of nanocarriers within the malignant stroma, usually up to 2 to 24 h. This has led to the recent developments to improve the extend the persistent of the PLNPs, which enables long afterglow or long-lasting phosphorescence that could last several hours after optical excitation. For instance, Thomas Maldiney et al. [48] observed persistent luminescence in mice tumour cells after 4 h of administration of chromium-doped zinc gallate. From 1 to 6 h after the injection, the luminescence intensity in the liver increased from 18% to about 50% of the total emission.

The type of radiation which is used for biomedical imaging is also an important parameter. The optical transmission of the biological tissues in the near-infrared (NIR) range (750–1000 nm) allows higher light penetration, resulting in lower autofluorescence and reduced light scattering, which gives clear image contrast.

Therefore, probes which are excitable in the NIR range are preferable for both *in vitro* and *in vivo* imaging. As mentioned above the nanoparticles can be optically excited under ultraviolet light before their injection into small animals to emit a NIR persistent luminescence, which can be monitored *in vivo* for up to 1 h after their systemic injection. This short span has been the limitation of the first-generation persistent luminescence nanoparticles (PLNPs), as the long-term imaging *in vivo* needs permeability and retention effect of nanocarriers within the malignant stroma, usually upto 2 to 24 h. This has led to the recent developments to improve the extend the persistent of the PLNPs, which enables long afterglow or long-lasting phosphorescence that could last several hours after optical excitation. For instance, Thomas Maldiney et al. [48] observed persistent luminescence in mice tumour cells after 4 h of administration of chromium-doped zinc gallate. From 1 to 6 h after the injection, the luminescence intensity in the liver increased from 18% to about 50% of the total emission.

## 24.5 Band Structure Modelling of Nanophosphors

Apart from experiments, it is essential to compute the quantized energy states of nanophosphors for understanding the carrier absorption and recombination processes that lead to bright luminescence. The theoretical concepts which explain these experimental observations can be utilised for controlling and optimising the parameters and helps in affecting the necessary modifications. Theoretical modelling in nanophosphors or QDs calls for the laws of quantum mechanics and the solution of three-dimensional Schrödinger's equation which can be used to engineer its optical properties [49, 50]. The Schrödinger solver computes the emission wavelength associated with the photoluminescence (PL) peak and also can be used to calculate the full PL spectrum. A very good correlation with the experimental results is found in the paper of Srujan et al. and the work can be implemented for any type of QD nanostructures [50]. Using the same process, Barmparis et al. [51] also computed the shape-dependent single electron levels of gold nanoparticles. After knowing the quantized energy levels, a rate equation can be formulated for each of the quantum levels. This provides information about the carrier absorption and recombination phenomena occurring in the QD which is used to compute the intensity of light emission or luminescence. Using a three-level rate equation model, Hu et al. thus modelled carrier dynamics in QD and described the power-dependent PL [52]. The intensity of luminescence obtained from the rate equation model can be used further to describe the optical transmission, scattering, absorption and colour conversion process in the QDs and the theoretical fit to experimental data is found to be greater than 96% [53]. Theoretical accuracy can thus be used as a guideline for synthesising the nanophosphors with desired optical properties and performance in specific applications.

## 24.6 Clinical and Pre-clinical Studies for Bioimaging

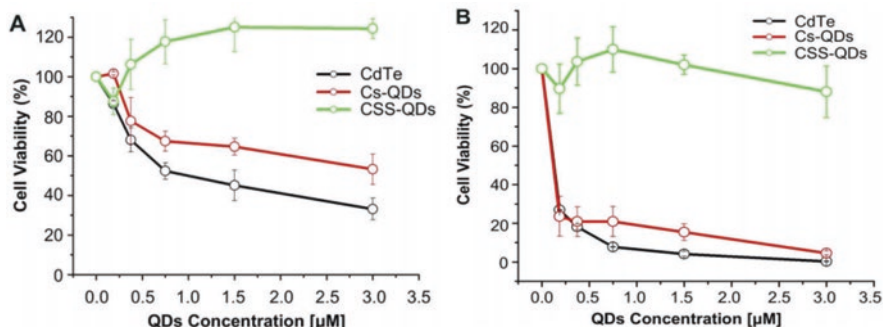
The biomarkers need to be confirmed and validated before it becomes clinically approved test for human use. Several correlative *in vitro* and *in vivo* studies have been conducted which have contributed to the data that are essential for interpreting and defining the precision and effectiveness of the biomarker endpoint. This can guide the medical professionals in the choice of the best treatment option. For *in vitro*, the patient-derived xenografts models are in use where cells from patient tissues are propagated in mice and are therefore closer to the clinical situation.

Pre-clinical *in vivo* micro-imaging techniques offer superior technical possibilities compared to current human imaging modalities because of (i) the immobility of the studied specimen (e.g. *ex vivo* lymph node and anaesthetized animal), (ii) higher spatial resolutions (e.g. special coils, higher frequency probes or higher magnetic fields), and (iii) possible use of novel contrast-agents, not approved for clinical use.

In spite of the success and the expected growth of non-invasive imaging by II–VI semiconductor nanophosphors as biomarkers, made over the last decades; it falls yet short of entering the clinics and becoming the standard neoadjuvant procedure. Several assessment studies including biodistribution, clearance, haematology, serum chemistry and histopathology studies have been conducted to assess the feasibility of the acceptance of the II–VI semiconductor nanophosphors as suitable biomarkers.

Studies have indicated that the insoluble nanoparticles can cross the protective barriers and get accumulated showing toxic effects such as reduced cell viability, induction of apoptosis, oxidative stress and cell morphology changes in the lungs, brain, liver, spleen and bone [54–56]. Salmi et al. [57] conducted an experiment to study the toxicological effects of CdSe due to bioaccumulation on land snail *Helix aspersa* and concluded that the species is sensitive to the presence of the material by inducing stress and enzymatic mechanisms.

Researchers have come up with surface coating and surface modification to reduce the cytotoxicity and these approaches have been validated with the biodistribution, pharmacokinetic and toxicity studies. Long-term and short-term *in vivo* pre-clinical studies were conducted by Su et al. [58] showing that water-dispersed CdTe QDs, CdTe/CdS core–shell QDs and CdTe/CdS/ZnS core–shell–shell QDS can be well tolerated even at high concentration incubation for a long time by various cell line as shown in Fig. 24.10. This is assumed to be due to the protective impact of the ZnS shell, impeding the release of Cd ions from the inner side. Further antimicrobial and biocompatibility study conducted by Mir et al. [59] suggested that the surface modification of ZnSe with ZnS shell helps to enhance the fluorescence property, making these more biocompatible for biomedical applications.



**Fig. 24.10** Cell viability study of HEK293T cells with different concentrations of CdTe QDs, CdTe/CdS core-shell QDs (Cs-QDs) and CdTe/CdS/ZnS (CSS-QDs) core-shell-shell QDs for 24 h (a) and 48 h (b), respectively. (Reprinted with permission from Ref. [58]. Copyright 2009: Elsevier)

## 24.7 Future Direction and Conclusion

In summary, we have given a detailed review of the latest research on important II–VI nanophosphors, process of synthesis, surface modification, bioconjugation, toxicity issues and various bioimaging modalities. Although there is a huge possibility of utilising these nanoparticles for sensing and imaging in biomedical industry, some challenges still exist that need to be addressed before it enters the clinical trials and audits. One of the challenges involves photoexcitation of these nanoparticles using ultraviolet radiation due to higher band gap and this poses photodamage to cells and tissues. So here research scope exists in upconverting the nanoparticles by doping with lanthanides or other novel materials. These UCNs can be utilised for absorbing the incoming radiation in the near-infrared range instead of using harmful UV rays for photoexcitation. A detailed discussion is given about various research which has provided novel methodologies for effectively utilising these nanoparticles in detecting various biomolecules, malignant tumours and biomarkers. Research can be focused on enhancing the luminescence of the UCNs for the development of high-sensitivity biosensors and imaging applications.

One important factor is based on cadmium-based nanophosphors which can pose a serious problem in the level of toxicity and thus can be barred for *in vivo* imaging applications if adequate steps are not taken. Thus, non-cadmium-based materials are recommended for biomedical imaging and medical diagnostics. In this domain, researches can be done with non-toxic zinc-based compounds such as ZnO, ZnS in the aforesaid applications although it needs to be kept in mind that increased levels of zinc absorption can become toxic [60]. However, cadmium nanophosphors also exhibit high-intensity luminescence which is vital for improving bioimaging efficiency. Hence, to overcome the adverse issues of toxicity, a lot of researches have been carried out that reported effective capping and encapsulation of these nanoparticles with non-toxic compounds or rare earth elements that prevent the release of

$\text{Cd}^{2+}$  ions and led to a considerable reduction in toxicity. We have also suggested the usage of aptamer and block copolymer molecules which are found to be non-toxic, highly stable, that is resistant to extreme conditions and also offer higher sensitivity of detection and high contrast imaging. Peptide molecules are suggested for increasing the cell penetration depth of the nanoparticles which can be highly photostable, bright and can be used as a biocompatible luminescent probe. Thus, with proper encapsulation technology and suitable synthesis methodology, it is also found that the CdSe QDs are successfully implemented in both in vitro and in vivo imaging with no increase in toxicity.

After analysing toxicity, other crucial parameters which need to be considered for effective in vitro and in vivo imaging are the intensity and persistence of the luminescence of nanoparticles. Research needs to be carried out on the choice of suitable phosphors which can offer long-term luminescence. The elemental composition of the chosen phosphor needs to be optimised to improve the persistence and efficiency in luminescence. Here scope for theoretical research also exists, such as development of three dimensional Schrödinger's equation solver for computing the energy states and modelling the band structure. From the band structure, electron dynamics rate equation can be formulated which can provide useful guidelines on the energy transfer mechanism in nanophosphors. With this information, a new strategy can be proposed for improving the persistence and intensity of luminescence along with tuning the luminescence peak in a specified region of the electromagnetic spectrum.

Finally, the question arises on the possibility of commercialisation and whether these encapsulated nanophosphors can be clinically approved for human use. The results of the biodistribution, pharmacokinetic and toxicity studies conducted on animal models as well as the human cells have enlightened the path of feasibility of acceptance of II–VI semiconductors as suitable biomarkers. The toxicological studies of the encapsulated biomarkers were well tolerated and this has confirmed that the surface coating and modification is an assured biocompatible application to reduce the cytotoxicity as well as increase the fluorescence effect. With these developmental studies, the different intra-vital imaging approaches in the clinics and in pre-clinical settings have stimulated further research, and the future is likely to see many technological advances on signal detection and emission as well as image specificity and resolution to tackle current hurdles.

## References

1. Wu L, Xu J, Li Q, Fan Z, Mei F, Zhou Y, Yan J, Chen Y. Enhanced performance of  $\text{In}_2\text{O}_3$  nanowire field effect transistors with controllable surface functionalization of Ag nanoparticles. *Nanotechnology*. 2020;31:355703.
2. Tran DP, Pham TTT, Wolfrum B, Offenhäusser A, Thierry B. CMOS-compatible silicon nanowire field-effect transistor biosensor: technology development toward commercialization. *Materials (Basel)*. 2018;11(5):785.



- Bayan S, Bhattacharya D, Mitra RK, Ray SK. Self-powered flexible photodetectors based on Ag nanoparticle-loaded g-C<sub>3</sub>N<sub>4</sub> nanosheets and PVDF hybrids: role of plasmonic and piezoelectric effects. *Nanotechnology*. 2020;31:365401.
- Ghosh K, Kundu S, Halder N, Srujan M, Sengupta S, Chakrabarti S. Annealing of In<sub>0.45</sub>Ga<sub>0.55</sub>As/GaAs quantum dots overgrown with large monolayer (11 ML) coverage for applications in thermally stable optoelectronic devices. *Solid State Commun*. 2011;151:1394.
- Wang X, Liu K, Chen X, Li B, Jiang M, Zhang Z, Zhao H, Shen D. Highly wavelength-selective enhancement of responsivity in Ag nanoparticle-modified ZnO UV photodetector. *ACS Appl Mater Interfaces*. 2017;9(6):5574–9.
- Choi MS, Park T, Kim WJ, Hur J. High-performance ultraviolet photodetector based on a zinc oxide nanoparticle@single-walled carbon nanotube heterojunction hybrid film. *Nano*. 2020;10(2):395.
- Bharathi MV, Ghosh K, Paira P. Glycerol–water mediated centrifuge controlled green synthesis of oleic acid capped PbS quantum dots for live cell imaging. *RSC Adv*. 2017;7:40664.
- Gil HM, Price TW, Chelani K, Bouillard JSG, Calaminus SDJ, Stasiuk GJ. NIR-quantum dots in biomedical imaging and their future. *iScience*. 2021;24:102189.
- Mohamadi E, Moghaddasi M, Farahbakhsh A, Kazemic A. A quantum-dot-based fluoroassay for detection of food-borne pathogens. *J Photochem Photobiol B*. 2017;174:291.
- Bharathi MV, Maiti S, Sarkar B, Ghosh K, Paira P. Water-mediated green synthesis of PbS quantum dot and its glutathione and biotin conjugates for non-invasive live cell imaging. *R Soc Open Sci*. 2018;5:171614.
- Park HW, Kim DH. Intense visible luminescence in CdSe quantum dots by efficiency surface passivation with H<sub>2</sub>O molecules. *J Nanomater*. 2012;2012:892506.
- Borovaya MN, Burlaka OM, Naumenko AP, Blume YB, Yemets AI. Extracellular synthesis of luminescent CdS quantum dots using plant cell culture. *Nanoscale Res Lett*. 2016;11:100.
- Yang W, Yang H, Ding W, Zhang B, Zhang L, Wang L, Yuc M, Zhang Q. High quantum yield ZnO quantum dots synthesizing via an ultrasonication microreactor method *Ultrason. Sonochem*. 2016;33:106.
- Cui Y, Zhang C, Song L, Yang J, Hu Z, Liu X. Facile synthesis of near-infrared emissive CdS quantum dots for live cells imaging. *J Nanosci Nanotechnol*. 2018;18:2271.
- Ma YY, Ding Hui H, Xiong HM. Folic acid functionalized ZnO quantum dots for targeted cancer cell imaging. *Nanotechnology*. 2015;26(30):305702.
- Singh N, Mehra RM, Kapoor A, Soga T. ZnO based quantum dot sensitized solar cell using CdS quantum dots. *J Renew Sustain Energy*. 2012;4:013110.
- Lin KF, Cheng HM, Hsu HC, Lin LJ, Hsieh WF. Band gap variation of size-controlled ZnO quantum dots synthesized by sol–gel method. *Chem Phys Lett*. 2005;409:208.
- Loo JFC, Chien YH, Yin F, Kong SK, Ho HP, Yong KT. Upconversion and downconversion nanoparticles for biophotonics and nanomedicine. *Coord Chem Rev*. 2019;400:213042.
- Siegel RL, Miller KD, Fuchs HE, Jemal A. Cancer statistics, 2021. *CA Cancer J Clin*. 2021;71:7.
- Tou M, Mei Y, Bai S, Luo Z, Zhang Y, Li Z. Depositing CdS nanoclusters on carbon-modified NaYF<sub>4</sub>:Yb, Tm upconversion nanocrystals for NIR-light enhanced photocatalysis. *Nanoscale*. 2016;8:553.
- Balaji R, Reddy SKKL, Sharma V, Bhattacharyya K, Krishnan V. Near-infrared driven photocatalytic performance of lanthanide-doped NaYF<sub>4</sub>@CdS core-shell nanostructures with enhanced upconversion properties. *J Alloys Compd*. 2017;724:481.
- Luo Z, Zhang L, Zeng R, Su L, Tang D. Near-infrared light-excited core–core–shell UCNP@Au@CdS upconversion nanospheres for ultrasensitive photoelectrochemical enzyme immunoassay. *Anal Chem*. 2018;90(15):9568.
- Li Y, Li Y, Wang R, Xu Y, Zheng W. Enhancing upconversion luminescence by annealing processes and the high-temperature sensing of ZnO:Yb/Tm nanoparticles. *New J Chem*. 2017;41:7116.

24. Anjana R, Subha PP, Kurias MK, Jayaraj MK. Enhanced green upconversion luminescence in ZnO:Er<sup>3+</sup>, Yb<sup>3+</sup> on Mo<sup>6+</sup> co-doping for temperature sensor application. *Methods Appl Fluoresc.* 2017;6:015005.
25. Li YW, Dong L, Huang CX, Guo YC, Zhu Yang X, Xu YJ, Qian HS. Decoration of upconversion nanoparticles@mSiO<sub>2</sub> core-shell nanostructures with CdS nanocrystals for excellent infrared light triggered photocatalysis. *RSC Adv.* 2016;6:54241.
26. Slejko EA, Lugh V. Upconversion photoluminescence in colloidal CdSe/CdS nanocrystal-based solid films. *Nano-Struct Nano-Objects.* 2021;26:100742.
27. Yen Kung P, Huang LW, Shen TW, Wang WL, Su YH, Lin MI. Down-conversion photoluminescence sensitizing plasmonic silver nanoparticles on ZnO nanorods to generate hydrogen by water splitting photochemistry. *Appl Phys Lett.* 2015;106:023114.
28. Kundu J, Ghosh Y, Dennis AM, Htoon H, Hollingsworth JA. Giant nanocrystal quantum dots: stable down-conversion phosphors that exploit a large stokes shift and efficient shell-to-core energy relaxation. *Nano Lett.* 2012;12(6):3031.
29. Chu H, Liu X, Liu J, Lei W, Li J, Wu T, Li P, Li H, Pan L. Down-conversion phosphors as noble-metal-free co-catalyst in ZnO for efficient visible light photocatalysis. *Appl Surf Sci.* 2017;391(Part B):468.
30. Baig N, Kammakam I, Falath W. Nanomaterials: a review of synthesis methods, properties, recent progress, and challenges. *Mater Adv.* 2021;2:1821.
31. Vo NT, Ngo HD, Thi NPD, Thi KPN, Duong AP, Lam V. Stability investigation of ligand-exchanged CdSe/ZnS-Y (Y=3-mercaptopropionic acid or mercaptosuccinic acid) through zeta potential measurements. *J Nanomater.* 2016;2016:8564648.
32. Chan WCW, Nie SM. Quantum dot bioconjugates for ultrasensitive nonisotopic detection. *Science.* 1998;281(5385):2016.
33. Pinaud F, King D, Moore HP, Weiss S. Bioactivation and cell targeting of semiconductor CdSe/ZnS nanocrystals with phytochelatin-related peptides. *J Am Chem Soc.* 2004;126(19):6115.
34. Hezinger AFE, Tessmar J, Göpferich A. Polymer coating of quantum dots--a powerful tool toward diagnostics and sensorics. *Eur J Pharm Biopharm.* 2008;68(1):138–52.
35. Murcia MJ, Minner DE, Mustata GM, Ritchie K, Naumann CA. Design of quantum dot-conjugated lipids for long-term, high-speed tracking experiments on cell surfaces. *J Am Chem Soc.* 2008;130(45):15054.
36. Kodanek T, Banbela HM, Naskar S, Adel P, Bigalla NC, Dorfs D. Phase transfer of 1- and 2-dimensional Cd-based nanocrystals. *Nanoscale.* 2015;7:19300.
37. Bharathi V, Roy N, Moharana P, Ghosh K, Paira P. Green synthesis of highly luminescent biotin-conjugated CdSe quantum dots for bioimaging applications. *New J Chem.* 2020;44:16891.
38. Jaiswal JK, Mattoussi H, Mauro JM, Simon SM. Long-term multiple color imaging of live cells using quantum dot bioconjugates. *Nat Biotechnol.* 2003;21:47.
39. Gac SL, Vermes I, Berg AVD. Quantum dots based probes conjugated to Annexin V for photo-stable apoptosis detection and imaging. *Nano Lett.* 2006;6(9):1863.
40. Li L, Daou TJ, Texier I, Chi TTK, Liem NQ, Reiss P. Highly luminescent CuInS<sub>2</sub>/ZnS core/shell nanocrystals: cadmium-free quantum dots for *in vivo* imaging. *Chem Mater.* 2009;21(12):2422.
41. Wan Q, Liu X, Zu Y. Oligonucleotide aptamers for pathogen detection and infectious disease control. *Theranostics.* 2021;11(18):9133.
42. Chen S, Yang X, Fu S, Tao XQ, Chaoxin Y, Jiang MY. A novel AuNPs colorimetric sensor for sensitively detecting viable salmonella typhimurium based on dual aptamers. *Food Control.* 2020;115:107281.
43. Dubertret B, Skourides P, Norris DJ, Noireaux V, Brivanlou AH, Libchaber A. *In vivo* imaging of quantum dots encapsulated in phospholipid micelles. *Science.* 2002;298(5599):1759.
44. Ballou B, Lagerholm BC, Ernst LA, Bruchez MP, Waggoner AS. Noninvasive imaging of quantum dots in mice. *Bioconjug Chem.* 2004;15(1):79.

45. Yong KT, Hu R, Roy I, Ding H, Vathy LA, Bergey EJ, Mizuma M, Maitra A, Prasad PN. Tumor targeting and imaging in live animals with functionalized semiconductor quantum rods. *ACS Appl Mater Interfaces*. 2009;1(3):710.
46. Yang K, Cao YA, Shi C, Li ZG, Zhang FJ, Yang J, Zhao C. Quantum dot-based visual *in vivo* imaging for oral squamous cell carcinoma in mice. *Oral Oncol*. 2010;46(12):864.
47. Kobayashi H, Hama Y, Koyama Y, Barrett T, Regino CAS, Urano Y, Choyke PL. Simultaneous multicolor imaging of five different lymphatic basins using quantum dots. *Nano Lett*. 2007;7, 6:1711.
48. Maldiney T, Bessière A, Seguin J, Teston E, Sharma SK, Viana B, Bos AJJ, Dorenbos P, Bessodes M, Gourier D, Scherman D, Richard C. *Nat Mater*. 2014;13:418.
49. Ghosh K, Naresh Y, Reddy NS. Theoretical optimization of multi-layer InAs/GaAs quantum dots subject to post-growth thermal annealing for tailoring the photoluminescence emission beyond 1.3 $\mu$ m. *J Appl Phys*. 2012;112:024315.
50. Srujan M, Ghosh K, Sengupta S, Chakrabarti S. Presentation and experimental validation of a model for the effect of thermal annealing on the photoluminescence of self-assembled InAs/GaAs quantum dots. *J Appl Phys*. 2010;107:123107.
51. Barmparis GD, Kopidakis G, Remediakis IN. Shape-dependent single-electron levels for Au nanoparticles. *Materials*. 2016;9(4):301.
52. Hu X, Zhang Y, Guzun D, Ware ME, Mazur YI, Lienau C, Salamo GJ. Photoluminescence of InAs/GaAs quantum dots under direct two-photon excitation. *Sci Rep*. 2020;10:10930.
53. Xu S, Yang T, Lin J, Shen Q, Li J, Ye Y, Wang L, Zhou X, Chen E, Ye Y, Guo T. Precise theoretical model for quantum-dot color conversion. *Opt Express*. 2021;29:18654.
54. Mirnajafizadeh F, Ramsey D, McAlpine S, Wang F, Stride JA. Nanoparticles for bioapplications: study of the cytotoxicity of water dispersible CdSe(S) and CdSe(S)/ZnO quantum dots. *Nanomaterials (Basel)*. 2019;9(3):465.
55. Ali D, Alarifi S, Alkahtani SH, Almansour M. *Fresenius Environ Bull*. 2018;27(6):4298.
56. Esparza JR, Mena AM, Sancha IG, Fragoso PR, de la Cruz GG, Mondragón R, Fragoso LR. Synthesis, characterization and biocompatibility of cadmium sulfide nanoparticles capped with dextrin for *in vivo* and *in vitro* imaging application. *J Nanobiotechnol*. 2015;13:83.
57. Salmi A, Rouabhi R. Study of the toxicity of cadmium selenide (CdSe) on a model bio indicator *Helix aspersa*. *Arch Environ Contam Toxicol*. 2018;AESET-102. <https://doi.org/10.29011/AESET-102.10000>.
58. Su Y, He Y, Lu H, Sai L, Li Q, Li W, Wang L, Shen P, Huang Q, Fan C. The cytotoxicity of cadmium based, aqueous phase - synthesized, quantum dots and its modulation by surface coating. *Biomaterials*. 2009;30(1):19.
59. Mir IA, Alam H, Priyadarshini E, Meena R, Rawat K, Rajamani P, et al. Antimicrobial and biocompatibility of highly fluorescent ZnSe core and ZnSe@ZnS core-shell quantum dots. *J Nanopart Res*. 2018;20:174.
60. Agnew UM, Slesinger TL. Zinc toxicity. In: *StatPearls*. Treasure Island: StatPearls Publishing (2022). Available from: <https://www.ncbi.nlm.nih.gov/books/NBK554548/>

# Chapter 25

## Biosensors Based on II–VI Semiconductor Quantum Dots for Health Protection



Suria Mohd Saad and Jaafar Abdullah

### 25.1 Introduction: II–VI Semiconductor Quantum Dots-Based Biosensors for Health Protection

The result of human activities in daily life has adversely affected the environment to the point of polluting the soil for plant cultivation, drinking water and inhaled air. Undoubtedly, the issue of environmental pollution has led to the issue of global public health in various aspects of life. Clearly, efforts to intensify the development of biomonitoring are essential to enable the measurement of many environmental pollutants in ensuring public health. In diagnosis and health care, it is important to measure contaminants in biological samples. Therefore, fast, responsive, accurate and inexpensive assessment methods must be developed to detect such contaminants.

Quantum dots (QDs) is a bright luminescent nanoparticles (NPs) with average size of 2–20 nm which gives remarkable optical and conductivity features [1, 2]. In the periodic table, QDs are atoms located in groups II–VI, IV–VI or III–V and are semiconductor nanocrystals [3]. Many of the present insights into the optical properties of QDs have been reported [4] such as applications in biomedical [5],

---

S. M. Saad

Institute of Nanoscience and Nanotechnology, University Putra Malaysia,  
Serdang, Selangor, Malaysia

Biotechnology and Nanotechnology Research Centre, MARDI Headquarters, Persiaran  
MARDI-UPM, Serdang, Selangor, Malaysia

J. Abdullah (✉)

Institute of Nanoscience and Nanotechnology, University Putra Malaysia,  
Serdang, Selangor, Malaysia

Department of Chemistry, Faculty of Science, University Putra Malaysia,  
Serdang, Selangor, Malaysia

e-mail: [jafar@upm.edu.my](mailto:jafar@upm.edu.my)

fluorescence sensors [2], food science [6], solar cell [7] and food contaminants detection [8]. Many studies of nanocrystalline semiconductor QDs, particularly in biosensing using electron transfer (ET) have been explored for the past few decades. The ET-based sensing methods are not limited to the emission wavelengths provided by the QDs, due to the broad QDs excitation profile and in addition to its high photostability, thus providing the system with significant modularity. This allows each component in the sensing system to be easily replaced by another component to achieve the desired response.

The combination of selectivity and modularity is difficult to match with other sensing methods compared to ET-based sensing methods with QDs [9]. This is due to the fact that in energy transfer-based sensing methods, in order to provide sensitivity and modularity, it requires a special coupling between organic fluorophores with a specific material and diameter [10]. Due to this, in energy transfer sensing methods there is a limit of the combination of other materials with organic fluorophores which have a high potential of photobleaching [11]. This is in contrast to the use of QDs in ET as a sensing mode. QDs offer modular control for analyte types and from a sensitivity point of view due to their unique photophysical properties and size-tunable. This allows the surface of QDs to be functionalised with a variety of biological and chemical ligands in the ET system [12]. The nano-size of QDs increases the surface ratio leading to increase in signal density (signal/geometric surface area). The properties of the semiconductor QDs themselves, which have ion centres, accelerate electron transfer, indirectly improving biosensor performance [13].

So far, there has been an effective increase in selectivity and sensitivity also reduction and removal of interference in nanosensors based on surface functionalisation of QDs [8]. Studies by Zhu et al. [14] show that the use of functional CdSe/ZnS QDs to detect contaminants in food has increased the sensitivity of ratiometric fluorescent ELISA systems compared to traditional HRP-based ELISA methods. The use of QDs with dual-emission wavelengths provides two fluorescent intensities (FL) under the same excitation wavelength. This method can effectively get rid of the effects of variations in the study environment in probe concentration and excitation wavelength fluctuations.

Compared to conventional organic dyes, QDs are highly photostable and resistant to photobleaching. They can be repeatedly excited and fluorescence for hours without photobleaching and maintaining brightness, but organic dyes are fragile and bleached after just a few minutes of exposure to light. QDs also have broad excitation spectra compared to conventional organic dyes that have narrow excitation spectra. These properties allow QDs to be excited in a wide range of wavelengths compared to organic dyes that require an excitation light at certain wavelengths [15]. Therefore, QDs are very useful in multiple-colour imaging compared to organic dyes that have limited use for single-colour imaging. Even QDs are more useful for multiple-colour imaging, it also has a narrow emission spectrum which makes it easy to identify and separate one from another. In contrast, organic dyes have a broad emission spectrum that makes it more difficult to use in multiple target identification simultaneously. This behaviour could cause more overlap between the

emission spectra of different dyes than the emission spectra of different QDs that can be distinguished upon their size and composition [6].

In sensing application, as a biological labelling QDs have been demonstrated to be far more efficient fluorescence sensing donors than conventional fluorophores. Application of QDs in fluorescence sensing has been proven to improve fluorescence sensing efficiency and spectral overlap due to its wide spectral range and tuneable in size. The use of QDs in analysing tetrabromobisphenol A has been shown to increase sensing sensitivity around 1 order of magnitude lower than conventional ELISA [14]. The use of QDs has also been shown to facilitate and increase sensing efficiency by detecting two types of analytes simultaneously in one response [16].

Different sensing schemes have been developed with QDs such as displacement of a bound quencher, structural or conformational changes in proteins and biocatalysed replication of DNA. Probes labelled QDs can be constructed easily by modifying the surface of QDs with various sensing elements such as peptides, antibodies and DNA [17]. This offers flexibility in inventing diagnostic tools. Moreover, the capability to adjust QDs fluorescence emission in the visible spectrum and its integration into polymeric microbeads offers a flexible multiplex diagnostic platform which can identify multiple disease biomarkers simultaneously [18]. With its broad absorption characteristics and narrow emission spectrum, QDs have multiple excitations at a single wavelength. In addition, the use of QDs in the analysis of complex samples, improves the sensitivity and repeatability of detection. This is due to QDs have a brightness and stability against photobleaching of 20 times and 100 times higher compared to organic dyes [19].

In conclusion to the above discussion, it can be observed that the real advantages that come from the superior characteristics of QDs should always be distinguished from the disadvantages of the use of inorganic probes in biological systems. Where, in certain applications, QDs are an excellent choice, or can be a very bad recommendation. The advantages of using QDs in sensing systems are indeed indisputable. In this review, we present the main chemical and physical mechanisms used for the detection of various biological components such as bacterial pathogens, toxic materials, environmental pollutants, pesticides, allergens, etc. with the use of QDs. We present examples of the most successful QDs applications in health protection as lateral flow immunoassay, electrochemical and optical sensors. Next, we focus on perspectives for further advancement in this area.

## **25.2 Biosensors Based on II–VI Semiconductor Quantum Dots for Detection of Pathogenic Bacteria**

Diseases associated with pathogenic bacteria, are among the major threats to human health, especially to those with immuno-compromised, children and the elderly. Most of epidemic and infectious diseases in humans are due to pathogenic bacteria

because they can be found everywhere in the environment. Various techniques have been developed in the detection of bacterial pathogens. Traditional methods for the detection of bacterial pathogens in the environment are such as microbiological methods, which involve agar culture and followed by colony counting, which is complicated, time-consuming and inefficient [20].

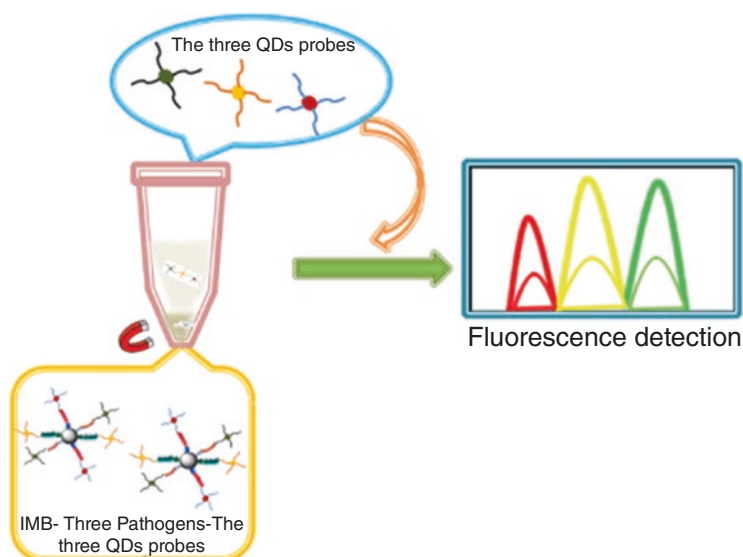
The application of polymerase chain reaction (PCR) followed by gel electrophoresis is faster, selective and sensitive [21] than traditional methods, but requires agarose gel electrophoresis in the process of DNA detection, which is carcinogenic [22]. Real-time PCR, on the other hand, involves expensive reagents, the use of sophisticated optical detection equipment and requires skilled personnel [23]. In addition, studies related to DNA as the target of analysis mostly struggle with the need for target amplification using a variety of strategies such as time-consuming and complicated isothermal amplification [24]. While fluorescent-based biosensors often face problems in terms of sensor performance and insensitive response [25].

Therefore, there is an urgent demand for simple techniques capable of detecting bacterial pathogens at high sensitivity, specificity, less toxic, stable and agile. So that testing for bacterial pathogens can be done anywhere and the tool is user-friendly and can provide accurate and immediate results. The limited monitoring processes and control techniques available in the market have raised public health concerns. Currently, no product can meet all of these criteria. In recent years, group II–VI of semiconductor quantum dots-based sensing has been considered an efficient and unique platform for rapid, selective, ultrasensitive, qualitative and quantitative detection of single or multiple pathogenic bacteria.

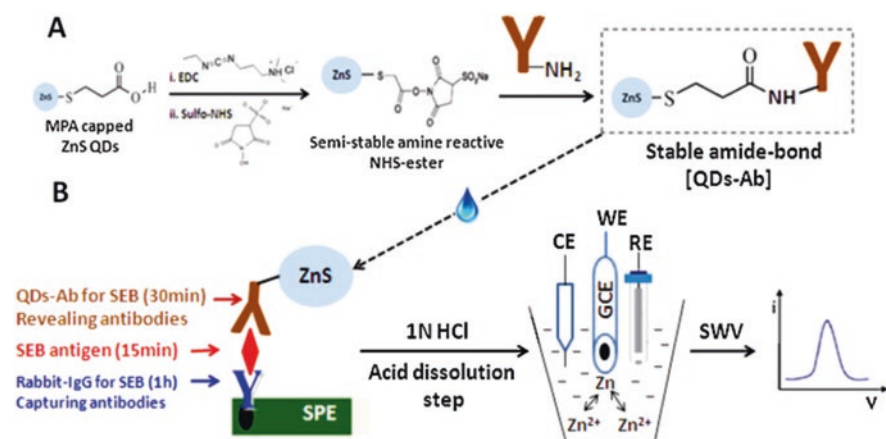
Studies by Wang et al. [26] have used the unique properties of QDs which is although they are different in sizes and excited at the same wavelength but yet emitting at different emission wavelengths. Three types of CdSe/ZnS QDs (330/430, 520 and 620 nm in the excitation/ emission wavelength evaluated) have been used in this study (Fig. 25.1). This unique property with different emission peaks has made it possible for the simultaneous detection of three types of pathogens.

Sharma et al. [27] have used electrochemical immunosensing method using ZnS QDs for detection of *Staphylococcal enterotoxin B* (SEB). In this study, ZnS QDs were functionalised with monoclonal antibodies (revealing antibodies) and used as signal materials in the electrochemical detection system. In this electrochemical method, ZnS was dissolved by the HCl through the oxidation process and turned into zinc ions ( $Zn^{2+}$ ) and function as indicators for the detection of SEB (Fig. 25.2). Although the detection sensitivity of this method is low compared to the conventional ELISA method but it meets the minimum concentration of SEB that can cause disease in humans. The more important is that this method has successfully shortened the analysis time and is suitable for on-field analysis because it is easy and fast.

Bui et al. [28] have used the doping technique of bare ZnSe QDs with transition-metal ions to improve fluorescence efficiency. A layer of ZnS is coated around the Mn-doped ZnSe QDs to enhance its optical properties. The developed method has successfully detected bacteria in 30 min with high sensitivity (Fig. 25.3). This QDs labelling method has the potential to be used in the food industry for the control and prevention of foodborne diseases.

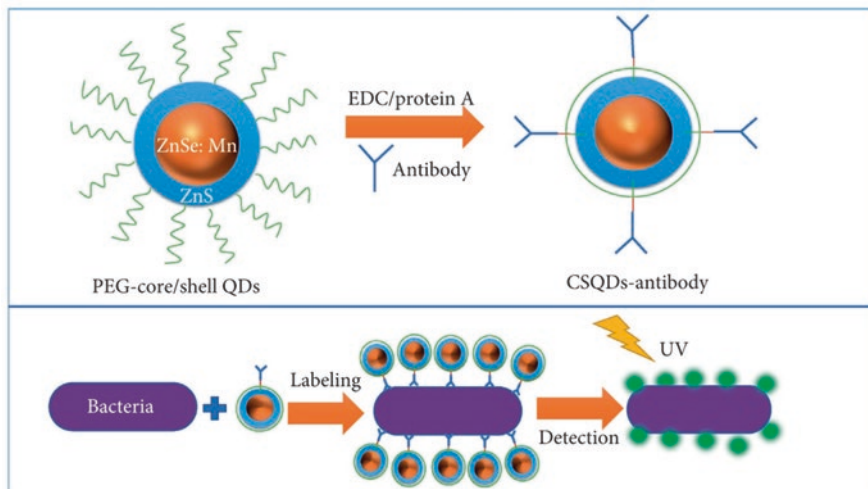


**Fig. 25.1** A peptide-mediated immunomagnetic separation technique and an immunofluorescence quantum dot technique for simultaneous and rapid detection of *Escherichia coli* O157:H7, *Staphylococcus aureus* and *Vibrio parahaemolyticus*. (Reprinted with permission from Wang et al. [26]. Copyright 2020: ACS)



**Fig. 25.2** Bioconjugation mechanism for the tagging of mice anti-SEB antibodies with mercapto-propanoic acid-capped ZnS QDs using EDC/NHS chemistry (a) and procedure for the QDs-based electrochemical immunosensing of SEB is shown in (b). (Reprinted with permission from Sharma et al. [27]. Copyright 2015: Elsevier)





**Fig. 25.3** The structure of synthesised CSQDs and its application in the bacteria detection. (Reprinted from Bui et al. [28]. Published 2020 by Hindawi Publ. as open access)

This review presented the detection of pathogenic bacteria, especially in contaminated food samples and thus helped prevent the outbreak of this foodborne disease. Therefore, it is clear those innovations in conventional methods for the detection of pathogenic bacteria have been actively pursued. Most of these efforts focus on the use of NMs especially in optical sensing to enhance detection sensitivity and miniaturisation of instrument to keep up with current developments in nanotechnology research.

### 25.3 Biosensors Based on II–VI Semiconductor Quantum Dots for Detection of Toxic Materials

Mycotoxins are a large secondary metabolite produced by fungi that are capable of posing a health threat to humans and animals due to their toxicity. It is one of the most important and toxic contaminants found in many foods and agricultural products [29].

Common methods used for the detection and confirmation of mycotoxins mainly include thin-layer chromatography (TLC) [30], liquid chromatography coupled with mass spectrometry (LC-MS) [31] and high-performance liquid chromatography (HPLC) [32]. However, such methods require complicated pretreatment, expensive and special instruments and even professional staff.

The emergence of semiconductor quantum dots (QD) in biosensor development has proven to be an efficient, attractive and convincing component material with high simplicity, rapidity, selectivity and sensitivity. CdSe QDs-based

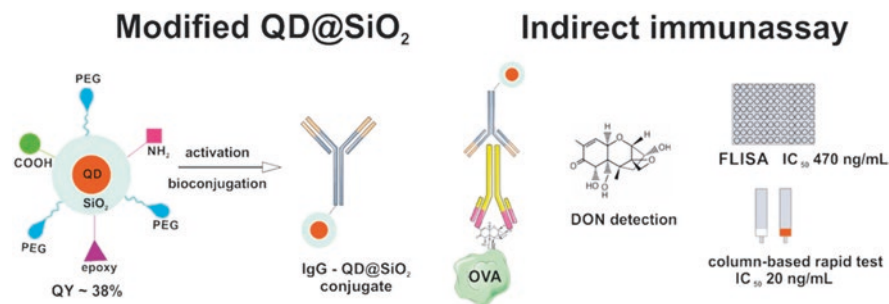
immunochemical techniques were successfully developed by Beloglazova et al. [33] for simultaneous screening of several mycotoxins. Simultaneous detection can occur because the conjugates of mycotoxin are labelled with fluorescent QDs having different spectra (orange, red and green emission), thus allowing to be scanned at different wavelengths as a result.

Goftman et al. [34] have modified the surface of QD@SiO<sub>2</sub> NPs with amino-, carboxyl- and epoxy-functional groups to obtain stable bright and sensitive fluorescent labels. The modified QD@SiO<sub>2</sub> was then conjugated with antibodies and used on a microtiter plate-based immunoassay and a quantitative column-based rapid immunotest for the detection of mycotoxin deoxynivalenol (Fig. 25.4).

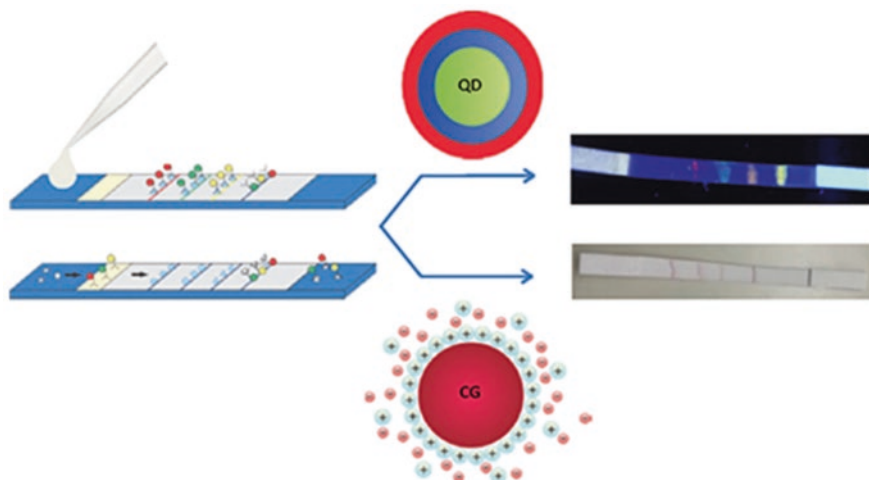
Foubert et al. [35] have innovated a tricolour-QD and CG-based LFIA system for the detection of DON, ZEN, T2 and HT2 mycotoxins. In this system, monoclonal antibodies (mAb) against DON, ZEN and T2 were labelled with CdSeS/ZnS QDs or colloidal gold (CG) allowing direct and correct comparison of developmental and performance characteristics (Fig. 25.5).

Vahid et al. [36] have developed an off-on probe based on chemiluminescence resonance energy transfer (CRET)-derived chemiluminescence (CL) emission of glutathione-modified CdSe quantum dots (GSH-CdSe QDs) for cyanide (CN<sup>-</sup>), poisonous toxin measurement. The synthesised GSH-CdSe QDs showed an increased effect on the intensity of CL emission and a reduced effect on the reaction time of this system. They catalyse the aforementioned CL responses, cooperate in the CRET process to act effectively as acceptors and generate a sensitising emission (Fig. 25.6).

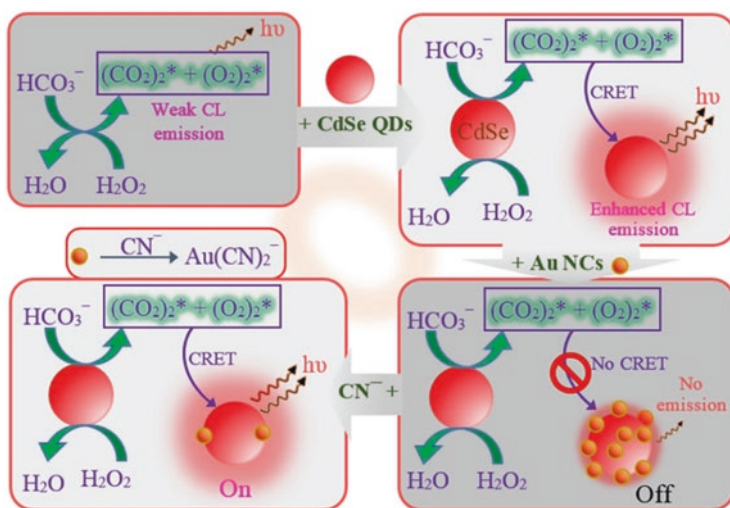
In conclusion, regular screening for mycotoxins is a necessity for health protection. In addition, it is very important to accurately investigate the worldwide distribution of mycotoxins, as well as their toxigenic potential. Further improvements are needed in detection procedures as well as the sensitivity of analytical methods to mycotoxins, with respect to recovery, accuracy and precision of measurements.



**Fig. 25.4** Functionalising of silica-coated CdSe quantum dots allow its bioconjugation with IgG in developing sensitive immunoassays. (Reprinted with permission from Goftman et al. [34]. Copyright 2016: Elsevier)



**Fig. 25.5** Colloidal gold- and quantum dot-based multiplex lateral flow immunoassay for simultaneous detection of four mycotoxins. (Reprinted with permission from Foubert et al. [35]. Copyright 2017: Elsevier)



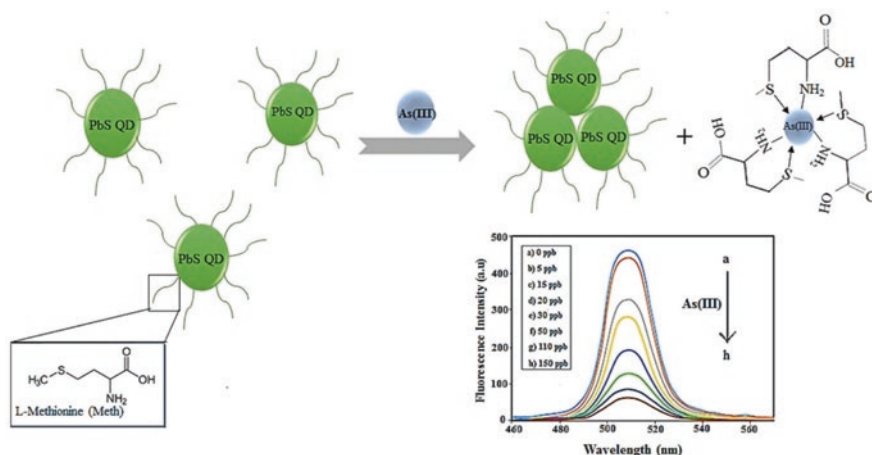
**Fig. 25.6** Design for off-on determination of cyanide based on CdSe QDs-improved CL and quenching effect of Au NCs. (Reprinted with permission from Vahid et al. [36]. Copyright 2019: Elsevier)

## 25.4 Biosensors Based on II–VI Semiconductor Quantum Dots for Detection of Environmental Pollutants

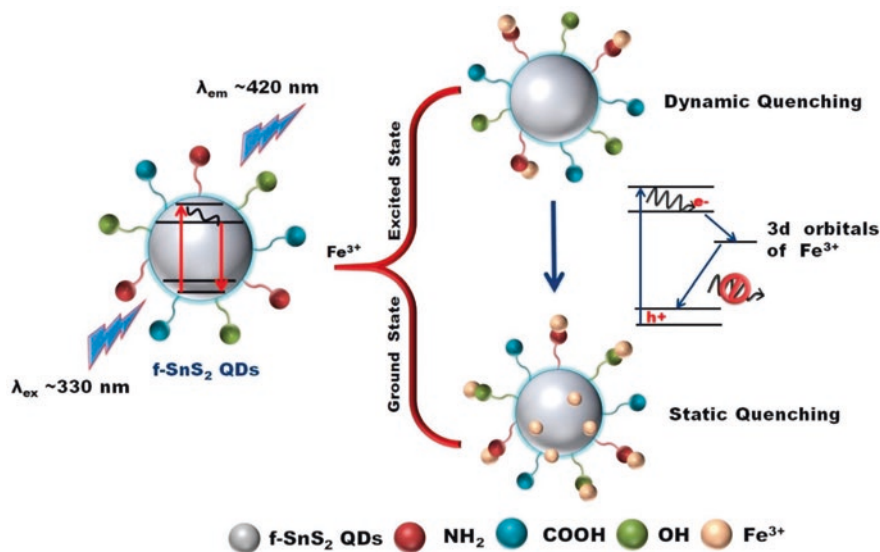
Environmental pollutants especially from heavy metal contamination usually occur in the developing countries due to industrial activities such as chemical manufacturing, metal processing, mining and soil fertilisation with improper management and treatment of metal ions [37]. Heavy metal pollution has a major impact on ecological systems and human health. Therefore, it is important to develop a sensitive, selective, portable and fast detection of heavy metal ions. To resolve the disadvantages of conventional methods which are time-consuming, less sensitive, complicated methods and high cost, quantum dots (QDs)-based nanomaterials have been used in developing sensors to improve the sensing performance [38].

The use of lead (II) sulphide (PbS) has been explored to improve the sensitivity and selectivity of QDs semiconductor nanocrystals. In this sense, Rahimi et al. [39] developed a system for the detection of arsenite (As(III)) ions in samples water based on Meth-capped PbS QDs that were synthesised using a simple aqueous chemical approach using L-methionine (Meth) as a template (see Fig. 25.7). This system was evaluated in solutions with different concentrations of As(III) ions, finding detection limits as low as 3.7 ppb proven through the fluorescence quenching. The mechanism involved in detection of As(III) is related to the formation of an S, N bidentate chelate ring by strong interaction between As(III) and Meth.

Other works report a fluorescence quenching system that involves the combination of both static and dynamic quenching process (Fig. 25.8). Srivastava et al. [40]



**Fig. 25.7** The Meth-capped PbS QDs acted as an effective fluorescent ‘turn-off’ probe for detection of As(III) ions. The sensor showed high sensitivity, selectivity and repeatability. (Reprinted with permission from Rahimi et al. [39]. Copyright 2021: Elsevier)



**Fig. 25.8** The proposed mechanism for fluorescence quenching of fluorophore (f-SnS<sub>2</sub> QDs) in presence of quencher (Fe<sup>3+</sup> ions). (Reprinted with permission from Srivastava et al. [40]. Copyright 2020: Elsevier)

developed a system based on optical sensor of 0D tin disulphide quantum dots (SnS<sub>2</sub> QDs) for detection of Ferric ion (Fe<sup>3+</sup>). Initially, this system showed a fluorescence compatible with the static quenching phenomenon, in which the interaction of the hydroxyl group present in f-SnS<sub>2</sub> QDs through non-radiative electron/hole recombination annihilation with Fe<sup>3+</sup> ion is essential. In the excited state with successive addition of Fe<sup>3+</sup> ions, coordination between electron-rich amino group and electron-deficient Fe<sup>3+</sup> ions is produced, leading to a dynamic quenching process. Finally, significant fluorescence quenching of f-SnS<sub>2</sub> QDs occurred following the successive addition of Fe<sup>3+</sup> ions. The system showed excellent detection of Fe<sup>3+</sup> ions up to 0.84 μM when excited at 330 nm.

Demand for rapid detection biosensors will increase as the world becomes increasingly aware of the adverse consequences of environmental pollution on ecosystems and public health. However, despite all these efforts, properties such as the toxicity of systems using semiconductor QDs in biosensor development in the environment must be evaluated. Biosensors need to be able to convince potential users, taking into account that the commercialisation of new devices and their use in the detection of contaminants in water sources will not generate additional pollution problems [37].

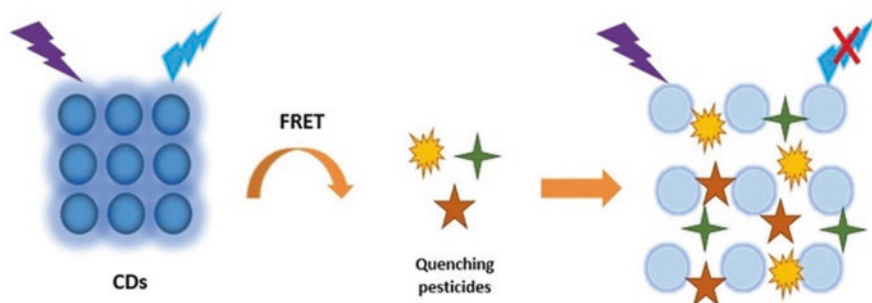
## 25.5 Biosensors Based on II–VI Semiconductor Quantum Dots for Detection of Pesticide

Large amounts of pesticides have been used in agriculture every year to increase crop yield. However, its widespread use in agriculture is risky because disclosure of pesticide residues through food is five times higher than disclosure through drinking water or air [41]. The increasing use of pesticides in agriculture is becoming increasingly significant, posing a threat to global human health as a result of the use and exposure of contaminated water and soil. Based on the fact that pesticide residues are a global threat to human health and the environment, accurate and rapid detection methods have become a major focus of researchers around the world.

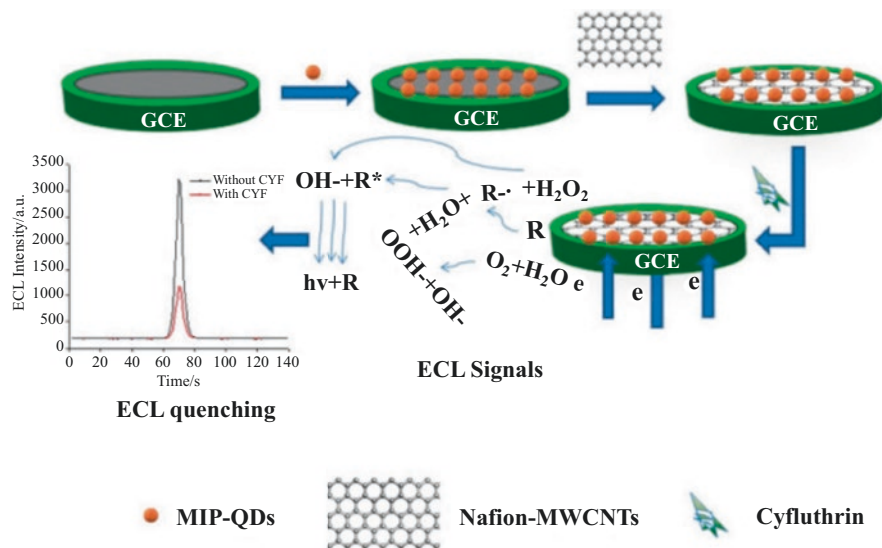
There are many pesticide verification methods including gas chromatography-tandem mass spectrometry (GCMS) [42], liquid chromatography-tandem mass spectrometry (LCMS) [43], molecular printing polymers [44] and capillary electrophoresis [45]. However, this method is not suitable for on-field testing as it requires skilled manpower, sophisticated equipment and high cost. Recently, the study of semiconductor QDs-based has attracted the interest of many researchers because of their high sensitivity, simplicity, controllability and test repeatability.

Tafreshi et al. [46] have used the green method, namely by using cauliflower as a precursor to CDs synthesis. The synthesised CDs were then used in development of ultrasensitive fluorescent sensor to detect diazinone, glyphosate and amicarbazone pesticides. The use of CDs in FRET system has proven to be cost-effective, reproducible, sensitive, applicable for real samples and user-friendly (Fig. 25.9).

A study by Xu et al. [47] for the detection of Cyfluthrin (CYF) showed success in increasing the sensitivity of molecularly imprinted-quantum dots (MI-QDs)-based detection systems. The use of cadmium selenide quantum dots (CdSe QDs) has increased electrical conductivity through an increase in electron transfer capability. The QDs used in this study are proven to have good electrochemiluminescence (ECL) properties and superior in conductivity (Fig. 25.10). Therefore, it significantly helps to improve the ECL signal.



**Fig. 25.9** The principle of FRET system through CDs fluorescence quenching by pesticides. The acceptors are three different pesticides and donors are CDs. (Reprinted by permission from Tafreshi et al. [46]. Copyright 2020: PLoS One)

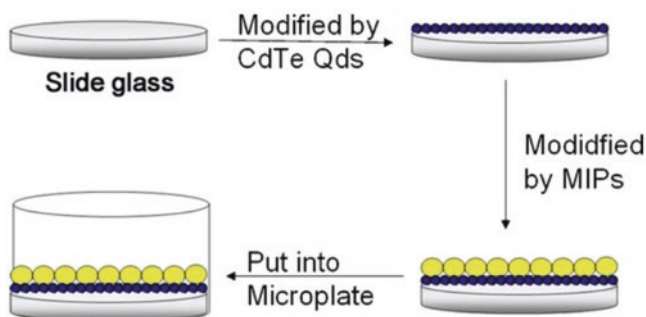


**Fig. 25.10** Schematic representation of MIECL sensor development. (Reprinted from Xu et al. [47]. Published 2020 by MDPI as open access)

Tran et al. [48] has started a study using CdSe and CdTe QDs in developing fabricated fluorescence biosensor for the detection of parathion methyl (PM) pesticide. This study has applied the principle of inhibition of the acetylcholinesterase (AChE) enzyme by pesticides that disrupt the hydrolytic rate of acetylthiocholine (ATCh) eventually leading to changes in the photoluminescence intensity (PL) of CdSe or CdTe QDs. This study has successfully developed a highly sensitive fluorescent biosensor with good performance in detecting PM pesticides up to 0.05 ppm.

Many studies involving the use of semiconductor QDs for pesticide detection have been initiated long ago. Ge et al. [49] also showed that the sensitivity and stability of chemiluminescence (CL) sensors modified with CdTe were successfully improved compared to bare sensors without modification with CdTe. This study has shown that the process of electron transfer from electron-rich organic molecules to CdTe QDs, a good semiconductor has effectively disrupted the excitonic recombination process (i.e., electron–hole pair). The success of manipulating this electron transfer basis has been applied in the detection of small organic molecules (Fig. 25.11).

The consequences of the harmful effects on human health from long-term consumption of pesticide-contaminated foods lead to the tendency and demand for portable and rapid pesticide detection technologies. Pesticide-contaminated food analysis faces constant modification due to the complexity of the matrix, the low concentration of target compounds and the increase in the number of pesticides approved for use. Through the development of sensing technology, innovative methods based on nanoparticles (NPs) in pesticide detection have attracted more attention due to their high sensitivity and low cost.



**Fig. 25.11** Modification of 96 well micro-plate with MIP-CdTe QDs. (Reprinted with permission from Ge et al. [49]. Copyright 2011: Elsevier)

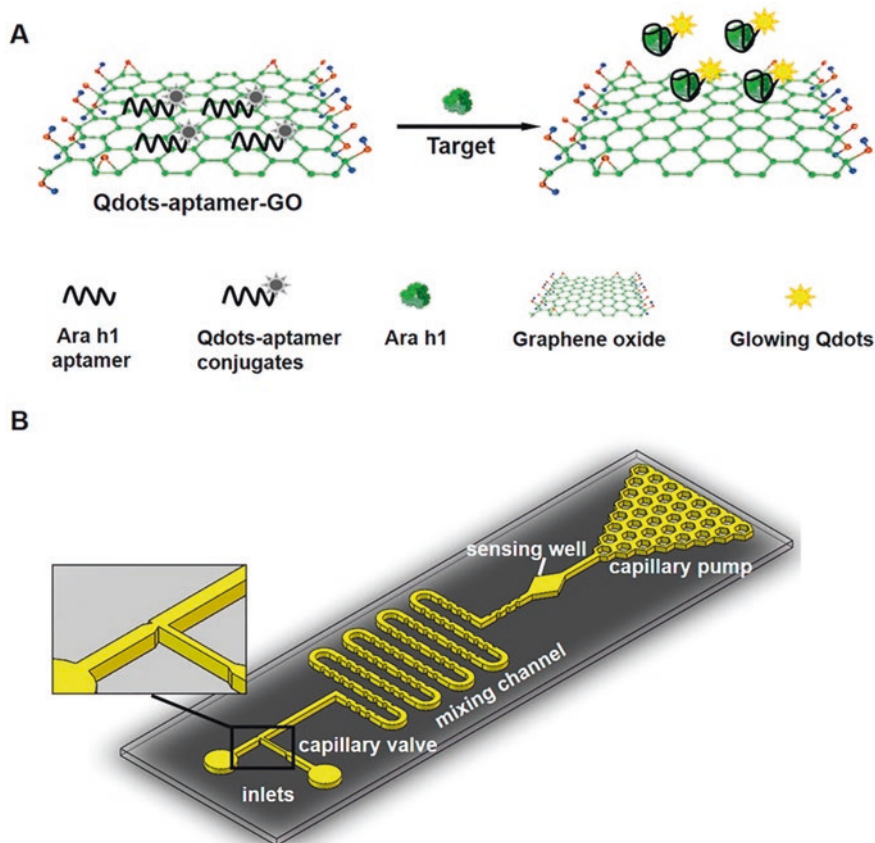
## 25.6 Biosensors Based on II–VI Semiconductor Quantum Dots for Detection of Allergens

Food allergy is an abnormal immune response to food which usually trigger by severe immunoglobulin E (IgE)-mediated allergic reactions, such as atopic dermatitis, emesis, diarrhoea, urticaria, angioedema and may even endanger [50]. Common food allergens that are always reported such as milk, eggs, fish, shellfish, tree nuts, peanuts, wheat and soybean. World Health Organization and International Union of Immunological Societies (WHO/IUIS) have recognised about 740 allergens which 260 molecules (35%) were labelled as food allergens, belonging to the Animalia (phyla: Arthropoda, Chordata, Mollusca and Nemata) and to the Plantae (phyla: Liliopsida and Magnoliopsida) kingdoms, twelve allergens (4.6% of known food allergens) are not real food molecules because they are all proteins from *Anisakis simplex* [51].

Current techniques for the detection of food allergens in industries such as enzyme-linked immunosorbent assay (ELISA) or lateral flow test using strips [52] have been developed for detection of proteins from the allergenic foods are convenient for onsite application as compared to PCR analysis. However, they have several drawbacks, which involve several steps of operation, are not practical for large number of samples and require photodetector for quantitative measurement. Therefore, simple, rapid and sensitive method is urgently needed for the detection of allergens in food.

A microfluidic system integrated with CdSe quantum dots (Qdots) functionalised graphene oxide (GO) coupled with aptamer nano-biosensor for simple, rapid and sensitive food allergen detection has been developed [53]. The food allergen is *Arachis hypogaea* 1 (Ara h1), one of the major allergens in peanuts. The biosensor based on Qdots/GO/aptamer complexes interact with the food allergens (Ara h1) resulting in fluorescence changes where the fluorescence quenching and recovering properties of GO through the adsorption and desorption of QDots-conjugated aptamers (Fig. 25.12). The microfluidic biosensor system

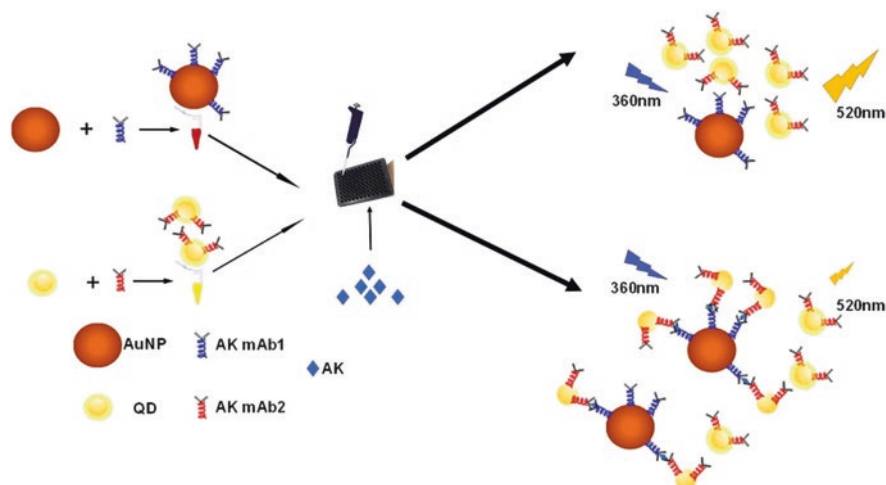




**Fig. 25.12** (a) Schematic of the sensing mechanism of the Qdots-aptamer-GO quenching system, (b) Schematic diagram of microfluidic chip design. (Reprinted with permission from Weng & Neethirajan [53]. Copyright 2016: Elsevier)

took approximately 10 min for the quantitative detection of Ara h1 with a detection limit of 56 ng/mL.

Wang et al. [54] have reported a sensitive immunosensor based on FRET mechanism using combination of gold nanoparticles (AuNP) and InP/ZnS quantum dots (QD) for the detection of arginine kinase (AK) which is one of the vital allergens in shrimp products. In this work, the first antibody was conjugated with AuNP (AuNP-Ab1) and the secondary antibody conjugated with QD (QD-Ab2). In the presence of AK, immunoreaction between AuNP-Ab1/AK/QD-Ab2 occurred, and the proximity interaction of AuNPs and QDs in the immuno-complex quenched the fluorescence signal (Fig. 25.13). The change in fluorescence intensity was proportional to the logarithm of AK in the concentration range of  $1.0 \times 10^{-6}$  –  $1.0 \times 10^{-3}$  mg/mL ( $R^2 = 0.9909$ ) with the detection limit of 0.11 ng/mL. The sensor took about 30 min for the detection of AK.



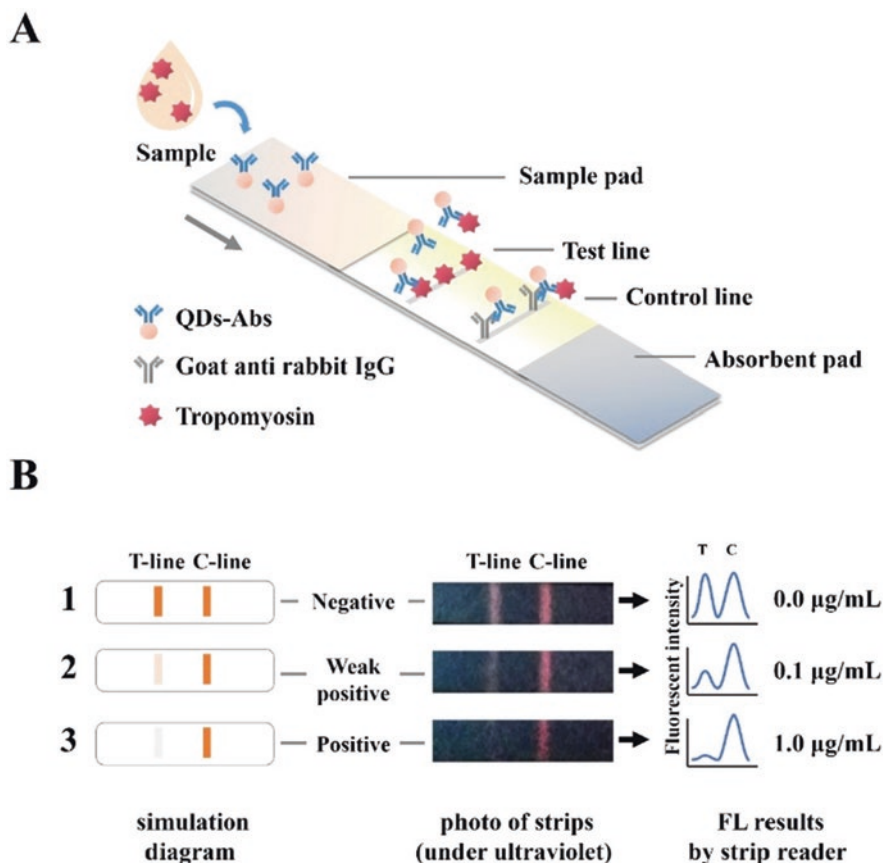
**Fig. 25.13** Schematic illustration of the proposed immunosensor based on FRET between antibody-modified AuNP and InP/ZnS QD for arginine kinase (AK) detection. (Reprinted with permission from Wang et al. [54]. Copyright 2021: Elsevier)

A rapid and sensitive detection method for crustacean allergen tropomyosin (TM) has been developed by Wang et al. [55]. In the study, polyclonal antibodies were labelled with CdSe/ZnS core-shell quantum dots using the lateral flow technique has been explored (Fig. 25.14). The results of the developed sensor can be obtained within 30 min with a visual limitation of 0.5  $\mu\text{g}/\text{mL}$  and with an instrumental limitation of 0.05  $\mu\text{g}/\text{mL}$ .

In Fig. 25.15, an electrochemical immunosensor device based on 3D printed mini cell integrated two thermoplastic electrodes and a disposable screen-printed carbon working electrode modified with  $\text{Sb}_2\text{O}_5/\text{SnO}_2$  for determination of adulteration of cheese produced from ewe/goat's milk with cow's milk has been demonstrated [56]. The system operated in two steps, first: a competitive immunoassay on the surface of the screen-printed working electrode using biotinylated anti-bovine k-casein labelled with streptavidin-conjugated CdSe/ ZnS quantum dots (QDs), second: detection of Cd(II) released after the acidic dissolution of Cd-based QDs by using stripping voltammetric technique. Under the optimal experimental condition, the limit of detection of 0.07% (v/v) of cow's milk in ewe/goat's cheese has been achieved.

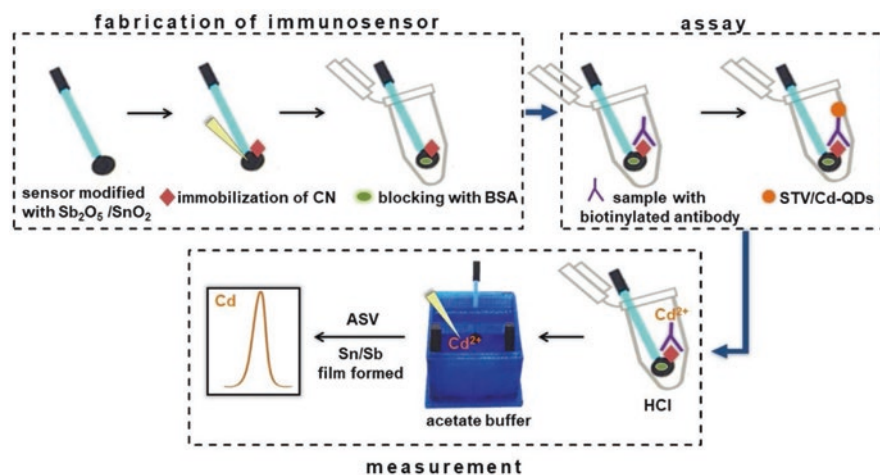
## 25.7 Summary

This review summarised the development of different biosensor systems by highlighting the current trend and potential solutions in achieving affordability, portability, higher accuracy and adaptability for health protection monitoring. The principle of the developed biosensor has been described in detail in terms of biorecognition used in the detection, type of quantum dots, sensitivity, technique of detection



**Fig. 25.14** Schematic diagram of the lateral flow immunoassay. (a) The QDs-based competitive reorganisation on the strip. (b) The real photos of lateral flow strip. As the T-line decreased, the sample is judged to be positive. Degrees of the fluorescence decrease indicated the level of TM. The strip is invalid in the absence of C-line. (Reprinted with permission from Wang et al. [55]. Copyright 2019: Elsevier)

(lateral flow test, optical or electrochemical), apart from its conventional and latest detection method in various types of samples. In this context, electrochemical technique shows potentially a powerful solution where the electrochemical setup can offer high sensitivity and high specificity, in conjunction with the portable reader and low power consumption of the setup; however, it is very sensitive to extreme environmental changes or interference of electroactive species. In addition, lateral flow test offers fast and low-cost analysis, qualitative or quantitative and simple procedure; however, its limitation is less sensitive, inaccurate sample volume reduces precision and requires good antibody preparation. The improvement of current approaches in combination with quantum dots-based materials will hopefully provide simple, sensitive, selective and rapid analysis for biosensing in real-world applications. The major route of health threat contaminants and their allied health hazards are described in Table 25.1.



**Fig. 25.15** Schematic diagram of the immunoassay-based sensor for the determination of adulteration of ewe/goat's cheese with cow's milk. (Reprinted with permission from Livas et al. [56]. Copyright 2021: Elsevier)

**Table 25.1** Major route of health threat contaminants and their allied health hazards

Major routes	Common contaminants	Health risks	References
Pathogenic bacteria	<i>Escherichia coli</i> O157:H7, <i>Staphylococcus aureus</i> , <i>Vibrio parahaemolyticus</i> and <i>Staphylococcal enterotoxin B</i>	Food poisoning	[26, 27]
Toxic materials	Mycotoxin	Carcinogenesis	[34, 35]
	Cyanide	Hypoxia and fatal	[36]
Environmental pollutants	Arsenite (As(III)) ions	Skin damage, circulation system problem and dead	[39]
	Ferric ion ( $Fe^{3+}$ )	Dysfunction of organs, hemochromatosis and Alzheimer's neurodegenerative diseases	[40]
Pesticide	Organophosphorous Pesticides	Mutagenicity, nervous system problems, carcinogenesis	[46]
	Cyfluthrin	Toxic effect on the respiratory, nervous, immune and reproductive system	[47]
	Deltamethrin	Neurotoxin	[49]
Allergens	Peanut allergen	Severe food-induced allergic reactions	[53]
	Arginine kinase	Severe food allergic reactions	[54]
	Crustacean major allergen tropomyosin	Adverse allergic reactions	[55]

## References

1. Chandan HR, Schiffman JD, Balakrishna RG. Quantum dots as fluorescent probes: synthesis, surface chemistry, energy transfer mechanisms, and applications. *Sensors Actuators B Chem.* 2018;258:1191–214.
2. Saha J, Datta Roy A, Dey D, Bhattacharjee D, Arshad Hussain S. Role of quantum dot in designing FRET based sensors. *Mater Today: Proc.* 2018;5:2306–13.
3. Reiss P, Protière M, Li L. Core/shell semiconductor nanocrystals. *Small.* 2009;5(2):154–68.
4. Vijayakumar V, Seshasayanan R. Optical characteristics of quantum dot transistor with front side illumination. *Mater Today: Proc.* 2015;2(9):4632–5.
5. Chen F, Gao W, Qiu X, Zhang H, Liu L, Liao P, et al. Graphene quantum dots in biomedical applications: recent advances and future challenges. *Front Lab Med.* 2018;1:192–9.
6. Bonilla JC, Bozkurt F, Ansari S, Sozer N, Kokini JL. Applications of quantum dots in food science and biology. *Trends Food Sci Technol.* 2016;53:75–89.
7. Ahmad Z, Najeeb MA, Shakoor RA, Al-Muhtaseb SA, Touati F. Limits and possible solutions in quantum dot organic solar cells. *Renew Sust Energ Rev.* 2018;82:1551–64.
8. Kong W, Yang X, Yang M, Zhou H, Ouyang Z, Zhao M. Photoluminescent nanosensors capped with quantum dots for high-throughput determination of trace contaminants: strategies for enhancing analytical performance. *Trends Anal Chem.* 2016;78:36–47.
9. Callan JF, Raymo FM. *Quantum Dot Sensors.* Danvers: Pan Stanford Publishing; 2013.
10. Yu X, Zhang C-X, Zhang L, Xue Y-R, Li H-W, Wu Y. The construction of a FRET assembly by using gold nanoclusters and carbon dots and their application as a ratiometric probe for cysteine detection. *Sensors Actuators B.* 2018;263:327–35.
11. Shangguan J, Huang J, He D, He X, Wang K, Ye R, Yang X, Qing T, Tang J. Highly Fe<sup>3+</sup>-selective fluorescent nanoprobe based on ultrabright N/P codoped carbon dots and its application in biological samples. *Anal Chem.* 2017;89(14):7477–84.
12. Sai-Anand G, Sivanesan A, Benzigar MR, Singh G, Gopalan AI, Baskar AV, et al. Recent progress on the sensing of pathogenic bacteria using advanced nanostructures. *Bull Chem Soc Jpn.* 2019;92(1):216–44.
13. Farzin MA, Abdoos H. A critical review on quantum dots: from synthesis toward applications in electrochemical biosensors for determination of disease-related biomolecules. *Talanta.* 2021;224:121828.
14. Zhu Y, Chao J, Zhu N, Zhang Q, Gyimah E, Yakubu S, et al. Ratiometric fluorescence immunoassay based on FAM-DNA-functionalized CdSe/ZnS QDs for the sensitive detection of tetrabromobisphenol A in foodstuff and the environment. *Anal Bioanal Chem.* 2020;412:3605–13.
15. Lesiak A, Drzozga K, Cabaj J, Bá Nski M, Malecha K, Podhorodecki A. Optical sensors based on II-VI quantum dots. *Nano.* 2019;9(192):1–24.
16. Jiao X, Zhou Y, Zhao D, Pang D, Wang C, Du H, Wen Y, Zhang X. An indirect ELISA-inspired dual-channel fluorescent immunoassay based on MPA-capped CdTe/ZnS QDs. *Anal Bioanal Chem.* 2019;411:5437–44.
17. Akinfiyeva O, Nabiev I, Sukhanova A. New directions in quantum dot-based cytometry detection of cancer serum markers and tumor cells. *Crit Rev Oncol Hematol.* 2013;86(1):1–14.
18. Kim J, Mohamed MAA, Zagorovsky K, Chan WCW. State of diagnosing infectious pathogens using colloidal nanomaterials. *Biomaterials.* 2017;146:97–114.
19. Ma F, Li CC, Zhang CY. Development of quantum dot-based biosensors: principles and applications. *J Mater Chem B.* 2018;6(39):6173–90.
20. Paniel N, Baudart J, Hayat A, Barthelmebs L. Aptasensor and genosensor methods for detection of microbes in real world samples. *Methods.* 2013;64(3):229–40.
21. Afendy M, Son R. Pre-enrichment effect on PCR detection of salmonella Enteritidis in artificially-contaminated raw chicken meat. *Int Food Res J.* 2015;22(6):2571–6.
22. Nakano M, Ding Z, Suehiro J. Comparison of sensitivity and quantitation between microbead dielectrophoresis-based DNA detection and real-time PCR. *Biosensors.* 2017;7(44):1–11.

23. Pang B, Zhao C, Li L, Song X, Xu K, Wang J, Liu Y, Fu K, Bao H, Song D, Meng X, Qu X, Zhang Z, Li J. Development of a low-cost paper-based ELISA method for rapid *Escherichia coli* O157:H7 detection. *Anal Biochem.* 2017;542:58–62.
24. Donmez S, Çağdaş L, Arslan H, Arslan F. Electrochemical nucleic acid hybridization biosensor based on poly(L-Aspartic acid)-modified electrode for the detection of short oligonucleotide sequences related to hepatitis C virus 1a. *Prep Biochem Biotechnol.* 2019;49(9):900–7.
25. Saleviter S, Wing Fen Y, Mohd Daniyal WMEM, Abdullah J, Sadrolhosseini AR, Sheh Omar NA. Design and analysis of surface plasmon resonance optical sensor for determining cobalt ion based on chitosan-graphene oxide decorated quantum dots-modified gold active layer. *Opt Express.* 2019;27(22):32294–307.
26. Wang D, Lian F, Yao S, Liu Y, Wang J, Song X, et al. Simultaneous detection of three food-borne pathogens based on immunomagnetic nanoparticles and fluorescent quantum dots. *ACS Omega.* 2020;5:23070–80.
27. Sharma A, Rao VK, Kamboj DV, Gaur R, Upadhyay S, Shaik M. Relative efficiency of zinc sulfide (ZnS) quantum dots (QDs) based electrochemical and fluorescence immunoassay for the detection of staphylococcal enterotoxin B (SEB). *Biotechnol Rep.* 2015;6:129–36.
28. Bui TD, Nguyen QL, Luong TB, Le VT, Doan VD. Utilization of Mn-doped ZnSe/ZnS core/shell quantum dots for rapid detection of *Escherichia coli* O157:H7 and methicillin-resistant *Staphylococcus aureus*. *Adv Mater Sci Eng.* 2020;9718706:10 p. <https://doi.org/10.1155/2020/9718706>.
29. Guo X, Wen F, Zheng N, Saive M, Fauconnier ML, Wang J. Aptamer-based biosensor for detection of mycotoxins. *Front Chem.* 2020;8:195.
30. Sokolovic M, Simpraga B. Survey of trichothecene mycotoxins in grains and animal feed in Croatia by thin layer chromatography. *Food Control.* 2006;17:733–40.
31. Abia WA, Warth B, Sulyok M, Krska R, Tchana AN, Njobeh PB, et al. Determination of multi-mycotoxin occurrence in cereals, nuts and their products in Cameroon by liquid chromatography tandem mass spectrometry (LC-MS/MS). *Food Control.* 2013;31:438–53.
32. Pietri A, Fortunati P, Mulazzi A, Bertuzzi T. Enzyme-assisted extraction for the HPLC determination of aflatoxin M 1 in cheese. *Food Chem.* 2016;192:235–41.
33. Beloglazova NV, Speranskaya ES, Wu A, Wang Z, Sanders M, Gofman VV, et al. Novel multiplex fluorescent immunoassays based on quantum dot nanolabels for mycotoxins determination. *Biosens Bioelectron.* 2014;62:59–65.
34. Gofman VV, Aubert T, Ginste V, Van Deun R, Beloglazova NV, Hens Z, et al. Synthesis, modification, bioconjugation of silica coated fluorescent quantum dots and their application for mycotoxin detection. *Biosens Bioelectron.* 2016;79:476–81.
35. Foubert A, Beloglazova NV, De Saeger S. Comparative study of colloidal gold and quantum dots as labels for multiplex screening tests for multi-mycotoxin detection. *Anal Chim Acta.* 2017;955:48–57.
36. Vahid B, Hassanzadeh J, Khodakarami B. CdSe quantum dots-sensitized chemiluminescence system and quenching effect of gold nanoclusters for cyanide detection. *Spectrochim Acta A Mol Biomol Spectrosc.* 2019;212:322–9.
37. Gaviria-Aroyave MI, Cano JB, Peñuela GA. Nanomaterial-based fluorescent biosensors for monitoring environmental pollutants: a critical review. *Talanta Open.* 2020;2:100006.
38. Wang X, Kong L, Zhou S, Ma C, Lin W, Sun X, et al. Development of QDs-based nanosensors for heavy metal detection: a review on transducer principles and in-situ detection. *Talanta.* 2022;239:122903.
39. Rahimi F, Anbia M, Farahi M. Aqueous synthesis of L-methionine capped PbS quantum dots for sensitive detection and quantification of arsenic (III). *J Photochem Photobiol A: Chem.* 2021;417:113361.
40. Srivastava RR, Singh VK, Srivastava A. Facile synthesis of highly fluorescent water-soluble SnS 2 QDs for effective detection of Fe<sup>3+</sup> and unveiling its fluorescence quenching mechanism. *Opt Mater.* 2020;109:110337.

41. Farina Y, Munawar N, Abdullah MP, Yaqoob M, Nabi A. Fate, distribution, and bioconcentration of pesticides impact on the organic farms of Cameron Highlands, Malaysia. *Environ Monit Assess.* 2018;190:386.
42. Chen H, Yin P, Wang Q, Jiang Y, Liu X. A modified QuEChERS sample preparation method for the analysis of 70 pesticide residues in tea using gas chromatography-tandem mass spectrometry. *Food Anal Methods.* 2014;7:1577–87.
43. Zhang H, Li Y, Zhu J, Li H, Li D, Liu Z, et al. Disposable pipette extraction (DPX) coupled with liquid chromatography-tandem mass spectrometry for the simultaneous determination of pesticide residues in wine samples. *Food Anal Methods.* 2019;12:2262–72.
44. Wei M, Yan X, Liu S, Liu Y. Preparation and evaluation of superparamagnetic core-shell dummy molecularly imprinted polymer for recognition and extraction of organophosphorus pesticide chemical routes to materials. *J Mater Sci.* 2018;53:4897–912.
45. Islam K, Chand R, Han D, Kim Y-S. Microchip capillary electrophoresis based electroanalysis of triazine herbicides. *Bull Environ Contam Toxicol.* 2015;94:41–5.
46. Tafreshi FA, Fatahi Z, Ghasemi SF, Taherian A, Esfandiari N. Ultrasensitive fluorescent detection of pesticides in real sample by using green carbon dots. *PLoS One.* 2020;15(3):1–17.
47. Xu J, Zhang R, Liu C, Sun A, Chen J, Zhang Z, et al. Highly selective electrochemiluminescence sensor based on molecularly imprinted-quantum dots for the sensitive detection of cyfluthrin. *Sensors.* 2020;20(3):1–15.
48. Tran TKC, Vu DC, Ung TDT, Nguyen HY, Nguyen NH, Dao TC, et al. Fabrication of fluorescence-based biosensors from functionalized CdSe and CdTe quantum dots for pesticide detection. *Adv Nat Sci Nanosci Nanotechnol.* 2012;3:035008.
49. Ge S, Zhang C, Yu F, Yan M, Yu J. Layer-by-layer self-assembly CdTe quantum dots and molecularly imprinted polymers modified chemiluminescence sensor for deltamethrin detection. *Sensors Actuators B Chem.* 2011;156(1):222–7.
50. Neethirajan S, Weng X, Tah A, Cordero JO, Ragavan KV. Nano-biosensor platforms for detecting food allergens – new trends. *Sens Bio-Sens Res.* 2018;18:13–30.
51. Ciardiello MA, Tamburrini M, Liso M, Crescenzo R, Rafeaianni C, Mari A. Food allergen profiling: a big challenge. *Food Res Int.* 2013;54:1033–41.
52. Hideshima S, Saito M, Fujita K, Harada Y, Tsuna M, Sekiguchi S, et al. Label-free detection of allergens in food via surfactant-induced signal amplification using a field effect transistor-based biosensor. *Sensors Actuators B.* 2018;254:1011–6.
53. Weng X, Neethirajan S. A microfluidic biosensor using graphene oxide and aptamer-functionalized quantum dots for peanut allergen detection. *Biosens Bioelectron.* 2016;85:649–56.
54. Wang Y, Ma J, Li H, Zhou J, Zhang H, Fu L. A sensitive immunosensor based on FRET between gold nanoparticles and InP/ZnS quantum dots for arginine kinase detection. *Food Chem.* 2021;354:129536.
55. Wang Y, Li Z, Lin H, Siddanakoppalu PN, Zhou J, Chen G, Yu Z. Quantum-dot-based lateral flow immunoassay for the rapid detection of crustacean major allergen tropomyosin. *Food Control.* 2019;106:106714.
56. Livas D, Trachioti M, Banou S, Angelopoulou M, Economou A, Prodromidis M, Petrou P, Kakabakos S, Kokkinos C. 3D printed microcell featuring a disposable nanocomposite Sb/Sn immunosensor for quantum dot-based electrochemical determination of adulteration of ewe/goat's cheese with cow's milk. *Sensors Actuators B.* 2021;334:129614.

# Chapter 26

## Application of II–VI Semiconductor-Based Biosensors in Nanomedicine and Bioanalysis



Bruno Gabriel Lucca and Jacqueline Marques Petroni

### 26.1 Introduction

Inorganic semiconductor crystals, also called quantum dots (QDs) are a class of nanoparticles with spherical or quasi-spherical shape and size ranging between 2 and 20 nm that has gained great interest in recent years. It may be attributed to their unique photophysical features, which include a wide absorption spectrum, narrow and tunable emission profile, long fluorescence life and photo-stability. These interesting electronic properties are attributed to the confinement of excited electrons that are bound to the existing interstices in the valence band. The quantum effect occurs when the size of these nanoparticles gets close to the dimension of excited electron. As the size of QDs decreases, the effective bandgap increases. It generates attractive optical and spectroscopic features that depend on the nanocrystal size [1]. The excellent optical properties of QDs have been widely used in biomedicine and bioanalysis. Moreover, the good biocompatibility makes semiconductor QDs a very promising material for use in medical applications. QDs are also utilised in therapy, diagnostics and various sensing platforms [2]. So, this chapter will cover some applications of QDs in nanomedicine and biosensing. The focus will be on semiconductor QDs classified as group II–VI (CdS, CdSe, CdTe, ZnO, ZnS, ZnSe and ZnTe). The main idea is to introduce the reader to current trends in the use of QDs for medical procedures and bioanalytical sensing.

---

B. G. Lucca (✉) · J. M. Petroni  
Federal University of Mato Grosso do Sul, Campo Grande, MS, Brazil  
e-mail: [bruno.lucca@ufms.br](mailto:bruno.lucca@ufms.br)

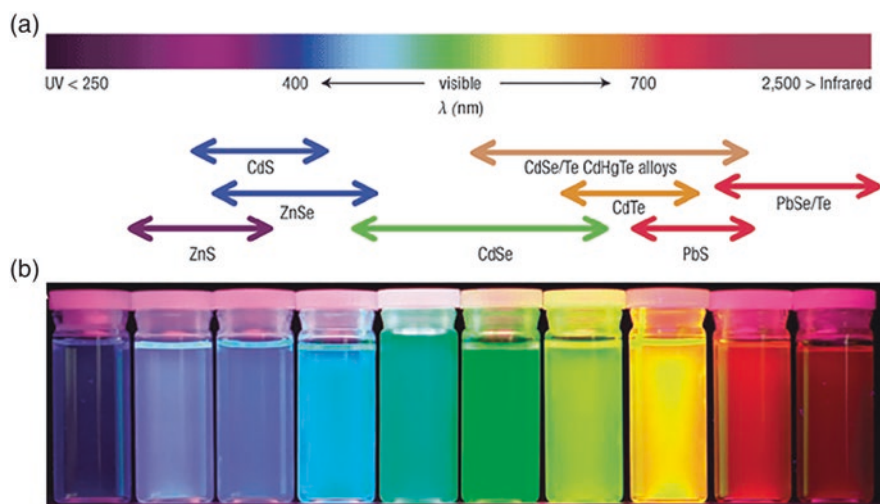
© The Author(s), under exclusive license to Springer Nature  
Switzerland AG 2023

G. Korotcenkov (ed.), *Handbook of II-VI Semiconductor-Based Sensors and Radiation Detectors*, [https://doi.org/10.1007/978-3-031-24000-3\\_26](https://doi.org/10.1007/978-3-031-24000-3_26)



### 26.1.1 Groups II–VI Quantum Dots

The first studies regarding QDs utilised compounds from groups II to VI, due to the fact that synthesis of metal-based sulphides is not difficult and the necessary precursors are easily acquired. Up to now, CdX compounds (where X is Se, S or Te) are the most explored quantum dots. In a pioneering work from 1981, Kalyanasundaram and collaborators first synthesized colloidal CdS in an aqueous media. A very interesting finding made by them was that, as the dimension of the CdS particles become smaller, the photoactivity becomes more intense [3]. Posteriorly, in 1983, Rossetti and collaborators studied the effect of QDs size in the emission bands, which expanded the scope for utilisation of QDs [4]. Currently, QDs of groups II–VI are one of the most developed and most explored in several areas, including medical applications. However, the presence of heavy metal cadmium in groups II–VI is a drawback aiming for applications in medicine. Fortunately, the element zinc is also a member of same group and has features and structures close to cadmium. This way, zinc has been an interesting alternative to overcome the limitation of use due to the toxic nature of cadmium. Furthermore, the tunable emission spectrum of semiconductor QDs, which ranges from ultraviolet (UV) until the near-infrared (NIR), can be adjusted to suit the desired application. Figure 26.1 demonstrates the emission range covered by some semiconductor QDs of groups II–VI.



**Fig. 26.1** Wavelength range covered by the emission band of some semiconductor QDs (a) and fluorescence colours obtained from CdSe QDs under different wavelengths (b). (Reprinted with permission from Bian et al. [5]. Copyright 2019: John Wiley and Sons)

## 26.2 QDs in Nanomedical and Bioanalytical Applications

Since the development and synthesis of QDs achieved a mature stage, researchers directed their work to applications involving these particles. Due to biocompatibility, one of the areas where QDs are most explored is within medical research [6]. However, biological applications require the modification of QDs surface. It can be achieved using a wide variety of binders. These ligands play a crucial role in regulating compatibility, bioconjugation and water dispersibility between QDs and biological media. Some requirements for ideally biocompatible QDs are to form stable colloids in aqueous media, present salt and pH stability, demonstrate high target selectivity for specific biological agents, exhibit high photoluminescent effect and have minimal size [7]. The most explored procedures for modification of QDs are silanisation [8], encapsulating using amphiphilic ligands [9], ligand exchange [10] and coating with phospholipid micelles [11]. In the next topics, some QDs-based approaches applied in nanomedicine and bioanalysis will be discussed. They will be focused on biosensing probing, drug delivery, therapy approaches and applications in electrochemical/photo-electrochemical/optical detection.

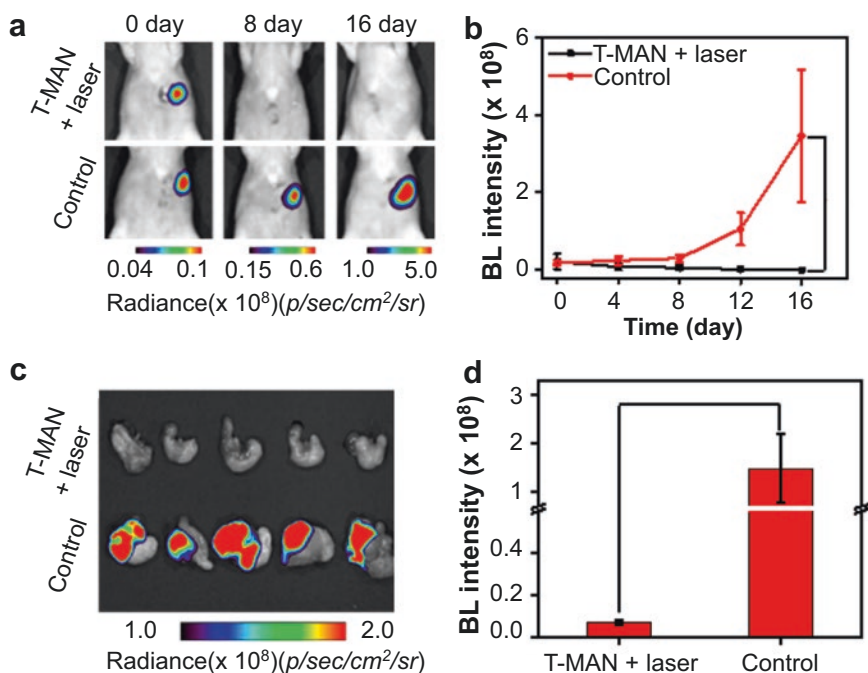
### 26.2.1 QDs-Based Therapy and Drug Delivery Approaches

In the last decade, the exploration of QDs in medical approaches such as diagnostics and drug delivery has also shown promising application potential. The electronic and tunable properties of semiconductor QDs make them more interesting to such applications in comparison with organic fluorophores. Thus, the possible uses of semiconductor QDs as therapeutic agents have drawn the attention of several researchers. The most explored application of QDs in medical therapy aims to treat cancer, which is one of the deadliest diseases of modern times [12, 13]. The successful detection and imaging of cancer are fundamental to track the tumour, defining the best therapeutic options and monitoring the treatment evolution [14].

In this context, Lefojane and colleagues recently demonstrated the cytotoxic properties of CdO QDs, which were synthesized via a green chemical pathway, against some breast cancer cell lines. An important advantage of cadmium oxide is that it has lower toxicity compared to semiconductor nanoparticles and is not harmful to human cells [15]. Jing et al. [16] evaluated the cytosolic delivery of CdSe/CdZnS QDs in lymphocyte cells. The biocompatibility of QDs was improved by coating them with a cell-penetrating peptide that consisted of an Asp-Ser-Ser (DSS) repeated sequence. In comparison with control QDs, the DSS-coated QDs presented higher mobilities and a greater propensity to remain in the monomeric state, showing great potential for *in vivo* drug delivery and gene therapy. Mansur and collaborators synthesized new inorganic–organic hybrids CuS-based QDs using a green aqueous procedure and carboxymethylcellulose (CMC) as a capping ligand. They explored the feasibility of these novel nanocrystals in nanotheranostics for the first

time. The nanostructures were functionalised with folic acid and complexed with anti-cancer drugs aiming for effective targeting in cancer cells. The approach was successfully utilised to kill breast cancer cells *in vitro* [17].

In another work, Shi et al. [18] reported a novel magnetic CuS QDs doped with gadolinium. This semiconductor nanoparticle was engineered in a tumour-targeting/matrix metalloproteinase-2 (MMP-2) activatable nanoprobes (called as T-MAN) by covalent modification and explored for treatment of gastric cancer by near-infrared photothermal therapy. The T-MAN particles presented good photothermal conversion efficiency (ca. 70%) and showed effectiveness on the production of heat aiming killing tumour cells in living mice. As shown in Fig. 26.2, the results suggested that stomach tumours were successfully removed from mice after 16 days of photothermal treatment, whereas tumours continued to grow in untreated mice, utilised as control. Tsolkile and colleagues [19] investigated the feasibility of glutathione-capped core/shell CuInS/ZnS QDs conjugated to 5,10,15,20-tetrakis(3-hydroxyphenyl)porphyrin for therapy approaches. These conjugated QDs presented higher cytotoxicity regarding human leukaemia cells (death rate > 60%) in comparison with the bare QDs, besides improved cell uptake.



**Fig. 26.2** Bioluminescence images (a) and mean bioluminescence magnitude (b) of gastric tumours obtained from non-treated (Control) and treated with T-MAN and laser live mice; Ex vivo bioluminescent images (c) and bioluminescent intensities (d) of gastric tumours obtained from mice which were non-treated (control) and treated with T-MAN and laser for 16 days. (Reprinted with permission from Shi et al. [18]. Copyright 2019: American Chemical Society)

Nanomaterials also benefit therapeutic activities such as drug delivery. As nanomaterials can accumulate at the diseased sites in higher concentrations than conventional drugs, systemic toxicity is reduced and target delivery is optimised. Cai and colleagues developed a drug delivery platform based on pH-responsive ZnO QDs. These QDs-based nanocarriers were utilised to carry out the controlled release of doxorubicin (DOX) molecules into lung cancer cells. The ZnO QDs were protected with dicarboxyl-terminated poly(ethylene glycol) (PEG), which yielded good stability at physiological pH conditions. The specific binding of QDs to the glycoprotein CD44 in cancer cells was achieved by conjugation of hyaluronic acid (HA), which acted as targeting ligand. Results showed concentration-dependent and time-dependent cytotoxicity, indicating a consistent and controllable drug delivery activity for the HA-ZnO-DOX system [20]. Yang et al. [21] reported a simple and environmentally friendly method for the synthesis of ZnS-coated quercetin/CdSe QDs (QCZ-QDs). Quercetin has known properties against inflammation, bacteria and cancer, in addition, to be an efficient anti-ageing agent. The results of in vitro experiments showed that QCZ-QDs presented higher antibacterial activity against *Escherichia coli* and *B. subtilis* in comparison with sole quercetin or CdSe nanoparticles. The QCZ-QDs also showed increased anticancer activity compared to raw quercetin and CdSe nanoparticles, demonstrating promising application potential.

Application of QDs in theragnostic approaches has also been explored. Theragnostic requires the utilisation of two agents, one for therapy and another for diagnosis. The use of theragnostic may be a better way to monitor the effectiveness of treatment response, expediting therapeutic decisions and improving the life quality of patients. Within this topic, Olerile et al. demonstrated the potential of co-loaded NLC (nanostructured lipid carriers) as a multifunctional drug delivery system for cancer theragnostic. The NLC consisted of CdTe/CdS/ZnS QDs and paclitaxel (PTX), which is one of the most effective anticancer drugs known. This co-loaded NLC was obtained by emulsion-evaporation and low temperature-solidification methods. Results showed that the co-loaded NLC inhibited the growth of cancer tumours in 78%. In addition, imaging obtained through in vivo and ex vivo experiments suggested that the NLC targeted and detected the cancer tumours with good selectivity, demonstrating the great performance of this parenteral drug delivery system aiming at cancer theragnostic [22]. Lv and colleagues [23] explored the use of CuInS/ZnS (ZCIS) QDs as an ‘all-in-one’ theragnostic platform with imaging and therapeutic potential. The QDs were employed for multispectral optical tomography (MSOT) imaging and synergistic photodynamic/photothermal therapy (PDT/PTT). The in vivo imaging of tumour sites could be successfully performed. In addition, ZCIS QDs also showed effective photothermal and photodynamic capabilities, resulting in satisfactory therapy effectiveness against cancer tumours (tumour regression was observed after 12 days of treatment). Other promising and exciting applications of semiconductor QDs in bio-applications and therapeutic approaches have been reported [24–28].

## 26.2.2 QDs in Biosensing

The development and improvement of analytical methods for detection of biological species is a frequent demand and have attracted the interest of many researchers. It led to extraordinary progress in the field of biosensing. A biosensor can be defined as an integrated analytical sensor able to give quantitative information based on the interaction of a biological receptor that is coupled to an electronic transduction device. Biosensors are classified as biocatalytic or affinity-based, depending on how biorecognition occurs. Biocatalytic biosensors often utilise immobilised enzymes to identify a particular substrate, while affinity-based biosensors contain species that are selective and only capture the target analyte, such as antibodies [29, 30].

Nanocrystals such as semiconductor QDs are great options for use in biosensors as they can enhance analytical performance regarding selectivity and sensitivity. Going further, nanotechnology has also provided custom analytical devices which are defined as nanosensors [31, 32]. Some of these approaches will be discussed below.

### 26.2.2.1 Electrochemical Applications of QDs in Bioanalysis

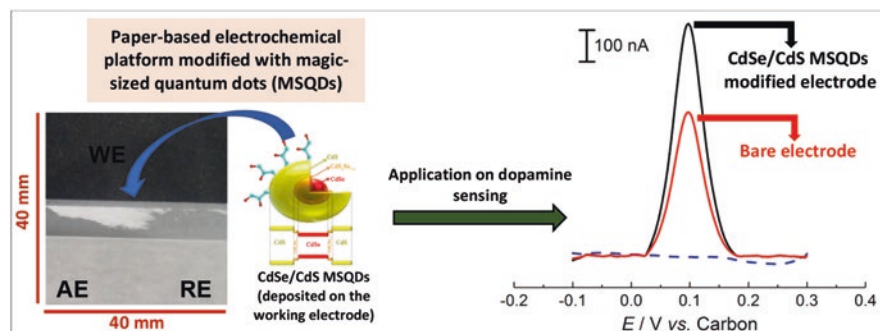
The use of semiconductor QDs in electrochemical sensing can enhance the analytical performance and favour the electron transfer process. It may be attributed to the good electrocatalytic activity and high area-to-volume ratio of such nanoparticles, which significantly increases the electroactive area of the sensors, resulting in higher peak currents. Moreover, QDs have also been explored as signal markers in development of highly sensitive electrochemical biosensors [33, 34].

Recently, Karaman and collaborators [35] reported an electrochemical immunosensor for detection of heart-type fatty acid-binding protein (h-FABP), which is a biomarker used in the diagnosis of acute myocardial infarction (AMI). The sensor consisted of a glassy carbon electrode modified with  $\text{Cd}_{0.5}\text{Zn}_{0.5}\text{S}$  QDs, which were utilised to conjugate the second antibody via  $\pi$ - $\pi$  and electrostatic interactions. This sensor showed improved analytical performance. It was attributed to the synergistic effect of  $\text{Cd}_{0.5}\text{Zn}_{0.5}\text{S}$ , which aided the electron transfer process and amplified the analytical signal. A low limit of detection (3.30 fg/mL) was achieved with this modified sensor. In another novel work, Moazampour and colleagues proposed a label-free electrochemical sensor for detection of microRNA-200a (miR-200), which is an important biomarker in the diagnosis of ovarian cancer. This genosensor consisted of a glassy carbon electrode modified with ZnS QDs functionalised with L-cysteine. These functionalised QDs were attached to the electrode surface by electrodeposition. This modified electrodic surface showed itself as an appropriate substrate for the coupling of  $\text{NH}_2$ -probe (ssDNA) used for measurement. The amino groups present in the ssDNA showed strong interaction with the carboxylic groups present in the L-cysteine-ZnS-QDs, favouring probe capture and increasing the number of active sites. After optimising all conditions, this sensor exhibited

excellent sensitivity (the limit of detection achieved was 8.4 fM) and allowed the quantification of miR-200 in human blood plasma samples without amplification procedures [36].

De França et al. [37] explored, for the first time, the application of magic-sized quantum dots (MSQDs) for modification of electrochemical sensors. The MSQDs are a class of nanocrystals that show smaller particle size, wider spectra and greater stability in comparison with conventional QDs. Among other applications, the MSQDs are a very promising nanomaterial for use in electrochemical sensing. In this pioneering work, a simple and inexpensive paper electrochemical device (PED) was proposed. The carbon-based working electrode was modified with core-shell CdSe/CdS MSQDs, which were synthesized according to the method described by Silva et al. [38–40]. To demonstrate the analytical feasibility, this modified PED was applied for clinical quantification of dopamine in biological samples, as represented in Fig. 26.3. Dopamine is an important biomarker, whose lack is associated with progressive neurodegenerative disorders such as Parkinson's disease. This modified PED presented improved analytical signal (ca. 46% higher), lower charge transfer resistance (32 vs. 169  $\Omega$ ) and larger superficial area (0.28 vs. 0.14 cm<sup>2</sup>) in comparison with the bare PED. It can be attributed to the presence of CdSe/CdS nanocrystals in the sensor, which favoured the electron transfer. The electroanalysis of dopamine in real human blood serum samples was successfully carried out and the limit of detection obtained (96 nM) was lower than other recent reports that utilise more complex electrochemical platforms for detecting the same analyte.

Xu and colleagues [41] proposed a novel electroanalytical method for detection of interleukin-8 (IL-8). This compound is a pro-inflammatory cytokine considered an important biomarker for oral cancer diagnosis. The proposed approach consists of treating IL-8 with a reducing agent in order to generate thiol groups. These thiol groups react with maleimide groups from maleimide-modified DNA-templated CdTe/CdS QDs (DNA-QDs), which were utilised as electrochemical reporters. Measurements were carried out using a mercury film-modified glassy carbon



**Fig. 26.3** Picture of the paper electrochemical device containing the pencil-drawn carbon electrodes used in the work, representation of modification of the working electrode with CdSe/CdS MSQDs and voltammetric response of dopamine regarding the bare and modified electrodes. (Reprinted with permission from De França et al. [37]. Copyright 2020: Elsevier)

electrode. This method enabled the quantification of IL-8 at extremely low levels, reaching a limit of detection of 3.4 fg/mL. The feasibility of the method for biomedical applications was investigated by analysing human serum samples spiked with IL-8. Recovery rates ranged between 97% and 104%, suggesting great potential for use in diagnosing oral cancer. In another approach focused on cancer diagnosis, Freitas et al. reported the development of a simple disposable electrochemical immunosensor for measurement of the ExtraCellular Domain of the Human Epidermal growth factor Receptor 2 (HER2-ECD), which is a biomarker for breast cancer. Core/shell CdSe@ZnS QDs were utilised as an electroactive label, while screen-printed carbon electrodes were employed as transducer. This biosensor showed excellent sensitivity for HER2-ECD detection, providing a limit of detection of 2 ng/mL. The biomedical applicability of this sensor was successfully tested by performing recovery studies in spiked human serum samples, with satisfactory precision and accuracy [42]. Beyond these few examples, many other applications of QDs in electrochemical biosensing are available in literature [43–47].

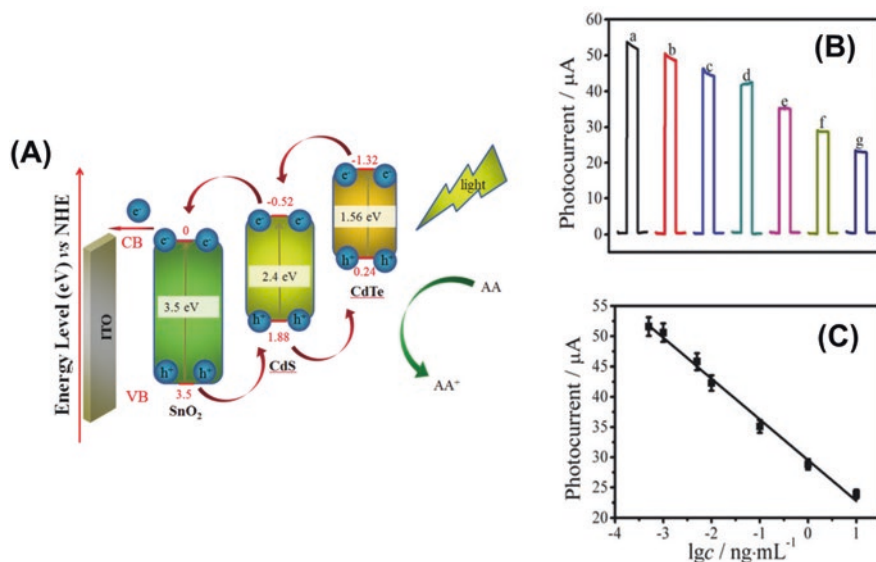
#### 26.2.2.2 Photo-Electrochemical Applications of QDs in Biosensing

Photo-electrochemical (PEC) detection has attracted the attention of many researchers in the last few years. Basically, PEC consists of the excitation of a semiconductor material by an excitation source (light), which generates a photocurrent as readout signal. PEC is an analytical technique that has grown and developed quickly, exhibiting advantages such as high sensitivities, easiness of operation and low noise levels [48, 49]. In recent years, PEC has also been utilised in biosensing approaches by combination with recognition species such as antibodies, proteins and enzymes. However, the most commonly utilised photoactive agents have as disadvantages a low photo-conversion efficiency and vulnerability in relation to photobleaching [50]. Regarding these drawbacks, nanostructured materials, such as QDs, have been frequently explored to improve the performance of PEC-based sensors, as will be demonstrated in the sequence.

In a recent work, Cai et al. [51] described the development of a biosensor aiming for photoelectrochemical measurement of human immunodeficiency virus (HIV). This sensor utilised CdSe QDs, which were linked with amino-modified DNA1 or DNA2 to generate CdSe QDs-DNA nanonetwork. This CdSe-based nanonetwork was then dropped onto an ITO glass electrode containing a mesoporous SnO<sub>2</sub> nanoflower film to form a heterojunction. The PEC sensor presented an excellent performance in detecting HIV, with a very low limit of detection (1.38 fM). Moreover, the analysis of human serum samples provided recoveries between 92% and 103%, suggesting great potential for practical biomedical applications. In another fresh paper, Gao and collaborators [52] developed a PEC sensor for biosensing of human haemoglobin. This biosensor was based on CdS QDs and TiO<sub>2</sub> nanorod arrays, which were used to form a heterojunction and improve the charge-transfer efficiency regarding visible light, resulting in increased photo-currents. The selectivity of this PEC sensor was achieved with the use of a molecularly imprinted polymer

(MIP) film deposited over the sensor. This MIP layer has the function of specifically binding to human haemoglobin. Haemoglobin captured by the sensor served to catalyse the oxidation of 4-chloro-1-naphthol by  $\text{H}_2\text{O}_2$ , forming an insoluble product on the surface of the PEC sensor and decreasing the analytical signal (photocurrent). This PEC sensor provided a limit of detection of  $0.53 \text{ pg/mL}$  and showed good applicability for the analysis of spiked urine samples simulating haemoglobinuria. The recoveries rates ranged from 97% to 101%.

Zhang and colleagues, in another interesting work [53], proposed a label-free PEC immunosensor for detection of amyloid  $\beta$ -protein ( $\text{A}\beta$ ). This protein is seen as an important biomarker for diagnosis of Alzheimer's disease, as its monitoring can prognosticate possible neurodegeneration and cognitive decay. The construction of the immunosensor was carried out by dropping an aqueous suspension of  $\text{SnO}_2$  nanoflowers on an ITO electrode. This substrate was then coated with CdTe QDs and, after this, CdS QDs were deposited by ionic layer adsorption. This  $\text{SnO}_2/\text{CdTe}/\text{CdS}$  sandwich showed high photocurrent magnitude and served as substrate for the immobilisation of  $\text{A}\beta$  antibody species. The detection of  $\text{A}\beta$  was successfully carried out, as presented in Fig. 26.4, with an excellent limit of detection ( $0.18 \text{ pg/mL}$ ). Studies performed in spiked human serum samples showed recoveries between 99% and 106%, indicating great accuracy. Moreover, great concordance was reached during validation, which was carried out by comparing the results with commercial enzyme-linked immunosorbent assay (ELISA) method. In addition to the works



**Fig. 26.4** Assembling scheme of PEC immunosensor for detection of  $\text{A}\beta$ -protein (a); photocurrent responses for different concentrations of  $\text{A}\beta$ -protein (b); logarithmic calibration curve obtained (c). (Reprinted with permission from Zhang et al. [53]. Copyright 2020: Royal Society of Chemistry)

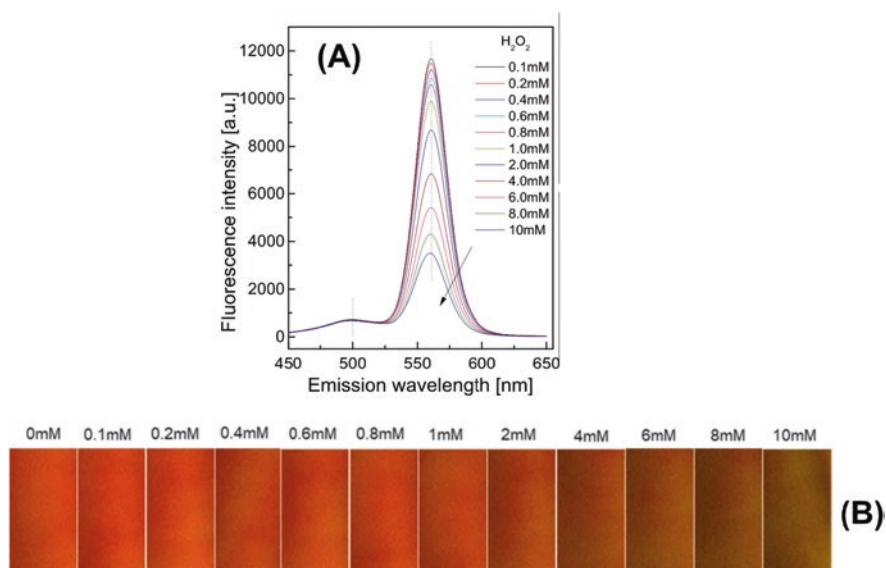


mentioned here, other researchers have contributed to the development of approaches involving the use of semiconductor QDs in PEC biosensing [54–58].

### 26.2.2.3 Applications of QDs in Optical Biosensing

The already mentioned exciting optical properties of quantum dots also make them very attractive options for use in optical detection. The coupling of quantum dots with biological species allows the conversion of the biological response in an optical response, which can be measured by the read-out platform. Moreover, the biocompatibility and low toxicity of QDs make them very suitable for biosensing applications involving optical methods [59, 60].

Recently, Duong and collaborators showed the synthesis of carboxyl group functionalised-CdSe/ZnS QDs and aminofluorescein (AF)-encapsulated polymer particles for application in a sensing membrane aiming  $\text{H}_2\text{O}_2$  detection. Horseradish peroxidase (HRP) enzyme was immobilised on the QDs-AF membrane surface to increase the sensitivity. The redox reaction of  $\text{H}_2\text{O}_2$  led to the fluorescence quenching of CdSe/ZnS QDs, while AF was employed as a reference dye. It was observed a correlation between the ratiometric fluorescence intensity of CdSe/ZnS-AF and  $\text{H}_2\text{O}_2$  concentration. Using this membrane, a linear concentration range between 0.1 and 10 mM and a limit of detection of 0.016 mM were observed for  $\text{H}_2\text{O}_2$ , as shown in Fig. 26.5. The HRP-QDs-AF membrane was successfully employed for



**Fig. 26.5** Emission spectra of CdSe/ZnS-AF membrane for different concentrations of  $\text{H}_2\text{O}_2$  (a); Fluorescence quenching of the sensing membrane after exposition to increasing  $\text{H}_2\text{O}_2$  concentrations (b). (Reprinted from Duong and Rhee [61]. Published 2019 by MDPI as open access)

quantification of  $\text{H}_2\text{O}_2$  in wastewater [61]. Ripoll et al. [62] reported the use of CdSe/ZnS QDs modified with aminophenylboronic acid (APBA) for glucose sensing. The incorporation of APBA on the surface of QDs results in the quenching of photoluminescence. After glucose binding to APBA, the photoluminescence was restored. This nanosensor provided a linear response for glucose in the range of 0.5 to 50 mM and a limit of detection equal to 0.1 mM. As proof of concept, glucose levels in MDA-MB-231 live cells were successfully monitored using the QDs-APBA nanosensor, demonstrating great potential for intracellular sensing.

In another work, Rahman and colleagues [63] have described the use of core-shell CdSe/ZnS QDs for sensitive glucose detection in aqueous samples. The synthesis of CdSe QDs was performed by a hot injection technique. In addition, the formation of ZnS was carried out via a process called SILAR (successive ionic layer adsorption and reaction). The average size of the prepared QDs was in the range of 10–12 nm. Aiming to achieve water-soluble nanoparticles, the core-shell QDs were modified with thio-glycolic acid (TGA). These CdSe/ZnS QDs capped with TGA presented fluorescence emission similar to that observed for the pure QDs. The maximum emission was observed at 620 nm. The CdSe/ZnS/TGA QDs were treated with glucose oxidase (GOx) and horseradish peroxidase (HRP) enzymes aiming for the analysis of glucose. The detection of glucose was based on the fluorescence quenching effect of the QDs, which is linked to the chemical reactions between the conjugated enzymes and analyte. The fluorescence intensity of GOx:HRP/CdSe/ZnS-TGA QDs showed good correlation with glucose concentration in the range from 0 to 10 mM. In addition, the limit of detection obtained was 0.045 mM. Besides the reports shown here, other approaches demonstrating the use of QDs in optical sensing are described in literature [64–66].

#### 26.2.2.4 Detection of Other Specific Targets

Besides their promising applications in electrochemical, photo-electrochemical and optical sensing, QDs have also been utilised for the biosensing of multiple other specific biomarkers and compounds of clinical and diagnostic interest, such as metallic ions, cells and viruses. Biosensors based on NIR QDs have been largely explored for such applications due to features such as deep penetration into biometrics, minimal photodamage and reduced fluorescence background. Wang et al., for example, developed a NIR aptasensor for thrombin turn-on determination based on electrochemiluminescence resonance energy transfer (ECL-RET) of CdTe/CdS core small/shell thick QDs to gold nanorods (AuNRs). This sensor presented a lower background interference and diminished photochemical degradation from NIR, in addition to an extremely low limit of detection equal to 31 aM (based on a signal/noise ratio = 3). The aptasensor could be successfully applied to thrombin sensing in real serum samples [67]. Tao and colleagues produced NIR-emitting CdTe/CdS QDs in an aqueous solution using 3-mercaptopropionic acid (MPA) as a stabiliser. These NIR-QDs were applied as a highly sensitive and fast-responsive sensors for  $\text{Cu}^{2+}$  detection through in vitro and in vivo fluorescent imaging. The

aggregation of NIR-QDs caused by the competitive interaction between MPA and the  $\text{Cu}^{2+}$  present in the solution resulted in the quenching of NIR light. This approach provided a low limit of detection (50 nM) and a wide linear range (from 100 nM to 50  $\mu\text{M}$ ). The monitoring of  $\text{Cu}^{2+}$  concentration in living cells was successfully performed, demonstrating the remarkable potential of this NIR nanosensor [68].

In another work, Gui and collaborators [69] developed a NIR-emitting CdTe/CdS core/shell QDs-based photoluminescence (PL) sensor aiming the selective and sensitive detection of  $\text{Cd}^{2+}$ . This sensor worked on the basis of an interesting PL 'OFF-ON' mode. First, adding ammonium pyrrolidinedithiocarbamate (APDC) to QDs caused pronounced PL quenching, which was attributed to the APDC partial breakage of surface Cd-thiol layers and formation of Cd-APDC complex over QDs. Then, as the  $\text{Cd}^{2+}$  concentration increased, the PL of APDC surface-modified QDs (QDs-APDC) was gradually reestablished. This effect can be explained by the occurrence of Cd-thiol passivation layers again on the QDs surface. This biosensor showed linear dependence on  $\text{Cd}^{2+}$  concentration range from 0.1 to 2  $\mu\text{M}$  with a limit of detection of 6 nM. The sensor also provided high selectivity against other cations present in biological fluids, such as  $\text{Mg}^{2+}$ ,  $\text{Zn}^{2+}$ ,  $\text{Na}^+$  and  $\text{Na}^+$ . As proof of concept, the QD-based biosensor was successfully utilised for determination of  $\text{Cd}^{2+}$  in liposome solutions, showing good concordance with the results found by ICP-AES and demonstrating promising potential for medical applications.

Wang and colleagues [70] synthesized N-acetyl-L-cysteine (NAC) capped CdTe/CdS@ZnS-SiO<sub>2</sub> NIR-emitting QDs with high luminescence, good stability and low toxicity via aqueous solution using a microwave irradiation reduction route for the first time. For this, thiol-capped CdTe/CdS QDs were employed as core templates and ZnCl<sub>2</sub>, NAC and tetraethyl orthosilicate were utilised as shell precursors. In comparison with the original CdTe/CdS QDs, these CdTe/CdS@ZnS-SiO<sub>2</sub> QDs presented improved properties such as enhanced stability, higher brightness, stronger NIR emission and lower cytotoxicity, which is especially interesting in aiming sensing applications in biological systems. Such novel QDs were utilised as a novel sensing probe for detection of  $\text{Hg}^{2+}$ . It was observed that the presence of  $\text{Hg}^{2+}$  ions led to a quench in the fluorescence of QDs. Under the best conditions, the QDs fluorescence decreased linearly with  $\text{Hg}^{2+}$  concentration in the range of 5 nM to 1  $\mu\text{M}$ . The limit of detection obtained was 1 nM (based on a signal/noise ratio of 3). As demonstration, this novel NIR-QDs sensor was successfully applied for monitoring the levels of  $\text{Hg}^{2+}$  in living cells, presenting satisfactory results. In another interesting work, Nguyen et al. reported the specific biosensing of H5N1 influenza virus using CdTe QDs. The biosensor utilised was based on luminescent CdTe/CdS QDs, chromatophores obtained from *Rhodospirillum rubrum* bacteria and the antibody of  $\beta$ -subunit. This core was attached to the biosensor through biotin-streptavidin-biotin bridge and linked to the H5N1 antibody, enabling the detection of the virus by change in photoluminescence response promoted by the interaction between antigen and antibody. This biosensor presented a linear dependence between photoluminescence response and H5N1 concentration in the range of 3 to 50 ng/L. The limit of detection achieved was 3 ng/L [71]. Yao and collaborators [72] studied the application of highly luminescent CdTe quantum dots synthesized in

aqueous media through an eco-friendly method. These QDs were applied on the biosensing of hemin, which is an iron-based complex considered as an essential regulator of gene expression and growth promoter of hematopoietic progenitor cells. In a slightly basic media, it was observed that hemin has the ability to quench the fluorescence of CdTe QDs. This quenching was proportional to the hemin concentration in the range of 0.2–20  $\mu\text{M}$ . The limit of detection obtained was 80 nM. There was no shift in the fluorescence emission spectra when the hemin concentration changed, suggesting that CdTe QDs do not congregate in the presence of quencher. It is known that electron and hole recombination is responsible for causing QDs to fluoresce. Hemin, acting as a fluorescence quencher, contributes with one electron to the QDs, occupying the hole and causing the radioactive recombination process that results in quenched fluorescence.

Apart from these reports, QDs have been used for the biosensing of many other compounds. Considering all approaches described in this section, it's clear that the detection of biomolecules is a vast field that has been attracting the attention of many researchers. In addition to the numerous direct measurements that have already been carried out, a number of indirect measurements, such as reaction byproducts or the use of intercalating molecules, have already been used as tactics to avoid the often difficult-to-implement direct measurement procedures. Overall, this has resulted in a wide range of biomolecules that can now be identified using QDs-based biosensors, a study field that is constantly expanding. Table 26.1 summarises some other approaches based on groups II–VI QDs that have been used for the sensing of important biological species. Different detection techniques are utilised. The performances of these systems in terms of linear range and limits of detection can be compared with each other.

### 26.3 Conclusions and Perspectives

The main objective of this chapter was to give to the reader an overview of some applications of group II–VI semiconductor QDs in medical and bioanalytical applications. For this, the use of QDs in the biosensing of several important species was shown. In addition, the use of II–VI QDs in drug delivery, diagnosis and therapy, as well as in electrochemical, photoelectrochemical and optical biosensing, was presented and discussed. These few examples demonstrate the enormous potential of QDs in nanomedicine and bioanalysis. QDs can improve the selectivity, sensitivity and efficiency of medical procedures, improving the patients' quality of life and facilitating therapeutic decision-making. Although the use of QDs in these areas is in an advanced stage, it is clear that there are still challenges to increasing the number of research focused on this area. The main difficulties of researchers around the world are related to the synthesis of QDs, which in most cases is laborious and time-consuming, and to the procedures for assembling QDs-based biosensors, which often require many hard-working steps. Thus, the development of simpler and faster strategies to produce QDs, as well as ready-to-use sensors, can boost research

**Table 26.1** Some biosensing approaches based on groups II–VI QDs utilised for detection of various species. The order of appearance is categorised by the type of analyte, going from ions and simple molecules to macromolecules, viruses and cells

Analyte and (samples)	Nanomaterial used	Detection mode	Linear range	Limit of detection	Reference (Year)
Hg <sup>2+</sup> (environmental samples)	CdSe/ CdScore shell QDs	ECL	1 pM to 1 μM	0.1 pM	[73]
Pb <sup>2+</sup> (environmental samples)	CdSe/ CdScore shell QDs	ECL	1 fM to 10 pM	0.98 fM	[74]
Cu <sup>2+</sup> (vegetable samples)	CdSeTe alloyed QDs	Fluorescence	20 nM to 2 μM	7.1 nM	[75]
O <sub>2</sub> and glucose (application in samples not demonstrated)	CdSe/ ZnScore shell QDs	Photo- electrochemical detection	0.1–5 mM	Not given	[76]
H <sub>2</sub> O <sub>2</sub> and glucose (whole blood)	CdTe/ CdScore shell QDs	Fluorescence resonance energy transfer	0.2–4 mM (H <sub>2</sub> O <sub>2</sub> ) and 0.1–5 mM (glucose)	0.1 mM (H <sub>2</sub> O <sub>2</sub> ) and 0.05 mM (glucose)	[77]
H <sub>2</sub> O <sub>2</sub> (environmental samples)	CdSeQDs	ECL	0.5– 500 μM	0.5 μM	[78]
Glucose (saliva)	CdTe/CdS core–shell QDs	Amperometric detection	10 pM to 10 nM	3 pM	[79]
Ascorbic acid (fruits and nude mice)	PbS QDs	Fluorescence	3–40 μM	1.5 μM	[80]
Cysteine (application in samples not demonstrated)	CdS QDs	Photo- electrochemical detection	0.2–2.8 μM	0.1 μM	[81]
Organophosphate pesticides (vegetables)	CdTe QDs	ECL	0.2–10 ng/ mL	0.06 ng/ mL	[82]
Cholesterol (biological fluid and food samples)	CdTe QDs	ECL	1 μM to 1 mM	0.33 μM	[83]
Deoxyguanosine-5'-phosphate (DNA samples)	CdTe/ ZnScore shell QDs	ECL	1–150 nM	0.1 nM	[84]
C-reactive protein (human serum)	PbS QDs	Anodic stripping voltammetry	0.2– 100 ng/mL	0.05 ng/ mL	[85]
Carbohydrate antigen 19–9 (human serum)	CdTe QDs	ECL	0.005– 100 pg/mL	0.002 pg/ mL	[86]

(continued)

**Table 26.1** (continued)

Analyte and (samples)	Nanomaterial used	Detection mode	Linear range	Limit of detection	Reference (Year)
Cancer biomarker P53 (human serum)	CdS QDs	ECL	20–1000 fg/ml	4 fg/ml	[87]
Human interleukin-6 (serum samples)	CdSe QDs	ECL	0.5 pg/mL to 10 ng/mL	0.17 pg/mL	[88]
Human carcinoembryonic antigen (synthetic sample)	CdTe QDs	ECL	1 fg/mL to 10 pg/mL	0.2 fg/mL	[89]
MicroRNA (human serum)	CdTe QDs	ECL	0.1–100 pM	33 fM	[90]
Human papillomavirus 18 (biological fluid)	CdTe QDs	Fluorescence	1.0–50 nM	0.2 nM	[91]
Norovirus (human serum)	CdZnSeS alloyed QDs	Photoluminescence	2–16 copies/mL	8.2 copies/mL	[92]
Hepatitis B virus surface antigen (human serum)	CdTe/CdS core shell QDs	ECL	3 fg/mL to 0.3 ng/mL	0.80 fg/mL	[93]
Colon cancer cells (application in samples not demonstrated)	CdSe/ZnS core shell QDs	Fluorescence-coupled capillary electrophoresis	Not given	Not given	[94]

involving these nanomaterials and accelerate development in the area. Considering the very broad field and a large number of publications available on the subject, the authors apologise for the possible neglect of important contributions that are not mentioned in this chapter.

## References

1. Somers RC, Bawendi MG, Nocera DG. CdSe nanocrystal based chem–/bio-sensors. *Chem Soc Rev.* 2007;36:579–91.
2. Reshma VG, Rajeev KS, Manoj K, Mohanan PV. Water dispersible ZnSe/ZnS quantum dots: assessment of cellular integration, toxicity and bio-distribution. *J Photochem Photobiol B.* 2020;212:112019.
3. Kalyanasundaram K, Borgarello E, Duonghong D, Grätzel M. Cleavage of water by visible-light irradiation of colloidal CdS solutions; inhibition of photocorrosion by RuO<sub>2</sub>. *Angew Chem Int Ed Engl.* 1981;20:987–8.
4. Rossetti R, Nakahara S, Brus LE. Quantum size effects in the redox potentials, resonance Raman spectra, and electronic spectra of CdS crystallites in aqueous solution. *J. Chem Phys.* 1983;79:1086–8.

5. Bian F, Sun L, Cai L, Wang Y, Zhao Y. Quantum dots from microfluidics for nanomedical application. *Wiley Interdiscip Rev Nanomed Nanobiotechnol.* 2019;11:e1567.
6. Hao N, Nie Y, Zhang JXJ. Microfluidic synthesis of functional inorganic micro-/nanoparticles and applications in biomedical engineering. *Int Mater Rev.* 2018;63:461–87.
7. Yang P, Ando M, Murase N. Highly luminescent CdSe/Cd<sub>x</sub>Zn<sub>1-x</sub>S quantum dots coated with thickness-controlled SiO<sub>2</sub> shell through silanization. *Langmuir.* 2011;27:9535–40.
8. Gofman VV, Aubert T, Ginste DV, Van Deun R, Beloglazova NV, Hens Z, et al. Synthesis, modification, bioconjugation of silica coated fluorescent quantum dots and their application for mycotoxin detection. *Biosens Bioelectron.* 2016;79:476–81.
9. Schmidtke C, Pösel E, Ostermann J, Pietsch A, Kloust H, Tran H, et al. Amphiphilic, cross-linkable diblock copolymers for multifunctionalized nanoparticles as biological probes. *Nanoscale.* 2013;5:7433–44.
10. Zhou J, Liu Y, Tang J, Tang W. Surface ligands engineering of semiconductor quantum dots for chemosensory and biological applications. *Mater Today (Kidlington).* 2017;20:360–76.
11. Dubertret B, Skourides P, Norris David J, Noireaux V, Brivanlou Ali H, Libchaber A. In vivo imaging of quantum dots encapsulated in phospholipid micelles. *Science.* 2002;298:1759–62.
12. Wegner KD, Hildebrandt N. Quantum dots: bright and versatile in vitro and in vivo fluorescence imaging biosensors. *Chem Soc Rev.* 2015;44:4792–834.
13. Liu Q, Das M, Liu Y, Huang L. Targeted drug delivery to melanoma. *Adv Drug Del Rev.* 2018;127:208–21.
14. Liang Z, Khawar MB, Liang J, Sun H. Bio-conjugated quantum dots for cancer research: detection and imaging. *Front Oncol.* 2021;11:749970.
15. Lefojane RP, Sone BT, Matinise N, Saleh K, Direko P, Mfengwana P, et al. CdO/CdCO<sub>3</sub> nano-composite physical properties and cytotoxicity against selected breast cancer cell lines. *Sci Rep.* 2021;11:30.
16. Jing H, Palmal M, Saed B, George A, Snee PT, Hu YS. Cytosolic delivery of membrane-penetrating QDs into T cell lymphocytes: implications in immunotherapy and drug delivery. *Nanoscale.* 2021;13:5519–29.
17. Mansur AAP, Amaral-Junior JC, Carvalho SM, Carvalho IC, Mansur HS. Cu-In-S/ZnS@carboxymethylcellulose supramolecular structures: fluorescent nanoarchitectures for targeted-theranostics of cancer cells. *Carbohydr Polym.* 2020;247:116703.
18. Shi H, Sun Y, Yan R, Liu S, Zhu L, Liu S, et al. Magnetic semiconductor Gd-doping CuS nanoparticles as activatable nanoprobe for bimodal imaging and targeted photothermal therapy of gastric tumors. *Nano Lett.* 2019;19:937–47.
19. Tsolekile N, Nahle S, Zikalala N, Parani S, Sakho EHM, Joubert O, et al. Cytotoxicity, fluorescence tagging and gene-expression study of CuInS/ZnS QDS - meso (hydroxyphenyl) porphyrin conjugate against human monocytic leukemia cells. *Sci Rep.* 2020;10:4936.
20. Cai X, Luo Y, Zhang W, Du D, Y. Lin, pH-sensitive ZnO quantum dots—doxorubicin nanoparticles for lung cancer targeted drug delivery. *ACS Appl Mater Interfaces.* 2016;8:22442–50.
21. Yang X, Zhang W, Zhao Z, Li N, Mou Z, Sun D, Cai Y, Wang W, Lin Y. Quercetin loading CdSe/ZnS nanoparticles as efficient antibacterial and anticancer materials. *J Inorg Biochem.* 2017;167:36–48.
22. Olerile LD, Liu Y, Zhang B, Wang T, Mu S, Zhang J, Selotlegeng L, Zhang N. Near-infrared mediated quantum dots and paclitaxel co-loaded nanostructured lipid carriers for cancer theragnostic. *Colloids Surf B Biointerfaces.* 2017;150:121–30.
23. Lv G, Guo W, Zhang W, Zhang T, Li S, Chen S, Eltahan AS, Wang D, Wang Y, Zhang J, Wang PC, Chang J, Liang X-J. Near-infrared emission CuInS/ZnS quantum dots: all-in-one theranostic nanomedicines with intrinsic fluorescence/photoacoustic imaging for tumor phototherapy. *ACS Nano.* 2016;10:9637–45.
24. Zhao T, Liu X, Li Y, Zhang M, He J, Zhang X, Liu H, Wang X, Gu H. Fluorescence and drug loading properties of ZnSe:Mn/ZnS-Paclitaxel/SiO<sub>2</sub> nanocapsules templated by F127 micelles. *J Colloid Interface Sci.* 2017;490:436–43.

25. Wang Y, Wang Y, Chen G, Li Y, Xu W, Gong S. Quantum-dot-based theranostic micelles conjugated with an anti-EGFR nanobody for triple-negative breast cancer therapy. *ACS Appl Mater Interfaces*. 2017;9:30297–305.
26. Rasekholghol A, Fazaeli Y, Moradi Dehaghi S, Ashtari P, Kardan M, Feizi S, Samiee Matin M. CdTe quantum dots on gold-198 nano particles: introducing a novel theranostic agent. *Radiochim Acta*. 2021;109:55–60.
27. Tandale P, Choudhary N, Singh J, Sharma A, Shukla A, Sriram P, et al. Fluorescent quantum dots: An insight on synthesis and potential biological application as drug carrier in cancer. *Biochem Biophys Rep*. 2021;26:100962.
28. Xu G, Mahajan S, Roy I, Yong K-T. Theranostic quantum dots for crossing blood–brain barrier in vitro and providing therapy of HIV-associated encephalopathy. *Front Pharmacol*. 2013;4:140.
29. Zhao G-Z, Wei M, Wang Y-J, Wang X-W, Zhao H, Shen J, et al. Detection of four phenolic oestrogens by a novel electrochemical immunosensor based on a hexestrol monoclonal antibody. *RSC Adv*. 2020;10:8677–84.
30. Campaña AL, Florez SL, Noguera MJ, Fuentes OP, Ruiz Puentes P, Cruz JC, et al. Enzyme-based electrochemical biosensors for microfluidic platforms to detect pharmaceutical residues in wastewater. *Biosensors (Basel)*. 2019;9:41.
31. Farzin L, Shamsipur M, Samandari L, Sheibani S. Recent advances in designing nanomaterial based biointerfaces for electrochemical biosensing cardiovascular biomarkers. *J Pharm Biomed Anal*. 2018;161:344–76.
32. Zhang W, Wang R, Luo F, Wang P, Lin Z. Miniaturized electrochemical sensors and their point-of-care applications. *Chin Chem Lett*. 2020;31:589–600.
33. Ehzari H, Safari M, Shahlaei M. A signal amplification by QDs used for ferrocene-labeled sandwich aptasensor for determination of  $Hg^{2+}$  in water samples. *J Iran Chem Soc*. 2019;16:2555–64.
34. Ehzari H, Safari M, Shahlaei M. A new sensing strategy based on thymine bases– $Hg^{2+}$ –methylene blue coordination on the electrospun PES–QDs platform for detection of  $Hg^{2+}$  in fruit juice samples. *J Iran Chem Soc*. 2019;16:2269–79.
35. Karaman C, Karaman O, Atar N, Yola ML. Electrochemical immunosensor development based on core-shell high-crystalline graphitic carbon nitride@carbon dots and  $Cd_{0.5}Zn_{0.5}S/d-Ti_3C_2T_x$  MXene composite for heart-type fatty acid-binding protein detection. *Mikrochim Acta*. 2021;188:182.
36. Moazampour M, Zare HR, Shekari Z. Femtomolar determination of an ovarian cancer biomarker (miR-200a) in blood plasma using a label free electrochemical biosensor based on L-cysteine functionalized ZnS quantum dots. *Anal Methods*. 2021;13:2021–9.
37. de França CCL, Meneses D, Silva ACA, Dantas NO, de Abreu FC, Petroni JM, et al. Development of novel paper-based electrochemical device modified with CdSe/CdS magic-sized quantum dots and application for the sensing of dopamine. *Electrochim Acta*. 2021;367:137486.
38. Silva ACA, Deus SLVD, Silva MJB, Dantas NO. Highly stable luminescence of CdSe magic-sized quantum dots in HeLa cells. *Sens Actuators B Chem*. 2014;191:108–14.
39. Silva ACA, da Silva SW, Morais PC, Dantas NO. Shell thickness modulation in ultrasmall CdSe/CdS<sub>x</sub>Se<sub>1-x</sub>/CdS core/shell quantum dots via 1-Thioglycerol. *ACS Nano*. 2014;8:1913–22.
40. Silva ACA, Silva MJB, da Luz FAC, Silva DP, de Deus SLV, Dantas NO. Controlling the cytotoxicity of CdSe magic-sized quantum dots as a function of surface defect density. *Nano Lett*. 2014;14:5452–7.
41. Xu J, Yu X, Xie L, Shao M. Facile incorporation of DNA-templated quantum dots for sensitive electrochemical detection of the oral cancer biomarker interleukin-8. *Anal Bioanal Chem*. 2020;412:2599–606.
42. Freitas M, Neves M, Nouws HPA, Delerue-Matos C. Quantum dots as nanolabels for breast cancer biomarker HER2-ECD analysis in human serum. *Talanta*. 2020;208:120430.



43. Wang C, Qian J, An K, Lu X, Huang X. A semiconductor quantum dot-based ratiometric electrochemical aptasensor for the selective and reliable determination of aflatoxin B1. *Analyst (Lond)*. 2019;144:4772–80.
44. Cadkova M, Kovarova A, Dvorakova V, Metelka R, Bilkova Z, Korecka L. Electrochemical quantum dots-based magneto-immunoassay for detection of HE4 protein on metal film-modified screen-printed carbon electrodes. *Talanta*. 2018;182:111–5.
45. Napi MLM, Sultan SM, Ismail R, How KW, Ahmad MK. Electrochemical-based biosensors on different zinc oxide nanostructures: a review. *Materials (Basel)*. 2019;12:2985.
46. Yu H-W, Zhang Z, Jiang J-H, Pan H-Z, Chang D. Simple strategy for sensitive detection of dopamine using CdTe QDs modified glassy carbon electrode. *J Clin Lab Anal*. 2018;32:e22320.
47. Mokwebo KV, Oluwafemi OS, Arotiba OA. An electrochemical cholesterol biosensor based on a CdTe/CdSe/ZnSe quantum dots-poly (propylene imine) dendrimer nanocomposite immobilisation layer. *Sensors (Basel)*. 2018;18:3368.
48. Zhao W-W, Xu J-J, Chen H-Y. Photoelectrochemical immunoassays. *Anal Chem*. 2018;90:615–27.
49. Zang Y, Lei J, Ju H. Principles and applications of photoelectrochemical sensing strategies based on biofunctionalized nanostructures. *Biosens Bioelectron*. 2017;96:8–16.
50. Zhao W-W, Xu J-J, Chen H-Y. Photoelectrochemical enzymatic biosensors. *Biosens Bioelectron*. 2017;92:294–304.
51. Cai Q, Wu D, Li H, Jie G, Zhou H. Versatile photoelectrochemical and electrochemiluminescence biosensor based on 3D CdSe QDs-DNA nanonetwork-SnO<sub>2</sub> nanoflower coupled with DNA walker amplification for HIV detection. *Biosens Bioelectron*. 2021;191:113455.
52. Gao B, Liang Z, Han D, Han F, Fu W, Wang W, et al. Molecularly imprinted photoelectrochemical sensor for hemoglobin detection based on titanium dioxide nanotube arrays loaded with CdS quantum dots. *Talanta*. 2021;224:121924.
53. Zhang N, Wang Y, Zhao G, Wang C, Li Y, Zhang Y, et al. A photoelectrochemical immunosensor based on CdS/CdTe-cosensitized SnO<sub>2</sub> as a platform for the ultrasensitive detection of amyloid  $\beta$ -protein. *Analyst (Lond.)*. 2020;145:619–25.
54. Liu S-T, Liu X-P, Chen J-S, Mao C-J, Jin B-K. Highly sensitive photoelectrochemical biosensor for microRNA159c detection based on a Ti<sub>3</sub>C<sub>2</sub>/CdS nanocomposite of breast cancer. *Biosens Bioelectron*. 2020;165:112416.
55. Zhang M, Guo S, Weller D, Hao Y, Wang X, Ding C, et al. CdSSe nanowire-chip based wearable sweat sensor. *J Nanobiotechnol*. 2019;17:42.
56. Dashtian K, Hajati S, Ghaedi M. L-phenylalanine-imprinted polydopamine-coated CdS/CdSe n-n type II heterojunction as an ultrasensitive photoelectrochemical biosensor for the PKU monitoring. *Biosens Bioelectron*. 2020;165:112346.
57. Wei Q, Wang C, Li P, Wu T, Yang N, Wang X, et al. ZnS/C/MoS<sub>2</sub> nanocomposite derived from metal-organic framework for high-performance photo-electrochemical immunosensing of carcinoembryonic antigen. *Small*. 2019;15:e1902086.
58. Liu XP, Chen JS, Mao CJ, Jin BK. A label-free photoelectrochemical immunosensor for carcinoembryonic antigen detection based on a g-C<sub>3</sub>N<sub>4</sub>/CdSe nanocomposite. *Analyst (Lond.)*. 2021;146:146–55.
59. Trapiella-Alfonso L, Pons T, Lequeux N, Leleu L, Grimaldi J, Tasso M, et al. Clickable-zwitterionic copolymer capped-quantum dots for in vivo fluorescence tumor imaging. *ACS Appl Mater Interfaces*. 2018;10:17107–16.
60. Pons T, Bouccara S, Loriette V, Lequeux N, Pezet S, Fragola A. In vivo imaging of single tumor cells in fast-flowing bloodstream using near-infrared quantum dots and time-gated imaging. *ACS Nano*. 2019;13:3125–31.
61. Duong HD, Rhee JI. Development of ratiometric fluorescence sensors based on CdSe/ZnS quantum dots for the detection of hydrogen peroxide. *Sensors (Basel)*. 2019;19:4977.
62. Ripoll C, Orte A, Paniza L, Ruedas-Rama MJ. A quantum dot-based FLIM glucose nanosensor. *Sensors (Basel)*. 2019;19:4922.

63. Abd Rahman S, Ariffin N, Yusof NA, Abdullah J, Mohammad F, Ahmad Zubir Z, et al. Thiolate-capped CdSe/ZnS core-shell quantum dots for the sensitive detection of glucose. *Sensors (Basel)*. 2017;17:1537.
64. Abd Rahman S, Ariffin N, Yusof NA, Abdullah J, Ahmad Zubir Z, Nik Abd Aziz NMA. Cdse/Zns capped thiolate for application in glucose sensing. *Biosensors J*. 2017;6:1000143.
65. Saran AD, Bellare JR. CdSe quantum dots to quantum rods: transition studies and evaluation of sensitivity as transducers for biosensing glucose. *Nanosci Nanotechnol-Asia*. 2020;10:29–38.
66. Jung E-Y, Ye J-H, Jung S-H, Choi S-H. Electrochemiluminescence biosensor based on thioglycolic acid-capped CdSe QDs for sensing glucose. *J Nanomater*. 2016;2016:1–9.
67. Wang J, Jiang X, Han H. Turn-on near-infrared electrochemiluminescence sensing of thrombin based on resonance energy transfer between CdTe/CdS coresmall/shellthick quantum dots and gold nanorods. *Biosens Bioelectron*. 2016;82:26–31.
68. Tao J, Zeng Q, Wang L. Near-infrared quantum dots based fluorescent assay of  $\text{Cu}^{2+}$  and in vitro cellular and in vivo imaging. *Sens Actuators B Chem*. 2016;234:641–7.
69. Gui R, An X, Su H, Shen W, Chen Z, Wang X. A near-infrared-emitting CdTe/CdS core/shell quantum dots-based OFF-ON fluorescence sensor for highly selective and sensitive detection of  $\text{Cd}^{2+}$ . *Talanta*. 2012;94:257–62.
70. Wang J, Li N, Shao F, Han H. Microwave-assisted synthesis of high-quality CdTe/CdS@ZnS– $\text{SiO}_2$  near-infrared-emitting quantum dots and their applications in  $\text{Hg}^{2+}$  sensing and imaging. *Sens Actuators B Chem*. 2015;207:74–82.
71. Nguyen TH, Ung TDT, Vu TH, Tran TKC, Dong VQ, Dinh DK, Nguyen QL. Fluorescence biosensor based on CdTe quantum dots for specific detection of H5N1 avian influenza virus. *Adv Nat Sci Nanosci Nanotechnol*. 2012;3:035014.
72. Yao J, Yang M, Duan Y. Highly fluorescent CdTe nanocrystals: synthesis, characterization, property, mechanism, and application as a sensor for biomolecule analysis. *J Mater Res*. 2014;29:633–40.
73. He Z-J, Kang T-F, Lu L-P, Cheng S-Y. An electrochemiluminescence sensor based on CdSe@CdS-functionalized  $\text{MoS}_2$  and a GOD-labeled DNA probe for the sensitive detection of  $\text{Hg}(\text{II})$ . *Anal Methods*. 2020;12:491–8.
74. Du X-L, Kang T-F, Lu L-P, Cheng S-Y. An electrochemiluminescence sensor based on CdSe@CdS functionalized  $\text{MoS}_2$  and hemin/G-quadruplex-based DNAzyme biocatalytic precipitation for sensitive detection of  $\text{Pb}(\text{II})$ . *Anal Methods*. 2018;10:51–8.
75. Liang G-X, Liu H-Y, Zhang J-R, Zhu J-J. Ultrasensitive  $\text{Cu}^{2+}$  sensing by near-infrared-emitting CdSeTe alloyed quantum dots. *Talanta*. 2010;80:2172–6.
76. Tanne J, Schäfer D, Khalid W, Parak WJ, Lisdat F. Light-controlled bioelectrochemical sensor based on CdSe/ZnS quantum dots. *Anal Chem*. 2011;83:7778–85.
77. Yu M, Zhao K, Zhu X, Tang S, Nie Z, Huang Y, Zhao P, Yao S. Development of near-infrared ratiometric fluorescent probe based on cationic conjugated polymer and CdTe/CdS QDs for label-free determination of glucose in human body fluids. *Biosens Bioelectron*. 2017;95:41–7.
78. Hu Y, Chen C, Liu Y, Wang S, Guo Z, Hu Y. Dual-signals electrochemiluminescence ratiometry based the synergic effect between luminol and CdSe quantum dots for direct detection of hydrogen peroxide. *J Electroanal Chem (Lausanne)*. 2018;815:61–7.
79. Zhiguo G, Shuping Y, Zaijun L, Xiulan S, Guangli W, Yinjun F, Junkang L. An ultrasensitive electrochemical biosensor for glucose using CdTe–CdS core–shell quantum dot as ultrafast electron transfer relay between graphene-gold nanocomposite and gold nanoparticle. *Electrochim Acta*. 2011;56:9162–7.
80. Zhao P, He K, Han Y, Zhang Z, Yu M, Wang H, Huang Y, Nie Z, Yao S. Near-infrared dual-emission quantum dots–gold nanoclusters nanohybrid via co-template synthesis for ratiometric fluorescent detection and bioimaging of ascorbic acid in vitro and in vivo. *Anal Chem*. 2015;87:9998–10005.
81. Long Y-T, Kong C, Li D-W, Li Y, Chowdhury S, Tian H. Ultrasensitive determination of cysteine based on the photocurrent of nafion-functionalized CdS–MV quantum dots on an ITO electrode. *Small*. 2011;7:1624–8.

82. Liang H, Song D, Gong J. Signal-on electrochemiluminescence of biofunctional CdTe quantum dots for biosensing of organophosphate pesticides. *Biosens Bioelectron.* 2014;53:363–9.
83. Huan J, Liu Q, Fei A, Qian J, Dong X, Qiu B, Mao H, Wang K. Amplified solid-state electrochemiluminescence detection of cholesterol in near-infrared range based on CdTe quantum dots decorated multiwalled carbon nanotubes@reduced graphene oxide nanoribbons. *Biosens Bioelectron.* 2015;73:221–7.
84. Zhao P, Zhou L, Nie Z, Xu X, Li W, Huang Y, He K, Yao S. Versatile electrochemiluminescent biosensor for protein–nucleic acid interaction based on the unique quenching effect of deoxyguanosine-5'-phosphate on electrochemiluminescence of CdTe/ZnS quantum dots. *Anal Chem.* 2013;85:6279–86.
85. Kokkinos C, Prodromidis M, Economou A, Petrou P, Kakabakos S. Disposable integrated bismuth citrate-modified screen-printed immunosensor for ultrasensitive quantum dot-based electrochemical assay of C-reactive protein in human serum. *Anal Chim Acta.* 2015;886:29–36.
86. Gan N, Zhou J, Xiong P, Li T, Jiang S, Cao Y, Jiang Q. An ultrasensitive electrochemiluminescence immunoassay for carbohydrate antigen 19-9 in serum based on antibody labeled Fe<sub>3</sub>O<sub>4</sub> nanoparticles as capture probes and graphene/CdTe quantum dot bionanoconjugates as signal amplifiers. *Int J Mol Sci.* 2013;14:10397–411.
87. Heidari R, Rashidiani J, Abkar M, Taheri RA, Moghaddam MM, Mirhosseini SA, Seidmoradi R, Nourani MR, Mahboobi M, Keihan AH, Kooshki H. CdS nanocrystals/graphene oxide-AuNPs based electrochemiluminescence immunosensor in sensitive quantification of a cancer biomarker: p53. *Biosens Bioelectron.* 2019;126:7–14.
88. Liu P-Z, Hu X-W, Mao C-J, Niu H-L, Song J-M, Jin B-K, Zhang S-Y. Electrochemiluminescence immunosensor based on graphene oxide nanosheets/polyaniline nanowires/CdSe quantum dots nanocomposites for ultrasensitive determination of human interleukin-6. *Electrochim Acta.* 2013;113:176–80.
89. Gao X, Fu K, Fu L, Wang H, Zhang B, Zou G. Red-shifted electrochemiluminescence of CdTe nanocrystals via Co<sup>2+</sup>-doping and its spectral sensing application in near-infrared region. *Biosens Bioelectron.* 2020;150:111880.
90. Zhu H-Y, Ding S-N. Dual-signal-amplified electrochemiluminescence biosensor for microRNA detection by coupling cyclic enzyme with CdTe QDs aggregate as luminophor. *Biosens Bioelectron.* 2019;134:109–16.
91. Shamsipur M, Nasirian V, Mansouri K, Barati A, Veisi-Raygani A, Kashanian S. A highly sensitive quantum dots-DNA nanobiosensor based on fluorescence resonance energy transfer for rapid detection of nanomolar amounts of human papillomavirus 18. *J Pharm Biomed Anal.* 2017;136:140–7.
92. Adegoke O, Seo M-W, Kato T, Kawahito S, Park EY. An ultrasensitive SiO<sub>2</sub>-encapsulated alloyed CdZnSeS quantum dot-molecular beacon nanobiosensor for norovirus. *Biosens Bioelectron.* 2016;86:135–42.
93. Babamiri B, Hallaj R, Salimi A. Ultrasensitive electrochemiluminescence immunosensor for determination of hepatitis B virus surface antigen using CdTe@CdS-PAMAM dendrimer as luminescent labels and Fe<sub>3</sub>O<sub>4</sub> nanoparticles as magnetic beads. *Sens Actuators B Chem.* 2018;254:551–60.
94. Liu F, Wang J, Yang L, Liu L, Ding S, Fu M, Deng L, Gao L-Q. Developing a fluorescence-coupled capillary electrophoresis based method to probe interactions between QDs and colorectal cancer targeting peptides. *Electrophoresis.* 2016;37:2170–4.

# Chapter 27

## Specific Applications of II–VI Semiconductor Nanomaterials-Based Biosensors for Food Analysis and Food Safety



Xiaodong Guo, Jiaqi Wang, Mengke Zhang, and Marie-Laure Fauconnier

### 27.1 Introduction

Food quality and safety issue is the most important challenge in food processing industry. For instance, the regular occurrence of bacterial contamination in food supplies is a growing concern as it has recently led to multiple deaths in the USA and Europe. Rapid and noninvasive means of detecting bacterial contamination in food products are therefore highly desirable for monitoring the safety of the food supply at a reasonable cost [3, 12, 32, 83]. However, pathogenic bacterial are made of the same major constituents including amides, proteins, nucleic acids, polysaccharides, and phospholipids which complicates a highly selective identification

---

X. Guo (✉)

School of Agriculture and Biology, Shanghai Jiao Tong University, Shanghai, China

Laboratory of Quality and Safety Risk Assessment for Dairy Products of Ministry of Agriculture and Rural Affairs, Institute of Animal Science, Chinese Academy of Agricultural Sciences, Beijing, China

Chimie générale et organique, Gembloux Agro-Bio Tech, Université de Liège, Gembloux, Belgium

e-mail: [guoxiaodong233@sjtu.edu.cn](mailto:guoxiaodong233@sjtu.edu.cn)

J. Wang

Laboratory of Quality and Safety Risk Assessment for Dairy Products of Ministry of Agriculture and Rural Affairs, Institute of Animal Science, Chinese Academy of Agricultural Sciences, Beijing, China

e-mail: [jiaqiwang@vip.163.com](mailto:jiaqiwang@vip.163.com)

M. Zhang

School of Agriculture and Biology, Shanghai Jiao Tong University, Shanghai, China

M.-L. Fauconnier

Chimie générale et organique, Gembloux Agro-Bio Tech, Université de Liège, Gembloux, Belgium

between different strains based on simple chemical analysis [39]. Although much time and effort are spent on methods for this, more efficient sensing platforms are of great importance and urgency.

Traditional biosensors are widely used for this purpose as reported in the bibliography. The development of biosensors is an emergent area, in response to the demand for simple, reliable, and low-cost techniques against food residues [22]. However, major problems like low sensitivity, lack of practicality, and time-consuming response have limited their wide application in food hazard analysis. II–VI semiconducting nanomaterials, possessed different morphologies, semiconductors, and characterisation technologies, mainly included zinc oxide (ZnO) [68, 69, 73, 80, 82, 86], zinc sulphide (ZnS) [37, 44, 67, 75, 76, 87], cadmium sulphide (CdS) [59, 60, 62, 70, 71, 85], cadmium selenide (CdSe) [18, 29, 30, 48, 53, 59, 60], cadmium teluride (CdTe) [40, 46, 52, 54, 66, 75, 79], etc. They are attracting more and more attention from scientists for biosensor applications due to their advanced optical, catalytic, sensing and electrochemical properties [41, 55–57, 65, 70–72, 77].

These nanomaterials offered a large surface area for biomolecules recognition elements like antibody [19, 24], and nucleic acid aptamer [28, 42, 43, 55, 56, 84] to specific interaction with target analytes, and the improved sensitivity of biosensors was achieved. Compared to traditional biosensors, nanomaterials integrated biosensors have significant superiorities, including high sensitivity, rapid response, enhanced practicality and facile devices. The current research highlighted an increasing implementation of nanomaterials in biosensor development for both molecule recognition and signal transduction [1, 2, 7, 10, 47, 58]. Pathogens and food toxins are detected by optics coated with antibodies. Water-soluble vitamins, drug residues, or other small molecules can be detected and measured through a variety of immuno- and ligand-binding assays embedded on II–IV-based sensor systems. These sensors are widely used across the food industry. Nanosensors can advance the food sector by improving food processing, packaging, and quality monitoring [8]. More importantly, the advantages of nanobiosensors can lead to their use in the whole food industry: from raw material preparation, food processing (quality control), monitoring of storage conditions and use of these devices as cost-effective tools for quality and process controls as well as to ensure food safety.

This book chapter will provide a new view to the readers that II–VI semiconducting nanomaterials have been widely utilised by sensor construction for food analysis and food safety field (Fig. 27.1), and highlight the recent advances and future prospects. First of all, we introduce the characteristics and classification of II–VI semiconducting nanomaterials. Then a brief introduction of the application of II–VI semiconducting nanomaterials-based sensing platform for food quality and safety control was discussed. In addition, we comprehensively analyse and summarise the practical application of these nanomaterials in certain food samples.

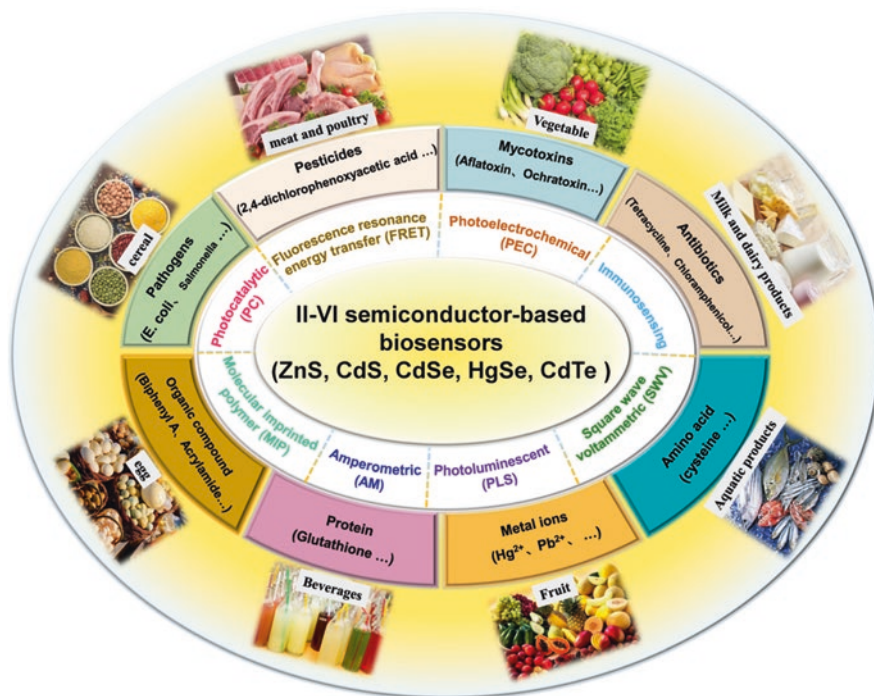
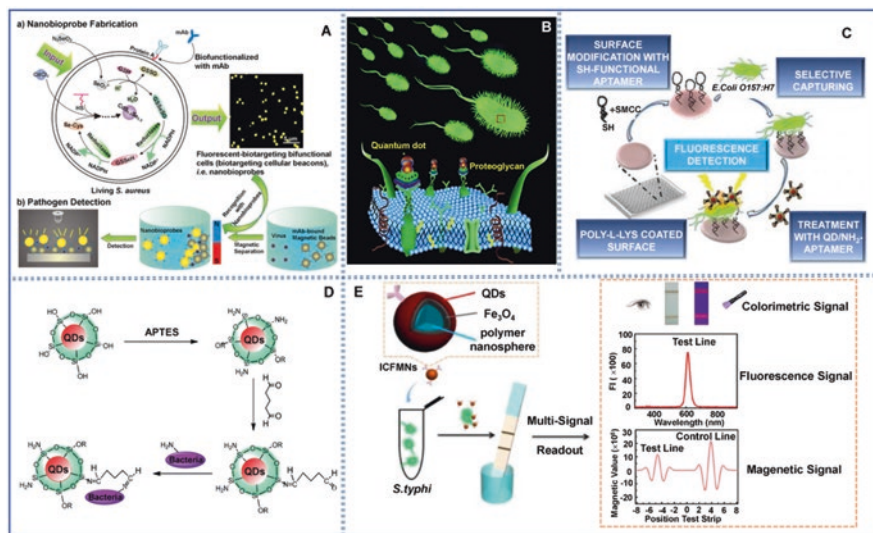


Fig. 27.1 Scheme illustration of II–VI semiconducting nanomaterials-based biosensors for food analysis and food safety

## 27.2 II–VI Semiconducting Nanomaterials for Food Analysis

### 27.2.1 Detection of Pathogenic Bacteria

Due to the growing concern of the risk that food- and water-borne pathogens pose to human health, there is an increasing demand from regulatory agencies to ensure a safe food supply. As shown in Fig. 27.2, II–VI semiconducting nanomaterials-based biosensing strategies for pathogens were illustrated. Xiong et al. reported the biosynthesis of CdSe QDs intracellularly and employed them as nanoprobe for the detection of bacteria (Fig. 27.2a). The bacteria detection involves a space-time-coupling strategy for converting the bacteria (*Staphylococcus aureus*) into fluorescent cells (cellular beacons) [61]. Typically, a low detection limit of 8.94 ng/mL was reported. The proposed scheme has many advantages like fluorescent probes being monodispersed with uniform size, high luminance with outstanding photostability. Also, the probes are highly accurate, reliable, and repeatable. By the suitable selection of the antibody conjugation, this kind of new bioprobe can be extended towards the sensitive detection of various other bacterial pathogens including pseudorabies virus, baculovirus, *Salmonella typhimurium*, and SKBR-3 cells [38]. CdSe was also



**Fig. 27.2** (a) Schematic representation of nanobioprobes fabrication for pathogen detection based on fluorescent CdSe QDs. (Reprinted with permission from Ref. [61]. Copyright 2014 American Chemical Society). (b) Schematic illustration of fluorescent detection of pathogenic bacteria *Vibrio harveyi* based on CdSe/ZnS QDs. (Reprinted with permission from Ref. [5]. Copyright 2016 Royal Society of Chemistry). (c) Schematic illustration of optical analysis of *E. coli* O157:H7 employing CdSe/ZnS QDs coupled with NH<sub>2</sub>-aptamer. (Reprinted with permission from Ref. [11]. Copyright 2015: Taylor & Francis). (d) Schematic illustration of fluorescent sensing of *Salmonella typhi* based on the preparation and conjugation of CdSe/ZnS QDs. (Reprinted with permission from Ref. [51]. Copyright 2014: Royal Society of Chemistry). (e) Schematic representation of CdSe/ZnS QDs-based multimodal sensing of *S. typhi* in lateral flow immunoassay (LFIA). (Reprinted with permission from Ref. [14]. Copyright 2018: American Chemical Society)

employed for multi-QDs detection. For instance, Arshad et al. reported the use of CdSe/ZnS QDs for the detection of *Vibrio harveyi* in solution and in animal cells [5]. Techniques such as fluorescence microscopy, elastase assay, polyacrylamide gel electrophoresis (PAGE), and comet assay are used to evaluate the interactions of QDs with *V. harveyi*. The appearance of bright yellow fluorescence when different concentrations of QDs were applied confirms the perfect attachment of the QDs to the bacteria (Fig. 27.2b). It was also demonstrated that the toxicity level of CdSe/ZnS QDs is genetically and cytotoxically safe for labelling the bacteria allowing live imaging and tracking of the microorganisms.

*Escherichia coli*, a common pathogenic bacterium, is one of the main reason for food-borne diseases. Toxins can occur by *E. coli* strains and further affect human health. The development of high efficient method for detection of *E. coli* is of great importance. In a novel research, the stability of the sensors was significantly enhanced by using oligonucleotide microarray combined with CdSe/ZnS QDs as fluorescent labels. The bacterium was identified with PerkinElmer Gx microarray scanner displaying a sensitivity of 10 CFU mL<sup>-1</sup>. Fluorescence detection of *E. Coli* O157: H7bacteria was obtained by using CdSe/ZnS QDs with carboxylic functional

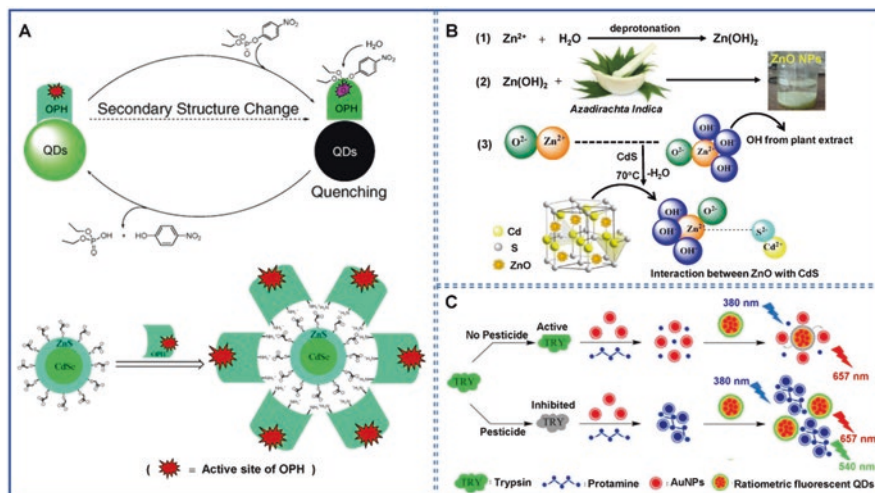
groups [11]. The 72-mer aptamer is used as the probe and sensing element where detection limit of  $10^2$  CFU  $\text{mL}^{-1}$  could be achieved (Fig. 27.2c). In addition, ZnO is an advanced nanomaterial, which is widely used for biosensors construction due to its unique optical and electrochemical characteristics. Azmy et al. introduced a ZnO coupled with reduce graphene oxides (ZnO-rGO) nanocomposite for high sensitive detection of *E. coli* [6]. More importantly, gamma radiation was applied to evaluate the analytic performance of the sensing strategy. Result demonstrated that the structure and morphology of the ZnO-rGO nanocomposite were improved by gamma radiation. Notably, the defects on the surface of ZnO allowed its adsorption towards various biomolecules.

Food-borne pathogens, commonly presented in food products, have a hazard impact on human health. Typically, of them, *Salmonella* is one of the most important food-borne pathogens. It was worth noting that the occurrence and mortality rate of *Salmonella* infection were obviously serious in numerous developing countries because of weak medical conditions. Taking the *Salmonella* infection risks into consideration, the rapid and sensitive detection methods are essential for *Salmonella* monitoring in food. Wang et al. first introduced a fluorescent sensing of *Salmonella typhimurium* based on CdSe/ZnS QDs (Fig. 27.2d). Notably, the  $\text{SiO}_2$  spheres were embedded on CdSe/ZnS QDs for enhanced fluorescent signal [51]. The detection limit was calculated to be  $3.3 \times 10^2$  CFU  $\text{mL}^{-1}$ . Based on similar mechanisms, the CdSe/ZnS QDs were synthesised and employed for multimodal sensing of *S. typhi* in lateral flow immunoassay (LFIA). In this study, colorimetric-fluorescent-magnetic multimodal signals were achieved by utilising the nanospheres for analyte separation and enrichment (Fig. 27.2e). The proposed sensing platform allowed ten-fold sensitivity improvement [14]. In particular, the colorimetric signal has exhibited a LOD of  $1.88 \times 10^4$  CFU  $\text{mL}^{-1}$ , and that of  $3.75 \times 10^3$  CFU  $\text{mL}^{-1}$  was realised in magnetic signal. It was demonstrated that two to four orders of magnitude enhancement were detected over the conventional LFIA. In addition, the multimodal sensing strategy was validated by successful application for *S. typhi* monitoring in milk analysis. In addition, Viter et al. reported the ZnO nanorods-based photoluminescence sensing of *Salmonella* for food pathogens. The Anti-*Salmonella* antibody was employed to interact with *Salmonella* as a result the surface charge changed. The achieved sensing performance was attributed to the photoluminescence signal quenching under the presence of *Salmonella* [50].

### 27.2.2 Detection of Pesticides

In view of the great toxicity and hazards in food and agricultural product safety, it is urgent and essential to develop advanced nanomaterials for the degradation and removal of pesticides (Fig. 27.3). Inspired by this consideration, an example of biosensing based on the use of QDs/OPH bioconjugate for paraoxon detection has been first reported by Ji et al. The CdSe/ZnS core-shell QDs were modified with OPH using electrostatic interactions between negatively charged QDs surfaces and





**Fig. 27.3** (a) Schematic illustration of photoluminescence sensing of paraoxon based on CdSe/ZnS QDs. (Reprinted with permission from Ref. [17]. Copyright 2005: American Chemical Society). (b) Schematic diagram of photodegradation of pesticides using ZnO@CdS nanoparticles. (Reprinted with permission from Ref. [36]. Copyright 2021: Elsevier). (c) Schematic illustration of optical sensor for detection of parathion-methyl (PM) based on two colored CdTe QDs. (Reprinted with permission from Ref. [64]. Copyright 2015: Elsevier)

the positively charged protein side chain and ending groups (NH<sub>2</sub>). Photoluminescence (PL) intensity of the OPH/QDs bioconjugate was quenched in the presence of paraoxon (Fig. 27.3a). It was observed that the PL intensity of the OPH/QDs bioconjugate to different concentrations of paraoxon exhibited a decrease as the paraoxon concentration increased [17].

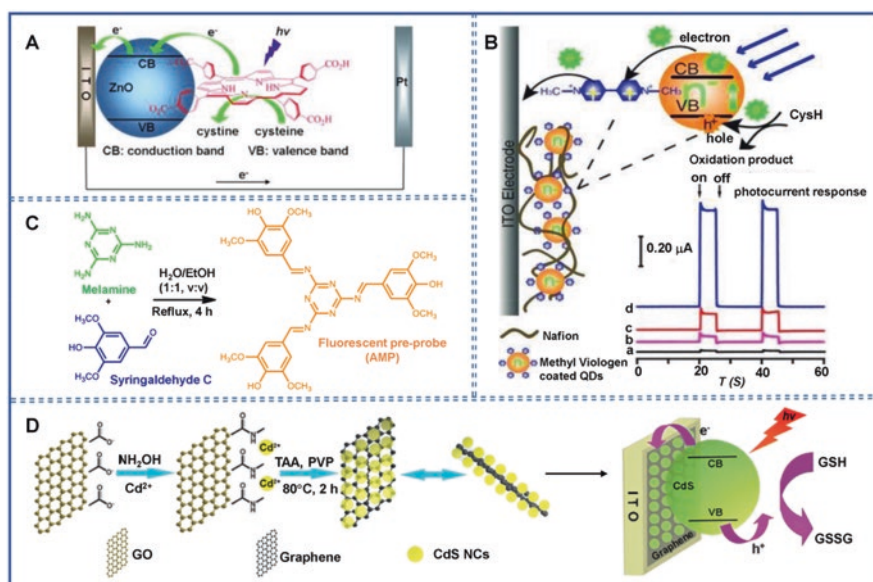
Furthermore, Vinayaka et al. [49] have developed a biosensor based on competitive fluoroimmunoassay for the analysis of the 2,4-dichlorophenoxyacetic acid using CdTe QD. This herbicide can cause human health problems even at low levels, hereby is very important to carry out a detection and quantification for applications in food analysis. The developed fluoroimmunoassay used an immunoreactor column which has been packed by immobilising anti-2,4-dichlorophenoxyacetic (2,4-D) antibodies; by this way it was possible to detect 2,4-D up to 250 pg mL<sup>-1</sup> in 50 mM phosphate buffer solution (pH 7.4).

Very recently, a novel and sustainable zinc oxide coupled with cadmium sulphide nanocomposite (ZnO@CdS) were prepared with the characteristic of green synthesis by plant leaf and high enriched product [36]. The photocatalytic activity of synthesized ZnO@CdS nanocomposite was highly enhanced compared to ZnO and CdS (Fig. 27.3b). In addition, the ZnO@CdS nanocomposite displayed optimised surface area (111 m<sup>2</sup>g<sup>-1</sup>), and reduced band energy (1.67 eV), resulting in great degradation efficiency towards pesticide residues in the range of 89–91%. In addition, two coloured CdTe QDs were synthesized and utilised in the fluorescent sensor for detection of parathion-methyl (PM). The red emissive QDs on silica sphere were

employed as the background signal, while the green emissive QDs on the surface of the silica acted as the measurement signal [64]. The fluorescent signal produced by the green emissive QDs were obviously quenched upon the utilisation of Au NPs. In the presence of protamine, the interaction between Au NPs and protamine were observed via the electrostatic attraction, which induced the aggregation of Au NPs, and further the recovery of the fluorescent signal (Fig. 27.3c). The proposed optical sensor allowed the sensitive detection of PM with a low LOD of  $18 \text{ pg mL}^{-1}$ . The successful application of this method was achieved for PM determination in milk and rice samples.

### 27.2.3 Detection of Amino Acids

Cysteine is an essential member of glutathione (GSH), which poses an important role in functional foods field. There are great requirements for development of sensitive and selective detection technology against cysteine (Fig. 27.4). Photoelectrochemical biosensor was also utilised in the analysis of cysteine with



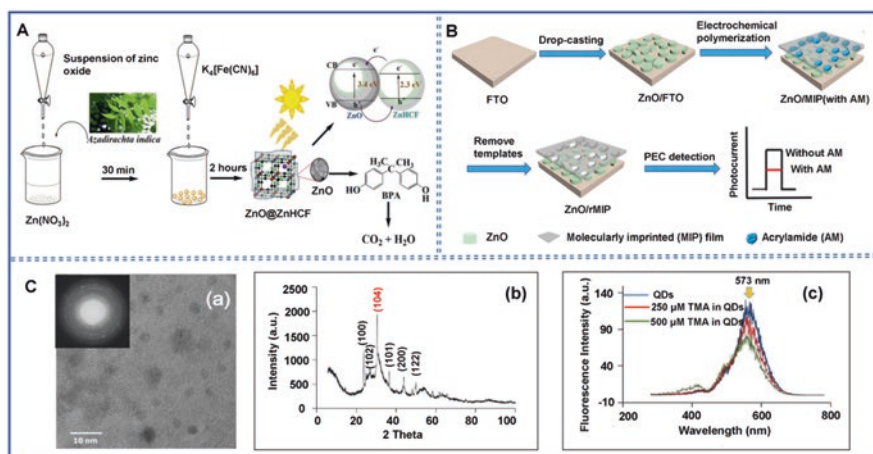
**Fig. 27.4** (a) Schematic representation of photoelectrochemical detection of cysteine at ZnO-coated ITO electrode. (Reprinted with permission from Ref. Tu et al. [45]. Copyright 2011: Wiley). (b) Schematic diagram of the photocurrent detection of cysteine at Nafion/CdS-MV decorated ITO electrode. (Reprinted with permission from Ref. Long et al. [26]. Copyright 2011: Wiley). (c) Diagram of fluorescent biosensing of cysteine based on ZnO QDs and fluorescent probe. (Reprinted with permission from Ref. [21]. Copyright 2021: Springer Nature). (d) Schematic illustration of photoelectrochemical detection of glutathione (GSH) at graphene-CdS decorated ITO electrode. (Reprinted with permission from Ref. [78]. Copyright 2012: Royal Society of Chemistry)

high sensitivity and specificity. A novel sensing platform was introduced for photoelectrochemical detection of cysteine based on free-base-porphyrin-functionalised ZnO NMs. In this design, ZnO NMs was employed to interact with functional nano-hybrid, which was coated on an indium tin oxide (ITO) electrode (Fig. 27.4a). When cysteine existed, the photocurrent signal was significantly enhanced under irradiation. Achieved by this performance, the photoelectrochemical signal was a dynamic response versus target cysteine concentrations in the range of 0.6–157  $\mu\text{mol L}^{-1}$ , and its detection of limit was 0.2  $\mu\text{mol L}^{-1}$ . It has been demonstrated that ZnO-based semiconductor nanoparticles provided a potential application for biomolecules analysis [45]. Based on similar photoelectrochemical biosensing, methyl viologen was coated on CdS QDs, and the efficient electron was transported from cysteine to the QDs when cysteine existed (Fig. 27.4b). The electron transfer on the electrode was surveyed [26]. Upon light irradiation, electron transportation was performed from CdS QDs to methyl viologen, leading to efficient electron transportation to the indium tin oxide (ITO) electrode. The photocurrent signal was proportionally enhanced versus the levels of cysteine. A dynamic response was obtained ranging from 0.2 to 2.8  $\mu\text{M}$ . Its detection limit was down to 0.1  $\mu\text{M}$ . Very recently, ZnO QDs were first synthesized and characterised for fluorescent detection of cysteine with high sensitivity (LOD = 0.642  $\mu\text{M}$ ) (Fig. 27.4c) [21].

Glutathione (GSH) was not only used for drugs but also applied in functional foods for the improvement of immunosystem function. The detection of GSH levels was thus much in demand. The graphene/CdS nanomaterials were synthesized and employed to construct the photoelectrochemical sensing strategy for sensitive GSH determination [78]. It was confirmed that the current graphene/CdS nanomaterials improved the photoelectric properties like the great electron transport and the spatial separation, and further enhance the photocurrent signals (Fig. 27.4d). A good linear relationship was achieved between the photocurrent signals and concentrations of GSH. Its detection limit was calculated to be 0.003 mM. Results demonstrated that the graphene/CdS nanomaterials offer great potential in functional foods application due to their significantly enhanced photoelectric properties.

### 27.2.4 Detection of Organic Compounds

Bisphenol A (BPA), a common contaminant in foods and water, was extensively used in food products and food package. Bisphenol A posed a great hazard to food safety. Thus, the detection and degradation of bisphenol A was attracted increasing interest from researches, especially in the exploration of low-cost and efficient methods. Rani et al. reported a novel ZnO doped with zinc-hexacyanoferrate (ZnO@ZnHCF) nanomaterials for high BPA degradation [35]. Through this synthesis and design, the surface area and band gap of ZnO@ZnHCF nanomaterials were obviously improved in comparison with ZnO or ZnHCF (Fig. 27.5a). Therefore, it was demonstrated that the proposed methods indicated the degradation pathway of BPA and the promising practicality of ZnO@ZnHCF nanomaterials.



**Fig. 27.5** (a) Schematic diagram of photocatalytic degradation of bisphenol A using ZnO@ZnHCF nanocubes. (Reprinted with permission from Ref. [35]. Copyright 2018: Elsevier). (b) Schematic diagram of photoelectrochemical detection of acrylamide based on ZnO/polypyrrole nanocomposites. (Reprinted with permission from Ref. [81]. Copyright 2021: Elsevier). (c) Schematic illustration of electrochemiluminescence detection of trimethylamine (TMA) using thioglycolic acid-CdSe QDs. (Reprinted with permission from Ref. [33]. Copyright 2021: Elsevier)

Acrylamide (AM), a group 2A carcinogen classified by international regulation, was a common contaminant produced in potato chips and biscuits during the high-temperature operation. Given its severe hazards for food safety and human health, simple, sensitive and reliable detection approaches are much in demand. A ZnO nanocomposite-based molecular imprinting (MIP) platform for photoelectrochemical sensing of AM was introduced [81]. The ZnO nanocomposite was synthesized and employed as a special photoelectron material, and the polypyrrole (PPy) was modified on ZnO nanocomposites for specific recognition of target AM. When AM was presented, the adsorption of AM on PPy-ZnO caused the electron transport, and further led to the reduced photocurrent signal (Fig. 27.5b). A dynamic response was observed between the photocurrent signals and AM concentrations ranging from  $10^{-1}$  to  $2.5 \times 10^{-9}$  M. Its limit of detection was  $2.147 \times 10^{-9}$  M. The developed PPy-ZnO-based photoelectrochemical sensing platform has a great potential to ensure food safety.

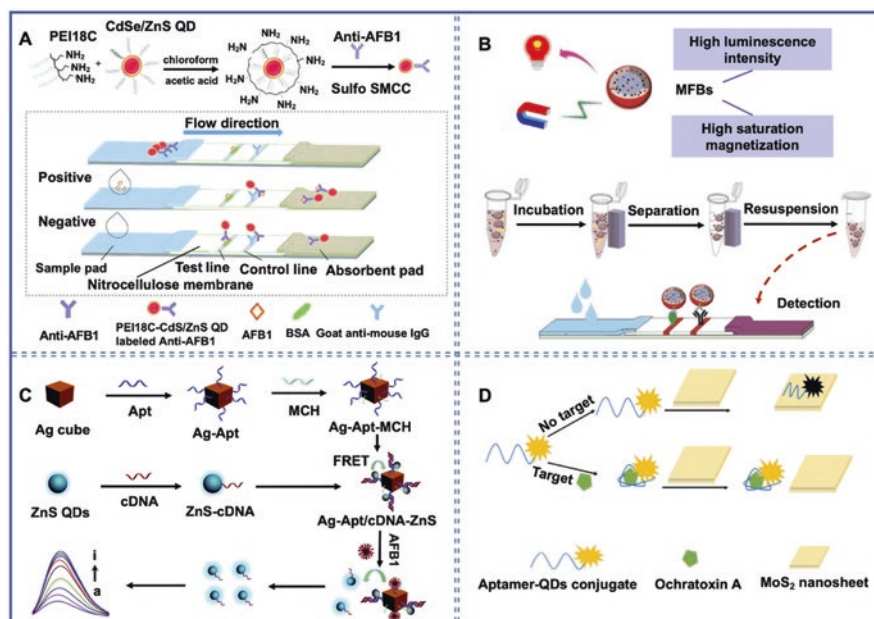
A paper-based electrochemiluminescence device ( $\mu$ PAD-ECL) for the estimation of trimethylamine (TMA) concentration in fish was developed using tris(2,2'-bipyridyl)ruthenium(II) complex coupled with water-soluble thioglycolic acid-capped CdSe quantum dots on the inkjet-printed paper-based device [33]. The quenching effect of tertiary amines on the ECL intensity was found to be sensitive and concentration-dependent. This effect allows the measurement of TMA at low concentrations (Fig. 27.5c). Under the optimal conditions, the linear concentration range was exhibited from  $1 \times 10^{-12}$  to  $1 \times 10^{-7}$  M and a detection limit of  $2.09 \times 10^{-13}$  M, with a relative standard deviation of 1.97%. The applicability of

$\mu$ PAD-ECL is demonstrated by the rapid estimation of trimethylamine concentration in fish tissue and could be used as a method for screening the total amount of tertiary amines in fishery products in remote communities. The results obtained using the paper-based devices agreed well with those obtained by applying high-performance liquid chromatography with benzoyl derivatisation, at a confidence level of 95%.

### 27.2.5 *Detection of Small Molecules Mycotoxins*

Aflatoxin B1 (AFB1), one of the most common and toxic mycotoxins in foods, has been recognised as group 1 carcinogen by the International Agency for Research on Cancer (IARC). Therefore, rapid, reliable, and sensitive methods for AFB1 determination are of great importance and urgency. Li et al. first developed a lateral flow immunoassay (LFIA) for rapid analysis of AFB1 in cereal products based on CdSe/ZnS QDs (Fig. 27.6a). The anti-AFB1 was immobilised on CdSe/ZnS QDs modified with amino [23]. The enhanced sensitivity was thus achieved with a low LOD of 5 pg mL<sup>-1</sup>. Inspired by this design, on the basis of CdSe/ZnS QDs, a novel iron oxide nanoparticle (IONP) was prepared and decorated by oleic acid. The CdSe/ZnS QDs were employed for the fluorescent signal amplification, while the IONPs were utilised to retain saturation magnetisation (Fig. 27.6b). The magnetic fluorescent beads (MFBs) were then synthesized with a highly fluorescent signal, and integrated into LFIA for AFB1 determination [13]. It was demonstrated that higher sensitivity was obtained with the LOD down to 3 pg mL<sup>-1</sup>. Moreover, nucleic acid aptamers, considered as “chemical antibodies”, possess high affinity and specificity that are similar to or even superior to antibodies. Accordingly, a novel ZnS QDs-based biosensor was established for the detection of AFB1 in peanuts via the specific aptamer recognition [55, 56]. In this work, ZnS-QDs were employed as the energy donors, while Ag nanocubes were used as the energy acceptors to produce fluorescence resonance energy transfer (FRET). When AFB1 was introduced, the conformational change of aptamer led to the release of the complementary strand DNA, which was modified on ZnS-QDs (Fig. 27.6c). The fluorescence signal was subsequently recovered. Compared to antibody-based immunoassay, enhanced analytical performance was achieved in this proposed aptasensor with high sensitivity (LOD = 2.67 pg mL<sup>-1</sup>).

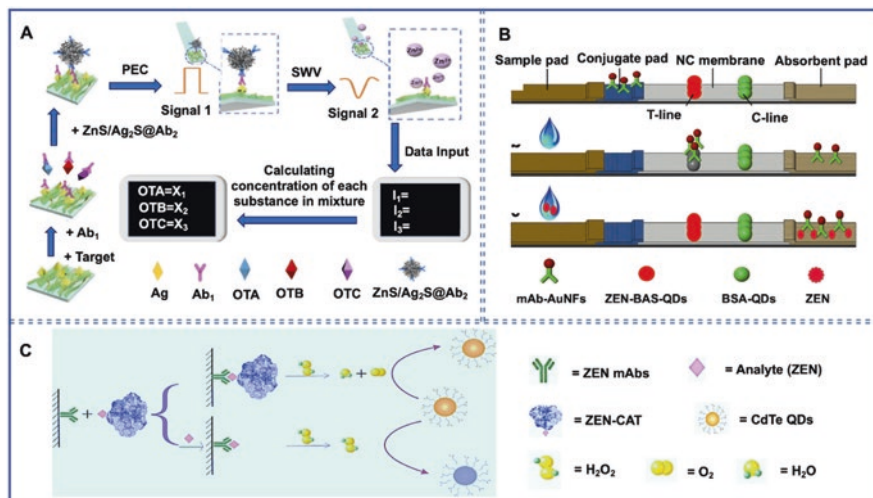
Based on a similar mechanism, CdTe QDs modified with the specific ochratoxin A (OTA) aptamer were utilised as the energy donors, and molybdenum disulphide (MoS<sub>2</sub>) was conjugated to quench the fluorescent signal produced by QDs (Fig. 27.6d). This proposed aptasensor was demonstrated to be sensitive and successfully applied for OTA determination in red wine [27]. Very recently, Qileng et al. reported an immunosensor for detection of ochratoxins in millet and maize combining MoS<sub>2</sub>-CdS with ZnS-Ag<sub>2</sub>S nanocages [34]. MoS<sub>2</sub>-CdS was prepared to immobilise antigens, and ZnS-Ag<sub>2</sub>S nanocages were employed to capture the



**Fig. 27.6** (a) Schematic illustration of fluorescent sensing of aflatoxin B1 based on CdSe/ZnS QDs and lateral flow immunoassay (LFIA). (Reprinted with permission from Ref. [23]. Copyright 2018: Royal Society of Chemistry). (b) Schematic diagram of fluorescent sensing of aflatoxin B1 based on CdSe/ZnS QDs and immunochromatographic assay (ICA). (Reprinted with permission from Ref. [13]. Copyright 2019: American Chemical Society). (c) Schematic illustration of FRET aptasensing of aflatoxin B1 based on ZnS QDs and Ag nanocubes. (Reprinted with permission from Ref. [55, 56]. Copyright 2021: Royal Society of Chemistry). (d) Schematic representation of fluorescent aptasensing of ochratoxin A using CdTe QDs and MoS<sub>2</sub> nanosheets. (Reprinted with permission from Ref. [27]. Copyright 2017: Elsevier)

antibody (Fig. 27.7a). The photoelectrochemical (PEC) signal and square wave voltammetric (SWV) signal were linear relationship with the levels of ochratoxins in the range of 1 ng L<sup>-1</sup> to 1 μg L<sup>-1</sup>. Their limits of detection were calculated to be 0.1 ng L<sup>-1</sup>, 0.5 ng L<sup>-1</sup> and 0.5 ng L<sup>-1</sup>, for OTA, OTB and OTC, respectively. Notably, this novel sensing platform provided a promising route for the analysis of mixture molecules.

Zearalenone (ZEN), a common mycotoxin in cereals, poses great hazards to agricultural products and food safety. For rapid response, even trace levels of ZEN [9], a novel LFIA platform was introduced for fluorimetric detection of ZEN based on CdSe QDs (Fig. 27.7b). Unlike fluorescent microspheres, the CdSe QDs were employed for the fluorescent quenching LFIA mechanism, which exhibited a sensitive and specific detection towards ZEN (LOD = 0.58 ng mL<sup>-1</sup>) in corn samples. For the improvement of detection sensitivity, the embedding of ZEN-labelled catalase in ELISA was used for H<sub>2</sub>O<sub>2</sub> reduction, and CdTe QDs were sensitive to H<sub>2</sub>O<sub>2</sub>. A fluorescent ELISA was then established for high sensitive analysis of ZEN



**Fig. 27.7** (a) Schematic diagram of the dual-signal immunosensing of ochratoxins based on ZnS/Ag<sub>2</sub>S. (Reprinted with permission from Ref. [34]. Copyright 2020: Elsevier). (b) Schematic illustration of fluorescent sensing of zearalenone (ZEN) based on CdSe QDs and lateral flow immunoassay (LFIA). (Reprinted with permission from Ref. [9]. Copyright 2019: Springer Nature). (c) Schematic diagram of fluorescent sensing of ZEN based on CdTe QDs and enzyme-linked immunosorbent assay (ELISA). (Reprinted with permission from Ref. [74]. Copyright 2016: Elsevier)

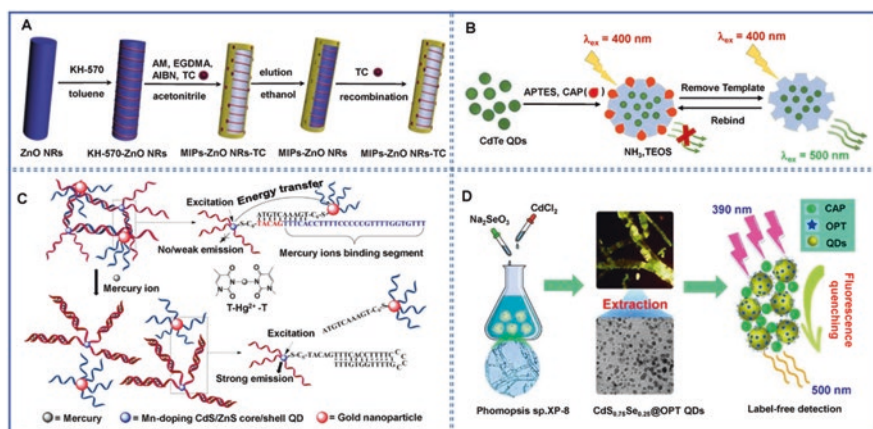
(Fig. 27.7c). Its limit of detection was calculated down to 4.1 pg mL<sup>-1</sup>, which was demonstrated nearly 140-fold improvement over the LFIA methods [74].

### 27.2.6 Detection of Other Analytes

Hydrogen peroxide (H<sub>2</sub>O<sub>2</sub>), one of the most important indicators in food industry, is widely used in food processing such as sterilising, bottling, transporting and packing instruments. However, excess levels of H<sub>2</sub>O<sub>2</sub> can cause the reduction of active components, and severe gastrointestinal disorders, as well as cellular damage, gene mutation, and even the cancer. Therefore, methods development for monitoring of H<sub>2</sub>O<sub>2</sub> levels in food is much in demand. A PVP-capped CoFe<sub>2</sub>O<sub>4</sub>@CdSe QDs core-shell magnetic composite was synthesized by one-pot co-precipitation approach via modifying the glassy carbon electrode surface simply by drop casting of its suspension on electrode surface [31]. The resulting nanosensor (CoFe<sub>2</sub>O<sub>4</sub>@CdSe QDs/RIF/GCE) exhibited an excellent catalytic activity on the electroreduction of H<sub>2</sub>O<sub>2</sub> attributed to the synergistic effect of CoFe<sub>2</sub>O<sub>4</sub>@CdSe QDs core-shell magnetic nanocomposite and RIF originating from the facile charge transfer between them. The proposed sensing platform was successfully applied to determine H<sub>2</sub>O<sub>2</sub> in milk and juice samples. Tetracycline (TC), a widely used and common antibiotic, posed severe hazards to milk and food upon its excessive use. To ensure food safety,

sensitive and selective sensing strategy for TC monitoring was of importance and urgency. Herein, a novel molecularly imprinted polymer captivity ZnO nanorods (NRs) was designed and synthesized for fluorescent sensing of TC [25]. Great performance was achieved via the formation of shield to decline the toxicity of ZnO and the fluorescence quenching for the selective signal determination (Fig. 27.8a), as well as the high sensitivity of  $1.02 \mu\text{mol L}^{-1}$ .

Heavy metal ion contamination in food was attracted more and more attention from scientists for decades owing to the great hazards towards humans. Notably, the occurrence of mercury (Hg) induced diverse toxic effects, including brain disease, kidney damage, as well as cognitive and physical disorders. In particular,  $\text{Hg}^{2+}$ , as the most common and stable mercury, was well studied since it possessed exciting water solubility. Accordingly, the Mn-doped CdS/ZnS QDs modified with single-stranded oligonucleotides (ssDNA) were prepared and employed as the fluorescent probe, while gold nanoparticles (Au NPs) decorated with complementary DNA were synthesized and used as the fluorescent quencher (Fig. 27.8c). In the absence of  $\text{Hg}^{2+}$ , the hybridisation of ssDNA into double-stranded DNA (ds DNA) caused that the fluorescent signal of CdS/ZnS QDs was quenched significantly. When  $\text{Hg}^{2+}$  existed, the conformational change of ssDNA was generated to form T-Hg<sup>2+</sup>-T structure, resulting in the release of complementary DNA and the recovery of the fluorescent signal [14]. The novel fluorescent sensing of  $\text{Hg}^{2+}$  was achieved with a limit of detection of 0.18 nM. Moreover, the integration of long-lifetime Mn-doped CdS/ZnS QDs was obviously reduced the background signal.



**Fig. 27.8** (a) Schematic representation of a novel molecularly imprinted polymer captivity ZnO nanorods (NRs) for fluorescent sensing of tetracycline (TC). (Reprinted with permission from Ref. [25]. Copyright 2020: Elsevier). (b) Schematic illustration of a fluorescent nanosensing for chloramphenicol (CAP) based on CdTe QDs and molecularly imprinted silica nanospheres. (Reprinted with permission from Ref. [4]. Copyright 2015: Wiley). (c) Schematic diagram of fluorescent sensing of  $\text{Hg}^{2+}$ , using Mn:CdS/ZnS QDs and Au NPs. (Reprinted with permission from Ref. [15]. Copyright 2012: American Chemical Society). (d) Schematic diagram of fluorescent sensing of CAP based on CdS<sub>x</sub>Se<sub>1-x</sub> QDs. (Reprinted with permission from Ref. [63]. Copyright 2020: American Chemical Society)



Chloramphenicol (CAP), one of the most broad-spectrum antibiotics, was extensively used for treating several infectious diseases. However, its severe side effects like aplastic anaemia and hypersensitivity in humans limit the wide applications. In particular, CAP was banned by European Commission in food-generating animals. Surprisingly, the utilisation of CAP was still well received in several countries due to its low cost, activity, as well as availability. Therefore, rapid, sensitive and selective analytical approaches for CAP monitoring in foods are of great importance and urgency. Owing to the excellent optical property, quantum dots (QDs) have attracted increasing interest in sensors and biosensors. Inspired by this knowledge, a fluorimetric sensing platform was established for detection of CAP in milk based on CdTe QDs (Fig. 27.8b). Notably, in this novel design [4], the molecularly imprinted silica nanospheres.

(SiO<sub>2</sub>@MIP) were integrated on CdTe QDs for preserving the fluorescence quantum yield. CAP, as a sensitive analyte probe, was observed to significantly quench the fluorescent signal produced by CdTe QDs via the electron transfer principle. The low limit of detection was measured to be 5.0 µg L<sup>-1</sup>. On the basis of this protocol, an in-depth investigation was made for the biological assembly of CdS<sub>x</sub>Se<sub>1-x</sub> QDs (Fig. 27.8d). It was found that the CdS<sub>0.75</sub>Se<sub>0.25</sub> QDs with diameter of 3.22 ± 0.07 nm possessed great water solubility and exciting fluorescent characteristics. Enlightened by this advance, the proposed CdS<sub>0.75</sub>Se<sub>0.25</sub> QDs were embedding to the fluorimetric sensor for the quantification of CAP in milk [63]. The detection sensitivity was improved over five-fold enhancement (LOD = 0.89 µg L<sup>-1</sup>). Consequently, quantum dots-based fluorescent sensing offers a promising trend towards label-free monitoring of antibiotics for food safety.

### 27.3 Challenges and Limitations

II–VI semiconducting nanomaterials-based sensors and biosensors are continuously attracted increasing attention from scientists for food safety hazard detection. As indicated in Table 27.1, the recent advances in II–VI semiconducting nanomaterials-based sensors and biosensors for food safety hazards were introduced and summarised. Although the great performance was achieved for targets analysis like glucose, vitamin, pathogenic bacteria, pesticides, metal ions, as well as mycotoxins, etc. There are still following vital challenges and limitations: (i) The exploration of more advanced nanomaterials for the construction of biosensors and sensor devices with the properties of high sensitivity, low cost, ease of use, and long life, which relies on the materials size, morphology, surface area, semiconducting band gap, optical activity, and chemical properties. (ii) For real sample analysis, especially for complex matrix like food, when nanomaterials existed, the interference of other substances for biosensor performance should be taken into account due to their interaction with the nanomaterials. (iii) Given the toxicity reaction, potential risk and safety issues of nanomaterials, toxicity evaluation should be required related to the size, morphology, surface charge and area, and composition. By this, environment-friendly nanomaterials-based biosensors are preferable. (iv) Nanomaterials like CdS, CdSe, CdTe integrated biosensors

**Table 27.1** Summary of II–VI semiconducting nanomaterials (NMs) based biosensors for the detection of food hazards

II–VI NMs composition	Detection methods	Transduction principle	Target	Dynamic Range	LOD	Samples	References
CdS	PEC	Graphene/CdS nanomaterials	GSH	0.01–1.5 mM	0.003 mM	Drug isethion	[78]
CdS	PEC	Methyl viologen-coated CdS QDs and light irradiation	Cysteine	0.2–2.8 $\mu$ M	0.1 $\mu$ M	NR	[26]
ZnO@CdS	EPCA	ZnO@CdS nanocomposite for degradation and removal of pesticides	Pesticides	NR	Quantitative removal of pesticides (89–91%)	NR	[36]
ZnO	PEC	Free-base-porphyrin-functionalised ZnO NMs and indium tin oxide (ITO) electrode	Cysteine	0.6–157 $\mu$ mol L <sup>-1</sup>	0.2 $\mu$ mol L <sup>-1</sup>	NR	[45]
ZnO	FL	ZnO QDs	Cysteine	0.1–600 $\mu$ M	0.642 $\mu$ M	Bovine serum albumin (BSA) and tap water	[21]
ZnO	ISABG	ZnO@ZnHCF nanomaterials for BPA degradation	BPA	NR	Half-life of BPA up to 2.8 h	NR	[35]
ZnO	FL	Molecularly imprinted polymer captivity ZnO nanorods (NRs)	TC	5.0–120 $\mu$ mol·L <sup>-1</sup>	1.02 $\mu$ mol L <sup>-1</sup>	Water	[25]
ZnO	PEC	ZnO nanocomposite-based molecular imprinting (MIP)	AM	10 <sup>-1</sup> to 2.5 $\times$ 10 <sup>-9</sup> M	2.147 $\times$ 10 <sup>-9</sup> M	Potato chips and biscuits	[80, 81]
CdS <sub>0.75</sub> Se <sub>0.25</sub>	FL	CdS <sub>0.75</sub> Se <sub>0.25</sub> @oligopeptide transporter	CAP	3.13–500 $\mu$ g L <sup>-1</sup>	0.89 $\mu$ g L <sup>-1</sup>	Milk	[63]

(continued)

Table 27.1 (continued)

II-VI NMs composition	Detection methods	Transduction principle	Target	Dynamic Range	LOD	Samples	References
CdSe	FL	CdSe QDs and fluorescent quenching lateral flow assay (LFIA)	ZEN	0.78 to 25 ng mL <sup>-1</sup>	0.58 ng mL <sup>-1</sup>	Corn	[9]
CdSe	FL	CdSe QDs and high luminance with photostability	<i>Staphylococcus aureus</i>	NR	8.94 ng mL <sup>-1</sup>	NR	Xiong et al. (2020)
CdSe	EC	PVP-capped CoFe <sub>2</sub> O <sub>4</sub> @CdSe QDs	H <sub>2</sub> O <sub>2</sub>	7–145 μM and 0.145–1.43 mM	0.38 μM	Milk and juice samples	[31]
CdSe	ECL	Tris (2,2'-bipyridyl) ruthenium(II) complex coupled with CdSe QDs	TMA	1 × 10 <sup>-12</sup> to 1 × 10 <sup>-7</sup> M	2.09 × 10 <sup>-13</sup> M	Fish	[33]
CdSe/ZnS	FL	CdSe/ZnS QDs combined with oligonucleotide microarray	<i>E. coli</i>	NR	10 CFU mL <sup>-1</sup>	Mock-contaminated food samples	[16]
CdSe/ZnS	FL	CdSe/ZnS QDs combined with lateral flow immunoassay (LFIA)	AFB1	0.001–10 ng mL <sup>-1</sup>	0.005 ng mL <sup>-1</sup>	Rice and peanuts	[23]
CdSe/ZnS	FL	CdSe/ZnS QDs and oleic acid-modified iron oxide nanoparticles (OA-IONPs)	AFB1	5–150 pg mL <sup>-1</sup>	3 pg mL <sup>-1</sup>	Sauce extract	[13]
CdSe/ZnS	FL	CdSe/ZnS@SiO <sub>2</sub> nanoparticles	<i>S. typhi</i>	6.6 × 10 <sup>2</sup> to 6.6 × 10 <sup>4</sup> CFU mL <sup>-1</sup>	3.3 × 10 <sup>2</sup> CFU mL <sup>-1</sup>	Different stains	[51]
CdSe/ZnS	FL	CdSe/ZnS QDs and colorimetric-fluorescent-magnetic nanospheres (CFMNs)	<i>S. typhi</i>	1.88 × 10 <sup>4</sup> to 1.88 × 10 <sup>7</sup> CFU mL <sup>-1</sup>	3.5 × 10 <sup>3</sup> CFU mL <sup>-1</sup>	Milk	[14]

ZnS	FL	ZnS-QDs-based fluorescence resonance energy transfer (FRET)	AFB1	5 pg mL <sup>-1</sup> –300 ng mL <sup>-1</sup>	2.67 pg mL <sup>-1</sup>	Peanut	[55, 56]
ZnS	PEC	MoS <sub>2</sub> -CdS with ZnS-Ag <sub>2</sub> S nanocages	OTs	1 ng L <sup>-1</sup> to 1 μg L <sup>-1</sup>	0.1 ng L <sup>-1</sup> , 0.5 ng L <sup>-1</sup> , and 0.5 ng L <sup>-1</sup> , for OTA, OTB, and OTC	Millet and maize	[34]
CdS/ZnS	FL	Mn:CdS/ZnS QDs and Au NPs	Hg <sup>2+</sup>	0 to 1 × 10 <sup>-9</sup> M	0.18 nM	Water	[15]
CdTe	FL	CdTe QDs and Molybdenum disulphide (MoS <sub>2</sub> ) nanosheet	OTA	1–1000 ng mL <sup>-1</sup>	1 ng mL <sup>-1</sup>	Red wine	[27]
CdTe	FL	CdTe QDs and fluorescent enzyme-linked immunosorbent assay (ELISA)	ZEN	2.4 pg mL <sup>-1</sup> –1.25 ng mL <sup>-1</sup>	4.1 pg mL <sup>-1</sup>	Corn	[74]
CdTe	FL	CdTe@SiO <sub>2</sub> @MIP nanoparticles	CAP	40–500 μg L <sup>-1</sup>	5 μg L <sup>-1</sup>	Milk	[4]
CdTe	FL	Tb/CdTe QDs and smartphone colour recogniser	Norflloxacin (NFX)	0–1200 nM	6.03 nM	Honey/water	[20]
CdTe	FIA	CdTe QDs-based competitive fluoroimmunoassay	2,4-D	250–1000 pg mL <sup>-1</sup>	250 pg mL <sup>-1</sup>	Phosphate-buffered solution	[49]

*EC* electrochemical, *ECL* electrochemiluminescence, *EPCA* enhanced photocatalytic activity, *FL* fluorescent, *FIA* fluoroimmunoassay, *ISABG* improved surface area and band gap, *LOD* Limit of detection, *NR* not reported; *PEC* photoelectrochemical, *AFB1* aflatoxin B1, *OTA* ochratoxin A, *ZEN* zearalenone, *CAP* chloramphenicol, *2,4-D* 2,4-dichlorophenoxyacetic acid, *TMA* trimethylamine, *TC* Tetracycline, *AM* acrylamide, *BPA* Bisphenol A, *GSH* glutathione, *E. coli* *Escherichia coli*, *ELISA* enzyme-linked immunosorbent assay, *FRET* fluorescence resonance energy transfer, *CFMNs* colorimetric-fluorescent-magnetic nanospheres, *QDs* quantum dots

proved to be highly expensive, especially for large-scale application or clinical analysis. Therefore, the researchers should take the cost into consideration for nanobiosensing development. (v) Biosensor development for point-of-care (POC) testing devices is the future trend for portable, and high-throughput analysis of food safety hazards. For decades' efforts, the most successful examples like personal glucose metres (PGM) or smartphones have been widely used for food field. Therefore, focusing on these advanced nanomaterials for POC biosensing devices would open a new insights and transfer them to the market.

## 27.4 Conclusions and Future Trends

Food safety issue, a cause of global concern, imposed severe hazards on human health. Therefore, the establishment of simple, sensitive, and reliable sensing platform against analytes determination in food safety was much in demand. Biosensors coupled with II–VI semiconducting nanomaterials displayed unique advantages such as rapid response, improved sensitivity and selectivity, enhancing sensing performance, as well as the versatile platform for food analysis. This book chapter was systematically introduced and discussed the application of II–VI semiconducting nanomaterials-based sensors and biosensors for detection of food hazards targets in recent years. Furthermore, future research direction will focus on the advanced integrated nanocomposites for the practical application in food safety field and the transition of biosensors platform to the market.

**Acknowledgements** This work was supported by the Special Fund for Agro-scientific Research in the Public Interest (201403071), the National Natural Science Foundation of China (No. 21305158), Modern Agro-Industry Technology Research System of the PR China (CARS-36). We thank the University of Liège-Gembloux Agro-Bio Tech and more specifically the research platform Agriculture Is Life for the funding of the scientific stay in Belgium that made this paper possible.

**Author Contributions** This work proposed in this book chapter was carried out in collaboration with all the authors. X.D.G. and M.K.Z. proposed the idea of the work, wrote the original paper and analysed the background, literatures, and materials. M.L.F. and J.Q.W. supported the structure and revised the book chapter.

## References

1. Agarwal C, Csóka L. Functionalization of wood/plant-based natural cellulose fibers with nanomaterials: a review. *TAPPI J.* 2018;17(2):92–111. <https://doi.org/10.32964/tj17.02.92>.
2. Albalghiti E, Stabryla LM, Gilbertson LM, Zimmerman JB. Towards resolution of antibacterial mechanisms in metal and metal oxide nanomaterials: a meta-analysis of the influence of study design on mechanistic conclusions. *Environ Sci Nano.* 2021;8(1):37–66. <https://doi.org/10.1039/d0en00949k>.

3. Aminloo ES, Montazer M. Clean sono-synthesis of ZnO on cotton/nylon fabric using dopamine: photocatalytic, hydrophilic, antibacterial features. *Fibers Polym.* 2021;22(1):97–108. <https://doi.org/10.1007/s12221-021-9237-4>.
4. Amjadi M, Jalili R, Manzoori J. A sensitive fluorescent nanosensor for chloramphenicol based on molecularly imprinted polymer-capped CdTe quantum dots. *Luminescence.* 2015;31:633–9. <https://doi.org/10.1002/bio.3003>.
5. Arshad E, Anas A, Asok A, Jasmin C, Pai SS, Singh IB, et al. Fluorescence detection of the pathogenic bacteria *Vibrio harveyi* in solution and animal cells using semiconductor quantum dots. *RSC Adv.* 2016;6(19):15686–93. <https://doi.org/10.1039/c5ra24161h>.
6. Azmy NAN, Bakar AAA, Arsad N, Idris S, Mohamad AR, Hamid AA. Enhancement of ZnO-rGO nanocomposite thin films by gamma radiation for *E. coli* sensor. *Appl Surf Sci.* 2017;392:1134–43. <https://doi.org/10.1016/j.apsusc.2016.09.144>.
7. Chaudhary P, Fatima F, Kumar A. Relevance of nanomaterials in food packaging and its advanced future prospects. *J Inorg Organomet Polym Mater.* 2020;30(12):5180–92. <https://doi.org/10.1007/s10904-020-01674-8>.
8. Chauhan N, Saxena K, Tikadar M, Jain U. Recent advances in the design of biosensors based on novel nanomaterials: an insight. *Nanotechnol Precis Eng.* 2021;4(4):045003. <https://doi.org/10.1063/1.50006524>.
9. Chen Y, Fu Q, Xie J, Wang H, Tang Y. Development of a high sensitivity quantum dot-based fluorescent quenching lateral flow assay for the detection of zearalenone. *Anal Bioanal Chem.* 2019;411:2169–75. <https://doi.org/10.1007/s00216-019-01652-1>.
10. Chikte RG, Paknikar KM, Rajwade JM, Sharma J. Nanomaterials for the control of bacterial blight disease in pomegranate: quo vadis? *Appl Microbiol Biotechnol.* 2019;103(11):4605–21. <https://doi.org/10.1007/s00253-019-09740-z>.
11. Demirkol DO, Timur S. A sandwich-type assay based on quantum dot/aptamer bioconjugates for analysis of *E. coli* O157: H7 in microtiter plate format. *Int J Polym Mater Polym Biomater.* 2016;65(2):85–90. <https://doi.org/10.1080/00914037.2015.1074906>.
12. Díez-Pascual AM. Sustainable green nanocomposites from bacterial bioplastics for food-packaging applications. In: *Handbook of composites from renewable materials, Nanocomposites: advanced applications, vol. 8.* Hoboken: Wiley; 2017. p. 229.
13. Guo L, Shao Y, Duan H, Ma W, Leng Y, Huang X, et al. Magnetic quantum dot Nanobead-based fluorescent immunochromatographic assay for the highly sensitive detection of aflatoxin B1 in dark soy sauce. *Anal Chem.* 2019;91(7):4727–34. <https://doi.org/10.1021/acs.analchem.9b00223>.
14. Hu J, Jiang YZ, Tang M, Wu LL, Xie HY, Zhang ZL, et al. Colorimetric-fluorescent-magnetic nanosphere-based multimodal assay platform for *Salmonella* detection. *Anal Chem.* 2018;91(1):1178–84. <https://doi.org/10.1021/acs.analchem.8b05154>.
15. Huang D, Niu C, Wang X, Lv X, Zeng G. “Turn-on” fluorescent sensor for Hg<sup>2+</sup> based on single-stranded DNA functionalized Mn:CdS/ZnS quantum dots and gold nanoparticles by time-gated mode. *Anal Chem.* 2013;85:1164–70. <https://doi.org/10.1021/ac303084d>.
16. Huang A, Qiu Z, Jin M, Shen Z, Chen Z, Wang X, et al. High-throughput detection of food-borne pathogenic bacteria using oligonucleotide microarray with quantum dots as fluorescent labels. *Int J Food Microbiol.* 2014;185:27–32. <https://doi.org/10.1016/j.ijfoodmicro.2014.05.012>.
17. Ji X, Zheng J, Xu J, Rastogi VK, Cheng TC, DeFrank JJ, et al. (CdSe)ZnS quantum dots and organophosphorus hydrolase bioconjugate as biosensors. *J Phys Chem B.* 2005;109:3793–9. <https://doi.org/10.1021/jp044928f>.
18. Jia M, Jia B, Liao X, Shi L, Zhang Z, Liu M, et al. A CdSe@CdS quantum dots based electrochemiluminescence aptasensor for sensitive detection of ochratoxin A. *Chemosphere.* 2022;287:131994. <https://doi.org/10.1016/j.chemosphere.2021.131994>.
19. Jiang Q, Zhang D, Cao Y, Gan N. An antibody-free and signal-on type electrochemiluminescence sensor for diethylstilbestrol detection based on magnetic molecularly imprinted polymers-quantum dots labeled aptamer conjugated probes. *J Electroanal Chem.* 2017;789:1–8. <https://doi.org/10.1016/j.jelechem.2017.02.020>.

20. Jiang R, Lin D, Zhang Q, Li L, Yang L. Multiplex chroma-response based fluorescent smart-phone sensing platform for rapid and visual quantitative determination of antibiotic residues. *Sensors Actuators B Chem.* 2022;350:130902. <https://doi.org/10.1016/j.snb.2021.130902>.
21. Kamaci UD, Kamaci M. Selective and sensitive ZnO quantum dots based fluorescent biosensor for detection of cysteine. *J Fluoresc.* 2021;31(2):401–14. <https://doi.org/10.1007/s10895-020-02671-3>.
22. Leonard P, Hearty S, Brennan J, Dunne L, Quinn J, Chakraborty T, et al. Advances in biosensors for detection of pathogens in food and water. *Enzym Microb Technol.* 2003;32:3–13. [https://doi.org/10.1016/S0141-0229\(02\)00232-6](https://doi.org/10.1016/S0141-0229(02)00232-6).
23. Li J, Mao M, Wu F, Li Q, Wei L, Ma L. Amino-functionalized CdSe/ZnS quantum dot-based lateral flow immunoassay for sensitive detection of aflatoxin B1. *Anal Methods.* 2018;10(29):3582–8. <https://doi.org/10.1039/c8ay00608c>.
24. Liao BY, Chang CJ, Wang CF, Lu CH, Chen JK. Controlled antibody orientation on Fe<sub>3</sub>O<sub>4</sub> nanoparticles and CdTe quantum dots enhanced sensitivity of a sandwich-structured electro-generated chemiluminescence immunosensor for the determination of human serum albumin. *Sensors Actuators B Chem.* 2021;336:129710. <https://doi.org/10.1016/j.snb.2021.129710>.
25. Liu X, Zhou Z, Wang T, Xu Y, Lu K, Yan Y. Molecularly imprinted polymers-captivity ZnO nanorods for sensitive and selective detecting environmental pollutant. *Spectrochim Acta A Mol Biomol Spectrosc.* 2020;228:117785. <https://doi.org/10.1016/j.saa.2019.117785>.
26. Long YT, Kong C, Li DW, Li Y, Chowdhury S, Tian H. Ultrasensitive determination of cysteine based on the photocurrent of nafion-functionalized CdS-MV quantum dots on an ITO electrode. *Small.* 2011;7(12):1624–8. <https://doi.org/10.1002/sml.201100427>.
27. Lu Z, Chen X, Hu W. A fluorescence aptasensor based on semiconductor quantum dots and MoS<sub>2</sub> nanosheets for ochratoxin A detection. *Sensors Actuators B Chem.* 2017;246:61–7. <https://doi.org/10.1016/j.snb.2017.02.062>.
28. Luo L, Liu X, Ma S, Li L, You T. Quantification of zearalenone in mildewing cereal crops using an innovative photoelectrochemical aptamer sensing strategy based on ZnO-NGQDs composites. *Food Chem.* 2020;322:126778. <https://doi.org/10.1016/j.foodchem.2020.126778>.
29. Marandi M, Nazari M. Application of TiO<sub>2</sub> hollow spheres and ZnS/SiO<sub>2</sub> double-passivating layers in the photoanode of the CdS/CdSe QDs sensitized solar cells for the efficiency enhancement. *Sol Energy.* 2021;216:48–60. <https://doi.org/10.1016/j.solener.2020.11.057>.
30. Mohan D, Pathak A, Resmi PE, Suneesh PV, Babu TS. Fluorescence imaging of E. coli using CdSe quantum dots. In: IOP conference series: materials science and engineering, vol. 577(1). IOP Publishing; 2019. p. 012107.
31. Mollarasouli F, Kurbanoglu S, Asadpour-Zeynali K, Ozkan SA. Non-enzymatic monitoring of hydrogen peroxide using novel nanosensor based on CoFe<sub>2</sub>O<sub>4</sub>@CdSeQD magnetic nanocomposite and rifampicin mediator. *Anal Bioanal Chem.* 2020;412(21):5053–65. <https://doi.org/10.1007/s00216-019-02306-y>.
32. Nazari A. Preparation of electroconductive, antibacterial, photoactive cotton fabric through green synthesis of ZnO/reduced graphene oxide nanocomposite. *Fibers Polym.* 2019;20(12):2618–24. <https://doi.org/10.1007/s12221-019-9180-9>.
33. Praoobon N, Siriket S, Taokaenchan N, Kuimalee S, Phaisansuthichol S, Pookmanee P, Satienerakul S. Paper-based electrochemiluminescence device for the rapid estimation of trimethylamine in fish via the quenching effect of thioglycolic acid-capped cadmium selenide quantum dots. *Food Chem.* 2022;366:128066. <https://doi.org/10.1016/j.foodchem.2021.130590>.
34. Qileng A, Liang H, Huang S, Liu W, Xu Z, Liu Y. Dual-function of ZnS/Ag<sub>2</sub>S nanocages in ratiometric immunosensors for the discriminant analysis of ochratoxins: Photoelectrochemistry and electrochemistry. *Sensors Actuators B Chem.* 2020;314:128066. <https://doi.org/10.1016/j.snb.2020.128066>.
35. Rani M, Shanker U. Insight in to the degradation of bisphenol A by doped ZnO@ZnHCF nanocubes: high photocatalytic performance. *J Colloid Interface Sci.* 2018;530:16–28. <https://doi.org/10.1016/j.jcis.2018.06.070>.

36. Rani M, Yadav J, Keshu, Shanker U. Green synthesis of sunlight responsive zinc oxide coupled cadmium sulfide nanostructures for efficient photodegradation of pesticides. *J Colloid Interface Sci.* 2021;601:689–703. <https://doi.org/10.1016/j.jcis.2021.05.152>.
37. Roushani M, Ghanbari K. A novel aptasensor based on gold nanorods/ZnS QDs-modified electrode for evaluation of streptomycin antibiotic. *Anal Methods.* 2018;10(43):5197–204. <https://doi.org/10.1039/c8ay01815d>.
38. Sai-Anand G, Sivanesan A, Benzigar MR, Singh G, Gopalan AI, Baskar AV, et al. Recent progress on the sensing of pathogenic bacteria using advanced nanostructures. *Bull Chem Soc Jpn.* 2019;92(1):216–44. <https://doi.org/10.1246/bcsj.20180280>.
39. Satpathy G, Chandra GK, Manikandan E, Mahapatra DR, Umaphathy S. Pathogenic *Escherichia coli* (*E. coli*) detection through tuned nanoparticles enhancement study. *Biotechnol Lett.* 2020;42(5):853–63. <https://doi.org/10.1007/s10529-020-02835-y>.
40. Shan Y, Zhang HL, Zhu Y, Wang Y, Song H, Shi C. Electrochemiluminescent CdTe nanocrystal/reduced graphene oxide composite films for the detection of diethylstilbestrol. *ACS Appl Nano Mater.* 2020;3(5):4670–80. <https://doi.org/10.1021/acsanm.0c00670>.
41. Shen H, Qileng A, Yang H, Liang H, Zhu H, Liu Y, et al. “Dual-signal-on” integrated-type biosensor for portable detection of miRNA: Cas12a-induced photoelectrochemistry and fluorescence strategy. *Anal Chem.* 2021;93(34):11816–25. <https://doi.org/10.1021/acs.analchem.1c02395>.
42. Tan J, Guo M, Tan L, Geng Y, Huang S, Tang Y, et al. Highly efficient fluorescent QDs sensor for specific detection of protein through double recognition of hybrid aptamer-molecular imprinted polymers. *Sensors Actuators B Chem.* 2018;274:627–35. <https://doi.org/10.1016/j.snb.2018.07.126>.
43. Tang T, Deng J, Zhang M, Shi G, Zhou T. Quantum dot-DNA aptamer conjugates coupled with capillary electrophoresis: a universal strategy for ratiometric detection of organophosphorus pesticides. *Talanta.* 2016;146:55–61. <https://doi.org/10.1016/j.talanta.2015.08.023>.
44. Tayebi M, Tavakkoli Yarak M, Ahmadi M, Mogharei A, Tahriri M, Vashae D, et al. Synthesis, surface modification and optical properties of thioglycolic acid-capped ZnS quantum dots for starch recognition at ultralow concentration. *J Electron Mater.* 2016;45(11):5671–8. <https://doi.org/10.1007/s11664-016-4792-y>.
45. Tu W, Lei J, Wang P, Ju H. Photoelectrochemistry of free-base-porphyrin-functionalized zinc oxide nanoparticles and their applications in biosensing. *Chemistry.* 2011;17(34):9440–7. <https://doi.org/10.1002/chem.201100577>.
46. Vaishnav SK, Korram J, Nagwanshi R, Ghosh KK, Satnami ML. Mn<sup>2+</sup> doped- CdTe/ZnS modified fluorescence nanosensor for detection of glucose. *Sensors Actuators B Chem.* 2017;245:196–204. <https://doi.org/10.1016/j.snb.2017.01.118>.
47. Van Duy L, Nguyen TT, Hung CM, Le DTT, Van Duy N, Hoa ND, et al. Ultrasensitive NO<sub>2</sub> gas sensing performance of two dimensional ZnO nanomaterials: Nanosheets and nanoplates. *Ceram Int.* 2021;47(20):28811–20. <https://doi.org/10.1016/j.ceramint.2021.07.042>.
48. Van MN, Li W, Sheng P, Van HP, Cai Q. Photoelectrochemical label-free immunoassay of octachlorostyrene based on heterogeneous CdSe/CdS/Pt/TiO<sub>2</sub> nanotube array. *J Electroanal Chem.* 2015;736:69–75. <https://doi.org/10.1016/j.jelechem.2014.10.033>.
49. Vinayaka AC, Basheer S, Thakur MS. Bioconjugation of CdTe quantum dot for the detection of 2,4-dichlorophenoxyacetic acid by competitive fluoroimmunoassay based biosensor. *Biosens Bioelectron.* 2009;24(6):1615–20. <https://doi.org/10.1016/j.bios.2008.08.042>.
50. Viter R, Savchuk M, Riekstina U, Poletaev N, Pleiko K, Ramanavicius A. Photoluminescence ZnO nanorod biosensors for medical and food safety applications. In: 2017 IEEE 7th international conference nanomaterials: application & properties (NAP). IEEE, 04NB16-1-04NB16-3; 2017.
51. Wang R, Xu Y, Jiang Y, Chuan N, Su X, Ji J. Sensitive quantification and visual detection of bacteria using CdSe/ZnS@SiO<sub>2</sub> nanoparticles as fluorescent probes. *Anal Methods.* 2014;6:6802–8. <https://doi.org/10.1039/c4ay01257g>.



52. Wang Y, Si B, Lu S, Liu E, Hu X, Fan J. Near-infrared excitation of CdTe quantum dots based on fluorescence resonance energy transfer and their use as fluorescent sensors. *Sensors Actuators B Chem.* 2017;246:127–35. <https://doi.org/10.1016/j.snb.2017.02.069>.
53. Wang S, Liu R, Li C. Highly selective and sensitive detection of Hg<sup>2+</sup> based on Förster resonance energy transfer between CdSe quantum dots and g-C<sub>3</sub>N<sub>4</sub> Nanosheets. *Nanoscale Res Lett.* 2018;13(1):1–7. <https://doi.org/10.1186/s11671-018-2647-6>.
54. Wang SN, Zhu J, Li X, Li JJ, Zhao JW. Fluorescence turn-on sensing of trace cadmium ions based on EDTA-etched CdTe@CdS quantum dot. *Spectrochim Acta A Mol Biomol Spectrosc.* 2018;201:119–27. <https://doi.org/10.1016/j.saa.2018.04.065>.
55. Wang Y, Li W, Hu X, Zhang X, Huang X, Li Z, et al. Efficient preparation of dual-emission ratiometric fluorescence sensor system based on aptamer-composite and detection of bis(2-ethylhexyl) phthalate in pork. *Food Chem.* 2021;352:129352. <https://doi.org/10.1016/j.foodchem.2021.129352>.
56. Wang C, Zhang W, Qian J, Wang L, Ren Y, Wang Y, et al. A FRET aptasensor for sensitive detection of aflatoxin B1 based on a novel donor-acceptor pair between ZnS quantum dots and Ag nanocubes. *Anal Methods.* 2021;13(4):462–8. <https://doi.org/10.1039/d0ay02017f>.
57. Wei J, Hu Q, Gao Y, Hao N, Qian J, Wang K. A multiplexed self-powered dual-photoelectrode biosensor for detecting dual analytes based on an electron-transfer-regulated conversion strategy. *Anal Chem.* 2021;93(15):6214–22. <https://doi.org/10.1021/acs.analchem.1c00503>.
58. Wong A, Santos AM, Cincotto FH, Moraes FC, Fatibello-Filho O, Sotomayor MD. A new electrochemical platform based on low cost nanomaterials for sensitive detection of the amoxicillin antibiotic in different matrices. *Talanta.* 2020;206:120252. <https://doi.org/10.1016/j.talanta.2019.120252>.
59. Xia H, He G, Peng J, Li W, Fang Y. Preparation and fluorescent sensing applications of novel CdSe-chitosan hybrid films. *Appl Surf Sci.* 2010;256(23):7270–5. <https://doi.org/10.1016/j.apsusc.2010.05.063>.
60. Xia H, Peng M, Li N, Liu L. CdSe quantum dots-sensitized FRET system for ciprofloxacin detection. *Chem Phys Lett.* 2020;740:137085. <https://doi.org/10.1016/j.cplett.2019.137085>.
61. Xiong LH, Cui R, Zhang ZL, Yu X, Xie Z, Shi YB, et al. Uniform fluorescent nanobioprobes for pathogen detection. *ACS Nano.* 2014;8:5116–24. <https://doi.org/10.1021/nn501174g>.
62. Xu R, Lu P, Wu B, Wang X, Pang X, Du B, et al. Using SiO<sub>2</sub>/PDA-Ag NPs to dual-inhibited photoelectrochemical activity of CeO<sub>2</sub>-CdS composites fabricated a novel immunosensor for BNP ultrasensitive detection. *Sensors Actuators B Chem.* 2018;274:349–55. <https://doi.org/10.1016/j.snb.2018.07.122>.
63. Xu X, Yang Y, Jin H, Pang B, Yang R, Yan L, et al. Fungal in situ assembly gives novel properties to Cd<sub>3</sub>Se<sub>1-x</sub> quantum dots for sensitive label-free detection of chloramphenicol. *ACS Sustain Chem Eng.* 2020;8:6806–14. <https://doi.org/10.1021/acssuschemeng.0c01698>.
64. Yan X, Li H, Han X, Su X. A ratiometric fluorescent quantum dots based biosensor for organophosphorus pesticides detection by inner-filter effect. *Biosens Bioelectron.* 2015;74:277–83. <https://doi.org/10.1016/j.bios.2015.06.020>.
65. Yan W, Xu H, Ling M, Zhou S, Qiu T, Deng Y, et al. MOF-derived porous hollow Co<sub>3</sub>O<sub>4</sub>@ZnO cages for high-performance MEMS trimethylamine sensors. *ACS Sens.* 2021;6(7):2613–21. <https://doi.org/10.1021/acssensors.1c00315>.
66. Yang P, Chen C, Wang D, Ma H, Du Y, Cai D, et al. Kinetics, reaction pathways, and mechanism investigation for improved environmental remediation by 0D/3D CdTe/Bi<sub>2</sub>WO<sub>6</sub> Z-scheme catalyst. *Appl Catal B Environ.* 2021;285:119877. <https://doi.org/10.1016/j.apcatb.2021.119877>.
67. You J, Ma L, He Y, Ge Y, Song G, Zhou J. ZnSe:Mn/ZnS quantum dots for the detection of microcystin by room temperature phosphorescence immunoassay. *Micro Nano Lett.* 2019;14(8):892–6. <https://doi.org/10.1049/mnl.2018.5690>.
68. Young SJ, Lai LT, Tang WL. Improving the performance of pH sensors with one-dimensional ZnO nanostructures. *IEEE Sensors J.* 2019;19(23):10972–6. <https://doi.org/10.1109/JSEN.2019.2932627>.

69. Young SJ, Chu YJ, Chen YL. Enhancing pH sensors performance of ZnO Nanorods with au nanoparticles adsorption. *IEEE Sensors J.* 2021;21(12):13068–73. <https://doi.org/10.1109/JSEN.2021.3062857>.
70. Yu Z, Huang L, Chen J, Li M, Tang D. Graded oxygen-doped CdS electrode for portable photoelectrochemical immunoassay of alpha-fetoprotein coupling with a digital multimeter read-out. *Sensors Actuators B Chem.* 2021;343:130136. <https://doi.org/10.1016/j.snb.2021.130136>.
71. Yu J, Lin J, Li J. A photoelectrochemical sensor based on an acetylcholinesterase-CdS/ZnO-modified extended-gate field-effect transistor for glyphosate detection. *Analyst.* 2021;146(14):4595–604. <https://doi.org/10.1039/d1an00797a>.
72. Yuan X, Zhang D, Zhu X, Liu H, Sun B. Triple-dimensional spectroscopy combined with chemometrics for the discrimination of pesticide residues based on ionic liquid-stabilized Mn-ZnS quantum dots and covalent organic frameworks. *Food Chem.* 2021;342:128299. <https://doi.org/10.1016/j.foodchem.2020.128299>.
73. Yue HY, Zhang HJ, Huang S, Lu XX, Gao X, Song SS, et al. Highly sensitive and selective dopamine biosensor using Au nanoparticles-ZnO nanocone arrays/graphene foam electrode. *Mater Sci Eng C.* 2020;108:110490. <https://doi.org/10.1016/j.msec.2019.110490>.
74. Zhan S, Huang X, Chen R, Li J, Xiong Y. Novel fluorescent ELISA for the sensitive detection of zearalenone based on H<sub>2</sub>O<sub>2</sub>-sensitive quantum dots for signal transduction. *Talanta.* 2016;158:51–6. <https://doi.org/10.1016/j.talanta.2016.05.035>.
75. Zhang F, Liu B, Sheng W, Zhang Y, Liu Q, Li S, et al. Fluoroimmunoassays for the detection of zearalenone in maize using CdTe/CdS/ZnS quantum dots. *Food Chem.* 2018;255:421–8. <https://doi.org/10.1016/j.foodchem.2018.02.060>.
76. Zhang H, Jin Q, Song X, Li H, Jia D, Liu T. Oxazine-functionalized CdSe/ZnS quantum dots for photochemical pH sensing. *ACS Appl Nano Mater.* 2020;3(11):10996–1006. <https://doi.org/10.1021/acsanm.0c02219>.
77. Zhang C, Zhou L, Peng J. Blue-light photoelectrochemical aptasensor for kanamycin based on synergistic strategy by Schottky junction and sensitization. *Sensors Actuators B Chem.* 2021;340:129898. <https://doi.org/10.1016/j.snb.2021.129898>.
78. Zhao X, Zhou S, Shen Q, Jiang LP, Zhu JJ. Fabrication of glutathione photoelectrochemical biosensor using graphene-CdS nanocomposites. *Analyst.* 2012;137(16):3697–703. <https://doi.org/10.1039/c2an35658a>.
79. Zhao Y, Tan L, Gao X, Jie G, Huang T. Silver nanoclusters-assisted ion-exchange reaction with CdTe quantum dots for photoelectrochemical detection of adenosine by target-triggering multiple-cycle amplification strategy. *Biosens Bioelectron.* 2018;110:239–45. <https://doi.org/10.1016/j.bios.2018.03.069>.
80. Zhao B, Deng S, Li J, Sun C, Fu Y, Liu Z. Green synthesis, characterization and antibacterial study on the catechin-functionalized ZnO nanoclusters. *Mater Res Express.* 2021;8(2):025006. <https://doi.org/10.1088/2053-1591/abe255>.
81. Zhao D, Zhang Y, Ji S, Lu Y, Bai X, Yin M, et al. Molecularly imprinted photoelectrochemical sensing based on ZnO/polypyrrole nanocomposites for acrylamide detection. *Biosens Bioelectron.* 2021;173:112816. <https://doi.org/10.1016/j.bios.2020.112816>.
82. Zheng Y, Fu L, Wang A, Peng F, Yang J, Han F. One-pot hydrothermal preparation of SnO<sub>2</sub>-ZnO nanohybrids for simultaneous electrochemical detection of catechol and hydroquinone. *Sens Lett.* 2015;13(10):878–82. <https://doi.org/10.1166/sl.2015.3543>.
83. Zheng L, Wan Y, Qi P, Sun Y, Zhang D, Yu L. Lectin functionalized ZnO nanoarrays as a 3D nano-biointerface for bacterial detection. *Talanta.* 2017;167:600–6. <https://doi.org/10.1016/j.talanta.2017.03.007>.
84. Zheng Y, Wang X, He S, Gao Z, Di Y, Lu K, et al. Aptamer-DNA concatamer-quantum dots based electrochemical biosensing strategy for green and ultrasensitive detection of tumor cells via mercury-free anodic stripping voltammetry. *Biosens Bioelectron.* 2019;126:261–8. <https://doi.org/10.1016/j.bios.2018.09.076>.

85. Zhong M, Yang L, Yang H, Cheng C, Deng W, Tan Y, et al. An electrochemical immunobiosensor for ultrasensitive detection of *Escherichia coli* O157:H7 using CdS quantum dots-encapsulated metal-organic frameworks as signal-amplifying tags. *Biosens Bioelectron.* 2019;126:493–500. <https://doi.org/10.1016/j.bios.2018.11.001>.
86. Zhou WH, Wang HH, Li WT, Guo XC, Kou DX, Zhou ZJ, et al. Gold nanoparticles sensitized ZnO nanorods arrays for dopamine electrochemical sensing. *J Electrochem Soc.* 2018;165(12):G3001–7. <https://doi.org/10.1149/2.001181jes>.
87. Zhu R, Lai M, Zhu M, Liang H, Zhou Q, Li R, et al. A functional ratio fluorescence sensor platform based on the graphene/Mn-ZnS quantum dots loaded with molecularly imprinted polymer for selective and visual detection sinapic acid. *Spectrochim Acta A Mol Biomol Spectrosc.* 2021;244:118845. <https://doi.org/10.1016/j.saa.2020.118845>.

# Index

## A

Active-matrix arrays (AMA), 15, 16  
Agricultural productions, 488–490, 492, 504  
Allergen, 635, 645–647, 649  
Ammonia (NH<sub>3</sub>), 234, 240–244, 246, 247  
Aptamers, 606, 607  
Atomic layer deposition (ALD), 205, 215, 217  
Attenuated total reflection (ATR), 589, 590

## B

Background signal, 517, 518  
Bacteria, 478, 485, 492, 495, 496  
Band gap, 36, 39–49, 56–60  
Bandgap tuning, 401  
Barrier modulation, 216  
Bioanalytical, 653, 655–665  
Bioanalytical applications, 509, 510  
Biocompatible, 623, 627, 629  
Bioconjugation, 628, 637, 639  
Bio-detection  
  acetylcholinesterase, 580  
  bacteria, 583  
  catechol, 580  
  cholesterol, 578, 579  
  glucose, 571  
  H<sub>2</sub>O<sub>2</sub>, 571, 579, 580  
  mercury, 582  
  pesticides, 581  
  *Staphylococcus aureus*, 583  
  uric acid, 577  
Bioimaging, 618, 620–628  
Biointerferences, 594

Biological compounds  
  DNA, 584  
  enzymes, 569, 584  
  oligonucleotides, 569  
Biomarkers, 593, 597, 600, 606, 607, 616, 618,  
  622, 627–629, 658–661, 663, 667  
Biomedical applications, 660  
Biomolecules, 665  
Bio-receptor  
  antibody, 443, 446, 451  
  aptamer, 464  
  biomolecule, 442, 453  
  DNA, 444, 450  
  enzyme, 443, 446, 450  
  protein, 442, 451  
  virus, 446  
Biorecognition  
  biomarker, 572  
  bio-selectivity, 572  
Biosensors, 475–504, 509–524,  
  633–648, 653–667  
  applications  
    agriculture, 465  
    detection of diseases, 463–465  
    detection of toxins and pathogen, 464  
    environmental monitoring, 444, 450,  
      461, 462, 465, 466  
    food quality control, 465  
  aptasensor, 450, 452  
  biochip  
    DNA, 448–451, 460  
    microfluidic, 460, 461  
    protein, 451, 460, 462, 463

- Biosensors (*cont.*)
- cell-based, 451, 452
  - configuration, 442
  - definition, 442
  - design, 450, 453–462
  - electrochemical, 674, 677, 689
  - electrochemiluminescence, 681, 689
  - fluorescent, 689
  - immunosensor, 446, 448, 451, 463, 465
  - performances, 446
  - photoelectrochemical, 679–681, 689
  - aptasensor, 537–540, 544
  - genosensor, 540, 544
  - immunosensor, 536, 537, 544
  - molecularly imprinted polymer-based sensor, 543, 544
- Broadband modulation absorption spectroscopy, 339
- Broad excitation spectra, 509
- C**
- Cadmium (Cd) chalcogenides, 396
- Cadmium selenide (CdSe), 203–205, 215–221, 238, 240, 241, 247, 419, 422, 425–427, 430, 432, 433, 593, 596, 597, 599, 601, 602, 605
- Cadmium sulfide (CdS), 238, 241–244, 247, 408, 422, 424, 425, 427, 435, 593
- Cadmium telluride (CdTe), 203, 205, 206, 208, 209, 221, 222, 238, 243, 244, 422, 423, 425–427, 430, 433, 434
- Cadmium tellurium (CdTe)
- CdTe detector, 137
- Cadmium-zinc telluride, 47
- Cadmium zinc tellurium (CZT)
- CZT detector, 137
- Cancer targeting, 656, 657
- Capacitance RH sensors
- CdS-ZnO heterostructures, 294
  - parameters, 294
  - polymer-based composites, 296
- Carbon-based materials, 396, 403
- Carbon nitride, 398
- CdTe and CdZnTe detectors, 37
- CdZnTe, 19
- Cell viability, 627, 628
- Chalcogenide semiconductors
- CdS, 571–575, 578
  - CdSe, 572–575, 578, 580
  - CdTe, 571, 574, 576, 578
  - ZnS, 577–580, 582, 583
  - ZnSe, 578
- Charge-collection efficiency, 10, 11, 15, 24, 26–28
- Charge transfer, 207, 210
- Chemiluminescence (CL), 509–524
- Chemiluminescence resonance energy transfer (CRET), 514, 517, 518, 521–523
- Clinical sensing, 659, 663
- Clinical trials, 616, 628
- Coating materials, 512
- Colloidal quantum dots, 639
- Colloidal synthesis, 202, 215, 220
- Composite, 397, 399–401, 404
- Compound semiconductors, 35, 36, 38, 41, 43–45, 47
- Computed tomography (CT), 137–145, 149, 151
- Conductometric RH sensors
- CdS, 285, 292, 293
  - CdS/PANI composite, 288, 289
  - hysteresis, 288, 289
  - illumination, 287, 288
  - impedance, 288, 289
  - parameters, 284, 285, 290
  - polyaniline (PANI), 285, 288, 289
  - self-powered device, 287
  - thin film sensors, 284, 285, 287, 289
  - ZnS, 285, 287, 290
  - ZnSe nanorods, 285, 286
- Conductometric (resistive) sensors
- advantages, 168
  - Fermi-level pinning, 166
  - gas sensing mechanism, 168
  - operating principle, 168
  - platforms, 168
- Core-shell, 423–424
- Core/shell quantum dots (QDs), 510–512
- Criminal, 501–504
- Crystal structure, 36, 46, 47, 49, 53, 54
- D**
- Dark current, 40, 42, 43, 46, 48, 66
- Detection efficiency, 39, 57
- Detection limit, 236, 244
- Detection mechanisms, 641
- Detective quantum efficiency (DQE), 20, 23, 24
- Detector construction, 36, 38, 39, 65
- Detector performance, 43, 54, 59
- Diagnosis, 381
- Dichalcogenides, 404
- Differential optical absorption spectroscopy (DOAS), 335, 336

- Digital radiography  
bone densitometry, 152  
chest X-ray imaging, 150  
computed mammography, 150–152  
dental digital radiography, 150–151  
mammography, 151  
planar molecular breast imaging (MBI), 151
- Direct absorption spectroscopy (DAS), 337–338, 346, 347, 353
- Direct conversion X-ray imaging detector, 16, 24
- Direct oxidation, 509, 514
- Downconversion, 616, 618–619
- Drug delivery, 655–657, 665
- E**
- Electrochemical biosensors  
amperometry, 553  
application, 552, 553, 555, 556, 558–560, 563  
fabrication, 555, 557, 559–561, 563  
impedimetry, 553  
non-portable, 554, 555  
operation, 560  
portable, 554–556  
potentiostats, 552, 554, 555  
voltammetry, 552, 560–562  
wearables, 563
- Electrochemical sensing, 658, 659
- Electrochemiluminescence (ECL), 663  
ECL mechanism, 531, 532, 534
- Electrochemiluminescent biosensor application  
biological defense, 544  
disease diagnosis, 539, 541, 544  
drug screening, 544  
environmental monitoring, 536, 540, 543, 544  
food testing, 544
- Electrochemiluminescent biosensor operation  
fast response, 531, 532, 544  
selectivity, 531  
sensitivity, 531, 535, 536, 543, 544  
signal transduction, 531, 534, 536  
simple operation, 531, 532, 544
- Electron and hole-injection, 515
- Electronic noise, 14, 15, 23–25
- Electron mobility, 403
- Electro-optical properties, 519
- ELISA assay, 607
- Emerging pollutants, 633, 635, 641, 649
- Emission, 509, 510, 514–523
- Energy resolution, 45, 54, 57, 59, 60, 62, 63, 68
- Environmental pollution, 393
- F**
- Fibre optics, 428–431
- Figure of merit (FOM), 593, 600, 608
- Fingerprints, 501, 502, 504
- Flat-panel X-ray imager (FPXI), 15, 18–22
- Fluorescence, 361–383, 420, 421, 427, 428, 431, 432, 434, 475–488, 490–504, 653, 654, 662–667
- Fluorescence resonance energy transfer (FRET), 605
- Food analysis  
amino acids, 679, 680  
chloramphenicol, 685, 686, 689  
hydrogen peroxide, 684  
metal ions, 685, 686  
mycotoxins, 682, 683, 686  
organic compounds, 680, 681  
pathogenic bacteria, 675, 676, 686  
pesticides, 677, 678, 686, 687
- Foodborne pathogens, 636, 638
- Food processing, 673, 674, 684
- Food safety, 492–496, 504, 673–690
- Förster resonance energy transfer, 618
- Frequency modulation spectroscopy (FMS), 337, 339, 346–348
- Fumed silica (FS), 602, 603
- Functionalisation, 512–514, 523
- G**
- Gamma camera, 138, 142
- Gas response, 236, 237, 240–243, 245–247
- Gas sensing systems, 335–357
- Gas sensor fabrication  
surface decoration, 186, 187  
thick films, 177, 178, 192  
thin films, 177, 179
- Gas sensor performance  
selectivity, 186, 194  
sensitivity, 186, 188, 191, 196  
stability, 191, 193
- Gas sensors, 201–224  
chemoresistors, 178, 179  
field of application, 170  
functionality, 178  
metal oxides, 165, 167–169  
monitoring, 161, 163, 165, 168

- Gas sensors (*cont.*)  
 photoactivated gas sensors, 178, 187  
 requirements, 165  
 resistive gas sensors, 178, 179, 184, 188  
 thermoactivated gas sensors, 178, 188–191
- Gas sensors classification  
 electrical sensors, 164  
 electrochemical sensors, 164  
 magnetic gas sensors, 164  
 mass-sensitive gas sensors, 164  
 optical gas sensors, 164  
 thermometric (calorimetric) sensor, 164
- Gas-sensitive II–VI semiconductors  
 CdS, 179, 185  
 ZnS, 179, 185, 190
- Gold triangular nanoprisms (AuTNPs), 600
- Groups of II–VI semiconductor materials, 510
- Growth-promoting hormone, 488–492, 504
- H**
- Health protection, 633–648
- Heavy metals, 496–500, 504, 641
- Hecht equation, 10
- Heterojunction, 207, 210, 214, 217, 221, 223, 224, 395–401, 408
- High performance liquid chromatography (HPLC), 602
- High quantum yields, 509, 523
- Hollow waveguide (HWG), 341, 345
- Human caused greenhouse gas emission, 308
- Humidity  
 water vapor, 281–285, 289, 290, 292–294, 299  
 water vapor influence, 289
- Humidity measurement  
 adsorption, 293  
 capillary condensation, 283  
 chemisorption, 283  
 mechanisms to humidity sensing, 282, 283
- HWG based-gas sensor, 341–345
- Hybrid, 202
- Hybrid materials, 404
- Hydrogen sulfide (H<sub>2</sub>S), 241, 242
- Hydrothermal synthesis, 205, 209, 211, 212
- I**
- II–VI compounds  
 advantages, 167  
 CdS, 169, 172, 510, 519, 520  
 CdSe, 169, 172, 510, 520  
 CdSe/ZnS, 510, 517, 521, 522  
 CdTe, 172, 510, 515–517, 520–523  
 parameters, 166  
 ZnS, 172  
 ZnSe, 510, 516
- II–VI compound semiconductors, 616, 618–619, 627, 629
- II–VI quantum dots, 475–504  
 high-quality quantum dots, 532  
 semiconductor QDs, 532, 544
- II–VI semiconducting nanomaterials  
 cadmium selenide, 674  
 cadmium sulfide, 678, 680, 682, 685, 687, 689, 690  
 cadmium telluride, 674  
 zinc oxide, 674, 678  
 zinc sulfide, 674
- II–VI semiconductor-based sensors  
 cadmium selenide, 559  
 cadmium sulfide, 560, 561  
 cadmium telluride, 559, 561  
 zinc sulfide, 562
- II–VI semiconductors, 336, 339, 340, 354, 357, 417–435  
 CdS, 259–261, 264, 266–271, 327  
 CdSe, 263–266, 317–319, 327, 329  
 CdTe, 322, 323, 327  
 ZnO, 313, 314, 319, 324–327  
 ZnS, 259, 260, 262–265, 269–271, 273, 274, 315, 316, 319, 322  
 ZnSe, 265, 266, 275, 314, 315  
 ZnSe image lag and ghosting, 20, 25–26
- II–VI semiconductors' synthesis  
 doping, 186, 187, 194  
 nanoflakes, 181, 184, 190, 193  
 nanoparticles, 187, 190, 193, 194  
 porous films, 184
- Image lag and ghosting, 25–26
- Imaging, 475, 477–479, 488, 489, 501, 504
- Immobilization  
 adsorption, 453  
 chemical methods, 442  
 covalent bonding, 453  
 physical methods, 442
- Immunosensor, 646, 647, 658, 660, 661
- Indirect enhancing, 509
- Inhibitory effects, 509
- Inorganic semiconductor, 653
- Interaction kinetics, 592, 596
- Interferometry, 429
- Intracellular, 422, 424, 427, 431, 432, 435
- In vitro imaging, 621, 622
- In vivo, 422, 424
- In vivo imaging, 621–624, 626, 628, 629

## Ion sensing

## heavy metals

- chromium, 378
- copper, 365, 372, 373, 383
- health effect, 362, 376
- lead, 376, 383
- mercury, 374, 375, 383
- source, 362

## implementation, 372–383

## optical, 362, 363

## performances, 373

## pH, 369, 373, 374, 380–383

## ratiometric sensing

- advantages, 370
- design, 370, 371, 382
- dual-emission, 369, 383

## Ionization energy, 8, 11, 19

## Isotopes

- $^{10}\text{B}$ , 77, 78, 81, 84, 87, 98
- $^3\text{He}$ , 77–79
- $^6\text{Li}$ , 77, 78, 80, 81, 95–98

**L**

## Laser absorption spectrometer (LAS)

- configuration, 336, 340
- principles, 336, 346
- prospects, 336, 357

## Lateral flow immunoassays, 635, 640, 648

## Layer-by-layer (LbL), 607

## Lead sulfide (PbS), 593

## Ligands

- capping agents, 365, 378
- glutathione, 377, 378
- L-Cysteine, 375
- TGA, 375

## Light activation, 207, 214–216

## Light-harvesting, 572, 575

## Liquid petroleum gas (LPG), 240–242, 244

Localized surface plasmon resonance (LSPR),  
590, 592–596, 600, 601, 604–608

## Long-term photostability, 509

## Lossy mode resonances (LMRs), 590, 607

## Luminescence, 615, 619, 624–626, 628, 629

## Luminescent probe, 623, 629

**M**

## Magnetic resonance imaging (MRT), 143

## Magnetron sputtering, 205, 206, 208, 209, 221

## Maxwell Garnett's (MG), 598, 599

## Mechanisms, 514, 515, 522, 523

## Medical diagnosis, 655

## Medical diagnostic, 628

## Metal-chalcogenides, 396–402

## Metal ions detection, 405

## Metal-oxides, 396, 402–404

## Mid-infrared (MIR), 595, 597

## Modulation transfer function (MTF), 20–23

## Molecular functionalization, 616, 621

## Multimodal systems

## PET/CT, 143

## PET/MRT, 139

## SPECT/CT, 144

## Multipass cell (MPC)

## chaotic multipass cell, 344

circular multi-reflection (CMR) cells, 340,  
341, 344

## Herriott cell, 340, 342

## multimirrors cells, 343

## white cells, 340–342

## Mycotoxin, 638–640, 649

**N**Nanocomposite, 201–224, 233–247,  
423–426, 430

## Nanocrystals, 653, 655, 658, 659

## Nanomaterial based biosensors

- advantages, 445, 446, 448, 449, 452
- bio-interfaces, 453, 454
- core-shell, 458
- metallic nanoparticles, 457
- performances, 446
- polymer nanoparticles, 458
- quantum dots, 455

Nanomaterials, 234–236, 238–240, 246, 247,  
641, 657, 659, 666, 667bottom-up approach, 255, 256, 268,  
269, 271

## chemical synthesis, 273

## classification, 558

## core-shell (CSh), 313, 315–317, 319, 329

## nanobelts, 320

## nanorods, 313

## nanowires, 313–315

## physical methods, 256

quantum dots (QDs), 312, 313, 315–317,  
319, 322–324, 327, 329

## top-down approach, 255, 256, 268, 272

Nanoparticles, 202–213, 216, 217, 238, 242,  
243, 245, 246, 615, 616,  
618–621, 624–629

## core shells, 577

## QDs, 567, 570–575, 577, 578, 580–583

## upconverting nanoparticles, 576



- Nanophosphors, 616–629
- Nanostructured semiconductors
- core-shell
    - CdSe/ZnS, 275
    - ZnO/ZnS, 266, 275
    - ZnS/In<sub>2</sub>O<sub>3</sub>, 275
    - ZnSe/SnO<sub>2</sub>, 275
  - one-dimensional, 254, 265–267
  - quantum dot, 255, 261–263, 265
  - three-dimensional
    - CdS/PbS/SnO<sub>2</sub>, 273
    - CdTe/ZnO/PSi, 272, 273
    - SnO<sub>2</sub>/ZnS, 273
    - ZnS, 270, 271
    - ZnSe/ZnO, 273
  - two-dimensional, 254, 259, 265–268, 270, 271
  - zero-dimensional, 254, 255, 257, 258, 261, 264, 267, 270
- Nanostructures, 397, 399, 400, 403, 405, 656
- Nanotechnology, 510
- Nanowire-based RH sensors
- advantages, 290
  - CdS nanowire, 289, 291
  - CdSSe nanowire, 290–292
  - polyimide (PI), 290, 292
  - reproducibility, 290
- Near-infrared (NIR), 593, 595, 597
- Neutron detectors
- alpha particles, 78
  - application, 76, 99
  - Bonner Sphere Spectrometer, 99
  - configuration, 87, 96, 99
  - detection efficiency, 91, 93, 96, 98, 99, 101
  - diffractometer, 93, 100, 101
  - fiber-coding, 90, 91
  - filters, 94
  - moderators, 87, 99
  - one-dimensional, 89
  - planar, 87, 89
  - reactions, 77–79, 81, 99
  - Si-APD, 87, 88
  - triton, 78
  - two-dimensional, 91, 100
  - WLSFs, 89–91
- Neutron detectors market
- BC-702, 95, 96
  - BC-704, 94–97, 101
  - BC-705, 95, 96
  - BC-720, 95, 96
  - performances, 88, 96
- Neutrons
- cross sections, 77–81, 94, 99
  - fast, 76, 78, 94, 95, 99–100, 103
  - parameters, 79, 80, 84, 85, 94, 96–98
  - sources, 75, 77, 79, 91, 93, 100
  - thermal, 76, 78–82, 84, 88, 93–97, 99, 103
- NIR sensor, 656
- Nitrogen dioxide (NO<sub>2</sub>), 234, 243, 247
- Nuclear medicine (NM), 137–146, 148
- Nuclear probes, 148–149
- O**
- Open path detection, 346–349
- Optical absorption, 430, 432
- Optical detection, 655, 662
- Optical gas sensors, 417–435
- cataluminescence (CTL), 309, 324
  - CdSe QDs, 171, 172
  - chemiluminescence, 309, 324
  - core-shell structures, 172
  - fiber optics, 327
  - fluorescence, 310, 322, 329
  - gas sensing techniques, 170
  - interferometry, 327, 329
  - longer periods of fiber gratings, 327
  - lossy mode resonances, 326, 327
  - non dispersive infrared, 327
  - optical absorption, 312, 324
  - photoluminescence, 171, 172, 309, 314, 319
  - photostability, 172
  - quantum dots (QD's), 170–172
  - surface plasmon resonance (SRP), 324, 326, 327, 329
- Oxidizing gases, 234, 235
- P**
- Paper-based RH sensors
- fabrication, 293
  - filter paper, 292
  - performance, 292
- Pathogens, 478, 479, 488, 495, 496, 504
- Persistence luminescence, 629
- Pesticides, 635, 643–644, 649
- Phase diagrams, 47, 49–51, 54, 56
- Phosphors
- fluorophores, 364
  - organic dyes, 364
- Phoswich detector
- Bi<sub>4</sub>Ge<sub>3</sub>O<sub>12</sub>, 103
  - CaF<sub>2</sub>, 103
  - EJ-212, 104
  - EJ-440, 103, 104
  - EJ-442, 103, 104
  - EJ-444, 103, 104

- NaI(Tl), 102, 103  
TCS-362, 103  
ZnS(Ag), 80–82, 84, 85, 88, 93, 95  
Photocatalytic properties, 260  
Photocurrent, 394, 395, 397–399,  
403–406, 408  
Photoelectrochemical biosensors  
  aptasensor, 575, 576  
  CRET, 570, 571  
  ELISA, 573, 574  
  enzyme immobilisation, 581  
  enzyme-sensing, 569  
  FRET, 578  
  immunoassay tests, 569, 572–575  
  immunosensors, 572–575  
  light stimulation, 568  
  photoexcitation, 569, 576  
  photo-voltammetry, 567  
Photoelectrochemical ion sensor, 393–409  
Photoelectrochemical sensing, 665  
Photoelectrochemistry, 394, 396  
Photoelectrode, 395, 400, 401  
Photoexcited electrons, 217, 220, 221  
Photoexcited holes, 216, 217, 220  
Photoluminescence (PL), 424, 595, 601  
Photomultipliers (PMTs)  
  flat-panel multi-anode, 91  
  multi-anode, 90–92  
Photonic crystal fiber-based surface plasmon  
  resonance (PCF-SPR), 600  
Photo-stability, 510  
Photovoltaics, 394, 396, 403  
Physical characteristics, 45–49  
Pixelated detectors, 5, 9, 26–28  
PL quenching  
  FRET, 367, 368, 370, 371, 377, 382  
  PET, 367, 368, 370, 382  
Planar and co-planar detectors, 5, 26  
Poly(3, 3''- dialkylquaterthiophene) (PQT-12),  
240, 241, 247  
Poly(3-hexylthiophene) (P3HT), 238, 240, 245  
Polyaniline (PANI), 238, 241–244, 247  
Polycrystalline mercuric iodide (poly-  
  HgI<sub>2</sub>), 19  
Polymer, 364, 373, 382, 383  
Polypyrrole (PPy), 242, 244  
Position sensitive semiconductor detectors,  
6, 26–28  
Positron emission tomography (PET)  
  brain scanner, 143  
  breast, 151  
  scanner, 139, 140, 143  
  whole body, 139  
Pre-clinical studies, 627–628  
Probes, 514, 519, 520, 523  
Proteins, 476–479, 482–485, 488, 489, 491,  
494, 504  
Pump suction system, 336, 340–341
- Q**  
QCM-based RH sensors  
  hysteresis, 299  
  parameters, 297  
  resonant frequency, 296–297  
  size effect, 297  
Quantum dots (QDs), 205, 208, 214, 216,  
218–221, 238, 240, 241, 246, 397,  
399–403, 417–435, 592, 615, 618,  
620, 621, 623, 624, 626, 627,  
633–648, 653–655, 659, 662, 664  
  advantages, 363, 377, 378  
  CdS, 363, 365, 367, 369, 372–375, 377,  
379, 380  
  CdSe, 365, 372, 374, 376  
  CdTe, 365, 366, 372, 373, 375, 376, 378,  
379, 382  
  core-shell, 373  
  functionalization, 365, 366
- R**  
Radiation  
  gamma radiation, 137, 141, 146, 147  
  neutrons, 146, 147  
  thermal neutrons, 147  
  X-ray, 137, 140, 141, 146, 149–151  
Radiation detectors, 3–28  
Radiation therapy  
  C-ion, 147  
Radionuclide, 137, 138, 146–149  
Radiopharmaceutical, 138  
Rapid detection, 637, 642, 643  
Rapid measurement, 645  
Reducing gases, 235, 240  
Refractive index (RI), 589–593, 596, 599, 602,  
604, 605, 608  
Residual pesticides, 477, 488, 491  
Room temperature radiation detection, 36,  
45–48, 59, 60
- S**  
Scintillation detectors  
  advantages, 79  
  GS20(Ce), 80  
  light yield, 80, 82–84, 98  
  <sup>6</sup>LiI(Eu), 80, 100

- Scintillation detectors (*cont.*)  
 mechanism, 84  
 ZnS(Ag)<sup>10</sup>B, 81  
 ZnS(Ag)<sup>6</sup>Li, 80
- Scintillation radiation detectors  
 application, 110, 114, 130, 131  
 II-VI compounds  
 advantages, 117  
 Bridgman Technique, 115, 119, 120  
 CdSe, 109–132  
 doping, 117, 124, 126, 128, 132  
 isovalent dopants, 124, 128  
 melt growth, 115, 119, 131  
 quantum dots, 115, 121–123  
 single crystal, 110, 118, 125, 128  
 ZnSe, 109–132  
 ZnSe-Al, 120  
 ZnSe<sub>(1-x)</sub>S<sub>x</sub>, 118, 119  
 ZnSe-Te, 120
- materials  
 bismuth germanium oxide, 112  
 cesium iodide (CsI: Tl), 112  
 gadolinium orthosilicate, 112  
 sodium iodide (NaI: Tl), 112
- parameters  
 afterglow, 111, 117, 118, 125–127  
 decay time, 111–113, 116–118, 121,  
 123, 129, 131  
 light yield, 111  
 radio-luminescence, 111
- performance, 123–128
- radiation  
 alpha, 113, 122, 124, 131  
 beta, 113, 124, 131  
 gamma, 118, 122–124, 126,  
 129–131
- scintillation  
 luminescence intensity, 128
- types  
 planar, 113  
 through-hole detectors,  
 113, 114  
 well-type, 113, 114
- Scintillator, 140, 142, 147, 148
- Security, 503, 504
- Selectivity, 235, 236, 238, 241–243, 245, 247,  
 475–477, 481–484, 487, 489,  
 494, 496–500
- Semiconductor detectors  
 Ge, 142  
 ZnS, 147, 148  
 ZnSe, 147
- Semiconductor dosimeters, 146
- Semiconductors, 394–396, 399, 401–403
- Sensitivity, 234–236, 238, 240–246, 394, 400,  
 401, 406–409, 475, 477, 478, 481,  
 484, 486–488, 491, 492, 494, 495,  
 498, 499, 502, 503
- Sensor chip, 594, 608
- Sensor operation  
 cross-sensitivity, 257, 276  
 room-temperature operation, 253, 259  
 selectivity, 259, 260, 267  
 sensitivity, 259, 260  
 stability, 257
- Sensors, 634–636, 641–644, 646, 647, 649  
 electrical, 257, 262, 265, 266, 270, 273,  
 275, 277  
 electronic, 257, 270, 273, 276, 277  
 gas, 253, 256–260, 262–266, 268–271,  
 273, 275–277
- Shockley-Ramo's theorem, 9, 26
- Silica, 372–374, 377
- Single photon emission computed  
 tomography (SPECT)  
 Discovery NM 530c, 142  
 D-SPECT, 141, 142
- Size-dependent luminescence, 509
- Small pixel effect, 26
- Solid-state detector, 39–45
- Solvothermal synthesis, 203, 204, 206, 210,  
 217, 221
- Sonochemical synthesis, 204, 217
- Spatial resolution, 21, 22
- Spectroscopic imaging, 336, 352–354
- SPR imaging (SPRi), 590
- Standoff sensing  
 standoff remote sensing, 340, 349, 357
- Streptavidine, 607
- Successive ionic layer adsorption and reaction  
 (SILAR), 203, 205, 206, 208, 222
- Surface plasmon resonance (SPR), 419, 420,  
 430, 431, 589–609
- Surface plasmon waves (SPW), 589, 590,  
 592, 594
- System performance, 20
- T**
- Temperature sensor (TS), 417–435
- Theranostics, 657
- Therapy, 653, 655–657, 665
- Thermal activation, 207–214, 224
- Thermal evaporation, 205, 208
- Thermal imaging, 431–435
- Thermometer, 417, 421
- Thick films, 63–67
- Thin film, 396, 399, 406, 424, 426, 430

- Toxic gases  
CO, 161, 162  
formaldehyde, 162  
NO<sub>x</sub>, 161–163  
SO<sub>2</sub>, 162  
VOCs, 162, 163
- Toxicity, 510, 519, 523
- Toxicology study, 629
- Transducer  
electrochemical  
amperometric, 444, 449, 450, 452, 463  
impedimetric, 444  
potentiometric, 444, 449, 463  
voltammetric, 444, 445  
optical  
bioluminescence, 447  
colorimetric, 447  
fiber-optic, 448, 449  
fluorescent, 446  
surface plasmon resonance, 447  
physical  
magnetic, 445, 446  
piezoelectric, 445, 446, 449, 463  
thermometric, 445
- Transition metal chalcogenides (TMCs), 254, 258–260, 264, 266, 268, 269, 271, 273, 275–277
- Tunable bandgap, 259
- Tunable diode laser absorption spectroscopy (TDLAS), 338, 340, 346, 348–352
- Tunable laser  
CdSe, 354  
CdTe, 354, 356  
ZnS, 354  
ZnSe, 354–356  
ZnTe, 354
- U**  
Upconversion, 616–619
- V**  
Viruses, 477–482, 485, 504  
Visible light activity, 397  
Volatile organic compounds (VOCs), 246, 601, 602
- W**  
Waste-water, 373  
Wavelength modulation spectroscopy (WMS), 337–339, 346–349, 351, 353  
Working principles, 480, 485, 486, 489, 492, 496, 499, 500
- X**  
X-ray damage, 11  
X-ray fatigue, 11  
X-ray interactions with photoconductor, 7  
X-ray photoconductors, 11, 16, 21  
X-ray sensitivity, 11, 19, 20, 25, 26  
X-ray spectroscopic detectors, 12
- Z**  
Zinc oxide (ZnO), 430, 593  
Zinc selenide (ZnSe), 203–205, 208–211, 215, 221, 245  
Zinc sulfide (ZnS), 203–206, 211–213, 216, 221, 223, 240, 245, 246, 422–428, 430, 435  
Zinc telluride (ZnTe), 203–205, 214, 246, 247  
ZnS-based phosphors  
activator, 81, 85  
annealing, 86  
emission maximum, 82  
ZnS:Ag,Cl, 85  
ZnS(Cu), 82, 86, 96